ISBN: 978-4-909106070 C3051

SEE PATTAYA 2021

Proceedings



EDITED BY

Zakaria Hossain
Suksun Horpibulsuk

November 10 – 12, 2021
The Zign Hotel & Villa Pattaya, Thailand

SEE 2021, PATTAYA, THAILAND
STRUCTURE, ENGINEERING AND ENVIRONMENT

PROCEEDINGS OF SEVENTH INTERNAONAL CONFERENCE – SEE 2021
STRUCTURE, ENGINEERING & ENVIRONMENT PATTAYA, THAILAND 10-12 NOVEMBER, 2021

Structure, Engineering and Environment

Edited by

Prof. Zakaria Hossain
Graduate School of Bioresources
Mie University, Japan

Prof. Suksun Horpibulsuk
School of Civil Engineering
Suranaree University of Technology, Thailand

THE GEOMATE INTERNATIONAL SOCIETY

Copyright @ 2021 by The GEOMATE International Society

All rights reserved. In principle, no part of this publication or the information contained herein may be reproduced in any form or by any means, translated in any language, stored in any data base or retrieval system, or transmitted in any form or by any means without prior permission in writing from the publisher.

Disclaimer: The editors and the publisher have tried their best effort to ensure the integrity and the quality of this publication and information herein. However, they give no warranty of any kind, expressed or implied with regard to the material contained in this book, and will not be liable in any event for the consequences of its use.

Published by:
The GEOMATE International Society
Tsu city, Mie, Japan
E-mail: society@geomate.org
http://www.geomate.org/

ISBN Number: 978-4-909106056 C3051

Table of Contents

	Preface	ix
	Organization	x
	Technical Papers	1
ID	***Structure***	2
7521	DEFECT DETECTION ON ASPHALT PAVEMENT BY DEEP LEARNING Jonpaul Nnamdi Opara, Aunt Bo Bo Thein, Shota Izumi, Hideaki Yasuhara and Pang-Jo Chun	3
7516	FIELD EVALUATION AND FATIGUE ASSESSMENTS OF BENT PLATE CONNECTIONS IN A HIGHLY SKEWED STEEL I-GIRDER BRIDGE Yousif Almoosi and Nazar Oukaili	9
7544	EFFECTS OF ELECTROLYZED WATER ON ULTRASTRUCTURAL CHANGES OF Fusarium oxysporum AND Escherichia coli Santirote Keatsirirote, Angkhana Chuajedton and Kanda Whangchai	16
7577	PERFORMANCE LEVEL PREDICTION OF STRUCTURE BUILDING USING LOG-SIGMOID METHODS Muhammad Gala Garcya, Reni Suryanita, Zulfikar Djauhari and Harnedi Maizir	21
7608	IS IT POSSIBLE TO APPLY GIG ECONOMY FOR FARMER IN INDONESIA? Siti Rochaeni and Diah Khairani	27
7609	COMPETITIVENESS OF INDONESIAN FROZEN SHRIMP AGAINST SEVEN MAJOR COMPETING COUNTRIES AND OVERVIEW OF PAPERLESS TRADE IN THE INTERNATIONAL MARKET Siti Rochaeni, Natasha Avinda Albertina, Iwan Aminudin and Rizki Adi Puspitasari	30
ID	***Engineering***	36
7507	VIBRATION ACTUATOR SYSTEM FOR INSPECTION OF LARGE COMPLEX IRON STRUCTURES Hiroyuki Yaguchi and Yusuke Itoh	37
7509	QUANTIFICATION OF SLOPE DEFORMATION BY FILTERING OF LASER POINT CLOUD OBTAINED BY MOBILE MAPPING SYSTEM Naoto Samori, Satoshi Nishiyama, Koki Sakita, Michinari Fuziki and Naoya Ono	43
7511	SOIL RETENTION TESTS FOR DETERMINING DISPERSION OF CLAYEY SOILS Saad Farhan Ibrahim Alabdullah, Yar Hassab, Zaman Teama and Suha Aldahwi	49
7520	STUDY ON SURFACE PREFORMANCE OF CONCRETE CONSTRUCTED BY PRECAST METHOD AND ON-SITE METHOD Yasuhide Mochida, Hiroshi Sakata and Hu Shaobo	56
7524	IMPROVEMENT IN MECHANICAL PROPERTIES OF FLEXIBLE POLY(L-LACTIDE)-b-POLYETHYLENE GLYCOL-b-POLY(L-LACTIDE) BIOPLASTIC BY MELT BLENDING WITH BORON NITRIDE Theeraphol Phromsopha and Yodthong Baimark	62
7525	INFLUENCE OF LOW MOLECULAR-WEIGHT POLY(D-LACTIDE)/POLY(L-LACTIDE) MIXTURES ON CRYSTALLIZATION BEHAVIOR AND MECHANICAL PROPERTIES OF HIGH MOLECULAR-WEIGHT POLY(L-LACTIDE) BIOPLASTIC Yodthong Baimark, Theeraphol Phromsopha, Yaowalak Srisuwan, Wuttipong Rungseesantivanon and Natcha Prakymoramas	67

7530	ATTITUDES AND PERCEPTIONS ON TRAVEL MODE CHOICE IN AN EMERGING URBAN AREA OF INDONESIA: THE CASE OF SOUTHERN SUMATERA Aleksander Purba	73
7532	MODIFIED RESILIENCE INDEX FOR WATER DISTRIBUTION NETWORKS Pornnapus Kongbuchakiat, Adichai Pornprommin and Surachai Lipiwattanakarn	80
7536	CONTEMPLATION OF VIBRATION AND SOUND SIGNALS OF A HYBRID-ENGINE CAR Suphattharachai Chomphan	85
7537	THE FACTOR ANALYSIS OF CONFLICT FACTOR EFFECT TO PROJECT MANAGEMENT IN GOVERNMENT CONSTRUCTION Korb Srinavin, Tanayut Chaitongrat, Bancha Teanngen, Wuttipong Kusonkhum and Watcharapong Deewong	91
7549	SEEPAGE FLOW ANALYSIS CONSIDERING THE EFFECTS OF INTERNAL EROSION DUE TO LONG-TERM SEEPAGE INTO GROUND COMPRISING SURFACE IMPERMEABLE GROUND Naoko Sakamoto and Mari Sato	98
7550	APPLICATION OF THREE-DIMENSIONAL LASER POINT CLOUDS TO RIVER MANAGEMENT Nanoka Akiyama, Satoshi Nishiyama, Koki Sakita and Fumiaki Yamazaki	104
7553	STUDY ON PHYSICAL PROPERTIES AND GRASS GROWTH CAPACITY OF POROUS CONCRETE Kensuke Yamaya, Yui Oyake, Yoshihiro Suenaga and Hidenori Yoshida	110
7557	GROUND EVALUATION METHOD BY PORTABLE DYNAMIC PENETRATION TEST BASED ON WAVE PROPAGATION THEORY Katsuya Iwai, Naoaki Suemasa, Kazuya Ito and Tsuyoshi Tanaka	116
7560	INFLUENCE OF RAINFALL INTENSITY ON INFILTRATION SURFACE FORMATION OF RIVER EMBANKMENTS Tsubasa Ichijo, Shin-ichi Kanazawa and Hisao Emoto	122
7561	ALTERED ROCKFALL BEHAVIOR OWING TO PARAMETERS IN ROCKFALL SIMULATION USING DISCONTINUOUS DEFORMATION ANALYSIS Hiroaki Kitauchi, Satoshi Nishiyama and Koki Sakita	128
7564	RIPPABILITY ASSESSMENT AT GRANITIC FORMATION: CASE STUDY USING SEISMIC REFRACTION, ELECTRICAL RESISTIVITY AND BOREHOLE Saiful Azhar Ahmad Tajudin, Muhammad Nur Hidayat Zahari, Aziman Madun, Muhammad Nizam Zakaria and Muhammad Haziq Taqiuddin Rezuwan	134
7567	METHOD OF EVALUATING CORROSION RISK FROM ELECTRICAL RESISTIVITY OF CONCRETE WITH REINFORCING BAR Yoko Sakakihara, Yuu Hashimoto, Sunao Fujimura and Shinichirou Okazaki	141
7568	APPLICATION OF THE PLACKETT AND BURMAN DESIGN FOR IMPROVED OLIGOSACCHARIDE EXTRACTION FROM YAM BEAN ROOT Mullika Teerakun, Nonthaphong Phonphuak, Weeranuch Wonkaonoi, Kanok-on Khampui and Piyawadee Saraphirom	147
7572	APPLICATION OF ARTIFICIAL INTELLIGENCE TO RIVER INSPECTION USING UAV Ryo Yahara, Satoshi Nishiyama, Tomohiro Shimono, Sayuri Yoshioka and Kohei Ogata	153
7578	PRODUCTION OF BIODIESEL AND VITAMIN E FROM A POOR QUALITY OF CRUDE PALM OIL BY ENZYMATIC TRANSESTERIFICATION PROCESS Mallika Tapanwong, Vittaya Punsuvon, Pinsuda Viravathana and Rayakorn Nokkaew	159
7583	SIMULATION OF INCOMPRESSIBLE THERMAL FLOW VIA MESHLESS FINITE POINT METHOD Chinnapat Buachart	165
7587	THE ADOMIAN DECOMPOSITION METHOD FOR SOLVING HEAT TRANSFER LIGHTHILL SINGULAR INTEGRAL EQUATION USING MAPLE Dalal Adnan Maturi	170

7591	JUSTIFICATION OF RESIDUE MATERIAL IN GROUND IMPROVEMENT OF COASTAL SOILS: AN APPLICATION OF COIR FIBER S. Islam, H. Islam, O. C. Debanath, M. A. Rahman and S. M. Farooq	176
7592	INFLUENCE OF TALCUM ON THERMAL AND MECHANICAL PROPERTIES OF STEREOCOMPLEX POLYLACTIDE-b-POLYETHYLENE GLYCOL-b-POLYLACTIDE BIOPLASTIC Yaowalak Srisuwan and Yodthong Baimark	180
7593	THE DEVELOPMENT OF COST-EFFECTIVE INSTRUMENT FOR WASTE REDUCTION Kantayut Trebooniti	185
7598	MACRO FABRIC MEASUREMENT WITH A NEW TECHNIQUE OF GLASGOW TILL Radhi Alzubaidi	189
7599	HIERARCHICAL BAYESIAN RJMCMC-BASED DETECTION FOR PIECEWISE CONSTANT SIGNAL UNDER RAYLEIGH MULTIPLICATIVE NOISE Suparman and M. Toifur	195
7607	ENGINEERING PROPERTIES OF RED BED SOIL FROM MAE MOH MINE FOR COVERING FINAL PIT WALL Suphamat Chaichana, Amarin Boontun and Suparit Tangparitkul	200
7610	APPLYING K-MEAN TECHNIQUE TO DEFINE THE SIZE OF GOVERNMENT PROJECT IN THE GOVERNMENT PROCUREMENT SYSTEM Wuttipong Kusonkhum, Tanayut Chaitongrat, Korb Srinavin, Worawit Phojan and Anuchat Leeanansaksiri	206
7611	A STUDY OF BEHAVIOR OF COST IN GOVERNMENT CONSTRUCITON PROJECTS WITH MACHINE LEARNING Wuttipong Kusonkhum, Korb Srinavin, Preenithi Aksorn, Narong Leungbootnak and Tanayut Chaitongrat	212
7616	EXPLORING THE EFFECTIVENESS OF HEALTH AND SAFETY REGULATIONS GOVERING CONSTRUCTION PROJECTS IN UAE Abdelrahman Abdalla Alhelo, Radhi Alzubaidi and Hamad Rashid	219
7635	PRODUCTION AND FRESH PROPORTIES OF SELF-COMPACTING CONCRETE CONTAINING MPF AND FPF FIBERS Osama M A Daoud and Nouraldaim F A Yagoub	226
7638	STUDY ON PROPERTIES OF CONCRETE MIXED WITH RICE HUSK ASH ADSORBING HEAVY METALS Ayane Yanaka, Takuto Ueno, Shinichiro Okazaki, Naomochi Matsumoto and Hidenori Yoshida	232
7639	A DECISION TOOL FOR LOCAL ROAD SAFETY MANAGEMENT IN THAILAND Patipat Kanha and Nopadon Kronprasert	238
7648	A STUDY OF HELMET USE BEHAVIOR CHANGES: A CASE STUDY OF KHON KAEN UNIVERSITY, THAILAND Jetsada Kumphong and Prach Amornpinyo	244
7663	DEEP NEGATIVE EFFECTS OF CONSPIRACY THEORIES AND MISLEADING INFORMATION ABOUT COVID-19 ON POPULATIONS THROUGH SOCIAL NETWORKS Mohamed Chakraoui, Naoual Mouhni, Abderrafiaa Elkalay and Mohamed Nemiche	250
7671	EVALUATION AND DEVELOPMENT OF TRADITIONAL GUTTIYA BUILDING AS A LOW COST SUSTAINABLE HOUSING TECHNIQUE IN EASTERN SUDAN May Y. Yousuf and Osama M. A. Daoud	256
7672	DEVELOPMET OF ARTIFICIAL INTELLIGENCE PROCESSING THROUGH CCTV CAMERA FOR DETECTING UNHELMETED MOTORCYCLISTS Jetsada Kumphong, Thaned Satiennam, Watis Leelapatra and Rujchai Ung-arunyawee	262

7673	A MATHEMATICAL MODEL AND SOLUTION APPROACH FOR A HETEROGENEOUS FLEET OPEN VEHICLE ROUTING PROBLEM Chansiri Singhtaun and Harit Piyapornthana	268
7680	DEVELOPMENT OF DECISION SUPPORT SYSTEM FOR RAILWAY MAINTENANCE: A CASE STUDY OF STATE RAILWAY OF THAILAND Thawatchai Phanyakit and Thaned Satiennam	274
7683	DESIGN OF A SENSOR MODULE FOR UNDERGROUND STRUCTURE MONITORING WITH ENERGY HARVESTED FROM SOIL Md Rubayatur Bhuyian, Kshirasagar Naik, Marzia Zaman and Gary Sakauye	280
ID	***Environment***	286
7540	STUDY ON EXTRACTION OF FALLING ROCK SOURCE USING AERIAL LASER DATA TO IMPROVE THE EFFICIENCY OF FALLING ROCK MEASURES Yuqing Zhang Koki Sakita, Satoshi Nishiyama and Takeharu Sato	287
7514	NOVEL STARTER FOR PRODUCING YOGURT CONTAINING ANGIOTENSIN CONVERTING ENZYME (ACE) INHIBITORY ACTIVITY Sri Yadial Chalid, Mu'izzah Irsyadi Putri, Fitriah Hatiningsih and Megga Ratnasari Pikoli	293
7522	ANTIBACTERIAL ACTIVITY OF LIQUID SMOKE POWDER FROM RICE HUSK Muriady, Hesti Meilina and Muhammad Faisal	299
7527	ON THE IMAGE OF URBAN SPACE EXTTRACTED BY COLORS Ami Hasegawa and Kazunari Tanaka	305
7529	STUDY OF THE TROPHIC STATUS AND ECOLOGICAL STATE OF THE COASTAL ZONES OF THE NATURAL MONUMENTS OF THE CHELYABINSK REGION (RUSSIA) OF THE TURGOYAK AND UVILDY LAKES Irina Mashkova, Anastasiya Kostryukova, Belov Sergey, Elena Shchelkanova and Viktor Trofimenko	311
7541	INFLUENCE OF DEGRADATION OF COASTAL ZONES ON THE SPECIES STRUCTURE OF PHYTOPLANKTON OF LAKES UVILDY AND TURGOYAK (SOUTH URAL, RUSSIA) Anastasiya Kostryukova, Irina Mashkova, Sergey Belov, Elena Shchelkanova and Viktor Trofimenko	317
7543	EFFECT OF ELECTROLYZED WATER ON INHIBITION OF *Colletotrichum capsici*, CAUSING ANTHRACNOSE DISEASE OF CHILLI Angkhana Chuajedton and Kanda Whangchai	323
7552	EXTERNAL COSTS CAUSED BY HOKKAIDO SIKA DEER-VEHICLE COLLISIONS IN HOKKAIDO, JAPAN Hideyuki Ito, Masanori Wada and Takahiro Fujii	328
7554	CHARACTERIZATION OF PHYSICALLY AND CHEMICALLY ACTIVATED CARBON FROM OIL PALM KERNEL SHELLS Hisbullah, Siti Kana, Nabila and Muhammad Faisal	335
7565	IMPROVEMENT OF ETHANOL PRODUCTION FROM THE PALM OIL MILL EFFLUENT WASTEWATER TREATMENT Andri Gumilar, Mindriany Syafila, Marisa Handajani and Syarif Hidayat	341
7569	THE RISE OF RAINBOW VILLAGE: OPTIMIZING AESTHETICAL PROGRAM TO ACCELERATE SANITATION ACCESS (CASE STUDY: KAMPUNG CIBUNUT BERWARNA AND KAMPUNG PELANGI 200, BANDUNG CITY, INDONESIA) L P Defi, I Kusumayanti, W M Fatimah, P W Sarli and P Soewondo	348
7575	DEGRADATION OF POLYETHYLENE TEREPHTHALATE AS SECONDARY MICROPLASTICS UNDER THREE DIFFERENT ENVIRONMENTAL CONDITIONS Ansiha Nur, Prayatni Soewondo, Ahmad Soleh Setiyawan and Katharina Oginawati	354
7588	FORMULATION AND ANTIOXIDANT ACTIVITY OF LIP BALM ENRICH BY BIDARA'S LEAVES EXTRACT (Ziziphus spina-christi L) Hendrawati, Siti Aidina, Maulidia, Nurhasni and Yulyani Nur Azizah	360
7594	MORPHOLOGICAL RESPONSES AND TISSUE ADAPTATIONS OF GAMMA-IRRADIATED BANANA TO STANDING SUBMERGENCE CONDITION Pimpan Pimonrat and Seyha Kong	367

7600	PASSIVE DESIGN ENERGY SAVING HOUSE BY NATURAL VENTILATION IN THAILAND Niran Watchrodom	372
7602	EFFECTS OF HIGH TEMPERATURE ON POLLEN VIABILITY AND TUBE GROWTH OF SOME INDIGENOUS PLANTS AND THE INFLUENCE OF GA3 ON TUBE GROWTH PROMOTION Pornanan Boonkorn	377
7604	THERMAL PERFORMANCE OF THE CLEAR BLOCK WALL FOR VENTILATION Thana Ananacha	383
7617	CONSOLIDATION OF INTERNATIONAL MARINE CONTAINER TERMINAL PORTS IN TOKYO BAY USING A MEGAFLOAT: A PROPOSAL Shinji Sato and Yusuke Miyajima	388
7618	EVALUATION OF THE RESOURCE EFFICIENCY OF PRINTED CIRCUIT BOARD WASTE SORTING AND TRANSFER PLANT USING MATERIAL FLOW COST ACCOUNTING Supanisara Wanwong, Suphaphat Kwonpongsagoon and Kanokwan Kingphadung	394
7619	PHYLOGENETIC ANALYSIS OF ENDOPHYTIC Colletotrichum spp. FROM QUINA PLANT (Cinchona calisaya Wedd.) BASED ON ITS rDNA AND ACTIN GEN AND ITS POTENTIAL AS QUINA PRODUCTION Nani Radiastuti, Dwi Ningsih Susilowati, Siti Nurbayti, Zhaira Amila Haqqa and Wiwid Wiladatul Solihah	400
7620	ANALYSIS OF SOIL QUALITY INDEX AT POTATO PRODUCTION CENTER IN THE UPSTREAM OF LEMBANG WATERSHED Aprisal, Bambang Istijono, Irwan Darpis, Mimin Harianti and Teguh Huria Aditia	411
7624	EFFECTS OF BA ON IN VITRO CALLUS DEVELOPMENT FROM LEAVES OF EUPHORBIA MILII Pantipa Limsanguan, Teerayut Klumchaun, Pennapha Suphatphol, Jutamas Taosanosieng and Onpreeya Chana-in	418
7633	THE MITIGATION PRIORITY OF ORGANIC FARMING RISK IN LOCAL FARMER PERSPECTIVE Ujang Maman, Arif Sumantri, Dwi Purwoko, Muskin and Lukman Effendy	422
7646	IMPACTS OF SEVEN INSECTICIDES ON THREE MAJOR NATURAL ENEMIES IN THE NORTHEASTERN THAILAND Ruchuon Wanna and Mongkol Wongsawas	428
7647	BIOMASS FUEL POTENTIAL FROM AGRICULTURAL PRODUCT WASTES IN SOUTHERN BORDER PROVINCES, THAILAND Saudee Maprasit, Piyaruk Pradabphetrat, Romsan Madmanang, Ratchada Boonkaew and Sidthipong Sathawong	434
7655	INDONESIA'S ESSENTIAL OILS IN THE GLOBAL MARKET Lilis Imamah Ichdayati, Rizki Adi Puspita Sari and Ratdin Cahyaning M.Warahmah	440
7628	AN IN SITU VOLCANIC GASEOUS EMISSIONS CONCENTRATION MEASUREMENT SYSTEM: A CASE STUDY FOR WELIRANG VOLCANO, MALANG, INDONESIA Arinto Yudi Ponco Wardoyo, Hari Arief Dharmawan, Muhammad Nurhuda, Arif Budianto and Azarine Aisyah Widhowati	446
7504	INVESTIGATION OF WATER-RESERVOIRS IMPACT MECHANISM ON GROUNDWATER AND INDICATOR SCHEME OF ASSESSMENT Matchavariani Lia, Metreveli Giorgi and Gulashvili Zaza	452
7685	STRENGTH AND MICROSTRUCTURE DEVELOPMENT OF RICE HUSK ASH WITH CEMENT STABILIZED SOIL Sayful Kabir Khan, Najmun Nahar, Alex Otieno Owino, Zakaria Hossain and Noma Tamaki	458

Preface

On behalf of the SEE 2021 Organizing Committee, it is our great pleasure to welcome you to the Seventh International Conference on Structure, Engineering & Environment, held at Pattaya City, Thailand, organized in conjunction with Suranaree University of Technology, Thailand, The GEOMATE International Society, Useful Plant Spread Society, Glorious International, AOI Engineering, HOJUN, JCK, CosmoWinds and Beppu Construction, Japan.

The conference covers three major themes with many specific themes including:

Advances in Building Structure
Advances in Infrastructures
Advances in Civil Engineering
Advances in Structural Engineering
Advances in Geological Engineering
Advances in Geometics Engineering
Advances in Chemical Engineering
Advances in Environmental Engineering
Advances in Geotechnical Engineering
Advances in Architectural Engineering
Advances in Industrial Engineering
Advances in Manufacturing Engineering
Advances in Materials Engineering
Advances in Mechanical Engineering
Advances in Petroleum Engineering
Advances in Process Engineering
Advances in Environmental Technology
Advances in Geophysics
Advances in Hydrology
Advances in Recycle Solid Wastes
Advances in Use of reclaimed Waters
Advances in Water Distribution
Advances in Water Treatment
Advances in Irrigation and Drainage
Advances in Farm Structures

Due to COVID-19, this year we have received less submissions from different countries all over the world. The technical papers were selected from the vast number of contributions submitted after a review of the abstracts. The final papers in the proceedings have been peer reviewed rigorously and revised as necessary by the authors. It relies on the solid cooperation of numerous people to organize a conference of this size. Hence, we appreciate everyone who support as well as participate in the joint conferences.

Last but not least, we would like to express our gratitude to all the authors, session chairs, reviewers, participants, institutions and companies for their contribution to SEE 2021. We hope you enjoy the conference and find this experience inspiring and helpful in your professional field. We look forward to seeing you at our upcoming conference next year.

Best regards,

Prof. Dr. Zakaria Hossain, Chairman (General)



Prof. Dr. Suksun Horpibulsuk (Program)



Organization

Conference Honorary Chairman:

Dr. Sohji Inoue, Emeritus Professor, Mie University, Japan

Conference Chairmen:

Prof. Dr. Zakaria Hossain, Mie University, Japan (General)
Prof. Dr. Suksun Horpibulsuk, Suranaree University of Technology, Thailand (Program)

Conference Organizing Committee:

Dr. Zakaria Hossain, Prof. Mie University, Japan (Chair)
Prof. Dr. Suksun Horpibulsuk, Suranaree University of Technology, Thailand (Program)
Dr. Satoshi Kaneco, Prof., Mie University, Japan (Co-Chair)
Dr. Sohji Inoue, E/Prof. Mie University, Japan (Co-Chair)
Dr. Toshinori Sakai, Prof. Mie University, Japan (Co-Chair)
Dr. Takamitsu Kajisa, Prof. Mie University, Japan (Co-Chair)
Dr. Masaaki Kondo, A/Prof. Mie University, Japan (Co-Chair)

National & International Advisory Committee:

Dr. Fumio Tatsuoka, Prof., Tokyo University of Science, Japan
Dr. Junichiro Takeuchi, Prof., Kyoto University, Japan
Dr. Kingshuk Roy, Prof., Nihon University, Japan
Dr. Nakib Dad Khan, A/Prof. Mie University, Japan
Dr. Sai Vanapalli, Prof., University of Ottawa, Canada
Dr. Musharraf Zaman, Prof. Univ. of Oklahama, USA
Dr. Rafiqul Tarefder, Prof. University of New Mexico, USA
Dr. M. Bouassida, Prof., National Sch. of Engg. of Tunis
Dr. L.R. Austriaco, Prof., Angles Univ. Found., Philippines
Dr. A.S.M. Abdul Awal, Prof., Univ. Technology Malaysia
Dr. M. Ibn Ibrahimy, Prof., Int. Islamic Univ., Malaysia
Dr. Mohammad Shariful Islam, Prof., BUET, Bangladesh.
Dr. Bujang B.K. Huat, Prof., Univ. Putra Malaysia
Dr. Nemy Banthia, Prof., UBC, Canada
Dr. Ian Jefferson, Prof., Univ. of Birmingham, UK
Dr. John Bolander, Prof., Univ. of California, USA
Dr. Shamsul Chowdhury, Prof., Roosevelt Univ., USA
Dr. Isabel Pinto, Prof., University of Coimbra, Portugal
Dr. Mark Jaksa, Prof., University of Adelaide, Australia
Dr. Hj. Ramli Bin Hj. Nazir, A/Prof., UTM, Malaysia
Dr. M.S. Hossain, Prof., International Islamic Univ. Bangladesh
Dr. Md. Ariful Islam, A/Prof. Dhaka University, Bangladesh
Dr. Md. Nurul Amin, Prof. Dhaka University, Bangladesh

International Technical Program Committee:

Prof. Adolf Heinrich Horn, Geological Institute - Federa University of Minas Gerais, Brazil
Prof. Bang-Fuh Chen, National Sun Yat-sen University, Taiwan
Prof. Bindeshwar Singh, Kamla Nehru Institute of Technology, India
Prof. Catherine Mulligan, Concordia Institute of Water, Energy and Sustainable Systems, Canada
Prof. Chi-Min Liu Chienkuo Technology University, Taiwan
Prof. Daffalla Rabih, Kenana Sugar Company, Sudan
Prof. Essaid Bilal, Ecole Nationale Superieure Des Mines De Saint Etienne, France
Prof. Hakan Caliskan, Usak University, Faculty of Engineering, Turkey
Prof. Ibrahim Maiyza, National Institute of Oceanography & Fisheries, Egypt
Prof. Loc Nguyen, Sunflower Soft Company, Vietnam
Prof. Marilia Hagen, Indiana University, United States
Prof. Md Najib bin Ibrahim, Universiti Teknologi MARA, Malaysia
Prof. Md. Abdul Baset Mia, BSMR Agri. Univ., Bangladesh
Prof. Mihaela Popescu, University of Craiova, Romania
Prof. Mohamed Abdou, Faculty of Education Department of Mathematics, Egypt
Prof. Mohamed Tahiri, Présidnce de l'Université Hassan II de Casablanca, Morocco
Prof. Nazar Oukaili, University of Baghdad, Iraq
Prof. Radim Cajka, Technical University Ostrava, Faculty of Civil Engineering, Czech Republic
Prof. Rajaraman Jambunathan, AMET University, India
Prof. Saad Farhan Ibrahim Alabdullah, University of Almustansiriyah, Iraq
Prof. Salem Alsanusi, Benghazi, Libya
Prof. Sudhir Kumar Das, Retired Senior Project Manager of Indian Railways, India
Prof. Zachary Senwo, Alabama A&M University, United States
Prof. Imed Jabri, University of Tunis, Tunisia
A/Prof. Bindeshwar Singh Kamla Nehru Institute of Technology, India
A/Prof. Hasi Rani Barai, Yeungnam University, South Korea
A/Prof. Jamaluddin Mahmud, Universiti Teknologi MARA, Malaysia
A/Prof. Mohamed Ramadan, University of Hail, Saudi Arabia
A/Prof. Najam Hasan, Dhofar University, Oman
A/Prof. Nosina Krishna Chaitanya, Jawaharlal Nehru Technological University, India
A/Prof. Nurbek Saparkhojayev, Almaty Management University, Kazakhstan
A/Prof. Pandian Vasant, Universiti Teknologi Petronas, Malaysia
A/Prof. Teodor Lucian Grigorie, University of Craiova, Romania
A/Prof. Zawawi Daud, Universiti Tun Hussein Onn Malaysia
A/Prof. Abdull Halim Abdul, OIl and Gas department, Malaysia
A/Prof. Baoping Cai, China University of Petroleum, China
A/Prof. Dariusz Jakóbczak, Koszalin University of Technology, Poland
A/Prof. Edgar Allan Mendoza, University of the Philippines
A/Prof. Lakhveer Singh, Universiti Malaysia Pahang (UMP) Malaysia, Malaysia
A/Prof. Lidia Sas Paszt, Research Institute of Pomology, Poland
A/Prof. Mahmood Barbooti, University of Yechnology, Iraq
A/Prof. Majid Mirzaei, Universiti Tunku Abdul Rahman, Malaysia
A/Prof. Najeh Lakhoua, University of Carthage, Tunisia
A/Prof. Ryan Joseph Calinao, Lyceum of the Philippines University-Laguna
A/Prof. Sarawut Thepanondh, Mahidol University, Thailand
A/Prof. Yasir Al Hussein, Jerash University, Faculty of Engineering, Jordan
A/Prof. Grigorie Teodor Lucian, University of Craiova, Romania
A/Prof. Hêriş Golpîra, Islamic Azad University, Sanandaj, Iran
A/Prof. Muhammad Aslam, King Abdulaziz University, Saudi Arabia
A/Prof. Tomasz Plech, Medical University of Lublin, Poland
A/Prof. Fellah Mamoun, Abbes laghrour University, Algeria
A/Prof. R. S. Ajin, GeoVin Solutions Pvt. Ltd., India
A/Prof. Roman Szewczyk, Industrial Research Institute for Automation and Measurements, Poland

Dr. Abolghasem Akbari, University Malaysia Pahang, Malaysia
Dr. Ahmad Safuan A Rashid, Universiti Teknologi Malaysia, Malaysia
Dr. Akinola Johnson Olarewaju, Federal Polytechnic Ilaro, Ogun State, Nigeria
Dr. Alexandre Costa, Federal University of the valleys of Jequitinhonha and Mucuri, Brazil
Dr. Angelo Gallone, Scotland's Rural College (SRUC), United Kingdom
Dr. Azizul Azhar Ramli, Universiti Tun Hussein Onn Malaysia
Dr. Bashir Dar, University of kashmir Delina Baramulla J&K India, India
Dr. Bassam Abdellatif, National Authority for Remote Sensing and Space Sciences, Egypt
Dr. Binh Phu Nguyen, National University of Singapore, Singapore
Dr. Cazacu Gabriela, S.C. Geotech Dobrogea, Romania
Dr. Chengen Yang, Intel Corporation, United States
Dr. Dayang Norulfairuz Abang Zaidel, Universiti Teknologi Malaysia
Dr. Evgeni Starikov, KIT, Karlsruhe, Germany; Chalmers, Gothenburg Sweden, Germany
Dr. Fatma Khanchel, University of Tunis El Manar, Tunisia
Dr. Hamidreza Khataee, Griffith University, Australia
Dr. Hêriş Golpîra, Islamic Azad University, Iran
Dr. Iskhaq Iskandar, Dept. Physics, University of Sriwijaya, Indonesia
Dr. Jingwei Zhao, University of Wollongong, Australia
Dr. Jitendra Agrawal, Rajiv Gandhi Proudyogiki Vishwavidyalaya, India
Dr. Liza Patacsil, Malayan Colleges Laguna, Philippines
Dr. Mohamed Amine, Ferrag Guelma University, Algeria
Dr. Mohd Afendi Rojan, Universiti Malaysia Perlis, Malaysia
Dr. Mohd Altaf, University of kashmir Delina Baramulla J&K India, India
Dr. Mohd Hairy Ibrahim, Sultan Idris Education University, Malaysia
Dr. Mostafa Khater, Egypt - El sharqia - Zagazig, Egypt
Dr. Najam Hasan, Dhofar University, Oman
Dr. Namir Alkawaaz, University of Almustansiriyah, Iraq
Dr. Nashrul Fazli Mohd Nasir, Universiti Malaysia Perlis, Malaysia
Dr. NaufaL Mansor Kampus Uniciti Alam, Universiti Malaysia Perlis (UniMAP), Malaysia
Dr. Obed Majeed Ali, Northern Technical University, Iraq
Dr. Piyapong Janmaimool, King Mongkhut' University of Technology, Thailand
Dr. Po-Sheng Chiu, National Cheng Kung University, Taiwan
Dr. Prabu Mohandas, Adhiyamaan College of Engineering, India
Dr. Raman Kumar, D A V Institute of Engineering and Technology, India
Dr. Riccardo Colella, University of Salento, Italy
Dr. Rolando Javellonar, Romblon State University, Philippines
Dr. Shikha Agrawal, Rajeev Gandhi Technical University, India
Dr. Stefania Tomasiello CORISA, University of Salerno, Italy
Dr. Sumiyyah Sabar, Universiti Sains Malaysia, Malaysia
Dr. Suphaphat Kwonpongsagoon, Mahidol University, Thailand
Dr. Wei Hong Tan, Universiti Malaysia Perlis, Malaysia
Dr. Yoshiro Fujii, Shin Kobe Dental Clinic, Japan
Dr. Yuk Feng Huang, Universiti Tunku Abdul Rahman (UTAR), Malaysia
Dr. Zongyan Zhou, Monsh University, Australia
Dr. Purnanand Savoikar, Goa Engineering College, India
Dr. Ahmed Toaha Mobashsher, University of Queensland, Australia
Dr. Chupong Pakpum, Maejo University
Dr. Emanuele Quaranta, Politecnico di Torino, Italy
Dr. Jiangling Yin, Apple Inc., Cupertino, CA, United States
Dr. Khor Shing Fhan, Universiti Malaysia Perlis, Malaysia
Dr. Mario Chauca, Ricardo Palma University, Peru
Dr. Santosh Gaikwad, Model College, Ghansawangi, India
Dr. Tse Guan Tan, Universiti Malaysia Kelantan
Dr. Vikas Panthi, National Institute of Technology, India
Dr. Watoo Phrompittayarat, Naresuan University, Thailand

Dr. Hamidreza Namazi, Nanyang Technological University, Singapore
Dr. Parichat Phumkhachorn, Ubon Ratchathani University, Thailand
Dr. Subhasis Roy, University of Calcutta, India

Conference Correspondence:

Prof. Dr. Zakaria Hossain (Director)
Dept. of Environmental Science and Technology, Mie University, Japan
Mr. Md. Aminul Islam (Secretary)
Dept. of Environmental Science and Technology, Mie University, Japan
E-mail: conference@geomate.org
Tel & Fax: +81-59-231-9578

Editorial and Executive Committee:

Prof. Dr. Zakaria Hossain
Engr. Alex Otieno Owino
Engr. Md. Aminul Islam
Ms. Najmun Nahar
Mr. Sayful Kabir Khan

Technical Papers

Structure

7th Int. Conf. on Structure, Engineering & Environment (SEE),
Pattaya, Thailand, Nov.10-12, 2021, ISBN: 978-4-909106070 C3051

FRACTURE SIMULATION OF THE ADHESIVE POST-INSTALLED ANCHOR APPLIED TO EXISTING CONCRETE STRUCTURES

Takuma Kadono[1], Shinichiro Okazaki[2], Taro Nakamura[3] and Mao Kurumatani[3]
[1]Graduate School of Engineering, Kagawa University, Japan; [2] Faculty of Engineering and Design Associate Professor, Kagawa University, Japan; [3] Faculty of Engineering and Design, Kagawa University, Japan;
[4] Department of Urban and Civil Engineering College of Engineering, Ibaraki University, Japan

ABSTRACT

The aim of this research is to investigate the applicability of a fracture simulation method based on concrete damage model and to construct a framework for evaluating the load capacity of adhesive post-installed anchor according to a failure mode and load resistant mechanism. A continuum damage model based on the fracture mechanics of semi-brittle materials is used for the simulation and interface elements are set at boundary between adhesive and concrete. The interface elements are used to simulate the contact state at the fracture boundary. The friction contact model is used to simulate the contact behavior by maintaining the initial stiffness in the direction perpendicular to the interface. As a result, by setting the appropriate friction coefficient and fracture occurrence strain in the interface elements, combined fracture mode of adhesion and cone fracture which is a characteristic failure mode of adhesive post-installed anchors are precisely simulated.

Keywords: Adhesive post-installed anchor, Fracture mechanics, Cone failure mode, Adhesion failure mode, Combined fracture mode

INTRODUCTION

Post-installed anchors are a widely used technology for repair and renewal in the concrete structures. In recent years, a reliability of the adhesive post-installed anchor has become a social problem in Japan, due to the accident such as collapsing ceiling boards in a road tunnel caused by the failure of the adhesive post-installed anchors. Although several organizations have proposed methods for evaluating the performance of post-installed anchors as guidelines and manuals [1]-[4], they have not always been standardized in Japan. In addition, various experiments and studies [e.g.5] have been conducted, however, there are few research cases to evaluate the structural capacity based on a failure mode and load resistant mechanism.

Ryu et al [6] showed that the failure mode of the adhesive post-installed anchor subjected to uniaxial tension is a combined fracture of cone fracture of the surface layer and adhesion of deep layer of base material (combined fracture). In addition, Mikura et al [7] showed that the pull-out strength decreases when the edge distance is 15 times or less of the anchor diameter, or when the anchor spacing is 20 times or less of the anchor diameter based on the results of the static pull-out test with parameters as the edge distance and the anchor spacing which evaluate an effect when the anchors are close to each other of when they are close to the edge of the base material. These studies were mainly based on the results of the loading tests, and there is a problem that the crack propagation process inside the base material cannot be understood. It is necessary to construct a numerical simulation method for grasping a damage process and the progress of microscopic cracks in addition to the experimental approach in order to construct an evaluation method to understand the damage process and progress of micro cracks in addition to the experimental approach.

The aim of the study is to construct a numerical simulation method to evaluate the structural capacity of adhesive post-installed anchors according to the failure mode and load resistant mechanism. A specifically, we verify a reproduction of a fracture behavior of the uniaxial pull-out test of adhesive post-installed anchor as a verification example by Ryu et al [6], using a continuum damage model based on the fracture mechanics of semi-brittle materials and a damage model considering frictional contact at an interface of damage.

FRACTURE SIMULATION METHOD

Continuum Damage Models Considering Fracture Mechanics of Reinforcing Bars and Concrete

In this research, we verify using a continuum damage model considering fracture mechanics semi-brittle material which is proposed by Kurumatani et al [8].

The von-Mises plastic model based on the nonlinear isotropic hardening law is applied to reinforcing bars. As shown in Equation (1) and

Equation (2), a total strain is additively decomposed into an elastic strain and a plastic strain, and it is assumed that only an elastic component of the stress contributes.

$$\varepsilon = \varepsilon_E + \varepsilon_P \quad (1)$$
$$\sigma = c : \varepsilon_P = c : (\varepsilon - \varepsilon_P) \quad (2)$$

Where, ε is the micro strain tensor, ε_E is the elastic strain tensor, ε_P is the plastic strain tensor, σ is the Cauchy stress tensor, and c is the elastic modulus tensor. The yield function as $f \leqq 0$ is adopted the nonlinear isotropic hardening law given by the exponential function shown in Equation (3).

$$f = \sigma_V - \sigma_{y0} - Q(1 - e^{-bp}) \quad (3)$$

Where, σ_V is the equivalent stress of the von-Mises, σ_{y0} is the initial yield stress, p is the equivalent plastic strain, and Q and b are parameters for expressing plastic hardening. In addition, the plastic flow rule is followed the related flow rule and is given by Equation (4).

$$d\varepsilon_P = dP \cdot \partial f / \partial \sigma = dpn \quad (4)$$

An isotropic damage model [9] based on the modified von-Mises model considering the fracture mechanics of semi-brittle material is applied to concrete, and we model the cracks growth behavior after the elastic limit of concrete. The model used targets the genuine equilibrium problem of the elastic bodies in the process of the damage, and an equilibrium equation, a strain matching condition equation, and each constitutive equation is shown in Equation (5), Equation (6) and Equation (7).

$$\nabla \cdot \sigma + \bar{b} = 0 \quad \text{in } \Omega \quad (5)$$
$$\varepsilon = \frac{1}{2}\{\nabla u + (\nabla u)^T\} \quad \text{in } \Omega \quad (6)$$
$$\sigma = C_D(\varepsilon) \quad \text{in } \Omega \quad (7)$$

Where, u is a displacement vector, Ω is an object region, C_D is a constitutive function considering the damage of the material. In addition, the modified von-Mises model proposed by De Vree et al. [10] shown in Equation (8) is applied to an equivalent strain ε_{eq}.

$$\varepsilon_{eq} = \frac{k-1}{2k(1-2\nu)} I'_1 + \frac{1}{2k}\sqrt{\left(\frac{k-1}{1-2\nu} I'_1\right)^2 + \frac{12k}{(1+\nu)^2} J'_2} \quad (8)$$

Where, ν is the Poisson's ratio, k is compressive tensile strength ratio, I'_1 is a first invariant of a strain tensor, and J'_2 is a second invariant of a deviation strain tensor. The k of the concrete is approximately 10, and substituting this k into Equation (8) can make possible to express the fracture characteristics that are weak in tension and strong in compression. A relationship between ε_{eq} and an equivalent stress σ_{eq} is expressed by Equation (9), and a damage variable D is expressed a degree of the damage by $0 \leqq D \leqq 1$. If there is no damage, it will be 0, and if it is completely destroyed, it will be 1.

$$\sigma_{eq} = [1 - D(\varepsilon_{eq})] E \varepsilon_{eq} = \left[1 - \left\{1 - \frac{\varepsilon_0}{\varepsilon_{eq}} exp\left(-\frac{E\varepsilon_0 h_e}{G_f}(\varepsilon_{eq} - \varepsilon_0)\right)\right\}\right] E\varepsilon_{eq} \quad (9)$$

Where, σ_{eq} is an equivalent stress, D is a damage variable, ε_0 is a fracture occurrence strain, and h_e is an element length. The damage variable $D(\kappa)$ is expressed assuming that the damage that has occurred is not recovered and the equivalent strain ε_{eq} in the damage variable $D(\varepsilon_{eq})$ is represented by $\kappa \leqq 0$ as the maximum value of the equivalent strain in a deformation history.

$$D(\kappa) = 1 - \frac{\kappa_0}{\kappa} exp\left(-\frac{E\kappa h_e}{G_f}(\kappa - \kappa_0)\right) \quad (10)$$

Where, κ_0 is an equivalent strain at a start of the damage. These models are analyzed using the augmentation method and the iterative solution method by Newton-Raphson method. If a convergent solution cannot be obtained, the modified Newton-Raphson method which updates the node stiffness for each step, is applied for analysis.

A Damage Model Considering Frictional Contact at a Fracture Boundary

In this research, we decide to reproduce the damage to a boundary near post-installed anchor that receives tensile load on the uniaxial using a damage model considering frictional contact of a boundary which proposed by Soma et al. [10]. The damage model considering the frictional contact at the interface is based on the structural relationship in the local coordinate system and uses a strain ε'_1 in the direction perpendicular to the interface to determine a contact state of the fracture surface. In the case of the fracture surface comes into contact, a contact behavior is expressed by maintaining an initial rigidity in the direction perpendicular to the interface. In addition, the Coulomb's friction law is introduced in order to consider an adhesion and a slippage of the interface in the contact state. Where, a friction stress τ_f is expressed by Equation (11) using a stress σ'_1 in the direction perpendicular to the interface.

$$\tau_f = \mu\sigma_n = \mu|\sigma'_1| \quad (11)$$

Where, μ is the coefficient of the friction and σ_n is the normal stress. In this model, a shear stress τ'_{12} and τ'_{31} in the local coordinate system are the forces

acting along the interface, and the maximum value of the forces acting along the interface is expressed by Equation (12).

$$\tau'_s = \sqrt{\tau'^2_{12} + \tau'^2_{31}} \quad (12)$$

A slip of the fracture surface is determined comparing τ'_s with the friction stress τ_f. It is assumed that the shear rigidity is equal to the initial rigidity because the fracture surface is fixed in a non-slip state. On the other hand, in the case of a slip state, it is needed to consider a shear stress that combines damage and friction, because the fracture progresses with frictional slip. A model shown in Equation (13) which expresses a behavior of the fracture progressing with friction slip is used by combining the shear stress acting on a non-damage area and the frictional stress acting on a damaged area.

$$\tau'_{12} = (1-D)G\gamma'_{12} + D\tau_f \frac{\gamma'_{12}}{\sqrt{\gamma'^2_{12}+\gamma'^2_{31}}}$$
$$\tau'_{31} = (1-D)G\gamma'_{31} + D\tau_f \frac{\gamma'_{31}}{\sqrt{\gamma'^2_{12}+\gamma'^2_{31}}} \quad (13)$$

Where, G is the shear rigidity and γ'_{ij} is the strain in the shear direction.

EXAMINATION BY THREE DIMENTE ELEMENT ANALYSIS

Verification Example

In this research, we decide to use the results of embedded lengths of 3ϕ, 5ϕ and 7ϕ as verification example among the uniaxial pull-out tests of the adhesive post-installed anchors conducted by Ryu et al. [6]. Where, ϕ is a diameter of an anchor bar, and a D25 which is deformed bar was used. Anchor bars were embedded in concrete specimen which size is width 900mm ×length 900mm×height 500mm, and experiments were conducted using a loading test equipment shown in Fig. 1. Table 1 shows physical characteristic of each material used in the pull-out test. The pull-out tests were performed using 3 specimens in each case.

When the embedded length is 3ϕ as shown in Fig.2(a), caracks were grew diagonally from the bottom tip of the anchor bar and came out in a cone shape, reaching the maximum load (cone failure). The average vale of the maximum load at that time was 62.3 kN. When the embedded lengths are 5ϕ and 7ϕ as shown in Fig.2(b) and (c), the cone failure was not formed from the bottom of the anchor bar, however a cone failure surface was formed from a position of about 4ϕ to 5ϕ from the surface layer of concrete, and a depth of below the concrete failure surface was pulled out by a adhesion failure reaching the maximum load (combined failure). The average vales

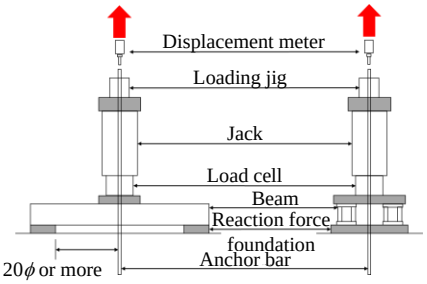
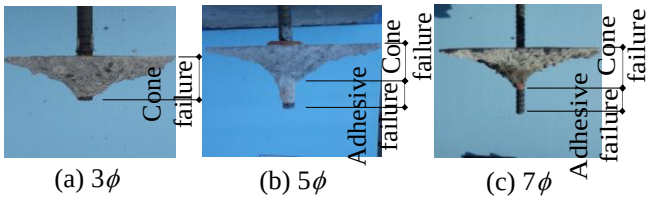


Fig. 1 Loading test equipment [6]

Table 1 Material property values of each material [6]

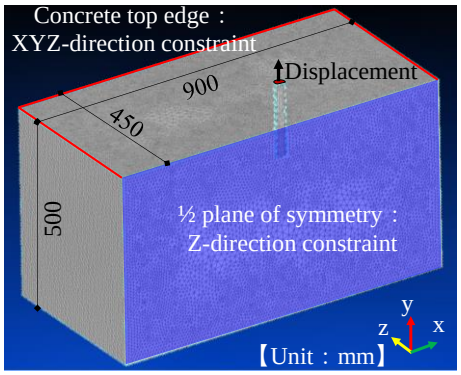
Epoxy resin		Concrete		Anchor bar
σ_{te} (N/mm^2)	σ_{ce} (N/mm^2)	σ_{cc} (N/mm^2)	E_c (kN/mm^2)	σ_{ea} (N/mm^2)
75.7	109	28.5	28.2	1,006

Note: σ_{te} is the tensile strength of the epoxy resin, σ_{ce} is the compressive strength of the epoxy resin, σ_{cc} is the compressive strength of the concrete, E_c is the elastic modulus of the concrete, σ_{ea} is the yield strength of the anchor bar.

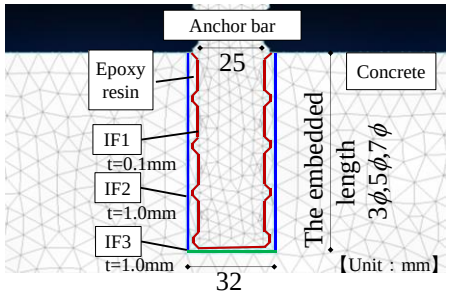


(a) 3ϕ (b) 5ϕ (c) 7ϕ

Fig. 2 Fracture status at the time of pull-out test



(a) Overall view



(b) Detail view

Fig. 3 Outline of analysis model

of the maximum load at those time were 123.9 kN and 193.9kN.

Outline of an Analysis

Fig.3 shows an outline of an analysis model. The analysis model is defined a 1/2 symmetric model of the pull-out test specimens. Materials are defined the concrete, the anchor bar, the epoxy resin, an interface element between the anchor bar and the epoxy resin boundary (IF1), an interface element between the epoxy resin on the side surface of the anchor bar and the concrete boundary (IF2), and an interface element between the epoxy resin and the concrete boundary on the bottom of the anchor bar (IF3). Material constitutional rules are used in the analysis are defined as shown in Table 2 with reference to the material property values at the time of the experiment shown in Table 1. The fracture energy G_f and ε_0 are defined to sufficiently large values that the anchor bar and the epoxy resin would not be damaged during the analysis.

Elements are meshed by tetrahedral element, and numbers of element are 646,009 elements, 660,073 elements and 652,038 elements respectively, in the models with embedded length of 3ϕ, 5ϕ and 7ϕ. A 1/2 plane of symmetry is constrained Z direction which is its normal direction. In addition, three sides excluding the side in contact with the 1/2 plane of symmetry are completely constrained to simulate a reaction force foundation. Displacement of 0.05mm per step is given in Y direction, and the analysis is performed up to 100 steps.

In this research, an effect on the analysis results is grasped by changing μ and ε_0 of IF2 as shown in Table 3. A notation after here is, e.g., in the case of the Case1 with the embedded length is 3ϕ is written "Case1-3ϕ".

Results and Considerations

Fig.4 shows the contour plot of the damage variables at the maximum load in Case1. Here, the distribution of the damage variable is exactly the distribution of the damage; however, it can be regarded as an approximate distribution of cracks because an element size is small. Focusing on Fig.4(a), the cracks do not reach the surface layer at the maximum load, although the cracks occur diagonally from the bottom of the anchor bar toward the surface of the concrete, and the maximum load has been reached due to combined failure. Therefore, it is not possible to reproduce the failure behavior during the experiment shown in Fig. 2. Also, focusing on Fig.4(b) and (c), although small cone failures are formed on the concrete surface, the damage is concentrated near the interface between epoxy resin and concrete and cone failure on the surface layer of the concrete reaches the maximum load. Therefore, it is not possible to reproduce the failure behavior during the experiment shown in Fig. 2.

Table 2 Table of material composition rules

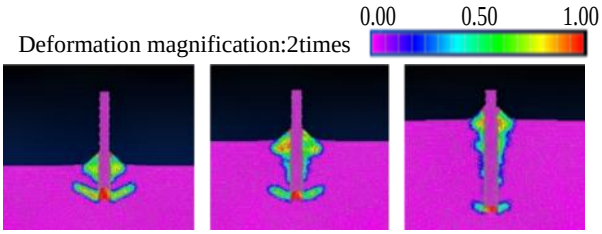
Case	Material composition rules of IF2					
	E (N/mm^2)	ν	μ	k	G_f (N/mm)	ε_0
Case1	28,200	0.2	0.6	13.3	0.0829	7.61E-5
Case2	28,200	0.2	0.1	13.3	0.0829	7.61E-5
Case3	28,200	0.2	1.0	13.3	0.0829	7.61E-5
Case4	28,200	0.2	1.5	13.3	0.0829	7.61E-5
Case5	28,200	0.2	0.6	13.3	0.0829	2.00E-4
Case6	28,200	0.2	0.6	13.3	0.0829	4.00E-4
Case7	28,200	0.2	0.6	13.3	0.0829	6.00E-4

Table 3 Table of analysis cases

Material	E (N/mm^2)	ν	k	G_f (N/mm)	ε_0
Concrete	28,200	0.2	13.3	0.0829	7.61E-5
Anchor bar	200,000	0.3	1.00	1.0000	1.0E+11
Epoxy resin	1,090	0.3	1.44	1.0000	1.0E+11
IF1	28,200	0.3	13.3	1.0000	1.0E+11
IF3	28,200	0.2	100	0.0829	7.61E-5

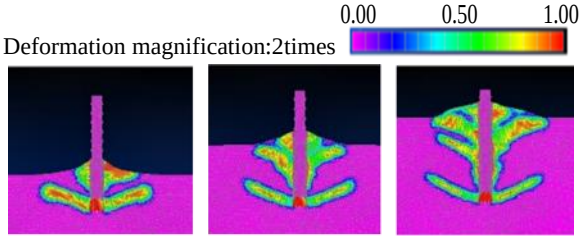
Fig.5 shows the relationship between μ and the maximum load for the analysis results of Case1 to Case4 with varying μ. The maximum load does not change even if the friction coefficient μ is increased. This is thought to be because the shape of IF2 is not uneven, so there is almost no variation in stress in the normal direction. The maximum load value obtained by the analysis is smaller than the maximum load at the time of the experiment, and the analysis cannot be reproduced the experiment. The distributions of the damage variable from Case2 to Case4 also show the approximately the same failure mode, although there was some variation in the size of the small cone failure in the surface layer. Therefore, we have decided to proceed with this research based on the general coefficient of friction between concrete, 0.6.

Fig. 6 shows the damage variation contour at the maximum load in Case6. Focusing on Fig.6 (a), diagonal cracks occur from the bottom of the anchor bar toward the concrete surface and reaching the maximum load. Therefore, the failure behavior as cone failure at the time of the experiment shown in Fig.2 can be reproduced. We focus on Fig.6 (b) and (c), a growth of the cracks in the diagonal direction from the bottom of the anchor bar toward the surface of the concrete can be confirmed however the growth remains inside the concrete. Damage is concentrated



(a) Case1-3ϕ (b) Case1-5ϕ (c) Case1-7ϕ

Fig. 4 Diagram of the damage variable contour



(a) Case6-3ϕ (b) Case6-5ϕ (c) Case6-7ϕ

Fig. 6 Diagram of the damage variable contour

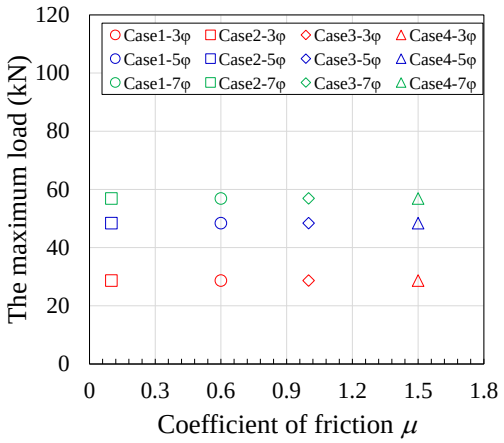


Fig. 5 Relationship between μ and maximum load

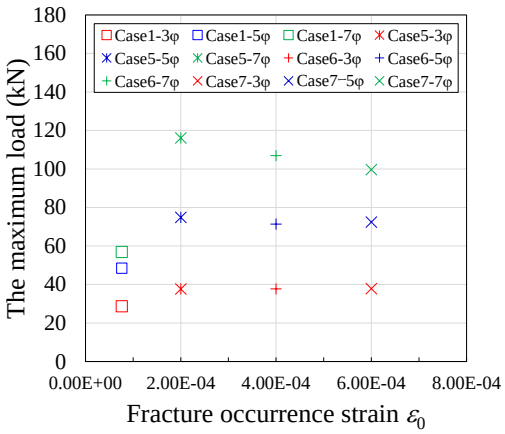
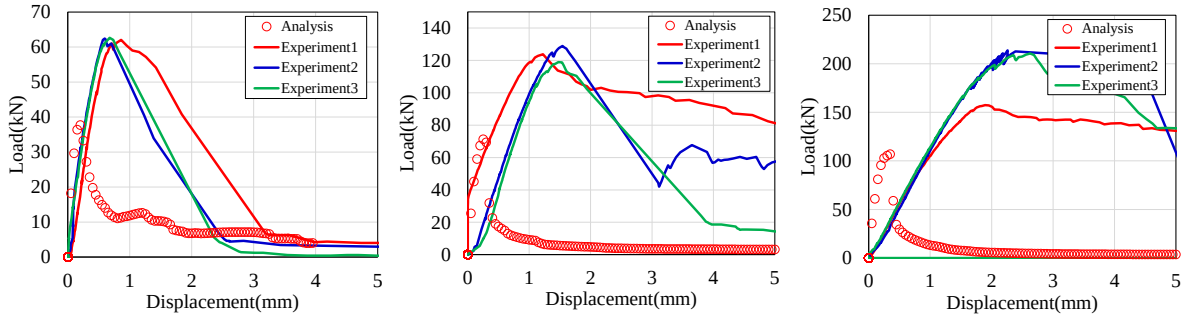


Fig. 7 Relationship between ε_0 and maximum load



(a) Case6-3ϕ (b) Case6-5ϕ (c) Case6-7ϕ

Fig. 8 Relationship between load and displacement in the loading point

near the interface between the epoxy resin and the concrete in the deep part of the anchor bar, and the cone failure on the surface layer of the concrete reaches the surface layer, and reaching the maximum load. Therefore, it is possible to reproduce the failure behavior as a combined failure during the experiment shown in Fig. 2.

Fig.7 shows Relationship between ε_0 and the maximum load based on the analysis results of Case1 and Case5 to Case7 with varying ε_0. The maximum load at the time of the analysis increases by increasing ε_0, however the increase trends is converged when ε_0 exceeds 2E-4. Distribution of the damage variables in the Case5 and Case7 were almost the same as the distribution of the damage variables in the Case6 shown in Fig.6. Fig.8 shows relationships between load and displacement in the loading point. In the figure, relationships between load and displacement in the loading point at the time of the experiments are also shown. The maximum loads at the time of the analysis are approximately 50% to 60% of the maximum load at the time of the experiments. And, we focus an initial rigidity, the Case6-3ϕ is almost the same as an initial rigidity at the time of the experiment. On the other hand, initial rigidities of Case6-5ϕ and Case6-7ϕ tends to be higher than the initial rigidities at the time of the experiments. This was probably due to the elastic deformation of the anchor bar and the elongation of the loading jig during the experiment.

From these results, we show that the failure behavior of the adhesive post-installed anchor can be reproduced roughly by changing the fracture occurrence strain ε_0 of the IF2. On the other hand, we could not reproduce the maximum load at the time of

the experiments. In the future, it is going to be necessary to further improve an accuracy of the analysis by considering the fluctuation of the compressive strength according to restraining effect of the concrete elements in this model.

CONCLUSIONS

The aim of this research is to investigate the applicability of a fracture simulation method based on a concrete damage model and to construct a framework for evaluating the load capacity of the adhesive post-installed anchor according to a failure mode and load resistant mechanism. A continuum damage model based on the fracture mechanics of semi-brittle materials is used for the simulation and interface elements are set at boundary between adhesive and concrete. The interface elements are used to simulate the contact state at the fracture boundary. The friction contact model is used to simulate the contact behavior by maintaining the initial stiffness in the direction perpendicular to the interface. As a result, by setting the appropriate friction coefficient and fracture occurrence strain in the interface elements, combined failure mode of adhesion and cone failure which is a characteristic failure form of adhesive post-installed anchors are precisely simulated.

ACKNOWLEDGMENTS

We received kind cooperation from the Railway Technical Research Institute in Japan in order to the data of the experimental results as a verification example. We would like to express our gratitude to them.

REFERENCES

[1] Railway Technical Research Institute in Japan, " Atosekouanka- no sekkei sekou no tebiki"(The manual of design and construction for the post-installed anchor), 2018

[2] Japan Society of Civil Engineers,"Konkuri-to no atosekouanka-kouhou no sekkei sekou shishin(an)"(The guideline of design and construction for the post-installed anchor in the concrete(Draft)), 2014

[3] EOTA, ETAG001 Part five: BONDED ANCHOR, 2013

[4] American Concrete Institute, 355.4-11 Qualification of Post-Installed Anchors in Concrete and Commentary, 2011

[5] e.g. Kazuhito Muramatsu and Eiichi Sou, "Epokishijushianka- no hipparitsuyosa ni kansuru jikkentekikenkyu"(Experimental study on the tensile length for the epoxy resin post-installed anchor), Annual Journal of Japan Concrete Institute, Vol.6, 1984, pp.389-392.

[6] Yuichiro Ryu, Toshiya Tadokoro, Masaru Okamoto and Takutoshi Furuya, Consideration on the pull-out capacity for post-installed anchor based on a load-bearing mechanism, Annual Journal of Japan Concrete Institute, Vol.37, No.2, 2015, pp.505-510.

[7] Hiroaki Mikura, Toshiya Tadokoro, Masaru Okamoto and Yuichiro Ryu, Effects of edge distance and anchor spacing on strength degradation of post-installed bonded anchor, Annual Journal of Japan Concrete Institute, Vol.39, No.2, 2017, pp.463-468.

[8] Mao Kurumatani, Yuki Nemoto, Yuto Soma and Kenjiro Terada, 3D fracture simulation of reinforced concrete based on fracture mechanics for concrete and its performance assessment, Transactions of JSCES, 2016, Paper No.2016004

[9] Mao Kurumatani, Kenjiro Terada, Junji Kato, Takashi Kyoya and Kazuo Kashiyama, An isotropic damage model based on fracture mechanics for concrete and its evaluation, Transactions of JSCES, 2013, Paper No.20130015

[10] J.H.P. de Vree, W.A.M Brekelmans, M.A.J. van Gils : Comparison of nonlocal approaches in continuum damage mechanics, Comput. Struct., 55, 1995, pp.581-588

[11] Yuto Soma and Mao Kurumatani, Fracture simulation of reinforced concrete using damage model considering frictional contact on interface, Journal of JSCE A2 (Applied Mechanics), Vol.75, No.2, 2019, pp.I_165-I_173

FIELD EVALUATION AND FATIGUE ASSESSMENTS OF BENT PLATE CONNECTIONS IN A HIGHLY SKEWED STEEL I-GIRDER BRIDGE

Yousif Almoosi[1] and Nazar Oukaili[2]

[1] PhD Candidate, Department of Civil Engineering, College of Engineering, University of Baghdad, Baghdad, Iraq
[2] Professor of Structural Engineering, Department of Civil Engineering, College of Engineering, University of Baghdad, Baghdad, Iraq

ABSTRACT

Bent plate connection is often used in skew bridges to connect the cross-frames to the girder and aligned parallel to the skew angle. Such a connection provides little if any warping restraint. While bent plate connections can simplify fabrication, the flexibility of the plate due to the connection eccentricity may compromise the effectiveness of the cross-frame in stabilizing the girders against lateral-torsional buckling. In many recent investigations reported on fatigue performance of existing steel and composite bridges, it has been found that the most common fatigue damage types are caused by secondary effects, so-called distortion-induced fatigue cracking. Design codes and evaluation methods generally provide little guidance on how this kind of fatigue damage should be accounted for or prevented. Strain measurements under various load passes of a weighed load vehicle were collected on the girders to cross-frames connections of a skewed I-girder bridge, mainly, US13 Bridge in Delaware State, USA. The fatigue evaluation used the field and FEA data generated in this work as input into the AASHTO MBE (2018) procedures to conclude that the Constant-Amplitude Fatigue Threshold (CAFT) is exceeded due to the use of bent plate connection. The results showed that distortion-induced fatigue can be exacerbated for the bent plate connection used between the end cross-frame and the girder at the abutment cross-section. At this location, the CAFT is exceeded when considering the principal stress ranges and realistic travel speeds of 100 km/h (65 mph). Thus, this data highlights some vulnerabilities of this connection detail.

Keywords: Skew Bridge, Field Test, Cross-Frames, Bent Plates, Fatigue Life.

1. INTRODUCTION

Braces in straight bridge systems, improve the lateral-torsional buckling resistance of the girders by reducing the unbraced length, while in horizontally curved and skew bridges, the braces are primary structural elements for controlling deformations by engaging adjacent girders to act as a system to resist the potentially large forces and torques caused by the curved or skewed geometry of the bridge. The cross-frames are usually designed as torsional braces, which increase the overall strength and stiffness of the individual girders by creating a girder system that translates and rotates as a unit along the bracing lines. However, when they transmit the truck's live load forces, they can produce fatigue cracks at their connections to the girders.

AASHTO/NSBA "Steel Bridge Erection Guide Specification", required that the end cross-frame be placed parallel to the skewed support, and hence at an angle to the girders [1], and to provide access for welding during fabrication and erection, bent plate connection is often used to connect the cross-frames to the girder and aligned parallel to the skew angle. Such a connection provides little if any warping restraint.

While bent plate connections can simplify fabrication, the flexibility of the plate due to the connection eccentricity may compromise the effectiveness of the cross-frame in stabilizing the girders against lateral-torsional buckling. For small skew angles, the bent plate performs adequately; however, problems can occur for larger support skews [2].

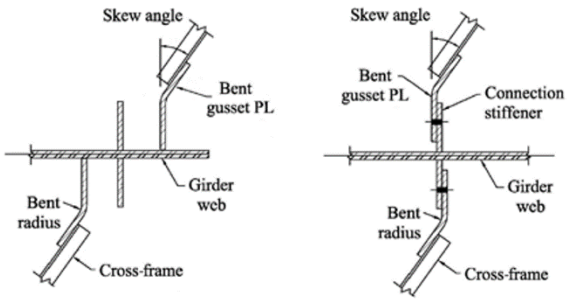
Results from laboratory tests and three-dimensional finite element studies have demonstrated that the eccentricity causes out-of-plane bending of the members resulting in a reduction in the stiffness of the cross-frame [3]. The eccentric connections lead to member bending that results in uncertain behavior for strength, stiffness, and especially fatigue.

Many recent investigations reported on fatigue performance of existing steel and composite bridges have been found that the most common fatigue damage types are caused by secondary effects, so-called distortion-induced fatigue cracking. This type of fatigue damage is often the result of secondary restraining forces generated by unintentional or overlooked interactions between different members of the bridge. Poor detailing, along with abrupt changes in stiffness at the connections between

girders and cross-frames increases the possibility of prone fatigue cracking in such details [4].

Many surveys and reports stated that distortion-induced fatigue, which often occurs in the vicinity of cross-frame to girder connections, is the most frequently observed type of fatigue observed [5]. Several studies have explored various specific examples of this phenomenon at cross-frame to girder connections [6] - [10].

This paper investigates the effect of using bent plate connections and their impacts on both, girder's stresses, and fatigue ratings. Field testing data of skewed steel girders bridge (US13 Bridge in Delaware, USA) under various load passes of a weighed load vehicle incorporated with a validated 3D full-scale finite element model are presented in this study. The bent plate connection type is widely adopted in bridges with skew abutments and pier support regions (see Fig. 1a and 1b, respectively). It is also used in the bridge of interest of the present study (US13 Bridge).



(a) (b)

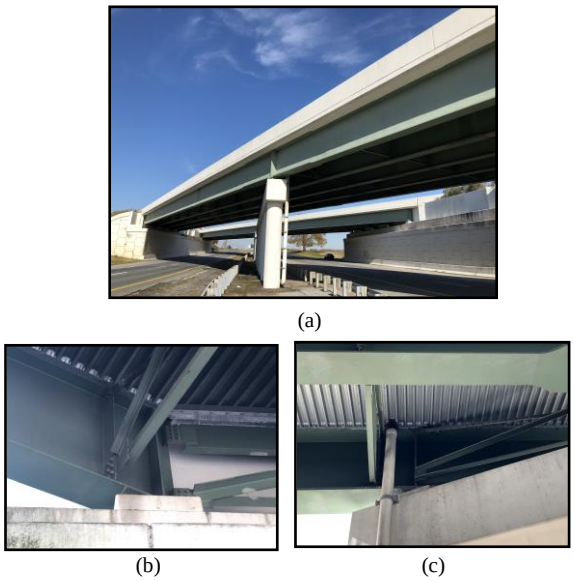
Fig. 1 Bent plate connection details used in US13 Bridge (subjected bridge), (a) bent plate connection in US13 Bridge abutment skew support, and (b) bent plate connection in US13 Bridge pier skew support.

2. BRIDGE FIELD TESTING

2.1 BRIDGE GENERAL DESCRIPTION

The bridge of interest, labeled US13 Bridge, is a 65° heavily skewed steel I-girder bridge in Delaware State, USA (Fig. 2). Twin spans carry the north- and southbound lanes. The bridge consists of two continuous spans of equal 50 m (165 ft) lengths. There are five girders spaced 2.9 m (9.5 ft) on center with exterior girders spaced 0.86 m (2.83 ft) and 1.16 m (3.83 ft) away from the outer edge of the bridge concrete guard wall on the west and east sides, respectively. The subjected bridge was constructed in 1999.

The bridge contains inline X-shaped cross-frames (between girders and at pier location) oriented perpendicular to the girders, which are connected to the girders using full-depth connection plates. Also, inline K-shaped cross-frames are used in the vicinity of the abutment supports and connected to the girders using bent plates, see Fig. 2b.



(a)

(b) (c)

Fig. 2. US13 Bridge, (a) general view (twin routes) (b) bent plate connection in skew abutment support, and (c) bent plate connection in skew pier support.

2.2 INSTRUMENTATION LAYOUT AND LOADING PATTERN

Bridge Diagnostics Inc. ST-350 strain gauges (BDI gauges) [11] and their associated data-acquisition system were used in the field test. Sections D and E (Fig. 3) are adopted for the present study since these sections include the bent plate connections that are used to connect K-Type abutment cross-frame with both, girder#4 and girder#5 respectively.

Section D and E had the same instrumentation plan (Fig. 4) with four gauges per section placed on opposite sides of the web in the longitudinal direction at two locations; one pair placed at the top intersection point between the girder's web (G4 and/or G5 webs) and the abutment K-Type cross-frame top chord. The other pair of gauges are located at the intersection point between both G4 and/or G5 web's bottom region and the K-Type cross-frame bottom chord.

The loading for the field testing consisted of driving loaded and weighed tri-axle dump trucks across the bridge while the bridge was closed to all other traffic. The truck positions were selected to maximize the stress range in the instrumented locations. The driving speeds and transverse positions of the field trucks are illustrated in Fig. 5.

3. FINITE ELEMENT MODELING AND ANALYSIS

The geometry of the bridge for both static and dynamic FEA models was created according to the structural plans provided by the bridge owner (the Delaware Department of Transportation).

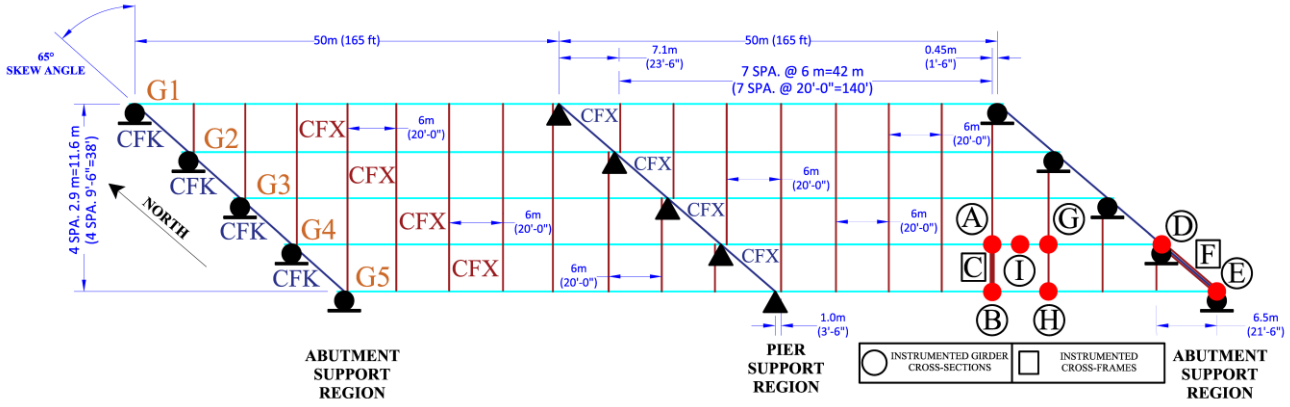


Fig. 3. Framing plan and instrumentation locations for US13 Bridge.

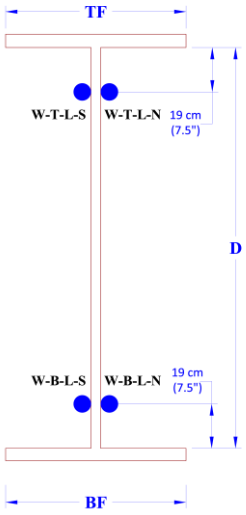


Fig. 4. Instrumentation layout for both, sections D and E.

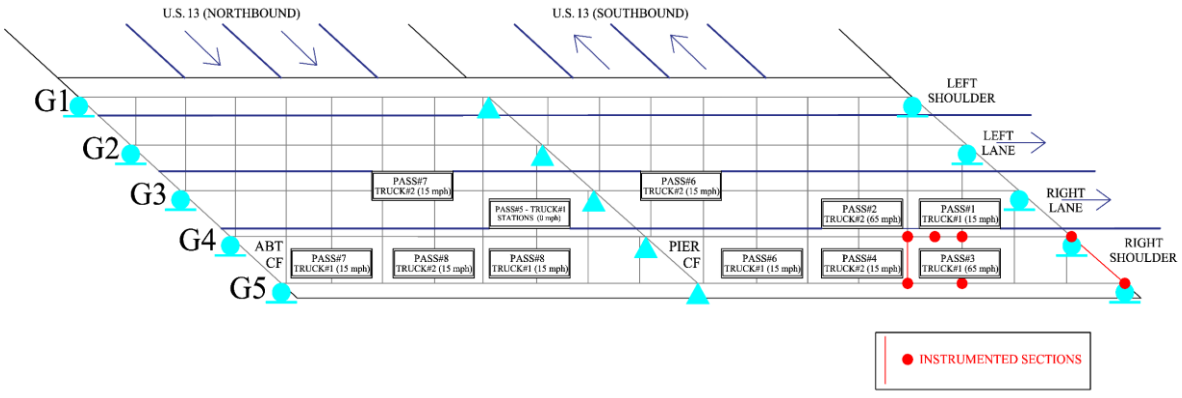


Fig. 5. Loaded passes schemes implemented in the field test.

Software like AutoCAD - 3D, FEMAP, NX Nastran, and ABAQUS/CAE were all used to perform the bridge final finite element model [12] - [14], see (Fig. 6). Four-node reduced-integration shell elements were used for modeling all girders, cross-frames, and stay-in-place profiled metal deck forms in each of the static and dynamic models.

For modeling the concrete deck, haunch, and

concrete guard wall, four-node reduced-integration shell elements (S4R) were used in the static models, compared to dynamic models in which three-dimensional eight-node reduced-integration brick elements (C3D8R) [12] - [14] were used instead. Two different approaches were used for modeling the static versus dynamic load passes. In the static models, the loading truck was modeled using six-point loads (one to represent each physical wheel of the loading vehicle) [12] - [14].

A One-dimensional (1D) dynamic model in which the vehicle is modeled as a spring-mass of one or two degrees of freedom was adopted in the present study for the modeling of truck dynamic loading. Truck wheels were modeled as a moving mass by defining a load versus time history for each axle, which is constant, and a displacement history for the position versus time. Consequently, both load and inertia are used to evaluate the dynamic effects of the moving load. Surface-based contact with a rigid pressure-overclosure relationship and frictionless tangential behavior was used to model the interaction between the bridge and moving masses [12] - [14].

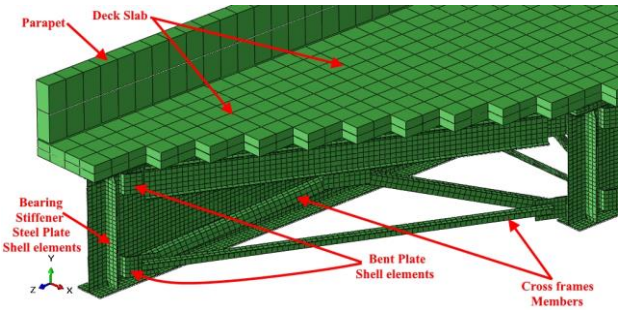


Fig. 6. Abaqus finite elements model (static/shell model), for pier support region of for US13 Bridge.

4. FATIGUE LIFE ANALYSIS

The principal stress range is used to evaluate the fatigue assessments of the US13 Bridge based on the procedures listed in AASHTO LRFD *Bridge Design Specifications* (AASHTO LRFD, 2017) [4], in which it provides a code-based procedure for determining load types and combinations specific to fatigue loading. AASHTO MBE *Manual for Bridge Evaluation* (AASHTO MBE 2018) [15], provides a procedure for evaluating load-induced fatigue through identifying the fatigue-sensitive details, traffic data, strain ….etc., then, a fatigue assessment evaluation will be done based on the rating ranges listed in Table .1. As the first step in the evaluation, an infinite-life check is performed. AASHTO LRFD, Table 6.6.1.2.3-1 [4] provide the stress threshold values, $(\Delta f)_{TH}$. If the check fails, finite fatigue life (Y_f) is calculated. Once the present age of the detail (a) is subtracted from the finite fatigue life, the remaining fatigue life can be calculated, and then, the fatigue serviceability index can be obtained.

Table 1. Types of fatigue rating and assessment outcomes [15].

Fatigue Serviceability Index, Q	Fatigue Rating	Assessment Outcome
1.00 to 0.50	Excellent	Continue Regular Inspection
0.50 to 0.35	Good	Continue Regular Inspection
0.35 to 0.20	Moderate	Continue Regular Inspection
0.20 to 0.10	Fair	Increase Inspection Frequency
0.10 to 0.00	Poor	Assess Frequently
< 0.00	Critical	Consider Retrofit, Replacement or Reassessment

For field stresses [15]:

$(\Delta_f)_{max}$ = Max [2.2 $(\Delta_f)_{eff}$ or $(\Delta_f)_{field}$]

$(\Delta_f)_{eff} = R_p R_s (\Delta_f)_{field}$

$(\Delta_f)_{field}$ = the stress range measured in the field testing.

For FEA stresses [15]:

$(\Delta_f)_{max}$ = Max [$(\Delta_f)_{FEA\ 1}$ or [$(\Delta_f)_{FEA\ 2}$]

$(\Delta_f)_{FEA\ 1} = R_p (\Delta_f)_{FEA}$

$(\Delta_f)_{FEA\ 2} = 2.2\ R_p R_s (\Delta_f)_{FEA}$

Δ_f = stress range calculated based on the AASHTO fatigue truck and factored using load factors for the Fatigue I limit state of 1.75 for live load and 1.17 for impact.

Where:

R_s = 0.95 (Minimum Expected Fatigue Life Analysis).

R_p = 1.018, which is a function of a present ADTT of 4167, a span length of 50 m (165 ft), and two lanes on the subject bridge.

Table 2 reports the stress ranges outputs for five different data types for the tested bridge: (1) the field measured stress ranges, which are measured in the longitudinal direction of the girders; (2) the corresponding (i.e., longitudinal) data from the FEA with the simulated FE field truck; (3) the maximum principal stress from the FEA with the simulated field truck; (4) the longitudinal stress ranges from the FEA with the AASHTO fatigue truck [4]; (5) the maximum principal stress from the FEA with the AASHTO fatigue truck.

The various FEA data types allow for investigation of fatigue performance using both the longitudinal stresses, as is commonly done in practice, and the worst-case scenario of maximum principal stresses given that fatigue cracks rarely occur perfectly orthogonal to the girder geometry.

Table 2. Field vs FEA stress ranges for the tested truck/s and the fatigue HS-20 AASHTO standard truck/s.

US-13 Bridge Stresses Data Webs - Bottom Region - Longitudinal Direction									
Gauge Label (for the gauges installed in section D, see Fig. 3)	Passes and Trucks Information			Field (NORMAL) Stresses - $(\Delta F)_{FIELD}$	Tested Truck/s Stress Range - $(\Delta F)_{FEA}$		Fatigue HS-20 Truck/s Stress Range - $(\Delta F)_{FEA}$		$(\Delta F)_{CALC}$ = MAX [NORMAL or MAX PRIN ABS] Stresses
	Pass No.	Trucks No.	Speed km/h		FEA (NORMAL) Stresses	FEA (MAX PRIN ABS) Stresses	FEA (NORMAL) Stresses	FEA (MAX PRIN ABS) Stresses	
				MPa	MPa	MPa	MPa	MPa	MPa
D-W-BH-NS	4	1	24	18.940	18.071	24.142	26.075	34.947	34.947
D-W-BH-NS	3	1	104	31.730	29.579	38.174	39.516	51.255	51.255
D-W-BH-NS	8	2	24	42.368	40.141	54.277	55.275	74.979	74.979

Table 4.

5. FATIGUE RATINGS AND ASSESSMENTS OUTCOMES

The gauge location listed in Table 2 experiences the highest stress ranges within the two investigated instrumented cross-sections evaluated in the present study that included the bent plate connections (section D & E). This location is a Category C' fatigue detail, which means that the constant amplitude fatigue threshold (CAFT) is 82 MPa [4].

The results of the fatigue life evaluation shown in Table 3 for Minimum Expected Fatigue Life Analysis (safe analysis) indicate that section D (Gauge D-W-BH-NS) exceeds the CAFT. Section D experiences stress ranges exceeding the CAFT during Load Pass #8 and when maximum principal stresses resulting from a single AASHTO fatigue truck in Load Pass #3 are considered. The high magnitude of these stress ranges is likely exacerbated by the cross-frame framing into the abutment cross-section, which is a configuration that current design specifications (AASHTO 2017) advise against [4].

When a negative fatigue serviceability index is obtained according to Article 7.2.6 [15], the detail's fatigue serviceability index may be updated using the Equations (3.4 through 3.8), {Article 7.2.7.2.3 (AASHTO MBE 2018)} [15], for mean, and minimum lives evaluations provided a field inspection finds no evidence of fatigue cracking at the detail. Table 4 illustrates the outputs of updating serviceability index for Minimum Expected Fatigue Life Analysis. Both the longitudinal and maximum principal stress ranges are included to make clear that the conclusions will dramatically differ depending on what type of stress is considered. If only longitudinal stresses or static analyses are considered, it would be concluded that the girders of this bridge have infinite fatigue life. If principal stresses and dynamic effects are considered, the minimum fatigue life of 29 years is predicted, see

6. CONCLUSIONS

Field testing data of different passes of a weighed load vehicle incorporated with a validate full-scale 3D FEA model of a highly skewed steel girder bridge, created using the commercial FEA software ABAQUS/CAE, are all used to investigate the fatigue life analysis of skew steel I-girders bridge (US13 Bridge) due to the use of steel bent plate to connect K-Type cross-frames to the web of the bridge girders at the abutment skew support region. The results of this study lead to the following conclusions:

1- One of the difficulties in using cross-frames parallel to the skew angle (case of US13 Bridge) can be the connection details that are used between the brace (cross-frame) and the girders. In many applications, the bent plate may be used to make the connection between the brace and the connection plate (web stiffener for the case of pier skew support region), and/or girder's web (in the abutment skew support region). Such detail allows the fabricator to utilize a connection plate that is perpendicular to the web; however, the bent plate connection can dramatically reduce the effectiveness of the brace due to the flexibility introduced by the eccentric connection.

2- The abutment K-Type cross-frame members are connected to the web of section D directly without a connection stiffener plate (only bent plates are used). Both, the top and bottom horizontal chords of the K-Type cross-frame experienced large magnitudes of tensile forces in which they transmitted through the steel bent plate and concentrated in the top and bottom regions of the web. The main source of these high tensile forces is the lateral stresses (Miner Axes Bending) resulting from the lateral movement of the K-Type cross-frame members.

Table 3. Fatigue finite-life check, serviceability index, rating and assessment - Minimum Expected Fatigue Life.

Finite-Life Check and Fatigue Serviceability Index Calculations (*Minimum Expected Fatigue Life)* Webs - Bottom - Longitudinal Direction											
Gauge Label (for the gauges installed in section D, see Fig. 3)	Pass	$(\Delta F_{FEA})_1 = R_p(\Delta F_{FEA})$ [$Rp=1.018$]	$(\Delta F_{FEA})_2 = 2.2R_pR_S(\Delta F_{FEA})$ [$Rp=1.018$, $RS=1.0$]	$(\Delta f)_{eff} = R_pR_S(\Delta F_{FEA})$ [$Rp=1.018$, $RS=0.95$]	$(\Delta f)_{MAX} = MAX[(\Delta F_{FEA})_1, (\Delta F_{FEA})_2]$	$(\Delta f)_{TH}$	AASHTO Fatigue Details Categories	Finite and Infinite -Life Check	Fatigue Finite-Life Y (Years) [$(\Delta f)_{eff}$] [$R_R=1$]	Fatigue Serviceability Index Q	Fatigue Rating and Assessment Outcome
		MPa	MPa	MPa	MPa	MPa					
D-W-BH-NS	4	35.576	78.268	33.797	78.268	82	C'	Infinite	…	…	…
D-W-BH-NS	3	52.178	114.791	49.569	114.791	82	C'	Finite	16.302	-0.042	Critical - Consider Retrofit, Replacement or Reassessment
D-W-BH-NS	8	76.328	167.923	72.512	167.923	82	C'	Finite	6.722	-0.129	Critical - Consider Retrofit, Replacement or Reassessment

Table 4. Fatigue finite-life check, serviceability index, rating, and re-assessment - Minimum Expected Fatigue Life.

Finite-Life and Fatigue Serviceability Index Re-Assessments Calculations *(Minimum Expected Fatigue Life)* Webs - Bottom - Longitudinal Direction											
Gauge Label (for the gauges installed in section D, see Fig. 3)	Pass	$(\Delta F_{FEA})_1 = R_p(\Delta F_{FEA})$ [$Rp=1.018$]	$(\Delta F_{FEA})_2 = 2.2R_pR_S(\Delta F_{FEA})$ [$Rp=1.018$, $RS=1.0$]	$(\Delta f)_{eff} = R_pR_S(\Delta F_{FEA})$ [$Rp=1.018$, $RS=0.95$]	$(\Delta f)_{MAX} = MAX[(\Delta F_{FEA})_1, (\Delta F_{FEA})_2]$	$(\Delta f)_{TH}$	AASHTO Fatigue Details Categories	Finite and Infinite -Life Check	Reassessments Values: Fatigue Finite-Life Y (Years) [$(\Delta f)_{eff}$] [$R_R=1$]	Reassessments Values: Fatigue Serviceability Index Q	Reassessments Values: Fatigue Rating and Assessment Outcome
		MPa	MPa	MPa	MPa	MPa					
D-W-BH-NS	3	52.178	114.791	49.569	114.791	82	C'	Finite	29.468	0.076	Poor - Assess Frequently

3- Fatigue Assessment and Evaluation Procedure adopted by the AASHTO LRFD [4] and AASHTO MBE [15] manuals suggested that this type of connection (bent plate) may increase the susceptibility of the US13 Bridge girders to induced fatigue stresses due to its low fatigue ratings and assessments outcomes.

4- Both the longitudinal and maximum principal stress ranges are important in the prediction of finite or in-finite fatigue life checks for the details under consideration.

7. REFERENCES

[1] AASHTO/NSBA, 2014, American Association of State Highway and Transportation Officials/National Steel Bridge Alliance), Guidelines for the Analysis of Steel Girder Bridges, G13.1. 2nd Ed., Washington, D.C.

[2] Quadrato C., Wang W., Battistini A., Wahr A., Helwig T., Frank K. and Engelhardt M., "Cross-Frame Connection Details for Skewed Steel Bridges." Texas Department of Transportation, Report No. FHWA/TX-11/0-5701-1, 2010, Austin Texas University, Austin, TX.

[3] Battistini, A. D., Wang, W., Helwig, T. A., Engelhardt, M. D., and Frank, K. H., "Stiffness

Behavior of Cross Frames in Steel Bridge Systems." J. Bridge Eng., ASCE, 2016, 21(6): 04016024-1 - 04016024-11.

[4] AASHTO LRFD, 2017, American Association of State Highway and Transportation Officials/Load and Resistance Factor Design Specifications. 8th Ed., Washington, DC.

[5] Bowman, M.D., Fu, G., Zhou, Y.E., Connor, R.J., and Godbole, A.A., "Fatigue Evaluation of Steel Bridge." National Cooperative Highway Research Program, NCHRP Report 721, 2012, Transportation Research Board, Washington, D. C.

[6] McConnell, J., Chajes, M., and Michaud, K., "Field Testing of a Decommissioned Skewed Steel I–Girder Bridge: Analysis of System Effects." J. Struct. Eng., ASCE, 2015, 141(1): D4014010.

[7] Reza Haghani, Mohammad Al-Emrani, and Mohsen Heshmati., "Fatigue-Prone Details in Steel Bridges." Buildings 2012, 2, 456-476; doi:10.3390/buildings 2040456.

[8] Connor, R. J., and Fisher, J. W., "Identifying Effective and Ineffective Retrofits for Distortion Fatigue Cracking in Steel Bridges Using Field Instrumentation." J. Bridge Eng., 2006, /(ASCE) 11: 6(745), 745–752.

[9] Barth Grider, A. S., and Bowman, M. D., "Fatigue Behavior of Welded Diaphragm-to-Beam Connections." J. Struct. Eng., 2001, 10.1061/(ASCE)0733-9445(2001)127:10(1145), 1145–1152.

[10] Stallings, J. M., Cousins, T. E., and Tedesco, J. W., "Fatigue of diaphragm-girder connections." Final Rep. RP 930-307, 1996, Auburn University, Highway Research Center, Auburn University, Auburn, Ala.

[11] BDI (Bridge Diagnostics, Inc.), 2006, strain transduce ST-350 specifications sheet,Boulder, CO.

[12] Y. Almoosi, J. McConnell and N. Oukaili, "Structural Modeling of Cross-Frame Behavior in Steel Girder Bridges." *12th International Conference on Developments in eSystems Engineering (DeSE)*, Kazan, Russia, October 2019, pp. 620-625, doi: 10.1109/DeSE.2019.00117.,.

[13] Y. Almoosi, J. McConnell and N. Oukaili, "Evaluation of the Variation in Dynamic Load Factor Throughout a Highly Skewed Steel I-Girder Bridge", Engineering Technology and Applied Science Research, Vol. 11, No. 3, 2021, 7079-7087, 2021.

[14] Y. Almoosi, and N. Oukaili, "The Response of a Highly Skewed Steel I-Girder Bridge with Different Cross-Frame Connections", Engineering Technology and Applied Science Research, Vol. 11, No. 4, 2021, 7349-7357, 2021.

[15] AASHTO MBE, 2018, American Association of State Highway and Transportation Officials/The Manual for Bridge Evaluation, 3rd Edition, Washington, D. C.

7th Int. Conf. on Structure, Engineering & Environment (SEE), Pattaya, Thailand, Nov.10-12, 2021, ISBN: 978-4-909106070 C3051

EFFECTS OF ELECTROLYZED WATER ON ULTRASTRUCTURAL CHANGES OF *Fusarium oxysporum* AND *Escherichia coli*

Santirote Keatsirirote[1] Angkhana Chuajedton[3] and Kanda Whangchai[1,2]

[1]Postharvest Technology Innovation Center, Ministry of Higher Education, Science, Research and Innovation, Bangkok, Thailand
[2]Department of Biology, Faculty of Science, Chiang Mai University, Chiang Mai, Thailand
[3]Department of Biology, Faculty of Science, Lampang Rajabhat University, Lampang, Thailand

ABSTRACT

The problem during postharvest on Zingiberaceae is the microbial contamination. This research investigated the effects of different electrolyzed water concentrations on ultrastructural changes of pathogenic microorganisms (*Fusarium oxysporum* and *Escherichia coli*). The mycelial disks and spore suspension were soaked with acidic electrolyzed water (AcEW)(pH 2.39-2.64) at free chlorine concentrations of 0 (distilled water), 100, 200, 300, and 400 mg/L for 10 minutes. And then, morphological damage to mycelial cells was observed under scanning electron microscopy (SEM). It was shown that AcEW at 100 mg/L was damaged cell structure, and the mycelia cell structure represented abnormal cells. The increasing concentrations of AcEW at 200-400 mg/L showed that contorted mycelium and conidia structure showed cell rupture and collapsed when compared to control. And the second group, *E. coli* treated with AcEW at different concentrations and alkaline electrolyzed water (AlEW) (pH 10.29-10.84) with NaOH concentrations of 0 (distilled water), 125, 250, 500, and 750 mg/L for 10 minutes. It was shown that AcEW and AlEW at all concentrations were damaged cell surface when compared to control. Therefore, the effect of electrolyzed water indicated that it could control pathogenic microorganisms during postharvest.

Keywords: Electrolyzed water, Escherichia coli, Fusarium oxysporum, Ultrastructural changes

INTRODUCTION

Thailand is one of the major exporters countries for turmeric [1,2]. Moreover, it is an edible and medicinal plant in the family Zingiberaceae. The main problem of fresh turmeric is the microbial contamination during harvest [3]. In Thailand, the harvested turmeric distributed in the markets is washed with clean water only. Typically, the fungi and bacteria are present in the packing-house and the field after harvest. Naruemon and Dariwan [4] reported that the contamination of turmeric was due to mold (40.45%) and Escherichia coli (62.34%). Postharvest disease control can be done with many methods, such as chemical disinfection, hot water treatment, or washing with clean water. Moreira [5] reported that the symptoms of rot ginger (Zingiber officinale Roscoe) rhizomes in Brazil were due to *Fusarium oxysporum* (74%). Electrolyzed water has recently been reported to have strong anti-bacterial effects on most pathogenic bacteria [6]. As well as, electrolyzed water is a powerful bactericidal agent and is applied in a wide range of fields, including aquaculture, agriculture, and food industry [7,8]. Buck [9] found that the used electrolyzed water to treat 22 fungal species and found that it significantly reduced the growth of the thin-walled fungi (e.g., *Botrytis* spp. and *Monilinia* spp.) within 30 seconds. Additionally, it substantially reduces the growth of the thicker-walled, pigmented fungi, Curvularia, and Helminthosporium within 2 minutes or less. In addition, Hung [10] reported that electrolyzed water treated with strawberries and broccoli significantly reduced *E. coli* 0157:H7. Paola [11] found that washing lettuce with electrolyzed water for 5 minutes significantly inhibited Listeria monocytogenes. Deza [12] found that tomato peel treated with electrolyzed water resulted in a decline of bacteria such as *Escherichia coli* 0157:H7, *Salmonella enteritidis*, and *L. monocytogenes*, without any effect on the environment. Guentzel [13] also found that spraying electrolyzed water at the surfaces of food service areas on spinach and lettuce reduced microbes' growth. Whangchai [14] found that electrolyzed water treatment on tangerine cv. Sai Nam Pung at a free chlorine concentration of 215 ppm for 120 and 240 seconds, completely inhibited the growth and development of *Penicillium digitatum*.

This study aimed to determine the effect of electrolyzed water on ultrastructural changes of pathogenic microorganisms (*Fusarium oxysporum* and *Escherichia coli*).

MATERIALS AND METHODS

Preparation of Electrolyzed Water

Acidic electrolyzed water (AcEW) and alkaline electrolyzed water (AlEW) was generated by electrolysis in a cell with positively and negatively charged titanium electrodes separated by a polypropylene membrane. The electrodes were subjected to a direct current of 8 volts. A 5% NaCl solution was added to the above system. The pH of AcEW water was recorded with pH/ion meter. Free–chlorine concentration was determined by using N, N -diethyl-P-phenylene diamine (DPD) test, and AlEW was recorded with available NaOH by titration technique. Oxidation-reduction potential (ORP) was measured by pH/ ORP meter (AZ, model 86502).

Preparation of *E. coli* Suspensions and *F. oxysporum*

E. coli was obtained from the Department of Medical Science, Bangkok, Thailand. Cell suspension of *E. coli* was prepared from stock culture, which inoculated into trypticase soy broth (TSB) and incubated at 37°C for 10 hr. Cell suspension turbidity was measured by using a spectrophotometer at OD 600 nm. After that, the dilution of serials in TSB and spread plate technique on trypticase soy agar (TSA) evaluated cell suspension at OD 600 nm (approximately 10^8 CFU/ml).

F. oxysporum was separated fungal codinia from Department of Biology, Faculty of Science, Chiang Mai University, Chiang Mai, Thailand. Mycelial growth, 1 cm diameter mycelial disk of *F. oxysporum* was cut by a sterile cork borer and put in a plate placed at the center of a potato dextrose agar (PDA) plate and then incubated at 27°C for 48 hr. Spore suspension, the fungus was cultured on PDA plate at 27°C, and then a spore suspension was harvested by pouring four days old cultures with sterile distilled water. Subsequently, the spore suspension was transferred into 100 ml of sterile distilled water in a 250 ml in flask. Then, the suspension was shaken for 10 min on an orbital shaker at 27°C, and it was filtered through two layers of sterile muslin cloth. The cell numbers were counted with a haemacytometer, and the initial concentration was adjusted with sterile distilled water to a concentration of 10^6 CFU/ml.

Effect of Acidic Electrolyzed Water (AcEW) and Alkaline Electrolyzed Water (AlEW) on Ultrastructural Changes of *E. coli* and *F. oxysporum* Scanning electron microscopy

Cell suspension of *E. coli* was prepared from the stock culture, inoculated into trypticase soy broth (TSB), and incubated at 35°C with 24 hr. The culture was usually diluted to give approximately 10^8 CFU/ml. One milliliter of the culture was added to 9 ml of ACEW water with various concentrations (100, 200, 300, and 400 ppm) of available chlorine and ER water with different concentrations (125, 250, 500, and 750 ppm) of available NaOH for 10 min. Then, determined by scanning electron microscope (SEM). For *F. oxysporum*, mycelial growth, 1 cm diameter mycelial disk of *F. oxysporum* was cut by a sterile cork borer and put in a plate containing 9 ml of ACEW water. After that, treated with various concentrations (100, 200, 300, and 400 ppm) of available chlorine and ER water with different concentrations (125, 250, 500, and 750 ppm) of available NaOH and spore suspension also treated same treatments. The treated in all three groups were then fixed and prepared for scanning electron microscope (SEM) using 2.5 % glutaraldehyde for 24 hours. Then they were dehydrated with serials in ethanol 50, 70, 90 %, and absolute ethanol. Each three ethanol concentrations were immersed for 10 min 3 times. After that, samples were critical point dried and sputter-coated with gold. Samples were examined under SEM (JEOL, JSM 5910LV).

RESULTS AND DISCUSSION

Effect of Acidic Electrolyzed Water (AcEW) and Alkaline Electrolyzed Water (AlEW) on Ultrastructural Changes of *E. coli*

Scanning electron micrograph (SEM) showed well-formed bacterial cells attachment of *E. coli* on the surface of control in Figure 1. Well-formed bacterial cells represented cells survival on the surface. After treated with AcEW water at the different concentrations, it showed cell destruction of *E. coli* on the surface in Figure 3. Hypochlorous acid damages the microbial cell by oxidizing nucleic acids and proteins, causing lethal damage [15]. As a result, Deza [12] found that tomato peel treated with electrolyzed water resulted in a decline of bacteria such as *E. coli* 0157:H7, *Salmonella enteritidis*, and *Listeria monocytogenes*. Hung [10] reported that electrolyzed water treatment on strawberries and broccoli significantly reduced *E. coli* 0157:H7. Electrolyzed water had been washed lettuce for 5 minutes, and inhibited *L. monocytogenes* [11]. Electrolyzed water has been reported to have strong anti-bacterial effects on most pathogens and is released as hydroxyl and chlorine radical, destroying the cell structure [6]. In another report, Issa-Zacharia [16] demonstrated that electrolyzed water significantly reduced the total aerobic mesophilic bacteria from Chinese celery, lettuce, and daikon sprouts. Bacterial cell structure indicated that the dehydrated cell and damage site after treated with AlEW water at the different concentrations in Figure 4. Moreover, individual bacterial cells were ruptured after treated with AlEW at 500 mg/L in Figure 4 C. Khalid [17] reported that alkaline electrolyzed water (AlEW) had high efficacy sanitizing contamination.

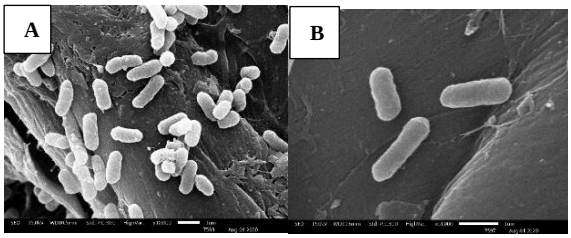


Fig. 1 SEM photographs were presented well-formed of bacterial cells (*E. coli*) (10000X); A, (18000X); B on the surface of the control.

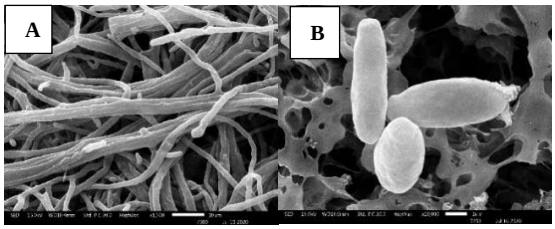


Fig. 2 SEM photographs were well-formed and continuous mycelia of *F. oxysporum* (1500X); A , and spore (10000X); B on the surface of the control.

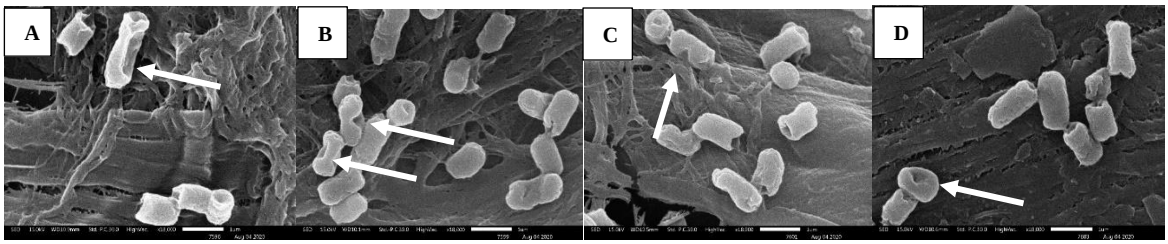


Fig. 3 SEM photographs of *E. coli* after treated with AcEW 100 mg/L (A), AcEW 200 mg/L (B), AcEW 300 mg/L (C), AcEW 400 mg/L (D). Arrow indicated that (A-D) the damage site of surface.

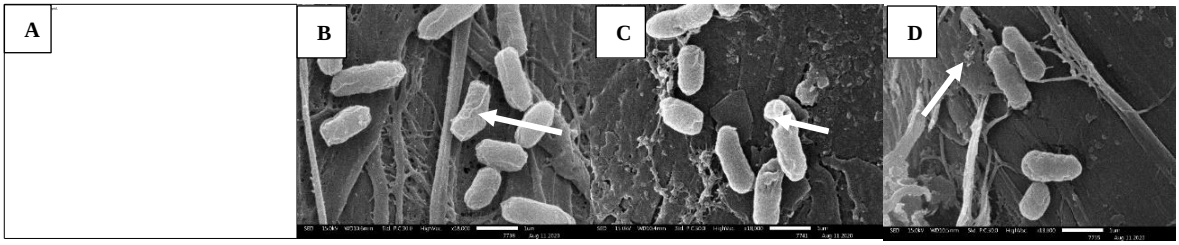


Fig. 4 SEM photographs of *E. coli* after treated with AlEW 125 mg/L (A), AlEW 250 mg/L (B), AlEW 500 mg/L (C), AlEW 750 mg/L (D). Arrow indicated that (A-D) the dehydrated cell and damage site of surface.

Effect of Acidic Electrolyzed Water (AcEW) on Ultrastructural Changes of *F. oxysporum*

The effect of AcEW on *F. oxysporum* structure indicated that morphological damage to mycelial cells was observed under scanning electron microscopy (SEM) in Figure 2, 5 and 6. The well-formed and continuous mycelia of *F. oxysporum* and spore showed on the surface of the control in Figure 2. It was shown that AcEW at 100 mg/L was damaged cell structure, and the mycelia cell structure represented abnormal in Figure 5 A. The increasing concentrations of AcEW at 200-400 mg/L showed that contorted mycelium. Significantly, the conidia structure showed cell rupture and collapsed when compared to control in Figure 2 and 5. As a result, Whangchai [18] reported that washing orange with electrolyzed water and exposure to ozone gas for 2 hours per day significantly controlled *P. digitatum*. As well as, Sierra [19] reported that acidic electrolyzed water showed inhibit conidia germination at 10 ppm and 50 ppm after 7 minutes of exposure time. Tomás-Callejas [20] found that electrolyzed water showed an inhibitory effect on natural microflora after wash fresh-cut baby mizuna leaves. Also, the low pH of the electrolyzed water could damage the membranes of the microorganisms and electrolyzed water has a strong oxidation potential that can be used as a disinfectant. This solution has a strong oxidation potential in which oxidation-reduction potential (ORP) occurred in AcEW at 400 mg/L (data not shown). The ORP showed more oxidation efficiency, which promoted the rising of oxidation efficiency by the concentrations. Suslow [21] reported that an ORP had the activity to eliminate the pathogens that promoted the rising of ORP. An ORP at 650-700 mV reduced the sterilization time of *Escherichia coli*, *Salmonella* sp., and *Listeria* sp. compared with the ORP lower than 485 mV.

The effect of AcEW on spore suspension indicated that AcEW at 100 mg/L was damaged cell structure

and represented abnormal cells. The increasing concentrations of AcEW at 200-400 mg/L showed that conidia structure was cell rupture and collapsed compared to control. (Figure 6) Electrolyzed oxidizing water (pH < 2.7, ORP > 1100 mV) and hypochlorous acid were produced at the anode side. The result of this study conformed to other reports that Buck [9] reported that electrolyzed water treated 22 fungal species, and it significantly reduced the growth of the thin-walled fungi (e.g., *Botrytis* spp. and *Monilinia* spp.) within 30 seconds. Additionally, it significantly reduces the growth of the thicker-walled, pigmented fungi, *Curvularia*, and *Helminthosporium* within 2 minutes or less.

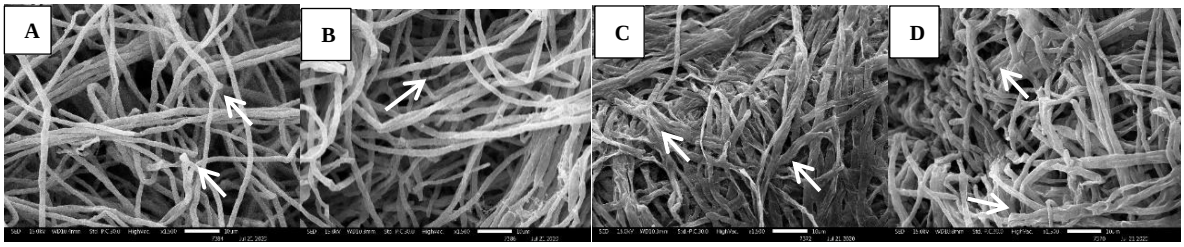


Fig. 5 SEM photographs of *F. oxysporum* after treated with AcEW 100 mg/L (A), AcEW 200 mg/L (B), AcEW 300 mg/L (C), AcEW 400 mg/L (D). Arrow indicated that (A-D) contorted and uneven mycelia.

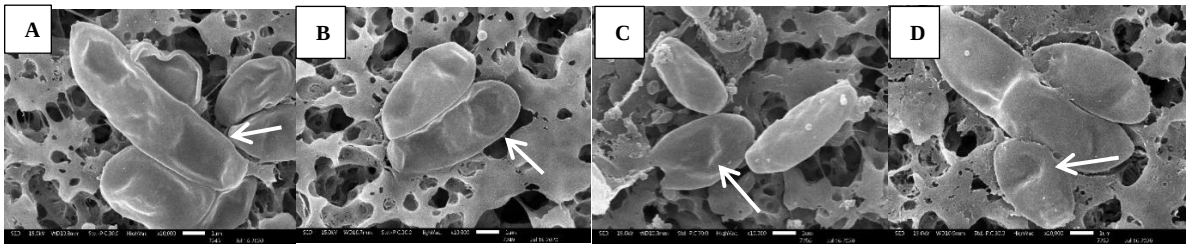


Fig. 6 SEM photographs of conidia of *F. oxysporum* after treated AcEW 100 mg/L (A), AcEW 200 mg/L (B), AcEW 300 mg/L (C), AcEW 400 mg/L (D). Arrow indicated that (A-D) cell rupture and collapsed.

CONCLUSION

The cell structure of *Fusarium oxysporum* and *Escherichia coli* represented abnormal cells after treated with AcEW and AlEW. The morphological damage to mycelial cells was contorted and uneven of *F. oxysporum*. All treatments decreased bacterial cell viability, and bacterial cell structures were observed under SEM showed cell rupture and collapsed of *E. coli*. Bacterial cell structures showed the dehydrated cell and damage site of surface. Therefore, AcEW and AlEW could control pathogenic microorganisms.

ACKNOWLEDGMENTS

This work has been supported by Postharvest Technology Research Center, Faculty of Agriculture, Chiang Mai University, Chiang Mai and Postharvest Technology Innovation Center, Ministry of Higher Education, Science, Research and Innovation, Bangkok.

REFERENCES

[1] TNAU Agritech Portal. 2015. Tumeric (Online) Available: http://agritech.tnau.ac.in/banking/PDF/Tumeric.pdf (April.17.2019).

[2] Selvan. S. 2016. Pre & postharvest processing of turmeric. (Online) Available: https://www.slideshare.net/senthamizhselvan1481/turmeric-processing.html (April.17.2019).

[3] Monton, C. Microbial contamination of turmeric capsules produced at a secondary government hospital in the northeastern Thailand. Thai Journal of Pharmaceutical Science, Vol. 40, Supplement Issue, 2016, pp. 143-145.

[4] Naruemon C., and Dariwan S. Microorganism contamination and standard of supplement products consumed in household case study: Municipal of Thapra, Muang District, Khon Kean Province. KKU Research Journal, Vol. 14, Issue 3, 2014, pp. 81-91.

[5] Moreira S. I., Dutra D.C., Rodrigues A. C., Oliveira J. R., Dhingra O. D., and Pereira O. L. Fungi and bacteria associated with post-harvest

rot of ginger rhizomes in Espírito Santo, Brazil. Tropical Plant Pathology, Vol. 38, Issue 3, 2013, pp.218-226.

[6] Al – Haq M. I., Seo Y., Oshita S. and Oshita Y. Disinfection effects of electrolyzed oxidizing water on suppressing fruit rot of pear caused by *Botryosphaeria berengeriana*. Food Research International, Vol. 35, 2002, pp. 657–664.

[7] Whangchai N., Nomura N. and Matsumura M. Factors affecting phytoplankton removal by electro- oxidation of artificial seawater. Chiangmai Journal of Science, Vol. 30, 2003, pp.255 – 259.

[8] Kim C., Hung Y.C. and Brackett R.E. Efficacy of electrolyzed oxidizing (EO) and chemically modified water on different types of foodborne pathogens. International Journal of Food Microbiology, Vol. 61, 2000, pp.199–207.

[9] Buck J.W., Van Iersel M.W., Oetting R.D. and Hung C.Y. In vitro fungicidal activity of acidic electrolyzed oxidizing water. Plant Disease, Vol. 86, 2002, pp. 278-281.

[10] Hung Y. C., Tilly P. and Kim C. Efficacy of electrolyzed oxidizing (EO) water and chlorinated water for inactivation of *Escherichia coli* 0157:H7 on strawberries and broccoli. Journal of Food Quality, Vol. 33, 2010, pp. 559-577.

[11] Paola C. L., Vivian R. C., Mercado M., Deaz M., and Carrascal A. K. Effectiveness of electrolyzed oxidizing water for inactivating *Listeria monocytogenes* in lettuce. Universitas Scientiarum, Vol. 10, 2005, pp.97-108.

[12] Deza M.A., Araujo M. and Garido J. M. Inactivation of *Escherichia coli* O157:H7, *Salmonella enteritidis* and *Listeria monocytogenes* on the surface of tomatoes by neutral electrolyzed water. The Society for Applied Microbiology, Vol. 37, 2003, pp. 482-487.

[13] Guentzel J. L., Liang L. K., Callan M. A., Emmons S. A. and Dunham V. L. Reduction of bacteria on spinach, lettuce, and surfaces in food service areas using neutral electrolyzed oxidizing water. Food Microbiology, Vol. 25, Issue 1, 2008, pp. 36-41.

[14] Whangchai K., Saengnil K., Singkamanee, C. and Uthaibutra J. Use of Electrolyzed oxidizing water to control postharvest disease during storage of tangerine cv. Sai Nam Pung. Acta Horticultrae, Vol. 837, 2009, pp. 211-215.

[15] Acher A., Fisher E., Turnheim R., and Manor,Y. Ecologically friendly wastewater disinfection techniques. Water Research, Vol. 31, 1997, pp. 1398–1404.

[16] Issa-Zacharia A., Kamitani Y., Miwa N., Muhimbula H., and Iwasaki K. Application of slightly acidic electrolyzed water as a potential non-thermal food sanitizer for decontamination of fresh ready-to-eat vegetables and sprouts. Food Control, Vol. 22, 2010, pp. 601-607.

[17] Khalid, N.I., Sulaiman, S., Ab Aziz, N., Taip, F.S., Sobri, S. and Nor-Khaizura, M.A.R. 2018. Electrolyzed water as a green cleaner: chemical and physical characterization at different electrolysing parameters. Food Research, Vol. 2, Issue 6, 2018, pp. 512 – 519.

[18] Whangchai, K., Saengnil, K., Singkamanee, C. and Uthaibutra, J. Effect of electrolyzed oxidizing water and continuous ozone exposure on the control of *Penicillium digitatum* on tangerine cv. Sai Nam Pung during storage, Crop Protection. Vol. 29, 2010, pp. 386-389.

[19] Sierra B. E. G., Meza A. X. S. and Sanchéz L. T. G. Antifungal activity of acidic electrolyzed water against strawberry postharvest molds (*Fragaria* x *ananassa* Duch cv. *Camarosa*. Acta Agronómica, Vol. 68, Issue 2, 2019, pp. 126-133.

[20] Tomás-Callejas A., Martinez-Hernandez G.B., Artés F., Artés-Hernández F., and Trevor V.S. Neutral and acidic electrolyzed water as emergent sanitizers for fresh-cut mizuna baby leaves. Postharvest Biology and Technology, Vol. 55, 2011, pp.114 -120.

[21] Suslow T. V. Oxidation-reduction potential (ORP) for water disinfection monitoring, control, and documentation. University of California. Division of Agriculture and Natural Resources, Publication, 2004, pp.8149.

MICROSTRUCTURAL AND PHISICAL CHARACTERIZATION OF CORDIERITE-MULLITE CERAMICS REFRACTORIES

Sibpawishkon Sittiakkaranon[1]

[1]Faculty of Agricultural and Industrial Technology, Rajabhat Nakhon Sawan University, Nakhon Sawan 60000, Thailand

ABSTRACT

The morphologies of the synthesized cordierite and mullite samples as well as their physical-mechanical properties were investigated and characterized by x-ray diffraction spectroscopy (XRD). The cordierite and mullite was shown to be successfully synthesized by XRD results and represented phases of mullite cordierite and alumina, indicating the creation of materials having interesting combinations of sample ceramics refractories properties. After sintering at 1300°C and 1350°C temperatures, physical properties, such as shrinkage (varied from 10.1% to 13.1% and 10.4% to 13.6%), bulk density (range of 2.33-2.41g/cm^3 and 2.22-2.36g/cm^3), water absorption (varied from 0.07% to 5.49% and 0.01% to 4.12%), apparent porosity (varied from 0.51% to 12.87% and 0.15% to 9.15%), flexural strength (range of 37.7-43.5MPa and 40.6-56.9MPa), thermal expansion coefficients (5.02-6.60x10^{-6}/°C and 4.70-6.22x10^{-6}/°C), respectively. The microstructure of cordierite and mullite ceramics refractories in sintered samples, in which consists of short cordierite and mullite grains by SEM imaging. It was found that a new sample sintering at 1350°C. They are most suitable for the manufacture of refractory materials.

Keywords: Refractory, Clay Cordierite, Mullite

INTRODUCTION

Refractory is a material that is able to resist the intense heat without altering the structure, mullite is refractory the stable crystalline phase in the aluminosilicate system. Its chemical composition ranges from $3Al_2O_3.2SiO_2$ to $2Al_2O_3.SiO_2$, mullite formed in refractory materials has a chemical composition $3Al_2O_3.2SiO_2$ with a melting point of about 3362ºF (1850ºC). It contains about 73.0 percent alumina [1]. It can be produced by sol–gel methods [2] or by a sintering process reaction of mixed Al_2O_3 and SiO_2 mullite materials [3]. It has received significant attention during the last decade as a potential structural material for high-temperature applications, presenting properties including low thermal expansion coefficient, low thermal conductivity, good strength at high temperature, low dielectric constant and chemical stability [4-6], when it was mixed with cordierite to supplement the properties of kiln products. Cordierite is important ceramic constituent of the MgO-SiO_2-Al_2O_3 system with the mixture compositions which can be in either 1:1:2 or 2:2:5 ratios. It has excellent properties of low thermal expansion coefficient, low dielectric constant, high chemical mechanical durability and good thermal shock resistance [7-9]. The mixed together in an appropriate ratio, cordierite and mullite will result has fracture strength and good resistance to thermal shock and it can be used products refractory various industrial applications such as kiln furniture, ceramic filters, converter substrates and electrical insulating porcelains, etc. The mullite-cordierite phase can be synthesized from natural raw materials including some of the starting raw materials to form talc, calcined alumina and fly ash [10], talc, kaolinitic clay, and gibbsite [11], kaolin, talc, silica, sepiolite and feldspar [12] and kaolin and talc [13]. The mixed together in an appropriate ratio, cordierite and mullite will result has fracture strength and good resistance to thermal shock and it can be used products refractory various industrial applications such as kiln furniture, ceramic filters, converter substrates and electrical insulating porcelains, etc.

The aim of this research was to characterized and investigate crystal formation of cordierite and mullite specimen bodies and to study differences in phase composition, physical and mechanical properties of the ceramic samples to obtain the research results aimed at creating products that can be used in high temperatures by to create mullite and cordierite crystals within the clay body through a single sintering. This simplifies the production of mullite and cordierite crystals used to produce equipment inside the kiln.

EXPERIMENTAL

1. Preparation of the test samples

The raw materials in this experiment were natural clay, talc and alumina powder. The chemical compositions of the synthesized materials were investigated by X-Ray Fluorescence technique (XRF: Mesa-500W, Horiba, Japan) and the phase compositions of clay were identified using X-ray diffraction (XRD: X' Pert PRO MPD, Philips, Netherland)

2. Samples preparation

The raw material ingredients were weighed and mixed in different ratios by various weight percent of alumina (wt.% Al_2O_3). They were rectangular in shape and were formed using a hydraulics press at 150 kg/cm^2 by using 5% water as a binder and used metal molds of around 1cm.x1cm.x8cm. The specimens were given a furnace soaking time at 100°C for 24 h. The sintering process was carried out at a temperatures of 1300°C and 1350°C in air atmosphere with a heating rate of 3°C/min and a soaking time of 1 hour.

3. Testing method of the test samples

The samples with the addition of different weight percentages of Al_2O3 at 0wt.%, 5wt.%, 10wt.%, 15 wt.% and 20wt.%. The cordierite-mullite phase compositions of samples were identified using X-Ray diffraction (XRD: X' Pert PRO MPD, Philips, Netherland) .The physical and mechanical properties of test samples by water absorption, bulk density and apparent porosity of the sintered samples were measured by conventional liquid displacement method based on ASTM C373- 88 [14], while the measuring flexural strength was determined by using a universal testing machine according to the standard of ASTM (C02–1161C) [15]. The Coefficients of Expansion (COE: DIL 420C, Netzsch, Germany) of the samples were measured as a function of temperature using a dilatometer and analyses of the microstructure of cordierite and mullite were performed by using Scanning Electron Microscopy with X-ray Energy-Dispersive System (SEM and EDS:JEOL JSE-5410 LV).

RESULTS AND DISCUSSION

1. Properties of raw materials

The starting properties of the cordierite and mullite ceramics were the chemical analysis of the investigated raw materials included clay, talc, and alumina by XRF and loss on ignition are given in Table 1. It was found that the clay had a high amount of contaminant of 0.79% ferric oxide and by the loss on ignition of 23.53% talc which causes porosity in the clay body. The analyses of the mineral compositions by XRD are shown in Fig.1.

2. Results of samples analysis

In this study, cordierite and mullite ceramics were fired at temperatures of 1300ºC and 1350ºC and analyzed and tested for physical properties shows in Fig.2. The samples of 0, 5, 10, 15 and 20 wt.% alumina addition had a firing shrinkage 10.1%-13.1% and 10.4%-13.6%, bulk density of 2.33-2.41 g/cm^3 and 2.22-2.36 g/cm^3 water absorption 0.07%-5.49% and 0.01%-4.12% and apparent porosity 0.51%-12.87% and 0.15%-9.15%, respectively. In general, firing shrinkage of the clay occurs because of the loss of water and organic matter in the clay body after high temperature burning, there are causing the clay particles to move closer and causing clay shrinkage. The addition of alumina to the clay caused the percentage of shrinkage to decrease as the amount of alumina increased at both temperatures. It is predicted that the added alumina has some parts that do not react with the clay and talc because the alumina itself is a heat-resistant material. It has a high melting point at 2053°C [16], high purity and the inserted alumina has a large particle structure and has very little change in particle size, with 0.17% loss on ignition shown in Table 1, which makes alumina result in a lower shrinkage when added in higher quantities, thus creating more gaps and pores between the edges. Therefore, the increase of alumina content causes the percentage of shrinkage to decrease as shown in Fig.2 (a). On the other hand, it increases the sample bulk density shown in Fig.2 (b). Additionaly as the amount of alumina increased, it clearly made increases in porosity and water absorption, as shown in fig.2 (c) and (d). The results of the addition of 20% alumina sintered at 1300°C were the highest, at 12.87% apparent porosity and 5.49% water absorption, and when sintered at 1350°C had the effect that both results were reduced 9.15% apparent porosity and 4.12% water absorption. Thus it is deduced that the alumina added to the clay and sintered at 1300°C and 1350°C temperatures contains some alumina, contributing to the crystalline, cordierite and mullite structure. It also contains a higher amount of free

Table 1 Chemical analysis (wt.%) and particle size of raw materials.

Compositions	Raw materials		
(wt.%)	Clay	Talc	Alumina
SiO_2	55.48	40.38	0.04
Al_2O_3	31.23	-	99.50
K_2O	1.67	-	-
CaO	0.10	1.17	-
MgO	-	34.18	-
Na_2O	-	-	0.29
Fe_2O_3	0.79	0.71	0.02
LOI	10.73	23.56	0.17

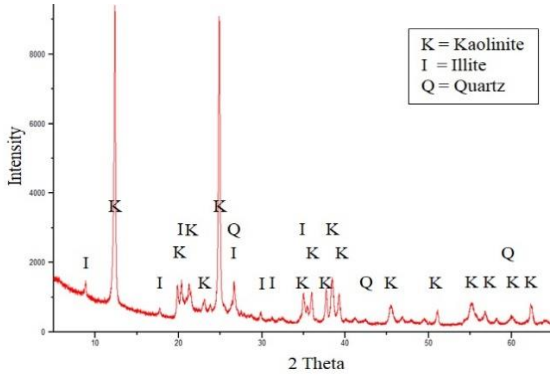


Fig. 1 XRD pattern of clay raw materials.

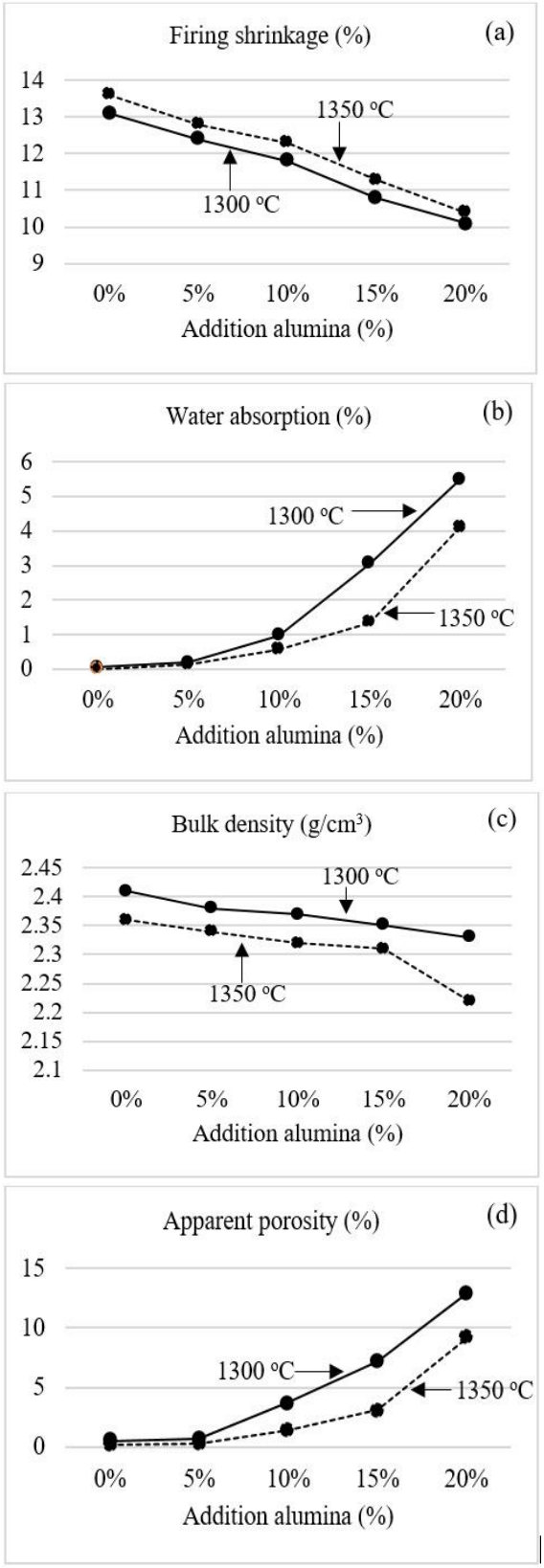


Fig. 2 Physical properties of samples sintering at 1300°C and 1350°C (a) firing shrinkage, (b) water absorption, (c) bulk density and (d) apparent porosity.

alumina, which is a major contributor to higher gaps and porosity. This is due to the large size of the alumina and little structural change for both sintering temperatures, the gap between the grain is increased, with the gap and porosity caused by the loss of on ignition of the 23.53% talc and the 10.73% clay shown in table 1. The mixture becomes a crystal structure of the cordierite and mullite crystals. The crystal structure of the cordierite has a high porosity which creates gaps and pores within the sample. And when sintered at a temperatures of 1350°C, the sample contracted at higher values. The crystals of the cordierite, mullite and free alumina became closer to each other, and the gap and pore size were reduced, thus reducing porosity and decreasing water absorption. Flexural strength is related to physical properties and sintering temperature, with the more gapped and porous samples having lower density, lower shrinkage and higher water absorption, resulting in low flexural strength values. From the analysis of the increased alumina content ceramics, it reduced the strength. In the sample sintered at 1300°C it produced a maximum flexural strength of 43.5MPa at 0% alumina addition and a minimum of 37.7MPa at 20% alumina addition. When sintered at 1350°C temperature, the flexural strength was increased to 56.9MPa and 40.6MPa, respectively as shown in Fig.3.

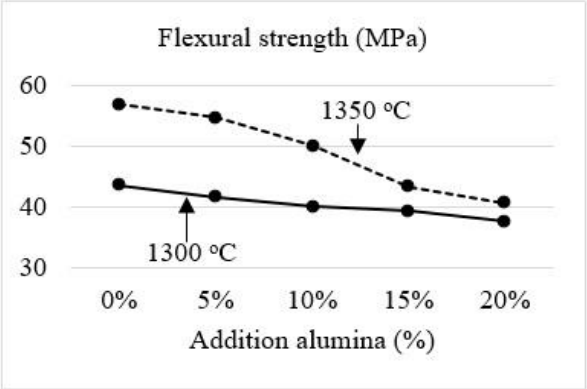


Fig. 3 Flexural strength of samples sintering at 1300°C and 1350°C.

This is because when sintering at 1350°C there is an increase in cordierite and mullite reaction and the higher the mullite content the higher the internal strength. This is because mullite has a needle-shaped structure that is overlapping and connected. This mechanical bonding occurs during firing, giving the ceramic texture a high mechanical strength and good heat resistances. Mullite provides the strength needed, while cordierite supplies resistance to shock. The presence of cordierite also lowers the reaction temperature and decreases the firing shrinkage. Both mullite and cordierite were added in different proportions either as grog or raw material [17].

Sintering at 1350°C found higher cordierite and mullite content than sintering at 1300°C by the X-ray diffraction pattern of the XRD form of the ceramic sample. Mullite and cordierite are the main components and we also found a small amount of alumina is shown in Fig.4.

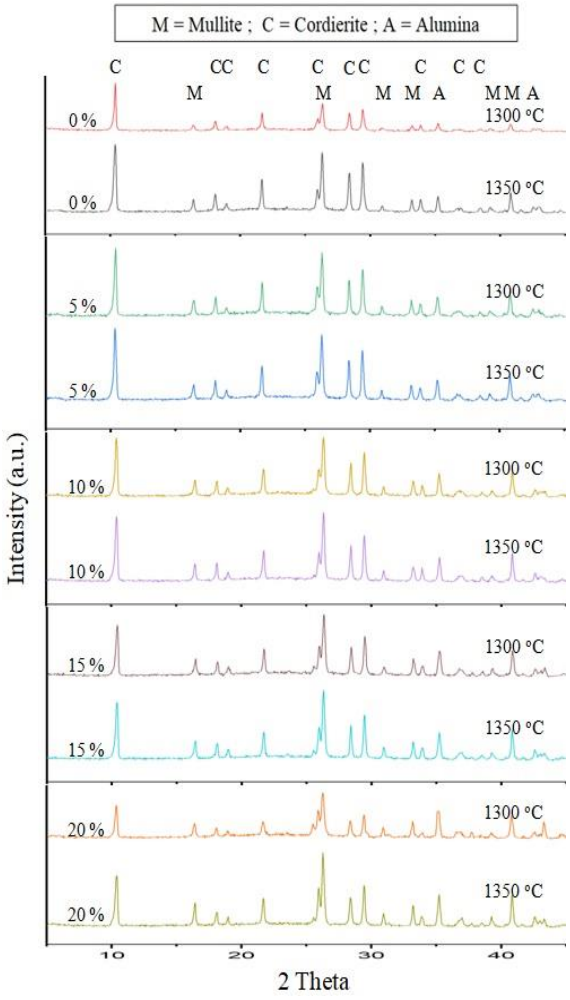


Fig. 4 XRD patterns of the investigated ceramic samples after sintering at 1300°C and 1350°C.

Considering the peaks in the main graph of mullite cordierite and alumina, the increase in 0-20% alumina results in increased mullite and alumina at both temperatures. This may be due to the presence of added alumina contributing to the formation of mullite and cordierite crystals. As 5% and 10% alumina added the cordierite amount increased. As both chemical compositions contain alumina, they support their crystallization. But when 15-20% alumina was added, cordierite amount was reduced, possibly due to the formation of cordierite crystals. Talc was a structural component that was completely reacted during the addition of 5-10% alumina. This is different from the mullite that can still produce more crystals according to their structure and chemical composition.

Morphology of the ceramic samples used in this study by scanning electron microscope (SEM) analysis crystal structure at 20,000 magnification finds crystals of cordierite and mullite. The crystals mullite were shaped as overlapping needles with their particle size smaller than 5 microns, and the crystals of cordierite have a cotton ball shape and a porous sheet and their particle size is smaller than 2 microns. The mullite crystallization content increased when sintered at 1350°C as shown in Fig.5. They have confirmed elements of mullite and cordierite crystals in samples with 10% added alumina sintering at 1350°C. Through Energy dispersive spectrometer (EDS) by spectrum 1 is crystal of mullite shown in Fig.6 (a) and spectrum 2 is crystal of cordierite shown in Fig.6 (b). The samples were tested for thermal expansion, and found that the COE curve of the all-ceramic samples showed low thermal expansion [18] during the heating period from room temperature to 1200℃.

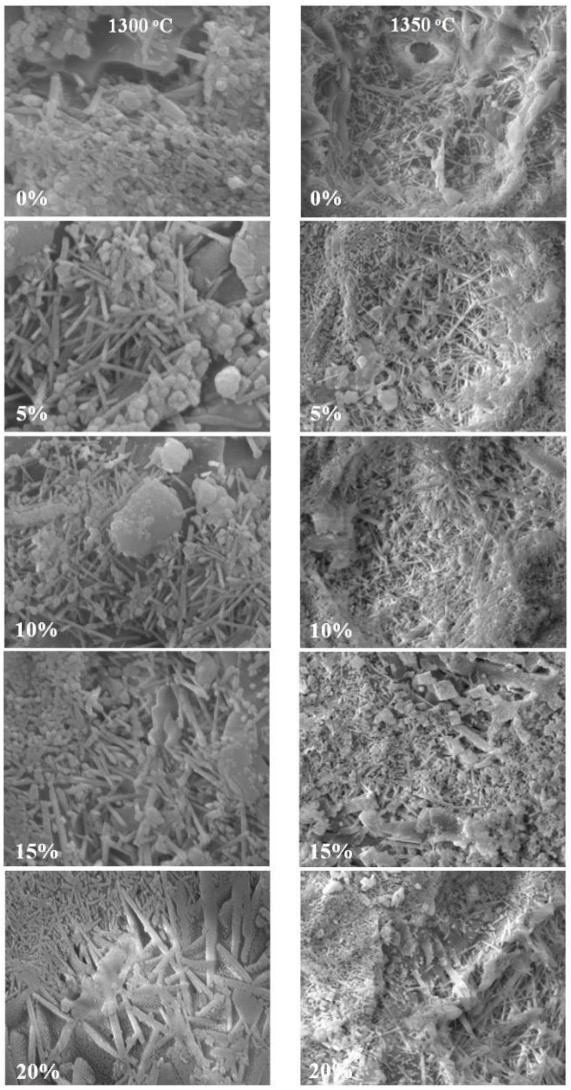


Fig. 5 SEM micrographs of the investigated mullite and cordierite crystals samples after sintering at 1300°C and 1350°C.

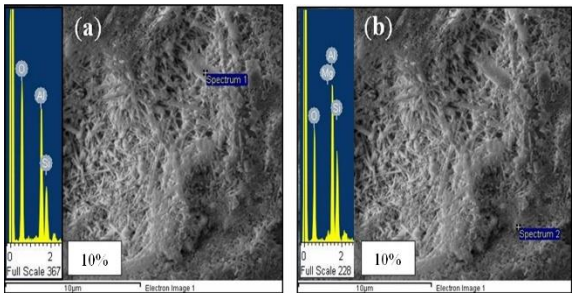


Fig. 6 EDS micrographs of the investigated cordierite and mullite ceramic samples 10% added alumina sintering at 1350°C: (a) crystal mullite and (b) crystal cordierite.

It was found that the thermal expansion of the sintered ceramic sample at 1350℃ was between 4.70-6.22x10^{-6}/°C. Lower values than the firing at 1300℃, with values between 5.02-6.60x10^{-6}/°C and the expansion due to heat tended to increase as the content of alumina increased. It can be predicted that the excess alumina contained in the samples of crystal cordierite and mullite structure which has a melting point that is higher than the temperature of sintering at 1350℃. So that when heated, it will expand more by proportion with the increased amount of alumina. Considering the heating and cooling graph of the sample sintered at 1300℃ and 1350℃, showing expansion during heat increase and graph showing sample contraction during heat decline, it is a graph which overlaps the same line, because when the sample is cooled, it shrinks back to its original position at room temperature. This demonstrates that it has thermal elastic properties and a low coefficient of thermal expansion which it helps to support for properties of thermal shock resistant as well [19]. This is different from the sample sintered at 1300℃, as shown in Fig.7.

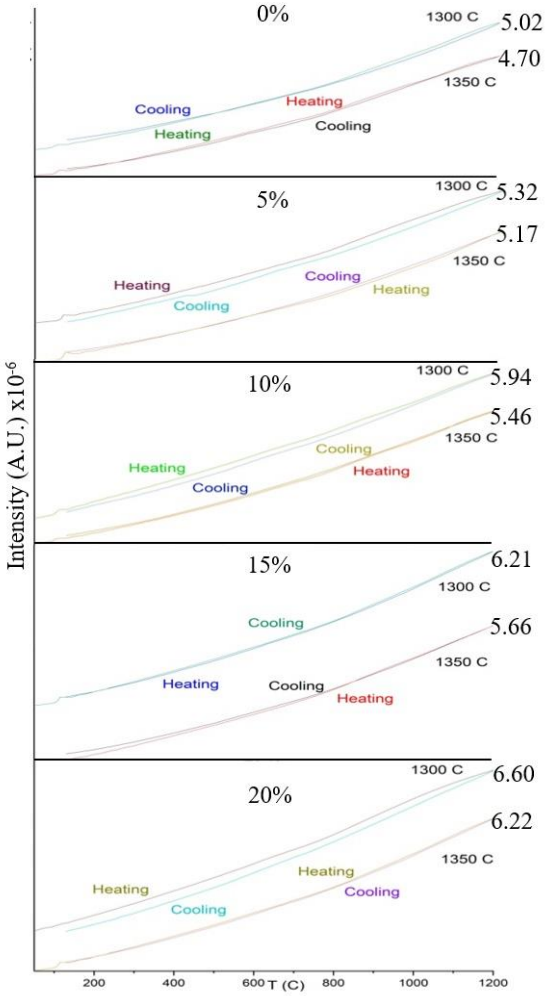


Fig. 7 COE curve of the investigated cordierite-mullite ceramic samples after sintering at 1300°C and 1350°C.

CONCLUSIONS

This research is a study of the characteristics of cordierite and mullite ceramics from mixing clay, talc and alumina raw materials and by varying alumina added at 0%, 5%, 10%, 15% and 20% and sintering at 1300°C and 1350°C, the XRD results indicated graph main phases of crystals of mullite and crystals of cordierite, which has a spreading feature throughout its body, confirmed by WDS images. All the samples were evaluated for their mineralogical, microstructure, physical and mechanical properties. It was found that, when the amount alumina increases, it increased the amount of mullite crystals formation but the number of cordierite crystals formed was decreased, and this has an influence on bulk density and a decrease in flexural strength but higher water absorption, porosity, and thermal expansion coefficients. In particular this indicates that flexural strength is controlled by the continuous mullite microstructure and porosity. The significant characteristic of mullite crystals is that they are found in the shape of needles and cordierite in the shape of cotton balls and a porous sheet from image SEM. This shows that alumina can react with clay and talc raw materials formed into a crystal structure cordierite and mullite at 1300°C and 1350°C, even if it has a melting point which is higher, and can form mullite and cordierite crystals This can be achieved within the ceramics body with a single firing, which reduces the cost of producing ceramics made from mullite and cordierite materials. It can be used to produce ceramic refractories as cups and plates ceramics that are well used in microwave ovens, sagger or kiln furniture

ACKNOWLEDGMENTS

The authors also would like to gratefully thank to Rajabhat Nakhon Sawan University for financial support.

REFERENCES

[1] Norton F. H., Refractory, New York, McGraw-Hill. 1968.

[2] Kleebe H. J., Siegelin F., Straubinger T. and Ziegler G., Conversion of Al_2O_3-SiO_2 powder mixtures to 3:2 mullite following the stable or metastable phase diagram, Journal of the European Ceramic Society, vol. 21, 2001, pp. 2521-25337.

[3] Jung J. S., Park H. C. and Stevens R., Mullite ceramics derived from coal fly ash, Journal of Materials Science Letters, vol. 20, 2001, pp. 1089-1091.

[4] Hamidouche M., Bouaouadjd N., Olagnon C. and Fantozzi G., Thermal shock behaviour of mullite ceramic, Ceramics International. vol. 29, 2003, pp. 599-609.

[5] Schneider H. S., Schreurer J. and Hildmann B., Structure and properties of mullite, Journal of the European Ceramic Society, vol. 28(2), 2008, pp. 329-344.

[6] Torrecillas R., Calderon J. M. and Moya J. S., Suitability of mullite for high temperature applications, Journal of the European Ceramic Society, vol. 19(13-14), 1999, pp. 2519-2527.

[7] Kurama S. and Ay N., Effect of Grinding Time and MgO Source on Cordierite Formation, Journal of the American Ceramic Society, vol. 81[11), 2002, pp. 58-61.

[8] Sevinçtav S. T., Marşoğlu M. and Kordiyerit V., Ceramics Congress With International Participations/TÜRKİYE, 2001, pp. 318-324.

[9] Goren R., Gocmez H. and Ozgur C., Synthesis of cordierite powder from talc diatomite and alumina, Ceramics International, vol. 32, 2006, pp. 407-409.

[10] Kumar S., Singh K. K. and Ramachadrarao P., Synthesis of cordierite from fly ash and its refractory properties, Journal of Materials Science Letters, vol. 19, 2000, pp. 1263-1265.

[11] Tamborenea S., Mazzoni A. D. and Aglietti E. F., Mechanochemical activation of minerals on the cordierite synthesis, Thermochim. Acta, vol. 411, 2004, pp. 219-224.

[12] Acimovic Z., Pavlovic L., Trumbulovic L., Andric L. and Stamatovic M., Synthesis and characterization of the cordierite ceramics from nonstandard raw materials for application in foundry, Journal of Materials Science *Letters*, vol. 57, 2002, pp. 2651-2653.

[13] Trumbulovic L., Acimovic Z., Panic S. and Andric L., Synthesis and characterization of cordierite from kaolin and talc for casting application, FME Trans. vol. 31, 2003, pp. 43-47.

[14] ASTM C373-14a, Standard Test Method for Water Absorption, Bulk Density, Apparent Porosity and Apparent Specific Gravity of Fired White ware Products Ceramic Tiles, and Glass Tiles, ASTM Book of Standards, vol. 15.02, 2014.

[15] ASTM C1161-02c, Standard Test Method for Flexural Strength of Advanced Ceramics at Ambient Temperature, ASTM Book of Standards; vol. 15.02, 2008.

[16] WILEY-VCH Verlag GmbH & KGaA Co., Weinheim, Ceramic Material Classes, Ceramics Science and Technology, ISBN: 978-3-527-31156-9, vol. 2, 2010.

[17] Ibrahim D. M., Naga S. M., Kader Z. A. and Salam E. A., Cordierite-mullite refractories, Journal of Ceramics International, vol. 21, 1995, pp. 265-269.

[18] Costa Oliveira F. A. and Fernandes C. J., Mechanical and thermal behaviour of cordierite-zirconia composites, Journal of Ceramics International, vol. 28, 2002, pp. 79-91.

[19] Donald Askeland R. and Phule Pradeep P., The Science and Engineering of Materials, Cengage Learning, 2010.

7th Int. Conf. on Structure, Engineering & Environment (SEE), Pattaya, Thailand, Nov.10-12, 2021, ISBN: 978-4-909106070 C3051

IS IT POSSIBLE TO APPLY GIG ECONOMY FOR FARMER IN INDONESIA?

Siti Rochaeni[1] and Diah Khairani[2]
[1]Faculty of Science and Technology, State Islamic University Syarif Hidayatullah Jakarta, Indonesia;
[2] Faculty of Economics and Management, Bogor Agricultural University, Indonesia

ABSTRACT

The gig economy keeps growing along with the development of digital technology and internet accessibility. The gig economy already applied to various sectors, especially to digital-based jobs. The gig economy is going to optimize the farmer performance only is the farmers have the knowledge of digital technology, internet access, and the digitalized farming system. This research approached the farming activities and the farming environment that affected the application of the gig economy. The gig economy can apply to the farming activities that required more labor, such as planting, harvesting, and product marketing. The offline gig worker can involve in the planting and harvesting activities. The online gig worker can participate in the product marketing activities using the reseller or drop-shipping system to reach deeper into the market. The internal factor that should get attention is the farmer's readiness to hire the gig worker, especially the labor training. The external factors that should get attention are government policies, applicable law, and the health issue due to current pandemics condition.

Keywords: Gig economy, Gig farming, Digital farmer, Online marketing

INTRODUCTION

Indonesia's economy is facing the challenging time due to the global pandemic in 2020 which hit both the demand and supply side of the economy [1]. The pandemic of Covid-19 affected the economic activity in Indonesia, including the mass dismissal of employment [2] and panic buying [3]. The gig economy could support economic resilience in Indonesia by providing jobs and business opportunities [4].

Food security is important during a pandemic due to efforts to limit mobility and panic buying that affect food supplies [5]. Agricultural inputs, farms, food processing, and distribution are need attention so that food can flow in adequate amount from farm to fork [6]. Farmers and other workers in agriculture need to keep working to meet agricultural needs while maintaining health protocols related to pandemic situations. The next step in feeding the world's rapidly growing population involves self-driving tractors, precision farming, and Internet of Things sensors to quantify agriculture in vast new ways [7].

The gig economy keeps growing along with the development of digital technology and internet accessibility. The gig economy already applied to various sectors, especially to digital-based jobs. Some gig jobs are available to be done online, while other must do the offline jobs, such as food delivery, day-labor, and odd-jobs task [8]. The gig economy is a source of income from informal sectors by relying on digital technologies through third-parties platform as a connector between the gig worker and the employer [9]. To enter the gig economy, internet access and digital literacy is a must. The gig economy is going to optimize the farmer performance only is the farmers have the knowledge of digital technology, internet access, and the digitalized farming system.

The pandemic has also increased internet access and the use of digital technology. It can be an opportunity for farmers to open insights into digital technology and take advantage of the gig economy to increase agricultural productivity. Therefore, this research aimed to analyze the readiness of Indonesian farmers to implementing a gig economy in their farming systems.

METHOD

This paper used secondary data from scientific articles and official government publications. The data was summarized to predict the future possibility of applying gig economy for farming activities. The data was analyzed by Strengths, Weaknesses, Opportunities, and Threats (SWOT) analysis.

The SWOT analysis used the farmer as the object. The strengths and weaknesses are based on the farmer's internal environment, such as competency, skill, and capability. The opportunities and threats are based on the farmer's external environment, such as policy, climate, and competitiveness.

RESULTS

The gig economy can apply to the farming activities that required more labor, such as planting,

harvesting, and product marketing. The offline gig worker can involve in the planting and harvesting activities. The online gig worker can participate in the product marketing activities using the reseller or drop-shipping system to reach deeper into the market.

Strength Analysis

Indonesian millennial farmers, range from age 19 to 39 years old, digital literate, and got supports from the government [10]. The important factor for applying gig economy is digital literate because the gig economy used digital platform for the operation. The millennial farmers are the great pillar for the gig economy because they understand the online system. The best part is that the millennials farmers got supported from the government, makes them got powers to do a lot of innovations for their farming systems.

Weakness Analysis

Indonesian old farmers are unable to understand the digitalization, which led to underdeveloped for the agriculture system in Indonesia. The traditional farming method relied on the farmers skill on field. Old farmers only act as the food producer, take care everything on field, without exposed to the digitalization. The agriculture products were handled by the other parties, caused the old farmers stay in the agricultural vicious circle and poverty.

Opportunities Analysis

The gig economy is related to internet users [11]. The number of Indonesian internet users in 2020 is 196.7 million people [12]. Compared with a population of 270.2 million people [13], internet users in Indonesia are around 73%. The users are predicted to keep increase until almost all the citizens are become the internet user in 2025 [14]. The coverage also almost available in every place in Indonesia, so it can be a great basis for the gig economy application.

Another opportunity is that a lot of labor and job seeker in Indonesia. The unemployment still a problem so there are a lot of gig worker available for work, online and offline.

Threats Analysis

The agriculture products from Indonesian farmers faces a big competition with the imported products due to the government policy. This caused the local farmers lost to the cheap imported products and unable to sustain their agricultural business. The local farmers need protection for their product so they can compete fairly with the imported products.

The gig economy is something new and still no official regulation for the gig worker, platform, and employer. There still no regulation for the labor fee, employer rights, and other related issues. This is a threat for the farmer to apply gig economy because the uncertainly could led to a high-risk decision.

DISCUSSION

The gig economy can be done in two ways, which are online and offline. The offline gig job is a job that require the worker to done something on a real world, such as harvesting, while the online gig job require more performance in the virtual world, such as marketing.

Strength:	Weakness:
Millennial farmers	Old farmers
Opportunities:	**Threats:**
-Internet users and coverage -Local workforce	-Imported products -Labor policy

Fig. 1 SWOT analysis of applying gig economy

The farming activities are before planting activities, planting activities, harvesting activities, and post-harvesting activities. Each activity required worker to done it. Usually, the farmers done it themselves or handed it over to other parties without future control about it. By applying gig economy, with the farmer get a role as an employer, the farmer can get more control and benefit from each activity that can lead into the increase of farmer welfare.

The before planting activities are included the planning, procurement of production facilities and the land preparation for planting. The planning activity is to identified farming objectives and needs. The procurement activities are choosing and buying the production materials and facilities, such as seeds and agrimotor. The land preparation activity is prepared a planting medium that is contain no weeds.

CONCLUSION

The gig economy is applicable only if the farmer is the millenial farmer. The old farmers could not apply gig economy to their farming system due to their digital illiterate and fixed traditional product distribution flow. The application of gig economy to all farmers in Indonesia needs a strong power, such as government, to protect and control the process.

ACKNOWLEDGMENTS

This is an independent research. No funding must be reported. There is no interest from any party mentioned in this paper.

REFERENCES

[1] K. Verico, Global Pandemic 2020: Indonesia's Output Gap and Middle-Income Trap Scenario, Jakarta: LPEM-FEBUI, 2021.

[2] M. I. Modjo, "Memetakan Jalan Penguatan Ekonomi Pasca Pandemi," *Jurnal Perencanaan Pembangunan: The Indonesian Journal of Development Planning*, vol. 4, no. 2, pp. 103-116, 2020.

[3] M. A. Shadiqi, R. Hariati, K. F. Hasan, N. I'anah and W. A. Istiqomah, "Panic Buying pada Pandemi Covid-19: Telaah Literatur dari Perspektif Psikologi," *Jurnal Psikologi Sosial*, vol. 18, 2020.

[4] R. Suparno, "Gig Economy Supports Indonesia's Economic Resilience," *The Jakarta Post*, 4 September 2020.

[5] M. Nicola, Z. Alsafi, C. Sohrab, A. Kerwan, A. Al-Jabir, C. Iosifidis, M. Agha and R. Agha, "The Socio-Economic Implication of the Coronavirus Pandemic (COVID-19): A Review," *International Journal of Surgery*, vol. 78, pp. 185-193, 2020.

[6] D. Laborde, W. Martin, J. Swinnen and R. Vos, "Covid-19 Risks to Global Food Security," *American Association for the Advancement of Science*, vol. 369, no. 6503, pp. 500-502, 2020.

[7] T. Maddox, "Agriculture 4.0: How Digital Farming is Revolutionizing the Future of Food," 12 December 2018. [Online]. Available: https://www.techrepublic.com/article/agriculture-4-0-how-digital-farming-is-revolutionizing-the-future-of-food/. [Accessed 3 May 2021].

[8] S. Vallas and J. B. Schor, "What Do Platforms Do? Understanding the Gig Economy," *Annual Reviews of Sociology*, vol. 46, pp. 273-294, 2020.

[9] N. Koutsimpogiorgos, J. van Slageren, A. M. Herrmann and K. Frenken, "Conceptualizing the Gig Economy and Its Regulatory Problems," *Policy & Internet*, vol. 12, no. 4, pp. 525-545, 2020.

[10] S. Fatimah, "Cerita Duta Petani Milenial Kementan, yang Bertani Sejak Usia 22 Tahun," 1 March 2021. [Online]. Available: https://news.detik.com/berita-jawa-barat/d-5476391/cerita-duta-petani-milenial-kementan-yang-bertani-sejak-usia-22-tahun. [Accessed 6 May 2021].

[11] M. Graham, I. Hjorth and V. Lehdonvirta, "Digital Labour and Development: Impact of Global Digital Labour Platforms and the Gig Economy on Worker Livelihood," *Transfer: The European Review of Labour and Research*, vol. 23, no. 2, pp. 135-162, 2017.

[12] Asosiasi Penyelenggara Jasa Internet Indonesia, "Survei Pengguna Internet APJII 2019-Q2 2020: Ada Kenaikan 25,5 Juta Pengguna Internet Baru di RI," Asosiasi Penyelenggara Jasa Internet Indonesia, Jakarta, 2020.

[13] Badan Pusat Statistik, "Hasil Sensus Penduduk 2020," Badan Pusat Statistik, Jakarta, 2021.

[14] H. Nurhayati-Wolff, "Indonesia: Number of Internet Users 2015-2025," 13 August 2020. [Online]. Available: https://www.statista.com/statistics/254456/number-of-internet-users-in-indonesia/. [Accessed 6 May 2021].

COMPETITIVENESS OF INDONESIAN FROZEN SHRIMP AGAINST SEVEN MAJOR COMPETING COUNTRIES AND OVERVIEW OF PAPERLESS TRADE IN THE INTERNATIONAL MARKET

Siti Rochaeni[1], Natasha Avinda Albertina[2], Iwan Aminudin[3] and Rizki Adi Puspitasari[4]
[1,2,3,4]Agribusiness Department, State Islamic University Syarif Hidayatullah Jakarta, Indonesia

ABSTRACT

Competitiveness could be said with the ability of a country to compete in international markets. This study describes the state of Indonesia's frozen shrimp commodity competitiveness against seven major competing countries. In the leading exporter of frozen shrimp, we also see the paperless trade policy's overview. This policy can accelerate trade and support the environment because the developing system being electronic format. Hence, this research is based on developing the world's frozen shrimp competition and increasingly advanced technology. This research aims to analyze competitiveness through the comparative advantage of Indonesia's frozen shrimp commodity against seven major competitor countries, the competitive advantage seen from five periods of international events, the market structure, and an overview of paperless trade policies. Data sourced from secondary data with data panels analyzed from 2000 to 2019 in the scope of competitiveness and based on the UN Global survey on digital and sustainable trade facilitation to overview the paperless trade policy. The analysis tools used in this research RCA to measure comparative advantage, EPD to measure competitive advantage, HHI8 and CR8 to see the market structure, and study literature to overview paperless trade. HS code used is 030613 or 030616 and 030617 after revision. The result shows Indonesia has a comparative advantage but does not has a competitive advantage in frozen shrimp commodities with the Oligopoly market structure increasingly concentrated. The impact of paperless trade has a good development impact and reduces trading costs.

Keywords: Frozen Shrimp, Comparative Advantage, Competitive Advantage, Market Structure, and Paperless trade

INTRODUCTION

Competitiveness at the country's level is based on the ability to compete in the global market. It can be defined as a set of institutions, policies, and any factors [1]. Indonesia is one of the active countries conducting international trade, especially in the marine and fisheries sector. It can be seen, one of the fisheries and marine commodities that have the most excellent export value is shrimp, with the shrimp trend from 2015 to 2019 is 4.49% [2]. Shrimp commodity generally has three types of products or forms for export: fresh shrimp, processed shrimp, and frozen shrimp. Judging from developing the export value of each type of Indonesian shrimp from 1990 to 2019 on the UN Comtrade [3] and International Trade Center (ITC) [4], frozen shrimp outperformed than other two types of shrimp. Frozen shrimp has an annual average export value of 939.883,69 (.000 US $), processed shrimp of 144.333,26 (.000 US $) and fresh shrimp of 15.504,55 (.000 US $). As seen before, this research focuses on frozen shrimp commodities. Shrimp production in Indonesia between 1990 and 2018 has a great trend of 9.62% from Fishtat J-FAO [5] and One Data from the Ministry of Maritime Affairs and Fisheries [6].

However, according to WITS, Indonesian frozen shrimp has a good export value rating, but has never been ranked first in export value. It differs from India, Vietnam, and Thailand, which dominated the world frozen shrimp market share [7]. Based on Globefish, we see the problem with competing countries with advantages in shrimp commodities, especially Ecuador. This country was increasing the quality of shrimp, and from 2018 to 2019, the second place has the most significant positive changed in export volume among other countries 24.3%. Meanwhile, Indonesia with the fourth place has decreased in negative 6.4%. The decline rate was bigger than Thailand, which was in the sixth place with negative values of 3.9%, and Argentina, which was in the seventh position with a negative value of 2.9% [8]. Seeing competitiveness competitively, we will divide into five periods of international events.

There are obstacles in any process in international trade, both tariff and non-tariff, the most famous ones being the SPS and TBT [9]. Since technology has grown, many policies come up for a good chance in the trading process. One of them is the paperless trade policy, the first initiation of the Free Trade Agreement (FTA) at the World Trade Organization's 9th Ministerial Conference 2013 in Bali [10]. The benefit of paperless trade policy for traders is the faster movement of goods, greater efficiency at border

agencies closely related to trade administration, and reductions in trade costs and efficiency via paperless trade can be beneficial for small and medium-sized enterprises (SMEs) [11]. Governance also greatly benefits, such as playing a pivotal role in cross-border regulatory cooperation [12]. SDG'S Statement also related to trade with three dimensions: economic, social, and environmental simultaneously [13]. This research also looks at this policy on the leading frozen shrimp exporting countries.

The whole research questions in this study are as follows:

a. How does comparative competitiveness of Indonesian frozen shrimp to seven major countries competitors?
b. Does Indonesia have a competitive advantage in frozen shrimp in the international market, seen from the five periods of international events?
c. How does the market structure for frozen shrimp in the international market?
d. How does the overview of the paperless trade policy on the main frozen shrimp export countries?

LITERATURE REVIEW

Related Research

Table 1 Previous Research

REF	Research Purpose	Tools Analysis
[22]	To analyze the competitive position of Indonesian fresh and frozen shrimp in the main export destination countries.	RCA, RSCA, and ECM
[23]	Compares the comparative analysis of export competitiveness from Indonesia and Thailand to export destination countries, Japan and the United States.	RCA
[24]	To Analyze the competitiveness of Indonesian fishery products in the ASEAN and Canadian markets.	RCA, EPD, and X-Model Product Export
[25]	To Analyze the impact of non-tariff measures on exports of shrimp and processed products from Indonesia.	Gravity model

TABLE 1. Describes research related to this research. It is used to broaden the writer's insight in terms of previous research and current research. Several reliable sources were also taken to enrich this writing.

Overview of The World Frozen Shrimp

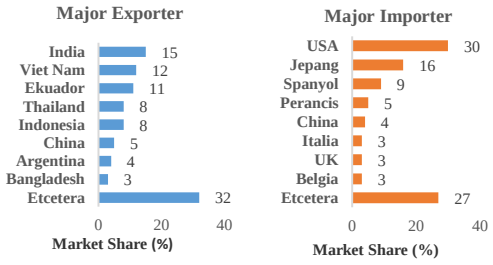


Fig. 1 Top Exporter and Importer

The data shows that eight countries are the largest exporters and importers of frozen shrimp in the world. It is sourced from ITC and UN Comtrade processed. Furthermore, the data will help analyze the competitiveness of the main exporting countries. At the top exporter, it appears that the major exporter countries controlling the shrimp market are in the Asia Pacific region. While the Latin America region only represents the two countries. USA and Japan are the major importing countries of frozen shrimp.

Conceptual Framework

Figure 2 shows that the framework serves to determine the flow of this research. In the scope of competitiveness, there are comparative advantages, competitive advantages, and market structure. At the same time, the policy is seen in paperless trade. David Ricardo popularized the comparative advantage in 1823 has considered the opportunity cost in which the country will specialize in cheap production costs and vice versa [14]. Competitive advantage grows fundamentally from the value the company can create for its buyers beyond its line of creating that value [15]. The market structure is commonly called the connections and characteristics of different elements in the market [16]. Paperless trade is one of the other policies related to trade that used empowerment of technology.

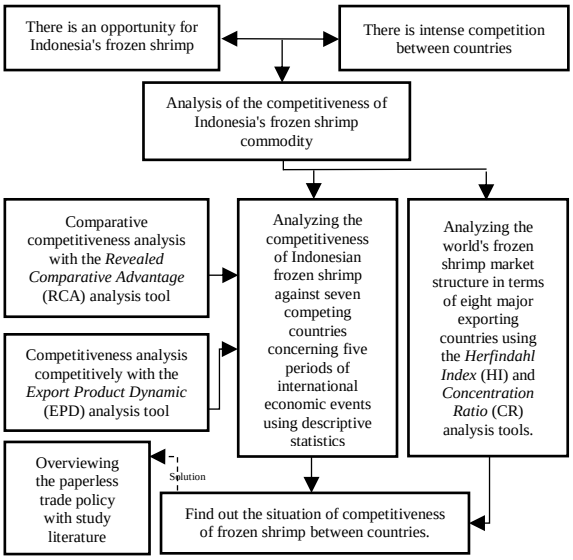


Fig. 2 Conceptual Framework

RESEARCH METHODOLOGY

We used Harmonized System (HS) with Code HS 030613 or HS 030616 and HS 030617 after revision. The data are in time series and focus on frozen shrimp exporting countries, including Indonesia, Ecuador, Bangladesh, Vietnam, India, Argentina, Thailand,

and China. Secondary data come from the International Trade Center (ITC) and UN Comtrade to see the export value of the countries analyzed from 2000 to 2019. Meanwhile, the data to overview the paperless trade policy is sourced from the UN global survey on digital sustainable trade facilitation [17]. This study uses several analytical tools following:

Revealed Comparative Advantage (RCA)

RCA analysis is used to measure competitiveness comparatively. The RCA measurement or the "Balassa Index" was popularized by Balassa in 1965. However, Balassa was not the first to use the comparative advantage index calculation, but Liesner in 1958 [18]. The formulation in general follows.

$$RCA = (X_{ij}/X_{it})/(W_i/W_t) \quad (1)$$

In this formula, X_{ij} is the Export value of frozen shrimp from country j (US$); X_{it} is the Total export value of all country commodities j (US$); W_i is the Export value of frozen shrimp commodities from the world (US$); Wt is the total export value of all world commodities (US$). The result means that if the RCA is more than one, then the country has a comparative advantage and vice versa.

Export Product Dyunamic (EPD)

EPD is used to reckon the dynamics of the frozen shrimp market position in the world. It Combines X-axis and Y-axis with four categories: rising star, falling star, lost opportunity, and retreat [18]. The ideal market position is a rising star. The systematic formulation in general as follows:

Export market share (X-axis)

$$\frac{\sum_{t=1}^{n}\left(\frac{X_i}{W_i}\right)_t \; x\; 100\% - \sum_{t=1}^{n}\left(\frac{X_i}{W_i}\right)_{t-1} \; x\; 100\%}{T} \quad (2)$$

Product market share (Y-axis)

$$\frac{\sum_{t=1}^{n}\left(\frac{X_t}{W_t}\right)_t \; x\; 100\% - \sum_{t=1}^{n}\left(\frac{X_t}{W_t}\right)_{t-1} \; x\; 100\%}{T} \quad (3)$$

In this formula, X_i is the export value of the frozen shrimp country i; Xt is the total export value of the country i; W_i is the export value of frozen shrimp commodities from the world; W_t is the total export value of all world commodities; T is the number of years analysis; t is the year to-t.

Herfindahl Index (HI) and Concentration Ratio (CR)

HI is a tool for measuring market concentration in the form of the square of all company's market share, which means considering all company's. This formulation was pioneered by Orris C Herfindahl and Albert O Hirschman. CR is calculated as the percentage of the market share largest companies in the industry concerned [19]. The formulation steps are as follows:

$$Sij = X_{ij}/X_i \quad (4)$$

$$HI = S_1^{\,2} + S_2^{\,2} + S_3^{\,2} + \ldots + S_N^{\,2} \quad (5)$$

$$CR_n = \sum_{i=1}^{n} Si \quad (6)$$

In this formula, Sij is country i frozen shrimp market share in the international market; X_{ij} is the frozen shrimp export value i-country in the international market; X_i is the total cumulative export value of frozen shrimp for all countries in the international market; S and S_i is the market share of the i-country in the world frozen shrimp trade; N is the number of countries involved in the world frozen shrimp trade. Determination of the results of HI and CR follows [20][21].

Table 2 Market Types in the Industry

Feature	Monoply	Dominant Firm	Oligopoly	Monopolistic competition	Pure Competition
Herfindahl Index (HHI)	HHI = 1	0,25 < HHI < 1	0,01 < HHI < 0,18	0,01 < HHI < 0,18	HHI < 00,1
Entry/Exit barrier	Very high	High	High	Low	Very low

Data source: Hasibuan (1993); Alistar (2004); Kuncoro (2007) inside Khavidhurrohmaningrum (2013: 224)

Table 3 The Dimensions of Measure According to Joe S. Bain in the Oligopoly Category

Oligopoly Category	Criteria
Type of I A (Full oligopoly)	1. CR_3 → Dominating the market ± 87% 2. CR_8 → Dominating the market ± 99%
Type of I B (Full oligopoly)	1. CR_4 → Dominating the market ± 90% 2. CR_8 → Dominating the market ± 95% 3. CR_{20} → Dominating the market ± 99%
Type of II (Highly concentrated)	1. CR_4 → Dominating the market ± 65% 2. CR_8 → Dominating the market ± 85% 3. CR_{20} → Dominating the market ± 95%
Type of III (High moderate concentration)	1. CR_4 → Dominating the market 50% - 65% 2. CR_8 → Dominating the market 70% - 85% 3. CR_{20} → Dominating the market ± 95%
Type of IV (Low moderate concentration)	1. CR_4 → Dominating the market 35% - 50% 2. CR_8 → Dominating the market 45% - 70% 3. CR_{20} → Dominating the market ± 70%
Type of V (Low grade oligopoly)	1. CR_4 → Dominating the market < 35% 2. CR_8 → Dominating the market < 45%
Type of VI	Oligopoly approaches a competitive market where there are no sellers who can influence other sellers.

Data source: Source: Joe S. Bain (1959: 125-133)

RESULT AND DISCUSSION

We now answer the questions in this research

Comparative Competitiveness of Indonesia Frozen Shrimp

The comparative advantage is the analysis by comparing the competitiveness of a country on frozen shrimp commodities relative to other commodities which are calculated based on the opportunity cost with other countries. Based on Table 4 of eight major

exporting countries, including Indonesia, the comparative advantage of Indonesian frozen shrimp is in the sixth position out of 8 countries

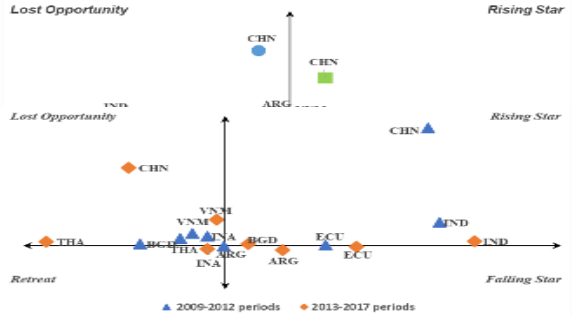
Table 4 Comparative Advantage of 8 Main Frozen Shrimp Exporting Countries Based RCA Analysis

Year	Countries							
	INA	ECU	BGD	VNM	IND	ARG	THA	CHN
2000	11,26	42,34	48,11	32,53	15,65	7,09	15,88	0,94
2001	11,83	45,67	37,14	31,28	13,91	11,58	13,98	0,80
2002	11,79	42,92	46,52	34,76	14,95	8,36	9,77	0,72
2003	11,54	40,90	41,81	40,97	12,44	11,46	9,39	0,83
2004	11,62	45,30	46,46	42,11	10,76	6,69	8,76	0,75
2005	11,13	53,64	44,45	41,28	10,27	2,52	9,73	0,51
2006	11,62	57,56	50,97	38,37	8,97	9,89	10,07	0,24
2007	9,93	61,84	65,69	40,40	8,15	7,46	10,10	0,21
2008	9,57	60,25	46,71	33,07	6,27	8,67	11,38	0,26
2009	7,33	58,88	24,69	27,56	5,16	7,12	10,79	0,75
2010	6,56	63,43	29,41	28,01	5,94	9,06	11,10	0,71
2011	6,69	71,58	27,49	23,78	7,18	8,48	9,93	0,76
2012	7,43	77,84	14,98	19,29	8,58	8,68	9,09	0,75
2013	8,14	87,34	21,78	18,45	9,40	9,89	4,96	0,67
2014	8,88	97,18	0,00	16,52	11,54	11,07	3,75	0,60
2015	8,50	130,21	12,62	11,24	12,26	14,11	3,24	0,47
2016	8,20	141,44	11,62	9,53	12,24	15,99	4,07	0,48
2017	7,29	137,46	10,51	9,54	13,53	17,86	3,49	0,37
2018	7,55	149,81	8,46	8,17	13,53	21,12	2,88	0,30
2019	7,33	167,95	7,46	7,07	13,63	15,58	2,67	0,22
AVG	**9,21**	**81,68**	**29,84**	**25,70**	**10,72**	**10,63**	**8,25**	**0,57**

Information: ARG = Argentina, BGD = Bangladesh, CHN = China, ECU = Ecuador, IND = India, INA = Indonesia, THA = Thailand, VNM = Vietnam
Data source: International Trade Center (ITC) and UN Comtrade *(processed)*

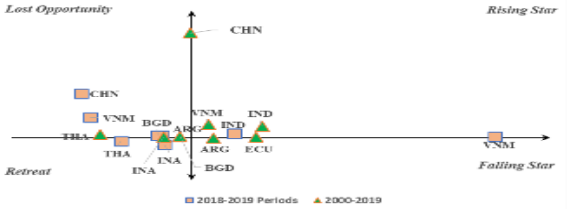
It can be seen that the value of Indonesia's RCA tends to decline in 2009-2012, which can be indicated because of the economic crisis in the USA and Europe. In line with research [22], some factors affect Indonesian exports to the USA market. One of the factors is the USA GDP variable, where GDP has a positive and significant effect at the 5% fundamental level on the competitiveness of Indonesian frozen shrimp, where an increase in GDP can be interpreted as an increase in demand in the USA market. Indonesia and Vietnam have tight competition in terms of shrimp competitiveness based on [23], in 1989-2010. This study stated that Thailand's frozen shrimp in the USA market had a more significant comparative advantage than Indonesia, with a ratio of 18.57:10.29, and in the Japanese market, with 5.61: 5.21. The study was analyzed in years 2000-2019. It is known that Indonesia can outperform Thailand in terms of the frozen shrimp exports in the international market. Ecuador has the most significant comparative advantage, whereas China does not have.

Competitive Advantage of Frozen Shrimp in the International Market



Information: ARG = Argentina, BGD = Bangladesh, CHN = China, ECU = Ecuador, IND = India, INA = Indonesia, THA = Thailand, VNM = Vietnam

Fig. 3 EPD Matrix Results



The first period in 2000-2006, indicates the post-Asian crisis. Indonesia is in a retreat position. In line with the growth in the average share of the Indonesian frozen shrimp exports, it decreased by 0.20%. Vietnam and Bangladesh position the rising star position. The lost opportunity position is to refer to India, Ecuador, Thailand, and China. The country of Argentina occupies the falling star position. The 2007-2008 period describes the events of the Global Financial Crisis (GFC). Indonesia is in a lost opportunity position followed by India and Argentina. Retreat occupied by Bangladesh. The rising star position send to India, Vietnam, Ecuador, Thailand, and China. China seems to have risen so that ASEAN countries and Canada entered into a Free Trade Agreement (FTA) to deal with this situation [24].

The third period 2009-2012, started the economic crisis in the USA and Europe and its early post. Indonesia is in the same position in the previous period, namely lost Opportunity. This position is also placed in Vietnam, Thailand, and Bangladesh. India, Ecuador, and China own rising star position. Meanwhile, the position of retreat was held by Argentina has experienced a setback in the sale of frozen shrimp commodities in the international market. The post-crisis period in the USA and Europe includes 2013-2017. Indonesia's position is in a retreat position. The countries that have a rising star position are India and Bangladesh. Both countries have good growth in both export and product share. Bangladesh can improve on its previous position, which lost market share. Lost Opportunity, there are Vietnam, Thailand, and China. China experienced a loss of market share, as seen from the average growth in frozen shrimp exports, which fell by 0.72%.

The period 2018-2019 reflects the state of the frozen shrimp trade during the trade war between the USA and China. Indonesia is in the same position as the previous period, which experienced a setback in frozen shrimp exports as a whole. Indonesia does not have a competitive advantage. Meanwhile, countries that have advantages from a competitive side include Ecuador, Vietnam, and India. Porter's theory reveals that the factors of demand conditions affect competitive advantage. It is evident from the results

of the acquisition of X-axis measured based on demand growth which has a positive value for Ecuador of 0.54%, Vietnam 0.14%, and India 0.59%.

Market Structure for Frozen Shrimp

HI is obtaining between 0.05 and 0.12 with an average value of 0.07 means the type of oligopoly market. The eight countries that export frozen shrimp have a market share of 67%. The characteristics of oligopoly are high barriers to entry and exit. Barriers can be in the form of tariffs and non-tariff. The Concentration Ratio has a type four (low-moderate) oligopoly structure in 2000-2013 with the concentration value of 45-70% and oligopoly three (high-moderate) with a concentration value of 70-85% in 2014-2019.

Table 5 Analysis Results HI and CR of Frozen Shrimp Producing Countries in the International Market

Year	Market Share	
	HI	CR
2000	0,06	59,21%
2001	0,06	58,55%
2002	0,05	55,83%
2003	0,05	56,70%
2004	0,05	55,05%
2005	0,05	56,35%
2006	0,05	59,59%
2007	0,06	59,70%
2008	0,05	58,80%
2009	0,06	60,63%
2010	0,06	65,94%
2011	0,07	69,08%
2012	0,07	68,79%
2013	0,08	69,78%
2014	0,09	70,14%
2015	0,09	71,17%
2016	0,09	73,47%
2017	0,10	74,32%
2018	0,10	73,19%
2019	0,12	73,89%
AVG	0,07	64,51%

Data source: International Trade Center (ITC) and UN Comtrade *(processed)*

Entry barriers to the oligopoly market, especially in the frozen shrimp market, have several regulations following exporting countries. The impacts of non-tariffs that are often implemented on international markets amount to seven policies. However, Sanitary and Phytosanitary (SPS) and Technical Barriers on Trade (TBT) are the most frequently applied ones. Ardiyanti & Saputri's research regarding the impact of these two policies and TBT implementation in export destination countries resulted in a more significant negative impact, namely 30.2% compared to SPS 21.3% [25]. In addition, there are still several cases of shrimp rejection from Indonesia. Recorded in the Import Refusal Report (IRR) issued by the United States Food and Drug Administration (USFDA), there were 827 cases of rejection of Indonesian shrimp from 2002 to 2020 [26]. From the European sides, the Rapid Alert System for Food and Feed (RASFF). It can be seen that some trade flows for frozen shrimp commodities are hampered due to non-compliance with standardization. It was recorded that from 1998 to 2018, there were approximately 48 cases of frozen shrimp commodities from Indonesia. These records include the categories of unauthorized imports, prohibition of sale, crushing, product recall, official containment, and some unsuitable ingredients such as nitrofuran, chloramphenicol, oxytetracycline, and salmonella [27].

Overview Paperless Trade Policy on the Main Frozen Shrimp Export Country

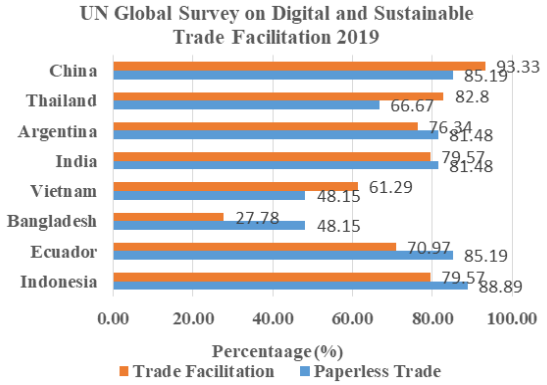


Fig. 4 Percentage of Trade Facilitation and Paperless Trade

Based on the UN global survey on digital sustainable trade facilitation 2019. Indonesia implemented a paperless trade policy with 88.89%, where this value was higher than the seven countries. From this percentage, it can be seen that Indonesia has implemented good traceability regarding several standards including the environment. However, for the total value of Trade Facilitation, Indonesia lost from China.

Implementation of paperless trade policy relates to the electronic/automated customs systems availability of internet connection to customs also other agencies at border-crossings are extensively in other regions. Many countries use advanced measures such as Electronic Single Window Systems. Indonesia is one of the countries that use the single window systems—known as Indonesia National Single Windows (INSW) in 2007 [28]. Hence, Indonesia can take an excellent opportunity for this system. In 2017, known as Buku Tarif Kepabeanan Indonesia 2017. The changes are areas related to HS Code Submission.

Several agencies have well-coordinated these changes in HS Code Submission and INSW to implement AHTN 2017. China Overall, the use of China's trade facilitation is very superior. It is known that the country is developing existing trade facilitation elements such as agricultural trade facilitation. The China e-cert is open to all authorities in the trading countries to verify the certificates

issued by local China Inspections and Quarantine (CIQ) authorities [17].

CONCLUSION AND RECOMENDATION

Indonesian frozen shrimp commodity has a comparative advantage in sixth out of 8 countries with an average RCA value of 9.21. Only China does not have a comparative advantage. Overall, Indonesia did not have a competitive advantage in 2000-2019 and was in a position of lost opportunity with the Oligopoly market structure that is increasingly highly concentrated. Indonesia implements paperless trade with the highest value gain among its competitors. However, China's trade facilitation is the most superior.

Increasing the competitive and comparative advantage. Improvements can be made by providing input subsidies to reduce the cost of Indonesian shrimp production, improving the existing standardization process, both locally and internationally. In facing the oligopoly market with high barriers, it is recommended to conduct a Mutual Recognition Agreement (MRA) in partner countries. For a good assessment of the implementation of Paperless Trade, it is hoped that Indonesia will maintain and develop the existing elements to support the Facilitation Trade. Efforts for environmental sustainability is a concern.

For future research, we recommended analyzing the effect of international events on the status of the world frozen shrimp trade and the impact of technological developments by following the changing times on state trade especially in environment issues.

REFERENCES

[1] G. L. Jamil, S. M. Lopes, A. M. Da Silva, and F. Ribeiro, "Handbook of research on effective project management through the integration of knowledge and innovation," in *Handbook of Research on Effective Project Management through the Integration of Knowledge and Innovation*, Portugal: IGI Global, 2015, pp. 1–602.

[2] Food and Agriculture Organization of the United Nations, *Globefish Highlights*. 2019.

[3] UN Comtrade, "Data on the Export Value of Indonesian Shrimp and Competing Countries," 2020. [Online]. Available: https://comtrade.un.org/. [Accessed: 23-Sep-2020].

[4] International Trade Center (ITC), "Data on the Export Value of Indonesian Shrimp and Competing Countries," 2020. [Online]. Available: https://www.trademap.org/Index.aspx. [Accessed: 23-Sep-2020].

[5] FishtatJ-FAO, "Total Production." 2020.

[6] One Data from the Ministry of Maritime Affairs and fisheries, "Total Production," *2021*, 2021. [Online]. Available:https://statistik.kkp.go.id/home.php?m=total&i=2#panel-footer. [Accessed: 06-Mar-2021].

[7] World Integrated Trade Solution (WITS), "Crustaceans; shrimps and prawns, frozen (whether in shell or not, whether or not cooked by steaming or by boiling in water) exports by country |2019." [Online]. Available: https://wits.worldbank.org/trade/comtrade/en/country/ALL/year/2019/tradeflow/Exports/partner/WLD/product/030613. [Accessed: 22-Jun-2020].

[8] H. Josupeit *et al.*, *Globefish Highlights*, 3rd issue., no. July. 2019.

[9] TRAINS-UNCTAD, "Non-Tariff Measures and Sanitary and Phytosanitary." [Online]. Available: https://trains.unctad.org/. [Accessed: 14-Nov-2020].

[10] "WTO | Trade facilitation." [Online]. Available: https://www.wto.org/english/tratop_e/tradfa_e/tradfa_e.htm. [Accessed: 25-May-2021].

[11] UNECE-UN/CEFACT, "White Paper: Paperless Trade," 2018, p. 8.

[12] UNECE-UN/CEFACT, "White Paper: Paperless Trade," 2018, p. 9.

[13] UNCTAD, "Trading into Sustainable Development: Trade, Market Access, and the Sustainable Development Goals," p. ix, 2016.

[14] P. . Krugman and M. Obstfeld, *International Economics Theory & Policy*, 8th Editio. Boston: Pearson Education, 2009.

[15] M. E. Porter, *Competitive Advantage: Creating and Sustaining Superior Performance*. New York: The Free Press, 1985.

[16] W. Zeng, M. Yu, D. Zhang, and Q. Zhao, "Holistic Innovation, Market Structure, and Performance-Research on a Computer Decision-Making Method," *IEEE Access*, vol. 8, no. 2013, p. 180445, 2020, doi: 10.1109/ACCESS.2020.3028065.

[17] UNESCAP, "UN Global Survey on Digital and Sustainable Trade Facilitation 2019," 2021. [Online]. Available: https://unnext.unescap.org/content/un-global-survey-digital-and-sustainable-trade-facilitation-2019.

[18] D. Esterhuizen, "An Evaluation of the Competitiveness of the South African Agribusiness Sector," University of Pretoria, 2006.

[19] I. Pavic, F. Galetic, and D. Piplica, "Similarities and Differences between the CR and HHI as an Indicator of Market Concentration and Market Power," *Br. J. Econ. Manag. Trade*, vol. 13, no. 1, pp. 1–8, 2016, doi: 10.9734/bjemt/2016/23193.

[20] Khavidhurrohmaningrum, "Strategi dan Periilaku Industri Pengolahan di Kota Semarang Tahun 2007-2011," *Econ. Dev. Anal. J.*, vol. 2, no. 3, pp. 220–223, 2013.

[21] J. S. Bain, *Industrial Organization*. Berkeley: University of California, 1959.

[22] U. Ashari, Sahara, and S. Hartoyo, "Competitiveness of Indonesian Fresh and Frozen Shrimp in Main Export Destination Countries," *J. Manaj. Agribisnis*, vol. 13, no. 1, pp. 1–13, 2016, doi: 10.17358/jma.13.1.1.

[23] L. A. Wati, C. Wen-I, and M. M. Mustadjab, "Competitiveness of Indonesian Shrimp Compare with Thailand Shrimp in Export Market," *Wacana*, vol. 16, no. 1, pp. 24–31, 2013.

[24] E. S. Luhur, S. Mulatsih, and E. Puspitawati, "Competitiveness Analysis of Indonesian Fishery Products in ASEAN and Canadian Markets," *Signifikan J. Ilmu Ekon.*, vol. 8, no. 1, pp. 105–120, 2019, doi: 10.15408/sjie.v8i1.7301.

[25] S. T. Ardiyanti and A. S. Saputri, "Dampak Non Tariff Measures (NTMs) Terhadap Ekspor Udang Indonesia," *Bul. Ilm. Litbang Perdagang.*, vol. 12, no. 1, pp. 14–18, 2018.

[26] USFDA, "Import Refusal Report," *United States Food and Drug Administration (USFDA)*, 2020. [Online]. Available: https://www.fda.gov.

[27] European Commission, "RASFF Portal," 2020. [Online]. Available: https://webgate.ec.europa.eu/rasff-window/portal/?event=SearchForm&cleanSearch=1.

[28] ASEAN Single Window, "Indonesia General Information." [Online]. Available: https://asw.asean.org/index.php/nsw/indonesia/indonesia-general-information.

Engineering

7th Int. Conf. on Structure, Engineering & Environment (SEE),
Pattaya, Thailand, Nov. 10-12, 2021, ISBN: 978-4-909106070 C3051

VIBRATION ACTUATOR SYSTEM FOR INSPECTION OF LARGE COMPLEX IRON STRUCTURES

Hiroyuki Yaguchi[1] and Yusuke Itoh[1]
[1] Faculty of Engineering, Tohoku Gakuin University, Japan

ABSTRACT

In recent years, many large structures have been constructed all over the world due to economic development. Especially in Japan, more than 50 years have passed since the intensive construction of large structures during the period of high growth known as the Japanese economic miracle. As these structures age, they need to be inspected, and numerous robots have been proposed for structural inspection. However, the technology for inspection of large structures by robots remains immature. This paper proposes a vibration actuator system that can move a robot over an iron structure having a complicated surface, such as a stepped surface. A prototype vibration actuator system was built, in which four vibration actuators and wheels containing magnets were combined with a flexible silicone rubber "backbone." Actual climbing tests showed that this actuator system can move smoothly over vertical steps. Further, this system can be equipped with an automatic tapping device, which might allow it to inspect the main towers of a large bridge.

Keywords: vibration, actuator system, inspection, magnetic wheel, complex iron structure.

INTRODUCTION

In recent years, many large structures have been constructed in every country due to economic development. Especially in Japan, more than 50 years have passed since the intensive construction of large structures during the period of high growth known as the Japanese economic miracle. Therefore, the maintenance requirements for these structures have increased since 2010. Within 20 years, it is expected that more than 50% of Japan's social infrastructure will be more than 50 years old. Old infrastructure was built without seismic standards, so there is a risk of collapse in the event of a major disaster. For this reason, inspection and maintenance of social infrastructure, such as large bridges and storage tanks, is extremely important. In particular, there is a high demand for inspection at the cable joint of a cable-stayed bridge having a height of a main tower over 200 m.

Numerous robots have been proposed for structural inspection. Adhesion methods for wall surface movement include the following proposed techniques: mimicking of a living leech [1], roller structure with a belt and suction cups [2], van der Waals forces [3], negative pressure produced by a pump [4], adhesive materials [5], and a claw gripper [6]. Multiple actuators are always mounted on the drive unit of these robots. Additionally, these methods involve complicated mechanisms and require the adhered device to have a relatively large weight. In recent years, robots that apply drone technology have been developed. However, drone inspection technology has not advanced because it requires skill in investigations due to the effects of strong winds and thunderstorms.

The authors previously proposed an actuator capable of movement on a ferromagnetic material by coupling an electromagnetic force and a mechanical vibration [7 - 9]. Although this actuator can climb vertically, it cannot move over a stepped surface. Therefore, it cannot be used for inspection of iron structures having a complicated shape. Moreover, because this actuator has a low propulsive force, it cannot be equipped with a heavy sensor, such as an automatic tapping device.

This paper proposes a vibration actuator system that can move over an iron structure having a complicated surface with, for example, steps. First, the movement characteristics of the vibration actuator were examined. Next, a vibration actuator system prototype was built having four vibration actuators and magnetic wheels combined with flexible silicone rubber. Actual climbing tests showed that this actuator system can move smoothly over a stepped surface. This actuator system can be equipped with an automatic tapping device, and it has been shown that it may be applicable to inspection of the main towers of a large bridge.

STRUCTURE OF VIBRATION ACTUATOR

Fig. 1 shows a diagram of the vibration actuator capable of movement on a ferromagnetic material. The vibration actuator consists of a permanent magnet, a translational spring, an electromagnet, a triangular acrylic frame, a second permanent magnet attached to the bottom of the frame, and a natural rubber sheet. The upper permanent magnet, which made up the mass of the vibration component, was cylindrical in shape and was composed of NdFeB magnetized in the axial direction. This magnet was 15 mm in diameter and 6 mm in height. The surface magnetic flux density measured using a tesla meter was 380 mT. The translational spring was a stainless-steel compression coil having an outer diameter of 14 mm, a free length of 30 mm, and a spring constant k of 4,812 N/m. The electromagnet consisted of an iron core having a diameter of 5 mm and a length of 25 mm with 1,000 turns of 0.2-mm-diameter copper wire. This electromagnet was inserted into the translational spring.

The permanent magnet attached to the bottom of the frame had a diameter of 12 mm and a thickness of 5 mm. The average surface magnetic flux density was 383 mT. A natural rubber sheet 1 mm in thickness was attached to this permanent magnet to increase the frictional force. The vibration component was inclined at an angle α from the horizontal plane. The vibration actuator had a height of 42 mm, a width of 15 mm, and a total mass of 30 g.

The angle α of the vibration component was set to 60° based on the results obtained in a previous study [8]. The attractive force generated by the permanent magnet attached at the support part acts on the vibration actuator when it is placed on a ferromagnetic material, as shown in Figs. 2(a) and 2(b). The frictional force between the rubber sheet

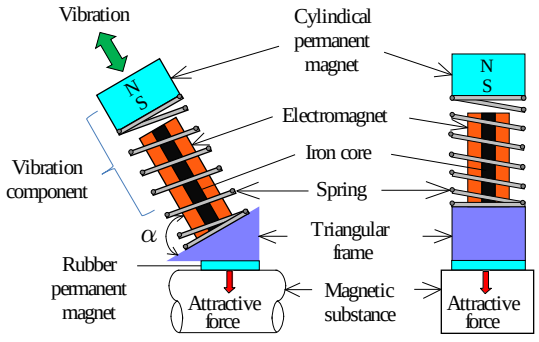
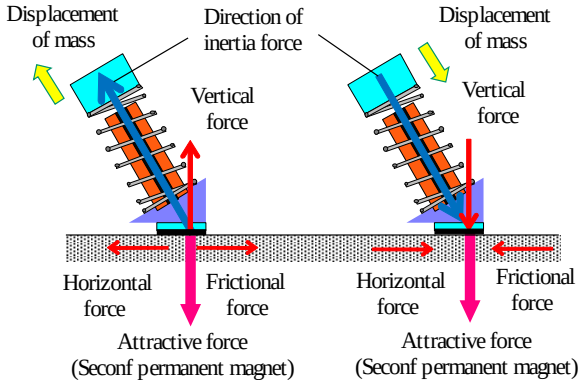


Fig. 1. Structure of the vibration actuator.



(a) Sliding (b) No sliding

Fig. 2. Principle of locomotion.

and the magnetic substance alternates periodically during one cycle of vibration. Because the horizontal component of the inertial force exceeds the frictional force, the vibration actuator is propelled by the difference between the frictional forces in the forward and backward directions acting on the rubber sheet, as shown in a previous study [8].

LOCOMOTION CHARACTERISTICS OF VIBRATION ACTUATOR

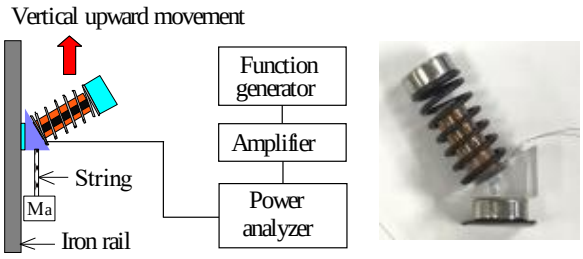
An experiment was conducted using the vibration actuator shown in Fig. 3. An iron rail with a width of 50 mm, a thickness of 50 m, and a length of 1,000 mm was used as the target magnetic structure. The vibration component was driven at a resonance frequency of 106 Hz using a signal generator and an amplifier. The attractive force F between the actuator unit and the iron rail was 11 N. The coefficient of friction between the iron rail and the natural rubber as measured in the experiment was 0.67. Fig. 3 also shows a photograph of the vibration actuator.

Fig. 4 shows the relationship between the load mass and the vertical upward speed of the actuator when the input power was 0.6, 0.9, and 1.4 W. In this figure, the actuator can move upward at a speed of 9.1 mm/s even with a load mass of 850 g.

Fig. 5 shows the relationship between the load mass and the self-propulsion efficiency of the actuator. The efficiency η is expressed:

$$\eta\,[\%] = \left(M_a + M_m\right) v_{up}\, g \times 100 \,/\, P_I\,, \qquad (1)$$

where M_a is the total mass of the actuator, M_m is the load mass, v_{up} is the vertical upward speed, g is the acceleration due to gravity, and P_I is the input power.



(a) Schematic (b) Photograph

Fig. 3. Experimental apparatus and actuator.

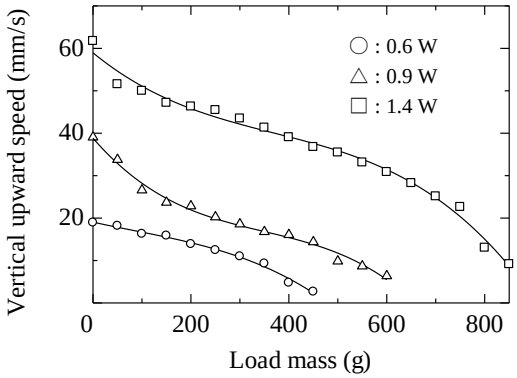


Fig. 4. Relationship between load mass and vertical upward speed for single actuator.

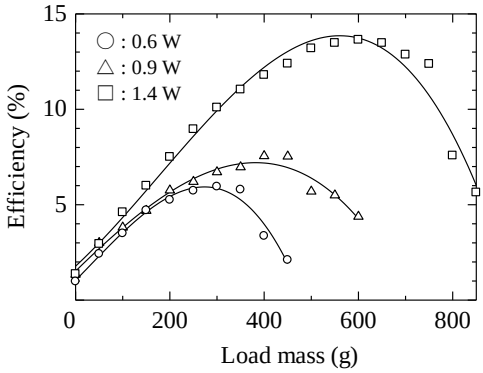


Fig. 5. Relationship between load mass and efficiency for single actuator.

It was observed that the maximum efficiency of this actuator is about 14%.

VIBRATION ACTUATOR SYSTEM CAPABLE OF MOVEMENT OVER A STEP

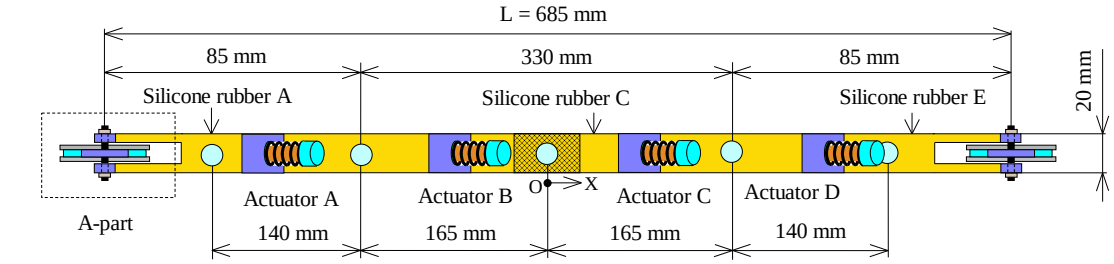
To move on a complex iron structure having a stepped surface, the new vibration actuator system has a flexible frame capable of deformation over uneven parts of the structure surface. Silicone rubber was used for the flexible frame, and the attractive force was generated by multiple permanent magnets.

Fig. 6 shows a vibration actuator system in which four actuators (A, B, C, D) capable of movement are connected by a flexible silicone rubber frame. The silicone rubber is divided into five segments. The lengths of silicone rubber segments A, B, C, D, and E and are L_1, L_2, L_3, L_4, and L_5, respectively. A magnetic wheel is attached to opposite ends of silicone rubber segments A and E. By attaching a magnetic wheel to the tip of the actuator system, it is possible to exert an appropriate attractive force on the iron structure and provide a guide for movement over a step. The magnetic wheel has a three-layer structure in which a ring-type permanent magnet is sandwiched between two acrylic disks having outer diameters of 30 mm and a thickness of 2 mm. In addition, auxiliary permanent magnets are placed at distances x_1, x_2, x_3, x_4, and x_5 from the origin O to adhere to an iron structure during movement over a stepped surface.

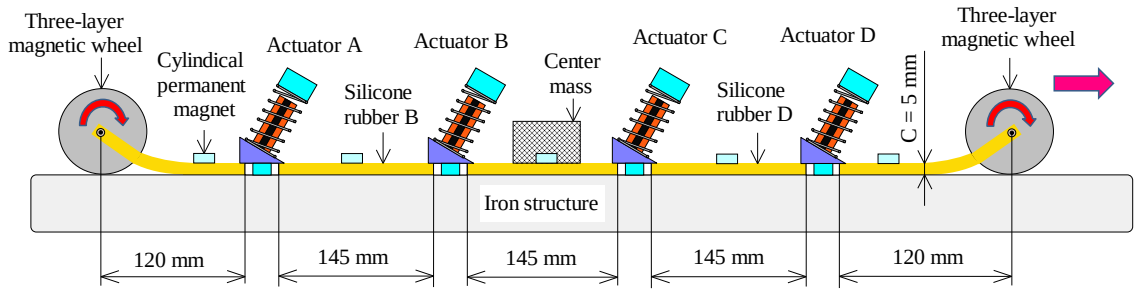
The longitudinal stiffness of the silicone rubber connecting the four actuators has a significant effect on the traction and movement over a step. Furthermore, the attractive force exerted by the magnetic wheel also affects the movement over the step. Because there are countless combinations of parameter for designing the actuator system, the following four criteria were introduced:

1) The total length of the actuator system is approximately 700 mm to allow portability.
2) Considering long cable traction over 200 m, the traction force for the actuator system is more than 15 N (load mass of 1,500 g).
3) In the future, an automatic tapping device mass weighing 260 g can be installed in the center of the actuator system.
4) The height of the step over which the actuator system can move does not exceed 25 mm in the vertical plane.

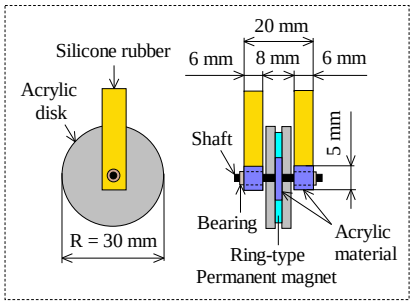
Preliminary experiments were conducted to satisfy the above design criteria. By trial and error, the dimensions of the silicone rubber material were determined. All silicone rubber segments A, B, C, D, and E had a thickness of 5 mm. In addition, the width B and length L of the silicone rubber were set to B = 20 mm and L_1 = 120 mm, L_2 = 140 mm, L_3 = 140 mm, L_4 = 140 mm, and L_4 = 120 mm. As the auxiliary attractive force, cylindrical permanent magnets were arranged at x_1 = 0 mm, x_2 = 165 mm, x_3 = 305 mm, x_4 = -165 mm and x_5 = -305 mm in



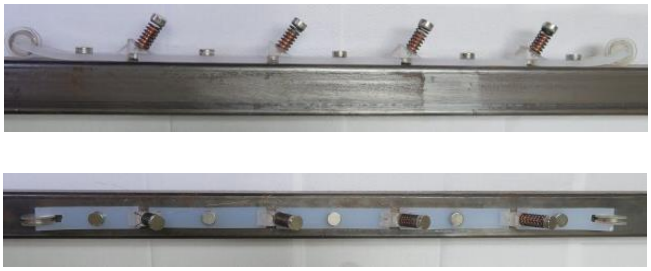
(a) Plan view



(b) Front view



(c) Details of Area A in (a)



(d) Photograph of actuator system

Fig. 6. Vibration actuator system capable of movement over a step.

segments A, B, C, D, and E. Cylindrical permanent magnets with an outer diameter of 15 mm and a thickness of 6 mm were attached at these positions. The attractive force on the iron rail for this magnet was 1.8 N.

The ring-shaped permanent magnet for the magnetic wheels had an outer diameter of 16.5 mm, an inner diameter of 8.5 mm, a thickness of 4 mm, and a magnetic flux density of 356 mT. A three-layered wheel with a shaft with an outer diameter of 1 mm in the center was attached to the silicone rubber via bearings. The attractive force for the magnetic wheel was 0.9 N.

The overall length of the actuator system was 715 mm, and the distance between the magnetic wheels was L = 685 mm. The width, height, and total mass of the actuator system were 20 mm, 42 mm, and 250 g, respectively. In this system, the attractive force F for each vibration actuator was set to 11 N. Fig. 6(d) shows photographs of the vibration actuator system.

LOCOMOTION CHARACTERISTICS OF VIBRATION ACTUATOR SYSTEM

Measurements were performed using the experimental apparatus shown in Fig. 3. In the measurement, a square iron pipe with a width and height of 50 mm, and a total length of 2,000 mm was used. The traction characteristics of the prototype actuator system were measured experimentally. The load mass was attached to the silicone rubber with a string. When a central mass of 300 g, which is heavier than a tapping device (260 g), was mounted on the actuator system, vertical upward motion was possible at a speed of 7.2 mm/s even when the maximum design load mass of 1,500 g was attached to the main body.

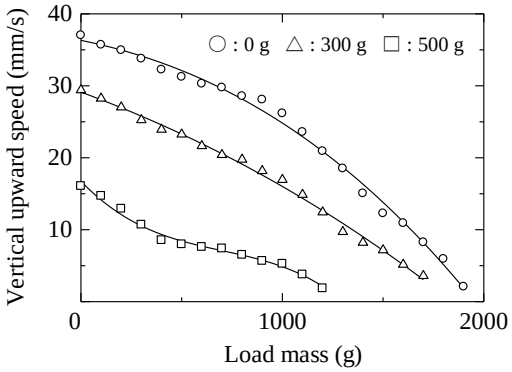


Fig. 7. Relationship between load mass and vertical upward speed with different central masses.

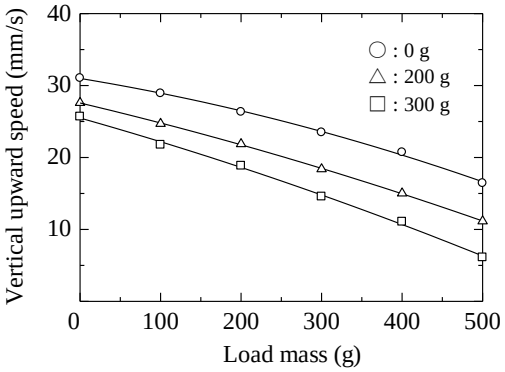


Fig. 9. Relationship between load mass and vertical upward speed for single infinite step.

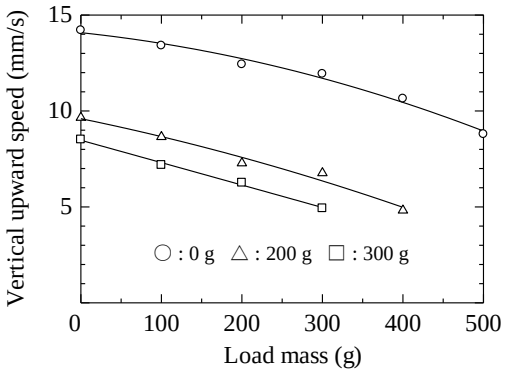
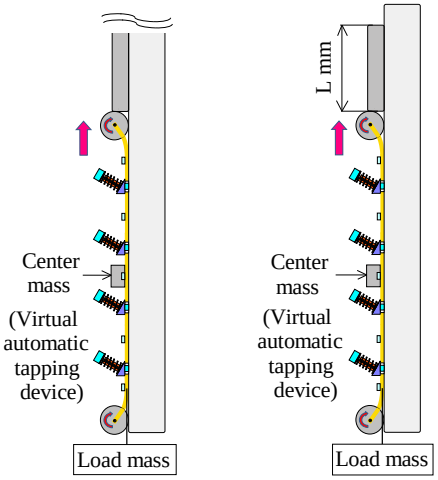


Fig. 10. Relationship between load mass and vertical upward speed for finite double step.

STEP MOVEMENT CHARACTERISTICS OF VIBRATION ACTUATOR SYSTEM

The locomotion characteristics of the vibration actuator system for two step patterns were measured. First, as shown in Fig. 8(a), an iron structure having a single step with an infinite length was examined. In these experiments, the measurement distance was set to 750 mm. The power input to each actuator was 1 W.

Fig. 9 shows the relationship between the load mass of the actuator system and the vertical upward speed for a single step with a height of 25 mm by varying for central masses of 0, 200, 300, 400, and 500 g. It was found that even with a central mass of 300 g, a traction force of 5 N (load mass of 500 g) was generated. However, the speed was only 6 mm/s. In the future, it will be necessary to take measures to increase the speed, such as changing the magnetic



(a) Single infinite step (b) Two steps

Fig. 8. Two step patterns for vertical iron structure.

circuit in the vibration component.

Furthermore, as shown in Fig. 8(b), the complex iron structure having two steps (defined as a single step of finite length, where the actuator system must crawl up the step where it begins and down the step where it ends) was examined. The power input to each actuator was 1 W. In the experiment, the step height was fixed at 25 mm, and the effect of the step length L on the movement of the actuator system with no load mass was investigated. The step length L was varied from 50 to 550 mm at intervals of 50 mm, and the vertical upward speed was measured. The step lengths over which the actuator system could move were 350, 500, and 550 mm or more. This is due to the placement interval of the vibration actuators in the system. An arrangement of vibration actuators that can handle any step length is an issue for the future.

The speed of the actuator system for the two-step case shown in Fig. 8(b) was measured. In these experiments, the step length was set to 500 mm. The power input to each actuator was 1 W.

Fig. 10 shows the relationship between the

load mass and the vertical upward speed for a finite-length step 25 mm in height and central masses of 0, 200, and 300 g. Even for a central mass of 300 g, the system could move over the vertical surface while generating a traction force of 5 N.

The movement speed of the actuator system has been extremely reduced at the step. This is because three actuators required large propulsive forces to overcome the attractive force between the permanent magnet in the holding part of one actuator and the stepped part of the iron structure. In the future, it will be necessary to improve the holding part using a design that combines a permanent magnet and an electromagnet. This will allow control of the attractive force according to the movement conditions.

In addition, this actuator system cannot switch the movement direction. To solve this problem, it is necessary to change the actuator to a structure that uses a vibration phase difference, as previously proposed by the author [9].

CONCLUSIONS

The demand for inspection of structures is increasing all over the world. However, it is very difficult to move on a complex iron structure having a step on a vertical surface. In this paper, a new vibration actuator system for inspection of complex iron structures has been proposed and tested.

At first, a single vibration actuator was prototyped and measured. The experimental results revealed that this vibration actuator was able to move with a load mass of 850 g. It is maximum efficiency about 14% for the case of carrying only its own weight for electromagnet input power of 0.6 W. Furthermore, from the actual machine test, the vibration actuator produces a tractive force of approximately 28 times its own weight.

Next, to move on a complex iron structure having a stepped surface, the vibration actuator system was prototyped with four vibration actuators and magnetic wheels combined with a flexible silicone rubber frame. The actuator system produced a traction force of 19 N. In addition, even for a load mass of 300 g, the approximate weight of an automatic tapping device, the system could move vertically over a step 25 mm tall. Thus, this actuator system can move on complex iron structure which is difficult even for a robot equipped with a complicated control system. In addition, with only a simple device and the actuator system, the possibility of internal inspection of the main tower of a large bridge over 200 m was shown.

However, this actuator system cannot switch its direction of movement. To solve this problem, it is necessary to change the actuator to a structure that uses a vibration phase difference, as previously proposed by the author [9].

REFERENCES

[1] Kanada A., Giardina F., HowisonT.,Mashimo T. and Iida F., “Reachability Improvement of a Climbing Robot based on Large Deformations induced by Tri-Tube Soft Actuators, Soft Robotics Vol. 6, No. 4(2019)

[2] Ge D., Ren C., Ma S. and Matsuno T., Guide Rail Design for a Passive Suction Cup based Wall-Climbing Robot, in Proc. 2016 IEEE/RSJ International Conference on Intelligent Robots and Systems (IROS2016), pp. 5776-5781, 2016.

[3] Kim S., M. Spenko, S. Trujillo, B. Heyneman, V. Mattoli and M. R. Cutkosky, ”Whole body adhesion hierarchical directional and distributed control of adhesive forces for a climbing robot”, IEEE International Conference on Robotics and Automation, (2007).

[4] Subramanyam A., Mallikarjuna Y., Suneel S.and Bhargava K. L., ” Design and Development of a Climbing Robot for Several Applications”, International Journal of Advanced Computer Technology, Vol. 3, No. 3, pp. 15-23 (2011).

[5] Unver O. and Sitti M., ” Tankbot: A Miniature, Peeling Based Climber on Rough and Smooth Surfaces”, in Proc., IEEE International Conference on Robotics and Automation, pp. 2282-2287 (2009).

[6] Provancher W., Ensen-Segal S. and Fehlberg M., ” ROCR: An Energy-Efficient Dynamic Wall-Climbing Robot”, IEEE Transaction on Mechatronics, Vol. 16, No. 5, pp. 897-906 (2011).

[7] Yaguchi H. and Sakuma S., ” Characteristic Improvement of a Magnetic Actuator Capable of Movement on a Magnetic Substance”, IEEE Trans. Magn., Vol. 52, No. 7, Article#: 10.1109/TMAG.2016.2533433 (2016).

[8] Yaguchi H., and Sakuma S., Vibration Actuator Capable of Movement on Magnetic Substance Based on New Motion Principle, Journal of Vibroengineering, Vol. 19, Issue 3, 2017, pp. 1494 - 1508.

[9] Yaguchi H., A new type of electromagnetically propelled vibration actuator for appearance inspection of iron structure, International Journal of GEOMATE, Vol. 20, No. 77, pp. 69 - 76 (2021).

7th Int. Conf. on Structure, Engineering & Environment (SEE),
Pattaya, Thailand, Nov.10-12, 2021, ISBN: 978-4-909106070 C3051

QUANTIFICATION OF SLOPE DEFORMATION BY FILTERING OF LASER POINT CLOUD OBTAINED BY MOBILE MAPPING SYSTEM

Naoto Samori[1], Satoshi Nishiyama[2], Koki Sakita[3], Michinari Fuziki[4] and Naoya Ono[5]
[1,2,3] Graduate school of environmental and life science, Okayama University, Japan,
[4,5] Kokusai Kogyo Co., Ltd, Japan

ABSTRACT

In recent years, the magnitude and frequency of heavy rains have been increasing worldwide. As a result, the possibility of slope failure has increased. It is important to inspect slopes to detect deformation, which is a sign of collapse. Slope inspections in Japan are mainly conducted through close visual inspections. The results could therefore vary depending on the inspecting engineer. In this study, we used a sensing device (mobile mapping system, MMS) that can acquire point cloud while the vehicle to which it is mounted is in motion, to quantitatively evaluate the shape of structures, and a differential analysis method that can extract slope deformations. We verified the effectiveness of these methods as an aid for slope inspection and as a screening method. Point clouds were acquired on two separate days for four slope frames. For the second measurement, deformed specimens were placed on the slope to verify that changes could be extracted. Because the acquired point cloud contained vegetation and noise generated during the measurement, it was filtered, and we analyzed the filtered point cloud. The deformation on the slope was determined by analyzing the unfiltered point clouds obtained on the two days. The results indicated that the filtering process was successful in removing vegetation and noise, and that the desired deformation could be clarified. This method is expected to play an important role as an aid in slope inspection.

Keywords: Slope, Point cloud, Mobile Mapping System, Iterative Closest Point, Inspection, Filtering

INTRODUCTION

In recent years, the magnitude and frequency of heavy rains have been increasing worldwide owing to the increasing size of typhoons and the occurrence of linear precipitation zones [1]. As a result, the possibility of slope failure has increased [2]. The collapse of slopes associated with transportation infrastructure can have a significant impact on the surrounding area, resulting in huge economic losses. Therefore, it is important to inspect slopes to detect deformations, which may become collapse. Slope inspections in Japan are mainly performed through close visual [3]. The results obtained by this method are qualitative and depend on the experience and skill of engineers. They vary depending on inspectors [4].

In recent years, surveying using laser scanners that can acquire point cloud data that can quantitatively evaluate the shape of structures has become widespread [5]. A point cloud is a set of points with three-dimensional coordinate information (X, Y, Z(H)) and color information (RGB) obtained from the camera image data. The acquired point cloud can be rotated and zoomed in and out to extract only the necessary points (Fig. 23). Because a point cloud consists of quantitative data, it can be used to quantitatively represent the deformation of a slope.

As most laser scanners are fixed and can only acquire a point cloud around the installation point, when measuring slopes constructed over a wide area, it is necessary to install the laser scanner several times to change the acquisition point. In this study, to acquire a point cloud, we used a mobile mapping system (MMS), a sensing device that can acquire the surrounding point cloud while the vehicle to which it is attached is in motion (Fig. 2).

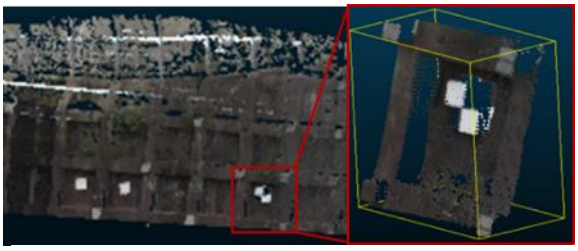


Fig. 1 Point cloud of the slope acquired by MMS.



Fig. 2 MMS acquiring a point cloud of a slope.

Using this point cloud, we attempt to extract the deformation at two time points using the differential analysis method. In this study, point clouds of a slope surface were acquired using MMS, and a differential analysis method was used to extract the slope deformation. The analysis was performed using the point cloud of the entire slope surface and the point cloud of the slope surface filtered to remove the point cloud of the part that could have interfered with the analysis. It was verified that this method could extract the deformation of the slope. Furthermore, we discuss the feasibility of using the method as a screening method for slope inspection as a method for quantitatively determining slope deformation.

MATERIAL AND METHOD

In this chapter, the equipment and methods used in this study and the slopes targeted are described.

Mobile Mapping System (MMS)

The MMS enables rapid acquisition of continuous high-precision laser point clouds while the vehicle to which it is mounted is in motion. The MMS system is divided into two parts: a navigation system that measures the vehicle's position and attitude, and a part that acquires information around the vehicle. The former has a global navigation satellite system (GPS), inertial measurement unit (IMU), and odometer, and the latter has a laser scanner and camera, which allows for the acquisition of accurate three-dimensional (3D) information on the road.

In general, the position of the acquired 3D laser point cloud is calculated using the position and attitude of the MMS vehicle. Therefore, the accuracy of the self-position of the vehicle has a significant influence on the accuracy of the acquired laser point cloud. The self-position of the MMS vehicle is determined by GNSS positioning based on the position of a fixed station, such as an electronic reference point. Currently, MMS is used for 3D topographic mapping of road facilities, road facility management, road maintenance management, and disaster risk management [6] (Fig. 3).

Differential Analysis Method

The differential analysis method is an application of the iterative closest point (ICP) algorithm (Fig. 4), which utilizes a scan matching algorithm called the simultaneous localization and mapping (SLAM) algorithm. SLAM simultaneously performs self-localization and map construction. Scan matching is a technique for aligning two scans (point clouds) to match their shapes [7]. The ICP algorithm performs the following processes. First, the point cloud is divided into a square grid called a mesh. It maps the closest points in the point cloud that are co-located

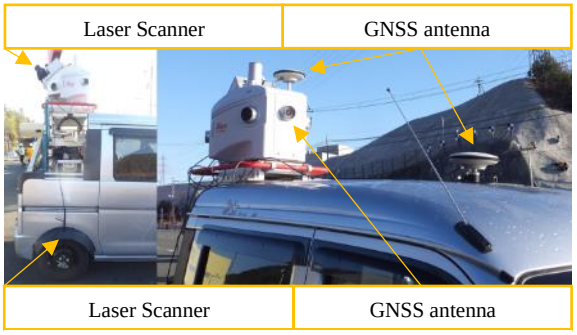


Fig. 3 Equipment installed in the MMS vehicle. These devices were used to acquire the coordinate and color data of point clouds while the vehicle is in motion.

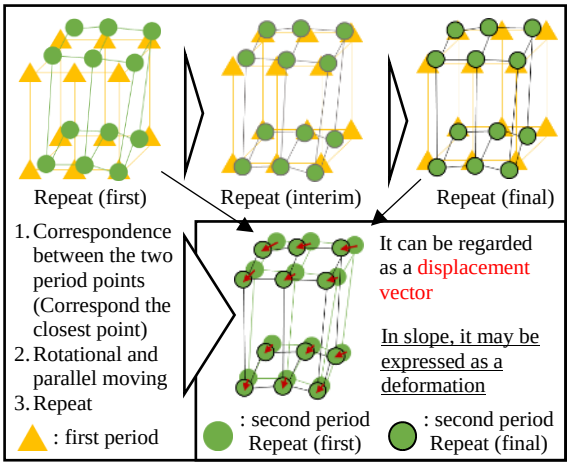


Fig. 4 Algorithm of the ICP method and differential analysis method.

with the mesh at two periods of the point cloud, and optimizes the position (rotation and translation moving) of the entire point cloud. The mapping and optimization are repeated, and the algorithm is terminated when the distance between each of the two point clouds is the closest. In the difference analysis method, the point cloud obtained after application of the ICP was utilized. We compared the coordinate values of the points that were associated with the two point clouds and created a vector. Then, we took the average value of the vectors in each mesh and regarded that value as the change in the mesh. This method is thought to be able to detect the change as a vector. The above equipment and methods were used to extract the slope deformations at the two time points.

Target Slope

The measurement target was a slope with a slope frame with a length and height of 70 m and 10 m, respectively, along National Highway No. 9 (Fig. 5). In 1987, the road was widened with cut-earth, and the section was sloped by the ground anchor method with

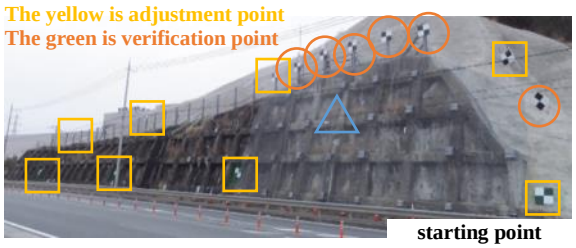


Fig. 5 Panoramic view of the target slope. The circles are verification point. The squares are adjustment point. The triangular is area where concrete has fallen.

slope frame. On May 1, 2016, the protective concrete of the anchor head fell, and a piece of concrete fell onto the roadway. After that, various investigations and observations were carried out, and it was judged that the slope around the anchor failure point would be displaced toward the starting point, although no significant expansion of deformation was observed. In this study, we use this slope as a potential landslide slope to verify whether the method can extract the signs of landslides. The target used for verification was placed on a slope. A total of 14 targets, each 0.7 m on a side, were set up. Eight of these points were placed around the entire slope as reference points for adjustment. The remaining six, which served as verification points, were placed on the slope at the starting point. A reference point for adjustment is a point that is used to correct the misalignment of an acquired point cloud.

The coordinates of the reference point for adjustment of the slope acquired by the MMS were converted to the coordinates acquired by the total station (TS) to correct the distortion of the entire point cloud [8]. The point clouds used in this verification were corrected. Verification points are used to verify the accuracy of the acquired point cloud. By comparing the difference between the coordinates acquired by TS and those acquired by MMS, one can determine whether the actual slope is fluctuating.

VERIFICATION METHOD

The first measurement was taken on January 13, 2018, and the second was taken on May 28, 2018. The MMS-equipped vehicle was driven at 50 km/h in the overtaking lane, where the distance from the target slope was approximately 12 m, and the point cloud of the slope was acquired (Fig. 6). In this study, slope frames were used. They were referred to as A1 or B3 using the letters and numbers shown in the diagram (Fig. 7). Verification was performed on four slope frames labelled A1 to A4 (the area enclosed in red). A test specimen of the deformation was placed in these slope frames, and the changes were checked.

This section describes the slope frames from A1 to A4 (Fig. 8). During the first period of measurement,

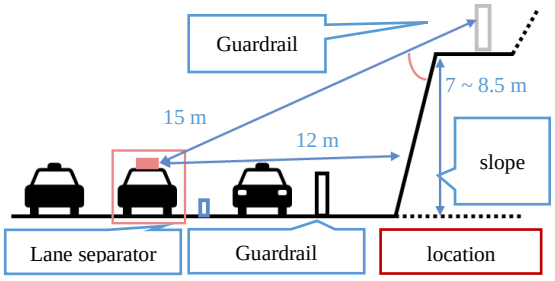


Fig. 6 Situation around the MMS vehicle during point cloud acquisition.

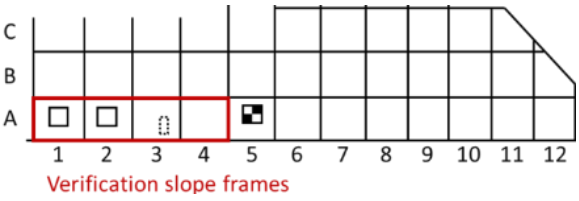


Fig. 7 Four verification slope frames and the name of each slope frame. The red frames are the unverified slope frames of A1–A4.

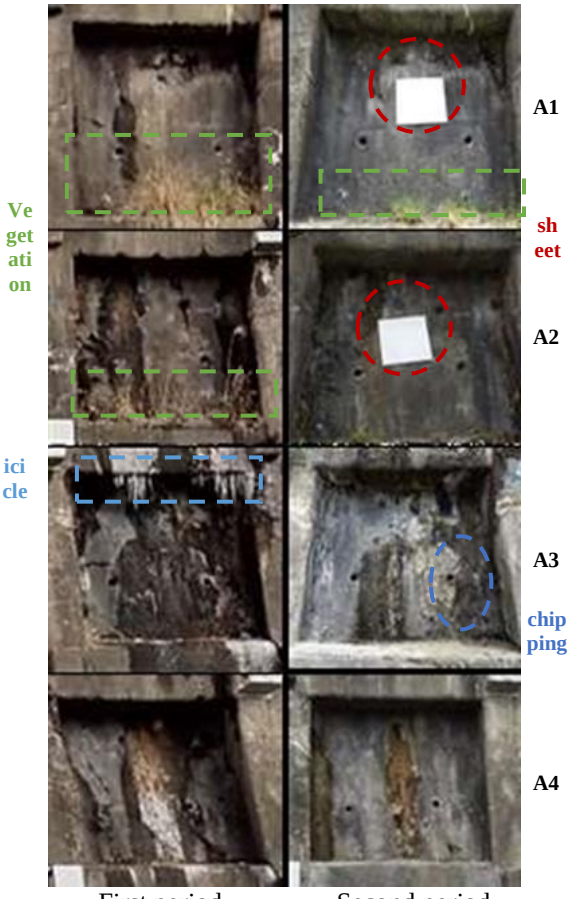


Fig. 8 Photograph of the slope frame with the specimen installed on the verification slopes.

nothing was placed on these slopes, and during the second period, the specimens described below were placed on the slopes. A 20-mm-thick sheet was placed on the slope of A1 to simulate a landslide warning flap, and a 10-mm-thick sheet was placed on A2. For the slope of A3, the surface of the slope was cut to a depth (chipping) of approximately 40 mm to provide a deformation that simulates a crack. No specimen of deformation was placed on the slope of A4. Changes were not observed when the second measurement was made. We expected to obtain the results shown (Fig. 9) when the frames were analyzed on the two days.

After analyzing the point clouds of the four normal frames, filtering was performed to remove a portion of the point cloud, and the analysis was performed again. In this verification, the vegetation on the slope and the noise that may have been generated during the measurement were removed from each slope point cloud. We compared and evaluated the results of the analysis of the point cloud before filtering with the results of the analysis of the point cloud after filtering.

In this verification, the point cloud before filtering and the point cloud after filtering were combined for the analysis. The difference analysis method was performed with a mesh size of 0.2.

VERIFICATION RESULTS AND DISCUSSION

The point density at the bottom of the slope (A level) acquired in this study was 1500–1800 points/m for both measurement time points.

The color scale show the deformation extraction results (Fig. 10 and Fig. 11). The magnitude of the change indicated by the color of the point cloud on the heat map (the closer the color approaches from blue to red, the larger the change). The value to the right of each normal frame is the change amount (unit : m). Changes of 0.01 m or less, which are measurement errors, and changes of 0.5 m or more, which are considered to be outliers, were excluded.

Analysis Results of Slope Frames Before Filtering

For slopes of A1 and A2, as shown in the installed specimens, deformation was observed at the point where the sheet was installed. Sheets of 20 mm and 10 mm were installed, but the amount of deformation could not be extracted. In addition, as vegetation existed at the bottom of the slope, they also showed changes for the two measurement periods. On the slope of A3, we can see that the slope surface was scraped at the point where the suspension was removed. In the slope frame of A4, there is general deformation, but no major change can be confirmed.

As described above, we were able to extract the expected deformations for each slope frame. On the other hand, owing to the vegetation on the slope and the noise during the measurement, many deformations were observed on the slope.

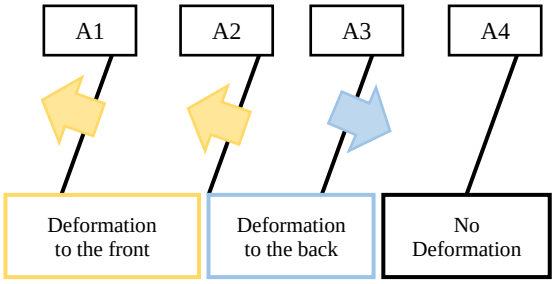


Fig. 9 Deformation predictions based on the analysis.

Analysis Results of Slope Frames After Filtering

Sheet deformation can be observed in the slopes of A1 and A2 (Fig. 11). The amount of deformation at the point where the sheets was installed could not be expressed in terms of the thicknesses of the sheets, which were 10 mm and 20 mm. The slope of A3 exhibits a suspension drop, and the slope of A4 exhibits no major deformation.

In addition to the results before filtering, we were able to extract the deformations. By filtering out the vegetation and noise, the number of large deformations outside the area where the specimen was installed was reduced, but the number of deformed areas was not reduced. This result represents the value of the change represented in a grid of 0.2 m per side, as shown by the mesh size.

Analysis Results of the Slope After Filtering.

The analysis was performed by filtering the slope near the place where the anchor head protection concrete fell (Fig. 12). In addition, the amount of deformation is larger on the upper slope. The amount of deformation is larger in the upper slopes. This is because the MMS vehicle is running on the ground surface, and the angle of the point cloud acquisition becomes larger at the upper part of the slope, resulting in larger point cloud errors. When we looked at the entire slope surface, we could not see any overhanging deformations as in A1, where the deformed specimen was installed. Therefore, it is confirmed that there is no fear of landslide on the target slope in this verification.

From the above analysis results of the slope frame and slope surface, it was confirmed that even without filtering, it was possible to extract deformations that simulated a 10 mm overhang.

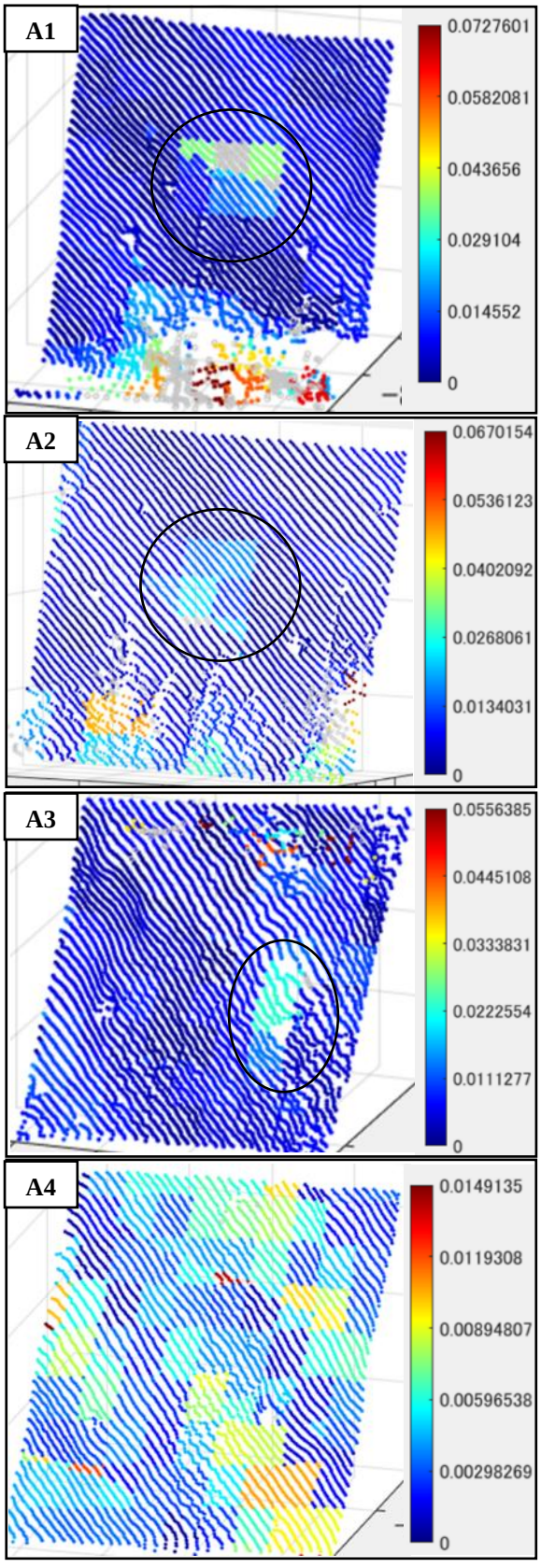


Fig. 10 Analysis results of the slope frames before filtering. The black circle is the location of the altered specimen. The unit of deformation is m.

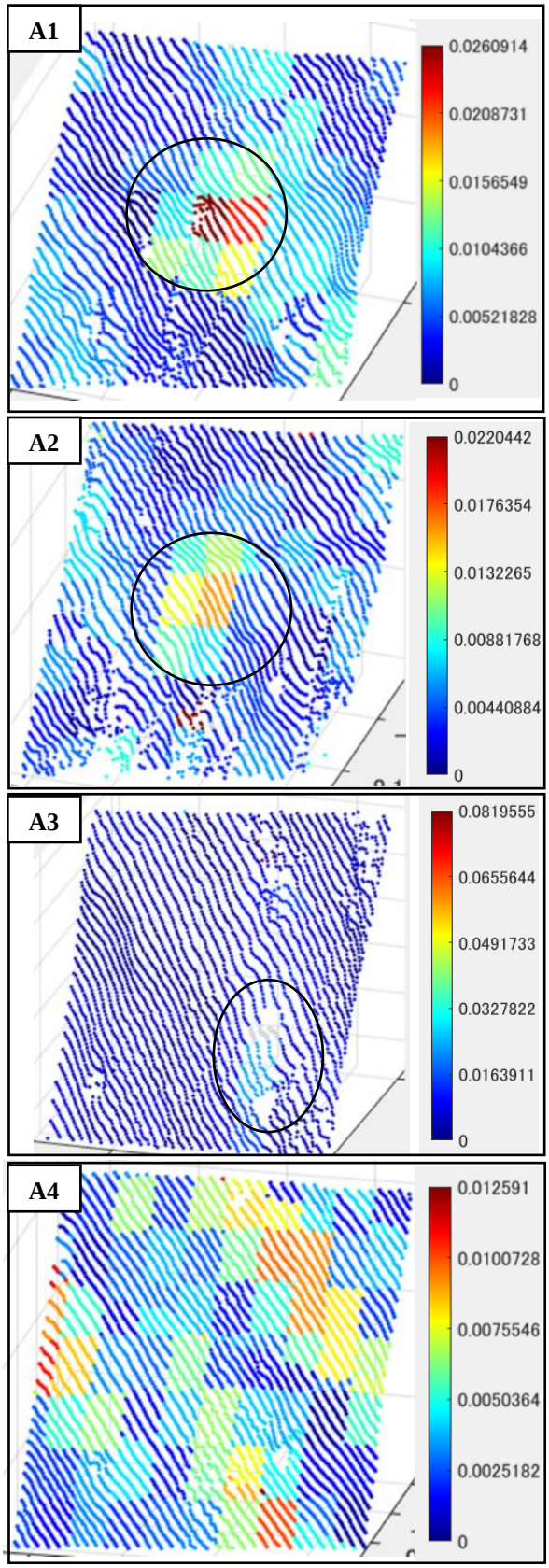


Fig. 11 Analysis results of the slope frames after filtering. The black circle is the location of the altered specimen. The unit of deformation is m.

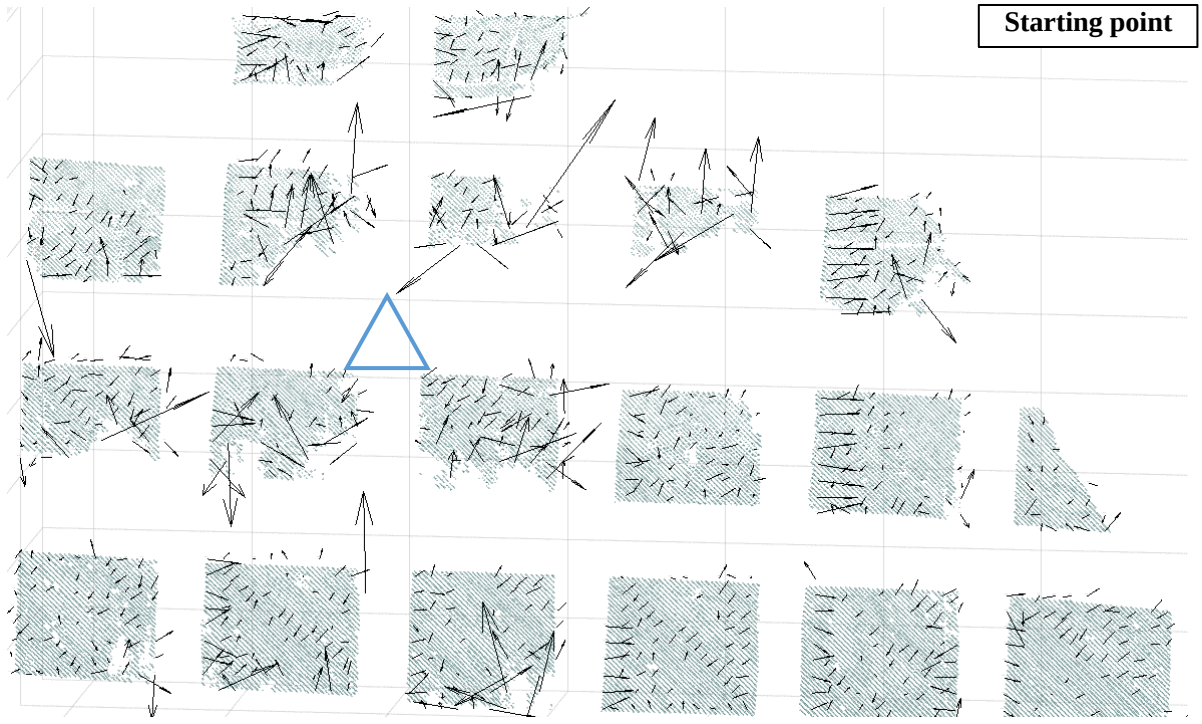


Fig. 12 Analysis results of the slope after filtering. Filtering is done to remove point clouds such as lawn and vegetation. The triangle in this figure shows the location where the anchor head protection concrete fell.

CONCLUSION

The conclusions of this study are as follows.We have verified that the MMS and the differential analysis method can be used to extract the slope deformation. As a result, we were able to extract some deformations. Among them, we were able to extract the deformation of a 10 mm thick sheet. Thus, the method of acquiring point clouds by MMS and extracting slope deformations using the differential analysis method was found to be an aid to inspection.

Therefore, this method can be effective for future maintenance by managing each frame of the slope. The future tasks are to improve the accuracy of the quantification of the deformation obtained as a result of the analysis and to reduce the number of deformation points.

ACKNOWLEDGEMENTS

We wish to thank Kokusai Kogyo Co., Ltd., West Japan Branch Public Project Consulting SBU.

REFERENCES

[1] Japan Meteorological Agency, Ministry of Land, Infrastructure, Transport and Tourism, “Climate Change Monitoring Report 2020”, https://www.data.jma.go.jp/cpdinfo/monitor/2020/pdf/ccmr2020_all.pdf, (refer to July 6, 2021)

[2] Ministry of Land, Infrastructure, Transport and Tourism Kinki Regional Development Bureau Kinki Regional Technical Office, “The Handbook for Road Slope Maintenance”, https://www.kkr.mlit.go.jp/kingi/database/26/01.pdf”, (refer to July 6, 2021)

[3] Ministry of Land, Infrastructure, Transport and Tourism, Bureau of Roads, "Guidelines for the Inspection of Road Geotechnical Structures", https://www.mlit.go.jp/road/sisaku/yobohozen/tenken/ty_h2908.pdf, (refer to June 2, 2021)

[4] Samori N., Nishiyama S., Sakita K., Fuziki M., Ono N., Quantitation of Slope Deformation Using Laser Point Cloud Data By Mobile Mapping System, 10th Int. Conf. Geotechnique, Const. Mat. Environ, Melbourne, Australia, 11-13 November 2020, pp. 641-646

[5] Tachibana K., Mano K., Shimamura H., Nishiyama S., The Application of Mobile Mapping System to River Embankment Measurement, Photogrammetry Remote Sensing, Vol. 4, Issue 54, 2015, pp. 166-177

[6] Ishikawa K., Road Survey Using Mapping System, J. Inst. Mech. Eng., Vol. 79, No. 5, 2013, pp. 397-400

[7] Besl P. J. and McKay N. D., A Method for Registration of 3-D Shapes, IEEE Pattern Anal. Mach. Intell.,Vol.14, No. 2, 2019, pp. 239-256

[8] Okamoto N., Sada T., Emori H., Verification of the Correction Effect of Mobile Mapping System with Marking Points at Different Traveling Speeds, Proc. Symposium Civil Eng. Informatics, Vol. 41, 2016, pp. 35-39

7th Int. Conf. on Structure, Engineering & Environment (SEE), Pattaya, Thailand, Nov.10-12, 2021, ISBN: 978-4-909106070 C3051

SOIL RETENTION TESTS FOR DETERMINING *DISPERSION* OF CLAYEY SOILS

Saad Farhan Ibrahim Alabdullah[1], Yar Hassab[2], Zaman Teama[3], Suha Aldahwi[4]

[1,4]Faculty of Engineering, Isra University, Amman, Jordan; [2,3]Baghdad University, Baghdad, Iraq

ABSTRACT

The basic nature of dispersive clays was firstly noticed by soil scientists and agricultural engineers of U.S. Dams, highway embankments and natural formations of high sodium dispersive clay were recorded as severely damaged by internal (tunnel) erosion of water flowing in the form of concentrated leaks within cracks. These dispersive clays which cannot be differentiated from ordinary erosion –resistant clays by the routine civil engineering tests erode rapidly in slow – moving (or even quite) water by individual colloidal particles going into suspension. In Iraq, few studies were interested in such types of soils that's why the present study takes into consideration dispersion of Baghdad clayey soil soils brought from three different Zones in Baghdad the first soil is brought from Al.Kazaliyah district Zone (A), This soil is classified as (CH) according to Unified Soil Classification System (USCS). The second soil is brought from Al.Qadisiya District Zone (B), it is classified as (CH), while the third soil is Al.Dora region Zone (C), it is classified as (CL) .The conventional testing and interpretation are found to be inapplicable to analyze and identify the Dispersion soils due to the existence of Na+. The effect of water content studied in two different tests for each soil; the pinhole test and soil retention test. The behavior of dispersive soil is not affected by water content but water content may change the time to failure. This fact gives a good and new indicator of the maximum time to failure.

Keywords: Dispersion, Retention, Soil Security, Pinhole

INTRODUCTION

Some natural clay soils disperse or deflocculates in the presence of relatively pure water and are, therefore, highly susceptible to erosion and piping. The tendency for dispersive erosion in a given soil depends upon such variables as the mineralogy and chemistry of the clay and dissolved salts in the soil pore water and in the eroding water. Standard tests for classifying for engineering purposes don't identify this property of a fine-grained soil [1].

Dispersive clay soils can be a problem for many practices or structures. In appearance, they are like normal clays that are stable and somewhat resistant to erosion, but in reality they can be highly erosive and subject to severe damage or failure. It is important to understand the nature of these soils and to be able to identify them so they can be treated or avoided [2].

Ordinary clays have a flocculated or aggregated structure because of the electrochemical attraction of the particles to each other and to water. This accounts for these soils' cohesive, nonerosive behavior. Dispersive clays have an imbalance in the electrochemical forces between particles. This imbalance causes the minute soil particles in a dispersive clay to be repulsed rather than attracted to one another. Consequently, dispersive clay particles tend to react as single-grained particles and not as an aggregated mass of particles. Dispersive clays are most easily eroded by water that is low in ion concentration, such as rain water. Runoff water has the opportunity to attain ions from land surface contact making it more in ionic balance with the dispersive clays and less erosive [3]. Typically, dispersive clays are low to medium plasticity and classify as CL in the Unified Soil Classification System (USCS).Other USCS classes that may contain dispersive clays are ML, CLML, and CH. Soils classifying as MH rarely contain dispersive clay fines [4-5].

The natural tendency of some fine-grained soils to deflocculated and disperse in the presence of water under certain circumstances creates problems when excessive removal and transport of the soil material cause erosion and piping. The dominant feature of such soils, which are generally identified as dispersive clays, is the presence of individual separate submicron-size particles or deflocculated small flocs where interaction between the particles or flocs is characterized by net repulsive forces [6-7].

Ordinary clays have a flocculated or aggregated structure because of the electrochemical attraction of the particles to each other and to water [8]. This accounts for these soils cohesive, nonerosive behavior [9]. Dispersive clays have an imbalance in the electrochemical forces between particles[10]. Consequently, dispersive clay particles tend to react as single-grained particles and not as an aggregated mass of particles. Dispersive clays are most easily eroded by water that is low in

ion concentration, such as rain water [11]. Runoff water has the opportunity to attain ions from land surface contact making it more in ionic balance with the dispersive clays and less erosive [12]. Typically, dispersive clays are low to medium plasticity and classify as CL in the Unified Soil Classification System (USCS).Other USCS classes that may contain dispersive clays are ML, CLML, and CH. Soils classifying as MH rarely contain dispersive clay fines Clay loss is common in bare soils subjected to rainfall or sprinkler irrigation. In a dispersed state, clays can be easily transported by the surface runoff [13] reported that anions interact with 1:1 clay minerals, where kaolinite is the most dominant clay mineral. In recent years, dispersion properties of the pure clay minerals under the influence of anions have received much attention [14]. However, the effect of anions on making surface charge more negative and dispersion properties of such kaolinite-rich soil clays has been neglected [15]. Organic anions originate from the exudation of plant roots and microorganisms, and the decomposition of soil organic matter is ubiquitous in soils, especially in the rhizosphere [16]. Inorganic anions such as sulfate and chloride may enter into soils through the degradation of soil organic matter and the application of mineral fertilizers. At acidic conditions, positively-charged edge sites of the clay minerals might favor the formation of edge-to-face structures, the so-called "card house", which facilitates coagulation. Adsorption of inorganic anions (SO_4^{2-} and Cl^-) onto these positively charged edge sites may counteract clay coagulation [17]. Similarly, low-molecular-weight organic anions such as acetate, oxalate and citrate can also associate with positively-charged edge sites and result in a decrease of the zeta potential of the clay particle [18] . However, effects of these organic anions on dispersion properties have not been studied systematically. Test tube experiments [19], have been utilized to study colloidal properties of clay minerals but this technique requires a highly concentrated suspension of clay. In contrast, dynamic light [19]

scattering is known as a suitable technique for investigating clay coagulation at lower clay concentrations[20] . Few comparable investigations on the dispersion of clay particles using both of these methods, however, have been reported. In the present work, a combination of dynamic light scattering and test tube experiments has been employed to investigate the dispersion state of the clay fraction under the influences of anions (Cl^-, SO_4^{2-}, acetate, oxalate and citrate) as a function of both pH and ionic strength. was also investigated to provide more information on the adsorption of anions on clay minerals [21].

In general, the net repulsion between particles occurs when double-layer repulsion overwhelms Van der Waals attraction. Although this phenomenon is by and large attributed to situations where an excessive amount of sodium ions exists in relation to the total salt concentration in the pore water, two other events can contribute to the development of net repulsion. These two other circumstances are [22]:

1. Low salt concentration in the pore fluid that results in desorption of the ions.
2. The presence of potential determining anions such as bicarbonates, carbonates, hydroxides, phosphates, etc.

The various tests used to aid in the identification and characterization of dispersive clays generally involve two basic parameters:

1. The force required detaching particles.
2. The floc size and double-layer interactions between various particles and floc, i.e., between various micro fabric units.

AIMS AND SCOPE OF THE STUDY

To analyze the effect of availability of dispersive characteristic and the property of soil of these zones in Baghdad city: Zone(A), Zone (B) and Zone (C).All samples are disturbed samples and taken from depth between 3.5 to 5m below the ground.

This study is concerned with the following:

1- Classifying soil of Baghdad Region as dispersive or not.
2- Introducing a new Laboratory test to identify the dispersion

DISPERSION OF CLAYEY SOILS

Clay is an assemblage of microscopic platelets formed by chemical decomposition of rock minerals. These platelets are held together by various forces. A high exchangeable sodium percentage (ESP) in the clay causes the platelets to be loosely bonded [3].

The sodium acts to increase the thickness of the diffused double water layer surrounding individual clay particles, and hence, to decrease the attractive force between the particles making it easier for individual particles to be detached from the mass [4]

The degree of dispersion is one of the best measures for predicting the erosion and piping potential of a clay material. But their own nature, dispersive clay particles being unable to form stable aggregates, are easily detached from other soil materials ,and thus, are easily suspended and carried away by the movement of water. Because of this characteristic; therefore, the presence of critical dispersion is sometimes easily detectable in the

field, particularly in areas of strong relief [5].

RECOGNITION OF DISPERSIVE CLAY

Clays are said to be dispersive when the interparticle forces are such that, there is a net repulsion between the clay platelets. Some efforts to recognize the dispersive properties of clay specimens utilize laboratory experimentation in which the field behavior is simulated to varying degrees, depending upon the type of the test performed. In other procedures, the chemical constituents of the soil are determined. These are extrapolated empirically to predict dispensability based on previous experience with similar materials. No single test provides results that have a satisfactory level of reliability. In general, a number of different types of tests have to be performed before a confident recognition of clay dispensability can be made [6].

The various methods used to identify the dispersive nature of clays can be categorized as (a) qualitative methods and (b) quantitative methods. The dispersion ratio tests developed by the Soil Conservation Service (SCS), the crumb test, and pinhole test developed by Sherard [22]. are qualitative in nature. The free swell test, the rotating cylinder, and the flume test provide quantitative criteria for the determination of the dispersive nature of clays. In 1977, predictive criteria based on the amount and type of clay, SAR (Sodium Adsorption Ratio), concentration of pore fluid and the shear stress required to initiate erosion have been proposed [7].

GEOLOGIC ORIGIN AND TOPOGRAPHY OF DISPERSIVE SOILS

The various origins of dispersive clay are not well known. Most of them encountered alluvial clays in the form of flood- plain deposit, slope wash, lake bed deposits, and loess deposits. In some areas, it has been found that clay stone and shales laid down as marine deposits, have the same pore water salts as dispersive clay, and their residual soils are dispersive.

Dispersive clays have been red, brown, gray (some nearly white), yellow, and all transitions among these. No black-colored soils, with obviously high organic content, have tested dispersive.

Many deposits of dispersive clay studied are situated in flat flood plains or gentle rolling topography with low relief and smooth, relatively flat slopes. Usually in areas where there are no manmade excavations or embankments in the area, there is little or no evidence from the surface appearance that the soil is highly erodible. The ground surface is covered with a thin layer of protective silty sand from which the dispersive clay particles have been removed, or has a protective layer of topsoil and vegetation.

Where steep topography and dispersive clay coexist, the peculiar ground surface topography is easily recognized by deep rapidly forming channels and tunnels.

It was indicated dispersive soils in nature, causing trouble with agriculture and hydraulic structures, were found most commonly in arid and semiarid regions and commonly had alkaline pore water (pH greater than about 8.5). Studies (including studies of damaged dams) have found many dispersive soils in humid areas, and many have pH well on the acid side [1].

LABORATORY TESTS

General

To distinguish the behavior and the properties of dispersion. Soil brought from three different locations in Baghdad City. Al.Kazalia (Zone A), Al.Qadisiyah (Zone B) and Al.Dora (Zone C) Zones. All disturbed samples taken from depth between 3.5m to 5.0m.below the ground surface transported to the soil Mechanics Laboratory, Civil Engineering department, collage of engineering Al.Mustansiria University [23] and [24] . The physical properties of Soil for each Zones are shown in Table 1.

Table 1 Physical properties of Soil used

specs	Soil From		
Tests	ZONE A	ZONE B	ZONE C
Specific gravity	2.68	2.654	2.70
Liquid limit %	56.0	51.5	34.4
Plasticity Index	30.5	28.1	17.2
Unified classification	CH	CH	CL
Sand size fraction %	6.4	8.5	11.7
Silt size fraction %	41.6	40.5	48.3
Clay size fraction %	52.0	51.0	39.0
Activity	0.58	0.55	0.44
Maximum dry unit wt.(kN/m^3)	14.9	17.4	17.25
Optimum Moisture Content %	21.0	17.05	16.4

There are four laboratory tests for identifying of dispersive clays and another one recommended here according to Tadinar [25].

The Soil Conservation Service (Double Hydrometer) Test

This test was developed by Volk [26] and has been widely used by the U.S. Soil Conservation Service. The particle size distribution is first measured by using the standard hydrometer test, in which the sample is dispersed in the hydrometer bath with strong mechanical agitation and a chemical dispersant. A second hydrometer test is made

without strong mechanical agitation and without chemical dispersant [8].
The degree of dispersion may be expressed by the ratio, degree of dispersion= percent finer than 0.005 mm without chemical dispersant or mechanical agitation divided by percent finer than 0.005 mm with chemical dispersant and mechanical agitation [7].

The Crumb Test

The crumb test first applied in Australia by Emerson [27] and later introduced to SCS engineers by Sherard [22], is useful as a quick field identification test by geologists during site investigation or by inspectors during construction [5]. The test was described in detail by [9]. The procedure consists of preparing a cubical specimen of a bout 15mm on a side, and is carefully placed in about 250ml of distilled water. As the soil crumb begins to hydrate, the tendency for colloidal sized particles to deflocculates and go into suspension is observed.
The crumb test, as originally developed by Emersion [27], was called the aggregate coherence test and had seven different categories of soil-water reactions. Sherard [8], later simplified the test by combining some soil-water reactions to use only four categories, or grades of soil dispersion. The crumb test has some limitations on its usefulness as an indicator of dispersive clay. A dispersive soil may sometimes give a nondispersive reaction in the crumb test. Soils containing kaolinite with known field dispersion problems have nondispersive in the crumb test. However, if the crumb test indicates dispersion, the soil is probably dispersive [9].

Chemical test

This is a standard test of the agricultural soil scientist described briefly as follows:

1. Soil is mixed with distilled water to a consistency near the Atterberg liquid limit.
2. A pore-water sample (saturation extract) is sucked out by vacuum using a filter.
3. The saturation extract is tested to determine the quantities of the four main metallic cations in solution (calcium, magnesium, sodium, and potassium) in milliequivalents per liter. The "total dissolved salts"(TDS) equals the total of these four cations, and "percent sodium" equals the quantity of sodium divided by the TDS, all in milliequivalents per liter [10].

Pinhole Test

The pinhole test had been developed for direct measurement of the dispersibility of compacted fine-grained soils in which water is caused to flow through a small hole punched in a specimen. The water running through samples of dispersive clay carries a cloudy colored suspension of colloidal particles, whereas the water running through erosion resistant clays is crystal clear [8]. Sherard classified the dispersive nature of soils under three categories. Dispersive soils are considered to fail under a flow caused by 50-mm head of distilled water. Intermediate soils erode slowly under 50 or 180-mm head of water, whereas nondispersive soils are supposed to produce no colloidal erosion under 380 or 1020-mm head of water [7].

Soil water Retention Test

This test has been developed and applied in Geo-mechanics laboratory of the Newsouth Wales Public Works Department since 1979. This test is based solely on water-retention properties and has the advantages of simplicity, reproducibility. The indication of multiple failure modes (not merely dispersive soil tunneling) the test involves filling a central hole in a compacted soil cylinder with water, and measuring the time taken to fail, the mode of failure is also recorded. This test is repeated for a limited range of compaction and soil moisture conditions to determine the optimal performance conditions and the range of acceptable behavior [11].
Depending on material type and compaction condition, failure occurs due the following:

1. Expansive cracking of the cylinder wall.
2. Hole (tunnel) formation.
3. Seepage through the cylinder base or wall.
4. Complete or partial collapse of the cylinder wall.

These classifications depend on the results proposed by [11].
A number of soil known to be dispersive, non-dispersive or marginal by other tests, together with (for some of dispersive soils) lime-modified samples of the same samples, were submitted to the test and to other test methods by [11].
These soils were also characterized by Sherard determinations.
Tadanier [28] showed that a more comprehensive soil security test for proposed water retaining structures can be operated quite simply and at least as effectively as other tests, this test yields information on dispersity, slaking and swelling (cracking) propensity simultaneously.
The test also defines the limits for soil moisture content or dry density which must be achieved to obtain a safe structure.

RESULT AND DISCUSSION

Soil Retention Test

Soils of Zone (A), (B) and (C) are submitted to the soil retention test. The characteristic failure time is defined quite analogously to maximum dry density as that failure time which is a maximum (T_{max}) in relation to variable moisture content. T_{max} can be determined from a plot of T_f (time to failue) versus moisture content.

In the persent test, T_{max} for each soil could be recognized in Figs. (1) (3) and (5) Ingles and wood proposed that any soil with T_{max}>420 $_{min}$ may be accepted without question. Obviously maximum time of failure for each soil in the present test is less than 420 minutes. For soil (A), T_{max} occurs on dry side of optimum, while T_{max} for soil (B) and soil (C) occurs at wet side of optimum. Therefore the last two samples are in the working range of 0-3% over optimum, on the other hand soil (A) could be considered as dangerous case and treatment may change it's result. With respect to air voids, it is safer to say simply that more than 6% is an acceptable (but remembering that less than 6% does not necessarily mean an acceptable resistance to failure, depending on soil type and moisture content). This absolute prohibition of air voids more than 6% was suggested by Ingles and wood, 164 within their study for defloculation phenomena in Earth Dams. This suggestion is applies here as it clear in figs. (2), (4) and (6).Tadainer [28] agreed that T_{max} more than 45 minutes could be accepted where adequate construction control is exercised. This seems okay with the results. T_{max} of soil (A) and soil (B) seems to be satisfied, while T_{max} of soil (C) is less than 45 and treatment may change its results

.

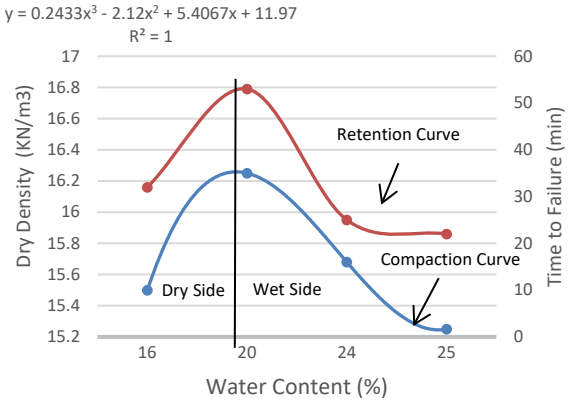


Fig. (1): Compaction and time to failure curves for zone (A)

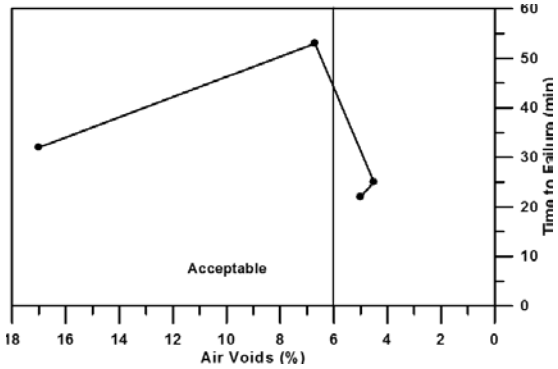


Fig. (2): Air voids versus time to failure curve for zone (A)

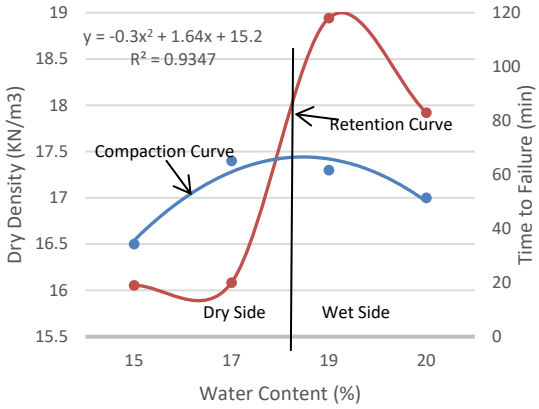


Fig. (3): Compaction and time to failure curves for zone (B)

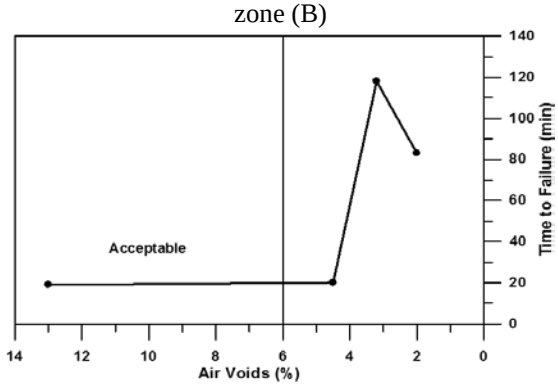


Fig. (4): Air voids versus time to failure curve for zone (B)

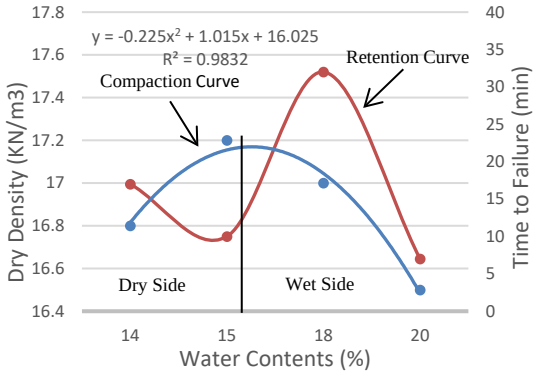


Fig. (5): Compaction and time to failure curves for zone (C)

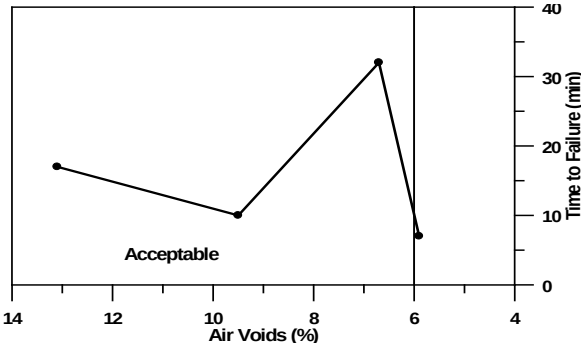


Fig. (6): Air voids versus time to failure curve for zone (C)

Pinhole Test

The test is applied to three soils Zone and the results shown that: Soil (B) shows high dispersion, while soil (A) and (C) are moderately dispersive**.**

INFLUENCE OF SAMPLE CURING AFTER COMPACTION

In the present investigation, pinhole test is applied to dispersive and intermediate dispersive samples of soils after ten days of curing in a compacted state. Samples are stored in a polythene bags and cured in a moist humid environment to prevent drying show. Results show that sample of grade ND4 has the same grade after ten days of curing, while sample of grade D2 gets better resistance to dispersion by having grade ND3 instead D2 after ten days of curing. Specimen(C) is of grade ND3 after ten days of curing instead of grade ND4**.**

INFLUENCE OF COMPACTION WATER CONTENT AND DENSITY

A series of pinhole test is applied to soils, dry of optimum and wet of optimum water content.

On dry side of optimum, soil (A) is intermediate to highly dispersive, while soil (B) and (C) are highly dispersive on dry side of optimum water content. Thus, the three soils are recorded as highly dispersive soil on dry side.

On wet side of optimum, soils (A) and (C) are intermediate to highly dispersive, while soil (B) is highly dispersive. Thus on wet side dry density and water content may increase the grade of depressiveness.

CONCLUSIONS

1. Dispersion clays are distinguished in some region of Baghdad city.
2. To evaluate soil due to dispersion, the soil security test should be carried out.
3. The limits of soil moisture content or dry density could be reduced the effect of dispersion on structure.
4. Curing modify the results of dispersion in Baghdad City.
5. Soil with high activity would be much erodible than other soils possess low activity.
6. Dispersion could be eliminated or mostly treated by adding 4% of $ca(OH)_2$.
7. Sampling and testing for dispersive soil should become a routine part of geotechnical investigation and testing program in areas where dispersive soil is known to be occur.
8. Adopting carrying out security test as main test provided for embankment

.

REFERENCES

[1] Sherard, J. L., Dunnigan, L. P., Decker, R. S.," Identification and Nature of Dispersive Soils," Journal of the Geotechnical Engineering Division, ASCE, Vol. 112, No.GT4, April 1976-b.

[2] Ghuman O. S., Allen, R. L., and McNeill, R. L., "Erosion, Corrective Maintenance, and Dispersive Clays," Symposium on Dispersive Clays, Related Piping and Erosion in Geotechnical Projects, ASTM STP 623, 1977.

[3] Chrorom M., Rengasamy, P., 1995. Dispersion and zeta potential of pure clays as related to net particle charge under varying pH, electrolyte concentration and cation type. European Journal of Soil Science 46, 657–665.

[4] Heinzen, R. T., and Arulanandan, K., "Factors Influencing Dispersive Clays and Methods of Identification, " Symposium on Dispersive Clays, Related Piping and Erosion in Geotechnical Projects, ASTM STP 623, 1977.

[5] .Holthoff, H., Egelhaaf, S.U., Borkovec, M., Schurtenberger, P., Sticher, H., 1996. Coagulation rates of colloidal particles by simultaneous static and dynamic light scattering. Langmuir 12, 5541–5549.

[6] Lagaly, G., Schulz, O., Ziemehl, R., 1997. Dispersionen und Emulsionen: Eine Einführung in die Kolloidik feinverteilter Stoffe einschließlich der Tonminerale. Steinkopff Verlag, Darmstadt.

[7] Sherard, J. L., Dunnigan, L. P., Decker, R. S., and Steel, E. F., "Pinhole Test for Identifying Dispersive Soils," Journal of the Geotechnical Engineering Division, ASCE, Vol. 102, No.GT1, January 1976-a.

[8] Mori, Y., Togashi, K., Nakamura, K., 2001. Colloidal properties of synthetic hectorite clay dispersion measured by dynamic light scattering and small angle X-ray scattering. Advanced Powder Technology 12, 45–59.

[9] Yong, R. N., Sethi, A. J., Ludwig, H. P., and Jorgensen, M. A., "Interparticle Action and Rheology of Dispersive Clays,"Journal of the Geotechnical Engineering Division, Vol. 105, No. GT 10, October 1979.

[10] Obut, A., 2005. Sedimentation characteristics of kaolin and bentonite in concentrated solutions. Acta Montanistica Slovaca 10, 145–150.

[11] Schmidt, C.U., Lagaly, G., 1999. Surface modification of bentonites: I. Betaine montmorillonites and their rheological and colloidal properties. Clay Minerals 34, 447–458.

[12] USBR "Procedure for Determining Dispersibility of Clayey Soils by the Crumb Test Method," 1984-a.

[13] Sherard, J. L., and Decker, R. S., eds. , " Dispersive Clays, Related Piping and Erosion in Geotechnical Projects," ASTM STP 623, 1977.

[14] Murphy, E.M., Zachara, J.M., 1995. The role of sorbed humic substances on the distribution of organic and inorganic contaminants in groundwater. Geoderma 67, 103–124.

[15] Penner, D., Lagaly, G., 2001. Influence of anions on the rheological properties of clay mineral dispersions. Applied Clay Science 19, 131–142.

[16] Strobel, B.W., 2001. Influence of vegetation on low-molecular-weight carboxylic acids in soil solution — a review. Geoderma 99, 169–198.

[17] Nguyen, N.M., Dultz, S., Kasbohm, J., Le, D., 2009. Clay dispersion and its relation to surface charge in a paddy soil of the Red River Delta, Vietnam. Nutrition and Soil Science 172, 477–486.

[18] Xu, R., Li, C., Ji, G., 2004. Effect of low-molecular-weight organic anions on electro kinetic properties of variable charge soils. Journal of Colloid and Interface Science 277, 243–247.

[19] Ketzschmar, R., Holthoff, H., Sticher, H., 1998. Influence of pH and humic acid on coagulation kinetics of kaolinite: a dynamic light scattering study. Journal of Colloid and Interface Science 202, 95–103.

[20] Ryker, N. L., "Encountering Dispersive Clays on Soil Conservation Service Projects in Oklahoma," Symposium on Dispersive Clays, Related Piping and Erosion in Geotechnical Projects, ASTM STP 623, 1977.

[21] Wagener, F. V., Harmse, H. J., Stone, P., and Ellis, W., "Chemical Treatment of a Dispersive Clay Reservoir, "Proceedings of the Tenth International Conference on Soil Mechanics and Foundation Engineering, Stockholm, Vol. 3, 1981.

[22] Sherard, J. L., Decker, R. S., and Ryker, N. L., "Piping in Earth Dams of Dispersive Clay," Proceedings of the Specially Conference on Performance of Earth and Earth-Supported Structures, Vol.1, Part 1, 1972.

[23] Ibrahim, Saad F., Gandhi G. Sofia, and Zaman T. Teama. 2014. An Approach in Study Behavior of Sand Dunes to Use as a Subgrade in Pave Road under. Congress on Technical Advancement, ASCE 2017

[24] Ibrahim, Saad F., Gandhi G. Sofia, and Zaman T. Teama. Evaluation of Using Geosynthetic Material and the Process of Grouting to Improve Pavement Performance over Sand Dunes Subgrade, International Conference on Transportation and Development 2016, ASCE. https://doi.org/10.1061/9780784479926.078

[25] Frenkel, H., Fey, M.V., Levy, G.J., 1992. Organic and inorganic anion effects on reference and soil clay critical flocculation concentration. Soil Science Society of America Journal 56, 1762–1766.

[26] Volk, G. M. 1937. Method of determination of degree of dispersion of the clay fraction of soils. Proceedings Soil Science Society of America 2: 561-567

[27] W.W. Emerson, A classification of soil aggregates based on their coherence in water, Australian Journal of Soil Research, 2 (1967), 211-217.

[28] Tadanier, R. and Ingles, O. G., "Soil Security Test for Water Retaining Structures", Journal of the Geotechnical Engineering Division, Vol. 111, No. 3, March 1985.

7th Int. Conf. on Structure, Engineering & Environment (SEE), Pattaya, Thailand, Nov.10-12, 2021, ISBN: 978-4-909106070 C3051

STUDY ON SURFACE PREFORMANCE OF CONCRETE CONSTRUCTED BY PRECAST METHOD AND ON-SITE METHOD

Yasuhide Mochida[1], Hiroshi Sakata[2] and Hu Shaobo[3]
[1]Ritsumeikan University, Japan
[2]KENKEN Co.,Ltd., Japan
[3]Graduate School of Science and Engineering, Ritsumeikan University, Japan

ABSTRACT

Compared to on-site concrete, precast concrete can be cured under strict control in a stable environment, and can be constructed with higher strength and low slump. As a result, it is possible to achieve high precision and high quality, which is also effective for maintenance. This study focuses on improving the solid performance of the surface of the precast method to prevent them. Through non-destructive testing, the surface performance is quantitatively evaluated by comparison with the on-site method. It is hoped that this content will be useful in future efforts to extend the life of buildings by the precast method.

Keywords: Concrete Surface Performance, Precast Concrete, Surface Water Content Test, Surface Air Permeability Test, Surface Water Absorption Test, Electrical Resistivity Test

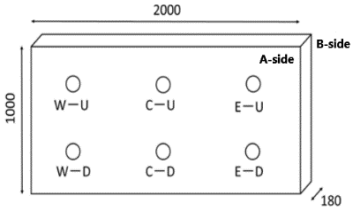
INTRODUCTION

One of the measures against the chronic shortage of construction workers in recent years is the utilization of the Precast Concrete method (Hereinafter, it is abbreviated as the PCa method.) as a method for improving the productivity of site operation in Japan.

On the other hand, against the background of the global environmental problems, one of the energy-saving efforts during construction and maintenance is the utilization of the PCa method. In this study we focus on improving the density performance of the surface layer of the PCa method in order to prevent neutralization and to quantitatively evaluate the surface layer performance through non-destructive inspection compared to the conventional method. We hope that this research will be useful for future efforts to extend the life of RC buildings by the PCa method.

Table.1 Blend of concrete and compressive strength test

Specimen Name	Nominal Strength	FC	Slump	Aair-Volume	W/C	Unit Weight(kg/m2)					Average Compressive Strength
	(N/mm²)	(N/mm²)	(cm)	(%)	(%)	Water	Cement	Fine Aggregate	Course Aggregate	Admixture	(N/mm²)
Conventional 24	27	24	19.5	5.7	53	184	374	914	844	3.47	35.8
Conventional 36	40	36	20	4.3	41	174	422	795	926	3.59	46.4
PCa36	—	36	10.5	1.7	39	165	423	776	1051	2.33	42.2
PCa50	—	50	10	2	35	165	471	739	1046	3.06	55.8
PCa60	—	60	14	1.4	30	165	550	710	1005	3.3	63.2



W：West side of the specimen
C：Central of the specimen
E：East side of the specimen
U：Upper part of the specimens
D：Down part of the specimens
Unit：mm
A-side：Bed side of PCa method (South side) and the south side of conventional method
B-side：Trowel finished surface of PCa (North side) and North side of conventional method

Fig.1 Shape and measurement position of the specimens

OUTLINE OF THE SPECIMENS

Specimens type, material, and measurement position

As shown in Table 1, the blend of concrete and the results of the compressive strength testing. Fig 1. shows the shape and measurement position of the specimens.

The types of test specimens are the design standard strength (Fc) used in standard buildings, With the PCa method, three types of Portland cement and early strengthening Portland cement are used: 36, 50, 60 N/mm^2. With the conventional method, Portland cement of 24 and 36 N/mm^2 are used. The compressive strength test results show that, with the standard cured PCa method cured for 7 days, and the average value of three test body with conventional method cured for 28 days, the average compressive strength of all the test specimens moderately satisfied the specified design strength.

The shape of the test specimens was 2000mm in width, 1000mm in height, 180 mm in thickness, 40 mm in cover thickness, and 200 pitch double wall reinforcement of D10, and all the test specimens were made of reinforced concrete and had the same shape. The measurement positions were divided into two vertically and three horizontally on both sides of each test piece, each of the grid which was near the center, and a total of 12 measurements were performed on both sides of 6 points on one side. Formwork joints, spacers, and the concrete layered area of the conventional method of the 12 points were measured at almost the same points in each test. The names of

these measurements position for the PCa method has A- side as the bed surface and the B-side as the trowel finished surface. While for the conventional method the south side is the A-side and the north side is the B-side. The vertical direction is U for the top, D for the bottom, W for the west, C for the center, and E for the east in the horizontal direction.

Specimen construction time and construction method

The PCa method uses a flat steel formwork specification. PCa36 was cast on November 21, 2018 and demolded on November 22, 2018. PCa50 was cast on 19th November, demolded on November 20, 2018. PCa60 was cast on November 20, 2018 and demolded on November 21, 2018. The concrete was cast horizontally smoothly with a hopper, and the surface (B-side) was finished with a trowel. The conventional construction method is to build a normal vertical wooden decorative formwork with normal wall specifications, and both conventional 24 and conventional 36 were formwork on October 29, 2018 and removed on November 5, 2018. And the vertical placement was formwork in 3 layers.

Curing method of the specimens.

Both the conventional method and the PCa method were cured according to standard building specifications. In the conventional method, the sheet was cured for one week and then demolded. After that, it was covered with a sheet and kept at all times without natural exposure. In the PCa method, the upper surface was troweled, and heat cured. The next day, it was covered with a sheet after demolding. The precast factory used in this research is a factory that mainly handles building materials and manufactures precast products of various sizes and shapes. Quality is ensured by centrally managing, which is using temperature sensors and control devices.

OUTLINE OF EXAMS

All the test specimens were measured 3 times at 6 points on each side for 12 points total. As for the test method, four types of non-destructive comparative test, which have been used in the concrete surface performance test in the previous research [1], were used. The four tests conducted were: surface water content test, surface air permeability test, surface water absorption test, and electrical resistivity test.

Measurement time

The first measurement age is according to the design standard strength development date of concrete, which is November 28, 2018 (7 days after casting) for PCa36, November 29, 2018 (10 days after casting) for PCa50, and November 30, 2018 (10 days after placement) for PCa60. Both the conventional 24 and conventional 36 were on November 27, 2018 (29 days after the placement), and after the concrete was placed, the PCa method was about age 9 days and the conventional method was about age 29 days. The second measurement age is about half a year after. The 3rd time of measurement age is about one year after.

Surface water content test

Using high-frequency capacitance type Handy Moisture Analyzer HI-520 to measure the surface water content. Since the thickness is 40 mm or more according to the specifications, after setting the thickness correction dial to 40 mm, set it in the specified position and lightly press it to detect. According to the past research [2], the recommended water content used as a guideline for management is less than 5.5%.

Surface air permeability test

Surface air permeability test[4][5][6] (Trent method: adopted from the developer's name), the concrete surface layer is evacuated by suction in the double chamber, then suction by the vacuum pump is stopped, and the time until the air pressure in the chamber recovers is primary. This is a method for evaluating the air permeability of surface concrete in one-dimensional direction. From the state where the air in the chamber was sucked up, the air permeability coefficient kt（$x10^{-16}$ m^2）, which indicates the measured of the change in the air pressure within a certain period of time.

The lower the kt (the smaller the amount of pressure change), the denser the surface concrete is evaluated. As a guideline for grading [3], 0.001 to 0.01 (excellent), 0.01 to 0.1 (good), 0.1 to 1 (general),1 to 10 (poor),10 to 100 (extremely inferior) were adopted.

Surface water absorption test

In the surface water absorption test [2] [5], water was injected by gravity using a tube installed at the bottom of a water absorption cup and a water injection tank to fill the upper edge of the cylinder with water. The injection is completed in about 10 seconds. After the water absorption cup is brought into close contact with the concrete surface and the water absorption cup is filled with water, the change of the water level in the cylinder is read and the water absorption rate is measured (ml/m^2/s) on the surface. After 600 seconds of completion of water injection, the water absorption

rate P_{600} (ml/m^2/s) is evaluated. As a guideline for grading[3], 0.25 or less (good), 0.25 to 0.5 (general), 0.5 or more (poor) were adopted.

Electrical resistivity test

For the measurement, a 4-point WENNER probe type Resipod was used. The method for finding the resistance is using four electrodes arranged at equal intervals pressed against the surface to be measured. An alternating current is applied from the outer current electrode, and electricity is applied using the measured value of the potential difference between the alternating current flowing to the measurement target and the potential difference electrode and the evaluation formula. The electrical resistivity ρ(kΩ ㎝) of concrete can be measured simply and completely non-destructively, but since it is easily affected by the contact state of the surface concrete, a small amount of water is applied to the contact part and repeated measurements are performed to measure a stable value. In addition, because of the influence of the reinforcing bars, the position was set to avoid the reinforcing bars near the measurement surface.

AGE AND TEST RESULTS

The results of various tests at the 1st, 2nd and 3rd age are summarized below.

Relationship between age and surface water content

Fig.2 shows the relationship between the age of the material and the surface water content. In all the test specimens, the water content of the surface layer decreased as the material age increased, and the rate of decrease decreased as the material age increased. The surface water content tended to decrease in the order of the A-side of PCa, the conventional, and the B-side of PCa at the age of the 3rd measurement.

Relationship between age and air permeability coefficient kt

Fig.3 shows the relationship between the age of the material and the air permeability coefficient kt. In all the test specimens, the air permeability coefficient kt increased as the material age increased, and the rate of increase decreased as the material age increased. The increase in the air permeability coefficient kt from 206 days to 373 days of PCa age is extremely small, but the increase in air permeability coefficient kt from 226 days to 393 days of the conventional material age is large for the conventional24 days and extremely small for the conventional36. The air permeability coefficient kt tended to decrease in the order of

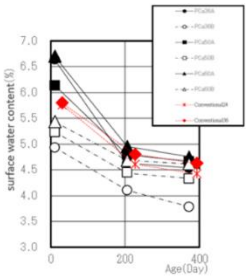


Fig.2 Relationship between age and surface water content

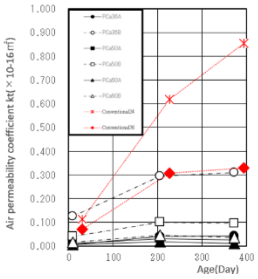


Fig.3 Relationship between age and air permeability coefficient kt

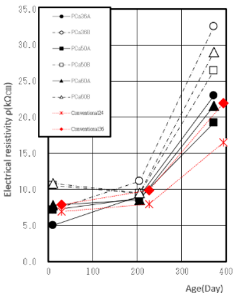


Fig.4 Relationship between age and water absorption rate P_{600}

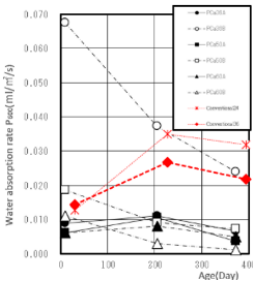


Fig.5 Relationship between age and electrical resistivity ρ

conventional, PCa B-side, and PCa A-side at all three ages. The grading is in the range of 0.01 to 0.1 (good) for the A-side of PCa, but 0.001 to 0.1 (excellent) is age 9 days for PCa36A and PCa50A and PCa60A, 0.1 to 1 (general) was all ages of conventional 24 and age 226 days and 393 days of conventional 36, and there is no grade above one (inferior or extremely inferior).

Relationship between age and water absorption rate P_{600}

Fig. 4 shows the relationship between the age of the material and the water absorption rate P_{600}.
For water absorption speed P_{600}, the A-side of PCa increased slightly from 9 to 206 days of age and decreased from 206 to 373 days of age. The conventional ones increased more than double from 29 days to 226 days and decreased slightly from 226 days to 393 days. On the B-side of PCa, the age decreases by about 1/2 from 9 days to 206 days, further decreased from 206 to 373 days, and decreased in a nearly linear state. The water absorption rate P_{600} showed a large difference between the A-side and the B-side of PCa at 9 days of age, the A-side had extremely small value and small variation, and the B-side had a large variation and large values. In all the grading results, the water absorption rate P_{600} was in the range of 0.25 or less (good), and the A-side of all PCa showed relativity small values.

Relationship between age and electrical resistivity ρ

Fig.5 shows the relationship between the age of the material and electrical resistivity ρ. The increase in electrical resistivity is extremely small from age 9 to 206 days of PCa and age 29 to 226 days of conventional method, but the electrical resistivity ρ

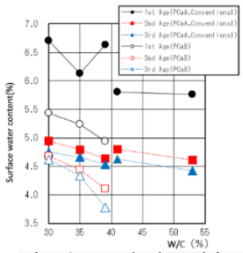


Fig.6 Relationship between W/C and surface water content

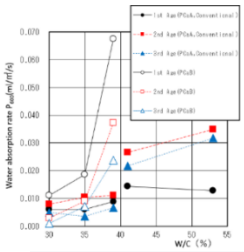


Fig.8 Relationship between W/C and water absorption rate P_{600}

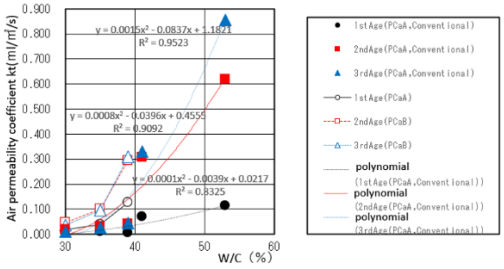


Fig.7 Relationship between W/C and air permeability coefficient kt

almost doubled when age 206 to 373 days of PCa A-side, and age 226 to 393 days of conventional. The increase in electrical resistivity ρ from age 206 to 373 days of PCa B-side was about threefold. The electrical resistivity ρ of PCa B-side was higher than others of all ages.

WATER-CEMENT RATIO (W/C) AND TEST RESULTS

There were 5 types of water-cement ratio (W/C) of the test specimens: 30% of PCa60, 35% of PCa50, 39% of PCa36, 41% of conventional 36, and 53% of conventional 24. It was organized based on the results of tests of 1st (age of 9 days of PCa A-side and age 29 days of conventional), and 2nd (age of 206 days of PCa A-side and age 226 days of conventional), and 3rd (age of 373 days of PCa A-side and age 393 days of conventional). Since there is tendency that the B-side of PCa is different to A-side of PCa and conventional one, the result of each age of the B-side of PCa are shown separately.

Relationship between water-cement ratio (W/C) and surface water content

Fig.6 shows the relationship between water-cement ratio (W/C) and surface water content. Apart from the A-side of the PCa36, the surface water content tends to decrease when the W/C increased from 30% to 53% at all ages. In all W/C, the surface water content decreases as age progresses. In particular, because the change of the age from the 1st test to the 2nd test, the decrease of surface water content is extremely large. The B-side of PCa was the same as above, and the surface water content at all ages and W/C was smaller than the A-side.

Relationship between water-cement ratio (W/C) and air permeability coefficient kt

Fig.7 shows the relationship between water-cement ratio (W/C) and air permeability coefficient kt. At all ages, when W/C increased from 30% to 53%, the air permeability coefficient kt also tended to increase. In all W/C, the air permeability coefficient kt increases with age. On the B-side of PCa, the air permeability coefficient kt was larger than the A-side of PCa at all ages and all W/C. Compared to the A-side of PCa36 with W/C=39%, the conventional 36 with W/C=41% showed an extremely large value. The air permeability coefficient kt for each age of PCa and the age of conventional can be evaluated by W/C by the following Eq. 1 as shown in Fig.24.

$$kt=k_1 \cdot W/C^2+k_2 \cdot W/C+k_3 \quad (1)$$

Kt：Air permeability coefficient (×10-16 ㎡)
W:Surface water content(%)
(1st age)K_1=0.0001,K_2=-0.0039, K_3=-0.0217
（R^2=-0.8325）
(2nd age)K_1=0.0008,K_2=-0.0396, K_3=-0.4555
（R^2=0.9092）
(3rd age)K_1=0.0015,K_2=-0.0837, K_3=-1.1821
（R^2=0.9523）

Relationship between water-cement ratio (W/C) and water absorption rate P_{600}

Fig.8 shows the relationship between water-cement ratio (W/C) and water absorption rate P_{600}. At all ages, when W/C increased from 30% to 53%, the water absorption rate P_{600} also tended to increase. With W/C=42% and 53%, the water absorption rate P_{600} of conventional one increased in the order of age of 1st,3rd, and 2nd. However, on the A-side of PCa with W/C=30%, 35%, and 39%, it increased in the order of ages of 3rd, 1st, and 2nd.On the B-side of PCa, it increas0de in the order of the ages of 3rd, 2nd , and 1st, and the 1st was extremely large. The water absorption rate P_{600} tended to increase remarkably in the conventional 36 with W/C=41% compared with the A-side of PCa36 with W/C=39%.

Relationship between water-cement ratio (W/C) and electrical resistivity ρ

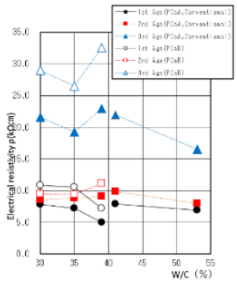


Fig.9 Relationship between W/C and electrical resistivity ρ

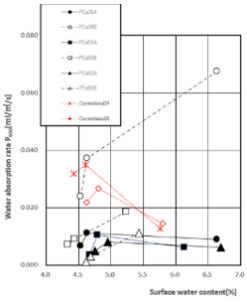


Fig.11 Relationship between surface water content and water absorption rate P_{600}

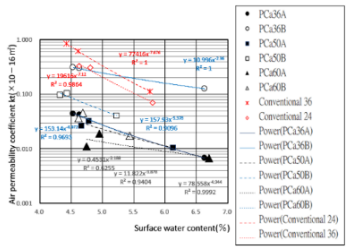


Fig.10 Relationship between surface water content and air permeability coefficient kt

Fig.9 shows the relationship between water-cement ratio (W/C) and electrical resistivity ρ. In all W/C, except for W/C=30% and W/C=35% on the B surface, the electrical resistivity ρ tends to increase with age, and in particular, it showed a large value due to variations in the 3rd age. For PCa and conventional, W/C had a tendency to decrease as electrical resistivity ρ increased. The electrical resistivity ρ on the B-side of PCa was larger than the A-side of PCa of all age and W/C.

SURFACE WATER CONTENT AND TEST RESULTS

Relationship between surface water content and air permeability coefficient kt

Fig.10 shows the relationship between surface water content and air permeability coefficient kt. As the surface water content increased, the air permeability coefficient kt tended to decrease. The air permeability coefficient kt is evaluated for each test specimens by the surface water content using the following Eq 2.

$kt=k_1 \cdot W^{k2}$ (2)

Kt：Air permeability coefficient (×10-16 ㎡)

W:Surface water content(%)

(PCa36A)K_1=78.558,K_2=-4.944（R^2=0.999）

(PCa50A)K_1=11.822,K_2=-3.878（R^2=0.9404）

(PCa60A)K_1=0.4531,K_2=-2.188（R^2=0.6255）

(Conventional24)K_1=77416,K2=-7.676（R^2=0.9992）

(Conventional36)K_1=19616,K2=-7.120（R^2=0.9864）

(PCa36B)K_1=10.996,K_2=-3.360 （R^2=1.0）

(PCa50B)K_1=157.93,K_2=-5.378 （R^2=0.9096）

(PCa60B)K_1=153.14,K_2=-4.972 （R^2=0.9693）

Relationship between surface water content and water absorption rate P_{600}

Fig.11 shows the relationship between surface water content and water absorption rate P_{600}. On the A-side of PCa, the water absorption rate P_{600} was concentrated at about 0.01 (ml/m²/s), and there was no effect on the increase in the surface water content, but on the B-side of PCa, an increase was observed in all specimens. The conventional one had no significant change observed when the surface water content was about 4.7% and when it reached about 5.8% the water absorption rate P_{600} decreased significantly.

Relationship between surface water content and electrical resistivity ρ

Fig.12 shows the relationship between surface water content and electrical resistivity ρ. In all specimens, the electrical resistivity ρ decreased as the surface water content increased. When the surface water content was in the range of 4.5% to 5.0%, the rate of decrease in the electrical resistivity was extremely large, but it was small when it was 5.0% or more. At the 2nd age, the surface water content was about 4.7(%) and the electrical resistivity was about 8 (kΩ ㎝). Unlike other tests, the A-side and B-side of PCa were close to each other.

AIR PERMEABILITY COEFFICIENT KT AND TEST RESULTS

Relationship between air permeability coefficient kt and water absorption rate P_{600}

Fig.13 shows relationship between air permeability coefficient kt and water absorption rate P_{600} at all ages. On the A-side of PCa, even if the air permeability coefficient kt fluctuates between 0.007 to 0.043 (x 10^{-16}m²), the water absorption rate P_{600} is about 0.01(ml/m²/s) and the change was small. On the B-side of PCa, the water absorption rate P_{600} decreased when the air permeability coefficient kt of PCa50B and PCa36B increased in the range of about 0.04 to 0.31(x 10^{-16}m²). For conventional ones, when the air permeability coefficient kt increased in the range of 0.07 to 0.86 (x 10^{-16}m²), the water absorption rate P_{600} also increased.

Relationship between air permeability coefficient kt

and electrical resistivity

Fig.14 shows the relationship between air permeability coefficient kt and electrical resistivity. It was graded as "good" for the air permeability coefficient kt as all the A-side and B-side of PCa was in the range of about 0.007 to 0.001 ($x10^{-16}m^2$), and the electrical resistivity was in the range of about 5 to 30 (kΩ cm). For conventional ones, it was graded as "normal" for the air permeability coefficient kt was in range of about 0.07 to 1.000 ($x10^{-16}m^2$), and the electrical resistivity was in the range of about 7 to 20 (kΩ cm).

CONCLUSIONS

From the results of various tests from age 1 week to 1 year, the following contents were clarified. The coefficient variation in the test result of the PCa method tends to be smaller compare to the conventional method. Regarding the surface water content, the one-week age bed surface of the PCa method is larger than conventional method, and it is about the same at the age of half a year. In the surface air permeability test, the bed surface of the PCa method is good, some are excellent, and the conventional method is average. In the surface water absorption test, all the results were good. The air permeability coefficient kt for each age could be evaluated quantitively by W/C. The air permeability coefficient kt for each test specimens could be evaluated quantitively by the surface water content.

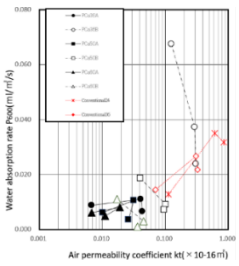


Fig.13 Relationship between air permeability coefficient kt and water absorption rate P_{600}

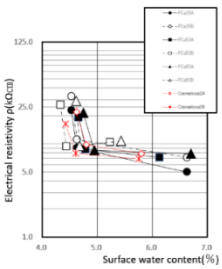


Fig.12 Relationship between surface water content and electrical resistivity ρ

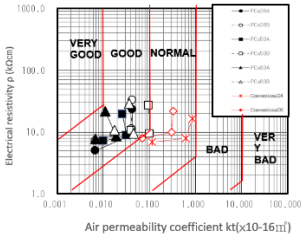


Fig.14 Relationship between air permeability coefficient kt and electrical resistivity ρ

REFERENCES

[1] Japan Society of Civil Engineers: Concrete Quality and Durability Performance Verification System Research Subcommittee Results Report (335 Committee) Results Report and Symposium Lecture Summary, Concrete Technology Series, No. 80,2008.

[2]Lin Heyan, Hosoda Jun: Development of surface water absorption test method applicable to concrete structures, Annual Proceedings of Concrete Engineering, Vol.33,No.1, 1769-1774, 2011.7.

[3]Ministry of Land Tohoku Regional Development: Guidance for ensuring the quality of concrete structures (draft), 21-28, 2015.12.

[4]Zou Shige, Michihiko Hironaga: Propose of a non-destructive evaluation method for concrete surface layer quality considering the water content dependence of the air permeability coefficient, Cement and Concrete Papers, Vol.65, No.1, 2011.

[5]Reiji Komatsu: Surface Quality Evaluation Method for Concrete Structures-How to Use Surface Water Absorption Test and Attention-Series "Quality Assurance Story for Concrete Structures" 10, Road Structure Journal NET, 2016.

[6]Keiichi Imamoto: Current Status and Issues of Surface Air Permeation Test Method for Concrete, Annual Papers on Concrete Engineering Vol.53, No.7,2015.7.

7th Int. Conf. on Structure, Engineering & Environment (SEE), Pattaya, Thailand, Nov.10-12, 2021, ISBN: 978-4-909106070 C3051

IMPROVEMENT IN MECHANICAL PROPERTIES OF FLEXIBLE POLY(L-LACTIDE)-*b*-POLYETHYLENE GLYCOL-*b*-POLY(L-LACTIDE) BIOPLASTIC BY MELT BLENDING WITH BORON NITRIDE

Theeraphol Phromsopha and Yodthong Baimark

Biodegradable Polymers Research Unit, Department of Chemistry and Center of Excellence for Innovation in Chemistry, Faculty of Science, Mahasarakham University, Mahasarakham 44150, Thailand

ABSTRACT

Poly(L-lactide)-*b*-polyethylene glycol-*b*-poly(L-lactide) triblock copolymer (PLLA-PEG-PLLA)/boron nitride (BN) composites with BN contents of 1, 2 and 4 wt.% were prepared by melt blending. Scanning electron microscopy (SEM), thermogravimetric analysis (TGA), differential scanning calorimetry (DSC) and tensile testing were carried out to characterize the phase morphologies, thermal properties and mechanical properties of composite films. The BN particles showed good distribution and dispersion throughout the film matrices as observed from SEM. DSC analysis showed that increasing crystallinity content and decreasing half crystallization-time of PLLA-PEG-PLLA/BN composites were obtained when the BN content was increased. The ultimate tensile stress significantly increased and strain at break steadily decreased with an increase in the BN content. These results showed that the BN particles enhanced crystallizability and mechanical properties of PLLA-PEG-PLLA.

Keywords: Bioplastics, Polymer composites, Poly(L-lactide), Block copolymer, Boron nitride

INTRODUCTION

Poly(L-lactic acid) or poly(L-lactide) (PLLA) is a potential bioplastic to replace petroleum-based plastics because of its biocompatibility, biodegradability, bio-renewability, high mechanical strength and good processability [1–3]. Unfortunately, slow crystallization and poor flexibility of PLLA limit some of its applications [4,5]. PLLA-*b*-polyethylene glycol-*b*-PLLA triblock copolymers (PLLA-PEG-PLLA) were found to be more flexible than PLLA because of PEG middle-blocks enhanced plasticizing effect for PLLA end-blocks [6, 7]. PLLA-PEG-PLLA have been widely investigated for use in medical and pharmaceutical applications due to their being biocompatible and biodegradable polymers [8–10]. However, PLLA-PEG-PLLA has lower mechanical strength than PLLA [7].

Previous studies reported that various fillers including natural fibers [11], cellulose nanocrystals [12], nanoclay [13] and boron nitride [14] can be used to improve mechanical strength of PLLA. Among these fillers, boron nitride is one of the most interesting reinforcing fillers because of its good thermal and chemical stability, low reactivity and high mechanical-strength [15, 16]. Boron nitride has used as a reinforcing filler for PLLA [14]. Moreover, boron nitride powder can accelerate crystallization of PLLA [16] and poly(3-hydroxybutyrate) (PHB) [17] by acting as a heterogeneous nucleating agent to increase their crystallinity content.

To the best of our knowledge, there have not been any reports on the effect of boron nitride on crystallization behavior and mechanical properties of PLLA-PEG-PLLA. In this study, we aimed to improve the crystallization and mechanical strength of PLLA-PEG-PLLA by blending with boron nitride.

MATERIALS AND METHODS

Materials

Chain-extended PLLA-PEG-PLLA were synthesized through ring-opening polymerization in the presence of 2 phr Joncryl® ADR4368 as described in our previous work [18]. Melt flow index of this PLLA-PEG-PLLA at 190˚C under 2.16 kg load was 31 g/10 min. Boron nitride (BN) powder with particle size of 1 μm was obtained from Qinghe Chuangya Welding Material Co., Ltd. (China) was used without further modification. The morphology of BN particles is shown in Fig. 1.

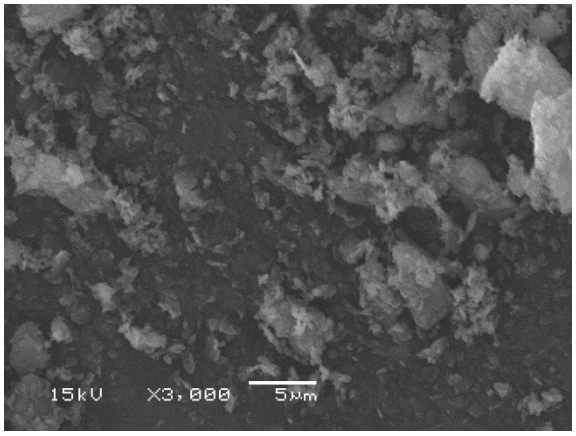


Fig. 1 SEM images of BN particles. Bar scale = 5 μm.

Preparation of PLLA-PEG-PLLA/BN Composites

PLLA-PEG-PLLA and BN were dried in vacuo at 50˚C overnight to remove moisture before melt blending using a Rheomix batch mixer (HAAKE Polylab OS). Melt blending was performed at 190˚C with a rotor speed of 100 rpm for 4 min. PLLA-PEG-PLLA composites with different BN contents (1, 2 and 4 wt.%) were prepared. PLLA-PEG-PLLA without BN was also prepared by the same method for comparison.

The composites were dried in vacuo at 50˚C overnight before film formation with a compression moulding machine (Auto CH Carver). The biocomposites were heated at 200˚C for 3 min without any force before compressing under 5 ton load for 1 min. The obtained films were 100 × 100 mm in size and were quickly cooled to 25˚C with water flow for 1 min.

Characterization of PLLA-PEG-PLLA/BN Composites

Thermal transition properties of the composites were determined using a differential scanning calorimeter (DSC, Perkin-Elmer Pyris Diamond) under nitrogen gas flow. The composites were first heated at 200 ˚C for 3 min to remove thermal history, then fast quenched before heating from 0 to 200 ˚C at a rate of 10 ˚C/min to detect glass transition (T_g), cold crystallization (T_{cc}) and melting (T_m) temperatures as well as enthalpies of melting (ΔH_m) and cold crystallization (ΔH_{cc}). The degree of crystallinity (X_c) of the PLLA phases was calculated from Eq. (1).

$$X_C(\%) = [(\Delta H_m - \Delta H_{CC}) / (93.7 \times W_{PLLA})] \times 100 \quad (1)$$

where the 93.7 J/g is the ΔH_m for 100%X_c PLLA [19]. W_{PLLA} is the PLLA weight-fraction of the composites calculated from PLLA fraction (PLLA-PEG-PLLA = 0.83 obtained from ^{1}H-NMR [7]) and the BN content.

For half crystallization-time ($t_{1/2}$) determination, the composites were first heated at 200˚C for 3 min to completely erase thermal history, then quenched to 120˚C at a rate of 50˚C/min and then isothermal scanned at 120˚C until the completion of crystallization [20]. The $t_{1/2}$ is the time required to achieve half of the final crystallinity.

Thermal decomposition behaviors of the composites were determined using a thermogravimetric analyzer (TGA, TA-Instrument SDT Q600). TGA was carried out in the range of 50 to 800˚C at a heating rate of 20˚C/min under a nitrogen gas flow.

Phase morphology of the composite films was observed using a scanning electron microscope (SEM, JEOL JSM-6460LV). The composite films were cryogenically fractured after immersing in liquid nitrogen and were sputter coated with gold to avoid charging before scanning at an acceleration voltage of 15 kV.

Tensile properties of the composite films were measured using an universal mechanical testing machine (Liyi Environmental Technology LY-1066B) with a load cell of 100 kg, a crosshead speed of 50 mm/min and a gauge length of 50 mm. The film sizes were 100 mm × 10 mm. The averaged tensile properties were obtained from at least five measurements.

RESULTS AND DISCUSSION

Thermal Transition Properties

DSC has been widely used to determine the thermal transition properties of PLLA-based composites [1, 16]. The DSC heating curves of pure PLLA-PEG-PLLA and their composites are shown in Fig. 2 and DSC results are reported in Table 1. It was found that the T_g of PLLA-PEG-PLLA/BN composites was in range 27–29˚C, indicating that the T_g was not significantly changed by the addition of BN.

BN blending caused shifting of T_{cc} peaks of PLLA-PEG-PLLA to lower temperature. This indicates that the BN enhanced stronger PLLA crystallizability by acting as a heterogeneous nucleating agent [16]. Therefore, the X_c of composites increased as the BN content increased. The T_m peaks of composite did not change with the BN content.

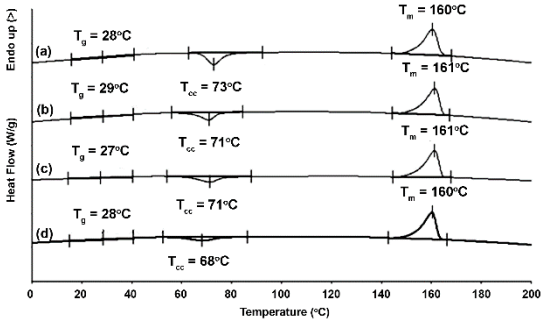


Fig. 2 DSC heating curves of PLLA-PEG-PLLA/BN composites (a) without BN and with BN contents of (b) 1, (c) 2 and (d) 4 wt.%.

Isothermal crystallization of pure PLLA-PEG-PLLA and its composites was observed from DSC exothermic curves as shown in Fig. 3. The $t_{1/2}$ values are also reported in Table 1 where it is seen that they significantly decreased as the BN content increased. This confirms that the addition of BN can accelerate crystallization of PLLA blocks corresponding to non-isothermal crystallization results as described above.

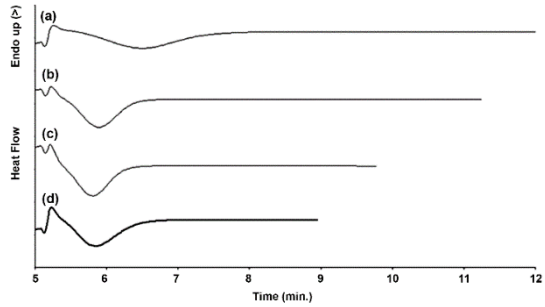


Fig. 3 DSC exothermic curves for the isothermal crystallization temperature at 120ºC of PLLA-PEG-PLLA/BN composites (a) without BN and with BN contents of (b) 1, (c) 2 and (d) 4 wt.%.

Table 1 DSC results of PLLA-PEG-PLLA/BN composites

BN (wt.%)	T_g [a] (˚C)	T_{cc} [a] (˚C)	T_m [a] (˚C)	X_c [a] (%)	$t_{1/2}$ [b] (min)
-	28	73	160	23.7	1.8
1	29	71	161	30.3	1.0
2	27	71	161	30.0	0.9
4	28	68	160	35.0	0.8

[a] Obtained from DSC heating curves in Fig. 2; [b] Obtained from DSC exothermic curves in Fig. 3.

Thermal Decomposition Behaviors

The thermal-decomposition behavior of composites provides important information on the processing window for melt processing that was investigated from thermogravimetric (TG) curves as reported in Fig. 4.

The TG curves of pure PLLA-PEG-PLLA are shown in Fig. 4 (black line) indicating that it had two thermal-decomposition steps in ranges 250–350˚C and 350–450˚C assigned to thermal decompositions for PLLA and PEG blocks, respectively [18]. The addition of BN did not change thermal-decomposition behavior of PLLA-PEG-PLLA.

The remaining weights at 1,000˚C for composites without and with BN contents of 1, 2 and 4 wt.% were 0.2%, 1.4%, 2.5% and 4.1%, respectively. Undoubtedly, the remaining weights of composites increases with increasing BN content. This suggested homogeneity of the BN within the composites [14].

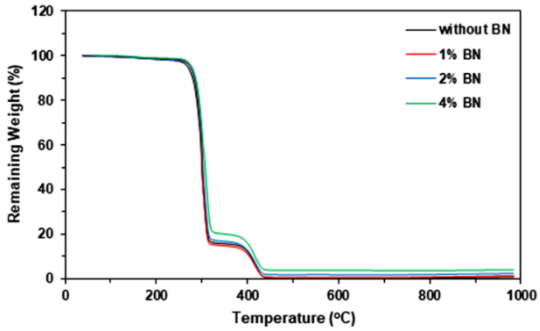


Fig. 4 TG curves of PLLA-PEG-PLLA/BN composites without and with BN.

Phase morphology

Phase morphology including distribution and dispersion of BN particles in the composite films was observed from SEM images of film cross-sections as shown in Fig. 5. The number of BN particles increased with the BN content. Good distribution and dispersion of the BN particles were found for all the composite films. This suggests that the BN particles were well compatible with PLLA-PEG-PLLA.

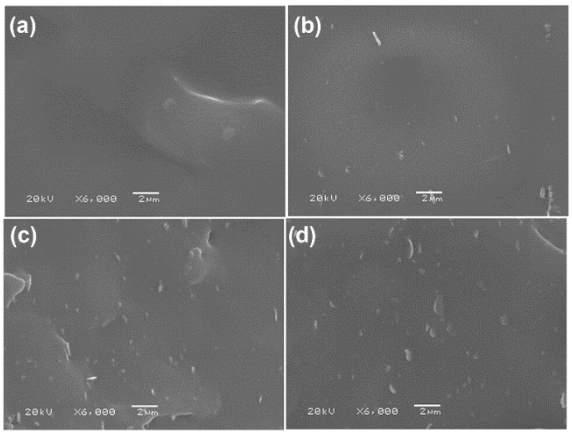


Fig. 5 SEM images of cryo-fractured cross-sections of PLLA-PEG-PLLA/BN composite films

(a) without BN and with BN contents of (b) 1, (c) 2 and (d) 4 wt.%. All bar scales = 2 μm.

Tensile Properties

Selected tensile curves of composite films are presented in Fig. 6. The averaged tensile properties are summarized in Table 2. All the PLLA-PEG-PLLA/BN composite films showed a yield point indicating that they were flexible. The PEG middle-blocks enhanced flexibility of PLLA-PEG-PLLA/BN composite films [6, 7].

The ultimate tensile stress and Young's modulus of the composite films increased while strain at break decreased steadily when the BN content was increased. The results indicated the BN particles induced a reinforcing effect on PLLA-PEG-PLLA films similar to that in PLLA films [14].

It should be noted that the ultimate tensile stress of composite films did not drop when the BN content was higher than 2 wt.%. This can be explained by good distribution and dispersion of BN particles in the PLLA-PEG-PLLA matrices as previous described from SEM analysis. The results indicated that the interfacial adhesion on PLLA-PEG-PLLA/BN composites was strong enough to enhance stress transfer from the PLLA-PEG-PLLA matrix to the BN particle surfaces to improve the stress at break and Young's modulus of these composite films [14].

However, from results of tensile properties, the PLLA-PEG-PLLA/BN composite films were still more extensible than the pure PLLA films (5–10% strain at break) [7].

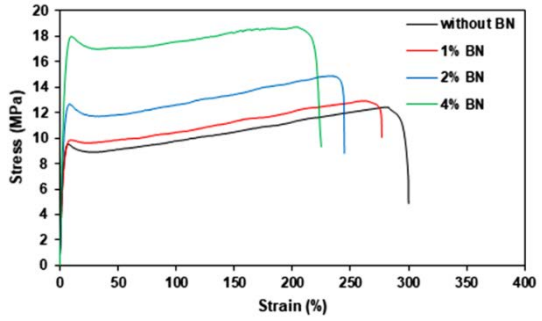


Fig. 6 Tensile curves of PLLA-PEG-PLLA/BN composite films without and with BN.

Table 2 Tensile properties of PLLA-PEG-PLLA/BN composited films

BN (wt.%)	σ [a] (MPa)	ε [b] (%)	E [c] (Mpa)
-	10.1 ± 1.9	288 ± 11	132 ± 18
1	12.9 ± 1.4	277 ± 15	163 ± 25
2	14.9 ± 2.6	245 ± 12	182 ± 15
4	18.7 ± 3.4	225 ± 27	252 ± 23

[a] Ultimate tensile stress; [b] Strain at break; [c] Young's modulus.

CONCLUSIONS

PLLA-PEG-PLLA/BN composite films have been successfully prepared by melt blending following compression molding. The effect of BN content on the thermal, morphological and mechanical properties of composites was investigated. DSC study indicated that the addition of BN enhanced PLLA crystallization. The $\%X_c$ of PLLA-PEG-PLLA increased significantly with increasing BN content. Good phase compatibility between the PLLA-PEG-PLLA matrix and BN filler was found as observed from SEM images. Tensile properties of the composite films indicated that the ultimate tensile stress significantly increased with increasing BN content. It was concluded that the crystallizability and mechanical properties of PLLA-PEG-PLLA can be improved by BN blending. Thus, the PLLA-PEG-PLLA/BN composites could be appropriate for use as highly flexible bioplastics in packaging applications.

ACKNOWLEDGEMENTS

This research was financially supported by the Office of National Higher Education Science Research and Innovation Policy Council (NXPO), Thailand (grant no. PMU B05F630023). The Center of Excellence for Innovation in Chemistry (PERCH-CIC), Office of the Higher Education Commission, Ministry of Education, Thailand is also acknowledged.

REFERENCES

[1] Hamad K., Kaseem M., Ayyoob M., Joo J., and Deri F., Polylactic acid Blends: the Future of Green, Light and Tough. Progress in Polymer Science, Vol. 85, 2018, pp. 83–127.

[2] Samitthiwetcharong S., and Chavalparit O., Enhancement of Methane Production from Alkaline Pretreated Poly(lactic acid) Waste by the Co-digestion Process. International Journal of GEOMATE, Vol. 16, Issue 56, 2019, pp. 171-176.

[3] Yin G.–Z., and Yang X.–M., Biodegradable Polymers: A Cure for the Planet, But a Long Way to Go. Journal of Polymer Research, Vol. 27, 2020, Article No. 38.

[4] Garlotta D., A literature review of poly(lactic acid). Journal of Polymer and the Environment, Vol. 9, 2001, pp. 63–84.

[5] Zhang X., Meng L., Li G., Liang N., Zhang J., Zhu Z., and Wang R., Effect of Nucleating Agents on the Crystallization Behavior and Heat Resistance

of Poly(L-lactide). Journal of Applied Polymer Science, Vol. 133, 2016, Article No. 42999.

[6] Yun X., Li X., Jin Y., Sun W., and Dong T., Fast Crystallization and Toughening of Poly(L-lactic acid) by Incorporating with Poly(ethylene glycol) as a Middle Block Chain. Polymer Science Series A, Vol. 60, 2018, pp. 141–155.

[7] Baimark Y., Rungseesantivanon W., and Prakymoramas N., Improvement in Melt Flow Property and Flexibility of Poly(L-lactide)-*b*-poly(ethylene glycol)-*b*-poly(L-lactide) by Chain Extension Reaction for Potential Use as Flexible Bioplastics. Materials & Design, Vol. 154, 2018, pp. 73–80.

[8] Stolnik S., Illum L., and Davis S. S., Long Circulating Micropaticlate Drug Carriers. Advanced Drug Delivery Reviews, Vol. 16, 1995, pp. 195–214.

[9] Basu A., Kunduru K. R., Doppalapudi S., Domb A. J., and Khan W., Poly(lactic acid) Based Hydrogels. Advanced Drug Delivery Reviews, Vol. 107, 2016, pp. 192–205.

[10] Danafar H., Rostamizadeh K., Davaran S., and Hamidi M., Drug-conjugated PLA-PEG-PLA Copolymers: A Novel Approach for Controlled Delivery of Hydrophilic Drugs by Micelle Formation. Pharmaceutical Development and Technology, Vol. 22, Issue 8, 2017, pp. 947–957.

[11] Lotfi A., Li H., Dao D.V., and Prusty G., Natural Fiber–reinforced Composites: A Review on Material, Manufacturing, and Machinability. Journal of Thermoplastic Composite Materials, Vol. 34, Issue 2, 2021, pp. 238–284.

[12] Pracella M., Haque M.M.U., and Puglia D., Morphology and Properties Tuning of PLA/Cellulose Nanocrystals Bio-nanocomposites by Means of Reactive Functionalization and Blending with PVAc. Polymer, Vol. 55, Issue 16, 2014, pp. 3720–3728.

[13] Singha S., and Hedenqvist M.S., A Review on Barrier Properties of Poly(Lactic Acid)/Clay Nanocomposites. Polymers, Vol. 12, Issue 5, 2020, Article No. 1095.

[14] Bindhua B., Renishaa R., Robertsb L., and Vargheseb T.O., Boron Nitride reinforced polylactic acid composites film for packaging: Preparation and Properties. Polymer Testing, Vol. 66, 2018, pp. 172–177.

[15] Dumludag F., Yener M.Y., Basturk E., Madakbas S., Kahraman V., Umer M.A., Yahsi U., and Tav C., Effects of Boron Nitride in Thermoplastic Polyurethane on Thermal, Electrical and Free Volume Properties. Polymer Bulletin, Vol. 76, 2019, pp. 4087–4101.

[16] Kong D., Zhang D., Guo H., Zhao J., Wang Z., Hu H., Xu J., and Fu C., Functionalized Boron Nitride Nanosheets/Poly(L-lactide) Nanocomposites and Their Crystallization Behavior. Polymers, Vol. 11, Issue 3, 2019, Article No. 440.

[17] Kai W., He Y., and Inoue Y., Fast Crystallization of Poly(3-hydroxybutyrate) and Poly(3-hydroxybutyrateco-3-hydroxyvalerate) with Talc and Boron Nitride as Nucleating Agents. Polymer International, Vol. 54, 2010, pp. 780–789.

[18] Baimark Y., Rungseesantivanon W., and Prakymoramas N., Synthesis of Flexible Poly(L-lactide)-*b*-polyethylene glycol-*b*-poly(L-lactide) Bioplastics by Ring-opening Polymerization in the Presence of Chain Extender. e-Polymers, Vol. 20, 2020, pp. 423–429.

[19] Li Y., Zhou H., Wen B., Chen Y., and Wang X., A Facile and Efficient Method for Preparing Chain Extended Poly(lactic acid) Foams with High Volume Expansion Ratio. Journal of Polymers and the Environment, Vol. 28, 2020, pp. 17–31.

[20] Li L., Cao Z.–Q., Bao R.–Y., Xie B.–H., Yang M.–B., and Yang W., Poly(L-lactic acid)-polyethylene glycol-poly(l-lactic acid) Triblock Copolymer: A Novel Macromolecular Plasticizer to Enhance the Crystallization of Poly(L-lactic acid). European Polymer Journal, Vol. 97, 2017, pp. 272–281.

7th Int. Conf. on Structure, Engineering & Environment (SEE), Pattaya, Thailand, Nov.10-12, 2021, ISBN: 978-4-909106070 C3051

INFLUENCE OF LOW MOLECULAR-WEIGHT POLY(D-LACTIDE)/POLY(L-LACTIDE) MIXTURES ON CRYSTALLIZATION BEHAVIOR AND MECHANICAL PROPERTIES OF HIGH MOLECULAR-WEIGHT POLY(L-LACTIDE) BIOPLASTIC

Yodthong Baimark[1], Theeraphol Phromsopha[1], Yaowalak Srisuwan[1], Wuttipong Rungseesantivanon[2] and Natcha Prakymoramas[2]

[1] Biodegradable Polymers Research Unit, Department of Chemistry and Center of Excellence for Innovation in Chemistry, Faculty of Science, Mahasarakham University, Mahasarakham 44150, Thailand;
[2] National Metal and Materials Technology Center (MTEC), 114 Thailand Science Park (TSP), Phahonyothin Road, Khlong Nueng, Khlong Luang, Pathum Thani 12120, Thailand

ABSTRACT

The crystallization behavior and mechanical properties were determined for poly(L-lactide) with a molecular-weight (M.W.) of 90 kg/mol (PLLA90k) blended with poly(D-lactide)/PLLA with M.W. of 6 kg/mol (PDLA6k/PLLA6k) mixtures. These blends were prepared by melt blending. PLLA90k/PDLA6k/PLLA6k ratios of 90/10/0, 90/7.5/2.5, 90/5/5, 90/2.5/7.5 and 90/0/10 wt.% were investigated. The presence of PDLA6k/PLLA6k mixture decreased the half crystallization-time of PLLA90k and this decrease was related to increased the PDLA6k content. The 90/10/0 and 90/0/10 blend films were brittle but 90/7.5/2.5, 90/5/5 and 90/2.5/7.5 blend films were not. It was demonstrated that the presence of PDLA6k/PLLA6k mixtures enhanced crystallizability of PLLA90k. The PDLA6k/PLLA6k mixtures exhibited synergistic effects to improve mechanical properties of the PLLA90k/PDLA6k/PLLA6k blend films. In conclusion, the crystallization behaviors and mechanical properties of these PLLA90k-based blends could be controlled by adjusting the PDLA6k/PLLA6k ratio.

Keywords: Bioplastics, Poly(L-lactide), Stereocomplex, Crystallization, Mechanical properties

INTRODUCTION

Poly(L-lactic acid) or poly(L-lactide) (PLLA) is a biodegradable bioplastic derived from renewable resources such as sugarcane and corn that is expected to replace petroleum-based plastics [1–3]. Moreover, reduced energy consumption and lower CO_2 release have been reported during production of PLLA compared with some commodity petroleum-based plastics such as polypropylene and poly(ethylene terephthalate) [4].

However, the slow crystallization-rate of PLLA is the main problem for many applications [5]. Highly amorphous molded-PLLA with low crystallinity-content are often obtained from melt processing. The low crystallinity PLLA exhibited poor heat-resistance [6, 7]. Therefore many researchers have reported on ways of increasing crystallization rate of PLLA by addition of nucleating agents [5–8].

It has been shown that stereocomplex crystallites were obtained by blending PLLA and poly(D-lactide) (PDLA) exhibited improved homo-crystallization of PLLA [9] due to stereocomplex crystallites providing nucleating sites. The stereocomplex crystallites of polylactide (PLA) had melting temperatures (around 210–240˚C) higher than PLA homo-crystallites (around 150–170˚C) due to stronger interaction between PLLA and PDLA chains [10–12]. PDLA with shorter chains or lower molecular-weight (M.W.) showed better stereocomplex formation [13, 14]. In addition, low M.W. PLLA has been used to accelerate crystallization of high M.W. PLLA by enhancing its chain mobility [15–17]. However, low M.W. PDLA and PLLA have not been blended together for improving crystallization of high M.W. PLLA.

Therefore, the aim of this work was to investigate effects of low M.W. PDLA/low M.W. PLLA blends on crystallization behavior and mechanical properties of high M.W. PLLA.

MATERIALS AND METHODS

Materials

High M.W. PLLA (PLLA90k), low M.W. PDLA (PDLA6k) and low M.W. PLLA (PLLA6k) were synthesized by ring-opening polymerization in bulk at 165˚C for 2.5 h under nitrogen atmosphere as described in our previous works [18, 19]. Molecular-weight characteristics from gel permeation chromatography (GPC) are reported in Table 1.

Table 1 Molecular-weight characteristics from GPC

analysis

PLA	M_n[a] (g/mol)	Đ[b]
PLLA90k	90,500	2.7
PDLA6k	5,700	1.9
PLLA6k	6,200	1.4

[a] Number-average molecular weight; [b] Dispersity index

Preparation of PLLA90k/PDLA6k/PLLA6k Blends

PLLA90k, PDLA6k and PLLA6k were dried in vacuo at 50˚C overnight to remove moisture before melt blending at 190˚C with a rotor speed of 100 rpm for 4 min using a Rheomix batch mixer (HAAKE Polylab OS). Blends with PLLA90k/PDLA6k/PLLA6k ratios of 90/10/0, 90/7.5/2.5, 90/5/5, 90/2.5/7.5 and 90/0/10 wt.% were prepared.

The blends were dried in vacuo at 50˚C overnight before film formation. The blend films were fabricated by a compression moulding machine (Auto CH Carver) at 200˚C for 3 min without any force before compressing under a 5 ton load for 1 min. The obtained films were 100 × 100 mm in size and were quickly cooled to 25˚C during 1 min.

Characterization of PLLA90k/PDLA6k/PLLA6k Blends

Thermal transition properties of the blends were studied using a differential scanning calorimeter (DSC, Perkin-Elmer Pyris Diamond) under nitrogen gas flow. The blends were first heated at 200˚C for 3 min to erase thermal history, then fast quenched before heating from 0 to 200˚C at a rate of 10˚C /min to measure glass transition (T_g), cold crystallization (T_{cc}) and melting (T_m) temperatures as well as enthalpies of melting (ΔH_m) and cold crystallization (ΔH_{cc}). The degree of crystallinity from DSC (DSC-X_c) of the PLLA phases was calculated from Eq. (1).

$$DSC - X_C(\%) = [(\Delta H_m - \Delta H_{CC})/(93.7)] \times 100 \quad (1)$$

where the 93.7 J/g is the ΔH_m for 100%X_c PLLA [20].

To investigate crystallization behaviour, the blends were melted at 200˚C for 3 min to remove thermal history before cooling from 200 to 0˚C at a rate of 10˚C /min to detect crystallization temperature (T_c) and enthalpy of crystallization (ΔH_c).

For half crystallization-time ($t_{1/2}$) determination, the blends were first heated at 200˚C for 3 min to completely erase thermal history, then quenched to 120˚C at a rate of 50˚C/min and isothermally scanned at 120˚C until the completion of crystallization [21]. The $t_{1/2}$ is the time required to achieve half of the final crystallinity.

Crystalline structures of the blend films were investigated using a wide angle X-ray diffractometer (XRD, Bruker D8 Advance) in the angle range of 2θ = 5˚–30˚ equipped with a copper tube operating at 40 kV and 40 mA producing Cu–Kα radiation. Scan speed was 3˚/min. The X_c from XRD (XRD-X_c) of the PLLA phases was calculated from Eq. (2).

$$XRD - X_C(\%) = [(A_c)/(A_c + A_a)] \times 100 \quad (2)$$

where the A_c and A_a are areas of XRD peaks of PLA crystallites and amorphous halo, respectively.

Tensile properties of the blend films were determined using an universal mechanical testing machine (Liyi Environmental Technology LY-1066B) with a load cell of 100 kg, a crosshead speed of 50 mm/min and a gauge length of 50 mm. The film sizes were 100 mm × 10 mm. The averaged tensile properties were obtained from at least five measurements.

RESULTS AND DISCUSSION

Thermal Transition Properties

The thermal transition properties of blends were studied from DSC analysis. Fig. 1 shows DSC heating curves of the blends and the DSC results are summarized in Table 1. The T_g of blends slightly decreased with increasing PLLA6k content. This may be due to the PLLA6k chains induced a plasticizing effect to enhance chain mobility of PLLA90k for glassy-to-rubbery transition [17]. However, the PDLA6k formed as stereocomplex crystallites with the PLLA chains [13, 14]. Both the T_{cc} and T_m peaks of blends did not change significantly.

The DSC-X_c of blends for PLLA homo-crystallites decreased from 21.9% to 18.1% when PDLA6k content decreased from 10% to 7.5%. The stereocomplex crystallites from PLLA6k/PDLA6k blends acted as nucleating sites for PLLA90k homo-crystallization [10]. Therefore, decreasing the PDLA6k content reduced stereocomplex-crystallite contents to decrease nucleating sites [14].

However, the DSC-X_c of blends increased again as the PLLA6k content increased up to 5%. This may be explained by the plasticizing effect of short PLLA6k chains enhancing the chain mobility during PLLA homo-crystallization [17].

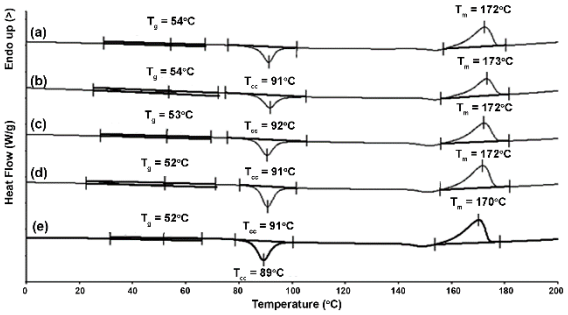


Fig. 1 DSC heating curves of blends with PLLA90k/PDLA6k/PLLA6k ratios of (a) 90/10/0, (b) 90/7.5/2.5, (c) 90/5/5,(d) 90/2.5/7.5 and (e) 90/0/10 wt.%.

Table 2 DSC results of PLLA90k/PDLA6k/PLLA6k blends

Blend ratio (wt.%)	T_g [a] (˚C)	T_{cc} [a] (˚C)	T_m [a] (˚C)	*DSC*-X_c [a] (%)	$t_{1/2}$ [b] (min)
90/10/0	54	91	172	21.9	0.87
90/7.5/2.5	54	92	173	18.1	1.18
90/5/5	53	91	172	19.3	1.25
90/2.5/7.5	52	91	172	23.8	1.47
90/0/10	52	89	170	24.3	3.36

[a] Obtained from DSC heating curves in Fig. 1; [b] Obtained from DSC exothermic curves in Fig. 3.

DSC cooling curves of the blends were also carried out as illustrated in Fig. 2 to show the T_c peaks and ΔH_c. The T_c peaks of pure PLLA90k, PDLA6k and PLLA6k were 96ºC, 105ºC and 104ºC, respectively (DSC cooling curves are not shown). The low M.W. PDLA and PLLA were easier to crystallize than the high M.W. PLLA because the shorter chains are more mobile, aiding crystallization.

The T_c peaks of 90/10/0, 90/7.5/2.5, 90/5/5, 90/2.5/7.5 and 90/0/10 blends were 131ºC, 124ºC, 123ºC, 122ºC and 101ºC, respectively. The T_c peaks of blends were steadily shifted to lower temperature as the PLLA6k content increased, suggesting that the crytsallization was more difficult when the PLLA6k content was increased. The 90/10/0 blend exhibited the T_c peak at the higest temperature (130ºC). This was due to the stereocomplex crystallites from 10% PDLA6k blending enhancing the crystallization of PLLA90k homo-crystallites by acting as nucleating sites [5]. Inceasing the PLLA6k content, results in a decrease of nucleating sites from stereocomplex crystallites. This promoted shifting of T_c peaks to lower temperatures. The results of cooling scans suggeted that stereocomplex crystallites from PDLA6k blending had more efficiency than the plasticizing effect from PLLA6k blending for homo-crystallization of PLLA90k.

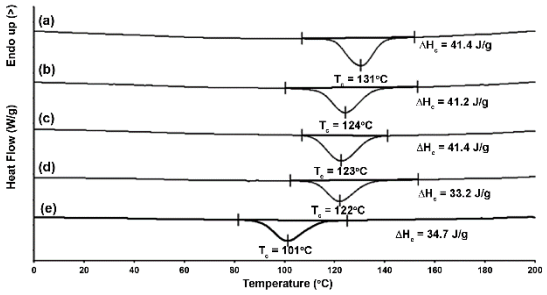


Fig. 2 DSC cooling curves of blends with PLLA90k/PDLA6k/PLLA6k ratios of (a) 90/10/0, (b) 90/7.5/2.5, (c) 90/5/5, (d) 90/2.5/7.5 and (e) 90/0/10 wt.%.

Isothermal crystallization of blends was observed from DSC exothermic curves as shown in Fig. 3. The $t_{1/2}$ of blends from Fig. 3 are also reported in Table 1 and it is evident that they steadily increased as the PLLA6k content increased. The $t_{1/2}$ of pure PLLA was 6.14 min (DSC exothermic curve is not shown). The 90/10/0 blend exhibited the fastest crystallization at 0.87 min due to the sterecomplex crystallites from 10% PDLA6k blending. The stereocomplex crystallinities decreased as the PDLA content decreased [10, 14]. This reduced the crystallization-rate (or increased $t_{1/2}$) when the PDLA6k content was decreased. This confirms that the PDLA fraction accelerated crystallization of PLLA90k, corresponding to results obtained from DSC cooling scans.

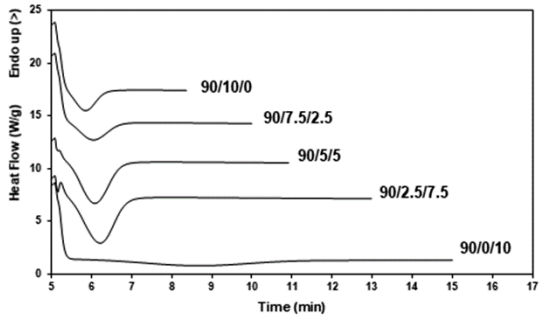


Fig. 3 DSC exothermic curves at the isothermal crystallization temperature of 120ºC of with various PLLA90k/PDLA6k/PLLA6k ratios.

Crystalline Structures

The crystalline structures of blend films were determined from XRD patterns as shown in Fig. 4. The blend films were prepared by a compression moulding method. The obtained films were immediately cooled to room temperature after compression.

The 90/10/0 blend films in Fig. 4 (a) had XRD

peaks at 2θ = 12º, 21º and 24º attributable to the stereocomplex crystallites [22, 23]. There were no XRD peaks of homo-crystallites at 2θ = 15º, 17º and 19º [24]. This demonstrated that the homo-crystallization did not take place during compression molding. According to the XRD pattern of 90/0/10 blend films in Fig. 4 (e), there were no XRD peaks indicating that this film had completely amorphous character. The PDLA6k/PLLA6k mixtures could not improve homo-crystallization during compression molding.

The intensities of XRD peaks of blends significantly decreased when the PDLA5k content was decreased. This can be explained by stereocomplexation decreasing as the PDLA content decreased. The XRD-X_c of 90/10/0, 90/7.5/2.5, 90/5/5, and 90/2.5/7.5 blend films were 19.6%, 17.3%, 12.7% and 5.6%, respectively. These are crystallinities of stereocomplex crystallites.

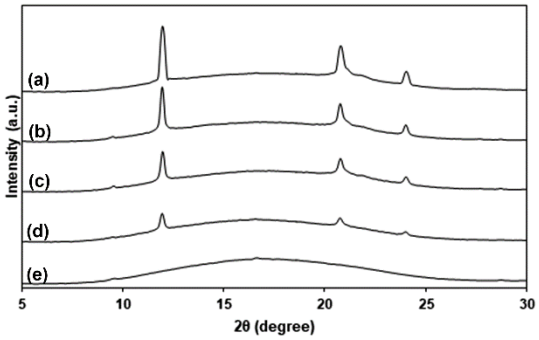


Fig. 4 XRD patterns of blend films with PLLA90k/PDLA6k/PLLA6k ratios of (a) 90/10/0, (b) 90/7.5/2.5, (c) 90/5/5, (d) 90/2.5/7.5 and (e) 90/0/10 wt.%.

Mechanical Properties

Fig. 5 shows tensile curves of the blend films. The averaged tensile properties are summarized in Table 3. The ultimate tensile stress, strain at break and Young's modulus of pure PLLA90k film in this work were 45.6 MPa, 5.5% and 883 MPa, respectively (tensile curve is not shown). It can be seen that both the 90/10/0 and 90/0/10 blend films had brittle characteristics. Their tensile properties were low. This may be explained by large fractions of short PDLA and PLLA chains inducing brittleness of films.

It is surprising that the 90/7.5/2.5, 90/5/5, and 90/2.5/7.5 blend films had higher ultimate tensile stress, strain at break and Young's modulus than both the 90/10/0 and 90/0/10 blend films. These films were not brittle. The tensile results indicated that the stereocomplex formation from PDLA6k blending and plasticizing effect from PLLA6k blending exhibited a synergic effect to improve mechanical properties of PLLA90k-based films.

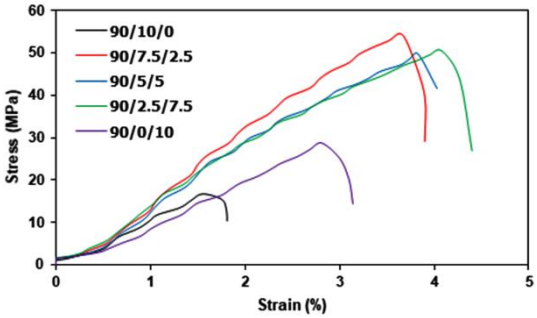


Fig. 5 Tensile curves of blend films with various PLLA90k/PDLA6k/PLLA6k ratios.

Table 3 Tensile properties of PLLA90k/PDLA6k/PLLA6k blend films

Blend ratio (wt.%)	σ [a] (MPa)	ε [b] (%)	E [c] (MPa)
90/10/0	17.5 ± 1.2	2.3± 0.5	225 ± 58
90/7.5/2.5	51.6 ± 2.5	3.7 ± 0.1	934 ± 73
90/5/5	45.8 ± 3.2	3.8 ± 0.3	888 ± 75
90/2.5/7.5	50.9 ± 1.7	4.2 ± 0.1	956 ± 34
90/0/10	27.9 ± 0.7	3.0 ± 0.3	465 ± 35

[a] Ultimate tensile stress; [b] Strain at break; [c] Young's modulus.

CONCLUSIONS

PLLA90k-based films containing PDLA6k/PLLA6k mixtures were successfully prepared by melt blending before compression moulding. The influence of PDLA6k/PLLA6k ratio on the crystallization and mechanical properties of blend films was determined.

The crystallizability of PLLA90k was directly related to PDLA6k content as revealed by DSC. The compressed blend films had only stereocomplex crystallites as indicated by XRD. The blend films containing 10% PDLA6k and 10% PLLA6k showed high brittleness. However the PDLA6k/PLLA6k mixtures improved the mechanical properties of the blend films.

It was concluded that the crystallizability and mechanical properties of PLLA-based films can be adjusted by varying the PDLA6k/PLLA6k ratio. These PLLA90k-based films with controllable crystallization and mechanical-properties could be applied for use as high performance bioplastics.

ACKNOWLEDGEMENTS

This research was financially supported by the Office of National Higher Education Science Research and Innovation Policy Council (NXPO), Thailand (grant no. PMU B05F630023). The Center

of Excellence for Innovation in Chemistry (PERCH-CIC), Office of the Higher Education Commission, Ministry of Education, Thailand is also acknowledged.

REFERENCES

[1] Silva D., Kaduri M., Poley N., Adir O., Krinsky N., Shainsky-Rotiman J., and Schroeder A., Biocompatibility, Biodegradation and Excretion of Polylactic acid (PLA) in Medical Implants and Theranostic Systems. Chemical Engineering Journal, Vol. 340, 2018, pp. 9−14.

[2] Samitthiwetcharong S., and Chavalparit O., Enhancement of Methane Production from Alkaline Pretreated Poly(lactic acid) Waste by the Co-digestion Process. International Journal of GEOMATE, Vol. 16, Issue 56, 2019, pp. 171−176.

[3] Yin G. –Z., and Yang, X. –M., Biodegradable Polymers: A Cure for the Planet, but a Long Way to Go. Journal of Polymer Research, Vol. 27, 2020, Article No. 38.

[4] Masutani K., and Kimura Y., Present Situation and Future Perspectives of Poly(lactic acid), in: Di Lorenzo M. L., and Androsch R. (Eds), Synthesis, Structure and Properties of Poly(lactic acid). Advances in Polymer Science, Vol. 279, 2018, pp. 1−27.

[5] Saeidlou S., Huneault M. A., Li H., and Park C. B., Poly(lactic acid) Crystallization. Progress in Polymer Science, Vol. 37, 2012, pp. 1657–1677.

[6] Zhang X., Meng L., Li G., Liang N., Zhang J., Zhu Z., and Wang R., Effect of Nucleating Agents on the Crystallization Behavior and Heat Resistance of Poly(L-lactide). Journal of Applied Polymer Science, Vol. 133, 2016, Article No. 42999.

[7] Vadori R., Mohanty A. K., and Misra M., The Effect of Mold Temperature on the Performance of Injection Molded Poly(lactic acid)-based Bioplastic. Macromolecular Materials and Engineering, Vol. 298, Issue 9, 2013, pp. 981–990.

[8] Battegazzore D., Bocchini S., and Frache A., Crystallization kinetics of poly(lactic acid)-talc composites. eXPRESS Polymer Letters, Vol. 5, Issue 10, 2011, pp. 849–858.

[9] Shi X., Jing Z., and Zhang G., Influence of PLA Stereocomplex Crystals and Thermal Treatment Temperature on the Rheology and Crystallization Behavior of Asymmetric Poly(L-Lactide)/Poly(D-lactide) Blends. Journal of Polymer Research, Vol. 25, 2018, Article No. 71.

[10] Tsuji H., Poly(lactic acid) Stereocomplexes: A Decade of Progress. Advanced Drug Delivery Reviews, Vol. 107, 2016, pp. 97–135.

[11] El-Khodary E., Fukui Y., Yamamoto M., and Yamane H., Effect of the Melt-Mixing Condition on the Physical Property of Poly(L-lactic acid)/Poly(D-lactic acid) Blends. Journal of Applied Polymer Science, Vol. 134, 2017, Article No. 45489.

[12] Shi X., Jing Z., and Zhang G., Influence of PLA Stereocomplex Crystals and Thermal Treatment Temperature on the Rheology and Crystallization Behavior of Asymmetric Poly(L-lactide)/Poly(Dlactide) Blends. Journal of Polymer Research, Vol. 25, 2018, Article No. 71.

[13] Shao J., Xiang S., Bian X., Sun J., Li G., and Chen X., Remarkable Melting Behavior of PLA Stereocomplex in Linear PLLA/PDLA Blends. Industrial & Engineering Chemistry Research, Vol. 54, 2015, pp. 2246–2253.

[14] Srisuwan Y., and Baimark Y., Controlling Stereocomplexation, Heat Resistance and Mechanical Properties of Stereocomplex Polylactide Films by Using Mixtures of Low and High Molecular Weight Poly(D-lactide)s. e-Polymers, Vol. 18, 2018, pp. 485–490.

[15] Burgos N., Tolaguera D., Fiori S., and Jiménez A., Synthesis and Characterization of Lactic Acid Oligomers: Evaluation of Performance as Poly(lactic acid) Plasticizers. Journal of Polymers and the Environment, Vol. 22, 2014, pp. 227–235.

[16] Avolio R., Castaldo R., Gentile G., Ambrogi V., Fiori S., Avella M., Cocca M., and Errico M. E., Plasticization of Poly(lactic acid) Through Blending with Oligomers of Lactic Acid: Effect of the Physical Aging on Properties. European Polymer Journal, Vol. 66, 2015, pp. 533–542.

[17] Di Lorenzoa M. L., and Androschb R., Accelerated Crystallization of High Molar Mass Poly(L/D-lactic acid) by Blending with Low Molar Mass Poly(L-lactic acid). European Polymer Journal, Vol. 100, 2018, pp. 172–177.

[18] Srisuwan Y., and Baimark Y., Controlling stereocomplexation, Heat Resistance and Mechanical Properties of Stereocomplex Polylactide Films by Using Mixtures of Low and High Molecular Weight Poly(D-lactide)s. e-Polymers, Vol. 18, Issue 6, 2018, pp. 485–490.

[19] Baimark Y., Pasee S., Rungseesantivanon W., and Prakymoramas N., Flexible and High Heat-Resistant Stereocomplex PLLA-PEG-PLLA/PDLA Blends Prepared by Melt Process: Effect of Chain Extension. Journal of Polymer Research, Vol. 26, 2019, Article No. 218.

[20] Li Y., Zhou H., Wen B., Chen Y., and Wang X., A Facile and Efficient Method for Preparing Chain Extended Poly(lactic acid) Foams with

High Volume Expansion Ratio. Journal of Polymers and the Environment, Vol. 28, 2020, pp. 17–31.

[21] Li L., Cao Z. –Q., Bao R. –Y., Xie B. –H., Yang M. –B., and Yang W., Poly(L-lactic acid)-polyethylene glycol-poly(l-lactic acid) Triblock Copolymer: A Novel Macromolecular Plasticizer to Enhance the Crystallization of Poly(L-lactic acid). European Polymer Journal, Vol. 97, 2017, pp. 272−281.

[22] Han L., Yu C., Zhou J., Shan G., Bao Y., Yun X., Dong T., and Pan P., Enantiomeric Blends of High Molecular-Weight Poly(lactic acid)/Poly(ethylene glycol) Triblock Copolymers: Enhanced Stereocomplexation and Thermomechanical Properties. Polymer, Vol. 103, 2016, pp. 376–386.

[23] Cui L., Wang Y., Guo Y., Liu Y., Zhao J., Zhang C., and Zhu P., Effects of temperature and external force on the stereocomplex crystallization in poly(lactic acid) blends. Advances in Polymer Technology, Vol. 37, Issue 4, 2018, pp. 962–967.

[24] Baimark Y., Rungseesantivanon W., and Prakymoramas N., Improvement in Melt Flow Property and Flexibility of Poly(L-lactide)-*b*-poly(ethylene glycol)-*b*-poly(L-lactide) by Chain Extension Reaction for Potential Use as Flexible Bioplastics. Materials & Design, Vol. 154, 2018, pp. 73−80.

7th Int. Conf. on Structure, Engineering & Environment (SEE), Pattaya, Thailand, Nov.10-12, 2021, ISBN: 978-4-909106070 C3051

FACTORS AFFECTING TRAVELER'S MODE CHOICE IN AN EMERGING URBAN AREA OF INDONESIA: THE CASE OF SOUTHERN SUMATERA

Aleksander Purba[1]
[1]Engineering Faculty, University of Lampung, Indonesia

ABSTRACT

Trans Sumatera toll road connects the southern end of Bakauheni to Palembang for 450 km has been operated almost for a year. With a right of way width of about 100 meters, the government planned the railway line to be built parallel to the toll road: with a cheaper investment cost because almost without land acquisition and access location is already open. Railway mode is possible immediately built on the Bakauheni – Bandar Lampung corridor to compete with the dominance of conventional modes such as AC-bus, non-AC bus, auto and motorcycle. The state preference technique has been applied to the study area to explore the attitude and perception of more than 500 respondents with the operation of new mode railways in line with toll road operating earlier. The railways will stretch for 109 km linking the port of Bakauheni in the south of Sumatera to Bandar Lampung This emerging urban area continues to grow dynamically due to the support of adequate transportation infrastructure and geographical proximity to the capital of Jakarta. The output of the mode choice model with the attributes of fare, travel time, headway and delay shows that the greatest potential in the existing conventional mode for shifting to railways is the non-AC bus user group by almost 25% followed by AC-bus 20%, auto user by 4% and motorcycle user by 1%.

Keywords: Attitude, Indonesia, Mode choice, Perception, Southern Sumatera

INTRODUCTION

Unlike the toll road that is usually built far apart from the railway lines, the trans Sumatera toll road, on the third largest island of Indonesia, which stretches from Bakauheni to Palembang is designed with a right of way width of about 100 meters. Right of way planned including for railway lines that are fully parallel with the toll road.

This condition allows the bargaining position of the railway mode to be more competitive because the location of the station and bus stops / terminals allows close proximity so that interchanges, especially passengers, can be designed more quickly, easily and smoothly. Meanwhile referring to the PT ASDP Indonesia Ferry data, 2017-2018, where the port of Merak - Bakauheni is one of the main contributors, the number of ship trips increased from 179,016 (2017) to 185,344 (2018); the number of passengers increased from 5,519,642 to 5,866,688 and the number of four or more wheeled vehicles to be transported increased from 2,065,421 to 2,196,808 in the same period.

As the main port connecting Java and Sumatera, the presence of the Bakauheni - Palembang toll road, which began operating in early 2019, will trigger an increase in passenger and logistic flows from Sumatera to Java and vice versa, not only because of the shorter travel times but also the addition of new infrastructure capacity on toll roads and ferry terminals.

To anticipate the use of overly dominant highway modes, the Ministry of Transportation plans to build a railway line from Bakauheni to Bandar Lampung on the right of way of the toll road that has been operated; far earlier the railway had operated from Bandar Lampung to Palembang, so that the expansion of the new rail mode from Bakauheni Port to Bandar Lampung for 109 km, would later be connected to the existing railway lines of 387 km that had been served by PT KAI Regional IV as an operator since a few decades ago (Fig. 1).

This paper aims to explore changes in the travel behaviour of users of various modes of transportation along the corridor when a new mode of railway is offered as an alternative from Bakauheni to Bandar Lampung and to compete with conventional modes such as AC-bus, non-AC bus, auto and motorcycle. The uniqueness of this study is to explore respondents' attitudes and perceptions with the stated preference technique for railway modes that are still missing links and will be fully aligned with the toll roads that are already operating in corridors of emerging urban areas that are dynamically growing and is closest to capital Jakarta outside the Java island.

The impact of changing attitudes and perceptions on travellers has been discussed by He & Thøgersen [1] on megacity in China but is more associated with car ownership aspects. In India a series of research is carried out to determine changes in respondents'

attitudes and perceptions related to bike route improvement strategies [2] and the relationship between urban transport and community severance [3,4].



Fig. 1 Map of Sumatera island and proposed railway line [5]

Research group Paleti et al., [6] emphasizes the impact of individual daily travel patterns associated with value of time; a number of other researchers focus on discussing the estimation of value of travel time for work trips and bus service configuration, real time traffic information, individual grouping based on cluster analysis and service desired by public transport users [7,8,9,10,11], and discuss the user response to parking policy change [12].

While the attitude and response of respondents in this study are related to the existence of the railway mode that will be connected to the existing line in the capital of Lampung province, which in total will reach a length of nearly 500 km to the capital city of South Sumatera province, competing with the dominant road-based mode with a length of toll road which is almost the same but offers flexibility of departure time and door to door service, especially auto and motorcycle modes.

It is important to note that both Lampung and south Sumatera provinces are the two most dynamic growth provinces in the southern part of Sumatera because of the support of their natural resources and benefited by the additional capacity of trans Sumatera toll road where the travel time from and to capital Jakarta has decreased significantly. Findings of the research will be interesting compared to the phenomenon of commuting behavior in emerging urban areas in developed countries, such as Napoca, Romania [13] and case study city in London [14] and Palermo [15].

METHODS AND DATA

The survey method applied was a paper based interview with a stated preference technique; the substance explored included socioeconomic respondents, travel characteristics and respondents' attitudes and perceptions related to the expansion of the new railway modes along the Bakauheni - Bandar Lampung corridor.

The survey covers as many as 567 respondents, each of which is an AC-bus (150), non-AC bus (154), Auto (153) and motorcycle (110) user. Commercial areas, offices and settlements are the main points of data collection. Fig. 2 shows the route of Bakauheni – Palembang toll road that has been operated and development plan for railway line connecting Bakauheni to Bandar Lampung.

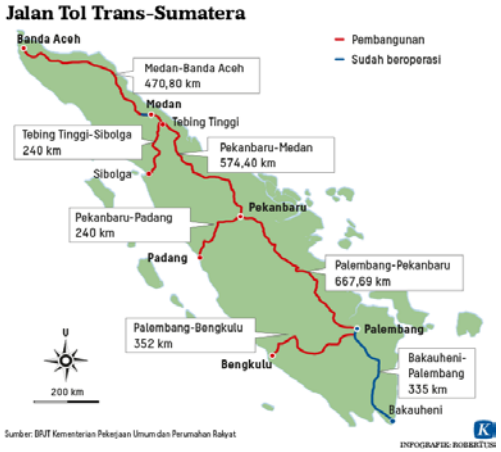


Fig. 1 Bakauheni – Palembang section

MODELS AND ANALYSIS

Socioeconomics

The overview of the respondent socioeconomics is shown in Fig. 2 to Fig. 4, respectively expressing age range and mode of transport used, education level and occupation of respondent.

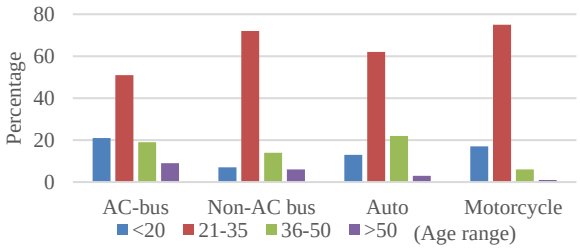


Fig. 2 Transport mode and age range.

As can be seen in Fig. 2 above, the 21 to 35 years' age group dominates the journey for all modes of transportation followed by the age group of 36 to 50 for auto and less than 20 years old and the age of 36 to 50 years for AC-bus. It is alleged that the 21 to 35 years old group dominated about 75% for the motorcycle mode followed by a less than 20 age group with nearly 20%. The respondent education level and transport mode commonly used by respondents throughout the study corridor are shown in Fig. 3.

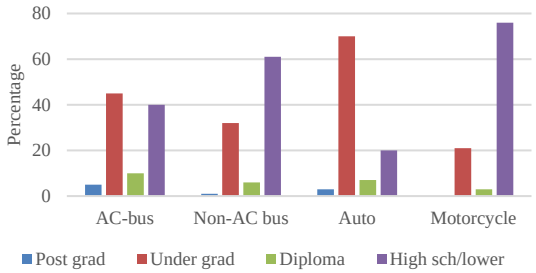


Fig. 3 Transport mode and education level

TABLES, FIGURES AND EQUATIONS

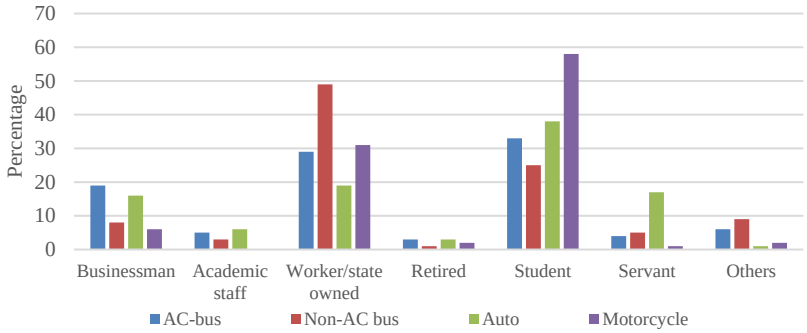


Fig. 4 Transport mode and occupation.

As shown in Fig. 3 that the level of education equivalent to high school or lower dominates trips using motorcycle and non-AC bus modes while undergraduate education levels dominates trips for auto and AC-bus modes. Post graduate and diploma education levels only contribute less than 10% of all modes of transportation in the Bandar Lampung - Bakauheni corridor. The current occupation of respondent and the modes of transportation used to support the activities are shown in Fig. 4.

As previously thought it turns out that motorcycle mode is the main choice of students when traveling in the corridor with a percentage of almost 60% followed by auto and AC-bus, while the workers are more inclined to choose non-AC bus with a percentage of almost 50%; motorcycle and AC-bus users show almost the same figures of 31% and 29% respectively for groups of worker/state owned company. One surprising finding shows that businessman and servant groups were recorded using auto and AC-bus mode with a range of only 16% to 19% of the total trips in the study area.

Utility Function

Data analysis using the stated preference in this study is to estimate the probability that respondents will choose the railway compared to existing modes such as AC-bus, non-AC bus, auto and motorcycle with the attributes offered by each mode. Assuming the utility function to be quasi-linear consisting of the attributes of the fare, travel time, delay and headway, the difference in utility values in the two modes can be expressed in the form of the difference in these attributes.

Table 1a Mode choice competition model (AC-bus and non-AC bus).

	AC bus			Non-AC bus		
	Coeff.	SE	t-Stat	Coeff.	SE	t-Stat
A constant	-1.822	1.8072	-1.0082	-1.347	1.4644	1.6025
Fare	-1.05E-05	-1.78E-05	-1.18E+00	-1.18E-05	-1.69E-05	1.39E+00
TT	-0.0491	-0.3348	-1.4670	-0.0035	-0.3181	1.1023
Headway	-0.0053	-0.0367	-0.1454	-0.0032	-0.0348	0.0932
Delay	-4.44E-05	1.22E-03	-0.0364	-1.52E-04	1.16E-03	-0.1304
R^2		0.62			0.65	

SE: standard error TT: travel time

Table 1b Mode choice competition model (auto and motorcycle).

	Auto			Motorcycle		
	Coeff.	SE	t-Stat	Coeff.	SE	t-Stat
A constant	-3.212	1.3606	0.7439	-4.413	0.0810	-2.6362
Fare	-3.05E-06	-9.38E-06	6.51E-01	-1.05E-07	-4.00E-07	2.63E-01
TT	-0.2288	-0.2651	0.1726	-0.1734	-0.0210	-8.2593
Headway	-0.0386	-0.0290	-1.3281	-0.0064	-0.0380	-0.1675
Delay	-5.45E-04	9.68E-04	0.5628	-9.09E-05	1.27E-03	-0.0718
R^2		0.68			0.71	

SE: standard error TT: travel time

For example, for auto user respondents as the existing mode, the difference between the utility function value between choosing railway and auto is as shown in Equation (1):

$$U_{rail} - U_{auto} = a_0 + a_1(Fare_{rail} - Fare_{auto}) + a_2(TT_{rail} - TT_{auto}) + a_3(Delay_{rail} - Delay_{auto}) + a_4(Headway_{rail} - Headway_{auto}) \quad (1)$$

In the equation the a_0 is a constant and a_1, a_2, a_3, and a_4 are the coefficients of the fare, travel time, delay and headway attributes which are obtained using multiple linear regression method. The results of multiple linear regression analysis are shown in Table 1a and Table 1b above. Table 1a presenting mode choice competition model AC-bus and non-AC bus and Table 1b showing mode choice competition model between auto and motorcycle, respectively.

Mode Choice Elasticity

In principle the value of elasticity indicates sensitivity changes in magnitude of the utility as a result of changing the value of attributes of fare, travel time, headway and delay; the specified mode selected by respondent indicates the utility value of the mode is higher compared to others. Further direct elasticity mean change of elasticity function related to changing the value of fare, travel time, headway and delay attributes in the corresponding mode, while indirect elasticity (cross elasticity) reflects change of the elasticity function for changing the value of the fare, travel time, headway and delay attributes between one mode and its competitors' modes. The following Table 2 shows the results of mode choice elasticity model expressing direct elasticity and indirect elasticity, respectively.

Table 2 Direct elasticity and indirect elasticity.

	Fare	Travel Time	Headway	Delay
Rail-AC bus	-5.27E-02	-1.79E-02	-6.42E-03	-4.46E-05
Rail-Non AC bus	-7.72E-02	-1.67E-03	-5.11E-03	-1.99E-04
Rail-Auto	-2.80E-03	-1.53E-02	-8.48E-03	-9.99E-05
Rail-Motorcycle	-3.37E-05	-4.05E-03	-4.90E-04	-5.83E-06

	Fare	Travel Time	Headway	Delay
Rail-AC bus	-2.10E-01	-7.14E-02	-2.56E-02	-1.78E-04
Rail-Non AC bus	-2.17E-01	-4.70E-03	-1.44E-02	-5.59E-04
Rail-Auto	-7.35E-02	-4.01E-01	-2.23E-01	-2.62E-03
Rail-Motorcycle	-2.59E-03	-3.11E-01	-3.77E-02	-4.49E-04

As shown in the tables above, the respondents of AC-bus and non-AC bus users show that the fare attribute is the most influential in changing utility values to shift to railway mode (direct and indirect elasticity). If railway travel cost is cheaper, the respondent group is potentially shifting from AC-bus and non-AC bus to railway. Conversely, the group of respondents using auto and motorcycle considered travel time as the most important attribute in terms of shifting to railway followed by headway (direct and indirect elasticity). The faster railway the more auto and motorcycle users will be shifting to railway.

Rail Mode Share

The next analysis is to estimate the proportion of users who will shifting using the rail mode from previous modes of AC-bus, non-AC bus, auto and motorcycle along the corridor of Bandar Lampung – Bakauheni. The proportions are calculated by entering the coefficient values of each attribute contained in Table 1a and Table 1b including the rail mode attributes proposed in the mode choice elasticity model.

Table 3 Attributes data of the rail and other modes (distance 100 km)

	Fare (Rp)	TT (hr)	Headway (hr)	Delay (min)
Rail	25,000	1.8	3.0	5.0
AC-bus	66,940	2.4	0.3	30.0
Non-AC bus	52,542	3.0	0.3	30.0
Auto	68,742	1.9	0.0	30.0
Motorcycle	28,600	2.4	0.0	5.0

Service attribute values of each existing mode based on field observations are shown in Table 3, except the value of rail mode attribute based on assumptions referring to service parameters of Bandar Lampung – Palembang railway line which has been operate.

Based on the attribute values listed in Table 3, the output of mode choice model results in the proportion of users of the existing modes that shifting potentially to rail mode shown in Fig. 5. As shown in Fig. 5, the largest proportion of existing modes that have the potential to shift if a new railway is developed is the non-AC bus user group by nearly 25% followed by the AC-bus user group with a potential shifting of 20%.

Surprisingly, auto users with the potential to shift less than 5%, while motorcycle users who have the potential to shift to rail mode only 1%. However, the findings in this study did not differ significantly compared to the results of previous studies, especially regarding the attitude and perception of the auto user group, which does offer flexibility of departure, more private and door to door service compared to railway mode.

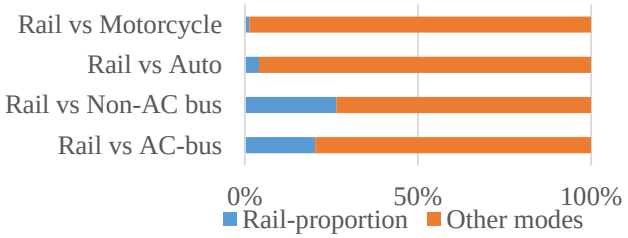


Fig. 5 Potential rail proportion

RESULTS AND DISCUSSION

As a newcomer mode in the Bakauheni - Bandar Lampung corridor, railways are still considered to be less financially feasible by investors compared to the toll road project even in the trans Sumatera toll road corridor that already provides right of way so that it does not require fees for land acquisition. This kind of land acquisition model for competing and fully aligned modes is the first project in Indonesia, although the railway project has not yet ensured its realization after almost a year of toll roads are operated.

On the other hand, the central government's alignment with rail mode development in the study corridor does not seem to be as strong as the commitment to realize the toll road project, which was built relatively quickly through a national strategic project scheme. In fact, if the railways and toll road infrastructure is built together, theoretically it will be able to reduce investment costs, especially since land-sharing and land acquisition are only done once by the central government and local government along the corridor. The tendency of the government to prioritize the operation of toll roads ahead of railways, may have influenced the attitude and

perception by respondents as shown in Figure 5 which only provides a 4% shifting chance by auto users even though railways offers faster travel time and 36% cheaper fare compared to auto. Findings of this research show an overview of the community in Indonesia and in particular the study area of Bakauheni - Bandar Lampung, which expresses attitude and perception relatively differ compared to the habits in developed countries such as Romania, UK and Italy [13,14,15] which more consider service quality such as travel time while choosing transport mode even though the purpose of trip sometimes also influences the choice.

Interestingly some findings of these research are in line with the previous research that there are six additional functions of the trans Sumatera toll project which can generate additional revenue, namely rest area development, tourism park development, railways integration, dry port integration, motorcycle lane integration, and optic fiber networking [16].

Another uniqueness of the results of this study which rarely occurs in developed countries is the attitude and perception of motorcycle user groups that are not affected by the presence of new modes of railways although travel time across the 109 km route on the Bakauheni - Bandar Lampung corridor requires 2.4 hours with a high risk of accidents using a motorcycle compared to 1.8 hours travel time using railways with minimal accident risk. The AC-bus and non-AC bus user groups in the study area were detected as the two groups with the highest flexibility for shifting to railways gradually as the service attributes increased, especially headway which at the beginning of operation was assumed every three hours. Based on observations at the Bakauheni bus terminal, bus departures to Bandar Lampung vary between 1 to 3 hours depending on the volume of passengers moving from Java to Sumatera. The shorter headway offered by railway will potentially attract more passengers since the corridor is growing rapidly because it supported adequate infrastructure capacity.

CONCLUSION

This study has succeeded in measuring the impact of attitudes and perceptions on travel mode choice in dynamically growing corridors Bakauheni - Bandar Lampung in southern Sumatera, Indonesia in terms of the presence of railway modes that will compete with conventional road-based modes. The AC-bus and non-AC bus user groups show that the fare attribute is the most important consideration for choosing railway mode, while the auto and motorcycle user groups consider the travel time attribute as the most important followed by the headway attribute.

Hence, the proportion of passengers who have the potential to shift to railway mode is the non-AC bus user group by nearly 25% followed by the AC-bus user group by 20%. The group of auto users with potential shifting is 4% and motorcycle users are only 1%. The last two groups seem to be difficult to shifting to railway mode since auto and motorcycle offers flexibility, more private and door to door service for its users as also revealed by results of previous research in other cities and countries.

ACKNOWLEDGMENTS

The project presented in this article are supported by PT Aria Graha Consultant and Dinas Perhubungan Provinsi Lampung, which provides a lot of data making it possible to use and produce this scientific work.

REFERENCES

[1] He S.Y. and Thøgersen J., The impact of attitudes and perceptions on travel mode choice and car ownership in a Chinese megacity: the case of Guangzhou, J. of Research in Transportation Economics, Vol. 62, 2017, pp. 57-67.

[2] Majumdar B.B. and Mitra S., Analysis of bicycle route-related improvement strategies for two Indian cities using a stated preference survey, J. of Transport Policy, Vol. 63, 2018, pp. 176-188.

[3] Anciaes P.R. Boniface S. Dhanani A. Mindell J. and Groce N., Urban transport and community severance: Linking research and policy to link people and places, J. of Transport & Health, Vol. 3, Issue 3, 2016, pp. 268-277.

[4] Anciaes P.R. Jones P. and Metcalfe P.J., A stated preference model to value reductions in community severance caused by roads, J. of Transport Policy, Vol. 64, 2018, pp. 10-19.

[5] https://www.dlaiqa.com/2017/12/kereta-api-malam-limex-sriwijaya.html

[6] Paleti R. Vovsha P. Givon D. and Birotker Y., Impact of individual daily travel pattern on value of time, J. of Transportation, Vol. 42, 2015, pp. 1003-1017.

[7] Athira I.C. Muneera C.P. Krishnamurthy K. and Anjaneyulu M.V.L.R., Estimation of value of travel time for work trips, J. of Transportation Research Procedia, Vol. 17, 2016, pp. 116-123.

[8] Bourgeat P., A revealed/stated preference approach to bus service configuration, J. of Transportation Research Procedia, Vol. 6, 2015, pp. 411-423.

[9] Tseng Y.Y. Knockaert J. and Verhoef E.T., A revealed-preference study of behavioural impacts of real-time traffic information, J. of Transportation Research Part C Emerging Technologies, Vol. 30, 2013, pp. 196-209.

[10] Ding L. and Zhang N., A Travel Mode Choice Model Using Individual Grouping Based on Cluster Analysis, J. of Procedia Engineering, Vol.

137, 2016, pp. 786–795.
[11] dell'Olio L. Ibeas A. and Cecin P., The quality of service desired by public transport users, J. of Transport Policy, Vol. 18, Issue 1, 2011, pp. 217-227.
[12] Milosavljević N. and Simicevic J., User response to parking policy change: A comparison of stated and revealed preference data, J. of Transport Policy, Vol. 46, 2016, pp. 40-45.
[13] Tosa C. Sato H. Morikawa T. and Miwa T., Commuting behavior in emerging urban areas: Findings of a revealed-preferences and stated intentions survey in Cluj-Napoca, Romania, J. of Transport Geography, Vol. 68, 2018, pp. 78-93.
[14] Matyas M. and Kamargianni M., Survey design for exploring demand for mobility as a service plans, J. of Transportation, Vol. 46, 2019, pp. 1525–1558.
[15] Migliore M. Catalano M. Castelluccio F. Burgio A. and Giovanna M., The Latent Factors Behind the Urban Travel Behaviour, J. of Procedia - Social and Behavioral Sciences, Vol. 111, 2014, pp. 282-291.
[16] Berawi M.A. Zagloel T.Y.M. Berawi A.R.B. and Abdurachman Y., Feasibility Analysis of Trans-Sumatera Toll Road Using Value Engineering Method. International Journal of Technology, Vol. 6, Issue 3, 2015, pp. 388-399.

7th Int. Conf. on Structure, Engineering & Environment (SEE), Pattaya, Thailand, Nov.10-12, 2021, ISBN: 978-4-909106070 C3051

MODIFIED RESILIENCE INDEX FOR WATER DISTRIBUTION NETWORKS

Pornnapus Kongbuchakiat[1], Adichai Pornprommin[1] and Surachai Lipiwattanakarn[1]
[1]Department of Water Resources Engineering, Faculty of Engineering, Kasetsart University, Thailand

ABSTRACT

Urban water distribution networks (WDNs) require reliability to provide adequate pressure and good water quality. One way to assess WDNs' reliability is through a resilience index. Typically, a resilience index is an index of how the surplus of the required variables such as energy or chlorine mass compares to a system input of such variables. In this paper, we modify the resilience index to include a target value of pressure (Target Hydraulic Resilience Index, THRI) and free residual chlorine concentration (Target Chlorine Resilience Index, TCRI). We applied the THRI and TCRI to a district metering area. The results showed that both RIs clearly explain the state of the reliability of the WDNs comparing to target values. The impact of water loss on each RI is that less water loss resulted in a higher THRI while less water loss gave a lower TCRI. The THRI and TCRI can also be presented in both time and space. Hence, we can assess the deficits of temporal and spatial resilience indices from targets. Therefore, they can be used for pressure and chlorine management to improve the WDNs' reliability.

Keywords: Resilience index, Water distribution networks, Free residual chlorine, Reliability

INTRODUCTION

Performance evaluation of water distribution networks (WDNs) is crucial for establishing the reliability of WDNs. One of the key performances of the WDNs is resilience. Resilience refers to the ability of the WDN to supply water with standard quality, sufficient quantity, and within the appropriate pressure range for consumers under normal and abnormal operating conditions. Gunawan I. Schultmann F. Zarghami S.A. [1] proposed two metrics for evaluating WDN performance, the structural metrics and the hydraulic metrics. Water quality metric was introduced by [2] but they did not evaluate this metric.

Todini [3] proposed a strong concept of hydraulic resilience index that measures the hydraulic capability of the WDN to cope with failures, which is indirectly related to system reliability. This resilience index has further adjusted and combined with other indices to assess network reliability [4]-[7]. However, this resilience index is focused on the existing system resilience or reliability. Hence, we modified Todini's resilience index by substituting input power with a target value for operational purposes.

Water quality metric has been evaluated based on water quality values before and after the failures [2], [8]. As chlorine is one of the most used for controlling water quality in the WDNs [9]. In this paper, we modified Todini's resilience index for the water quality metric using free residual chlorine mass as the indicator. We then explored variations of both hydraulic and water quality resilience indices on both time and space. We also investigated the impact of water losses on the indices.

MATERIALS AND METHODS

Study Area

The study area is one of the district metering areas (DMAs) in the Samut Prakarn branch office service area, Metropolitan Waterworks Authority (MWA), Thailand. The DMA is DMA170104, as shown in Fig. 1. There are 3 of each pressure and free residual chlorine measurement points in the DMA. The characteristics of the study area are shown in table 1.

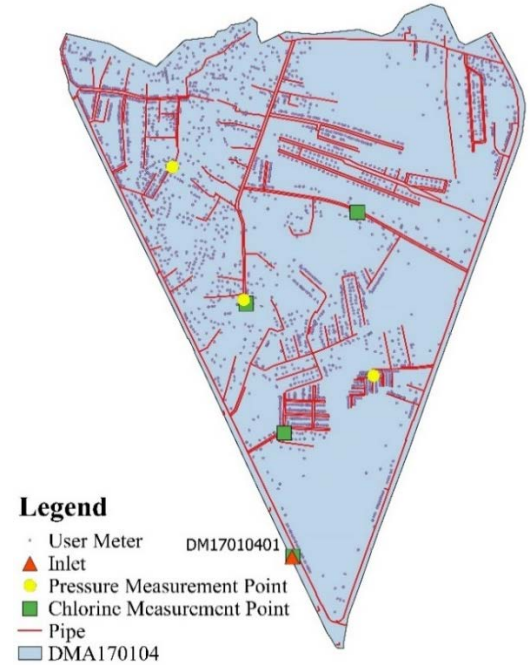


Fig. 1 DMA170104

Table 1 Main characteristics of the study area

Data	Details
Area (km^2.)	1.43
No. of customers	2,669
Total pipe length (km.)	24.61
Average pressure head (m.)	6.95
Water loss (%)	44.3

Methodology

Model

The EPANET model [10] was applied to simulate a water distribution network. We obtained the primary data from the MWA, such as customer meters, pipe diameters, pipe lengths, and demand patterns. Each customer type had different demand patterns and was connected to pipes using valves with no friction loss. Water loss was distributed throughout the network and simulated by the emitter function as shown in eq.1. The hydraulic and quality models were already calibrated by MWA. We simulated the model for 10-day and used the last 24-hr results for calculating resilience indices. There were two cases in this study: WDNs with existing (44.3%) and planned (19%) percentages of water loss conditions [11].

$$Q_{leak} = CP^{N1} \quad (1)$$

where Q_{leak} and P are leakage flow (m^3/hr) and pressure (m.), respectively. N1 is a leakage exponent and equals 1.0 since a pressure step test [12] was conducted and N1 was found to be close to 1.0.

Resilience index

The resilience index (RI) by Todini [3] is the ratio of the excess power and the difference between the total available power at the entrance in WDNs and the total minimum power at user nodes. If the delivery head is more than or equal to the required or minimum head at each node, the customers will receive the desired demand. The RI can measure the reliability of WDNs when pipes fail [3]. RI can be calculated by using the following equation.

$$RI = \frac{\sum_{i=1}^{n_n} Q_i(h_i - h_i^*)}{\sum_{k=1}^{n_r} Q_k H_k - \sum_{i=1}^{n_n} Q_i h_i^*} \quad (2)$$

where h_i and h_i* are head (m.) and minimum satisfied head (m.) at each node i, respectively. n_n is the number of nodes. Q_i is the demand (m^3/hr). Q_k and H_k are discharge (m^3/hr) and head (m.) of each reservoir k. n_k is the number of reservoirs.

Target hydraulic resilience index

For the low pressure WDNs which need to increase the pressure, the original RI in eq. (2) cannot indicate the appropriate pressure level needed to apply to improve the WDNs reliability. In this study, we modified the RI to incorporate a target pressure level as a target hydraulic resilience index (THRI) as follows.

$$THRI = \frac{\sum_{t=1}^{24}\sum_{i=1}^{n} Q_{i,t}P_{i,t} - \sum_{t=1}^{24}\sum_{i=1}^{n} Q_{i,t}P_{min}}{\sum_{t=1}^{24}\sum_{i=1}^{n} Q_{i,t}P_{target} - \sum_{t=1}^{24}\sum_{i=1}^{n} Q_{i,t}P_{min}} \quad (3)$$

where t and n are time (hr.) and the number of user meters, respectively. Qi,t is satisfied demand at each node i at time t (m^3/hr). $P_{i,t}$ is pressure at each node i at time t (m.). P_{min} is the minimum pressure (m.) defined as MWA service level of 5 m. P_{target} is the target pressure (m.) from MWA strategic plan [11] defined as 9.5 m.

Target chlorine resilience index

The free residual chlorine (FRC) is typically used as one of the water quality indicators in the WDNs [9]. To calculate the RI of FRC, we modify the RI using FRC mass instead of power. The target chlorine resilience index (TCRI) can be expressed as:

$$TCRI = \frac{\sum_{t=1}^{24}\sum_{i=1}^{n} Q_{i,t}C_{i,t} - \sum_{t=1}^{24}\sum_{i=1}^{n} Q_{i,t}C_{min}}{\sum_{t=1}^{24}\sum_{i=1}^{n} Q_{i,t}C_{target} - \sum_{t=1}^{24}\sum_{i=1}^{n} Q_{i,t}C_{min}} \quad (4)$$

where $C_{i,t}$ is FRC concentration (mg/l) at each node i at time t. C_{min} is the minimum FRC concentration as recommended by World Health Organization (WHO) as 0.2 mg/l [9]. C_{target} is the target FRC concentration (mg/l) which should not exceed the odor threshold value of 0.6 mg/l [13].

RESULTS AND DISCUSSIONS

Target Hydraulic Resilience Index Analysis

The THRI results of the whole network are 0.151 and 0.205 for WDNs with existing water loss (44.3%) and 19% of water loss, respectively. They imply that the average powers of WDNs are 15.1% and 20.5% above the minimum power and 84.9% and 79.5% below the target power. The THRI of the 19% of water loss case increases by 0.055 (36.2%) indicates that decreasing water loss can improve system hydraulic reliability. We calculated the original RI to be 0.179 which only indicated that the surplus power of the system was 17.9% above the minimum requirement. It did not state the surplus power condition comparing to target value.

The hourly THRI in Fig. 2 shows the improvement of THRI every hour when the water loss

reduces to 19%. Between 11.00 to 15.00, the THRIs of the existing case are lower than 0 because of the dropping pressure. It means that users will get pressure lower than the service level. By examining the hourly THRI, we can manage the system pressure. We will know what time the THRI approaches the target or below the service level, so we can increase or decrease pressure.

Figure 3 shows the spatial distribution of THRI. We can see that in Fig. 3(a), the higher THRI is mostly near the inlet and the THRI values become smaller and smaller as they are further away from the inlet. The low-reliability areas can be identified, so we can apply the appropriate measures to the problemed areas. After reducing water loss to 19% as shown in Fig. 3(b), the THRI becomes better in all areas. Therefore, reducing water loss will make the WDNs have higher THRI and reliability in both time and space.

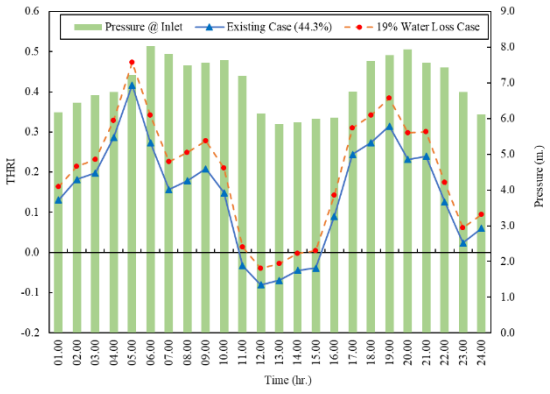
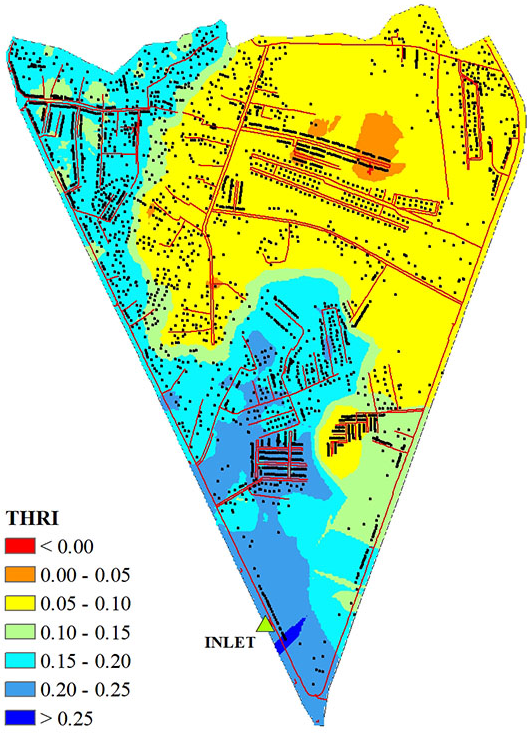


Fig. 2 Hourly THRI and pressure at inlet

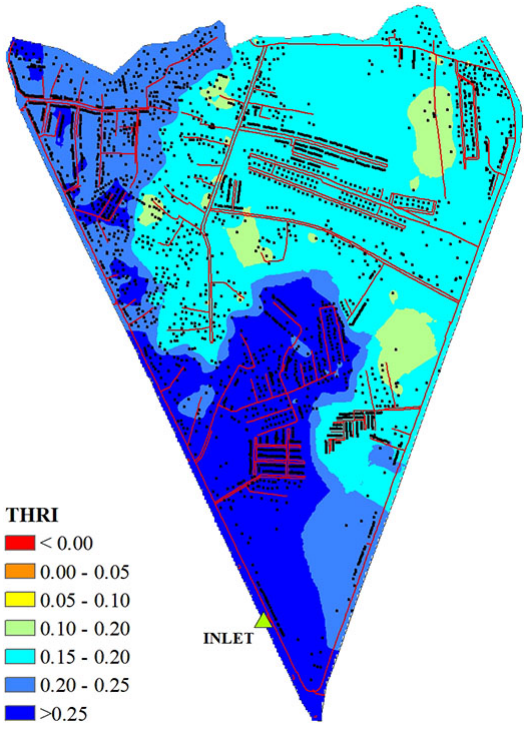
Target Chlorine Resilience Index Analysis

The results of TCRI of the whole network are 1.759 and 1.690 for WDNs with existing case (44.3%) and 19% of water loss, respectively. They imply that the WDN had 75.9% and 69.0% of FRC mass above the target FRC level, respectively. These values conform with users' complaints of chlorine odors. The TCRI of the water loss reduction case slightly decreases by 0.069 (3.91%). We also calculated the chlorine resilience index using system FRC mass inputs instead of the target FRC level. The value is 0.650 which only indicates that on average users receive 65.0% of the FRC system mass. The 0.650 value did not identify the problem of chlorine overdoses.

The hourly TCRI in Fig. 4 shows that when water loss is reduced, the WDN has a lower TCRI. The TCRI decreases during nighttime more than daytime due to longer water ages. Since both cases of TCRIs are above 1 (above the target value), we can reduce chlorine input at the inlet.



(a) Existing Case (44.3% WL)



(b) 20% Water Loss Case

Fig. 3 Spatial THRI

Figure 5 shows the spatial distribution of TCRI. Figure 5(a) shows that almost all users have TCRI above 1. The water near the inlet will have an unpleasant odor and taste because FRC is considerably higher than 0.6 mg/l. Figure 5(b) shows that water loss reduction makes TCRI smaller. The less water loss makes the water age increases which affects chlorine decay. Therefore, water loss reduction decreases chlorine resilience in the system. Comparing to THRI, the impact of water loss reduction increases hydraulic resilience in the system. The hourly and the spatial TCRI can help manage chlorine dosing rates in WDNs to improve chlorine reliability.

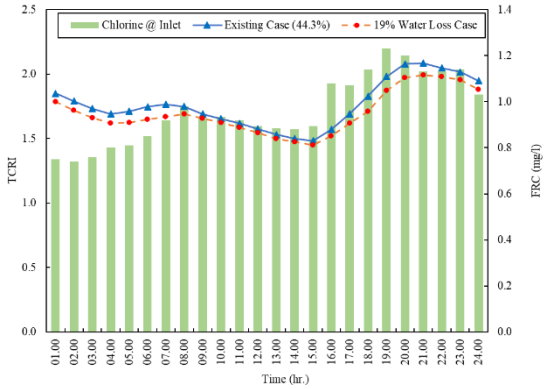


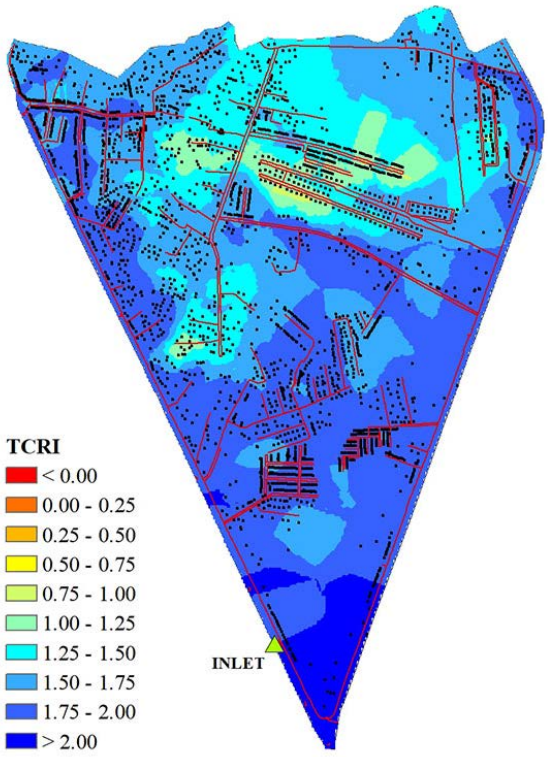
Fig. 4 Hourly TCRI and chlorine at inlet

CONCLUSIONS

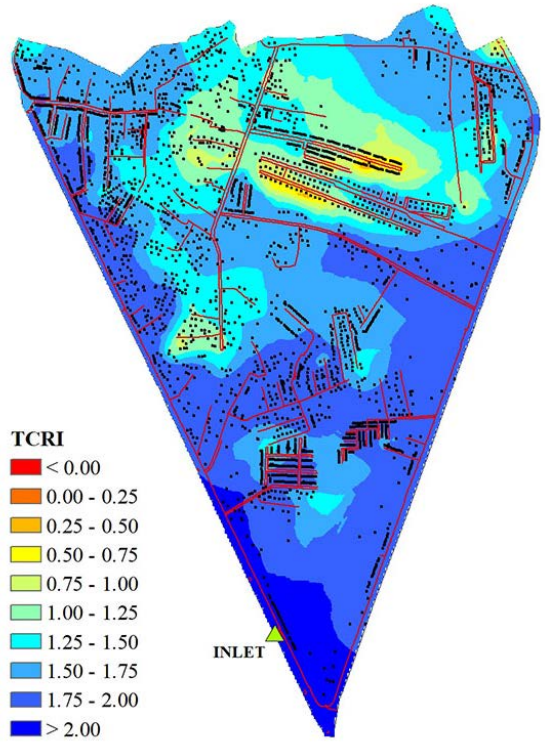
The resilience index by Todini can measure the reliability of WDNs when the pipe fails by calculating the surplus energy over required energy. We modified the resilience index to include a target value of pressure and free residual chlorine concentration, so we could compare the delivery values to the target values. We applied both RIs to a district metering area on time and spatial aspects and investigated the impact of water loss on the RIs.

The THRI results of the whole network are 0.151 and 0.205 for WDNs with existing water loss (44.3%) and 19% of water loss, respectively. They imply that the average pressures of WDNs are 15.1% and 20.5% above the minimum pressure. By examining the hourly THRI, the time when the THRI approaches the target or below the service levels can be identified. In the spatial distribution of THRI, we can identify the low-reliability areas. Appropriate measures can be implemented accordingly. After reducing water loss, the THRIs are better in both time and space. Therefore, reducing water loss will make the WDNs more hydraulic reliable.

The results of TCRI of the whole network are 1.759 and 1.690 for WDNs with existing (44.3%) and 19% of water loss, respectively. They indicate that the WDN had 75.9% and 69.0% of FRC mass above the



(a) Existing Case (44.3% WL)



(b) 19% Water Loss Case

Fig. 5 Spatial TCRI

target FRC level. Both hourly and spatial TCRIs indicate where and when FRC problems occur for low and high chlorine contents. Therefore, the TCRI can help manage chlorine dosing rates in WDNs to improve reliability. After reducing water loss, the water age increases, so chlorine decays higher and the TCRI decreases. Unlike the THRI, water loss reduction has a negative impact on chlorine resilience.

Hence, by using the THRI and TCRI we can assess the deficits of temporal and spatial resilience indices from targets which can be used for pressure and chlorine management to improve the WDNs' reliability.

ACKNOWLEDGMENTS

This study is funded by the Faculty of Engineering, Kasetsart University, researcher scholarship. The authors gratefully acknowledge Metropolitan Waterworks Authority (MWA) for providing data using in this study.

REFERENCES

[1] Gunawan, I., Schultmann, F., Zarghami, S.A., The four Rs performance indicators of water distribution networks: a review of research literature, International Journal of Quality & Reliability Management, Vol. 34, Issue 5, 2017, pp.1-9.

[2] Cimellaro, G.P., Tinebra, A., Renschler, C., Fragiadakis, M., New Resilience Index for Urban Water Distribution Networks, Journal of Structural Engineering, 142(8): C4015014, 2016, pp.1-13

[3] Todini E., Looped water distribution networks design using a resilience index based heuristic approach, Urban Water, 2(2), 2000, pp.115-122.

[4] Baños R., Juan R., Martínez J., Gil C. and Márquez A.L., Resilience Indexes for Water Distribution Network Design: A Performance Analysis Under Demand Uncertainty, Water Resources Management, 25, 2011, pp.2351–2366.

[5] Creaco E., Franchini M., and Todini E., The combined use of resilience and loop diameter uniformity as a good indirect measure of network reliability, Urban Water, 13:2, 2016, pp.167-181.

[6] Jeong G., Wicaksono A., and Kan D., Revisiting the Resilience Index for Water Distribution Networks, Journal of Water Resources Planning and Management, 2017, 143(8): 04017035 (pp.1-13)

[7] Zhan X., Meng F., Liu S., and Fu G., Comparing Performance Indicators for Assessing and Building Resilient Water Distribution Systems, Journal of Water Resources Planning and Management, Volume 146 (12), 2020, 06020012.

[8] Diaoa K., Sweetapplea C., Farmania R., Fua G., Warda S., and Butle D., Global resilience analysis of water distribution systems, Water Research Vol. 106, 2011, pp.383-393.

[9] WHO (World Health Organization). 2011. Guidelines for drinking-water

[10] Rossman L.A., EPANET 2 USERS MANUAL. CINCINNATI, OH, USA, 2000, pp.1-200.

[11] MWA (Metropolitan Waterworks Authority), Enterprise strategic plan no.5, 2020, p. 58. (in Thai)

[12] McKenzie R.S., and Langenhovenm S., Presmac pressure management program. Pretoria, South Africa: Water Research Commission, 2001.

[13] NHMRC, Australian drinking water guidelines paper 6 national water quality management strategy. National Health and Medical Research Council, National Resource Management Ministerial Council, Commonwealth of Australia, Canberra, 2011, 7-5.

7th Int. Conf. on Science, Engineering & Environment (SEE),
Pattaya, Thailand, Nov.10-12, 2021, ISBN: 978-4-909106032 C3051

CONTEMPLATION OF VIBRATION AND SOUND SIGNALS OF A HYBRID-ENGINE CAR

Suphattharachai Chomphan
Faculty of Engineering at Sriracha, Kasetsart University, Thailand

ABSTRACT

In the present day, hybrid-engine cars are becoming popular before moving to the age of electric vehicles (EV). An analysis of vibration and sound signals of a hybrid-engine car with three different modes at some different positions within the passenger room to evaluate the quality of service comparatively has been conducted in this paper. The Honda Accord Hybrid 2015 model has been selected in this study due to its popularity. The vibration measuring positions are at the right front or driver's seat, the left front seat, and the rear seat, while the sound measuring position is at the rear seat. Three measuring scenarios include EV-drive, hybrid-drive, and engine-drive modes. The experimental data are collected and subsequently, the dominant frequency extraction is conducted. The experimental results have been finally concluded. It can be seen that the hybrid-drive mode shows the highest level of vibration magnitude for all tested speeds ranging from 750 to 3750 rpm, however, some scenarios of engine-drive mode are higher than hybrid-drive mode due to the engine and battery setups. When comparing the engine speeds, the level of vibration magnitude directly varies with the engine speed. On the other hand, when comparing among the measuring positions, the level of vibration magnitude is lowest at the rear seat, meanwhile, the levels of those other front seats are rather similar. Last but not least, the sound signal analysis is performed with the same scenarios. It has been seen that the level of sound magnitude directly varies with the engine speed.

Keywords: Hybrid engine, Vibration signal analysis, Sound signal analysis, Fast Fourier transform, Dominant frequency extraction

INTRODUCTION

The increasing consumption of petroleum poses a serious threat to the environment with the problem of global warming, therefore wide-ranging automotive manufacturers focus on producing hybrid electric vehicles (HEVs) while gaining the advantages of both pure electric vehicles (EVs) and traditional internal combustion engines. However, the noise and vibration produced during the HEV operation reduce the comfort of the passengers. They also cause stress, fatigue, and adversely affect the drivers [1], [2].

In addition, noise, vibration, and soreness (NVH) issues affect the retina and visible objects, resulting in a blurry view of the drivers. In addition, competition in the automotive market is required to have a vehicle's acoustic and vibration dampening properties for optimal performance [3].

From the previous study, the analysis of vibration and sound signals has been inaugurated and developed for many years. The external and internal factors which affect the working conditions of the vehicles have been continuously performed. One study of the environmental effects of the road surface type and condition on the traffic flows management mode in the case of directive management has been explored by Novikov et al., [4]. Its focus is the method of assessment of the effect of the road surface type and condition on the capacity rate of the signalized area and therefore its effects on the traffic flow management mode. It has been concluded that there is a correlation between the friction coefficient and the capacity of the managed area resulting in the change of the traffic lights cycle, which is also corroborated by the conducted field experiment on a signalized intersection.

Another external factor that affects vehicle durability has been conducted by Hu and Zhong in 2019. They applied a conventional finite element model for linear and nonlinear analysis for multibody full-vehicle-durability simulation. Six different kinds of test road surfaces are conducted in the simulation, finally, it has been concluded that the explicit–implicit co-simulation techniques are efficient and accurate enough for engineering purposes [5].

Moreover, the interaction between the type and technical condition of road surfaces, dynamic vehicle loads, and the level of vibration propagated to the environment has been studied by Czech [6]. It has been insisted that the type of road surface and the technical condition and varied dynamic vehicle loads are explicitly affecting the level of vibration propagated to the environment.

A study of the discomfort caused by vibration for three models of micro commercial vehicles running in four types of road conditions has been performed by Huang and Li [7] since the main

environmental stress of vibration affected the vehicles implicitly. Another external factor analysis has been conducted by Litak and his colleagues. They investigated the chaotic vibration which was the effect of critical Melnikov amplitude of the road surface profile to a quarter car model [8]. Blekhman and Kremer also conducted a study of the effect of road unevenness on the dynamics of the averaged longitudinal motion of a vehicle [9].

As for internal factor analysis, a study of detection and diagnosis of the faults in rotating machinery, a number of the mechanical vibration-based studies have been tremendously pursued [10]-[12]. Inspecting the associated signal processing for machine diagnosis, an amount of research on signal processing adaptation has been investigated for fault diagnosis [11]. The discrete wavelet transform (DWT) in the temporal and spatial domain was successfully applied with the vibration signal for the engine fault diagnosis of the diesel engine and the gearbox [11], [12]. The other successful techniques of the power spectrum analysis with high order, cepstrum analysis, and neural network approach were utilized for the fault diagnosis and the indication of some of the specific induction motors [13]. Another interesting applied technique of the Fourier transform has been widely used in signal processing, for example, the Fourier transform coefficients adopted in the features of mel-cepstral HMM-based speech modeling for speech synthesis [14]. It is consequently adapted to the correlation analysis of vibration and sound signals for a gasoline-engine car [15]. Moreover, the power of signal analysis with less time consumption and the low computational cost was conducted in a comparative study of LPG-modified engine and normal oil-usage engine [16], and also in a fault diagnosis of rolling element bearings [17]. Another internal analysis has been introduced, the problems of gasoline substitution with LPG boiling system installation cause some significant variation in vibration and sound signals of the modified engines [18]-[21]. Subsequently, some analysis techniques of the vibration and sound signals were proposed to differentiate between the LPG-modified engine and the conventional gasoline engine, subsequently, some significant attributes were used to indicate the irregularities of the corresponding engines [22], [23]. Another internal factor study of vibration and sound signal analysis for a gasoline engine with LPG-installation and some specified fault simulations was investigated, LPG-installation and the specified faults concretely affected the engine efficiency degradations [24]-[26].

This paper applies engineering knowledge to study and analyze the vibration and sound of an HEV car from one worldwide manufacturer. The study includes all operating modes of EV-drive, hybrid-drive, and engine-drive scenarios where all internal factors directly affect the HEV. In vibration measuring, the positions are defined at the right front or driver's seat, the left front seat, and the rear seat inside the passenger room. In sound measuring, a microphone is located at the rear seat inside the passenger room.

A couple of principle purposes are to compare the vibration affecting from all three operating modes with three different measuring positions and to compare the sound affecting from all three operating modes. The Fast Fourier Transform is adopted to extract the signal spectrum and the corresponding features in the analysis procedure [15], [16], [25], [26].

MATERIAL AND METHODS

In this section, hybrid electric vehicles have been generally explained in principle. The experimental procedure has been illustrated step by step. Finally, the experimental setups have been therefore presented.

Hybrid Electric Vehicles

The hybrid electric vehicle is defined literally as a vehicle that uses oil and electricity. The energy from the oil has been partially converted to electricity stored in a specific type of rechargeable battery. It is aimed at reducing combustion engine consumption, reducing pollution, reducing internal vibration, and also saving total fuel consumption [1].

The term “hybrid” means the combination use of both the conventional internal combustion engine and the electric motor in the vehicle system process. In the electric charging subprocess, the generated electrical energy while the engine braking period slows down is stored in the battery. On the other hand, during the EV-drive mode, the stored energy is released to run the drive motor without the fuel consumption. In addition, the reduction in fuel consumption occurs when the engine is always running at the optimal engine speed. In summary, when the vehicle's energy demand is greater than the volume that the engine produces, the vehicle is supplementarily powered by an extra battery [2], [3]. The driving modes of the HEV are concluded as follows.

The EV-drive mode: the vehicle is powered by electric power from a Lithium-ion battery via an electric motor.

The hybrid-drive mode: the engine and electric motor work together with good acceleration. While the accelerator pedal is being released, the engine stops working.

The engine-drive mode: the engine drives all of the power directly to the front wheels without using electric power.

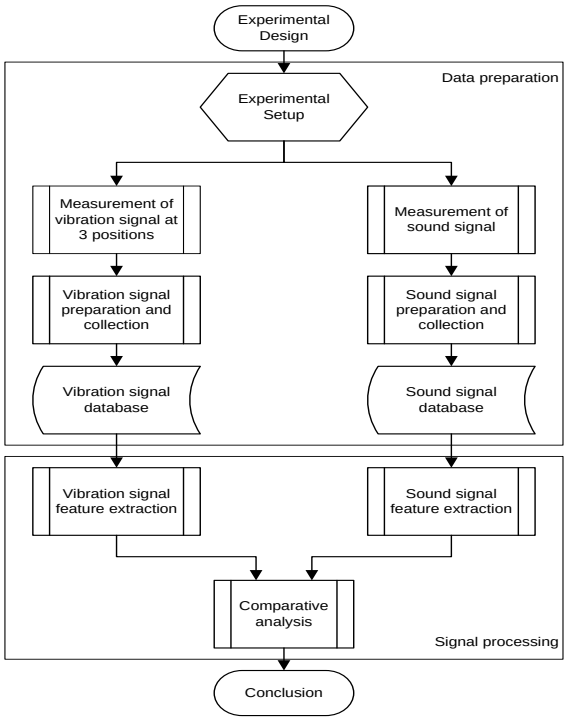


Fig. 1 Experimental Procedure.

The Sports Drive Mode: the engine sends all the power directly to the front wheels, but gives a higher rpm than normal operation. This mode is ignored since it is rarely used in practical use.

Experimental Procedure

The experimental procedure consists of a couple of consequential stages of data preparation and signal processing sub-procedures as depicted in Fig. 1. A brief explanation of the procedure is presented as follows.

Initially, the experimental design process has been performed. All experimental equipment includes a personal HEV car (Y2015 Honda Accord hybrid (DOHC) i-VTEC with a 2.0-liter engine, 4 cylinders, and 16 valves), vibration sensors and their accessories, a condensed microphone and its complementary parts, NI card for interfacing with a computer, and a computational program for signal processing.

At the data preparation, the experimental setup is conducted to retrieve the vibration and sound signals simultaneously from the experimental car with five different numbers of engine speeds; 750, 1500, 2250, 3000, and 3750 rpm at standstill condition. Thereafter, the measurement, preparation and collection, and database implementation are performed respectively.

The vibration and sound signal retrieving setups have been arranged during the experimental setup process. Three sets of high-frequency vibration sensors and a condensed microphone are allocated at different positions within the passenger room. The corresponding signals are then transferred into the processing computer through a group of NI interfacing cards.

The vibration sensors are allocated at three positions including at the right front or driver's seat, the left front seat, and the rear seat. The condensed microphone is attached at the mid of the rear seat beside the vibration sensor. Three vibration sensor wires and the microphone wire are connected with the NI cards which are attached to the NI rack. The rack is also connected to the computer which the signals are retrieving into the Labview program.

All of the sensors apply the sampling frequency of 50,000 Hz. The signals are measured with 10 samples and 5-second periods of time at 5 different engine speeds of 750, 1500, 2250, 3000, and 3750 rpm, respectively.

The preliminary process of signal segmentation is performed after the vibration and sound signals arrive at the input ports through the Labview program. The collection of signals from all different sensor positions with all different engine speeds are categorized.

At the signal processing, the feature extraction and comparative analysis are performed respectively.

The signal analysis technique of Fast Fourier transform has been applied with all of the portions of the signals for all groups within the database to obtain their corresponding frequency spectrum. From the output frequency spectrum, the most dominant peak appearing in the frequency domain is extracted. The frequency and magnitude at the peak are analyzed. Monitoring the frequency spectrum brings about some frequencies at the dominant peak points and their corresponding amplitudes. These highest peaks are assumed to represent the important components of the vibration signal inherited from the movement of the HEV. These extracted features are consequently utilized in the final process of the comparative analysis.

The extracted features are averaged among all corresponding samples. Several comparative analyses are conducted with different aspects. As for the vibration signals, the operating modes including EV-drive, hybrid-drive, and engine-drive modes are compared. Moreover, the positions of sensors include the right front, the left front seat, and the rear seat are also compared. As for the sound signals, the aspect of operating mode is performed as same as those of the vibration signals.

The interpretation of the output comparative analysis is performed. Finally, the discussion for all aspects has been completed.

EXPERIMENTAL RESULTS

In the signal feature extraction process, the FFT technique has been adopted to extract the significant

features as described in the previous studies [15], [25], [26]. The extracted features are consequently utilized in the final process of the comparative analysis using the statistical averaging technique. The following bar charts are constructed and presented in this section.

As for vibration comparative analysis, the comparisons of the averaged magnitude of emerging peak of the frequency spectrum of the vibration signal measured at three different positions in gravitational acceleration unit (g) with different engine speeds for three operating modes are presented in Figs. 2-4. On the other hand, the comparisons of the averaged magnitude of the emerging peak of the frequency spectrum of the vibration signal measured at three operating modes in the gravitational acceleration unit (g) with different engine speeds for three different positions are presented in Figs. 5-7.

As for sound comparative analysis, the averaged magnitude of the emerging peak of the frequency spectrum of the sound signal measured of three operating modes at the rear seat has been plotted and presented in Fig. 8.

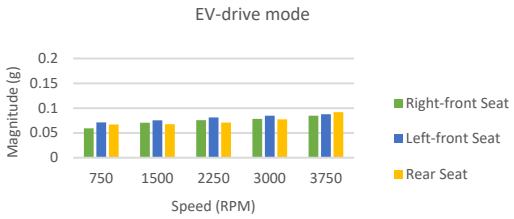


Fig. 2 The averaged magnitude of emerging peak of the frequency spectrum of the vibration signal measured at three different positions of EV-drive mode.

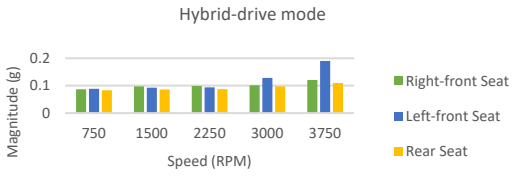


Fig. 3 The averaged magnitude of emerging peak of the frequency spectrum of the vibration signal measured at three different positions of hybrid-drive mode.

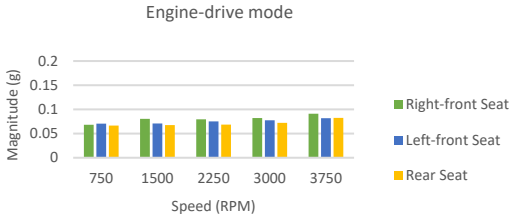


Fig. 4 The averaged magnitude of emerging peak of the frequency spectrum of the vibration signal measured at three different positions of engine-drive mode.

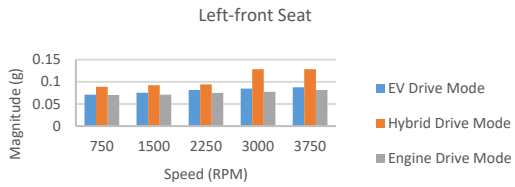


Fig. 5 The averaged magnitude of emerging peak of the frequency spectrum of the vibration signal measured of three operating modes at the left-front seat.

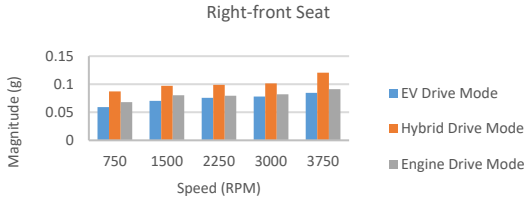


Fig. 6 The averaged magnitude of emerging peak of the frequency spectrum of the vibration signal measured of three operating modes at the right-front seat.

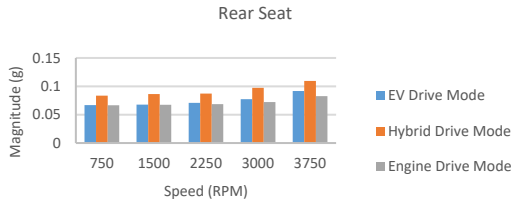


Fig. 7 The averaged magnitude of emerging peak of the frequency spectrum of the vibration signal measured of three operating modes at the rear seat.

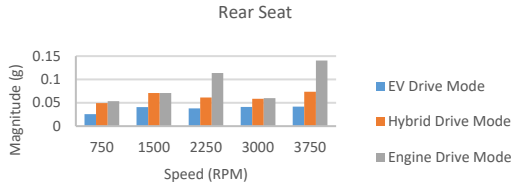


Fig. 8 The averaged magnitude of emerging peak of the frequency spectrum of the sound signal measured of three operating modes at the rear seat.

Based on the previous study of an analysis of vibration for a gasoline-engine car driving on three types of roads [27], the results are analyzed accordingly. From Figs. 2-4, the averaged magnitude of the emerging peak of the frequency spectrum of the vibration signal increases while the engine speed is being raised. This finding is highly consistent with the result of the previous study.

From Fig. 2 with focusing at the EV-drive mode, the averaged magnitude of the emerging peak of the

frequency spectrum of the vibration signal increases while the engine speed is being increased. The left-front seat reflects the highest impact to the averaged magnitude when comparing with the others. Furthermore, it can be noticed that the magnitude of the rear seat emerges as the highest value when the speed arrives at 3750 rpm.

From Fig. 3 with focusing at the hybrid-drive mode, the averaged magnitude of the emerging peak of the frequency spectrum of the vibration signal increases while the engine speed is being raised as same as that of the EV-drive mode depicted in Fig. 2. It can be seen that the magnitudes of the left-front seat trends to increase much more than those of the others.

From Fig. 4 with focusing at engine-drive mode, the averaged magnitude of the emerging peak of the frequency spectrum of the vibration signal has the same movement along the engine speed axis with an increasing upward trend. The magnitude of the right-front seat noticeably tends to increase more than those of the others.

From Fig. 5 with focusing the left-front seat, the averaged magnitude of the emerging peak of the frequency spectrum of the vibration signal increases while the engine speed is being raised for all of the vibrations at all operating modes of the HEV. The hybrid-drive mode gives the highest level to the averaged magnitude when comparing with the others, meanwhile, the engine-drive mode gives the least level.

From Fig. 6 with focusing on the right-front seat, the trends of all averaged magnitudes are as same as those of the left-front seat in Fig. 5. However, it has been seen that the EV-drive mode gives the least level among all operating modes.

From Fig. 7 with focusing on the rear seat, the trends of all averaged magnitudes are closely similar to those of the left-front seat in Fig. 5.

From Fig. 8 with focusing the sound signal to which the microphone is attached at the surface of the rear seat, the trends of all averaged magnitudes are closely similar to those of the right-front seat in Fig. 6.

CONCLUSIONS

An analysis of vibration and sound signals of a hybrid-engine car with three different operating modes at three different positions within the passenger room has been initiated. The locations of vibration sensors are at the right-front seat, the left-front seat, and the rear seat, meanwhile the microphone is attached to the rear seat. The important frequency spectral features have been extracted for five different engine speeds ranging from 750 to 3750 rpm. As for the vibration analysis with positioning focus, the left-front seat presents the highest levels of averaged magnitudes for EV-drive mode and hybrid-drive mode, meanwhile, the right-front seat shows the highest levels of averaged magnitudes for engine-drive mode. As for the vibration analysis with operating mode focus, the hybrid-drive mode gives mostly the highest levels of averaged magnitudes for all sensor positions. As for the sound analysis, the engine-drive mode reflects the highest levels of averaged magnitudes for operating modes. Concentrating on varying engine speeds, the levels of vibration and sound magnitudes directly vary with the engine speed. All in all, the study summarizes that the proposed analysis technique of vibration and sound signals can be used to distinguish the signal features of all scenarios of an HEV car. In future works, this study is anticipatively applied with other types of new electric vehicles with some improved signal processing techniques.

ACKNOWLEDGMENTS

The study was supported by Kasetsart University, Faculty of Engineering at Sriracha. The associated working equipment was arranged by the members of the Mechanical System and Signal Processing research group.

REFERENCES

[1] Sarrazin M., Gillijns S., Anthonis J., Janssens K., Auweraer H. V. D., Verhaeghe K., NVH Analysis of a 3 Phase 12/8 SR Motor Drive for HEV Applications, in Proc. Int. Conf. on World Electric Vehicle Symposium and Exhibition, 2013, pp. 1-10.

[2] Liao L., Zuo Y., Meng H., Liao X., Research on the Technology of Noise Reduction in Hybrid Electric Vehicle with Composite Materials, Advances in Mechanical Engineering, Vol. 10, Issue 3, 2018, pp. 1-8.

[3] Liao L. Y., Zuo Y. Y., Liao X. H., Study on Hybrid Electric Vehicle Noise and Vibration Reduction Technology. Advanced Materials Research, Vol. 764, 2013, pp. 141-148.

[4] Novikov A., Novikov I., Shevtsova A., Study of the Impact of Type and Condition of the Road Surface on Parameters of Signalized Intersection, Transportation Research Procedia, Vol. 36, 2018, pp. 548-555.

[5] Hu H., Zhong Z., Explicit–Implicit Co-Simulation Techniques for Dynamic Responses of a Passenger Car on Arbitrary Road Surfaces, Engineering, Vol. 5, Issue 6, 2019, pp. 1171-1178.

[6] Czech K. R., The Impact of the Type and Technical Condition of Road Surface on the Level of Traffic-Generated Vibrations Propagated to the Environment, Procedia Engineering, Vol. 143, 2016, pp. 1358-1367.

[7] Huang Y., Li D., Subjective Discomfort Model of the Micro Commercial Vehicle Vibration over Different Road Conditions, Applied Acoustics, Vol. 145, 2019, pp. 385-392.

[8] Litak G., Borowiec M., Friswell M. I., Szabelski K., Chaotic Vibration of a Quarter-Car Model Excited by the Road Surface Profile, Communications in Nonlinear Science and Numerical Simulation, Vol. 13, Issue 7, 2008, pp. 1373-1383.

[9] Blekhman I., Kremer E., Vibrational Resistance to Vehicle Motion Due to Road Unevenness, Journal of Sound and Vibration, Vol. 405, 2017, pp. 306-313.

[10] Yujun L., Peter W. T., Xin Y., Jianguo Y., EMD-Based Fault Diagnosis for Abnormal Clearance between Contacting Components in a Diesel Engine, Mechanical Systems and Signal Processing, Vol. 24, Issue 1, 2010, pp.193–210.

[11] Xia W., Changwen L., Fengrong B., Xiaoyang B., Kang S., Fault Diagnosis of Diesel Engine based on Adaptive Wavelet Packets and EEMD-Fractal Dimension. Mechanical Systems and Signal Processing, Vol. 41, Issue 1-2, 2013, pp. 581–597.

[12] Binqiang C., Zhousuo Z., Chuang S., Bing L., Yanyang Z., Zhengjia H., Fault Feature Extraction of Gearbox by using Over Complete Rational Dilation Discrete Wavelet Transform on Signals Measured from Vibration Sensors. Mechanical Systems and Signal Processing, Vol. 33, Issue 11, 2012, pp. 275–298.

[13] Liang B., Iwnicki S. D., Zhao Y., Application of Power Spectrum, Cepstrum, Higher Order Spectrum and Neural Network Analyses for Induction Motor Fault Diagnosis. Mechanical Systems and Signal Processing, Vol. 39, Issue 1-2, 2013, pp. 342–360.

[14] Chomphan S., Towards the Development of Speaker-Dependent and Speaker-Independent Hidden Markov Model-Based Thai Speech Synthesis. Journal of Computer Science, Vol. 5, Issue 12, 2009, pp. 905-914.

[15] Chomphan S., Wongchai B., Correlation Analysis of Vibration and Sound Signals of a Gasoline-Engine Car, International Journal of GEOMATE, Vol.18, Issue 67, 2020, pp. 195-201.

[16] Chomphan S., Chaimanatsakun A., Sakornsin R., Khumneungratavongsa S., Rattanarat K., A Comparative Study of LPG-modified Engine and Normal Oil-usage Engine. in Proc. Int. Conf. on Engineering and Applied Sciences, 2016, pp. 219-225.

[17] Akhand R., Upadhyay S. H., A Review on Signal Processing Techniques Utilized in the Fault Diagnosis of Rolling Element Bearings, Tribology International, Vol. 96, Issue 4, 2016, pp. 289-306.

[18] Ahmad T. A., Barat G., Teymour T. H., Seyed S.M., Vibration Analysis of a Diesel Engine Using Biodiesel and Petro Diesel Fuel Blends, Fuel, Vol. 102, Issue 12, 2012, pp. 414–422.

[19] Zunmin G, Jin C., Barry H., Analysis of Engine Vibration and Design of an Applicable Diagnosing Approach. International Journal of Mechanical Sciences, Vol. 45, Issue 8, 2003, pp. 1391–1410.

[20] Xianhua L., Randall R. B., Jerome A., Blind Separation of Internal Combustion Engine Vibration Signals by a Deflation Method. Mechanical Systems and Signal Processing, Vol. 22, Issue 5, 2008, pp.1082–1091.

[21] Xianhua L., Randall R. B., Blind Source Separation of Internal Combustion Engine Piston Slap from other Measured Vibration Signals. Mechanical Systems and Signal Processing, Vol. 19, Issue 6, 2005, pp. 1196–1208.

[22] Zbigniew S., Jan W., Application of Vibration Signals in the Diagnosis of Combustion Engines – Exploitation Practices. Journal of KONES Powertrain and Transport, Vol. 18, Issue 3, 2011, pp. 405-412.

[23] Carlucci A. P., Chiara F. F., Laforgia D., Analysis of the Relation Between Injection Parameter Variation and Block Vibration of an Internal Combustion Diesel Engine. Journal of Sound and Vibration, Vol. 295, Issues 1–2, 2006, pp. 141–164

[24] Boonsit S., Chomphan S., Vibration Signal Analysis for LPG-modified Engine and Normal Oil-usage Engine with Different Engine Speeds and Faults. in Proc. International Congress on Engineering and Information, 2017, pp. 102-107.

[25] Chomphan S., Vibration Signal Analysis of a Motorcycle, International Journal of GEOMATE, Vol.16, Issue 56, 2019, pp. 27-32.

[26] Chomphan S., Kingrattanaset T., Boonsit S., Signal Analysis for LPG-modified Gasoline Engine with Engine Faults, International Journal of GEOMATE, Vol.16, Issue 56, 2019, pp. 65-72.

[27] Chomphan S., An Analysis of Vibration for A Gasoline-engine Car Driving on Three Types of Roads, International Journal of GEOMATE, Vol.20, Issue 80, 2021, pp. 29-35.

FACTOR ANALYSIS OF CONFLICT FACTOR EFFECT TO PROJECT MANAGEMENT IN GOVERNMENT CONSTRUCTION

Bancha Teanngen [1],Korb Srinavin[2*], Tanayut Chaitongrat[3], Wuttipong Kusonkhum[4], and Watcharapong Deewong[5]
[1,2]Department of Civil Engineering, Khon Kaen University, Khon Kaen, Thailand
[3]Faculty of Architecture, Urban Design and Creative Arts, Mahasarakham University, Mahasarakham, Thailand.
[4]Department of Civil Engineering, Faculty of Engineer, Northeastern University, Khon Kaen, Thailand
[5]School of Civil Architecture, UdonThani Rajabhat University, UdonThani, Thailand

ABSTRACT

Conflict is one parameter that is critical to the success of a construction project. In general, projects have different objectives and formats. In addition, throughout project management, each project is different. There are many different factors in a construction project and these factors cause conflicts between stakeholders. Thus, this study aims to identify groups of conflict factors that affect project success. In this study, data were collected by questionnaire from government agencies which response rate was more than 70%. Moreover, the data was analyzed by exploratory factor analysis. The finding of this study demonstrates groups of conflict factors in project management. Further, the groups were divided into two groups: construction contract management and construction management in the execution phase. Construction contract factor includes conflicts from contract management and conflicts from construction management. And construction management factor in the execution phase includes carelessness or a negative attitude of the project participants, the delayed decision of the project owner, confusing needs of the project owner, the project participants lack of management and supervision of the project, working functional defects, quality of construction materials or machines and on-site condition.

Keywords: Construction management, Conflict management, Factor analysis, Conflict factor.

INTRODUCTION

The construction industry is unique, complicated, and different from other industries. Additionally, there are limitations such as working outdoor, weather conditions, and limit of time which affect the working process [1-3]. Moreover, the construction project must be successful by the cooperation of a project owner, an architect, a construction supervisor, a contractor, and other stakeholders [4].

Since the cooperation consists of parties, it causes misunderstanding, dissatisfaction, and disagreement among each other. Further, it can delay the project, increase the higher budget and reduce the productivity of works, which affects the business damage [5-7]. The conflict is unavoidable for construction projects at all levels, which is considered a normal situation [7-9]. In addition, the study work of Pétursson, B. K. (2015) has found that the efforts to resolve conflicts and disputes caused an average financial loss of 32.2 million USD per year. Additionally, each project required 13 months to recover on average [10]. Moreover, the conflicts and disputes [10]. Moreover, the conflicts and disputes in a construction project happened from 4 big problems as follows; Contractual problems, Behavioral problems, Technical problems [7-8], and Communication problems. Additionally, in the communication problem, some personnel have private relation issues involved, which could affect the reduced collaboration efficiency.

Conflicts in a construction project are an essential issue that affects various aspects of project management. Thus, this article aims to analyze conflict factors affecting project management in government constructions. As well as to understand the conflicts of government construction projects, and to apply this understanding as a guideline for preventing and coping with the occurrence of conflicts.

LITERATURE REVIEW

Conflict Management

A conflict is a different situation between two people or two groups of people. Those people have expressed different cognitive behaviors causing misunderstanding and different needs. In addition, Project Management Institute (2013) suggested that factors that affect conflicts in the project consisted of limited sources, a priority of time schedules, and individual rules, procedures, and performance. Nevertheless, the conflicts can be reduced by understanding and setting the common goals between those stakeholders [12].

Cause of Construction Conflict

The conflicts affect various issues of the construction project [6] such as increased budgets, delay in the project, reduced productivity of work, loss of benefits, and business relations. In addition, three main problems cause the conflicts: Behavioral problems, Contractual problems, and Technical problems [8], [13-14]. The conflicts affect the performance of the project stakeholders including the project owner, an architect, a supervisor (advisor), a contractor, and a subcontractor. Those will lead to poor communication, delay in payment, and Contractual claims which causes an argument afterward [15-17]. From what was mentioned above, the main problems are as follows.

Behavioral problems

Interaction between human, personality, cultures, and professional background of each participant in the project. Additionally, there are other related behavioral problems such as Individual ambition, Frustration, Dissatisfaction, Desire for growth, Faith, Fraud, Communication, and level of power, etc. [3], [5].

Contractual problems

Variation, extension of time, payment, quality of technical specifications, availability of information, administration and management, unrealistic client expectation, and determination [1], [5-6].

Technical problems

Such as unrealistic contract duration, late instructions or information from an architect or an engineer, overdesign, inadequate site report, complete technical specifications [3], [5].

Cause of Construction Conflict

From literature review of conflict factors affecting project management in constructions, it can be summarized and categorized as shown in table 1.

Factors Analysis

The Factors Analysis is a statistical analysis technique used to explore or identify the latent variables hidden in the observed variables [18]. In addition, the variables can be group into groups called factors. The Exploratory Factor Analysis consists of 4 processes [18-19] as following.

1) The first process of factors analysis is to find the straight-line relationships between two variables by using the Pearson Correlation formula. Each pair of variables which required to be group will be in Correlation Matrix.

2) The second process is Factor Extraction. This process is to find some factors that can explain the correlation. Factor extraction is divided into two main principles: Principal Component Analysis (PCA) and Common Factor Analysis (PCA).

3) The third process is indicating which group each variable should be in. In addition, there are two kinds of rotation: Orthogonal and Oblique Rotation.

4) The fourth process is Factor Meaning. This process is to indicate a name or define a meaning for the factor or variable by considering that each factor consists of which variables.

Preliminary agreement and audit criteria for exploratory elemental analysis consist of at least 300 samples [16], the variables must have ordinary contributions [15-19]. And that needs to be tested by the value of Skewness and Kurtosis. Moreover, the value of Skewness and Kurtosis needs to be between -2 to 2, and the value of Correlation needs to be between 0.3 to 0.9 [15]. Additionally, it is necessary to verify that Metrix Correlation of discrepancy of variables must reject the hypothesis, or p-Value < 0.05 [18-19], Eigenvalue must be more than 1.00 [18-19] and Kaiser-Meyer-Olkin (KMO) test value must be higher than the standard of 0.50. Thus the data would be considered suitable data for factors analysis. Moreover, there is Bartlett's Test of Sphericity which is used for testing the hypothesis to see if this correlation matrix is the unity matrix or not [18-22].

Table 1 Conflict factors affecting project management in constructions in contexts.

Coding	Factors	Reference
IO1	carelessness or negative attitude of the project participants.	[Jaffar, N., et al., 2011]
IO2	Delayed decision of the project owner.	[Chaitongrat, T., et al., 2021]
IO3	Working does not meet the requirements.	[Jaffar, N., et al., 2011]
IO4	Confusing the needs of the project owner.	[Pétursson, B. K., 2015]
IO5	Lack of efficiency in the work of the contractor.	[San Loke, Y., 2013]
IO6	Lack of efficiency in the work of the sub-contractor.	[Jaffar, N., et al., 2011]
IO7	Those participants in the project lack the management and supervision of the project.	[Pétursson, B. K., 2015]
IO8	Functional defects	[Acharya, N. et al., 2006]
IO9	The quality of materials or machines used in the construction.	[Jaffar, N., et al., 2011]
IO10	On site condition	[Pétursson, B. K., 2015]

RESEARCH METHODOLOGY

This research is a factors analysis of conflict factors that affect the government's construction projects. In addition, this study is quantitative research which is conducted as follows.

The population and sample

The samples in this study were 454 government construction projects, the Department of Public Works and Town & Country Planning. those projects were the budget year of 2019. According to the preliminary agreement of using statistics for Factor Analysis, it indicated that there must be no less than 300 samples [23] in the study. Thus all of the samples were the participants in the study.

Research instrument

A questionnaire is used in this research. It has been divided into two parts: The first part is about general information of the participants and the second part is issues, problems, conditions of the contract for architecture and construction supervision. Additionally, the questionnaire is a close-ended question. And the samples are measured with the Rating Scale. This measurement passed the Index of Item-Objective Congruence (IOC) test by three experts [24].

In addition, the questionnaire can indicate the Reliability value by using Try out method with a similar group of 30 populations who were not the sample. Moreover, this instrument has Cronbach's Alpha value of 0.958, which is more than 0.70, so it is considered reliable and suitable for collecting data [25].

Data collection

This research collected the data by using Web Surveys [22], which had been helped by Department of Public Works and Town & Country Planning in contacting those engineers who were in charge of the government construction projects.

In addition, there were 339 projects responded which are considered 73.81% from the whole number of government projects that the Department had contacted for data collection.

Data Analysis

There are three levels of statistical analysis in this research as follows; (1) Single Variate Analysis, such as number, percentage, mean, standard deviation (SD), skew and kurtosis. (2) Bivariate Analysis, this is to find Correlation value by using Pearson Product Moment test to identify the correlation coefficient value between variables, the value is between 0.3 to 0.9 [19]. And (3) Multivariate Analysis, this one uses the Principal Component Factor Analysis method and performs Orthogonal rotation by Varimax method which considers factor loading.

Additionally, the factor loading value higher than 0.30 is focused. After all, the statistical values for each factor from exploratory factors analysis will be compared with factors from the literature review. Moreover, those factors will be given names analyzed to find the reliability value of Cronbach's alpha for each factor [19].

Furthermore, the data of general information of the participants have been analyzed by using basic statistics which is a percentage. In addition, the issues, problems, conditions of the contract for architecture and construction supervision have been measured by estimation of Likert [26].

After that, factor analysis has been performed to group the group of conflicts factors that affect the government construction projects.

RESULTS

The results of the study of conflict factors which affect the government construction projects have been divided into two parts which are characteristics of the participants and results of descriptive data analysis. The details are as follows.

General Information of Participant

Most of the participants are male for 54.4%, age between 30-40 years old for 50%, education background with Bachelor's degree for 100%, with experience in government construction project management for 9.5 years on average (SD = 7.6). Those participants were also in charge of all government construction projects, and those project values were not over 50 million THB for 50%.

Results of Descriptive Data Analysis

The results have found that the government projects have had opinions toward conflict factors that affect the government construction projects at the lowest significant level, which accounted for 2.26 points (SD=1.10). In addition, to consider each factor, it has been found that the lack of efficiency of a subcontractor had the highest average point of the significant level at 2.94 (SD = 1.19). The second highest point was the lack of efficient contractors, which the average point was at 2.74 (SD = 1.13). The following one was not working follows the requirements, the average point of the significant level was at 2.53 (SD=1.39). The next factor was the project participants' lack of management and supervision of the project; the average point was at 2.4 (SD = 1.05). And the last two factors with very low points were carelessness or negative attitude of the project participants at the average point of the significant level at 1.67 (SD=0.69). The data has shown in Table 2.

Conflict Factors Affecting Government Construction Projects

Preliminary examination results have found that all observed variables had a normal distribution. In addition, Correlation Coefficient analysis between 10 variables by the Pearson Correlation test, which correlation coefficient value was between 0.300 to 0.818, had a statistically significant positive correlation at the level of 0.01.

The statistic met the Correlation Coefficient criteria which its suitable value should be between 0.3-0.9 [16]. The results were as below.

Table 2 Percentage, standard deviation (SD) and significant levels of conflict factors affecting the government construction projects. (n = 337)

No.	Factor ID	Conflict factors	Significance		
			Mean	SD	Level
1	IO1	Carelessness or negative attitude of the project participants.	1.67	0.96	Very low
2	IO2	Delayed decision of the project owner.	2.04	1.15	Low
3	IO3	Not working follows the requirements.	2.53	1.39	Low
4	IO4	Confusing needs of the project owner.	1.94	1.12	Very low
5	IO5	Lack of efficiency of a contractor.	2.74	1.13	Medium
6	IO6	Lack of efficiency of a contractor.	2.94	1.19	Medium
7	IO7	The project participants lack of management and supervision of the project.	2.40	1.05	Low
8	IO8	Working functional defects.	1.99	1.01	Low
9	IO9	Quality of construction materials or machines.	2.28	1.00	Low
10	IO10	On site conditions.	2.07	1.03	Low
		Total	2.26	1.10	Low

Analysis of conflict factors in time management of the government construction projects was performed by using Principal Component Analysis (PCA). The results have found that Kaiser-Meyer-Olkin (KMO) value was at 0.821, which was more than 0.05 to 1 and was considered as high.

This indicated that the analyzed data was suitable to use for factors analysis. Moreover, Bartlett's test of Sphericity was also performed. It has found that the Chi-square value was at 3109.435, and p-Value < 0.01, less than 0.05, which meant that the received correlation matrix was not in the line with the unity matrix. It demonstrated that 10 variables had relations between each other. Thus, it was suitable to use for factors analysis (Table 3).

In addition, Factor Extraction by Principal Component Analysis, was performed by using the Orthogonal Rotation with the Varimax method. The received factors were the conflict factors of time management of the government construction projects considering from components which had a variance of the variables (Eigenvalue) more than once. Additionally, there were two components (Table 4-6) that followed the criteria and consisted of 40 variables. However, four variables were cut off since they did not follow factor loading. The variance values of all variables were 74.85% and it is shown in Figure 1.

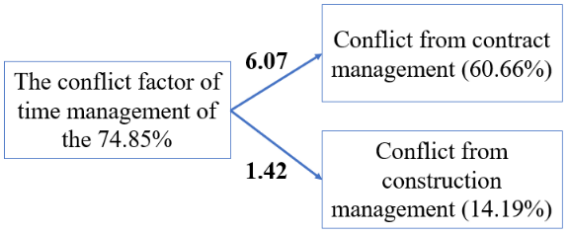


Fig. 1 Conflict factors affecting the government construction projects.

Table 3 The result of suitability examination of unity matrix between variables

Variable	KMO		Bartlett's test	
	Suitable value	Received value	Suitable value	Received value
14 variables	More than 0.50 (>0.9 = very good)	0.821	P-value < 0.05	<0.01

Table 4 Components, Eigen Value, percentage of variance and percentage of cumulative variance

Component	Conflict factors affecting the government construction projects	Number of questions	Eigen values	% of Variance	Cumulative % of Variance
1	Conflicts from contract management	7	6.07	60.66	60.66
2	Conflicts from construction management	3	1.42	14.19	74.85

This research study has found two components of conflicts which affect the government construction

projects. They were considered from high point to low point.

1) Component of conflicts from contract management. This component affects the government construction at 60.66%. In addition, this component consists of 7 observed variables: carelessness or negative attitude of the project participants, the delayed decision of the project owner, confusing needs of the project owner, the project participants lack of management and supervision of the project, working functional defects, quality of construction materials or machines, and on-site condition. Additionally, those factors conform to the finding of Sutthi Suntharanurak in 2012. His research has found that the accuracy of the price estimation for the contractor from the poor management and organization would affect contract management during the process [27]. Moreover, the research study of Anita Rauzana in 2016 has divided the groups of conflict factors. It consists of a project owner, the project supervisor, and contract management [28]. Further, the variables of this research conform to the results of other study works, such as conflicts from the corruption procurement among the contractors [29-31].

Table 5 Component 1 Conflicts from contract management

Variables	**Conflict factors**	**Factor loadings**
IO1	Carelessness or negative attitude of the project participants.	0.866
IO2	The delayed decision of the project owner.	0.842
IO4	Confusing needs of the project owner.	0.686
IO7	The project participants lack of management and supervision of the project.	0.652
IO8	Working functional defects.	0.592
IO9	Quality of construction materials or machines.	0.605
IO10	On site condition.	0.844
7 factors	Eigenvalues	6.07
	Percent of variance	60.66

Table 6 Component 2 Conflicts from construction management

Variables	Conflict factors	Factor loadings
IO5	Lack of efficiency of a contractor	.911
IO6	Lack of efficiency of a subcontractor	.915
IO3	Not working follows the requirements.	.801
3 factors	Eigenvalues	1.42
	Percent of variance	14.19
	Cronbach's Alpha	XXX

2) Component of conflicts from construction management. This component demonstrates conflicts that affect the government construction at 14.19%. In addition, this component consists of 3 observed variables: lack of efficiency of a contractor, lack of efficiency of a subcontractor, and not working follows the requirements. Additionally, those 3 factors conform to the research study of Bancha Teanngen in 2020 which indicated that the risks affecting cost management and project timing mainly arise from stakeholders, including their management or cooperation among the stakeholders themselves [9], [23]. Moreover, it has found that the observed of this study conform to the results of Organization for Economic Co-operation and Development's research in 2016, which mentioned about the project participants or the stakeholders who take part in the corruption during procurement can lead to conflicts during process of the project and would affect the image of the project [32-33].

CONCLUSIONS

The contribution of this study is the defining conflict in construction that affects project management. The conflicts could be divided into two groups. The first group is the construction contract group which includes conflicts from contract management and conflicts from construction management.

And the second group is the construction management group in the execution phase. It includes carelessness or negative attitude of the project participants, the delayed decision of the project owner, confusing needs of the project owner, the project participants lack of management and supervision of the project, working functional defects, quality of construction materials or machines, and on-site condition.

SUGGESTIONS FOR FURTHER RESEARCH

From the study of conflict factors affecting the government construction projects, it has found two components of conflicts. Those two components consist of conflicts from contract management and conflicts from construction management. Both conflicts components could demonstrate the problems in construction projects. Thus, this information could be used to raise awareness, find solutions and prevent conflicts affecting government construction projects. A recommendation to those project participants includes the project owner, the contractor, and the project supervisor is that they should have created a working system as a guideline when there is a conflict through a meeting and a common direction.

ACKNOWLEDGMENTS

The researchers would like to express our sincere thank to the directors and personnel from the Comptroller General's Department, Ministry of Finance, the Department of Public Works and Town

& Country Planning, Ministry of Interior, Khon Kaen University, Northeastern University and Maha Sarakham University for your invaluable helps. Your helps were truly useful and were the part to make this research study successful.

REFERENCES

[1] Jervis, B.M.; Levin, P. Construction law, principles and practice; McGraw-Hill College, 1988.

[2] Boonyarit Chonpitakwong, Wuttipong Kusonkhum, Tanayut Chaitongrat, Korb Srinavin, and Phatsaphan Charnwasununth, Hindrance of Applying Big Data Technology for Construction Management in Thai Government. Journal of Advances in Information Technology, 2021, 12(2), May 2021, pp. 159-163,

[3] Chaitongrat,T., Leungbootnak, N., Kusonkhum, W., Deewong,W., Srinavin, K., Measurement model of good governance in government procurement. IOP Conference Series Materials Science and Engineering, 2018, 639:012024. 639(1), 0120204.

[4] Surachai Thasuwanin, Factors Affecting the Construction Conflict Between Consultant and Contractor, 201, Chiang Mai University.

[5] Khahro, S. H., & Ali, T. H., Causes Leading to Conflicts in Construction Projects: A Viewpoint of Pakistani Construction Industry. In International Conference on Challenges in IT, Engineering and Technology (ICCIET 2014). Phuket: International Institute of Engineers.

[6] San Loke, Y., A Study of Causes and Effects of Conflict in Construction Industry, (Doctoral dissertation, UMP).

[7] Jaffar, N., Tharim, A. A., & Shuib, M. N., Factors of conflict in construction industry: a literature review. Procedia Engineering, 2011, 20, 193-202.

[8] Pétursson, B. K., Disputes and Conflicts within Construction Contracts in the Icelandic Construction Industry, 2015.

[9] Bancha Teanngen, Wuttipong Kusonkhum, Surapong Liwthaisong, Tanayut Chaitongrat and Korb Srinavin., Risk factors affecting conflict management for construction government project in Thailand. Multidisciplinary Technologies for Industrial Applications, 2020, pp. 94–105, doi: https://doi.org/10.13052/rp-9788770225823.

[10] Khaled Al Shami., Investigating the use Building Information Modeling (BIM) in Managing Construction Claims. PM World Journal, 2018, Vol. VII, Issue II – February 2018.

[11] Enshassi, A., Mohamed, S., & Abushaban, S., Factors affecting the performance of construction projects in the Gaza strip. Journal of Civil engineering and Management, 2019, 15(3), 269-280.

[12] PMI, A., guide to the project management body of knowledge (PMBOK guide). In Project Management Institute (Vol. 5), 2015.

[13] Leungbootnak, N., Chaithongrat, T., & Aksorn, P., An Exploratory Factor Analysis of Government Construction Procurement Problems. MATEC Web of Conferences 192, 2018, 02053 (2018), pp.1-4,

[14] Korb Srinavin, Wuttipong Kusonkhum, Boonyarit Chonpitakwong, Tanayut Chaitongrat, Narong Leungbootnak, and Phatsaphan Charnwasununth., Readiness of Applying Big Data Technology for Construction Management in Thai Public Sector. Journal of Advances in Information Technology, 2021, 12(1), February 2021, pp. 1-5.

[15] Khahro, S. H., & Ali, T. H., Causes leading to conflicts in construction projects: a viewpoint of Pakistani construction industry. In International Conference on challenges in IT, Engineering and Technology (ICCIET'2014), 2014, July (pp. 17-18).

[16] Acharya, N. K., Dai Lee, Y., & Im, H. M., Conflicting factors in construction projects: Korean perspective. Engineering, construction and architectural management, 2006.

[17] Zidane, Y., & Andersen, B., Causes of delay and their cures in major Norwegian projects, 2018.

[18] Chaichana, C. Using multivariate statistics for research: designing, analyzing, and interpreting, Bangkok: Chulalongkorn University Printing House, 2015.

[19] Andy Field. Discovering Statistics Using IBM SPSS Statistics. 4th ed. London: Sage Publications Ltd, 2012.

[20] Pranee, l. Finding quality of measurement and evaluation tools, Yala: Yala Rajabhat University, 2016.

[21] Nonglak, W. LISRELL Model: Statistical Analysis for Research, Bangkok: Chulalongkorn University Printing House, 1999

[22] Hair, J.F., Black, W.C., Babin, B.J., Anderson, R.E., and Tatham, R.L. Multivariate data analysis. 6th ed. New Jersey: Pearson Education, 2006.

[23] W. Lawrence Neuman. Qualitative and Quantitative approaches. 6th ed. Boston: Allyn and Bacon, 2006.

[24] Kangpheng, S, Gunlong, S and Kaewin, D. Mixed Methods: Paradigms of Research for the 21st Century. Khon Kaen: Apichat, 2016.

[25] Vorakitkasemsakul, S. Applied Statistics for Behavioral and Social Science Research, Udon Thani: Aksonsin, 2011.

[26] Siljaru, T. Research and Analysis of Statistical Data with SPSS, 9th ed. Bangkok: Se-education, 2008.

[27] Suthe, S. Economics of Bid Rigging : A Review of Literature, NACC Journal, 2011, 4 (1), pp. 94-117.

[28] Rauzana, A., Causes of conflicts and disputes in construction projects. Journal of mechanical and civil engineering, 2016, 13, 44-48.

[29] Goldberg, P., Anderson, M., & Aubertine, A. Bid Rigging Detection Government, 2004. Available from: http://www.osbar.org/_docs/sections/antitrust/attr_cle_bid_rigging.pdf. [Accessed 20 August 2016]

[30] OECD. Preventing Corruption in Public Procurement, Organization Economic Co-operation and Development, 2016. Available from: from www.oecd.org/document/19/…. [Accessed 22 August 2016]

[31] Joras, F., Ioana D. & Brigitte U. Corruption in Public Procurement: Finding the Right Indicators. Eur J Crim Policy Res, 2017, 23 (2), pp. 245–267. DOI 10.1007/s10610-016-9312-3.

[32] Teanngen, B., Kusonkhum, W., Rattanapongwanich, S., Chaitongrat, T., & Srinavin, K., The Factor of Conflict Effect to Government Construction Project. Engineering Journal of Research and Development, 2021, 32(1), 77-88.

[33] Chaitongrat, T., Liwthaisong, S., Aksorn, P., Kusonkhum, W., Leungbootnak, N., Causal Relationship Model of Problems in Public Sector Procurement. International Journal of GEOMATE,2021, 20(80), pp. 52–58.

7th Int. Conf. on Structure, Engineering & Environment (SEE), Pattaya, Thailand, Nov.10-12, 2021, ISBN: 978-4-909106070 C3051

SEEPAGE FLOW ANALYSIS CONSIDERING THE EFFECTS OF INTERNAL EROSION DUE TO LONG-TERM SEEPAGE INTO GROUND COMPRISING SURFACE IMPERMEABLE GROUND

Naoko Sakamoto[1], Mari Sato[2]
[1]Graduate school of environmental and life science, Okayama University, Japan;[2]Academic Assembly, Shimane University, Japan

ABSTRACT

There have been several reports on ground disasters such as soil piping due to heavy rainfall. This is commonly observed when the ground consists of a surface low-permeable layer containing clay or silt, and a foundation composed of high-permeable layer. However, repeated infiltration might have hidden effects on the ground even during normal rainfall. The aim of this study is to elucidate the effect of fine particle movement caused by long-term water infiltration into the ground. Based on the results of previous modeling experiments that examined long-term penetration into a ground model with a lower high permeability layer and an upper low permeability layer and by performing the measurement of particle movement in the ground, we performed steady seepage analysis considering a change in the local coefficient of permeability due to internal erosion. Specifically, a steady seepage analysis was performed on a two-layer ground model, considering cases where the water permeability coefficient distribution is uniform in each of the two layers before erosion, and then water permeability coefficient distribution was changed by considering particle movement after erosion. We compared the results obtained by changing the location, width of inflow and outflow, and analytical ground saturated permeability. According to the results, when water is infiltrated from the lower high permeability layer, the downward hydraulic gradient tended to be larger after erosion near the boundary on the upper low permeability layer. Clogging in the vicinity of the boundary layer is estimated to cause the phenomenon.

Keywords: Internal erosion, Steady seepage flow analysis, Finite element method, Riverbank

INTRODUCTION

In recent years, several cases of ground disasters such as piping during heavy rains have been reported on the ground with a low permeable foundation layer containing clay or silt and a upper surface layer of the permeable layer [1]. The internal situation before the piping occurs is often unknown. In addition, there is a possibility that there are hidden effects due to repeated infiltration during normal rainfall. In this study, we aim to clarify the effect of fine-grains movement on the ground due to long-term penetration, called internal erosion in this paper. Research on fine-grains transfer has been studied; Horikoshi and Takahashi [2] conducted an embankment model experiment, and Sato and Kuwano [3] did a basic study on triaxial compression test equipment. However, several situations related to the actual ground, where the layers are mixed complexly and the seepage flow is concentrated in a high permeable layer [4], have not been elucidated. In this study, a steady osmosis flow analysis was performed considering the change in local permeability due to the movement of fine grains in the ground. This study was based on the results of a model experiment of a previous study [5] that simulated long-term penetration into a ground model with a below high permeability layer and above a low permeable layer. After the infiltration and internal erosion, the particle size distributions were measured at some points of the ground. Then the local permeability change by the erosion was estimated.

ANALYSIS CONDITIONS OVERVIEW

In this study, VGFlow2D Ver.3 was applied for creating a two-layer ground model, and analyzing saturated and unsaturated seepage flow for three cases under six different ground conditions, for a total of 18 cases. The governing equation is Richards' equation, which is expressed in Eq. (1). Here, ρ is the fluid density, $K(\theta)$ is the hydraulic conductivity, t is time, ϕ is the pressure head, z is the positional head, and θ is the volumetric water ratio. In the analysis, based on the results of the model-scale experiment [5], the permeability was calculated considering the effect of internal erosion. Before erosion, the soil was assumed to be uniform in the upper fine-grained soil layer and the lower coarse-grained soil layer. However, after erosion, the hydraulic conductivity was corrected to have distribution within the soil due to the effect of internal erosion. As the soil movement inside the ground was assumed to be converged for a long

period time, at a constant hydraulic head difference, a steady-state analysis was adopted, and the skyline method (direct method) was used to calculate until convergence to the set judgment error. The details are explained as follows.

$$\nabla^T[\rho K(\theta)\nabla(\phi + z)] = \frac{\partial}{\partial t}(\rho\theta) \quad (1)$$

Analytical Ground Model

The analytical ground model is a two-dimensional, two-layer ground model, as shown in Figs. 1 and 2. The two-layer ground model is 30 cm in length and 30 cm in width. The mesh width was 2 mm near the drainage outlet and 4 mm near the water supply outlet. For Ground I, fine-grained soil and sand (approximately 10 times difference in permeability) were used as analysis materials, and for Ground II, alluvial soil and sand (approximately 20 times difference in permeability) were used to increase the difference in permeability between the upper and lower layers. 'Ground a' represents the pre-erosion ground before correction of saturated hydraulic conductivity, and 'Ground b' represents the post-erosion ground with correction of saturated hydraulic conductivity only at the points where the particle size distribution was measured in the model experiment [5]. 'Ground c' represents post-erosion ground where the saturated hydraulic conductivity was corrected only measured points in Ground b, but also at the unmeasured points; for the unmeasured area, the average of the post-erosion saturated hydraulic conductivity $K_{\mathrm{ea}}(\theta_s)$ of the neighboring sampling areas was used. The details are described later. The name of the ground model expressed as a combination of the abovementioned ground model (I or II) and the hydraulic conductivity correction conditions (a: before erosion, b: after erosion without hydraulic conductivity correction at unmeasured locations, c: after erosion with hydraulic conductivity correction at unmeasured locations; details are given later). Table 1 summarized the ground conditions. Figs. 1 and 2 show the two-dimensional meshes before erosion and after erosion, respectively, and the corresponding element definition partitions. Specifically, for the pre-erosion Grounds Ia and IIa, the uniform ground was set for the upper and lower layers, respectively, as shown on the left side of Figs. 1 and 2. In Ground Ia (Fig. 1, left), the upper layer of fine-grained soil is represented by olive, and the lower layer sand is represented by brown, while in Ground IIa (Fig. 2, left), the upper layer alluvium is green, and the lower layer sand is brown as in Ground Ia. In the upper layers of Grounds Ib, Ic (Fig. 1, right), and IIc (Fig. 2, right) after erosion, the areas where the particle size distribution was measured are numbered 14, 36, and 8, called measured points. The unmeasured areas are numbered 2, 5, 7, and 9. The areas where the particle size distribution was measured in the lower layer after erosion are numbered (1) (4), (3) (6), (5) (8), and the unmeasured areas are numbered (2), (7), and (9). In the post-erosion Grounds Ib, Ic, and IIc, the upper layers 14, 36, and 8 are light blue; the unmeasured upper layers 2, 5, 7, and 9 are olive in ground Ib and Ic and green in ground IIc; the measured lower layers (1) (4), (3) (6), and (5) (8) are purple; and the unmeasured lower layers (2), (7), and (9) are brown (Table 4).

Table 1 Analysis ground conditions

Ground model name	Upper fine-grained soil layer	Lower coarse soil layer	Internal conditions	Unmeasured point permeability correction
Ia	Fine-grained soil	Sand	Before erosion	
Ib	Fine-grained soil	Sand	After erosion	No correction
Ic	Fine-grained soil	Sand	After erosion	Correction
IIa	Alluvial soil	Sand	Before erosion	
IIc	Alluvial soil	Sand	After erosion	Correction

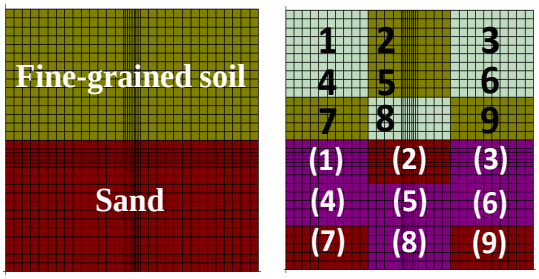


Fig. 1 Left: Element definition for Ground Ia.
Right: Element definition for Grounds Ib, Ic.

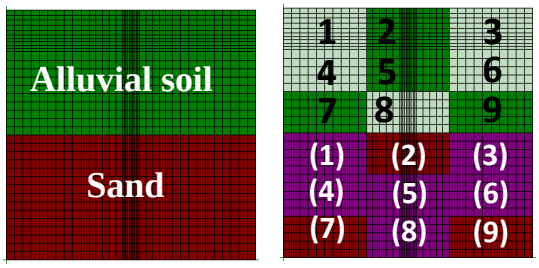


Fig. 2 Left: Element definition for Ground IIa.
Right: Element definition for Ground IIc.

Inlet Outlet Conditions

The analytical conditions for the three cases are shown in Table 2, simulating similar situations to model-scale experiments [5]. For the drainage conditions of the three cases, a hydraulic head difference of P = 0 cm was set as the boundary of seepage surface with an opening width of 6 mm or 20 mm in the center of the height of 0 cm. For the water supply condition, the known boundary of the water head was set as the water head difference N = 30 cm, and at the left and right ends: at the upper layer height of 25 cm in Case 1, and at the lower layer height of 12 cm in the Case 2 and 3, both with a width of 20 mm. All other boundaries are impermeable. For the results of the analytical ground models Ia, Ib, Ic, IIa, and IIc calculated in this study, they are summarized as IaIb, IaIc, and IIaIIc to compare the results before and after erosion, and the results of Cases 1–3 are discussed.

Table 2 Analysis conditions

Case name	Inlet (mm)	Outlet (mm)	Head boundary N (cm)	Seepage surface boundary P (cm)	Inflow position
Case1	20	6	30	0	upper layer 25 cm
Case2	20	6	30	0	Lower layer 12 cm
Case3	20	20	30	0	Lower layer 12 cm

ESTIMATION METHOD OF LOCAL SATURATED PERMEABILITIES AFTER EROSION AND OTHER PARAMETERS

To simulate the hydraulic conductivity of the upper layer No. 7 silica sand and the lower layer No. 3 silica sand in the model tests, two types of geomaterials with different hydraulic conductivities, as described above, were set as the materials for the analysis, and the ground was assumed to be isotropic. The van Genuchten model was used as the unsaturated seepage property, provided as typical parameters in VGFlow2D. The specific infiltration characteristics of each ground material are shown in Table 4. The parameters shown in Table 4 were the same before and after erosion. To predict the saturated hydraulic conductivity of each layer before erosion, we used Creager's estimation equation based on the original 20% particle size distribution values of No. 3 and 7 silica sand. This is $K_{\mathrm{o}}(\theta_{\mathrm{s}})$ in Eq. (2). For post-erosion, the saturated hydraulic conductivity is corrected by Creager's equation using 20% of the particle size at the points where the particle size distribution was investigated [5] after the penetration. The corrected saturated hydraulic conductivity after erosion is $K_{\mathrm{e}}(\theta_{\mathrm{s}})$. The analytical values of the saturated hydraulic conductivity for the fine-grained soil and sand samples for analysis are determined to change in the same ratio as that of K_{o} and K_{e} before and after erosion. $K_{\mathrm{oa}}(\theta_{\mathrm{s}})$ is the predetermined saturated hydraulic conductivity before erosion in the analytical soil model, combined with unsaturated properties by VGFlow2D. Then, the saturated hydraulic conductivity after erosion, $K_{\mathrm{ea}}(\theta_{\mathrm{s}})$ can be obtained using Eq. (2).

$$\frac{K_{\mathrm{e}}(\theta_s)}{K_{\mathrm{o}}(\theta_s)} = \frac{K_{\mathrm{ea}}(\theta_{\mathrm{s}})}{K_{\mathrm{oa}}(\theta_{\mathrm{s}})} \tag{2}$$

The specific values of $K_{\mathrm{oa}}(\theta_{\mathrm{s}})$ in three soils, are sand: 3.1×10^{-4} (m/s), fine-grained soil: 4.0×10^{-5} (m/s), and alluvial soil: 1.81×10^{-6} (m/s). Table 3 shows the saturated hydraulic conductivity conditions for Ground IaIb, Table 5 shows Ground IaIc, and Table 6 shows Ground IIaIIc. For unmeasured areas, the hydraulic conductivity cannot be determined by the method described above, but for Ground Ib, the value of $K_{\mathrm{oa}}(\theta_s)$ was used without correction for unmeasured areas as described earlier. For Grounds Ic and IIc, the average of the saturated hydraulic conductivities of adjacent sample locations was used.

Table 3 List of saturated permeability (Ground IaIb)

Permeability analysis value (m/s)			
	Case 1	Case 2	Case 3
Sand	$\mathbf{3.100\times10^{-4}}$	$\mathbf{3.100\times10^{-4}}$	$\mathbf{3.100\times10^{-4}}$
(1) (4)	$\mathbf{3.100\times10^{-4}}$	$\mathbf{3.100\times10^{-4}}$	$\mathbf{3.028\times10^{-4}}$
(3) (6)	$\mathbf{3.100\times10^{-4}}$	$\mathbf{2.958\times10^{-4}}$	$\mathbf{3.100\times10^{-4}}$
(5) (8)	$\mathbf{3.028\times10^{-4}}$	$\mathbf{2.958\times10^{-4}}$	$\mathbf{3.028\times10^{-4}}$
Fine grained soil	$\mathbf{4.000\times10^{-5}}$	$\mathbf{4.000\times10^{-5}}$	$\mathbf{4.000\times10^{-5}}$
1 4	$\mathbf{4.000\times10^{-5}}$	$\mathbf{2.345\times10^{-5}}$	$\mathbf{2.345\times10^{-5}}$
3 6	$\mathbf{4.000\times10^{-5}}$	$\mathbf{3.429\times10^{-5}}$	$\mathbf{3.765\times10^{-5}}$
8	$\mathbf{3.882\times10^{-5}}$	$\mathbf{2.089\times10^{-5}}$	$\mathbf{2.089\times10^{-5}}$

Table 4 Penetration characteristics

Color and pattern	Specific storage S_s (1/m)	Inclination angle of stratum ϕ_z (°)	α (1/m)	n	Residual water ratio θ_r	Saturation water ratio θ_s
	0	0	6.32	1.405	0	0.410
	0	0	1.02	2.130	0.199	0.517
	0	0	1.65	3.220	0.426	0.697

Table 5 List of saturated permeability coefficients (Ground IaIc)

Permeability analysis value (m/s)							
	Case 1	Case 2	Case 3	Layer	Case 1	Case 2	Case 3
Sand	3.100×10^{-4}	3.100×10^{-4}	3.100×10^{-4}	Lower	Unmeasured point		
(1) (4)	3.100×10^{-4}	3.100×10^{-4}	3.028×10^{-4}	(2)	3.076×10^{-4}	3.005×10^{-4}	3.052×10^{-4}
(3) (6)	3.100×10^{-4}	2.958×10^{-4}	3.100×10^{-4}	(7)	3.064×10^{-4}	3.029×10^{-4}	3.028×10^{-4}
(5) (8)	3.028×10^{-4}	2.958×10^{-4}	3.028×10^{-4}	(9)	3.064×10^{-4}	2.958×10^{-4}	3.064×10^{-4}
Fine grained soil	4.000×10^{-5}	4.000×10^{-5}	4.000×10^{-5}	Upper	Unmeasured point		
1 4	4.000×10^{-5}	2.345×10^{-5}	2.345×10^{-5}	2 5	3.961×10^{-5}	2.621×10^{-5}	2.733×10^{-5}
3 6	4.000×10^{-5}	3.429×10^{-5}	3.765×10^{-5}	7	3.941×10^{-5}	2.217×10^{-5}	2.217×10^{-5}
8	3.882×10^{-5}	2.089×10^{-5}	2.089×10^{-5}	9	3.941×10^{-5}	2.759×10^{-5}	2.927×10^{-5}

Table 6 List of saturated permeability coefficients (Ground IIaIIc)

Permeability analysis value (m/s)							
	Case 1	Case 2	Case 3	Layer	Case 1	Case 2	Case 3
Sand	3.100×10^{-4}	3.100×10^{-4}	3.100×10^{-4}	Lower	Unmeasured point		
(1) (4)	3.100×10^{-4}	3.100×10^{-4}	3.028×10^{-4}	(2)	3.076×10^{-4}	3.005×10^{-4}	3.052×10^{-4}
(3) (6)	3.100×10^{-4}	2.958×10^{-4}	3.100×10^{-4}	(7)	3.064×10^{-4}	3.029×10^{-4}	3.028×10^{-4}
(5) (8)	3.028×10^{-4}	2.958×10^{-4}	3.028×10^{-4}	(9)	3.064×10^{-4}	2.958×10^{-4}	3.064×10^{-4}
Alluvial soil	1.810×10^{-6}	1.810×10^{-6}	1.810×10^{-6}	Upper	Unmeasured point		
1 4	1.810×10^{-6}	1.061×10^{-6}	1.061×10^{-6}	2 5	1.792×10^{-6}	1.186×10^{-6}	1.237×10^{-6}
3 6	1.810×10^{-6}	1.551×10^{-6}	1.704×10^{-6}	7	1.784×10^{-6}	1.003×10^{-6}	1.003×10^{-6}
8	1.757×10^{-6}	9.453×10^{-7}	9.453×10^{-7}	9	1.784×10^{-6}	1.248×10^{-6}	1.325×10^{-6}

ANALYSIS RESULTS

Vertical Downward Hydraulic Gradient of the Upper Layer of the Ground

Figure 3 shows the flow net overlaid on the contour plot of the vertical dynamic gradient in the upper layer. The left figure shows the results before erosion (a), and the right figure shows the results after erosion (b or c). To highlight the changes before and after erosion, the scale is narrowed to a certain range by focusing only on the vertically downward direction where the largest difference is observed. The scale is -0.89–0 m for Case 1, -0.50–0 m for Case 2, and -0.55–0 m for Case 3. The specific values of the mean vertical hydraulic gradients in Cases 1, 2, and 3 near the boundary between the upper and lower layers and in the middle of the upper layer are shown in Table 7. In particular, the average vertical hydraulic gradient values for the 0.15 m wide and 0.07 m high part of the upper layer surrounded by the four points (0.07,0.15), (0.22,0.15), (0.07,0.22), and (0.22,0.22) were obtained as the upper layer just above the boundary. In the middle part of the upper layer, the average vertical hydraulic gradient of the 0.15 m wide and 0.02 m high part of the ground surrounded by the four points (0.07, 0.23), (0.22,0.23), (0.22,0.25), and (0.07,0.25) was calculated. The figure shows that the vertical downward hydraulic gradient just above the boundary between the upper and lower layers (y-axis 0.150 m) tends to be larger in Case 2 and Case 3 of all ground models after erosion than that before erosion. Table 7 also shows that the vertical downward hydraulic gradient just above the boundary of the two layers is approximately 10–20% larger after erosion than that before and the vertical downward hydraulic gradient after erosion decreases in the middle part of the upper layer (around 0.225 m y-axis) compared with that before erosion. Note that the rate of decrease was relatively small in the case of IaIc. Conversely, in Case 1, there was almost no difference in the hydraulic gradient before and after erosion regardless of calculated locations or the ground models.

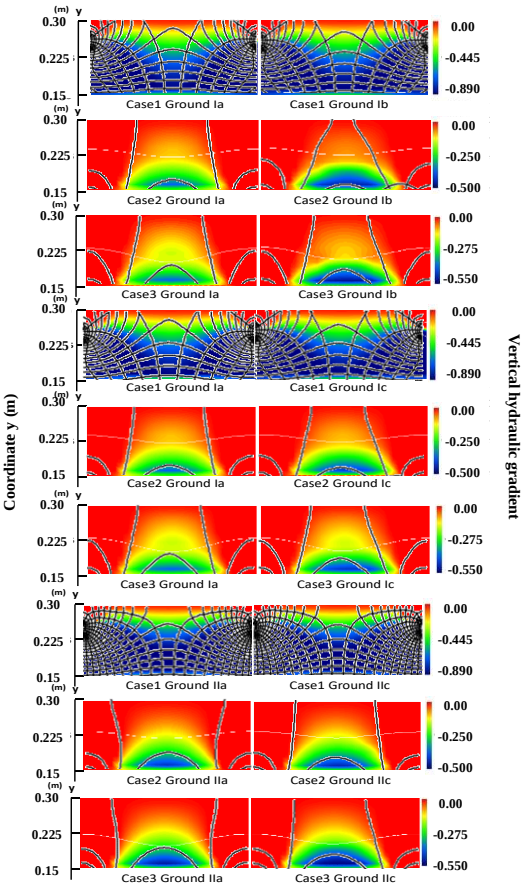


Fig. 3 Vertical hydraulic gradient contour diagram. (vertical downward direction only)

Table 7 Average vertical gradient

Average vertical gradient				
Ground model	Case	Erosion	Directly above the boundary	The middle of the upper layer
Ground IaIb	Case 1	before	-0.8015	-0.5707
		after	-0.7011	-0.5462
	Case 2	before	-0.1970	-0.0718
		after	-0.2410	-0.0520
	Case 3	before	-0.2220	-0.1060
		after	-0.2680	-0.0807
Ground IaIc	Case 1	before	-0.8015	-0.5707
		after	-0.8089	-0.5688
	Case 2	before	-0.1970	-0.0718
		after	-0.2190	-0.0702
	Case 3	before	-0.2220	-0.1060
		after	-0.2510	-0.1020
Ground IIaIIc	Case 1	before	-0.9702	-0.7058
		after	-0.9768	-0.7024
	Case 2	before	-0.2320	-0.0770
		after	-0.2680	-0.0585
	Case 3	before	-0.2770	-0.0916
		after	-0.3250	-0.0712

Average flow rate

The average flow velocities before and after erosion in the entire upper fine-grained soil layer and the lower erosion, after long time seepages. As a result, Case 2 and 3 showed significant changes after erosion but coarse-grained soil layer were calculated for all cases of ground models IaIb, IaIc, and IIaIIc. The results of each mean flow velocity are shown in Table 8. For example, the results for Ia in IaIb and IaIc are described as before erosion of Ground IaIb and IaIc. From the results of the mean flow velocity before and after erosion in the upper fine-grained soil layer and the lower coarse-grained soil layer, no significant difference in the flow velocity before and after erosion in the lower layer was observed in either ground model. Comparing the mean flow velocity between Cases 2 and 3 in Grounds IaIb and IaIc, the difference in the velocity between before and after erosion is highlighted in Ground Model IaIc, and the flow velocity tends to decrease after erosion. Comparing the ground model IaIc with the ground model IIaIIc, it can be observed that the flow velocity in the upper layer of the ground model IIaIIc is smaller after erosion as in the ground model IaIc. Furthermore, in Cases 2 and 3, where water was supplied to the lower layer in both ground models, a large difference in the average flow velocity between the upper and lower layers was observed due to the difference in the original permeability.

Table 8 Average flow velocity (Ground models IaIb, IaIc, and IIaIIc)

Average flow velocity (m/s)					
		Erosion	Ground IaIb	Ground IaIc	Ground IIaIIc
Case 1	Upper	before	1.027×10^{-5}	1.027×10^{-5}	2.126×10^{-6}
		after	1.028×10^{-5}	1.028×10^{-5}	2.112×10^{-6}
	Lower	before	6.653×10^{-5}	6.653×10^{-5}	3.670×10^{-6}
		after	6.618×10^{-5}	6.600×10^{-5}	3.649×10^{-6}
Case 2	Upper	before	7.375×10^{-6}	7.375×10^{-6}	4.127×10^{-7}
		after	6.100×10^{-6}	4.623×10^{-6}	2.303×10^{-7}
	Lower	before	2.317×10^{-4}	2.317×10^{-4}	2.316×10^{-4}
		after	2.233×10^{-4}	2.228×10^{-4}	2.230×10^{-4}
Case 3	Upper	before	8.218×10^{-6}	8.218×10^{-6}	4.913×10^{-7}
		after	7.036×10^{-6}	5.363×10^{-6}	3.077×10^{-7}
	Lower	before	2.634×10^{-4}	2.634×10^{-4}	2.628×10^{-4}
		after	2.587×10^{-4}	2.583×10^{-4}	2.518×10^{-4}

DISCUSSION AND CONCLUSIONS

The seepage flow analysis was conducted on the ground including the local permeability distributions, due to the soil particles movement, invisible internal

Case 1 didn't. From the results of the analysis of the vertical hydraulic gradient in Fig. 3, it is shown that the downward hydraulic gradient slightly increased locally at the boundary on the fine-grained soil in Cases 2 and 3. On the other hand, the below permeable layer was not affected and the flow rate of a permeable layer was almost constant before and after the erosion because there is almost no change in analytical saturated permeability on the permeable layer before and after the erosion. The velocity decreasing of above soil layer is occurred by decreasing of analytical saturated permeability after erosion in Case 2 and 3. The results of the model-scale experiment [5] show that the particle size distribution changed from a downward convex shape to a slightly upward convex shape, suggesting that the presumed "clogging" might have occurred [6], inducing a local increase of hydraulic gradient at the boundary. It is commonly said that internal erosion is imposed at a critical hydraulic gradient or critical hydraulic velocity [7]. These simulations didn't simulate such as critical conditions but the results of the analysis in this study suggest that the fine particles might not have completely flowed out from the upper layer when the water is penetrated from the lower permeable layer compared with that from the upper impermeable layer, because of the inadequate velocities; the overall average velocity in the upper fine-grained soil layer was smaller in Cases 2 and 3 than that in Case 1 both before and after erosion, because water is directly penetrated to the upper layer in Case 1.

In Case 1, where water flowed in from the fine-grained soil layer, there was almost no change in analytical permeability before and after erosion according to the estimation of permeability by 20% grain size; the effect of erosion did not appear in the analysis. However, the results of the model-scale experiment [5] showed that fine grains were discharged in a range smaller than 20% grain size. Therefore, our proposed method was difficult to simulate the situations such as Case 1, and development of the method is required for more accurate simulations.

In the case that the saturated permeability is uncorrected in the unmeasured points of the experiments, the decrease in flow velocity was less than the case that the values were estimated from the measured points. It is mentioned that the changes in the ground due to internal erosion can be clearly understood if the permeability is corrected at unmeasured areas by the use of mean values of neighboring measured areas. However, the overall trend of this analysis condition was not significantly affected by the presence or absence of the correction of unmeasured areas. The overall trend of the ground can be captured without the correction of permeability in unmeasured areas. From the entire analytical simulations, it is suggested that above-mentioned tendencies occur regardless of the difference in initial soil saturated permeabilities when water flows into the lower coarse-grained, covered by a fine-grained soil layer. In addition, the influences of internal erosion are obvious in the area where the direction of penetrations changes from upward to downward, observed by the flow net; such areas can be estimated also in the large-scale embankment models by the flow net.

The method proposed in this paper enabled the analysis of the seepage flow considering the change in the internal condition of the ground before and after the internal erosion. However, the improvement of the method is necessary for simulating more situations of internal erosion.

REFERENCES

[1] Komatsu, M., Nakahara, T. and Takahashi, K., Model experiments on seepage failure patterns in river levees, the Japanese Geotechnical Society, proceedings of annual research meeting Chugoku chapter, public interest incorporated foundation, Ground engineering, Vol. 37, No. 1, pp. 61-69, 2019, in Japanese.

[2] Horikoshi, K. and Takahashi, A., Effects of re-deposition of fines on seepage-induced fines transport in embankments, Japanese Geotechnical journal, Vol. 10, No. 4, pp. 473-488, 2015, in Japanese.

[3] Sato, M. and Kuwano, R., Laboratory testing for evaluation of the influence of a small degree of internal erosion on deformation and stiffness, Soils and foundations, Vol. 58, No. 3, pp. 547-562, 2018, in Japanese.

[4] Azuma, T., Akiba, S., Ishihara, M. and Sasaki, T., Detailed investigations and factor analysis of disaster for levee destruction of Futatsumori-river due to Typhoon No.10 in 2016, Advances in river engineering, pp. 577-582, 2018, in Japanese.

[5] Sato, M., Influence of the long-term seepage on the ground consists of low permeable surface layer and high permeable foundation, the 56th Annual Meeting of the Japan National Conference on Geotechnical Engineering, 12-5-1-07, 2021.

[6] Kondo, A., Yamada, T. and Maeda, K., Effects of the pore structure caused by the grading for internal erosion and clogging, the 24th Chubu Geotechnical Engineering Symposium, pp. 71-78 2012.

[7] Bonelli, S. (ed.), Erosion of Geomaterials, ISTE Ltd and John Wiley & Sons, Inc., 2012.

7th Int. Conf. on Structure, Engineering & Environment (SEE),
Pattaya, Thailand, Nov.10-12, 2021, ISBN: 978-4-909106070 C3051

APPLICATION OF THREE-DIMENSIONAL LASER POINT CLOUDS TO RIVER MANAGEMENT

Nanoka Akiyama[1], Satoshi Nishiyama[2], Koki Sakita[3] and Fumiaki Yamazaki[4]
[1,2,3] Graduate School of Environmental and Life Science, Okayama University, Japan;
[4] KASIKA-VISION, Japan

ABSTRACT

The number of record rainfall cases has increased due to climate change in recent years. Therefore, disasters such as levee breaks occur almost every year throughout Japan. Moreover, the current river management inspection is a qualitative visual inspection conducted every 200 m. Therefore, point cloud surveying has attracted considerable attention. It can acquire data that can be viewed as a plane; thus, it is expected to lead to more efficient and sophisticated river management. The purpose of this study is to examine the application of three-dimensional laser point clouds to river management using a drone equipped with a green laser scanner and a portable laser measurement system with simultaneous localization and mapping (SLAM) technology. The former extracted the deformation of the levee, and the latter verified the characteristics of SLAM technology. The results indicated that the accuracy of the former was within ±50 mm, which could grasp the displacement in the local range. In addition, the accuracy of the latter was approximately 0.3 m, achieved by dividing the levee into sections of approximately 150 to 200m. Consequently, the former is effective in managing the height and shape of the levees in terms of area by setting control points and taking measurements to obtain an accuracy within 50 mm at high density. In addition, the latter can be expected to be applied to small and medium-sized rivers with short river lengths by walking between river distance markers installed every 200 m.

Keywords: Three-dimensional laser point clouds, River management, Drone equipped with the green laser, SLAM

INTRODUCTION

In recent years, rainfall volumes have been increasing due to factors such as global warming, causing large-scale disasters such as levee breaches throughout Japan every year. In Japan, in 2017 and 2018, not only national rivers but also prefectural rivers broke their levees, causing extensive damage. Thus, it is becoming increasingly important to carefully examine the robustness of the levees over significant distances. However, the paucity of engineers and financial resources at the national and local government levels has become severe, leading to difficulties in performing detailed levee inspections. In addition, the current river management inspection is qualitatively conducted by visual inspection every 200 m. Therefore, a measurement method that can acquire data efficiently and quantitatively for river levee management is required.

Recently, point cloud surveying has attracted significant attention. It is a surveying method that obtains high-density and three-dimensional (3D) topographic data of the ground surface and river beds using laser surveying systems. In conventional surveying, topographic data are created by connecting "points" that are surveyed point by point. However, point cloud surveying can acquire data that can be viewed as a “plane”. With this surveying method, we can grasp the topography in detail, and obtain quantitative data. In addition, it is possible to survey a large amount of high-density data thoroughly within a short time, thus improving the efficiency of surveying. This is expected to lead to more efficient and sophisticated river management.

Therefore, the purpose of this study is to examine the application of 3D laser point clouds to river management using a drone survey and a portable laser measurement system.

EQUIPMENT USED

Drone Equipped With Green Laser Scanner

In this study, a system equipped with a green laser scanner was used for the drone surveys. Figure 1 shows the drone equipped with a green laser scanner, Figure 2 shows the green laser scanner, and Table 1 presents the scanner specifications. The drone is equipped with a GNSS system with ±10 mm horizontal and ±20 mm altitude positioning accuracy. The green laser can penetrate water and grasp the shape of the area under the water surface as a plane. In addition, the method is expected to be able to acquire continuous 3D data from above the ground surface to below the water surface, thereby enabling surveys with the same degree of accuracy as that of conventional surveys using near-infrared lasers.



Fig. 1 Drone equipped with green laser scanner



Fig. 2 Green laser scanner

Table 1 Specifications of green laser scanner

Laser wavelength	532±1nm
Laser reflective angle	90°
Laser pulse rate	60,000Hz
Scan speed	30scan/s
Beam divergence	0.3mrad
Weight (main body only)	2.6kg

Portable Laser Measurement System

We introduced Simultaneous Localization and Mapping (SLAM) technology, which has been practically applied in autonomous vehicle technology in recent years. SLAM is a mapping technology commonly used in cleaning robots. Although GPS is generally used for self-positioning, it is possible to estimate the self-position without GPS. Because the system configuration is simple, 3D laser surveying while walking can be realized by combining it with a portable laser scanner. Table 2 details the system characteristics, including the specifications of the laser scanner, while Figure 3 shows the portable laser measurement system used in this study. The laser used was in the near-infrared wavelength range.

Table 2 Specifications of the portable laser measurement system

Laser wavelength	903 nm
Laser max range	80–100 m
Laser pulse rate	300,000Hz

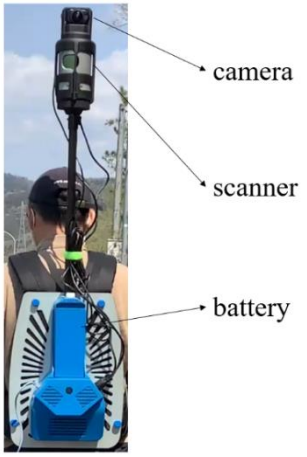


Fig. 3 Portable laser measurement system

3D LASER POINT CLOUD ANALYSIS

Measurement Site And Process

Figure 4 shows the measurement site where 3D laser point clouds were acquired. We carried out measurements in an approximately 600m section from 14.8 to 15.4km of the Asahikawa River, Okayama Prefecture, denoted by the red frame in Fig. 4. The drone equipped with the green laser scanner was used for measurement over two periods in March and October 2020. Measurements were conducted at an altitude of 50 m above the ground (water surface), with a side lap of 75% and a flight speed of 2.5 m/s in both periods. The drone flew five courses over approximately 120 min. In addition, the portable laser measurement system was used to obtain measurements in April 2020, in approximately 90 min on foot over the range shown in Fig. 4. In the measurement using the portable laser measurement system, we verified the data obtained by continuously walking the entire 600 m section and integrating the data of the results obtained via 150 to 200m section increments without installing landmarks.



Fig. 4 Measurement site

System Characteristics According To Measurement Results

Riverbed measurement results obtained by drone equipped with green laser scanner

The green laser can grasp the shape of the area under the water surface as a plane. Figure 5 shows the results. The blue point clouds represent measurements obtained near the water surface, and the green point clouds represent those after removing the point clouds near the water surface. The water depth that can be measured depends on the transparency; however, it was shown that at this site (first period), the shape could be measured up to a water depth of approximately 2.0 m.

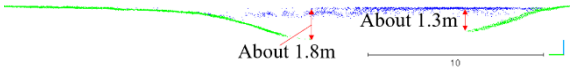


Fig. 5 Riverbed measurement results

Results of 3D model creation

Figures 6 and 7 show the river levee reproduction results obtained by the drone equipped with the green laser scanner and the portable laser measurement system, respectively. In both cases, the levee can be reproduced with a high point density. Because taking measurements while walking on a flood-channel using the latter is easy, it is possible to grasp the sluice gate shape in detail, unlike the measurements taken from the sky using the former.



Fig. 6 Results of reproduction by drone equipped with green laser scanner



Fig. 7 Results of reproduction by portable laser measurement system; continuous walking

Accuracy verification results

Table 3 shows the results of accuracy verification by comparing the total station (TS) results with the drone survey results, using the adjustment points and verification points installed within the measurement range. The adjustment points and verification points were set up at every five points. In the table, X and Y refer to the horizontal directions and Z to the elevation direction. In addition, root mean squared error (RMSE) is the square root of the mean square difference between the drone and the TS results. All X, Y and Z values are within ±50 mm of the average or RMSE with respect to the TS results.

Table 3 Accuracy verification results for drone equipped with green laser scanner

(Unit: mm)	X	Y	Z
Average difference	0	13	8
RMSE	43	16	29

Table 4 shows the accuracy results of the portable laser measurement system at the same site compared to the accuracy of the drone equipped with the green laser scanner measured. RMS is the root mean square error. We obtained an accuracy of approximately 0.3 m by walking in sections. Because this corresponds to the tolerance for ascertaining the shape of river management facilities, it is expected to grasp the shape of such river management facilities on land. The difference between the results of continuous and segmented walking may be due to the problem of accumulating errors in SLAM technology. Therefore, when using SLAM technology, we must walk in sections.

Table 4 Accuracy verification results for portable laser measurement system

(Unit: m)	RMS
Continuous walking	0.49
Walking in sections	0.31

Extraction Of Deformations By The Drone

We extracted the deformation between two periods of measurement data obtained using the drone equipped with the green laser scanner. We applied the iterative closest point (ICP) algorithm, which is a form of scan matching using SLAM technology. We used this method because it can quantitatively express the deformation to regard the movement and direction of points as displacement vectors and enable the analysis as point clouds. Figure 8 shows a total of 200 m levee from 15.2 to 15.4 km in two periods, which was divided into the levee slope and crown, 20 m longitudinally, for analysis. In this study, the mesh

size was set to 1 m per side.

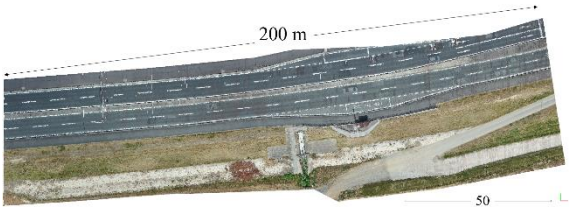


Fig. 8 Point clouds of river levee in two periods

Some of the deformation extraction results at the two periods are shown below. The deformations are represented using a color scale. Figures 8–13 are related to the levee crown, and Figs. 14–18 are related to the levee slope. In addition, the point clouds in Fig. 18 are green for the first period and blue for the second period.

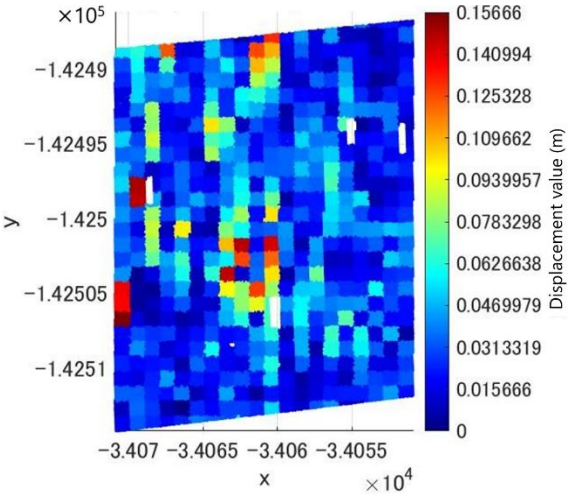


Fig. 9 Composition displacement of levee crown

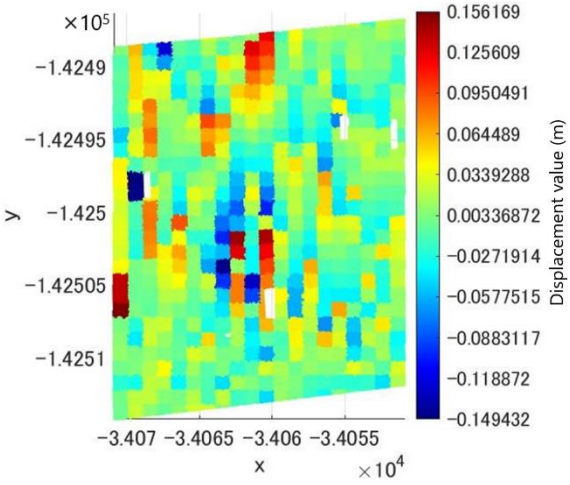


Fig. 10 X displacement of levee crown

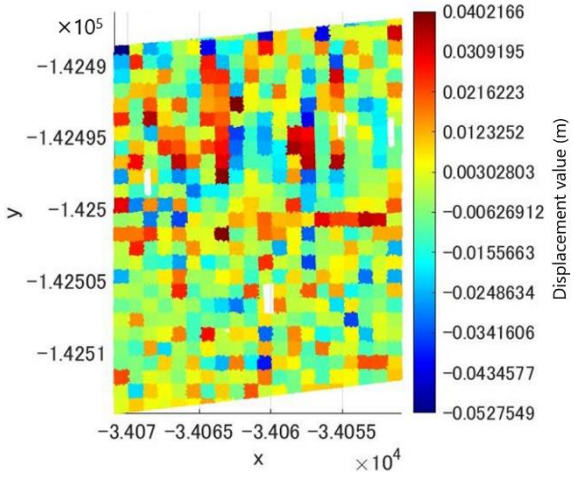


Fig. 11 Y displacement of levee crown

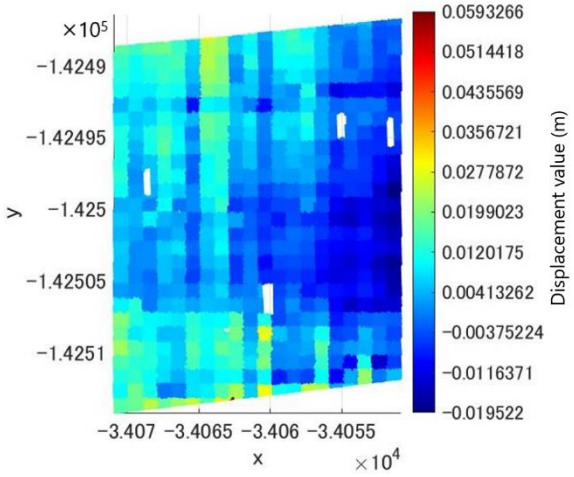


Fig. 12 Z displacement of levee crown

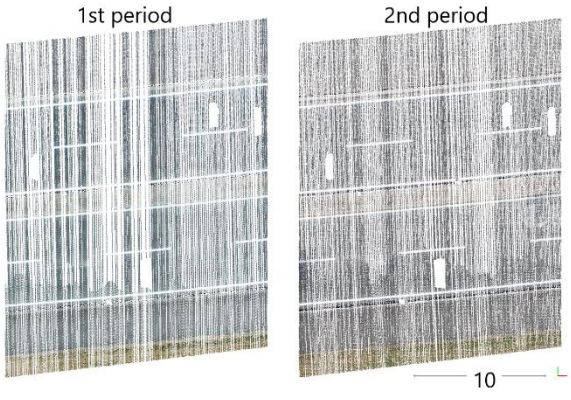


Fig. 13 Point clouds of levee crown in two periods

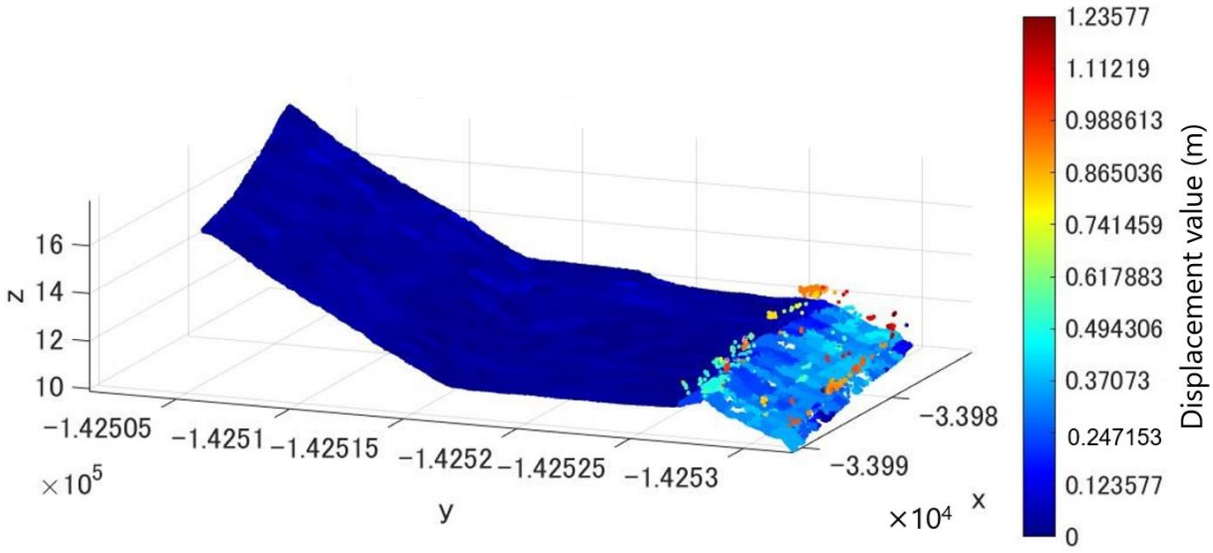


Fig. 14 Composition displacement of levee slope

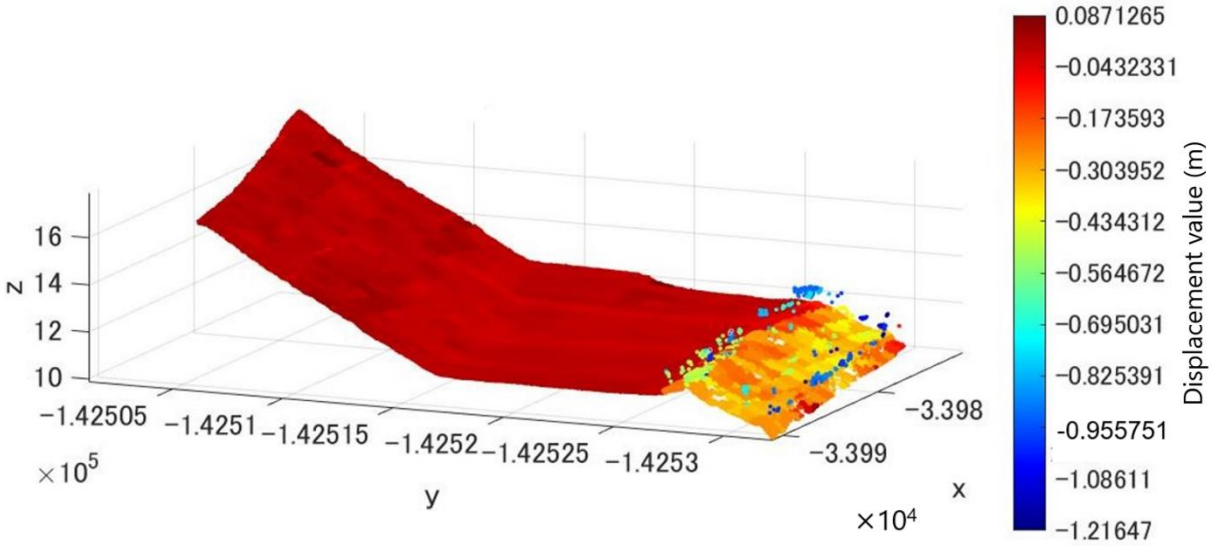


Fig. 15 Z displacement of levee slope

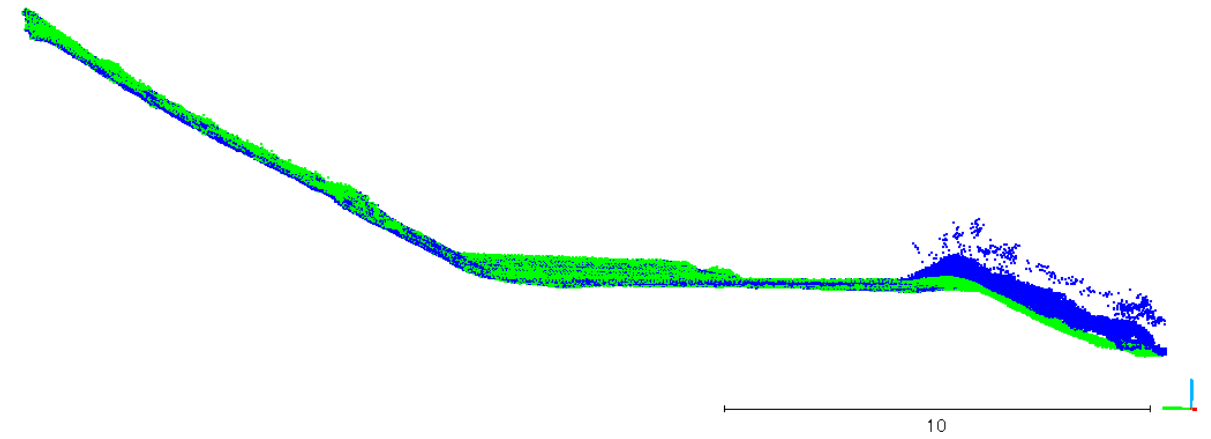


Fig. 16 Point clouds of levee slope in two periods

At the levee crown, we observed displacements of up to 30 cm in the composition. In the Z direction, displacements of less than approximately 6 cm were observed. However, displacements of more than 5 cm were mostly observed in the vegetation area, not in the road area. We considered that the levee crown had not settled. The large displacements in the composition, X, and Y directions identified are thought to be due to differences in the density of the local point clouds, as shown in Fig. 13. In contrast, at the levee slope, we observed displacements of up to 1.5 m in the Z direction. It can be seen from Fig. 16 that this is due to the growth of the vegetation during the two periods. Thus, it is possible to grasp the deformations in the local area. However, we consider that processing for the filtering of vegetation and the interpolation completion of areas with few point clouds will be necessary to achieve higher deformation extraction accuracy.

CONCLUSIONS

In this study, we attempted to measure the shape of a river levee using a drone equipped with a green laser scanner and a portable laser measurement system with SLAM technology as methods for reproducing the 3D shape of the river levee. Both methods are expected to be applied to river management in the future. The potential use of each method for river management is presented as follows.

A drone equipped with a green laser scanner can measure, from the air, the riverbed to the levee as a plane. In addition, it exhibits an accuracy within 50 mm. Therefore, it is expected that this method can be used to plan the levee height management. It is shown that it is possible to determine the amount of deformation in the local area. It is effective in the management of both the levee height and shape via setting up verification points and carrying out measurements, which can obtain an accuracy within 50 mm with high density. It is also expected to improve the efficiency of data management by extracting the deformations of the levee crown and slope. In addition, we believe that this method can aid in grasping the shape of foot protections, etc. for small and medium-sized rivers within depth of 2.0 m.

A configuration of a portable laser measurement system is simple; thus, 3D laser surveying while walking can be realized via combining it with a portable laser scanner. In addition, the shape of the sluice gate can be measured near the ground, which is easier to measure using a portable laser measurement system than a drone equipped with a green laser scanner. However, SLAM technology has the problem of accumulating position estimation errors while walking, which was observed in this study; yet, it does not depend on the accuracy of GNSS positioning. Nevertheless, by measuring sections of approximately 150–200 m, the accuracy of approximately ±0.3 m could be obtained, which is useful for grasping the shape of river management facilities on land. Therefore, it is expected to be applied to small and medium rivers with short river lengths by walking between river distance markers placed every 200 m.

In the future, we will need to investigate the extraction of deformations for a riverbed using a drone equipped with a green laser scanner and river levees using a portable laser measurement system, as well as the problem of accumulating errors associated with walking with SLAM technology.

ACKNOWLEDGMENTS

This study was conducted under the project research of the Okayama Office of River, Ministry of Land, Infrastructure, Transport and Tourism.

REFERENCES

[1] Pacheco J. F., Ascencio J. R., and Rendon J.M.: Visual simultaneous localization and mapping: a survey. Artif Intell Rev. 43, 2015, pp. 55-81.
[2] Zou D. Tan P. and Yu W.: Collaborative visual SLAM for multiple agents: A brief survey. Virtual Reality & Intelligent Hardware. Vol. 1, Issue 5, 2019, pp. 461-482.
[3] Itsukushima R.: Countermeasures against floods that exceed design levels based on topographical and historical analyses of the September 2015 Kinu River flooding. Journal of Hydrology; Regional Studies. Vol. 19, 2018, pp. 211-223.
[4] Smith M. W.: Direct acquisition of elevation data: Terrestrial Laser Scanning. Geomorphological Techniques. Chap. 2, Sec. 1.5, 2015.
[5] Gallay M.: Direct Acquisition of Data: Airborne laser scanning. Geomorphological Techniques. Chap. 2, Sec. 1.4, 2013.
[6] Nishimura S. Takeshita Y. Nishiyama S. Suzuki S. Shibata T. Shuku T. Komatsu M. and Kim B.: Disaster report of 2018 July heavy rain for geo-structures and slopes in Okayama. Soils and Foundations. Vol. 60, Issue 1, 2020, pp. 300-314.
[7] Javanmardi E. Javanmardi M. Gu Y. and Kamijo S.: Factors to Evaluate Capability of Map for Vehicle Localization. IEEE Access. Vol. 6, 2018, pp. 49850-49867.
[8] Jo K. Kim C. and Sunwoo M.: Simultaneous Localization and Map Change Update for the High Definition Map-Based Autonomous Driving Car. Sensor. Vol. 18, Issue 9, 2018.
[9] Bailey T. and Durrant-Whyte H.: Simultaneous Localization and Mapping (SLAM): Part Ⅱ. IEEE Robotics & Automation Magazine. Vol. 13, Issue 3, 2006, pp. 108-117.

7th Int. Conf. on Structure, Engineering & Environment (SEE),
Pattaya, Thailand, Nov.10-12, 2021, ISBN: 978-4-909106070 C3051

STUDY ON PHYSICAL PROPERTIES AND GRASS GROWTH CAPACITY OF POROUS CONCRETE

Kensuke Yamaya[1], Yui Oyake[2], Yoshihiro Suenaga[3] and Hidenori Yoshida[4]
[1] Graduate School of Engineering, Kagawa University, Japan; [2,3,4] Faculty of Engineering and Design, Kagawa University, Japan

ABSTRACT

In Japan, sufficient consideration is required for natural ecosystem and landscape in the plan of river revetment. The current river act in which the environment was newly added to conventional flood control and water utilization as a purpose of river management was enforced in 1997. Furthermore, the basic guideline of nature-oriented river planning was presented in 2006, and the good river environment was recovered by river planning considering nature ecosystem and landscape, and the relationship between human and river would be reconstructed. Due to the backgrounds as has mentioned above, river revetments using porous concrete have been focused on. Porous concrete is an environmentally friendly concrete in which plant roots, water, and air can pass through the pores and organisms can grow. It is required to have the strength necessary for safety as a revetment and have many pores. In this study, when the condition of "Low cost" was added to these conditions, hydroxyapatite (FbP) of the fishbone derivation was noticed in order to clear all these conditions. Also, physical property (strength, permeability, and porosity) tests and test on growth of western turf grass are carried out for the FbP mixed porous concrete. According to the test results, the target values for physical properties of the FbP mixed porous concrete are achieved. Furthermore, the FbP has a function to improve the plant growth environment of porous concrete since the leaf length of the germinated western turf in the FbP mixed specimens is longer than that in the non-FbP mixed specimens.

Keywords: Porous concrete, Green concrete, FbP, Grass growth capacity, Western turf grass

INTRODUCTION

In Japan, sufficient consideration is required for the natural ecosystem condition of flora and fauna inhabiting and growing in rivers and landscape of rivers in the plan of river revetment. The current river act in which the environment was newly added to conventional flood control and water utilization as a purpose of river management was enforced in 1997. Furthermore, the basic guideline of nature-oriented river planning was presented in 2006, and the good river environment was recovered by the river planning considering nature ecosystem and landscape, and the relationship between human and river would be reconstructed. Due to the backgrounds as has mentioned above, river revetments using a new material called porous concrete in which the plants can grow have been focused on. Porous concrete is an environmentally friendly concrete in which plant roots, water, and air can pass through the pores, and organisms can grow. Porous concrete was developed in Western Europe around the middle of the 19th century, and it was introduced to Japan via USA. The main application of porous concrete in Western Europe and USA was pavement. When porous concrete was introduced to Japan, it was utilized as not only pavement but also environment-conscious concrete such as flood control, water purification, sound absorption, sound isolation, plants growth, and particularly the planting base [1]. It is necessary for porous concrete as the planting base to satisfy the contradictory condition, high strength condition necessary for the safety as a river revetment and high porosity condition. While porous concrete which has the strength necessary for the safety as a river revetment and has many pores is most ideal, the strength of porous concrete generally tends to decrease with an increase in voids. Therefore, it is difficult to satisfy the conditions that porous concrete has both enough strength and many pores. The valid technology for achieving both conditions is the carbonation curing of concrete. Generally, the carbonation reaction of concrete is regarded as a cause of deterioration of concrete since it destroys nonconductive coating film for protecting steel. However, it has reported to significantly densify concrete by carbonation reaction according to curing method and reaction period, also it has already revealed to increase concrete strength by carbonation curing while adding special admixture [2], [3]. Furthermore, it has revealed to secure nitrate-nitrogen necessary for growing plants by lowering pH value of porous concrete to near neutral due to carbonation curing [4]. As has stated above, carbonation curing is considering to be the most effective method for the production of porous concrete which simultaneously

achieves both purposes of enough strength and maintenance pores and, has excellent plant growth capacity. However, in order to stably supply a large amount of carbon dioxide gas, a gas supply source such as a carbon dioxide bombe is required, so that the production of carbonation concrete requires a high cost. To solve the above issue, in this study, hydroxyapatite (hereafter, FbP) of the fishbone derivation is noticed. The physical property (strength, permeability, and porosity) tests and western turf grass growth test are carried out for the FbP mixed porous concrete. Through the tests, the property of the application of the FbP mixed porous concrete for revetment facilities is verified.

FISHBONE POWDER (FBP)

Hydroxyapatite is a representative apatite having a basic structure of $M_{10}(ZO_4)_6X_2$, and it is basic calcium phosphate whose chemical formula is $Ca_{10}(PO_4)_6(OH)_2$. Hydroxyapatite has many characteristics such as high adsorption property, ion exchange property, catalytic, and ion electric conductivity [5], [6], [7]. In this study, fishbone hydroxyapatite (Fishbone Powder: FbP, Fig. 1) developed by a part of the author is adopted as an admixture of porous concrete. The FbP is manufactured by burning and crushing fishbones discarded at fishing ports. Previous studies have reported that the strength of concrete increases when calcium ions dissolved in water combine with cement components [8], [9]. Additionally, it is revealed that phosphorous-adsorbed concrete has a plant growth promoting function [10]. Furthermore, it is confirmed that there is a strong correlation between the amount of phosphorus absorbed and the root volume of plants [11]. Therefore, it is expected that the improvement of plant growth capacity and the strength of porous concrete are increased by the mixing FbP of which main component is calcium phosphate in porous concrete, since the FbP supplies phosphorus and calcium (Fig. 2). Also, it is possible to realize the coexistence of sufficient strength and excellent plant growth capacity at low cost, because the FbP is manufactured from fishbone which is food wastes.



Fig. 1 Fishbone Powder (FbP)

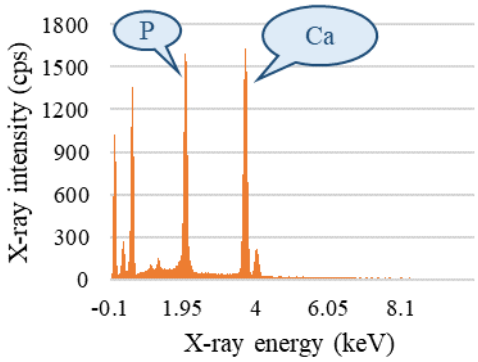


Fig. 2 Spectrum of FbP by EDS

TEST METHOD

Physical Property Test

To determine the physical property of the FbP mixed porous concrete, strength, permeability, and porosity tests are conducted on the specimens. Preparation of specimens, permeability test, and porosity test are conducted in accordance with the report of the committee on the establishment of design and construction methods of porous concrete of the Japan Concrete Institute [12]. Materials such as cement and admixtures are mixed according to the mixing conditions, poured into a cylindrical mold of ϕ 10 × 20 cm, and placed in 3 times by using a rod and a hammer. Five specimens are prepared for each case and cured in water for 7 or 28 days. The mixing promotion of porous concrete prepared in this study is shown in Table 1.

Table 1 Mixing promotion

	Mixing ID	
Materials	Blank	FbP
W/C (%)	25	25
Water (kg/m^3)	84	84
Cement (kg/m^3)	337	337
Gravel (kg/m^3)	1547	1547
Admixture* (% cement)	1	1
FbP (% cement)	0	1

*Admixture is polycarboxylic acid-based water reducing agent.

The design porosity is 26 % and the water-cement ratio is 25 %. The admixture amount of the FbP is 1% substitution for the cement mass. In addition, the uniaxial compression test is conducted according to the compression test method of concrete (JIS A 1108). Also, the porous concrete adopts either “revetment type emphasizing strength” or “revetment type emphasizing vegetation” according to the design flow velocity of the place where the porous concrete is installed. In both types, strength and porosity are respectively determined. In this study, the target

values are as follows: porosity 21 ~ 30 %, permeability 2.5 ~ 5.0 cm/s, compressive strength 10 N/mm^2 referring to the porous concrete of revetment type emphasizing vegetation.

Grass Growth Test

To verify the plant growth capacity of the FbP mixed porous concrete, the growth of western turf grass test is conducted on the specimens. The test period is from December 1, 2020, to February 1, 2021, and it is conducted in the plastic greenhouse installed outdoors. The aspect of the grass growth test is shown in Fig. 3.

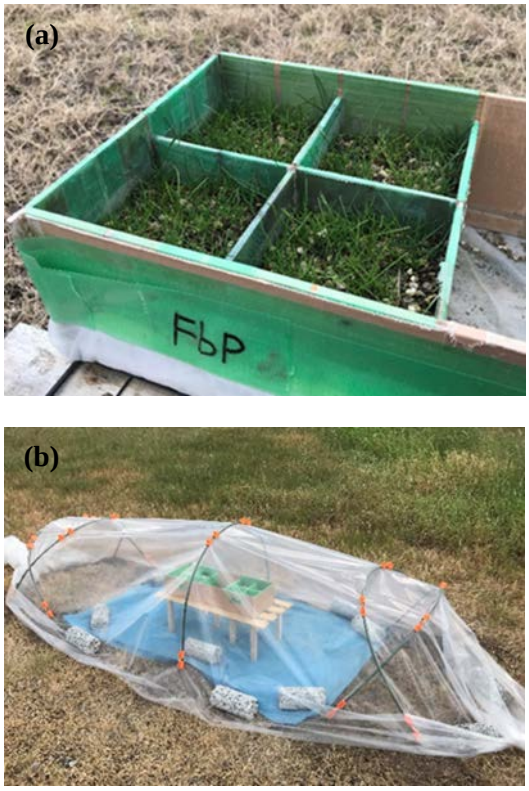


Fig. 3 Grass growth test ((a) is a close-range view, (b) is a distant view)

Peat moss slurry (water powder mass ratio = 1: 1) is filled on the pore of the porous concrete placed on a square column 10 cm in length, 10 cm, in width and 6 cm in thickness. The outline of the specimens is shown in Fig. 4. The material age of the porous concrete for grass growth test is set at 7 days and 5 specimens are prepared in each case. In this study, the test plant in which 3 species; Kentucky bluegrass, Perennial ryegrass and Creeping red Fescue is employed as a test plant with considering the test period. The soil cover is covered with peat moss of 2 cm on the specimen, and the seeds of the western turf grass are uniformly disseminated on it. Water is supplied once a day before germination and once every two days after germination. From 14 days after sowing, the leaf length is measured once a week with referring to Tsukioka and Yonemoto [13]. Leaf length is measured at 5 places for one test-peace, and the mean leaf length measured at 5 places is adopted as the test result. It is noted that the withered leaf is excluded from measuring objects. Additionally, the soil pH value of the covering soil and the inside of the specimens is measured since the soil pH value of the planting base seems to affect the growth of plants [14].

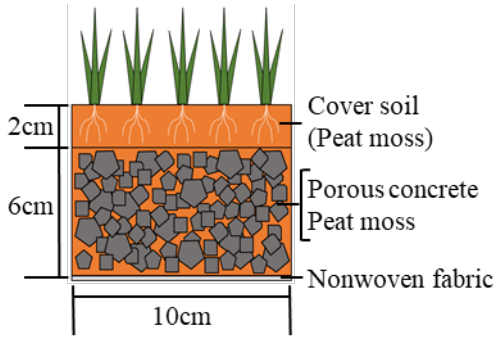


Fig. 4 Cross section of specimen for grass growth test

RESULTS AND DISCUSSION

The results of the physical property and grass growth tests for each specimen are summarized in graphs. Five specimens for the physical property test and four specimens for the grass growth test are prepared to ensure reproducibility. Therefore, the values in the figure are the average of each.

Physical Property Test

The results of the porosity test are shown in Fig. 5 (Total porosity) and Fig. 6 (Continuance porosity). “Blank” is the specimen to which FbP is not mixed. The porosity and curing period of porous concrete are shown in the vertical and horizontal axes, respectively. According to the test results, the porosity of both “Blank” and the FbP mixed specimens satisfies the target value (21-30 %). The porosity in the design is 26 %, but the porosity of produced porous concrete exceeds this value. As this reason, it seems that the filling property of the part which contacts the form in a specimen molding is hindered by weir effect [15]. Also, the general tendency that the porosity decrease in proportion to the curing days is confirmed. In addition, the proportion of continuous porosity occupied in total porosity of the “Blank” specimen or the FbP mixed one is about 99 %, and it can be said that those porous concrete are suitable for the growth of plants.

The results of the permeability test are shown in Fig. 7. The coefficient of permeability of both the “Blank” specimen and the FbP mixed specimen satisfies the target value (2.5-5.0 cm/sec). Generally, the coefficient of permeability tends to decrease as

the curing period becomes longer, but such tendency is not confirmed in this study. It is considered that the porosity distribution in a specimen affects permeability. Therefore, it is necessary to investigate the state of porosity in detail by X-ray photography.

The results of the uniaxial compression test are shown in Fig. 8. The compressive strength of both the "Blank" specimen and the FbP mixed specimen after 28 days curing exceeds the target value (10 N/mm²).

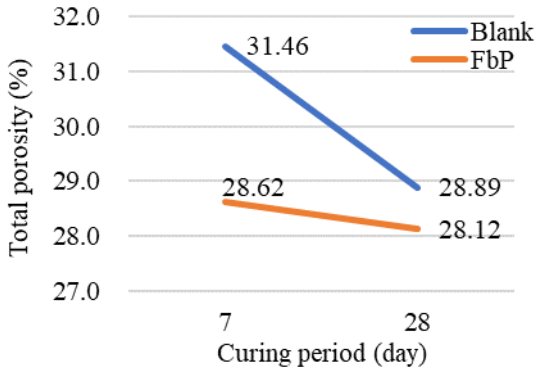


Fig. 5 Porosity test results (Total porosity)

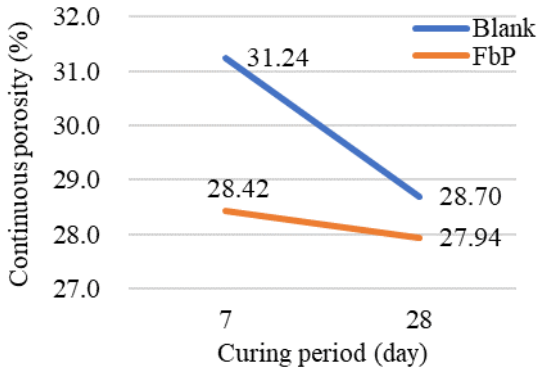


Fig. 6 Porosity test results (Continuance porosity)

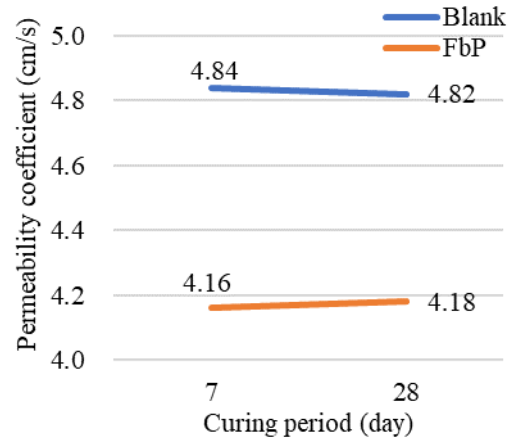


Fig. 7 Permeability test results

The strength of the FbP mixed specimen is almost the same as that of the "Blank" specimen despite the reduction of cement. It is considered that calcium is supplied to porous concrete from the mixture of FbP. In the future, it is necessary to examine the relation between the amount of FbP mixing and the strength of porous concrete by adjusting the amount of FbP mixing.

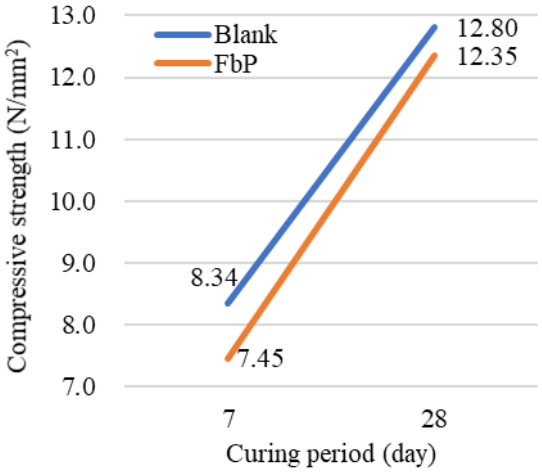


Fig. 8 Uniaxial compressive test results

Grass Growth Test

The results of the grass growth test are shown in Fig. 9. The leaf length and elapsed days are shown in the vertical and horizontal axes, respectively. Also, the results of the measuring soil pH value are shown in Fig. 10. From the test results, it is proven that the leaf length of the FbP mixed specimen is longer than "Blank" specimen from the start to end of measurement. Additionally, it is confirmed that the growth period of western turf grass on the FbP mixed specimen is longer than the "Blank" specimen since the FbP mixed specimen does not show the growth lowering of the leaf length after 42 days. Comparing the soil pH value of the "Blank" specimen and that of the FbP mixed specimen, the soil pH value of the FbP mixed specimen is lower than that of the "Blank" one. It is considered that the growth of grass is improved since the soil pH value became more neutral by the reduction of cement content and the mixture of FbP. In addition, phosphorus which is one of the three elements of fertilizer is supplied to the grasses by the mixture of FbP, which may support the growth of grasses. In order to verify this, it is necessary to analyze the phosphorus content of plants.

CONCLUSIONS

· The FbP mixed porous concrete has physical properties required as river revetment.

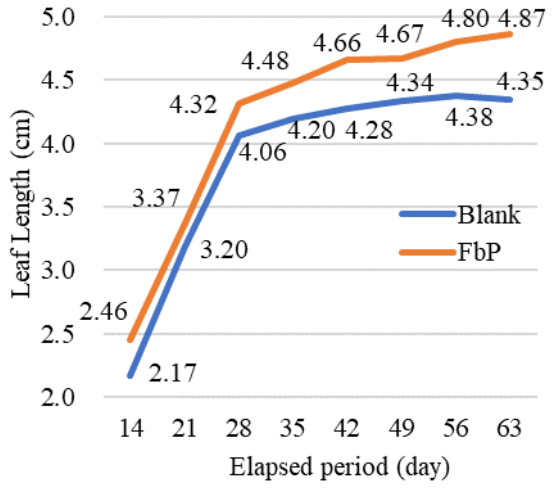


Fig. 9 Leaf length in grass growth test

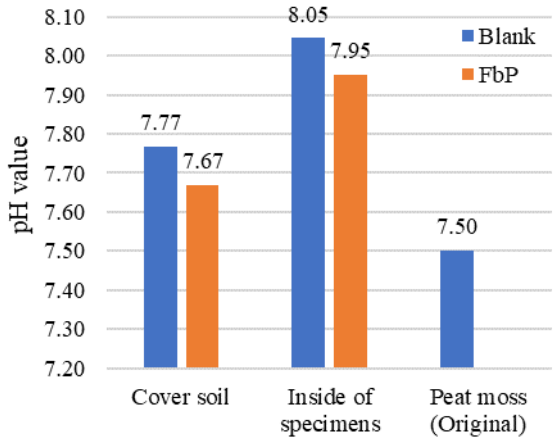


Fig. 10 Soil pH value in grass growth test

・The compressive strength of the FbP mixed porous concrete was almost the same as that of the “Blank” one despite the reduction of cement.
・The soil pH value on FbP mixed porous concrete is lower than that of the “Blank” one.
・The leaf length and growth period of grasses on the FbP mixed porous concrete are better than that of the “Blank” one. Phosphate acid which is one of the main components of FbP may affect the growth of grass. Thus, it is necessary to analyze the phosphorus content of the test plant.
・In this study, only the case in which the FbP was mixed with the porous concrete at a rate of 1 % of the cement amount was conducted. In the future, it is necessary to examine physical properties and the plant growth capacity when the mixing amount of FbP is changed.
・In this study, the test period was short, 9 weeks. In the future, it is necessary to extend the test period to annual units to examine long-term effects on physical properties and the plant growth capacity.

ACKNOWLEDGMENTS

This work has been supported by JSPS KAKENHI Grant Number JP20K04684. Additionally, to perform this study, Nihon Kogyo Co., Ltd. provided FbP. We express our gratitude here.

REFERENCES

[1] Okamura T., Naka S., Porous Concrete, Concrete Journal, Vol. 54, No. 5, 2016, pp. 542-547.
[2] Watanabe K., Yokozeki K., Torichigai T., Sakata N., High Durability Concrete using Mineral Admixtures cured with CO_2 Gas, Concrete Journal, Vol. 45, No. 7, 2007, pp. 31-37.
[3] Ushiro M., Higuchi T., Arano N., Morioka M., CARBONATION OF QUICK-HARDENING CEMENT CONTAINING γ-C₂S, Cement Science and Concrete Technology, Vol. 70, No. 1, 2016, pp. 209-214.
[4] Yokozeki K., Torichigai T., Takayama H., Higuchi T., Study on Plant Growth Capacity of Porous Concrete, Proceedings of the Japan Concrete Institute, Vol. 35, No. 1, 2013, pp. 1405-1410.
[5] Hamada M., Nagai T., Inorganic Components of Bones of Fish and Their Advanced Utilization, The Journal of Shimonoseki University of Fishers, Vol. 43, No. 4, 1995, pp. 185-194.
[6] Aoki H., Yajima T., Koyama T., Apatite as a Marvelous Biomaterial and the Surface Technology, The Journal of the Surface Finishing Society of Japan, Vol. 58, No. 12, 2007, pp. 744-750.
[7] Shigeta H., Enomoto T., Sugihara T., Development of a Medical Grinding Tool Considering Material Properties of Wet Bone for Minimally Invasive Surgery, Transactions of the Japan Society of Mechanical Engineers Series C, Vol. 79, No. 804, 2013, pp.2917-2928.
[8] Morimura T., Nomura M., Study on Influence Given to Mortar and Concrete Strength Outbreak Putting in Ionizing Ca, Research reports of the School of Engineering, Kinki University, No. 38, 2004, pp. 71-76.
[9] Ota K., Morimura T., Ohiro M., Proposal and pilot strength test of high-performance concrete with water containing Ca [2+], Research reports of the School of Engineering, Kinki University, No. 42, 2008, pp. 33-36.
[10] Abe K., Hyodo M., Sato T., Nomura T., Research on recycling use methods of phosphorous adsorption concrete, Transactions of the Agricultural Engineering Society, Vol. 2007, No. 249, 2007, pp. 269-275.
[11] Yoneyama T., Horie H., Takebe M., Tanno F., Absorption of Phosphorus from Soil by Crops: II. The Relationship between Root Mass and Phosphorus Absorption, Journal of the science of

soil and manure, Japan, Vol. 61. No. 4, 1990, pp. 382-385.
[12] Japan Concrete Institute, Report of the committee on the establishment of design and construction methods of porous concrete, 2003.
[13] Tsukioka S., Yonemoto T., Growth Experiment of the turf Grass Using the Vegetation Type Concrete, Journal of the Japanese Society of Irrigation, Drainage and Reclamation Engineering, Vol. 74, No. 2, 2006, pp. 127-130.
[14] Research Committee of Japanese Institute of Landscape Architecture, Ground Maintenance Manual in Landscape Planting, Journal of the Japanese Institute of Landscape Architecture, Vol. 63, No. 3, 2000, pp. 224-241.
[15] Saito T., Demura K., INFLUENCE OF WALL EFFECT OF MOLD FOR SPECIMEN ON VOIDS DISTRIBUTION AND COMPRESSIVE STRENGTH OF POROUS CONCRETES, Cement Science and Concrete Technology, Vol. 70, No. 1, 2016, pp. 290-296.

7th Int. Conf. on Structure, Engineering & Environment (SEE),
Pattaya, Thailand, Nov.10-12, 2021, ISBN: 978-4-909106070 C3051

GROUND EVALUATION METHOD BY PORTABLE DYNAMIC PENETRATION TEST BASED ON WAVE PROPAGATION THEORY

Katsuya Iwai[1], Naoaki Suemasa[1], Kazuya Ito[1], Tsuyoshi Tanaka[1]
[1]Architecture and Civil Engineering, Tokyo City University, Japan

ABSTRACT

The Portable Dynamic Cone Penetration Test is a ground survey method often used for small-scale buildings. In this test, the N_d-value is obtained from the number of blows and a conversion formula from the N-value of the standard penetration test (SPT) to the N_d-value has been proposed. However, the problem with this method is that the N_d-value is likely to be overestimated because the shaft friction increases as penetration depth increases. While the Dynamic Load Test is a method of estimating a bearing capacity and load-displacement relationship. This study aims to evaluate the ground strength by the Portable Dynamic Cone Penetration Test based on the wave propagation theory of the Impact Load Test of single piles, which is one of the Vertical Load Tests of piles. In this report, after carrying out a Portable Dynamic Cone Penetration Test on a model ground, the ground resistance estimated from load and acceleration measured at the pile head was compared with those measured at the pile toe. In addition, to clarify the response mechanism of shaft friction applied to the rod, the stress wave toward the toe and the response wave from the toe were measured at the middle of the rod and analyzed in detail. Experimental results showed not only that the calculation method of the Impact Load Test of single piles could be applied even in the Portable Dynamic Cone Penetration test, but also that a ground resistance with higher accuracy could be obtained by the estimated frictional resistance.

Keywords: Case method, Dynamic penetration test, Wave propagation theory, Impact load test of single piles

1. INTRODUCTION

The Portable Dynamic Cone Penetration Test has often been used for survey of natural slope and evaluation of bearing capacities of small-scale buildings. In this test, the N_d-value is obtained from the number of blows and a conversion formula from the N-value of the Standard Penetration Test to the N_d-value has been proposed. Although this test has an advantage to be conducted easily, its disadvantage is that the N_d-value is likely to be overestimated because the skin friction increases as penetration depth increases. The previous study showed that this problem could be solved by measuring transmitted energy at the cone head and the rod end during penetration and applying the obtained energy efficiency to the N_d value correction so that the corrected N_d value is similar to the N value even at depths greater than 10m to 15m (Yoshizawa et al, 2016).

On the other hand, there is another method, the Dynamic Load Test, which estimates a bearing capacity and load-displacement relationship in pile foundation structure of building. Fig. 1 shows the appearance of the Dynamic Load Test. In the Dynamic Load Test, (information of) frictional resistance can be understood by the ground resistance in depth direction obtained from response of an upwards traveling wave (Nishimura, 2001).

This study aims to evaluate the ground strength by the Portable Dynamic Cone Penetration Test based on the wave propagation theory of the Impact Load Test of single piles, which is one of the Vertical Load Tests of piles. In this report, after carrying out dynamic load tests on the model sand ground, the ground resistances estimated from load and acceleration measured at the pile head were compared with those measured at the pile end. Then, to clarify the response mechanism of skin friction applied to the rod, more tests were carried out with additional measuring equipment.



Fig. 1 Appearance of Dynamic Load Test

2. CALCULATION METHOD ADAPTING WAVE PROPAGATION THEORY

In the Impact Load Test, the bearing capacity of pile is calculated by the Case Method. This method is proposed by Goble et al. (1975), and in which the wave propagation theory is applied to the analysis mechanism of dynamic load test of piles. A total driving resistance was calculated based on the mechanism that a sum of a downwards and an upwards traveling wave is equal to the ground end resistance, here, the downwards traveling wave represents a wave produced by an impact force at the pile head and it travels to the pile end and turns around to become an upwards traveling wave. The downwards and the upwards traveling waves were calculated using a pile force and a particle velocity measured by measurements of strain-gauge and an accelerometer installed at the pile head. The calculation formulas are given as

$$F_d = \frac{(F(t)+z*v(t))}{2} \quad (1)$$

$$F_u = \frac{(F(t)-z*v(t))}{2} \quad (2)$$

$$z = \frac{(E*A_p)}{c} \quad (3)$$

$$R = F_d(t) + F_u(t + \frac{2L}{c}) \quad (4)$$

where F(t) is pile force, F_d is a downwards traveling wave, F_u is an upwards traveling wave, z is impedance, v(t) is particle velocity, E is elastic modulus, A_p is cross-sectional area, c is response velocity, R is ground strength and L is length of a rod.

3. DEMONSTRATION TEST OF CASE METHOD

In this study, Portable Cone Penetration Tests were carried out using a 63.7N weight on the model ground with relative densities Dr=80%. Fig. 2 and Fig. 3 show the summary of test machine and equipment positions, respectively. A load cell and an accelerometer were installed on each measurement point, right below the anvil, point A and B, and the distances to each point from the rod end were 2.90m, 2.25m and 1.33m, respectively. In order to measure ground strength, an additional load cell was installed on the cone-shaped rod end with 16mm diameter and 60 degrees point angle. A shock absorber with 20mm thickness was also installed on the contact surface between the anvil and the weight.

Two types of tests were conducted, with and without friction for comparison. In the case of applying frictional force, the middle of points A and B on the rod was sandwiched with two woods of 30mm thickness using an air cylinder. Fig. 4 shows the method to apply frictional force. The test procedure was as follows; a weight was dropped from a height of 330mm, and force, acceleration and displacement were measured at every impact. After that, the downwards traveling wave and the upwards traveling wave were calculated by measuring the impact force and the acceleration, and then the total penetration residence, the "Case-value" was calculated using the Case Method. By comparing the Case-value with the load measured at the rod end, the accuracy of the Case-value was confirmed.

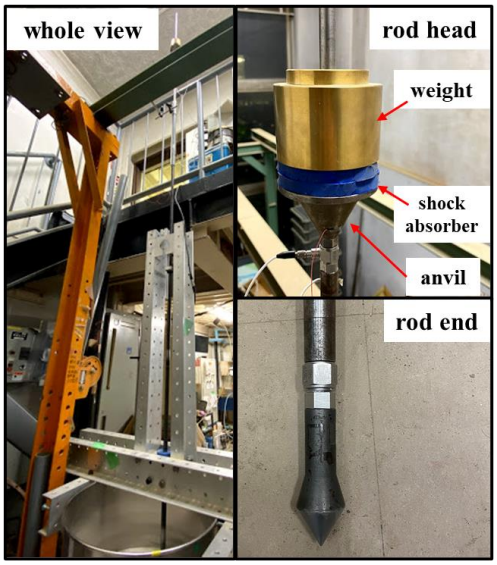


Fig. 2 Summary of test machine

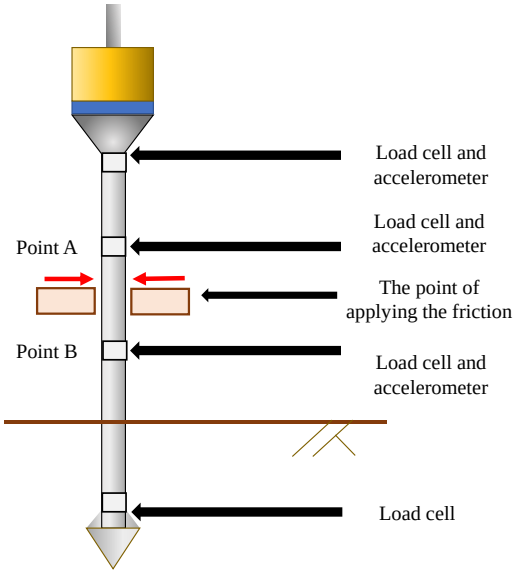


Fig. 3 Summary of equipment positions

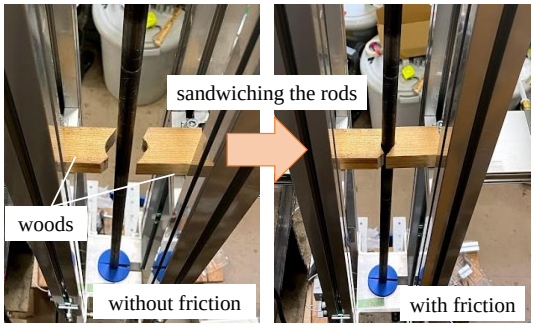


Fig. 4 Method of applying friction.

3-1. FRICTIONLESS CASE (CASE 1)

A dynamic test was carried out without applying frictional force. Fig. 5 shows downwards traveling waves F_d and upwards traveling waves F_u calculated with force and acceleration measured at each position. As seen in Fig. 5, the downwards traveling waves and the upwards traveling waves did not converge to 0. In order to confirm the accuracy of the measurement results, the measured displacement value was compared with the calculated displacement value which was obtained by second order integration of acceleration. Fig. 6 shows the displacement values actually measured and calculated with acceleration. The calculated displacement values rapidly increased because right after the weight dropped, negative acceleration was measured larger than the actual value. Therefore, a correction was made to suppress the negative acceleration and to make the measured acceleration at each point closer to the actual displacement. Afterwards, all the downwards traveling waves and the upwards traveling waves were recalculated from the corrected acceleration.

Fig. 7 shows the corrected downwards traveling wave and the corrected upwards traveling wave and Fig. 8 shows the corrected displacement. From the results, all values were converged to 0.

Fig. 9 shows the results of measured value and the Case-value at 300mm depth without friction. The Case-value calculated from the downwards traveling wave and the upwards traveling wave was approximately 500N larger than the end force, which represents the ground resistance. In addition, it was confirmed that the response time histories of the Case-value and the end force were similar to each other.

As seen in Fig. 10, although the downwards traveling wave and the upwards traveling wave at each point were different in the response time history and the downwards traveling wave slightly decreased as measured position became lower, basically the values at three points were almost equal. Here, the displacement per impact was 12.6mm.

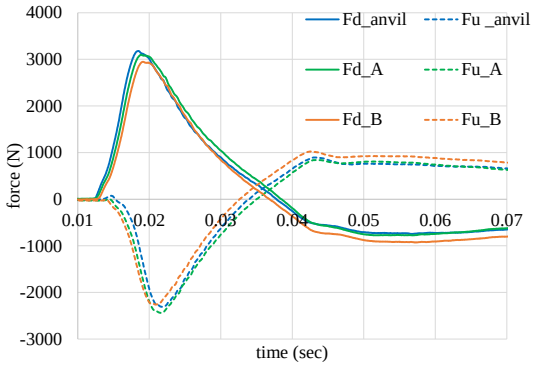


Fig. 5 Downwards traveling wave and Upwards traveling wave.

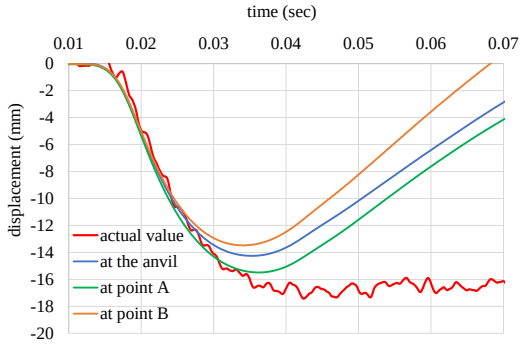


Fig. 6 Measured displacement value and calculated displacement values

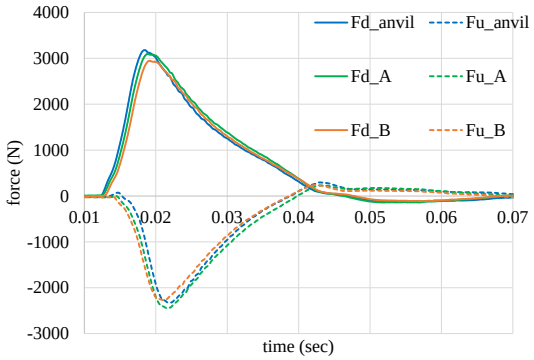


Fig. 7 Corrected the downwards traveling wave and the upwards traveling wave.

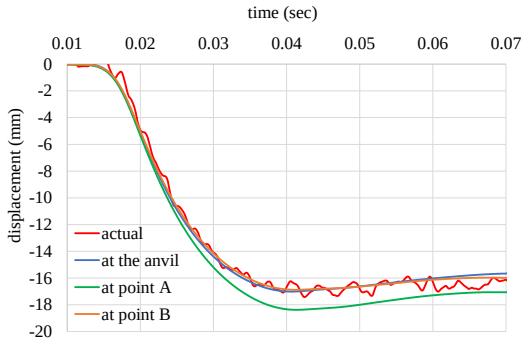


Fig. 8 Displacement from corrected acceleration.

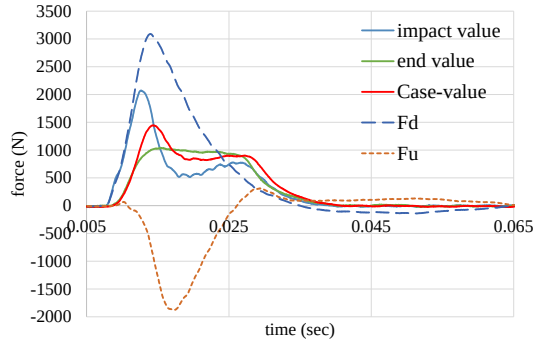


Fig. 9 Results of measured value and Case-value (frictionless case)

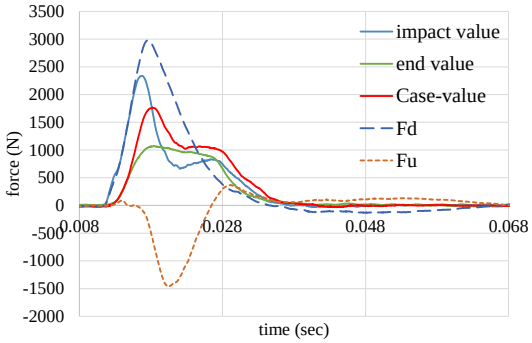


Fig. 11 Results of measured values and Case-value (friction case)

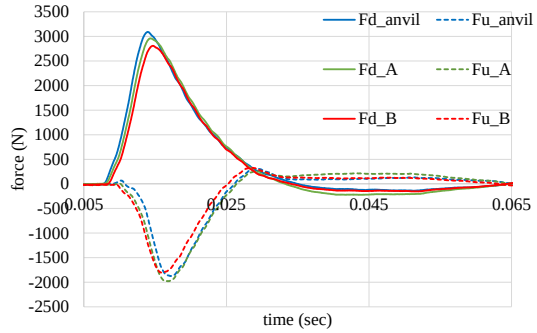


Fig. 10 Downwards traveling waves and upwards traveling waves (frictionless case)

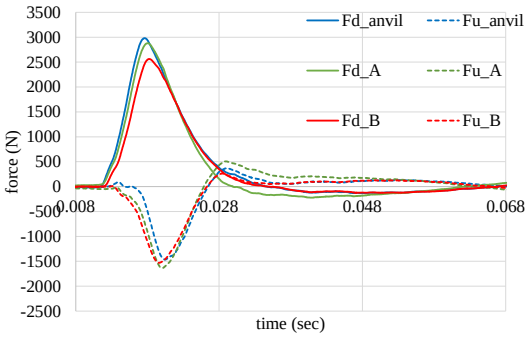


Fig. 12 Downwards traveling waves and upwards traveling waves (friction case)

3-2. FRICTION CASE (CASE 2)

This time, frictional force was applied to the rod during a dynamic test while maintaining the penetration state of case 1. Fig. 11 shows the results of measured values and the Case-value with applying the frictional force. Compared Fig. 9 with 11, as the end forces of the friction and the frictionless cases were very close, it was revealed that the ground strength of both cases were similar. On the other hand, the Case-value of the frictionless case was approximately 700N larger than the end force, which implies the accuracy of friction case was worse than the frictionless case. Besides, although the downwards traveling waves of the friction case were similar to those of the frictionless case, the peaks of negative upwards traveling waves of the friction case decreased because of the friction.

In order to confirm the frictional mechanism in detail, the downwards traveling wave and the upwards traveling wave at each point were compared. Fig. 12 shows the downwards traveling waves and the upwards traveling waves. Compared the downwards traveling wave at right below the anvil with that at point B, the peak of the downwards traveling wave of point B was decreased by approximately 500N, which was likely to be due to the frictional force added to the rod. In addition, it could be seen that, compared to the frictionless cases, the starting time of the downward force working on the upwards traveling wave at right below the anvil was lagged behind in the frictional cases. The cause could be considered that the friction force generated by sandwiching the rod influenced the upward traveling wave. Here, the displacement per impact was 8.98mm.

4. COMPARISON BETWEEN CASE-VALUE AND END VALUE AT EACH POINT

Additionally, two pairs of dynamic tests were carried out with and without friction after case 1 and case 2 and a comparison was made between the Case-values at each point and end force. All the cases from case 1 to 6 were successively conducted. Table 1 shows the summary of the experiment and the results and Fig. 13 shows the comparison of the Case-values calculated from acceleration at each point and the actual value measured at the rod end in case 1 to 6.

Compared the displacements of both cases, it could be seen that the displacements of frictional cases were smaller than the counterparts of

Table 1. Summary of experiment and results

position		case1	case2	case3	case4	case5	case6
	with or without the friction	without	with	without	with	without	with
	displacement (mm)	12.6	8.98	17.9	11.6	28.8	15.6
anvil	Case-value (N)	1445	1765	1208	1600	1069	1409
point A		1076	1376	845	1183	710	1018
point B		1168	1225	929	985	794	850
rod end	actual value	1039	1071	706	763	501	617

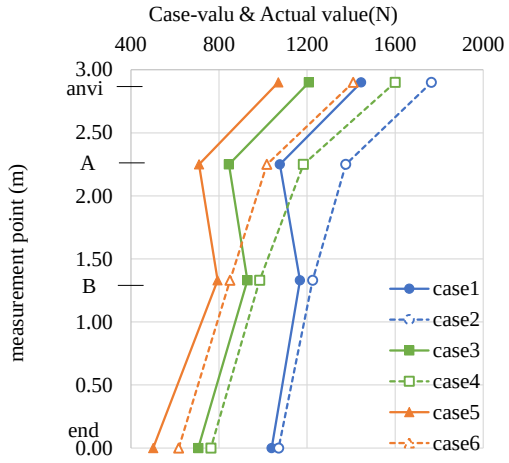


Fig. 13 Case-values and actual values

frictionless cases. It is likely that the displacement was decreased by the friction force generated by sandwiching the rod. Accordingly, it could be confirmed the friction generated for the rod. It could be seen that while the difference in the Case-values of point A and B were small in frictionless cases 1, 3 and 5, the Case-values of point A were larger than B in the friction cases 2, 4 and 6. As a result, it is likely that the Case-values above the part that frictional force was added such as the point A were overestimated due to the influence of the friction, and the Case-values below the part such as the point B, were not affected by the friction. Which is also confirmed from the results that the Case-values at point B were similar in the both friction and frictionless cases and that the Case-values at right below the anvil were overestimated in the friction cases same as the point A. As regards the cause of the decrease in the Case-values from the point anvil to points A and B even in the frictionless conditions, it could be considered that the impact energy was not transmitted accurately due to the rolling of the rod during impact loading.

5. CONCLUSIONS

This study investigated the frictional mechanism using the Case Method, compared the downwards traveling wave with the upwards traveling wave under the different conditions with and without providing frictional force during impact loading. Moreover, the effects from the friction on the energy transmission was also studied with comparing the Case-values with actual values. The findings obtained from the experiments are shown below.

(1) It was confirmed that the Case Method could estimate the end resistance of the ground to some extent using the measurement results of the rod head.

(2) Regardless of friction, the reason that the Case-values were calculated larger than the end force values could be due to the rolling of the rod at the time of impact.

(3) Since the difference between the Case-values and the end force values in the frictionless cases was smaller than that in the friction cases, the accuracy of the Case-method might be decreased due to friction.

(4) From the result that there was a difference in the Case-values above and below the point where frictional force was added by catching the rod with the woods, it is necessary to examine the effect of friction on the Case Method in more detail.

6. REFERENCES

[1] Japanese Geotechnical Society, "Japanese Geotechnical Society Standard, Method for dynamic cone penetration test", 2016

[2] Yoshizawa D., Uemura K., Fuji N., Nobumoto M., "Development of Piezo Drive Cone with load measurement", Oyo technical report, No.35, 2016

[3] Nishimura S., "Points of a Signal matching analysis for Dynamic Load test", Proceeding of the Japan national conference on geotechnical engineering, 2001.
[4] Goble G., Linkins G., Jr., Rausche F., "Bearing Capacity of Piles from Dynamic Measurements", Final Report, Dept of Civil Engineering, Case Western University.
[5] Japanese Geotechnical Society, "Japanese Geotechnical Society Standard, Method for vertical load test", pp.227-244, 2002
[6] Matsumoto T., "Theoretical Background of Application of Stress-Wave Theory on piles", Symposium for pile driving property and application of wave theory to piles, pp.7-21, 1989
[7] Kojima E., "Verification of measurement method in impact load test of piles and consideration of signal matching analysis", Japanese Geotechnical Journal, vol. 8, No.2, pp.349-359, 2013

7th Int. Conf. on Structure, Engineering & Environment (SEE),
Pattaya, Thailand, Nov.10-12, 2021, ISBN: 978-4-909106070 C3051

INFLUENCE OF RAINFALL INTENSITY ON INFILTRATION SURFACE FORMATION OF RIVER EMBANKMENTS

Tsubasa Ichijo[1], Shin-ichi Kanazawa [2] and Hisao Emoto[3]
[1,3] Social Environmental Systems Engineering Course, National Institute of Technology, Fukushima College, Advanced Course Program, Japan; [2] Niigata University,Japan

ABSTRACT

In recent years, a local downpour occurs frequently at a various part of Japan and there is an embankment destroyed by the downpour. River embankments are important structures to protect residents from floods and other disasters. Many of long embankments are historical products of flood control that have been reinforced by raising them with age. However, the structure of the river embankment was developed based on the experience of the disaster that actually occurred, and the design and analysis of the destruction of the structure were not analyzed. Furthermore, up to now, the mechanism of the levee collapse has been discussed, and it has not been fully elucidated.In this study, we perform a numerical analysis considering the infiltration boundary of the slope of the embankment, and express the difference in stress behavior in the embankment before and after considering the infiltration boundary. We analyzed the stress behavior of the embankment when the river water level rises by analysis, and tried to analyze the collapse mechanism of the river embankment by analyzing the effect. In addition, we observed the stress behavior when precipitation was applied, and performed a detailed analysis closer to the actual problem. Also, it was analytically confirmed that the fracture mode of the embankment differs depending on the presence or absence of the infiltration boundary. At that time, it was analytically confirmed that the failure mode of the embankment was different depending on the difference in the water level rising speed.

Keywords: River embankment, Unsaturated soil, Penetration, Collapse

1. INTRODUCTION

Due to global climate change, there have been frequent reports of local torrential rains in various parts of Japan in recent years, with associated river dike collapse. Among these, the breach of the embankment of the Chikuma River caused by Typhoon No.19 in October 2019 stands out. An embankment is an extremely important disaster prevention structure that protects the lives of riverside residents from floods, and it is necessary to ensure the safety of these structures. If a river embankment breaks or collapses due to heavy rain damage, large-scale damage to the inland area due to inundation, as well as enormous damage such as isolated settlements, missing persons, and outflow of houses will occur.

Regarding water infiltration resistance, erosion resistance and seismic resistance ratings required for river levees, the existing rules for satisfying the earth levee principle and cross-sectional shape have been revised, and the magnitude of the external force applied to the levees before the earth structure is constructed has been stipulated. As a general rule, the design of levees for each river should be optimized considering topography, weather, and river shape. However, the mechanism of destabilization and deformation of levees due to floods or earthquakes has not yet been fully elucidated [1], and the current guidelines do not necessarily represent well-established technical knowledge.

On the other hand, the difficulty of elucidating the mechanisms of river levee infiltration and stability problems is because these problems deal with unsaturated soil, intermediate soil, compacted soil and unsteady phenomena. Overflow, erosion, seepage, and earthquakes are the causes of riverbank breakage due to changes in the outside water level. Of these, all except for earthquakes are caused by rainfall, and the risk of riverbank breakage is increasing due to the recent local heavy rainfall. Currently, as an evaluation method for embankment structures, arc slip analysis is performed using the infiltration analysis results, such as rainfall, in the embankment design method Nonetheless, deformation analysis is not performed, and infiltration analysis and stability analysis are performed individually. However, the infiltration problem and the deformation problem are coupled, and it is hard to say that the current embankment evaluation method is sufficient.

It is thought that local torrential rain will increase in the future, and it can be said that the risk of bank breakage will increases alongside this. There is an urgent need to take measures against embankment destruction, and for that purpose it is important to elucidate the mechanism of embankment destruction.

In previous studies, Kodaka, Lee, Kubo, Ishihara, Nakayama, Li, and Fujita [2] have investigated the stress state and collapse mechanism inside the

embankment using their respective methods, but all of them are in service. On the other hand, there is no discussion about continuous state changes and rainfall intensity.

In this study, embankment analysis was performed using the unsaturated soil / water / air coupled element finite method analysis program (DACSAR-MP) [3]. In the analysis program, the slope of the embankment is used as the drainage boundary when the water level rises, but since the water level is maintained as the water level rises, the infiltration boundary was considered in this study by returning the slope of the embankment to the position head when the water level rises. Improved to an analysis program.

The purpose of this study is to analytically elucidate river levee collapse mechanisms by analytically expressing the stress behavior in the levee body during river water level rise due to and considering the effect of rainfall. In addition, by changing the water level rise speed, we can see the difference in the fracture form due to the difference in speed**.**

2. RESEARCH METHOD

2.1 Soil/Water/Air Coupled Finite Analysis Code

The finite element analysis code (DACSAR-MP) [3] used in this study formulates the unsaturated soil constitutive model proposed by Ohno, Kawai, and Tachibana [4]. This model is framed as the soil/water/air coupled problem using the three-phase mixture theory. Equation (1) shows the effective stress. Equation (2) shows the base stress tensor and suction stress. Equation (3) shows suction.

$$\boldsymbol{\sigma}' = \boldsymbol{\sigma}^{\mathbf{net}} + p_s \mathbf{1} \tag{1}$$

$$\boldsymbol{\sigma}^{\mathbf{net}} = \boldsymbol{\sigma} - p_a \mathbf{1} \ , \quad p_s = S_e s \tag{2}$$

$$s = p_a - p_w \ , \quad S_e = \frac{S_r - S_{rc}}{1 - S_{rc}} \tag{3}$$

Here, $\boldsymbol{\sigma}'$ is the effective stress tensor; $\boldsymbol{\sigma}^{\mathbf{net}}$ is the base stress tensor; $\mathbf{1}$ is the second order unit tensor; $\boldsymbol{\sigma}$ is the total stress tensor; s is the suction; p_s is the suction stress; p_a is the pore air pressure; p_w is the pore water pressure; S_r is the degree of saturation; S_e is the effective degree of saturation; and S_{rc} is the degree of saturation at s→∞. Equations (4), (5), (6) and (7) provide the yield function.

$$f\left(\boldsymbol{\sigma}', \zeta, \varepsilon_v^p\right) = MD \ln \frac{p'}{\zeta p_{sat}'} + \frac{MD}{n_E}\left(\frac{q}{Mp'}\right)^{n_E} - \varepsilon_v^p = 0 \tag{4}$$

$$\xi = \exp\left[(1 - S_e)^{n_s} \ln a\right] \ , \quad MD = \frac{\lambda - \kappa}{1 + e_0} \tag{5}$$

$$p' = \frac{1}{3}\boldsymbol{\sigma}' : \mathbf{1} \ , \quad q = \sqrt{\frac{3}{2}\mathbf{s} : \mathbf{s}} \tag{6}$$

$$\mathbf{s} = \boldsymbol{\sigma}' - p'\mathbf{1} = \mathbf{A} : \boldsymbol{\sigma}' \ , \quad \mathbf{A} = \mathbf{I} - \frac{1}{3}\mathbf{1} \otimes \mathbf{1} \tag{7}$$

Here, n_E is the shape parameter; ε_v^p is the plastic volume strain; M is the q/p' in the limit state; D is the dilatancy coefficient; p_{sat}' is the yield stress at saturation; a and n_s are the parameters representing the increase in yield stress due to unsaturation; λ is the compression index; and κ is the expansion index. Equation (8) shows pore water velocity. Equation (9) shows air velocity. Pore water and air flow follow Darcy's law.

$$\tilde{v}_w = -\mathbf{k}_\mathbf{w} \cdot \mathrm{grad} h \tag{8}$$

$$\tilde{v}_a = -\mathbf{k}_\mathbf{a} \cdot \mathrm{grad} h_a \ , \quad h_a = \frac{p_a}{\gamma_w} \tag{9}$$

Here, $\tilde{v}_\mathrm{w}$ is the pore water velocity; $\tilde{v}_\mathrm{a}$ is the air velocity; $\mathbf{k}_\mathbf{w}$ is the hydraulic conductivity; $\mathbf{k}_\mathbf{a}$ is the coefficient of air permeability; h is the total head; γ_w is the unit weight of water; and h_a is the pneumatic head. Equations (10)-(11) show hydraulic conductivity and the coefficient of air permeability by way of Mualem's [5] formula and the Van Genuchten [6] formula.

$$\mathbf{k}_\mathbf{w} = k_{rw}\mathbf{k}_\mathbf{wsat} = S_e^{1/2}\left[1 - \left(1 - S_e^{1/m}\right)^m\right]^2 \mathbf{k}_\mathbf{wsat} \tag{10}$$

$$\mathbf{k}_\mathbf{a} = k_{ra}\mathbf{k}_\mathbf{ares} = \left(1 - S_e\right)^{1/2}\left(1 - S_e^{1/m}\right)^{2m} \mathbf{k}_\mathbf{ares} \tag{11}$$

Here, k_{rw} is the ratio of hydraulic conductivity; k_{ra} is the ratio of coefficient of air permeability; m is the Mualem constant; $\mathbf{k}_\mathbf{wsat}$ is the hydraulic conductivity at saturation; $\mathbf{k}_\mathbf{ares}$ is the coefficient of air permeability in dry conditions. Equations (12)-(13) show the continuous formula of pore water and air using three-phase mixture theory.

$$n\dot{S}_r - S_r\dot{\varepsilon}_v + \mathrm{div}\tilde{v}_w = 0 \tag{12}$$

$$(1 - S_r)\dot{\varepsilon}_v + n\dot{S}_r - n(1 - S_r)\frac{\dot{p}_a}{p_a + p_0} - \mathrm{div}\tilde{v}_a = 0 \tag{13}$$

Here, n is porosity; $\dot{\varepsilon}_v$ is volumetric strain; and p_0 is atmospheric pressure. The elasto-plastic constitutive model obtained from Equation (4) and the equilibrium equation [Equations (12) - (13)] are formulated as the soil/water/air coupled problem.

2.2 Moisture Characteristic Curve Used in the Analysis

For a soil-water characteristic curve model, a model capable of hysteresis expression, as proposed by Kawai, Wang and Iizuka [7], is used. In addition, to determine the logistic curve in the case of DRY and WET, derived from arbitrary suction and the degree of saturation, the logistic curve equation of Sugii and Uno [8] was used. This makes it possible to grasp the moisture conditions of sloped ground where complex water balance occurs.

3. INTERIOR CHANGES IN THE DIKE WITH EMBANKMENT COMPLETION

3.1 Rewriting analysis code

In the analysis program, the slope of the embankment is used as the drainage boundary when the water level rises, but since the water level is maintained as the water level rises, the infiltration boundary was considered in this study by returning the slope of the embankment to the position head when the water level rises. Improved to an analysis program. This schematic is shown in Figure 1.

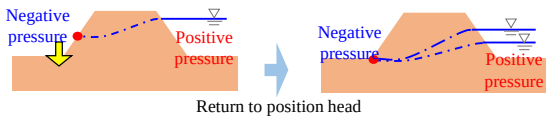


Fig.1 Finite element mesh diagram

3.2 Analysis Conditions

Figure 2 shows the analytical model. The foundation ground was 3m long and 45m long, and the dam body was 5m long, 5m at the top, and 25m at the bottom, with a slope of 1: 2 [9]. The mesh of the model is 1m each for the foundation ground, 10 cm for the levee body, and it was divided into 25 parts horizontally. The right side of the analytical model was assumed to be the river side, and the drainage layer was 0.6m in length and 6m in width from the left end of the embankment.

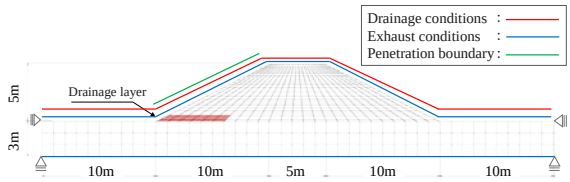


Fig. 2 Finite element mesh diagram

The material used in the analysis was silt mixed with sand for the foundation ground and sand mixed with silt for the dam body. Table 1 shows the material constants, and Figure 3 shows the moisture characteristic curve. Table 1.1 is the material constant used for the foundation ground, and Table 1.2 is the material constant used for the dam body. Figure 3.1 shows the moisture characteristic curve used for the foundation ground, and Figure3.2 shows the moisture characteristic curve used for the dam body. The material constants shown in Table 1 are λ: swelling index, k: compression index, M: critical stress ratio, m: shape parameter of unsaturated hydraulic conductivity, n: magnification parameter of consolidation yield stress in unsaturated state, nE: Fitting parameter of EC model, e_0: Initial void ratio, v: Poisson's ratio, k_x: Horizontal hydraulic conductivity, K_Y: vertical hydraulic conductivity, S_{r0}: critical saturation, and G_s: soil particle specific gravity. The initial saturation of the material used for embankment was set to 60%, and the initial suction was determined from Figure3.2. The drainage layer has a permeability coefficient and an air permeability coefficient set to 500 times that of the embankment. The material constants other than the permeability coefficient and the permeability coefficient of the

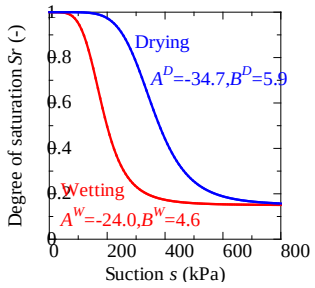


Fig.3.1 Soil-water characteristic curve (Foundation ground)

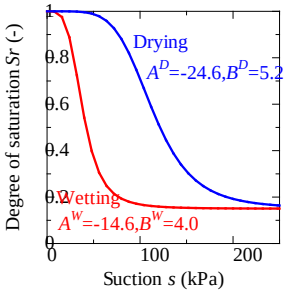


Fig. 3.2 Soil-water characteristic curve (Levee)

λ	k	M	m	n	nE
0.18	0.037	1.33	0.8	1	1.3
e_0	v	kx(m/day)	ky(m/day)	Sr_0	Gs
1.2	0.33	0.1	0.1	0.15	2.7

Table 1.2 Levee material parameters

λ	k	M	m	n	nE
0.18	0.013	1.33	0.8	1	1.3
e_0	v	kx(m/day)	ky(m/day)	Sr_0	Gs
1	0.33	8.7	8.7	0.15	2.7

drainage layer are the same as those of the bank body. The displacement boundary was fixed vertically at the bottom of the foundation ground and horizontally at the top of the foundation ground.

For the hydraulic boundary, the lower and upper ends of the foundation ground and the upper part of the dam body were drained. As for the air boundary, the upper end of the foundation ground and the upper end of the dam were exhausted.

3.3 Analysis Method

In the embankment analysis, layers were spread one-by-one. An evenly distributed load was applied, and compaction was repeated until the height of the embankment reached 5m. Layers of 0.3m were prepared. The rolling strength was 300kPa. In the analysis, elements were generated to create a heap, and loading and unloading was repeated with an evenly distributed load to simulate compaction. This schematic diagram is shown in Figure 4.

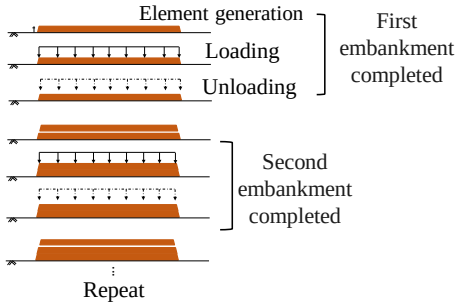


Fig.4 Embankment analysis schematic

3.4 Analysis Result

Figure 5 shows a visualization of each stress at the completion of the embankment. From the top, the mean effective stress *p'*, void ratio *e*, deviatoric stress *q*, shear strain ε_s, suction *s*, and degree of saturation S_r are shown. First, the mean effective stress *p'* exhibits a higher value in the foundation ground than in the embankment due to the effect of compaction during embankment construction. In addition, the gap ratio e increases toward the upper part of the embankment body. Next, the shear strain ε_s shows a higher value near the boundary between the foundation and the levee than in the levee.

Therefore, it is possible that there was already weakening when the embankment was completed, although not enough to cause failure. In addition, as the position where the drainage layer is located contains more water than the surrounding area, the void ratio *e* is low.

4. CHANGES IN THE LEVEL DUE TO RISINGWATER LEVELS

Water level fluctuation analysis was carried out using the analytical model used for embankment analysis. The right side of the embankment was used to raise the water level. This is expressed by applying water pressure to the levee body and the foundation

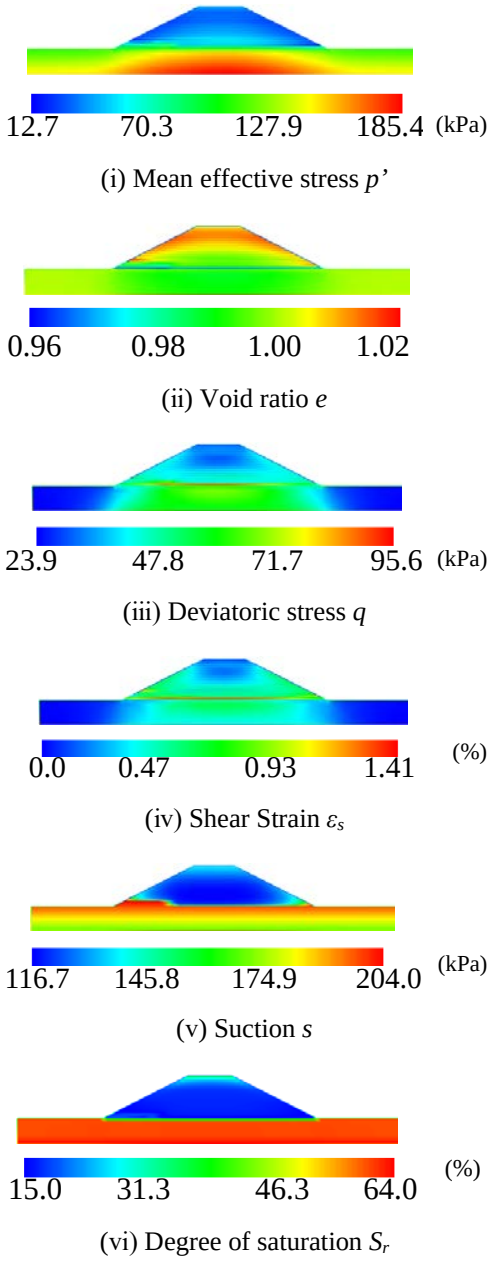
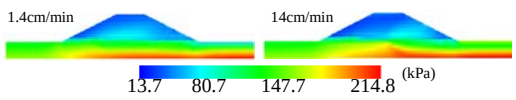


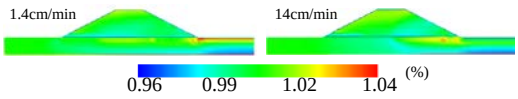
Fig. 5 Summarizes analysis results

ground after raising the head of water on the right slope of the embankment where water infiltrates, along with the foundation ground. The water head and water pressure applications were repeated until the crown reached 3m. In addition, the rate of water level rise was set to 1.4cm /min and 14cm/min [10].

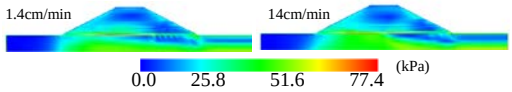
Next, we paid attention to the difference in the speed of water level rise. Figure 5 shows the analysis results for each stress. Each figure shows the average effective principal stress *p'*, axial differential stress *q*, shear strain ε_s, void ratio e, suction s, and degree of saturation S_r from the top.
First, from results of the mean effective stress *p'*, strength is considered to decrease as the water level rises, and the value inside the levee decreases from the infiltration surface. In addition, the void ratio *e* also decreases inside the levee from the infiltration surface as the water level rises, and volume compression is considered to occur. Second, from the degree of saturation S_r, it can be seen that values for the foundation ground and the lower part of the levee become lower as the water level rises. At a slower velocity of 1.4cm/min this value is higher than at a faster velocity of 14cm/min. Finally, the shear strain ε_s indicates that the value at the tail end of the embankment is higher, suggesting that the tail end becomes a weak part of the embankment as the water level rises. For each stress, the change in velocity in 1.4cm/min was more remarkable than that in 14cm/min. This is probably because at the slower the rising speed, the infiltration time of the river water was longer. In particular, the degree of saturation S_r was significantly different with different rising speeds, and a large difference in the formation of the infiltration surface was confirmed. The velocity 1.4cm/min formed a smooth infiltration surface, and the velocity14cm/min formed a vertical infiltration surface. It is considered that 1.4cm/min first infiltrated from the foundation ground and then infiltrated upward from the ground to the bank body.
At this time, the levee body can be considered as subject to buoyancy due to leftward infiltration from the levee exterior and upward infiltra tion from the foundation ground, suggesting the possibility of piping. In contrast to 1.4cm/min, 14cm/min is considered to have caused infiltration only from the lower left side of the embankment to form a vertical infiltration surface, suggesting that water overflow may occur.



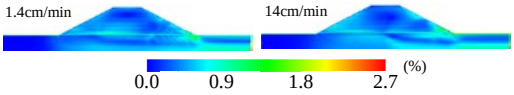
(i) Mean effective stress *p'*



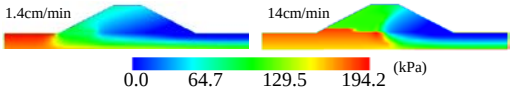
(ii) Void ratio *e*



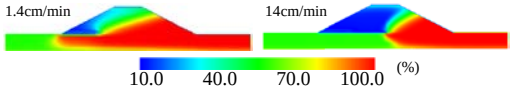
(iii) Deviatoric stress *q*



(iv) Shear Strain ε_s



(v) Suction *s*

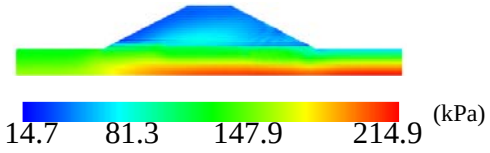


(vi) Degree of saturation S_r

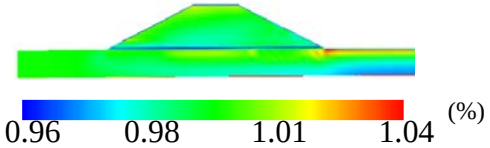
Fig. 6 Summarizes analysis results

5. PRECIPITATION ANALYSIS

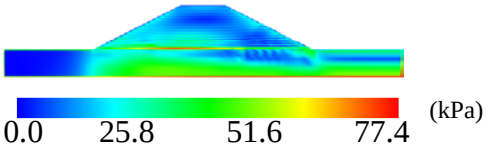
Precipitation analysis was performed using an analysis model that performed embankment analysis and water level fluctuation analysis. Precipitation was about 7.1 mm / h.
Figure 7 shows a visualization of each stress after precipitation analysis.
First, the value is lower than the average effective principal stress p'with precipitation, and it is considered that the strength is decreasing. In addition, the gap ratio e shows that the value of the right tail is higher than that in the embankment. As a result, it is possible that the right hip is particularly weak.



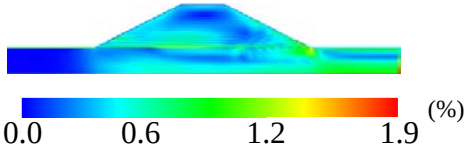
(i) Mean effective stress *p'*



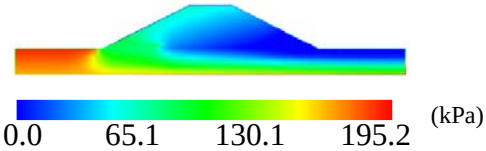
(ii) Void ratio *e*



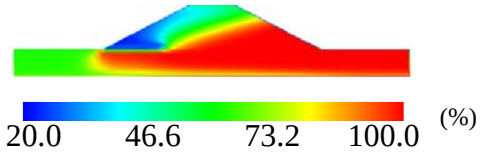
(iii) Deviatoric stress q



(iv) Shear Strain ε_s



(v) Suction s



(vi) Degree of saturation S_r

Fig. 7 Summarizes analysis results

6. CONCLUSION

Based on the results obtained from the embankment analysis and the water level rise analysis, the following conclusions are developed.

(1) As the water level rises, the strength inside the levee decreases, the volume is compressed, and the inside of the levee is saturated, thus collapse is considered to occur within the levee. In addition, collapse progresses into the levee body as the water level rises.

(2) When the rate of water level rise is slow there is a high possibility of collapse due to the long infiltration time of river water. If the ascendingspeed is high, it is likely that the river will overtop the levee before collapse occurs.

(3) A gentle infiltration surface formed when the speed of water level rise was slow, and a vertical infiltration surface was formed when the water velocity was high. In particular, when the speed is slow, the dam body may be subjected to upward penetration from the foundation ground in addition to leftward penetration from the outside of the embankment. This results in buoyancy and the formation of water channels in the foundation ground to cause Penetration destruction.

(4) It was found that the river embankment becomes more prone to collapse when it is rained.

REFERENCES

[1] Japan Institute of Country-ology and Engineering：River embankment guide (Revised edition),2012, p.1.

[2] Kodaka T., Lee K., Kubo Y., Ishihara M., Nakayama Y., Li Z., Fujita K: Shear Strength Test Method for River Embankment Penetration, Proceedings of the 7th River Embankment Symposium, 2019, p.35.

[3] Kanazawa S., Toyoshima K., Kawai K., Tachibana S. and Iizuka, A.: Analysis of mechanical behavior of compacted soil with F.E. method, journal of JSCE, No.68 (2), 2012, pp.291-298.

[4] Ohno S., Kawai K. and Tachibana S.: Elastoplastic constitutive model for unsaturated soil applied effective degree of saturation as a parameter expressing stiffness, Journal of JSCE, Vol.63/No.4,2007, pp.1132-1141.

[5] Mualem Y.: A new model for predicting the hydraulic conductivity of unsaturated porous media, Water Re-sources Research, Vol.12, No.3, 1976, pp.514-522.

[6] Van Genuchten: A closed-form equation for predicting hydraulic of unsaturated soils, Soil Science Society American Journal, Vol.44, 1980, pp.892-898.

[7] Kawai K., Wang W. and Iizuka, A.: The expression of hysteresis appearing on water characteristic curves and the change of stresses in unsaturated soils, Journal of applied mechanics, Vol.5, 2002, pp.777-784.

[8] Sugii T. and Uno T: Modeling the New Moisture Characteristic Curve, Journal of JSCE, 1995, pp.130-131.

[9] Japan Road Association, Roadway Workers - Fill Construction Guidelines, 2010, p.163.

[10] Ministry of Land, Infrastructure, Tranceport and Tourism Hokuriku Regional Development Bureau: Chikuma River Embankment Survey Committee materials, 2019, p.7-8.

7th Int. Conf. on Structure, Engineering & Environment (SEE),
Pattaya, Thailand, Nov.10-12, 2021, ISBN: 978-4-909106070 C3051

ALTERED ROCKFALL BEHAVIOR OWING TO PARAMETERS IN ROCKFALL SIMULATION USING DISCONTINUOUS DEFORMATION ANALYSIS

Hiroaki Kitauchi[1], Satoshi Nishiyama[2] and Koki Sakita[3]
[1,2,3]Environmental and life science, Okayama University, Japan

ABSTRACT

To rationally design rockfall countermeasures, it is necessary to predict detailed rockfall behavior using numerical simulations according to the conditions of slopes and rockfalls. In this study, we conducted rockfall simulations using the discontinuous deformation method. This method is used to analyze the motion between blocks comprising polygons of arbitrary elastic bodies. In this method, to reproduce rockfall dynamics in detail, selection of parameters such as the rock shape and the velocity energy ratio indicating the energy attenuation at the time of the rockfall collision have considerable influence on rockfall behavior. In this study, we modeled the shape of an actual slope and rockfall from data measured through an aerial laser survey, and quantitatively evaluated rockfall behavior by performing simulations with varying rock shapes and velocity energy ratios. In this paper, we discuss the use of simulations in determining the design of rockfall countermeasures, such as changes in energy and jump height owing to differences in the shape and physical properties of slopes and rockfalls.

Keywords: Discontinuous deformation analysis, Slope shape, Rockfall shape, Velocity energy ratio

INTRODUCTION

In planning for rockfall disaster prevention measures, it is important to not only identify the source of rockfall and evaluate its stability, but to also predict and evaluate rockfall behavior for designing rockfall countermeasures. To forecast rockfall behavior, an estimation formula based on past rockfall experiment data is generally used; however, the formula estimates a comprehensive upper limit of fall speed and jump height based on limited experimental data [1]. Therefore, it is difficult to predict the change in speed corresponding to the topographical change in the middle of a slope. In contrast, the introduction of a numerical analysis method (rockfall simulation) aimed at predicting rockfall behavior has been promoted in recent years, and by establishing such a simulation technology, the details of rockfall behavior can be predicted. Using such simulations, it is expected that the study of rational and economical countermeasure construction methods would be improved considerably.

Rockfall simulation methods that analyze rockfall behavior are divided as mass point system analysis methods that model rockfalls as mass points or simple rigid bodies and non-mass point system analysis methods that model rockfalls as polygonal blocks [2]. The former method assumes a spherical rock shape, whereas the latter method considers a polygonal rock shape. So, in the non-mass point system analysis method, discontinuities can be considered, and the moments and rotations generated at the contact points between rocks and slopes can be calculated.

Discontinuous deformation analysis (hereinafter referred to as DDA) is a typical method for solving non-mass point systems. In DDA, analysis is based on Hamilton's principle and a penalty function is introduced into the contact mechanism to evaluate energy in a quadratic form. The specific features are that the law of energy conservation and the uniqueness and convergence of the solution are guaranteed for the entire analysis target, and that a large deformation process such as block contact can be analyzed [3].

Regarding the applicability of DDA rockfall simulation, although the effectiveness is determined through case analysis of past rockfall experiments, it has been highlighted that establishing a method for setting analysis parameters that determine rockfall behavior is a challenge [2]. The analysis parameters used in the DDA rockfall simulation are divided into parameters related to physical properties such as rockfall density and elastic modulus, and parameters related to shape, such as rock shape and unevenness of slopes. Among them, the velocity energy ratio and the shape of the rock/slope, which are parameters indicating the attenuation of energy at the time of collision, have a considerable influence on rockfall behavior when a block collides. However, the effects of these parameters on rockfall behavior are not fully understood, and the operational mode of the DDA simulation has not been determined. Therefore, in this

study, we focused on two-dimensional DDA rockfall simulations to determine the effects of rock/slope shape and velocity energy ratio on rockfall behavior. Based on the results, we examine the operational mode of the DDA rockfall simulation for the design of rockfall countermeasures. To investigate the effect of each parameter on rockfall behavior, a sensitivity analysis was performed to quantitatively determine the magnitude of the effect of the modified parameter.

In the following sections, we first explain the outline of the DDA rockfall simulation, and then describe the design of rockfall countermeasures and sensitivity analysis, present the results of the sensitivity analysis, and finally, examine the operational mode of the simulation.

DDA ROCKFALL SIMULATION

DDA is a method for analyzing the motion between blocks comprising polygons of arbitrary elastic bodies [3]. The equation describing the motion of the block is formulated based on Hamilton's principle and is finally expressed by Eq. (1), including translation, rotation, and elastic strain.

$$\mathbf{M}\ddot{\mathbf{u}}^{t+\Delta t} + \mathbf{C}\dot{\mathbf{u}}^{t+\Delta t} + \mathbf{k}\mathbf{u}^{t+\Delta t} = \mathbf{F}^{t+\Delta t} \quad (\mathbf{1})$$

where, $\mathbf{M}$: mass matrix, $\mathbf{C}$: damping matrix, $\mathbf{K}$: stiffness matrix, $\mathbf{F}$: outer matrix, $\ddot{\mathbf{u}}$: center of gravity acceleration, $\dot{\mathbf{u}}$: center of gravity velocity, $\mathbf{u}$: center of gravity displacement, $\boldsymbol{t}$: arbitrary time, and $\boldsymbol{\Delta t}$: time step. The equation of motion described in Eq. (1) is converted into simultaneous equations related to incremental displacement using the β and γ methods of Newmark, and the motion of the block can be obtained by solving these at each time interval. In DDA, it is assumed that each block has a constant stress and constant strain, and the displacement at any point on the block is discretized by six sets of displacement variables, including rigid body displacement and rigid body rotation (Fig. 1).

In Fig. 1, $\mathbf{u_0}$, $\mathbf{v_0}$: x-direction and y-direction rigid body displacement, respectively; $\mathbf{r_0}$: block center of gravity rigid body rotation; and $\boldsymbol{\varepsilon_x}$, $\boldsymbol{\varepsilon_y}$, $\boldsymbol{\gamma_{xy}}$: block x-direction vertical strain, y-direction vertical strain, and shear strain.

In DDA, the viscosity coefficient C is introduced for the air resistance to the collapsed rock mass and the damping effect owing to contact with vegetation [4], and the velocity energy ratio γ is introduced for the energy damping effect at the time of contact [5], and both are incorporated into the analysis.

$$\boldsymbol{C = \eta M} \quad (\mathbf{2})$$

$$\boldsymbol{\gamma = V_{out}^2 / V_{in}^2} \quad (\mathbf{3})$$

where, $\boldsymbol{\eta}$: viscosity coefficient, $\boldsymbol{V_{out}^2}$: post-contact velocity, and $\boldsymbol{V_{in}^2}$: pre-contact velocity.

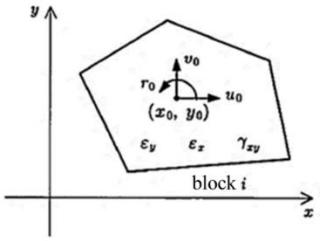


Fig. 1 Variable in DDA

ROCKFALL COUNTERMEASURE DESIGN

In this study, we examined the operational mode of rockfall simulation for designing rockfall countermeasures [1]. Therefore, the outline of the design method for rockfall countermeasures followed in Japan is explained below.

Prediction of Rockfall Behavior

When designing a rockfall countermeasure, the energy and jump height of the rockfall, which are targets of the countermeasure, are predicted. To predict rockfall behavior, an estimation formula based on past rockfall experiment data is generally used in energy prediction and is expressed as:

$$\boldsymbol{E = 1.1\left(1 - \frac{\mu}{\tan\theta}\right) W \cdot H} \quad (\mathbf{4})$$

where $\boldsymbol{E}$: kinetic energy of the falling rock, $\boldsymbol{\mu}$: equivalent friction coefficient, $\boldsymbol{\theta}$: slope gradient, $\boldsymbol{W}$: falling rock weight (kN), and $\boldsymbol{H}$: falling rock height (m). The equivalent friction coefficient is a coefficient that represents the characteristics of rockfalls and slopes, and the values listed in Table 1.

This formula estimates the comprehensive upper limit of energy based on limited experimental data, and it is not possible to predict the energy corresponding to topographical changes in the middle of the slope. In addition, the jump height of rockfalls is generally designed to be 2 m or less; however, if the vertical fall distance of rockfalls exceeds 10 m, the jump height of rockfalls may exceed 2 m. Therefore, rockfall simulations are used when detailed energy and jump height predictions corresponding to the slope shape are required.

Table 1 The value of equivalent friction coefficient

Classification	Rockfall and slope characteristics	μ
A	Hard rock, round uneven small, no standing trees	0.05
B	Soft rock, round / square uneven medium / large, no standing trees	0.15
C	Sediment / Cliff cone, round / square uneven small / medium, no standing trees	0.25
D	Cliff cone, square uneven medium / large, no standing tree / standing tree	0.35

Types and Uses of Rock Fall Countermeasures

Rockfall countermeasures are divided into rockfall prevention and rockfall protection interventions. Rockfall prevention involves a construction method that works directly on the rockfall source to prevent the occurrence of rockfall, such as removing dangerous stones that are expected to fall and fixing the dangerous stones on the slope. In contrast, rockfall protection involves a construction method that catches rocks falling down a slope and absorbs and dissipates kinetic energy to prevent the rocks from reaching the conservation target. Generally, when the energy of rockfall is extremely large, rockfall prevention interventions are used, and when the energy of rockfall can be absorbed and dissipated, rockfall protection interventions are used. Typical types of rockfall protection interventions include rockfall protection fences and rockfall protection nets, as shown in Fig. 2. The types of interventions used here differ depending on the rockfall behavior, such as the energy and jump height of the target rockfall. Fig. 3 shows a guideline for the energy coverage of rockfall protection fences and rockfall protection nets. Generally, the height of the rockfall protection measure is designed with 2 m as the standard, but if a jump height of the rockfall exceeding 2 m is expected, it is necessary to alter the corresponding height of the rockfall protection measure.



Fig. 2 Rockfall fence (left) and rockfall net (right)

SENSITIVITY ANALYSIS

In this study, a sensitivity analysis was performed to understand the effects of the DDA parameters of rock/slope shape and velocity energy ratio on rockfall behavior. The parameters used for the sensitivity analysis are explained below.

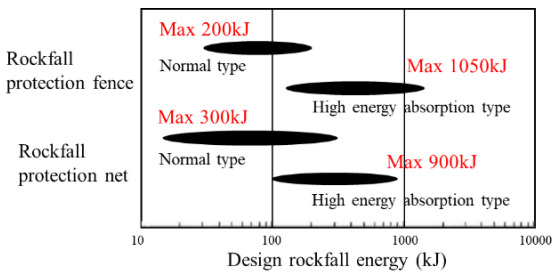


Fig. 3 Scope of energy absorption

Slope Shape

For the sensitivity analysis, we used a flat slope with no irregularities and a model of the actual shape of the slope with irregularities and compared the effects of slope shape on rockfall behavior. Three-dimensional data of the slope shape along National Route 53 in Okayama Prefecture obtained through aerial laser survey were used to create the actual slope. In this type of data, the shape of trees and noise are acquired together with the shape of the ground surface at the time of measurement. For this analysis, only the ground surface data were extracted by filtering [6]. In this study, the dangerous stones found from the field survey (Fig. 4) were assumed to flow in the valley direction of the slope and the fall path of these stones was used to create the slope shown in Fig. 5. And a flat slope was created, as shown in Fig. 6, with the same inclination angle and vertical height as the actual slope. During the simulation, all rockfalls were dropped naturally from the positions in contact with the slopes shown in Figs 5 and 6.



Fig. 4 Dangerous stone (Diameter aprx.1.2 m)

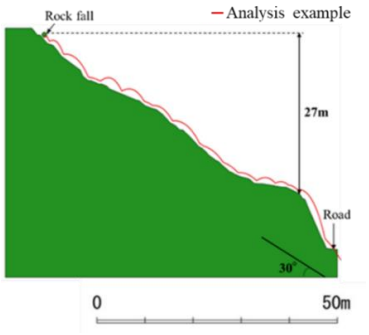


Fig. 5 An actual slope used for sensitivity analysis

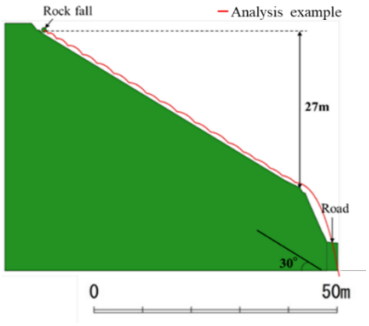
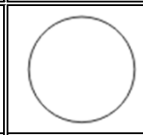


Fig. 6 A flat slope used for sensitivity analysis

Rockfall Shape

To determine the effect of rock shape in the sensitivity analysis, a sphere and the actual shape as shown in Table 2 were used, and the effects of the rock shape on the rockfall behavior were compared. Here, the actual shape is based on the rock shown in Fig. 6, and the shape is reproduced by assuming floating rocks. The sphere, in effect was a regular 32-sided object, but is described as a sphere because the shape is close to that of a sphere. The area of each rock shape was 0.7 m^2, and the scale was the same. In the simulation, 10 types of analyses were performed for each rock shape by rotating the rockfall position by 36° to show the variation in rockfall behavior depending on the rockfall position.

Table 2 Rockfall shape used for sensitivity analysis

Classification	sphere	Actual shape
shape		

Physical Characteristics Parameters

Table 3 shows the values of the physical property parameters used during analysis in this study [7], [8]. Two velocity energy ratios, 0.8 and 1.0, were used to represent the energy decay at the time of contact, and the effects of the velocity energy ratio on rockfall behavior were compared.

Table 3 Physical characteristics parameters

Type	Rockfall	Slope	Type	
Density[kN/m^3]	26	26	Viscosity coefficient	0.01
Elastic modulus[MPa]	2000	2	Velocity energy ratio γ	0.8, 1
Poisson's ratio	0.17	0.40	Analysis time step[s]	1.0×10^{-4}
Friction angle[°]	25	35	Penalty coefficient[kn/m]	1.0×10^{6}
Adhesive force[kPa]	0	50		

RESULTS OF SENSITIVITY ANALYSIS

It is important to predict the maximum value of rockfall energy and jump height when studying the design of rockfall countermeasures [9]. The results of the sensitivity analysis for the maximum values of the rockfall energy and jump height are summarized below. Here, the jump height is the height in the vertical direction with respect to the slope of the center of gravity of the jumping rock.

Figs 7 and 8 show the maximum energy and maximum jump height for each fall height (vertical fall distance) of each rock shape when $\gamma = 0.8$ and 1.0, respectively, on a flat slope. Fig. 7 also shows the results of the energy estimation formula ($\mu = 0.25$) for comparison.

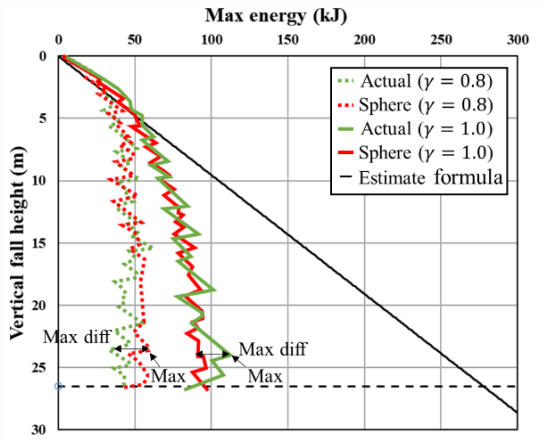


Fig. 7 Maximum energy and fall height of falling rocks (flat slope)

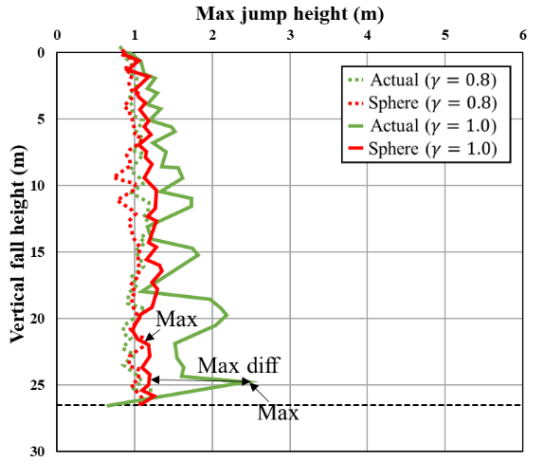


Fig. 8 Maximum jump height and fall height of falling rocks (flat slope)

As seen in Fig. 7, the maximum energy of rockfall with $\gamma = 0.8$, on a flat slope, was the largest for the actual shape of the rock with a fall height of 23.5 m, at approximately 60 kJ. The maximum energy of falling rocks with $\gamma = 1.0$ was the largest for the actual shape of the rock with a falling height of 24 m, at approximately 115 kJ. The energy difference of the rock shape for each fall height is approximately 10 kJ or less for both $\gamma = 0.8$ and $\gamma = 1.0$; however, when the fall height increases, a difference of approximately 20 kJ was observed. In addition, when compared with the result of the estimation formula, the simulation result had more energy than the estimation formula up to a drop height of 5 m. In addition, beyond a fall height of 5 m, the values obtained from the energy estimation formula became larger than those with the simulation, and the difference between the two increased as the fall height increased.

As seen in Fig. 8, the maximum jump height of the rockfall with $\gamma = 0.8$, on a flat slope, was approximately 1.2 m, for a sphere with a fall height

of 22 m. The difference in the jump height of the rock shape for each fall height was within approximately 0.5 m. The maximum jump height of a rock fall with γ = 1.0 was the largest for the actual shape of the rock with a fall height of 24.5 m, at approximately 2.5 m. Here, the largest jump height of the sphere with γ = 1.0 was approximately 1.3 m, and the change in jump height owing to the velocity energy ratio was small compared to that because of the actual shape. The difference in jump height due to the rock shape for each fall height with γ = 1.0, was the largest at a fall height of 24.5 m, at approximately 1.2 m.

As with the flat slope, Figs 9 and 10 show the maximum energy and maximum jump height for each fall height (vertical fall distance) of each rock shape when γ = 0.8 and 1.0 are used on the actual slope. Fig. 9 also shows the results of the energy estimation formula (μ = 0.25) for comparison.

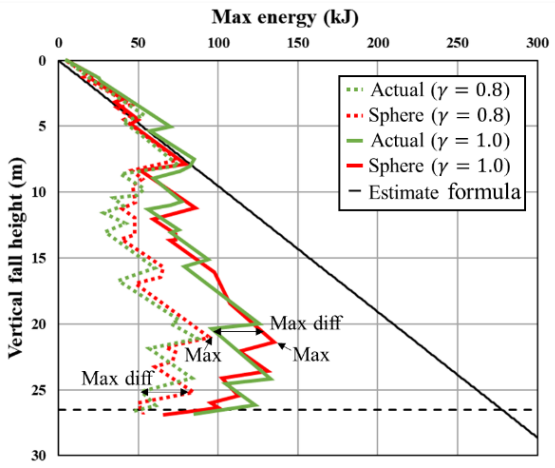


Fig. 9 Maximum energy and fall height of falling rocks (actual slope)

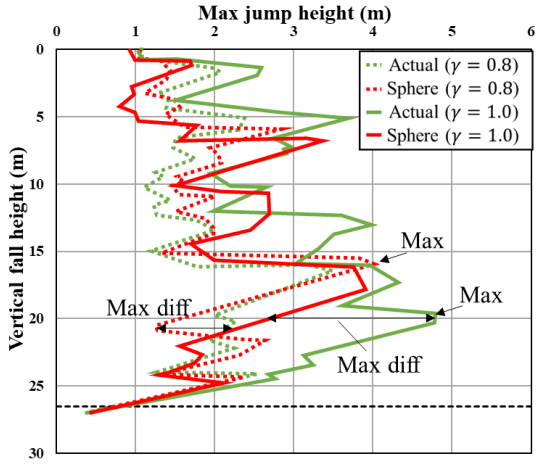


Fig. 10 Maximum jump height and fall height of falling rocks (actual slope)

As seen in Fig. 9, the maximum energy of the rockfall with γ = 0.8, on the actual slope, was approximately 95 kJ for a sphere with a fall height of 21 m. The maximum energy of falling rocks (γ = 1.0) was the largest in a sphere with a falling height of 21.5 m, at approximately 135 kJ. The energy difference of the rock shape for each fall height was within approximately 10 kJ; however, when the fall height increased, a difference of approximately 25 kJ was observed. In addition, when compared with the results of the estimation formula, the energy values obtained with the simulation were larger than those with the estimation formula up to a fall height of 5 m for all rock shapes and velocity energy ratios. In addition, beyond a fall height of 5 m, the values obtained with the energy estimation formula became larger than those obtained with the simulation, and the difference between the two increased as the fall height increased.

As seen in Fig. 10, the maximum jumping height of the rockfall with γ = 0.8, on the actual slope, was approximately 4 m for a sphere with a fall height of 16 m. The difference in the jump height of the rockfall shape for each fall height was the largest at a fall height of 21 m, at approximately 1 m. The maximum jump height of a rock fall with γ = 1.0 was the largest for the actual shape of the rock with a fall height of 20 m, at approximately 4.8 m. Here, the largest jump height of γ = 1.0 was approximately 3.9 m for a sphere and the change in jump height owing to the velocity energy ratio was smaller than that of the actual shape. The difference in the jump height of the rockfall shape for each fall height of γ = 1.0, was the largest at a fall height of 20 m, at approximately 2 m.

Comparing the rockfall behavior between the flat slope and the actual shape of the slope, the largest energy in the flat slope was approximately 60 kJ at γ = 0.8 and 115 kJ at γ = 1.0, and in the actual slope was approximately 95 kJ at γ = 0.8, and 135 kJ at γ = 1.0. Therefore, it can be confirmed that the energy of falling rocks increases owing to the unevenness of the slope shape. In terms of jump height, the largest jump height on a flat slope was approximately 1.2 m at γ = 0.8 and 2.5 m at γ = 1.0, and on the actual slope was approximately 4 m at γ = 0.8 and 4.8 m at γ = 1.0. Thus, it can be confirmed that the jump height of the falling rock increases owing to the unevenness of the slope shape as well as the energy. Regarding the difference in rockfall behavior depending on the rock shape for both slope shapes, it can be seen that the difference in rockfall behavior between both slope shapes was approximately 10 kJ or less and did not change significantly depending on the slope shape. Regarding the jump height, when γ = 1.0, the maximum jump height of the flat slope was approximately 2.5 m, and the largest jump height of the actual shape slope was approximately 4.8 m. Therefore, from the viewpoint of designing countermeasures, the large difference in jump height depending on the shape of the slope should be taken into consideration.

EXAMINATION OF THE OPERATIONAL MODE OF DDA ROCKFALL SIMULATION

We next examine how to select each shape parameter for the DDA rockfall simulation when designing rockfall countermeasures.

First, regarding the method of setting the slope shape in the sensitivity analysis performed this study, a flat slope and an actual slope with unevenness were used. Thus, it was confirmed that the energy and jump height increased owing to the unevenness of the slope. In particular, regarding the jump height, on the actual slope, a jump height exceeding 2 m, which was rare on the flat slope, was frequently confirmed, and a jump height exceeding 3 m was also confirmed (Fig. 10). From this result, considering that the standard height of rockfall protection interventions is 2 m, the design of the rockfall protection measure should differ depending on the slope shape; therefore, it is considered important to reproduce the actual slope shape.

Regarding the rock shape, a sphere and an actual shape of a rock were used in this study. Our results indicated that the energy difference between the sphere and the actual shape at each drop height was approximately within 10 kJ (Figs. 7 and 9). The DDA also has a simple analysis method using the rockfall shape as a sphere. Comparing this result with the result of the estimation formula, it is considered that the approximate energy of the actual shape can be predicted even if a sphere is used for the rockfall shape. However, it should be noted that when the scale and velocity of rockfalls are larger than those used in this analysis, the difference in energy owing to the rockfall shape also increases. Regarding the jump height, it was frequently confirmed that the difference in jump height owing to the rock shape for each fall height was 1 to 2 m at $\gamma = 1.0$, on the actual slope (Fig. 10). This difference in jump height is not negligible considering that the standard height of the rockfall protection interventions is 2 m. Therefore, if a sphere is used as the rock shape at $\gamma = 1.0$, it is possible to underestimate the jump height of the actual rock shape. At $\gamma = 0.8$ on the actual slope, the difference in jump height because of the shape of the falling rock for each fall height was approximately 0.5 m or less (Fig. 10). Therefore, when setting a velocity energy smaller than 0.8, it is possible to easily predict the approximate jump height of the actual shape using a sphere as the shape of the rock.

In this study, 0.8 and 1.0 were used as the velocity energy ratios in the sensitivity analysis. On the actual slope, the difference in energy for each drop height owing to the velocity energy ratio was the largest for a sphere with a drop height of 23 m, and a difference of approximately 70 kJ was observed (Fig. 9). In terms of jump height, that of the actual shape with a falling height of 20 m was the largest, with a difference of 2.5 m (Fig. 10). The value of the velocity energy ratio is generally determined by the geology of the site; however, when using a high value exceeding the velocity energy ratio of 0.8, a slight difference in the value may cause a large difference in the result obtained. Therefore, it is necessary to set the velocity energy ratio carefully.

CONCLUSIONS

In this study, a sensitivity analysis of model parameters was performed to examine the operational mode of the DDA rockfall simulation. Based on our results, the effects of the slope, rock shape, and velocity energy ratio on rockfall behavior could be explained, and we were able to study the operational mode of the DDA rockfall simulation. In the future, we will verify other rockfalls, slope shapes, and velocity energy ratios, and expand the study of the operational mode of the DDA rockfall simulation.

REFERENCES

[1] Japan Road Association, Rockfall Countermeasures Handbook, Maruzen, 2002, pp.422.

[2] Japan Road Association, Reference Materials for Rockfall Countermeasures Handbook, Maruzen, 2002, pp.448.

[3] Shi, G.H., Goodman, R.E., Discontinuous deformation analysis, Proc 25th U.S.Symposium on Rock Mechanics, 1984, pp.269-277.

[4] Ohnishi Y., Yamamukai K., Chen G-Q., Application of DDA in rock fall analysis, Proc. of the 2nd North America Rock Mechanics Symposium, 1996, pp.2031- 2037.

[5] Hagiwara I., Sasaki T., Nishiyama S., Ohnishi Y., Estimation and simulation of vegetation effect on rockfall using discontinuous deformation analysis, Proceedings of the ISRM International Symposium, Third Asian Rock Mechanics, Vol.2, 2004, pp.1249-1252.

[6] Sakita K., Imanishi M. and Nishiyama S., Creation of Microtopography Analysis Drawings Suitable for Slope Inspection using ALB Data, In Proceedings of the 15th Domestic Symposium on Rock Mechanics, 2021, pp.378.

[7] Hagiwara I., Ohnishi Y., Sasaki T. and Nishiyama S., Examination of Rockfall Shape Index in Non-mass Point Rockfall Simulation, Soil Engineering Journal Vol. 4, No. 4, 2009, pp.357-367.

[8] Simauchi T., Nakamura K., Sasaki T., Nishiyama S., Ohnishi Y., Research on analysis parameter determination method for rockfall analysis by DDA, 40th Symposium on Rock Mechanics Lectures, 2011, pp.294-298.

[9] Kokugan S., Ohta H., Hayashi Y., On the effective rock fall countermeasure in the slope from the medium-scale to the large-scale, Ohta-geoResearch Co., Ltd., pp.1-4.

7th Int. Conf. on Structure, Engineering & Environment (SEE), Pattaya, Thailand, Nov.10-12, 2021, ISBN: 978-4-909106070 C3051

RIPPABILITY ASSESSMENT AT GRANITIC FORMATION: CASE STUDY USING SEISMIC REFRACTION, ELECTRICAL RESISTIVITY AND BOREHOLE

Saiful Azhar Ahmad Tajudin[1,3], Muhammad Nur Hidayat Zahari[2,4], Aziman Madun[2,4], Muhammad Nizam Zakaria[1,3] and Muhammad Haziq Taqiuddin Rezuwan[1]

[1]Faculty of Civil Engineering and Built Environment, Universiti Tun Hussein Onn Malaysia, 86400 Parit Raja, Johor, MALAYSIA

[2]Faculty of Electric and Electronic Engineering,Universiti Tun Hussein Onn Malaysia, 86400 Parit Raja, Johor, MALAYSIA

[3]GeoStructure & Rehabilitation Centre, Universiti Tun Hussein Onn Malaysia, 86400 Parit Raja, Johor, MALAYSIA

[4]Preston GeoCEM Sdn. Bhd. No.33A Jalan Universiti 4, Taman Universiti, 86400 Parit Raja, Johor, MALAYSIA

ABSTRACT

Geophysical surveys of Seismic Refraction and Electrical Resistivity Tomography (ERT) were conducted in granitic rock formation. This study aims to assess the material rippability and to determine the rock head. The rippability assessment using seismic refraction, electrical resistivity and verified using borehole test that were conducted at two locations in Melaka, denoted as chainage (CH) 900 and 2100. The seismic refraction survey used 24 channel geophones and ABEM Terraloc MK8 seismograph. The geophones were spaced at 5 m interval and total survey length was 115 m. Electrical resistivity survey was performed using ABEM Terrameter LS using two resistivity land cables, 41 electrodes and spacing of 5.0 m at length of 200 m adopted Schlumberger protocol. The outcomes show that there are discrepancies of depth bedrock layer between seismic refraction and borehole tests. The seismic refraction test result at CH 900 shows deeper marginal rippable at 20 m below ground surface, while borehole test indicated that the bedrock is 13 m from ground surface. For CH 2100, seismic test shows deeper marginal rippable at 25 m, and borehole shows the hard material at 4.5 m. These huge differences between marginal ripple and rock or hard material are due to several reasons; (1) the percentage of soil with isolated corestones or boulders is influenced the seismic wave refraction and propagated wave, and thus affected the value of seismic velocity, i.e. reduce the seismic velocity, and (2) the rock head is masked by the isolated corestones, and thus effected the accuracy to determine the bed rock. Finally, the resistivity test unable to identify rock head due to low groundwater table, but it is able to identify saturated material.

Keywords: Rippability, Granitic formation, Seismic refraction, Electrical Resistivity, Borehole

INTRODUCTION

Rippability of rock mass assessment is adopted the parameters obtained from core boring and/or geophysical work [1]. There are six parameters which are type of rock, rock structures, rock hardness, weathering grade, rock fabric and seismic wave velocity [2]. Seismic refraction is a geophysical method used for investigating the thickness of overburden, depth bedrock and assessing rippability parameters. The seismic wave velocity method for rippability assessment was developed by the Caterpillar Tractor Company [3]. The speed of a seismic wave depends on the stiffness, density and the degree of cementation of materials, thus the seismic waves move faster through the rock than in the soil.

In general, a lower seismic wave velocity indicates material more easily rippable [4]. Caterpillar Tractor Company found that a comparison of the wave velocities recorded with those obtained in a similar material from previous experience gives a good indication of ripper performance. They have published charts in Fig 1 showing ripper performance as related to seismic wave velocities for D8R ripper equipment [3]. Rippability may be qualitative: rippable, marginal, and/or non-rippable.

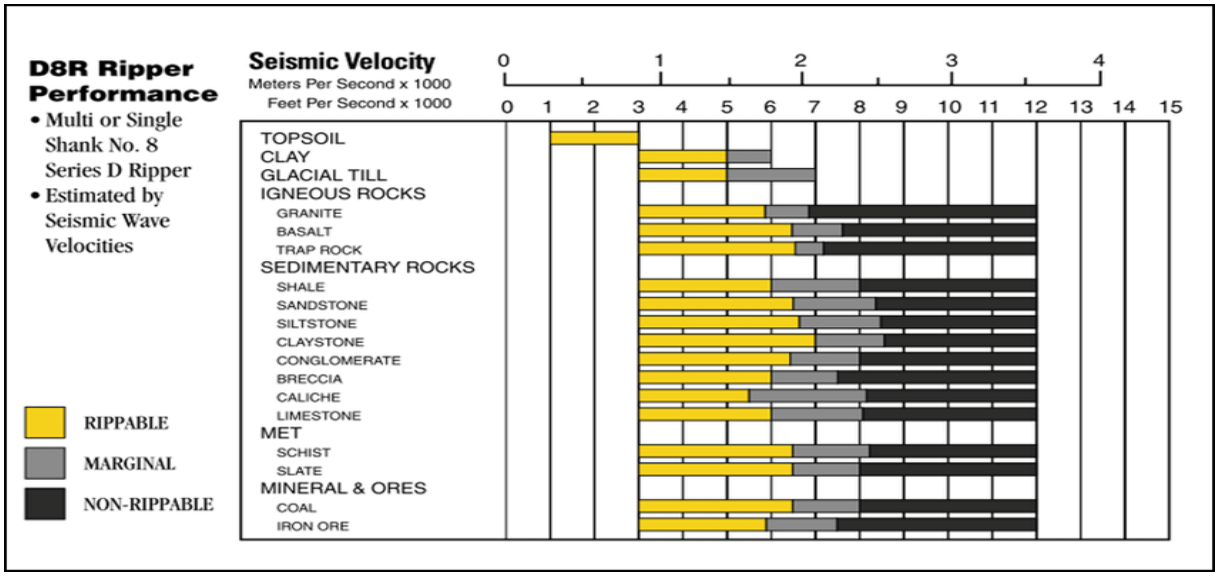


Fig. 1 Rippability classification of different rock masses according to their P-wave seismic velocity values [3].

Or it may be semi-quantitative on a scale of rippability ratings from 0-100: 0 being highly rippable and 100 being non rippable. In either description, rippability is dimensionless. The degree of difficulty of earthwork was crucial to classify to rippable, marginal or non-rippable due to affecting the cost of project. Rock rippability is evaluated via site trial excavation, however this method is time consuming and costly due to require to have ripper machine on the site. The problems of the conventional excavation evaluation may not effective when dealing with large earthwork scale and rough terrain. Thus alternative approach is using the geophysical method with particular reference to seismic refraction method has increasingly adopted for the excavation assessment [5].

The resistivity is measured the ground resistant to the injected direct current, which measured in ohm.m. The resistivity method basically measures the bulk resistivity of the subsurface material. Table 1 shows the resistivity value of some of the typical rocks, soil materials and water [6]. Rocks materials typically have high resistivity values compared to soils. The resistivity of these rocks are mainly dependent on the degree of fracturing and the present of groundwater. The greater the fracturing and moist, the lower is the resistivity value of the rock. As an example, the resistivity of sandstone varies from 8 ohm-m in saturated condition to 4000 ohm-m in dry. Also, clay has a significantly lower resistivity value than sand due to capability of holding the water. However, earth materials is mixed between rock, sand, clay at different percentage of water, thus the typical resistivity value is just for guidance in interpretation. The higher resistivity ground is referred to the dry material, which can be interpreted as solid rock mass or dry soil. Thus, understanding the geological model of the study area is crucial in interpretation of resistivity result. In this study, the resistivity is used to support the result obtained from the seismic refraction technique. Third test is the borehole, which is conducted to verify the result from both geophysical testing. In addition, the bore hole test is to provide subsurface profile via SPT test and soil sampling, however only information at the actual drilling location.

Table 1 Typical resistivity value of selected rocks, soil and water [6]

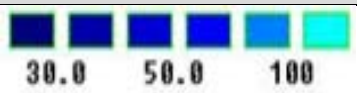
Material	Resistivity (ohm-m)
Granite	**500 - 50000**
Marble	**10 - 10000**
Sandstone	**8 - 4000**
Shale	**20 - 2000**
Clay	**1 - 100**
Sand and Gravel	**100 - 10000**
Soil	**10 - 1000**
Fresh water	**10 - 100**
Sea water	**0.15**

In term of geophysical investigation, the bedrock has higher velocity of primary wave (P-wave) and higher resistivity value. The P-wave propagation velocity is depending on the density of the materials in subsurface. High density material generates a high velocity of P-wave, where the P-wave velocity is higher in a bedrock compared to the weathered granite/soil. For the resistivity, the soil and weathered are normally loose and moist, and expected will generate a lower resistivity values compared to the fresh rock. However, the fractured rock mass can be filled with water or wet clay mineral are also expected will generate a low resistivity value compared to solid fresh rock. The objectives of the survey is to estimate the thickness of the residual soil and depth of the bedrock at the study area. Thus, the result is applied for the rippability assessment.

Table 2 The rippability chart in granite

Description of Material	P-wave Velocity, (Vp)	N-Values	Rippability assessment	Colour
Residual Soil (Grade VI)	350 – 750	< 30	Rippable	Blue
Completely weathered rock (Grade V)	750 - 1500	31 - 49	Rippable	Green
Highly weathered rock (Grade IV)	1500 - 2000	50 - 65	Marginal	Yellow
Moderately weathered to fresh rock	>2000	>65	Non-rippable	Red

Table 3 The resistivity value interpretation for this study

Resistivity Value (Ωm)	Legends	Grade	Interpretation
< 100		Grade V-VI	Residual soil, highly weathered granite or fractured rock contained water
1000 - 3000		Grade III - IV	Medium weathered granite
>3000		Grade I - II	Low weathered to fresh granite

This study is adopted seismic P-wave velocity to assess the rippability of igneous rock formation via conducting the seismic refraction test and supported by the electrical resistivity tomography test at Melaka new road from Tebong to Hutan Percha.

GEOLOGY OF STUDY AREA

The geological setting of the study area is intrusive rock, which consists of granite rock as illustrated as shown Fig. 2. The overburden materials mainly consist of weathered rock to residual soils, which are derived from the weathering of granitic rock and generally consists of silty sand and sandy silt with traces of gravel. Field observation also revealed the formation and occurrences of isolated boulders in the studied sites (Fig.3).

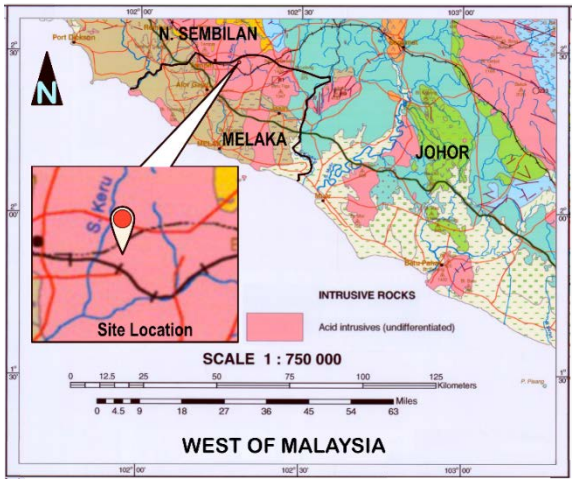


Fig. 2 Geological setting at site location [7]



Fig. 3 Exposed boulders at testing location

METHODOLOGY

The spread lines for seismic refraction and resistivity were parallel and at similar center line position. Two (2) lines of seismic refraction and two (2) lines of electrical resistivity tomography were carried out along the proposed road alignment at CH 900 and CH 2100. The seismic refraction survey was applied using a sledge hammer weighing of 7 kg, hammering on a striker plate as a source. For receiver, a 24 channel vertical geophone was used based on 28 Hz of frequency. Meanwhile, ABEM Terraloc MK8 seismograph was used for field data recording. The spread line was arranged and the geophones were spaced at 5 m interval as given total line length was 115 m. In order to generate the subsurface seismic tomography profile, the seismic raw data was analyzed using Optim software [8].

Electrical resistivity imaging (2-D electrical resistivity survey) was performed using ABEM Terrameter LS. A single spread line of electrical

resistivity survey was performed across at each location. The test configuration was based on Schlumberger array using two resistivity land cables, 41 electrodes and 42 jumper cables. Equal electrode spacing of 5.0 m was used for all 41 electrodes producing total electrical resistivity for a survey length of 200 m. Schlumberger array was used during the data acquisition since it is able to provide dense near-surface coverage of resistivity data. Raw data obtained from data acquisition was processed using commercialized RES2DINV software to provide an inverse model that approximates the actual subsurface structure. The inversion algorithm of RES2DINV was used to process the data, as proposed by in order to replicate the 2-D model of the subsurface profile [9]. Bore holes were drilled at the point of geophysical survey ah CH 997.5 and CH 2215. The standard penetration test (SPT) and soil samples were carried out at 1.50 m interval. The drilled was terminated when five (5) consecutive SPT-N blows more than 50 to penetrate 0.3 m depth or 6.0 m length of continuous coring for rocks. The interpretation of seismic refraction was based on recommendation by D8R ripper equipment [3]. The rippability chart that corresponding to the rock weathering grade, P-wave velocity and SPT N-blow. Meanwhile, for interpretation of resistivity values is yet to standardize due to the resistivity value is effected by many parameters, such as type of rocks and soils, degree of saturation and concentration of ion contents in groundwater [10][11]. Thus, to simplify the resistivity value interpretation, this study considered the resistivity values correspondent to grade of weathered rock material and rock / soil degree of saturation as shows in Table 3.

RESULT AND DISCUSSION

Survey at CH900

At CH 900 of study area, the granite boulders were exposed on ground surface as shown in Fig 4a. Figure 4 shows the tomography plots of seismic velocity profile and the resistivity profile as well as borehole position at location CH 900. The seismic spread length was 115 m and obtained up to 35 m depth. The result indicate the ripple material varies from 10 m to 25 m thickness for velocity below 1500 m/s, follows by marginal 1500 m/s to 2000 m/s and non-rippible for material more than 2000 m/s. Meanwhile, the resistivity spread length was 200 m and obtained up to 55 m depth. However from the resistivity tomography indicates that majority of material less than 200 ohm-m indicates the ground material is influences by groundwater. It worth to note the groundwater table at 4.3 m below ground level. The borehole 1 at CH 997.5 tabulated at Table 5 indicates that 6 m coring begin at 13 m below ground level, which is considered as non-ripple material. Besides, the seismic result shows rippable material at 13 m depth. It seems that borehole terminated on the boulder based on the visual inspection shows that the area has many boulders at variable size.

Survey at CH 2100

At CH 2100 of study area, the granite boulders were also exposed on ground surface as shown in Fig 4b. Figure 6 shows the tomography plots of seismic velocity profile and the resistivity profile as well as borehole position at location CH 2100. The seismic spread length was 115 m and obtained up to 35 m depth. The result indicate the ripple material from 15 m to 25 m thickness for velocity below 1500 m/s, follows by marginal material more than 1500 m/s. The resistivity spread length was 200 m and obtained up to 55 m depth. However from the resistivity tomography indicates that majority of material less than 1000 ohm-m and decreased to less than 100 ohm-m at deeper layer, which indicates the resistivity profile is influences by groundwater. It worth to note the groundwater table at 5 m below ground level. However, at horizontal position 120m, it seems a solid rock mass at size of 20m x 10m, which is buried at 15m below ground surface. The result of borehole 2 at CH 2215 is tabulated at Table 4 indicates that hard layer begin at 4.5 m below ground surface and terminated at 12.45 m. Besides, the result of seismic shows the ripple material at 4.5 m depth contrast with borehole.



(a)



(b)

Fig. 4 Exposed granite boulders at (a) CH 900 (b) CH 2100

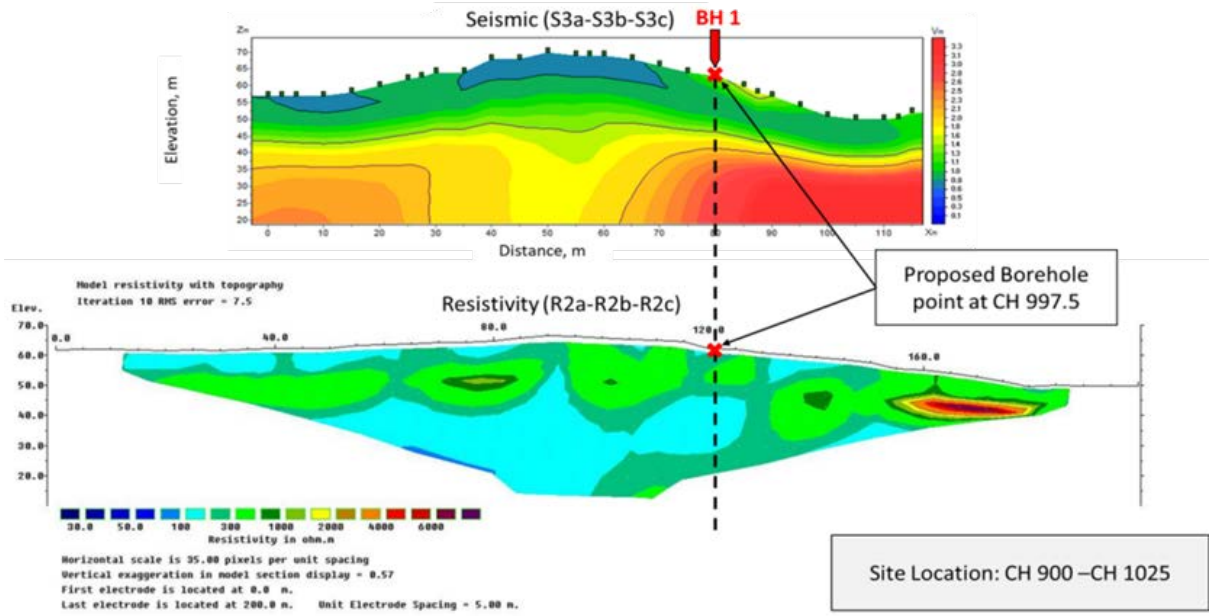


Fig.5 The tomography plots of seismic velocity profile and resistivity profile at CH900 to CH1025 as well as borehole # 1 position at CH997.5

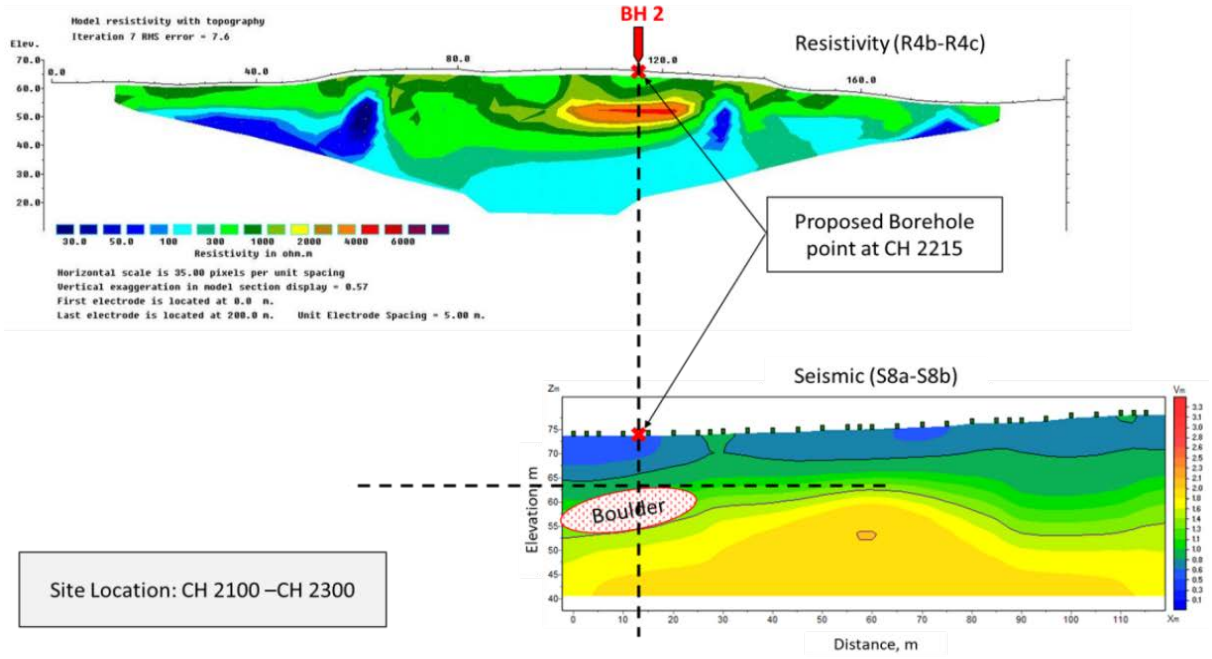


Fig.6 The tomography plots of resistivity profile and seismic velocity profile at CH2100 to CH2300 as well as borehole position # 2 at CH2215

Discussion

The rippability assessment using seismic refraction, electrical resistivity and verified using borehole test were conducted at the boulders areas. This discrepancy results between seismic and borehole at both location may due to (1) the effect of seismic wave refraction propagated along the bedrock head not on boulders, and (2) the seismic velocity influences by the volume of measurement due to the volume ratio between soil and boulders [12][13].

Surprisingly, the results show that the occurrences of boulders below the ground surface significantly affected the accuracy of seismic refraction to

determine the rock profile. The site investigation works are challenging due to heterogeneous of subsurface as shown in Fig. 7. The existence of isolated corestones have been detached from the rock mass and sometimes boulders (corestones) exposed on the ground surface.

The seismic refraction method disregard the corestones via averaging the seismic values based on the volume of measurement. Therefore the percentage of soil with isolated corestones (embedded boulders) is influenced the seismic wave refraction and wave propagation, and thus affected the seismic velocity value. The second issues is related to the rock profile, which is masked by the corestones, and thus effected the accuracy of rock head depth.

The resistivity test is unable to differentiate between the soil and corestones because of the influences of shallow groundwater at 5 m deep below ground surface. This finding indicates that the resistivity method is not suitable to determine the heterogeneous weathered rock profile with fully saturated condition. Otherwise, it is recommended to use this method for profiling purposes in unsaturated soil. Borehole is only provides single subsurface information from the drilled hole.

Therefore, to apply this method in a boulder zone may affect the accuracy of result due to the heterogeneous characteristics of the area. Furthermore in the geological complex area, interpolation between borehole and geophysical result may involve some degree of uncertainty.

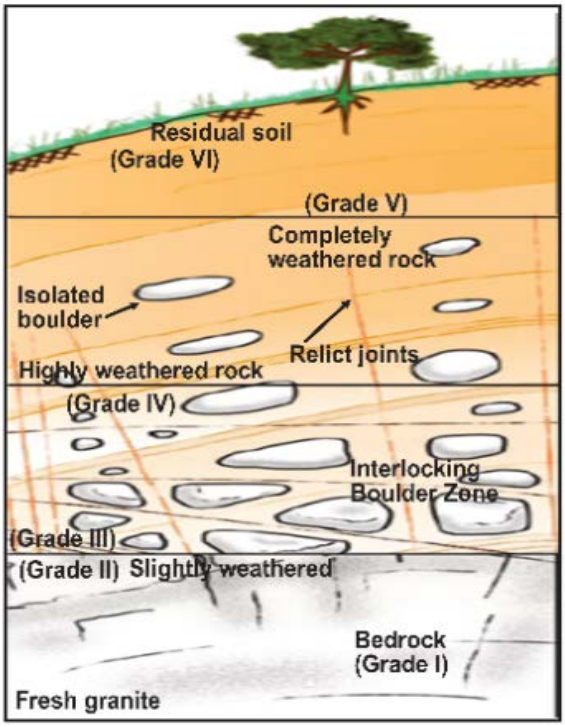


Fig. 7 Typical weathering profile in granitic rock

Table 4 Summary of Borehole Data

Borehole no.	Material	SPT	RQD value (%)	Depth	Termination depth (m) & Final Type of Soil/SPT/Rock Type	Ground Water Level
BH 1	Residual Soil	< 30	-	0.0m – 9.45m	Borehole 1 terminated at depth 19.00m. Coring: Granite	4.3m from G.L
	Hard Layer	30 < N < 50	-	10.50m – 12.45m		
	Granite	-	C1: 61.33	12.00m – 19.00m		
			C2: 36			
			C3: 49.33			
			C4: 52.67			
BH 2	Residual Soil	< 30	-	0.0m – 3.45m	Borehole 1 terminated at depth 12.45m. SPT: 50	5 m from G.L
	Hard Layer	30 < N < 50	-	4.50m – 12.45m		

CONCLUSION

The rippability assessment using seismic refraction, electrical resistivity and verified using borehole test was conducted at the boulders area.

The testing shows that there are discrepancies outcomes of determining the bedrock/hard material layer between seismic refraction and borehole tests. The seismic test result at CH 900 shows deeper marginal rippable at 20 m, while borehole shows rock head at 13 m. Similar trend at CH 2100 show deeper marginal rippable at 25 m using seismic refraction, while borehole shows hard material at 4.5 m. These huge differences depth between marginal ripple and rock / hard material are due to several reasons; (1) the

percentage of soil with isolated corestones is influenced the seismic wave refraction and propagated wave, and thus affected the value of seismic velocity, i.e. reduce the seismic velocity, and (2) the rock head is masked by the isolated corestones, and thus effected the accuracy to determine the bed rock. Finally, the resistivity test unable to identify rock head due to low groundwater table, but able to identify saturated material.

ACKNOWLEDGMENTS

This work was collaboration between Universiti Tun Hussein Onn Malaysia and Preston GeoCEM Sdn Bhd. The authors wish to acknowledge gratefully to Mr. Zailani Mansur for his supported in this research.

REFERENCES

[1] Weaver, J. M. (1975). Geological factors significant in the assessment of rippability. Civil Eng S Afr., 17(12), 313-316.

[2] Bieniawski, Z.T. (1989). Engineering rock mass classifications. New York: Wiley.

[3] Caterpillar (2001). Performance Handbook Edition 32. Caterpiller Inc., Peoria, Illinois

[4] Mohamad, E. T., Kassim, K. A., & Komoo, I. (2005). An overview of existing rock excavatability assessment techniques. Jurnal Kejuruteraan Awam, 17(2), 46-59

[5] Aziman, M., Firdaus, M. D. M., Faizal, P., Azhar, A.T.S., Nordiana, M., Ashraf, M. I. M. and Nor' Aishah, M. A. (2019). Sedimentary rock mass rippability assessment using seismic refraction survey, AIP Conference Proceedings 2129, 020110.

[6] Keller, G.V. and Frischknecht, F.C. (1966). Electrical methods in geophysical prospecting: Pergamon Press, New York, pg. 517.

[7] Mineral and Geoscience Department Malaysia, Geological Map of Peninsular Malaysia, 8th Ed. Ministry of Natural Resources and Environment (1985).

[8] Hazreek Z.A.M., Faizal, T.B.M., Aziman, M, Azhar, A.T.S., Rosli, S., Ashraf, M.I.M. and Hafizan, S.M. (2017). Subsurface Profile Mapping using 3-D Compressive Wave Imaging. MATEC Web of Conferences, 2017.

[9] Loke, M.H., Chambers, J.E., Rucker, D.F. and Wilkinson, P.B. (2013). Recent developments in the direct-current geoelectrical imaging method. Journal of Applied Geophysics, 95, 135-156.

[10] Ismail, M.A.M., Kumar, N.S., Abidin, M.H.Z. and Madun, A. (2018). Identification Of Rippability And Bedrock Depth Using Seismic Refraction. Journal of Physics: Conference Series, 995.

[11] Hazreek, Z.A.M, Rosli, S., Devapriya, C.W., Fauziah, A, Faizal, T.B.M., Azhar, A.T.S. and Aziman, A. (2017). The Influences of Basic Physical Properties of Clayey Silt and Silty Sand on Its Laboratory Electrical Resistivity Value in Loose and Dense Conditions. Sains Malaysiana, Universiti Kebangsaan Malaysia, vol. 46(10), p. 1959-1969.

[12] Madun, A., Ahmad Supa'at, M.E., Ahmad Tajudin, S.A., Zainalabidin, M.H., Sani, S., Yusof, M.F.. (2016). Soil investigation using Multichannel Analysis of Surface Wave (MASW) and borehole. ARPN Journal of Engineering and Applied Sciences, 11 (6), pp. 3759-3763.

[13] Madun, A., Tajuddin, S.A.A., Abdullah, M.E., Abidin, M.H.Z., Sani, S., Siang, A.J.L.M., Yusof, M.F. (2016). Convertion Shear Wave Velocity to Standard Penetration Resistance. IOP Conference Series: Materials Science and Engineering, 136 (1), art. no. 012009.

7th Int. Conf. on Structure, Engineering & Environment (SEE),
Pattaya, Thailand, Nov.10-12, 2021, ISBN: 978-4-909106070 C3051

METHOD OF EVALUATING CORROSION RISK FROM ELECTRICAL RESISTIVITY OF CONCRETE WITH REINFORCING BAR

Yoko Sakakihara[1], Yuu Hashimoto[1], Sunao Fujimura[2] and Shinichirou Okazaki[3]
[1] Graduate School of Engineering, Kagawa University, Japan;
[2] Penta-Ocean Construction Co., Ltd., Japan;
[3] Faculty of Engineering and Design, Kagawa University, Japan

ABSTRACT

The effect of water penetration is a major factor in the deterioration of reinforced concrete (RC) structures. Water reaching the reinforcing bars triggers the corrosion of the steel, which causes cracks in the concrete. Therefore, a technology that nondestructively signals contact between water and these steel bars is required to properly maintain RC structures. In this study, the relationship between the contact of water with the reinforcing bars and the electrical resistivity of the RC was investigated using the four-electrode method. The result of the experiment showed that the electrical resistivity of the RC specimen was much lower than that of a non-RC specimen, and when water reached the RC, the electrical resistivity decreased significantly. Furthermore, analytical findings indicated that water reached the reinforcing bars when the resistance value suddenly decreased due to water penetration. Thus, it found as an indicator that water has contacted the reinforcement that the rate of decrease in electrical resistivity instantly increases once the water reaches the reinforcement.

Keywords: Four-electrode method, Corrosion risk estimation, Electrical resistivity, Numerical analysis

INTRODUCTION

Concrete is used in civil engineering structures as a main construction material due to its workability, economy, and availability. However, RC structures have been reported to deteriorate due to salt attack, carbonation, and ASR and so on. In particular, when water penetrates into carbonated cover concrete, reinforcing bar corrosion occurs, and the cover concrete delaminates due to the increase in expansion pressure [1], leading to serious problems such as bridge collapse [2]. It is also known that even if the cover concrete is carbonated, if water is not supplied, the reinforcing steel will not be corroded. Therefore, in considering the corrosion of steel bars in deteriorated RC structures, it is the most important to know whether water has reached the steel bars or not, but a simple and non-destructive method has not yet been established. For example, assessment methods for reinforced corrosion have been devised around the world, and research is underway on a method for directly measuring corrosion by attaching an optical fiber to the reinforcement [3], measurement by a combination of SEM/EDS analysis and strain gauging [4], and measurement by an embedded sensor [5], among others.

In this study, we focus on electrochemical measurement [6]-[8] and propose a method to evaluate the contact of water with the reinforcement from the change in electrical resistivity caused by the penetration of water in the RC. The relative permittivity values of dry and wet concrete are about 4–6 and 8–20, respectively. whereas the relative permittivity of steel can be considered infinite. In cases where water gradually infiltrates from the surface while the cover concrete is dry, the electric current will initially flow mainly through the concrete; as the water infiltrates, the electric current will flow to the reinforcement, and the electrical resistivity of the cover concrete, including the reinforcement, will decrease significantly. Figure 1 shows a schematic diagram of this mechanism. In this paper, we proved this hypothesis, confirmed that we can assess the risk of reinforcement corrosion, and confirmed the validity of this experiment via simulation.

EVALUATION METHOD FOR CONTACT OF WATER WITH REINFORCEMENT

Four-Electrode Method

There are many methods of evaluating electrical resistivity, depending on how the electrodes are arranged [9]. The two-electrode method is greatly affected by the contact resistance of the current-carrying electrodes, and the four-electrode method A, which is standardized in JSCE-K 562, is unsuitable for field measurement because the measurement point must be sandwiched between current-carrying electrodes. Therefore, the four-electrode method B, which was proposed in the same paper [9], was

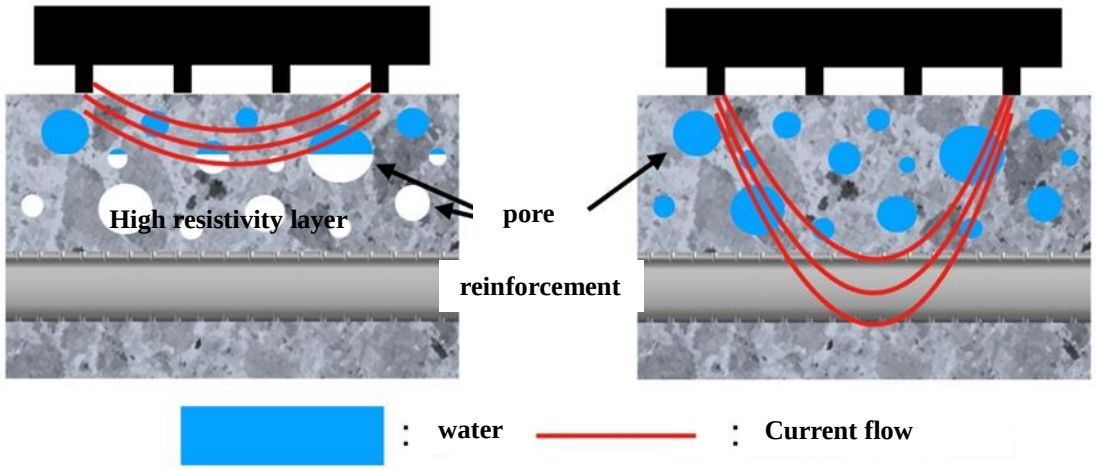


Fig. 1 Change in current flow as a result of water penetration

adopted in the present study.

We verified the hypothesis that the electrical resistivity of concrete changes when water penetrating from the surface of the concrete reaches the reinforcement. This method of measuring the electrical resistivity of concrete is based on JSCE-K 562-2008. As shown in Fig. 2, in the four-electrode method, the current I (A) is applied from the outer current-carrying electrodes, and the potential difference V (V) is measured at the inner electrodes. The electrode spacing is L (m), and the surface electrical resistivity ρ (Ωm) can be calculated by the following equation:

$$\rho = 2\pi LV/I. \quad (1)$$

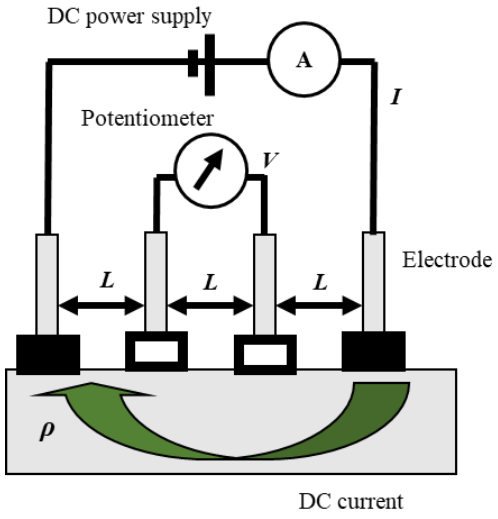


Fig. 2 Schematic diagram of four-electrode method

Electrode Distance

In general, the four-electrode method is used to estimate the apparent diffusion coefficient of chloride ions and to evaluate the mass transfer resistance of concrete structures [6]. The disadvantage of this method is that it is affected by reinforcement and aggregate.

The effect of reinforcement becomes larger as the distance between electrodes lengthens, and the effect of coarse aggregate becomes larger opposite the distance between electrodes.

In this study, the distance of the electrodes was set so that they would be affected by the reinforcement but not the coarse aggregate. Specifically, the electrode distance was 50 mm for the maximum coarse aggregate particle size of 25 mm. The experiment was conducted so that the effect of the coarse aggregate was small while retaining the effect of the reinforcement.

EXPERIMENT

Experimental Procedure

Experiments were conducted to test the hypothesis that the electrical resistivity of concrete changes when water infiltrating from the surface of the concrete reaches the reinforcement.

Ordinary Portland cement (3.15 g/cm^3), fine aggregate (2.60 g/cm^3), and coarse aggregate (2.61 g/cm^3) were used. AE water-reducing agent was used as the admixture. The concrete mix ratio is shown in Table 1. The concrete specimens were 100 mm wide, 100 mm high, and 380 mm deep. Four cases were made: no reinforcement and with reinforcement (25, 50, and 70 mm of the thickness of the cover concrete); three specimens were made per case. The W/C values of the two cases were 40% and 60%. The reinforcement was D13 steel bars.

In 24 h after the placement of concrete, the specimens were immediately demolded, sealed with plastic wrap, and cured for 28 days.

While water was supplied from the measurement surface, the electrical resistance and the current

flowing through the reinforcement were measured every 24 h until the 28th day. A photo of the specimens is shown in Fig. 3.

Table 1 Concrete mixture ratios

W/C	Water kg/m^3	Cement kg/m^3	Sand kg/m^3	Gravel kg/m^3	Ad. %
0.4	175	438	790	964	1
0.6	175	292	843	1029	1

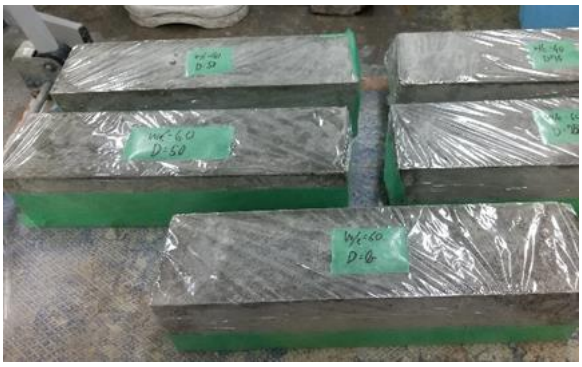


Fig. 3 Sealed curing with plastic wrap

Experimental Results

The relationship between the measured electrical resistivity and the time elapsed since the start of water supply is shown in Fig. 4-1 and 4-2. The electrical resistivity of the specimens with reinforcement was lower than that of the non-reinforced specimens, and the electrical resistivity increased with the thickness of the cover concrete. The decrease in electrical resistivity due to water penetration generally converged in 48 h, regardless of the thickness of the cover concrete.

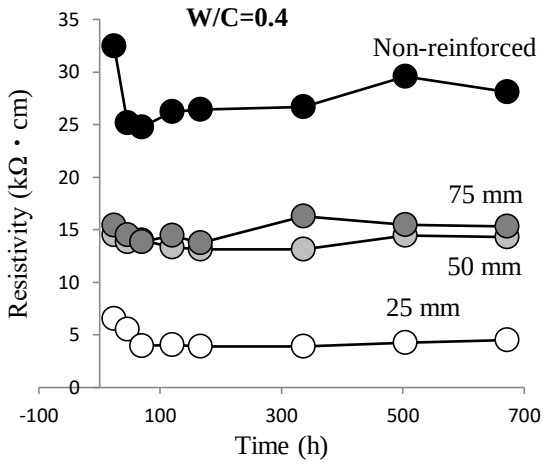


Fig. 4-1 Relationship between electrical resistivity of each cover concrete thickness and time (W/C=0.4)

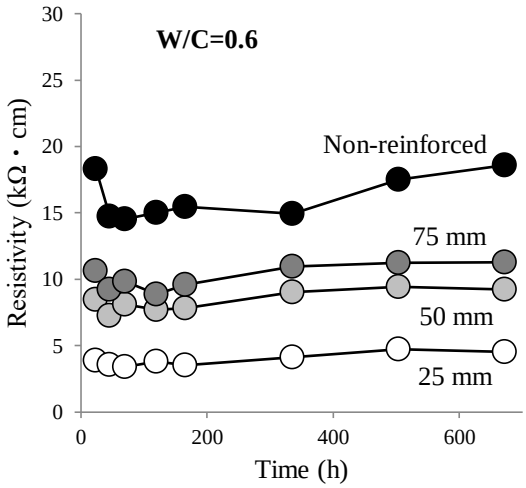


Fig. 4-2 Relationship between electrical resistivity of each cover concrete thickness and time (W/C=0.6)

The change in electrical resistivity that was caused by the difference in the cover thickness and the contact of water with the reinforcement could not be confirmed in detail because of the long measurement time interval. The converging tendency may indicate the contact of water with the reinforcement.

SIMULATION

Simulation Conditions

A simulation study was conducted on the basis of the two-dimensional finite element method [10]. It for the four-electrode method was performed using the V5.6 AC/DC module of COMSOL Multiphysics® software.

A model with the same dimensions as the specimen set in the experiment study was used, and the electrode distance for the four-electrode method was set in the same way. Figure 5 shows the model used in this simulation. The applied current was 1 A/m. The material characteristic values were decided with a specific resistance of 5×10^4 (Ω·cm) for dry concrete and 6×10^3 (Ω·cm) for wet concrete, in accordance with the work of Sudjono et al. [11]. The material constant of the reinforcing bars was set to 1.62×10^3 (S/m). The electrical resistivity was calculated by determining the measurement point from the electrode spacing and measuring the electric potential, as in Wenner's four-electrode method (used in the experimental study). The model for reproducing the water penetration was generated by setting the material property values of the dry and wet concrete in layers of 5 mm each. The penetration of water to the iron bars was reproduced by gradually replacing the material property values from dry to wet.

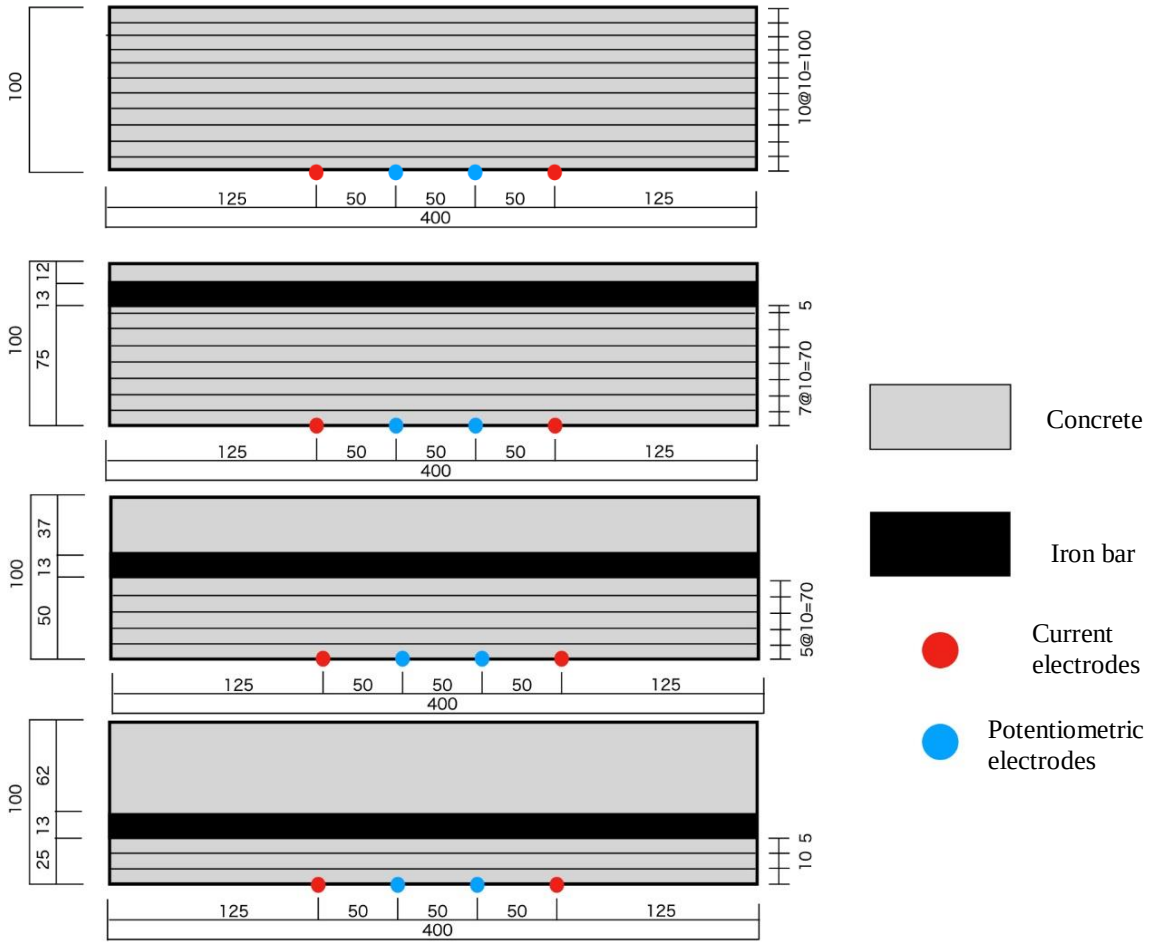


Fig. 5 Simulation model dimensions (top: non-RC, upper middle: 75 mm cover concrete, lower middle: 50 mm cover concrete, bottom: 25 mm cover concrete)

Simulation Results

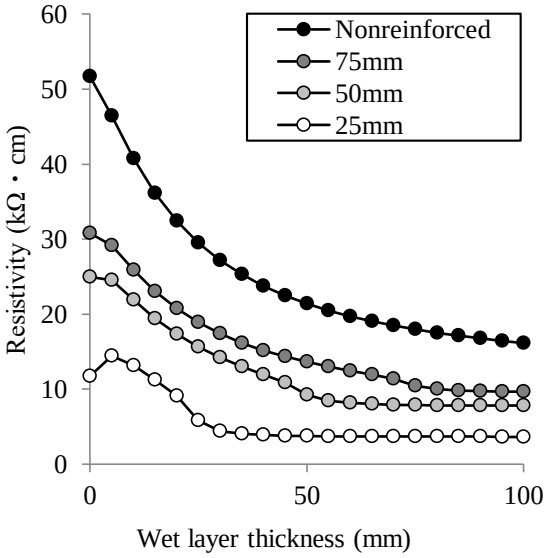


Fig. 6 Relationship between electrical resistivity and water penetration

Figure 6 shows the simulation results of the water penetration distance and electrical resistivity. As in the experimental study, the electrical resistivity of the non-reinforced specimens was the highest, and the electrical resistivity was lower in the cases with reinforcement. Findings showed that the thinner the cover thickness, the lower the electrical resistivity. For the specimens with reinforcement, the resistivity converged when the water penetrated the reinforcement.

Figure 7 shows the electrical resistivity ratio when the material property values of the dry concrete were given to all layers of the model and the electrical resistivity at each measurement point when water penetrated. With the behavior of the non-reinforced specimen as the reference line, the water reaches the position of the reinforcement when it deviates from the behavior of the non-reinforced specimen. However, as mentioned in the experimental study, it is difficult to apply this method in the field because the resistivity may converge when the water penetration reaches a steady state in the non-reinforced specimen.

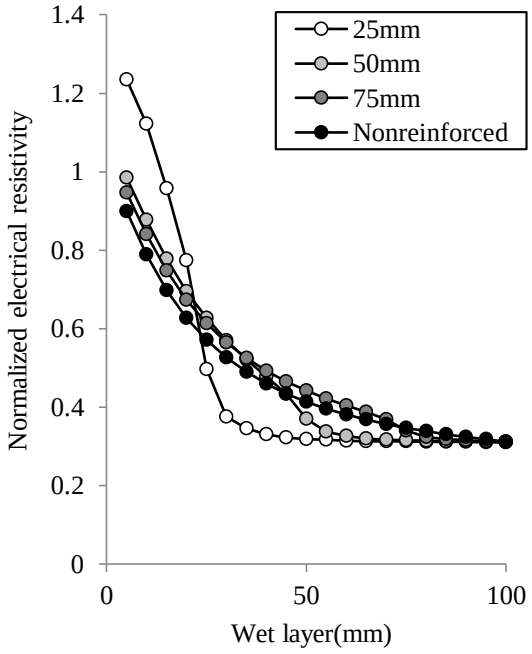


Fig. 7 Normalized electrical resistivity

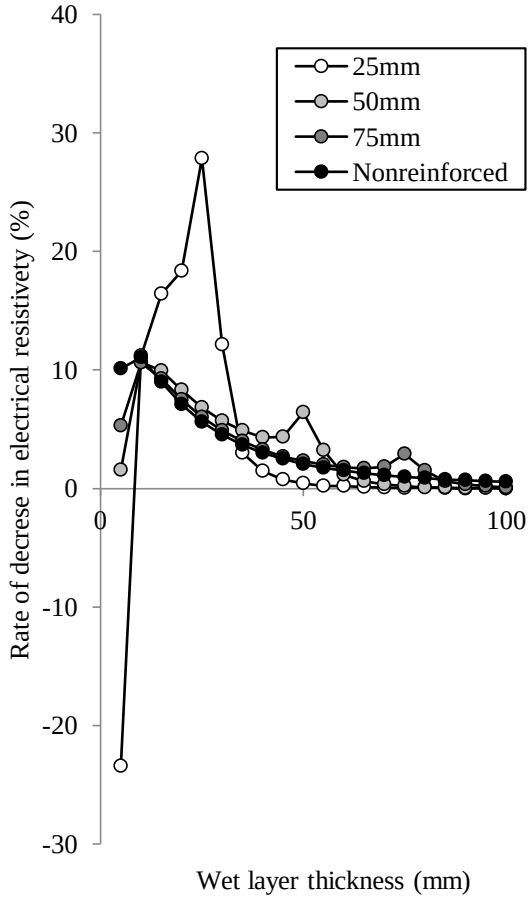


Fig. 8 Relationship between rate of decrease in electrical resistivity and location of water penetration

In the case of the 25 mm cover concrete in Fig. 6, there was a considerable change in the rate of decrease in electrical resistivity near the distance at which the water contacted the reinforcement. The graphs show that the electrical resistivity changed just when the water reached the rebar location, even in the cases with cover thicknesses of 50 mm and 75 mm. Therefore, the rate of change in electrical resistivity may be related to the arrival of water at the rebar, so we calculated the rate of decrease in electrical resistivity.

The decrease in electrical resistivity was calculated by subtracting the electrical resistivity at (x-5) mm from the electrical resistivity at x mm, divided by the electrical resistivity at 0 mm, and multiplied by 100 for the percentage.

Figure 8 shows the rate of decrease in electrical resistivity between each point. The rate of decrease in electrical resistivity instantly increases once the water reaches the reinforcement. Thus, this may serve as an indicator that water has contacted the reinforcement.

Given the simulation results, we again considered the experimental results. Figure 9 shows a graph of the resistivity decrease rate in experimental study. This experimental study confirmed that the rate of decrease in electrical resistivity exhibited a peak at the initial stage of water supply. In the case of W/C = 0.4 and 25 mm cover concrete, the resistivity decreased by 25% at 72 h and then converged, suggesting that the water had penetrated the position of the reinforcement.

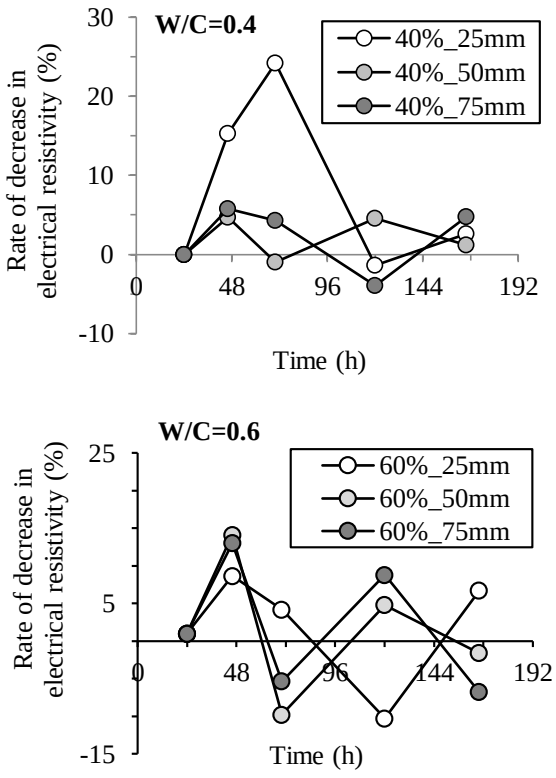


Fig. 9 Graphs showing rate of decrease in electrical resistivity at each time (top: W/C = 0.4, bottom: W/C = 0.6)

In the case of w/c = 0.6, there was no significant change in the resistance reduction rate. Compared to w/c = 0.4, w/c = 0.6 is more porous, suggesting that water reached the steel bars at an earlier stage. It was not possible to capture the change since the measurement interval was every 24 hours.

CONCLUSIONS

In this study, the four-electrode method was used to investigate a non-destructive method to know when water reaches the reinforcement. The experimental results show that the electrical resistivity of the RC specimens is much lower than that of the non-reinforced specimens, and the electrical resistivity decreases significantly when water reaches the reinforcement.

In the simulation study, the experimental results were confirmed by numerical analysis, where the resistance decreased rapidly as the water reached the reinforcement. It was newly found that the rate of decrease in electrical resistivity has the maximum value when the water reaches the reinforcement, because the electrical resistivity decreases significantly when the water reaches the reinforcement. Based on this result, the experimental results were summarized again, and it was confirmed that w/c = 0.4 and 25 mm cover concrete had the maximum value as well.

Thus, it found as an indicator that water has contacted the reinforcement that the rate of decrease in electrical resistivity instantly increases once the water reaches the reinforcement.

ACKNOWLEDGMENTS

This research was supported by JSPS KAKENHI (grant number JP 19K04554) and the Ministry of Land, Infrastructure, Transport and Tourism, Construction Technology Research and Development Grant Program (CRD).

The authors would like to thank Enago (www. Enago.jp) for the English language review.

REFERENCES

[1] Ishibashi T., Furuya T., Hamazaki N., Suzuki H., Investigation of falling on concrete fragments from RC structure, Proceedings of JSCE, No.711 V-56, 2002, pp.125-134

[2] Pilz M., The Collapse of the K-B Bridge in 1996, A MSc Dissertation at the Imperial College London, 2007

[3] Fan L., Zhang Q., Meng W., Chen G., Bao Y., Monitoring corrosion of steel bars in reinforced concrete based on helix strains measured from a distributed fiber optic sensor, Engineering structures, Vol.204, 2020

[4] Bazan A.M., Galvez J.C., Reyes E., Gale-Lamuela D., Study of the rust penetration and circumferential stresses in reinforced concrete at early stages of an accelerated corrosion test by means of combined SEM, EDS and strain gauges, Construction and Building Materials, Vol.184, 2018, pp.655-667

[5] Tondolo F., Cesetti A., Matta E., Quattrone A., Sabia D., Smart reinforcement steel bars with low-cost MEMS sensors for the structural health monitoring of RC structures, Construction and Building Materials, Vol.173, 2018, pp.740-753

[6] Hou T., Nguyen V.K., Su Y., Chen Y., Chen P., Effects of coarse aggregates on the electrical resistivity of Portland cement concrete, Construction and building Materials, Vol.133, 2017, pp.397-408

[7] Seki H., Miyata K., Kitamine H., Kaneko Y., Experimental study on permeability of concrete based on electrical resistivity, Journal of JSCE, No. 451/V-17, 1992, pp. 49-57

[8] Badr J., Fargier Y., Palma-Lopes S., Deby F., Balayssac J., Delepine-Lesoille S., Conttineau L., Villain G., Design and validation of a multi-electrode embedded sensor to monitor resistivity profiles over depth in concrete, Construction and buildings Material, Vol. 223, 2019, pp.310-321

[9] Sub-Committee on Test Methods and Specifications for Concrete, Committee on Concrete, JSCE STANDARDS "Test method for measuring resistivity of patching repair materials with four electrodes", Journal of JSCE Ser. E, Vol. 64-No. 3, 2008, pp.427-434

[10] Alhaji M.A., Pal,a-Lopes S., Villain G., Accounting for steel rebar effect on resistivity profiles in view of reinforced concrete structure survey, Construction and Building Materials Vol.223, 2019, pp.898-909

[11] Sudjono A.S., Seki H., Prediction of pore structure of concrete based on conductivity value, Proceedings of the Japan Concrete Institute, Vol.20-No.2, 1998, pp.727-732

7th Int. Conf. on Structure, Engineering & Environment (SEE), Pattaya, Thailand, Nov.10-12, 2021, ISBN: 978-4-909106070 C3051

APPLICATION OF THE PLACKETT AND BURMAN DESIGN FOR IMPROVED OLIGOSACCHARIDE EXTRACTION FROM YAM BEAN ROOT

Mullika Teerakun[1], Nonthaphong Phonphuak[2], Weeranuch Wonkaonoi[3], Kanok-on Khampui[4], and Piyawadee Saraphirom[3]
[1]Faculty of Agricultural Technology, Kalasin University, Thailand; [2]Faculty of Engineering, Rajabhat Mahasarakham University, Thailand; [3]Faculty of Science and Technology, Rajabhat Maha Sarakham University, Thailand; [4]Faculty of Education, Rajabhat Maha Sarakham University, Thailand

ABSTRACT

This research aimed to screening of significantly effects factors for enhanced oligosaccharide extraction from yam bean (*Pachyrhizus erosus* (L.) Urban. The Plackett and Burman design matrix was employed to adjust 5 factors effecting on extraction of prebiotic in the form of oligosaccharide i.e., sample size, extraction temperature, extraction time, ethanol concentration and pH. Optimum conditions for increasing the oligosaccharide yield were determined using statistical methodology as follows: 2 mm of sample size, extraction temperature of 60°C, 99.93 min of extraction time, 50% (v/v) ethanol concentration and pH of 7.0. Under these optimal conditions, predicted oligosaccharide yield was found to be 35.58 wt% at 0.89 of R-Squared.

Keywords: Oligosaccharide, Yam bean, Model development, Optimization

INTRODUCTION

Jicama (yam bean) is a leguminous root crop native to Thailand as shown in Fig.1. The edible part is the crispy root contains starch and sugars. It is a good source of fiber, ascorbic acid, thiamin, riboflavin, niacin and minerals [1]. Fiber from yam bean root is a prebiotic fructan (oligofructose inulin) carbohydrate because it is not digested in the human digestive system but is fermented in the intestines [2]. The prebiotic properties of oligofructose inulin in yam bean root can be used as a nutrient of probiotics, promoting the efficiency of the digestive system and immunity. [3].



Fig. 1 Yam bean)*Pachyrhizus erosus* (L.) Urban(

The consumption of yam bean in Thailand is mostly fresh tubers or processed into various products, but it is not very widespread. The quality control of yam bean yield and the process of the chemical composition analysis still involve efficient extraction methods. Although it was found that the extraction of prebiotics from legumes was possible at the laboratory scale or pilot plant. However, extraction methods that optimum yield of prebiotics from yam root extract have been reported relatively rarely. Previous study reported that, extraction efficiency and quantity of plant prebiotic extracts depended on several factors, including temperature, extraction time, reactor ratio and the type of solvent, etc. [4].

Plackett and Burman design (PBD) is an experimental manipulation that can be considered as part of a factorial experimental manipulation to select multiple factors to be the primary effecting factor. The number of experimental units can be reduced without large-scale experiments, but the disadvantage is the inability to study the interactions of various factors [5]. Thus, this research focused on the using of Plackett and Burman design to estimate an optimal condition of oligosaccharide extraction enhancement. The results were expected to provide the optimal conditions for improving and enhancing the oligosaccharide concentration potential from yam bean root.

MATERIALS AND METHODS

Raw Material Preparation Method

Fresh yam bean root (90 days) was harvested before cleaned using tap water. Then peeled and cut into thin slices, dried for 6 hours and then baked with hot air oven at 55 ºC for 6 hours. The dried yam bean root was cut into 2 and 10 mm and stored in a ziplock bag in a desiccator at room temperature before use.

Extraction Method and Sample Analysis

Extraction and concentration

The 20 g of dried yam bean samples were immersed in ethanol solution at a sample:extract ratio of 1:5 and then were well mixed for the specified extraction time and temperature. The residue was

then filtered out and centrifuged at 4,000 rpm for 10 min then evaporated at 40 °C for 1 hour. The extract was incubated using a hot air oven at 50°C for 48 hours before freeze-dried at -55 °C for 12 hours. The extract sample was weighed to calculate the total extracted yield, then refrigerated.

Chemical composition analysis

Total sugar was analysed by phenol sulfuric acid method [6]. The reducing sugar content was analyzed by the 3, 5-dinitrosalicylic acid (DNS method) [7]. The content of oligosaccharide (non-reducing sugar) in yam bean root extract was performed according to [8] as in,

Non-reducing sugar = total sugar - reducing sugar (1)

The yield of oligosaccharide extract was analysed by equation:

Yield of oligosaccharide (wt%) = (W_o/W_d) x 100 (2)

where, W_o is the dry weight of oligosaccharide extract (g) obtained and W_d is the dry weight of dried yam bean samples (g).

Experimental Design and Statistical Analysis

Plackett Burman design (PBD)

The PBD was used to examine the result of 5 factors including sample size, extraction temperature, extraction duration, ethanol concentration and pH on oligosaccharide extraction in yam bean root. Placket-Burman experimental design is based on the first order model:

$$Y = \beta_0 + \sum \beta_i X_i \quad (3)$$

where, Y is the response, β_0 is the model intercept and β_i is the linear coefficient, and X_i is the level of the independent variable. Based on the PBD, each factor was prepared in two levels: -1 for low level and +1 for high level. Five designated variables were screened in twelve experimental designs. Levels of each factor used in the experimental design and the design matrix were shown in Table 1 and Table 2, respectively. The effect of each variable was established by equation:

$$E_{(Xi)} = \frac{2\left(\sum M_{i+} - M_{i-}\right)}{N} \quad (4)$$

where, E_{Xi} is the concentration effect of the tested variable, M_{i+} and M_{i-} are oligosaccharide yield obtained from runs where the variable (X_i) measured was present at the high and low concentration, respectively, and N is the number of run (12).

Table 1 Level of variables in PBD

Code	Variable	(-1)	(+1)
X_1	Sample size (mm)	2	10
X_2	Extraction temp (ºC)	30	60
X_3	Extraction duration (min)	30	100
X_4	Ethanol conc (% v/v)	30	50
X_5	pH	5.0	7.0

Statistical analysis

The statistical analysis of the experimental results was divided into model validation, analysis of decision coefficients (R-Square) and analysis of variance (ANOVA). The statistical software package Design-Expert 7.0.0, Stat-Ease, Inc., Minneapolis, MN, USA was used as a tool for statistical analysis.

Table 2 PBD design matrix for evaluating factors influencing oligosaccharide yield from yam bean root.

Run order	X_1		X_2		X_3		X_4		X_5		Yield of oligosaccharide extract (wt%)
	code	actual	Code	actual	code	actual	code	actual	code	actual	
1	+1	10	+1	60	+1	100	-1	30	-1	5.0	18.81
2	-1	2	-1	30	-1	30	+1	50	-1	5.0	22.50
3	-1	2	+1	60	+1	100	-1	30	+1	7.0	28.98
4	+1	10	+1	60	-1	30	+1	50	+1	7.0	25.83
5	-1	2	+1	60	-1	30	+1	50	+1	7.0	36.00
6	+1	10	-1	30	+1	100	+1	50	+1	7.0	24.70
7	+1	10	-1	30	-1	30	-1	30	+1	7.0	14.25
8	+1	10	+1	60	-1	30	-1	30	-1	5.0	11.01
9	-1	2.	-1	30	+1	100	-1	30	+1	7.0	17.15
10	+1	10	-1	30	+1	100	+1	50	-1	5.0	14.70
11	-1	2	+1	60	+1	100	+1	50	-1	5.0	25.45
12	-1	2	-1	30	-1	30	-1	30	-1	5.0	8.94

Statistical analysis

The statistical analysis of the experimental results was divided into model validation, analysis of decision coefficients (R-Square) and analysis of variance (ANOVA). The statistical software package Design-Expert 7.0.0, Stat-Ease, Inc., Minneapolis, MN, USA was used as a tool for statistical analysis.

RESULTS

The Yield of Oligosaccharide Extract from Yam Bean Root

The results of evaluation factors influencing oligosaccharide yield from yam bean root was shown in Table 2. The maximum of oligosaccharide yield at 36 wt% was obtained under optimal conditions of 2 mm sample size, 60ºC extraction temperature, 30 min extraction duration, 50 % (v/v) ethanol concentration and pH of 7.0 (run 5).

Statistical Analysis

Model validation

The normal distribution test is used to check the residual of the data whether there is a normal distribution. The results showed that is distributed along a straight line. Considering the distribution of residual values as shown in Fig. 2.

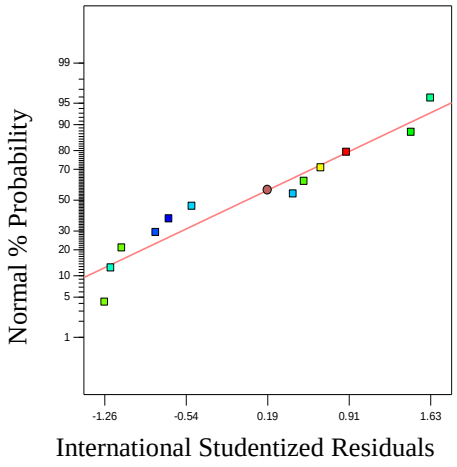


Fig. 2 Normal probability of residual plot.

It was shown that residues from the experimental results of oligosaccharide yield from yam bean root showed no abnormalities. Therefore, it can be concluded that the residual value has a normal distribution. The test for the independence of the residual values is performed by determining the distribution chart. The data of the distribution characteristics of the points representing the data on the chart represents the independent form of the data.

Figure 3 shows that the residual of oligosaccharide yield from yam bean root does not have a specific arrangement, or it cannot be estimated to be an exact form. The residuals of the data were evenly distributed, indicating that the data were independent.

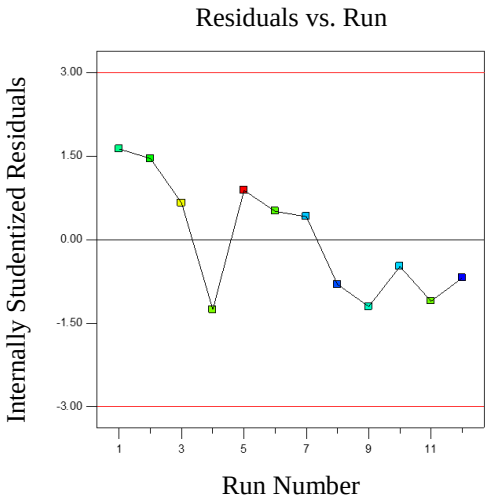


Fig. 3 Studentized Residuals and Run number.

Figure 4 shows the stability of the variance by using residual distribution charts at each factor level. The results showed that the residuals of the experimental results of oligosaccharide yield from yam bean root were evenly distributed in both positive and negative ways, indicating that the data was stable with variance. Validation of the experimental model revealed that the residual values of the data obtained from experiments were based on three assumptions: (1) residuals were normally distributed, (2) residual values were independent, and (3) the variance was stable. Therefore, it can be concluded that the data obtained from this experiment are accurate and suitable for analysis of decision coefficients and analysis of variance.

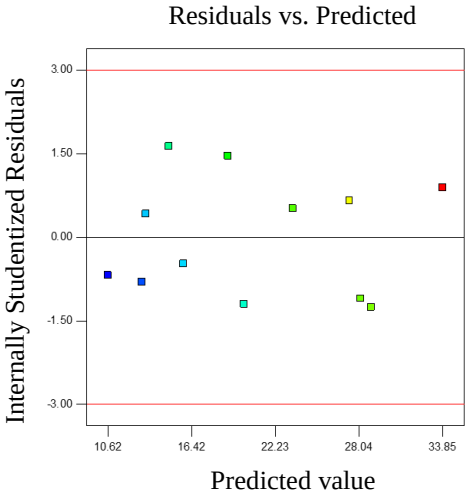


Fig. 4 Studentized Residuals and Predicted values.

Coefficient of decision and analysis of variance (ANOVA)

The coefficient of decision (R-Squared) is used to analyses a dependent variable and independent variables in the regression equation. The results of the coefficient analysis of the regression equation show that independent variables can describe at a confidence level of 89% (Table 3). The experimental results show that the model can be used to create the predictive equations for the precise and appropriate response.

Table 3 Coefficient of decision and analysis of variance (ANOVA)

Source	Sum of Squares	df	Mean Square	*F* Value	*p*-value Prob > F	Remark
Model	625.5352	5	125.107	10.53954	0.0062*	significant
A-Sample size	73.55701	1	73.55701	6.196752	0.0472*	
B- Extraction temp	160.3083	1	160.3083	13.50505	0.0104	
C- Extraction duration	10.56563	1	10.56563	0.890093	0.3819*	
D- Ethanol conc	208.5834	1	208.5834	17.57194	0.0057*	
E-pH	172.5208	1	172.5208	14.53388	0.0088*	
Residual	71.22152	6	11.87025			
Cor Total	696.7567	11				
Std. Dev. = 3.445323; Mean = 20.695; C.V. % = 16.6481; PRESS = 284.8861; R-Squared = 0.897781; Adj R-Squared = 0.812599; Pred R-Squared = 0.591125; Adeq Precision = 9.535981						

Effect of independent factors

The yield of oligosaccharide extract was obtained from the range of 8.94-36 wt% (Table 2). The Pareto chart (Fig. 5) indicates that the independent variables i.e. sample size, extraction temperature, extraction duration, ethanol concentration, and pH requires significant influence on the yield of oligosaccharide extract.

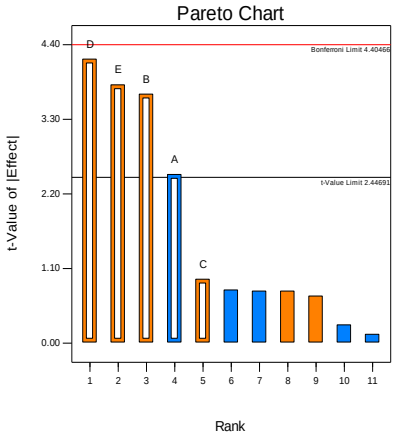


Fig. 5 Pareto chart of the standardized effects of independent variables on the yield of oligosaccharide extract.

In the Pareto chart, effects above the Bonferroni limit are most likely significant, effects above the t-value limits are possibly significant and effects below the t-value limits are not likely to be significant. The ANOVA results also confirm that all the five factors show *P* values less than 0.05, which indicating that all the five factors having significantly different from zero and 95% confidence level (Table 3). The ethanol concentration, pH, extraction temperature and sample size were effect cross the Bonferroni limit, that is, it showed great influence on the yield of oligosaccharide extract (Fig. 5). The negative coefficient value of effect suggested that the increase in sample size decreased the yield of oligosaccharide extract. The positive coefficient value of effect suggested that the increasing in ethanol concentration, pH and extraction temperature increased the yield of oligosaccharide extract (Table 4).

Table 4 Effect of independent factors.

Term	Effect	Sum of Squares	% Contribution
Sample size	-4.95	73.55	10.55
Extraction temp	7.31	160.30	23.00
Extraction duration	1.87	10.56	1.51
Ethanol conc	8.33	208.58	29.93
pH	7.58	172.52	24.76

Prediction equation

The multiple regression analysis can establish models or equations that predict the experimental

results of each factor. The results obtained from this experimental was a non-linear quadratic correlation model. Results of the yield of oligosaccharide extract are shown as follows:

$$\gamma = 20.69 - (2.47 * X_1) + (3.65 * X_2) + (0.93 * X_3) + (4.16 * X_4) + (3.79 * X_5)$$

where, $\boldsymbol{\gamma}$ is the yield of oligosaccharide extract, $\boldsymbol{X_1}$ $\boldsymbol{X_2}$, $\boldsymbol{X_3}$, $\boldsymbol{X_4}$ and $\boldsymbol{X_5}$ is representing sample size, extraction temperature, extraction duration, ethanol concentration, and pH, respectively.

Optimal condition

The statistical analysis of the experimental results was divided into model validation, analysis of decision coefficients (R-Square) and analysis of variance (ANOVA). The statistical software package Design-Expert 7.0.0, Stat-Ease, Inc., Minneapolis, MN, USA was used as a tool for statistical analysis. Optimization function in the statistical software was used to predict the optimal conditions for oligosaccharide extraction from yam bean root. The optimization function was also used to determine the optimal factor and measure composite desirability: D, which ranged from 0–1. The composite desirability effect of 1 means that the response is completely satisfied. Results reveals optimal condition as follows: 2 mm of sample size, extraction temperature of 60°C, 99.93 min of extraction duration, 50% (v/v) ethanol concentration and pH of 7.0. Under these optimal conditions, predicted oligosaccharide yield was found to be 35.58 wt% at the composite desirability of 0.985 (Fig. 6).

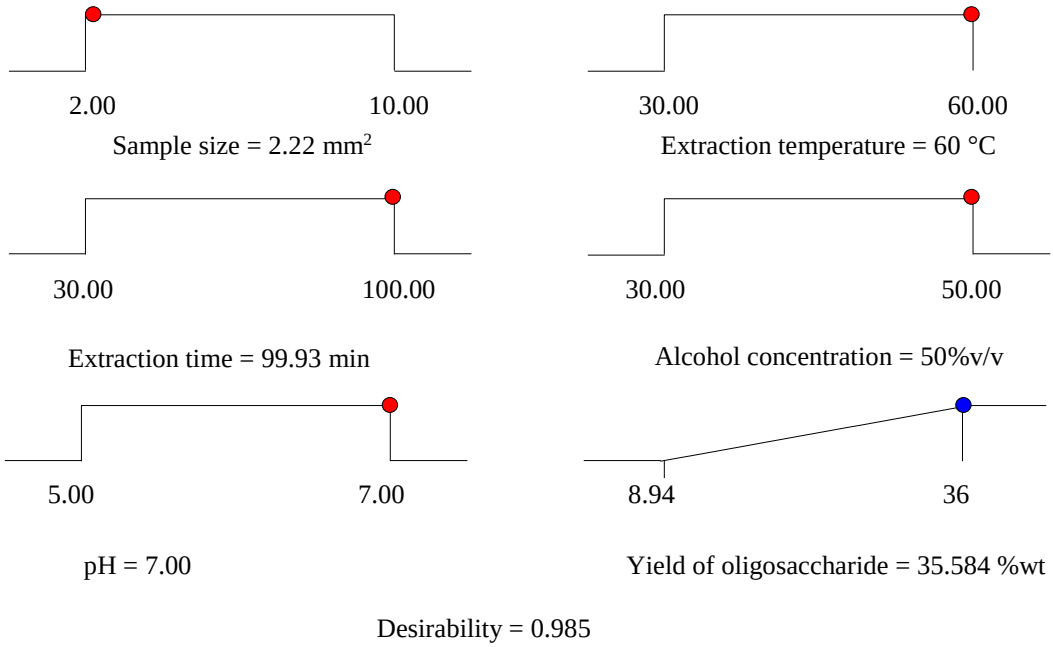


Fig. 6 The optimal conditions for on the yield of oligosaccharide extract from yam bean root.

DISCUSSION

The optimal conditions of oligosaccharide from yam bean root extraction obtained from Fig. 6. The predicted oligosaccharide yield was found to be 35.58 wt%. The results indicated that increasing the concentration of ethanol resulted in higher extract content. This is because the structure of the ethanol solution consists of both polar and non-polar parts. Dilution with water thus increases the polarity of the solution, causing the small molecules to can be dissolved while large carbohydrate molecules will be precipitated out at higher concentrations. The effect of high temperature is also resulting in higher extract content because at high temperatures the solvent can dissolve sugars better than at less than a temperature. The effect of the increased extraction duration resulted in an increase in the total sugar and the reducing sugar content due to the increased solute-solvent contact time. The smaller sample size results in more extraction as it increases the contact area between the sample and the solvent. Reducing the sample size destroys the cell wall, allowing for better diffusion of the extracted substance into the solvent. Usually at high acid concentrations or low pH, it is better digested than at low acid or high pH values. This is because high acidity is more intense, so it is easier to break the connected bonds of sugar molecules than in low acidic environments.

CONCLUSIONS

The observation of experiment revealed the maximum of oligosaccharide yield at 36 wt% was obtained under optimal conditions of 2 mm sample size, 60ºC extraction temperature, 30 min extraction duration, 50 % (v/v) ethanol concentration and pH of 7.0. The result is close to using the prediction of optimum conditions using statistical analysis shows optimal condition as follows: 2 mm of sample size, extraction temperature of 60°C, 99.93 min of extraction duration, 50% (v/v) ethanol concentration and pH of 7.0.

ACKNOWLEDGMENTS

This research was partially supported by the Center of Excellence on Biodiversity, Thailand. We thank our colleagues from Rajabhat Maha Sarakham who provided insight and expertise that greatly assisted the research.

REFERENCES

[1] Ekvall J., Stegmark R., Nyman M. Optimization of Extraction Methods for Determination of the Raffinose Family Oligosaccharides in Leguminous Vine Peas (*Pisum sativum* L.) and Effects of Blanching, Journal of Food Composition and Analysis, Vol. 20, 2007, pp. 13-18.

[2] Kim S. Kim W., Hwang I.K. Optimization of the Extraction and Processing Commercial Prebiotics, International Dairy Journal, Vol. 18, 2003, pp. 287-293.

[3] Gibson G. R. and Roberfroid M. B. Dietary Modulation of the Human Colonie Microbiota Introducing the Concept of Prebiotics, Jounal Nutrition. Vol.125, 1995, pp. 1401–1412.

[4] Miller G.L. Use of Dinitrosalicylic Acid Reagent for Determination of Reducing Sugar, Analytical Chemistry, Vol. 31, 1959, pp. 420-428.

[5] Wu Y., Cui S. W., Tang J., and Gu X. Optimization of Extraction Process of Crude Polysaccharides from Boat-fruited Sterculia Seeds by Response Surface Methodology, Food Chemistry, Vol. 105, Issue 4, 2007, pp. 1599-1605.

[6] Dubois M., Gilles K.A., Hamilton J.K., Roberts P.A. and Smith F. Colorimetric Method for Determination of Sugars and Related, Substances, Analytical Chemistry, Vol. 28, Issue 3, 1956, pp. 350- 356.

7th Int. Conf. on Structure, Engineering & Environment (SEE), Pattaya, Thailand, Nov.10-12, 2021, ISBN: 978-4-909106070 C3051

APPLICATION OF ARTIFICIAL INTELLIGENCE TO RIVER INSPECTION USING UAV

Ryo Yahara[1], Satoshi Nishiyama[2], Tomohiro Shimono[3], Sayuri Yoshioka[4], and Kohei Ogata[5]
[1,2]Environmental and Life Science, Okayama University, Japan; [3,4,5] Kokusai Kogyo Co., Ltd., Japan

ABSTRACT

In recent years, torrential rains have been occurring frequently, leading to an increase in the frequency of disasters, such as bank breaks. As a result, river inspections are becoming more important for monitoring river conditions on a daily basis. However, river inspections are currently conducted qualitatively by river inspection officers visually, and inspecting long embankments is labor-intensive. In this study, we aimed to improve the efficiency of river inspections using UAV (Unmanned Aerial Vehicle) and artificial intelligence (AI) techniques. We captured images of the river using a UAV equipped with a camera and automatically extracted objects listed in river inspection items, such as illegally dumped objects from the images using AI techniques. We compared the accuracy of machine learning and deep learning as AI methods and confirmed that the deep learning method is useful for river inspection. We then summarized the effects of the ground resolution and angle of the image on the object detection of deep learning and its application to various rivers. As a result, the detection accuracy decreases owing to the decrease in ground resolution and the difference in the background between the teacher data and the validation images. In the future, we will study object detection that is not affected by ground resolution and create a versatile machine that can be used in various rivers.

Keywords: Artificial Intelligence, Machine Learning, Deep Learning, Object Detection

INTRODUCTION

Short-term heavy rainfall exceeding 50 mm per hour is increasing, and large-scale flood damage is also increasing in Japan. To prevent these disasters or detect them at an early stage, river inspection work to grasp the state of rivers on a daily basis is becoming more important. Therefore, the Ministry of Land, Infrastructure, Transport, and Tourism launched an innovative river technology project in November 2016 to develop technologies, such as low-cost water level gauges, simple river monitoring cameras specializing in flood observation, and unmanned flow rate observation. Efforts, such as the technological development of automation, are being made. This verification was conducted as a part of this project. River inspections were conducted by patrol cars, etc., and in places where it is difficult for cars to enter, such as river banks, abnormal parts are inspected on foot or by boat. Therefore, the inspection of a long embankment is labor-intensive, and there is room for improvement from the viewpoint of the absence of technicians and the possibility of oversight. Therefore, in this study, to improve the efficiency of river inspection, we investigated a method for automatically extracting dumped material from images captured by a UAV equipped with a camera using artificial intelligence (AI).

In recent years, UAVs have been expected to play an active role in the field of inspection, and inspections for cracks in bridges and fixed points for plant growth are also being conducted. [1]–[4] Even in river inspections, it is expected that work efficiency will be improved by taking a wide range of images using a UAV equipped with a camera and acquiring a large amount of information. In addition, because finding an abnormal part from these images is also a labor-intensive task, the purpose is to improve the efficiency of the work by automatically extracting the abnormal part using AI technology. In this verification, using AI technology, we compared machine learning methods and deep learning methods, and examined the teacher data specifications required for learning.

ARTIFICIAL INTELLIGENCE

AI technology has developed remarkably in recent years. It is active in a wide range of fields, such as autonomous driving technology, face identification, and games. In addition, in the field of civil engineering, it is used for damage prediction, crack inspection, and flow rate prediction to create hazard maps [5]–[7]. Although the definition is ambiguous, it may be possible for machines to perform the work that humans have performed this far. One of these methods is machine learning, which is a technology that allows a machine to learn known data and learn its features and patterns to perform regression and classification of unknown data. At that time, humans must specify what to

learn as a feature quantity, and setting an appropriate feature town is a labor-intensive task. Conversely, deep learning technology is a type of machine learning method that can solve more complicated tasks by connecting neurons in multiple layers, and has drawn considerable attention in recent years. Because the machine selects an appropriate feature amount by itself, it is freed from feature amount selection, such as machine learning, and more accurate learning can be performed [8], [9].

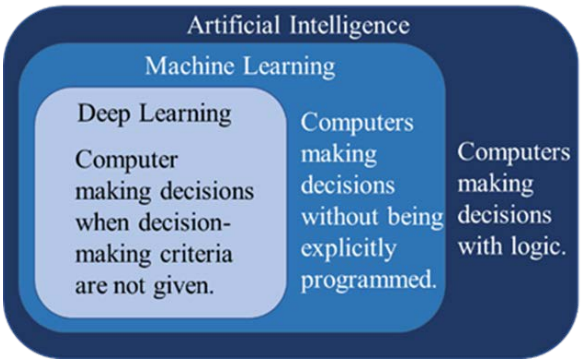


Fig. 1 Outline of Artificial Intelligence

Machine Learning

In this verification, the OpenCV traincascade was used as the training model, and LBP features were used as the features. The LBP features were developed by Ojala [10], and a histogram was created from the difference in the brightness values of each pixel. It is a feature quantity that is widely used as a feature amount [11]–[13]. It has the advantage of being strong against the difference in overall illuminance because it takes the difference in brightness value. Figure 2 shows the procedure for extracting the LBP features. First, the image is divided, and a part is extracted. Furthermore, we focused on the extracted part of the 3 × 3 pixels. In this method, a local area of 3 × 3 pixels was used, but the size of the local area was arbitrary. The numerical value in the area represents the brightness of each pixel. First, the brightness levels of the central and peripheral pixels were compared. That is, the difference in brightness between the central and peripheral pixels was calculated. If the brightness value of the peripheral pixels is high (if the difference in brightness value is positive), the value of the peripheral pixels is set to 1, and if it is low (if the difference is negative), it is set to 0. As in this example, when eight pixels adjacent to the center pixel are selected as the peripheral pixels, the LBP value of the center pixel is represented by 8 bits. The LBP value can be obtained by assigning a weight of 2^i (i = 0, ..., 7) clockwise from the upper left pixel of the center pixel.

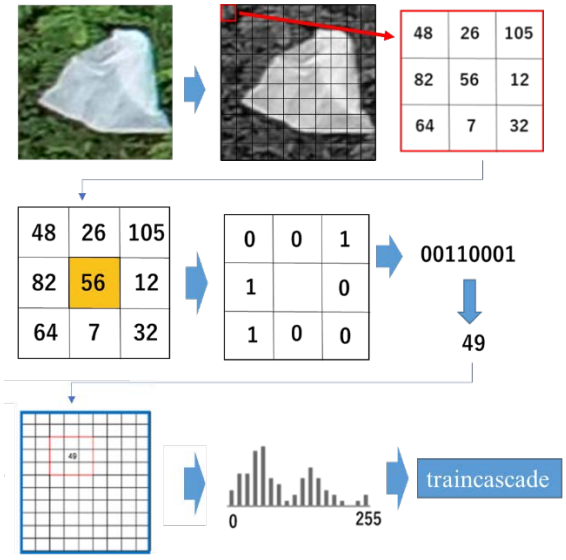


Fig. 2 Machine learning procedure

Deep Learning

Retinanet was used as the deep learning method. The object detector model that introduces the convolutional neural network (CNN), which is the key to deep learning, is roughly divided into two types: one-step detection model and two-step detection model. The difference between these two models is whether the region proposal and classification of the objects contained in each region are performed simultaneously or in two stages. Most of the two-step object detection models have an R-CNN-based two-step detection configuration [14], and while high accuracy is expected, there are problems with inference speed and model complexity. Therefore, concurrently, networks, such as YOLO [15] and SSD [16] have been proposed to detect objects at high speed with one-step detection. However, while the one-step detection models are fast, they also have the problem of being inferior to the two-step detection models in terms of accuracy. Conversely, an approach to improve the detection accuracy by devising a network structure, such as the feature pyramid network, is known. Tsung-Yi Lin developed a one-step detection model that can achieve high accuracy while maintaining the inference speed to solve the above-mentioned problems, and RetinaNet was proposed in a paper published in August 2017 [17]. As shown in Figure 3, RetinaNet is an implementation of FPN (Feature Pyramid Network) in the one-step detection. In this method, the conventional one-step detection model cannot achieve the same accuracy as the two-step detection model because of "Class Imbalance," which is a general loss function for improving accuracy. They proposed a loss function called "focal loss" that is different from the cross-entropy loss that is commonly used as an error function.

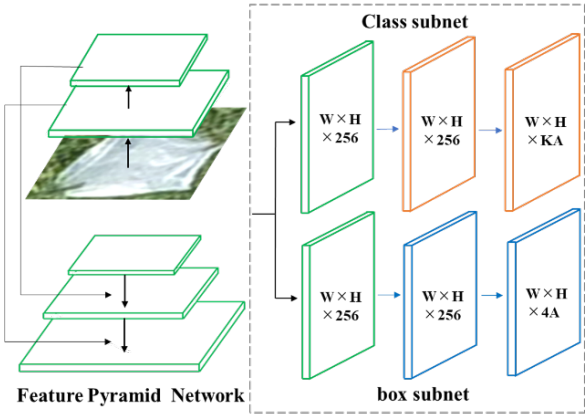


Fig. 3 RetinaNet structure

OVERVIEW OF VERIFICATION

We compared the accuracy of machine learning and deep learning and verified the versatility of the teacher data. The photographs were taken at two locations, Rivers A and B, which are the first-class rivers in Japan. The shooting in River A was conducted in August, and the shooting in River B was performed in November. Multiple garbage bags were placed in these rivers as illegal dumping, and the images were captured with a UAV equipped with a camera while changing the angle and altitude. Figure 4 shows an example of a photograph of each river. Subsequently, annotations were added to tag the garbage bags in the captured images such that the machine could be learned. There were 3166 annotations in River A and 2774 in River B.



Fig. 4 Annotation example (left: River A, right: River B)

EVALUATION METHOD

The results obtained from the shooting were organized by the ground resolution calculated from the angle and altitude. The ground resolution is the distance on the ground indicated by one pixel of a digital image, and the smaller this value, the clearer the image. Figure 5 compares shooting cases with ground resolutions of 2.0, 3.0, and 4.0 cm.



Fig. 5 Ground resolution

Evaluation Equation

The detection accuracy was evaluated using three indices: recall rate, precision rate, and F value. Each evaluation method was described using the following four types of detection patterns.
(1) TP: Number of objects that actually exist and are correctly judged by the detector.
(2) FP: The number of objects mistakenly determined to be an object other than the object.
(3) FN: The number of objects that the detector mistakenly determined not to be the object, although it is actually the object.
(4) TN: The number of objects other than the object that is judged not to be the object.

Recall refers to the ratio of the number of correctly determined objects to the number of actually existing objects. That is, if the recall is low, the rate at which objects are actually detected but not detected (missing rate) is high. This can be calculated using the following formula:

$$\textbf{recall rate} = \frac{TP}{TP+FN} \quad (3)$$

Precision is an index that evaluates the accuracy of the detector and indicates the ratio of the number of detection frames that have been judged to be correct by the detector and are actually judged correctly to the output detection frames. That is, if the matching rate is low, the rate at which the detector determines that the target object is included (erroneous detection rate) is high, even though it is not actually the target object. This can be calculated using the following formula:

$$\textbf{precision rate} = \frac{TP}{TP+FP} \quad (2)$$

The F value is an index showing the balance between recall and precision, and is a value calculated by the harmonic mean of recall and precision. This was calculated using the following formula:

$$\textbf{F Value} = \frac{\textbf{2} \times \textbf{recall rate} \times \textbf{precision rate}}{\textbf{ecall rate} + \textbf{precision rate}} \quad (3)$$

RESULT AND DISCUSSION

First, we compared the accuracy of the deep learning method and the machine learning method. The teacher image and the verification image are only those of the river A, and the verification images are 17 images taken at an angle of 90°. About teacher images in deep learning, we trained all 3166 annotated images and created a classifier. Regarding the machine learning method, it was not possible to learn when many images were loaded. It is probable that the results diverged without being able to identify the features. Therefore, in the machine learning method, we reduced the number of images and trained 864 teacher images to create a classifier. The maximum F value was 76% and 40.0% on average for machine learning, and the maximum F values were 100% and 92.4% on average for deep learning. Machine learning was vulnerable to changes in ground resolution, and the accuracy decreased significantly as the altitude changed. In contrast, deep learning detected garbage bags even at high altitudes. It was confirmed that in the machine learning model using LBP features, no significant change was observed in the detection results, even if the illuminance changed. In deep learning, it was found that when the illuminance changed, some garbage could not be detected. It was found to be excellent in that it can be used properly according to the specific purpose because the feature values can be specified by oneself in machine learning. However, it is considered unsuitable for actual business use because its accuracy is not high at present.



Fig. 6 Detection example of machine learning with a ground resolution of 2.0 cm and an angle of 90°



Fig. 7 Detection example of deep learning with a ground resolution of 4.0 cm and an angle of 90°

Versatility of Teacher Data

Creating teacher data requires a great deal of effort. Therefore, it is desirable that appropriate detection can be performed by learning as few images as possible, so we verified the versatility of teacher data. The classifier created the three patterns listed in Table 1. The results obtained were organized by angles of 45°, 60°, and 75 ° and ground resolutions of 2.0, 3.0, and 4.0 cm. The number of learning photos was 3166 for river A and 2774 for river B. Verification images are also prepared for each condition, and the total is 159 for river A and 198 for river B.

Table 1 Types of classifiers

Classifier	Classifier A	Classifier B	Classifier C
Teacher data	River A	River B	River A + River B

Figure 8 shows the results when classifier A was applied to River A and classifier B was applied to River B. The average F value can be detected with high accuracies of 80.1% and 83.1%, respectively, and a river using a UAV was used. It is thought that it can contribute to improving the work efficiency during inspection.

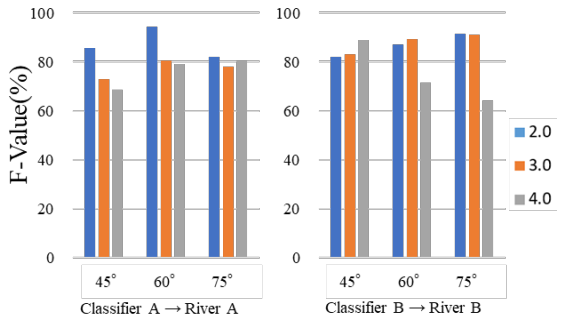


Fig. 8 Detection accuracy result when river and classifier are matched

Next, the results when classifier B is applied to River A and classifier A are applied to River B are shown in Fig. 9. The accuracy was lower than that in the previous section, and the average F values were 31.4% and 36.1%, respectively. The average F value decreased even though the target object was a garbage bag common to both rivers because the machine learned included background information in addition to the object garbage bag. As shown in Fig. 10, the shooting time was August in River A, and most of the target garbage bags were placed on the green vegetation. Conversely, in River B, the shooting time was October, and it was performed under the condition that many garbage bags were placed on the stone. In addition, because the annotation of the teacher data is performed in a square shape, it is highly possible that the information on the background in which the garbage bag is placed is also learned. Therefore, it is considered that the accuracy was different in different rivers even though the objects were similar.

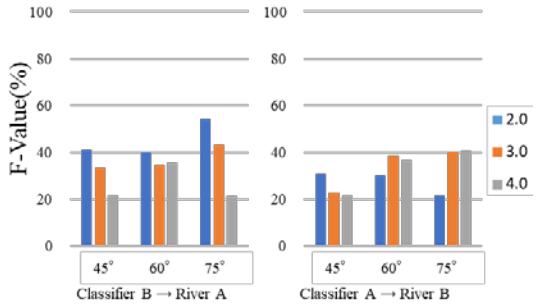


Fig. 9 Detection accuracy results when rivers and classifiers are staggered



Fig. 10 Difference between river A and river B

Finally, Fig. 11 shows the results when classifier C, in which both Rivers A and B were trained as teacher data, was applied to each river. The average F values were 73.0% and 66.2%, respectively. Although the accuracy was slightly inferior to that shown in Fig. 8, the detection accuracy in the two rivers was maintained at approximately 70% in the F value with only one type of classifier. Therefore, using the images taken in rivers with different environments as batch teacher data, it is thought that a classifier corresponding to a wide range of rivers can be created. It is also expected that the collection of teacher data will be easier if different river data can be used for teacher images.

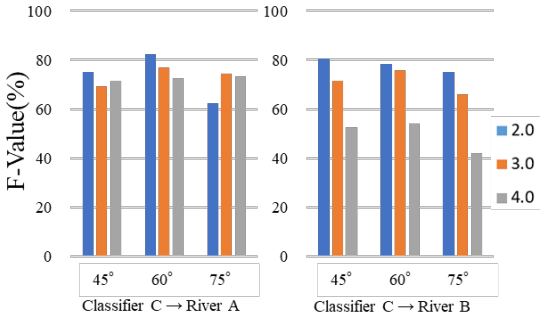


Fig. 11 Detection accuracy results of when applying multiple classifiers

Ground Images Verification

If detection can be performed from a UAV without using UAV teacher data, teacher data creation will be much easier. Therefore, we also examined the use of ground images to verify their versatility. We used 461 Ground-based image of a garbage bag prepared for shooting with UAV, and 771 images of the above-ground garbage bag of River B stored in the River Management Data Intelligent System (RiMADIS), which is a database created to support river maintenance operations in Japan.



Fig. 12 Ground image (left: River A, right: River B)

As a result, although some detection was possible, it was found that the accuracy was extremely low, with an F value of 29.6%, for River A and 24.7% for River B, compared to the case where the UAV image was used as teacher data. The ground image can also be used as teacher data by finding out what difference occurs from the viewpoint of AI between the reduced ground image and the UAV image and correcting it.

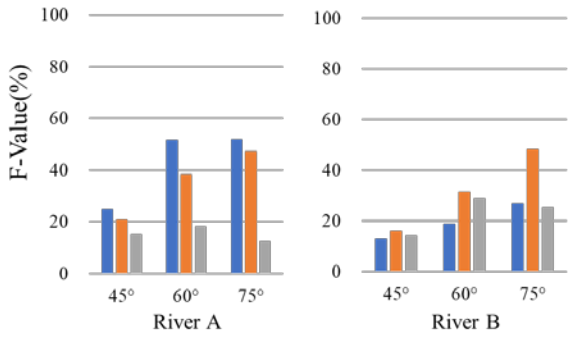


Fig. 13 Detection result by ground image

CONCLUSIONS

In this study, the applicability of AI to river inspections using UAVs was examined. For this purpose, we compared the accuracy of machine learning and deep learning and verified the versatility of the teacher data. The results are summarized below.

- Regarding the efficiency of river inspection, deep learning can be expected to have a higher detection accuracy than machine learning.
- The detection accuracy is reduced owing to the influence of the ground resolution and the difference in the background between the teacher data and the verification image.
- One can create a classification machine for a wide range of rivers by collectively using images taken from different rivers as teacher data.

In the future, if one can detect images taken at high altitudes and in a wide range, it will lead to more efficiency; therefore, it is a highly versatile machine that can handle various rivers, including examination of object detection that is not affected by ground resolution.

REFERENCES

[1] Metni N. Hamel T. and Derkx F., A UAV for bridge's inspection: visual servoing control law with orientation limits, IFAC Proceedings Volumes, Vol. 37, Issue 8, 2004, pp. 454–459.

[2] Seo J. Duque L. Wacker J., Drone-enabled bridge inspection methodology and application, Automation in Construction, Vol. 94, 2018, pp. 112–126.

[3] Nakshmi J.V.N., Hemanth K.S., and Bharath J., Optimizing Quality and Outputs by Improving Variable Rate Prescriptions in Agriculture using UAVs Procedia Computer Science, Vol. 167, 2020, pp. 1981–1990.

[4] Wang X. Sun H. Long Y. Zheng L. Liu H. and Li M., Development of Visualization System for Agricultural UAV Crop Growth Information Collection, IFAC-PapersOnLine, Vol. 51, Issue 17,2018, pp. 631–636.

[5] Kuchi A. Hoque M.T., Abdelguerfi M. Flanagin M.C., Machine learning applications in detecting sand boils from images, Array, Vol. 3–4, 2019, Article 100012.

[6] Li Y. Wang X. Zhao Z. Han S. and Liu Z., Lagoon water quality monitoring based on digital image analysis and machine learning estimators, Water Research, Vol. 172, 2020, Article 115471.

[7] Schmitt J. Bönig J. Borggräfe T. Beitinger G. and Deuse J., Predictive model-based quality inspection using Machine Learning and Edge Cloud Computing, Advanced Engineering Informatics, Vol. 45, 2020, Article 101101.

[8] Fujiyoshi H. Hirakawa T. and Yamashita T., Deep learning-based image recognition for autonomous driving, IATSS Research, Vol. 43, Issue 4, 2019, pp 244–252.

[9] Lundervold A. S., and Lundervold A., An overview of deep learning in medical imaging focusing on MRI, Zeitschrift für Medizinische Physik, Vol. 29, Issue 2, 2019, pp 102–127.

[10] Ojala T. Pietikäinen M. and Harwood D., A comparative study of texture measures with classification based on featured distributions Pattern Recognition, Vol. 29, Issue 1, 1996, pp 51–59.

[11] Lahiani H. and Neji M., Hand gesture recognition method based on HOG-LBP features for mobile devices, Procedia Computer Science, Vol. 126, 2018, pp 254–263.

[12] Mahale V. H., Ali M. M. H., Yannawar P. L., and Gaikwad A. T., Image Inconsistency Detection Using Local Binary Pattern (LBP), Procedia Computer Science, Vol. 115, 2017, pp 501–508.

[13] Smolka B. and Nurzynska K., Power LBP: A Novel Texture Operator for Smiling and Neutral Facial Display Classification, Procedia Computer Science, Vol. 51, 2015, pp 1555–1564.

[14] Girshick, R., Donahue, J., Drrell, T. and Malik, J.: Rich feature hierarchies for accurate object detection and semantic segmentation, 2013.

[15] Redmon, J., Divvala, S., Girshick, R. and Farhadi, A.: You Only Look Once: unified, Real-Time Object Detection, 2015.

[16] Liu, W., Anguelov, D., Erhan, D., Szegedy, C., Reed, S., Fu, C. and Berg, A.: SSD: Single Shot MultiBox Detector, 2015.

[17] Lin, T., Goyal, P., Girshick, R., He, K., and Dollár, P.: Focal Loss for Dense Object Detection, 2017.

7th Int. Conf. on Structure, Engineering & Environment (SEE), Pattaya, Thailand, Nov.10-12, 2021, ISBN: 978-4-909106070 C3051

PRODUCTION OF BIODIESEL AND VITAMIN E FROM A POOR QUALITY OF CRUDE PALM OIL BY ENZYMATIC TRANSESTERIFICATION PROCESS

Mallika Tapanwong[1], Vittaya Punsuvon[1,2], Pinsuda Viravathana[1,2], Rayakorn Nokkaew[2]
[1]Department of Chemistry, Faculty of Science, Kasetsart University, Bangkok, 10900 Thailand;
[2]Center of Excellence-Oil Palm Kasetsart University, Bangkok, 10900 Thailand

ABSTRACT

Thailand has community palm oil mills for more than 120 factories. The press cake is the by-product from the oil production process which the press cake remained a high oil yield. The crude palm oil (CPO) had a high free fatty acid (28.33%) indicated that the poor-quality CPO. The value-added from the oil by the biodiesel and vitamin E production is the aim of this research. Response Surface Methodology (RSM) was applied to optimize the enzymatic transesterification for biodiesel and vitamin E production. The RSM evaluated the relationship between the amount of enzyme, alcohol, water, and reaction time. The result showed that the optimum condition was 19.48% of enzyme, 4.43 mole of methanol, 11.21% of water content for 5.47 hr. at 55°C. This condition gave 94.24% of fatty acid methyl ester content and 5,305.42 ppm of total vitamin E concentration. The amount of catalyst and water factors were significant for yield of biodiesel and vitamin E. The advantages of transesterification using the biocatalyst were tocotrienol conservation, eco-friendly process, and reduction of operating time and solvent amount when compared with the conventional process.

Keywords: Biodiesel, Vitamin E, Poor Quality Crude Palm Oil, Enzymatic Transesterification

INTRODUCTION

At present, a CPO and a press cake are only incomes of the community palm oil mill (CPOM). The CPO contained in the press cake more than 10% which was a high yield of residue oil. The FFA of CPO from CPOM is about 6-15% while the FFA of CPO from the press cake is about 20-30% which the high FFA indicated the poor oil quality. But the CPO is resource of rich an anti-oxidant substrate, consists of tocopherols and tocotrienols (600-1000 ppm of total vitamin E) that the composition of vitamin E was 45% of g-tocotrienol, 23% of a-tocopherol, and 21% of a-tocopherol [1]. The strength of CPO has a high content of tocotrienol of vitamin E. Tocotrienol is interested because it's a high effect in protecting against heart related diseases and certain cancers [2]. Many researches reported that Vitamin E is a powerful antioxidant, it protects body cells from damage caused by free radical, especially protect of blood cells, the nervous system, skeletal muscle and retinas in the eyes [3, 4]. Komiyama and Yamoka [5] reported the effectiveness of tocotrienol from palm oil against mice tumors.

The value-added of CPO is biodiesel production and palm phytonutrients (by-production of biodiesel production) that biodiesel is important renewable energy for the sustainability of the world. In the production of palm biodiesel, CPO is transesterified in alcohol with an alkaline catalyst (a low free fatty acid (FFA) in the oil). Transesterification or alcoholysis is the reaction of oil/fat (triglyceride) with alcohol to produce monoester and glycerol products. The catalysts for biodiesel production are alkaline, acid, and enzyme depended on the amount of FFA in the oil. Using alkaline or acid catalysts know as chemical transesterification (the conventional biodiesel production) [6]. The enzyme catalyst is a biocatalyst for the environment because reduces the consumption of solvent and energy for production and is not produces wastewater when compared with conventional production. The biodiesel production from CPO gives the red biodiesel which it has rich in palm phytonutrients concentrate (a rich source of carotenoids and vitamin E). The separation of vitamin E from biodiesel was a short path distillation technology with minimal loss or degradation of both products [7, 8]. The biodiesel distillation, a colorless liquid is a biodiesel while a dark red mixture is the palm phytonutrients.

Many reports use enzymes for biodiesel as it produces high purify products (monoester and glycerol). Advantages of enzymatic transesterification are easy separation between monoester and glycerol, the catalyst is an environment, is not produce wastewater from the production process [9-11]. Devanesan [12] reported 72% biodiesel of maximum yield from enzyme catalyst of Jatropha oil. The optimum condition was 1:4 molar ratio of oil to methanol at 40°C, pH 7.0, 3 grams amount of beads, and 48 hr. of reaction time.

this research investigated a value-added from the press cake by oil extraction for the raw material of biodiesel and vitamin E products. Due to, the chemical catalysts have effect on vitamin E degradable. So, an enzyme catalyst is interested in the production of biodiesel and vitamin E for this research. RSM technique applied to experimental design for determination of the optimum condition and studied an interactive variables effect on biodiesel and vitamin E concentration.

MATERIAL AND METHOD

Material

A press cake is a raw material for the oil extraction process by a screw press machine in CPOM. The oil remained in press cake about 10-15% to depend on the moisture content of dried palm fruit and screw press efficiency. The CPO for the experiment used the solvent extraction method from press cake and the solvent was distilled by a vacuum rotary evaporator. The chemical reagents for the experiment were analytical grade and HPLC grade for HPLC analysis.

Method

The production of biodiesel and vitamin E has two processes. The first process is transesterification with liquid lipase of an enzyme catalyst for biodiesel production. The second process is vacuum distillation for the separation of vitamin E and biodiesel products. In the transesterification reaction; the triglyceride is transferred to monoester (biodiesel) which causes a reduction of molecular weight of the product and to easy for separation between biodiesel and vitamin E by distillation. The residue distillation is the vitamin E while the monoester was distilled. All experiments were designed by the RSM technique.

Experimental design

RSM with central composite design (CCD) was used to optimize the biodiesel and vitamin E production and to investigate the influence of different process variables on the fatty acid methyl ester (FAME) and total vitamin E (Vit. E) content. A five-level-four-factor of independent variables has ranging from +2 to -2 for 27 experiment runs. The variables and levels selected for the biodiesel and vitamin E production optimization were: enzyme amount (A: 6-30%); methanol amount (B: 1-7 mole); water content (C: 3-5%) and reaction time (D: 2-12 hr.) (Table 1). The all data (Table 2) was divided into three sets: training set, testing set and validating set.

The experimental data were analyzed by using a second-order polynomial (Eq. (1)) to analyze the relationship between the independent variables, FAME and total vitamin E.

$$\mathbf{Y = \beta_0 + \sum_{i=1}^{3} \beta_i X_i + \sum_{i=1}^{3} \beta_{ii} X_i^2 + \sum_{i=1}^{2} \sum_{j=i+1}^{3} \beta_{ij} X_i X_j} \quad (\mathbf{1})$$

where Y is the response (%FAME and total vitamin E), β_0 is the intercept, β_i, β_{ii} and β_{ij} are the linear, quadratic, and interactive coefficients, respectively, and X_i and X_j are the independent variables. Statistical analysis of the equation was employed to evaluate the analysis of variance (ANOVA) and Design-Expert 8.07 software (State Ease Inc., Minneapolis, MN, USA) was used to design the experiments and carry out the regression and graphical analysis of the data.

Table 1 Independent variables and level for the Central Composite Design (CCD) of transesterification reaction with enzyme catalyst

Variables	Range of levels				
	-2	-1	0	1	2
Enzyme (%)	6.0	12.0	18.0	24.0	30.0
MeOH (mole)	1.0	2.5	4.0	5.5	7.0
Water (%)	3.0	6.0	9.0	12.0	15.0
Time (hr.)	2.0	4.5	7.0	9.5	12.0

Fatty acid methyl ester analysis

FAME content was analyzed to follow by BS EN 14103:2003. The analysis used gas chromatography (Agilent technologies, 6890N, USA) with DB-WAX capillary column (0.32mm×30m× 0.25µm film) and a flame ionization detector. The operated temperatures for analysis were 270°C and 300°C of injector and detector, respectively. The oven temperature program was 80°C of initial temperature and increased until to 270°C with the rate of 10°C/min. Helium was a carrier gas at 3 ml/min of flow rate. Equation 2 is FAME calculation.

$$\text{FAME}(\%) = \frac{(\sum \mathbf{A}) - \mathbf{A_{Is}}}{\mathbf{A_{IS}}} \times \frac{\mathbf{C_{IS} \times V_{IS}}}{\mathbf{W}} \times \mathbf{100} \quad (2)$$

When ΣA is total area, A_{IS} is area of internal standard, C_{IS} is concentration of internal standard (ppm), V_{IS} is value of internal standard (ml) and W is amount of sample (mg).

Vitamin E analysis

Vitamin E composition (α-, γ- and δ-tocotrienol; α-, γ- and δ-tocopherol) was determined by High performance liquid chromatography (Yonglin Instrument, Acme 9000 Isocratic pump, Absorbance detector UV 730D, Korea) with Unison UK-Silica column (UKS05, 150 x 4.6 mm, 3 µm, Imtak, USA).

The mobile phase was composed of 0.5% isopropanol in hexane and 1 ml/min of flow rate. The sample was dissolved in hexane to inject as 20 µl at 295 nm of wavelength. The concentration of each tocopherol and tocotrienols were determined from the calibration curve of vitamin E composition.

RESULT AND DISCUSSION

The chemical properties of raw material are shown in Table 2. The CPO has a high FFA (28.33%) The antioxidants (carotenoids and vitamin E) were low value because the CPOM performances a high temperature (100-150°C) and a long time (10-15 hr.) for the drying process of palm fruit before the oil extraction process. Both factors are an important effect on oil oxidation reaction that causes antioxidants to degrade in the oil [13].

Table 2 Chemical properties of CPO from press cake of the CPOM

Properties	Value
FFA (%)	28.33±0.98
Total carotenoids (ppm)	359.03±7.76
Total vitamin E (ppm)	535.46±63.20
Vitamin E composition (%)	
α-TP	39.46±0.12
α-TT	15.93±0.06
γ-TT	32.41±0.11
δ-TT	12.20±0.05

TP is Tocopherol, TT is Tocotrienol

Optimization condition by RSM

The relationships between the responses (FAME and vit. E concentration) and the four variables (catalyst concentration, methanol to oil molar ratio, water content, and reaction time) were evaluated using RSM. The results based on the experiment runs are presented in Table 3. Twenty-seven experiments were performed in duplicate. Regression analysis was employed to fit the empirical model with the generated response variable data. The response obtained in Table 4 and Table 5 were correlated with the four independent variables using a polynomial equation (Eq. (1)). The results from Table 3 revealed the FAME varies between 25.98 - 96.23% while the total vitamin E varies between 760.31 - 6,523.02 ppm. The condition for the FAME synthesis of the maximum value was 18% of the enzyme, 4 mole ratio of methanol and oil, 9% of water for 2 hr. of reaction time while the vitamin E condition of the maximum value was 24% of enzyme, 5.5 mole ratio of methanol and oil, 12% of water for 9.5 hr. of reaction time. The results observed that a high concentration of FAME synthesis (>90%) provided a high concentration of vitamin E (>4,000 ppm). Due to, at a low FAME concentration of biodiesel had to operate a high temperature and a long time for distillation process which both factors can destroy vitamin E. Design-Expert 8.07 software was employed to determine and evaluate the coefficients of the full regression model equation and their statistical significance. The second polynomial model for the FAME and vitamin E were regressed, as shown in Eq. (3) and Eq. (4), respectively:

$$\text{FAME} = -230.48+9.57A+35.03B+17.91C+14.76D+0.08AB-0.18AC+0.26AD+1.01BC-1.32BD+0.36CD-0.22A^2-4.95B^2-0.91C^2-1.18D^2 \quad (3)$$

$$\text{Vit. E} = -16470.18+409.24A+3572.36B+541.05C+1618.77D+12.66AB-5.52AC+25.87AD+32.93BC-64.04BD+68.71CD-13.51A^2-463.44B^2-43.91C^2-157.52D^2 \quad (4)$$

The ANOVA revealed that the response of FAME concentration was significant while the response of total vitamin E concentration was insignificant (Table 4 and Table 5). The FAME and total vitamin E were fitting with the quadratic (second-order) polynomial model which the correlation coefficients (R^2) of the responds were 0.76 and 0.77 at 95% confident interval. The ANOVA explaining of FAME and total vitamin E indicated that variables of enzyme and water were high significant (p value < 0.05). shown in Table 4 and Table 5, respectively.

The contour plots of FAME and total vitamin E present the variables effect that shown in Fig.1 and Fig. 2, respectively. The graphs were plotted by two variations while the last one kept constant at the center point which Fig. 1 presents the graphical two-dimensional plot from Eq. (2). Fig. 1 (a), Fig. 1 (b), and Fig. 1 (c) are clear that enzyme amount was a significant variable on FAME concentration. Increasing enzyme amount is increase the FAME concentration. Especially, more than 16% of catalyst provide more than 90% of FAME. Fig. 1 (b), Fig. 1 (e), and Fig. 1 (f) are clear that water content in transesterification reaction has a significant factor on FAME concentration. When the increased water content in the reaction affects increasing of FAME concentration. From the contour plots observe that About 8.3% of catalyst could increase FAME concentration more than 90%. Fig. 2 presents the graphical two-dimensional plot from Eq. (3). Fig. 2 (a), Fig. 2 (b), and Fig. 2 (d) are clear that enzyme factor was significant on vitamin E concentration. Fig. 2 (b), Fig. 2 (c), and Fig. 2 (f) are clear that water content was a significant variable on vitamin E concentration too. Due to, when increasing both factors to can increase the vitamin E concentration too.

Table 3 FAME and total vitamin E values of biodiesel and vitamin E production from RSM design

No.	Enzyme (%)	MeOH (mole)	Water (%)	Time (h)	FAME (%)	Vit. E (ppm)
1	12.0	2.5	6.0	4.5	32.85	760.31
2	12.0	2.5	6.0	9.5	35.43	1,442.78
3	12.0	2.5	12.0	4.5	48.63	1,068.28
4	12.0	2.5	12.0	9.5	90.97	5,049.08
5	12.0	5.5	6.0	4.5	29.05	1,153.48
6	12.0	5.5	6.0	9.5	25.98	1,118.93
7	12.0	5.5	12.0	4.5	58.87	1,641.95
8	12.0	5.5	12.0	9.5	66.22	2,332.94
9	24.0	2.5	6.0	4.5	49.86	1,260.73
10	24.0	2.5	6.0	9.5	90.92	4,482.62
11	24.0	2.5	12.0	4.5	54.11	1,502.24
12	24.0	2.5	12.0	9.5	90.91	3,962.76
13	24.0	5.5	6.0	4.5	35.62	1,447.38
14	24.0	5.5	6.0	9.5	56.99	1,879.60
15	24.0	5.5	12.0	4.5	79.49	1,108.25
16	24.0	5.5	12.0	9.5	94.56	6,523.02
17	18.0	4.0	3.0	7.0	32.32	1,584.84
18	18.0	4.0	15.0	7.0	94.59	6,262.03
19	6.0	4.0	9.0	7.0	33.11	1,721.24
20	30.0	4.0	9.0	7.0	94.80	5,386.58
21	18.0	1.0	9.0	7.0	68.13	1,285.39
22	18.0	7.0	9.0	7.0	34.92	1,381.33
23	18.0	4.0	9.0	2.0	96.23	2,156.18
24	18.0	4.0	9.0	12.0	36.83	976.73
25	18.0	4.0	9.0	7.0	93.14	4,547.57
26	18.0	4.0	9.0	7.0	94.04	5,614.83
27	18.0	4.0	9.0	7.0	95.53	5,753.85

Table 4 ANOVA for the response surface quadratic model of biodiesel production

Source	Sum of Squares	df [a]	Mean Square	F Value	P value [b]
Model	13990.07	14	999.29	2.67	0.048
A	3524.50	1	3524.50	9.42	0.010
B	563.76	1	563.76	1.51	0.243
C	5063.42	1	5063.42	13.53	0.003
D	94.80	1	94.80	0.25	0.624
AB	8.44	1	8.44	0.02	0.883
AC	173.58	1	173.58	0.46	0.509
AD	241.03	1	241.03	0.64	0.438
BC	332.52	1	332.52	0.89	0.364
BD	390.66	1	390.66	1.04	0.327
CD	113.53	1	113.53	0.30	0.592
A^2	1376.59	1	1376.59	3.68	0.079
B^2	2647.66	1	2647.66	7.08	0.021
C^2	1419.77	1	1419.77	3.79	0.075
D^2	1164.80	1	1164.80	3.11	0.103
Residual	4490.16	12	374.18		
Pure Error	2.91	2	1.46		
Lack of Fit	4487.25	10	448.72	307.97	0.003

[a]df is degree of freedom; [b]p>0.05 is not significantly different at the 5% level

Table 5 ANOVA for the response surface quadratic model of vitamin E production

Source	Sum of Squares	df [a]	Mean Square	F Value	p value [b]
Model	74810945.51	14	5343638.	2.80	**0.**041
A	9287119.42	1	9287119.	4.87	0.048
B	189280.75	1	189280.7	0.10	0.758
C	15037027.86	1	15037027	7.89	0.016
D	8748591.08	1	8748591.	4.59	0.053
AB	207719.46	1	207719.4	0.11	0.747
AC	158167.28	1	158167.2	0.08	0.778
AD	2410015.62	1	2410015.	1.26	0.283
BC	351308.11	1	351308.1	0.18	0.675
BD	922680.32	1	922680.3	0.48	0.499
CD	4248803.09	1	4248803.	2.23	0.161
A^2	5072264.42	1	5072264.	2.66	0.129
B^2	23196159.13	1	23196159	12.17	0.005
C^2	3332370.33	1	3332370.	1.75	0.211
D^2	20675974.58	1	20675974	10.85	0.006
Residual	22867178.03	12	1905598.		
Pure Error	871160.64	2	435580.3		
Lack of Fit	21996017.39	10	2199601.	5.05	0.177

[a]df is degree of freedom; [b]p>0.05 is not significantly different at the 5% level

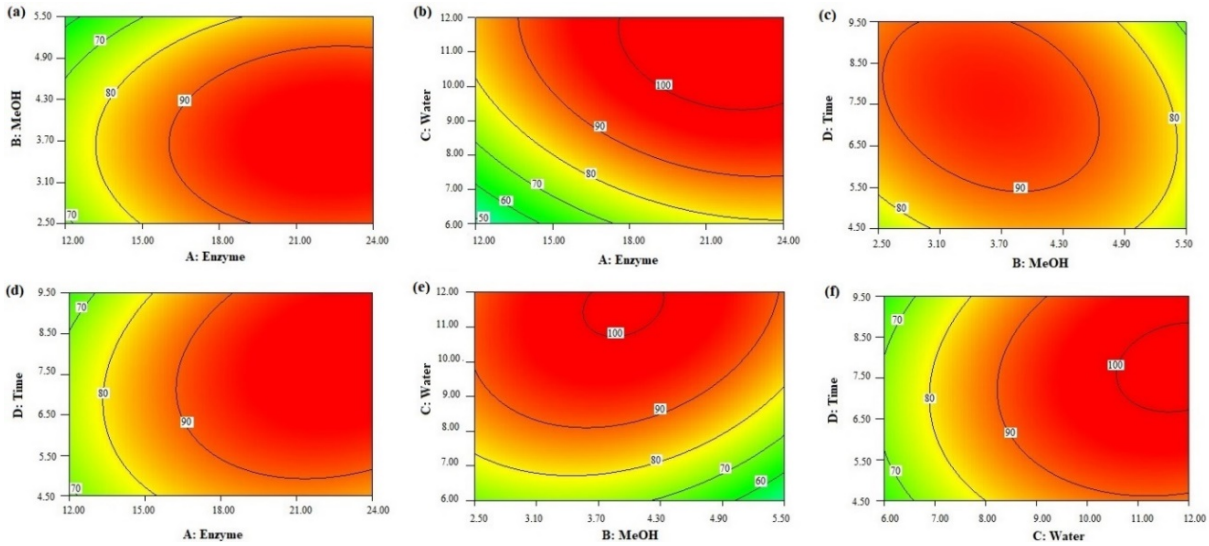


Fig. 1 Contour plots explaining the effects of variables on percentage of FAME

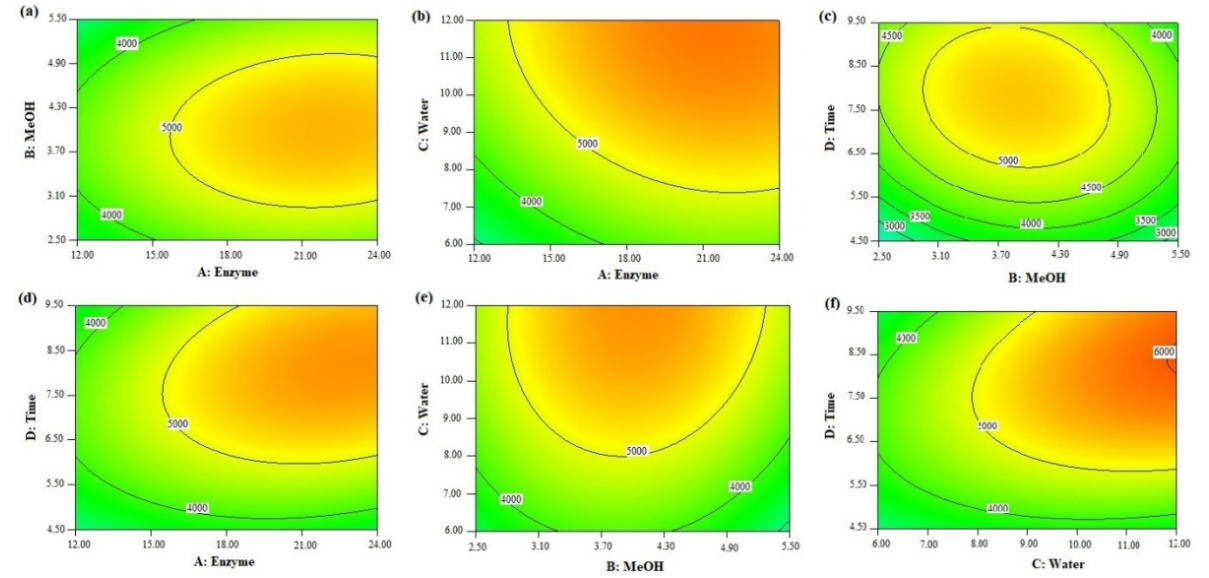


Fig. 2 Contour plots explaining the effects of variables on the total vitamin E

The optimum condition for the production of biodiesel and vitamin E was predicted by applying numerical optimization with the Design Expert software using RSM. The criteria of optimum condition was more than 90% of FAME concentration and more than 5,000 ppm of vitamin E concentration. So, the optimal condition was 19.48% of enzyme, 4.43 mole of methanol, 11.21% of water content for 5.47 hrs. at 55°C. This condition gave the average of FAME concentration and vitamin E concentration were 94.24% and 5,305.42 ppm, respectively. Table 6 presents the concentration of biodiesel and vitamin E from the optimal condition of transesterification reaction that repeated triplicate experiments.

Fig. 3 presents the vitamin E composition from different catalysts in the production process. Lipase enzyme catalyst used in transesterification process which it was one step for production and did not occur waste from the process. Chemical catalysts (KOH and H_2SO_4) are used in the conventional process for biodiesel production. This process provided two steps, there is esterification with the acid catalyst for reducing high acid in the oil. The next step was transesterification with the alkaline catalyst for FAME synthesis. Each step of the conventional process occurs a large of wastewater [6]. The result of vitamin E analysis revealed a low degradation of the chemical structure of all tocotrienols in enzyme catalyst because the α-, γ-, and δ-tocotrienol have remained in vitamin E. The chemical catalyst could not found tocotrienol but the vitamin E product found high α-tocopherol content. Although the total vitamin E of chemical catalyst had yield nearly as enzyme catalyst but tocotrienol is an anti-oxidant substrate more than tocopherol. The high tocopherol concentration from the conventional process may be

occurred changing of tocotrienol chemical structure to tocopherol chemical structure. From results of the vitamin E analysis indicated that the enzyme catalyst for production is a milder reaction than the chemical catalyst.

Table 6 Numerical optimization of the reaction conditions using RSM

Product	repeat	value	Average	SD
FAME (%)	1	93.14	94.24	1.21
	2	94.05		
	3	95.53		
Total vit. E (ppm)	1	4,547.57	5,305.42	659.99
	2	5,614.83		
	3	5,753.85		

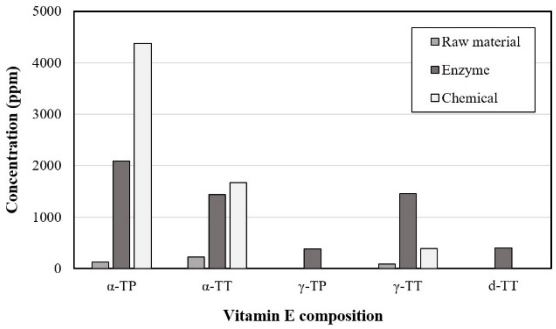


Fig. 3 Vitamin E composition from raw material, and vitamin E products

CONCLUSIONS

RSM was performed to determine the optimum condition of enzymatic transesterification. This optimum condition gave 93.79% FAME of biodiesel and 5,305.42 ppm of total vitamin E. The catalyzing and water factors were significant in the production process. The advantages of biocatalyst were conservation of tocotrienol, save of chemicals and operated time when compared with the conventional process.

ACKNOWLEDGMENTS

This research was supported by Agricultural Research Development Agency (Public Organization) (ARDA), The Research and Researchers for Industries (RRI), and Sang Arun Palm Oil Ltd., Co.

REFERENCES

[1] Jalani B. S., Cheah S. C., Rajanaidu N., and Darus A., Improvement of Oil Palm Through Breeding and Biotechnology. Journal of the American Oil Chemists' Society, Vol. 47, 1977, pp.1451-1455.

[2] Gunstone F. D., Vegetable Oils in Food Technology Composition, Properties and Uses. Blackwell Publishing, France, 1st ed., 2002.

[3] CHOO Y. M., and TAY B. Y. P., Valuable Minor Constituents of Commercial Red Palm Olein: Carotenoids, Vitamin E, Ubiquinones and Sterols. J. Oil Palm Research, Vol. 12, 2002, pp.14-24.

[4] Sen C. K., KHANNA S., and ROY S., Tocotrienols in Health and Disease: The Other Half of The Natural Vitamin E Family. Molecular Aspects of Medicine, Vol. 28, 2007, pp.693-728.

[5] Komiyama, K., and Yamaka M., Anti Tumor Activity of Tocotrienols in Vitamin E in Health and Disease. Marcel Dekker Inc., New York, 1993.

[6] Nwosu-Obieogu K., Chiemenem L. I., and Adekunle K. F., Biodiesel Production from Plant Seed Oil - A Review. International Journal of Scientific Research in Science, Engineering and Technology, Vol. 3, Issue 18, 2016, pp.2394-4099.

[7] OOI C. K., Minor Components of Palm Oil. Palm Oil Technical Bulletin, Vol. 38, 1999, pp.29-32.

[8] CHOO Y. M., MA A. N., CHUAH C. H., KHOR H. T., and BONG S. C., A Developmental Study on the Appearance of Tocopherols and Tocotrienols in Developing Palm Mesocarp (Elaeis guineensis). Lipids, Vol. 39, Issue 60, 2004, pp.561-564.

[9] Banerjee A., and Chakraborty R., Parametric Sensitivity in Transesterification of Waste Cooking Oil for Biodiesel Production-A Review, Resour. Conserv. Recy., Vol. 53, 2009, pp.490-497.

[10] Refaat A. A., Attia N. K., Sibak H. A., El Sheltawy S. T., and El Diwani G. I., Production Optimization and Qualify Assessment of Biodiesel from Waste Vegetable Oil. Int. Journal Environ. Sci. Tech., Vol. 5, Issue 1, 2008, pp.75-82.

[11] Abigor R. D., Uadia P. O., Foglia T. A., and Obibuzor J. U., Lipase-Catalyed Production of Raphia Hookeri Oil Methyl Esters for use as Biodiesel Fuel. Nigerian journal of Palms and Oil Seed, Vol. 15, 2002, pp.87-93.

[12] Jackson M. A., and King J. W., Methanolysis of Seed Oils in Supercritical Carbon. Journal of the American Oil Chemists Society, Vol. 73, 1996, pp. 353-356.

[13] Choe E., and Min D. B., Mechanisms and Factors for Edible Oil Oxidation. Comprehensive Reviews in Food Science and Food Safety, Vol. 5, 2006, pp.169-186.

7th Int. Conf. on Structure, Engineering & Environment (SEE), Pattaya, Thailand, Nov. 10-12, 2021, ISBN: 978-4-909106070 C3051

SIMULATION OF INCOMPRESSIBLE THERMAL FLOW VIA MESHLESS FINITE POINT METHOD

Chinnapat Buachart
Faculty of Engineering, Chiang Mai University, Thailand

ABSTRACT

In this work, techniques to stabilize the convection dominated problems are adopted to solve two-dimensional steady-state incompressible Navier-Stokes problems via meshless finite point method (FPM). The trial functions and gradients are computed based on weighted-least-square (WLS) approximation. The numerical instability due to convection terms are alleviated by improving the gradient approximation. These techniques were developed based on edge stabilization with analytical solution of equivalent one-dimensional convection dominated equation. Numerical tests of incompressible thermal flow with various Rayleigh numbers are performed. The predicted value of nodal velocities are computed using explicit time integration of conservative momentum equation incorporate with stabilized convection term in each time step. Then, the nodal pressure are computed by implicitly solve matrix equation of Laplace equation derived from incompressibility. Finally, the corrected values of nodal velocities and temperature are recomputed using nodal pressure obtained from previous calculation step. The distribution of velocity and temperature at steady state from proposed method are closed to analytical solution available from literatures.

Keywords: Edge-based stabilization, Incompressible thermal flow, Meshless method, Weighted-least square

INTRODUCTION

Many fluid flow problems in engineering are governed by the so-called convection-diffusion equations, in which, there are both convective and diffusive terms. To analyze the convection-diffusion problems, the conventional finite element method (FEM), the finite difference method (FDM), or the finite volume method (FVM) has been widely used.

However, there is a well-known instability issue of convection-diffusion problem; the highly oscillatory solution will occurs when the convective term is dominated. Hence, the special treatment is required to stabilize the numerical solution. A lot of studies have been performed to solve the instability problem in conventional numerical schemes, and excellent documentation on stabilization techniques can be found in many finite element book [1].

In recent years, meshfree or meshfree methods have attracted more and more attention from many researchers in computational mechanics field, especially in computational fluid mechanics [2-7]. These meshfree methods do not required a mesh to discretize the problem domain, because the shape function is constructed entirely based on a set of scattered nodes. They are categorized to be two groups. First category is based on the collocation techniques, for example the finite point method (FPM) and the hp-cloud method [6-10]. Other meshfree methods are based on weak form, e.g. the element-free Galerkin method [3], the reproducing kernel particle (RKP) method [4], the meshfree local Petrov-Galerkin (MLPG) method, and so on [7], this category of meshfree method require numerical integration to approximate the weak form. Hence, the first category is defined to be truly meshfree, i.e. no mesh required to perform numerical integration.

Only very few studies on solving convection dominated problems using meshfree method have been reported [8-10]. In this work, the finite point method was applied to the convection dominated problem with upwinding for the first derivative or with characteristics approximation, and then applied this technique to solve for incompressible thermal flow problem.

THEORETICAL BACKGROUND

In this section, the governing equations of viscous thermal flow is described. Then the derivation of stabilized term of convection equation and time stepping procedure are explained.

Incompressible Thermal Flow

The set of equations which will be used in simulation of fluid flow are two dimensional thermal viscous incompressible Navier Stokes equations consist of the conservation of mass:

$$\frac{\partial u}{\partial x}+\frac{\partial v}{\partial y}=0 \quad (1)$$

conservation of momentum in *x* and *y* directions:

$$\rho\frac{\partial u}{\partial t}+\rho\left(u\frac{\partial u}{\partial x}+v\frac{\partial u}{\partial y}\right)=-\frac{\partial p}{\partial x}+\mu\left(\frac{\partial^2 u}{\partial x^2}+\frac{\partial^2 u}{\partial y^2}\right)+\rho g_x\left[1-\beta\left(T-T_0\right)\right] \quad (2a)$$

$$\rho\frac{\partial v}{\partial t}+\rho\left(u\frac{\partial v}{\partial x}+v\frac{\partial v}{\partial y}\right)=-\frac{\partial p}{\partial y}+\mu\left(\frac{\partial^2 v}{\partial x^2}+\frac{\partial^2 v}{\partial y^2}\right)+\rho g_y\left[1-\beta\left(T-T_0\right)\right] \quad (2b)$$

and conservation of energy:

$$\rho\frac{\partial T}{\partial t}+\rho c\left(u\frac{\partial T}{\partial x}+v\frac{\partial T}{\partial y}\right)=\mu\left(\frac{\partial^2 T}{\partial x^2}+\frac{\partial^2 T}{\partial y^2}\right)+f \quad (3)$$

where *u* and *v* represent velocity of fluid in *x* and y-directions, respectively. The variable *T* is absolute temperature and T_0 denote the reference temperature. The variable *p* is fluid pressure.

The parameters in Eqs. (1) to (3) are listed as follow. The coefficients β is volumetric coefficient of thermal expansion, and *k* is thermal conductivity. The variable μ is fluid viscosity. The specific heat at constant volume is denoted by *c*. The density and gravitational accerelation are denoted by ρ and *g*, respectively.

Weighted-Least Square Approximation

In this work, the spatial discretization of dependent variables; *u*, *v*, *T*, and *p*; in conservative equations, Eqs. (1) to (3), are approximated by weighted-least square (WLS) procedure proposed in [6]. Let suppose Ω_i is an local approximation domain (cloud) of unknown function $\phi(\boldsymbol{x})$ consists of *star point* $\boldsymbol{x}_i$, and set of surrounding points $\boldsymbol{x}_j$, j = 1, 2,…,*np* as shown in Figure 1. Then, the local approximation of ϕ can be defined by

$$\hat{\phi}\left(\boldsymbol{x}\right)=\sum_{k=1}^{m}p_k\left(\boldsymbol{x}\right)\alpha_k=\boldsymbol{p}^{\mathrm{T}}\left(\boldsymbol{x}\right)\boldsymbol{\alpha} \quad (4)$$

where $\boldsymbol{p}(\boldsymbol{x})$ is a vector whose their components are the terms of a complete polynomial basis functions, and $\boldsymbol{\alpha}$ is a vector of coefficients to be determined. In this work, complete quadratic polynomial basis in two dimensional domain are employed, *i.e.* $\boldsymbol{p}^{\mathrm{T}}(\boldsymbol{x})$ = [1, *X*, *Y*, X^2, *XY*, Y^2]. Note that the capital symbol in each component of $\boldsymbol{p}$ represent point coordinates which relative to the star point position.

For each region Ω_i the number of could nodes is larger than number of parameter $\boldsymbol{\alpha}$, *np* > *m*. The approximation parameter $\boldsymbol{\alpha}$, is solved to minimized weighted-sum square error defined as

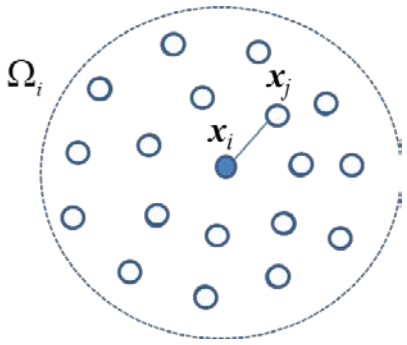


Fig. 1 Local approximation domain in WLS [11]

$$J_i=\sum_{j=1}^{np}W_{ij}\left(\hat{\phi}_j-\hat{\phi}_i\right)^2 \quad (5)$$

in which W_{ij} is a weighting factor at surrounding point $\boldsymbol{x}_j$. In this paper the following normalized Gaussian (exponential) weighting function is adopted

$$W_{ij}=\frac{\exp\left[-\left(wd_{ij}/\gamma d_{\max}\right)^2\right]-\exp\left(-w^2\right)}{1-\exp(-w^2)} \quad (6)$$

where *dij* is the distance between star point x_i and surrounding point x_j in cloud. The parameters *w* and γ govern the shape of the weighting function. In this work, the value of γ = 1.01, and initial value of *w* = 3.5. The value of largest distance $d_{\max}$ and shape parameter *w* are computed iteratively to obtain acceptable approximation accuracy according to procedure proposed in [10].

The minimization of Eq. (5) with respect to parameter $\boldsymbol{\alpha}$ leads to the following results

$$\boldsymbol{\alpha}=\mathbf{A}\boldsymbol{\phi} \quad (7)$$

in which

$$\mathbf{A}=\left(\mathbf{P}^{\mathrm{T}}\mathbf{W}\mathbf{P}\right)^{-1}\mathbf{P}^{\mathrm{T}}\mathbf{W} \quad (8)$$

where the matrices $\mathbf{W}$ = diag[W_{ij}], and $\mathbf{P}^{\mathrm{T}}$ = [$\boldsymbol{p}(\boldsymbol{x}_1)$, $\boldsymbol{p}(\boldsymbol{x}_2)$, …, $\boldsymbol{p}(\boldsymbol{x}_{np})$]. Then, an approximation value of $\phi(\boldsymbol{x})$ at the star point is then computed according to Eq. (4)

$$\hat{\phi}\left(\boldsymbol{x}_i\right)=\sum_{j=1}^{np}a_{1j}\phi_j\ . \quad (9)$$

where a_{kj} indicates the *k*th entry in *j*th column in

matrix **A**. An approximated value of first derivatives of unknown variable are also computed by take derivatives of polynomial basis in Eq. (4)

$$\frac{\partial \hat{\phi}_i}{\partial x} = \sum_{j=1}^{np} a_{2j}\phi_j \,, \tag{10}$$

$$\frac{\partial \hat{\phi}_i}{\partial y} = \sum_{j=1}^{np} a_{3j}\phi_j \,, \tag{11}$$

and Laplacian

$$\frac{\partial^2 \hat{\phi}_i}{\partial x^2} + \frac{\partial^2 \hat{\phi}_i}{\partial y^2} = \sum_{j=1}^{np} 2\left(a_{4j} + a_{6j}\right)\phi_j \,. \tag{12}$$

THE SOLUTION PROCEDURE

In this section, the stabilization technique of convection term in Eqs. (2) and (3) are described. Then the numerical solution scheme of Eqs. (1) to (3) are explained.

The Upwinding Scheme

The convection term, second term at left side of Eqs. (2) and (3) usually caused the non-smooth numerical results. So, the upwinding scheme is needed to alleviate this problem. The upwinding scheme is applied to the weighted-least squares (WLS) approximation of convection terms as follows [11]:

$$u\frac{\partial \hat{\phi}_i}{\partial x} + v\frac{\partial \hat{\phi}_i}{\partial y} = \sum_{j\neq i} b_{ij}\left(1-\zeta_{ij}\right)\left(\phi_j - \phi_i\right) \tag{13}$$

where $b_{ij} = u_i\, a_{2j} + v_i\, a_{3j}$ indicates the algebraic divergence operator approximated from weighted-least square scheme, connected between node *i* and *j*, as shown in Fig. 1. The dissipation coefficient ζ_{ij} is expressed as follows:

$$\zeta_{ij} = \coth \eta_{ij} - \frac{1}{\eta_{ij}} \tag{14}$$

in which η_{ij} is the stencil Peclet number, defined as

$$\eta_{ij} = \frac{\rho\left[u_i\left(x_j - x_i\right) + v_i\left(y_j - y_i\right)\right]}{2\mu} \,. \tag{15}$$

Time Stepping Procedure

The velocities and temperature in Eqs. (2) and (3) are solved using Euler time stepping scheme. The predicted increment nodal velocities at iteration number *n* are first computed

$$\Delta u^* = -\Delta t\left\{\begin{array}{r}\left(uu_{,x} + vu_{,y}\right) - \frac{\mu}{\rho}\left(u_{,xx} + u_{,yy}\right) + \\ g_x\left[\beta\left(T - T_0\right) - 1\right]\end{array}\right\}^n \tag{16a}$$

$$\Delta v^* = -\Delta t\left\{\begin{array}{r}\left(uv_{,x} + vv_{,y}\right) - \frac{\mu}{\rho}\left(v_{,xx} + v_{,yy}\right) + \\ g_y\left[\beta\left(T - T_0\right) - 1\right]\end{array}\right\}^n \tag{16b}$$

and incremental nodal temperature

$$\Delta T = -\Delta t\left[\left(uT_{,x} + vT_{,y}\right) - \frac{k}{\rho c}\left(T_{,xx} + T_{,yy}\right)\right]^n \,. \tag{17}$$

The corrected value of nodal pressure at next iteration is solved from Laplacian equation

$$\frac{\Delta t}{\rho}\left(p_{,xx} + p_{,yy}\right)^{n+1} = \left(u^n + \Delta u^*\right)_{,x} + \left(v^n + \Delta v^*\right)_{,y} \tag{18}$$

Then the corrected values of nodal velocities and temperature at next step are computed from corrected pressure as follow

$$u^{n+1} = u^n + \Delta u^* - \Delta t\frac{\partial p^{n+1}}{\partial x} \,, \tag{19}$$

$$v^{n+1} = v^n + \Delta v^* - \Delta t\frac{\partial p^{n+1}}{\partial y} \,, \tag{20}$$

$$T^{n+1} = T^n + \Delta T \,. \tag{21}$$

The iteration process according to Eqs. (16) to (21) are repeat until the steady state are reached, *i.e.*

$$\frac{\sum_i\left(\left|\Delta u_i\right| + \left|\Delta v_i\right| + \left|\Delta T_i\right|\right)}{\sum_i\left(\left|u_i^{n+1}\right| + \left|v_i^{n+1}\right| + \left|T_i^{n+1}\right|\right)} \le 10^{-4} \tag{22}$$

The size of local time step at star point *i* is set according to convection time to nearest node,

$$\Delta t_i = \frac{\min\limits_{j \neq i}\left(\sqrt{\left(x_j - x_i\right)^2 + \left(y_j - y_i\right)^2}\right)}{\sqrt{u_i^2 + v_i^2}}. \qquad (23)$$

In the next section, the performance of finite point method with upwinding scheme and time stepping algorithm are tested.

RESULTS

In this section, the finite point method with upwinding scheme are used to solve two test cases, convection dominated flow and natural convection flow problems

Test on Upwinding Scheme

To test the upwinding scheme, analysis of two-dimensional thermal convection-diffusion a square domain under a uniform heat source f = 10 using a regular square grid of 8 × 8 points with diagonal convective velocity $u = v$ = 1 m/s and coefficient $k/\rho c$ = 0.005 m^2/s. A prescribed zero value, *i.e.* homogeneous boundary condition, of the temperature at the boundary has been taken. Figure 2 shown the results for temperature. The numerical solution is free of oscillations and coincides with the expected result [6].

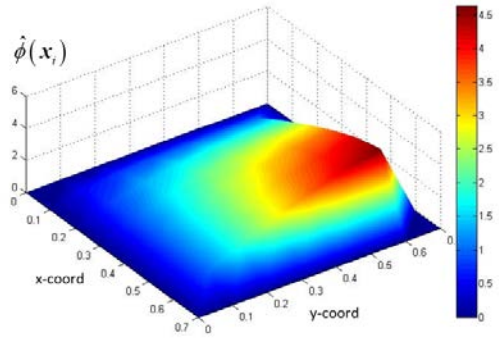


Fig. 2 Contour of Temperature

Thermal Flow in Square Domain

To test the algorithm proposed in previous section. The problem of thermal flow in square domain will be solved. The unit square domain containing a fluid inside is discretized by irregular 352 points. The temperature on left and right wall are set to be difference values. The temperature on left wall is colder than the right wall. The velocity of fluid on the four sides of wall are set to be zero. The dimensionless Prandtl number and Rayleigh numbers are used to categorize the problems.

The Prandtl number $Pr = \mu c/k$ is measure of ratio between momentum diffusivity versus thermal diffusivity. The Rayleigh number measures the ratio between buoyancy forces due to temperature change versus viscosity forces, $Ra = (g\beta L^3 \Delta T/\mu^2)Pr$. Two test cases of flow in unit square are performed using Pr = 1, Ra = 10^4 and 10^5, respectively. The solutions are shown in Figs 3 and 4. The solution are similar with finite element solution following in literature [11]. Increasing the value of Rayleigh number, cause the flow vector separated to be two vertex as shown in Fig. 4. The effect of buoyancy forces guide the flow to be separated and form in the H-shape.

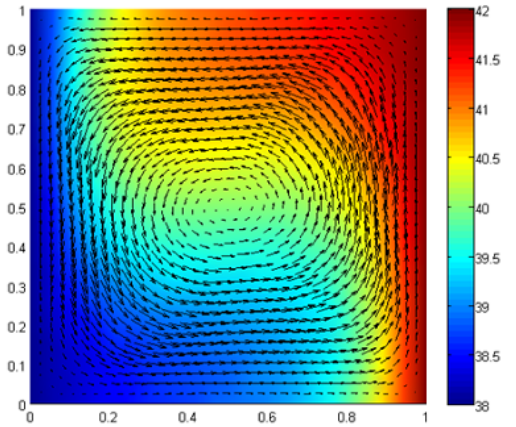


Fig. 3 Temperature and velocities (Ra = 10^4)

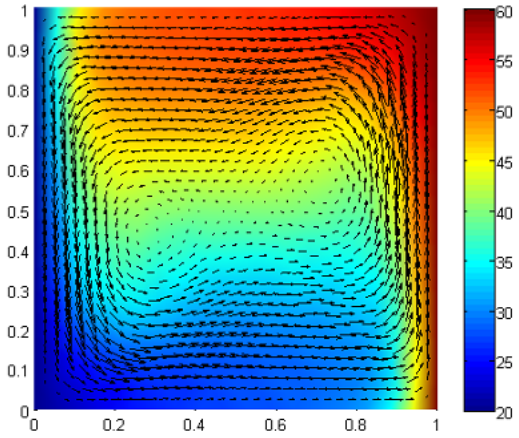


Fig. 4 Temperature and velocities (Ra = 10^5)

CONCLUSIONS

The main objective of this research is to provide the

algorithm to solve incompressible thermal flow based on finite point (FPM) method. The results from two test cases can be conclude as follow:

- The convection stabilization is work well in steady state two dimensional problem.
- The solution of thermal flow in unit square domain is corresponding with available numerical solution via well-known finite element scheme.

ACKNOWLEDGMENTS

This research had been financial supported by The Murata Science Foundation 2017.

REFERENCES

[1] Zienkiewicz, O. C. and Taylor, R. L., The Finite Element Method: Volumn 3 Fluid Dynamics, Oxford: Butterworth-Heinemann, 2000.

[2] Lancaster, P. and Salkauskas, K., Surfaces Generated by Moving Least Squares Methods. Math. and Comp., Vol. 37, 1981, pp. 141–158.

[3] Belytschko, T., Lu, Y. Y and Gu, L, Element-free Galerkin Methods, Int. J. Num. Meth. Eng., Vol. 37, 1994, pp. 229–256.

[4] Liu, W. K., Jun, S. and Zhang, Y., Reproducing Kernel Particle Methods, Int. J. Num. Meth. Fluids, Vol. 20, 1995, pp. 1081–1106.

[5] Duarte, C. A. and Oden, J. T., Hp clouds-A Meshfree Method to Solve Boundary-value Problems, TICAM report No. 95-05 (May), 1996.

[6] Oñate, E., Idelsohn, S., Zienkiewicz, O. C. and Taylor, R. L., A Finite Point Method in Computational Mechanics. Applications to Convective Transport and Fluid Flow, Int. J. Num. Meth. Eng., Vol. 39, 1996, pp. 3839–3866.

[7] Atlutri, S. N. and Shen, S. P., The Meshfree Local Petrov-Galerkin (MLPG) Method, Tech Science Press., Encino USA, 2002.

[8] Gu, Y. T. and Liu, G. R., Meshfree Techniques for Convection Dominated Problems, Comp. Mech., Vol. 38, 2006, pp. 171–182.

[9] Ortega, E., Oñate, E. and Idelsohn, S., An Improved Finite Point Method for Tri-dimensional Potential Flows, Comp. Mech., Vol. 40, 2007, pp. 949–963.

[10] Buachart, C., Kanok-Nukulchai, W., Ortega, E. and Oñate, E., A Shallow Water Model by Finite Point Method, Int. J. Comp. Meth., Vol. 11, Issue 1, 2014.

[11] Buachart, C. and Kanok-Nukulchai, W., Finite Point Method for Convection-dominated Flow Problems. GMSARN International Journal, Vol. 8, 2014., pp. 79–84.

[12] Dechaumphai, P. And Kanjanakijkasem, W., A Finite Element Method for Viscous Incompressible Thermal Flows. Science Asia, Vol. 25, 1999, pp. 165–172.

7th Int. Conf. on Structure, Engineering & Environment (SEE), Pattaya, Thailand, Nov.10-12, 2021, ISBN: 978-4-909106070 C3051

THE ADOMIAN DECOMPOSITION METHOD FOR SOLVING HEAT TRANSFER LIGHTHILL SINGULAR INTEGRAL EQUATION USING MAPLE

Dalal Adnan Maturi [1]

[1]Departement of Mathematics, Faculty of Science, King Abdulaziz University, Jeddah, Saudi Arabia

ABSTRACT

In this paper, we study the mathematical physics model, which is an Abel-type Volterra integral equation that describes the distribution Temperature of heat along the surface when the heat transfer to it is balanced by radiation from it. We applied the adomian decomposition method to the heat transfer Lighthill Singular integral equation and by converting it to the nonlinear singular Volterra equation of the second kind using the Maple program. The nonlinear term can easily be handled with the help of Adomian polynomials. The solution takes the form of a convergent series with easily computable terms. The method is based on the application of Heat Transfer to a nonlinear Integral equation. The Pad e approximants are used effectively in the study to capture the solution's critical behavior. The method's efficiency and reliability are demonstrated by numerical examples. For a broad range of linear and nonlinear singular Integral equations, the approach is very effective and useful in finding analytical and numerical solutions. It gives you more concrete series solutions that converge quickly.

Keywords: Adomian Decomposition Method, Heat Transfer, Lighthill Singular Integral Equation, Maple18.

INTRODUCTION

Many areas of applied mathematics depend on knowledge of integral equations, as they arise naturally in various applications in mathematics, engineering, physics, and technology. They can be used to model a wide range of physical problems such as thermal conductivity, propagation and continuity, mechanics, geophysics, electricity, magnetism, neutron transport, traffic theory, and many more. Integrative equations provide solutions in designing effective parameter algorithms for algebraic curves, surfaces, and superficial surfaces. Many associated elementary and boundary value problems can be reformulated as integral differential equations. Weak singular and scalar integral equations are of particular interest because they are accustomed to solving inverse boundary value problems whose domain is fractal curves, where classical calculus cannot be used. Abel's equations and other fractional integral equations have been extensively studied and are used in the modeling of various phenomena in biophysics, elastic viscosity, electrical circuits, etc.

The solubility and properties of Volterra's integral equations have been studied using various analytical and approximate methods.

In this paper, we consider the second kind of nonlinear weakly-singular Volterra integral equations are provided by

$$u(x) = f(x) + \int_0^x \frac{\beta}{\sqrt{x-t}} F\big(u(t)\big)dt, \quad x \in [0,T] \quad (1)$$

And

$$u(x) = f(x) + \int_0^x \frac{\beta}{[g(x)-g(t)]^{\alpha}} F\big(u(t)\big)dt, \quad 0 < \alpha < 1, \quad x \in [0,T], \quad (2)$$

where $F(u(t))$ is a nonlinear function of $u(t)$ and β is a constant. The generalized nonlinear weakly-singular Volterra equation (2) is also known as the Volterra equation. Many mathematical physics and chemistry applications use these equations, including stereology, heat conduction, crystal formation, and heat radiation from a semi-infinite material. Singular equations with singular kernels include the nonlinear weakly-singular and extended nonlinear weakly-singular equations (1) and(2)

$$K(x,t) = \frac{1}{\sqrt{x-t}},$$
$$K(x,t) = \frac{1}{[g(x)-g(t)]^{\alpha}}, \quad 0 < \alpha < 1, \quad (3)$$

Several authors have investigated the numerical solvability of (1). In [1], Diogo et al. used a collocation with graded mesh. A hybrid collocation approach was introduced in [2] for (1). After a smoothing adjustment, a Nystrom type technique [3] was also considered (1).

The Jacobi spectral collocation method [4] was recently proposed for the solution of (1). Ortiz and Samara [5] introduced an operational strategy based on the conventional Tau approach for the numerical solution of nonlinear ordinary differential equations with certainly added constraints in 1981. Ordinary differential equations (ODEs), partial differential

equations, integral equations, and integro-differential equations have all been solved using the Tau technique [8, 7, 6].

The kernels in many applications modeled by integral equations are not smooth, making it difficult to identify a solution and numerically approximate it, as the convergence of approximation methods is dependent on the smoothness of the solution in general. As a result, traditional analytical approaches, such as projection methods, perform poorly in such situations, as the linear system that they lead to is often poorly conditioned and difficult to solve.

When classical calculus cannot be utilized, proving convergence and estimating error can be time-consuming. They frequently have a significant implementation cost. As a result, fast, easy-to-use numerical algorithms for these types of equations are in high demand.

The adomian decomposition approximation of the second kind weakly singular nonlinear Volterra-Hammerstein integral equations is the subject of this research.

THE ADOMIAN DECOMPOSITION METHOD (ADM)

Consider the differential equation [11]. Because Eq. (1) is a particular case of the generalized nonlinear weakly-singular Volterra equation (2), the Adomian decomposition method will be used to solve it. $\alpha = 1\,2$, $g(x) = x$ .As previously said, we will provide a brief overview of the method's framework. We substitute the decomposition series for the decomposition series to (2) find the solution $u(x)$ of $u(x) = \sum_{n=0}^{\infty} u_n(x)$

$$u(x) = \sum_{n=0}^{\infty} u_n(x), \tag{4}$$

And

$$F\big(u(x)\big) = \sum_{n=0}^{\infty} A_n(x),$$

$$A_n = \frac{1}{n!}\frac{d^n}{d\lambda^n}\left[F\Big(\sum_{n=0}^{\infty}\lambda^i u_i\Big)\right]_{\lambda=0}, n = 0,1,2,\cdots \tag{5}$$

where an is the Adomian polynomials, and (2) on both sides to get

$$\sum_{n=0}^{\infty} u_n(x) = f(x) + \int_0^x \frac{\beta}{[g(x)-g(t)]^{\alpha}}\left(\sum_{n=0}^{\infty} A_n(t)\right)dt, \quad 0 < \alpha < 1, \tag{6}$$

$$u_0(x) = f(x)$$

$$u_1(x) = \int_0^x \frac{\beta}{[g(x)-g(t)]^{\alpha}} A_0(t)dt,$$

$$u_2(x) = \int_0^x \frac{\beta}{[g(x)-g(t)]^{\alpha}} A_1(t)dt,$$

$$u_3(x) = \int_0^x \frac{\beta}{[g(x)-g(t)]^{\alpha}} A_2(t)dt,$$

$$u_4(x) = \int_0^x \frac{\beta}{[g(x)-g(t)]^{\alpha}} A_3(t)dt, \tag{7}$$

and so forth. After determining the components $u0(x), u1(x)$, and $u2(x)$, the solution $u(x)$ of (2) will be determined as a series by substituting the (4) derived components in the formula.

Definition 1.

Let $(\boldsymbol{X}, ||\cdot||)$ be a Banach space. A mapping $\boldsymbol{T}: \boldsymbol{X} \to \boldsymbol{X}$ is called a $\boldsymbol{q}-$contraction if there exists a constant $\boldsymbol{0} \leq \boldsymbol{q} < \boldsymbol{1}$ such that

$$\big||\boldsymbol{Tx} - \boldsymbol{Ty}|\big| \leq \boldsymbol{q}||\boldsymbol{x} - \boldsymbol{y}||,$$

for all $\boldsymbol{x}, \boldsymbol{y} \in \boldsymbol{X}$. On Banach spaces, the well known contraction principle holds:

Theorem 1.

Consider a Banach space $(\boldsymbol{X}, ||\cdot||)$ and let

be a q−contraction. Then $\boldsymbol{T}: \boldsymbol{X} \to \boldsymbol{X}$

(1) $\boldsymbol{T}$ has exactly one fixed point, which means equation $\boldsymbol{x} = \boldsymbol{Tx}$ has exactly one solution $\boldsymbol{x}^* \in \boldsymbol{X}$;

(2) the sequence of successive approximations $\boldsymbol{x_{n+1}} = \boldsymbol{Tx_n}, \boldsymbol{n} \in \boldsymbol{N}$, converges to the solution$\boldsymbol{x}^*$, where $\boldsymbol{x_0}$ can be any arbitrary point in $\boldsymbol{X}$;

(3) for every $\boldsymbol{n} \in \boldsymbol{N}$, the following error estimate $||\boldsymbol{x_n} - \boldsymbol{x}^*|| \leq \frac{\boldsymbol{q_n}}{\boldsymbol{1-q}} ||\boldsymbol{Tx_0} - \boldsymbol{x_0}||$ holds.

We utilize Banach's theorem to prove the existence and uniqueness of a solution to Equation (1) under particular conditions, and to approximate it by applying the operator consecutively. The values of the solution at specific nodes are then approximated using an appropriate numerical integration scheme.

SEVERAL EXAMPLE

Example1. Consider the heat transfer Lighthill Singular integral equation

$$u(x) = 1 - \frac{\sqrt{3}}{\pi}\int_0^x \frac{t^{\frac{1}{3}}u^4(t)}{(x-t)^{\frac{2}{3}}}dt,$$
$$x\epsilon[0,1]$$

Applying the Adomian Decomposition Method using Maple, we find

Table 1 Numerical results and exact solution of heat transfer Lighthill Singular integral equation for example 1

x	$u(x)$	$Exact = \sqrt{x}$	$Error$
0.00100	0.0316228	0.0316227	0.0000001
0.00200	0.0447214	0.0447209	0.0000005
0.00300	0.0547723	0.0547710	0.0000013
0.00400	0.0632456	0.0632429	0.0000027
0.00500	0.0707107	0.0707060	0.0000047
0.00600	0.0774597	0.0774523	0.0000073
0.00700	0.0836660	0.1475523	0.0000108
0.00800	0.0894427	0.0894277	0.0000151
0.00900	0.0948683	0.0948481	0.0000202
0.01000	0.1000000	0.0999737	0.0000263

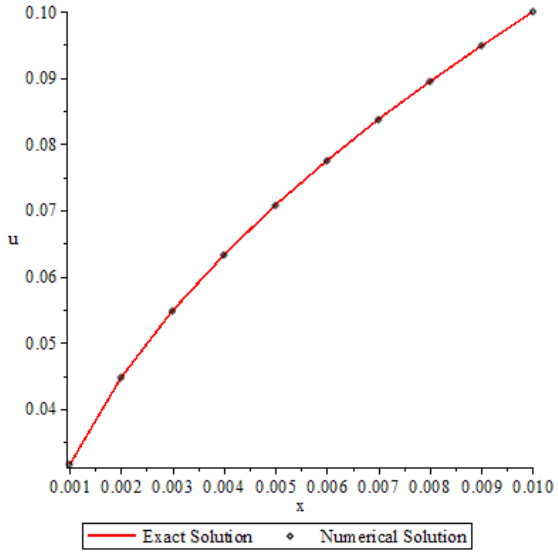


Fig. 1 Plot 2D of the exact solutions result of heat transfer Lighthill Singular integral equation for example 1.

Example2. Consider the heat transfer Lighthill Singular integral equation

$$u(x) = x + \frac{4}{3}x^{\frac{3}{2}} - \int_0^x \frac{1}{\sqrt{x-t}}u(t)dt$$
$$x\epsilon[0,1]$$

Applying the Adomian Decomposition Method using Maple, we find

Table 2 Numerical results and exact solution of heat transfer Lighthill Singular integral equation for example 2.

x	$u(x)$	$Exact = x$	$Error$
0.00100	0.0010000	0.0010001	0.0000001
0.00200	0.0020000	0.0020003	0.0000003
0.00300	0.0030000	0.0030008	0.0000008
0.00400	0.0040000	0.0040017	0.0000017
0.00500	0.0050000	0.0050030	0.0000030
0.00600	0.0060000	0.0060047	0.0000047
0.00700	0.0070000	0.0070069	0.0000069
0.00800	0.0080000	0.0080096	0.0000096
0.00900	0.0090000	0.0090129	0.0000129
0.01000	0.0100000	0.0100168	0.0000168

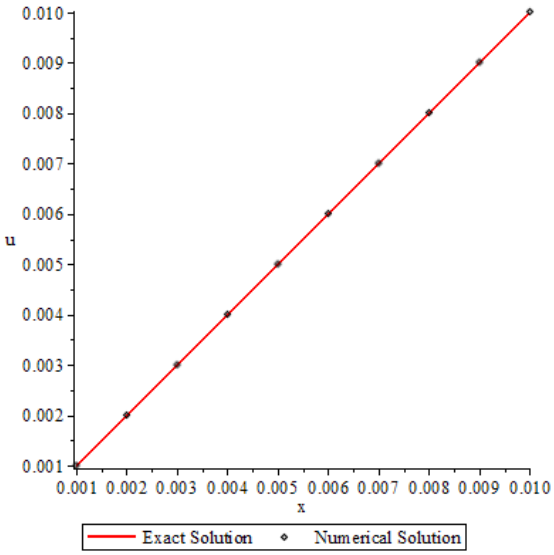


Fig. 2 Plot 2D of the exact solutions result of heat transfer Lighthill Singular integral equation for example 2.

Example3. Consider the heat transfer Lighthill Singular integral equation

$$u(x) = 2\sqrt{x} - \int_0^x \frac{1}{\sqrt{x-t}}u(t)dt$$
$$x\epsilon[0,2]$$

Applying the Adomian Decomposition Method using Maple, we find

Table 3 Numerical results and exact solution of heat transfer Lighthill Singular integral equation for example 3.

x	$u(x)$	$Exact = 1 - e^{\pi x} erfc(\sqrt{\pi x})$	$Error$
0.00100	0.0602316	0.0602315	0.0000002
0.00200	0.0835154	0.0835145	0.0000009
0.00300	0.1007661	0.1007636	0.0000025
0.00400	0.1149105	0.1149055	0.0000050
0.00500	0.1270797	0.1270710	0.0000087
0.00600	0.1378525	0.1378389	0.0000136
0.00700	0.1475722	0.1475523	0.0000199
0.00800	0.1564618	0.1564341	0.0000277
0.00900	0.1646760	0.1646391	0.0000370
0.01000	0.1723273	0.1722794	0.0000479

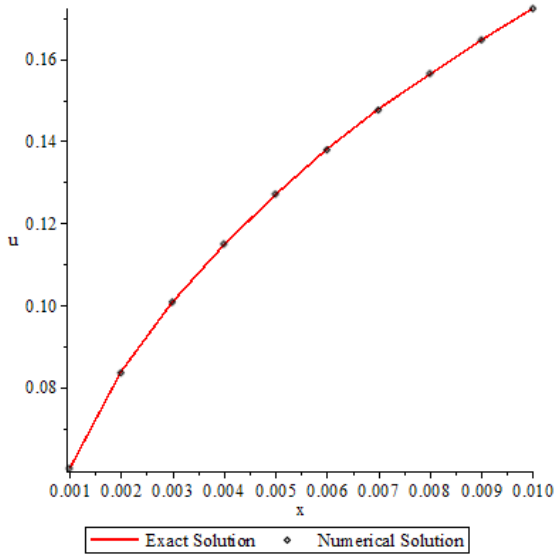


Fig. 3 Plot 2D of the exact solutions result of heat transfer Lighthill Singular integral equation for example 3.

CONCLUSIONS

In this paper, we are frequently directed to integral Volterra equations that are difficult to solve analytically when addressing numerous nonlinear issues in thermal conductivity, boundary layer heat transfer, chemical kinetics, and superfluidity. The domain decomposition method is provided in this article for solving nonlinear Volterra integral equations with a single weak core. The Maple program was used to produce numerical results as well as drawings illustrating the degree of accuracy between the numerical and accurate solutions. Some examples are given to demonstrate the scheme's applicability and accuracy. Other numerical methods can be used in the future, and the results of the numerical solution can be compared to the exact solution.

Some examples are given to demonstrate the scheme's applicability and accuracy. We can apply different numerical methods in the future, and we may extend the current method to a system of nonlinear Volterra integral equations and nonlinear Volterra integral equations of the mix type or the first type by comparing the results of the numerical solution with the exact solution.

ACKNOWLEDGMENTS

This paper was supported by the Deanship of Scientific Research (DSR), King Abdulaziz University, Jeddah.

REFERENCES

[1] T. Diogo, J. Ma, M. Rebelo, Fully discretized collocation methods for nonlinear singular Volterra integral equations, J. Comput. Appl. Math. 247 (2013), 84-101.

[2] M. Rebelo, T. Diogo, A hybrid collocation method for a nonlinear Volterra integral equation with weakly singular kernel, J. Comput. Appl. Math. 234 (2010), 2859-2869.

[3] P. Baratella, A Nystrom interpolant for some weakly singular nonlinear Volterra integral equations, J. Comput. Appl. Math. 237 (2013), 542-555.

[4] S. S. Allaei, T. Diogo, M. Rebelo, The Jacobi collocation method for a class of nonlinear Volterra integral equations with weakly singular kernel, J. Sci. Compute.

[5] E. L. Ortiz, H. Samara, An operational approach to the Tau method for the numerical solution of nonlinear differential equations, Computing. 27 (1981), 15-25.

[6] G. Ebadi, M. Y. Rahimi-Ardabili, S. Shahmorad, Numerical solution of the nonlinear Volterra integro-differential equations by the Tau method, Appl. Math. Comput. 188 (2) (2007), 1580-1586.

[7] F. Ghoreishi, M. Hadizadeh, Numerical computation of the Tau approximation for the Volterra-Hammerstein integral equations, Numer. Algor. 52 (2009), 541-559.

[8] S. M. Hossieni, S. Shahmorad, Tau numerical solution of Fredholm integro diff erential equations with arbitrary polynomial bases, Appl. Math. Model. 27 (2003), 145-154.

[9] G. Adomian, Solving Frontier Problems of Physics: The Decomposition Method, Kluwer Academic Publishers, Dordrecht. (1994).

[10] A.M. Wazwaz, The variational iteration method; a reliable tool for solving linear and nonlinear wave equations, Comput. Math. Appl., 54 (2007) 926–932.

[11] A.M. Wazwaz, A First Course in Integral Equations, World Scientific, Singapore, (1997).

[12] A.M. Wazwaz, Suheil A. Khuri, The variational iteration method for solving the Volterra integro-differential forms of the lane-Emden and the Emden-Fowler problems with initial and boundary value conditions, DE GRUYTER Open Eng. (2015);5:31-41.

[13] J. H. He, "Homotopy perturbation technique", Computer Methods in Applied Mechanics and engineering. 178, 1999, pp. 257-262.

[14] J. H. He, "A coupling method of a homotopy technique and a perturbation technique for non-linear problems", International Journal of Non-Linear Mechanics, Vol. 35, 2000, pp. 37-43.

[15] J. H. He, "Homotopy perturbation method: anew non-linear analytical technique", Applied Mathematics and Computation, Vol. 135, 2003, pp.73-79.

[16] J. H. He, "Asymptotology by homotopy perturbation method", Applied Mathematics and Computation. 156, 2004, pp. 591-596.

[17] J. H. He, "Application of homotopy perturbation method to nonlinear wave equations", Chaos, Solitons and Fractals, Vol. 26, 2005, pp. 695-700.

[18] J. H. He, "Homotopy perturbation method for solving boundary value problems", Physics Letters A, Vol. 350, 2006, pp. 87-88.

[19] J. H. He, "New interpretation of homotopy perturbation method", International Journal of Modern Physics B, Vol. 18, 2006, pp. 2561-2568.

[20] V. Balakumar, K. Murugesan, Numerical Solution of Systems of Linear Volterra Integral Equations Using Block-Pulse Functions, Malaya Journal of Matematik, S(1)(2013)77-84.

[21] L.C. Becker and M. Wheeler, Numerical and Graphical Solutions of Volterra Equations of the Second Kind, Maple Application Center, 2005.

[22] R.L. Burden and J. Douglas Faires, Numerical Analysis, 8th ed., Thomson Brooks/Cole, Belmont, CA, 2005.

[23] T. A. Burton, Volterra Integral and Differential Equations, 2nd ed., Mathematics in Science & Engineering, 202, Elsevier, 2005.

[24] M.I. Berenguer, D. Gamez, A. I. Garralda-Guillem, M. Ruiz Galan, and M.C. Serrano Perez, Biorthogonal Systems for Solving Volterra Integral equation Systems of the Second Kind, Journal of Computational and Applied Mathematics,235(7) (2011),1875-1883.

[25] J. Biazar and M. Eslami, Modified HPM for Solving Systems of Volterra Integral Equation of the Second Kind, Journal of King Saud University-Science, 23(1) (2011),35-39.

[26] P. Linz, Analytical and Numerical Methods for Volterra Equations, Studies in Applied Mathematics 7, SIAM, Philadelphia, 1985.

[27] P. Linz, A simple approximation method for solving Volterra integro-differential equations of the first kind, J. Inst. Math. Appl., 14 (1974) 211–215.

[28] F. Mirzaee, Numerical Computational Solution of the Linear Volterra Integral Equations System Via Rationalized Haar Functions, Journal of King Saud University- Science, 22(4) (2010),265-268.

[29] A.M. Wazwaz, Linear and Nonlinear Integral Equation: Methods and Applications, Springer, 2011.

[30] S. Effati and M.H. NooriSkandari, Optimal Control Approach for Solving Linear Volterra Integral Equations, I.J. Intelligent Systems and Applications, 2012,4,40-46.

[31] D.A. Maturi, Numerical Solution of System of Two Nonlinear Volterra Integral Equations, International Journal of Computers & Technology, Vol12, No.10, pp.3967-3975,2014.

[32] D.A. Maturi, A.Z. Bajamal, B.M.AlGethami, Numerical Solution of Volterra Integral Equation of Second Kind Using Implicit Trapezoidal, Journal of Advances In Mathematics, Vol8, No.2, pp.1540-1553,2014.

[33] Dalal A. Maturi, Adomian Decomposition Method of Fredholm Integral Equation of the Second Kind Using Maple, Journal of Advances In Mathematics, Vol9, No.1, pp.1868-1875,2014.

[34] Dalal A. Maturi, Application of Adomian Decomposition Method for Solving of Fredholm Integral Equation of the Second Kind, European Journal of Science and Engineering, Vol9, No.2, pp.1-9,2014.

[35] H.H. Sorkun, S. Yalcinbas, Approximate solutions of linear Volterra integral equation systems with variable coefficients, Applied Mathematical Modeling, 34(2010) 3451-3464.

[36] Dalal A. Maturi, Honaida M. Malaikah, Numerical Solution of System of Three Nonlinear Volterra Integral Equation Using Implicit Trapezoidal, Journal of Mathematics Research; Vol. 10, No. 1; February 2018, ISSN

1916-9795 E-ISSN 1916-9809, doi:10.5539/jmr.v10n1p44URL: https://doi.org/10.5539/jmr.v10n1p44.

[37] Dalal Adnan Maturi, The Modified Decomposition Method For Solving Volterra Integral Equation Of The Second Kind Using Maple, International Journal of GEOMATE, Oct. 2019 Vol.17, Issue 62, pp. 23-28.

[38] Dalal Adnan Maturi, Amal Ibrahim Aljedani, Eman Salem Alaidarous, Finite Difference Method For Solving Heat Conduction Equation Of The Granite, International Journal of GEOMATE, Sept. 2019 Vol.17, Issue 61, pp. 135 -140. ISSN: 2186-2982 (P), 2186-2990 (O), Japan.

[39] Dalal Adnan Maturi, Finite Difference Method For Solving Heat Conduction Equation Of The Brick, International Journal of GEOMATE, April ,2020 Vol.18, Issue 68, pp. 114-119.

[40] Dalal Adnan Maturi, Eman Ahmed M. Simbawa, The Modified Decomposition Method For Solving Volterra Fredholm Integro-Differential Equation Using Maple, International Journal of GEOMATE, March 2020 Vol.18, Issue 67, pp. 84-89.

7th Int. Conf. on Structure, Engineering & Environment (SEE), Pattaya, Thailand, Nov.10-12, 2021, ISBN: 978-4-909106070 C3051

JUSTIFICATION OF RESIDUE MATERIAL IN GROUND IMPROVEMENT OF COASTAL SOILS: AN APPLICATION OF COIR FIBRE

S. Islam[1], H. Islam[1], O. C. Debanath[1], M. A. Rahman[1], S. M. Farooq[1]

[1]Department of Civil Engineering, Chittagong University of Engineering & Technology, Chattogram-4349, Bangladesh

ABSTRACT

Living in the downstream end of the Himalayan Belt, Bangladesh is suffering significantly due to the presence of soft, fine-grained soils at the upper stratum. The scenario is worst along the coastline of the country. Conventional pile foundation can overcome this problem; however, the project cost is very high and may not be feasible for a developing country like Bangladesh. Instead, the ground improvement technique is a plausible approach. Among several approaches, the replacement of soft soils with eco-friendly materials has spotlighted in recent years. In line with the trend, this research evaluates the suitability of using coir fibre as a replacement of soils, keeping an aim to increase the bearing capacity of existing soft soils. A series of Unconfined Compressive Strength (UCS) tests have been conducted for different fibre contents and lengths to check the improvement of bearing capacity. Significant improvement of strength has been observed with the increment of both fibre length and percentage. The maximum UCS has been found for soil improved with 0.6% fibre content having 50mm length, which are around 2.75 times of original soil. This is because coconut coir fibre's combined effect changes the soil's brittle behaviour to ductile behaviour.

Keywords: Soft clay, Coir fibre, Coastal soil, Unconfined compressive strength, Ground improvement

INTRODUCTION

Ground improvement is a general term for any physical, chemical, mechanical, biological, or combined method of changing a natural soil to meet an engineering purpose. Improvements include increasing the bearing capacity, tensile strength, and overall performance of in-situ subsoil.

Huge number of waste materials are composed worldwide because of the expeditious industrialization and urbanization, causing frightful menace to public health and the ecosystem. Yet, in practice, the application of these waste materials needs standardized experiments to pursue their feasibility. By scrutinizing these circumstances, a numerous number of investigations and experiments have been occurred over the last few years. The most used by-product materials and natural fibres for soil strengthening are cement, rice-husk-ash, fly ash, date fibre, jute fibre, polypropylene fibre, coconut fibre, bamboo strip, flax fibre etc. The use of natural fibres, agro-wastes are increasing since the last decade as a soil reinforcing agent. Natural fibres have some advantage over other soil reinforcing materials due to their lightweight, high strength, biodegradability and availability throughout the world [1]–[4].

The fibres increase the cohesion among the soil particles; a combination of bamboo strips and flax fibre increase the cohesion of clay soil by 26% [5]. In addition, the interaction of the fibres among themselves and the fibres' flexibility makes them behave as a structural mesh that holds the soil together, increasing the soil structural integrity. The length and diameter of fibre govern the improvement characteristics, generally higher length shows better performance in terms of strength improvement.

Around 1.5 to 2.0 % of jute fibre is enough to substantially improve the CBR value of soft soil [6], [7]. Jute fibre is also efficient to increase the shear resistance of soft and expansive soil. However, higher water content induces a lubricating effect at the soil-fibre interface hence reduce the reinforcing effect [2].

Coconut trees grow widely in tropical areas worldwide, such as Asia, Central and South America, and Africa. Coconut fibre, mostly known as coir fibre is significantly stronger than other fibre, even with a smaller diameter, and more available worldwide than date palm fibre and cheaper than polypropylene. Coir is biodegradable and it takes approximately 20 years to decompose above ground. Typically 0.5 to 2.0% of coir fibre is optimum for soil reinforcement [8]. Application of industrial by-products like rice husk ash along with coir fibre presents better efficiency; in some cases higher compressive strength around 140 kPa was obtained [9].

Bangladesh is a deltaic plain, and most of its formation is sedimentary deposition in the upper stratum and undergoes rapid urbanization and industrialization to meet up the increasing economic growth of the country. Chattogram is the second largest city of Bangladesh and the major seaport of

the country. Consequently, the coastal area of Chattogram has given high priority for the upcoming developments of the country's infrastructures. Due to the presence of soft soil layer, laying a safe foundation is a concerning issue for the engineering community. This research aims to investigate the feasibility of using coir fibre to improve the bearing capacity of coastal soil. Specifically, the improvement of strength characteristics was examined by laboratory tests.

MATERIALS

The coastal soil used for this study was collected from two distinct points on the eastern bank of river Karnaphuli along the Chattogram coastal line. The samples were collected from shallow depth. Fig. 1 shows the study area map representing the sampling location, and fig. 2 shows the distribution of particle sizes (ASTM D 7928) for soils. The engineering properties of the soil samples are shown in table 1. As the liquidity index of both samples was found above 0.5, the soils are soft in their natural state. According to the unified soil classification system (ASTM D 2487), the soil samples were classified as clay (CL).

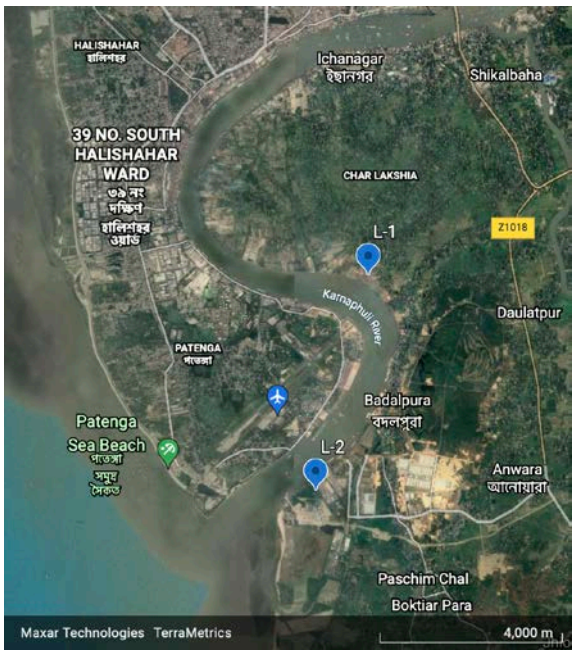


Fig. 1 Location map of the study area

Coconut fibre is a natural fibre extracted from the husk of Coconut. It is manufactured from retted coconut husks through a process called defibring. The coir fibre thus extracted is then combed using steel combs to make the fibre clean and remove short fibres. The coir fibre used for the current study was collected from a local factory and then cut into desired lengths. Two different fibre length (30mm & 50mm) was used for sample preparation, and varying percentage of fibre content up to 0.6% was replaced.

Table 1 Geotechnical properties of used soil

Properties	Location -1	Location -2
Specific gravity	2.79	2.75
Water content (%)	32.5	32.6
Liquid limit (%)	38.0	41.2
Plastic limit (%)	21.00	23.0
Plasticity index (%)	17.0	18.2
Liquidity index (%)	0.68	0.53

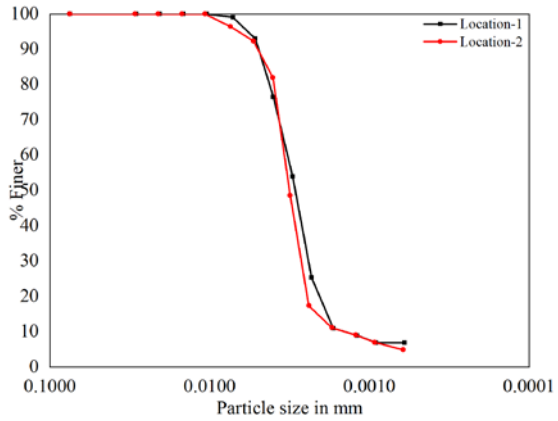


Fig. 2 Grain size analysis of parent soils

EXPERIMENTAL PROGRAM

The collected soil samples were dried, pulverized and stored for the next step, and the coir fibre was prepared at the desired length. Previous literature suggested that up to 1% fibre content is sufficient for soil reinforcing [10]. In this experimental program, the fibre content was varied by two lengths, 30mm and 50mm, along with the following percentage of fibre by weight of dry soil: 0, 0.2, 0.4 and 0.6%. At the first step of the research, standard proctor test was conducted for each soil-fibre mix to determine the moisture density relationship of each mix.

Unconfined compressive strength (UCS) tests were conducted at three different curing ages (0, 7 and 28 days) for various soil-fibre combinations compacted to their corresponding optimum moisture content. Fibre reinforced specimens for UCS tests were cured in air sealed conditions to intact the optimum moisture until testing.

RESULT AND DISCUSSION

Compaction characteristics

Figure 3 represents the compaction characteristics of coir fibre treated and untreated coastal soils with different fibre content percentages. The maximum

dry unit weight decreases with the increasing percentage of fibre content, whereas the optimum moisture content shows the reverse trend.

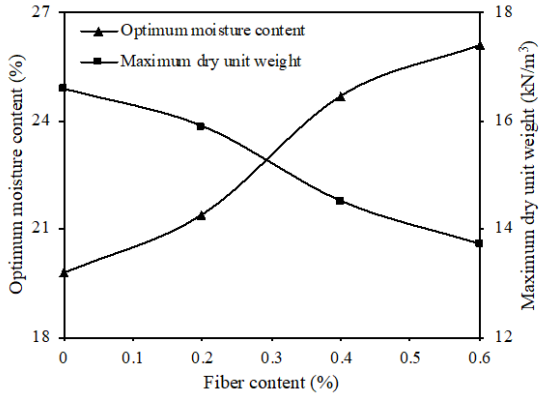


Fig. 3 Variation of compaction characteristics

The optimum moisture content of soil-fibre mixes varied within 1 to 5% of the parent soil. Similarly, the maximum dry density varied between 13.7 to 16.58 kN/m^3. The coir fibre specimens absorb water during the mixing process, leading to the continuous increment of optimum moisture content. Consequently, the decreases in dry unit weight of fibre reinforced soil specimen are due to the replacement of heavy soil portions with relatively lower density of fibre [10], [11].

Strength of fibre reinforced coastal soil

A series of unconfined compression test were performed on coir fibre treated coastal soil. The improvement of strength characteristics of fibre treated soil was determined by unconfined compressive strength. To observe the strength improvement during curing period, the samples were kept in a moisture sealed condition for up to 28 days and tested at 0, 7 and 28 days. The unconfined compressive strength of fibre treated coastal soil of location 1 and location 2 is plotted in fig. 4 and 5, respectively.

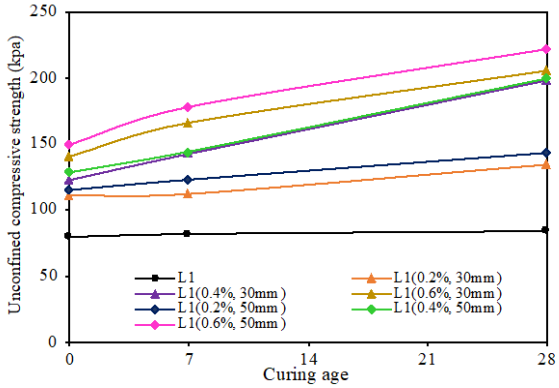


Fig. 4 UCS of fibre treated soil (Location-1)

The addition of coir fibre increases the unconfined compressive strength of soil for both locations. The UCS value of untreated soil was found 70 and 81kpa, respectively for locations 1 and 2, which indicates the soils are soft clay in the natural state. And the maximum strength was found 225 kpa for 0.6% fibre content and 50 mm fibre length. However, the variation of UCS due to the varying length of fibre was found within a close range. At the early stage of curing (0 and 7days), sufficient improvement of strength of coir fibre treated soils was found, indicating that the fibre reinforcement of soil is time independent and provides instantaneous improvement, whereas the other ground improvement techniques are curing time-dependent.

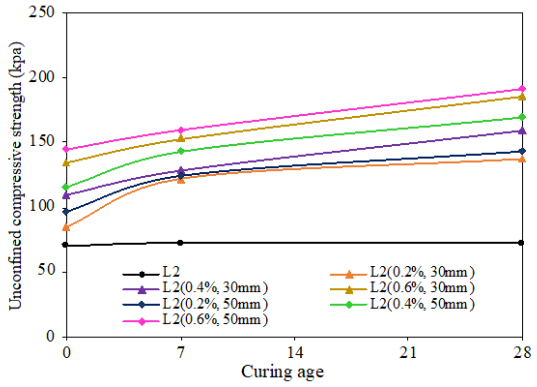


Fig. 5 UCS of fibre treated soil (Location-2)

The insight mechanism continuous strength improvement due to increment of fibre content can be explained as follows:
When shear failure occurs at the of the soil-fibre reinforced UCS samples, the tensile stress developed in the failure interface is taken by the fibre and the relative displacement of fibre surface and the surrounding soil particle is restrained [2]. Hence, the resistance to the soil-fibre interface is continuously increasing due to the increasing percentage of coir fibre in soil and shows an increasing trend of UCS value for all cases regardless of the fibre length.

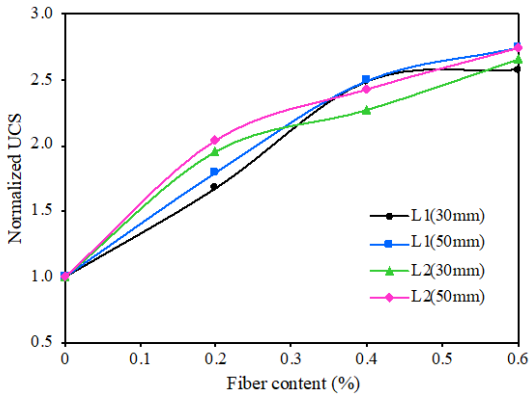


Fig. 6 Normalized UCS vs fibre content

Figure 6 represent the variation of normalized UCS with fibre content of 0 to 0.6% after 28 days of curing age. The normalized UCS value is the ratio of the UCS of untreated soil to that of the fibre treated soil. A steep increment of normalized strength was observed for fibre content of 0.2%, which is around 2.0 times of untreated soil and become slow down after that, which indicates that the improvement process reaches near to optimum. The maximum normalized UCS was found as 2.75 for 0.6% fibre content. After the final curing age, all the normalized UCS values lies within a close range regardless of the sampling location. Another reason for increasing UCS due to fibre inclusion is to increase their energy absorbing capacity or toughness so that the soil-fibre exhibit a more ductile behavior.

CONCLUSIONS

A series of unconfined compressive strength tests were conducted on unreinforced and coir fibre reinforced coastal soil specimens (having varying fibre content and length) prepared at corresponding optimum moisture content. The experimental results of this study bring forth to the following conclusions:

- The maximum dry unit weight decreases with the increment of coir fibre content, whereas the optimum moisture content shows the reverse trend.
- The unconfined compressive strength of both locations increases with the increment of fibre content and length. However, the effect of fibre length variation can be taken as negligible.
- The UCS values of fibre reinforced soil specimens shows instantaneous (0 days) strength improvement, which eliminates the time barrier of conventional ground improvement.
- The maximum UCS value was found 225 kpa that is approximately 2.75 times that of untreated coastal soil, and only 0.6% fibre content is sufficient to develop this strength.

This indicates that the coir fibre reinforcing is an efficient technique for coastal soil improvement, and 0.6% fibre content can be taken as optimum based on the current study

REFERENCES

[1] Qu J. and Zhao D., Stabilising the cohesive soil with palm fibre sheath strip. *Road Mater. Pavement Des.*, Vol. 17, Issue 1, 2016, pp. 87 - 103.

[2] Yixian W., Panpan G., Shengbiao S., Y Haiping., and Binxiang Y., Study on Strength Influence Mechanism of Fiber-Reinforced Expansive Soil Using Jute. *Geotech. Geol. Eng.*, Vol. 34, Issue 4, 2016, pp. 1079-1088.

[3] Ayininuola G. M. and Oladotun P. O., Geotechnical Properties of Coconut Coir Fiber Soil Mixture. *J. Civ. Eng. Res.*, Vol. 6, Issue 4, 2016, pp. 79-85.

[4] Al Adili A., Azzam R., Spagnoli G., and Schrader J., Strength of soil reinforced with fiber materials (Papyrus). *Soil Mech. Found. Eng.*, Vol. 48, Issue 6, 2012, pp. 241-247.

[5] Tong F., Ma Q. and Xing W., Improvement of Clayey Soils by Combined Bamboo Strip and Flax Fiber Reinforcement. *Adv. Civ. Eng.*, Vol. 2019, 2019, pp. 1-10.

[6] Kumar D., Nigam S., Nangia A. and Tiwari S., Improvement in CBR Values of Soil Reinforced with Jute Fibre. *Int. J. Eng. Tech. Res.*, Vol. 3, Issue 5, 2015, pp. 290–293.

[7] Y. Sharma, D. G. M. Purohit, and S. Sharma, "Improvement of Soil Properties by Using Jute Fibre as Soil Stabilizer," *Am. J. Eng. Res.*, Vol. 6, no. 10, pp. 123–129, 2017.

[8] V. Anggraini, "Potential of Coir Fibres as Soil Reinforcement," *Pertanika J. Sch. Res. Rev.*, Vol. 2, no. 1, pp. 95–106, 2016.

[9] Nandan M. S., Sai K. V., Rakesh P., Kumar N. S. and Chamberlin K. S., Stabilisation of Red Soil By using Coconut Coir Fibre and Rice Husk Ash. *Int. J. Innov. Technol. Explor. Eng.*, Vol. 9, Issue 3, 2020, pp. 535–540.

[10] Amadi H. O., Eberemu A.A., and Momoh A.O., Use of coir fiber reinforcement technique to improve strength of cement kiln dust treated black cotton soil subgrade. In *Int. Conf. on Geosynthetics for Water Resources and Energy Challenges*, 2013, pp. 223–229.

[11] Shukla D., Rajan S., Saxena A. K. and Jha A. K., Soil Stabilization Using Coconut Coir Fibre. *Int. J. Res. Appl. Sci. Eng. Technol.*, Vol. 3, Issue 9, 2015, pp. 305–309.

7th Int. Conf. on Structure, Engineering & Environment (SEE), Pattaya, Thailand, Nov.10-12, 2021, ISBN: 978-4-909106070 C3051

INFLUENCE OF TALCUM ON THERMAL AND MECHANICAL PROPERTIES OF STEREOCOMPLEX POLYLACTIDE-*b*-POLYETHYLENE GLYCOL-*b*-POLYLACTIDE BIOPLASTIC

Yaowalak Srisuwan and Yodthong Baimark

Biodegradable Polymers Research Unit, Department of Chemistry and Center of Excellence for Innovation in Chemistry, Faculty of Science, Mahasarakham University, Mahasarakham 44150, Thailand;

ABSTRACT

Stereocomplex polylactide-*b*-polyethylene glycol-*b*-polylactide triblock copolymer (scPLA-PEG-PLA)/talcum composites were prepared by melt blending of poly(L-lactide)-*b*-polyethylene glycol-*b*-poly(L-lactide) (PLLA-PEG-PLLA), poly(D-lactide)-*b*-polyethylene glycol-*b*-poly(D-lactide) (PDLA-PEG-PDLA) and talcum (0–8 wt.%). The PLLA-PEG-PLLA/PDLA-PEG-PDLA ratio was kept constant at 80/20 w/w. Differential scanning calorimetry (DSC), X-ray diffractometry (XRD), dynamic mechanical analysis (DMA) and tensile testing were carried out to characterize the thermal and mechanical properties of the composites. The DSC and XRD results indicated that degrees of crystallinity for PLA homo-crystallites of the composites were increased with the talcum content but there was no increase for PLA stereocomplex-crystallites. The heat resistance of composite films increased as the talcum content increased as determined from DMA. The talcum did not affect tensile properties of the composite films. These results showed that the talcum acted as a nucleating agent to enhance crystallizability on only homo-crystallites of scPLA-PEG-PLA.

Keywords: Bioplastics, Poly(L-lactide), Stereocomplex, Nucleating agent, Heat resistance

INTRODUCTION

Poly(L-lactic acid) or poly(L-lactide) (PLLA) is an important bioplastic that has been widely investigated for use instead of commodity petroleum-based plastics to reduce plastic-waste pollution. This is due to the PLLA being non-toxic, bio-renewable, biodegradable and easily processable [1–3]. However its low flexibility and poor heat-resistance have limited some applications such as hot-fill packaging and microwave applications, etc. [4, 5].

PLLA-*b*-polyethylene glycol-*b*-PLLA triblock copolymers (PLLA-PEG-PLLA) are highly flexible because the PEG middle-blocks induced plasticizing effects for PLLA end-blocks [6, 7]. The PLLA-PEG-PLLA are also biocompatible and biodegradable [8, 9]. However, the flexible PLLA-PEG-PLLA still showed poor heat-resistance.

Stereocomplex polylactides (scPLA) are polymer blends between PLLA and poly(D-lactide) (PDLA) chains [10-12]. Stereocomplex crystallites of stereocomplex polylactides (scPLA) exhibited higher melting-temperatures (approximately 210–240˚C) and faster crystallization-rate than the homo-crystallites of PLLA [10]. However, scPLA-PEG-PLA or PLLA-PEG-PLLA/PDLA-PEG-PDLA blends still had low heat-resistance [13].

It has been reported that the heat resistance of PLLA can be improved by increasing their crystallinity-contents [5, 14]. Talcum is an effective nucleating-agent for developing the crystallinity content of PLLA [5, 15]. The high crystallinity-content PLLA obtained by talcum blending promoted good heat-resistance [5]. scPLA-PEG-PLA/talcum composites have not been reported in the literature. Therefore, this paper studied the effect of talcum on crystallizability, heat resistance and mechanical properties of scPLA-PEG-PLA.

MATERIALS AND METHODS

Materials

PLLA-PEG-PLLA and PDLA-PEG-PDLA were synthesized by ring-opening polymerization in bulk at 165˚C for 6 hours under nitrogen atmosphere as described in our previous work [13]. PEG with molecular weight of 20,000 g/mol and stannous octoate were employed as the initiating system. Molecular-weight characteristics obtained from gel permeation chromatography (GPC) are reported in Table 1. Talcum powder with 10 μm in particle size was supplied by Thai Poly Chemical Co., Ltd. (Thailand).

Table 1 Molecular-weight characteristics from GPC analysis

Triblock copolymer	M_n[a] (g/mol)	Đ[b]
PLLA-PEG-PLLA	90,000	2.8

PDLA-PEG-PDLA	85,400	2.1

[a] Number-average molecular weight; [b] Dispersity index

Preparation of scPLA-PEG-PLA/talcum Composites

PLLA-PEG-PLLA, PDLA-PEG-PDLA and talcum were dried in vacuo at 50˚C overnight to remove moisture before melt blending using a Rheomix batch mixer (HAAKE Polylab OS). Melt blending was performed at 190˚C with a rotor speed of 100 rpm for 4 minutes. The PLLA-PEG-PLLA/PDLA-PEG-PDLA ratio was kept constant at 80/20 w/w. Composites with different talcum contents (1, 2, 4 and 8 wt.%) were prepared. PLLA-PEG-PLLA/PDLA-PEG-PDLA blend without talcum was also prepared by the same method for comparison.

The composite films were fabricated using a compression molding machine (Auto CH Carver) at 200˚C for 3 minutes without any force before compressing under 5 ton load for 1 minute. The obtained films were 100 × 100 mm in size and were then quickly cooled to 25˚C with water flow for 1 minute. The composites were dried in vacuo at 50˚C overnight before film compression.

Characterization of ScPLA-PEG-PLA/Talcum Composites

Thermal transition properties of the composites were studied using a differential scanning calorimeter (DSC, Perkin-Elmer Pyris Diamond) under nitrogen gas flow. The composites were first heated at 200˚C for 3 min to erase thermal history, then fast quenched before heating from 0 to 200˚C at a rate of 10˚C/min to measure glass transition (T_g), cold crystallization (T_{cc}) and melting (T_m) temperatures as well as enthalpies of melting (ΔH_m) and cold crystallization (ΔH_{cc}). The degree of crystallinity for homo-crystallites from DSC (DSC-$X_{c,hc}$) of the composites was calculated from Eq. (1).

$$DSC - X_{c,hc}(\%) = [(\Delta H_m - \Delta H_{CC})/(93.7 \times W_{PLA})] \times 100 \quad (1)$$

where the 93.7 J/g is the ΔH_m for 100%X_c PLA [16]. W_{PLA} is the PLA weight-fraction of the composites calculated from PLLA fraction (PLLA-PEG-PLLA and PDLA-PEG-PDLA = 0.83 obtained from ^{1}H-NMR [13]) and the talcum content.

Crystalline structures of the composite films were determined using a wide angle X-ray diffractometer (XRD, Bruker D8 Advance) at 25˚C in the angle range of 2θ = 5˚–30˚ equipped with a copper tube operating at 40 kV and 40 mA producing Cu–Kα radiation. Scan speed was 3˚/min. The X_c from XRD for homo-crystallites (XRD-$X_{c,hc}$) and for stereocomplex crystallites (XRD-$X_{c,sc}$) of composites were calculated from Eq. (2) and (3), respectively. Total X_c from XRD (XRD-X_c) was calculated from Eq. (4).

$$XRD - X_{c,hc}(\%) = [(A_{c,hc})/(A_{c,hc} + A_{c,sc} + A_a)] \times 100 \quad (2)$$

$$XRD - X_{c,sc}(\%) = [(A_{c,sc})/(A_{c,hc} + A_{c,sc} + A_a)] \times 100 \quad (3)$$

$$XRD - X_c(\%) = (XRD - X_{c,hc} + XRD - X_{c,sc}) \quad (4)$$

where the $A_{c,hc}$ and $A_{c,sc}$ are areas of XRD peaks of homo- and stereocomplex crystallites, respectively. The A_a is an area of amorphous halo.

Tensile properties of the composite films were determined using an universal mechanical testing machine (Liyi Environmental Technology LY-1066B) with a load cell of 100 kg, a crosshead speed of 50 mm/min and a gauge length of 50 mm. The film sizes were 100 mm × 10 mm. The averaged tensile properties were obtained from at least five measurements.

RESULTS AND DISCUSSION

Thermal Transition Properties

The thermal transition properties of composites were studied from DSC analysis. Fig. 1 shows DSC heating curves of the blends and the DSC results are summarized in Table 1.

The T_g of composites could not be found. The T_{cc} peaks had disappeared when the talcum content was increased up to 4 wt.%. DSC-$X_{c,hc}$ of composites increased with the talcum content. This indicates that talcum enhanced crystallization of scPLA-PEG-PLA by acting as a heterogeneous nucleating agent [5, 15]. The T_m peaks of composites did not change significantly.

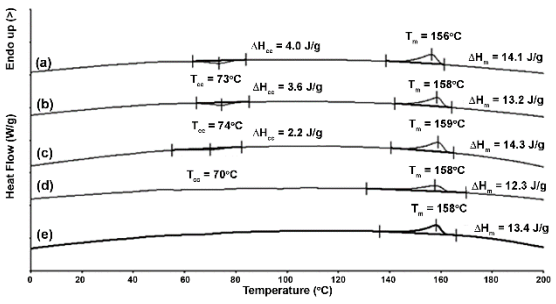


Fig. 1 DSC heating curves of scPLA-PEG-PLA blends (a) without talcum and with talcum contents of (b) 1, (c) 2, (d) 4 and (e) 8 wt.%.

Table 2 DSC results of scPLA-PEG-PLA/talcum

composites.

Talcum (wt.%)	T_{cc} (˚C)	T_m (˚C)	DSC-$X_{c,hc}$ (%)
-	73	156	13.2
1	74	158	13.7
2	70	159	16.2
4	-	158	16.8
8	-	158	20.0

Crystalline Structures

The crystalline structures of compressed films were investigated from XRD patterns as presented in Fig. 2. The scPLA-PEG-PLA film without talcum in Fig. 2 (a) had XRD peaks at 2θ = 12º, 21º and 24º assigned to the stereocomplex crystallites [17, 18] and at 2θ = 17º and 19º attributed to homo-crystallites [7].

All the composite films had XRD peaks of talcum at 2θ = 9.5º and 28.7º [19]. The various degrees of crystallinities of composite films are summarized in Table 3. It was found that the %$X_{c,hc}$ of composite films trended to increase but the %$X_{c,sc}$ did not change significantly as the talcum content increased. Therefore the %X_c also increased with increasing %$X_{c,hc}$. The talcum addition affected only homo-crystallization of scPLA-PEG-PLA but did not influence stereocomplex crystallization.

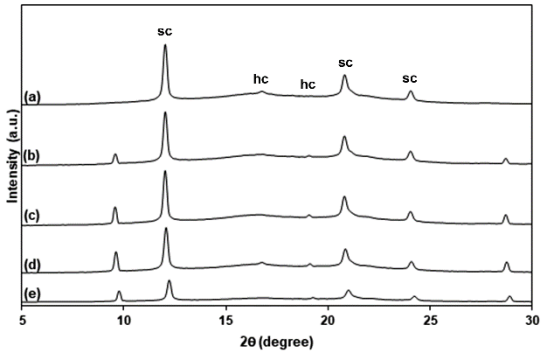


Fig. 2 XRD patterns of scPLA-PEG-PLA blend films (a) without talcum and with talcum contents of (b) 1, (c) 2, (d) 4 and (e) 8 wt.%.

Table 3 Degree of crystallinities from XRD patterns of scPLA-PEG-PLA/talcum composite films

Talcum (wt.%)	XRD-$X_{c,hc}$[a] (%)	XRD-$X_{c,sc}$[b] (%)	XRD-X_c[c] (%)
-	5.3	26.5	31.8
1	5.6	26.9	32.5
2	6.2	26.8	33.0
4	6.9	26.8	33.7
8	7.4	27.1	34.5

[a] Degree of crystallinity for homo-crystallites from XRD; [b] Degree of crystallinity for stereocomplex crystallites from XRD; [c] Total degree of crystallinity from XRD

Thermo-Mechanical Properties

Storage-modulus changes with a temperature scan from DMA analysis have been used to determine the heat resistance of scPLA [20, 21]. Poor heat-resistance of amorphous PLLA was reflected in decreased storage modulus in the region of glassy-to-rubbery transition before rising up again due to cold crystallization [5, 22]. Meanwhile the storage modulus of high crystallinity-content PLLA slowly dropped in the T_g region indicating that it had good heat-resistance [5].

Fig. 9 shows storage-modulus changes from DMA of composite films. It can be seen that the storage moduli of composite films decreased more slowly when the talcum content was higher. The results indicated that stiffness of composite films containing higher talcum-content were better maintained. This is due to the talcum acting as a heterogeneous nucleating agent to increase the XRD-X_c as reported in Table 3. Then, the heat resistance of scPLA-PEG-PLA films could be improved by talcum addition similar to the PLLA as described in the literature [5].

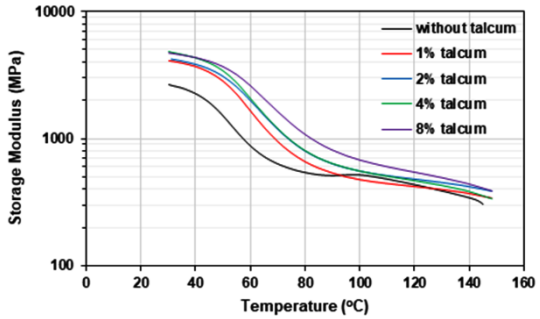


Fig. 3 Storage modulus changes as the function of temperature from DMA analysis of scPLA-PEG-PLA films without and with talcum.

Mechanical Properties

The mechanical properties of composite films were determined from tensile tests. The results are summarized in Table 4. It can be seen that the addition of talcum did not significantly change tensile properties of the composite films.

Table 4 Averaged tensile properties of scPLA-PEG-PLA/talcum composite films

Talcum (wt.%)	σ [a] (MPa)	ε [b] (%)	E [c] (MPa)

-	18.2 ± 2.6	33 ± 6	243 ± 29
1	17.1 ± 2.1	26 ± 5	242 ± 26
2	15.2 ± 1.8	34 ± 7	236 ± 23
4	16.8 ± 1.9	32 ± 4	251 ± 31
8	17.5 ± 1.2	37 ± 8	248 ± 36

[a] Ultimate tensile stress; [b] Strain at break; [c] Young's modulus.

CONCLUSIONS

The scPLA-PEG-PLA/talcum composite films were successfully prepared by melt blending following compression molding. The effects of talcum content on the crystallization, heat resistance and mechanical properties of composite films were determined. Talcum addition enhanced only homo-crystallization of scPLA-PEG-PLA as revealed by DSC and XRD data. The tensile properties of composite films were not affected by talcum addition. However, these composite films showed more extensibility (strain at break = 26–37%) than the PLLA film (strain at break = 5–10%) [7].

It was concluded that the crystallizability and heat resistance of scPLA-PEG-PLA films can be improved by talcum addition. scPLA-PEG-PLA composite films could be applied for use as flexible and efficient heat-resistant bioplastics.

ACKNOWLEDGEMENTS

This research was financially supported by the Office of National Higher Education Science Research and Innovation Policy Council (NXPO), Thailand (grant no. PMU B05F630023). The Center of Excellence for Innovation in Chemistry (PERCH-CIC), Office of the Higher Education Commission, Ministry of Education, Thailand is also acknowledged.

REFERENCES

[1] Castro-Aguirre E., Auras R., Selke S., Rubino M., and Marsh T., Enhancing the Biodegradation Rate of Poly(lactic acid) Films and PLA Bio-nanocomposites in Simulated Composting through Bioaugmentation. Polymer Degradation and Stability, Vol. 154, 2018, pp. 46–54.

[2] Silva D., Kaduri M., Poley N., Adir O., Krinsky N., Shainsky-Rotiman J., and Schroeder A., Biocompatibility, Biodegradation and Excretion of Polylactic acid (PLA) in Medical Implants and Theranostic Systems. Chemical Engineering Journal, Vol. 340, 2018, pp. 9–14.

[3] Samitthiwetcharong S., and Chavalparit O., Enhancement of Methane Production from Alkaline Pretreated Poly(lactic acid) Waste by the Co-digestion Process. International Journal of GEOMATE, Vol. 16, Issue 56, 2019, pp. 171-176.

[4] Nuzzo A., Coiai S., Carroccio S. C., Dintcheva N. T., Gambarotti C., and Filippone G., Heat-Resistant Fully Bio-based Nanocomposite Blends Based on Poly(lactic acid). Macromolecular Materials and Engineering, Vol. 299, 2014, pp. 31−40.

[5] Zhang X., Meng L., Li G., Liang N., Zhang J., Zhu Z., and Wang R., Effect of Nucleating Agents on the Crystallization Behavior and Heat Resistance of Poly(L-lactide). Journal of Applied Polymer Science, Vol. 133, 2016, Article No. 42999.

[6] Yun X., Li X., Jin Y., Sun W., and Dong T., Fast Crystallization and Toughening of Poly(L-lactic acid) by Incorporating with Poly(ethylene glycol) as a Middle Block Chain. Polymer Science Series A, Vol. 60, 2018, pp. 141−155.

[7] Baimark Y., Rungseesantivanon W., and Prakymoramas N., Improvement in Melt Flow Property and Flexibility of Poly(L-lactide)-b-poly(ethylene glycol)-b-poly(L-lactide) by Chain Extension Reaction for Potential Use as Flexible Bioplastics. Materials & Design, Vol. 154, 2018, pp. 73–80.

[8] Basu A., Kunduru K. R., Doppalapudi S., Domb A. J., and Khan W., Poly(lactic acid) Based Hydrogels. Advanced Drug Delivery Reviews, Vol. 107, 2016, pp. 192–205.

[9] Danafar H., Rostamizadeh K., Davaran S., and Hamidi M., Drug-conjugated PLA-PEG-PLA Copolymers: A Novel Approach for Controlled Delivery of Hydrophilic Drugs by Micelle Formation. Pharmaceutical Development and Technology, Vol. 22, Issue 8, 2017, pp. 947–957.

[10] Tsuji H., Poly(lactic acid) Stereocomplexes: A Decade of Progress. Advanced Drug Delivery Reviews, Vol. 107, 2016, pp. 97–135.

[11] El-Khodary E., Fukui Y., Yamamoto M., and Yamane H., Effect of the Melt-Mixing Condition on the Physical Property of Poly(L-lactic acid)/Poly(D-lactic acid) Blends. Journal of Applied Polymer Science, Vol. 134, Issue 44, 2017, Article No. 45489.

[12] Li Y., Li Q., Yang G., Ming R., Yu M., Zhang H., and Shao H., Evaluation of Thermal Resistance and Mechanical Properties of Injected Molded Stereocomplex of Poly(L-lactic acid) and Poly(D-lactic acid) with Various Molecular Weights. Advances in Polymer Technology, Vol. 37, Issue 6, 2018, pp. 1674–1681.

[13] Pasee S., and Baimark Y., Improvement in Mechanical Properties and Heat Resistance of PLLA-b-PEG-b-PLLA by Melt Blending with PDLA-b-PEG-b-PDLA for Potential Use as High-Performance Bioplastics. Advances in

Polymer Technology, Vol. 2019, 2019, Article No. 8690650.

[14] Vadori R., Mohanty A. K., and Misra M., The Effect of Mold Temperature on the Performance of Injection Molded Poly(lactic acid)-based Bioplastic. Macromolecular Materials and Engineering, Vol. 298, Issue 9, 2013, pp. 981–990.

[15] Saeidlou S., Huneault M. A., Li H., and Park C. B., Poly(lactic acid) Crystallization. Progress in Polymer Science, Vol. 37, 2012, pp. 1657–1677.

[16] Li Y., Zhou H., Wen B., Chen Y., and Wang X., A Facile and Efficient Method for Preparing Chain Extended Poly(lactic acid) Foams with High Volume Expansion Ratio. Journal of Polymers and the Environment, Vol. 28, 2020, pp. 17–31.

[17] Han L., Yu C., Zhou J., Shan G., Bao Y., Yun X., Dong T., and Pan P., Enantiomeric Blends of High Molecular-Weight Poly(lactic acid)/Poly(ethylene glycol) Triblock Copolymers: Enhanced Stereocomplexation and Thermomechanical Properties. Polymer, Vol. 103, 2016, pp. 376–386.

[18] Cui L., Wang Y., Guo Y., Liu Y., Zhao J., Zhang C., and Zhu P., Effects of temperature and external force on the stereocomplex crystallization in poly(lactic acid) blends. Advances in Polymer Technology, Vol. 37, Issue 4, 2018, pp. 962–967.

[19] Battegazzore D., Bocchini S., and Frache A., Crystallization kinetics of poly(lactic acid)-talc composites. eXPRESS Polymer Letters, Vol. 5, Issue 10, 2011, pp. 849–858.

[20] Si W. –J., An X. –P., Zeng J. –B., Chen Y. –K., and Wang Y. –Z., Fully Bio-Based, Highly Toughened and Heat-Resistant Poly(L-lactide) Ternary Blends via Dynamic Vulcanization with Poly(D-lactide) and Unsaturated Bioelastomer. Science China Materials, Vol. 60, 2017, pp. 1008−1022.

[21] Masutani K., Kobayashi K., Kimura Y., and Lee C.W., Properties of Stereo Multi-Block Polylactides Obtained by Chain-Extension of Stereo Tri-Block Polylactides Consisting of Poly(L-lactide) and Poly(D-lactide). Journal of Polymer Research, Vol. 25, Issue 3, 2018, Article No. 74.

[22] Vadori R., Mohanty A. K., and Misra M., The Effect of Mold Temperature on the Performance of Injection Molded Poly(lactic acid)-Based Bioplastic. Macromolecular Materials and Engineering, Vol. 298, Issue 9, 2013, pp. 981−990.

THE DEVELOPMENT OF COST-EFFECTIVE INSTRUMENT FOR WASTE REDUCTION

Kantayut Trebooniti
[1]Faculty of Industrial Education, Rajamangala University of Technology Suvarnabhumi, Thailand

ABSTRACT

The gasket is the consumable equipment in the production line that needs to be replaced once deteriorated with ages or has an accident. Besides, producing different sizes of the gaskets by the plant itself without any suitable equipment usually causes much waste and time spending. To reduce production time and production costs, the researcher has developed the gasket cutting dividers from used spare parts within the factory. Then, the equipment was tested at various cutting angles to achieve the engineered tool performance and speed in the manufacture of custom gaskets. The gasket cutting divider was developed. The results of the preparation of the special tools as gasket cutting dividers enabled the plant to build self-made gaskets instead of ordering finished gaskets. In the 1st month, the invented gasket cutting tool reduced the cost of ordering gaskets by USD 2,240. In addition, replacing finished gaskets with own-cut gaskets reduced USD 2,356 gasket costs in the 2nd month. For the 3rd month, replacing finished gaskets with own-cut gaskets decreased the gasket budget by USD 2,524. Therefore, during the experimental 3-month period, the factory could save more than USD 2,373 on average for 3 months. Also, changing from ordering ready-made gasket to self-producing allowed employees within the factory to upskill the capability to build gasket cutter and create awareness of the possibility to increase cost-effectiveness from innovation.

Keywords: Cost Effectiveness, Cost Reduction, Gasket, Gasket Cutting Divider, Compasses, Self-Made Tool

INTRODUCTION

Fibers have been used by humans for the manufacturing of textiles and garments for a long time. Fibers can be classified into synthetic fibers, chemical fibers (from natural polymers), inorganic fibers, natural fibers. Natural fibers are usually plant-derived fibers but they could also be animal fibers [1]. Animal fibers are usually composed of amino acids that make up proteins, such as fibers from wool, goat hair, etc. Synthetic fibers could be sub-divided into polymerization fibers, polycondensation fibers, and polyaddition fibers. Synthetic fibers are often produced from petroleum products or petrochemicals. They involve bringing together monomers to form larger molecules in the form of polymers. Then the polymers are spun through the fiber press glasses. Synthetic fiber production can be done in 3 ways. The main method is dry spinning. The method applies a solvent suitable for the fiber to dissolve. Then inject the fibers through hot air to harden the fibers. The second method is wet spinning. With this method, fibers are produced by injecting the fibers from the fiber press glasses and cooled by passing them into water or a suitable solution to wash off the chemicals The third method is melt spinning. It is a method of injecting raw materials through fiber press glasses. Then, they are brought through hot air to harden the fibers [8].



Fig. 1 Synthetic fiber factory in Thailand.

Synthetic fiber factories often use a large number of circular tubes for the main passage of water, oil, CH2 reagents, gases, and chemicals. Between the pipe connections contains the gaskets with different sizes and designs to prevent heat leakage at every point. General Inspection of pipe flanges often finds that the gaskets have been deteriorated or have ended their service life rapidly and often need to be replaced. This short lifetime of usage increases the overall production cost. Finding solution to manage the gasket costs potentially decrease the cost of the factory and reduce the use of materials. This will also

help reduce the use of the world's resources, waste, and create savings for industrial plants which could decrease waste problem that industrialization generally contributed to [2-7].

Therefore, the researcher initiated to study and use the waste material inside the factory to make a tool gasket cutting dividers to replace the use of gaskets from the outside for the company's cost-saving.

METHODOLOGY

The researcher cut 304 stainless steel pipes with 10-mm. diameter to be 70 cm long. Then, the 70-cm. the pipe was arc weld with after head and ball bearing by applying Tungsten Inert Gas. A lock-slid rail behind the stainless steel pipe, a lock-slid saw blade holder, and a small saw blade was prepared. After that, all parts were assembled into gasket cutting dividers.



Fig. 2 Gasket cutting dividers.



Fig. 3 Finished workpiece.



Fig. 4 Sheet gasket cutting.

RESULT AND DISCUSSION

Applying invented gasket cutting dividers to cut gasket made the factory could produce 7 pieces of the 4-inched gasket in 15 minutes, 5 pieces of 8-inched gasket per 15 minutes, and 3 pieces of the 12-inched gasket in 15 minutes.

Table 1 Gasket cutting time

Gasket	No. of Pieces Produced	Production Time (Minutes)
4-inched gasket	7	15
8-inched gasket	5	15
12-inched gasket	3	15

In the 1st month, the start of the made gasket cutting tool reduced the cost of ordering gaskets. In addition, replacing finished gaskets with own-cut gaskets reduced USD 2,240 gasket costs per month. Out of this USD 2,240, USD 516 saving for 4-inched gasket, USD 600 saving for 8-inched gasket and USD 820 saving for the 12-inched gasket.

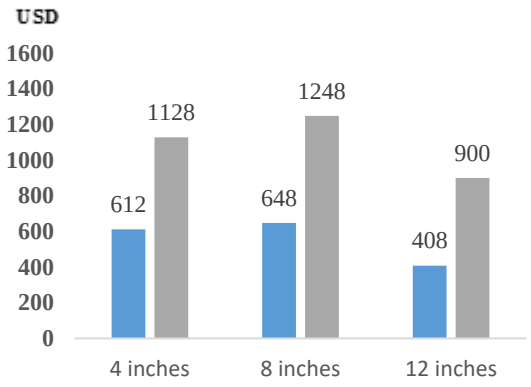


Fig. 5 Cost saving for the first month.

In the 2nd month, the start of the made gasket cutting tool reduced the cost of ordering gaskets. In addition, replacing finished gaskets with own-cut gaskets reduced USD 2,356 gasket costs per month. Out of this USD 2,356, USD 436 saving for 4-inched gasket, USD 680 saving for 8-inched gasket, and USD 1,240 saving for the 12-inched gasket.

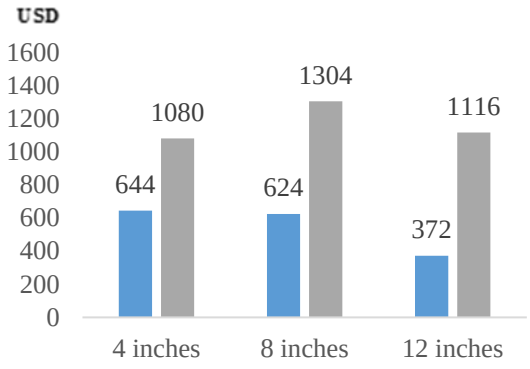


Fig. 6 Cost saving for the second month.

In the 3nd month, the start of the made gasket cutting tool reduced the cost of ordering gaskets. In addition, replacing finished gaskets with own-cut gaskets reduced USD 2,524 gasket costs per month. Out of this USD 2,524, USD 388 saving for 4-inched gasket, USD 696 saving for 8-inched gasket and USD 1,440 saving for the 12-inched gasket.

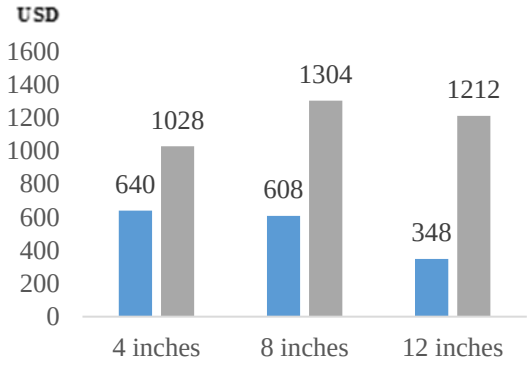


Fig. 7 Cost saving for the third month.

Average amount of cost-saving for 3 months, the start of the made gasket cutting tool reduced the cost of ordering gaskets. In addition, replacing finished gaskets with own-cut gaskets reduced USD 2,373 gasket costs for 3 months. Out of this USD 2,373 USD 632 saving for 4-inched gasket, USD 658 saving for 8-inched gasket, and USD 700 saving for the 12-inched gasket.

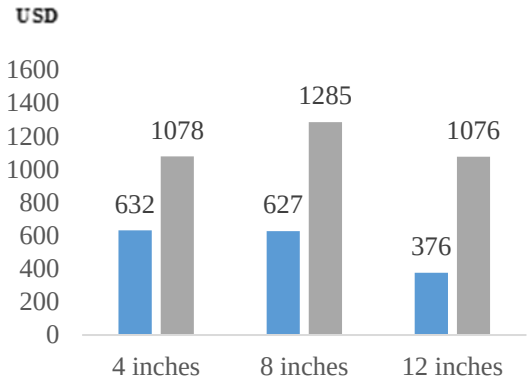


Fig. 8 Cost saving for the third month.

CONCLUSION

This study aimed to create the tool to cut the gasket from recycled materials that are available in the industrial plant in Suphan Buri and apply such tools for the factory's benefits. The second purpose was to find a way to reduce the use of working material and production cost for the factory. The gasket cutting dividers were developed from used spare parts within the factory and was tested at various cutting angles to achieve the engineered tool performance. When applying the self-made gaskets instead of ordering finished gaskets, the factory could save more than USD 2,373 on average for 3 months. In the 1st, 2nd and 3rd month, the invented gasket cutting tool reduced the cost of ordering gaskets by USD 2,240, USD 2,356 and USD 2,524 consecutively. Also, changing from ordering ready-made gasket to self-producing enhanced employees' capability to build gasket cutter and create awareness of the possibility to increase cost-effectiveness from innovation.

ACKNOWLEDGMENTS

The results of this experiment can be accomplished with great assistance from the consultation of the Faculty of Mechanical Engineering. Thank you to the Research and Development Institute. Rajamangala University of Technology Suvarnabhumi, the budget for the research and the Faculty of Mechanical Engineering, Faculty of Industrial Education Suphan Buri Center Providing facilities, tools, and support. The researcher is highly appreciated. including Synthetic fiber factory in Suphan Buri Province, Thailand. who contributed to the support of this research.

REFERENCES

[1] Franz Fourne., Synthetic Fibers Machines and Equipment, Manufacture Properties, pp. 5.

[2] Ngoc, U. N. and Schnitzer, H. Sustainable Solutions for Solid Waste Management in Southeast Asian Countries. Waste Management, Vol. 29, No. 6, 2009, pp. 1982–1995.

[3] Dhokhikah, Y. and Trihadiningrum, Y. Solid Waste Management in Asian Developing Countries: Challenges and Opportunities. Journal of Applied Environmental and Biological Science, ISSN: 2090-4274, Vol. 2, No. 7, 2012, pp. 329–335.

[4] Medina, M., The World's Scavengers Salvaging for Sustainable Consumption and Production. Globalization and the Environment, 2007.

[5] Arvind, K., Singh, S. K., Singh, G. P., and Gupta, P.K.Sustainable Municipal Solid Waste Management in Low Income Group of Cities: A Review. Tropical Ecology, Vol. 52, No. 1, 2011, pp. 123–131.

[6] Mohamad Satori, Erri N. Megantara, Ina Primiana F.M.S, Budhi Gunawan. Review of The Influencing Factors of Integrated Waste Management. International Journal of Geomate, Vol.15, Issue 48, 2018, pp.34-40.

[7] Kantayut Trebooniti., Thermal Energy Evaluation of the Incinerator Medical Waste, International Journal of GEOMATE, May., 2021, Vol.20, Issue 81, pp.112-117.

[8] Rudolf Hufenus, Yurong Yan, Martin Dauner and Takeshi Kikutani., Melt-Spun Fibers for Textile Applications. August 2020. pp. 2.

7th Int. Conf. on Structure, Engineering & Environment (SEE), Pattaya, Thailand, Nov.10-12, 2021, ISBN: 978-4-909106070 C3051

MACRO FABRIC MEASUREMENT WITH A NEW TECHNIQUE OF GLASGOW TILL

Prof. Radhi Alzubaidi

College of Engineering, University of Sharjah, United Arab Emirates

ABSTRACT

Glacial drift as embracing all rock material in transport by glacier ice, all deposits made by glacier ice, and all deposits predominantly of glacier origin made the sea or in bodies of glacial melt water, whether rafted in icebergs or transported in the water itself. Fissured are conventionally measured either from the block or cavity techniques. In present research a new techniques is utilized in which a sufficient number of oriented borehole samples are adopted. The study of Glasgow till clay fissures data include, fissure orientation, area, spacing, intensity, asperity and surface material. The fissures are found to be arranged in a definite geometric pattern, one near horizontal set and two vertical sets. Close agreement is found between the fissures data obtained from the new technique and those from other studies in the till using other techniques.

Keywords: Fissures, Glacial till, Macro fabric, Spacing, Intensity

INTRODUCTION

In Europe at the beginning of the nineteenth century most geologists regarded glaciers as a phenomenon peculiar to high altitude and latitudes with no role in geological processes elsewhere [1].Data were developed that challenges the canonical view that the Younger Drayas (c.12.9-11.7ka) was of glacier expansion across the North Atlantic[2]. They stated that 14 Boulders on moraines located within the inner sector of the Scottish Loch Lomond 15 Stadial (≈ Younger Dryas) ice cap yield cosmogonic exposure ages 12.8 – 11.3 ka with 16 a best estimate moraine age of 11.5 ± 0.6 ka. [3] conducted a 1:25,000 scale geomorphological map of the Glasgow region, western central Scotland, an area that was glaciated during the Last Glacial Maximum and, in part, during the Younger Dryas glaciation. They concluded that the geomorphological maps shows that the ice owed from the west to the east during most of the LGM, then changed to ow towards the southeast at the later stages of ice thinning and wastage, in response to topographic control. During the YD glaciation the ice owed southwards as a piedmont lobe into the southern end of the Loch Lomond Basin where it formed a well-developed end-moraine ridge. [4] reviewed existing information on the last glaciation of Caithness and presents new evidence for additional till units and for long distance ice-flow paths based on till palynomorphs, indicator erratics and striae. They stated that the multiple ice-flow events is consistent with the dynamic behavior of the last ice sheet exhibited in mathematical simulations. [5] stated that glacial deposits make up the biggest volume of deposits of the Quaternary system in Lithuania. In their study they explore the stiffness and deformation of till soils of the Medininkai glacial period and compare the obtained values with the glacial till soil properties with other tills. The results showed that the mechanical properties of till soils of the Medininkai glacial period shows that values obtained by different laboratory methods may be correlated, but may be rarely compared with values presented in the literature. [6] studied a number of failure in deep trenches and slope exaction in west central Scotland, they concluded that these failure occurred due to the presence of macrofabric features such as fissures. The influence of these fissure patterns on undrained shear strength and consolidation properties have been assessed using test specimens ranging from 76 to 254 mm diameter and correlations between observed laboratory anisotropic behavior and behavior in excavations have been suggested. [7]investigated into Dublin boulder clay ,laboratory tests to measure the undrained strength conducted using the triaxial machines ,they found that the behaviour of earth retained structures that intact, clayey, Dublin boulder clay formations are two to three times stiffer than assessed from high-quality laboratory tests on block samples. Dublin boulder clay is shown to be significantly stiffer than other well-characterised tills. They also concluded the measured engineering parameters for the Dublin boulder clay are favourable for many construction projects.

CLASSIFICATION AND FORMATION OF FISSURES

The first measurement of the attitude of fissures were reported by [8]during the investigation into Siwalik clay. Fookes defined the fissures as “small fractures existing in clay and silty- stone beds but not crossing the boundary of the bed or horizons with the bed”. Observations of fissures in London clay were carried out by [9]. The field observations of fissures includes, orientation, area, surface, geometric form of discontinuities, polish and stain. Orientation of fissures was defined by measuring the strike and dip of discontinuities using a compass and inclinometer. The area measurement includes the irregular dimensions of each fissure. The surface of fissures was classified into very rough, rough, moderately rough, smooth and very smooth.

TECHNIQUE OF MACROFABRIC STUDY

There are two types of techniques normally used in fabric study and termed by [10] as, cavity techniques and block technique .Both of the techniques were used to define the stone orientation and fissures study. The cavity technique is undertaken in the field by gradually digging a cavity extending to about 1 m3 while making the various observations about fissure orientation, coating etc. The block technique is undertaken un the laboratory on a large block of soil, collected in the field and re-oriented in the laboratory in its fields position. The observations as for the cavity technique are then made.

TECHNIQUE ADOPTED IN PRESENT STUDY

[11] used a technique called sample technique that developed by [12].Cumulative data from a number of 100 mm diameter borehole samples provide the description of fissuring. One sample set up for observation is shown in Fig. 1, the analyzing arrangement is simply formed from two Perspex plates mounted vertically and perpendicular to each other and fixed to a Perspex base. The three planes so formed provide the X, Y and Z axes of references. The perspex base carries a circular clamp within which the test sample is located and oriented with its cylindrical axis vertical.

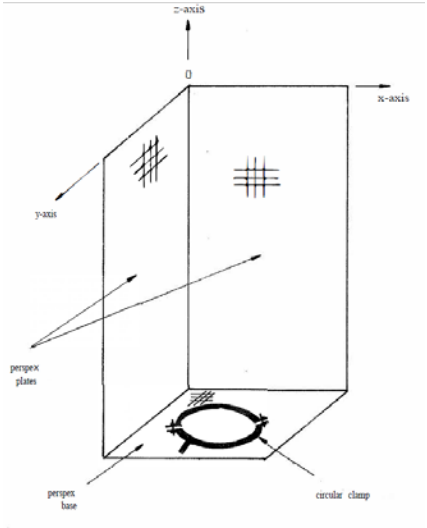


Fig. 1 Sample Technique Sketch

SAMPLING PROCEDURE

The field includes extracting the U100 samples by means of open drive sampling tubes of 100 mm internal diameter. The bottom of the sampling tube is fitted with a rigid cutting shoe. The tube is driven using a sliding hammer. Before driving the sampler, a line indicating the north direction is marked on the ground surface at the borehole using the compass, as the sampling tube is entered into the borehole the north direction is also marked on it. The tube is advanced far enough into the soil and removed from the borehole and the ends of the tube sealed with several layers of wax. A circular paper with an arrow placed over the wax to indicate the north direction of the sample

GRAIN SIZE DISTRIBUTION

The results of grain size distribution of the weathered and unweathered till at Springburn site are shown in Fig. 2 and Fig.3 respectively. The weathered till was found to extend to a depth about 1.7 m. It can be seen the till is well graded with multi modal grading curve and no split in the grading.

LABORATORY PROCEDURE FOR FABRIC ASSESSMENT

Alzubaidi (1984) used undisturbed sample that extract from the tube and placed on the base plate of the analyzing arrangement. The X- axis is oriented to compass north and the sample is then also oriented to same compass north and held in place with the clamp.

The sample is considered being positioned as it was in situ and search for fissure proceeds as follows:

1- A small spatula is used to explore the surface of sample, the end is pressed about 10 mm into the soil near the top of the cylinder and lifted gently. When the fissure is encountered the resistance to lifting is relatively small, the soil separating at the fissure, still using the spatula the fissure is gradually exposed and its extent.

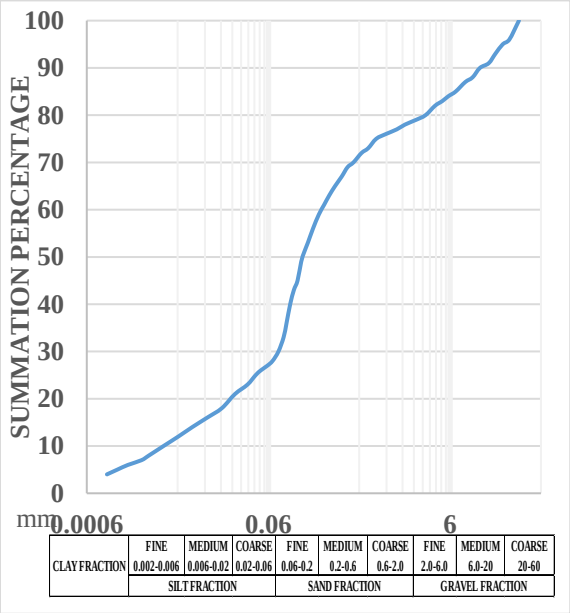


Fig. 2 Grading Curve of Weathered till from

Springburn Site

2-The center of the use area of the visible fissure so exposed is determined and the co-ordinates are recorded, with reference to X, Y and Z and the arbitrary origin 0, defined in Fig.1.

3- Using the spirit level, a level line is located on the exposed fissure and marked, from the line the dip and strike of the fissure are measured using clinometer and compass.

4- The dimensions of the largest rectangle contained within the exposed area of the fissure are measured for record purposes.

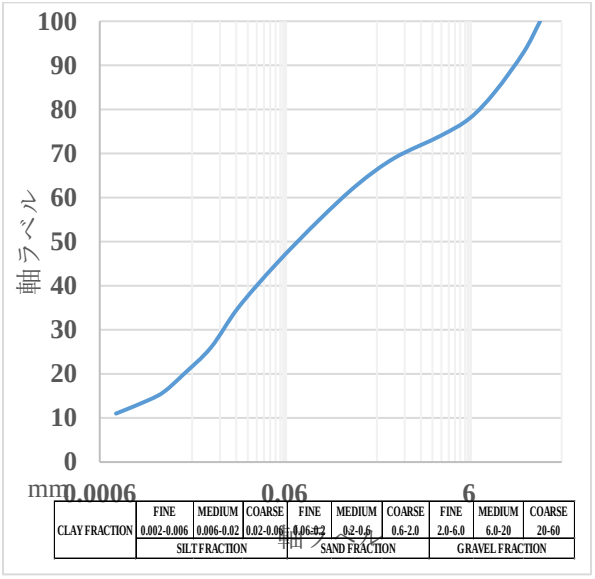


Fig.3 Grading Curve of Unweather till from

Springburn Site

5- The characteristics of the fissure surface are then recorded, geometry, asperity, coatings and stains.

This procedure is repeated throughout the entire sample perhaps logging 40-60 fissures, with a number of samples analyzed at each location, the requisite total of fissure is recorded.

PRESENTATION OF FISSURE ANALYSIS

To display the orientation of the fissures in a clay, an equal area stereographic projection is used. The poles representing the fissures planes on the lower hemisphere plot are identified and their intensity noted. The recorded data were plotted by a computer program using the program originally written by [13].The distribution of the fissure area, spacing, asperity and stain been presented in the form of histograms.

FISSURE STUDY AT SPRINGBURN SITE

[11] carried out fissure study at Springburn site which is located within the city of Glasgow, UK on a drumlin area as seen from Fig. 4. The till at this site is brown-grey in color and stones are dominantly of local origin. The samples used in assembling the fissure date were all taken from 2 m depth and the number of fissures recorded was 302 fissures. Almost all of these fissures recorded were planner.

PRESENTATION OF RESULTS

Alzubaidi (1984) carried out sample technique on 102 mm samples from Glasgow till the results presented in the following sections.

INTENSITY AND SPACING OF FISSURES

The intensity of fissures was found to be 7 m^2/m^3 , therefore the intensity of fissured is classified as "low" according to [10] classification. The frequency distribution of the fissures spacing in the directions of X, Y and Z axes are shown in Fig. 5 ,6 and 7

The average spacing in the directions of X, Y and Z axes are 208mm, 205mm and 23 mm respectively

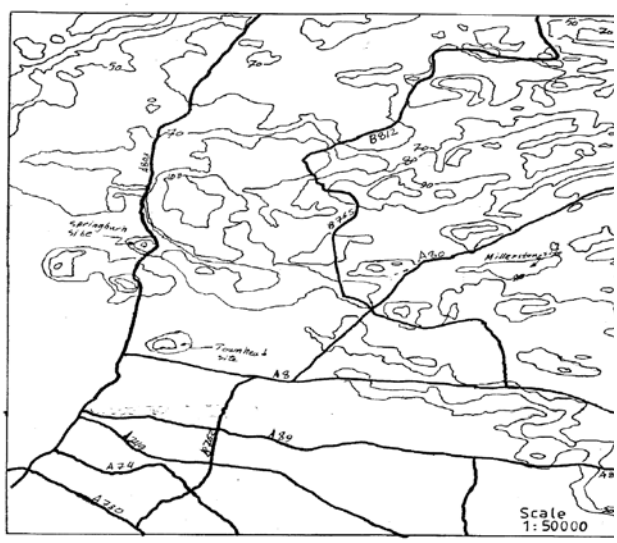


Fig. 4 Contour Map of The Area Around Study

Site (after Ordnance Survey , Survey Map Sheet 64)

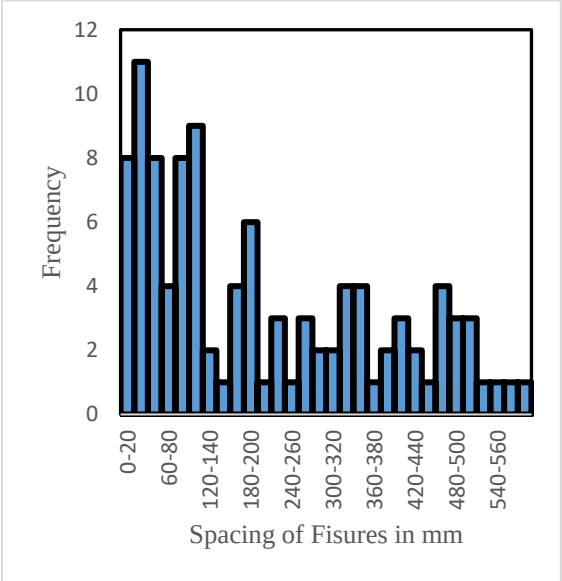


Fig. 5 Frequency Distribution of Fissure Spacing in the Direction of X-Axis

ASPERITY, SUFRACE MATERIAL AND AREA OF FISSURES

The asperity distribution of fissures in set is shown in Fig. 8 , it seems that the near horizontal fissures have lower asperity than the near vertical sets. Fig.9 shows the material at the fissure surface, and it can be noticed that 35% of the near horizontal set are coated with silty sand material whereas the majority of the near vertical fissures are clean. The frequency distribution of fissure areas and the average areas in each set (F1,F2 and F3) are shown in Fig.3.10 and Table.1 , where F1 is near horizontal and F2 F3 are near vertical , the fissure areas lie mostly between 200 $x10^{-6}$ m^2 to 4000 $x10^{-6}$ m^2. Therefore the fissures are classified as small fissures according to [10] classification

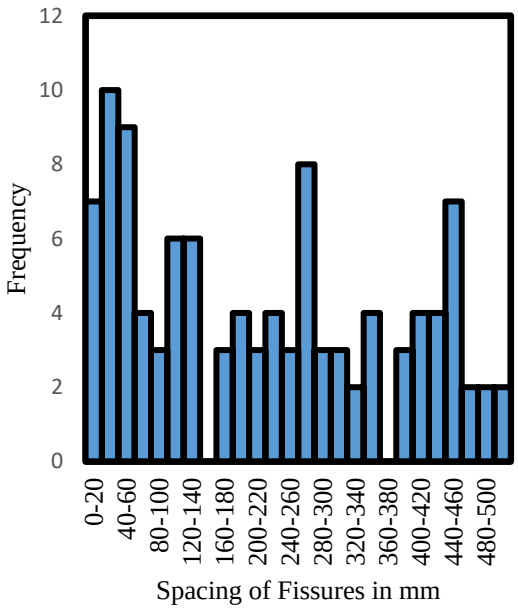


Fig. 6 Frequency Distribution of Fissure Spacing in the Direction of Y-Axis

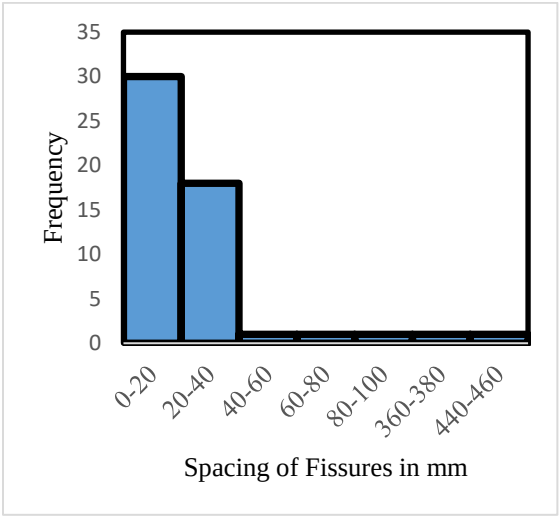


Fig. 7 Frequency Distribution of Fissure Spacing in the Direction of Z-Axis

CONCLUSSIONS

Based on the present research results, some conclusions can be drawn as follow:

1- The glacial till of the Springburn drumlin was found to be fissured, the fissures are arranged in a definite geometric pattern, one set horizontal, approximately parallel to original ground surface, and two near vertical sets conjugate about the drumlin elongation.

2-The areas of the fissures are found to classify as small fissures according to [10] classification.

3- Some near horizontal fissures are covered with a very thin silty sand coating , the near horizontal fissures are believed to be of depositional origin while the near vertical fissure are either clean or weathered and they are rougher than the near horizontal fissures.

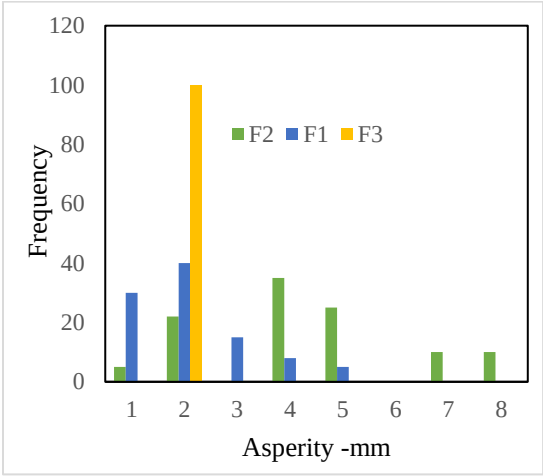


Fig.8 Asperity of Fissures

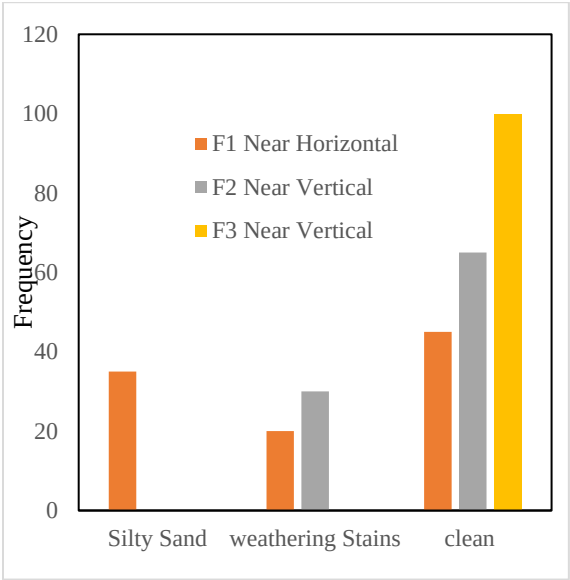


Fig. 9 Material of Fissure Surface

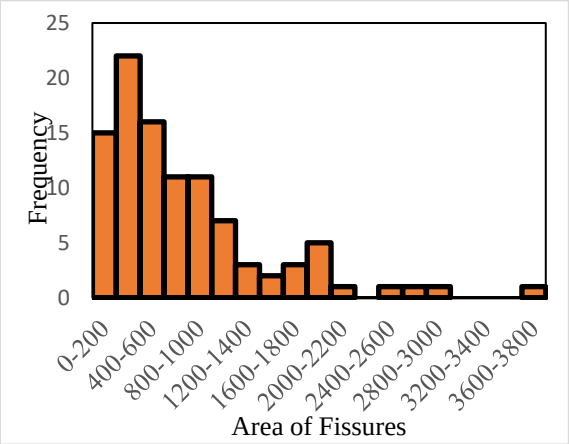


Fig.10 Frequency Distribution of Area of Fissures

Table .1 Total and Average Area of Fissures

Fissure Set	No. of Fissures	Total Area X 10^{-6} m^2	Average Area X 10^{-6} m^2
F1	45	52765	1172
F2	13	9475	729
F3	1	575	575

4- The new technique (sample technique) used in the present study seems to agree very well with block and cavity technique.

5- The grain size distribution grading curves of Springburn till contained particles ranging from boulder to clay size, with no significant gap.

REFERENCES

[1]Hansen B., The early history of glacial theory in British geology, Journal of Glaciol,Vol. 9 , 1970 ,pp 135-141

[2]Small D., and Fabel D., Was Scotland DE glaciated during the Younger Dryas., Quaternary Science Reviews, Vol.145, 2016, pp. 259-263.

[3]Rose J., and Smith J., Glacial geomorphological maps of the Glasgow region, western central Scotland, Journal of Maps ,vol.4 ,issue 1,2008,pp 399-416

[4]Hall A., and Riding J., The last glaciation in Caithness, Scotland: revised till stratigraphy and ice-flow paths indicate multiple ice flow phases ,Scottish Journal of Geology ,Vol.52 .Issue 7,2016, pp 77-89.

[5]Lekstutytėa I., Gadeikisa S., Žaržojusa G., and Skuodisb S., (2019) Engineering geological and geotechnical properties of till soil of the Middle Pleistocene glacial period , Estonian Journal of Earth Sciences, Vol. 68, Issue 2,2019, pp 101–111

[6]McGown A., and Radwan A., The Presence and Influence of Fissures in the Boulder Clays of West Central Scotland , Canadian Geotechnical Journal ,Vol.12,Issue 1,2011, pp 84-97

[7]Long M., and Menkiti C., Geotechnical properties of Dublin Boulder Clay, Geotechnique, Vol. 57 , Issue 7 ,2007,pp 595-611

[8]Fookes P.G., Orientation of Fissures in Stiff Over-consolidated Clays of the Siwalik System. Geotechnique , vol.15,1965, pp195-202

[9] Fookes P.G., and Parrish D.G., Observation on Small Scale Structural Discontinuities in London Clay and Their Relationship to Regional Geology. Quarterly Journal Engineering Geology, Vol.1, 1969, pp 217-240.

[10]Fookes P.G., and Denness B., Observational Studies on Fissure Pattern in Cretaceous Sediments of South East England. Geotechnique , Vol.19 ,1969,pp 453-477.

[11]Alzubaidi R., Pressuremeter Practice in Testing Glacial Till, PhD Thesis, civil Engineering. Department, University of Strathclyde, 1984, UK

[12]Hadidi F., The total fabric of natural clayey soils and its relevance to their engineering behavior. PhD Thesis, College of Engineering, Civil Engineering Department, University of Strathclyde, 1983, UK

[13]Warner J., FORTRAN program for construction of PI diagram with the Univac 1108 computer ,computer contribution 33, State Geol. Surv. University ,Kansas ,1969, Lawrence 1-38

7th Int. Conf. on Structure, Engineering & Environment (SEE), Pattaya, Thailand, Nov.10-12, 2021, ISBN: 978-4-909106070 C3051

HIERARCHICAL BAYESIAN RJMCMC-BASED DETECTION FOR PIECEWISE CONSTANT SIGNAL UNDER RAYLEIGH MULTIPLICATIVE NOISE

Suparman[1], M. Toifur[2]
[1]Department of Mathematics Education, Universitas Ahmad Dahlan, Indonesia;
[2]Department of Physics Education, Universitas Ahmad Dahlan, Indonesia

ABSTRACT

Piecewise constant models have been used in signal processing. The signal contains noise so that noise needs to be eliminated. Several research results have used the assumption that noise has a normal, gamma, or Laplace distribution. However, the signal may have noise with other distributions. This study aims to propose a piecewise constant model in which noise is assumed to have a Rayleigh distribution. This study also proposes a method for estimating the parameters of a piecewise constant model that includes Rayleigh noise. The parameters of the piecewise constant model were estimated in the Bayesian framework by adopting the reversible jump Markov Chain Monte Carlo (RJMCMC) method. This research shows that the dimension of the parameter space is a combination of several spaces with different dimensions. Bayes estimators for the parameters of the piecewise constant model cannot be stated explicitly. The RJMCMC method is used to calculate the Bayes estimator. The results of this study have a significant contribution in providing Rayleigh noise as an alternative noise in signal processing. This research has a novelty, namely: the use of Rayleigh noise in the piecewise constant model and the Bayesian hierarchical procedure to estimate the parameters of the piecewise constant model. Further research can be extended to a piecewise polynomial model under Rayleigh noise.

Keywords: Hierarchical Bayesian RJMCMC, Multiplicative noise, Piecewise constant model, Rayleigh distribution, Signal detection

INTRODUCTION

Piecewise is a stochastic mathematical model. The piecewise models are widely used in change-point analysis, for example [1], [2], and [3]. One of the piecewise models used in signal processing is the piecewise constant model. The piecewise constant model contains a noise. Several authors use additive noise, for example [4], [2]. Several other authors use multiplicative noise, for example [5], [6]. Noise is usually assumed to follow a distribution. Some researchers use the piecewise constant model with Gamma noise, for example [5] and [6]. In [5], the value of the Gamma distribution parameter is given. In applications, the value of this parameter is generally unknown. In [6], the value of one parameter is given and the value of the other parameter is assumed to be unknown. This parameter is estimated based on the data. However, in various applications of the piecewise constant model, the noise of the mathematical model is not Gamma distributed. There is little literature on piecewise constant models with multiplicative noise that is not a gamma distribution. This article provides a solution by proposing a piecewise constant model with Rayleigh noise. In this article, noise is assumed to have a Rayleigh distribution. The use of Rayleigh noise in piecewise constant is an innovation because the piecewise constant model with Rayleigh noise has not been studied by previous researchers. However, the piecewise constant model has a complex structure because the number of constant models is also a parameter. This article provides a solution by proposing a reversible jump MCMC (RJMCMC) algorithm to estimate the parameters of the piecewise constant model.

This article aims to find the procedure for estimating the piecewise constant model with Rayleigh noise based on RJMCMC algorithm.

LITERATUR REVIEW

Rayleigh Distribution

Suppose that $\boldsymbol{z}$ is a random variable. The random variable z is said to have a Rayleigh distribution with parameter σ, written as $z \sim Rayleigh(\sigma)$, if the probability density function of z is [7]

$$\boldsymbol{g(z|\sigma) = \frac{z}{\sigma^2} exp - \frac{z^2}{2\sigma^2}.}$$

Piecewise Constant Model with Multiplicative Noise

Let $y = (y_1, \cdots, y_n)$ be a data set where n is the

number of observations. The data is said to have a piecewise constant model with multiplicative noise if this data satisfies the stochastic equation

$$\boldsymbol{y_t = \mu_t z_t}$$

where μ_t is a constant function [8]:

$$\mu_t = \begin{cases} h_1, & \tau_1 < t \leq \tau_2 \\ h_2, & \tau_2 < t \leq \tau_3 \\ \dots & \dots \\ h_{k+1}, & \tau_{k+1} < t \leq \tau_{k+2} \end{cases}$$

where $\boldsymbol{\tau_1 = 0}$ and $\boldsymbol{\tau_{k+2} = n}$. Here, $\boldsymbol{z_1, \cdots, z_n}$ are noise and $\boldsymbol{k}$ is the number of change-point. The quantity $\boldsymbol{\tau = (\tau_1, \dots, \tau_k)}$ is the location of the change-point. The quantity $\boldsymbol{h = (h_1, \dots, h_{k+1})}$ is the height of the constant function. The piecewise constant model with multiplicative noise is used in modeling the Synthetic Aperture Radar (SAR) signal [9]. Research related to SAR signal can also be found in [10], [5], and [6]. In [5] and [6], the noise is assumed to have a Gamma distribution. In this article, the noise $\boldsymbol{z_t}$ is assumed to have a Rayleigh distribution with the parameter $\boldsymbol{\sigma}$. Figure 1 shows a piecewise constant model with Rayleigh noise.

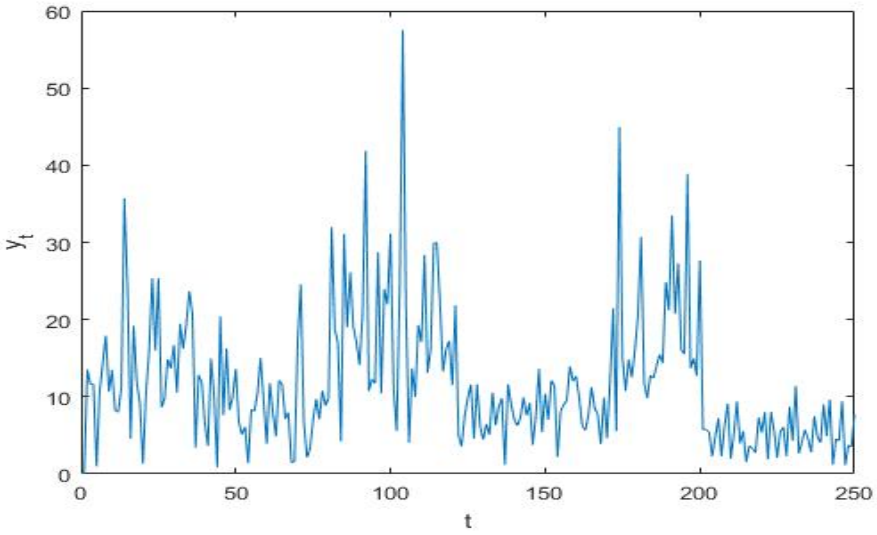


Fig. 1 Piecewise constant with noise Rayleigh

Bayesian Approach

Let $\theta = (k, \tau, h, \sigma)$ be the parameter of the piecewise constant model. As in [11], the parameter θ was estimated using the Bayesian approach. In the Bayesian approach, the parameter θ is considered as a random variable that has a prior distribution. The prior distribution of parameter θ is combined with the likelihood function of y_t $(t = 1, 2, \cdots, n)$ to produce the posterior distribution of parameter θ. Since the number of change-point k is also a parameter, the parameter space of θ is a combination of k parameter spaces with different dimensions. As a result, the posterior distribution of the parameter θ becomes very complex. So the Bayes estimator of the parameter θ cannot be calculated explicitly. To solve this problem, the Bayesian estimator is calculated using the Reversible Jump Markov Chain Monte Carlo (RJMCMC) algorithm.

RJMCMC

The RJMCMC method proposed by Green [12]. The RJMCMC method is an extension of the standard MCMC method. In the standard MCMC, the simulation of the posterior distribution is only in spaces with the same dimensions. In the RJMCMC, Markov chains can move from one space to another space with different dimensions. In this article, the RJMCMC is used to calculated the Bayes estimator of the parameter θ.

The basic idea of the RJMCMC is to create a Markov chain that has a limit distribution close to the posterior distribution. This Markov chain is used to determine the estimator of the parameter θ. For example, this Markov chain is used to determine the Posterior Marginal Maximum estimator [13].

METHODOLOGY

The data used in this article is the data that will be modeled with the piecewise constant model. Procedures for change-point detection include data collection, data modeling, and estimation of model parameters. The steps in estimating the model

parameters consist of determining the likelihood function, selecting the prior distribution, determining the posterior distribution, and calculating the Bayes estimator. The Bayes estimator was determined using the RJMCMC algorithm. The estimated model is used for change point detection. This procedure is presented in Figure 2.

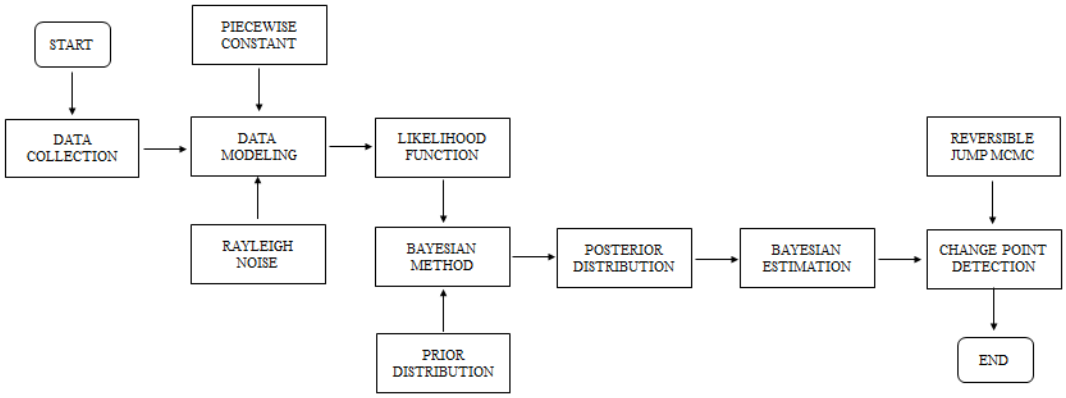


Fig. 2 Flow chart

RESULTS AND DISCUSSION

Likelihood Function

Let $y = (y_1, \dots, y_n)$ be data. This data is assumed to have a piecewise constant model with multiplicative noise. In this article, the noise $z_t \sim Rayleigh(\beta)$ where $\beta = \frac{1}{\sigma^2}$. Therefore the probability function of z_t can be written as

$$g(z_t|\beta) = \beta z_t \, exp - \frac{1}{2}\beta z_t^2$$

So the likelihood function of data y becomes

$$f(y|k,\tau,h,\beta) = \prod_{i=1}^{k+1} \prod_{t=\tau_i+1}^{\tau_{i+1}} \beta y_t \frac{1}{h_i^2} exp - \beta \frac{1}{2}\left(\frac{y_t}{h_i}\right)^2 = \beta^n \prod_{i=1}^{k+1} y_t^{n_i} \frac{1}{h_i^{2n_i}} exp - \beta \frac{s_i}{h_i^2}$$

where $s_i = \frac{1}{2}\sum_{t=\tau_i+1}^{\tau_{i+1}} y_t^2$ and $n_i = \tau_{i+1} - \tau_i$ for $i = 1, \dots, k+1$.

Prior Distribution

As in [6], the prior distribution of the number of change-points k is Binomial distribution with parameters k_{max} and λ, written $k \sim B(k_{max}, \lambda)$. Therefore, the probability function of the change-point k can be written as

$$\pi(k|\lambda) = \binom{k_{max}}{k} \lambda^k (1-\lambda)^{k_{max}-k}$$

for $k = 0, 1, \dots, k_{max}$. Here, k_{max} is the maximum value of k. Furthermore, the prior distribution of λ is a uniform distribution on the interval $(0,1)$. The uniform distribution was chosen because it is a conjugate prior distribution.

As in [12], the prior distribution of change-point locations $\tau_1, \dots, \tau_k$ is an ordered statistic. Therefore, the probability function of the change-point locations $\tau_1, \dots, \tau_k$ can be written as

$$\pi(\tau_1, \dots, \tau_k|k) = \frac{1}{C_{2k+1}^{n-2}} \prod_{i=1}^{k+1} (\tau_i - 1)$$

Here, C_k^n is the number of k combinations of the set containing n objects.

The prior distribution of height $h_1, \dots., h_{k+1}$ is chosen so that the prior distribution of $h = (h_1^2, \dots, h_{k+1}^2)$ is an inverse exponential distribution with parameter $\nu > 0$.

$$\pi(h_1^2, \dots, h_{k+1}^2|k,\nu) = \prod_{i=1}^{k+1} \frac{\nu^u}{\Gamma(u)} (h_i^2)^{-2} exp - \nu \frac{1}{h_i^2} = \upsilon^{(k+1)} \left(\prod_{i=1}^{k+1} h_i^2\right)^{-2} exp - \upsilon \sum_{i=1}^{k+1} \frac{1}{h_i^2}$$

Then the prior distribution of ν is the Jeffreys distribution. So the probability function of υ can be written as $\pi(\upsilon) \propto \upsilon^{-1}$.

Finally, the prior distribution of β is also the Jeffreys distribution. So the probability function of β can be

written as $\pi(\beta) \propto \beta^{-1}$.
Thus, the joint prior distribution of $\theta = (k, \tau, h, \lambda, \nu, \beta)$ becomes

$$\pi(k,\tau,h,\beta) = C_k^{k_{max}} \lambda^k (1-\lambda)^{k_{max}-k} \frac{1}{C_{n-2}^{2k+1}} \prod_{i=1}^{k+1}(n_i - 1)\, \upsilon^{(k+1)} \left(\prod_{i=1}^{k+1} h_i^2\right)^{-2} exp - \upsilon \sum_{i=1}^{k+1} \frac{1}{h_i^2} \frac{1}{\beta} \frac{1}{\nu}.$$

Posterior Distribution

Let $\theta = (\theta_1, \theta_2)$ be a parameter. Here, $\theta_1 = (k, \tau, h)$ and $\theta_2 = (\lambda, \nu, \beta)$. According to Bayes Theorem, the posterior distribution of the parameter $\theta = (\theta_1, \theta_2)$ is

$$\pi(\theta_1, \theta_2 | y) \propto \frac{\beta^{\alpha n - 1}}{(\Gamma(\alpha))^n} \prod_{i=1}^{k+1} y_t^{n_i} \frac{1}{h_i^{2n_i}} \exp -\beta \frac{s_i}{h_i} C_k^{k_{max}} \lambda^k (1-\lambda)^{k_{max}-k} \frac{1}{C_{n-2}^{2k+1}} \prod_{i=1}^{k+1} (n_i - 1)\ \upsilon^k \left(\prod_{i=1}^{k+1} h_i^2\right)^{-2} exp - \upsilon \sum_{i=1}^{k+1} \frac{1}{h_i^2}.$$

RJMCMC

Gibbs algorithm is used to estimate the parameter (θ_1, θ_2). The Gibbs algorithm procedure is as follows:

1. Simulate the distribution $\pi(\theta_2 | \theta_1, y)$
   1.1. $\beta \sim G\left(2n, \sum_{i=1}^{k+1} \frac{s_i}{h_i}\right)$
   1.2. $\lambda \sim B(k+1, k_{max} - k + 1)$
   1.3. $\upsilon \sim G\left(k+1, \sum_{i=1}^{k+1} \frac{1}{h_i^2}\right)$
2. Simulate the distribution $\pi(\theta_1 | \theta_2, y)$

The distribution $\pi(\theta_1 | \theta_2, y)$ is simulated using the RJMCMC algorithm. As in [6], the RJMCMC algorithm uses 3 transformations, namely: change-point location shift, change-point birth, and change-point death. These transformations have been used in [6] so that more detailed calculations in [6] can be used but Gamma noise is replaced by Rayleigh noise. Although the calculations in Suparman and the calculations in this article are similar, they are conceptually different.

If the results of this study are compared with previous studies. In [6], previous researchers used gamma noise. But in this study, the author uses noise with Rayleigh distribution. Thus, this article complements the results of previous studies. This article provides an alternative for modeling data that has Rayleigh noise. In terms of noise, the Rayleigh distribution is a special case of the Weibull distribution, so in general the research can be extended to the piecewise constant model with Weibull noise. In terms of function, constant function is also a special form of linear function so that the research can be extended to the linear piecewise model.

CONCLUSIONS

This research has studied the parameter estimation procedure of the piecewise constant model with Rayleigh noise based on the RJMCMC algorithm. The results have shown that the RJMCMC algorithm can estimate the parameters of the piecewise constant model with Rayleigh noise simultaneously. In addition, the research results can add to the literature related to signal modeling using piecewise constant models with Rayleigh noise. Further research can be extended to the estimation procedure of the piecewise constant with Weibull noise. In addition, further research can be developed on the estimation procedure of the piecewise linear model with Weibull noise.

ACKNOWLEDGMENTS

The authors would like to thank the Directorate of Research and Community Service (DRPM), Ministry of Education, Culture, Research and Technology (Indonesia) for providing research grants with a basic research scheme. Furthermore, the authors would also like to thank Universitas Ahmad Dahlan for facilitating this research. Finally, the authors would like to thank the reviewers of the 7th International Conference on Structure, Engineering & Environment in Pattaya, Thailand, who provided comments and suggestions to improve the quality of this article.

REFERENCES

[1] C. Beaulieu, J. Chen, and J. L. Sarmiento, "Change-point analysis as a tool to detect abrupt climate variations," *Philos. Trans. R. Soc. A Math. Phys. Eng. Sci.*, vol. 370, no. 1962, pp. 1228–1249, 2012, doi: 10.1098/rsta.2011.0383.

[2] F. Sadia, S. Boyd, and J. M. Keith, "Bayesian change-point modeling with segmented ARMA model," *PLoS One*, vol. 13, no. 12, pp. 1–23, 2018, doi: 10.1371/journal.pone.0208927.

[3] M. jeanne Buscot *et al.*, "Bayesian hierarchical piecewise regression models: a tool to detect trajectory divergence between groups in long-term observational studies," *BMC Med. Res. Methodol.*, vol. 17, no. 1, pp. 1–16, 2017, doi: 10.1186/s12874-017-0358-9.

[4] N. B. Khoolenjani and M. H. Alamatsaz, “Extension of de Bruijn’s identity to dependent non-Gaussian noise channels,” *J. Appl. Probab.*, vol. 53, no. 2, pp. 360–368, 2016.

[5] G. Aubertt and J. F. Aujol, “A variational approach to removing multiplicative noise,” *SIAM J. Appl. Math.*, vol. 68, no. 4, pp. 925–946, 2008, doi: 10.1137/060671814.

[6] Suparman, “Bayesian estimation in piecewise constant model with gamma noise by using reversible jump MCMC,” *Math. Stat.*, vol. 8, no. 2, pp. 17–22, Mar. 2020, doi: 10.13189/ms.2020.081303.

[7] D. J. Best, J. C. W. Rayner, and O. Thas, “Easily applied tests of fit for the Rayleigh distribution,” *Sankhyā Indian J. Stat. Ser. B*, vol. 72, no. 2, pp. 254–263, 2008.

[8] S. C. Dass, C. Y. Lim, T. Maiti, and Z. Zhang, “Clustering curves based on change point analysis : a nonparametric Bayesian approach,” *Stat. Sin.*, vol. 25, no. 2, pp. 677–708, 2015, doi: 10.5705/ss.2012.308.

[9] C. Oliver and S. Quegan, *Understanding Synthetic Aperture Radar Images*. SciTech, 2004.

[10] C.-S. Yang and K. Ouchi, “Application of Velocity Bunching Model to Estimate Wave Height of Ocean Waves using Multiple Synthetic Aperture Radar Data,” *J. Coast. Res.*, vol. 79, no. 10079, pp. 94–98, 2017.

[11] J. Hu *et al.*, “Bayesian detection of embryonic gene expression onset in C. elegans,” *Ann. Appl. Stat.*, vol. 9, no. 2, pp. 950–968, 2015.

[12] P. J. Green, “Reversible jump Markov chain Monte Carlo computation and Bayesian model determination,” *Biometrika*, vol. 82, no. 4, pp. 711–743, 1995.

[13] J. Heikkinen and H. Hogmander, “Fully Bayesian Approach to Image Restoration with an Application in Biogeography,” 1994.

7th Int. Conf. on Structure, Engineering & Environment (SEE), Pattaya, Thailand, Nov.10-12, 2021, ISBN: 978-4-909106070 C3051

ENGINEERING PROPERTIES OF RED BED SOIL FROM MAE MOH MINE FOR COVERING FINAL PIT WALL

Suphamat Chaichana[1], Amarin Boontun[2], Suparit Tangparitkul[3]

[1,2,3]Department of Mining and Petroleum Engineering, Faculty of Engineering, Chiang Mai University, Chiang Mai Thailand

ABSTRACT

Red bed soil is the waste from operation mining of Mae Moh mine. It will be excavated and taken to the waste area to open the mine. But in the final plan, the thick overburden red bed soil of Huai Luang formation in the last pit C of Mae Moh coal mine is prepared to be the covering materials on the coal outcrop in the final pit slope. The red bed soil is divided into 10 parts. Part 9 and Part 10 will not be mined and planned to use as covering materials in the final pit wall. The soil samples will be tested for basic engineering properties and strength parameters. Using unified soil classification, the red bed soil was classified into three groups: sandy lean clay, gravelly lean clay, and sandy fat clay. The three groups of red bed soil will be remolded at optimum water content for the triaxial test. Furthermore, the mixture of the three soil groups at a field ratio will be investigated as well. The results will be compared and the relevant physical properties of red bed soil will be discussed.

Keywords: Red bed soil, Mae Moh mine, Triaxial test, Optimum water content

INTRODUCTION

"Red bed" is the name of soil in Mae Moh mine. The position of the red bed is between topsoil and J-seam lignite in Na Kheam formation [1]. In the field, the topsoil and red bed layers must be excavated and taken to the dumping area via a conveyor belt and left to be reused. In 2051, the Mae Moh power plant is going to shut down. Mae Moh mine must manage and rehabilitate the mining area corresponding to the environmental impact prevention and correction statement recommended in the environmental impact assessment report (EIA report). The red bed is similar to clay as not explicitly stated. Typical characteristics of clay are soils and sediments particles having diameters of less than 2 μm. They are sticky when wet and hard when dry [2] and also have very low permeability. They have good chemical absorbency and depend on the type of compound in clay. Clay minerals are classified by their chemical composition and structure [3]. With these characteristics, EGAT will use the red bed for covering the exposed coal seams in the final pit wall. As known that the nature of coal beds may consist of sulfide mineral which turn to be acidic in water and the acidic water will dilute some of the heavy metals. There will be the big problem if some mine materials contain such toxic heavy metals. For prevention, the coal seams crop out in the pit slope must be eliminated or covered with proper materials and the red bed clay is one of the selected materials.

In addition to chemical properties, There are also important geotechnical properties [4] to be considered. This paper will focus on the geotechnical or engineering properties of the red bed soil for using as covering materials on mine pit slope. Many tests are conducted which are; soil classification, Atterberg limits, moisture content, specific gravity, dry density, unconfined compression test, compaction test, and triaxial test. All of the tests are following American Society for Testing and Materials (ASTM). The results from the tests are parameters that will be used to design proper pit slope covering with the red bed clay.

The red bed clay samples were collected from Mae Moh Mine, Lampang, Thailand. The core samples are collected from two drill holes located at N13W19 and N3W22 in a min pit as shown in Fig.1. The depth of the drill core is about 170 meters. The samples are collected as undisturbed as possible.

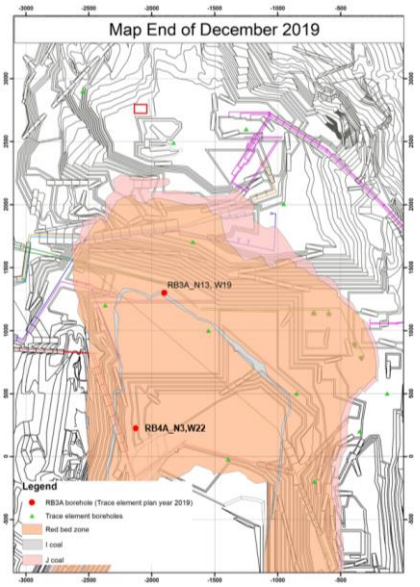


Fig. 1 Location map of the samples

METHODOLOGY

The test begins with soil classification using Unified Soil Classification System (USCS). After grouping the soil, the random samples of each group is taken to test for other engineering properties.

The following tests are performed in this study: grain size analysis, Atterberg limits, moisture content, specific gravity, dry density, compaction, and strength of soil. In the moisture content and the unconfined compression tests, undisturbed samples were used. The other tests used the disturbed samples.

CLASSIFICATION OF RED BED SOILS

The whole samples are divided into 17 samples with 10 meters apart along the depth of the borehole (RB3A_N13, W19). Grain size analysis and Atterberg's limits from disturbed samples are applied to classify according to Unified Soil Classification System [5]. The results from sieve analysis indicate that all red bed soil are fine grained soils due to that more than half of the soil passed No. 200 sieve.

From Atterberg's limit tests, the results show that the range of the values of liquid limit (L.L) are about 26-53%, plastic limit (P.L.) 11-21%, plastic index (PI) 12-36%, liquid index (L.I.) 1.33-1.96% and shrinkage index (S.I) 13 -43% as shown in Table 1. All values are plot in Fig. 2. As a result, the red bed soil is classified into 3 groups, CL-sandy lean clay, CL-gravelly lean clay and CH-sandy fat clay according to their properties (Table 2). The core samples from drill hole RB4A_N3W22 and classified accordingly.

Table1 Results from Atterberg's limit tests

SAMPLE NO.	DEPTH (m.)	LIQUID LIMIT (L.L.) (%)	LIQUID INDEX (L.I.) (%)	PLASTIC LIMIT (P.L.) (%)	PLASTIC INDEX (P.I) (%)	SHRINKAGE LIMIT (S.L.) (%)
1	0.00-10.00	36.06	1.54	14.38	21.68	43.40
2	10.00-20.00	37.29	1.56	15.02	22.26	19.51
3	20.00-30.00	32.37	1.65	14.22	18.15	6.30
4	30.00-40.00	31.38	1.57	12.99	18.39	17.99
5	40.00-50.00	32.65	1.52	12.70	19.95	28.45
6	50.00-60.00	36.83	1.53	14.31	22.51	26.05
7	60.00-70.00	38.23	1.74	17.64	20.59	27.75
8	70.00-80.00	50.22	1.36	15.10	35.12	15.21
9	80.00-90.00	42.70	1.42	14.58	28.12	17.39
10	90.00-100.00	53.28	1.41	17.52	35.76	23.33
11	100.00-110.00	39.64	1.70	17.87	21.78	18.70
12	110.00-120.00	36.88	1.33	10.89	25.98	19.49
13	120.00-130.00	46.21	1.54	17.83	28.38	32.26
14	130.00-140.00	34.82	1.96	18.36	16.46	22.75
15	140.00-150.00	40.13	1.93	20.63	19.50	17.42
16	150.00-160.00	36.76	1.80	17.71	19.05	12.98
17	160.00-170.00	25.76	1.94	13.96	11.80	26.37

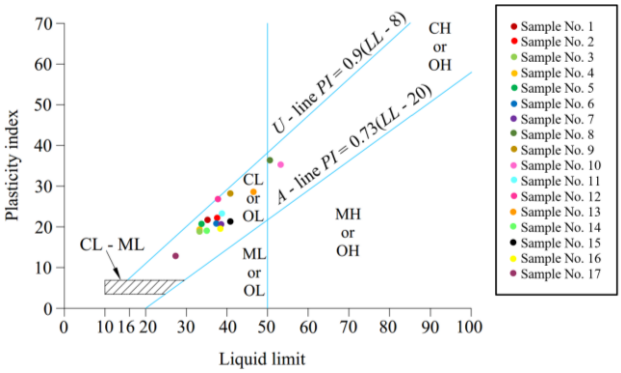


Fig. 2 Plasticity chart

Table 2 Red bed soil groups along the depth of drill hole (RB3A_N13, W19)

SAMPLE NO.	DEPTH (m.)	Unified Soil Classification System (USCS)	
		Group Symbol	Group Name
1-3	00.00-30.00	CL	Sandy lean clay
4-6	30.00-60.00	CL	Gravelly lean clay
7	60.00-70.00	CL	Sandy lean clay
8	70.00-80.00	CH	Sandy fat clay
9	80.00-90.00	CL	Sandy lean clay
10	90.00-100.00	CH	Sandy fat clay
11-15	100.00-150.00	CL	Sandy lean clay
16-17	150.00-170.00	CL	Gravelly lean clay

After the red bed soil is defined and grouped into 3 groups according to USCS, the further tests will be conducted using the random samples from each group.

BASIC ENGINEERING PROPERTIES

The samples are random taken from each sample group and the tests for basic engineering properties; moisture content, specific gravity and density, are conducted. The results are shown in Table 3.

Table 3 Basic engineering properties of red bed soil

Basic Engineering Properties of Red Bed Soil	Group Name		
	Sandy Lean Clay	Gravelly Lean Clay	Sandy Fat Clay
Moisture Content (%)	2.54	2.49	2.63
Specific Gravity	2.24	2.26	2.20
Density (g/cm^3)	2.24	2.26	2.20

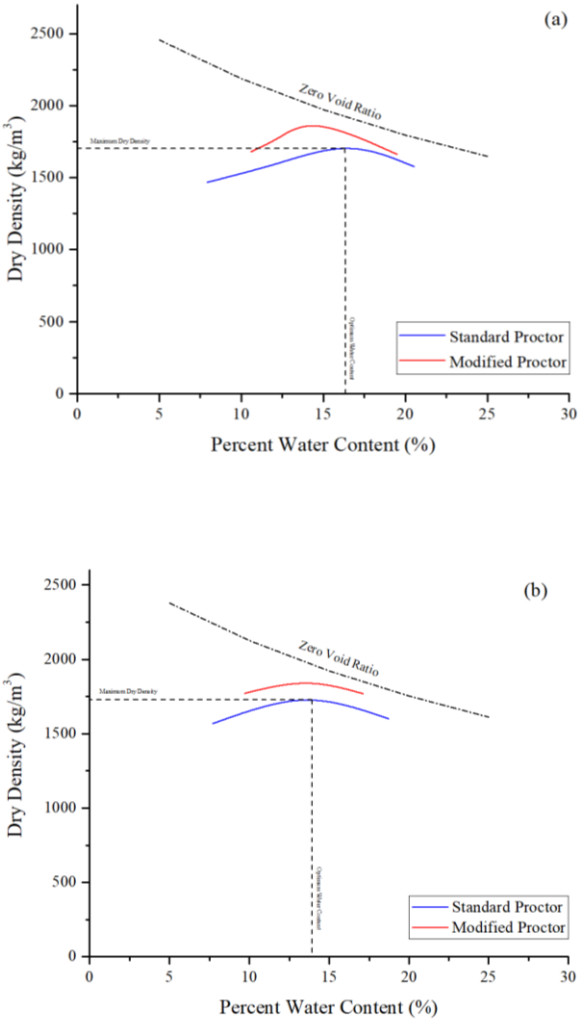
It is found that sandy fat clay has the highest values of moisture content and specific gravity but having the lowest value of density. Gravelly lean clay has the lowest moisture content and specific gravity values. The general properties of solids are denser than liquids and less moisture content than liquids [6]. In this basic engineering properties of red bed soil, .

gravelly lean clay has a higher percentage of gravel than other two groups which are considered to be more solid as shown Table 3

COMPACTION TEST

Compaction is the densification of soils by the application of mechanical energy. It may also involve a modification of the water content as well as the gradation of soil [7]. For the use of covering in the mine, the optimum water content (the peak point of the curve) of soil is very important. This information will be used in conjunction with the shear strength of each type of red bed soil. The standard proctor and modified proctor tests of each soil group are performed, and the results are shown in Fig. 3 and Table 4.

There are found that the gravelly lean clay has the lowest of the optimum water content and related to maximum dry density. The optimum water content and maximum dry density values of sandy lean clay and sandy fat clay are not much different.



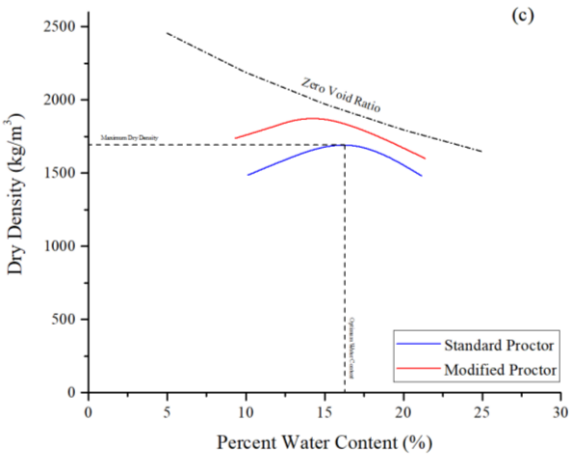


Fig. 3 Standard and Modified Proctor compaction test results for the Red Bed soil (a) Sandy Lean Clay (b) Gravelly Lean Clay (c) Sandy Fat Clay

Table 4 Maximum dry density and optimum water content of red bed soils from standard proctor and modified proctor tests

SAMPLE NAME	STANDARD PROCTOR		MODIFIED PROCTOR	
	MAXIMUM DRY DENSITY (kg/m^3)	OPTIMUM WATER CONTENT (%)	MAXIMUM DRY DENSITY (kg/m^3)	OPTIMUM WATER CONTENT (%)
SANDY LEAN CLAY	1760.26	16.59	1926.22	14.29
GRAVELLY LEAN CLAY	1751.04	14.55	1867.40	13.77
SANDY FAT CLAY	1763.03	16.76	1934.36	14.92

STRENGTH PARAMETERS

The strength of soil defines its ability to support the load of a building or to remain stable upon a hillside. Engineers must include soil strength in the design of buildings, embankments, road cuts and, other civil works [8]. Similarly, the red bed soil is used to cover the coal outcrop in the final pit. The strength parameters are important to design the slope for the covering in the mine pit (the design slope isn't mentioned in this paper). The tests of strength properties are unconfined compression tests, and unconsolidated undrained triaxial tests. The parameters obtained from triaxial tests are cohesion and friction angle of the red bed soil which will be used as covering materials. The thick red bed soil covering layer will be compacted with maximum dry density from standard proctor tests and will be cut as a proper slope design.

Unconfined Compression test

The unconfined compression test is a quick test for estimation the cohesion of soft and medium clay.

The cohesion is the electrochemical bonds between the soil and the friction is particle interlocking and surface friction [9]. The test used the undisturbed samples taken from each soil group and applied the axial load to the samples to cause failure. However, the unloading of the test is not a long period. The results are shown in Table 5.

Table 5 The results of unconfined compression test

Unconfined Compression test	Group Name		
	Sandy Lean Clay	Gravelly Lean Clay	Sandy Fat Clay
Unconfined Compressive Strength (t/m^2)	6.34	6.31	4.87
Undrained Cohesion (t/m^2)	3.17	3.15	2.43
Consistency	Soft	Soft	Very Soft

In clay samples that the friction angle was zero because of clay properties. The cohesion indicates the relationship between unconfined compressive strength and consistency of clay found that sandy fat clay is very soft but sandy lean clay and gravelly lean clay is medium. The sandy fat clay has the lowest strength which is about 4.87 t/m^2.

Triaxial tests

Triaxial tests are usually apply to determine shear strength parameters that a primary criterion in all stability analyses [10]. The parameters that the total angle of shearing resistance (θ) and the shear stress (c). There are defined the Mohr – Coulomb effective stress failure envelope as shown in the following equation:

$$\tau = c + \sigma \tan \theta$$

In this case, the unconsolidated undrained triaxial (UU) test [11]. Due to the properties of red bed soil from classified by the Unified Soil Classification System, this method is suitable for testing the red bed soil samples. The remolded samples of each soil group and the mixture of soils from every group are used to tests.

The samples are remolded according to optimum water content obtained from the compaction tests. The proportion of soil mixture is calculated according to the proportion of soil found in Table 1(sandy lean clay: gravelly lean clay: sandy fat clay = 6: 3 :1, and the optimum water content from sandy lean clay is used since it is the most commonly found group. The samples are a cylinder with a diameter of 3.5 centimeters, a height of 7.15 centimeters. The confining pressures applied are 10 kPa, 30 kPa, and 50 kPa (Fig. 4).



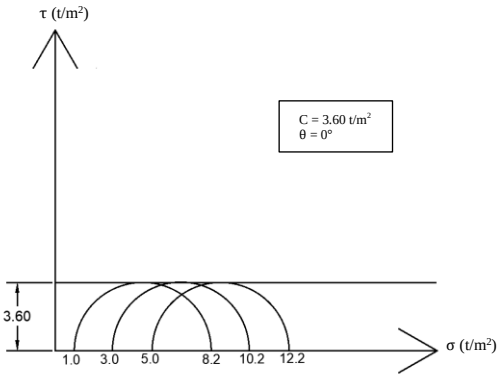
Fig. 4 Unconsolidated Undrained Triaxial test

The results of this test (Table 6 and Fig. 5) indicate that the red bed soil has very low friction angle which is about 0.00 - 0.14 degree. The gravelly lean clay has the highest cohesion value of 3.69 t/m^2, the sandy lean clay has 3.60 t/m^2. The sandy fat clay has the lowest cohesion value which is 2.95 t/m^2. The cohesion value of mixture of red bed soil is 3.30 t/m^2.

Table 6 Results of Unconsolidated Undrained triaxial test of remolded samples

UU test	Group Name			Mix Red Bed
	Sandy Lean Clay	Gravelly Lean Clay	Sandy Fat Clay	
Cohesion (t/m^2)	3.60	3.69	2.95	3.30
Friction angle (degree)	0^o	0.14^o	0^o	0^o

(a)



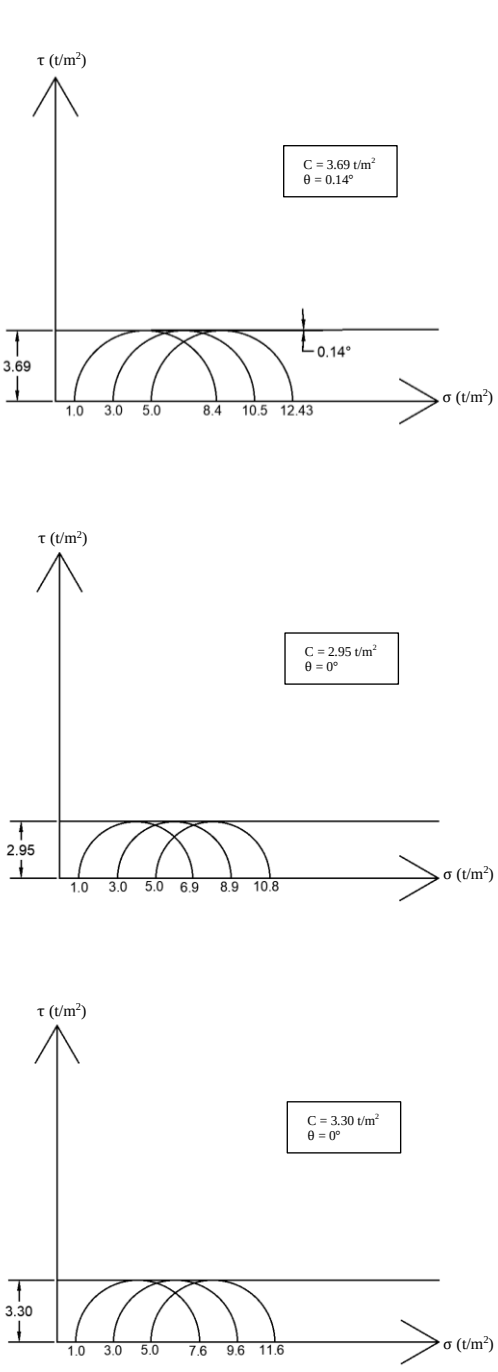


Fig. 5 Total stress Mohr's circles and failure envelope from Unconsolidated Undrained triaxial test (a) Sandy Lean Clay (b) Gravelly Lean Clay (c) Sandy Fat Clay (d) Mix Red Bed

DISCUSSION AND CONCLUSIONS

1. The study found that the red bed soil from the Mae Moh mine can be divided into 2 group symbols as CL and CH and 3 group names; Sandy Lean Clay, Gravelly Lean Clay, and Sandy Fat Clay.
2. Sandy Fat Clay has the highest moisture content, that is the cause of the lowest strength parameter. This type of clay is not proper to use for covering at optimum water content.
3. Sandy Lean Clay and Gravelly Lean Clay have 3.60 t/m^2 and 3.69 t/m^2 of the cohesions. They are soft from consistency property. They can be used for covering but it is not easy to separate them from other soil types.
4. Mix Red Bed soil has 3.30 t/m^2 of cohesion at the optimum water content of sandy lean clay. The mixture of the red bed soils is convenient for material handlings and the strength property is sufficient to use for covering and slope cut design. It should be more efficiently used than using a single group type of red bed soil.

ACKNOWLEGEMENT

The authors would like to thank the Electricity Generating Authority of Thailand (EGAT), Faculty of Engineering, Chiang Mai University, Thailand (CMU) and Faculty of Engineering, Rajamangala University of Technology Lanna, Thailand (RMUTL) for helps through this work.

REFERENCES

[1] EGAT, Thailand –Australia Lignite Mines Development Project, , in Mae Moh Mine Geotechnical Report 1985: Mae Moh Mine, Thailand.
[2] The dictionary of physical geography / edited by David S.G. Thomas ; International Advisory Panel David Dunkerley, Giles Foody, Andrew Goudie, Michael Meadows, David Montgomery, Sharon Nicholson, Tom Spencer. Fourth Edition. ed.: Hoboken, NJ : John Wiley & Sons Inc., 2016.
[3] Budhu, M., Soil mechanics and foundations. 3rd ed. 2011: John Wiley & Sons, Inc.
[4] Ural, N., The Importance of Clay in Geotechnical Engineering, in Current Topics in the Utilization of Clay in Industrial and Medical Applications. 2018.
[5] Das, B.M., Fundamentals of Geotechnical Engineering, Fourth International Edition. 2012: CL Engineering.
[6] Liquids. [cited 2021 3 June]; Available from: http://www.pkphysicalscience.com/article/481/liquids.
[7] Robert D. Holtz and W.d. Kovacs, An Introduction to Geotechnical Engineering. 1981: New Jersey : Prentice-Hall.
[8] Wagner, J.F., Chapter 9 - Mechanical Properties of Clays and Clay Minerals, in Developments in Clay Science, F. Bergaya and G. Lagaly, Editors. 2013, Elsevier. p. 347-381.
[9] Fam, M. and M. Dusseault, Effect of unloading duration on unconfined compressive strength.

Canadian Geotechnical Journal, 2011. 36: p. 166-172.
[10] Ekawita, R., et al., A Simple Unconsolidated Undrained Triaxial Compression Test Emulator. Applied Mechanics and Materials, 2015. 771: p. 104-107.
[11] ASTM, Standard Test Method for Unconsolidated-Undrained Triaxial Compression Test on Cohesive Soils. ASTM International, West Conshohocken, 2015.

7th Int. Conf. on Structure, Engineering & Environment (SEE), Pattaya, Thailand, Nov.10-12, 2021, ISBN: 978-4-909106070 C3051

APPLYING K-MEAN TECHNIQUE TO DEFINE THE SIZE OF GOVERNMENT PROJECT IN THE GOVERNMENT PROCUREMENT SYSTEM

Wuttipong Kusonkhum[1], Tanayut Chaitongrat[2*],
Worawit Phojan[3], Anuchat Leeanansaksiri[4], Rangsri Nantasarn[5] and Chinawat Muktabhant[6]
[1,3,4,5,6]Department of Civil Engineering, Faculty of Engineer, Northeastern University, Khon Kaen, Thailand
[2]Faculty of Architecture, Urban Design and Creative Arts, Mahasarakham University, Mahasarakham, Thailand.

ABSTRACT

Thai government has kept the data regrading to procurement process in e-Government Procurement system. At present, Thai government projects can be divided into four types including hire contract, purchase contract, construction contract, and service contract. However, only the construction project could be the defined the size of projects. There are four size of construction project. The construction project was defined by budget of project. This study aims to define the size of project for another type of Thai government projects. The data was collected from all projects in e-Government Procurement system. There are 698,124 projects within four types of contracts. In addition, Classification techniques was selected for classify the size in each contract types and K-mean was used as analysis technique. The finding of this study could be used to define purchase contract in five classes, hire contract into five classes, service contract into three classed and consult contract into three classes.

Keywords: Procurement management, Construction management, Budgeting, Size of project, K-mean.

INTRODUCTION

In this era, technology disruption affects public sections and private sections through the construction industry. This effort them to improve their organizations with new technology. One factor that works with the tradition process is to apply the tradition data with analytical technique to define or to understand the problem or opportunity for improve their works. In addition, Thailand is one country regarding develop data with technology [1].

Construction industry is such an industry that many processes have been applied in, such as project price estimation, contractor selection for construction project, construction labor productivity assessment [2] [3], and also procurement [4].

Nowadays, the Thai government agency who is in charge of procurement system has developed the procurement electronic system in order to use for the whole country, the system is called Electronic Government Procurement (e-GP) [5]. In addition, there are 5 types of hiring contracts including hire contract, purchase contract, Service contract, Construction contract, and Consultant contract. At present, for the ease of project management, the contracts can be divided according to types of hiring, and construction works can be separated according to type of constructions as well [6].

Additionally, construction contract is the only contract that needs to be defined a project's size. This is for the ease of management and for being used in the study of operational transparency in the procurement process of the government sector [7]. Thus, this research study aims to define the size of a project from the project prices of the 4 types of contracts: Hire contract, Purchase contract, Service contract and Consultant contract. The data is from 2019, collected in Electronic Government Procurement (e-GP).

LITERATURE REVIEW

Procurement project management

Procurement project management is a process of providing products and services according to the objective of a project [8]. On the other hand, there are different aspects and contexts of the procurement depending on responsibility and order of the project's stakeholders [9]. In addition, the project owner is the one who takes part in selecting the employees to work in each process, such as a main contractor, an architect or an advisor. Moreover, the project owner also works on clustering contracts in order to select dealers of necessary products or materials for the project. The management is different between the government agencies and the private companies [10] [11]. Additionally, in Thailand, the government agency takes responsible for procurement management [12].

Thai Procurement management

Recently in Thailand, Comptroller General's Department is the government agency which takes responsible for management and procurement of the private companies to work for the government

according to the law. In addition, Thai government has clustered the type of hiring contracts into 5 types including *hire contract, purchase contract, service contract, construction contract, and Consultant contract.* Further, for the transparency of the operation, e-Bidding selection specific method [6] is used for selecting the contractors in each different type of contract. However, there are many studies that examined the risk of corruption in government procurement, and the results have found that the government officers tend to be surreptitious in operation [5]. Because of this, it is necessary that the government agencies must adjust and improve the operational transparency by planning to bring the technologies into data management or other regulations. Additionally, to reduce the risk of operational corruptions [8] [12], it is also necessary to study or specify clarity in areas that are not yet detailed or that are too difficult for the officers to use [12].

Thai government contract type

To adjust and improve the operational transparency, it is necessary that the government agency must have plans to bring the technologies for data management or other regulations [1] [13]. Additionally, to reduce the risk of operational corruptions [6] [8], it is also necessary to study or specify clarity in areas that are not yet detailed or that are too difficult for the officers to use [12].

Clustering with K-Mean technique

K-means clustering is easy to apply even in large data sets, particularly when using heuristics such as Lloyd's algorithm. It has been successfully used in market segmentation, computer vision, and astronomy among many other domains. Moreover, it is often used as a preprocessing step for other algorithms, for example, to find a starting configuration.

In cluster analysis, the k-means algorithm can be used to partition the input data set into k partitions (clusters). However, the pure k-means algorithm is not very flexible, such as there is limitation of use (except for when vector quantization as above is actually the desired use case). In particular, the parameter k is known to be hard to choose (as discussed above) when it is not given by external constraints. Another limitation is that it cannot be used with arbitrary distance functions or on non-numerical data. For these use cases, many other algorithms are superior. [14]

Project level

At present, Thailand divides the size of construction projects into three sizes as follows; small size with project price between 1 to 5 million Thai Baht. Medium size with project price between 5.01 to 10 million Thai Baht and large size with project price more than 10.01 million Thai Baht [7]. Additionally, Thailand also divides a government construction project into 5 classes according to level of risk and effects from factors affecting the project [8]. It is important and necessary to divide the size of a project because it is easier to manage the paper works and the process, and it helps avoid the corruption for the government units as well [12].

RESEARCH METHODOLOGY

Population in the study

The population is Thai government projects organized in 2019. The data was collected from 4,010,275 projects which included four types of contracts including hire contracts, purchase contract, service contract, and Consultant contract. In addition, the factors are collected from e-GP system and those factors has won bidding prices from bidders. The sample is over 45 percentages from total 4,010,275 projects in 2019 [15].

Data processing

Since the collected data has missing values and it affects a project value which is the important part of data analysis by using *K-Mean technique*. Thus, for the most effective data analysis and the results that conform to the theory, the only projects which have values between 30 to 70% are selected for data processing [6].

Analysis technique

There are two types of analysis for this study as follows.

Descriptive statistics [15]

The statistics has been used to analyze three part of a questionnaire: part one, which is about demographic factor. Part two, which is about online purchasing for products or services via social media. And part three, which is about reactions when seeing online marketing campaigns via social media.

Inferential statistics

The implement of software **SPSS version 26** is used in data analysis. In addition, **Operator K-Mean** is also used for indicating the best group and the characteristics from each group. Additionally, to

cluster the groups, it is according to the literature review, which is between 3 to 5 groups to see the suitability and distribution of information.

RESULT AND DISCUSSION

All the project type was collected, including hiring contracts including hire contract, purchase contract, Service contract and Consultant contract. The most preferable contract type for the Thai government is the service contract, which accounts for 86.85% from all contract type, as shown in Table 1.

Table 1 This is an example of table formatting

Contract type	Amount (projects)	%
Hire	64,407	3.63
Purchase	719,236	40.49
Service	990,384	55.75
Consult	2,373	0.13
Sum	1,776,400	100

There are 698,124 projects for analysis process including hire contract, which consists of 25,765 projects, purchase contract, which consists of 287,665 projects, service contract, which consists of 383,869 project and hire contract, which consists of 825 projects, as shown in Table 2. In addition, the analysis of K-mean technique is significant as shown that in Table 3.

Table 2 This is an example of table formatting

Contract type	Amount (projects)	%
Hire	25,765	3.69
Purchase	287,665	41.21
Service	383,869	54.99
Consult	825	0.12
Sum	698,124	100

Table 3 ANOVA

Contract type	F test	Sig.
Hire	140,519.999	0.000
Purchase	1,128,592.001	0.000
Service	1,570,631.244	0.000
Consult	2,958.363	0.000

In clustering process, K mean technique is used as a tool to analyze characteristics of each group from the big data. Additionally, K-Mean analysis is widely accepted for cluster analysis and characteristics analysis for each group based on various research studies [16][17][18]. The projects can be clustered following type of contracts as follows; Hire contract, Purchase contract, Service contract, and consult contract.

The cluster of hire contract

Hire contract is a contract that the government units make an announcement to find dealers who can provide products or equipment for them to rent. In addition, the contract could be a daily contract, monthly contract or annual contract [6]. From clustering of contracts, there are clustered into five classes. In addition, Initial cluster centers of cluster one is 7,500 Thai baht, Initial cluster centers of cluster two is 7,608 Thai baht, Initial cluster centers of cluster three is 8,000 Thai baht, Initial cluster centers of cluster four is 20,002 Thai baht and Initial cluster centers of cluster five is 28,910 Thai baht, as shown in Table 4.

The final cluster centers of cluster one is 8,324 Thai baht, final cluster centers of cluster two is 10,439 Thai baht, final cluster centers of cluster three is 13,868 Thai baht, final cluster centers of cluster four is 19,544 Thai baht, and final cluster centers of cluster five is 25,732 Thai baht as shown in Table 5. In addition, the number of projects in each cluster is as follows; cluster one consists of 6,788 projects, cluster two consists of 5,229 projects, cluster three consists of 6,249 projects, cluster four consists 4,339 projects and cluster five consists of 3,090 projects as shown in Table 6.

Finally, the results have shown the length of contract price for each cluster as follows; the cluster one is under 9,000 Thai baht, cluster two is between 9,001 to 11,917 Thai baht, cluster three is between 11,918 16,639 Thai baht, cluster four is contract price in 16,640 between 22,503 Thai baht, and cluster five is over 22,504 Thai baht as shown in Table 7.

Table 4 Initial cluster centers

Cluster	Price (Thai baht)
1	7,500
2	7,608
3	8,000
4	20,002
5	28,910

The cluster of purchase contract

Purchase contract is a contract that the government units make an announcement to find traders who can provide products or equipment for the government units to purchase [6]. From the analysis, the contract values are clustered into five classes depending on the contract price as follows; Initial cluster centers of cluster one is 8,080 Thai baht, Initial cluster centers of cluster two is 38,330 Thai baht, Initial cluster centers of cluster three is 39,937

Thai baht, Initial cluster centers of cluster four is 39,974 Thai baht and Initial cluster centers of cluster five is 28,910 Thai baht as shown in Table 8.

Table 5 Final Cluster Centers

Cluster	Price (Thai baht)
1	8,324
2	10,439
3	13,868
4	19,544
5	25,732

Table 6 Number of projects in each cluster

Cluster	Project
1	6,788
2	5,299
3	6,249
4	4,339
5	3,090
Sum	25,765

Table 7 length of contract price

Cluster	Price (Thai baht)
1	< 9,000
2	9,001-11,917
3	11,918-16,639
4	16,640-22,503
5	> 22,504

The final cluster centers of cluster one is 11,558 Thai baht, final cluster centers of cluster two is 19,685 Thai baht, final cluster centers of cluster three is 27,796 Thai baht, final cluster centers of cluster four is 33,795 Thai baht, and final cluster centers of cluster five is 38,418 Thai baht as shown in Table 9. In addition, the numbers of projects in each cluster are as follows; cluster one consists of 128,043 projects, cluster two consists of 76,055 projects, cluster three consists of 46,785 projects, cluster four consists of 22,956 projects and cluster five consists of 13,826 projects as shown in Table 10.

Finally, the results have shown the length of contract price for each cluster, for the cluster one, the contract price is contract price under 15,930 Thai baht, cluster two is contract price between 15,931 to 24,172 Thai baht, cluster three is contract price between 24,173 to 31,208 Thai baht, cluster four is contract price between 31,209 to 36,387 Thai baht, and cluster five is contract price over 36,388 Thai baht as shown in Table 11.

Table 8 Initial Cluster Centers

Cluster	Price (Thai baht)
1	8,080
2	38,330
3	39,937
4	39,974
5	40,000

The cluster of service contract

Service contract is a contract that the government units make an announcement to find dealers to provide service or work as a part of the government units. Additionally, the service contract will be made according to the tasks assigned by the government units [6]. From the analysis, the contract values are clustered into three classes depending on the contract price as follows; Initial cluster centers of cluster one is 8,000 Thai baht, Initial cluster centers of cluster two is 10,336 Thai baht, and Initial cluster centers of cluster three is 30,000 Thai baht as shown in Table 12.

Table 9 Final Cluster Centers

Cluster	Price (Thai baht)
1	11,558
2	19,685
3	27,796
4	33,795
5	38,418

Table 10 Number of projects in each cluster

Cluster	Project
1	128,043
2	76,055
3	46,785
4	22,956
5	13,826
sum	287,665

Table 11 length of contract price

Cluster	Price (Thai baht)
1	< 15,930
2	15,931-24,172
3	24,173-31,208
4	31,209-36,387
5	>36,388

The final cluster centers of cluster one is 10,390 Thai baht, final cluster centers of cluster two is 17,121 Thai baht, and final cluster centers of cluster three is 25,438 Thai baht as shown that in Table 13. In addition, the number of projects in each cluster is as

follows; cluster one consists of 181,805 projects, cluster two consists of 124,868 projects, and cluster three consists of 77,196 projects as shown in Table 14.

Finally, the results have shown the length of contract price in each cluster, for the cluster one, contract price is under 13,727 Thai baht, cluster two is between 13,728 to 21,246 Thai baht and for cluster three is over 21,247 Thai baht as shown in Table 15.

Table 12 Initial Cluster Centers

Cluster	Price (Thai baht)
1	8,000
2	10,336
3	30,000

Table 13 Final Cluster Centers

Cluster	Price (Thai baht)
1	10,390
2	17,121
3	25,438

Table 14 Number of projects in each cluster

Cluster	Project
1	181,805
2	124,868
3	77,196
sum	383,869

Table 15 length of contract price

Cluster	Price (Thai baht)
1	< 13,727
2	13,728-21,246
3	> 21,247

The cluster of consult contract

Consult contract is a contract that the government units announce to seek for the specialists to be advisors in specific issues, which is necessary for the government projects and process of their works. In addition, the consult contract will be made according to the accepted standard contract prototype [1 9]. From the analysis, the contract values are clustered into three classes depending on the contract price as follows; Initial cluster centers of cluster one is 850,000 Thai baht, Initial cluster centers of cluster two is 1,055,000 Thai baht, and Initial cluster centers of cluster three is 4,080,000 Thai baht as shown in Table 16.

The final cluster centers of cluster one is 1,198,114 Thai baht, final cluster centers of cluster two is 2,166,271 Thai baht, and final cluster centers of cluster three is 3,301,230 Thai baht as shown in Table 17. Further, the number of projects in each cluster as follows; cluster one consists of 301 projects, cluster two consists of 274 projects, and cluster three consists of 250 projects as shown in Table 18.

Finally, the results have shown the length of contract price, for the cluster one, the contract price is under 1,672,800 Thai baht, for cluster two is between 1,672,801 to 2,730,000 Thai baht and for cluster three, the contract price is over 2,730,001 Thai baht as shown in Table 19.

Table 16 Initial Cluster Centers

Cluster	Price (Thai baht)
1	850,000
2	1,055,000
3	4,080,000

Table 17 Final Cluster Centers

Cluster	Price (Thai baht)
1	1,198,114
2	2,166,271
3	3,301,230

Table 18 Number of projects in each cluster

Cluster	Project
1	301
2	274
3	250
sum	825

Table 19 length of contract price

Cluster	Price (Thai baht)
1	< 1,672,800
2	1,672,801-2,730,000
3	> 2,730,001

CONCLUSIONS

This study could define purchase contracts into five classes, hire contract into five classes, service contract into three classes and consult contract into three classes. However, This defination could be used to improve the process of governnance works and make the government officers work easily to divide their project types.

The success of this study gives clearly definition and identify details of each class of those contract

types. In addition, that cold encourage the transparent in works for Thai government units [12].

ACKNOWLEDGMENTS

We would like to thank the Northeastern university for their funding support. We would also like to thank the Comptroller General's Department for their kindness of being a data provider for this study.

REFERENCES

[1] Korb Srinavin, Wuttipong Kusonkhum, Boonyarit Chonpitakwong, Tanayut Chaitongrat, Narong Leungbootnak, and Phatsaphan Charnwasununth, "Readiness of Applying Big Data Technology for Construction Management in Thai Public Sector," Journal of Advances in Information Technology, Vol. 12, No. 1, pp. 1-5, February 2021. doi: 10.12720/jait.12.1.1-5

[2] P. Carrillo, J. Harding, A. Choudhary, Knowledge discovery from post-project reviews, Construct. Manage. Econom. 29 (7) (2011) 713–723

[3] V.S. Desai, S. Joshi, Application of decision tree technique to analyze construction project data, in: Information Systems, Technology and Management, Springer, 2010, pp. 304–313.

[4] Bilal, M., Oyedele, L. O., Qadir, J., Munir, K., Ajayi, S. O., Akinade, O. O., ... & Pasha, M. (2016). Big Data in the construction industry: A review of present status, opportunities, and future trends. Advanced engineering informatics, 30(3), 500-521.

[5] Chaitongrat,T., Leungbootnak, N., Kusonkhum, W., Deewong,W., Srinavin, K., (2019). Measurement model of good governance in government procurement. IOP Conference Series Materials Science and Engineering 639:012024. 639(1), 0120204.

[6] The Government Procurement and Supplies Management Act B.E. 2560, Bangkok: The Comptroller General's Department, 2017.

[7] South, S. Economics of Bid Rigging : A Review of Literature, NAAC Journal, 2011, 4 (1), pp. 94-117

[8] PMI, A. (2013). guide to the project management body of knowledge (PMBOK guide). In Project Management Institute (Vol. 5).

[9] Jervis, B.M.; Levin, P. Construction law, principles and practice; McGraw-Hill College, 1988

[10] Burke, R. Project management: planning and control techniques, New Jersey, USA, 2013; pp. 26.

[11] Chitkara, K.K. Construction project management; Tata McGraw-Hill Education, 1998

[12] Chaitongrat, T., Liwthaisong, S., Aksorn, P., Kusonkhum, W., Leungbootnak, N., (2021). Causal Relationship Model of Problems in Public Sector Procurement. International Journal of GEOMATE, 20(80), pp. 52–58.

[13] Boonyarit Chonpitakwong, Wuttipong Kusonkhum, Tanayut Chaitongrat, Korb Srinavin, and Phatsaphan Charnwasununth, "Hindrance of Applying Big Data Technology for Construction Management in Thai Government," Journal of Advances in Information Technology, Vol. 12, No. 2, pp. 159-163, May 2021. doi: 10.12720/jait.12.2.159-163

[14] Lloyd, S. (1982). Least squares quantization in PCM. IEEE transactions on information theory, 28(2), 129-137.

[15] W. Lawrence, SOCIAL RESEARCH METHODS: Qualitative and Quantitative Approaches, Plus Mysearchlab... Without Etext. Pearson Education Limited, 2013.

[16] Balan, S., & Rege, J. (2017). Mining for social media: usage patterns of small business. Business Systems Research, 8(1), 43 -50.

[17] Boonjing, V., & Pimchangthong, D. (2017). Data mining for customers' positive reaction to advertising in social media. Proceedings of the Federated Conference on Computer Science and Information Systems, 945-948.

[18] Bradlow, E. T., Gangwar, M., Kopalle, P., & Voleti, S. (2017). The role of big data and predictive analytics in retailing. Journal of Retailing, 93(1), 79-85.

[19] des Ingenieurs Conseils, F. I. (1990). Client/consultant model services agreement. Fidic.

7th Int. Conf. on Structure, Engineering & Environment (SEE), Pattaya, Thailand, Nov.10-12, 2021, ISBN: 978-4-909106070 C3051

A STUDY OF BEHAVIOR OF COST IN GOVERNMENT CONSTRUCITON PROJECTS WITH MACHINE LEARNING

Wuttipong Kusonkhum[1], Korb Srinavin[2*,] Preenithi Aksorn[3],
Narong Leungbootnak[4], and Tanayut Chaitongrat[5]
[1,2,3,4]Department of Civil Engineering, Khon Kaen University, Khon Kaen, Thailand
[5]Faculty of Architecture, Urban Design and Creative Arts, Mahasarakham University, Mahasarakham, Thailand.

ABSTRACT

Nowadays, the technologies were disruptive in any industries even the construction industries phase according to Thai government effort to apply machine learning for forecasting fund for each Thai government construction projects. The aim of this study is to develop the machine learning model for forecasting behavior of Thai government construction projects. In addition, the data was collected from e-Government Procurement System in 2019 with eight attributes including groups of departments, types of projects, procurement methods, duration, standard price over budget, winning price over standard price, winning price over budget, and standard price over budget. Further, the four of classification algorithms were used for this study including K-nearest neighbor (KNN), Super vector machine (SVM), Artificial neural network and Decision tree. Additionally, the finding has shown that the artificial neural network has the high accuracy of forecasting. The mentioned accuracy value is higher than 0.77. Thus, the study could be confirming the Thai data from e-Government Procurement System is quite important and could be useful for technology disruptive era.

Keywords: Cost management, Procurement management, Machine learning, Government construction project, Behavior of forecasting

INTRODUCTION

Nowadays, many industries have applied the data management technology for an advantage of using data from the past. In addition, the construction industry is such an industry that has been affected by this change [1] [2]. One part of the Thai government process is that the government have been trying to find the way to study and improve procurement system which can help reduce conflicts in construction projects [3][4][5]. Even though there are some methods for reducing risks in project management including risk avoidance, transfer, or reducing risk [7], the conflicts still occur [5] and it cause a lack of transparency from the operations of government officers [7].

In the procurement process of a construction project, machine learning [2][8] is such a popular technology that has been applied in data management technology analysis. Moreover, it has been applied to increase the efficiency of construction management by focusing on studying data from the past to create the new knowledge, or trying to understand their own behavior of construction management [9] [10] [11].

Thai government have seen the opportunities and possibilities of machine learning implementation in Thai construction industry [1]. Though the working process might face some problems for the Thai government agencies, the government still attempt to find the solutions for those obstacles, and also find a way to study [12] about procurement system and to understand behavior of such a process in the past [7]. In addition to improve the more systematic of the process, one important factor of procurement process is to estimate costs before submitting them to an auction [6] [13] and set the standard price which conforms to the budget. That would help control the price for those bidders [14]. Thus, this study aims to build the knowledge collected from the behaviors of procurement systems in 2019. Additionally, those data were collected from all government construction projects including all type of construction projects to study and indicate the cost discrepancy of the winning bidder. Also, to see the behavior of the budget by machine learning implementation.

PROBLEM STATEMENT

The explanation of problems by linking the theories and researches under the relevant topics about Project cost and procurement management, Thai government procurement, Behavior in Thai government procurement and Conceptual framework.

Project cost and procurement management

The construction project is started by desire of a project owner or an authority who is in charge of the project. In addition, the project can be operated by hiring contractors for each work segment [6], and it is

necessary for the project owner to define a detailed scope of works in all areas [15] [16]. Moreover, one of an important part of hiring a contractor is the standard price of the project [13] [14]. In Thailand, the government is the one who indicate the standard price for all government construction projects in order to input the information into the government's procurement system called Electronic government procurement (e-GP) [14].

Thai government procurement

After set the budget from project presentation, the government, the owner of the project, will operate each project procurement [14]. Additionally, the incorrect project cost of the project is such a necessary information and is risky at causing conflicts [5] [13] [17]. Thus, cost estimation is actual important and necessary for the government officers in operations [6].

Behavior in Thai government procurement

According to data from the government units, there are still problems about winning price which is over a project budget. Moreover, the standard price of the project is also over a project budget which affects budget management of government units. It causes the gaps in excess value and lost value [1] [7]. Thus, to understand the behavior and examine the result of discrepancy in standard price estimation, the implementation of classification techniques from machine learning could be used in order to find the solutions [2] [18].

Conceptual framework

The conceptual framework of this study is behavior of Thai government procurement in a construction government project. The study will be inputting tradition data for analysis with machine learning technique in order to forecast the winning price and comparing with project budget. As shown in Figure1.

RESEARCH METHODOLOGY

In this research, the data was collected from the government procurement electronic system (e-GP), the permission to access was granted from the comptroller general's department for data collection. The required data were the information about all the government construction project in 2019 including three cases that concerned in this study. There were as follows; standard price over project budget, winning price over standard price and wining price over project budget.

According to the collection of the necessary data, the data was divided into two parts: 80% of the data were used for model training, and 20% of the data were used for model validation. In addition, the training data was analyzed by using K-nearest neighbor (KNN), Super vector machine (SVM), Artificial neural network and Decision tree and verified by a confusion matrix [2] [19].

A. Machine learning **Model Development**

The collected data needed to be prepared in a CSV file to ensure that there was no missing value and unknown category. Moreover, a computer program was necessary to perform KNN, SVM, ANN and Decision tree analysis. The hidden layer size of ANN is used for 100 [20]. The computer program was written in Python language and ran on Anaconda software.

Verifying the Model

The KNN model was verified for its accuracy, precision, and recall by constructing a confusion matrix and using the following equations (1–3) [21].

$$\text{Accuracy} = (TP-TN)/TP-TN-FP-FN) \quad (1)$$

$$\text{Precision} = TP/(TP-FP) \quad (2)$$

$$\text{Recall} = TP/(TP-FN) \quad (3)$$

where TP = true positive, TN = true negative, FP = false positive, and FN = false negative.

Accuracy is the ratio of the total number of correct classifications to the total number of predicted classifications, as calculated by a model. Further, precision is defined as the ability to obtain consistent results from repeated measurements. Precise values differ from one another because of random error, a type of observational error in information retrieval. In addition, Recall is the percentage of relevant documents that are successfully retrieved [19].

Data Collection

Table 1 has shown eight attributes of the input data collected from the traditional system of the Thai government. Each parameter has a different factor depends on its definition. The first parameter is groups of department name attribute which consist of 13 groups of departments in Thailand as shown in the Table 2. In addition, a project owner is one of the stakeholders involved conflicts in a construction project [13,15]. Moreover, they are the main of cost estimation influencers. For the type of project attribute, it consists of three factors including building roads and irrigation projects [14]. This attribute is an important factor that influences cost estimate, project budgeting and project procurement [16]. The Thai procurement method attribute has three factors including the chosen bidding method and specific method as show in the Table 3. In

addition, the procurement method is different in each country, but the goal is the same, i.e., to eradicate corruption [22]. For the procurement method, it is a significant factor influencing a contractor's cost [14,22]. Further, project levels consist five levels. The levels are separated by price range as shown in Table 4 [3] [23]. And the Duration, it is duration of construction project within contract.

The case of project attributes is the consideration of whether a project is under budget or over budget according to the Thai government policy. It consists two factors.

Table 1 Attributes in input data

No.	Attributes	Factor
1	Group of departments	13
2	Type of project	3
3	Procurement method	3
4	Duration	5
5	Standard price over budget	3
6	Winning price over standard price	3
7	Winning price over budget	3
8	Standard price over budget	3

Table 2 Group of departments in Thailand

No	Group	Detail
1	University	Construction under university
2	School	Construction under school
3	Hospital	Construction under hospital
4	Irrigation	Construction under department of irrigation
5	Public works and town and country planning	Construction under military agency department public works and town and country planning
6	Highway	Construction under department of highway
7	Rural road	Construction under department of rural road
8	Finance	Construction under ministry of finance
9	Local of administration	Construction under department of local of administration
10	Justice	Construction under department of court
11	Police	Construction under Thai police
12	Soldier	Construction under military agency
13	Other	Department in Thai land without group 1-12.

Table 3 Thai procurement method

Method of procurement	Detail
Bidding	every company could join and check the qualify of projects.
Chosen	Only the qualified company could bid with special condition of projects
Specific	The owners could select the contractor by themselves.

Table 4 Project level

Project level	Detail (Million baht)
L1	< 5,000,000
L2	5,000,001 - 10,000,000
L3	10,000,001 - 50,000,000
L4	50,000,001 - 250,000,000
L5	> 250,000,000

RESULT AND DISCUSSION

The result of this study has included three parts; 1. General information, 2. Machine learning model and 3. Verifying the model.

General information

The most preferable procurement method for the Thai government is the specific method, which accounts for 77.8% from all procurement methods as shown in Table 5.

Table 5 Method of procurement

Method of procurement	Amount (projects)	%
Bidding	56504	19.9
Chosen	6483	2.3
Specific	220557	77.8
Sum	283,544	100.00

Most of the group of departments for the Thai government data in 2019 is from the group of Other, which accounts for 67.5%. However, the groups of departments with the highest budget is local of administration, and second one is highway, as shown in Table 6 and Table 7.

Most of Thai government construction projects are road and building constructions. Infrastructure is one of various points that Thai government concern of the most for Thai people [7] [14] as shown in Table 7 and Table 8. This study has separated the case of budget in to three groups including standard price

over budget, winning price over standard price and winning price over budget as shown in Table 9, Table 10 and Table 11. In addition, most of the case found in standard price over budget is the group of Under, that means standard price is under budget. Moreover, most of the case found in a winning price over the standard price case is the group of Balance, the behavior is the same with winning price over budget case.

Table 6 Group of departments in Thailand

Group of departments	Amount (projects)	%
University	2,825	1.0
School	21,770	7.5
Hospital	8,065	0.2
Irrigation	2,873	0.6
Public works and town and country planning	1,044	7.2
Highway	5,281	7.7
Rural road	6,049	2.8
Finance	151	1.0
Local of administration	191,459	0.4
Justice	21,332	1.9
Police	541	2.1
Soldier	1,650	0.1
Other	20,504	67.5
Sum	283,544	100.00

Table 7 Value of departments in Thailand

Method of procurement	Price (million bath)	%
University	27,213,849,975	5.63
School	17,371,463,580	3.59
Hospital	12,104,583,298	2.50
Irrigation	24,759,861,792	5.12
Public works and town and country planning	29,724,273,461	6.14
Highway	100,506,037,775	20.78
Rural road	41,189,023,249	8.51
Finance	565,930,364	0.12
Local of administration	107,208,585,377	22.16
Justice	20,403,766,794	4.22
Police	10,585,518,443	2.19
Soldier	12,262,407,782	2.53
Other	79,881,003,280	5.63
Sum	483,776,305,170	100.0

Table 8 percentage of project type

Project type	Amount (projects)	%
Building	112,984	39.8
Road	159,753	56.3
Irrigation	10,807	3.8
Sum	283,544	100.00

Table 9 Standard price over budget

Case of projects	Amount (projects)	%
Under	179,925	63.5
Balance	66,252	12.4
Over	37,367	13.2
Sum	283,544	100.00

Table 10 Winning price over standard price

Case of projects	Amount (projects)	%
Under	92,097	32.5
Balance	190,781	67.3
Over	666	0.2
Sum	283,544	100.00

Table 11 Winning price over budget

Case of projects	Amount (projects)	%
Under	92,771	32.7
Balance	190,490	67.2
Over	283	0.1
Sum	283,544	100.00

In the result of general formation has shown that, there is a few of winning projects have prices over the budgets. However, it is a concerned point of this study because the corruption can happen from the officers [7]. There are 666 projects for the case of winning price over standard price, which means there is a mistake in The government's cost estimation process [5][6].

Machine learning model

There are four algorithms develop the model for classification the behavior of winning price including KNN, SVM, ANN and Decision tree. The Table 12 has shown that the accuracy of algorithm is nearly but the highest is ANN algorithm as 77.81 percentage. It is a popular algorithm technique to classify for large data [24]. In addition, the accuracy is not enough to forecast the fund because of cases of the concerned models are not many enough [25]. However, the result could show behavior of department in Thailand.

Table 12 Accuracy of each algorithm

Input	Accuracy
ANN	77.81
KNN	74.21
SVM	77.77
Decision tree	77.45

Verifying the model

The confusion matrix (Fig.1) [26] is used to calculate the model's classification accuracy. The matrix of ANN model showed that the model correctly predicted for 44,127 from 56,709 cases. The matrix of KNN model showed that the model correctly predicted for 42,089 from 56,709 cases. The matrix of SVM model showed that the model correctly predicted for 44,104 from 56,709 cases. And the matrix of decision tree model showed that the model correctly predicted for 43,925 from 56,709 cases as shown that in Table 13.

		Actual class		
		Under	Balance	Over
Predicted class	Under	A	B	C
	Balance	D	E	F
	Over	G	H	I

Fig. 1 Confusion matrix table

Furthermore, a confusion matrix is a table that reports the counts of true positives, false positives, true negatives, and false negatives which are defined as follows; True Positive (TP), the label belongs to the class, and it is correctly predicted. False Positive (FP), the label does not belong to the class, but classifier predicted as positive. True Negative (TN), the label does not belong to the class, and it is correctly predicted. And False Negative (FN), the label does belong to the class but it is predicted as negative [26] [27].

Similarly, the ANN model's precision can also be calculated by using the confusion matrix. The precision can be divided into three cases (i.e., Under Balance and Over cases), as shown in Table XII. For the first case, the Under case, the model achieved a precision of 84%. For the Balance case, the model achieved a precision of 77%. And for the Over case, the model achieved a precision of 0% as shown in the Table 14.

The KNN model's precision can also be calculated by using the confusion matrix. The precision can be divided into three cases (i.e., Under Balance and Over cases), as shown in Table 15. For the first case, the Under case, the model achieved a precision of 61%. For the Balance case, the model achieved a precision of 80%. And the Over case, the model achieved a precision of 12%.

The SVM model's precision can also be calculated by using the confusion matrix. The precision can be divided into three cases (i.e., Under Balance and Over cases) as shown in Table 16. For the first case, the Under case, the model achieved a precision of 83%. For the Balance case, the model achieved a precision of 77%. And the Over case, the model achieved a precision of 0%.

The decision tree model's precision can also be calculated by using the confusion matrix. The precision can be divided into three cases (i.e., Under Balance and Over cases) as shown in Table 17. For the first case, the Under case, the model achieved a precision of 84%. The next one is the Balance case, the model achieved a precision of 76%. And the Over case, the model achieved a precision of 0%.

Table 13 Confusion matrix of machine learning model

Algorithm	Confusion matrix
ANN	array ([[7,279, 11,178, 0], [1,341, 36,848, 0], [20, 43, 0]], dtype=int64)
KNN	array([[10,487, 7,976, 0], [6,587, 31,601, 7], [13, 37, 1]], dtype=int64)
SVM	array([[7,392, 11,048, 0], [1495, 36,712, 0], [19, 43, 0]], dtype=int64)
Decision tree	array([[7,209, 11,328, 0], [1,399, 36,716, 0], [23, 34, 0]], dtype=int64)

Table 14 ANN model validation

Input	Print (metrics.classification_report(y_test, predicted))				
		precision	recall	f1-score	support
Output	Under	0.84	0.39	0.54	18,457
	Balance	0.77	0.96	0.85	38,189
	Over	0.00	0.00	0.00	63
	Accuracy			0.78	56,709
	Macro avg	0.54	0.45	0.46	56,709
	Weighted avg	0.79	0.78	0.75	56,709

The precision of confusion matrix has shown that the ANN and decision tree algorithm could show the highest accuracy in the Under case and this point could prove that the traditional data have a relation for application data technology [1]. However, the

"Balance cases" has the highest accuracy with KNN algorithm, and the "Over cases" has the highest accuracy with KNN algorithm, anyway it is a low accuracy of precision relates that the KNN algorithm could be a good technique for classification [27], as shown in Table 18.

Table 15 KNN ANN model validation

Input	Print (metrics.classification_report(y_test, predicted))				
		precision	recall	f1-score	support
Output	Under	0.61	0.57	0.59	18,463
	Balance	0.80	0.83	0.81	38,195
	Over	0.12	0.02	0.03	51
	Accuracy			0.74	56,709
	Macro avg	0.51	0.47	0.48	56,709
	Weighted avg	0.74	0.74	0.74	56,709

Table 16 SVM ANN model validation

Input	Print (metrics.classification_report(y_test, predicted))				
		precision	recall	f1-score	support
Output	Under	0.83	0.40	0.54	18,440
	Balance	0.77	0.96	0.85	38,207
	Over	0.00	0.00	0.00	62
	Accuracy			0.78	56,709
	Macro avg	0.53	0.45	0.46	56,709
	Weighted avg	0.79	0.78	0.75	56,709

Table 17 Decision tree ANN model validation

Input	Print (metrics.classification_report (y_test, predicted))				
		precision	recall	f1-score	support
Output	Under	0.84	0.39	0.53	18,537
	Balance	0.76	0.96	0.85	38,115
	Over	0.00	0.00	0.00	57
	Accuracy			0.77	56,709
	Macro avg	0.53	0.45	0.46	56,709
	Weighted avg	0.79	0.77	0.75	56,709

CONCLUSIONS

The current study collected data from the traditional system of the Thai government. There are eight attributes including group of departments, type of project, procurement method, duration, standard price over budget, winning price over standard price, winning price over budget, and standard price over budget. In addition, the accuracy of four algorithms demonstrated that the data could be used to forecast behavior with the highest accuracy. However, if the number of input factors has increased, which is related the project management concept for cost management such as the start date of the contract or the date of handover project and etc. [1][6], the accuracy will be increased, and it could be applied for another knowledge for project management [1] [2].

Table 18 Accuracy of each algorithm

Cases	Algorithm	Accuracy
Under	ANN	84%
Balance	KNN	80%
Over	KNN	12%

ACKNOWLEDGMENTS

We would like to sincerely thank the Graduate School, Khon Kaen University for their funding support. In addition, we would like to thank the Comptroller General's Department for allowing their data to be used in this study. Without any of them, our research would not be accomplished.

REFERENCES

[1] Korb Srinavin, Wuttipong Kusonkhum, Boonyarit Chonpitakwong, Tanayut Chaitongrat, Narong Leungbootnak, and Phatsaphan Charnwasununth, "Readiness of Applying Big Data Technology for Construction Management in Thai Public Sector," Journal of Advances in Information Technology, Vol. 12, No. 1, pp. 1-5, February 2021. doi: 10.12720/jait.12.1.1-5

[2] Bilal, M.; Oyedele, L.O.; Qadir, J.; Munir, K.; Ajayi, S.O.; Akinade, O.O.; Owolabi, H.A.; Alaka, H.A.; Pasha, M., 2016. Big Data in the construction industry: A review of present status, opportunities, and future trends. Advanced Engineering Informatics. 2016, 30(3), 500-521.

[3] Chaitongrat, T., Leungbootnak, N., Kusonkhum, W., Deewong, W., Liwthaisong, S., & Srinavin, K., Measurement model of good governance in government procurement. In IOP Conference Series: Materials Science and Engineering, (Vol. 639, No. 1, p. 012024), 2019, IOP Publishing.

[4] Khahro, S. H., & Ali, T. H. Causes leading to conflicts in construction projects: a viewpoint of Pakistani construction industry. In International Conference on challenges in IT, Engineering and Technology (ICCIET'2014), 2014. July pp. 17-18.

[5] B. Teanngen, W. Kusonkhum, S. Liwthaisong, T. Chaitongrat, and K. Srinavin, "Risk factors affecting conflict management for construction government project in Thailand," Multidiscip.

Technol. Ind. Appl., pp. 94–105, 2020.
[6] PMI, A. Guide to the project management body of knowledge (PMBOK guide). Project Management Institute., 2013 Vol. 5.
[7] T. Chaitongrat, S. Liwthaisong, P. Aksorn, W. Kusonkhum, and N. Leungbootnak, "Causal Relationship Model of Problems in Public Sector Procurement," Int. J. GEOMATE, vol. 20, no. 80, pp. 52–58, 2021.
[8] Hurwitz, J.; Kirsch, D. Machine learning for dummies, 2018; pp. 75.
[9] Bai, S.; Li, M.; Kong, R.; Han, S.; Li, H.; Qin, L. Data mining approach to construction productivity prediction for cutter suction dredgers. Automation in Construction. 2019, 105, p.102833.
[10] Naganathan, H.; Chong, W.O.; Chen, X. Building energy modeling (BEM) using clustering algorithms and semi-supervised machine learning approaches. Automation in Construction, 2016, 72, 187-194.
[11] Poh, C.Q.; Ubeynarayana, C.U.; Goh, Y.M. Safety leading indicators for construction sites: A machine learning approach. Automation in Construction. 2018, 93, 375-386.
[12] Boonyarit Chonpitakwong, Wuttipong Kusonkhum, Tanayut Chaitongrat, Korb Srinavin, and Phatsaphan Charnwasununth, Hindrance of Applying Big Data Technology for Construction Management in Thai Government, Journal of Advances in Information Technology, Vol. 12, No. 2, pp. 159-163, May 2021. doi: 10.12720/jait.12.2.159-163
[13] Jervis, B. M., & Levin, P. Construction law, principles and practice. McGraw-Hill College., 1988.
[14] The Government Procurement and Supplies Management Act B.E. 2560, Bangkok: The Comptroller General's Department, 2017.
[15] Burke, R. Project management: planning and control techniques, New Jersey, USA, 2013; pp. 26.
[16] Chitkara, K.K. Construction project management; Tata McGraw-Hill Education, 1998.
[17] Maemura, Y., Kim, E., & Ozawa, K. Root causes of recurring contractual conflicts in international construction projects: Five case studies from Vietnam. Journal of Construction Engineering and Management, 2018, 144(8), 05018008.
[18] Dzuke, A.; Naude, M.J. Procurement challenges in the Zimbabwean public sector: A preliminary study. Journal of Transport and Supply Chain Management. 2015, 9(1), 1-9.
[19] Hernández-Torruco, J.; Canul-Reich, J.; Frausto-Solis, J.; Méndez-Castillo, J.J. Towards a predictive model for Guil-lain-Barré syndrome. In 2015 37th Annual International Conference of the IEEE Engineering in Medicine and Biology Society (EMBC), IEEE, August 2015, pp. 7234-7237
[20] Allen, K.; Berry, M.M.; Luehrs Jr, F.U.; Perry, J.W. Machine literature searching VIII. Operational criteria for designing information retrieval systems. American Documentation (pre-1986), 1955, 6(2), 93.
[21] Gondia, A.; Siam, A.; El-Dakhakhni, W.; Nassar, A.H. Machine learning algorithms for construction projects delay risk prediction. Journal of Construction Engineering and Management 2020, 146(1), p.04019085.
[22] Leungbootnak, N.; Chaithongrat, T.; Aksorn, P., An exploratory factor analysis of government construction pro-curement problems, 2018, In MATEC Web of Conferences (Vol. 192, p. 02057). EDP Sciences.
[23] Suntharanurak, S., Screening for bid rigging in rural road procurement of Thailand (Doctoral dissertation, Doctoral dissertation, National Institute of Development Administration), 2012.
[24] Juszczyk, M., Leśniak, A., & Zima, K. (2018). ANN based approach for estimation of construction costs of sports fields. Complexity, 2018.
[25] Domingos, P., A few useful things to know about machine learning. Communications of the ACM, 2012, 55(10), 78-87.
[26] Ali, M., Son, D. H., Kang, S. H., & Nam, S. R. (2017). An accurate CT saturation classification using a deep learning approach based on unsupervised feature extraction and supervised fine-tuning strategy. Energies, 10(11), 1830.
[27] Zhang, Z. Introduction to machine learning: k-nearest neighbors. Annals of Translational Medicine, 2016, 4(11).

7th Int. Conf. on Structure, Engineering & Environment (SEE),
Pattaya, Thailand, Nov.10-12, 2021, ISBN: 978-4-909106070 C3051

EXPLORING THE EFFECTIVENESS OF HEALTH AND SAFETY REGULATIONS GOVENRING CONSTRUCTION PROJECTS IN UAE

Abdelrahman Abdalla Alhelo[1],Radhi Alzubaidi[2],Hamad Rashid[3]
[1]PhD Student, College of Engineering, University of Sharjah, UAE
[2]College of Engineering, University of Sharjah ,UAE
[3]College of Engineeing ,University of Sharjah, UAE

ABSTRACT

The construction industry is the most critical modern sociotechnical industry when it comes to safety. There are various levels of regulations of safety - related requirements in the construction field globally. Although the construction sector in the United Arab Emirates (UAE) is considered one of the leading sectors internationally, however the sector required continuous developments of an all-encompassing regulatory platform that addresses the safety issues within construction sites nationally. This paper applies a qualitative methods approach to explore the current status of safety practices in the construction industry in UAE, specifically in regards to the active safety regulations, and the industry compliance with such regulations. The research further explores potential gaps within the active regulation and observes variation between multiple regulatory systems overlapping within the industry. Analysis of collective qualitative data highlighted multiple adverse issues within the current regulatory frames, thus specific recommendations were furnished to facilitate the development of a national safety regulatory platform applicable nationwide.

Keywords: Construction sites safety, Health and safety regulations, Compliance, National safety standards

1. INTRODUCTION

The Construction industry in UAE received distinctive developments and growths in term of residential, commercial and infrastructure projects. Safety and health is demanding to proceed with projects free from accidents and delays. [1] studied attempts to identify the health and safety, risks and causes of poor safety practice in construction projects. They concluded that site workers experienced a lack of information about site safety and not wearing protective equipment, which is considered as the main cause of poor safety practices in construction.

[2] conducted a study to identify safety management factors like risk management and site management, they selected 12 construction sites to compare their safety management and safety performance. In their research employed qualitative comparative analysis to predict case knowledge, compare the cases and identify connections between the factors and safety performance. They concluded that construction stakeholders should realize that the ability to conduct high safety performance in construction sites connected to key safety management, contextual factors and combinations of these factors. [3] proposed practical roles to reduce accidents during the construction stage in South Korea by considering the organically linked characterization with different stages, which represent, the client, consultant, supervisor and contractor in construction to understand preventive standards. They reviewed all the occupational safety and regulation and law of safety applicable in construction in South Korea. The study implemented a questionnaire with different coordinators to explore the implantation level of the present condition. They proposed some items to interconnect with current safety and health regulations stages during construction projects in South Korea. [4] developed a control structure model of construction in Australia to improve and understand the construction operating system. The suggested model has been developed by applying the System Theoretical and Accident Model and Process (STAMP) method to show the actors, organizations controls ,communication loops and relationships that are involved in managing safety through the construction sectors in Australia. They concluded that the proposed model provides a distinctive representation of maintaining and providing a useful incident investigation template in safety in the construction sector in Australia. [5]Carried out a case study on one of the international construction companies operating in UAE and Indonesia to assess the performance in terms of Health & Safety, the study concluded that tighter enforcement by the municipality in UAE has driven safety standards up to a level it is performing

better than in Indonesia. [6] conducted a practical study on some construction companies working in that there are many companies not applying the roles and regulations of safety and health due to lack of regulations and codes required for safety in construction sector. [7] investigate into the safety and health regulations in UAE and explore the safety and health regulations in the UK to improve the existing regulations in UAE, in their study concluded that many items of safety and health regulation are not applied properly and found that some safety managers were more concerned about cost rather than health and safety, and there is still a lack of preventive measures for reducing occupational safety and illness on construction sites.

2. SAFETY OF OPERATION IN CONSTRUCTION PROJECT

In construction industry safety play a great role in decreasing the accidents occurred in the projects, most of the construction companies conducting safety and health regulations and environmental management system to reduce accidents, illness and to provide a safe environment in the construction projects. [8]conducted a safety management survey in 20 construction sites projects in Hong Kong to explore the application of safety in these projects. The survey analysis provided useful information such as safety policy and standards, safety, organization, safety training, inspecting hazardous conditions, personal protection, plant and equipment, safety promotion, and management behaviour. They concluded that the information provided in their study represents useful guides to the construction companies, where construction safety awareness is not high. [9] adopted 4D building information modelling (BIM) to improve the safety aspects in the construction of Iraqi oil projects and study the impact of applying BIM on the scheduled time and cost. They concluded that conducting BIM will explore different hazards and prepare the acceptable solutions to mitigate the expected hazards and solving all safety and health problem in the early stages. [10]studied the effective safety management in the construction sector in Malaysia, they carried extensive questioner study through different construction projects and concluded that many factors affecting the safety issues like safety training and awareness, worker's attitude towards safety, availability of safety equipment, safety inspections and organization safety policy.

Abu Dhabi and Dubai to explore the level of applying the safety and health regulation ,the study showed

3. REGULATING THE CONSTRUCTION INDUSTRY

In construction sectors, failure to comply with the statutory requirements for safety and health regulations can have serious consequences regarding the safety of employees and others like extra costs, many countries urged to issues legislation and regulations concerning the health and safety practices. [11] conducted a study on the impact of environmental regulation on regional construction efficiency in China. The results showed that environmental regulation has a significant impact on the efficiency of the construction industry. [12] applied the Loughborough Construction Accident Causation "ConCA model" which presents new opportunities to understand accident causation by linking immediate accident circumstances with the distal shaping and originating influences. The results support integrating safety into primary activities to increase engagement, learning legacies to transfer knowledge between projects, multi-disciplinary teams to raise risk awareness, empowerment to combat their feelings of dissatisfaction and disloyalty, and collaboration in risk management to incorporate workers' expertise and ensure they feel valued. [13] conducted a case study on a Chinese international contractor to explore and evaluate the difficulties to implement safety practices. Difficulties identified were: Labor-only subcontracting and complex labor structure, high turnover rates of frontline workers, low safety awareness of local workers, and the failure of Chinese workers who work far from home. Eliminating these difficulties can help implementing safety practices and therefore improve safety performance. [14] Developed a hierarchical framework to illustrate how (13) factors influence safety on construction projects, it was validated by interviews with experts and confirmed that safety performance not only determined by management activities within project levels, but also by the interactions among factors at different hierarchical levels.

[15]evaluated the effectiveness of the Safety Management Systems (SMS) in improving construction safety and identified the factors that influence its implementation; interviews indicated that visible senior commitment, in terms of manpower and cost allocation, and competency of safety manager as key drivers for the SMS implementation. They also concluded that reduced accident rates and accident costs, schedules, and high labor turnover rate were the key challenges to the effective SMS implementation.

4. CURRENT PRACTICE IN UAE

The construction industry in UAE is one of the most developed sectors in the region, workers in construction are always threatened by the occurrence of accidents in their work. Employers of constructions around the world seek to reduce and control these incidents to save humans lives, and reduce projects delays due to these incidents. Only a few studies had been conducted on constructions health and safety in UAE. [6]Conducted a study to determine the level of safety in construction sites for 120 companies operating in Abu Dhabi and Dubai, the study showed that (25%) of employers do not provide personal protective equipment (PPE) to their workers; (26%) do not have a first aid kit; (21%) do not have fire safety measures; (16%) do not keep records of accidents; and (63%) of workers had almost deadly accidents in the past. Most of all the lack of regulations and codes required for safety in construction was the main problem. [7]tried to introduce the foundations on which appropriate health and safety systems may be built in UAE by exploring methods adopted in the UK to improve the existing code of practice. 130 out of 350 construction companies participated in the survey conducted. The study showed that (69%) have a lack of understanding of the importance of health and safety policy; (71%) have no training of H&S; (74%) believe that training when exists is outdated; (87%) agree that the culture causes a problem implementing H&S procedures; (86%) admitted that they did not adhere to an accident reporting procedures; (83%) admitted not recording accidents; and (71%) said that they were not provided with means of recording accidents which explains why only (54%) carry out follow up action after an accident. It was found that some safety managers were more concerned about the cost than health and safety, and there is still a lack of preventive measures for reducing occupational safety and illness on construction sites. Roddy (2014) carried out a case study on one of the international construction companies operating in UAE and Indonesia to assess the performance in terms of Health & Safety, he found that tighter enforcement by the municipality in UAE has driven safety standards up to a level it is performing better than in Indonesia.

According to the International Labor Organization (ILO), MOHRE is one of the governmental federal organizations in UAE that has part responsibility for occupational health and safety under Federal Law No. 8 of 1980. In addition, Order No. 32 of 1982 on Protection from Hazards and Ministerial Decision No. 37/2 of 1982, other regulations such as Federal Law No. 1 of 2002 on use, monitoring, and protection from radioactive material. The Occupational Health and Safety Department organizes periodic inspection visits to enterprises, of all sectors and industries, to ensure compliance with the OHS legal provisions and monitor OHS and living standards in the workers' dormitories and the health and safety department is not responsible for checking the health and safety in construction sites. Abu Dhabi Center for Occupational Safety and health (OSHAD) was established in 2010, to ensure the implementation of an integrated and sustainable system of occupational health and safety in the workplace, and supervision of all aspects of occupational health and safety in Abu Dhabi, to develop legal and legislative tools in the field of occupational safety and health. As part of the strategic plan, Dubai Municipality has published the "Code of Construction Safety Practice" as local legislation to be implemented in Dubai projects. To put the future standards in place in a time that witnesses global challenges and unprecedented competition to win the leading position in preparing infrastructure, planning, environmental, medical, construction, beautifying and recreational aspects of growing modern cities. The Code of Construction Safety Practice is set out to regulate working conditions in construction projects carried out in Dubai for all employees who work with main contractors or sub-contractors' companies. It is essential from literature review the importance of developing and implementing Health and Safety legislation, and the impact and importance of creating a Federal organization in UAE responsible to implement and enforce H & S regulations. The objective of the present research is to develop a concrete unified strategy with a validated supporting set of regulations and policies that can better empower health and safety regulations of the construction industry sector in UAE and should be controlled by a federal organization. Moreover an effort target to design and develop a framework that can be used by various stakeholders of the construction industry to implement the improved regulations and policies.

5. Methods and Data

The current research applies a qualitative approach of data collection and analysis to investigate to which extent have the safety culture and safety-related practices matured within the UAE fast - growing construction industry. Due to the specific nature of the construction industry in UAE, being of global representation, yet of many local features, the current research needed to try deeply explore the insights of various relevant professionals and other stakeholders. The overall design of the applied current research methodology is given in Figure1.

5.1 The Stratified Sampling Technique

The stratified sampling technique is utilized to assign the sample participants from the Emirate of Sharjah in the UAE. In statistics, stratified sampling is defined as a method of sampling from a population that can be partitioned into subpopulations. In statistical surveys, when subpopulations within an overall population vary, it could be advantageous to sample each subpopulation independently. A stratified sample number was calculated based on the number of companies of consultants and contractors eligible to work in Emirate of Sharjah. The data were collected from the municipality and economic department of Emirate of Sharjah, as shown in Tables .1and 2. The stratified sample size was calculated as shown in Tables 3and 4.

Table 1 Number of Construction companies in Sharjah

Emirate	Excellence Category	First Category	Second Category	Total
Sharjah	25	272	46	343

Table 2 Number of Consultant Companies in Sharjah

Emirate	Excellence Category	First Category	Second Category	Total
Sharjah	265	42	38	345

Table 3 Stratified Sample for Construction Companies

Emirate (strata)	Strata Sample Size
Sharjah	8.7

Table 4 Stratified Sample for Consultancies Companies

5.2. Data collection

The applied methods comprised a thorough literature review that highlighted possible gaps in terms of the lack of global obligatory regulations of safety practice that are internationally recognized, and resistance to change factors in regards to safety compliance in the global construction industry. The identification of this initial gaps was consolidated via direct observation of the local UAE construction industry. The semi-structured interviews technique was then selected as a main data collection tool. A sample of 18 company informants from the population of constructions and consultants working at the Sharjah-UAE construction industry was interviewed. Each interview was launched referring to a pre-settable of questions for both the practitioners. Interviews were fully recorded at the consent of participants. A pre-structured list of interview questions, as given in Table 5 and Table 6, was developed and used to drive the conversation during interviews.

5.3 Data analysis and Results

After conducting the questioner results with both engineers working with construction companies and consultancy offices at Sharjah. In the UAE health and safety are regulated respectively by the Ministry of Human Resources & Emiratization Law No. 8 of 1980 Regulating Labour Relations as amended by Federal Laws No. 24 of 1981, No.15 of 1985 , and No.12 of 1986 Law. The Law is federal and is therefore applicable to all the emirates of the federation. It is enforced by the Ministry of Labour, and some by local Municipality. An initial evaluation was first constructed building on the previous relevant literature findings, the insights from the initial field observations, and the factors highlighted in the interview records.

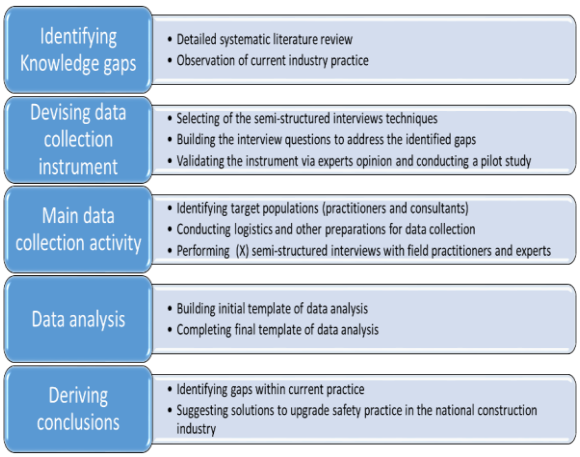


Figure 1. The applied research methodology

5.3.1 Results of Construction companies

According to the results of the interview , it can be noticed ,there is no specific governmental department responsible to follow up the implementation of health and safety regulations as found from the answers, 57% of the companies stated that municipalities are responsible for implanting the safety and health regulations, while 28% stated that they sometimes get inspected from MOHRE, and 15% stated that Department of Public Works is responsible for impending the regulations. The suggestions of all companies to improve the health and safety procedures can be briefed as follows:

- Health and safety regulations have to be provided and forced to be implemented with continuous follow - up by the Government.
- The specific governmental departments should be responsible for a qualified health and safety inspectors.
- Health and safety regulations have to be revised and updated regularly.
- Health and safety policy should be included in all construction contracts and sub-contracts.

One of significant factor concluded that 86% of the companies found that (nationalities, habit, and language) has a great effect on implementing health and safety regulations, as they come from different countries with different culture and languages.

There are some questions used in the interview to identify the health and safety procedures and policies followed by different sizes of construction companies at Sharjah (UAE). It was found that 84% of the companies have a written health and safety policy The results of the questioners showed that 56% of the companies do not have a written health and safety policies, while 33% of the companies have their health and safety policies, and 11% of the companies follow the health and safety regulations from municipalities. The findings also showed that 78% of the companies does not implements health and safety regulations during the design stage while 67% of the companies do not have formal health and safety training programs for their employees and do not have any department responsible for implementing health and safety procedures. All companies stated that they do not have external health and safety consultants, while 33% have internal health and safety consultants. It was found that 33% of the companies do not conduct any site visits to inspect implementing H&S regulations. Consultant companies have no direct role when accidents occur on - site, while 11% of the companies stated that the procedure is set out in the Main Contractor's responsibilities. The results exert that 22% of the which was developed by the companies themselves, where no local authority been distributed to the constructions sector the health and safety regulations. To understand the methods used for applying health and safety regulations within the company. The study found that all companies provide PPE to workers and use the Municipality health and safety guide boards on site, cranes and scaffolding are certified by a third-party specialist. Formal health and safety training is very important in the construction field as it helps reducing job - related injuries and accidents. 85% of the companies conduct formal health and safety training for workers, where43% of them have qualified health and safety officers to perform the training and inspections. Interviews concluded that 42% of the companies have a specific department to follow up implementing health and safety regulations. The study also found that minor accidents that occurred, been treated site , where major accidents always reported to authorities and 86% of the companies have all accident recorded, this can be used to reduce accidents in the future by learning from past mistakes. The distinctive types of accidents occurred on site were falling from heights where 71% of companies reported this type of accidents on sited. While 29% of the companies stated that falling objects can cause accidents on sites. The number of annual major accidents that occurred ranged from 1 to 5 accidents in most construction companies. All companies agreed that implementing health and safety regulations will increase the performance and productivity of the company and should reduce the cost of the project.

5.3.2 Results of Consultant companies

companies stated that falling from height is one of the issues that could cause accidents on - site and 33% of the companies referred those accidents might occur through not safe scaffoldings. The results also showed that 11% of the companies stated that tower cranes can cause major accidents. The interviews concluded that 33% of the companies keep records of all accidents, where 56% of the companies keep few records of accidents, and the rest do not keep any records. The study found that 67% of the companies stated that Sharjah Municipality is responsible for implementing health and safety policy in construction, and 33% of these companies claimed that they only received recommendations regarding health and safety regulations which is not enough support. All companies agreed that implementing health and safety regulations should improve organization performance. Neglecting the health and safety procedures will have an impact on the overall cost which will affect the project performance, it will also have a direct impact

on human life, therefore will cause a loss of time and money. With Zero accidents morale of workers at the site will increase and increase in productivity. Implementing health and safety regulations maintains a constant progressive outcome and prevents any setbacks or major delays and helps to assess potential risks and identify significant hazards. The suggestions of all companies to improve the H&S procedures can be briefed as follows:Health and safety policies should be implemented and forced by the government on the construction companies.

- Health and safety training should be mandatory in construction and consultant companies and can be delivered by third-party specialists.
- Environmental health and safety policies should be implanted.

All companies should have a clear written health and safety policy

3. CONCLUSIONS

Implementation of safety and health regulations represents one of the important issues in the construction sector in UAE, Emirate of Sharjah, from this research some conclusions can be drawn as follows:

1- There is no specific governmental department responsible for issuing and implanting health and safety regulations in the construction industry.
2- Different nationalities, habits , and languages were found to have a great effect on health and safety implantation.
3- A distinctive number of construction companies have written health and safety regulations that developed by the companies themselves.
4- All the construction companies provide their workers with PPE, and use the municipality health and safety guide boards on - site, where cranes and scaffolding are certified by a third-party specialist.
5- Most of the construction companies conducted formal health and safety training for their workers and some have qualified health and safety officers to perform the training and inspections.
6-Some of the construction companies do not have departments to implement the regulations of safety and health, while 42% of the companies have a specific department to follow the safety and health regulations.
7- All the minor accidents have been treated on - site, while the major accident reported and treated by health authorities.
8- The majority of the companies have a record of occurred accidents at sites.
9- The most distinctive accidents that occurred at the site are falling from height and falling objectives while working on site.
10- The number of annual major accidents that occurred ranged from 1 to 5 accidents in most construction companies.
11-All companies agreed that implementing health and safety regulations will increase the performance and productivity of the company and should reduce the cost of the project.
12- More than half of the consultant companies have no written health and safety policies , while some developed their policies and a few follow the municipality's policies.
13- Most of the consultant companies do not implement health and safety regulations during the design stage while 67% of the companies do not have formal health and safety training programs for their employees and do not have any department responsible for implementing health and safety procedures.
14- All the consultant companies do not hire external health and safety consultants, while some have internal consultants.
15- The majority of the consultant companies do not conduct site visits to inspect the safety and health regulations safety and have no role in occurred accidents.
16- Consultant companies have no direct role when accidents occur on - site, while 11% of the companies stated that the procedure is set out in the Main Contractor's responsibilities.
17- Some of the consultant companies stated that the major causes of the accidents are falling from height ,unsafe scaffolding , and falling tower cranes.
18- Few consultant companies keep records of accidents that occurred at the sites.
19- The majority of the consultant companies stated that Sharjah Municipality is responsible for implementing health and safety policy in construction, and some of these companies claimed that they only received recommendations regarding health and safety regulations which is not enough support

3. REFERENCES

[1]Vitharana V., Subashi G., and Sudhira D., Health hazards, risk and safety practice in construction sites – a review study. Engineer, Journal of the Institution of Engineer, Sri Lanka, 2015, Vol. 48, No.03, pp 35-44.

[2]Winge S., Albrechtsen E.m., and Amesen J., A comparative analysis of safety management and safety performance in twelve construction projects. Journal of Safety Research, 2019, Vol.71, pp 139-152

[3]Oh T., Kwon Y. , Oh B., Gwon Y.,and Yoon H., Suggestions for safety coordinator's roles at each construction stage (client,designer, supervisor, and contractor) to improve safety and health ctivities in South Korea, Safety Science , 020,https://doi.org/10.1016/j.ssci.2020.104994, Elsevier .

[4]Woolley M., Goode N., Salmon P., and Read G., Who is responsible for construction safety in Australia? A STAMP analysis, Safety Science, 2020, Vol.132.

[5]Roddy C., A review of health & safety in construction in the U.A.E. within an international construction company. Salford,2014,MSc thesis, University of Salford

[6]Al-Kaabi N. and Hadipriono, F., Construction safety performance in the United Arab Emirates. Civil Engineering and Environmental Systems, 2003, vol.20, issue 3, pp 197-212.

[7]Shibani A., Saidani M., and Alhajeri M., Health and safety influence on the construction project performance in United Arab Emirates, Journal of Civil Engineering and Construction Technology ,2013,Vol. 4,issue 2, pp. 32 – 44.

[8]Choudhry R., Fang D., and Ahmed S., Safety management in construction: best practice in Hong Kong. Journal of profession issues in engineering education and practice, 2020, Vol.134, Issues .1.

[9]Abed H., Hatem W., and Jasim N., Role of BIM technology in enhancing safety analysis of Iraqi oil projects. Asian Journal of Civil Engineering, 2020,Vol.21, pp695-706

[10]Othman I., Shafiq N., and Nuruddin M., Effective Safety Management in Construction Project. International Conference on Architecture and Civil Engineering, 2017, Malaysia

[11]Zhang J., Li H., Xia B., and Skitmore M., Impact of environment regulation on the efficiency of regional construction industry: A 3-stage Data Envelopment Analysis. Journal of Cleaner Production, 2018, p. 770 – 780

[12]Harvey E., Waterson P., and Dainty A., Beyond ConCA: Rethinking causality and construction accidents. Applied Ergonomics , 2018,vol 73, pp. 108 – 121.

[13]Gao R., Chan A.P.C., Lyu S., Zahoor H., and Utama W., Investigating the difficulties of implementing safety practices in international construction projects. Safety Science,2018, vol 108, p.39 – 47.

[14]Mohammadi A., Tavakolan M., and Khosravi Y., Factors infuencing safety performance on construction projects: A review, Safety Science, 2018, vol 109, p. 382 - 397.

[15]Yiu N., ze N., and Chan D., Implementation of safety management systems in Hong Kong construction industry – A safety practitioner's perspective. Journal of Safety Research, 2018, vol 64, pp. 1 – 9.

PRODUCTION AND FRESH PROPORTIES OF SELF-COMPACTING CONCRETE CONTAINING MPF AND FPF FIBERS

Osama.M. A Daoud [1] and Nouraldaim.F. A.Yagoub [2]
Building and Roads Research Institute[1], University of Khartoum[2], Khartoum, Sudan[3]

ABSTRACT

This paper presents the results of an experimental study conducted to performance of the self- compacting concrete containing the two types of fibers (Monofilament and "Fiber Guard-Fibrillated polypropylene) in Sudan. The primary objective of the study is to conduct an exploration work towards the development of a suitable SCC mix, with consideration focus on problems related to satisfactory segregation resistance, filling, and passing abilities thorough conducting a series of trial mixes. In addition, the paper investigates different fresh properties of SCC containing fibers and their interrelations at the fresh state. Different tests were carried out to characterize raw materials. All necessary modifications in proportioning and mixing are mentioned. The SCC with different percentages fibers mixes was produced and their fresh properties were studied by taking into consideration the length of the fibers. Some reliable statistical relations between fresh properties of SCC containing fibers were developed and presented. The effects of fibers content on fresh properties of SCC were also highlighted and the optimum amount of fibers was obtained. Results showed that the addition of the fibers adversely affected on the fresh state properties of self- compacting concrete such as (workability), this adverse effect could be avoided by increasing Super-plasticizers content so as to maintain self- compacting concrete properties.

Keywords: Self-Compacted Concrete, Polypropylene Fiber, Fly Ash, Concrete.

INTRODUCTION

Concrete is characterized by quasi-brittle failure, the nearly complete loss of loading capacity, once failure is initiated. This characteristic, which limits the application of the material, can be overcome by the inclusion of a small amount of randomly distributed fibers and can be practiced among others that remedy weaknesses of concrete, such as low growth resistance, high shrinkage cracking, low durability, etc. Fiber reinforced self-compacting concrete is the composite material containing fibers in the cement matrix in an orderly or randomly distributed manner. Its properties would obviously, depend upon the efficient transfer of stress between matrix and the fibers, which is largely dependent on the type of fiber, fiber geometry, fiber content, and distribution of the fibers, mixing and size and shape of the aggregate. Fiber reinforced self-compacted concretes exhibit property improvement caused by the fibers. (MPF and FPF) have great influence on the behavior of concrete under loading. Fibers of Fibrillated Polypropylene form a mesh structure which binds the coarse aggregates in it, resulting in less workability of self-compacting concrete. Fibrillated Polypropylene fibers actually inhibit the Formation of cracks in self-compacting concrete matrix. Fibrillated polypropylene fibers are slit and expanded into an open network thus offering a larger specific surface area with improved bond characteristics that is they do not absorb water. Therefore, when placed in a concrete matrix they need only be mixed long enough to insure dispersion in the concrete mixture. The mixing time of (MPF and FPF) fibers should be kept to a minimum to avoid possible shredding of the fibers. The type of polypropylene fiber recommended by manufacturers for paving applications is the collated fibrillated fiber.

MATERIALS USED

Cement

Ordinary Portland cement (Type I) was used. The chemical analysis of cement is presented in Table 1 [1].

Fly Ash

Class F Fly ash obtained from Zouxian power plant was used. The chemical analysis of fly ash is presented in Table 2. Chemical analysis was carried out according to the ASTM C311/C311M-18[2].

Table 1 Chemical analysis of cement

Test	% by mass
Loss on ignition at J OOO°C	4.63
Silica as Si02	19.53
Aluminum oxide as Al203	5.66
Ferric oxide as F~03	3.20
Calcium oxide as CaO Magnesium oxide as MgO	58.37 2.67

Table 2 Chemical analysis of fly ash

Test	Result according to BS
Moisture content	0.29%
Fineness	8.11%
Particle density	2031kg/m³
Water requirement	89%
Soundness	8.89 mm
Strength factor	0.88

Coarse Aggregates

Natural crushed igneous stones with maximum size 20 mm processed from the local quarries of Toryia Mountain were used as coarse aggregates (Fig.1). The average values of specific gravity and absorption were 2.8 and 1.8 %, respectively [3].

Chemical Admixtures

Sikament ® -R2004complies with ASTM C-494 Type G and BS 5075 part 3 was used. It is a modified synthetic dispersion brown liquid with density of 1.2 ± .005 kg/I at 20° C.

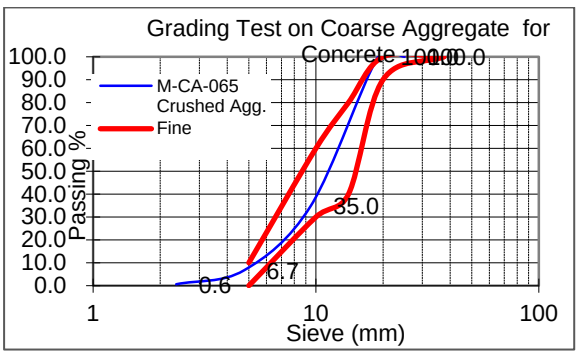


Fig.1 Particle size distribution of coarse aggregates using BSjacket.

Fine Aggregates

Locally available natural sand was used as fine aggregate. The sand used was classified as class M according to BS 882:1992. Physical properties of sand and sieve analysis are presented in Table 3 respectively [4].

Table 3 the physical properties of fine aggregates

Properties	Determined as
specific gravity	2.66
Apparent	2.63
Absorption %	0.7
Bulk density (Kg/m3)	1692
Fineness modulus(Sieve analysis)	2.36
Silt and clay content	3.47 %

EXPERIMENTAL WORK

A fixed mixing procedure takes 7 minutes was adopted and carried out throughout this research using a drum type concrete mixer. In order to achieve dispersion of the powder and fibres, and to avoid balling effect; the concrete was mixed in the flowing way [5]:

1. Binder and aggregate are mixed for one minute.

2. The 1st part (70%) of water was added and mixed for two minutes.

3. SP along with the 2nd part (30%) of water was added and mixed for two minutes.

4. The mix was stopped and kept rest for 1 minutes.

5. The mix was remixed for one minute.

6. Polypropylene Fiber added for the mix and discharged for SCC tests.

Uniformity of the mix was visually inspected continuously during all stages of mixing, sampling, and testing.

Following these steps, six different mixes of self-compacted concrete were prepared. Properties of the mixes are shown presented in Table 4.

Mix Proportioning

Table 4 Proportions of SCC Mixes.

Trial Mix. No	Total Powder Content (Kg/m³)	Cement (Kg/m³)	FA (Kg/m³)	Sand (Kg/m³)	C.A (Kg/m³)	S/C.A ratio	Water (Kg/m³)	W/P ratio	SP (L/m³)
1	528	528	0	950	792	1.19	190	0.36	8
2	528	528	0	793	898	0.88	212	0.40	9
3	528	536	0	910	803	1.13	198	0.37	8
4	550	412.5	137.5	829	829	1	187	0.34	9.9
5	550	412.5	137.5	829	829	1	190	0.35	10.45
6	550	412.5	137.5	829	829	1	198	0.36	11

RESULTS AND DISCUSSION

General

All data obtained for the fresh properties through the trials performed during the experimental work are presented graphically and discussed in the following sections. The succeeded trial that satisfied, self-compacting properties was the control trial mix (TR6). It is commonly accepted that a T50 < 5s, concrete flow diameter (Fd) > 650mm, and V-funnel < 12 s, and segregation index < 15% will produce a good performing SCC (EFNARC, 2002). The slump flow of the selected mix obtained approximately 770 mm which indicated good deformability [6].

The slump flow obtained is categorized as SF2, which is suitable for many normal applications (e.g. walls, columns). The effect of the two types of fibers (MPF and FPF) on workability has been examined. Test results of this research indicated that all SCC mixes satisfy the requirements of the allowable flow time and they are categorized as VS1/VF1; The selected mixes have similar slump flow times of average 2 seconds, consequently all the selected mixes have good flow ability even with congested reinforcement. The addition of fibers affected the slump flow time as indicated by the J-ring results (Fig.2).

All mixes exhibited good passing ability and no blockage was exhibited in any of the mixes. All mixes displayed good resistance to segregation categorizes as SR2 (Fig.3 and Fig.4).

Series of mixes were carried out on concrete to ensure the fresh and hardened properties of Self Compacting Concrete (SCC). The first step in the test program comprises developing six trial mixes to obtain the star up mix of SCC. Then the second step included developing control mix. All mixing proportions were kept fixed and both types of fibers had been added with varied percentages.



Fig.2 J-Ring test



Fig.3 V-funnel test



Fig.4 It explains the process of fiber weight.

Effect of Addition of (MPF and FPF) on Workability.

According to the results shown presented in fig. 5, 6,7and 8, it is clear that the workability (flow diameter) of self-compacted concrete containing fibers decreased with the increase of (MPF and FPF) content.

A linear relationship in the form of (y = -670.00x + 756.50 with R^2 = 0.881 for the type one 12mm "type two y = -456.00x + 774.70 with R^2 = 0.957 for 6mm, y = - 627x + 759 with R^2 = 0.932 for 12mm, y = - 456.00x + 774.70 with R^2 = 0.951 for 20mm") were obtained. But there was difference in workability for the two types of fibers due to thickness and length of the fibers. Furthermore the results obtained from J-ring and V-funnel achieved times (T50cm, T10s, andT5min) were more than that of control mix, indicating that low workability and Normal filling ability obtained using of two types of fibers (MPF and FPF) [7].

All mixes showed good passing ability as indicated by the step height parameter (Bj), and it seems that the addition of fibers did not make any difference. It was noticed that from the results obtained of J-ring test, the flow spread (Fd) decreases when the fibers content increases but at the same time indicating a good deformability, except the flow spread of 0.15% fibers (MPF and FPF) decreases by noticeable value .

All mixes with addition FPF fibers have similar slump flow times T50cm (average 2 seconds), except for the mix of 0.15% FPF has taken long time, that means the addition of fibers affected the slump flow time, but It was noticed that Monofilament polypropylene Fibers increased flow time for all mixes specially the mix of 0.15% MPF which was increased from 2.7 sec to 4.4 sec. from the results which obtained from the slump flow and j-ring test it is clear that the workability adversely affected when the ratio of the fibers increased from 0.1% to 0.15%. In spite of this the results obtained were still within the acceptance range [8].

Relationships Between Key Characteristics of The SCC with Addition of the (MPF and FPF) Fibers

The following sub-sections present the analysis and discussion of results including comparisons with previous researches. Relationships between fibers % in fresh Properties of SCC:

Fibers percentage vs. slump flow

It is clear from (Fig.5) that the addition of fibers decreases the slump flow for all mixes. The reduction in workability was varying due to the friction between the flowing and the surface, length and thickness of fibers.

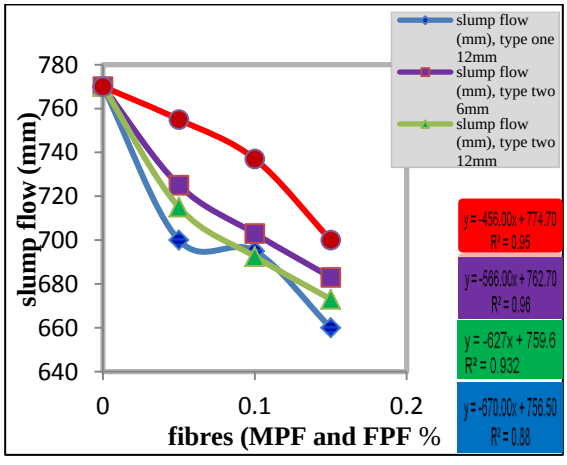


Fig.5 Relationships between Fibers % and slump flow(mm).

Fibers % vs. T50cm time

The obtained data shows almost linear relationship between fibers percentage andT50cm times as shown in(Fig.6), the time of the slump flow increased with an increase in the percentage of fibers. Straight lines were obtained from the data an equation in the forms of (y = 12.8x + 2.54 with R^2 = 0.994 for type one 12mm, type two "y = 10.82x + 2.556 with R^2 = 0.922 for 6mm, y = 9.46x + 2.203 with R^2 = 0.878 for 12mm, y = 4.44x + 2.677 with R^2 = 0.969 for 20mm"), which are ideal.

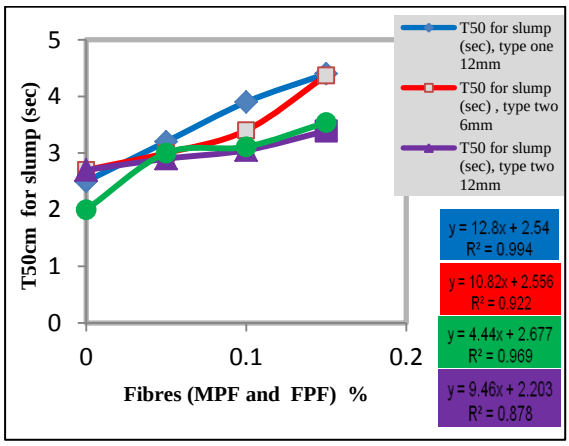


Fig.6 Relationships between Fibers %, and T 50cm for slump (sec)

Fibers percentage vs. (Bj) for J-Ring (mm)

The relationship between fibers percentage and (Bj) for J-Ring (mm) was demonstrated by plotting step height of J-ring as shown in (Fig.7). With the percentage of addition both types of fibers increased it means that the slump flow decreased and the step height of J-ring increased, as a result of that the tendency to blocking increased. Blocking criteria was unlikely to occur in this research as indicated from test results. The maximum value obtained for step height (Bj) was equal to 1.75mm which is close to acceptable value.

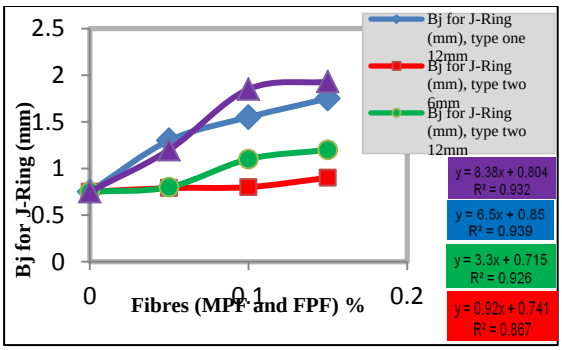


Fig 7 Relationships between Fibers %, and Bj- for J-Ring (mm).

Fibers percentage vs. V-Funnel.

It clear that from (Fig.8) with the increase of (MPF and FPF) fibers content the V-Funnel test shows an increase in the time to empty the V-Funnel as the percentage of fibers increases and the correlation coefficients were obtained.

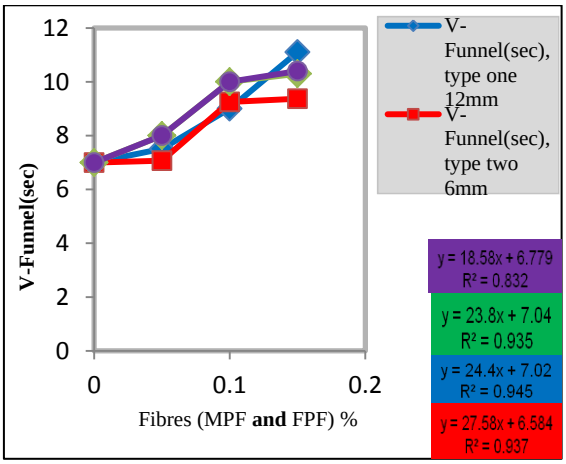


Fig.8 Relationships between Fibers %, and V-Funnel (sec).

Fibers percentage vs. L-Box (mm).

The Figure 9 shows the relationship between (MPF and FPF) fibers content and the L-Box test with the percentage of addition both types of fibers. It is clear that the fibers were not affected in passing ability due to obtained the result which confirms good passing abilities and within the range (h2/h1=0.8-1.0) according to EFNARC Guidelines, (2002).The distribution of data showed that most data have slump flow in the range of 600mm-800mm with v-funnel time lies in range of 6 – 12 sec, and step height of 0.75 to1.75 mm; which confirms good filling ability and passing ability according to European Guidelines, (2005)

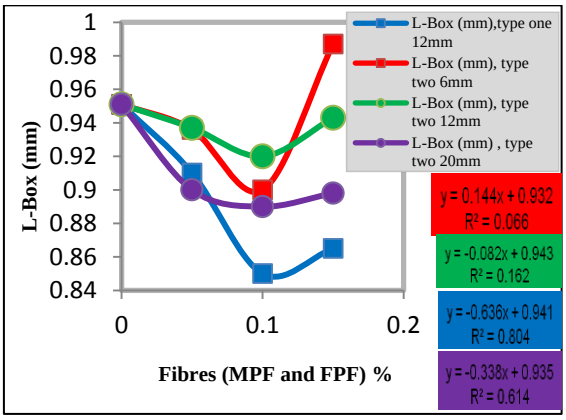


Fig.9 Relationships between Fibers %, and L-Box (mm).

CONCLUSIONS

SCC Powder has been successfully produced, using class F fly ash and replaced cement 25%.

SCC is very sensitive to small changes in constituent materials, so it requires careful attention during all production stages.

It was observed that the fresh properties for all tests samples from the self-compacting concrete containing fibers are good and within the acceptance range as compared to the control mix.

It was found that the addition of the fibers adversely affected the fresh properties of self-compacting concrete such as (workability), this adverse effect could be avoided with increasing Super-plasticizers content to maintain self-compacting concrete properties.

REFERENCES

[1] ASTM C150/C150M-20 Standard Specification for Portland cement.

[2] ASTM C311/C311M-18 Standard Test Methods for Sampling and Testing Fly Ash or Natural Pozzolans for Use in Portland Cement Concrete.

[3] ASTM C33/C33 M-18 Standard Specification for Concrete Aggregates.

[4] ASTM C 128 Standard Test Method for Density, Relative Density (Specific Gravity), and Absorption of Fine Aggregate.

[5] Andreas Huss and Hans W. Reinhardt, Design and Flow of Powder-type SCC with Crushed Aggregates, Design, Production and Placement of Self-Consolidating Concrete, Proceedings of SCC2010, Montreal, Canada, September 26–29, 2010, RILEM Bookseries 1, pp. 3-11.

[6] Lohaus, L., Ramge, P., Höveling, H. and Anders, S., Superplasticizer-Based Approach for Optimized Paste composition and Robustness of SCC, Proceedings of the 5th Int. RILEM Symposium on Self-Compacting Concrete - SCC2007, De Schutter, G., Boel, V. (Eds), RILEM Publications S.A.R.L. Bagneux, pp. 89-94.

[7] Kumar P., Self-compacting Concrete: Methods of Testing and Design, Journal of Institution of Engineers (India), IE(I) Journal-CV, Vol. 86, February 2006.

[8] Marcovic I., Walraven J. (2003), "Self-Compacting hybrid fiber Concrete-mix design, Workability and Mechanical Properties", Third International Symposium on Self-Compacting Concrete 2003, Reykjavik, pp. 763-775.

7th Int. Conf. on Structure, Engineering & Environment (SEE), Pattaya, Thailand, Nov.10-12, 2021, ISBN: 978-4-909106070 C3051

STUDY ON PROPERTIES OF CONCRETE MIXED WITH RICE HUSK ASH ADSORBING HEAVY METALS

Ayane Yanaka[1], Takuto Ueno[1], Shinichiro Okazaki[2], Naomochi Matsumoto[2] and Hidenori Yoshida[2]

[1] Graduate School of Engineering, Kagawa University, Japan; [2] Faculty of Engineering and Design, Kagawa University, Japan

ABSTRACT

Goals 12 of the Sustainable Development Goals (SDGs), “Sustainable Consumption and Production”, aims to achieve “Drastic reduction of waste generation through the prevention, reduction, recycling and reuse of waste” by 2030. In Asia, more than 100 million tons of rice husk are discharged annually, but the generation of wastes has not been drastically reduced, though they are utilized for biomass power generation as a reuse. Therefore, it is necessary to develop a method to realize a significant reduction of rice husk. The rice husk has the following features; it has the adsorption performance for heavy metals and incinerated rice husk contains a large amount of amorphous silica, which may increase the strength of concrete. Thus, firstly, untreated rice husk is utilized as an adsorbent for heavy metals. After that, it is used for biomass power generation to reduce its volume. Since heavy metals remained in the rice husk are concentrated at this stage, the rice husk ash used for biomass power generation is mixed as fine aggregate of concrete instead of being discarded as it is. In this study, fresh properties are examined by slump test and air volume test, hardening property is investigated by compressive strength test, and harmful substance elution is evaluated by dissolution test. As the result, the concrete has fresh properties with no problem in construction, the concrete mixed with rice husk ash has a higher compressive strength than ordinary concrete, and no harmful substance is eluted from the concrete mixed with rice husk ash.

Keywords: Rice husk ash, Recycling, Concrete admixture, Heavy metals

INTRODUCTION

In recent years, various environmental problems such as environmental pollutions and the shortage of waste disposal sites are faced by the mass consumption of resources and energy and the increase of waste discharge associated with the consumptions. Therefore, the formation of a recycling-oriented society becomes an urgent problem. As the initiatives to realize a recycling-oriented-society, the goal 12, “Sustainable Consumption and Production” which is one of the 17 goals raised in "Sustainable Development Goals (SDGs)" aims to achieve "Drastic reduction of waste generation through the prevention, reduction, recycling and reuse of waste" by 2030. Recently, as a part of the generation control and reduction of wastes, the recycling of food wastes which are regarded as a worldwide problem is promoted due to their enormous generation. In Asia, where rice is the staple food, more than 100 million tons of rice husk are discharged annually as food waste. As a reuse, as shown in [1], they are utilized as an energy resource for biomass power generation, which is one of the renewable energies. However, in biomass power generation, the amount of generation waste has not been drastically reduced in the true sense because a large amount of rice husk ash is generated as an energy resource after incinerating rice husk. Therefore, it is necessary to develop a method to realize a significant reduction of rice husk. In addition, it is also necessary to change the rice husk to a resource recycling material with high-added value in recycling the rice husk because it is important to implement the development method in society at an early stage. As reported in [2] and [3], even untreated rice husk has adsorption performance for heavy metals in an aqueous solution. Additionally, as described in [4], the incinerated rice husk contains a large amount of amorphous silica. In this study, at first, untreated rice husk is utilized as an adsorbent for heavy metals, and metals with high value are recovered after adsorption. After that, it is used for biomass power generation to reduce its volume. In this stage, since heavy metals remained in rice husk ash are concentrated, the rice husk ash in which heavy metals remain is mixed as fine aggregate of concrete instead of being discarded as it is. Since rice husk ash contains a large amount of amorphous silica, there is a possibility that the merits such as an increase of concrete strength are brought about as shown in [5] and [6] That is to say, in the achievement of zero-emission of rice husk which is a sort of food waste, it is very important whether rice husk ash can be mixed into concrete or not.

Therefore, in this study, the fresh and hardening properties are grasped for concrete mixed with rice husk ash containing heavy metals, and whether it can be used as concrete or not is evaluated. Furthermore,

the elution properties of heavy metals from concrete mixed with rice husk ash containing heavy metals are examined in order to assess environmental loading.

MATERIALS

Cement And Aggregate

Ordinary Portland Cement (density 3.16 g/cm^3) specified in JIS R 5210 Japanese Industrial Standards is used for cement. In addition, the mountain sand and crushed stone 2005 produced in Sanuki City, Kagawa Prefecture, Japan are used for fine aggregate and coarse aggregate, respectively. According to the properties of the used aggregate, the surface dry density and maximum particle size for fine aggregate are respectively 2.57 g/cm^3 and 2.5 mm, and those for coarse aggregate are respectively 2.62 g/cm^3 and 20mm.

Rice Husk Ash

According to [7], rice husk ash contains about 90 % silica by mass. The silica content of rice husk ash is higher than that of fly ash, and the content of rice husk ash is comparable to that of silica fume. Moreover, it is reported that silica as the amount of the amorphous state is large, the reactivity of the silica contained in rice husk ash increases. Therefore, as described in [8], it is expected to promote the pozzolanic reaction, which is related to the improvement of concrete strength. Thus, rice husk ash is noticed as a high silica material. Additionally, the research to use rice husk ash as a concrete admixture is studied, because the properties of dense and strength of concrete are improved due to amorphous silica. From the result of XRD analysis of rice hull ash incinerated at 600 ~ 1150 ºC conducted by Umeda et al.[9], it is reported that the incinerated at 1000 ºC or less is necessary in order to maintain the amorphous structure of silica. In addition, as shown in [10], in order to obtain amorphous silica, it is desirable to incinerate rice husk at low temperature as much as possible and in a minimum of time. Thus, in this study, rice husk is put into an alumina vessel, heated to 600 °C in an electric furnace for 2 hours, then incinerate at 600 °C for 3 hours, and then left to cool. Fig. 1 shows the rice husk ash prepared to use in this study. Then, in order to confirm whether silica contained in the prepared rice husk ash is amorphous or not, the crystal structure of the prepared rice husk ash is analyzed by XRD (X-ray Diffraction) analysis.

Fig. 2 shows the spectrum of the prepared rice husk ash analyzed by the XRD analysis. From the peak position and peak width of the spectrum obtained by the XRD analysis, it is possible to know the components and crystallinity of the prepared rice husk ash. The horizontal and vertical axes in Fig. 2 are the diffraction angle and the X-ray diffraction intensity, respectively. From Fig. 2, it can be seen that the intensity peak appears in the vicinity of 22 º to 23 º of 2θ. In addition, it is found that the peak width is wide, and that the X-ray diffraction pattern (called halo according to [11]) is continuous. As a result of XRD analysis, a broad peak (halo pattern) appeared between 15 º and 30 º around 22.5 º of 2θ, so it can be said that silica in the rice husk ash produced in this study is a typical amorphous state. Such fact is seen to have a good accordance with the references [12] and [13].



Fig. 1 Rice husk ash

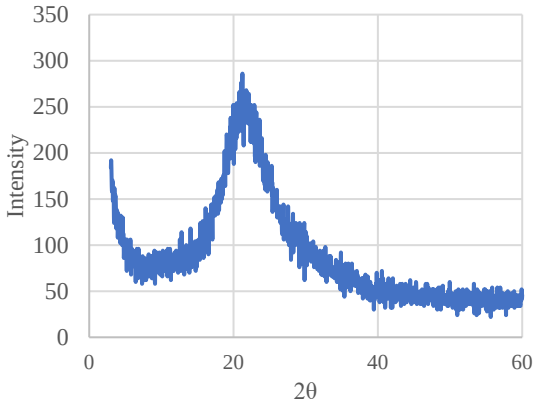


Fig. 2 Spectrum of rice husk ash by XRD

Chemical Admixture

For chemical admixtures, the air-entraining and high-range water-reducing admixture (AE-HR-WRA) and the air-entraining admixture (AE-A) are used, respectively. Regarding the main components of the used chemical admixture, the main component of AE-HR-WRA is a complex of a lignin sulfonic acid compound and a polycarboxylic acid ether, and the main component of AE-A is a modified rosinic acid compound-based anionic surfactant.

TEST METHOD

Concrete Mix Design

On the concrete in the tests, the mix proportion is designed at a water-cement ratio of 55 % and a fine aggregate ratio of 46 %. Table 1 shows the mix proportions of concrete in the test. “Blank” is ordinary concrete (concrete without rice husk ash), “RHA” is concrete mixed with rice husk ash, and “RHA(Cd)” is concrete mixed with rice husk ash adsorbing cadmium. The heavy metal which is mixed in the concrete of the test is cadmium which is known as a causative substance of pollution diseases in Japan and is a toxic heavy metal that affects living organisms and the environment. The mixing method of rice husk ash into concrete is so-called "outer percentage mixing" in which fine aggregate is replaced by the rice husk ash, and the replacement rate is 5 % for the volume of fine aggregate. 1.9 % (RHA and RHA(Cd)) for the cement mass, respectively. Then, the addition amount of AE-A is 0.001 % (all specimens) for the cement mass. Furthermore, as shown in [14], there are studies on the elution behavior of heavy metals from mortar containing heavy metals. However, there are few studies on the elution of heavy metals from concrete mixed with rice husk ash as admixture. Thus, in the test, a predetermined concentration of cadmium is adsorbed on the rice husk ash in advance. Concretely, the adsorption test (shaking test) of rice husk ash for cadmium is carried out using the cadmium nitrate solution prepared at the initial concentration of 1 ppm, and the residual concentration of cadmium is analyzed by ICP-AES after the shaking test. From the results, it is found that about 0.9 ppm of cadmium is adsorbed on the rice husk ash used in the tests. Therefore, this concentration (about 0.9 ppm) shall be taken as the initial concentration of cadmium in rice husk ash. In addition, mixing is carried out according to the following procedure. First, half of the aggregate (coarse aggregate, fine aggregate, rice husk ash), cement, and the rest of the aggregate are put to the mixer in that order. Rice husk ash is mixed with the fine aggregates in advance. After putting the materials into the mixer for 30 seconds, rotate the mixer to mix the materials. Then, pure water with a chemical admixture is poured into the mixer, and mix for 60 seconds for Blank specimen and for 90 seconds for RHA and RHA(Cd) ones.

Fresh Properties Test For Concrete

Regarding the fresh properties tests, each material (cement, aggregate, rice husk ash, and so on) is mixed using a mixer to prepare a concrete sample. After that, the slump test and air volume test are carried out according to JIS A 1101 Japanese Industrial Standards and JIS A 1128 Japanese Industrial Standards, respectively. In the slump test, first, the slump cone is filled with three layers of fresh concrete. In each time, approximately one-third of fresh concrete is filled into the slump cone, and the fresh concrete is struck 25 times with a rod. After filling the slump cone with fresh concrete, the fresh concrete which protrudes from the upper part of the slump cone is made flat in alignment with the upper end surface of the slump cone. After that, the slump cone is lifted vertically for 2 to 3 seconds, and the slump is measured. In the air volume test, the air volume measuring instrument is filled with fresh concrete in the same procedure as the slump test described above. After that, the side of the container is hit with a wooden hammer, fresh concrete protruding from the upper part of the container is removed and the upper part of the container is leveled. Next, the lid is gently attached to the container with the exhaust port opening, and four fasteners are tightened. Then, after the exhaust port and the pressure control valve are closed, the pressure in the container is raised using a pump and the pointer of the pressure gauge is adjusted to the scale of the initial pressure. Afterward, the actuated valve is opened for about 5 seconds, and the scale of the air volume of the pressure gauge is recorded to one decimal place. In the test, the target slump and air volume values are set to 12±2.5 cm and 4.5±1.5 %, respectively.

Preparing Of Test Specimen For Concrete

A cylindrical specimen of ϕ100 × 200 mm is prepared in accordance with JIS A 1132, the Japanese Industrial Standard. Two patterns of cylindrical specimens are prepared for compressive strength test and dissolution test. After preparing the specimens, they are cured in water for 28days. The upper surface of the specimen is grinded by a polishing grinder so that the specimen loading surface (upper surface) of the test specimen becomes flat.

Table 1 Mix proportions of concrete (kg/m^3)

	Water	Cement	Rice Husk Ash	Fine Aggregate	Coarse Aggregate	AE-HR-WRA	AE-A
Blank	175	318	0	785	940	2.86	0.003
RHA	175	318	32	746	940	6.05	0.003
RHA(Cd)	175	318	32	746	940	6.05	0.003

Hardening Properties Test For Concrete

After the specimens are cured in water for 28 days, the compressive strength test is carried out as a physical property test of concrete in accordance with JIS A 1108 of the Japanese Industrial Standard. In the procedure of the compressive strength test, the specimen is placed in the universal testing machine, and the specimen is loaded at a uniform speed so as not to give an impact to it. After that, the maximum load indicated by the testing machine is recorded and the compressive strength is calculated. The compressive strength is defined by the following equation (1).

$$f_c(N/mm^2) = \frac{P}{\pi d^2/4} \quad (1)$$

where, "*fc*" is the compressive strength, "*P*" is the maximum load and "*d*" is the measuring diameter of the cylindrical test specimen. In order to ensure reproducibility, the mean value of three tests is adopted as a test result in the tests.

Heavy Metals Elution Test From Concrete

In the test, the elution test of cadmium from concrete is conducted based on the Environment Agency Notification 46. First, the specimen is crushed to 5 mm or less with a hammer, and the crushed blocks passed through a sieve (mesh opening 2 mm) defined as a sample. Next, 50 mL of pure water is poured into a centrifuge tube, and 5 g of the sample is also added into the centrifuge tube. They are defined as the specimen in the test. The ratio of pure water to the sample in the specimens is 10 % of the weight-volume ratio. Then, the test specimens are shaken for 6 hours at 200 rpm at 20 °C. After shaking, the specimens are allowed to stand for 10 to 30 minutes, and they are centrifuged at 3000 rpm for 20 minutes. After centrifugation, the supernatant solution of the specimen is filtered through a membrane filter (pore size: 45 μm), and the concentration of cadmium in the filtered solution is analyzed by an ICP-AES. In order to ensure reproducibility, the mean value of the tests is calculated from the results obtained by three tests as well as the compressive strength test.

RESULTS AND DISCUSSION

Result Of Fresh Properties Test For Concrete

Table 2 shows the slump value and air volume value for the three cases of Blank, RHA and RHA(Cd) samples. From Table 2, it can be seen that the slump value and air volume value achieve the target values in all the fresh concrete. Although the air volume values of all the fresh concrete are within the allowable value, they are lower than the standard value of 4.5 %. In the tests, it is considered that the amount of air was not entrained than expected, because the amount of AE-A added in all the concretes was considerably small (0.001 % of cement mass). In all the samples, the slump value reaches the target one. However, compared to the slump value of Blank, RHA and RHA(Cd) sample and the slump shape of that (see Fig. 3 to Fig. 5), regarding the Blank sample, it can be seen that the slump value is the largest, and that the slump shape also collapses from the top. This is because material separation occurs in the fresh concrete of the Blank sample due to the uneven mixing of materials. In the RHA sample, the collapse of the slump from the top can be confirmed, though it is not as much as the Blank sample. According to this fact, it can be seen that the material separation occurs even in fresh concrete of the RHA sample. On the other hand, the slump of the RHA(Cd) does not collapse. Additionally, it is found that the fresh concrete of the RHA (Cd) specimen has a higher viscosity than that of other specimens. Further examinations are needed to obtain more detailed information on the fresh property of the RHA(Cd) specimen.



Fig. 3 Slump of the Blank



Fig. 4 Slump of the RHA

Table 2 Result of fresh properties test for concrete

	Slump value (cm)	Air volume value (%)
Blank	14.3	3.0
RHA	13.0	3.6
RHA(Cd)	10.3	3.1



Fig. 5 Slump of the RHA(Cd)

Result Of Hardening Properties Test For Concrete

Fig. 6 shows the compressive strength of Blank, RHA and RHA(Cd) concrete. From Fig. 6, it is found that the compressive strength of the RHA sample is much higher than that of the Blank one. This is due to the pozzolanic reactivity by amorphous silica contained in the rice husk ash. Additionally, according to [15], it is reported that the concrete mixed with rice husk ash with the addition of superplasticizer shows much higher compressive strength than that without superplasticizer. This is because the water-binding ratio decreases due to the addition of a superplasticizer. In the test, since the addition amount of AE-HR-WRA to the RHA is more than twice that to the Blank, the unit water content of the RHA decreases more than that of the Blank. As the water-cement ratio decreases, concrete strength increases. Therefore, it is considered that the compressive strength of the RHA is higher than that of the Blank. Additionally, there is not much difference between the compressive strength of the RHA(Cd) and that of the RHA. It is suggested that the presence or absence of Cd in rice husk ash has little effect on the strength of concrete in the low concentration of Cd in rice husk.

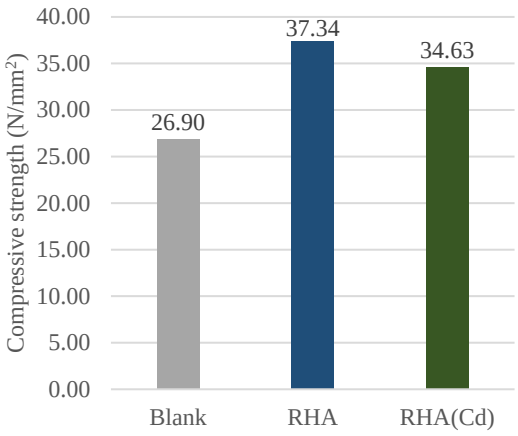


Fig. 6 Result of compressive strength test (28 days)

Result Of Heavy Metals Elution Test From Concrete

Fig. 7 shows the eluted concentration of Cd from Blank, RHA and RHA(Cd) concrete. The effluent standard for Cd in Japan is 0.03 ppm. From Fig. 7, the eluted concentration of Cd was less than 0.03 ppm for all concrete specimens, and the elution of Cd could hardly be confirmed. It is considered that Cd does not elute from concrete even when rice husk ash adsorbing Cd is mixed with concrete. Therefore, even if rice husk ash containing Cd at a low concentration is used as a concrete mixture, it can be said that there is no impact on the environment.

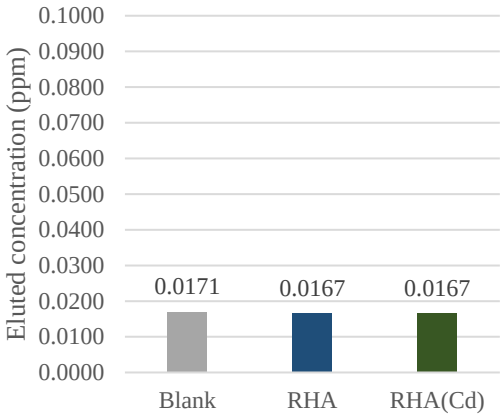


Fig. 7 Result of elution test

CONCLUSIONS

In this study, the fresh and hardening properties were grasped for concrete without rice husk ash (Blank), concrete mixed with rice husk ash (RHA) and concrete mixed with rice husk ash containing cadmium (RHA(Cd)), respectively, and whether RHA(Cd) can be used as concrete or not was evaluated. Furthermore, in order to assess environmental loading, whether cadmium elutes from RHA(Cd) or not was examined. The results obtained are as follows.

- The slump value and air volume value achieved the target values (slump: 12±2.5cm and air volume: 4.5±1.5%) in all the fresh concrete of Blank, RHA and RHA(Cd).
- From the slump shape of each fresh concrete, it was confirmed that the fresh concrete of the RHA (Cd) specimen has a higher viscosity than that of other specimens. Further examinations are needed to obtain more detailed information on the fresh property of the RHA(Cd) specimen.
- The compressive strength of the RHA sample was much higher than that of the Blank one. This is due to the pozzolanic reactivity by the amorphous

silica contained in the rice husk ash and the decrease of the RHA unit water volume by adding AE-HR-WRA.

- On the other hand, there is not much difference between the compressive strength of the RHA(Cd) and that of the RHA. It is suggested that the presence or absence of Cd in rice husk ash has little effect on the strength of concrete in the low concentration of Cd in rice husk.
- The elution of Cd could hardly be confirmed for all concrete specimens of Blank, RHA and RHA(Cd). Therefore, even if rice husk ash containing Cd at a low concentration is used as a concrete mixture, it can be said that there is no impact on the environment.

From these results, it is necessary to investigate the fresh properties of RHA(Cd) by changing the concentration of Cd adsorbed on the rice husk ash. In addition, it is needed to verify the long-term intensity expression of RHA(Cd) by extending the curing period. Furthermore, in order to grasp various trends of RHA(Cd), it is necessary to change the volume replacement rate of rice husk ash for fine aggregate and carry out various tests (slump test, air volume test, compressive strength test and heavy metals elution test).

ACKNOWLEDGMENTS

This work has been supported by JSPS KAKENHI Grant Number JP20K04684. Also, in carrying out this study, Japan Agricultural Cooperatives provided rice husk. We express our gratitude here.

REFERENCES

[1] Lim J. S., Manan Z. A., Alwi S. R. W. and Hashim H., A review on utilisation of biomass from rice industry as a source of renewable energy, Renewable and Sustainable Energy Reviews, Volume 16, Issue 5, 2012, pp. 3084-3094

[2] Chuah T. G., Jurnasiah A., Azni I., Katayon S. and Choong S. Y. T., Rice husk as a potentially low-cost biosorbent for heavy metal and dye removal: an overview, Desalination, Vol 175, Issue 3, 2005, pp. 305-316

[3] Lata S. and Samadder S. R., Removal of Heavy Metals Using Rice Husk: A Review, International Journal of Environmental Research and Development, Volume 4, Number 2, 2014, pp. 165-170

[4] Pode R., Potential applications of rice husk ash waste from rice husk biomass power plant, Renewable and Sustainable Energy Reviews, Volume 53, 2016, pp. 1468-1485

[5] Kajiwara N., Uehara T. and Saito K., Fundamental Study of Fresh and Hardening Property of Concrete with Non-crushed Rice Husk Ash, Concrete Research and Technology, Vol. 28, 2017, pp. 1-13

[6] Godwin A. A., Ephraim M. E., Akobo I. Z. S. and Ukpata J. O., Structural Properties of Rice Husk Ash Concrete, International Journal of Engineering and Applied Sciences, Vol. 3, No. 3, 2013, pp. 57-62

[7] Ishiguro S., Strength of Mortar Made with Rice Husk Ash Cement, Transactions of the Agricultural Engineering Society, Japan, Vol.68, No.210, 2000, pp. 83-89

[8] Morishita K., Sutou A., Hatori T., Miyashita T. and Kawakami K., Study on efficiency evaluation of rice husk ash as concrete admixture, National Institute of Technology, Oyama College, Research Bulletins, No. 51, 2018, pp. 16-19

[9] Umeda J., Kondoh K. and Michiura Y., Recycling process of rice husk ash to prepare high-purity amorphous silica, Proceedings of the Annual Conference of the Japan Society of Waste Management Experts, Vol. 18, 2007, pp. 413-415

[10] Yamamichi H., Kubota E., Shoya M. and Sugita S., Study on the Properties of Concrete with Highly Reactive Rice Husk Ash, Proceedings of the Japan Concrete Institute, Vol. 22, No. 2, 2000, pp. 139-144

[11] Ohara K., Halo in X-ray Diffraction, NEW GLASS, Vol. 31, No. 118, 2016, pp. 24-26

[12] Liu Y., Guo Y., Zhu Y., An D., Gao W., Wang Z., Ma Y. and Wang Z., A sustainable route for the preparation of activated carbon and silica from rice husk ash, Journal of Hazardous Materials, Volume 186, Issue 2-3, 2011, pp. 1314-1319

[13] Lu P. and Hsieh Y. L., Highly pure amorphous silica nano-disks from rice straw, Powder Technology, Volume 225, 2012, pp. 149-155

[14] Kawai K. and Kaya T., Heavy metal leaching behavior from mortar in several leaching tests, Cement Science and Concrete Technology, No. 56, 2002, pp. 353-359

[15] Khan R., Jabbar A., Ahmad I., Khan W., Khan A. N. and Mirza J., Reduction in environmental problems using rice-husk ash in concrete, Construction and Building Materials, Volume 30, 2012, pp. 360-365

7th Int. Conf. on Structure, Engineering & Environment (SEE), Pattaya, Thailand, Nov.10-12, 2021, ISBN: 978-4-909106070 C3051

A DECISION TOOL FOR LOCAL ROAD SAFETY MANAGEMENT IN THAILAND

Patipat Kanha[1] and Nopadon Kronprasert[2]
[1,2] Department of Civil Engineering, Faculty of Engineering, Chiang Mai University, THAILAND
[2] Excellence Center in Infrastructure Technology and Transportation Engineering (ExCITE), Chiang Mai University, THAILAND

ABSTRACT

Currently, road transport authorities are facing numerous pressures on a systematic process for conducting road safety improvement projects. In recent years, many countries have developed decision-making tools and information technologies that ensure effective and reliable engineering solutions. However, in developing countries, the decision on road safety improvement plans is questionable and is therefore arbitrarily made due to limited knowledge and understanding of road safety management and financial resources. This paper presented the practical decision support system that is being applied for road infrastructure safety management in Thailand. This decision tool has been developed based on limited data available from road authorities and expert panels. It consisted of three modules. First, the hazardous road segments and intersections within the road network were identified using a risk-based approach. Second, the risk of crash types at any specific locations were investigated in a proactive manner. Finally, the low-cost road safety treatments were properly recommended. In this study, pilot projects in local areas were presented. There were the high-risk four-legged unsignalized intersections. This study revealed that the proposed decision tools could overcome some rigid constraints during decision-making process, be flexible to decision-makers, and could be compatible with other local road authorities in a developing world.

Keywords: Road safety, Decision-making, Decision support system, Low-cost treatment, Safety management.

INTRODUCTION

Road crashes have become the major problem resulting in deaths and serious injuries particularly in low-and middle-income countries. In Thailand, there were about 42,000 fatal crashes with around 22,000 road fatalities annually corresponding to a rate of 32.7 per 100,000 population placing the country worst in Southeast Asia [1]. In Thailand, major roads are divided into three road networks by road administration including highways by Department of Highways, rural roads by Department of Rural Roads, and local and municipal roads by Department of Land Administration. According to the Report of Traffic Accidents on National Highways [2], local and municipal roads account for 85 percents of total road lengths in Thailand and contribute to more than 80 percents of road crashes, which are equivalent to 235.8 crashes per 1,000 km and 47.8 fatalities per 1,000 km as shown in Table 1.

The government has committed to continually managing road safety to reduce fatalities and injuries from road crashes. A key challenge for road agencies is to select proper road safety treatments for reducing crash frequency and severity. However, for developing countries, especially in Thailand, many local agencies lack personnel knowledge of effective road safety management; the capacity and skills are limited; and crash databases are poorly identified [3]. As a result, the decision to plan for local road safety improvements is not yet clear.

Table 1 Traffic crashes in Thailand by road network

Road Network	Distance (km.)	Crash rate per 1,000 km.	Fatality rate per 1,000 km.
Local and municipal roads	597,667	235.8	47.8
Highways	51,937	329.0	51.2
Rural Roads	48,598	34.1	7.6

The objectives of this study are to develop a practical decision-making tool for road safety management, and to apply to local road networks in Thailand. This tool aims to improve decision-making process in local road infrastructure planning and improvement programs and help local engineers and practitioners in assessing the safety of local road network, identifying safety deficiencies, and suggesting proper road safety measures.

LITERATURE REVIEW

Road Safety Management

Road safety management has been referred by most research studies when conducting road safety

improvement programs [4]–[6]. It involves identifying road safety problems and defining possible measures to address such issues. In general, there are six steps in road safety management process as shown in Fig. 1.

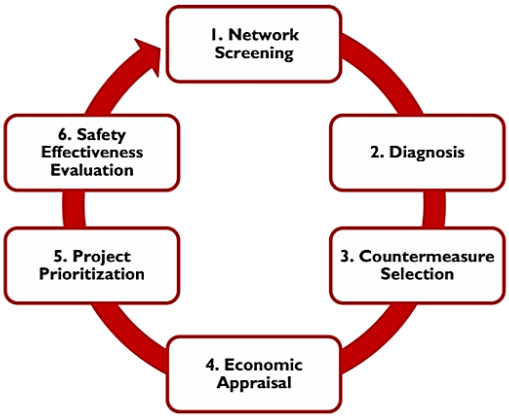


Fig. 1 Road Safety Management Process [7]

- Network screening is the step of identifying high-risk locations within a road network to ensure that resources are allocated such that the high-priority locations are treated, and their impacts are maximized.
- Diagnosis is the step of investigating a site to determine what contributing crash factors such as road user behaviors, road design elements and road environment may be present.
- Countermeasure selection is the step of recommending road safety measures that are expected to effectively address the identified problems.
- Economic appraisal is the step of evaluating how cost-effective each potential measure provides by means of a cost-benefit analysis.
- Project evaluation and prioritization is the step of creating a plan for ranking the safety measures across various road safety projects that maximize the benefits within the total budget allocated to safety remediation.
- Safety effectiveness evaluation is the step of assessing how well a countermeasure performs once it is implemented and evaluated with a Before/After study.

Decision Tools for Road Safety Management

To perform reliable and sustainable decision-making process in road safety planning and management, various decision tools have recently been developed to help engineers and practitioners in many developed countries. Such tools are available for road safety professionals to employ in developing road safety improvement projects at the global, regional, or local levels. Among the successful tools is the International Road Assessment Programme (iRAP) [8], AASHTOWare Safety Analyst [9], Road Safety Toolkit [10, 11], Australian Road Safety Engineering Tool [5], and The Crash Modification Factors Clearinghouse [12, 13].

The International Road Assessment Program (iRAP) also known as iRAP Star Rating is a risk assessment tool to assess the risk score of road segments and present a risk map for a planning purpose.

Safety Analyst by The American Association of State Highway and Transportation Officials (AASHTO) is a set of tools for developing site-specific road safety improvement program following the procedures in the Highway Safety Manual. This system incorporates road safety management approaches into computerized analytical tools for guiding the decision-making process.

Furthermore, a variety of tools are available for selecting proper interventions to address road safety risk. They provide information on possible treatments based on problems identified. The iRAP Road Safety Toolkit (http://toolkit.irap.org) provides information on the causes and countermeasures that can be taken to improve safety on the road to specific types of crashes involving specific road users [14].

The Austroads Road Safety Engineering Toolkit (http://engtoolkit.com.au) is a reference tool created for Australian and New Zealand road infrastructure and road services practitioners. This toolkit provides quick access to information on crashes and road safety deficiencies, and outlines the best-practice, low-cost, high return road safety engineering treatments to reduce the number and the risk of crashes.

The Crash Modification Factors Clearinghouse by The US Federal Highway Administration (FHWA) is an advanced and comprehensive system that maintains a database of countermeasures and their safety effectiveness. It helps transportation engineers identify the most appropriate countermeasure for their safety needs.

Such road safety management decision tools have been prepared for use on a different scope and purposes. Therefore, special care needs to be taken to ensure in selecting the tool for use. However, in Thailand, none of decision tools have been fully implemented to manage road safety in a national and local levels.

DEVELOPMENT OF DECISION TOOLS FOR LOCAL ROADS

The study developed a road safety management system as a decision tool for local engineers and practitioners to conduct the local and municipal road safety improvement projects in Thailand. It is called Local Road Safety Management toolkit for Thailand

(Thai-LRSM). This decision tool was developed with a Visual Basic for Applications (VBA) of Microsoft Excel. It was built based on limited data available from local road authorities and expert panels. The proposed Thai-LRSM encompasses three modules according to road safety management process: (i) Site Identification module; (ii) Diagnosis module; and (iii) Countermeasure Selection module.

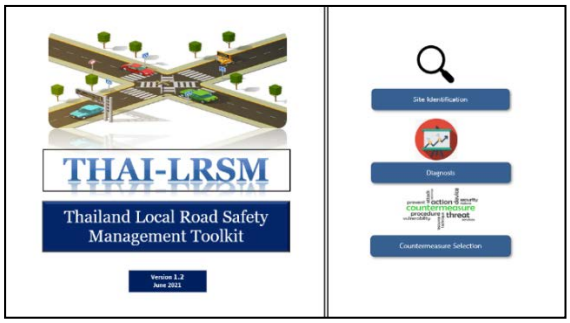


Fig. 2 Interface of the proposed decision tool

Site Identification Module

The 'Site Identification module" is used to identify hazardous road segments and intersections within a local road network. It employed a risk-based approach to assess the safety of a road network based on road characteristics. The road segment or intersection is assigned a risk score and iRAP Star Rating based on how well the road can reduce road users from fatality or serious injury. This module consists of three main interface pages as shown in Fig. 3. It includes:

- Part 1- Route information and input road attributes
- Part 2 - Street view at a site
- Part 3 - Star Rating and Chart by crash types

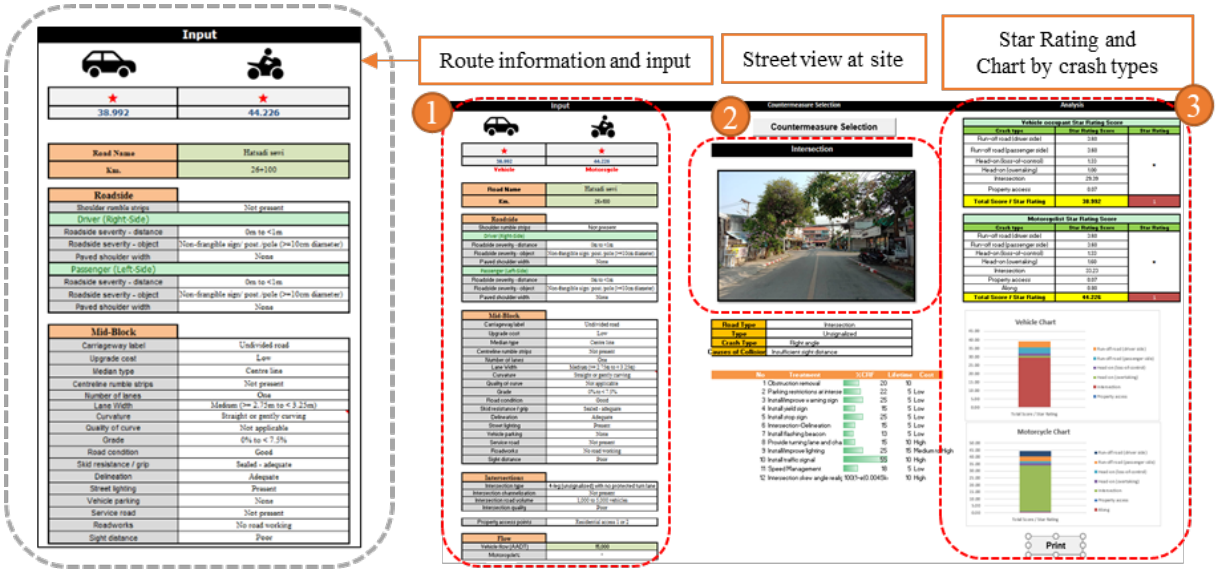


Fig. 3 Interface of 'Site Identification' module

Part 1: Route information and input road attributes code encompasses the following data:

- Route information
- Road details and context
- Observed flow
- Speed
- Mid-block attributes
- Roadside attributes
- Intersection attributes, and
- Supporting data attributes (e.g., attributes for collecting speed and flow)

Part 2: Street view at the site presents the attributes recorded from road survey imagery. The system enables digital images with a minimum 140-degree field of view (centered on the travel lane).

Part 3: Star Rating and Chart by crash types shows the Star Rating Scores (SRS) associated with road segments or intersections of the two road users (vehicle occupants and motorcyclists) by crash types:

$$SRS = \sum Crash\ Type\ Scores \quad (1)$$

The SRS represents the relative risk of all fatal and serious injury crash types of an individual road user based on iRAP Star Rating method.

Star Ratings are then allocated on a scale of one to five. A 5-star rating represents the lowest-risk road design for the prevailing speed environment, while a 1-star rating represents a road with poor infrastructure design for the speed environment.

Diagnosis Module

The 'Diagnosis' module is used to investigate the sites and identify the safety deficiencies using the risk factors derived from the 'Site Identification' module and crash data available from the scene. Road safety engineers and practitioners can review general site condition, current traffic operations, and crash history in the office, and further observe road user behaviors and site characteristics from a site visit during daytime and nighttime. It is essential to diagnose the causes of the problems before developing potential countermeasures.

Countermeasure Selection Module

The 'Countermeasure Selection' module is used for engineers and decision-makers to select road safety treatments to target the contributing factors of the underlying crashes. The decision can be made based on the following criteria: safety effectiveness by means of Crash Reduction Factor (CRF), treatment life, and cost of treatment.

It is noted that CRF provides a quick way of estimating crash reductions associated with road safety improvements and is used by many countries in planning to decide whether a specific treatment should be implemented and to determine the costs and benefits of selected treatments.

Furthermore, the decision tool will guide practitioners in assessing engineering needs at site-specific (both road segments and intersections) for more than 70 low-cost treatments; and conducting a cost-benefit analysis of every treatment for which the needs are identified.

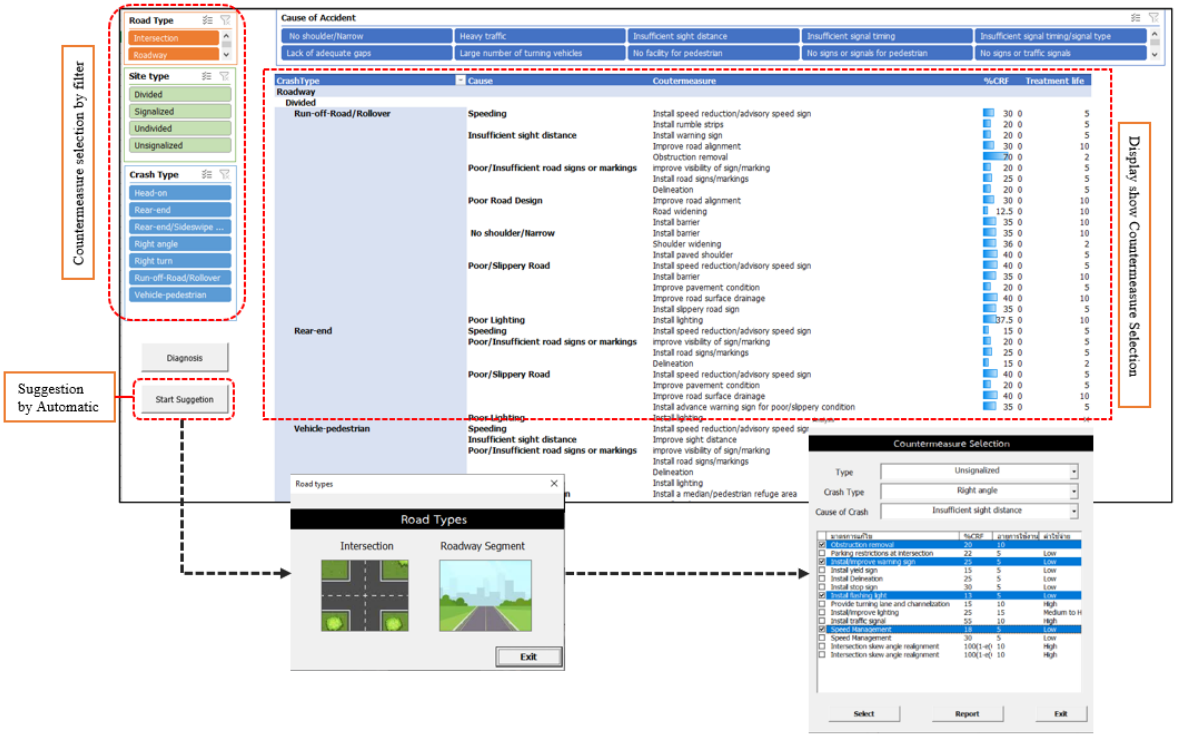


Fig. 4 Interface of Diagnosis and Countermeasure Selection module

APPLICATION TO LOCAL ROAD SAFETY IMPROVEMENT PROJECTS

The study applied the proposed Thai-LRSM decision tool to real-world local road safety improvement projects. One example here is the case study of hazardous intersection in Chiang Mai Province, Thailand. This intersection is a four-legged unsignalized intersection between two-lane paved local roads in an urban area as shown in Fig. 5.

Using the Thai-LRSM tool, we perform the road safety management for this study area. First, in 'Site Identification' module we determined the crash risk scores and star rating for both vehicle occupants and motorcyclists. The module showed that both vehicle occupants and motorcyclists at this intersection are at very high risk with 1-star rating (risk scores of 38.99 and 44.23 for vehicle occupants and motorcyclists, respectively) as shown in Fig. 6. The road attributes that contribute the risk of intersection crashes the

most are sight distance, intersection quality, and speed management as shown in Fig. 7.



(a) North-South approach



(b) East-West approach

Fig. 5 Street views of the study area

Vehicle occupant Star Rating Score		
Crash type	**Star Rating Score**	**Star Rating**
Run-off road (driver side)	3.60	★
Run-off road (passenger side)	3.60	
Head-on (loss-of-control)	1.33	
Head-on (overtaking)	1.00	
Intersection	29.39	
Property access	0.07	
Total Score / Star Rating	**38.992**	1

Motorcyclist Star Rating Score		
Crash type	**Star Rating Score**	**Star Rating**
Run-off road (driver side)	3.60	★
Run-off road (passenger side)	3.60	
Head-on (loss-of-control)	1.33	
Head-on (overtaking)	1.60	
Intersection	33.23	
Property access	0.07	
Along	0.80	
Total Score / Star Rating	**44.226**	1

Fig. 6 Risk scores and ratings of vehicle occupants and motorcyclists in the study area

Type of Risk Factor	Description	Risk Factor	Risk scores
Road attribute (likelihood)			
Intersection type	4-leg (unsignalized) with no protected turn lane	23.00	
Intersection quality	Poor	1.20	
Grade	0% to < 7.5%	1.00	
Street lighting	Present	1.00	
Skid resistance / grip	Sealed - adequate	1.00	
Sight distance	Poor	1.42	
Intersection channelization	Not present	1.20	
Speed management / traffic calming	Not present	1.25	
Product of road attribute (likelihood) risk factors			58.788
Road attribute (severity)			
Intersection type	4-leg (unsignalized) with no protected turn lane	50.00	
Product of road attribute (severity) risk factors			50.000
External flow influence	Intersection Ex Flow		0.125
Operating speed	60		0.080
Intersection Star Rating Score			29.394

Fig. 7 Risk factors associated with the study area

Second, in 'Diagnosis' module we identified the safety deficiencies using the risk factors and crash records. The asset database of this site showed that there was no intersection warning sign on east-west approach and the intersection sight distance was insufficient. In addition, crash data revealed that there were five crashes in last 3 years at this intersection; all of which are angle collisions and occurred at nighttime as shown in Fig. 8. The major causes of intersection crashes are due to the insufficient intersection sight distance; vehicles approach at high speed without slowing down.

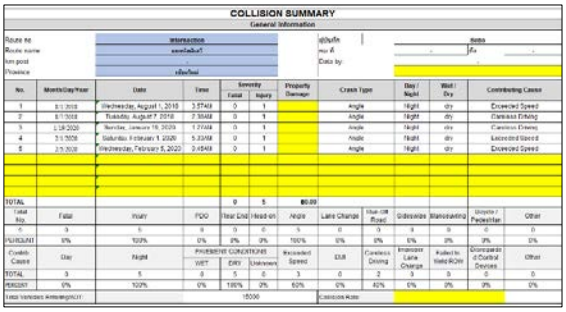


Fig. 8 Crash summary associated with the study area

Finally, in 'Countermeasure Selection' module the potential road safety countermeasures were listed as shown in Fig. 9.

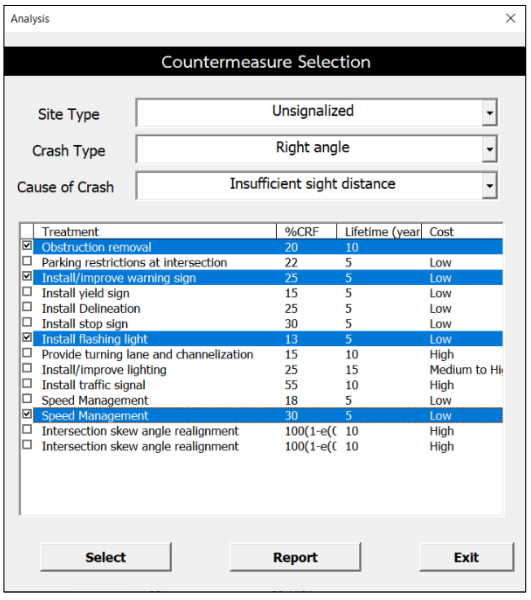


Fig. 9 Countermeasure Selection associated with the study area

For this study area, it is recommended that (i) flashing lights be installed to avoid the see-through effect of vehicles; (ii) warning signs be improved at the intersection; (iii) the obstruction of intersection

sight distance be removed; and (iv) the speed management be implemented on intersection approaches.

By introducing “Install LED flashing lights”, the attributes “intersection quality” and “sight distance” were improved, and the predicted speed reduced from 60 to 50 km/h. As a result, the star rating would change from 1 star to 3 stars.

The analysis results by this decision-making tool led local road authorities to decide the solutions to improve road safety including installing flashing lights and delineation at intersections, as shown in Fig. 10.



Fig. 10 Installation of LED flashing signal and delineation at the study area

CONCLUSIONS AND RECOMMENDATION

In this study, the road safety management tool called Thai-LRSM was developed as a decision support system for local road authorities in Thailand to conduct road safety improvement projects. The tool can identify risk spots on the local road networks by considering the risks of road characteristics that may cause crashes. Further, it integrates with crash history and allows users to analyze the cause of crashes. Finally, it can recommend potential safety measures in accordance with the road characteristics and road user behavior on local roads in Thailand.

This proposed decision-making tool currently performs testing and validation with more case studies including straight and curve road segments and intersections. In addition, the list of safety countermeasures is a low-cost treatment only. In the future, the medium- to long-term treatments should be included as more sustainable solutions when the resources are not constrained.

ACKNOWLEDGMENTS

The authors would like to gratefully acknowledge the technical and financial support of the research project from the Graduate School of Chiang Mai University, and the Faculty of Engineering, Chiang Mai University.

REFERENCES

[1] World Health Organization, The Global status report on road safety 2018. World Health Organization, 2018.

[2] Office of Transport and Traffic Policy and Planning, “Report of Traffic Accidents on National Highways 2019,” Bangkok, Thailand, 2019. Accessed on: June., 11, 2021. [Online]. Available: https://www.otp.go.th/uploads/tiny_uploads/PDF/2563-06/25630601-RoadAccidentAna2562_Final.pdf.

[3] World Health Organization, Review of Thailand’s status against voluntary global targets for road safety risk factors and service delivery mechanism. World Health Organization, 2020.

[4] American Association of State Highway and Transportation, Highway Safety Manual. Washington, DC, 2010.

[5] Jurewicz, C, Road safety engineering toolkit, Transportation Research Board, Transportation Research Board of the National Academies, Washington, D.C

[6] International Road Assessment Programme. iRAP Safety Assessment of National Highway 5: PakistanRAP, Transportation Research Board (TRB).

[7] F. Gross, T. Harmon, and K. Peach, “Reliability of Safety Management Methods,” Federal Highway Administration Office of Safety, USA, Tech. Rep. FHWA-SA-16-041 Sep. 2016.

[8] International Road Assessment Programme: iRAP, 2021. [Online]. Available from https://irap.org. [Accessed: June. 11, 2021].

[9] AASHTOWare Safety Analyst, 2021. [Online]. Available from https://www.aashtoware.org/ [Accessed: June. 11, 2021].

[10] International Road Assessment Programme: iRAP, 2010. [Online]. Available from http://www.toolkit.irap.org/. [Accessed: June. 11, 2021].

[11] Turner, B and Smith, G., The IRAP road safety toolkit: a website-based approach to addressing road safety problems, Transportation Research Board of the National Academies, Washington, D.C.

[12] Federal Highway Administration: FHWA, CMF Clearinghouse User Guide, Federal Highway Administration, Washington, D.C.

[13] Federal Highway Administration: FHWA, 2021. [Online]. Available from http://www.cmfclearinghouse.org/. [Accessed: June. 11, 2021].

[14] Road Safety Manual-World Road Association: PIARC,2021. [Online]. Available from roadsafety.piarc.org. [Accessed: June. 11, 2021].

7th Int. Conf. on Structure, Engineering & Environment (SEE), Pattaya, Thailand, Nov.10-12, 2021, ISBN: 978-4-909106070 C3051

A STUDY OF HELMET USE BEHAVIOR CHANGES: A CASE STUDY OF KHON KAEN UNIVERSITY, THAILAND

Jetsada Kumphong[1], Prach Amornpinyo[2]
[1,2] Faculty of Technical Education, Rajamangala University of Technology Isan Khon Kaen Campus, Thailand.

ABSTRACT

Based on the World Health Organization of Global Status Report on Road Safety 2018, Thailand has the high risk of death of motorcyclists in the world. The aim of the present study was to explain the motorcycle helmet use factors, using logistic regression analysis (N=16,097). Data were collected by CCTV-signaled intersection in Khon Kaen University, Thailand. The resulting helmet wearing rates were found to be significantly associated with rider status, absence of passengers, female riders, and daytime riding. The interesting point found was that at the road intersections during daytime, the helmet use rate was about 3.3 times higher than at nighttime, Motorcyclists riding in the helmet detection by CCTV wore helmets 1.4 times more frequently than those riding in the helmet use campaign and helmet checkpoint which was statistically significant. The outcome of this study could increase understanding of motorcyclist's helmet use, and it could be useful for development of safety measures to prevent accidents and injuries during 24 hours on campus roads.

Keywords: logistic regression, motorcycle, road safety, road intersection, CCTV.

INTRODUCTION

The 2018 report of the World Health Organization indicated 28% overall death rate of motorized 2-3 wheelers, compared to other vehicles. In South-East Asia, the death rate of motorized 2-3 wheelers was the highest, i.e., 43%, while it was 23% in America, 11% in Europe,9% in Africa, 15% in Eastern Mediterranean, and 36% in Western Pacific. In Thailand, the death rate of motorized 2-3 wheelers was 74%, which came as the third whereas road fatality ranked the ninth in the world.

In Thailand, there is a high death rate of motorcycle riders while the helmet wearing rate has been low. The group of injured and dead motorcyclists is often found to be the adolescent group. Motorcycles, in particular, are generally used for students' transportation in regional and upcountry universities. Many students in these universities are bought a motorcycle by their parents because it is easy to buy and is not expensive. Accidents and the death rates of motorcycle riders have become a major problem in Thailand [1-2] and other Asian countries. Helmet is the first accessory for motorcyclists to use in order to prevent head injury, which is one of the most frequent injuries that result from motorcycle accidents [3-4].

This research which was conducted in Khon Kaen, Thailand shows that riding without a helmet or while intoxicated can explain the increased fatality risk (increased risk among those aged 20–39 years.), suggesting that safety enforcements should be specifically targeted among teen riders [5].

Khon Kaen University (KKU) is a large university, with her campus consisting of a number of official buildings and educational institutions including a lot of educational establishments, hospitals, department stores, and residences. There is an extensive use of motorcycle transportation daily, while users especially students, often neglect wearing helmet while driving. As a consequence, the statistics reveals an average of one death and 3 injured people annually.

This study aims at investigating the influence of factors on student riders' helmet use. The findings should provide practical information for more effective measures to increase helmet use in Khon Kaen University, Thailand.

RESEARCH METHODOLOGY

Data collection

Khon Kaen University is a big university covering an area of 900 hectares, where education center and other organizations such as the university hospital are situated. At present, the university has rapidly grown and thus there are a great number of vehicles using the roads on campus. This leads to traffic accidents (roughly 40% per year), death (1 person per year), and injuries (20 people per year). The problem is of great concern among administrators, especially when this involves student motorcycle riders and the university has attempted to enforce law to ensure helmet wearing among student riders. Three phases of measures were expedited

under the campaign for helmet wearing: Phase 1 – public relating and helmet distribution; Phase 2 – setting a check-point for motorcyclists' helmet wearing and deducting the behavior score of violating students; Phase 3 – installing a CCTV camera to detect those not wearing helmet.

The researcher collected data by a CCTV installed at one intersection on KKU campus where students usually ride their motorcycles and where frequent accidents were recorded, as shown in Figure 1. Figure 2 depicts the example of the cross-section of the investigated intersection. The data was randomly collected during 24 hours of 2 weeks.

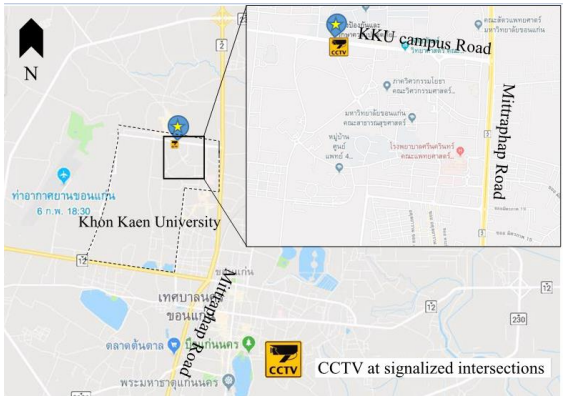


Fig. 1. Study area



Fig. 2. The cross-section of the investigated intersection

Variables of the study

The study of motorcycle riders' status could explain the helmet use behavior, which is similar to other studies in Khon Kaen [6]. The gender of motorcycle riders could also explain the helmet use, and is consistent with past research studies in Ghana, Germany, Ireland, Italy, Portugal and Turkey [7-8]. Moreover, the time and day of riding could explain the helmet use and agree with the past research study [6].

Table 1 shows the variables, categories and codes, which were used to develop the Helmet Use model for this study. For example, helmet use was treated as a dependent variable with the variables defined as 'yes' and 'no', whilst gender (male or female), time of day (daytime or nighttime), and passenger (with or without) were treated as independent variables. The data was collected from a sample group of motorcyclists riding on campus road in Khon Kaen University, Thailand.

Table 1 Description of the study variables

Variables	Code/Category
Wearing a helmet	1=Yes 0=NO
Riding status	1=Rider 0=Passenger
No. of passenger	1=None 0=≥One
Riding gender	1=Female 0=Male
Time	1= Daytime 0= Nighttime
Implementation period	1=Helmet use campaign 2=Helmet Checkpoint 3=Helmet detection by CCTV
M1	1= Helmet Checkpoint 0= Other
M2	1= Helmet detection by CCTV 0= Other

Data Analysis

All variables (status, no. of passenger, gender and time) were analyzed, based on a hypothetical model. The statistical association between the variables was assessed by Pearson chi-square Test and Logistic regression (odds ratio (OR)). For all analyses, p-values less than 0.05 were defined to be statistically significant based on Hair et al. (2010). The data were analyzed using the SPSS software.

RESULT AND DISCUSSIONS

Result of helmet use observation by characteristics

The research findings are summarized in Table 2. A total of 16,097 motorcyclists were observed at the intersection on KKU campus where the helmet wearing rate. We observed that motorcyclists riding during daytime often wore helmets compared with riders at nighttime.

Result of helmet use estimation

The results of Pearson chi-square test are summarized in Table 3. It reveals that all variables were correlated significantly with helmet wearing.

Table 4 shows the results of the logistic regression

analysis for variables associated with helmet use. The starting set of predictors was status (rider vs. passenger), number of passenger, driver gender (male vs. female), time of day (daytime vs. nighttime) and Implementation period (helmet use campaign vs. helmet checkpoint vs. helmet detection by CCTV). The analytical results demonstrate that all variables were significant predictors of helmet use among motorcyclists in KKU.

Overall, riders were 2.9 times more likely to wear a helmet compared to passengers. It was also found that motorcyclists who did not have passengers wear helmet 2.3 times more than when there was a passenger. We found that female riders were 1.7 times more likely to wear a helmet compared to male riders. The daytime helmet wearing rate was observed to be 3.3 times higher than the night time. Motorcyclists riding in the helmet detection by CCTV wore helmets 1.4 times more frequently than those riding in the helmet use campaign and helmet checkpoint.

The data analysis among helmet use campaign shows that riders were 3.1 times more likely to wear a helmet compared to passengers. Motorcyclists who did not have passengers wear helmet 2.3 times more than when there was a passenger. Female riders were 1.6 times more likely to wear a helmet compared to male riders. We found that the riders during the daytime were 1.9 times more likely to wear a helmet compared to nighttime riders.

The data analysis among helmet checkpoint shows that riders were 2.6 times more likely to wear a helmet compared to passengers. Motorcyclists who did not have passengers wear helmet 2.3 times more than when there was a passenger. Female riders were 1.5 times more likely to wear a helmet compared to male riders. We found that the riders during the daytime were 3.4 times more likely to wear a helmet compared to nighttime riders.

The data analysis among helmet detection by CCTV shows that riders were 3.3 times more likely to wear a helmet compared to passengers. Motorcyclists who did not have passengers wear helmet 2.4 times more than when there was a passenger. Female riders were 1.9 times more likely to wear a helmet compared to male riders. We found that the riders during the daytime were 4.3 times more likely to wear a helmet compared to nighttime riders.

Additionally, our data reveals that motorcycle riders' helmet use was associated with the gender, status, number of passenger and time. The logistic regression model indicates that helmet use was generally higher in KKU, particularly among riders and among the passenger. Moreover, helmet use by men was observed to be low. Similar to other studies.[6-8, 10], the results also show that the observed helmet use rates were lower than those reported from other studies conducted in ASEAN [11-13]. The helmet use rates were lower in the evening [6-8, 13]. These different patterns of use highlight the potential for designing helmet enforcement for improving helmet use rates in KKU. A similar conclusion was reported by Akaateba, M.A. et al. (2014).

CONCLUSION AND RECOMMENDATIONS

The aim of this study was to investigate the prevalence of helmet use among motorcyclists in Khon Kaen University, Thailand. The status of riders, absence of passenger, female motorcyclists and daytime were found to be significant with helmet use. In view of the increasing concerns on the problem arising from motorcyclist injuries and fatalities, we found that helmet can reduce the accident severity of the head. The higher the efficiency of helmet enforcement means more budget required to support the helmet usage. The results of this study can be used to guide the development of targeted countermeasures aimed at improving motorcycling safety for riders. This information will be valuable for the urban road and road safety in KKU when new policy is established in the future.

Motorcycle riders should be required to follow the instructions shown below, with suggestions of some concrete transport measures based on this research output.

1) Implement campus roads safety action plan (Helmet use 100%).

2) Set up the measures for safe motorcycle riders in the university.

3) Suggest punishment or fine for not using helmet such as deducting the student behavioral score.

4) Use 24-hour CCTV to supplement law enforcement [14].

Study in psychological variables in-depth of motorcycle helmet use [15].

ACKNOWLEDGMENTS

This work is dedicated to and in good remembrance of my Mr. Vutidach Kumphong, brother of a co-author, passed away from a road accident.

REFERENCES

[1] World Health Organization, Global Status Report on Road Safety 2018, Geneva, Switzerland, 2018.

[2] Kumphong J, Satiennam T, Satiennam W. Correlations among motorcycle-related deaths, helmet law enforcement and helmet usage for ASEAN countries. International Journal of GEOMATE; 2018, Sept. 2018, Vol.15, Issue 49, 72 -77.

[3] COST327. Motorcycle safety helmets: Final report of the action. European communities, Belgium.

[4] Fernandes FAO and Alves de Sousa RJ. Motorcycle helmets –a state of the art review, Accident Analysis and Prevention; 2013, 56, 1-21

[5] Nakahara S, Chadbunchachai W, Ichikawa M, Tipsuntornsak N, Wakai S. Temporal distribution of motorcyclist injuries and risk of fatalities in relation to age, helmet use, and riding while intoxicated in Khon Kaen, Thailand. Accident Analysis and Prevention; 2005, 37, 833-842.

[6] Kumphong J, Satiennam T, Satiennam W. The determinants of motorcyclists helmet use: Urban arterial road in Khon Kaen City, Thailand. *Journal of Safety Research*; 2018. (https://doi.org/10.1016/j.jsr.2018.09.011)

[7] Akaateda MA, Amoh-Gyimah R, Yakubu I. A cross-sectional observational study of helmet use among motorcyclists in Wa, Ghana. Accident Analysis and Prevention; 2014, 64, 18-22.

[8] Orsi C, Stenderdo A, Marinoni A, Gilchrist MD, Otte D, Chliaoutakis J, Lajunen T, Ozkan T, Dias Pereira J, Tzamalouka G and Morandi A. Motorcycle riders' Perception of helmet use: Complaints and dissatisfaction, Accident Analysis and Prevention; 2012, 44,pp 111 – 117.

[9] Hair, J.F., Black, W.C., Babin, BJ, Anderson RE. Multivariate Data Analysis a global perspective 7th ed. New Jersey; 2010.

[10] Xuequn Y, Ke L, Ivers R, Du W, Senserrick T. Prevalence rates of helmet use among motorcycle rider in a developed region in China. Accident Analysis and Prevention; 2011, 43, 214-219

[11] Trinh TA, Le TPL. Motorcycle Helmet Usage among Children Passengers: Role of Parents as Promoter, Proceedings of Sustainable Development of Civil, Urban and Transportation Engineering Conference, Procedia Engineering; 2016, 142, 10-17.

[12] Brijs K, Brijs T, Sann S, Trinh TA, Wets G, Ruiter RAC. Psychological determinants of motorcycle helmet use among young adults in Cambodia. Transportation Research Part F; 2014, 26, 273-290.

[13] Conrad P, Bradshaw YS. Helmet, Injuries and cultural definitions: motorcycle in Urban Indonesia. Accident Analysis and Prevention; 1996, 28, 193-200.

[14] Satiennam T, Kumphong J, Satiennam W, Klungboonkrong P, Jaensirisak S, and Ratanavaraha V. Change in helmet use behavior enforced by CCTV cameras with automatic helmet use detection system on an urban arterial road. Traffic Inj. Prev.; 2020, vol. 21, no. 7, pp. 494–499.

[15] Kumphong J, Satiennam T, Satiennam W, and Tu Anh Trinh. Psychological models for the development of motorcycle helmet use among students in Vietnam. Proceedings of IOP Conference Series: Earth and Environmental Science, Vol.143; 2018.

Table 2 Comparison of proportion of helmet usage

	Helmet use campaign					Helmet Checkpoint					Helmet detection by CCTV				
	Helmet-wearing (%)		Total		Dif.	Helmet-wearing (%)		Total		Dif.	Helmet-wearing (%)		Total		Dif.
	Yes	No	N	%		Yes	No	N	%		Yes	No	N	%	
Status															
Rider	42.5	57.5	2,491	77.6		47.0	53.0	5,517	77.2	4.5	51.1	48.9	4,514	78.6	4.1
Passenger	13.0	87.0	717	22.4		17.6	82.4	1,630	22.8	4.6	18.1	81.9	1,229	21.4	0.5
No. of passenger															
None	48.4	51.6	1,775	55.3		53.5	46.5	3,906	54.7	5.1	57.3	42.7	3,296	57.4	3.8
≥1	20.4	79.6	1,433	44.7		24.4	75.6	3,241	45.3	4	26.1	73.9	2,447	42.6	1.7
Gender															
Male	34.0	66.0	1,754	54.7		39.8	60.2	3,474	48.6	5.8	40.2	59.8	2,911	50.7	0.4
Female	38.2	61.8	1,454	45.3		40.8	59.2	3,673	51.4	2.6	48.0	52.0	2,832	49.3	7.2
Time															
Daytime	45.0	55.0	1,440	44.9		57.1	42.9	3,168	44.3	12.1	61.6	38.4	2,862	49.8	4.5
Nighttime	28.5	71.5	1,768	55.1		26.9	73.1	3,979	55.7	-1.6	26.6	73.4	2,881	50.2	-0.3
Total	35.9	64.1	3,208	19.9		40.3	59.7	7,147	44.4	4.4	44.0	56.0	5,742	35.7	3.7

Table 3 Proportion of helmet-wearing by Pearson chi-squared test

	Helmet use campaign					Helmet Checkpoint					Helmet detection by CCTV				
	Helmet-wearing (%)		Total		*p*-value	Helmet-wearing (%)		Total		*p*-value	Helmet-wearing (%)		Total		*p*-value
	Yes	No	N	%		Yes	No	N	%		Yes	No	N	%	
Status															
Rider	42.5	57.5	2,491	77.6	<0.001**	47.0	53.0	5,517	77.2	<0.001**	51.1	48.9	4,514	78.6	<0.001**
Passenger	13.0	87.0	717	22.4		17.6	82.4	1,630	22.8		18.1	81.9	1,229	21.4	
No. of passenger															
None	48.4	51.6	1,775	55.3	<0.001**	53.5	46.5	3,906	54.7	<0.001**	57.3	42.7	3,296	57.4	<0.001**
≥1	20.4	79.6	1,433	44.7		24.4	75.6	3,241	45.3		26.1	73.9	2,447	42.6	
Gender															
Male	34.0	66.0	1,754	54.7	0.012*	39.8	60.2	3,474	48.6	0.362	40.2	59.8	2,911	50.7	<0.001**
Female	38.2	61.8	1,454	45.3		40.8	59.2	3,673	51.4		48.0	52.0	2,832	49.3	
Time															
Daytime	45.0	55.0	1,440	44.9	<0.001**	57.1	42.9	3,168	44.3	<0.001**	61.6	38.4	2,862	49.8	<0.001**
Nighttime	28.5	71.5	1,768	55.1		26.9	73.1	3,979	55.7		26.6	73.4	2,881	50.2	
Total	35.9	64.1	3,208	19.9		40.3	59.7	7,147	44.4		44.0	56.0	5,742	35.7	

Table 4 Logistic regression analysis of variables associated with observed helmet use

	All			Helmet use campaign			Helmet Checkpoint			Helmet detection by CCTV		
	β	OR	*p*-value	β	OR	*p*-value	β	OR	*p*-value	β	OR	*p*-value
Status												
Rider	1.062	2.89	<0.001	1.120	3.07	<0.001	0.956	2.60	<0.001	1.188	3.28	<0.001
Passenger*												
No. of passenger												
None	0.837	2.31	<0.001	0.827	2.29	<0.001	0.824	2.28	<0.001	0.868	2.38	<0.001
≥1*												
Gender												
Male*												
Female	0.500	1.65	<0.001	0.478	1.61	<0.001	0.392	1.48	<0.001	0.648	1.91	<0.001
Time												
Day time	1.180	3.25	<0.001	0.614	1.85	<0.001	1.215	3.37	<0.001	1.454	4.28	<0.001
Night time*												
M1												
Helmet Checkpoint	0.213	1.24	<0.001	-	-	-	-	-	-	-	-	-
Other*												
M2												
Helmet detection by CCTV	0.298	1.35	<0.001									
Other*												
Constant	-2.762	0.06	<0.001	-2.511	0.08	<0.001	-2.415	0.089	<0.001	-2.808	0.06	<0.001
ρ^2		0.239			0.172			0.229			0.291	
-2LL		18623.401			3758.993			8309.919			6470.795	

Note: OR= odds ratio; *Reference parameter is set to zero because it is redundant.

7th Int. Conf. on Structure, Engineering & Environment (SEE),
Pattaya, Thailand, Nov.10-12, 2021, ISBN: 978-4-909106070 C3051

DEEP NEGATIVE EFFECTS OF CONSPIRACY THEORIES AND MISLEADING INFORMATION ABOUT COVID-19 ON POPULATIONS THROUGH SOCIAL NETWORKS

Mohamed CHAKRAOUI[1], Naoual MOUHNI[2], Abderrafiaa ELKALAY[3] and Mohamed NEMICHE[4]
[1]LS3M, Polydisciplinary Faculty of Khouribga, Soultan Moulay Slimane University, Béni mellal, Morocco;
[2]LAMIGEP EMSI Marrakech, Morocco; [3]RITM, EST, Hassan II University, Casablanca, Morocco;
[4]Faculty of Science, Ibn Zohr University, Agadir, Morocco

ABSTRACT

If pandemics kill humans and spread too quickly, misinformation is another scourge that puts people in danger. Health is what a person needs the most in the world to strive for great wealth and future. The novel Coronavirus Disease (COVID-19) outbreak has threatened massively human health on the 21 century (precisely on 2020). The spreading of COVID-19 pandemic press specialists to do more efforts in order to find a cure. The same reason makes people perform billions of queries on search engines and social networks about comprehending the origin of the virus, the spread mechanisms and existent cures. The virus that causes the pandemic is the new Coronavirus appeared in a unique market in Wuhan, in China on December 2019. This new Coronavirus is named coronavirus (COVID-19). In March 2020, the World Health Organization (WHO) announced the COVID-19 outbreak to be a pandemic. Throughout the ages, mankind has experienced many epidemics, but the distinction of the 21 century is technology development. The spread of misinformation is faster than that of the pandemic. With advent of big data, we can analyze the huge information shared in a second in social networks and it contains millions of misinformation. In this current, we analyze the belief frequency of misinformation in three languages, English, French and Arabic shared on Twitter users' timeline. Misinformation urges people against vaccination in different ways; many people are spreading misinformation to be famous or make money through views and sharing. Scientists and Journalists are concerned to reduce the likelihood of susceptibility to misinformation by comply with WHO guidance measure in social networks.

Keywords: Coronavirus; COVID-19; Sentiment analysis; Misinformation; Social networks; Misleading information treatment; Rumors about COVID-19

INTRODUCTION

There is quite a bit of research that has discussed this problem of fake news. These are mainly limited to the context of the 2016 US presidential election, concluding that exposure to fake news was quite limited among the population. Likewise, large-scale analyses of Facebook data in the context of anti-covid vaccine reluctance also find that anti-vaccination groups are growing. Always in this context of COVID-19, a recent research demonstrated on YouTube videos, found that more than 27% of the most viewed English videos contained fake news and exceeded 60 million views[1] [2]. what pushes us to predict more flow of misinformation concerning the progress of the vaccination [3] [4].

A study made by Ofcom precises that half of UK online adults came across false or misleading information about the coronavirus (Covid-19). 35% of UK online adults have seen a false information which claims that drinking more water can flush out the infection, and 24% of them have seen a misinformation that states coronavirus can be treated by gargling with saltwater, or avoiding cold food and drink. Our survey in Morocco about covid-19 misinformation spread make on evidence that:

- 65% of Moroccan population believe in conspiracy about the virus.
- More than 90% of Moroccans online adults have come across false or misleading information.
- More than 40% of Moroccans online adults are ignoring false claims about coronavirus.
- In addition, more than 60% of Moroccans online adult are finding it hard to know what is true or false about the virus.
- Younger people are following official channels.

Billions of information about health care are shared in Internet via social media. These information contain 70% of rumors, conspiracies and misleading information versus 30% of WHO and public health guidelines regarding COVID-19 information [5] [6].

Social structures and social relations can be modeled into social networks composed of multiple connections between individuals (which can

perform a group of persons) are used as a pattern issue. Social relations can be made by particular individuals or by groups, Facebook as an example. Institutional individual forms social organizations with consideration to macro level pattern [7].

Facebook Instagram and Twitter are the most used social networks around the world. In China, they use WeChat, Sina, Weibo and other platforms as well. In this paper we use Twitter due to its wide use and openness to researchers to get public data through Twitter API. 63% of Twitter users are between 35 and 65 years old, 71% of Twitter users are surfing in the platform to look for news according to the Pew Research Center. 80% of Twitter clients log in via mobile devices or smart phones. According to OMNICORE official web site, 93% of users watch Twitter videos by means of mobile devices. Any data scientist who get data from Twitter, asks this question: how many active users on Twitter?

The response is that Twitter active users are more than 330.000.000 per month. Of this figure, more than 40% (more than 166.000.000), are using the platform at least one time a day (Twitter, 2020).

After the peak of Twitter active users in January 2018, Twitter team accounts that monthly active users has raised up in the first quarter of 2020. These statistics give us great reliability in this platform.

The WHO has announced that to slow the spread of the pandemic, people must respect the social distancing measures (one meter minimum) by stopping transmissions of COVID-19 around the world. Then preventing new novel coronaviruses from appearing. WHO has announced later that mask wearing is another important measure which can stop the spread of COVID-19 [8]. Avoiding contact with contaminated persons and surfaces to stop the spreading of COVID-19 [9]. Teachers can perform video conference with students via Ms. Teams or ZOOM meeting for example. Consumers can buy their needs through many existent and trusted online sales web sites. Teleworking (work from home) is a good measure to avoid crowding and reduce pollution emitted by vehicles. Distance learning can be established by universities and schools platforms via local TVs, Radios and very importantly by social networks and video streaming. Mask wearing ought to be imposed by governments. “Stay-at-home” can be the slogan of COVID-19. Hence, limitation of transportation such as national and international flights and is a wise decision was taken. In addition to these measures, every one in every place must respect all measures against the spread of COVID-19, which are washing hands very frequently and using cough etiquette. On February 28 2020, the UN Secretary-General appealed on governments to make as much efforts as possible in order to contain COVID-19 epidemic.

Technologies, especially machine learning is involved deeply to stop the spread of the disease by encouraging researchers to engage in projects related to COVID-19 in order to end this pandemic. Enterprises, universities, schools changed the method of working by adopting Tele-working and tele-schooling (study-from-home). However, the enterprises, which provide daily needs and medical supplies-, should respect some working protocols such as social distancing and mask wearing. Connections between familial, personal and professional communities must be established by technology and virtual communications [10]. New Technologies, radio, televisions and mobile phones have to raise awareness by streaming videos and documents about the danger of COVID-19. “Figure 1” presents a world map of all affected countries by COVID-19 and “Fig. 2” presents histogram of the total cases and death rate of some affected countries until May 28 2020, according to the European Centre for Disease Prevention and Control (ECDC).

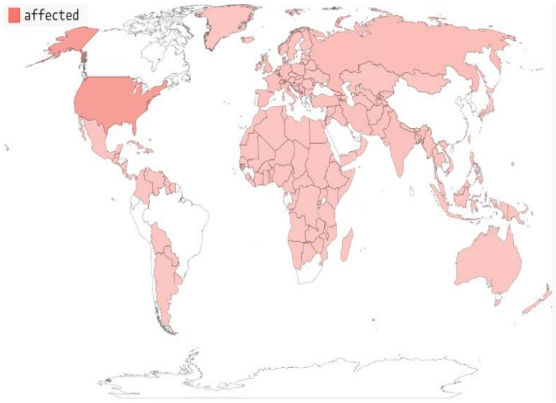


Fig. 1: Affected countries and territories around the world by COVID-19

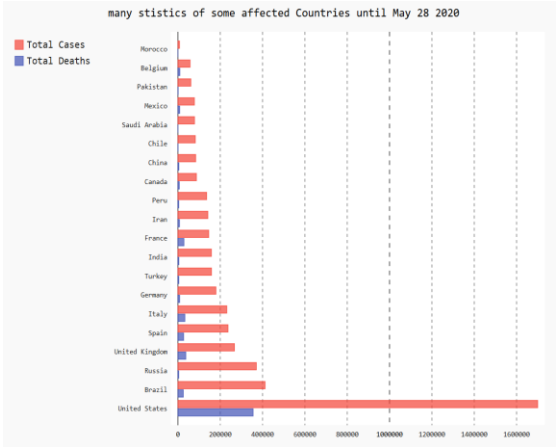


Fig. 2: COVID-19 total death and total cases for some countries

LITERATURE REVIEW

The damage that rumors and misinformation has caused to the economy

As COVID-19 affects health of international scale, its affection is parallel to the spread of misinformation around the world, especially the economic side [11]. A systematic approach to identify assesses and reduces the risks of this disaster, called disaster risk reduction (DRR). After weeks the fall of the economy caused by rumors about the disease is more than $20 trillion which is greater in number and size than the loss of 2008-2009 Great Recession... [12]

The lack of knowledge, non-based-science, poor coordination and uncertainty in the near future form the main wheel towards crisis and wrong decision-making. Reducing the economic activity and slump of capital markets caused by the immediate stop of activity have a direct negative impact on the economy. COVID-19 becomes a very costly lesson of RDD to save initial investments taking in consideration the medical infrastructure. To fight incoming diseases and mitigate future emergencies, supplies for at least some critical items must be in local production. Illiterate disaster economic policy tends to view redundancy as ineffective [13].

Medical statistics about COVID-19

Since WHO office in China announced a pneumonia detected in Wuhan, on 31 December 2019 and no one knows its origin. WHO is working day and night and collaborating with their partners to get more helpful data, in order to help people by providing them advice and increasing medical supplies. The number of affected people grows exponentially, it is declared as a public Health Emergency on 30 January 2020. 11 days later, WHO labeled it as COVID-19 and one day after, WHO reported it as a pandemic (March 12 2020).

Chinese Center for Disease Control and Prevention published a statistic, which shows that 80% of patients manifest with minor illness. Some studies of patients shown that symptoms begin slightly. In between symptoms are dry cough and fever accompanied by muscle aches and tiredness. The minority of these patients present abdominal troubles and diarrhea hours before major symptoms appear. The director-general of the World Health Organization confirmed that the seasonal flu is less severe compared to illness caused by COVID-19. The overall death rate is less than 2.3% and can increase until 8.0% with senior patients between 70 and 79 years old and 14.8% for those with age more than 80 years, “Fig. 3” gives an overview of COVID-19 death rate by country.

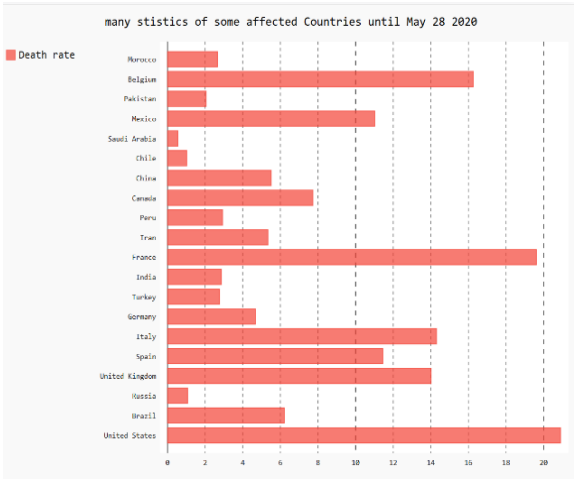


Fig. 3: Covid-19 death rate for some countries

According to a study of Dr. Dedier Raoult, Hydroxychloroquine has given very promising results in vitro against COVID-19.

Hydroxychloroquine shows higher safety than Chloroquine and admitted to increase of the dose of the day depending on the patient condition and less worry medication-medication interactions [14].

Chenghu Zhou et al. [15] constructed a decision making information system through significant subjects that take challenges. Analyses of geographic and spatiotemporal information systems make it possible to prevent and contain incoming diseases and epidemics by making decisions on the right time.

Sophisticated health services must be connected to the Internet to provide a mass overview of spatiotemporal data on different sources about the disease, then develop a geographic information system that collects and analyzes all the data of the epidemic in real time (per second) to allow precise, overly updated visualization. Building a cubic spatiotemporal model of mass of data collected about the disease, then model the heterogeneous multi data after its normalization chronologically and at the end create a system of historization, which normalizes and homogenizes these data. The development of a calculation engine, which makes it possible to describe, diagnose, predict diseases, the GIS, which is developed, is able to make a decision about diseases through straightforward queries. Programing a real-time spatiotemporal visualization platform scaled on multi-dimensions in order to get a visualization on levels of state, region, town, section and community to allow management and analysis of curves of multidimensional epidemic data under a normalized GIS data. New technologies with cloud architecture is taken over to set up a structure, which includes the management of the GIS. The masses of spatiotemporal data and interface of disease, that will eliminate some problems like the too congested relationships, the complexity and poor optimization

of code linked to traditional information systems, all this makes it possible to have a GIS adapted to emergency cases linked to epidemics [15].

Using Natural Language Understanding to extract misinformation about COVID-19

Natural language interfaces (NLI) can be called in order to get structured data about the disease stored in DBMS more straightforwardly. There are many kinds of NLI, the most solicited NLI is Natural Language Interfaces to Databases (NLIDB), which allow structured information to be stored in a relational database [16]. The disadvantage of this type of NLI is that of SQL which is not easy to use by end-users. Then, we are looking for an interface that can be interpreted by RDBMS as well as by humans [17]. Otherwise we can appeal to ontologies in order to treat information by using Natural Language Interfaces to Knowledge Bases (NLIKB) [16]. Natural language Interfaces can communicate with all RDBMS, and use close algorithm for interpretations of NLI queries and mapping them to RDBMS queries. Requests in database systems are optimized using parallel index partitioning [18].

MISINFORMATION STATISTICAL ANALYSIS

Natural Language Processing

Text data, Meta data are available in plenty on the Internet through social media networks. Natural language processing can be defined to be a branch of artificial intelligence that deals with interactions between machine and human using the natural language understanding as English, French, Arabic and other languages. Natural language processing which is usually shortened as NLP brings powerful technologies to help researchers derive immense value from that data.

Data scientist is a new field, which is interested on data analysis and visualization. We can say that this era of big data and sharing of the dataset in social networks is the big data revolution, which focuses less on the data placed by the governments (which represents less than 1% of the data distributed on the web). However, data is provided massively by enterprises, social medias and research stations (wildfire stations, weather stations, route traffic stations) etc. Consequently, the integration of heterogeneous data remains a challenge for GIS, which has pushed various stakeholders (universities, companies, governments) to establish targeted policies. At masses of data era, big data analysis, sentiment analysis, and cloud computing brought new methods of decision making by discarding the old methods, which are no longer valid.

"Opinion mining" widely known as sentiment analysis is a branch of data mining, which is interest into processing and interpreting text mining through natural language processing (NLP). NLP extracts the user's emotion or sentiment which is extracted by analyzing the subjective context of the text and can be positive, negative or neutral [19].

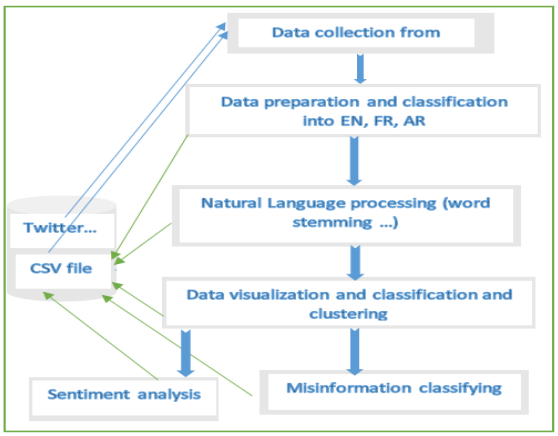


Fig. 4: Misinformation classification architecture

Data generated from social networks like Facebook conversations, publications or status, tweets, timelines and messages are part of unstructured data through the web. These datasets cannot be translated to traditional rows and columns (tables). Structured data (relational data) is widely used in the web because of its mathematical based theory and their straightforwardness. Unstructured data is difficult to process because it is generally inhomogeneous and disordered, it can be texts, messages or tweets…. Nevertheless, due to NLP, other fields are born like text information retrieval, which allow us to understand the meaning behind those words in the phrase syntax (its cognitive sense). To do this we have used many algorithms as follow:

- Tokenization
- Stop word removal
- Stemming
- Lemmatization
- Content word extraction
- Syntactic Analysis
- Sentiment analysis

As illustrated in "Fig. 4", we collect data tweets from Twitter and perform our NLP algorithm in order to preprocess these data then prepare them, after that we extract clean text out of URLs, special characters and no meaning words filtration. English, French and Arabic are three languages widely written and spoken on social networks and can be a powerful bank of data to get profit in this paper in order to catch and classify misinformation, misleading information and rumors spread about the virus. Through the last step, which is data visualization we extract statistics of sentiments of

adult connected people about these information in concern of COVID-19 pandemic. These extractions are done for tweets of English, French and Arabic separately. In the second step, we did the same statistics by continent, than by some countries. This can allow us to learn more about the spread of COVID-19 as well as its rate of transmission and mastering the situation.

May tools are used as python 3.7.6, Pandas 1.0.1, Numpy 1.18.1, Pip 20.0.2, Pygal 2.4.0, Sklearn …

Moreover, other packages running on an Intel® Core™ i7-4500 CPU @ 1.80GHz 2.40GHz Asus Laptop with 8GB of RAM, 64-bit operating system, x64-based processor.

Misinformation tweets similarity clustering

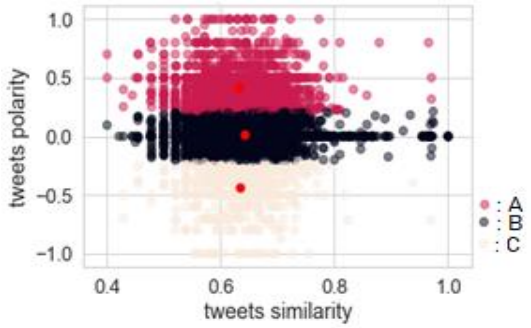


Fig. 5: Dissemination of negative COVID-19 information via English social networks

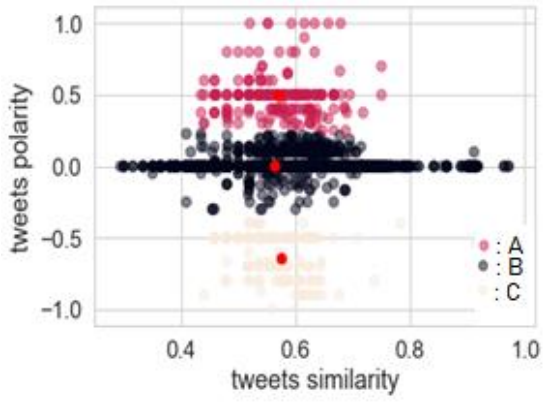


Fig. 6: Dissemination of negative COVID-19 information via French social networks

Clustering is a fundamental classification method which is frequently used in order to group together unlabeled (unsupervised learning) data with similar properties. It can be used in different fields such as pattern recognition (observations, data items feature vectors…), data mining, machine learning and statistics [20, 21]. “Figures 5 and 10” cluster three different tweets: misinformation (A), conspiracy theory (B) and rumors(C) for English tweets (Fig. 5) and French tweets (Fig. 6).

CONCLUSION

The Internet is the most popular source of information, it produces a large amount of information in different languages. This information is not always healthy, especially in social networks which disseminate millions of misinformation per second. The later can put people's lives at risk. When it comes to information about people's health, we have to make sure that the information we read and distribute is true. The misinformation which called into question the COVID-19 and which led to the reluctance to vaccination and to push people not to comply with the advice of the WHO and the public health service. Governments must develop algorithms to regularize the access and disposal of information relating to public health, especially when it comes to a disease like COVID-19,

REFERENCES:

[1] Heidi Oi-Yee Li, Adrian Bailey, David Huynh, and J. Chan, "YouTube as a source of information on COVID-19: a pandemic ofmisinformation?," *BMJ Global Health*, 2020.

[2] Latika Gupta, Armen Yuri Gasparyan, Durga Prasanna Misra, Vikas Agarwal, Olena Zimba, and M. Yessirkepov4, "Information and Misinformation on COVID-19: a Cross-Sectional Survey Study," *Journal of Korean Medical Science*, 2020.

[3] Jon Roozenbeek, Claudia R. Schneider, Sarah Dryhurst, John Kerr, Alexandra L. J. Freeman, Gabriel Recchia, *et al.*, "Susceptibility to misinformation about COVID-19 around the world," *Royal Society Open Science*, 2020.

[4] Jose Yunam Cuan-Baltazar, Maria José Muñoz-Perez, Carolina Robledo-Vega , Maria Fernanda Pérez-Zepeda, and E. Soto-Vega, "Misinformation of COVID-19 on the Internet: Infodemiology Study " *JMIR Public Health and Surveillance*, vol. 6, 2020.

[5] S. Tasnim, M. M. Hossain, and H. Mazumder, "Impact of Rumors and Misinformation on COVID-19 in Social Media " *Journal of Preventive Medicine and Public Health* vol. 53, 2020.

[6] Bright Opoku Ahinkorah, Edward Kwabena Ameyaw, John Elvis Hagan Jr.2, and A.-A. S. a. T. Schack, "Rising Above Misinformation or Fake News in Africa: Another Strategy to Control COVID-19

Spread," *Frontiers in Communication Health Communication*, 2020.

[7] John Scott and F. N. Stokman, "Social Networks," *International Encyclopedia of the Social & Behavioral Sciences*, vol. 2, pp. 473-477, 2015.

[8] J Ricard and J. Medeiros, "Using misinformation as a political weapon: COVID-19 and Bolsonaro in Brazil," *misinforeview.hks.harvard.edu*, 2020.

[9] Daniel A.Erku, Sewunet A.Belachew, SolomonAbrha, MahipalSinnollareddy, JacksonThomas, Kathryn J.Steadman, *et al.*, "When fear and misinformation go viral: Pharmacists' role in deterring medication misinformation during the 'infodemic' surrounding COVID-19," *Research in Social and Administrative Pharmacy*, vol. 17, 2021.

[10] WHO, "Coronavirus disease 2019 (COVID-19)Situation Report –72," *World Health Organization*, 1 april 2020 2020.

[11] MokterHossain, "The effect of the Covid-19 on sharing economy activities," 2020.

[12] Mrinal Gupta, Ayman Abdelmaksoud, Mohammad Jafferany, Torello Lotti, Roxanna Sadoughifar, and M. Goldust, "COVID-19 and economy," 2020.

[13] Riyanti Djalante, Rajib Shaw, and A. D, "Building resilience against biological hazards and pandemics: COVID-19 and its implications for the Sendai Framework," *Progress in Disaster Science*, 2020.

[14] Philippe Gautret, Jean-Christophe Lagier, Philippe Parola, Van Thuan Hoang, Line Meddeb, Morgane Mailhe, *et al.*, "Early diagnosis and management of COVID-19 patients: a real-life cohort study of 3,737 patients, Marseille, France," *International Journal of Antimicrobial Agents*, 20 march 2020 2020.

[15] Chenghu Zhou, Fenzhen Su, Tao Pei, An Zhang, Yunyan Du, Bin Luo, *et al.*, "COVID-19: Challenges to GIS with Big Data," *Geography and Sustainability*, vol. 77-87, 2020.

[16] Yongjun Zhu, Erjia Yan, and I.-Y. Song, "A natural language interface to a graph-based bibliographic information retrieval system," *Data & Knowledge Engineering*, 2017.

[17] Fei Li and H. V. Jagadish, "Constructing an Interactive Natural Language Interface for Relational Databases," *VLDB Endowment*, vol. 8, 2014.

[18] Mohamed Chakraoui and Abderrafiaa Elkalay, "Efficiency of indexing database systems and optimising its implementation in NAND flash memory," *Int. J. Systems, Control and Communications*, vol. 7, pp. 221-239, 30 June 2016 2016.

[19] Aditya Bhardwaja, Yogendra Narayanb, Vanrajc, Pawana, and M. Dutta, "Sentiment Analysis for Indian Stock Market Prediction UsingSensex and Nifty," *Procedia Computer Science*, vol. 92 (2016), 2015.

[20] A.K. JAIN, M.N. MURTY, and P. J. FLYNN, "Data Clustering: A Review," *ACM Computing Surveys*, vol. 31, 1999.

[21] Aristidis Likasa, Nikos Vlassisb, and J. Verbeekb, "The global k-means clustering algorithm," *pattern recognition*, 2003.

7th Int. Conf. on Structure, Engineering & Environment (SEE), Pattaya, Thailand, Nov.10-12, 2021, ISBN: 978-4-909106070 C3051

EVALUATION AND DEVELOPMENT OF TRADITIONAL GUTTIYA BUILDING AS A LOW COST SUSTAINABLE HOUSING TECHNIQUE IN EASTERN SUDAN

May Y. Yousuf[1], Osama M. A. Daoud[2]

Private Architectural Consultant, Sudan[1], Assistant Prof., BRRI, University of Khartoum, Sudan [2]

ABSTRACT

This paper presents and outlines a research project established in Sudan aiming at evaluation of some local traditional construction techniques in order to be developed, adapted and standardized with the international sustainability requirements. Guttiya is a traditional low cost housing technique based on construction of isolated rooms or verandas using natural woods and straws. This technique has been widely accepted for along time ago in eastern Sudan. The region where this technique has been applied is characterized by a heavy rainy windy season most of the year. The ground condition of this region suffered from the wide spread of expansive black cotton soils down to about seven meters below the ground surface. Internally these rooms may be finished as required using different finishing materials. A comparative study was carried out between Guttiya and other different low cost housing techniques (sand bags, rammed earth, clay bricks and stone walls) based on material availability, cost, affordability of construction technique and ground base soil conditions. The Guttiya technique was enhanced and developed by incorporating the traditional rammed earth technique for construction of walls while keeping the traditional wood and straw made inclined roof. This newly developed composite construction technique has many advantages over other different techniques. It utilizes the naturally available materials with the a low energy consumption and significant reduction in carbon foot print. The new developed technique has the advantage of being easy to implement by the local people themselves without the need for skilled labour or equipment. Some room Models designed using the developed technique is now under construction for final on site evaluation.

Keywords: Sustainable, Green Building, Guttiya, Wood and Grass, Environment.

INTRODUCTION

The Gedaref state is located in the north east of the Sudan between 12o - 17o N latitude and 34o-37o E longitude. The temperature is high all year around, the highest temperatures being in April above 40o C and in October around 36o C. January is the coolest month with the maximum temperature being 17o C. The total area is 72.000 thousand square kilometers, the soil characterized by heavy clay soils in the middle and south and light and semi sandy soils in the north and north-west, the topography is vary, where the surface is dominated by the elevation with some highlands and plateaus and valleys as in the sedimentary lands, there are four seasonal rivers in the state (Atbara Baslam – –Saiteet and Rahad River. The rainy season is characterized by low rain fall in the north (150–250mm) and medium to high in the middle and south of state (400 – 900mm), fluctuated in its amount and distribution with majority of rains at August, also characterized by low relative humidity especially in winter reaching its minimum in April and its maximum in August [1]

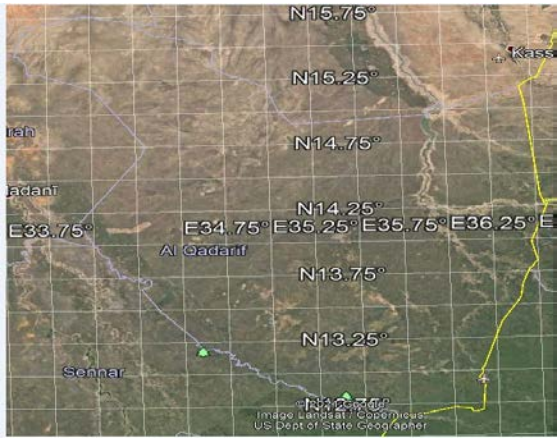


Fig. 1 Location of Gadarief state from google earth.

Guttiya is a traditional wood and grass building that has been used for a long time ago in the Gadarief state at eastern Sudan, east of Africa. It is a circular

house consisting of a single unit that forms a room so that the house surrounded by a wall with a main gate that opens onto the street is made up of a number of cats the size of the family or their standard of living. And the average in it consists of one or two cats for sleeping, a large one for reception and accommodation of guests called khilwa, and a small third such as a kitchen called Al-Takal, as well as other rooms. The Guttiya is built from a large circular wall of brick or mud bricks to the middle of the house, three meters long. It has one door and two or more small windows. It is topped by a roof in the form of a conical dome, the top of which is pointed on the outside. Its structure consists of local building materials such as sticks (branches) of thick trees called ileum Single cannulas that are connected by threads and ropes with other thin ones called canals, single canals in the form of circles and then covered with dry straw. A third of the conical roof is wiped from the inside with a layer of terracotta, which, after drying, is painted with white lime paint or another color in harmony with the circular brick wall paint. In the poorer neighborhoods, reeds and tree branches are used instead of bricks, where they are plastered with a layer of fermented mud mixed with animal dung and fine, crushed grass. The top of the outer cat is decorated with the addition of a straw head wrapped in black or colored wool ropes to give it an architectural beauty, and a crescent or ball of metal is placed on its top.

The floor of the cat may be paved from the inside with tiles, glass is placed on its door and windows, and then electricity is introduced to operate a fan or air conditioner, lighting lights, a TV, a refrigerator, and the like. The beauty of the cat is completed when it is surrounded by fresh trees and flowers. The cat, which is used as a reception room, is characterized by its spaciousness from the inside and the height of its ceiling. Sometimes it can accommodate more than ten people at one time.

The phenomenon of Al-Gatati buildings has started to decline in recent times, as there are neighborhoods where Al-Gatati is completely absent due to the high cost of construction and the lack of durability of building materials, so that Al-Qatati needs periodic maintenance at a rate of once a year, in addition to its rapid exposure to fires and home breakage, which is impractical in terms of urban planning Despite its harmony with the geographical and climatic environment of the region where there is a lot of rainfall and high temperatures in summer, in addition to the highly viscous clay soil without rocks [1].



Fig. 2 View of Guttiya

The soil of Gadarief state is mainly characterized by the spread and domination of expansive black cotton soils from the ground surface down to about 5-7m. This among other types of soils such as calcareous materials and silty sands makes it difficult to construct single or few stories buildings from any available building material due to very high uplift pressures that could damage the building.



Fig.3 Skeleton of Guttiya.

DEFINITION OF SUSTAINABILTY

Sustainability in construction means using renewable and recycled materials when building new structures, as well as reducing energy consumption and waste. The primary goal of sustainable construction is to reduce the industry's impact on the environment [2].

The construction industry, by its very nature, is a big user of natural resources. But with growing concerns over climate change and the finite nature of these resources, there is increasing pressure on construction firms to reduce their environmental impact.

Sustainable construction doesn't end when the

building is complete; the building itself should have a reduced impact on the environment over its lifespan. This means that the building design should incorporate elements that have an ongoing positive influence on the building's environmental impact. These can include proper insulation to prevent heat loss, solar panels to reduce energy consumption, and building materials with a long lifespan [2].

Requirements of Sustainability

Sustainable construction addresses these criteria through the following principles set by the conference:[3].

- Minimize ressource consumption (Conserve)
- Maximise ressource reuse (Reuse)
- Use renewable or recyclable resources (Renew/Recycle)
- Protect the natural environment (Protect Nature)
- Create a healthy, non-toxic environment (Non-Toxics)
- Pursue quality in creating the built environment (Quality)

Benefits of Sustainability

The advantages of green construction fall into three main categories: [4]

- environmental benefits;
- financial benefits; and
- social benefits.

Here are the most essential benefits of sustainable construction are; cost reduced increased productivity, improved health, waste minimization, better use of materials, environmental protection, noise avoidance, better quality of life, new market is emerging and finally room for experimentation.

BACKGROUND INFORMATION

Socio-economic Status of people at Gadarief State

The main socio-economic activity of Gadarief people is agriculture. Almost about 80% of peoples are working in different types of agricultural schemes. Most of the peoples are just farmers and seasonal workers, while plenty of them are land owners and investors. Gedarief is a very important strategic center for food security in Sudan and depends on mechanized rain-fed agriculture. It is characterized by large areas of arable land, and it has the largest rain-fed and mechanized agriculture projects in Sudan. The most important crops are: Sesame, as Sudan is the third largest producing country in the world after China and India. Gedarief is the largest producing area of sesame in Sudan, and sorghum and Sudan is among the three largest producing countries in the world, and Gedarief is one of the most important production areas in Sudan. Millet and gum arabic, and Sudan is the largest producer of it in the world, about 85% of global production, and Gedarief is one of the most important production areas in Sudan, and sunflower, in addition to horticultural crops that include fruits and vegetables such as lemons, guavas, tomatoes, okra, and others.
The city of Gedarief has the largest market for sesame, maize and millet crops. It also has the largest grain silos in Sudan [1].

Climate and Ecology of Gadarief State

Gedarif State is characterized by diverse ecological areas resulting from interaction of a number of complex interrelated factors such as climate, soil types, geological formations and human activities.

The Vegetation Cover in Gedarif State

There are three main types of the natural vegetation in Gedarief State. The Acacia trees, the major perennial type, including Acacia tertilus, Acacia Seyal and Acacia mellifera. The shrubs are the second perennial type of vegetation in Gedarif State, including bushy grasses scattered all over the region. The third type includes the annual grasses and herbs. E.g: Schoenefeldia gracilis (Gabash), Sorghum Purpureo Sericeum (Adar) and Sehima ischaemoids, while herbs include pemea cardiosepala) Hantut ,Ipomea Cordofana (Taber) and Blepharis edulis (Siha). These herbaceous plants are dominant during the wet season, but after the rainy season they wither and disappear and only a few species can be seen during the dry season. During the rainy season the low areas which are covered by water for a long time will become less vegetated due to the spoilage of seeds [1].



Fig.4 Vegetation Cover in Gedarif State.

Table 1 Sample of the most palatable plants that prevailed in Gedarif State.

#	Arabic name	Latin name	Family	Dominated area	palatability
1	Seha	Blephers edules	Acanthaceae	South, West	Most Plat.
2	Shara Ebil	Endogetera sp	Convolvulaceae	Central, West, South	Most Plat.
3	Tabar	Ipomea kordofanum	Convolvulaceae	North, East, South	Most Plat.
4	Hantot	Ipomea cardiesepala	Convolvulaceae	East, Central, North.	Most Plat.
5	Damblab	Schima ischaemoldes	Boaceae	Central, South	Most Plat.
6	Humaid	Selerocerta sp	Convolvulaceae	East, South	Most Plat.
7	Ghabash	Aristida sp	Boaceae	North	Most Plat.
8	Safary	Crotalaria senegalensis	Papilionaceae	North	Most Plat.

Table 2 Sample of ornamental plants in Gedarif State

No.	Arabic name	Latin name	Family	Dominated area	palatability
1	Hanzal	Colocynthis vulgaria	Cucurbitaceae	North, Central	Non plat.
2	Sena mecca	Cassia cena	Caeselpiniaceae	Central	Ornamental
3	Nal	Cymopogon nervatus	Boaceae	East, Central	Non plat.
4	Raihan	Ocimum basilicum	Lamaceae	East, Central	Non plat.
5	Maharaib	Cymopogon proximus	Boaceae	East, South.	Ornamental

Table 3 Sample of invasive and harmful plants In Gedarif State.

No.	Arabic name	Latin name	Family	Dominated area	Type
1	Jubain	Sulanum dubium	Solanaceae	Central	Herbivorous
2	Sekran	Datura sp	Solanaceae	East	
3	Ramtuk	Xanthiums brazilicum	Asteracaeae	North, East	
4	Fakha	Solanum nigram	Solanaceae	South	Herbivorous
5	Um galot	Leucas urticieolia		Central, South	Herbivorous

Some of the above mentioned plants are used for construction of Guttiya's skeleton and outer skin. Samples of these plants are Acacia nubica, Acacia senegala, Tamarindus indica, Acacia tortilis and Bamboos.

Definition and Important of Current Applied Research Project

The research project summarized in this paper is a part of the major Project of Gadarief Argo-innovation Laboratory. The PGAL is a development project recently brought to Sudan funded by International and local social enterprises aiming at enhancing the socio-economic status of the local people at Gadarief state, eastern Sudan. The main objective and long term purpose of the PGAL is to achieve long term food security for the people of the Gadarief state. Detailed objectives of the PGAL includes development of the agricultural and farming techniques, increase productivity of soils and introduction of modified and improved seeds for local corps, vegetables and fruits.

Finally, local government and international associates aimed at providing a comprehensive socio-economic development model for other states of Sudan as well as other countries in the region with the same climatic and ecological conditions [1].

STUDY METHODOLOGY

A comparative study was carried out in this research between different locally available building materials and techniques in Gadarief state. Beside the Guttiya technique it was found that some buildings were constructed using either clay bricks or rammed earth techniques. Also, some buildings were found to be constructed using stones or fired clay bricks. All available materials and techniques were studied based on the following criterion: cost, availability,

usability, power consumption, renewability, recyclability, satisfaction of health requirements and waste minimization. The main objective of the comparative study was to satisfy all sustainability requirements as much as possible.
In order to find the most efficient and sustainable power solution a solar analysis was conducted.

RESULTS AND DISCUSSION

Results of Soil Investigation

A soil investigation carried out during this study reveals that the general soil profile of the Gadarief state is a very stiff silty clay layer of high plasticity and with calcareous materials was encountered at upper 2.5 meters in the most boreholes (66 boreholes were drilled during this study). This layer was underlain by a medium dense to very dense silty sand layer. Avery dense clayey sand with calcareous material was encountered below 8m and extended down to the ends of boreholes. Highly weathered sand stone was encountered in all boreholes at depth ranging from 3m to 9m [5].
Based on the results of soil investigation it was clear that the most economic option for sustainable construction should utilize this available soil type.

Results of Vegetation survey

Based on the results previously stated about the vegetation cover of Gadarief state, it was also concluded that efficient utilization of the available natural materials in construction would lead to satisfaction of green and sustainable construction in the state.

Climatic Conditions

Based on the available data from the local and local and international meteorological agencies as well as local people experience it was obvious that any acceptable and efficient construction technique should be adaptable with the high rainy season and very high temperature most of the year in order to minimize energy consumption.

Results of Solar Analysis

Based on the data provided by local meteorological agencies regarding sunshine during the year a complete solar analysis was performed in order to reduce the yearly power consumption.
Results of the analysis and design of solar units are shown in figures 5-8.

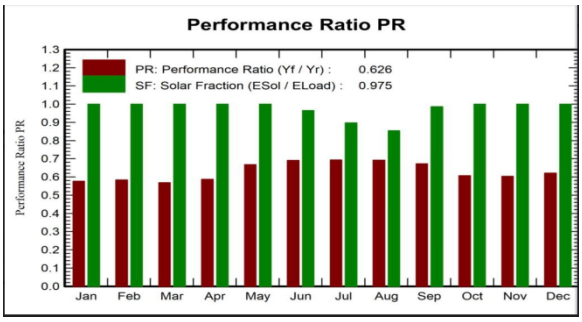


Fig.5 Yearly performance ratio of designed solar cell units

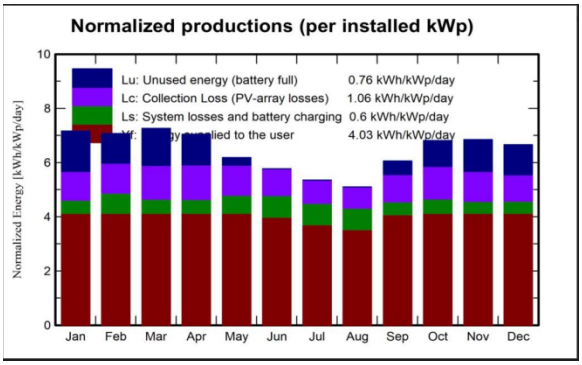


Fig.6 Yearly normalized production of designed solar cell units.

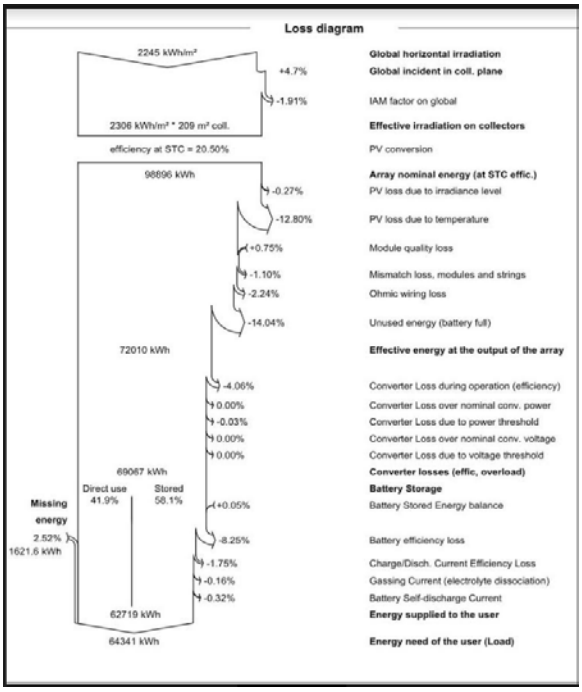


Fig.7 Loss diagram in radiation solar energy.

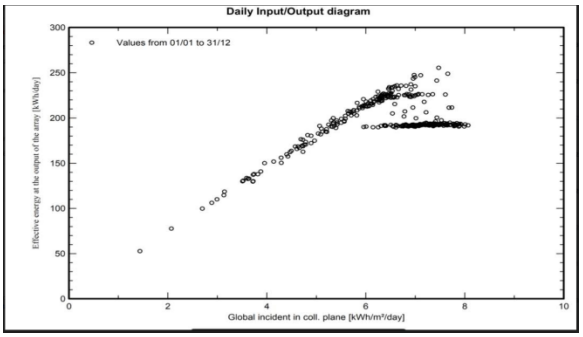


Fig.8 Daily input/output diagram.

CONCLUSIONS

Based on the survey, analysis, and comparative studied carried out and presented in this paper, the main conclusion was the adoption of the Guttiya building using a combined technique of rammed earth for the walls and wood and grass technique for the roof. Foundation of the Guttiya was designed as a strip foundation to be constructed from natural stones. An efficient deign of power supply system was designed utilizing the solar panels. Some figures presented below show details of the architectural and structural proposed design for the Guttiya building.

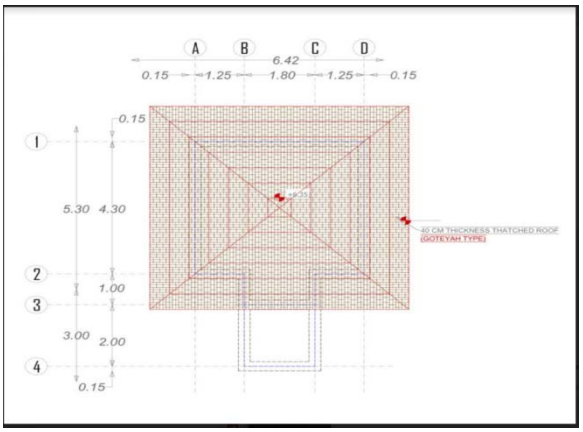


Fig.9 Plan of single Guttiya structure.

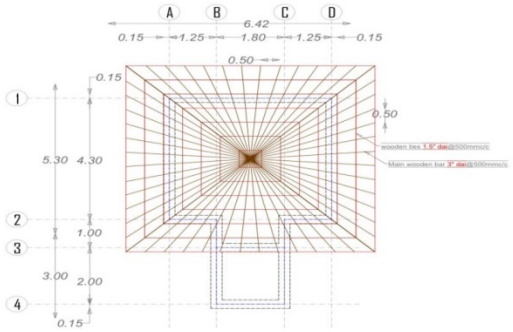


Fig.10 Plan of double Guttiya structure.

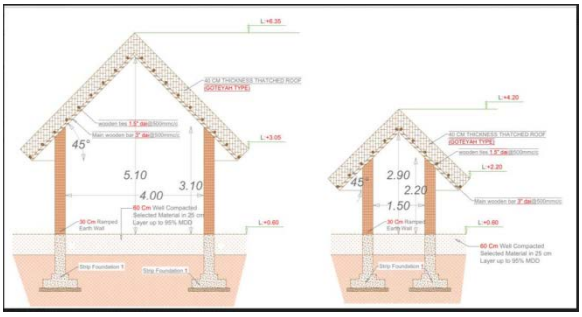


Fig.11 Cross-section of double Guttiya structure including foundation details.

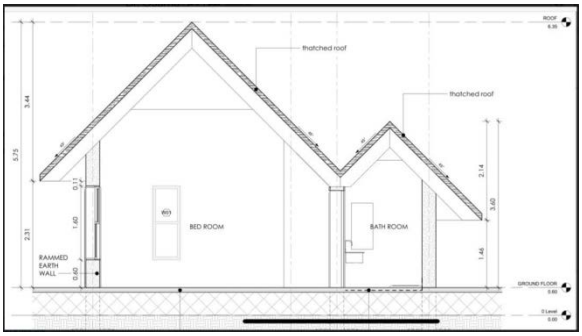


Fig.12 Elevation of double Guttiya module.

REFERENCES

[1] PGAL Study Report, prepared by Carnation company, Khartoum, Sudan, January 2021.
[2]Https://www.britishassesment.co.uklinsights/what-is-sustainable-construction-and-why-is-it-important/.
[3]Https://en.m.wikipedia.org/wiki/sustainability-in-construction.
[4] Https://www.constuctionexec.com/
[5] Soil investigation report, prepared by BRRI, Building and Road research Institute, University of Khartoum, May 2020.

7th Int. Conf. on Structure, Engineering & Environment (SEE), Pattaya, Thailand, Nov.10-12, 2021, ISBN: 978-4-909106070 C3051

DEVELOPMENT OF ARTIFICIAL INTELLIGENCE PROCESSING THROUGH CCTV CAMERA FOR DETECTING UNHELMETED MOTORCYCLISTS

Jetsada Kumphong[1], Thaned Satiennam[2], Watis Leelapatra[3]and Rujchai Ung-arunyawee[4]
[1,2,3,4]Faculty of Engineering, Khon Kaen University, Thailand

ABSTRACT

At present, Thailand's death rate from motorcycle accidents is very high while the rate of helmet wearing is low compared with other countries. Previous studies have shown that law enforcement can promote helmet wearing. This research aimed to develop an Artificial Intelligence (AI) program processing data recorded by Closed-Circuit Television (CCTV) cameras for detection of unhelmeted motorcyclists. Four steps for program development were performed, namely, 1) data collection, 2) program development in the C++ language and OpenCV library, 3) training the neural network of the program, and 4) checking the accuracy of the developed program. The result shows that the developed program can detect unhelmeted motorcyclists with 91% accuracy. This accuracy is practical for the law enforcement of Khon Kaen provincial police.

Keywords: Helmet, CCTV, Motorcycle, Detection

INTRODUCTION

The report of World Health Organization (WHO) in 2018 reveals that Thailand was in the top ten countries in the ranking of the number of road accidents and deaths, of which over 70% came from motorcycles. Past studies have shown that helmet wearing is an important factor that can reduce head injuries and deaths. [1] – [7].

The traffic laws of Thailand also govern motorcyclists, including drivers and passengers, to wear helmets. However, the efficiency of helmet wearing enforcement in Thailand is low. The police usually establish a temporary checkpoint to enforce riders who do not wear a helmet by issuing a ticket. Consequently, accidents sometimes occur at the check point because the traffic law violators attempt to escape by driving the wrong way, and also, there are conflicts between the traffic law violators and the police officer [8] – [10]. To increase the efficiency of law enforcement and avoid conflicts between police and road users, the application of CCTV cameras to law enforcement was introduced.

The authors previously developed a program to detect riders not wearing a helmet and achieved an accuracy of 74% [11]. This program has been extended and led to law enforcement by means of a CCTV camera under the enforcement program in Khon Kaen City. The system is compatible with the Thai Police Ticket Management System (PTM) that issues a ticket to a motorcycle rider who fails to conform to the law. This program increased 3.8% of helmet wear in the project area [8].

Although our previous developed program, [11], was practical for law enforcement police in Khon Kaen City, its detection accuracy was acceptable but still not high. Thus, the objective of this study is to further develop the program to improve its detection accuracy. This study applied Artificial Intelligence (AI) and collected more samples of unhelmeted motorcycles for training the program. In this paper, the next section explains the literature review. The third section presents the methodology. The fourth section presents the results and discussion. The last section presents the conclusions and recommendations.

LITERATURE REVIEW

CCTV cameras have been used to record events under surveillance for over 10 years, most of which involve recording the event and replaying it. The concept of CCTV image analysis arose in 2013 with the aim of object classification and object tracking [12].

Besides the use of CCTV cameras to record the evident image, CCTV cameras can also be used to increase the efficiency of law enforcement by police officers. Such operations require more officers according to the number of cameras in order to be able to detect the event abruptly and warn the person involved at once, and hence increase law enforcement efficiency [11] – [16]. The key element of the design of this detection system for motorcycle riders not wearing a helmet is object classification. The program is able to distinguish between the helmet and the head. The camera detects if the rider is wearing a

helmet or not. If not, the program will record the motorcycle image showing the number plate. The image showing the evident will be reported by the program and the officer will be able to issue a ticket at once [11].

Artificial neural networks can yield good results, but they require high-performance computerization such that real-time computation on personal computers is not possible. It was not until Nvidia, a producer of the graphic processor unit, publicized the software and allowed programmers to use it for more rapid computation of complex images than using the CPU only. Google then used this technique to develop software for creating machine learning. Thus, it is now possible to analyze images from CCTV cameras to the point that the machine is now able to distinguish and follow-up moving objects in real time [16].

When many images are found, the image of a doubtful object can be brought for further analysis. A rule is created and filed as a database for later decision on whether it is a helmet or not. In addition, Artificial Intelligence (AI) is being brought into use, such as the Artificial Neural Network. More conditions can also be added for decision making by training an interesting image for the system so that the system will be able to recognize a helmet image [16]. In our previous research, the HAAR algorithm was applied to analyze the motorcycle image prior to analyzing whether the rider was wearing a helmet or not, which made the whole process complicated [11].

From the studies discussed above, the HAAR HOG (Histogram of Oriented Gradients), Haar cascades, and YOLO (You only look once) have been selected to study the detection of unhelmeted riders to both detect and distinguish material types. Besides, the program first detects a motorcycle before analyzing if the rider is wearing a helmet or not.

RESEARCH METHODOLOGY

Data collection for program development

This study required a higher number of samples of unhelmeted motorcycles to develop the program with detection accuracy higher than our previous developed program [11]. The ten CCTV cameras were installed at three signalized intersections having a high number of motorcycles, including 1) Pratumuang intersection, 2) Mordindang intersection and 3) Charoensri intersection located along the Friendship Highway in Khon Kaen City as shown in Fig. 1.

To capture efficiently and effectively an image of an unhelmeted motorcyclist riding a motorcycle through the intersection, this study selected the CCTV camera with its specifications of 2 Megapixel resolution and 30 fps shutter speed, to be installed at the selected intersections. The CCTV cameras were installed at a height of 5.5 meters and an angle of 45 degrees from the road surface.

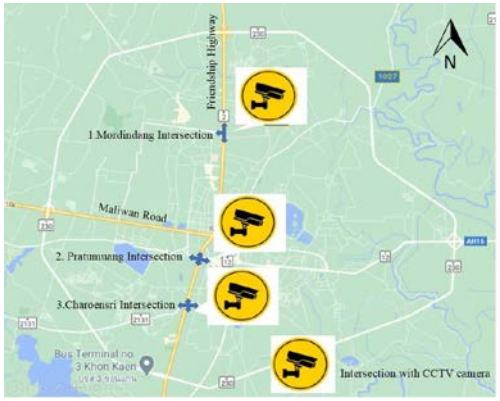


Fig. 1 Position of installation CCTV cameras

Program development

Image Record

This study recorded images of the study area (the method differs from previous studies, which recorded only the image of the rider's head [11]–[14], [17]). From the previous mentioned problems, this study was conducted on object classification and unhelmeted riders using CCTV cameras, as shown in Fig.2

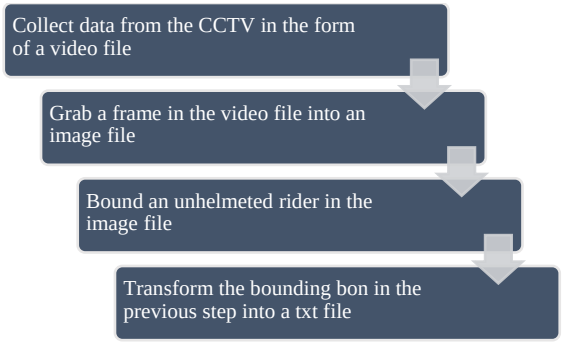


Fig. 2 Management of image file

Image Storage

This study stored about 1,119 images per one CCTV camera both during the daytime and nighttime for program development (1,019 images will be used for training and 100 images will be used for checking accuracy during the training). Images for training would contain various details which had to be recorded. An image may contain more than one unhelmeted rider. Some previous research could record only an unhelmeted head rider.

Table 1 shows variables, category, and codes in the developed program. This study developed the software - status (driver, passenger); No. of passenger (none, ≥ One); gender (female, male, and unidentified); apparent age (adult and child);

motorcycle class (engine size (CC)> 125, and other); side carriage – that is added on the motorcycle's side and is common in Thailand although illegal (yes, no) as shown in Fig. 3; time (daytime, night time); hairstyle (long hair, short hair, and unidentified); hair color (black, others, and unidentified); head ornaments – accessories put on the head, e.g., a hat that is not a helmet, a hairclip, or a bow (yes, no), as shown in Fig. 4 ; helmet type (full face, open-face, half-head, tropical and Unhelmet), as shown Fig. 5.

Table 1 Description of the study variables

Variables	Category and Codes
Status	1 = Driver 0 = Passenger
No. of passenger	1 = None 0 = ≥ One
Gender	1 = Female 0 = Male
Apparent age	2 = Unknown 1 = Adult 0 = Child
Motorcycle class	2 = Unknown 1 = Engine size > 125 CC 0 = Other
Side carriage	1 = Yes 0 = No
Time	1 = Daytime 0 = Nighttime
Hair style	1 = Long hair 0 = Other
Hair color	2 = Unknown 1 = Black 0 = Other
Head accessories	2 = Unknown 1 = Yes 0 = No
Helmet type	4 = Tropical 3 = Half-head 2 = Open-face 1 = Full face 0 = Unhelmet



Fig. 3 Example of a motorcycle with a side carriage

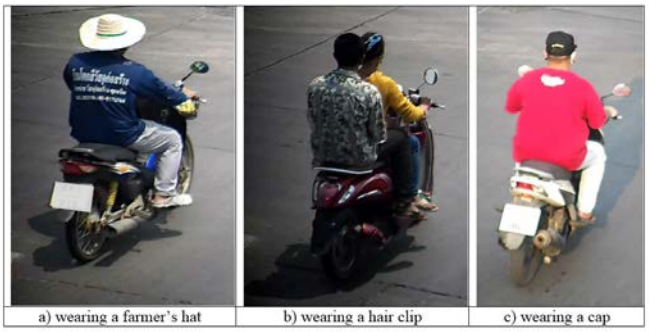


Fig. 4 Example of riders with local head accessories

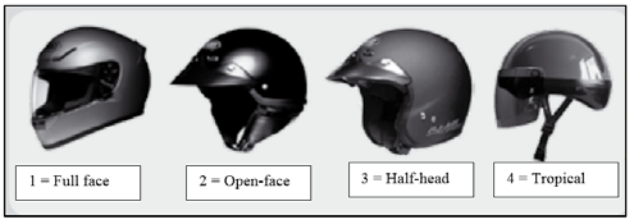


Fig. 5 Helmet styles [18]

Table 2 The results of Pearson's chi-square test of the percentage of the previous study, program development, and program verification found that the proportion of data divided by variables: the number of passengers, gender, status, and time, had differences that are of statistical significance- Apparent age and motorcycle class had no significant differences in statistics. Additionally, the results of Pearson's chi-square test of the percentage of the program development and program verification results found that the data divided by the following variables: side carriage, hairstyle, hair color, head accessories, and helmet type, had no significant differences in statistics. The results of this study were undertaken as a reference to further develop the program and check the validity of the program to ensure the appropriate proportion and sufficiency in comparison to the previous study's data proportion on motorcycles. The factors of riders' size and motorcycle class are part of the program development. Therefore, the data proportion for program development and validation had no differences compared to the data proportion of the motorcycle riders in this study.

Program Training

This study applied artificial neural networks to achieve more accuracy in detection. This study applied the principle of YOLO for detecting and distinguishing objects. The rider not wearing a helmet would be detected without detecting a motorcycle, as shown in Fig. 6.

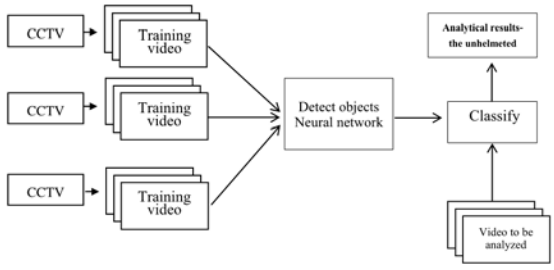


Fig. 6 Principle of the unhelmeted rider detection system using CCTV cameras

Testing accuracy of developed program

This study collected images from a sample of 100 images, which are not the same set as the images used in the training program (unknown to the training program). each to compare the number of riders not wearing helmets detected by the program and the number detected by the manual in order to evaluate the detection accuracy of the developed program.

RESULT AND DISCUSSIONS

Result of Program Development

In program development, 1,019 images consisting of 1,686 motorcyclists not wearing helmets were compiled. The characteristics of these motorcyclists are shown in Table 2. 64.5% and 35.5% of samples were drivers and passengers. 30.2% of samples were alone drivers and 69.8% of samples were drivers with passengers. 42.8%, 55.6%, and 21.3% of samples were female, male, and unidentified motorcyclists. 93% and 7% of apparent age were adults and children. 5.8% of the engine size of motorcycles was 125 CC. 4.1% of motorcycles had side carriages. 91.3% and 8.7% of samples were collected during the daytime and nighttime. 33.0%, 45.7%, and 21.3% of samples had long hair, short hair, and an unidentified hair style. 72.7%, 5.4%, 21.9% of samples had black, other colors, and unidentified colors. 29.8% of samples wore head accessary. 1.9%, 1.9%, 10.6%, 1.7% and 83.9% of helmet type samples had full face, open-face, half-head, tropical and unhelmet.

Each cycle requires roughly one hour, depending on the efficiency of the computer. The training process was similar to the previous study [16], but in this research, the training was carried out with unhelmeted riders only in order to increase the effectiveness of law enforcement, since this means training of the key target only. The program was able to distinguish between riders wearing hats and riders wearing helmets, as shown in Fig. 7.



Fig. 7 Example of detection of rider wearing hat (not wearing a helmet)

Verification of program accuracy

Verification of program accuracy was carried out by compiling 100 images of 163 riders not wearing and wearing helmets. The baseline data of the sample group included: status (63.8% riders, 36.2% passengers); No. of passenger (28.2% none, 71.8% ≥ One); gender (42.3% females, 57.7% males); apparent age (95.7% adult, and 4.3% child); motorcycle class (6.1%engine size (CC)> 125, and 93.9% other); side carriage (3.1% yes, 96.9% no); time (92% daytime, 8% night time); hairstyle (33.7% long hair, 47.3% short hair, and 19.0% unidentified); hair color (66.9% black, 9.8% other, and 23.3% unidentified); head ornaments (31.9% yes, 68.1% no); helmet type (1.8% full face, 9.2% half-head, 4.3% tropical and 84.7% unhelmet).These are shown in Table 2. The accuracy training of the learning program was 2,300 cycles and the accuracy was found to be 91%. The developed program detected a 9 percent error rate among helmeted motorcyclists because the shape and color printing of their helmets were sophisticated and distinctive.

Therefore, the accuracy of this developed program is higher than our previous developed program [11].

CONCLUSION AND RECOMMENDATIONS

The objective of this study was to develop an AI program to detect unhelmeted motorcyclists through CCTV cameras. The accuracy of the developed program was 91%, which was sufficiently effective for law enforcement by Khon Kaen provincial police. The misdetection of developed programs on unhelmeted motorcyclists is caused by their colorful helmets. Practically, the police would reject these cases during the process of ticket issue. To achieve higher accuracy in detection of unhelmet motorcyclists, more data on a variety of colors and types of helmets should be collected for more program training.

To extend the developed program to other areas, the same or higher specifications and installation position of CCTV cameras according to this study are required to maintain the detection accuracy.

Table 2 Pearson chi-square test, variable of program development and Variables for verification of program accuracy

Variables	Unhelmeted Motorcyclist						
	Previous study (Kumphong et al. , 2018)		Program Development (N=1,686)		Verification of program accuracy (N=163)		*p*-value
	Number	%	Number	%	Number	%	
No. Of passenger							
None	21,220	60.8	509	30.2	46	28.2	$p<0.05$
≥1	13,704	39.2	1,177	69.8	117	71.8	
Gender							
Male	22,201	63.5	938	55.6	94	57.7	$p<0.05$
Female	10,080	28.9	721	42.8	69	42.3	
Unknown	2,643	7.6	27	1.6	0	0	
Status							
Driver	27,977	80.1	1,088	64.5	104	63.8	$p<0.05$
Passenger	6,947	19.9	598	35.5	59	36.2	
Time							
Daytime	22,720	65.1	1,539	91.3	150	92.0	$p<0.05$
Nighttime	12,204	34.9	147	8.7	13	8.0	
Apparent age							
Adult	34,349	98.4	1,568	93.0	156	95.7	$p>0.05$
Child	468	1.3	118	7.0	7	4.3	
Unknown	107	0.3	0	0	0	0	
Motorcycle class							
Engine size (CC)> 125	2,648	7.6	97	5.8	10	6.1	$p>0.05$
Other	32,276	92.4	1,589	94.2	153	93.9	
Side carriage							
Yes	-	-	69	4.1	5	3.1	$p>0.05$
No	-	-	1,617	95.9	158	96.9	
Hair style							
Long hair	-	-	556	33.0	55	33.7	$p>0.05$
Others	-	-	770	45.7	77	47.3	
Unknown	-	-	360	21.3	31	19.0	
Hair color							
Black	-	-	1,225	72.7	109	66.9	$p>0.05$
Others	-	-	92	5.4	16	9.8	
Unknown	-	-	369	21.9	38	23.3	
Head accessories							
Yes	-	-	503	29.8	52	31.9	$p>0.05$
No	-	-	1,183	70.2	111	68.1	
Helmet type							
Tropical	-	-	28	1.7	7	4.3	$p>0.05$
Half-head	-	-	179	10.6	15	9.2	
Open-face	-	-	33	1.9	0	0	
Full face	-	-	33	1.9	3	1.8	
Unhelmet	-	-	1,419	83.9	138	84.7	

ACKNOWLEDGMENTS

This work has received scholarship under the Post-Doctoral Training Program from Khon Kaen University, Thailand. This work was dedicated to and in good remembrance of Mr. Vutidach Kumphong, a brother of a co-author, passed away from a road accident.

REFERENCES

[1] WHO, Global status report on road safety 2018, 2018.

[2] WHO, Global status report on road safety 2015, World Health Organization, 2015. Accessed: Sep. 16, 2019. [Online]. Available: https://sarf.org.za/who-global-status-report-on-road-safety-2018/.

[3] WHO, Global status report on road safety 2009, World Health Organization, 2009. Accessed: Sep. 16, 2019. [Online]. Available: https://www.who.int/violence_injury_prevention/road_safety_status/2009/en/.

[4] WHO, Global status report on road safety 2013, World Health Organization, 2013. Accessed: Sep. 16, 2019. [Online]. Available: https://www.who.int/violence_injury_prevention/road_safety_status/2013/en/.

[5] Ichikawa M., Chadbunchachai W., and Marui E., Effect of the helmet act for motorcyclists in Thailand, Accid. Anal. Prev., vol. 35, no. 2, pp. 183–189, Mar. 2003, doi: 10.1016/S0001-4575(01)00102-6.

[6] Kumphong J., Satiennam T., and Satiennam W., A correlation of traffic accident fatalities, speed enforcement and the gross national income of thailand and its cross-border countries, Int. J. Technol., vol. 7, no. 7, 2016, doi: 10.14716/ijtech.v7i7.4706.

[7] Kumphong J., Satiennam T., and Satiennam W., The determinants of motorcyclists helmet use: Urban arterial road in Khon Kaen City, Thailand, J. Safety Res., vol. 67, pp. 93–97, Dec. 2018, doi: 10.1016/J.JSR.2018.09.011.

[8] Satiennam T., Kumphong J., Satiennam W., Klungboonkrong P., Jaensirisak S., and Ratanavaraha V., Change in helmet use behavior enforced by CCTV cameras with automatic helmet use detection system on an urban arterial road, Traffic Inj. Prev., vol. 21, no. 7, pp. 494–499, 2020, doi: 10.1080/15389588.2020.1778170.

[9] Kumphong J., Satiennam T., and Satiennam W., Preliminary evaluation of helmet law enforcement by CCTV camera: Case of the phatumuang intersection, Khon Kaen City, Thailand, Inj. Prev., vol. 24, no. Suppl 1, p. A85, 2018.

[10] Oshima R., Fukuda A., Satiennam T., and Fukuda T., Study on Regulation of Motorcycle Taxi Service in Bangkok, J. East. Asia Soc. Transp. Stud., vol. 7, pp. 1828–1843, 2007, doi: 10.11175/easts.7.1828.

[11] Wonghabut P., Kumphong J., Satiennam T., Ung-arunyawee R., and Leelapatra W., Automatic helmet-wearing detection for law enforcement using CCTV cameras, IOP Conf. Ser. *Earth Environ. Sci.*, vol. 143, no. 012063, pp. 1–7, Apr. 2018, doi: 10.1088/1755-1315/143/1/012063.

[12] Silva R., Aires K., and Veras R., Detection of helments on motorcyclists, Multimed Tools Appl, 2017, doi: 10.1007/s11042-017-4482-7.

[13] Li J., Liu H., Wang T., Jiang M., Wang S., Li K., and Zhao X., Safety helmet wearing detection based on image processing and machine learning, in 9th International Conference on Advanced Computational Intelligence, *ICACI 2017*, 2017, pp. 201–205, doi: 10.1109/ICACI.2017.7974509.

[14] Vishnu C., Singh D., Mohan C.K., and Babu S., Detection of motorcyclists without helmet in videos using convolutional neural network, Proc. Int. Jt. Conf. Neural Networks, vol. 2017-May, no. November, pp. 3036–3041, 2017, doi: 10.1109/IJCNN.2017.7966233.

[15] Waranusast R., Bundon N., Timtong V., Tangnoi C., and Pattanathaburt P., Machine vision techniques for motorcycle safety helmet detection, Int. Conf. Image Vis. Comput. New Zeal., no. February, pp. 35–40, 2013, doi: 10.1109/IVCNZ.2013.6726989.

[16] Chairat A., Dailey M.N., Limsoonthrakul S., Ekpanyapong M., and Raj D.K.C., Low cost, high performance automatic motorcycle helmet violation detection, Proc. - 2020 IEEE Winter Conf. Appl. Comput. Vision, WACV 2020, pp. 3549–3557, 2020, doi: 10.1109/WACV45572.2020.9093538.

[17] Dahiya K., Singh D., and Mohan C.K., Automatic detection of bike-riders without helmet using surveillance videos in real-time,Proc. Int. Jt. Conf. Neural Networks, vol. 2016-Octob, pp. 3046–3051, 2016, doi: 10.1109/IJCNN.2016.7727586.

[18] WHO, helmets - a road safety manual for decision-makers and practitioners World Health Organization, 2006.

7th Int. Conf. on Structure, Engineering & Environment (SEE), Pattaya, Thailand, Nov.10-12, 2021, ISBN: 978-4-909106070 C3051

A MATHEMATICAL MODEL AND SOLUTION APPROACH FOR A HETEROGENEOUS FLEET OPEN VEHICLE ROUTING PROBLEM

Chansiri Singhtaun[1], Harit Piyapornthana [2]
[1,2]Department of Industrial Engineering, Faculty of Engineering, Kasetsart University, Thailand

ABSTRACT

This research proposes a new mathematical model and a solution method for a heterogeneous fleet open vehicle routing problem (HFOVRP). HFOVRP focuses on determining the set of customers and delivery routes for a mixed fleet of vehicles that does not return to the depot after servicing the last customer on a route. This situation usually occurs in manufacturing companies or warehouses that use outsource delivery companies, as well as in delivery companies that use third party logistics companies. In this research, HFOVRP is applied at a government enterprise that hires outsource delivery companies to distribute parts from the depot to 49 regional warehouses. At present, the company uses a point-to-point delivery system. Therefore, the company tries to collect orders from each destination warehouse until there is a full truckload or the lead time to reduce the transportation cost is met. However, a full truckload may not be achieved when the destination warehouse has to wait for parts for a very long time. This research proposes a new delivery system that collects the orders from every destination warehouse, and creates a cluster of destination warehouses and optimal vehicle routes, which is considered as a HFOVRP. The mathematical model is formulated by employing a modified heterogeneous fleet vehicle routing problem. The solution algorithm starts with clustering the warehouses, dealing with overload demand and solving problems by using a branch-and-cut algorithm. After performing the numerical experiments, the results show that the transportation cost was reduced by 15.02%.

Keywords: Mathematical Model, Heterogeneous fleet, Single depot, Open vehicle routing problem

INTRODUCTION

Transportation and distribution management has a crucial role in logistics management to enhance customer satisfaction and the company's core competency. The efficient distribution of products to customers at the lowest cost is one of the most challenging problems in logistics management. This problem involves finding the optimal assignment of customers to be visited by a fleet of vehicles, selecting the vehicle routes, and calculating the number of vehicles needed to serve the customers. This type of problem is called the Vehicle Routing Problem (VRP).

VRP has been extensively studied since it was first introduced by [1] in 1959. The current VRP models are very different from the first model as they increasingly aim to incorporate real-life complexities, such as time-dependent travel time, time windows for pickup and delivery, depot visiting after serving the last customer and input information that changes over time [2]. The open vehicle routing problem (OVRP) is well-known variant of VRP. The problem is first described in the literature by [3] in 1981 but has only recently attracted the attention of scientists and researchers [4]. It differs from the classical VRP in that a fleet of vehicles does not necessarily return to their original location after serving customers; if they do, they must follow the same path in the reverse order [5]. There are many applications in industry and service for businesses that do not usually have fleets [6]. These companies use outsource vehicles through third party logistic companies. In real-life routing applications, mixed fleets with variant capacity are common. When this condition is considered in VRP, it is known as the Heterogeneous Fleet Vehicle Routing Problem (HFVRP) or the mixed fleet vehicle routing problem [7]. In this paper, open routes are investigated in HFVRP. Consequently, the problem is a Heterogeneous Fleet Open Vehicle Routing Problem (HFOVRP). HFOVRP finds the optimal number of vehicles and designs optimal delivery routes to be used by a mixed fleet of vehicles to serve a set of customers at minimum delivery cost subject to the vehicle capacity constraint. The fleet of vehicles starts at a central depot and is characterized by different capacities and costs. After serving the last customer on the route, the vehicles do not return the depot. According to the literature review, there have been a few similar studies on the open routing version of HFVRP with a variant including constraints, such as [8] - [9]. Therefore, to explore the algorithms for HFOVRP, these articles and other variant versions of OVRP are studied.

OVRP is an NP-hard problem. Most mathematical models for the variant class of OVRP are constructed

by modifying the class of VRP. Most of them are integer programming problems. Classical exact algorithms such as the branch- and-cut algorithm [10], column generation [9], etc., are only efficient in instances of small problems. Therefore, most research focuses on heuristics and metaheuristics such as the ant colony algorithm [6], the hybrid genetic algorithm [8], tabu search [11], the particle swam algorithm [12], the hybrid algorithm [13], and so on.

Even though an exact algorithm takes more computational time than heuristic and metaheuristic algorithms, it guarantees an optimal solution. Moreover, a significant increase in the performance of computers due to new technology and the parallel computing technique dramatically reduces the limitation of problem size when solved by an exact algorithm. There is much software supporting exact algorithms. Most are commercial software but some are freeware such as OpenSolver, etc.

In this paper, the case study company is a government organization that is responsible for the provision of standardized electricity services and related business. To meet that mission, the warehouse management division at the case study organization needs to distribute supplies from its depot to 49 regional warehouses. At present, point-to-point delivery is carried out to all warehouses. The supply orders from each destination warehouse are collected until there is a full truckload or the delivery deadline is reached, whichever occurs first. These supplies are delivered by an outsource logistics company using two types of vehicle, which are 10-wheel trucks and trailer trucks. The types of vehicle are selected to match the quantity of delivered supplies. In each delivery round, each vehicle starts by loading supplies at the main warehouse (hereafter referred to as the depot), and then travels to only one destination warehouse without returning to the depot. The company is aware of the lateness and the high delivery cost of using the present delivery method and targets cost reductions. Therefore, the organization needs to improve the delivery policy by grouping the destination warehouses and by creating optimal vehicle routes to reduce transportation cost by at least 10%. Therefore, we propose HFOVRP instead of the current delivery system. The mathematical model of HFOVRP is obtained by modifying the HFVRP model proposed in [14]. At first, the customers are grouped by using the angular sweep algorithm. The branch-and-cut algorithm is then employed to solve the model in each cluster. The program using VBA and OpenSolver in Excel is constructed to support delivery planning.

The remainder of this paper is organized as follows. In the next section, the research methodology is presented. After that, an example of program implementation and the numerical results are shown. Finally, the conclusion and discussion on the results are presented.

RESEARCH METHODOLOGY

The research methodology has five parts: studying the current delivery problem and restrictions, formulating a mathematical model, developing the solution algorithm, developing a delivery planning program, and conducting numerical experiments.

Problem description and restrictions

The proposed delivery system, HFOVRP, changes the vehicle management of the current delivery system, which is point-to-point delivery, without changing the following conditions and restrictions. The organization outsources deliveries from the depot to 49 regional warehouses. The working hour limit of the driver is set at 8 hours. Nine out of these 49 warehouses require nearly 8 hours of travel time, so they cannot be delivered together with the others. Therefore, point-to-point delivery is still needed for these nine warehouses and the remaining 40 warehouses are considered in the study. The distance between each pair of warehouses and the distance between each warehouse and the depot are estimated with a geometric information system (GIS). The delivery cost includes driver wages and fuel cost, which depends on the type of vehicle and the distance.

Two types of vehicles, which are 10-wheel trucks and trailer trucks, have limited capacity at 24,000 units and 12,000 units respectively. The number and type of vehicles need to be decided. The maximum number of available vehicles is unlimited. All vehicles start at the depot, but they do not return to the depot. The traveling time, which ignores traffic conditions, is obtained by dividing the distance by the speed limit. Each warehouse is served by only one vehicle. The maximum order from any warehouse does not exceed the capacity of the available vehicles. The required space for all items is converted into the same unit of measurement.

Mathematical model formulation

The mathematical model representing the case study organization delivery problem is developed by modifying the mathematical model for HFVRP proposed by [14]. The travel cost of all returning paths to the depot are deleted from the objective function and the traveling time of these paths is not considered in the working hour constraint. The notations used in the formula are as follows. The vertex set $V = \{0, 1, \ldots, N\}$ is the set of $N+1$ nodes. Node 0 represents the factory, while the remaining node set $V' = V \setminus \{0\}$ corresponds to N customers. $K = \{1, \ldots, M\}$ is the vehicle set. The vehicles are indexed by parameter *k* running from 1 to *M* and each

type of vehicle has a different capacity (Q_k). M, which is total number of vehicles, is unknown at the first stage. The maximum number of 10-wheel trucks (M_1) and the maximum number of trailer trucks (M_2) are independently calculated by dividing the total quantity of demand by the capacity of the vehicles, which is used as the upper bound. The number of vehicles used can be less than or equal to this upper bound. M is the summation of M_1 and M_2. Indexes of k =1 to M_1 are used for 10-wheel trucks and k=M_1+1 to M are used for trailer trucks. Q_1 to Q_{M_1} equals 12,000 units and Q_{M_1+1} to Q_{M_2} equals 24,000 units. c_{ijk} is the delivery cost, which is the transportation charge, from node i to node j of vehicle k. The transportation charge consists of $c_{iik} = \infty$. Parameter q_i is the number of units of product at node i. t_{ijk} is traveling time from node i to node j by vehicle k. s_j is the service time at node j. The decision variables and the mathematical model of this problem are as follows.

$$x_{ijk} = \begin{cases} 1 \text{ if vehicle } k \text{ travels from node } i \text{ to node } j \\ 0 \text{ otherwise} \end{cases}$$

$$y_{ik} = \begin{cases} 1 \text{ if node } i \text{ is visited by vehicle } k \\ 0 \text{ otherwise} \end{cases}$$

u_{ik} = arbitary real numbers which satisfy constraints (7)

$$\text{Minimize} \quad Z = \sum_{k\in K}\sum_{i\in V}\sum_{j\in V'} c_{ijk} x_{ijk} \tag{1}$$

subject to

$$\sum_{i\in V'} q_i y_{ik} \le Q_k \qquad \forall k \in K \tag{2}$$

$$\sum_{k\in K}\sum_{i\in V} x_{ijk} = 1 \qquad \forall j \in V' \tag{3}$$

$$\sum_{k\in K}\sum_{j\in V} x_{ijk} = 1 \qquad \forall i \in V' \tag{4}$$

$$\sum_{i\in V} x_{ipk} - \sum_{j\in V} x_{pjk} = 0 \qquad \forall p \in V', \forall k \in K \tag{5}$$

$$u_{ik} - u_{jk} + n x_{ijk} \le n-1 \qquad \forall (i,j) \in V', i \ne j, \forall k \in K \tag{6}$$

$$\sum_{j\in V'} x_{0jk} \ge \sum_{j\in V} x_{ijk} \qquad \forall i \in V', \forall k \in K \tag{7}$$

$$\sum_{j\in V'} x_{0jk} \le 1 \qquad \forall k \in K \tag{8}$$

$$\sum_{j\in V'}\sum_{i\in V} x_{ijk}(t_{ijk} + s_j) \le L \qquad \forall k \in K \tag{9}$$

$$x_{ijk} \in \{0,1\} \qquad \forall (i,j) \in V, \forall k \in M \tag{10}$$

$$y_{ik} \in \{0,1\} \qquad \forall i \in V, \forall k \in M \tag{11}$$

The objective function (1) states that the total travel cost, excluding the cost of returning to the depot, is to be minimized. Constraint (2) ensures that the total quantity of product loaded on a vehicle is not over the truckload. Constraint (3) and (4) ensure that each customer is visited by one vehicle. Route continuity is represented by constraint (5), i.e., if a vehicle enters a demand node, it must exit from that node. Constraint (6) is the subtour-breaking constraint. Constraints (7) - (8) state that if a vehicle travels to any customer, then that vehicle must leave from the depot to only one customer. Constraint (9) states that the total time (travel time and service time) spent by each vehicle must not be over the daily working hour limit. The travel time to return to the depot is excluded in this constraint. Constraints (10) - (11) are logical constraints.

Solution algorithm

The algorithm is composed of three main steps: clustering the warehouses, dealing with the overload demand, and solving the vehicle routes. The first two steps are pre-process phases for the third step. They reduce the problem size using the transportation constraints to enhance the efficiency of the solution algorithm. These steps are described as follows.

Clustering the warehouse

In this step, the warehouses are clustered according to the limitation of daily working hours (8 hours). Regarding the traveling time and service time data, no more than 4 warehouses can be served by a single vehicle. Therefore, 40 warehouses are equally split into 10 clusters using the angular sweep algorithm. These clusters are shown in Table 1.

Table 1 Warehouses in each cluster

	BRANCH NAME		BRANCH NAME
	Cluster 1		**Cluster 6**
1	HuaHin	1	Phra Phutthabat
2	Pethaburi	2	Lopburi
3	Samut Sakhon	3	Tha Ruea
4	Samut Songkhram	4	Khok Samrong
	Cluster 2		**Cluster 7**
1	Samphran	1	Kabinburi
2	Nakhonchaisri	2	Saraburi
3	Ratchaburi	3	Nakhonnayok
4	Photharam	4	Prachinburi
	Cluster 3		**Cluster 8**
1	Suphanburi	1	Thanyaburi
2	Banpong	2	Chachoengsao
3	Kanchanaburi	3	Srakaew
4	Ladlumkaew	4	Panat Nikhom
	Cluster 4		**Cluster 9**
1	Sena	1	Rayong
2	Ladyao	2	Bang Pakong
3	Uthaithani	3	Klaeng
4	Chainat	4	Pluak Daeng
	Cluster 5		**Cluster 10**
1	Ang Thong	1	Sriracha
2	Ayuthaya	2	Chonburi
3	Singburi	3	Pataya
4	Nakhonsawan	4	Rangsit

Dealing with overload demand

In cases where the quantity of supplies from a warehouse is over the capacity of the trailer truck, the order is divided into two parts. The quantity that can fit in the trailer trucks is assigned to trailer trucks. Point-to-point delivery will apply for the full trailer loads. The capacity of a trailer truck is twice that of a 10-wheel truck but the unit travel cost is less than twice. Using one trailer truck is cheaper than using two 10-wheel trucks. The remaining quantity of supplies is considered in the next step of the algorithm.

Solving the vehicle routes

Having completed the previous two steps, the problem size is thus reduced. The mathematical model, which is an integer programing problem, is solved. To solve the problem, the branch-and-cut algorithm in OpenSolver is employed because of the free software license and user familiarity.

Delivery planning program development

To facilitate logistics planners, the delivery planning program is developed using Excel VBA. This program is divided into three parts: the data input part, the solver part, and the report part.

The data input spreadsheet shown in Fig. 1 is created to input the orders of each warehouse. The "Reset" button allows users to clear the past data in this spreadsheet. After the operators click the "Solve" button, the second part of the program, the solver spreadsheet, will be activated. The input demands that are over the trailer truck capacity (24,000 units) are subtracted from the trailer truck capacity and kept in the report spreadsheet. These orders will be delivered point-to-point. The remaining orders will be sent to the solver part.

The solver part consists of 10 spreadsheets corresponding to 10 clusters to respond for the case of a specific cluster is of interest. For example, Fig.2 shows the spreadsheet in the solver part of cluster 4. Quantity of demand of Sena warehouse identified with parameter d_1 in Fig.2 is the remaining quantity (36,000 – 24,000 = 12,000). In general use, only the spreadsheets of clusters that have demand are activated. They are solved one-by-one until all clusters that have demand are solved. In each spreadsheet, the related cells contain formula representing the mathematical model. The data used in the formula are imported from the data input spreadsheet. These cells are then referred in the OpenSolver and the problem is solved. The solutions are translated into a descriptive format as shown in the report spreadsheet (Fig.3). The report part informs the vehicle number to be used and their delivery routes.

The program is verified by testing with 30 randomly generated data sets to ensure the accuracy of the program before implementation with real data sets in the next step.

	BRANCH NAME	Demand (Units)
	Cluster 1	
1	HuaHin	
2	Pethaburi	
3	Samut Sakhon	
4	Samut Songkhram	
	Cluster 2	
1	Samphran	
2	Nakhonchaisri	
3	Ratchaburi	
4	Photharam	
	Cluster 3	
1	Suphanburi	23500
2	Banpong	6000
3	Kanchanaburi	
4	Ladlumkaew	5000
	Cluster 4	
1	Sena	36000
2	Ladyao	
3	Uthaithani	12000
4	Chainat	12000
	Cluster 5	
1	Ang Thong	6000
2	Ayuthaya	12000
3	Singburi	6000
4	Nakhonsawan	

	BRANCH NAME	Demand (Units)
	Cluster 6	
1	Phra Phutthabat	
2	Lopburi	5970
3	Tha Ruea	
4	Khok Samrong	18000
	Cluster 7	
1	Kabinburi	
2	Saraburi	36000
3	Nakhonnayok	6000
4	Prachinburi	4000
	Cluster 8	
1	Thanyaburi	
2	Chachoengsao	16500
3	Srakaew	
4	Panat Nikhom	
	Cluster 9	
1	Rayong	33030
2	Bang Pakong	5000
3	Klaeng	
4	Pluak Daeng	12000
	Cluster 10	
1	Sriracha	
2	Chonburi	12000
3	Pataya	
4	Rangsit	12000

Reset Solve

Fig. 1 Data input spreadsheet

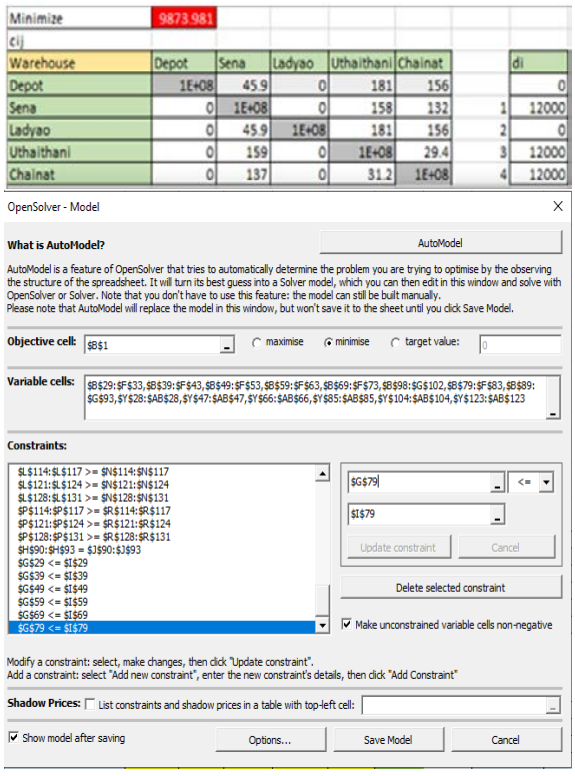


Fig.2 Solver spreadsheet of cluster 4

Cluster	Fleet Type	Route
Cluster 3	10-wheel truck	Depot-Ladlumkaew-Suphanburi
	Trailer truck	Depot-Suphanburi
Cluster 4	10-wheel truck	Depot-Sena
	Trailer truck	Depot-Sena
	Trailer truck	Depot-Chainat-Uthaithani
Cluster 5	10-wheel truck	Depot-Angthong-Singburi
	10-wheel truck	Depot-Ayuthaya
Cluster 6	Trailer truck	Depot-Lopburi-Khok Samrong
Cluster 7	10-wheel truck	Depot-Saraburi
	Trailer truck	Depot-Saraburi
	10-wheel truck	Depot-Nakhonnayok-Prachinburi
Cluster 8	Trailer truck	Depot-Chachoengsao
Cluster 9	10-wheel truck	Depot-Bang Pakong
	Trailer truck	Depot-Rayong
	Trailer truck	Depot-Pluak Daeng-Rayong
Cluster 10	10-wheel truck	Depot-Chonburi
	10-wheel truck	Depot-Rangsit

Number of 10-wheel truck	9
Number of trailer truck	8

Fig.3 Report spreadsheet of the example problem

The numerical experiments

After passing the verification step, the delivery planning program is implemented with 30 past weekly orders. The transportation cost and delivery plans obtained from the program are compared with the original plans of the case study company.

RESULTS AND DISCUSSION

The data set of a weekly delivery plan is shown in Fig.1 as an example. The demand column is filled in by the operators. In this data set, there are 20 warehouses requesting supplies from the depot. There are three warehouses; Sena, Saraburi, Rayong, with orders over the trailer truck capacity of 24,000 units.

By clicking the “Solve” button, the first 24,000 units of supplies for each of these warehouses is assigned to a trailer truck. These three trailer trucks make point-to-point deliveries. The remaining quantity of supplies are sent to the Solver part.

The Solver spreadsheets of Cluster 3 to Cluster 10 are then solved. The solutions are converted into a delivery route for each vehicle as shown in Fig.3. It shows that to deliver the supplies, nine 10-wheel trucks and eight trailer trucks are needed as shown in Fig 1. The transportation route for each vehicle is shown in each row. The transportation cost, which is 69,913.476 Baht, is not presented in this report but is recorded by the responsible department.

To deliver these orders by using the original delivery system, seventeen 10-wheel trucks and six trailer trucks are required. The transportation cost is 80,751.204 Baht. Point-to-point delivery is carried out to all warehouses. Each vehicle starts by loading supplies at the depot, and then travels to only one assigned destination warehouse without returning to the depot. Since the warehouses cannot share the space of vehicles, the number of vehicles is higher than that of the proposed delivery system.

After implementing the program with 30 real data sets, the program yields delivery plans within 5 minutes. The transportation cost of these data sets is illustrated in Fig. 4. The transportation cost of the proposed delivery system is lower than the transportation cost of the original delivery system for all data sets. According to the numerical results, the delivery cost is reduced by 15.02% on average.

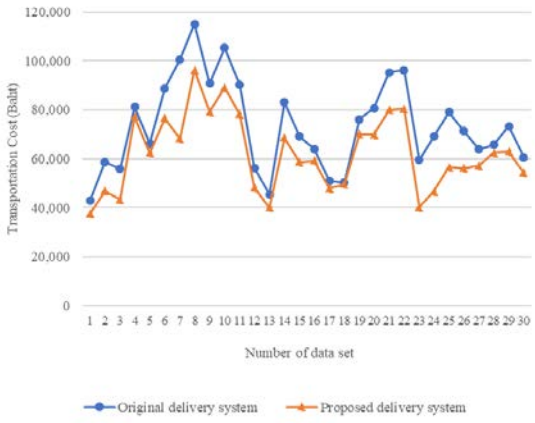


Fig.4 Comparison of transportation cost

CONCLUSION

In this research, a delivery planning program is developed to determine vehicle usage and to provide an optimal delivery route for a fleet of vehicles in each cluster of customers of the case study company. After program trial, the program allows the planners to make better decisions on delivery planning, the delivery cost is decreased by 15.02% on average. The new mathematical model applied in the program can represent real problems. The branch-and-cut algorithm in OpenSolver can solve the model, which is a MIP, in an acceptable computing time.

RECOMMENDATIONS

For the future research, there are two main extensions of this research. The first area is to modify the algorithm to find a tighter upper bound for the number of 10-wheel trucks and trailer trucks to reduce the computational time. In this paper, M1 and M2 are calculated independently, then M is much larger than the number of vehicles need. Therefore, the problem involves a lot of decision variables. The efficient heuristic algorithm is another alternative. The second extended version aims to expand the scope and enhance the realism of the mathematical model by considering conditions such as longer planning period, traffic conditions, split load and so on.

REFERENCES

[1] Dantzig G.B., and Ramser J.H., The Truck Dispatching Problem, Management Science, Vol. 6, Issue 1, 1959, pp. 80–91. https://doi.org/10. 1287/mnsc.6.1.80.

[2] Ren C., Research on Single and Mixed Fleet Strategy for Open Vehicle Routing Problem, Journal of Software, Vol. 6, Issue 10, 2011, pp. 2076–2081. https://doi.org/10.4304/jsw.6.10.20 76-2081.

[3] Schrage L., Formulation and structure of more complex/ realistic routing and scheduling problems, Networks, Vol. 11, Issue 2, 1981, pp. 229–232. https://doi.org/10.1002/net.32301102 12.

[4] Sedighpour M., Ahmadi V., Yousefikhoshbakht M., Didehvar F., and Rahmati F.,Solving the open vehicle routing problem by a hybrid ant colony optimization. vol. 41. 2014.

[5] Gurpreet E., and Vijay D., Open Vehicle Routing Problem by Ant Colony Optimization, International Journal of Advanced Computer Science and Applications, Vol. 5, Issue 3, 2014. https://doi.org/10.14569/ijacsa.2014.050308.

[6] Yousefikhoshbakht M., Dolatnejad A., Didehvar F., and Rahmati F., A Modified Column Generation to Solve the Heterogeneous Fixed Fleet Open Vehicle Routing Problem, Journal of Engineering (United Kingdom), Vol. 2016, 2016. https://doi.org/10.1155/2016/5692 792.

[7] Braekers K., Ramaekers K., and Van Nieuwenhuyse I., The Vehicle Routing Problem: State of the Art Classification and Review, Computers and Industrial Engineering, Vol. 99, 2016, pp. 300–313. https://doi.org/10. 1016/j.cie. 2015.12.007.

[8] Yilmaz Eroglu D., Caglar Gencosman B., Cavdur F., and Ozmutlu H.C., Introducing the MCHF/ OVRP/ SDMP: Multicapacitated/ heterogeneous fleet/ open vehicle routing problems with split deliveries and multiproducts, Scientific World Journal, Vol. 2014, 2014. https://doi.org/10.1155/2014/515402.

[9] Yousefikhoshbakht M., and Dolatnejad A., A Column Generation for the Heterogeneous Fixed Fleet Open Vehicle Routing Problem, International Journal of Production Management and Engineering, Vol. 5, Issue 2, 2017, pp. 55–71. https://doi.org/10.4995/ijpme. 2017.5916.

[10] Letchford A.N., Lysgaard J., and Eglese R.W., A Branch-and-Cut Algorithm for the Capacitated Open Vehicle Routing Problem, Journal of the Operational Research Society, Vol. 58, Issue 12, 2007, pp. 1642–1651. https://doi.org/10.1057/ palgrave.jors.2602345.

[11] Niu Y., Yang Z., Chen P., and Xiao J., A Hybrid Tabu Search Algorithm for a Real-World Open Vehicle Routing Problem Involving Fuel Consumption Constraints, Complexity, Vol. 2018, 2018. https://doi.org/10.1155/2018/57549 08.

[12] Marinakis Y., and Marinaki M.,A Hybrid Particle Swarm Optimization Algorithm for the Open Vehicle Routing Problem. Swarm Intell. ANTS 2012. Lect. Notes Comput. Sci., vol. 7461, Springer, Berlin, Heidelberg; 2012, p. 180–187. https://doi.org/10.1007/978-3-642-32 650-9_16.

[13] Maleki F., and Yousefikhoshbakht M., A Hybrid Algorithm for the Open Vehicle Routing Problem, Int J Optim Civil Eng, Vol. 9, Issue 2, 2019, pp. 355–371.

[14] Singhtaun C., and Tapradub S., Modeling and Solving Heterogeneous Fleet Vehicle Routing Problems in Draft Beer Delivery, International Journal of Engineering and Advanced Technology, Vol. 8, Issue 3S, 2019, pp. 353–356.

7th Int. Conf. on Structure, Engineering & Environment (SEE), Pattaya, Thailand, Nov.10-12, 2021, ISBN: 978-4-909106070 C3051

DEVELOPMENT OF DECISION SUPPORT SYSTEM FOR RAILWAY MAINTENANCE: A CASE STUDY OF STATE RAILWAY OF THAILAND

Thawatchai Phanyakit[1], Thaned Satiennam[2, *]

[1,2] Department of Civil Engineering, Faculty of Engineering, Khon Kaen University,

Khon Kaen 40002 Thailand

ABSTRACT

This research presents a development of decision support system for railway maintenance of the State Railway of Thailand (SRT). The 10 high experienced engineers, expertizing in railway maintenance from the State Railway of Thailand, were interviewed to give the weight of severity that caused rail breaks, cracks and deterioration based on the standard of the International Union of Railways (UIC). In analysis, factors influencing railway deterioration were considered for making pairwise comparison, and Fuzzy Analytic Hierarchy Process (FAHP) was used to consider factors influencing decision on choosing a plan for structure railway maintenance and rehabilitation. The major factors applied to decision making were railway quality, risk reduction of railway deterioration, and investment worthiness. According to the experts' opinions, the most important factor was railway quality, which showed the importance of 50.5%, followed by investment worthiness, which showed the importance of 27.4%, and risk reduction of railway deterioration, which showed the importance of 22.1%. The window-based program of decision support system was developed to facilitate in this research for analyzing the weight of each factor for railway engineers gaining better decision.

Keywords: Decision Support System (DSS), Fuzzy Analytic Hierarchy Process (FAHP), Railway Maintenance

INTRODUCTION

Currently, the State Railway of Thailand (SRT) has a 4,043 km railway network covering 47 provinces of Thailand, with 3,764 km of single track, 174 km of double track, and 105 km of triple track. Because the distance between double and triple tracks is relatively short, train operation on single track takes a long delay. Furthermore, the railway network has deteriorated (over 60% of railways have an average age of more than 30 years) and has not been maintained (Academic Report of National Assembly of Thailand, 2019). Thailand ranked 61st in terms of overall infrastructure quality in a World Economic Forum (WEF) report from 2013 to 2014, behind Singapore and Malaysia, which ranked 5th and 25th, respectively. For railway structure quality, Thailand ranked 72nd, behind Singapore, and Malaysia, which ranked 10th and 18th, respectively as shown in Table1.

Table 1 Ranking of Infrastructure Quality

Country	Ranking of Infrastructure Quality				
	Overall	Road	Rail	Airport	Port
Singapore	5	7	10	1	2
Malaysia	25	23	18	21	24
Thailand	62	42	72	34	56

Source: World Economic Forum (2013-2014)

The transport by railway is unlikely to be ready because the railway structure deterioration cannot be maintained and rehabilitated in a timely manner. According to an in-depth interview with experts from the State Railway of Thailand (SRT), two existing maintenance issues were found as follows.

(1) Inspection and evaluation of railway condition for maintenance cannot be properly performed based on the structure deterioration in each year due to the limitation in using EM120, an inspection car, for inspection because there is only one EM120 available. Considering the existing railway network, excluding the newest constructed one, with over 4,000 km that have been used for many decades, the railway deterioration cannot be evaluated progressively.

(2) There is not a process of data management to support a proposal as well as a budget approval request that is in accord with deterioration level in terms of systematically mathematical evaluation, but it is proposed based on previous experiences of railway engineers due to a lack of supportive tools for systematic thinking under the same standard. These principles are not possibly suitable for the happening deterioration since qualitative principles are often indistinct from the mentioned problem.

For these existing limitations, this study has attempted to develop a program of decision support system to facilitate railway engineers and

stakeholders in determining more appropriate plans for maintenance. This study applied an Analytic Hierarchy Process (AHP), one of decision-making methods deriving from Multi Criteria Decision Making (MCDM), because it is so simple and accurate, and it can be used to manage both abstract and concrete criteria [1]. AHP can help stakeholders to make decisions on choosing optimal criteria based on explicit and accurate values. This method has been widely used [2,3]. Although AHP is accurate in decision making process, it has some weak points because it cannot reflect human's concepts and ideas accurately. Also, the decision makers can have a sense of conflict when making a decision that leads to errors in values. Thus, this study applied a principle of Fuzzy for decision making process to cope with the problems that often happen during criteria analysis process. This study also applied a decision support system (DSS) since it is supportive technology that creates the distinctness in the right time for decision makers and gives optimal representatives in operation as well as certain cost [4]

METHODOLOGY

The methodology of this study for development of a decision support system to determine an appropriate plan for railway maintenance and rehabilitation as shown in Fig. 1. Each step was described as following sections.

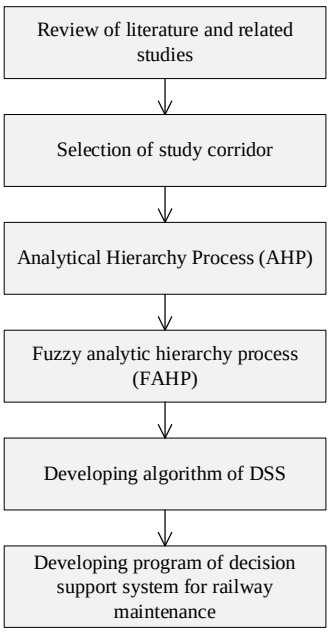


Fig. 1 Research Methodology

Selection of Study Railway Corridor

The Northeastern line (NE Line) from Thanon Chira junction to Nong Khai station was selected as the area of study, as shown in Fig. 2, because it is a rail transportation route heading to the upper northeastern region of Thailand. The destination of this line is Nong Khai station that is the province bordering Laos, which is considered as an important route for Thailand's logistics because the weight through track during 2007-2016 was higher in every year. Therefore, this has influenced higher rate of deterioration. The study corridor has the distance of 320.9 km approximately. The railway structure is ballasted track with 1.00-meter gauge.

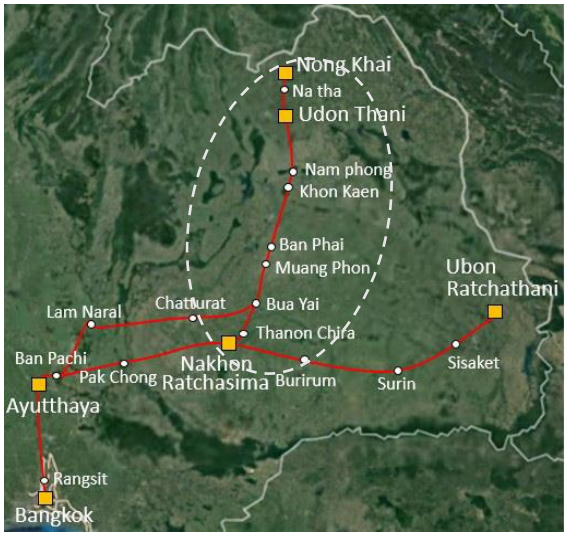


Fig. 2 Study Railway Corridor

Analytical Hierarchy Process

Decomposition of factors with a hierarchical decision structure

This study has divided decision elements into 4 levels under the aim of decision support system for railway maintenance as shown in Fig. 3.

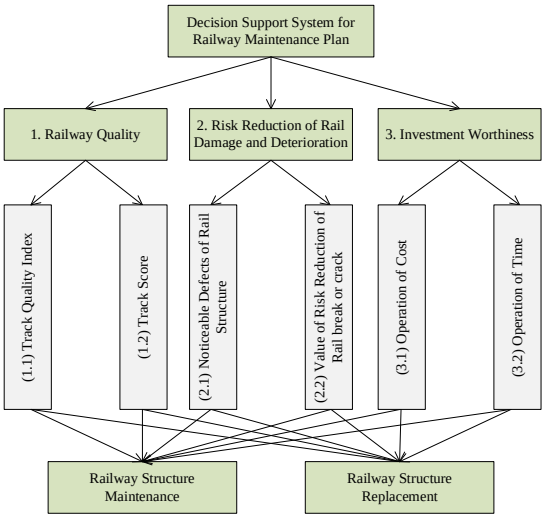


Fig. 3 Hierarchy Decision Structure

Prioritization

The next step is a calculation of importance of factors on each hierarchy. Scores for a calculation has received from interviewing the selected railway experts, including engineers, and technicians from the Civil Engineering Department of SRT through ratio scale questionnaire. The selected experts must have experiences in railway maintenance and rehabilitation for at least 15 years. This study applied the pairwise comparison with basic value from the previous study [6], to compare the factor at the same level.

Synthesis

Synthesis is a process conducted after receiving the importance of each factor. This study applied the Principle of Hierarchy Composition to synthesize the importance into global relative importance for considering optimal alternative. The weight of all last factors becomes important indicators of alternative and can consider optimal alternative.

Fuzzy Analytic Hierarchy Process

Fuzzy Analytic Hierarchy Process (FAHP) was developed based on the basic principle of Fuzzy set with MCDM. This study used Analytic Hierarchy Process (AHP) for decision process under the hypothesis that FAHP probably has Fuzzy data. Fuzzy data can be replaced by Fuzzy number [5].

Fuzzy Scoring Method

This study applied Fuzzy Scoring Method (FSM) to transform the fuzzy data into fuzzy number. This study applied the method, from the previous study [1], used both left and right sides of Utility Scoring Method in composite score calculation for each value of fuzzy numbers by considering highest and lowest scores. The scores would be ranged into low, medium, and high scores.

Composite Score Index Analysis

This study applied the Simple Additive Weight (SAW) through the utility theory, as shown in Eq. (1), to calculate the composite score index [5].

$$CI_i = \sum_{j=1}^{n} (W_j \times S_{ij}) \quad (1)$$

Where

CI_i = Composite Score Index of alternative i

W_j = Importance of criterion j

S_{ij} = Score weight of alternative i when considering criterion j

N = number of criteria

The results would prioritize the factors influencing decision on railway maintenance and rehabilitation, either plan 1: track structure maintenance or plan 2: track structure replacement.

Development Algorithms of Decision Support System

In this study, a computer-based decision support system has been developed to assist engineers and stakeholders of the State Railway of Thailand in making an appropriate decision on SRT railway maintenance plans. Algorithm of DSS has been developed with 6 steps as shown in Fig. 4.

Step 1 is Login where the user must enter email and password. When the login is successful, the user can access to the next step.

Step 2 is Input Data 1 where the user can input the details of parameters that influence railway deterioration. A decision rule was developed according to SRT standard and experts' decision from the given importance. Most of railway defect factors often occur with railway in Thailand. These factors are entered into DSS program in the Input 1 step, but the user must input the program whether there is any defect caused by these factors. There are two provided alternatives for the user to report the programs, either "Have" or "Have a few or Don't have".

Step 3 is Input Data 2 where the user inputs the utility scores from FSM, with 3 levels of low (0.20), medium (0.60), and high (1.00), to allow the program to analyze the importance of 6 factors: 1) Track Quality Index, 2) Track Score, 3) Noticeable Defects of Rail Structure, 4) Value of Risk Reduction of Rail Break or Crack, 5) Operation Cost and 6) Operation Time.

Step 4 is the process that the program calculates the composite scores through the Simple Additive Weight (SAW) method and displays the result of decision on optimal plan of railway maintenance and rehabilitation to the user. The railway maintenance and rehabilitation plan consist of 2 alternatives: (1) track structure maintenance and (2) track structure replacement.

Step 5 is the process where the user evaluates work value for railway maintenance and rehabilitation with known evaluator and decision maker in step 4. Bill of Quantity (BOQ) is also provided to use as appropriate and ask an authorized person for an approval in the next step.

Step 6 is the final step where all data on evaluation results can be printed out for making decisions on railway maintenance and rehabilitation plan.

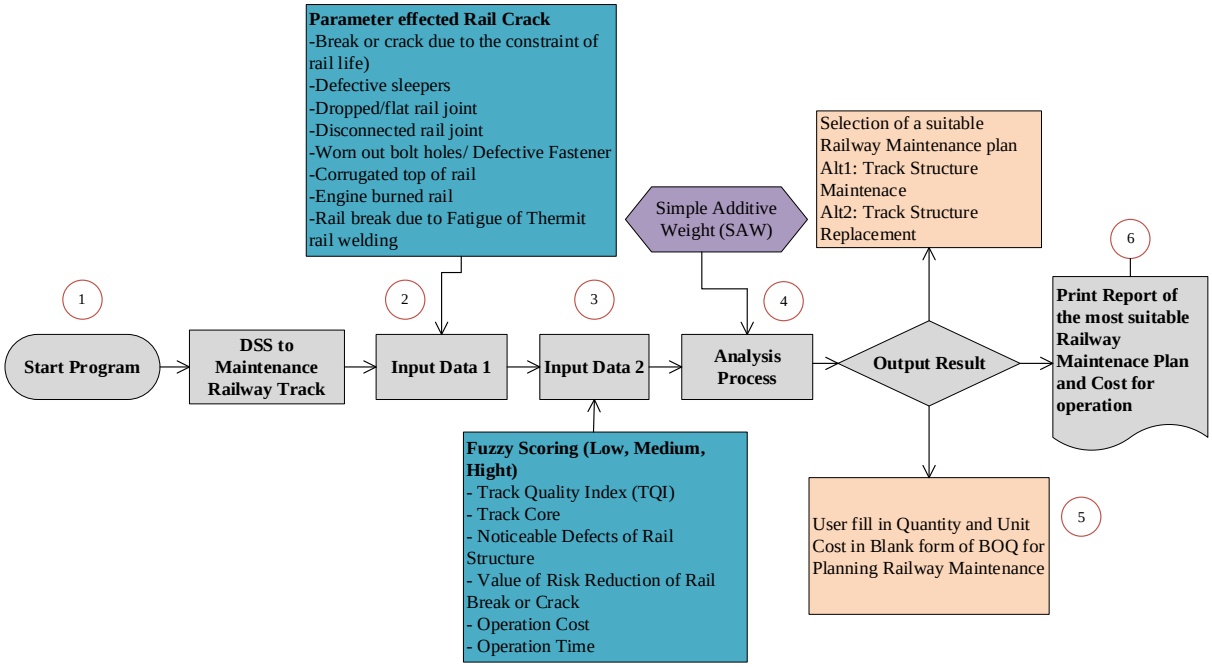


Fig. 4 Algorithm of Decision Support System

RESULTS AND DISCUSSIONS

Results of Calculation of Criteria Score

The results of calculation of importance weight from interviews with ten experts from Thailand's State Railway (SRT) by AHP for find prioritizing results of importance weight to affecting Decide on a railway maintenance plan as shown in table 3.

Results of Calculation of Composite Score index

The results of the analysis were used to determine the significance weights of each factor and the scores of each sub-factor by using AHP method and using FSM theory to determine the numerical values of low, medium, high scores. The next step was to combine group significance weights. with scores by using Simple Additive Weight (SAW) method by applying Utility Theory as shown in tables 3 and 4 to find composite scores and prioritizing results of factors affecting decide on a railway maintenance plan as detailed in table 5, 6.

Alternatives for railway maintenance and rehabilitation as shown on table 5 and 6, the results revealed that composite score index of maintenance and rehabilitation by track structure replacement (0.875) was higher than track structure maintenance (0.591). The sub criteria in terms of track quality index (TQI) were the most composite score index (CI) for both plans of maintenance and rehabilitation. Its composite score index in terms of maintenance method had the composite score index of 0.206 and track structure replacement has the composite score of 0.343. The importance given by the SRT experts in terms of railway quality was highest because they might see convenience and safety from derailment as more important than other factors and see that high quality of track can increase capacity in freight transportation based on the designed standard of track. The studies of RAIB (2015), Zhao and others (2006), Zakar and Mueller (2016), and Office of Rail and Road (2006) presented that most of the rail accidents and derailments were associated with rail defects. However, these accidents could be solved by inspecting the rail defects and evaluating rail serviceability as well as developing a technique to measure TQI. Higher accurate inspection can help maintenance management become more effective. In addition, the study of Udom (2003) under the Civil Engineering Department, SRT revealed that the importance of factor influencing decision on railway maintenance plan was track quality index (TQI), the details of SRT'S TQI has presented in previous study [6].

Result of Development of DSS Program

This study applied Java-script for program development. Electron-Vue Framework and Five-base were applied for user's account to login the system via e-mail and password as shown in Fig. 5. The developed program can only be compatible with Windows 10 or over. The objective of this study however is to develop the computer-based decision support system supporting railway engineers or stakeholders in analysis and decision for railway

maintenance and rehabilitation. Therefore, the program user should have knowledge on railway structure and an experience in railway deterioration.

Table 3 Importance weight of Factors in Decision on Railway Maintenance and Rehabilitation Plan

Main Criteria	Importance wt. of Main Criteria	Priority of Main Criteria	Sub Criteria	Importance wt. of Sub Criteria	Priority of Sub Criteria
(1) Railway Quality	0.505 (50.5%)	1	(1.1) Track Quality Index (TQI)	0.343 (34.3%)	1
			(1.2) Track Scores	0.163 (16.3%)	2
(2) Risk Reduction of Railway Deterioration	0.221 (22.1%)	3	(2.1) Noticeable Defects of Rail Structure	0.159 (15.9%)	3
			(2.2) Value of Risk Reduction of Rail Break or Crack	0.062 (6.2%)	6
(3) Investment Worthiness	0.274 (27.4)	2	(3.1) Operation Cost	0.157 (15.7%)	4
			(3.2) Operation Time	0.117 (11.7%)	5
Total	1.000 (100%)			1.00 (100%)	

Table 4 Scoring of Factors Influencing Decision on Railway Structure Maintenance and Rehabilitation Plan

Sub Criteria	Track Structure Maintenance			Track Structure Replacement		
	Criteria Score From Experts	Fuzzy Number [5]	Utility score by FSM [5]	Criteria Score From Experts	Fuzzy Number [5]	Utility score by FSM [5]
(1.1) Track quality Index (TQI)	0.270 or (27%) [6]	Medium	0.60	0.300 or (3%) [6]	High	1.00
(1.2) Track Scores	0.379	Medium	0.60	0.621	High	1.00
(2.1) Noticeable Defects of Rail Structure	[7]	Medium	0.60	[7]	High	1.00
(2.2) Value of Risk Reduction of Rail Break or Crack	0.332	Low	0.20	0.668	High	1.00
(3.1) Operation Cost	0.256	Low	0.20	0.744	Low	0.20
(3.2) Operation Time	0.625	Low	0.20	0.375	High	1.00

Table 5 Composite Score Index of Railway Maintenance Structure Plan

Sub Criteria	Importance from AHP	Scores from FSM	Composite Scores from SAW by (Eq.1)
(1.1) Track quality Index (TQI)	0.343	0.270 (Medium) 0.60	(0.343*0.60) 0.206
(1.2) Track Scores	0.163	0.379 (Medium) 0.60	(0.163*0.60) 0.098
(2.1) Noticeable Defects of Rail Structure	0.159	*** (Medium) 0.60	(0.159*0.60) 0.095
(2.2) Value of Risk Reduction of Rail Break or Crack	0.062	0.332 (Low) 0.20	(0.062*0.20) 0.012
(3.1) Operation Cost	0.157	0.256 (Low) 1.00	(0.157*1.00) 0.157
(3.2) Operation Time	0.117	0.625 (Low) 0.20	(0.117*0.20) 0.023
Composite Score Index (CI)			0.591

Table 6 Composite Score Index of Railway Structure Replacement Plan

Sub Criteria	Importance from AHP	Scores from FSM	Composite Scores from SAW by (Eq.1)
(1.1) Track quality Index (TQI)	0.343	0.030 (High) 1.00	(0.343*1.00) 0.343
(1.2) Track Scores	0.163	0.621 (High) 1.00	(0.163*1.00) 0.163
(2.1) Noticeable Defects of Rail Structure	0.159	**** (High) 1.00	(0.159*1.00) 0.159
(2.2) Value of Risk Reduction of Rail Break or Crack	0.062	0.668 (High) 1.00	(0.062*1.00) 0.062
(3.1) Operation Cost	0.157	0.744 (Low) 0.20	(0.157*0.20) 0.031
(3.2) Operation Time	0.117	0.375 (High) 1.00	(0.117*1.00) 0.117
Composite Score Index (CI)			0.875

CONCLUSIONS AND RECOMMENDATIONS

The main criteria applied to decision making were track quality, risk reduction of railway deterioration, and investment worthiness. According to the experts' opinions, the most important criterion was track quality, which showed the importance weight of 50.5%, followed by investment worthiness, which showed the importance of 27.4%, and risk reduction of railway deterioration, which showed the importance of 22.1% as shown in table 3. The window-based decision support system program was developed to facilitate in this research for analyzing the weight of each factor for railway engineers gaining better decision. The developed decision support system is only used in maintenance and rehabilitation of railway structure and ballasted track. Therefore, decision support system for slab track or ballast less track should be additionally developed because it has different structural components. Different deterioration of track structure leads to different plan of railway maintenance and rehabilitation. According to composite score index analysis by using FAHP for railway maintenance and rehabilitation, composite score analysis the results revealed that composite score index of maintenance and rehabilitation by track structure replacement (0.875) was higher than track structure maintenance (0.591).

ACKNOWLEDGMENTS

The authors would like to acknowledge the support from the Department of Civil Engineering, Faculty of Engineering, Khon Kaen University, and Expertizing in Railway Maintenance of State Railway of Thailand (SRT**)** for giving useful data and opinions that contributed to the success of this research.

REFERENCES

[1] Saaty, T.L. (1980). The Analytical Hierarchy Process. Priority setting, resource allocation. California: McGraw-Hill.

[2] P. K. Agarwal, A. Das, and P. Chakroborty, "Arational approach of prioritization of highway sections for maintenance," in Proceedings of the 6th International Conference on Managing Pavements, p. 12, Brisbane, Australia, October 2004.

[3] J.Farhan and T. F. Fwa, "Pavement maintenance prioritization using analytic hierarchy process," Transportation Research Record, vol. 2093, pp. 12–24, 2009.

[4] Rashidi, M., Lemass, B., and Gibson, P. (2010). "Decision support system for concrete bridge maintenance, ISCM II and EPMESC XII, PTS 1 and 2." AIP Conf. Proc., 1233, 1372–1377.

[5] Klungboonkrong, P. (1998). Development of A Decision Support Tool for The Multicriteria Environmental Impact Evaluation of Urban Road Networks. Ph.D. Dissertation. School of Geoinformatics, Planning and Building, University of South Australia.

[6] Phanyakit T., and Satiennam T., "Fuzzy Multi—Attribute Decision Making for the Selection of a Suitable Railway Track Maintenance Plan: A Case Study in Thailand," International Journal of GEOMATE, Aug. 2019, Vol.17, Issue 60, pp.96-104.

[7] Transport Rail Corp. 2012. TMC 226 rail defects handbook (version 1.2). Sydney, Australia: Australian Rail Track Corporation.

7th Int. Conf. on Structure, Engineering & Environment (SEE), Pattaya, Thailand, Nov.10-12, 2021, ISBN: 978-4-909106070 C3051

DESIGN OF A SENSOR MODULE FOR UNDERGROUND STRUCTURE MONITORING WITH ENERGY HARVESTED FROM SOIL

Md Rubayatur Bhuyian[1], Kshirasagar Naik[2], Marzia Zaman[3] and Gary Sakauye[4]
[1,2] University of Waterloo, Canada; [3]Cistel Technology, Canada; [4]Sanstream Technology, Canada

ABSTRACT

A large number of infrastructures are buried underground and are prone to corrosion. The Sacrificial Anode Cathodic Protection (SACP) technique is a well-known corrosion protection technique, where an anode block is deployed in the soil that replenishes the lost electrons and protects the steel structures from corrosion. This technique requires monitoring the depletion rate of the anode block for replacement purposes which is currently done manually by visiting each Sacrificial Anode (SA) site. This paper proposes a GSM-based wireless sensor network powered by the harvested energy from the existing SACP set up to automate the process. The nodes monitor the current flow from the anode to the cathode to eventually model the depletion rate. The paper outlines the design, development, and operation of the overall circuit. A self-sustaining energy harvesting approach has been considered where energy is harvested from the same cyber-physical system that the unit is monitoring. A prototype has been developed and deployed underground. The module periodically captures the required measurements and sends them to the cloud. The results from the deployed prototype illustrate that every 12~13 hour of charging can supply enough energy to operate the sensor module for approximately 60s. During this 60s period, the GSM module boots up, and two messages are communicated to the base station.

Keywords: Corrosion Monitoring, Sacrificial Anode Cathodic Protection, Energy Harvesting, Wireless Sensor Network.

INTRODUCTION

Sacrificial Anode Cathodic Protection (SACP) is a popular technique to protect underground structures, such as water and gas pipelines, oil tanks, etc., from corrosion. In this technique, steel structures are protected from natural corrosion by enabling an externally connected anode material to deplete over time [1]. The anode material that depletes over time is called the Sacrificial Anode (SA). Modeling is required to find the depletion rate of the anode for replacement purposes. To do so, human readers visit each SA site once a month to take voltage and current measurements. However, this approach is expensive and also prone to human errors.

Wireless Sensor Networks (WSN) can automate this system, but the sensor nodes need to be deployed underground due to the nature of the protection scheme. Therefore, finding a feasible and sustainable solution for powering the sensor nodes in an underground setup is critical. Different energy harvesting sources are available to power above-ground sensor nodes in a WSN, such as photovoltaic (PV), wind, piezoelectric, and thermoelectric energy harvesting [2]. But, when it comes to powering the WSNs in an underground setup, the options are minimal. Most traditional energy harvesting techniques fail in the underground environment due to their requirement for an above-ground structure [3]-[4]. For the application under consideration, the deployment needs to be underground due to the following reason.

- **Security:** Underground setup provides natural concealment facility, preventing vandalism of the monitoring infrastructure.
- **Zero access to above-ground land:** Underground deployment offers little to no obstruction to the place where it is deployed; thus, it does not hinder the above-ground operation of the land.

There are many applications in various fields, such as agricultural monitoring, structural monitoring, environmental monitoring, border patrol, etc., which require following the above criterion; thus, requiring an underground setup. Several works have reported the use of thermal gradient and piezoelectric vibration to power the sensor nodes for corrosion monitoring [5]-[6]. In few other applications, corrosion energy was suggested to produce the required energy to power the wireless sensor nodes [7]-[8].

Energy harvesting from the SACP setup has been proposed in [9] to power the underground sensor nodes. This technique exploits the electric current flowing from the cathode to the anode to energize the sensor node. This paper investigates the power requirement of a typical GSM module and the possibility of powering such a node using the harvested energy harvested from the SACP setup. A prototype has been developed that harvests energy from the SACP setup and powers a GSM module to

communicate data to the cloud. This paper outlines the design considerations, development, and operation of the overall circuit. The developed prototype is running in the backyard of one of the authors for more than a year. From the actual operation, we have observed that every 12~13 hour of charging could supply enough energy to operate the sensor module for approximately 60s. During this 60s period, the GSM module boots up, and two messages are communicated to the base station.

SACRIFICIAL ANODE CATHODIC PROTECTION

In the SACP technique, a slightly more active material (anode) is electrically connected to the structure (cathode) that needs to be protected. This setup allows electrons to flow from the anode to the cathode, replenishing the lost electrons due to corrosion.

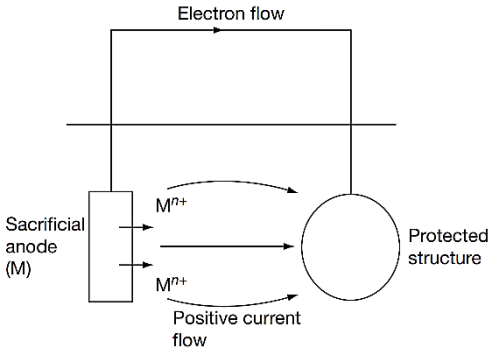


Fig. 1 Schematic diagram of cathodic protection using sacrificial anodes [1].

Figure 1 shows how the SACP technique works. The corrosion rate in the absence of SACP in place is determined by several factors such as soil chemical composition, availability of oxygen on the steel surface, moisture content of the soil, and temperature. In SACP, the anode block gradually dissolves in the soil by providing electrons to the cathode and minimizes the corrosion at the cathode. Therefore, it is crucial to estimate the lifetime of the anode block to replace the dissolved ones. A key parameter in modeling the anode's lifetime (T_s) is the electrical current (I) flowing between the anode and the cathode. From Faraday's law, the service life T_s can be derived as below [10]:

$$T_s = \frac{\alpha \times A_m}{C_m \times I} \quad (1)$$

Where,

A_m= The initial mass of the anode block

α = The part of the anode mass Am required to keep the protection system active

I = The mean value of the current $i(t)$, flowing between the anode and cathode,

C_m = Constant that depends on the anode material.

The challenge in applying Eq. (1) lies in finding the value of I. Therefore, T_s could be estimated by continuously monitoring $i(t)$ for an adequate period (several months).

MODULE DESCRIPTION

The GSM/3G network covers the majority percentage of the world's surface area; thus, this makes the connectivity option very attractive and easy where there is no other alternative. Fig. 2 shows the Arduino MKR GSM 1400 [11], which uses the cellular network to communicate data to the cloud. The board comes with a low-power Arm® Cortex®-M0 32-bit SAMD21 processor, and the GSM/3G connectivity is achieved using the module from u-blox called the SARA-U201, which is a low power chipset operating in different bands of the cellular range such as GSM 850 MHz, E-GSM 1900 MHz, DCS 1800 MHz, PCS 1900MHz.



Fig. 2 Arduino MKR GSM 1400 (WS Node) [11].

The MKR GSM 1400 can work as a standalone device without the need for any manager or AP. The device gets connected to the internet over 3G, as depicted in Fig. 3.

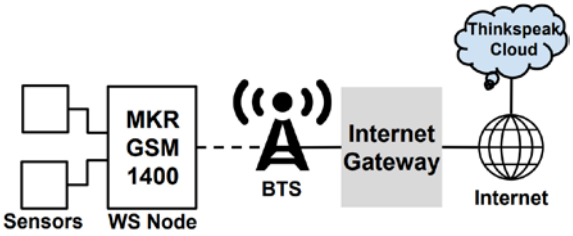


Fig. 3 MKR GSM 1400 connects to the internet over 3G.

Power Consumption Analysis of MKR GSM 1400

Figure 4 demonstrates the energy requirements of the MKR GSM 1400 module. During the startup (booting and network discovery), maximum power is consumed, around 760mW. It requires 310mA current from the supply during startup. Transmission of a message requires approximately 10 seconds, and

the power consumption is almost the same as the startup process. During standby conditions, the average power consumption is around 200mW, and the current requirements are about 80mA. The WS node takes about 20 to 25 seconds to startup and connects to a BTS. The board was tested using a DC power supply.

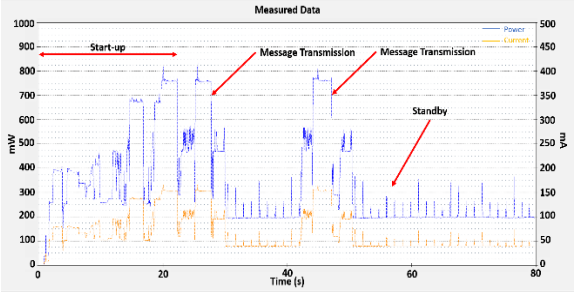


Fig. 4 Power and current consumption of MKR GSM 1400.

Underground Signal Strength Test of MKR GSM 1400

Table 1 shows the received signal strengths for MKR GSM 1400 at different burial depths. The signal strength is measured on a scale of 0 to 31, where 31 represents excellent signal strength and 0 represents the weakest. During the tests, the module was powered using a USB power bank, and it was programmed to report the signal strength data to the cloud at a specific interval.

Table 1 Signal strength of MKR GSM 1400 at different burial depth

Frequency Band	Range	Depth	Signal Strength
880MHz	>5km	Open Air	25/31
		1"	20/31
		2"	16/31
		6"	13/31

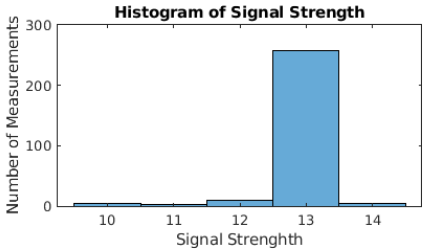


Fig. 5 Histogram of received signal strength at 6" under the soil.

Figure 5 shows the histogram of received signal strength at a burial depth of 6". For the application under consideration, the burial depth needs to be at least 6". We can observe that out of all the packets transmitted; most packets were received with signal strength 13/31. The reception signal strength is good enough to establish reliable communication with a node and a base station.

Compared to using Bluetooth, Zigbee, or Wi-Fi, using GSM/3G has the advantage of a long communication range and can connect directly to BTS without any intermediate node. This is an excellent advantage as it eliminates the management and power issues of relay nodes. Once the connection is established, the communication is reliable, and the data transfer rate is also very high. The drawback of using GSM/3G is the high-power consumption of the sending node.

SYSTEM OVERVIEW

The general structure of the proposed system is shown in Fig. 6. Solid, dashed, and dash-dotted lines represent the flow of energy, I/O control signal, and data paths, respectively. The overall system can be divided into five stages:

- **Stage 1: Energy Source**

In the SACP technique, steel structures are protected from natural corrosion by enabling an externally connected anode material to deplete over time. Due to this, there is a movement of electrons between the anode and cathode that are buried into the soil. We exploit this movement of electrons to harvest energy.

- **Stage 2: EH Module**

The EH module collects energy from the movement of electrons. The EH module mainly comprises an ultra-low voltage step-up DC/DC converter and a storage device. The DC/DC step-up converter operates at a very low voltage and converts the low voltage to a usable one, i.e., 3.15V. The onboard and the external capacitor together form the storage for the EH module, which is expandable if needed.

- **Stage 3: Voltage Switching and Control**

The voltage that builds up across the capacitor over time is fed to output pins when it reaches a specified level. The switching of voltage to the output pin is controlled at this stage, and it ensures that the sensor node is powered only when the output voltage has reached a specified level. The energy harvesting circuit is configured to turn on at 3.15 V to supply the load and turn off at 2.85 V.

- **Stage 4: Voltage Regulation**

Voltage is brought up to 5V to feed the WS Node. The maximum voltage the EH module provides is 3.15V which is boosted to 5V through a booster circuit. The capacitor voltage goes down with the energy usage and, the booster circuit helps maintain a constant voltage across the node.

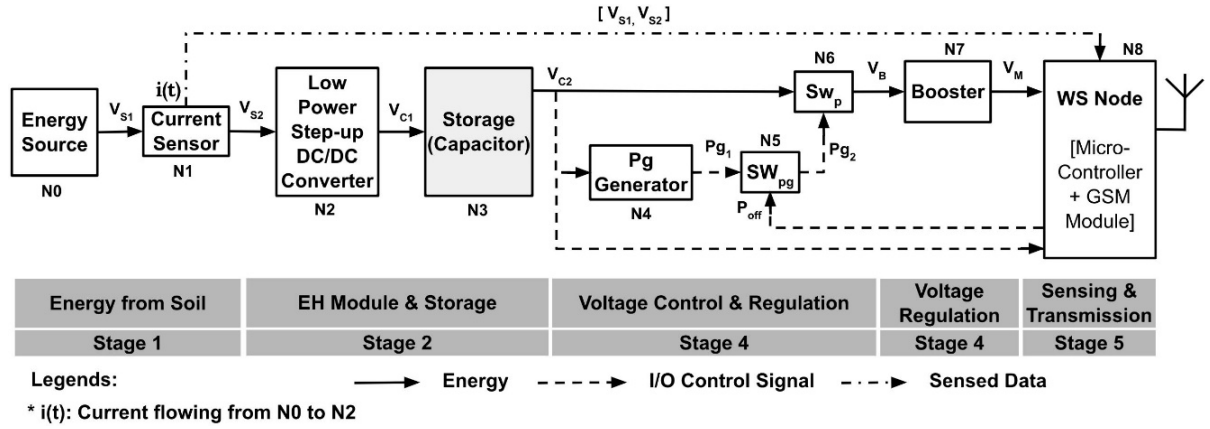


Fig. 6 Proposed system.

- **Stage 5: Sensing and Transmission**

The current flowing from the anode to the cathode is being sensed through the analog input port of the MKR GSM 1400 module and transmitted after processing. The WS node is responsible for sensing the current $i(t)$ and transmitting the data to the cloud. Once the module is turned on, it is programmed to sends data every 20 secs.

OPERATION OF THE PROPOSED SYSTEM

Detail operation of the proposed system, outlined in Fig. 6, is explained here. V_{S1} is the voltage across the source, and V_{S2} is the input voltage to the EH module. Here $V_{S1} > V_{S2}$ due to the small voltage drop across the resistor placed in series to measure the current $i(t)$. The micro-controller senses the voltage V_{S1} and $V_{S2,}$ respectively, which is the voltage of the two ends of the known resistor and runs a function to calculate the current $i(t)$. The measured current data is then reported to the cloud server. V_{C1} is the voltage across the capacitor that has been stepped up from V_{S2} by the EH module. Here, V_{C2}=V_{C1} and based on voltage V_{C2} the power to the WS node is controlled. The EH module generates a control signal, $P_{g1,}$ based on the capacitor output voltage V_{C2}. Figure 6 demonstrates the output and the control signal taken from the EH module. When the output voltage of the EH board reaches 3.15V, the control signal is ON/HIGH, and when the output voltage drops below 2.25V, the control signal is OFF/LOW. The on-broad control allows the capacitor to drain up to 2.25V before it disconnects the load. A lot of energy is wasted due to repeated transmission of the same reading. The change in current from the anode to the cathode at a particular time is insignificant. So, an additional control circuit has been placed to disconnect the load at a higher voltage and save energy. The circuit is designed to disconnect the load after two messages are sent or whenever the capacitor voltage reaches 2.85V.

The operation of different switches and function generators are shown below:

Operation of P_g Generator

$$P_{g1} = 1 \quad if\ V_{C2} \geq 3.15V$$
$$P_{g1} = 0 \quad if\ V_{C2} \leq 2.25V$$

Operation of switch SW_{pg} (PGOOD Switch)

Initially $P_{off} = 0$

$$P_{g2} = P_{g1} \quad if\ P_{off} = 0$$
$$P_{g2} = 0 \quad if\ P_{off} = 1$$

$P_{off} = 0$ (Feedback from Micro-controller)

$$P_{off} = 0 \quad if\ 3.15V \leq V_{C2} \leq 2.85V$$
$$P_{off} = 1 \quad if\ V_{C2} < 2.85V$$

Operation of switch SW_p (Power Switch)

$$V_B = V_{c2} \quad if\ P_{g2} = 1$$
$$V_B = 0 \quad if\ P_{g2} = 0$$

Operation of Booster

$$V_M = 5V \quad if\ 3.15V \leq V_B \leq 2.85V$$
$$V_M = 0V \quad if\ V_B < 2.85V$$

EXPERIMENTAL SETUP

Figure 7 shows the lab setup to replicate an actual SA site. A block of Magnesium is buried under the soil along with a galvanized steel pipe that needs to be protected. The steel pipe acts as a cathode, and the Magnesium block acts as an anode of an electrochemical cell, and the output is taken simply from the terminals of two metal blocks.

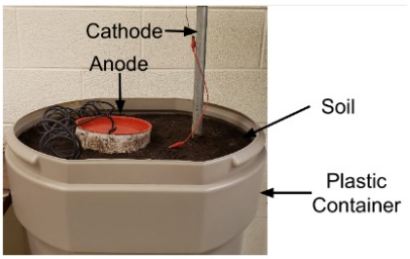


Fig. 7 Setup to replicate an actual SA site [9].

Figure 8 shows the hardware implementation of the proposed system. The EH module is realized by the demo board DC2042A from Analog Devices [12]. This board consists of four energy harvesting ICs. For our application, we utilize the energy harvester chip LTC3108. This chip is an integrated DC/DC converter ideal for harvesting and managing surplus energy from extremely low input voltage sources [13]. This can operate from input voltages as low as 20 mV. The WS node is realized by the Arduino MKR GSM 1400 from Arduino. This node connects to the internet using the GSM/3G network and operates in an 880 MHz frequency band. The DC-DC booster module is sourced from DFROBOT that can convert voltage between 0.9V~5V to standard 5V which is used to power up the GSM module. It integrates a PFM DC-DC boost control chip. A 40F 3.8V supercapacitor and two MOSFETs, LU024N and 18537N, have been used for this setup.

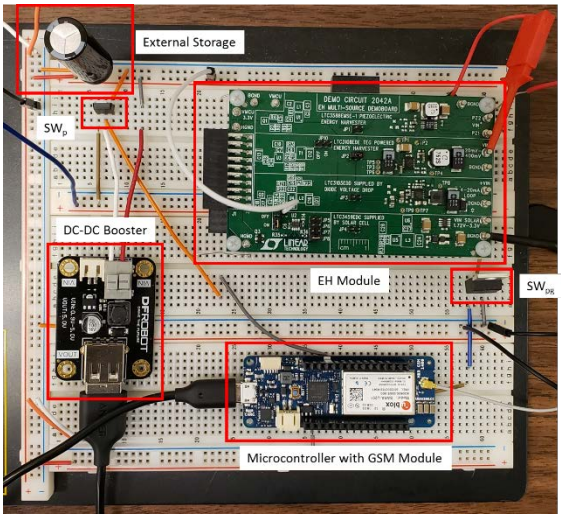


Fig. 8 The hardware platform of the proposed prototype.

SYSTEM PARAMETERS

The open-circuit voltage of the capacitor is approximately 890mv, whereas the short circuit current is about 23mA. The voltage across the energy source when connected to the module is 227mV and supplies a 12.15mA current. The energy harvester module takes an input voltage of 61mV and charges the capacitors to reach 3.15V. There are fifteen optional energy storage capacitors available onboard to be used by the load to store energy at the output voltage level, i.e., 3.15V. In parallel to those fifteen onboard capacitors, we have added one 40F 3.8V capacitor to meet the energy requirement of the node. The system is designed in a way that the capacitor will supply power to load when it reaches 3.15V and will disconnect the load when the voltage drops down to 2.85V. During this interval, two messages can be sent successfully. The DC-DC booster gets an input voltage in the range of 2.85V~3.15V and provides a constant output voltage of 5V to supply the WS Node.

RESULTS

Figure 9 shows the charging operation of the capacitor using the energy from the soil. A 40F capacitor requires one day and 8 hrs (111600s) to charge from 2.85V to 3.15V. The sharp drop in the voltage from 3.15V to 2.85V is due to the operation of the GSM module.

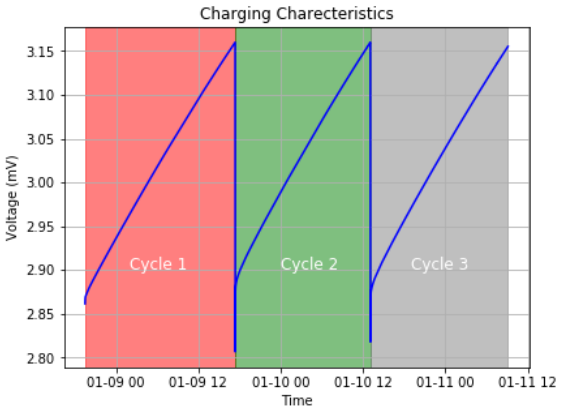


Fig. 9 Charging Operation.

Figure 10 shows the discharge operation of the capacitor. The module is programmed to disconnect from the source whenever it sends two messages, or the capacitor voltage goes below 2.85 V.

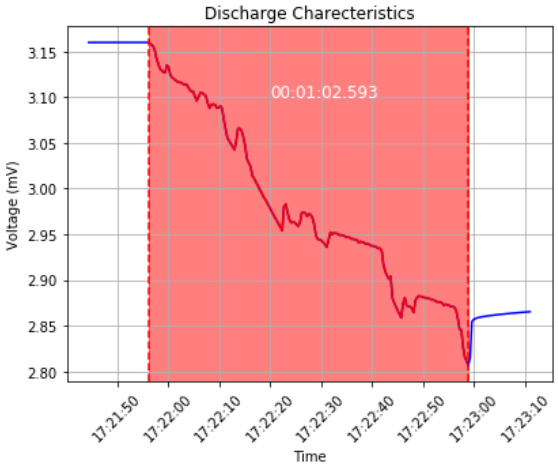


Fig. 10 Discharging Operation.

The sudden sharp voltage drop indicates the message transmission phase. Each message transmission phase lasts approximately 62secs.

Figure 11 shows the received messages at the cloud server. Messages get corrupted sometimes due to server issues. As a result, the broad is programmed in such a way that multiple measurements are taken and sent to the cloud to prevent data loss.

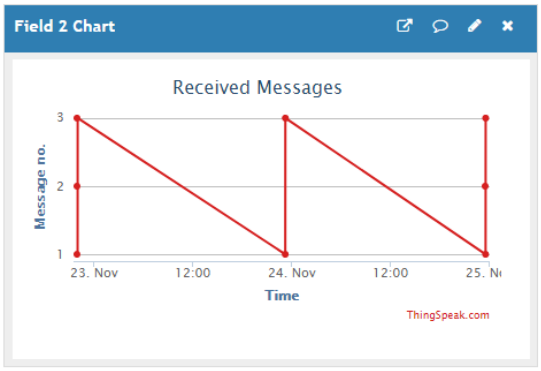


Fig. 11 Received messages at the Thinkspeak cloud.

CONCLUSIONS

The results indicate that harvested energy from an SACP setup is a promising solution for the sustainable operation of a GSM-based WS node in an underground environment. The solution can be used for underground deployments where most traditional energy sources fail. There are thousands of applications in environmental monitoring, agricultural monitoring, and structural monitoring sector where monitoring is essential but has minimal powering options. Moreover, for some applications, traditional powering options are not feasible at all. For such applications, harvesting energy from soil could be a promising solution. The harvested energy from the soil is in the order of a few milliwatts and applies to applications where reporting frequencies are less.

REFERENCES

[1] Ashworth V., 4.18. principles of cathodic protection. Shreir's Corros; Elsevier: NewYork, NY, USA, pages 2747–2762, 2010.

[2] Dziadak B., Makowski Ł., and Michalski A., Survey of energy harvesting systems for wireless sensor networks in environmental monitoring, Metrology and Measurement Systems, vol. 23, no. 4, pp. 495–512, 2016.

[3] Yu, X., Wu, P., Han, W. and Zhang, Z., Overview of wireless underground sensor networks for agriculture, African journal of biotechnology, vol. 11, no. 17, pp. 3942–3948, 2012.

[4] Parameswaran, V., Zhou, H. and Zhang, Z., Irrigation control using wireless underground sensor networks., in 2012 Sixth International Conference on Sensing Technology (ICST). IEEE, 2012, pp. 653–659.

[5] Su, D., Xia, Y. and Yuan, R., Self-powered wireless sensor network for automated corrosion prediction of steel reinforcement. Journal of Sensors, 2018.

[6] Aung, N.N., Crowe, E. and Liu, X., 2015. Development of self-powered wireless high temperature electrochemical sensor for in situ corrosion monitoring of coal-fired power plant. ISA transactions, 55:188–194, 2015.

[7] Yu, Y., Qiao, G. and Ou, J., Self-powered wireless corrosion monitoring sensors and networks. IEEE Sensors Journal, 10(12):1901–1902, 2010.

[8] Sun, G., Qiao, G. and Xu, B., Corrosion monitoring sensor networks with energy harvesting. IEEE Sensors Journal, 11(6):1476–1477, 2010.

[9] Bhuyian, M., Al-tekreeti, M., Naik, K., Plourde, B. and Sakauye, G., A Soil-Based Energy Harvester for Wireless Sensor Nodes to Monitor Corrosion Characteristics of Underground Water Pipes," in 2019 IEEE SENSORS. IEEE, 2019, pp. 1–4.

[10] Ward, C., Nanukuttan, S. and McRobert, J., The performance of a cathodic protection system in reinforced concrete structure: monitoring and service life modelling. Proceedings of Civil Engineering Research in Ireland (CERI), Belfast, Northern Ireland, 2014.

[11] Arduino. Arduino MKR GSM 1400, 2019.

[12] Analog Devices. Energy harvesting multi-source demo board, May 2019.

[13] Analog Devices. Ultralow voltage step-up converter and power manager, May 2019.

Environment

7th Int. Conf. on Structure, Engineering & Environment (SEE), Pattaya, Thailand, Nov.10-12, 2021, ISBN: 978-4-909106070 C3051

STUDY ON EXTRACTION OF FALLING ROCK SOURCE USING AERIAL LASER DATA TO IMPROVE THE EFFICIENCY OF FALLING ROCK MEASURES

YUQING ZHANG [1], KOKI SAKITA [1], SATOSHI NISHIYAMA [1] and TAKEHARU SATO [2]

[1]Okayama University, Okayama, Japan; [2] Okayama University of Science, Okayama, Japan

ABSTRACT: Due to the continuous rainfall, concentrated rainstorm, earthquake and so on caused by the rainy season and typhoon, the accidents caused by falling rock from hillside to road occur frequently. From these accidents, the opportunity to devote to the cause of falling stone countermeasures is improving. In the cause of falling stone countermeasures, road disaster prevention inspection and field investigation play a very important role. Selection of the survey areas and conduction the field survey is important on the project of falling rock measures. However, it is concerned that oversight of falling rock sources and waste of time at field survey, because of the diagram that cannot express the earth surface correctly. Also, it is difficult to express all data in a diagram made by aerial laser surveying although it is good at expression of the earth surface properly. So, we made micro topography highlight map to express the change in terrain finely and emphasize the steep cliff by combining diagrams. In this study, we extracted falling rock source on the desk and survey the selected area by micro topography highlight map. In addition, we verify its result by point cloud data. As a result, we report that we were able to extract steep cliffs of 1.4m or more in height and 60 degrees or more in terms of angle.

Keywords: micro topography highlight map， falling rock， aerial laser , on the desk

INTRODUCTION

In recent years, due to the continuous rainfall, concentrated rainstorm, earthquake and so on caused by Plum rains period and typhoon, the accidents caused by falling stone from hillside to road occur frequently. In the cause of falling stone countermeasures, road disaster prevention inspection and field investigation play a very important role. Now, in order to select the place of road disaster prevention and inspection, the source of falling stone is extracted by aerial photo interpretation, but it is difficult to extract the source of falling stone from the aerial photo of lush vegetation.

Therefore, it is a problem to omit the source of falling stone during inspection. In addition, due to the poor accuracy of the source of falling stone in the part of the subject, it may take a lot of time to carry out the investigation. As one of the methods to solve the problem, the manufacture of high precision drawings to capture the changes of micro terrain can be given. It can be considered that the efficiency of inspection and field investigation without omission and omission can be realized by extracting the location of the source of falling stone on the table in advance. In this study, the steep terrain below altitude is defined as the source of falling stone. By confirming the consistency between the results of table extraction based on high precision drawings and the local results, the possibility of table extraction of the source of falling stone is verified.

PURPOSE & RESEARCH

Establish an efficient and accurate inspection method for the source of falling rock.

[1] Method: Aerial laser surveying & Microtopographical emphasize analysis for laser data

[2] Map: Microtopograph highlight map

[3] Validation items and research contents:

Extraction of target parts on desk by using current inspection record

Field survey and Confirmation the validity of the map

Evaluation of the extracted target by using laser data

MEASUREMENT METHOD

Utilization of Aeronautical Laser

[1] Three-dimensional measurement by the nonprism-lasersnan.

[2] Using a helicopter, the measurement point increase.

[3] Following processing is done on the data.

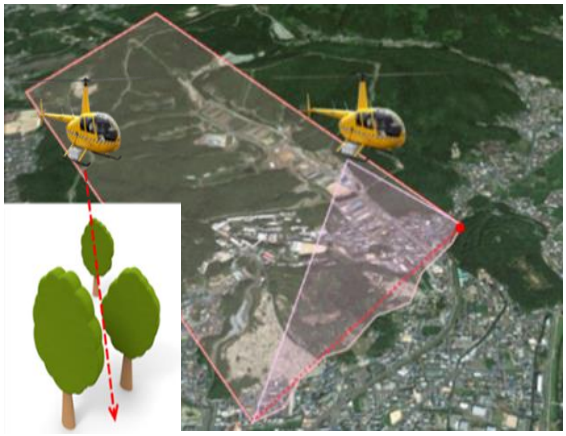


Figure1: Imaging Diagram of Aeronautical Laser Measurement

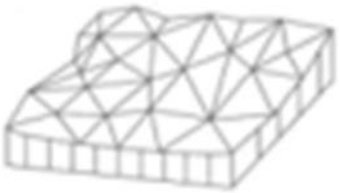


Figure2: Measuring helicopter

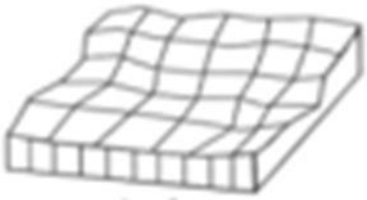
Table1: Measuring helicopter

LiteMapper-6800-400		
Operating AGL		30-1600m
Scan angle		45° ～60°
Pulse rate		80,000Hz～400,000Hz
Number of scans		10Hz～200Hz
Beam diameter		0.5mrad
Laser safety standard		Class3R
Nominal ocular hazard area		>1.5m(NOHD),>10m(ENOHD)
Measurable altitude	Pulse rate	MaxImum operating AGL
	80,000Hz	1600m
	100,000Hz	1100m
	300,000Hz	950m
	400,000Hz	800m
Equipment		GNSS/IMU:IGI AEROcontrol- II, DigiCAM-50

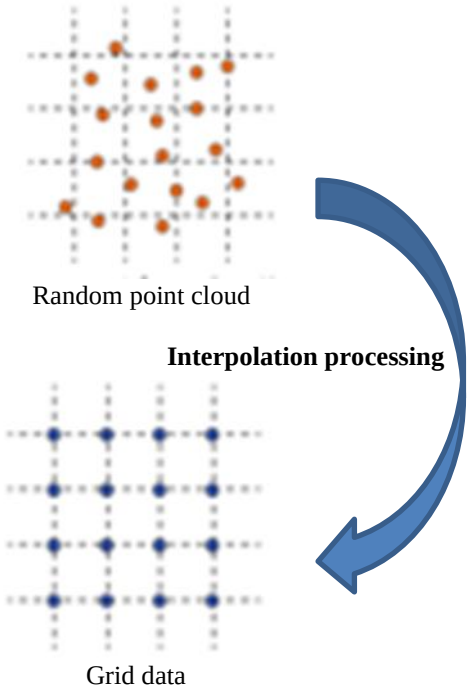
As a method of making high precision drawings to represent microtopography, aerial laser measurement is used. Aerial laser measurements can accurately capture the ups and downs of the surface even in the mountainous areas where the trees are located. In this study, the DEM data with 0.5m interval are compiled from the aerial laser measurement data.



Terrain representation by TIN (Irregular triangle)



Terrain representation by Grid date



MAP OVERVIEW

Contour map

Contour map is a curve on a map that draws a trajectory that connects to the same elevation (figure 3). In the dense performance, the oblique plane from the low angle to the middle angle is easier to understand, but because it cannot show the topographic change points between the contours, it is sometimes impossible to judge the micro-topography of the mountain path and so on.

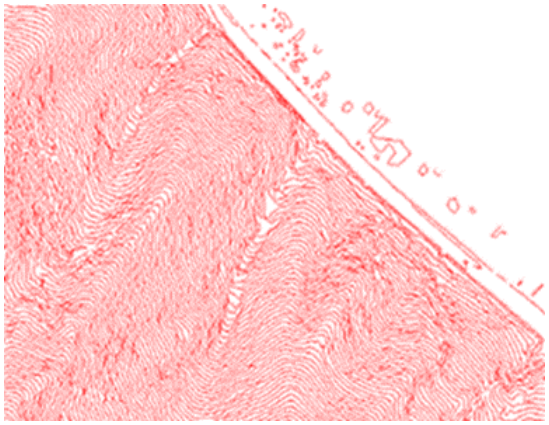


Figure3: Contour map

Inclination-amount map

Inclination-amount map is an image that calculates the tilt of each pixel of the grid data and changes the brightness according to that value to represent the terrain. (figure 4) this represents the tilting of the maximum tilt direction from the adjacent 9 points to the plane best described by the central point using the least square method (figure 5). The steep slope is bright (white) and the gentle slope is dark (black). The steep cliff can be extracted as the source of falling stone.

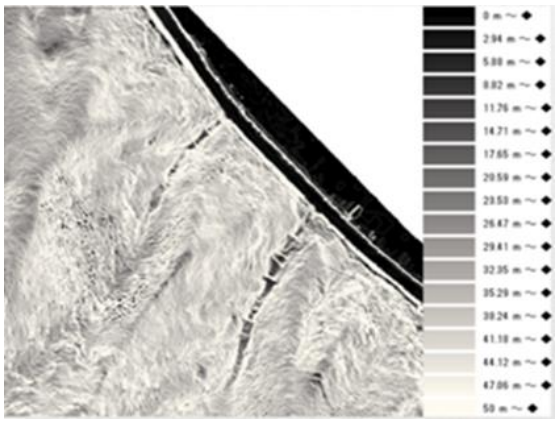


Figure4: Inclination-amount map

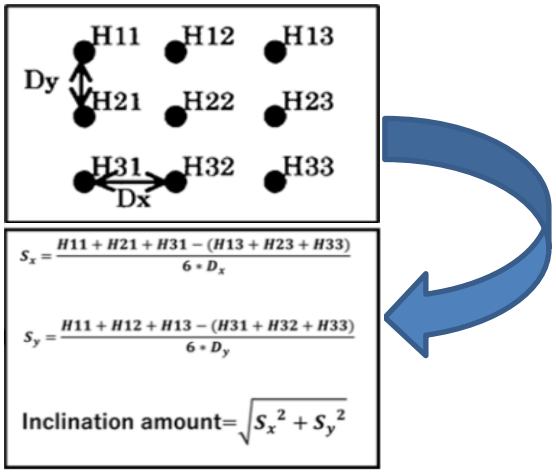


Figure5: Inclination amount

Laplacian map

Laplacian map is an index to represent the concavity and convexity of terrain and the sharp change of tilt in grid data. Contrary to ridge valley degree, concave terrain is represented on the positive side (higher than around the target point) black, and convex terrain on the negative side (lower than around the target point) pink.

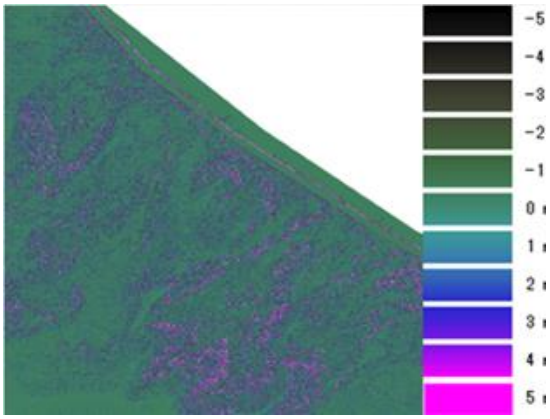


Figure6: Laplacian map

Microtopography highlight map

In the microtopographic representation monomer, it is difficult to extract the source of falling stone. As a result, microtopographic maps highlighting steep cliffs are made (figure 7). First of all, by transmission synthesis of Inclination-amount map with high sensitivity to tilt change (fugure 4) and Laplacian diagram (figure 5), which is easy to distinguish ridges and valleys, the fluctuation and concavity of mountain area can be easily captured by vision, and the source of falling stone can be extracted. Moreover, through the overlapping contour map (figure 3), the microtopographic emphasis map showing the fluctuation state and height difference information of oblique plane is made, and the source of falling stone is tried to be extracted.

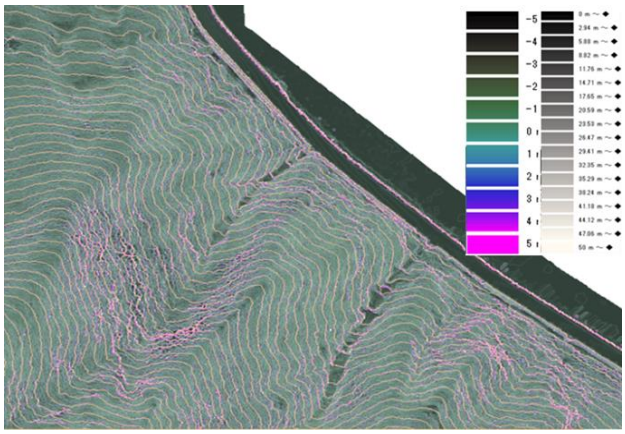


Figure7: Microtopography highlight map

[1] Each disadvantage will be supplemented
[2] Retaining the advantage of each map

RESULT AND DISCUSSION

The survey site is near otukusawa, North District of Okayama, No. 53 General National Highway of Okayama (figure 8). In order to investigate the road to prevent falling stone, the area where the rock may fall directly from the slope is selected.



Figure8: Survey of land

Extraction of target parts on desk

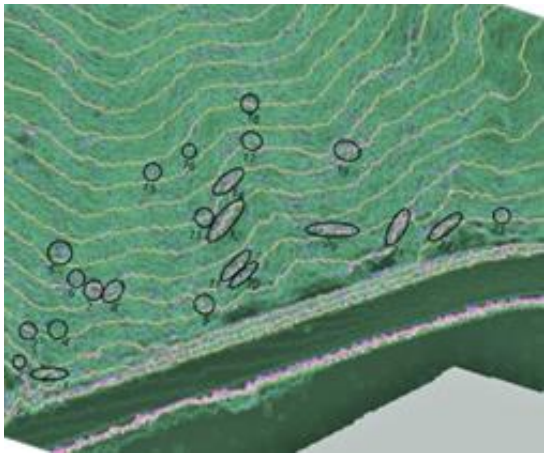


Figure9: Marked map

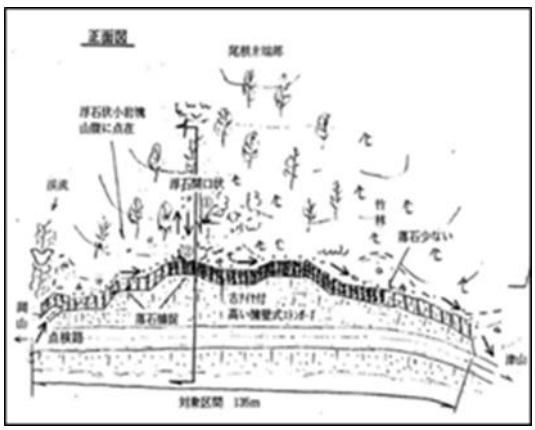


Figure10: Current inspection record

Current inspection record was used as material for the extraction on the map.

According to the microtopographic highlight map, the performance of the steep slope, which may be the source of the falling rock, is compared with the disaster prevention medical records in the area, as shown in figure 9. Considering the ease of comparison, the direction of the drawing is the micro-terrain highlight map, the disaster prevention medical records are the direction of the top of the mountain and the road on the lower side. In the microtopographic highlight map, as shown in the topographic representation of Laplacian map, there are more places in the survey site, represented by black circles, focusing on the pink representation of the possible source of falling rock. The possible source of falling rock can be clearly shown from the surface, and it can be said that the source of falling rock is represented by microtopography.

[1] Can create the map which express whole area.
[2] The reddish parts tended to mark as a target part.

Field Survey and confirmation on the validity of the map

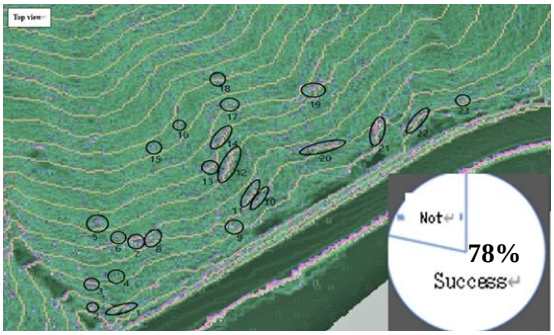


Figure11: Summary of extraction trial and field survey and 78 % of the 23 places were identified locally as the source of falling rock.

Table2: Summary of survey results

Number	Possibility of extraction	Investigation result
1	△	Steeo slope
2	△	Steeo slope
3	△	Hollow
4～17	○	Fallstone source
18	△	Hollow
19～22	○	Fallstone source
23	△	Valley

The images of the parts where each area corresponds to the individual survey result indicated in low right with color circle are shown.

The results of the field survey are shown in figure 11, and the following summarizes the status photos of the places corresponding to each number. No. 1 is the extraction of steep slope, 4, 5, 6, 7, 8, 9,

10, 11, 12, 13, 14, 15, 16, 17, 19, 20, 21, 22 is the extracted source of falling rock, 3, 18, 23 is the depression terrain, 2 is the valley terrain.



Figure12: Number2 Stereo slope



Figure13: Number3 Hollow



Figure14: Number7 Fall stone source



Figure15: Number19 Fall stone source

As a result, 78 percent of the 23 places were identified locally as the source of falling rock. In addition, outside 23 places, it is considered that this is a measure that can contribute to the substantial reduction of the efficiency of on-site investigation, from the point of view of the fact that no significant source of falling rock has been identified. In addition, using microtopographic highlight maps at various survey sites, it is also necessary to master the detailed conditions for the indicated source of falling rock.

[1] Can extract the source of falling rock.

[2] Various terrain (steep slope or hollow) was extracted.

Evaluation of the extracted target by using laser data

We graphed the relationship between the relative height and inclination angle by using base laser data.

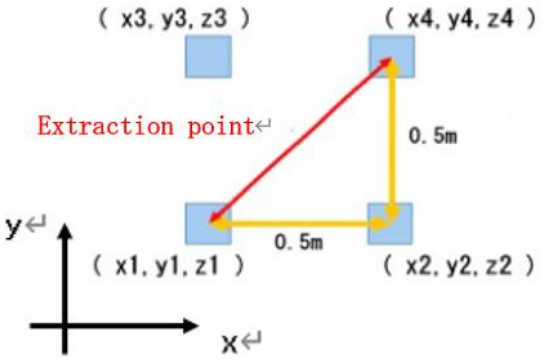


Figure16: Point cloud data viewed from above

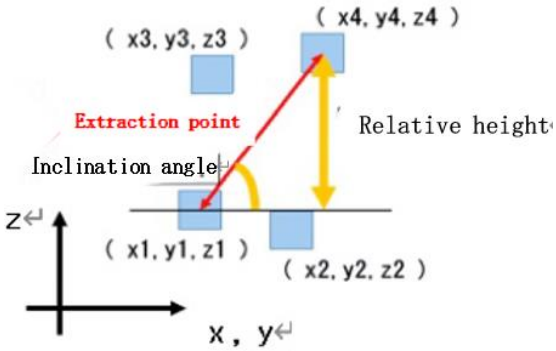


Figure17: Point cloud data with cross section

To quantitatively evaluate the possibility of extracting the sources of falling rocks, from the map, we use the grid data used for creating the map to examine the factors that affect the availability of extraction. We extract, from the grid data, the parts where extraction is feasible in the extraction and field survey results, and summarize this data for each factor. As the factor, we calculate the

inclination angle and the relative height of the falling rock source, respectively, using the coordinates of the steep cliff portion of the grid data.

Relative height = $|z4 - z1|$

Inclination angle = $\text{atan}\frac{|z4-z1|}{\sqrt{(x4-x1)^2+(y4-y1)^2}}$

The source of falling rocks more than 60 degree was extractable in the map.

CONCLUSION AND FUTURE WORK

In this study, by combining the contour map, ti lt map and Laplacian map of the microterrain repre sentation method based on the data obtained from t he aerial laser measurement, the microterrain emph asis map is made, and the table extraction of the fal ling rock source is discussed. Through field investi gation and point group data verification, the table e xtraction is evaluated from the aspects of accuracy and quantification. The following is a summary of the content of this study, and as a conclusion.

[1] Can Create drawings from the laser data that can see the whole of the target mountain.
[2] The created map can extract the source of falling rocks more than 60 degrees.

As a future issue, since there were rockfall sour ces that could not be represented by microtopograp hic highlighting maps, it is necessary to verify the analysis method to represent them. In addition, it is also necessary to grasp the detailed conditions of t he source of rockfall expressed by using microtopo graphic highlighting maps in various research sites . In addition, it will be necessary to verify the effec t of the angle of vegetation and slope on the point density of the laser.

REFERENCES

[1] Teriyaki Kikuchi, Akira Hartanto ceremony, Ryoudou Sendak and Satoshi Nishiyama: : Development and Oyo of fluctuation vector analysis technology in the landslide place where S - DEM data was used. 57-6, p.277-288, 2017.

[2] Chhatkuli, S., Kawamura, K., Manno, K., Satoh, T., and Tachibana, K. An approach to automatic detection and hazard risk assessment of large protruding rocks in densely forested hilly region, Int. Arch. Photogram. Remote Sens. Spatial Inf. Sci., XLI-B3, 195-199. 2016.

[3] Miyashita Masashi Imanishi Masahumi Miya Tame Takashi Satoshi Nishiyama: Basic inspection of falling rock source abstraction with 2 periods of different aerial edge laser data and the (69th time) Japan Society of Civil Engineers Chinese branch meeting for giving papers announcement outline collection in fiscal, p.373-Annan B., Unpublished Work but Accepted, Vol., Issue, Year 2017.

[4] Kamara kaya and Takeharu Sato: The rapurashian chart present technique in case of the mass movement geomorphic analysis and erosion control academic journal， Vol.67， No.1，pp.41-47，2014.5

[5] Hasegawa, A. and Ota, T, An estimation method of the distribution of rock-outcrops using DEM, Jpn. Soc. Eng. Geol., 115-116 2015.

[6] Gigli, G., Morelli, S., Fornera, S., and Casagli, N., Terrestrial laser scanner and geomechanical surveys for the rapid evaluation of rock fall susceptibility scenarios, Landslides, 11, 1-14. Hasegawa, A. and Ota, T. An estimation method of the distribution of rock-outcrops using DEM, Jpn. Soc. Eng. Geol., 115-116 2015.

[7] Mashita, K., Yokota, H., Okayama, K., Maki, A., Ibose, Y., Hiraoka, T., Onda, Y., and Suetsugi, T. Development of terrain analysis methods to draw a prediction map of landside waters inundation by using LiDAR data, Jpn. Geomorphol. Union, 33, 281-295.2015.

[8] Kamita, I., Tanaka, K., Hasegawa, H., Kuroki, T., Hayata, Y., Odagiri, S., and Masaharu, H., Production of slope map and its application, Jap Soc. Geoinform., 10, 76-79.1999.

[9] Thousands of Dalang: red Stereo-New Topographic representation, Earth, 44 Supplement, p. 14-15, 2006.

[10] Sasaki, H. and Mukoyama, S., Development of new mapping technique for interpretation of geographical features and its application – ELSAMAP (elevation and slope angle map) with airborne laser scanner DEM, J. Jpn. Soc. Eng. Geol., 49, 318-330.2009.

NOVEL STARTER FOR PRODUCING YOGURT CONTAINING ANGIOTENSIN CONVERTING ENZYME (ACE) INHIBITORY ACTIVITY

Sri Yadial Chalid[1*], Mu'izzah Irsyadi Putri[1], Fitriah Hatiningsih[2], Megga Ratnasari Pikoli[1]
[1]Faculty of Science and Technology, Syarif Hidayatullah State Islamic University, Jakarta Indonesia 15412
[2]Center for Integrated Laboratory, Syarif Hidayatullah State Islamic University, Jakarta Indonesia 15412

ABSTRACT

Novel traditional yogurt starter from *dadih* have been used for producing cow's milk yogurt which have ACE inhibitor activity. *Dadih* derived from Koto Malintang (A) and Padang Gadut (B) village. Cow's milk was added with *dadih* variation concentration of 2.5; 5.0; 7.5; and 10.0% (v/v) and fermented for 48 hours at room temperature. Lactic acid bacteria were obtained as much as $1.01x10^{11}$ CFU/mL and $2.146x10^{9}$ CFU/mL for A and B, respectively.Yogurt was tested organoleptically by 33 panelists then extracted using ethanol, degree of hydrolysis using trichoactic acid and ACE inhibitors were measured in vitro. The organoleptic test results indicate that the preferred yogurt was yogurt with starter A was 10% (v/v) and B was 2.5% (v/v). The degree of hydrolysis (DH) for yoghurt A and B was obtained by 10% and 12% respectively and the ACE-inhibitory activity of yogurt A and B were 93.81% and 65.29%, respectively. The results of this study can be concluded that *dadih* is a novel source of starter to produce yogurt which has angiotensin converting enzyme (ACE) inhibitory activity.

Keywords: Novel starter, ACE inhibitor activity, Dadih, Yogurt, Organoleptict test

INTRODUCTION

Dadih is buffalo milk which is naturally fermented in a bamboo tube and covered with banana leaves to produce lumpy milk. *Dadih* contains lactic acid bacteria (LAB) which acknowledged can be utilized as a *starter* in formulating yogurt. A total of 20 strains of lactic acid bacteria from *dadih* originating from Bukittinggi area were found, namely five strains of *Lactococcus lactis* subsp. *lactis* and three strains each of *Lb. brevis, Lb. plantarum, Lb. casei, Lb. paracasei*, and *Leu. Mesenteroides* [1].

Lactic acid bacteria (LAB) are probiotics that have functional properties such as antibacterial, antimutagenic, anti-cholesterol and antidiabetic. Lactic acid bacteria isolated from Boza has been shown to simulate the gastrointestinal tract and produce bacteriocins that are active against of pathogens [2]. Lactic acid bacteria produce several enzymes to hydrolyze macromolecules into smaller molecules that have functional properties as antioxidant [3] antihypertensive [4] and anti-diabetic [5]. González-Córdova [6] conducted skim milk fermentation with *Lactobacillus reuteri*, *Lb. johnsonii*, and *Lb. helveticus*, then tested the ACE inhibitory activity, they got a value of 86.36% for milk fermented with *Lb reuteri*. The addition of herbal extract to fermented cow's milk results in an increase in bioactive peptides which could inhibit ACE activity (Amirdivani & Baba, 2011) [7].

Chalid, Nurbayti, & Pratama [8] stated that the fermented buffalo milk protein hydrolyzate for one day was able to inhibit angiotensin connverting enzyme by 87.52%.

Researchers want to use *dadih* as a new starter to produce cow's milk yogurt. *Dadih* as a novelty of source contains lactic acid bacteria (LAB) was used is obtained from Koto Malintang (A) and Padang Gadut (B) villages. Cow's milk yogurt was made according to the Indonesian National Standard SNI 298:2009 Yoghurt [18]. This research begins with the examination of the number of lactic acid bacteria in starter A and B using the Total Plate Count Method [9].

EXPERIMENTAL SECTION

Raw Material and Chemicals

As stated previously, the main ingredients in this study were two sources of *dadih* namely A and B from Koto Malintang and Padang Gadut villages, respectively. Yogurt cultures starter A and B were one day fermented buffalo milk in bamboo tube. Also skim milk powder as a substrate purchased from trade Ciputat area. Meanwhile, the chemicals used were angiotensin-converting enzyme (ACE) from rabbit lungs (0,25U/mg), hippuryl-L-histidyl-L-leucine (HHL; Hydrate Powder) ≥ 98% (HPLC grade) were obtained from Sigma Chemical Co. (USA). Some solvents such as ethanol, hydrochloric acid, sodium hydroxide, ammonium bicarbonate, ethyl acetate, sodium tetraborate buffer, bouvine serum albumin and trochloroacetic acid were obtained from Merck. De Man Rogosa and Sharpe (MRS) medium and peptone were obtained from Merck. Genesys 10S UV-Vis UV-Vis spectrophotometer (Thermo

Scientific, USA), set of distillation devices and IWAKI soxhlets.

Counting the Number of Lactic Acid Bacteria (LAB)

The bacterial population in *dadih* and yogurt was calculated using decimal dilutions of 10^{-1}, 10^{-2}, 10^{-3}, to 10^{-9} by transferring 1 mL of milk dadih A and B into a test tube containing 9 ml of 0.1% (w/v) buffer peptone water (BPW) solvent. The test tube was homogenized using a tube shaker. Amount of 1mL solvent form the last 3 dilutions were planted in De Man Rogosa and Sharpe Agar (MRS). The inoculate tube were incubated anaerobically at 37 °C for 48 h in a reverse position. The calculation of growing colonies was done after 48 hours [9].

Preparation of Yogurt with *Dadih* as Starter

A total of 148.5g of powdered skim milk were dissolved in 900 mL of warm water and stirred using a magnetic stirrer until evenly dissolved. The liquid skim milk was piped as much as 100 mL and put in a glass jars and heated at heated at 85°C for 30 min. These bottles were allowed to warm.

The first glass jars as a control containing skim milk without adding *dadih*. The next glass jars are fermentation bottle containing skim milk and each glass jars was added starter *dadih* as much as 2.5; 5.0; 7.5; and 10.0% (v/v). The bottles were shaken until they were homogenous and then was incubated at room temperature for 48 hours and culture was stopped by pasteurization at 75°C for 1 minute [10].

Protein Extraction of Yogurt

Yoghurt A and B (100 mL) were homogenized with 100 mL of 75% ethanol. The mixture was incubated for 10 minutes and then centrifuged at 13.000 x g for 15 minutes at 4 °C [8]. The supernatant and pellet of yogurt A and B was collected for determination of dissolved protein level and degree of hydrolysis (DH). The protein filtrate level was determined by spectrometric method using bovine serum albumin solution as a standard (Bradford method).

Degree of Hydrolysis (Hoyle & Merritt, 1994)

The degree of hydrolysis (DH) of yogurt A and B was measured using by ratio soluble nitrogen to total nitrogen in yogurt. Meanwhile, the yogurt extract of 5 mL was added with 5 mL of 10% TCA (trychloroaceic acid w/v). The mixture was allowed to stand for 30 minutes for sedimentation, then the mixture was centrifuged at 10.000 ppm for 15 minutes. Nitrogen of supernatant and pellet of yogurt were analyzed by Kjeldahl method [11]. The degree of hydrolysis was calculated by the formula:

$$DH = \frac{\text{10\% TCA – soluble N in yogurt}}{\text{Total N in yogurt}}$$

Yogurt A and B measurements were performed in duplicate.

In Vitro ACE Inhibitor Activity of Yogurt

ACE inhibitory of yogurt was measured by spectrophotometric assay describe by Chusman and Cheung as applied to the study of inhibitory peptides by Arihara [12]. A total of 15 µL yogurt protein filtrate was dissolved with 125 µL of 100 mM sodium borate buffer solution (pH 8.3) containing 7.6 mM hippuryl-L-histidil-L-leucine and 608 mM sodium cloride (subtrate). The mixture was centrifuged at 12000 rpm for 2 minutes and pre-incubated for 5 minutes at 37 °C. The reaction began with an additional 50 µL of the 50 mU angiotensin converting enzyme (ACE). Correspondingly, the mixture was incubated for 30 minutes at 37 °C. 50 µL distilled water was used as blank. The process was conducted twice and stopped by the addition of 125 µL 1N HCl. Hippuric acid released during the reaction was extracted through adding 750 µL of ethyl acetate to the mixture and stirred using a vortex. The mixture were centrifuged at 1.200 rpm for 10 minutes at cold temperatures and number 500 µL of organic phase was transferred to a glass tube to be dried in an oven at 90 °C for 60 minutes.

Furthermore, the formed hippuric acid was dissolved with 1 mL of water and vortexed for one minute long. Meanwhile, the amount of absorbance was measured with a spectrophotometer at a wavelength of 228 nm. The ACE inhibitor activity was calculated according to the equation as follows:

$$\text{Inhibitory Activity (\%)} = (C - A)/(C - B) \times 100$$

Where A is the absorbance of sample, B is the absorbance of blank and C is the absorbance of control (distilate water)

RESULT AND DISCUSSION

Concentration of Lactic Acid Bacteria (LAB) in *Dadih*

The population of lactic acid bacteria in *dadih* A after incubation for 48 hours was obtained as much as 1.01×10^{11} colony-forming units/mL. Meanwhile, dadih B after incubating for 48 hours, the number of lactic acid bacteria was found to be 2.146×10^{9} CFU/mL. Some researchers suggest that the concentration of lactic acid bacteria in fermented milk is a minimum of 10^{7} colony-forming units per gram of media to obtain the desired health benefits

and a range of 1.9 x10^6 to 1.11x10^7 CFU on MRS media [13].

The results revealed that *dadih* A and B manage to be used as a *starter* in yogurt formulation. It is known that *dadih* A contains more LAB than *dadih* B, this was thought to be the result of several important factors such as differences in the type of food given to buffaloes that affect the chemical composition of buffalo milk, the type of bamboo as a fermenter and banana leaves as a cover for bamboo tubes. These factors influence the number of lactic acid bacterial cells in *dadih* and yogurt as a product.

The pH Value of Yogurt

Yogurt with traditional starter namely dadih, sourced from two different regions. Yogurt with dadih starter A from Koto Malintang village, and yogurt with dadih starter B from Padang Gadut village. The acidity of yogurt was measured using a pH-meter after the fermentation process was complete.

Table 1 showed the results of pH yoghurt with dadih starter A and yogurt with dadih starter B. Analysis of variance of these yogurts have a significantly different result (P<0.05). The acidity yogurt with dadih starter B from Padang Gadut village was higher than yogurt with dadih starter A from Koto Malintang village. pH value and acidity in fermented milk as a result of bacterial growth and caused by the type of bacteria contained in starter yogurt [14].

Acidity yogurt A dadih B dengan sumber dadih dari desa Koto Malintang (A) and Padang Gadut (B). yang berasal dari desa Padang Gadut lebih tinggi dibandingkan dengan keasaman dadih A yang berasal dari Koto Malintang.

The decrease in pH value that occurred in fermented milk was estimated relate to the metabolic activity and the viability of contained lactic acid bacteria [15].

Table 1. The pH value of yogurt with dadih starter A and yogurt with dadih starter B

Concentration of *dadih* as *starter* (%) (v/v)	Yogurt pH Value	
	Yogurt A	Yogurt B
2.5	4.27 ± 0.01^{b}	3.96 ± 0.02^{c}
5.0	4.28 ± 0.01^{b}	3.80 ± 0.01^{b}
7.5	4.18 ± 0.02^{a}	3.71 ± 0.02^{a}
10.0	4.20 ± 0.01^{a}	3.74 ± 0.02^{ab}

Note: Differ letter notations in the exact column indicates a significant difference (p<0,05)

Table 1 shows that the acidity of dadih B from Padang Gadut village is higher than the acidity of dadih A from Koto Malintang village.

Organoleptic Yogurt

In accordance with the analysis of variance in yogurt texture with the additional *starter A* showed a significantly different result (P<0.05). It was acknowledged that yogurt with additional 10% (v/v) of *starter* A was most preferred by the panelists with an average score of 2.91 (Table 2).

The result of analysis of variance consistency indicated a significant difference (P<0.05) in all variations of yogurt concentration with the additional *starter* A. Similary, yogurt with a concentration of 5.0; 7.5; and 10% (v/v) was identified as a mildly preferred yogurt by the panelists, as a result of the existence of several separate lumps. Moreover, the analysis of variance in yogurt aroma with the additional *dadih starter* also revealed significantly different results (P<0.05). Yogurt with the addition of 10% *dadih starter* A indicated to possessed a sharper distinctive aroma of yogurt and chosen as most preferred by the panelists. Analysis of variance in yogurt flavor with an additional *starter* A revealed a significant difference (P<0.05). Meanwhile, yogurt with *dadih* concentration of 5.0; 7.5; and 10.0% (v/v), placed at the exact notation which indicated that the typical sour taste of yogurt was most preferred by the panelists. The results of variance analysis towards panelists' general preference did not reveal any significant difference in yogurt A with various concentrations.

Furthermore, the results of the variance analysis in yogurt texture with the additional dadih starter showed a significantly different result (P<0.05). It was acknowledged that yogurt B with a total of 5.0% (v/v) concentration had a noticeable different notation and acknowledged as the most preferred yogurt by the panelists (Table 2). According to the results on the consistency of yogurt with dadih starter B revealed a significantly different result (P<0.05). Yogurt with the additional dadih starter B concentrated 2.5 and 5.0% (v/v) had a score of 2.97 and 2.82 in the exact notation indicated that it had a consistency that was most preferred by the panelists since it was homogeneous and no lumps had been found. Aside from that, the aroma of yogurt with the additional dadih starter B did not reveal any significant difference (P<0.05), this showed that the additional variance of dadih consistency did not affect the panelists' preference level towards the distinctive aroma of yogurt. Correspondingly, the results of analysis variance towards general preference did not reveal any significant difference in the yogurt products with the additional dadih starter B (P>0.05). Therefore, this indicated that variations on the concentration of *dadih* starter A and B in yogurt products did not affect the panelists' preference level against the general preference parameters.

Table 2. The result of organoleptic test on yogurt with dadih starter A and yogurt with dadih starter B

Concentration of *dadih starter* (%, v/v)	Yogurt	Texture	Consistency	Aroma	Taste	General Preference
2.5	A	2.12 ± 0.65^{b}	1.79 ± 0.41^{a}	2.24 ± 0.71^{a}	2.06 ± 0.61^{a}	1.79 ± 0.60^{a}
	B	2.48 ± 0.71^{a}	2.97 ± 0.17^{b}	2.61 ± 0.61^{a}	2.76 ± 0.43^{a}	2.30 ± 0.72^{a}
5.0	A	1.73 ± 0.72^{a}	2.42 ± 0.66^{b}	2.18 ± 0.63^{a}	2.39 ± 0.70^{b}	1.79 ± 0.69^{a}
	B	2.82 ± 0.39^{b}	2.82 ± 0.39^{b}	2.55 ± 0.61^{a}	2.70 ± 0.46^{a}	2.24 ± 0.75^{a}
7.5	A	2.55 ± 0.56^{c}	2.39 ± 0.60^{b}	2.21 ± 0.65^{a}	2.55 ± 0.66^{b}	1.97 ± 0.68^{a}
	B	2.36 ± 0.65^{a}	2.27 ± 0.62^{a}	2.61 ± 0.55^{a}	2.64 ± 0.60^{a}	1.97 ± 0.72^{a}
10.0	A	2.91 ± 0.29^{d}	2.61 ± 0.49^{b}	2.61 ± 0.55^{b}	2.67 ± 0.59^{b}	2.06 ± 0.74^{a}
	B	2.27 ± 0.57^{a}	2.21 ± 0.60^{a}	2.58 ± 0.61^{a}	2.61 ± 0.61^{a}	2.03 ± 0.72^{a}

Note: Differ letter notations in the exact column indicates a significant difference (p<0,05).

Dissolved Protein Levels of Yogurt

According to the results on dissolved protein levels of yogurt with dadih starter A and yogurt with dadih starter B revealed a significantly different result (P<0.05). Yogurt with a concentration of 2.5% starter A had the highest dissolved protein level, which was 210.87 ppm, while the addition of 7.5% *starter* only produced a total of 138.37 dissolved protein levels. The highest dissolved protein levels in yogurt with the additional *dadih starter* B was produced by a total of 7.5% concentration with a value of 233.37 ppm. The additional variations in the *dadih* concentration that produced dissolved protein levels with a fluctuating value was estimated as a consequence of the difference amount of bacterial contained in *dadih starter*. Accordingly, fermented milk with a low growth of LAB affected the dissolved protein levels to also be low because the amount of hydrolyzed protein was reduced.

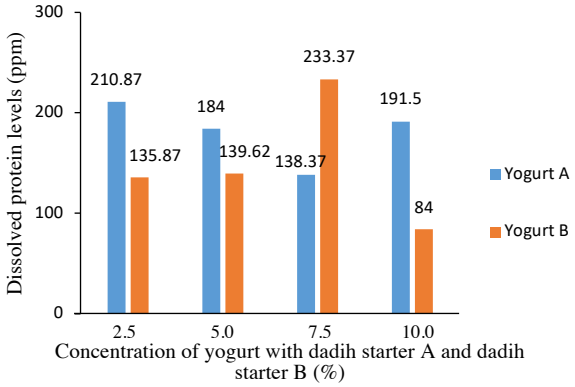


Figure 1. Dissolved protein levels of yogurt with dadih starter A and dadih starter B

The Hydrolysis Degree (DH) of Yoghurt

The result of analysis degree of hydrolysis yogurt with dadih starter A and yogurt with dadih starter B indicated a significant difference (P<0.05).

The highest hydrolysis degree results in this study was produced in yogurt with the addition of a 5.0% concentration of *starter* A, which was 11.17% (Fig.2). Yogurt with the additional 10% concentration of *starter* produced the highest degree of hydrolysis, which was 10.42% (Fig.2). Referred to Hernández-ledesma [16] the degree of hydrolysis is directly proportional to the concentration of dissolved protein, i.e. if the dissolved protein levels are large, the degree of hydrolysis is high. The results of this study were not in accordance with the mentioned theory, this was estimated as a result of several proteins that have not been completely degraded into smaller peptides. Accordingly, it was estimated the hydrolysis is less than optimal hence the contact between the protease enzyme produced by LAB and the substrate is not optimal in several yogurt products.

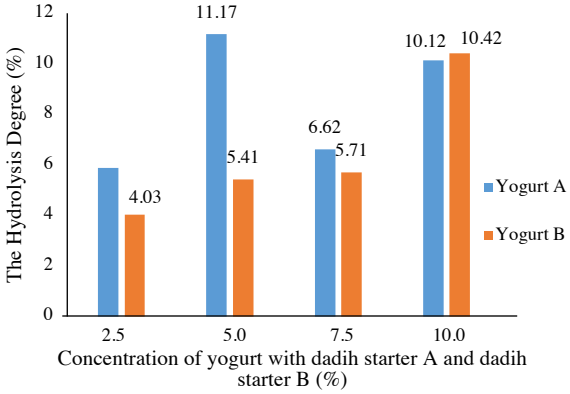


Figure 2. Degree of hydrolysis of yogurt with dadih starter A and yogurt with dadih starter B

ACE Inhibitor Activity of Yogurt

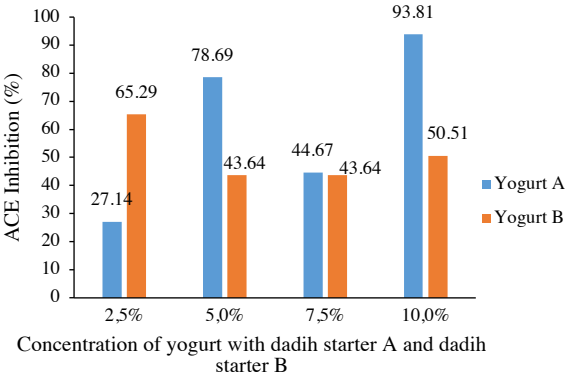
Analysis of ACE inhibitory actvity in yogurt with dadih starter A and yogurt with dadih starter B revealed a significant difference (P<0.05). Furthermore, yogurt A with an additional concentration of 10% starter was examined excellent since it had the highest. The ACE inhibitor activity of yogurt A which was 93.81% (Fig.3) with an IC_{50} result of 69.81 ppm. Yogurt with the addition of starter B which acknowledged having the highest ACE inhibitor activity was at a concentration of 2.5% with the percent inhibition result of 65.22% (Fig.3) and IC_{50} of 58.92 ppm. The difference results obtained in Yogurt A and B were

estimated due to the larger concentration of LAB in *dadih* A Koto Malintang compared to *dadih* B Padang Gadut which caused the ACE inhibitor activity was limited to 2.5% (v/v).

Figure 3. ACE inhibitory activity of yogurt with dadih starter A and dadih starter B

The Proximate Test on Yogurt

The results of water levels measurement in yogurt with the addition of 10.0% *dadih* A, was equal to 82.72% and water levels in yogurt with the additional 2.5% *dadih* B was equal to 82.57%. The highest ash levels in yogurt products were obtained in yogurt with the addition of 10.0% (v/v) starter A, which was 0.93%. Moreover, yogurts products with the additional 10.0% (v/v) of starter A and 2.5% (v/v) *starter* B already fulfilled the ash levels requirements in SNI, which is a maximum of 1%. Furthermore, the results of protein levels in yogurt with 10.0% (v/v) of starter A was 2.74% meanwhile in yogurt with 2.5% (v/v) of *dadih starter* B was 3.56%. The protein levels in yogurt products were determined by the number of lactic acid bacteria.



The higher amount of the LAB contained, the higher protein levels will be since most of the components of LAB are proteins [17]. Correspondingly, the fat levels in yogurt products with the additional 10.0% (v/v) of *dadih starter* A was 2.54%, while 2.5% (v/v) of *dadih starter* was 0.91%. This indicated that the fat levels in the additional 10.0% (v/v) of *starter* A was higher compared to the additional 2.5% (v/v) of *starter* B but still fulfilled the SNI 2981:2009 requirements on Yogurt Quality where fat levels in low-fat yogurt are 0.6 – 2.9 %. This was estimated due to the number of additional *dadih* since buffalo milk is acknowledged to contains higher fat.

Tabel 4. The results proximate test of yogurt
The data from the yogurt have the highest ACE inhibitor activity ie 10% for starter A and 2.5% for starter B

Parameter (%)	SNI (2009)	Results		
		Milk skim	A	B
Water levels	-	85.26 ± 0.43	82.72 ± 0.07	82.57 ± 0.60
Ash levels	Max. 1.0	0.90 ± 0.01	0.93 ± 0.004	0.87 ± 0.005
Protein levels	Min. 2.7	21,00	3.74 ± 0.12	3.56 ± 0.09
Fat levels	0.6 – 2.9	0,00*	2.54 ± 0.49	0.91 ± 0.07

*citation of nutrition value in IndoPrima Skim Milk on packaging

CONCLUSIONS

Admittedly, the optimal ACE inhibitor activity in yogurt with the additional 10.0% (v/v) of starter A with a percent inhibition value of 93.81% and IC_{50} was 69.81 ppm. The optimal ACE inhibitor activity in yogurt with additional starter B was 65.29% with IC_{50} of 58.92 ppm. Yogurt quality with an optimal ACE inhibitor activity were yogurts with the additional 10.0% (v/v) of starter A and 2.5% (v/v) of *starter* B which known had fulfilled the yogurt quality standards SNI 2981: 2009. The results of this study can be concluded that *dadih* is a novel source of starter contains lactic acid bacteria to produce yogurt which has angiotensin converting enzyme (ACE) inhibitory activity.

ACKNOWLEDGEMENTS

The researchers would like to express gratitude to the Head of Institute of Research and Community Services of Syarif Hidayatullah State Islamic University Jakarta for the college development research grant in 2019.

REFERENCES

[1] Surono. In Vitro Probiotic Properties of Indigenous Dadih Lactic Acid Bacteria. Asian-Australasian Journal Animal Sciences, Vol. 16, 2003, pp 726-731.

[2] Todorov, S. D., Botes, M., Guigas, C., Schillinger, U., Wiid, I., Wachsman, M. B., & Dicks, L. M. Boza. A Natural Source of Probiotic Lactic Acid Bacteria. Journal of Applied Microbiology, Vol. 2, Issue 104, 2008, pp 465-477.

[3] Virtanen, T., Pihlanto, A., Akkanen, S., & Korhonen, H. (2007). Development of antioxidant activity in milk whey during fermentation with lactic acid bacteria. Journal of applied microbiology, 102(1), 106-115.

[4] Pihlanto, A., Virtanen, T., & Korhonen, H. Angiotensin I Converting Enzyme (ACE) Inhibitory Activity and Antihypertensive Effect of Fermented Milk. International Dairy Journal, Vol.1, Issue 20, 2010, pp 3-10.

[5] Ayyash, M., Al-Dhaheri, A. S., Al Mahadin, S., Kizhakkayil, J., & Abushelaibi, A. In Vitro Investigation of Anticancer, Antihypertensive, Antidiabetic, And Antioxidant Activities of Camel Milk Fermented With Camel Milk Probiotic: A Comparative Study With Fermented Bovine Milk. Journal of dairy science, Vol.2, Issue 101, 2018, pp 900-911.

[6] González-Córdova, A. F., Torres-Llanez, M. J., Rodriguez-Figueroa, J. C., Espinosa-de-los-Monteros, J. J., Garcia, H. S., & Vallejo-Cordoba, B. Angiotensin Converting Enzyme Inhibitory Activity in Milks Fermented by Lactobacillus strains. CyTA-Journal of Food. Vol.2, Issue 9, 2011, pp 146–151.

[7] Amirdivani, S., & Baba, A. S. Changes in Yogurt Fermentation Characteristics, and Antioxidant Potential and In Vitro Inhibition of Angiotensin-1 Converting Enzyme upon the Inclusion of Peppermint, Dill And Basil. LWT-Food Science And Technology, Vol. 6, Issue 44, 2011, pp 1458-1464.

[8] Chalid, S. Y., Nurbayti, S., & Pratama, A. F. ACE Angiotensin Converting Enzyme (ACE) Inhibitory Activity Of Protein Fraction Of Fermented Buffalo Milk (*Bubalus bubalis*). Jurnal Ilmu Kefarmasian Indonesia. Vol.2, Issue 16, 2018, pp 214–224.

[9] Pelczar, M. J., & Chan, E. C. 1998. Microbiology, Fifth Edition. Tata Mc-Graw-Hill Education.

[10] Rodríguez-Figueroa, J. C., Reyes-Díaz, R., González-Córdova, A. F., Troncoso-Rojas, R., Vargas-Arispuro, I., & Vallejo-Cordoba, B. Angiotensin-Converting Enzyme Inhibitory Activity of Milk Fermented by Wild and Industrial *Lactococcus Lactis* Strains. Journal of Dairy Science, Vol. 11, Issue 93, 2010, pp 5032-5038.

[11] Association of Official Analytical Chemist (AOAC). Official Methods of Analysis (18th Ed). Washington, D. C, 2005.

[12] Arihara, K., Nakashima, Y., Mukai, T., Ishikawa, S., & Itoh, M. Peptide Inhibitors for Angiotensin I-Converting Enzyme from Enzymatic Hydrolysates of Porcine Skeletal Muscle Proteins. Meat Science, Vol.3, Issue 57, 2001, pp 319–324.

[13] Birollo, G. A., Reinheimer, J. A., & Vinderola, C. G. Viability of Lactic Acid Microflora in Different Types of Yoghurt. Food Research International, Vol. 9, Issue 33, 2000, pp 799-805.

[14] Sakul, S.E., Rosyidi, D., Radiati, L.E., Purwadi. The Effect of Different Starter Cultures on the Fermentation of Yogurt Added with Aqueous Extract of White Oyster Mushroom *(Pleurotus ostreatus)*. Jurnal Ilmu dan Teknologi Hasil Ternak, Vol.15, Issue 1, 2020, pp 46-51.

[15] Madigan, M.T., Tsai, Z.Y., Stahl, D.A. Biology of Microorganisms (13th ed). San Fancisco: Benjamin Cummings, 2011, pp 140.

[16] Hernández-ledesma, B., Contreras, M. del M., & Recio, I. Antihypertensive Peptides : Production, Bioavailability and Incorporation into Foods. Advances in Colloid and Interface Science, Vol. 1, Issue 165, 2011, pp 23–35.

[17] Winarno, F. G., & Fernadez, I. Dairy and Fermented Products. Bogor: M-Brio Press, 2007.

[18] Badan Standar Nasional. SNI 2981:2009 Yoghurt. 2009.

7th Int. Conf. on Structure, Engineering & Environment (SEE), Pattaya, Thailand, Nov.10-12, 2021, ISBN: 978-4-909106070 C3051

ANTIBACTERIAL ACTIVITY OF LIQUID SMOKE POWDER FROM RICE HUSK

Muriady[1], Hesti Meilina[2], Muhammad Faisal[1,2,3,*]
[1]Magister Program of Environmental Management, Universitas Syiah Kuala, Indonesia
[2]Department of Chemical Engineering, Universitas Syiah Kuala, Indonesia
[3]Halal Research Center, Universitas Syiah Kuala, Indonesia

ABSTRACT

The technological trend towards waste reduction has attracted the attention of researchers in utilizing rice husk as a value-added material. Rice husk, mainly composed of lignocellulose, is a promising feedstock for the production of liquid smoke powder which can be used in food preservation. The objective of the present work is to investigate the antimicrobial activity of liquid smoke powder from rice husk on some gram-positive and negative bacteria, i.e *Salmonella choleraesuis, Escherichia coli, Staphylococcus aureus,* and *Bacillus subtilis*. Liquid smoke was prepared through the pyrolysis of rice husk at a temperature of 300, 350, and 400°C**.** After purification by distillation, the liquid smoke was prepared into liquid smoke powder by spray drying method. The antibacterial activity test was conducted using the Kirby–Bauer method. Gas chromatography-mass spectrometry (GC-MS) analysis shows that rice husk liquid smoke contains various chemicals such as acetic acid, 2-propanone, butanal, propanoic acid, 2-cyclopenten and phenolic compounds. The liquid smoke powder could inhibit the growth of all the tested bacteria with various inhibition zone (6-9 mm). The results of this study show that liquid smoke powder from rice husk has the antimicrobial activity and could inhibit the growth of tested bacteria.

Keywords: Rice huks, Liquid smoke powder, Salmonella choleraesuis, Escherichia coli, Staphylococcus aureus, Bacillus subtilis, Inhibition zone

INTRODUCTION

The utilization of agricultural waste to produce value-added materials is a way to achieve a lifestyle based on the go green concept. Rice husks, a byproduct of the rice milling industry, is one of the agricultural wastes that interest the researchers as it could be processed into various kinds of products. Depending on the rice variety, the amount of rice husks produced from the rice milling industry ranges from 20-33% [1]. Like other biomass, rice husks have a high content of organic constituents with a total carbon of 45.28% (w / w) [2]. Rice husk is organic waste that is difficult to compost due to its hard texture, its strong material (i.e., not easily broken down), and its high silica content. However, contents including cellulose, hemicellulose, and lignin in rice husks make this biomass a suitable raw material to produce liquid smoke. Liquid smoke is the result of condensation of steam from pyrolysis, either directly or indirectly, from materials with high carbon content. Liquid smoke contains components derived from the thermal degradation of lignin, such as phenols which act as antioxidants, acids that act as antimicrobials, guaiacol and its derivatives, syringols and their derivatives, and alkyl aryl. Rice husks utilization to make liquid smoke provides many benefits, especially because it can reduce the volume of the husk waste pile. Liquid smoke from various biomass including palm kernel shell [3,4], durian husks [5,6], rice husk [7,8], bamboo [9], oil palm empty bunches [10,11], sawdust [12], and cacao bark [13] have been used as a natural preservative for various foodstuffs. Moreover, liquid smoke can also be used in agriculture as biological pest control, for example, to anticipate anthracnose in chilies [10]. With its various compositions, liquid smoke is also thought to have a positive effect on plants in terms of improving soil quality and neutralizing soil acidity, warding off pests and plant pathogens, as well as stimulating plant growth on roots, stems, tubers, leaves, flowers, and fruit.

In its application, liquid smoke is widely used in its liquid state, which is considered impractical, especially in the distribution and transportation process, because it requires special containers and handling. Phenolic compounds in liquid smoke are also prone to damage (oxidation). Therefore, a method is to protect the active components in liquid smoke and to make its handling easier is necessary, one of which is by transforming liquid smoke into powder. Generally, smoke powders are made by freeze-drying method with the addition of maltodextrin. Smoke powder also has antioxidant and antibacterial properties, just as the liquid smoke does. Until today, research and application of smoke powder to preserve food have not been extensively carried out, so that the antibacterial properties of smoke powders from various liquid smoke raw materials have not been well described. This paper

aims to study the antimicrobial activity of smoke powder derived from rice husks on several types of bacteria commonly found in food, namely, *Salmonella choleraesuis*, *Escherichia coli*, *Staphylococcus aureus*, and *Bacillus subtilis*.

METHODOLOGY

Preparation of Liquid Smoke

A total of 2 kg of rice husk was put into the pyrolysis reactor, in which it was pyrolyzed at temperatures of 300°C, 350°C, and 400°C to produce smoke, which was then condensed using a condenser to produce liquid smoke. The liquid smoke was purified in a distillation unit at a temperature of 190°C so that the liquid smoke was free from tar and other toxic compounds. The detailed procedure for making liquid smoke followed other studies [14-16].

Preparation of Liquid Smoke Powder

The preparation of smoke powder from liquid smoke derived from rice husks was carried out using a spray dryer. 1 liter of liquid smoke was added with maltodextrin (30% of the liquid smoke volume) then stirred thoroughly. After it was well blended, the mixture was put into a spray dryer, and the powdering process was carried out at a temperature of 170°C at a pressure of 2 bar for two hours.

RESULTS AND DISCUSSION

GC-MS Test

GC-MS test is to determine the composition contained in liquid smoke at each pyrolysis temperature. Pyrolysis temperature plays an important role in the composition of the liquid smoke [17], while the composition of liquid smoke is one of the parameters to determine the quality of liquid smoke produced. Liquid smoke has several compositions including phenol, acetic acid, ethanol, cyclopentanone, and propionic acid [6]. Tables 1-3 present the various chemical compounds obtained from the rice husks pyrolysis at 300-400°C.

Table 1 Chemical compounds of liquid smoke from rice husks (pyrolyzed at 300°C)

Retention time (min)	Component	Concentration (%)
9.193	Acetic acid (CAS) ethylic acid	40.50
9.622	2-Propanone, 1-hydroxy- (CAS) acetol	13.99
9.942	Butanal, 3-hydroxy- (CAS) 3-hydrocybutanal	1.23
10.616	Propanoic acid (CAS) propionic acid	1.44
12.017	2-Cyclopenten-1-one (CAS) cyclopentenone	0.64
14.109	3-Pentanone, 2-methyl- (CAS) 2-methyl-3-pentanone	1.12
14.476	phenol (CAS) izal	7.48
14.817	2-Buten-1-ol, 3-methyl- (CAS) prenol	4.17
15.618	Phenol, 2-methoxy- (CAS) guaiacol	8.52
16.026	Phenol, 2-methyl- (CAS) o-cresol	1.27
16.800	2-Methoxy-4-methylphenol	2.78
17.092	Phenol, 3-ethyl- (CAS) m-ethylphenol	1.66
18.543	Phenol, 2-methoxy-4-(2-propenyl)- (CAS) eugenol	6.66
18.718	trans-caryophyllene	7.29
28.875	Cyclohexanecarboxylic acid, 1-phenyl-, methyl ester (CAS)	1.25

Table 2 Chemical compounds of liquid smoke from rice husks (pyrolyzed at 350°C)

Retention time (min)	Component	Concentration (%)
8.305	Acetic acid (CAS) ethylic acid	40.54
8.708	2-hydroxymethyl-3-methyl-oxirane	4.43
8.927	Propanoic acid (CAS) propionic acid	17.29
9.475	N-nitroso-2-methyl-1,3-oxazolidine	2.02
9.922	3-Pentanone, 2-methyl- (CAS) 2-methyl-3-pentanone	1.96
12.609	Acetic acid, anhydride (CAS) acetic oxide	1.00
14.214	2-Butanone, 1-(acetyloxy)- (CAS) 1-acetoxy-2-butanone	0.63

14.587	2-Buten-1-ol, 3-methyl- (CAS) prenol	1.96
14.888	Phenol (CAS) izal	8.82
15.342	Ethane, 1,1,1	2.09
15.696	Phenol, 2-methoxy- (CAS) guaiacol	5.30
16.157	Phenol, 2-methyl- (CAS) o-cresol	3.47
16.950	2-Methoxy-4-methylphenol	0.69
18.735	Phenol, 2-methoxy-4-(2-propenyl)- (CAS) eugenol	7.91

Table 3 Chemical compounds of liquid smoke from rice husks (pyrolyzed at 400°C)

Retention time (min)	Component	Concentration (%
5.500	Bicylco [2.2.1] hepane,-5-(ethyl-1-amie)	0.98
8.125	Acetic acid (CAS) ethylic acid	43.87
12.677	2-Cyclopenten-1-one, 2-methyl- (CAS) 2-methyl-2-cyclopentenone	1.62
14.095	2-methylene-7-oxabicyclo[4.1.0]heptane	3.65
14.477	Phenol, 2-methyl- (CAS) o-cresol	1.27
14.792	5-Hydroxy-2-heptanone	7.42
15.320	phenol (CAS) izal	7.48
15.716	Phenol, 2-methoxy- (CAS) guaiacol	8.52
16.408	Bicyclo [4.1.0] heptane, 7-(1-methylethylidene)- (CAS) 7-isopropylenyl bic 11	1.11
16.811	Phenol, 3-ethyl- (CAS) m-ethylphenol	1.66
17.527	2,5-Dimethoxytoluene	1.95
18.362	Phenol, 2-methoxy-4-(2-propenyl)- (CAS) eugenol	6.66
18.645	trans-caryophyllene	9.44
5.500	Bicyclo [2.2.1] heptane ,-5-(ethyl-1-amine)	0.98

GC-MS analysis showed that the composition of liquid smoke after distillation which had been degraded at a pyrolysis temperature of 300°C was dominated by acetic acid content, which was 40.50%. Likewise, the acetic acid content in the liquid smoked pyrolyzed at 350°C and 400°C were 41.54% and 43.87% respectively. The acetic acid content tended to increase with increasing pyrolysis temperature. Acetic acid has an antibacterial role [18,19]. At a very low pH environment, acetic acid can cause enzyme denaturation and destabilize the cell membrane permeability of the bacteria, thus inhibiting its growth and decreasing the viability of bacterial cells. In addition, acidic compounds also determine smoked products in terms of taste, aroma, and product shelf life. The content of chemical compounds in rice husks after the pyrolysis process is similar to the results in a previous study on durian peel by Faisal et al. [6] where pyrolysis of durian peel at 300°C was dominated by acetic acid content of 36.37%

Tables 1-3 also show that phenolic compounds also increase with increasing pyrolysis temperature. The phenolic content obtained at the temperatures of 300, 350 and 400°C were 21.13, 26.19 and 28.37% respectively. Phenol is a pyrolysis product of lignin compounds [19]. Thus, the high phenol content in liquid smoke prepared from rice husks is due to the high lignin compounds in the rice husks. The identification results also show that phenol is the second-largest component in liquid smoke. The high phenolic content at a pyrolysis temperature of 400°C is probably due to the lignin decomposition process that occurred at a temperature of 300-450°C so that the higher the pyrolysis temperature, the higher the phenol concentration will be. Phenols are the main antioxidants in liquid smoke. The anti-oxidative role of liquid smoke is indicated by phenolic compounds with high boiling points, especially 2,6-dimethoxyphenols; 2,6 dimethoxy-4-methylphenol and 2,6-dimethoxy-4-ethylphenol which act as hydrogen donors to the free radicals and inhibit chain reactions. Generally, liquid smoke can be used as a preservative because it has a degree of acidity (pH) with a value of 2.8-3.1 so that it can inhibit the growth of pathogenic bacteria. Liquid smoke has been shown to suppress the growth of rotting bacteria and pathogens such as *Escherichia coli, Bacillus subtiliis, Pseudomonas* and *Salmonella* [20].

Effect of Liquid Smoke Powder on Gram-Positive Bacteria

The antibacterial activity of liquid smoke powder showed by the clear zones around the colony. Two Gram-positive bacteria (*S.aureus and B.subtilis*) have different sensitivity to the liquid smoke powder.

The diameter inhibitory zone in each treatment showed in Table 1-2, the antibacterial activity test results performed by the Kirby-Bauer method.

Table 4 Inhibition zone on *S.aureus* by liquid smoke powder

Liquid smoke	Inhibition zone diameter (mm)	Control + (mm)
LP1	6.67 ± 0.03^{A}	16.81
LP2	7.84 ± 0.12^{B}	
LP3	9.09 ± 0.34^{C}	

Note: The different superscript letter within a column shows the actual difference with an α=0.05
LP1= Liquid smoke obtained from pyrolysis of rice husks at 300°C
LP2= Liquid smoke obtained from pyrolysis of rice husks at 350°C
LP3= Liquid smoke obtained from pyrolysis of rice husks at 400°C

Table 2 Inhibition zone on *B. subtilis* by liquid smoke powder

Liquid smoke	Inhibition zone diameter (mm)	Control + (mm)
LP1	6.53 ± 0.0^{A}	24.84
LP2	6.58 ± 0.0^{A}	
LP3	6.69 ± 0.0^{A}	

Note: The different superscript letter within a column shows the actual difference with an α=0.05

Comparisons of the diameter of the inhibitory zone and pyrolysis temperatures were presented in Table 1-2 for Gram-positive bacteria. The antibacterial properties against S.aureus and B.subtilis were categorized in the medium category, the diameter of inhibitory zone of 6.67 mm – 9.09 mm, and 6.53 mm – 6.69 mm, respectively, for each treatment (LP1-LP3). Sample LP3 was the most effective against antibacterial tested. The pyrolysis temperature affected the composition of the liquid smoke and also the liquid smoke powder and in turn affected the antibacterial properties. The LSD test showed that the pyrolysis temperature was not significantly different for *B.subtilis*, although *S.aureus* was quite different. A previous study using liquid smoke from oil palm kernel shells could inhibit *Streptococcus* bacteria [4]. Liquid smoke from different biomass types produces a different composition (such as phenol, acetic acid, and carbonyl) that influences an antibacterial agent. Previous research has reported that liquid smoke from durian peel waste [6], oil palm empty bunches [15], cacao pod shells [13], rice hulls [7] and palm kernel shells [3] can inhibit the growth of bacteria.

Effect of Liquid Smoke Powder on Gram-Negative Bacteria

This study used two strains of Gram-negative bacteria, known as *E.coli and Salmonella*. The Gram-negative bacteria cell wall is surrounded by two membrane bilayers [21]. The cell wall (around 5-10 nm) contains high lipid and lipoprotein, lipopolysaccharide, and less susceptible to anionic detergent [22].

Table 3 Inhibition zone on *E.coli* by liquid smoke powder

Liquid smoke	Inhibition zone diameter (mm)	Control + (mm)
LP1	6.58 ± 0.03^{A}	18.10
LP2	6.99 ± 0.25^{A}	
LP3	7.58 ± 0.04^{B}	

Note: The different superscript letter within a column shows the actual difference with an α=0.05

Table 4. Inhibition zone on *Salmonella* by liquid smoke powder

Liquid smoke	Inhibition zone diameter (mm)	Control + (mm)
LP1	6.48 ± 0.0^{A}	27.58
LP2	6.65 ± 0.06^{A}	
LP3	7.36 ± 0.06^{B}	

Note: The different superscript letter within a column shows the actual difference with an α=0.05

The distilled water (negative control) was tested on Gram-positive, and harmful bacteria does not inhibit the growth of bacteria (inhibition zone= 0 mm). Tables 3 and 4 show that the diameter of an inhibitory zone for the liquid smoke powder was 6.48 mm to 7.58 mm, the antibacterial properties belonged to the medium category. However, the pyrolysis temperature increased (at LP3), the inhibition formed grew, which means rising antibacterial ability. Antibacterial activity in Gram-positive and negative bacteria will increase along with increasing pyrolysis temperature. Further, research by Desvita et al [23] found that liquid smoke from cacao pod shells can inhibit gram-positive and negative bacteria with the inhibition ranging zone diameter 6-7.36 mm. In a study by Desvita et al. [7], the use of 5% liquid smoke inhibited the growth of Salmonella and E.coli with inhibition zones of 7.75 mm and 7.07 mm, respectively.

Statistical analysis was applied by using a one-way ANOVA test with α=0.05 (significant differences) for each treatment. However, the LSD procedure showed the largest diameter inhibitory zone was obtained LP3; there is no significant difference for treatment LP1 and LP2. The different structures in cell walls from each bacterium (Gram-

positive and Gram-negative) may have affected the abilities to inhibit the growth of bacteria.

CONCLUSIONS

Liquid smoke from rice husks contains various organic compounds including acetic acid, carbonyl and phenolic compounds, which is potential in inhibiting some common bacterias in food. Temperature pyrolysis affected the number of the chemical component produced. The liquid smoke powder from rice husks has been found can inhibit the growth *S.aureus*, *B.subtilis*, *E.coli*, and Salmonella bacteria. The best results for inhibiting the growth of bacteria are achieved at liquid smoke produced at a pyrolysis temperature of 400ºC. Based on each bacterium, the liquid smoke powder most effective in inhibiting against *S.aureus.*

ACKNOWLEDGEMENTS

The work was financially supported by Universitas Syiah Kuala (Grant No. 166/UN11/ SPK/PNBP/ 2021).

REFERENCES

[1] Pode R., Potential Applications of Rice Husk Ash Waste from Rice Husk Biomass Power Plant. Renewable and Sustainable Energy Reviews, Vol. 53, 2016, pp. 1468-1485.

[2] Tsai W. T., Lee M. K., and Chang Y. M., Fast Pyrolysis of Rice Husk: Product Yields and Compositions. Bioresource Technology, Vol. 98, Issue 1, 2007, pp.22-28.

[3] Faisal M., Gani A., and Husin., Utilization of Liquid Smoke from Oil Palm Kernel Shell to Preserve Mackerel. Rasayan Journal of Chemistry, Vol. 11, Issue 3, 2018, pp. 1120-1125.

[4] Faisal M., Gani A., Husni., and Daimon H., A Preliminary Study of the Utilization of Liquid Smoke from Palm Kernel Shells for Organic Mouthwash. International Journal of GEOMATE, Vol. 13, Issue 37, 2017, pp. 116-120.

[5] Faisal M., Sunarti A. R. Y., Desvita H., Characteristics of Liquid Smoke from the Pyrolysis of Durian Peel Waste at Moderate Temperatures. Rasayan Journal of Chemistry, Vol. 11, Issue 2, 2018, pp. 871-876.

[6] Faisal M., Gani A., and Mulana F., Preliminary Assessment of the Utilization of Durian Peel Liquid Smoke as a Natural Preservative for Mackerel [version 6; peer review: 2 approved]. F1000Research, 8 (240), 2019, pp. 1-9.

[7] Desvita H., Faisal M., Mahidin., and Suhendrayatna. Preservation of Meatballs with Edible Coating of Chitosan Dissolved in Rice Hull-Based Liquid Smoke. Heliyon, Vol. 6(10), 2020, pp. e05228.

[8] Desvita H., Faisal M., Mahidin., and Suhendrayatna. Edible Coating for Beef Preservation from Chitosan Combined with Liquid Smoke. International Journal of Technology, Vol. 11, Issue 4, 2020, pp. 817-829.

[9] Triastuti W. E., Budhi P. A., Agustiani E., Hidayat R. A., Retnoningsih R., and Nisa A. A., Characterization of Liquid Smoke Bamboo Waste with Pyrolysis Method. IPTEK Journal of Proceedings Series, Vol. 3, 2019, pp. 114-117.

[10] Faisal M., Gani A., Husni., Baihaqi A., and Daimon H., Pyrolysis of Oil Palm Kernel Shell into Liquid Smoke and Its Application to Control Anthracnose Disease on Chili (Capsicum annum L). Journal of Engineering and Applied Sciences, Vol. 11, Issue 12, 2016, pp. 2583-2587.

[11] Faisal M., and Gani A., The Effectiveness of Liquid Smoke Produced from Palm Kernel Shells Pyrolysis as a Natural Preservative in Fish Ball. International Journal of GEOMATE, Vol. 15, Issue 47, 2018, pp. 145-150.

[12] Lingbeck J. M., Cordero P., O'Bryan C. A., Johnson M. G., Ricke S. C., and Crandall P. G., Functionality of Liquid Smoke as an All-Natural Antimicrobial in Food Preservation. Meat Science, Vol. 97, Issue 2, 2014, pp. 197-206.

[13] Desvita H., Faisal M., Mahidin, and Suhendrayatna. Characteristic of Liquid Smoke Produced from Slow Pyrolysis of Cacao Pod Shells (Theobroma Cacao L).International Journal of GEOMATE, Vol. 20, Issue 80, 2021, pp. 17-22.

[14] Faisal M., Chamzurni T., and Daimon H., A study on the Effectiveness of Liquid Smoke Produced from Palm Kernel Shells in Inhibiting Black Pod Disease in Cacao Fruit In Vitro. International Journal of GEOMATE, Vol. 14, Issue 43, 2018, pp. 36-41.

[15] Faisal M., Gani A., Mulana F., Desvita H., and Kamaruzzaman S., Effects of Pyrolysis Temperature on the Composition of Liquid Smoke Derived from Oil Palm Empty Fruit Bunches. Rasayan Journal of Chemistry, Vol. 13, Issue 1, 2020, pp. 514-520.

[16] Ginayati L, Faisal M, and Suhendrayatna Pemanfaatan Asap cair dari Pirolisis Cangkang

Sawit Sebagai Pengawet Alami Tahu, Jurnal Teknik Kimia USU, Vol. 4, No. 3, 2015, pp. 7-11.

[17] Budaraga K., Marlida Y., and Bulanin U., Liquid Smoke Production Quality from Raw Materials Variation and Different Pyrolysis Temperature. International Journal on Advanced Science, Engineering and Information Technology, Vol. 6, Issue 3, 2016, pp. 306-315.

[18] Malarut J. A., and Vangnai K., Influence of Wood Types on Quality and Carcinogenic Polycyclic Aromatic Hydrocarbons (PAHs) of Smoked Sausages. Food Control, Vol. 85, 2018, pp. 98-106

[19] Vega R. C., Figueroa K. H. N., and Oomah B. D., Cococa (Theobroma Cacao L.) Pod Husk: Renewable Source of Bioactive Compounds. Trends in Food Science and Technology, Vol. 81, 2018 , pp. 172-184.

[20] Darmadji, Aktivasi Anti Bakteri Asap Cair yang Diproduksi dari Bermacam-macam Limbah Pertanian, Agritech, Vol 16, Issue 4, 1999, pp. 19-22.

[21] Miller S.I., and Salama N. R., The Gram-Negative Bacterial Periplasm: Size Matters. PLoS biology, Vol. 16, Issue 1. 2018, pp. e2004935.

[22] Panawala L., Difference Between Gram Positive and Gram Negative Bacteria. Epedıaa, Vol. 3, 2017, pp.1-13.

[23] Desvita H, Faisal M, Mahidin and Suhendrayatna, Preliminary Study on the Antibacterial Activity of Liquid Smoke from Cacao Pod Shells (*Theobroma cacao L*), IOP Conf. Series: Materials Science and Engineering, 1098 (2021) 022004

7th Int. Conf. on Structure, Engineering & Environment (SEE), Pattaya, Thailand, Nov.10-12, 2021, ISBN: 978-4-909106070 C3051

ON THE IMAGE OF URBAN SPACE EXTTRACTED BY COLORS

Ami Hasegawa[1], Kazunari Tanaka[2]
[1] Graduate School of Engineering, Osaka Institute of Technology, Japan
[2] Osaka Institute of Technology, Japan

ABSTRACT

The urban space is full of various colors such as green from trees, and the various colors of buildings and cars. The colors of urban spaces themselves have a great influence on our impression. At the same time, livelier spaces given us a bright color impression and a lonely street gives us a dark color impression. The shops you visit often have cheerful color, and the noisy street has vivid color. By capturing these colors, it may extract an image of urban space.In this study, it was assumed that children who color on cognitive maps can freely draw without being influenced by stereotypes. The purpose is to extract the impression spaces by extracting the colors they use. We extracted the elements drawn on the cognitive maps of adults and children and compared the results. Then we clarified the difference in the image of the city between children and adults, and examined the method of study. Our goal is to propose attractive and comfortable urban space design, which people wish to inhabit longer. The research method is to investigate by the Basic Drawing Method. By extracting the drawn elements and analyzing the colors, we grasped the spatial cognitive structure of the street or space one uses. The results indicated that adults tend to color with a fixed concept, but children use their favorite colors wherever they like, and their image has a big effect, and there was indeed a clear difference between adults and children in color use.

Keywords: Color, Map, Image, Street

INTRODUCTION

Urban spaces are full of various colors such as greens from trees, various colors of buildings and cars. The colors of urban spaces themselves have a great influence on our impression. At the same time, the liveliness of a space given us a bright color impression and a lonely street gives us a dark color impression. The shops you visit often have a cheerful impression, and a noisy street has a vivid color image. By capturing these colors, we may be able to extract an image of urban space.

PURPOSE AND METHOD

In this study, it was assumed that children use colors on cognitive maps that they can freely draw with rich images without being influenced by stereotypes. The purpose is to extract the impression of the space by extracting the color. We extracted the elements drawn on the cognitive maps of adults and children and compare the results. Then we clarified the difference in the image of the city between children and adults, and examine the method of study.

There are two research methods for this study. One is to grasp the spatial cognitive structure of the street space in which we frequent by conducting a cognitive map survey using the basic drawing method and extracting the elements and analyzing the colors of the extracted elements. The second is to conduct a route selection experiment by the paired comparison method, and to understand what kind of route is preferred from the analysis of the ratio of elements in the photograph and the color.

Chris J. Boyatzsis and others [1] are conducting a questionnaire survey of children aged 4 to 7 to see what kind of emotions they associate with the colors they are shown. This study, which aims to clarify the relationship between children's emotions and colors, prepares uses nine-colors of drawing paper and asks the children to answer the emotions associated with each color and why they feel that way. As a result, it is clear that bright colors tend to receive positive emotions and dark colors tend to receive negative emotions. In addition, the difference in the results between males and females shows that girls receive more negative emotions from dark colors than boys. In addition, there was a tendency for more positive feelings toward dark colors to increase with age. Some of the children's emotional associations were empirical. From this, the author states that the image of emotions toward the color may diversify with age.

Hyun-min and others [2] asked Japanese participants aged 18 to 30 to put 10 basic colors of colored paper on a 3x3 cell to express their emotions. As a result, it was found that warm colors are often used to express happiness and surprise, and cool colors and achromatic colors are often used to express sadness, fear, and disgust. In addition, feelings of fear, disgust, and surprise tended to use five or more color schemes compared to other feelings.

Yukiko Shimada [3] is investigating the connection between words and colors for young children. In this

study, 21 color swatches were presented and each of the 15 words was selected one color at a time. As a result, black was selected for "scary" and pink for "gentle", "cute", "weak", "girl", and "sister". In addition, while the words for men tended to be bluish and the words for women tended to be red, white and gray tended to be selected for "grandfather" and "grandmother." In addition, since black, flesh color, pink, red, indigo, etc. were frequently used, the author states that these colors are familiar to young children and are easy to associate with the image.

ROUTE SELECTION EXPERIMENT

Experiment Contents

This experiment was conducted on 150 adults over the age 18, and 184 children aged 10 to 12 based on the Paired Comparison Method using 13 photographs. By converting 13 photos to a total of 130 pixels of 10 x 13 pixels and counting the number of pixels that contain the most elements, there were ratios of each element of a road surface, road area, and sky in the photos. Furthermore, the color and average brightness were extracted for each photograph as a whole or for each element, and the color ratio and the difference in color for each element were analyzed.

Experiment Contents

Percentage of each element

Fig.1 and Fig.2 show the area ratio of each element in the photographs from the 13 photographs, and compared them between adult and child together with the results of the paired comparison method.

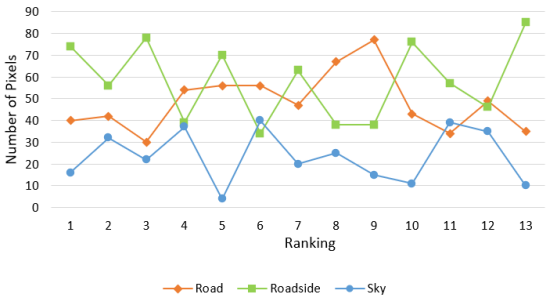


Fig. 1 Number of pixels in each adult element

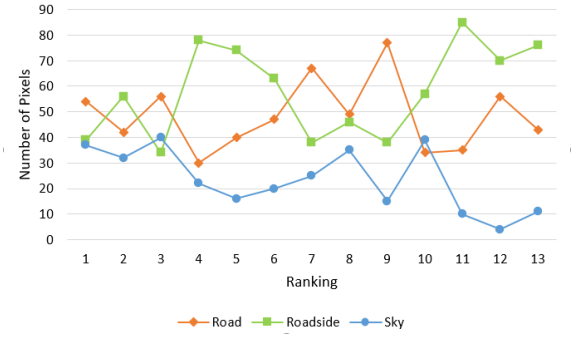


Fig. 2 Number of pixels in each children element

Although the results from the adults did not show a solid trend, the 4th to 9th ranks were ones where the number of pixels road surface almost 50 pixels or more, which has a value which accounts for more than 40% of the image. In the 1st to 3rd ranks, the number of pixels containing road surface is about 30 to 40 pixels, which is a value that occupies about 30% of the image. The children's results tended to have stronger trends than those of adults. From 1st to 3rd, it can be seen that all three elements of road surface, roadside, and sky are between 30 and 55 pixels. This percentage of each element which occupies the image is around 30-40%. In addition, the proportion of the road surface was found to be about 10% more than the percentage of the sky. In the 11th to 13th rank, the number of empty pixels is 0 to 11 pixels, which is the smallest among the 13 photographs, and the ratio of the image is less than 10%.

Luminance of each element

Fig.3 and Fig.4 shows the brightness of each element extracted from the 13 photographs, combined with the results of the paired comparison method for adults and children.

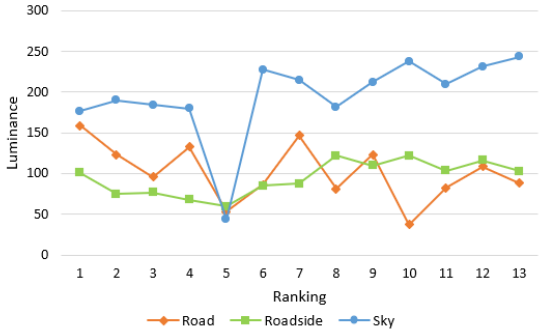


Fig. 3 Brightness of each element for adults

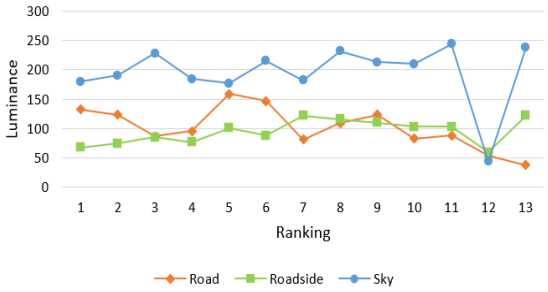


Fig. 4 Brightness of each element for children

For adults, it can be seen that the brightness of the sky is between 150 and 200 and the brightness of the road surface is between 100 and 160 in the 1st to 4th ranks. In addition, the sky, the road surface, and the side of the road are brighter in that order. It can be seen that in the 10th to 13th ranks, the brightness of the sky is relatively bright, 200 to 250, and the brightness of the road surface is relatively dark, 40 to 110. Also, focusing on the side of the road, it can be seen that the 1st to 7th ranks are between 50 and 100, and most of them are darker than the road surface. On the other hand, the 8th to 13th places are between 100 and 150, and it can be seen that most of them are brighter than the road surface. Focusing on the 10th to the lowest, many of them have a large difference in brightness between the sky and the road surface. As the luminance of the road surface is low, it is considered that the road surface is covered by shadow. (Fig.3)

The results of the children did not show as much tendency as adults, but it can be seen that the road surface was darker than the roadside in most of the 7th to 13th ranks, as in adults. Also, focusing on the side of the road, it can be seen that this is also between 50 and 100 in the 1st to 6th ranks, similar to adults. (Fig. 4)

Color

First, we will analyze by focusing on the colors of the road surface and the side of the road. Figures 5 and 6 show the colors extracted from each photograph and the ones with the highest selection rate for adults and children arranged in order from left to right. The colors are arranged in the order of the photographs with the highest selection rate from the left, and the colors that occupy the largest proportion in the photographs in order from the top.

In the same way, we also performed a comparative analysis from the color extraction of the roadside and road surfaces. For adults, 1st to 4th ranks are darker on the side of the road than on the road surface. The color of the road surface is mostly represented by yellow in the 13 photos. In the 5th to 9th ranks, there are no significant differences in the

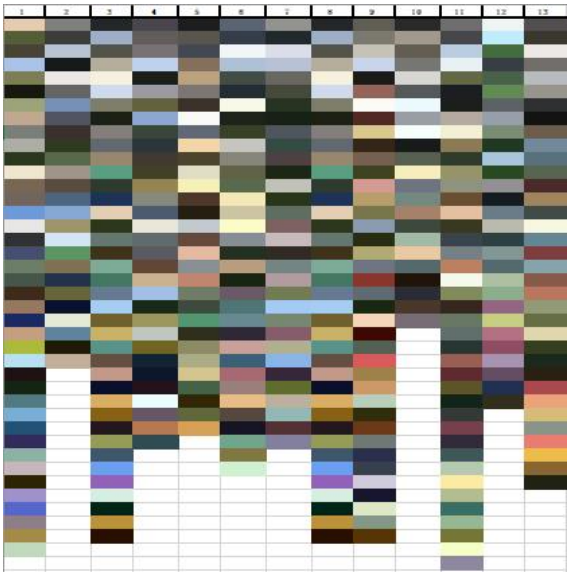


Fig. 5 The order of selected colors by adults from photographs

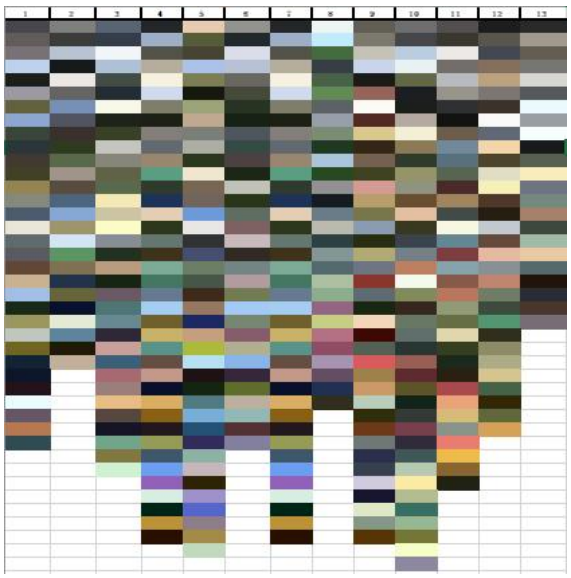


Fig. 6 The order of selected colors by children from photographs

colors of the road surface and the roadside, and the colors are similar. From 10th to 13th ranks, there is a difference in colors between the road surface and the roadside, with most of them being darker on the road surface than on the roadside. In addition, in the 1st to 4th ranks, the roadsides have similar colors and many types, and the road surface has the same color and only a few types. On the other hand, in the 8th to 13th ranks, many different colors can be seen on the roadsides. (Fig.5)

For children, from 1st to 3rd ranks, the colors on the roadside are dark with few colors, and most of the colors on the road surface are closer to cold colors. For 11th and 12th, it can be seen that most of the color

of the road surface is in the achromatic color range. From 5th to 10th ranks, various types and system colors can be seen on both the road surface and the roadside. (Fig.6)

Next, the analysis is performed focusing on the overall color tone.

For adults, we see that the selectivity tends to decrease as the number of warm colors increases, although the proportion is small. The 12th and 13th, cool colors accounted for most of the image, with a small ratio. On the other hand, the 1st to 4th contain cool colors evenly, regardless of whether the ratio is large or small.

For children, the 1st to 3rd have a calm color overall. The 11th to 13th contain almost no cool colors. In addition, the yellowish tint tends to increase as the selectivity decreases.

Consideration

It was difficult to see a tendency with adults for the number of pixels of each component, but there was a strong tendency with children. From the results, we think it is more likely that children are choosing the balance of the components that come into view than adults. Also, for children, the selection rate of roads with a high proportion of sky was high, while the selection rate of roads with a low proportion of sky was low, so we think roads with an open overhead may be preferred because they do not feel oppressed.

Regarding the brightness, since the selection rate of roads where the road surface is brighter than the roadside is high for both adults and children, I think that roads with shadows on the road surface were not really preferred.

As for colors, both adults and children have a low selectivity when warm colors increase and cool colors decrease, so the roads where emphasized colors are sporadic were not very popular. Cool colors that make up the whole of the color, also includes empty color, and we can consider that the 11th – 13th ranks for children do not include cool colors.

COGNITIVE MAP SURVEY

Experiment Contents

The cognitive map survey was conducted on children aged 10 to 12 who attend school A or B and 9 adults aged 20 and over who attend a regular university. Children drew a map of the road they take to school and its surroundings on an A2 size blank piece of paper and 12 colored pencils (Fig. 7, Fig. 8). Elements were extracted and analyzed for each elementary school. From the cognitive maps, 40 sheets from each elementary school was randomly selected for analysis. For adults, we had them draw a map of the surrounding university on a B3 size blank piece of paper and 12 colored pencils. Elements were extracted and analyzed. For the elements, what was drawn on the cognitive map was extracted by dividing it into letters and pictures. In this study, we focused on the colors used in the extracted elements, and analyzed the impression in the street space.

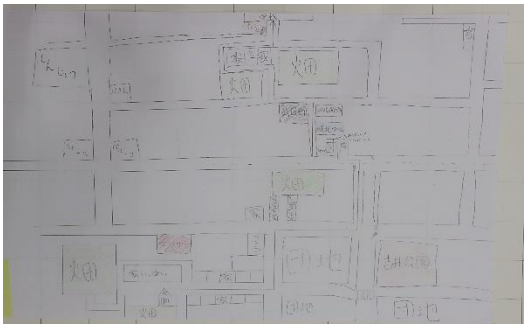


Fig. 7 cognitive map of school A

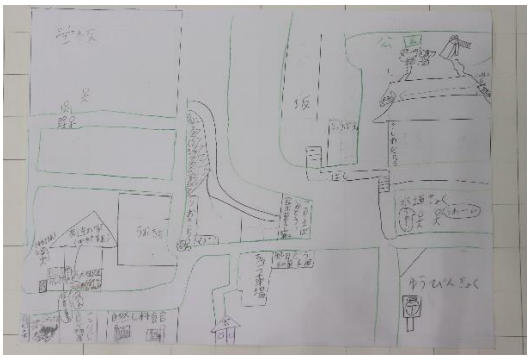


Fig. 8 cognitive map of school B

Experimental result

Children's cognitive map

Fig. 9 and Fig. 10 elements drawn on the child's cognitive map are extracted and classified, and the colors used are represented by school by combining the elements drawn in pictures and the elements drawn in letters.

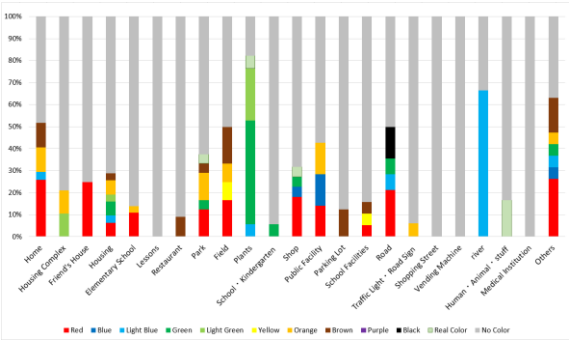


Fig. 9 Colors used in the cognitive map of school A

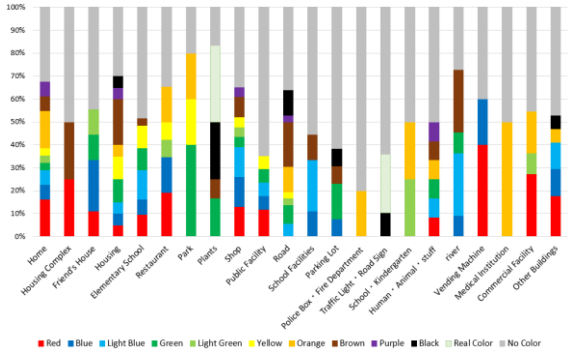


Fig. 10 Colors used in the cognitive map of school B

It can be seen that school A located in the suburbs has more elements drawn without using colors than school B located in the city. In addition, purple is used in school B, but was not used in school A. It can be seen that there are fewer elements drawn in black at School A. Focusing on the text elements, we can see that red is used for homes, friends' homes, elementary schools, fields, shops, public facilities, and roads. Also, yellow or orange was frequently used in parks, fields and public facilities. (Fig. 9) At School B, it can be seen that more than 60% of many elements are colored. Focusing on the text elements, it can be seen that red is often used in homes, apartments, restaurants, vending machines, and commercial facilities. In addition, yellow or orange was frequently used in homes, restaurants, parks, police/fire stations, medical facilities, and commercial facilities. Light blue or blue was frequently used in friends' homes, elementary schools, school facilities, and rivers. Among the many red colors used, school facilities and rivers are the elements that red was not used instead light blue or blue was often used. (Fig. 10)

Adult's cognitive map

Fig. 11 shows the elements drawn on the adult cognitive map extracted and classified, and the colors used are shown by combining the elements drawn with pictures and the elements drawn with letters.

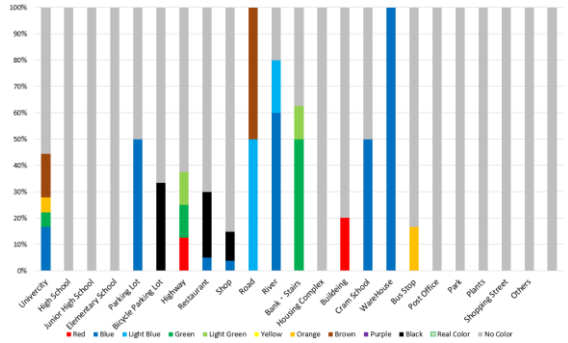


Fig. 11 Colors used in the cognitive map of adults

The adult cognitive maps show that the average number of elements was about twice as many as children, but the colors used are considerably less. In addition, red, which was often used in children's cognitive maps, was rarely used. The place where colors were most used was the university. Places where blue or light blue was often used were universities, parking lots, roads, rivers, and warehouses.

Consideration

From the results of the children's cognitive maps, they tend to use red for the locations were they have pleasant memories of friends and family. For this reason, the areas in red are considered as a place with a fun image. Also, we should consider the fact that those from the elementary school located in the city were using many colors, as the bustling street space would be visible in vivid color from the child's point of view, compared to the elementary school is located in the suburbs. Therefore, we think that the place where many colors are used is a lively and good impression place.

On the other hand, in the adult cognitive maps, colors were rarely used, and red is rarely used, so we recognize the place itself, not the feelings and memories of the place.

CONCLUSION

We thought that adults and children might change the way they perceive colors in the street space depending on the height of their eyes. Actually, there was a difference in recognition not only from the height of the line of sight but also from the difference in how they use the city. As you can see from the results of the cognitive map, it was noticed that adults remember the places they often use, but the other places are not so memorable. On the other hand, it is being investigated with the cognitive map and the conversation with children that they have many memories and images of the places they draw.

In addition, children tend to choose the path based on the color information and the proportion of components that come into view, but as adults, they tend to choose the path based on brightness rather than color and components. From the results, it was found that adults and children interpret different ways of feeling safe and reassurance.

This time, we will extract colors that may differ from the actual colors, and understand the differences between children and adult colors. From this, we have the possibility of extracting the image of a district or facility. In the future, we will clarify the specific contents and differences depending on the samples.

REFERENCES

[1] Chris J. Boyatzsis, Reenu varghese, Children's Emotional Association With Colors. The Journal of Genetic Psychology, Vol. 155, Issue 1, 1994, pp.77-78.

[2] Hyun-min, Akira Ishiguchi, Emotional Expression and Emotional Recognition by Color and Form, Proceedings of the Japanese Psychological Association Conference, Vol. 70, 2006, pp. 2433-7609.

[3] Yukiko Shimada, Toddler's color emotions, Journal of the Society of Art Science Education, Vol.22, 2001, pp. 95-104.

[4] T. Sakai, Urban distortion in children's spatial perception,

[5] H. Tsukaguchi and K. Matsuda, Pedestrian route selection behavior analysis, Japan Society of Civil Engineers Papers, Vol. 2002, Issue 709, 2002, pp. 117-126.

7th Int. Conf. on Structure, Engineering & Environment (SEE), Pattaya, Thailand, Nov.10-12, 2021, ISBN: 978-4-909106070 C3051

STUDY OF THE TROPHIC STATUS AND ECOLOGICAL STATE OF THE COASTAL ZONES OF THE NATURAL MONUMENTS OF THE CHELYABINSK REGION (RUSSIA) OF THE TURGOYAK AND UVILDY LAKES

Irina Mashkova[1*], Anastasiya Kostryukova[1], Belov Sergey [1], Elena Shchelkanova[2] and Viktor Trofimenko[3]
[1]Institute of Natural Sciences and Mathematics, South Ural State University, Russia; [2]Institute of Linguistics and International Communications, South Ural State University, Russia; [3]South Ural State Humanitarian Pedagogical University, Chelyabinsk, Russia

ABSTRACT

Human impact on the hydro-ecological state of water bodies affects every stage of water ecosystem formation. Such organisms as phyto and zooplankton, which constitute the basis for trophic chains, are especially sensitive to the impact. Under the complex load, conditions that adversely change species composition, diversity, size, mass and dominance in plankton communities are created. Such a load has certain patterns of the spatial distribution of coastal geosystems with different stages of degression as a result of the direct recreational impact on hydrological natural monuments. So, studying basic patterns of anthropogenic succession in lake geoecosystem, exploring phyto and zooplankton communities, revealing natural and anthropogenic factors that determine their life cycles and stating relationships between separate indices of a hydroecological state of the lakes in South Ural and an anthropogenic load of geocomplexes near-by are of the utmost importance, especially for hydrological natural monuments. The current paper researches the trophic status of Lake Turgoyak, Uvildy (Russia) and the degradation level of the coastal zones. Complex samples were taken in the summer of 2020 and will be continued in the summer of 2021. Several criteria were used to determine the trophic status. They are the taxonomic structure and biomass of zooplankton, some hydroecological indices and canonical correspondence analysis (CCA). The degradation level of the coastal zones was rated according to the herbaceous vegetation, biodiversity, coverage density and anthropogenic load of the given territories. All the trophic classifications of the lakes were based on dividing the trophic continuum.

Keywords: Lake, Trophic Status, Eutrophic, Degradation Level, Zooplankton

INTRODUCTION

Most of the research works are related to practical requests and the state of large aquatic ecosystems that have economic, recreational significance or belong to specially protected natural objects Chelyabinsk region [1]-[3]. There are many lakes in the Chelyabinsk region. Their numbers range from 1193 to 3170 [4], [5]. The lakes are located unevenly, the largest number of them is located in the northern and eastern parts of the region. They are located in different natural zones: mountain-forest, forest-steppe and steppe

At the end of the XX century, the spontaneous recreational development of the water bodies of South Ural led to the unauthorized development of coastal territories. Spontaneously organized nature management has increased the territorial contrast. As a result, a rather complex hierarchical network of natural and anthropogenic coastal territories was formed on the shores of tectonic lakes, with the degree of degression changing naturally in space. There are articles on the eutrophication of water bodies, which leads to restructuring the phytoplankton community, changing seasonal dynamics of biomass, and increasing the importance of individual species [6]. At that time, there were many articles related to the identification of indicators of the ecological state of water-bodies under anthropogenic impact both [7] Thus, phytoplankton communities of lakes were studied to identify indicator species of phytoplankton suitable for determining the water quality in the water-body and its trophic capacity [8]. It was found out that with an increase in the eutrophication rate, phytoplankton is one of the first to react to changes in habitat conditions [9]-[11]. Was shown that when the trophic status of water-bodies changes from oligotrophic to eutrophic, the number of species, varieties and forms increases, which begins to gradually decrease after the ecosystem reaches a certain critical level, with a minimum reached in highly polluted hypertrophic waters [11], [12].

The lakes of the Uvildy zone are actively used as sources of drinking water and industrial water supply, for drainage and recreation, for fishing purposes. The authors of this article have repeatedly studied the relationship of the trophic level of aquatic ecosystems of the forest zone of the Chelyabinsk region using

quantitative and qualitative methods for assessing the phytoplankton community [13]-[16].

The lakes under study are located in the Eastern foothills and mountains of the Southern Urals. Their location within the above-mentioned territories contributed to the wide development of tourism, recreation and healthcare services [4], [5]. The birch-pine forests prevailing in the catchments, as well as the lime and spruce forests, increase the attractiveness of the territory. On a ten-point scale, most of the parameters of the natural and recreational potential of water bodies are within 6-9 points [5], [6]. Most recreation facilities near the water bodies are concentrated in the area of twenty-minute walking distance from bus stops and railway stations, which determines the prospect of further development of recreation infrastructure in the study area.

Due to the increasing anthropogenic load on water bodies and the contrasting recreation, there was a problem of organizing a high-quality landscape and recreational structure of lake ecosystems. The purpose of this study is to carry out the zoning of the coastal landscape and recreational zones and the ecological state of coastal territories of tectonic lakes at various spatial levels.

MATERIALS AND METHODS

Study Area

Lake Uvildy is located in the north of the Chelyabinsk region (Fig. 1), 80 km northwest of Chelyabinsk. The lake is a natural monument, and since the 1970s it has been included in the international list of the most valuable lakes in the world. The main morphometric parameters of Lake Uvildy are: the height above sea level is 272 m, the water surface area is 68.1 km2, the maximum and average depths are 38 and 13 m [4]. The lake is a typical tectonic water body located in a deep front fault. The shores of Lake Uvildy are strongly indented by peninsulas and bays. The western and southwestern parts are characterized by a significant rise in depth [4]. Lake Uvildy belongs to the group of low-water basin lakes. The water is completely renewed in 17 years. Most of the winding coastline is covered with pine and mixed forests. The water in the lake is fresh, according to its chemical composition it belongs to the bicarbonate-calcium, and according to the ratio of ions - to the sulfate-sodium [4]. In the catchment area of the lake, there are sources of sapropel mud and radon, which contributed to the development of national resorts [4], [5]. The total volume of water in the lake is about 1000 million cubic meters. The bottom of the lake is sandy, with pebbles and silt. The water in the lake warms up very slowly due to the great depth, currently, it has a transitional status between oligo - and mesotrophic. In the coastal zone, over 90% of the forest stand is pine forests, the rest is birch and alder. As a result of a decreasing water level in the lake in the 1985-1990-s, the coastal part of the shallow waters was exposed on an area of about 200 hectares, and woody vegetation appeared on 10-15 % of this area [13]. Since the mid-twentieth century, Lake Uvildy has been used for recreational purposes. There are about seventy recreation centres, several sanatoriums, children's health camps and private cottages on its shores. Almost the entire coastline is built up (except for small areas in the south and northwest of the lake).

Lake Turgoyak belongs to the Eastern Foothill Limnological Region [4]. The main morphometric parameters of Lake Turgoyak are the following: the area of the lake is 26.4 km2, the length is 6.9 km, the maximum width is 6.3 km, the length of the coastline is 27 km. The lake is located in a deep intermountain basin, between the Ural-Tau and Ilmensky ridges at an altitude of 320 m above sea level. This is the deepest lake in South Ural. The maximum depth reaches 34 m, and the average is 19.2 m [4]. Stony soils (granites) are the most widespread in the catchment area, their outcrops are often found on the surface in the form of entire massifs and rock outcrops (the northern and eastern shores of the lake) and the form of clots and bolder stones on the mountain slopes. The soil layer covering granite massifs is low-power (0.3-0.5 m), unevenly podzolic in composition, and in river valleys, it is with an admixture of serozem. The hydrographic network of the catchment area is poorly developed - only six rivers and streams with a total length of 17 km. There are no marches on its territory, and a third of the area is occupied by the lake. A lake basin is of tectonic origin. It does not have a definite geometric shape; it is relatively rounded. At a distance of about 200 m from the shore, the depth of the lake reaches 15-18 m. The role of surface runoff in the water supply of the lake is small due to the small size of the catchment area. The total length of flows within the catchment area does not exceed 20 km. Groundwater plays a significant role in the nutrition of the lake. The nutrition of all aquifers occurs through the infiltration of atmospheric precipitation.

The catchment area of the lake is located in a zone of a sharply continental climate. The annual amplitude of the air temperature in the studied area is 33.6 °C. Winter is cold, long, and summer is warm but relatively short. A characteristic feature of the area is the late termination of spring and early resumption of autumn frosts in the air and on the soil surface. The Siberian anticyclone plays an important role in the formation of the climate in the Urals in winter, as well as cyclonic activity on the Arctic front. Intrusions of Arctic air masses lead to sudden weather changes. It is often influenced by southern cyclones moving from the Black, Caspian and Aral Seas, as well as «diving» cyclones from the Barents Sea [4]. The average annual precipitation is 496 mm. Most of

the precipitation falls during the warm period of the year with a maximum in July.

Field expedition studies were conducted in 2017-2021 on the lakes Uvildy, Turgoyak. Five sites were selected for the study on Lake Uvildy and Lake Turgoyak. The coordinates of the sites of Lake Uvildy: site 1 - 55 ° 32'9.13 "N, 60 ° 25'34.05" E, site 2 - 55°32'37.8"N 60°26'14.5"E, site 3 - 55°33'11.0"N 60°30'07.7"E, Site 4 - 55°31'12.1"N 60°34'26.5"E, site 5 - 55°28'45.4"N 60°29'36.0"E. Coordinates of Lake Turgoyak's sites: Site 1 - 55°10 '42.9"N 60°01'56.2" E, site 2 - 55°10'41.1"N 60°05 '43.9" E, Pad 3-55°09 '19.2"N 60°06 '35.3" E, Pad 4 - 55°07'44.6"N 60°04 '12.6" E, Pad 5 - 55°07'56.9"N 60°01'54.5" E. The selected sites are located in areas with different degrees of a recreational load of the coast (various sanatoriums, recreation centres, settlements).

To prepare for measurements and measure recreational load, the methods of trial areas, transect, mathematical-statistical and registration-measuring methods were used, according to OST 56-100-95 [17]. The degression stages (from 1 to 5) were determined by the ratio of the ground cover surface trampled to the mineral horizon to the total surface of the studied area (from 1.0 to 25.0 %, respectively) [17]. To assess the degression of forest recreational areas, the method of test sites in recreation areas with a size of at least 100 x 100 m. The level of degression at the test site was determined by an integral generalized assessment of fifteen characteristic criteria for the anthropogenic transformation of geosystems on a five-point scale. The estimated number of one-time visitors to the territory of parks, forest parks, forests, green zones was determined according to SP 42.13330.2016 (SNiP 2.07.01-89) [18].

Sampling of Zooplankton

Zooplankton was caught in the littoral part of the lakes. An automatic bathometer with a capacity of 5 litres was used for catching. The method of weighted average samples was applied. The volume of the selected water was, depending on the density of plankton, from 20 to 50 litres. The sample was concentrated immediately using a sieve from gas No. 64 to a volume of 35 ml. The work is started in May and is planned to finish in November. 25 samples have been worked out. The samples were examined on the day of collection. The material was fixed with 70° alcohol. To determine the species, classical determinants were used [19]-[20].

Water Quality Analysis

The following instream parameters including pH, dissolved oxygen (DO), and water temperature (WT) were measured in situ by a Portable Meter (Multitest IPL-513, Semico Ltd, Russia, Novosibirsk). Salinity (SALIN) were measured in situ by a Portable Meter (Multitest KSL-111, Semico Ltd, Russia, Novosibirsk) Air temperature was determined with a mercury thermometer.

At each site, water samples were also collected for further laboratory analysis including nitrate-nitrogen (NO_3^-), nitrite–nitrogen (NO_2^-), ammonium–nitrogen (NH_4^+), chlorides (Cl^-), sodium (Na^+), potassium (K^+), total hardness (H), calcium hardness (Ca^{2+}), bicarbonates (HCO_3^-), permanganate oxidability ([O]), total iron (Fe). All these parameters were measured in the lab of the Department of Chemistry of South Ural State University according to the standard methods. For spectrophotometric analysis the Spectrophotometer KFK-3 was used.

Data Analysis

The calculation of animal biomass was carried out according to the equations of proportional growth. Saprobity is determined by Pantle Buccu. All mathematical calculations and diagrams were performed in Excel 7.0. To assess the similarity of plankton in different lakes and to analyze the influence of abiotic factors on the formation of a zooplankton community, the Chekanovsky-Sorensen coefficient was used, which was determined using GRAFS [21].

RESULTS AND DISCUSSION

Tables 1 and 2 shows the results of physicochemical analysis of water in the sampling sites Lake Uvildy and Lake Turgoyak.

The field studies revealed the landscape differentiation of the catchment areas. 3 landscapes, 15 localities were revealed within the watershed of Lake Uvildy, [5]; 2 landscapes, 5 localities were revealed for Lake Turgoyak. More detailed landscape differentiation is revealed for the coastal 300-meter zone, which is intensively used in recreation. 101mesogeosystems are distinguished for Lake Uvildy; more than 40 – for Lake Turgoyak.

The area of recreation facilities near the studied lakes varies from 0.5 to 20.0 hectares, and the number of vacationers from 20 to 1500 people. The maximum one-time recreational load on the coastal territories of lakes ranges from 5 to 120 people/ha. The prevailing load is 25-50 people/ha since most facilities are represented by small recreation centres, where the maximum occupancy of vacationers is observed at this load.

The territorial pattern of the recreational infrastructure and especially its density have left a significant " imprint "on the formation of the spatial "pattern" of the degression of coastal geosystems of lakes. The assessment of the stages of degression of geosystems was based on 5 criteria according to the

matrix method of introducing weight parameters of degression.

Table 1 Physicochemical parameters Lake Uvildy

Chemical parameters	Site				
	1	2	3	4	5
TW, °C	24	24	22	22	21
DO, mgO/l	4.4	5.2	3.9	3.4	2.95
pH	8.45	8.47	8.86	8.89	8.95
SALIN, mg/l	192.3	194.9	195.5	209.4	215.1
NH_4^+, mg/l	0.39	0.42	0.75	0.95	0.96
NO_3^-, mg/l	2.48	1.67	2.51	2.51	3.34
NO_2^-, mg/l	-	-	0.008	0.006	0.005
Cl^-, mg/l	10.65	9.23	11.85	12.56	16.65
Na^+, mg/l	2.53	2.65	2.80	3.98	4.08
K^+, mg/l	1.79	1.59	1.80	1. 96	2.80
HCO_3^-, mmol/l щ	3.0	3.0	3.6	3.3	3.3
Ca^{2+}, mmol/l	0.08	0.08	0.18	0.19	1.18
H mg-eq/l	3.75	3.85	3.65	4.81	4.92
[O]	7.56	8.86	8.90	8.92	9.06

Table 2 Physicochemical parameters Lake Turgoyak

Chemical parameters	Site				
	1	2	3	4	5
TW, °C	21	21	21	18	21
DO, mgO/l	5.4	4.4	5.2	5.6	5.6
pH	7.54	7.43	7.58	6.93	7.41
SALIN, mg/l мир	190.1	191.4	185.5	192.3	194.9
NH_4^+, mg/l	0.08	0.05	0.13	0.02	0.13
NO_3^-, mg/l	1.46	2.46	2.79	2.05	1.51
NO_2^-, mg/l	-	-	-	0.01	0.01
Cl^-, mg/l	3.54	4.01	5.33	13.74	7.53
Na^+, mg/l	0.12	1.04	1.13	3.01	2.05
K^+, mg/l	0.56	0.66	1.36	3.49	5.31
HCO_3^-, mmol/l щ	1.2	1.15	1.2	1.4	1.35
Ca^{2+}, mmol/l	0.04	0.04	0.04	0.03	0.03
H mg-eq/l	1.45	1.75	1.55	1.85	1.65
[O]	6.16	7.37	8.17	7.05	7.37

According to the results of our research in 2017 in the three-hundred-meter coastal zone of the lake about 8 % of the territory is represented by geosystems with the 5th stage of degression, 27 % of the territory – with the 4th stage, about 65 % of the territory is with stage 2-3 [5]. In a similar zone of Lake Turgoyak 9 % of the territory is represented with stage 5, 26 % – with stage 4 and 65 % – with stage 2-3.

By 2021, there have been changes for the worse (Table 1). We calculated the ratio of taxa Rotifera (R): Copepoda (C): Cladocera (Cl), at which we took Cladocera as a unit (Table 3). The deterioration is associated with an increasing degree of degression as a result of an increasing number of vacationers. The increase in the load on the lakes is associated with quarantine measures for the coronavirus, which did not allow the population to leave the region.

Table 3 The ratio of the main zooplankton taxa in the lakes Uvildy and Turgoyak, depending on the degree of degression of the territory

Lake	Site	Degression degree		Relation of zooplankton groups R: C: Cl
		2017	2021	
Turgoyak	1	1	1	0.3:1.15:1
	2	4	4	1:1.5:1
	3	5	5	2.5:1.8:1
	4	2	5	2.2:1.6:1
	5	3	4	1.2:1.5:1
Uvildy	1	2	2	0.9:1.5:1
	2	1	1	0.2:0.19:1
	3	3	4	1.3:1.6:1
	4	4	4	1.5:1.8:1
	5	5	5	2.5:1.8:1

The 4-th and 5-th s degrees of degression prevail on the camping sites (Fig. 1) located not far than 50 m from the lake. The 3-d degree is at a distance of 50-200 m from the lake. The 2-nd degree dominates at a distance of 200-500 m.

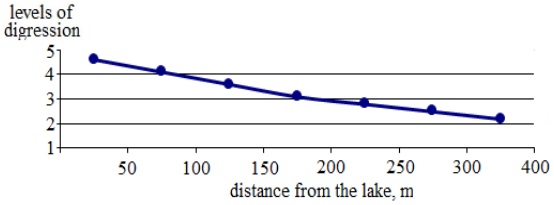


Fig. 1 Dependence of the remoteness of the territory from the lake's edge and the stage of its degression on the territory of camping sites.

Figure 1 shows that the decrease in the degree of degression on the territory of camping sites is almost directly proportional to the square of the distance from the lake. A significant improvement in the ecological state is observed here already at a distance of more than 200 m from the edge of large tectonic lakes.

When moving away from the lake's edge within large recreation centres, the degree of degression of the territory does not practically change, slightly decreasing from a distance of more than 200 m. On average, the 4-th degree of degression dominates (Fig. 2).

When moving away from the lake's edge within small recreation centres, the degree of degression of the territory decreases in proportion to the distance from the water bodies. At a distance of up to 150-200 m from the edge of water bodies, the 4-5 degrees of

digression dominates.

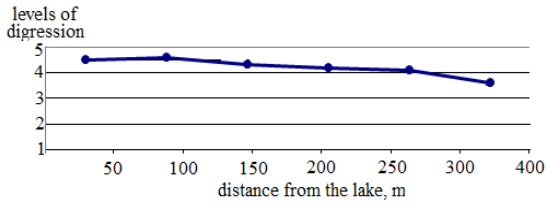


Fig. 2 The dependence of the remoteness of the territory from the lake's edge and the degree of its degression on the territory of large recreation centres.

Then degree 3 prevails, and areas with the 2nd one appear (Fig. 3).

A close relationship between the maximum recreational density and the degree of degression of the coastal territory of lakes is revealed (Fig. 3).

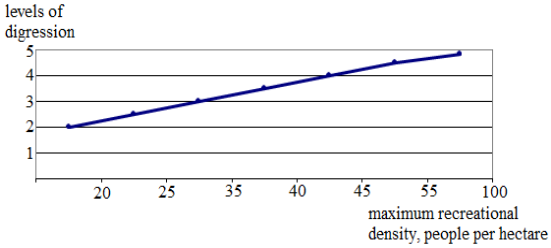


Fig. 3 The dependence of the degression of the territory on the recreational density.

In the plan, the areas with the 4-5 stage of degression at any of the considered spatial levels in the coastal territories have a radial linear-nodal or linear-block pattern. Nodes correspond to recreation facilities, lines are trails, roads and communications. In most recreation centres, geosystems with degrees 4-5 are distributed at a greater distance from lakes than similar geosystems of camping sites.

For coastal geosystems with the 3rd "threshold" degree of degression, the recreational density most often corresponds to from 20-25 (in spruce forests) to 40 people/ha (in birch and birch-lime forests).

Giving a brief characteristic of the distribution of zooplankton in lakes, it should be noted that Rotifera is distributed fairly evenly across all sites, with a total average number from 1176 animals/m^3 (Lake Turgoyak) to 2517 animals/m^3 (Lake Uvildy). Concerning crustaceans, the differences between the sites are very large. Cladocera is the leading group of zooplankton, prevailing in taxonomic diversity, occurrence, and coenotic significance. The density and biomass of zooplankton of Lake Turgoyak at sites 1 (5912 animals/m^3, 0.5323 g/m^3, respectively) and 2 (5731 animals/m^3, 0.4134 g/m^3) have the highest values for the lake, at site 3 - the lowest (401 animals/m^3, 0.0211 g/m^3), sites 4 (1452 animals/m^3, 0.0842 g/m^3) and 5 (1853 animals/m^3, 0.1322 g/m^3) occupy an intermediate position according to these indicators. The density and biomass of zooplankton of Lake Uvildy at sites 1 (15918 animals/m^3, 1.5453 g/m^3, respectively) and 2 (15731 animals/m^3, 1.2154 g/m^3) have the highest values for the lake, at site 5 - the lowest (1251 animals/m^3, 0.0617 g/m^3), sites 3 (8531 animals/m^3, 0.5842 g/m^3) and 4 (7867 animals/m^3, 0.4928 g/m^3). Table 1 shows that the ratio of the main groups of zooplankton varies depending on the state of the environment. The higher the degression of the territory, the greater the impact on the ecosystem, the more Rotifera are in the water, some of which are very stable.

CONCLUSION

It was determined that the natural basis for recreation is areas, mesogeosystems and facies (on the example of tectonic lakes), with territorial formations where recreation facilities are formed, playing the key role. The catchment areas of the studied lakes are more often represented by several landscapes and localities consisting of several dozen tracts. It was found that moving from the peripheral areas of recreational zones to the coasts and in the direction of territories with transport accessibility, the degree of degression increases from the 2nd to the 4th stage, and the recreational load increases from 5-10 to 100 people/ha or more. On 18-45 % of the coastal territories, the allocated maximum recreational density exceeds the permissible values according to OST 56-100-95 and ranges from 0.3 to 3-4 maximum permissible recreational loads. Most often, the contours of coastal geosystems with one degree of degression coincide with the contours of the landscape and recreational zones of the 3rd order. It is established that the larger the recreation facility is, the smaller the spatial differences in the ecological state of its geosystems. In general, littoral zooplankton is more abundant in those parts of the lake water area where there are optimal conditions for its development, the lowest recreational load and the lowest degree of degression.

ACKNOWLEDGMENTS

This research was funded by RFBR and Chelyabinsk Region (Russia), project number 20-45-740005.

REFERENCES

[1] Namsaraev Z., Melnikova A., Komova A., Ivanov V., Rudenko A., and Ivanov E., Algal bloom occurrence and effects in Russia, Water Vol. 12, Issue 1, 2020, 2020285.

[2] Wang J., Wu S., Fan B., and Chen W., Distribution Features of Phytoplankton and Its Correlation with Environmental Factors of Baima

Lake, IOP Conference Series: Materials Science and Engineering Vol. 730, Issue 1, 2020, 012055.
[3] Pratiwi H., Damar A., and Sulistiono, Phytoplankton community structure in the Estuary of Donan River, Cilacap, Central Java, Indonesia, Biodiversitas Vol. 19, Issue 6, 2018, 2104-2110.
[4] Andreeva M. A., Lakes of Middle and South Ural, South-Ural. Publishing house, Chelyabinsk, 1973, 270 p. [Russian]
[5] Zakharov S. G., Lakes of Chelyabinsk region, ABRIS, Chelyabinsk, 2010, 128 p. [Russian]
[6] Tkacheva V. A., and Rogozin A. G., Ecology of Lake Turgoyak, IGZ UrO RAS, Miass,1998, 154p. [Russian]
[7] Golubkov M. S., Primary production of plankton along the salinity gradient: dissertation ... candidate of Biological Sciences: 03.02.10 / Golubkov M. S., St. Petersburg, 2010, 247 p. [Russian]
[8] Song Y., Qi J., Liu L., Deng L., Liu H., Bai Y., Liu H., and Qu J., Eutrophication status and phytoplankton community structure in Chenghai Lake in summer and winter Huanjing Kexue Xuebao, Acta Scientiae Circumstantiae Vol. 39, Issue 12, 2019, 4106-4113.
[9] Suda H., Tanaka M., Oyagi M., Nobori M., and Yagi A., Water quality and compositions of the phytoplankton and zooplankton before and after building construction in Lake Fukami-ike, Japan, International Journal of GEOMATE Vol. 10, Issue 4, 2016, 1983-1988.
[10] Wang J., Wu S., Fan B., and Chen W., Distribution Features of Phytoplankton and Its Correlation with Environmental Factors of Baima Lake, IOP Conference Series: Materials Science and Engineering, Vol. 730, Issue 1, 2020, 012055.
[11] Najmus S. K., and Naznin A. T., Freshwater algal tolerance to organic pollution: a review, Poll Res. Vol. 39, Issue 4, 2020, 1297-1301.
[12] Yang Y., Du C., Qian Z., Jiang C., Chen H., Yu G., and Li Y., Phytoplankton Community Structure and Its Influencing Factors in Nanhan Polder Area of Dongting Lake, Research of Environmental Sciences, Vol. 33, Issue 1, 2020, 147-54.
[13] Kostryukova A.M., Mashkova I.V., Krupnova T.G., and Egorov N.O., Phytoplankton biodiversity and its relationship with aquatic environmental factors in Lake Uvildy, South Urals, Russia, Biodiversitas, Vol. 19, Issue 4, 2018, 1422–1428.
[14] Kostryukova A.M., Krupnova T.G., Mashkova I.V., Gavrilkina S.V., and Egorov N.O., Phytoplankton diversity in three lakes of South Ural, Russia, Biodiversitas, Vol. 19, Issue 4, 2018, 1459–1467.
[15] Kostryukova A.M., Mashkova I.V., Trofimenko V.V., and Vasilieva E.I., Taxonomic structure of phytoplankton in Shershnevskoe Reservoir (Chelyabinsk, Russia), an artificial lake, IOP Conference Series: Earth and Environmental Science Vol. 351, Issue 1, 2019, 012001.
[16] Kostryukova A., Mashkova I., Shchelkanova E., Trofimenko V., and Kornilova A., Analysis of water quality of rivers and reservoirs in Chelyabinsk region, South Ural, International Journal of GEOMATE Vol. 18, Issue 67, 2020, 120–127.
[17] Industry-standard 56-100-95, Methods and units for measuring recreational loads on forest natural complexes, 1995 [Russian].
[18] SNiP 2.07.01-89 Urban planning. Planning and construction of urban and rural, Moscow, 1994, 120 p. [Russian]
[19] Determinant of freshwater invertebrates of the European part of the USSR, Nauka, 1977, 290 p. [Russian]
[20] Determinant of freshwater invertebrates of Russia, Publishing house of ZIN RAS, St. Petersburg, 1994, 396 p. [Russian]
[21] Nowakowski A.B., Possibilities and principles of operation of the software module "Graphs", Automation of Scientific Research, Issue 27, 2004, 2-29. [Russian]

7th Int. Conf. on Structure, Engineering & Environment (SEE), Pattaya, Thailand, Nov.10-12, 2021, ISBN: 978-4-909106070 C3051

INFLUENCE OF DEGRADATION OF COASTAL ZONES ON THE SPECIES STRUCTURE OF PHYTOPLANKTON OF LAKES UVILDY AND TURGOYAK (SOUTH URAL, RUSSIA)

Anastasiya Kostryukova[1], Irina Mashkova[1], Sergey Belov[1], Elena Shchelkanova[2]and Viktor Trofimenko[3]
[1]Institute of Natural Sciences and Mathematics, South Ural State University, Russia; [2]Institute of Linguistics and International Communications, South Ural State University, Russia; [3]South Ural State Humanitarian Pedagogical University, Chelyabinsk, Russia

ABSTRACT

The current paper aims at analyzing the species structure of the phytoplankton community of two reservoirs on the territory of South Ural. The given water bodies are of different trophicity, namely, oligotrophic Lake Turgoyak and oligomesotrophic Lake Uvildy. Both lakes, being natural monuments, are subject to intensive recreational use. Based upon the research the current paper reveals spatial patterns in the distribution of recreational load on the coastal geosystems and the level of anthropogenic transformation of the territory. Concentric zones of recreational digression have been created around the lakes. They are of an approximately similar increase in the degree of geosystem transformation when moving to the lake edge. Some signs allow forecasting changes in the species composition of phytoplankton communities and the trophic status of the lakes depending on the degradation of the coastal zones. Diatoms (Bacillariophyta) have been dominant in plankton phytocoenosis of oligotrophic Lake Turgoyak and oligomesotrophic Lake Uvildy. Green and blue-green algae biodiversity has grown in oligomesotrophic Lake Uvildy.

Keywords: Phytoplankton, Lake, Taxonomy, Degression, Trophicity

INTRODUCTION

Plankton communities, especially their space-and-time reactions to the anthropogenic stress of the adjusting zones, are often viewed as one of the key parameters when water ecosystems are studied [1]-[4]. Various parameters of the aquatic environment have an impact on the state of phytoplankton communities. Niu et al. [1] established patterns of anthropogenic impact on phytoplankton based on long-term observation data of the Pearl River estuary. The constant influx of pollutants as a result of the discharge of wastewater and the washout of agricultural fertilizers from the catchment area has shifted the ratio of nutrients such as nitrogen and phosphorus towards an increase in nitrogen. This changed the species composition of the phytoplankton community of the studied water body. The species of the Bacillariophyta dominated in the early 1980s, then the species of the Ochrophyta and Miozoto became dominant in 2012-2016. The change in the species composition of diatoms (Dashahe Reservoir, China) [2] also occurred as a result of the increased anthropogenic load of nutrients (N and P). The combined predominance of planktonic and benthic species was replaced by the dominance of only planktonic species. The authors of [3] indicate that there was a change in dominant algae (cryptophytes were replaced by diatoms) as a result of improved water quality (decrease N) in the Yeongil Bay on the southeastern coast of Korea.

Currently, one of the important factors that can change the ecological state of various water bodies is intensive recreational activities that lead to any given stage of anthropogenic degradation of coastal zones. The heterogeneous recreational load caused by developing transport infrastructure and improving attractive coastal territory of water-bodies lead to the transformation of natural ecosystems. Unorganized mass recreation has a particularly negative effect.

There are not very many papers devoted to assessing the consequences of tourism activity on the state of water bodies. Tourism has a foremost impact on the soil and vegetation cover and tree and shrub vegetation [5], [6]. However, studies are showing that intensive recreational activity in the coastal zones of water-bodies leads to the intake of the increased amounts of biogenic elements, and, consequently, to the growth of certain species of macrophytic aquatic vegetation [6], which may lead to a deteriorating trophic status of water-bodies. Wang et al. [7] found a relationship between intense tourist activity and increased nitrogen levels in the Five-Color Lake (Jiuzhaigou Nature Reserve). This led to the growth of phytoplankton and filamentous algae. Also, tourist activity often leads to an increase in the amount of garbage left by tourists, littering of coastal areas and the water bodies themselves. This leads to a deterioration in the quality of the water. For example, the water quality of the West Lake Basin (Hangzhou, China) deteriorated with an increase in tourist traffic [8].

The Chelyabinsk Region belongs to the industrial regions of Russia (ferrous and non-ferrous metallurgy, fuel and energy industry, mechanical engineering). Pollution of water bodies in the Chelyabinsk region is one of the main environmental problems [9]. There are several hydrological natural monuments on the territory of the Chelyabinsk region (Russia), which have an exceptionally high biological conservation value. The existing anthropogenic stress threatens their natural conditions. At present, in addition to the impact of the industry in the pollution of water bodies, the contribution of tourism activities is also increasing. Lake Turgoyak and lake Uvildy, which are widely used for economic and recreational purposes, are especially vulnerable. Excessive anthropogenic load and the lack of proper arrangement of recreation areas lead to a significant deterioration of coastal territories and changes in the composition of aquatic biocenoses. Unfortunately, there are very few works devoted to assessing the impact of tourism activities on them, despite the great importance of the Turgoyak and Uvildy lakes for the region. They assess the degree of disturbance of the coastal area.

Phytoplankton is one of the most sensitive indicators of the state of water bodies. Previously, we studied the species composition of phytoplankton communities in Turgoyak and Uvildy lakes [10], [11]. The given work aims at identifying signs that allow forecasting changes in the species composition of phytoplankton communities of lakes depending on the degree of degression of coastal zones.

METHODOLOGY

Study Area

Two water bodies different in trophicity are taken as the subject of research. They are situated in South Ural: Turgoyak, an oligotrophic lake, and Uvildy, an oligomesotrophic lake (Fig. 1).

Lakes Turgoyak and Uvildy are large and deep lakes with a surface of more than 10 км[1]nd depth of more than 20 m. The morphology of the water bodies is given in Table 1.

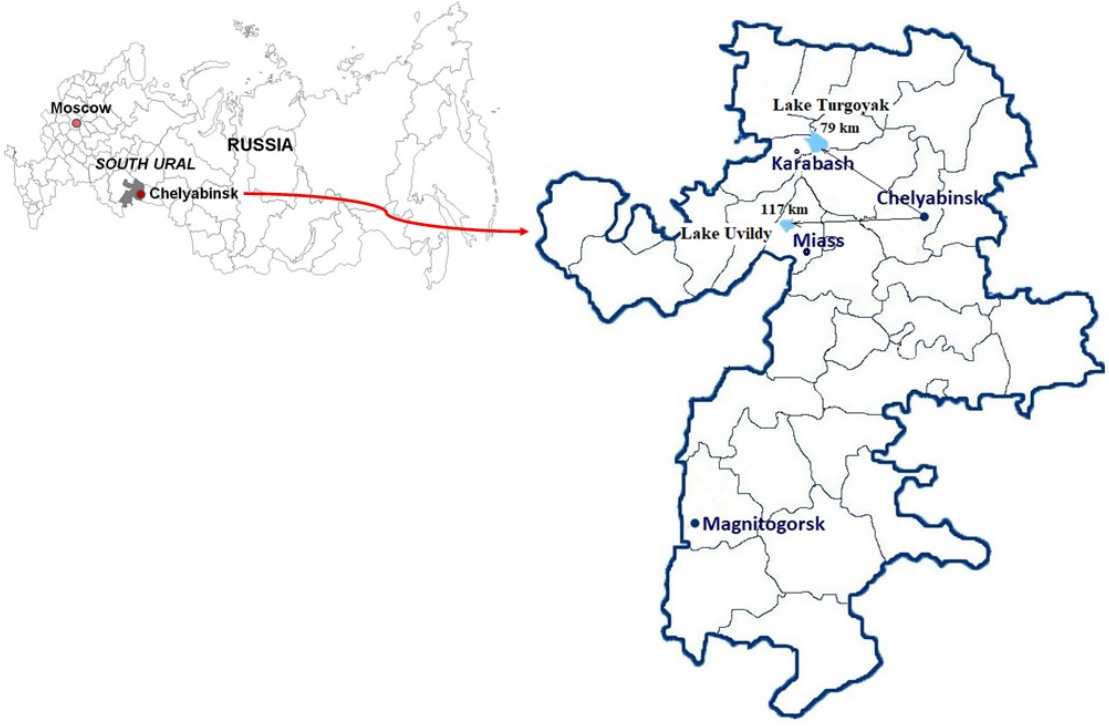


Fig.1 Quick map of water bodies.

Table 1 Morphological parameters of water-bodies

	Water-bodies	
	Turgoyak	Uvildy
High above sea level, (m)	318.9	272.0
Water surface, km^2	26.40	68.10
Water volume, mlnm^3	507.0	1014.0
Maximal depth, m	34.5	38.0
Average depth, m	19.2	13.0

Lake Uvildy is an oligo mesotrophic water body [10], [11]. The lake is one of the largest and unique lakes in the region. As a result of economic activity in the 1970-s (pumping about a quarter of the lake's water to the Argazinsky reservoir to supply Chelyabinsk), the reservoir shallowed a lot, with the water level fallen by almost 4 m. In the drainage zone, woody and shrubby vegetation has grown, which was flooded during the restoration of the water level in

2006. As a result, eutrophication has increased in coastal areas. The lake is also experiencing a recreational load. Along its shores, there are villages, sanatoriums and recreation centres, private houses. There are two facilities of the copper industry near the water body. Their performance has had an anthropogenic load on the landscapes nearby.

Lake Turgoyak is an oligotrophic lake with signs of mesotrophy [11]. The lake is located near the town of Miass. The lake also experiences a great recreational load. From 1952 to the early 90s, the water from Turgoyak was taken for economic purposes. The intake exceeded the average annual water balance of the lake.

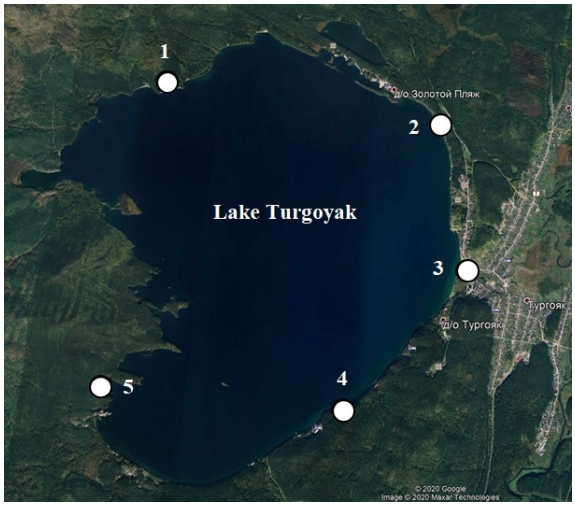
Both water bodies have the status of hydrological natural monuments.

Characteristics of Sampling Sites

The sampling was carried out during the vegetation period in June 2021 in 5 sites in Lake Uvildy and Lake Turgoyak (Fig. 2).

The characteristics of the sampling sites in Lake Turgoyak:

- site 1 - the coastal geosystems are represented by lime, lime-birch and lime-pine forests with almost completely preserved layering. The area is far from any recreation centres and large camping sites. To reach it you need to go through straits and swamps. The recreational load does not exceed 10 people/ha and is mainly associated with fishing, gathering mushrooms and berries, as well as local small-group camping holidays;
- site 2 - the coastal geosystems are represented by lime-pine and pine-birch forests with almost completely lost layering from anthropogenic impact. There are large recreation centres and large well-maintained camping sites on the territory. The recreational load ranges from 25 to 50 people/ha or more. Swimming, beach and camping holidays prevail;
- site 3 - the coastal geosystems are represented by sparse pine forests with lime and birch trees and meadow swampy glades of the City Beach with undergrowth almost completely lost from anthropogenic impact. The territory is dominated by a zone of stationary "wild" recreation. The recreational load ranges from 40 to 60 people/ha or more. For the beach, it is 1000-2000 people/ha or more. The swimming and beach recreation prevails;
- site 4 - the geosystems are represented by lime and lime-pine forests, where layering is noticeably disturbed by anthropogenic activity. The territory is occupied by camping sites and children's sports tent camps. The recreational load is 10-30 people/ha. Camping, sometimes swimming, beach and fishing holidays prevail;



a)



b)

Fig.2 Lake Turgoyak (a) and Lake Uvildy (b) with sampling sites.

- site 5 - the coastal geosystems are represented by lime, pine and lime-pine forests, where layering is significantly disturbed by anthropogenic activity. There are small recreation centres and camping sites on its territory. The recreational load ranges from 20 to 40 people/ha. Swimming, beach and camping holidays prevail.

The characteristics of the sampling sites in Lake Uvildy:

- site 1 - the geosystems are represented by lime and lime-pine forests, where layering is disturbed by anthropogenic activity. There are garden associations and fishermen's camping sites on the territory. The

area is slightly swampy and remote from public stops. The recreational load is 10-30 people/ha. Fishing and camping holidays prevail

- site 2 - the coastal geosystems are represented by lime, lime-birch and lime-pine forests with almost completely preserved layers. The territory is very far from any recreation centres or camping sites, as it needs to be reached through straits and swamps. The recreational load does not exceed 5 people/ha and is mainly associated with commercial recreation: hunting for mushrooms, berries;
- site 3 - the coastal geosystems are represented by lime-birch and lime-pine forests, with layering disturbed by anthropogenic activity. The territory is dominated by recreation centres and large camping sites. The recreational load ranges from 20 to 40 people/ha or more. Swimming, beach and camping holidays prevail;
- site 4 - the coastal geosystems are represented by lime-birch and birch forests with almost completely lost layering from anthropogenic impact. There are a recreation centre and large well-maintained camping sites on the territory. The recreational load ranges from 30 to 50 people/ha or more. Swimming, beach and camping holidays prevail;
- site 5 - the coastal geosystems are represented by lime-birch and birch forests with almost completely lost layering from anthropogenic impact. The territory is dominated by large recreation centres. The recreational load ranges from 30 to 60 people/ha or more. Swimming and beach holidays predominate, with rare camping holidays.

Assessing Recreational Degression of the Coastal Territories

Recreational degression is the process of negative changes in the biocenosis as a result of recreational exposure. The main signs of recreational digression are a trampled area, destroyed undergrowth, damaged trees, changing forest grasses to the meadow and then to weeds. The stage of recreational degression is the stage of changing biogeocenosis as a result of the recreational load [12]. There are 5 stages of degression:

- stage 1 is characterized by the absence of noticeable changes in the biocenosis as a result of human activity;
- stage 2 is minor changes;
- stage 3 is moderate changes;
- stage 4 is changes of a strong degree;
- stage 5 is almost completely degraded biocenosis.

The following methods were used to assess the degree of degression of the coastal territory:

- determination of the degree of anthropogenic transformation of geosystems [12]. This method determines the stages of recreational degression according to the degree of the relation of surface trampled to the mineral horizon of soil cover surface to the total surface of the studied area;
- methods for assessing the degression of natural complexes [13]. The methodology is based on an integral indicator based on a point-by-component assessment of 15 indicators of natural and anthropogenic genesis, identified according to the natural features of the landscape and the prevailing forms of anthropogenic impact;
- methods for assessing the stages of forest community degression [14]. In this method, the stages of recreational degression are determined depending on the surface of the trampled territory;
- methods for describing the stages of trail formation [15]. In this methodology, the stages of recreational degression are established depending on the state of the dominant trails in the recreation area.

Identification of Phytoplankton Species

At each site, samples were collected and filtered through a plankton net (mesh size: 100 μm). The retained organisms were transferred into glass containers. The collected material was preserved in 5% formalin.

Algae were analyzed using a magnification of 600× (Altami BIO 2T microscope, Altami Ltd, Russia, St. Petersburg.). Species were identified using handbooks [16], [17]. Taxonomic characteristics were specified following algae determinants [18], [19].

RESULTS AND DISCUSSION

The field landscape and ecological studies revealed that recreational facilities located near Lakes Uvildy and Turgoyak occupy from 40 to 80% of the length of the coastal zone and, as a rule, are closed into the single landscape and recreational complexes with a width of 200-300 meters (a zone of five-minute walking distance to the lakes). The vast majority of recreational facilities (more than 80%) belong to recreation centres. The maximum anthropogenic load, calculated through the recreational density of vacationers, is observed at recreation centres, garden associations and camping sites and is up to 100 people/ha or more. The average recreational density within recreation centres is 25-50 people/ha since the majority of recreational facilities represented by small recreation centres have maximum occupancy at this load. Such a recreational load has led to the formation of a very "motley" pattern of the degree of anthropogenic transformation of coastal geosystems of lakes. When the recreational load from vacationers approaches 30-50 people/ha, the 4-5 stage of digression is actively formed. However, if there is proper landscaping, it is possible to maintain a good condition even at a given recreational density.

It was also revealed that when the density of the path network in recreation areas is more than 200-250 m/ha, geosystems with 4-5 stages of digression predominate. As a result, the state of the coastal territory of Lake Turgoyak and Uvildy in the studied areas can be characterized as follows (Table 2).

Table 2 The degree of degression in the studied sites of Lakes Turgoyak and Uvildy

Site	Water-bodies	
	Turgoyak	Uvildy
1	1	2
2	4	1
3	5	3
4	4	4
5	4-5	5

The number of species of different departments of phytoplankton in the studied sites is presented in Table 3. Table 3 shows the dominance of diatom algae (Bacillariophyta) in plankton phytocenosis of the oligotrophic lake Turgoyak and the oligomesotrophic lake Uvildy. The biodiversity of green and blue-green algae has increased in the oligomesotrophic lake Uvildy. Comparison of the number of species of different departments of phytoplankton and the degree of degression of the site where sampling took place does not allow us to speak unambiguously about the relationship of these two parameters. For green algae, there is a tendency to increase species diversity with an increase in the degree of degression. This is due to the deterioration of trophic activity in these areas. The number of diatom species in the oligotrophic Lake Turgoyak mainly ranges from 10-12, regardless of the degree of degradation of the site. In other species, the picture is similar.

The dependence of the species diversity of diatoms on the degree of degradation is higher in Lake Uvildy with a higher degree of trophicity. The number of phytoplankton species is significantly less at sampling points with a higher degree of degression.

Table 3 Number of species of different divisions of phytoplankton in Lakes Turgoyak and Uvildy

Divisions	Sampling site				
	1	2	3	4	5
			Lake Turgoyak		
Bacillariophyta	12	11	10	5	11
Chlorophyta	1	4	3	4	6
Cyanobacteria	3	2	-	1	-
Euglenozoa	-	-	1	-	-
Ochrophyta	-	-	-	-	1
Miozoa	-	-	-	1	-
Charophyta	-	1	3	1	-
Total	16	18	17	12	18
			Lake Uvildy		
Bacillariophyta	15	11	5	6	6
Chlorophyta	2	7	4	6	2
Cyanobacteria	1	2	6	5	2
Euglenozoa	-	1	-	1	-
Ochrophyta	-	1	-	-	-
Miozoa	-	-	-	1	-
Charophyta	1	1	-	2	-
Total	19	23	15	21	10

CONCLUSIONS

A clear relationship between changes in the species structure of the phytoplankton community and the degree of degression of the sampling sites was not revealed. In the oligotrophic lakes Turgoyak and Uvildy, the algae of the Bacillariophyta department play the leading role in the formation of the plankton community. In the oligotrophic lake Uvildy with signs of mesotrophy, an increase in the proportion of Chlorophyta and Cyanobacteria is observed. In areas of water-bodies where the coastal territory is characterized by a 4-5 stage of digression, algae of the Chlorophyta department predominate in species diversity. The dependence of the species diversity of the remaining departments on the degree of degradation of coastal zones was not found.

ACKNOWLEDGEMENTS

This research was funded by RFBR and Chelyabinsk Region (Russia), project number 20-45-740005.

REFERENCES

[1] Niu L., Luo X., Hu S., Liu F., Cai H., Ren L., Ou S., Zeng D. and Yang Q., Impact of anthropogenic forcing on the environmental controls of phytoplankton dynamics between 1974 and 2017 in the Pearl River estuary, China, Ecological Indicators, Vol. 116, 2020, 106484.

[2] Lei Y., Wang Y., Qin F., Liu J., Feng P., Luo L., Jordan R.W., Jiang S., Garus-Oas C.H. and Julies E., Diatom assemblage shift driven by nutrient dynamics in a large, subtropical reservoir in southern China, Journal of Cleaner Production, Vol. 317, 2021, 128435.

[3] Kang Y., Moon C.-H., Kim H.-J., Yoon Y.H., Kang C.-K., Water quality improvement shifts the dominant phytoplankton group from cryptophytes to diatoms in a coastal ecosystem, Frontiers in Marine Science, Vol. 8, 710891.

[4] Mashkova I.V., Kostriykova A., Shchelkanova E., Trofimenko V. and Slavnaya A., Study of the zooplankton community as an indicator of the trophic status of reservoirs, International Journal of GEOMATE, Vol. 19, Issue 73, 2020, pp. 57-63.

[5] Liu Q. and Guan D., Non-polluted ecological impact of tourist activities in natural scenic area, Chinese Journal of Ecology, Vol. 24, Issue 4, 2005, pp. 443-447.

[6] Dynowski P., Senetra A., Źróbek-Sokolnik A. and Kozłowski J., The impact of recreational activities on aquatic vegetation in alpine lakes, Water (Switzerland), Vol. 11, Issue 1, 2019, p. 173.

[7] Wang L., Pan Y., Cao Y., Li B., Wang Q., Wang B., Pang W., Zhang J., Zhu Z. and Deng G., Detecting early signs of environmental degradation in protected areas: An example of Jiuzhaigou Nature Reserve, China, Ecological Indicators, Vol. 91, 2018. pp. 287-298.

[8] Sun Q. and Liu Z., Impact of tourism activities on water pollution in the West Lake Basin (Hangzhou, China), Open Geosciences, Vol. 12, Issue 1, 2020, pp. 1302-1308.

[9] Kostryukova A., Mashkova I., Shchelkanova E., Trofimenko V. and Kornilova A., Analysis of water quality of rivers and reservoirs in Chelyabinsk region, South Ural, International Journal of GEOMATE, Vol. 18, Issue 67, pp. 120-127.

[10] Kostryukova A., Mashkova I., Belov S., Shchelkanova E. and Trofimenko V., Short communication: Assessing phytoplankton species structure in trophically different water bodies of south ural, Russia, Biodiversitas, Vol. 22, Issue 8, 2021, pp. 3530-3538.

[11] Kostryukova A., Mashkova I., Shchelkanova E. and Trofimenko V., Retrospective analysis of phytoplankton community structure in water bodies of South Ural (Russia), IOP Conference Series: Earth and Environmental Science, Vol. 626, Issue 1, 2021, 012008.

[12] Industry-standard 56-100-95, Methods and units for measuring recreational loads on forest natural complexes, 1995 (Rus).

[13] Shaplygina T.V., Geoecological assessment of the state of natural complexes of the Curonian and Vistula spits, Immanuel Kant Baltic Federal University, Kaliningrad, 2010, pp. 1-197 (Rus).

[14] Kazanskay N.S., Lanina V.V. and Marfenin N.N., Recreational forests (state, protection, prospects of use), Timber industry, 1977, pp. 1-96 (Rus).

[15] Isakov N.S., Methods for identifying the recreational stability of the types of facies of the Kytlym midlands and displaying it on the schematic map, Landscape research in the Urals, 1985, pp. 82-92 (Rus).

[16] Yarushina M.I., Tanaeva G.V. and Eremkina T.V., Algae flora of water bodies of the Chelyabinsk region, Ekaterinburg, Ural Branch of Russian Academy of Sciences, 2004, pp. 3-304 (Rus)

[17] Al-Kandari M., Al-Yamani F. and Al-Rifaie K., Marine phytoplankton atlas of Kuwait's waters, Kuwait, Lucky Printing Press, 2009.

[18] Guiry M.D. and Guiry G.M., AlgaeBase. World-wide electronic publication, Galway, National University of Ireland, 2021, https://www.algaebase.org; searched on 28 June 2021.

[19] WoRMS Editorial Board 2019 World Register of Marine Species. Available from http://www.marinespecies.org at VLIZ.

7th Int. Conf. on Structure, Engineering & Environment (SEE), Pattaya, Thailand, Nov.10-12, 2021, ISBN: 978-4-909106070 C3051

EFFECT OF ELECTROLYZED WATER ON INHIBITION OF *Colletotrichum capsici*, CAUSING ANTHRACNOSE DISEASE OF CHILLI

Angkhana Chuajedton[1] and Kanda Whangchai[2,3]
[1]Department of Biology, Faculty of Science, Lampang Rajabhat University, Lampang, Thailand
[2]Postharvest Technology Innovation Center, Ministry of Higher Education, Science, Research and Innovation, Bangkok, Thailand
[3]Department of Biology, Faculty of Science, Chiang Mai University, Chiang Mai, Thailand

ABSTRACT

The mycelia of *Colletotrichum capsici* is one of the microbial contamination during postharvest on Solanaceae. This research investigated the effects of different electrolyzed water concentrations on inhibition of *Colletotrichum capsici*, causing anthracnose disease of chilli. The mycelial disks were soaked with acidic electrolyzed water (pH 1.95, ORP >1,100 mV) at free chlorine concentrations of 0 (distilled water), 100, 200, and 300 mg/l for 10 minutes. And then, morphological damage to mycelial cells was observed under light microscope and scanning electron microscopy (SEM). It was shown that electrolyzed water at 100 mg/l was damaged cell structure, and the mycelia cell structure represented abnormal and under microscopic observation. The increasing concentrations of the electrolyzed water at 200-300 mg/l showed that contorted mycelium showed cell rupture and collapsed in all treatments when compared to control. The inhibitory effect on the pathogenic fungi was determined by wounding on the chilli skin and washing with electrolyzed water at 100 mg/l, then stored at room temperature (28 ± 1 º C). It was found that the chilli treated with electrolyzed water could control the disease, which had normal fruit skin and storage life was eight days. Therefore, the effect of electrolyzed water indicated that it could control pathogenic fungi of chilli during postharvest.

Keywords: Anthracnose disease, Electrolyzed water, Chilli, Colletotrichum capsici,

INTRODUCTION

Chilli is one of the popular spicy plants in the family Solanaceae. It is an edible and essential plant for traditional Thai cooking and economy, such as the condiments food industry. The most popular chilli (*Capsicum* spp.) grown in Thailand are garden chili peppers. Sweet chilli peppers, sweet bell peppers, bell peppers, and capsicums, which farmers found important diseases causing damage to chilli plants, are anthracnose. *Colletotrichum* spp. *C. capsici* and *C. gloeosporioides* have been reported anthracnose disease of chilli grown in Thailand [1]. The product spoilage was contaminated from the production plot and anthracnose symptoms on chilli fruit showed sunken necrotic tissues [2]. Anthracnose disease found that pre- and postharvest damage to chilli fruits causing anthracnose. It showed small anthracnose lesions on chilli fruits to reduce their marketable value [3]. Therefore, fresh chilli was washed with water and disinfected.

Recently, acidic electrolyzed is a powerful bactericidal agent applied in various fields, including agriculture and the food industry [4] [5]. Buck [6] used acidic electrolyzed water to treat the fungi and reduced growth of *Botrytis* spp. and *Monilinia* spp., which were the thin-walled fungi, within 30 seconds. In addition, Guentzel [7] found that the use of acidic electrolyzed water to control the growth of microbes by spraying at the surfaces of food service areas on spinach and lettuce. Hung [8] reported that electrolyzed water treatment on strawberries and broccoli significantly reduced *E. coli* 0157:H7. Paola [9] found that washing lettuce with electrolyzed water for 5 minutes significantly inhibited the growth of *L. monocytogenes*.

Additionally, Mueller [10] reported that acidic electrolyzed water reduced the percentage of powdery mildew on greenhouse-grown gerbera daisy plants when applied twice per week. Whangchai [11] found that electrolyzed water treatment at a free chlorine concentration of 215 ppm for 120 and 240 seconds inhibited the growth and development of *Penicillium digitatum* on tangerine cv. Sai Nam Pung. Furthermore, the use of electrolyzed water to control fungal growth could be applied directly to the plants. Washing or spraying with electrolyzed water is used to treat harvested fruit by dipping during the growing. [7]. Hassan and Dann [12] found that electrolyzed oxidizing (EO) water reduced the severity of anthracnose and stem-end rot disease by 30–75% compared with water-treated control fruit in avocado after dipped for 30s.

Thus, the objective of this research was to determine the effects of different electrolyzed water concentrations on inhibition of *Colletotrichum*

capsici, causing anthracnose disease of chilli.

MATERIALS AND METHODS

The plant materials

Chilli (*Capsicum annuum* L.) was collected from farms in Mae-Tha, Lampang Province, Thailand, and transported to the Laboratory at Lampang Rajabhat University within three hours. After that, washed in tap water, the chilli (7 fruits) were sampled for each replicate. All the experiments were designed as a Completely Randomized Design (CRD), and each treatment was done in triplicate.

Preparation of *Colletotrichum capsici*

C. capsici was obtained from the Laboratory at Lampang Rajabhat University., Lampang, Thailand. Mycelial growth, 1 cm diameter mycelial disk of *C. capsici* was cut by a sterile cork borer and put in a plate placed at the center of a potato dextrose agar (PDA) plate and then incubated at 27°C for seven days. Spore suspension, the fungus was cultured on PDA plate, and then spore suspension was harvested with sterile distilled water. Subsequently, the spore suspension was transferred into 100 ml of sterile distilled water in 250 ml in a flask. Then, the suspension was shaken for 10 min on an orbital shaker, and it was filtered through two layers of sterile muslin cloth. The cell numbers were counted with a haemacytometer, and the initial concentration was adjusted with sterile distilled water to a concentration of 10^5 conidia/ml before inoculation.

Preparation of Acidic electrolyzed Water

Acidic electrolyzed water was generated by electrolysis in a cell with positively and negatively charged titanium electrodes separated by a polypropylene membrane. The electrodes were subjected to a direct current of 8 volts. A 5% NaCl solution was added to the above system for 30 minutes. The pH of acidic electrolyzed water was recorded with pH/ion meter. Free–chlorine concentration was determined by using N,N-diethyl-P-phenylene diamine (DPD).

Effect of Acidic Electrolyzed Water on Structural Changes of *Colletotrichum capsici*

Mycelial growth, 1 cm diameter mycelial disk of *Colletotrichum capsici* was cut by a sterile cork borer and put in a plate containing 9 ml of acidic electrolyzed water at free chlorine concentrations of 0 (distilled water), 100, 200, and 300 mg/l for 10 minutes. Then, mycelial cells were observed under light microscope, staining mycelial by using Lactophenol cotton blue. For scanning electron microscope (SEM), samples were fixed using 2.5 % glutaraldehyde for 24 hours. Then they were dehydrated with serials in ethanol 50, 70, 90 %, and absolute ethanol. Each three ethanol concentrations were immersed for 10 min 3 times. After that, samples were critical point dried and sputter-coated with gold. Samples were examined under SEM (JEOL, JSM 5910LV).

Effects of Acidic Electrolyzed Water on Inactivation of *Colletotrichum capsici In Vitro*

One milliliter of *Colletotrichum capsici* spore suspension (10^5 conidia/ml) was added to a tube containing 9 ml of acidic electrolyzed water at free chlorine concentrations of 0 (distilled water), 100, 200, and 300 mg/l for10 minutes. Then, 0.1 ml of the suspension from each free chlorine concentrations treatment at several times were spread on PDA plate and incubated at 27°C for 48 h. The survival of the fungus was expressed as the mean number of colony forming units (logCFU/ml).

Effect of Acidic Electrolyzed Water on the Reduction of *Colletotrichum capsici* after Inoculated on Chilli

Chilli fruit were inoculated to determine the efficacy of treatments with pathogen infection. Chilli were wounded at the skin approximately 2 cm diameter were two positions on each fruit to indicate sites for inoculation. *C. capsici* was inoculated using spore suspension $1x10^5$ conidia/ml. A volume of 10 µl droplet of *C. capsici* was placed with wounded skin. After the incubation period for 10 min, chilli fruits were immersed in 450 ml of acidic electrolyzed water at different concentrations (0, 100, 200, and 300 mg/L residual chlorine) for 10 minutes and then wounded-inoculated chilli fruit with *C. capsica* kept in trays within room temperature (28±2°C). Samples were investigated for fruit quality; Physical changes (weight loss, outer peel color, diameter of lesions).

Statistical Analysis

All experiments were replicated three times and evaluated with the regression procedure using SPSS version 17. Differences among treatments performed using Duncan's Multiple Range test ($P \leq 0.05$).

RESULTS AND DISCUSSION

Effect of Acidic Electrolyzed Water on Structural Changes of *Colletotrichum capsici*

The effect of acidic electrolyzed water on *C. capsici* structure indicated that morphological damage to mycelial cells was observed under light microscopy in Figure 1. It was shown that acidic electrolyzed water at 100 mg/L was damaged cell structure, and the mycelia cell structure represented abnormal-formed and contorted mycelia. The increasing concentrations at 200-300 mg/L showed that contorted mycelium (Figure 1). This solution has a powerful bactericidal agent in acidic electrolyzed water at 100-300 mg/l and strong oxidation potential in which oxidation-reduction potential (ORP). Suslow [13] reported that an ORP at 650-700 mV had the activity to reduced *Escherichia coli*, *Salmonella* sp., and *Listeria* sp. Significantly, scanning electron micrograph (SEM) showed contorted and uneven mycelia of *C. capsici* on the surface after treated with acidic electrolyzed water at 100 mg/L in Figure 2. The concentrations at 200-300 mg/L also showed abnormal-formed mycelia cells. As a result, Buck [6] reported that the electrolyzed water reduced the growth of the thin-walled such as *Botrytis* spp. and *Monilinia* spp. within 30 seconds. As well as, Sierra [14] reported that acidic electrolyzed water showed inhibit conidia germination at 10 ppm and 50 ppm after exposure time for 7 minutes.

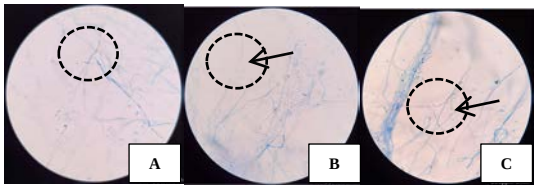


Fig. 1 Light photographs of *C. capsici* after treated with acidic electrolyzed water at 100 mg/L (A), 200 mg/L (B) and 300 mg/L (C). Arrow indicated that (A-C) contorted mycelia.

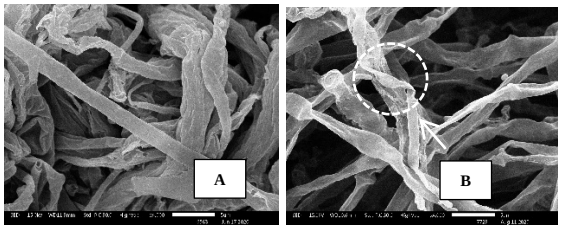


Fig. 2 SEM photographs were well-formed and continuous mycelia of *C. capsici* (4000X); A, and acidic electrolyzed water at 100 mg/L (4000X); B. Arrow indicated that contorted and uneven mycelia.

Effects of Acidic Electrolyzed Water on Inactivation of *Colletotrichum capsici* In Vitro

The reduction in *Colletotrichum capsici* is shown in Figure 3. Acidic electrolyzed water significantly inhibited the mycelial growth at 100-300 mg/l and obtained the best result in the reduction of *C. capsici* when compared to the control (Distilled water) in Figure 4. Acidic electrolyzed water was effective against mycelial cell which has an antibacterial action. Issa-Zacharia [15] demonstrated that electrolyzed oxidizing waters significantly reduced the total aerobic mesophilic bacteria from Chinese celery, lettuce and daikon sprouts. As a result, Xiong [16] reported that electrolyzed oxidizing waters were evaluated against *Aspergillus flavus* conidia and mycelia at 86.1 mg/l for 30s. Acidic electrolyzed water (pH 1.95, ORP >1,100 mV) represented hypochlorous acid were produced at the anode side and this solution has a strong oxidation potential in which oxidation-reduction potential (ORP) was measured for the oxidation reaction of all treatments. Also, the low pH of the acidic electrolyzed water could damage the membranes of the microorganisms as well as acidic electrolyzed water expressed strong antifungal and mycelium. *Aspergillus flavus* conidia and mycelia found the leakage of K^+ and Mg^{2+} results from damage to the normal cellular functions [16]. In another report, Whangchai [17]reported that washing orange with electrolyzed water and exposure to ozone gas for 2 hours per day significantly controlled *P. digitatum*. Tomás-Callejas [18] reported that washing fresh-cut baby mizuna leaves with electrolyzed water showed an inhibitory effect on natural microflora.

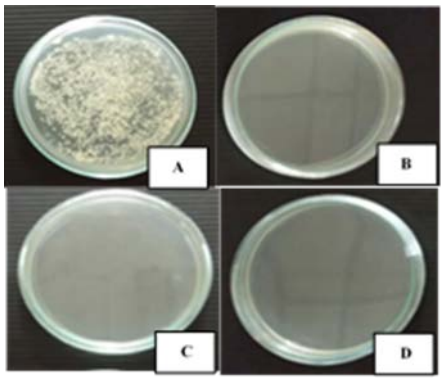


Fig. 3 Effect of acidic electrolyzed water: (A) control (distilled water), (B) 100 mg/l, (C) 200 mg/l and (D) 300 mg/l after treated for 10 minutes on growth inhibition of *E. coli* after incubation at room temperature (28±2°C) for 48 hr.

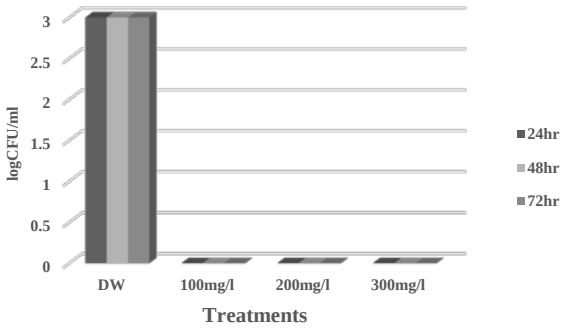


Fig. 4 Effect of acidic electrolyzed water on inactivation of *Colletotrichum capsici* after incubation at room temperature (28±2°C)**.**



Fig. 5 Chilli after washed with acidic electrolyzed water for 10 min; (a) control (b) acidic electrolyzed water at 100 mg/L for 8 days and storage at room temperature (28±2°C).

Table 1 Effect of acidic electrolyzed water for fruit quality change; physical changes (weight loss, outer peel color, diameter of lesions) after storage for 8 days.

Treatment	Color			Weight loss (%)	Disease (score)	Diameter of lesion (cm)
	L*	a*	b*			
Control	38.16a	5.60a	8.36a	0.38	2.33	1.32
100 mg/l	39.91a	7.66b	12.29b	0.32	1.33	0.5
200 mg/l	40.64a	8.77b	12.47b	0.32	1.00	0.4
300 mg/l	41.00a	8.97b	12.93b	0.31	1.00	0.5

Effect of Acidic Electrolyzed Water on the Reduction of *Colletotrichum capsici* after Inoculated on Chilli

Effect of acidic electrolyzed water for fruit quality change was shown in Table 1. The L* value represented a non-significant change of all treatments when compared to the control, and a*, b* were a slight increase in this parameter with the storage period for all treatments. The weight loss percentages of all treatments increased with storage time as a result, Artés [19] reported that the loss of weight was due to water evaporation during storage. Anthracnose disease after washed with represented acidic electrolyzed water expressed less than the fruit washed with distilled water (control) as well as the lesion in Figure 5. Huang [20] reported that acidic electrolyzed water could damage the normal morphological cell structures by increased the amount of hydroxyl radicals, and cell damage may arise due to available chlorine. In another report, Paola [9] found that washing lettuce with electrolyzed water for 5 minutes significantly inhibited growth of *L. monocytogenes*. Fujiwara [21] reported that acidic electrolyzed water reduced the severity of powdery mildew infection and phytotoxic symptoms on cucumber leaves.

CONCLUSIONS

The effective of acidic electrolyzed water on the suppression of plant pathogens and anthracnose diseases. The use of acidic electrolyzed water at 100 mg/L could inhibit the mycelial growth of *C. capsici*. The morphological damage to mycelial cells was contorted and uneven of *C. capsici*. *In vivo* assay on infected chilli, chilli treated with acidic electrolyzed water could control the disease, which had normal fruit skin. Therefore, washing with acidic electrolyzed water could control pathogenic microorganisms.

ACKNOWLEDGMENTS

This work was supported by Department of Biology, Faculty of Science, Lampang Rajabhat University for the financial and Postharvest Technology Innovation Center, Ministry of Higher Education, Science, Research and Innovation, Bangkok, Thailand.

REFERENCES

[1] Sangchote S. R., Pongpisutta B., Kongsamai N., Taweechai and S. Sukprakarn. Resistance of pepper to C*olletotrichum* spp. The first Announcement and Int. Conf. on Periurban Vegetable Production in the Asia – Pacific Region

for the 21 st Century, 1998, Kasetsart University, Bangkok.

[2] Manandhar J.B., Hartman G.L., and Wang T.C. Anthracnose development on pepper fruits inoculated with *Colletotrichum gloeosporioides*. Plant Disease, Vol.79, 1998. pp, 380-383.

[3] Than P. P., Prihastuti H., Phoulivong S., Taylor P.W.J. and Hyde K .D. Chilli anthracnose disease caused by *Colletotrichum* species. Journal of Zhejiang University, Vol.9, Issue 10, 2008, pp. 764 – 778.

[4] Whangchai N., Nomura N. and Matsumura M. Factors affecting phytoplankton removal by electro- oxidation of artificial seawater. Chiangmai Journal of Science, Vol. 30, 2003, pp.255 – 259.

[5] Kim C., Hung Y.C. and Brackett R.E. Efficacy of electrolyzed oxidizing (EO) and chemically modified water on different types of foodborne pathogens. International Journal of Food Microbiology, Vol. 61, 2000, pp.199–207.

[6] Buck J.W., Van Iersel M.W., Oetting R.D. and Hung C.Y. In vitro fungicidal activity of acidic electrolyzed oxidizing water. Plant Disease, Vol. 86, 2002, pp. 278-281.

[7] Guentzel J. L., Liang L. K., Callan M. A., Emmons S. A. and Dunham V. L. Reduction of bacteria on spinach, lettuce, and surfaces in food service areas using neutral electrolyzed oxidizing water. Food Microbiology, Vol. 25, Issue 1, 2008, pp. 36-41.

[8] Hung Y. C., Tilly P. and Kim C. Efficacy of electrolyzed oxidizing (EO) water and chlorinated water for inactivation of *Escherichia coli* 0157:H7 on strawberries and broccoli. Journal of Food Quality, Vol. 33, 2010, pp. 559-577.

[9] Paola C. L., Vivian R. C., Mercado M., Deaz M., and Carrascal A. K. Effectiveness of electrolyzed oxidizing water for inactivating Listeria monocytogenes in lettuce. Universitas Scientiarum, Vol. 10, 2005, pp.97-108.

[10] Mueller D.S., Y.C. Hung, R.D. Cetting, van M.W.Iersel, and J.W. Buck. Evaluation of electrolyzed oxidizing water for mangangement of powdery mildew of gerberadaisy. Plant Dis. 2003, Vol. 87, pp. 965 – 969.

[11] Whangchai K., Saengnil K., Singkamanee, C. and Uthaibutra J. Use of Electrolyzed oxidizing water to control postharvest disease during storage of tangerine cv. Sai Nam Pung. Acta Horticultrae, Vol. 837, 2009, pp. 211-215.

[12] Hassan M. K. and Dann E. Effects of Treatment with Electrolyzed Oxidizing Water on Postharvest Diseases of Avocado. Agriculture. Vol. 9, 2019, pp. 3-15.

[13] Suslow T. V. Oxidation-reduction potential (ORP) for water disinfection monitoring, control, and documentation. University of California. Division of Agriculture and Natural Resources, Publication, 2004, pp.8149.

[14] Sierra B. E. G., Meza A. X. S. and Sanchéz L. T. G. Antifungal activity of acidic electrolyzed water against strawberry postharvest molds (Fragaria x ananassa Duch cv. Camarosa. Acta Agronómica, Vol. 68, Issue 2, 2019, pp. 126-133.

[15] Issa-Zacharia A., Kamitani Y., Miwa N., Muhimbula H., and Iwasaki K. Application of slightly acidic electrolyzed water as a potential non-thermal food sanitizer for decontamination of fresh ready-to-eat vegetables and sprouts. Food Control, Vol. 22, 2010, pp. 601-607.

[16] Xiong K., Li X., Guo S., Li L. and Liu H. The Antifungal Mechanism of Electrolyzed Oxidizing Water against *Aspergillus flavus*. Food Sci. Biotechnol. Vol. 23, Issue 2, 2014, pp. 661-669.

[17] Whangchai, K., Saengnil, K., Singkamanee, C. and Uthaibutra, J. Effect of electrolyzed oxidizing water and continuous ozone exposure on the control of Penicillium digitatum on tangerine cv. Sai Nam Pung during storage, Crop Protection. Vol. 29, 2010, pp. 386-389.

[18] Tomás-Callejas A., Martinez-Hernandez G.B., Artés F., Artés-Hernández F., and Trevor V.S. Neutral and acidic electrolyzed water as emergent sanitizers for fresh-cut mizuna baby leaves. Postharvest Biology and Technology, Vol. 55, 2011, pp.114 -120.

[19] Artés F, Gómez, P., Aguayo. E., Escalona, V. and Artés-Hernández, F. Sustainable sanitation techniques for keeping quality and safety of fresh-cut plant commodities. Postharvest biology and technology. Vol. 59, 2009, pp. 287-296.

[20] Huang YR, Hung YC, Hsu SY, Huang YW, Hwang DF. Application of electrolyzed oxidizing water in the food industry. Food Control, Vol. 19, 2008, pp. 329-345.

[21] Fujiwara K., Fujii T and Park J.S. Successive spraying efficacy of acidic electrolyzed oxidizing water and alkalic electrolyzed reducing water on controlling powdery mildew infection and suppressing visible physiological disorder on cucumber leaves. Hortic. Environ. Biotechnol. Vol. 52, 2011, pp. 387–392.

7th Int. Conf. on Structure, Engineering & Environment (SEE), Pattaya, Thailand, Nov.10-12, 2021, ISBN: 978-4-909106070 C3051

EXTERNAL COSTS CAUSED BY HOKKAIDO SIKA DEER-VEHICLE COLLISIONS IN HOKKAIDO, JAPAN

Hideyuki Ito[1], Masanori Wada[2] and Takahiro Fujii[3]
[1,3]College of Science and Technology, Nihon University, Japan; [2]Hasuda City Hall, Japan

ABSTRACT

The population of Ezo sika deer (*Cervus nippon yesoensis*) inhabiting all of Hokkaido, Japan temporarily decreased due to heavy snowfall and overhunting during the Meiji period (1868-1912). However, the population has increased since the 1980s due to hunting bans and changes in the habitat. Due to the increase in the population, damage caused by Deer-Vehicle Collisions (DVCs) has become a serious problem, with 3,188 DVCs occurring annually in 2019. In addition, the occurrence of DVCs causes a variety of social costs such as economic loss due to damage to the vehicle, passenger injury, cost of processing Ezo sika deer and external diseconomy caused by roadkill of Ezo sika deer, but these social costs have not been clarified. Therefore, the purpose of this research is to estimate the social costs of DVCs occurrence including the external costs of the roadkill of Ezo sika deer in entire Hokkaido using Contingent Valuation Method (CVM) by internet survey to Hokkaido residents. As the result, it was shown that the social costs caused by roadkill of Ezo sika deer accounted for a high proportion of its cost of DVCs occurrence.

Keywords: Ezo sika deer, Contingent Valuation Method, Deer-Vehicle Collisions, Social costs

INTRODUCTION

The Ezo sika deer, a subspecies of the Japanese deer classified in the deer family, deer genus, inhabits all of Hokkaido, Japan. The Ezo sika deer inhabits forests from the land to the mountains, especially preferring forest margins with grasslands and meadows. Ezo sika deer have a head and body length of 140-180 cm and a body weight of 90-140 kg for males and 70-100 kg for females [1].

The Ezo sika deer was on the verge of extinction due to heavy snowfall, overhunting, and habitat destruction during the Meiji period. However, the population of Ezo sika deer has increased since the 1980s due to the implementation of hunting bans and other measures to protect them, the increase in *Abies sachalinensis* plantations that serve as wintering grounds, and the expansion of agricultural land that serves as their main feeding ground. According to data from the Hokkaido Government [2], it is estimated that by 2019 there will be approximately 670,000 Ezo sika deer living throughout Hokkaido.

This has led to an increase in the population of Ezo deer and a high incidence of DVCs (Deer-Vehicle Collisions); in 2019, there were 3,188 DVCs [3], which has become a serious social problem due to the risk of accidents for drivers, damage to vehicle body. According to data published by the Hokkaido Branch of the General Insurance Association of Japan [4], annual vehicle insurance claims paid in 2018 amounted to approximately 1.36 billion yen (Approximately US$120 million). Thus, there are various social impacts and significant external costs associated with the occurrence of DVCs, but there are few existing researches that have estimated the social costs associated with the occurrence of DVCs in Japan.

As previous researches in Japan that estimated the social costs caused by traffic accidents and roadkill, Koyama and Kishimoto [5] calculated the external costs of automobile traffic in Japan. The external costs of accidents were estimated by subtracting insurance company payments from human losses and property losses. Nakamura et al. [6] evaluated the loss value of native plants caused by Ezo sika deer using CVM (Contingent Valuation Method), and added traffic accident loss and agriculture and forestry damage loss to clarify the loss value of Ezo sika deer to society. A survey conducted by the Ministry of the Environment [7] asked households in Tsushima, Nagasaki Prefecture, Japan about their willingness to pay for restoring the population of the Tsushima leopard cat, an endangered species whose population has declined due to roadkill, from the current level of about 100 to 140 in 20 years. From the survey results, it was found that the annual payment per household for one Tsushima leopard cat is 1,015 JPY (approximately US$9.2)/household. In researches that estimated external cost and conducted the cost-benefit analysis of DVCs occurrence in foreign countries, Reed et al. [8] showed the cost efficiency of a 2.4-meter fence to reduce deer-vehicle accidents in six fences on Highway 82 and Interstate 70 in Colorado, and showed the accident-reducing facilities, and presented a cost-benefit analysis procedure for future highway planning with reduced deer accidents.

Kurt and Peter [9] examined the method of calculating the value of deer in deer-vehicle collisions. From the viewpoint of economics, they stated that most of the values of deer estimated in previous researches were basically expenditure indicators, not economic values, and suggested using consumer surplus or net WTP as a measure of deer value. Bissonette et al. [10] evaluated the costs associated with deer-vehicle collisions. They estimated that the total cost of 13,020 collisions in Utah, USA from 1996-2001 was $45,175,454, the estimated average annual cost was approximately $7,529,242, and the average collision cost was $3,470. The cost of human fatalities at $24,000,000, vehicle damage at $18,000,000, deer damage at $2,700,000, and human casualties at $1,000,000 were also estimated.

As a previous research that calculated the economic value based on the willingness to pay for the conservation of wildlife to be protected, Chambers and Whitehead [11] determined the willingness to pay for wolf management plans and wolf damage plans in Minnesota. They found that the WTP paid as a tax for wolf conservation was $67/household. Bandara [12] estimates the amount of additional charges for payments to insurance schemes by elephants in Sri Lanka based on the results of a questionnaire survey applying CVM. The estimated WTP was found to be 100 Indian rupees/household.

As described above, there are a few existing researches overseas that have estimated social costs due to accidents with animals, but there are no existing researches in Japan that have estimated the economic value of Ezo sika deer by estimating social costs due to DVCs. The purpose of this study is to estimate the annual social external costs of DVCs, including losses from running over and killing Ezo sika deer, for residents of Hokkaido.

Losses from running over and killing Ezo sika deer were estimated based on the results of calculating the economic value of each Ezo sika deer using the CVM for residents of Hokkaido. Losses due to vehicle damage, occupant health damage, Ezo sika deer disposal costs, and other social external costs were estimated based on existing data, and the total of each social external cost was defined as the social external cost due to the occurrence of DVCs.

ESTIMATION OF ECONOMIC VALUE OF EZO SIKA DEER

Outline of Questionnaire Survey

In order to estimate the economic value of running over and killing Ezo sika deer, a web-based survey by Rakuten Insight was conducted from January 6 to 12, 2021. We obtained 1,200 samples by assigning them to Rakuten Insight members living in Hokkaido, based on the population composition ratio of people aged 20 to 79 years [13] in the areas of 14 promotion bureaus (Table 1). The questionnaire was divided into three patterns, and 400 samples were collected for each pattern. From the 1,200 samples obtained, 17 respondents who were in favor of payment and 184 respondents who were against payment were excluded as invalid responses, resulting in 999 valid responses.

Table 1 Outline of questionnaire survey

Survey period	January 6 to 12, 2020
Implementation Method	Web survey by Rakuten Insight
Survey target	Rakuten Insight members residing in Hokkaido
Survey area	All areas in Hokkaido, Japan
Number of collections	1,200 samples (400 samples per pattern)
Number of valid samples	999 samples
Survey Items	-Amount of willingness to pay for conservation of Ezo sika deer -Reasons for choosing the amount of willingness to pay -Subjects' attributes (gender, age, residential area, occupation, annual income, environmental awareness, interest)

As a structure of the questionnaire, at the beginning, in order for respondents to understand the contents of the questionnaire, the ecosystem and role of Ezo sika deer and damage to crops by Ezo sika deer were explained using figures, tables and photographs. Also, a simple question about Ezo sika deer was asked to confirm whether the respondents understood the contents of the explanation, and only the samples of the respondents who answered correctly were collected. Next, we asked about the WTP for the conservation of Ezo sika deer. Assuming that Ezo sika deer are killed in traffic accidents between Ezo sika deer and automobiles on roads in Hokkaido, it was assumed that Ezo sika deer can be saved from traffic accidents by a one-time collection of donations from Hokkai residents by nature conservation organizations to build Ezo sika deer intrusion prevention fences and facilities for crossing roads to prevent accidents from occurring. The amount of money to be asked was divided into three patterns,

and the amount was presented in a double-bounded dichotomous choice as shown in Table 2. The offer prices were set at 10 JPY (approximately US$ 0.090), 30 JPY (approximately US$ 0.27), and 50 JPY (approximately US$ 0.45), and number of deer to be conserved was presented for one, five, and ten deer. In addition, a scoping response test was also conducted to check whether the willingness-to-pay amount corresponded to the number of deer to be preserved. In order to eliminate resistant responses, we divided the questions into those who answered that they were willing to pay at least once and those who answered that they were unwilling to pay for all questions.

Table 2 Offer price for each pattern

	Initial offer price	Number of deer to be protected								
		1 Deer		5 Deer			10 Deer			
Pattern 1	10 JPY	Yes	20 JPY	250 JPY	Yes	400 JPY	300 JPY	Yes	500 JPY	
		No	5 JPY		No	200 JPY		No	150 JPY	
Pattern 2	30 JPY	Yes	50 JPY	50 JPY	Yes	100 JPY	500 JPY	Yes	800 JPY	
		No	15 JPY		No	25 JPY		No	400 JPY	
Pattern 3	50 JPY	Yes	80 JPY	150 JPY	Yes	250 JPY	100 JPY	Yes	200 JPY	
		No	40 JPY		No	75 JPY		No	50 JPY	

Finally, personal attributes were asked in order to analyze the factors influencing WTP for conservation of Ezo sika deer. The following personal attributes were asked: "area of residence," "awareness of protection of natural environment and living things," "frequency of participation in activities to protect natural environment and living things," "knowledge of Ezo sika deer," "knowledge of roadkill," "frequency of seeing wild Ezo sika deer within living area," "occupation," "annual household income," "gender," and "age. We also asked them about their occupation, annual household income, gender, and age.

Results of Fundamental Analysis

The results of the questionnaire survey showed that more than half of the respondents, 61.3%, were male, and the largest age group was in their 60s, 19.3%, followed by those in their 40s, 19.0%. The percentage of respondents who knew about Ezo deer and roadkill were 95.5%, 28.2% respectively. The percentage of respondents who had seen wild Ezo sika deer in their living area was 55.7%, 31.3% had seen them outside their living area, and 13.1% had never seen them.

The most common reason given by the respondents for agreeing to pay donations for deer conservation was "because it will reduce traffic accidents" at 75.8%, followed by "because I think it is important for society to protect the lives of Ezo deer" at 15.6% as shown in Fig.1.

The most common reason given by respondents who answered "No" to all the suggested amounts for opposing the payment of donations was "Because I cannot make a decision based on this information," at 40.1%, followed by "Because I do not think that efforts to conserve Ezo deer are necessary," at 28.4% (Fig.2).

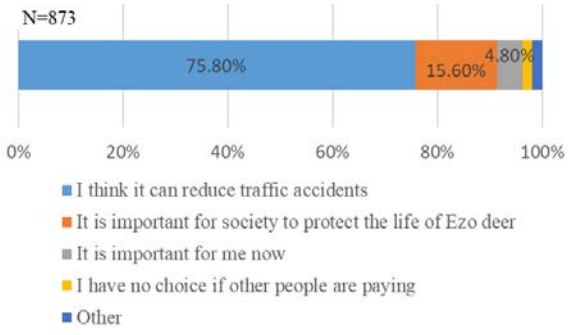


Fig. 1 Reasons in favor of paying a donation.

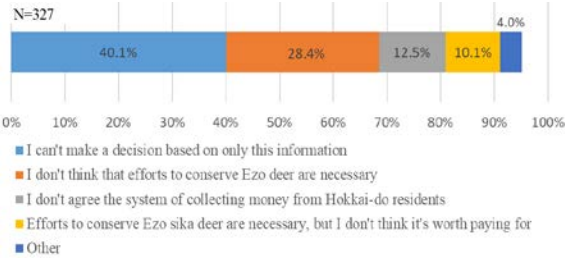


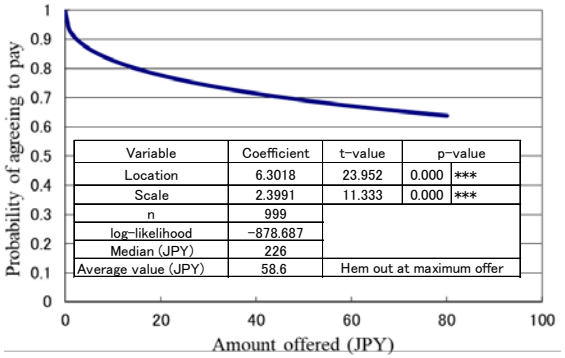
Fig. 2 Reasons for opposing the payment of donations.

Estimation Results of Economic Value of Ezo Deer

The economic value of Ezo sika deer was estimated based on 999 samples, excluding resistance responses from the 1,200 samples collected. For the estimation of the economic value, we estimated the nondiscrimination curve by applying the Weibull distribution using "CVM in Excel Version 4.0" provided by Kuriyama [14], obtained the median value, and estimated the survival rate curve of Ezo sika deer. Figures 3 to 5 show the estimation results of the survival rate curves for each number of Ezo sika deer.

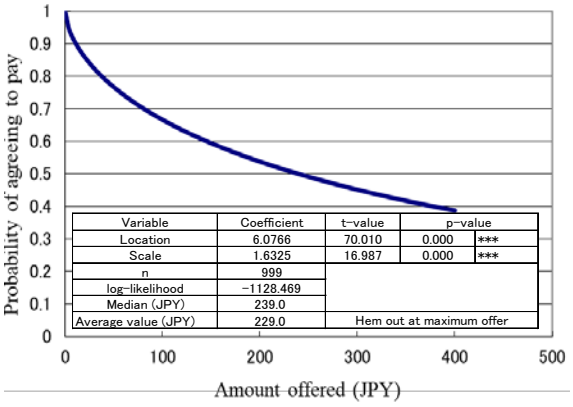
For estimating the economic value of Ezo sika deer, we used the median value, which is the lowest value when converted to one animal, in order to give a conservative evaluation in CVM. As a result, the economic value per 10 Ezo sika deer was 320

yen/person, and the economic value per a deer was 32.0 yen (approximately US$ 0.29)/person. One of the reasons for the low economic value of Ezo deer is that they are considered to be vermin to farmers, which may have resulted in the low value. This value was multiplied by the number of households in Hokkaido (31,594 households [13] and the number of DVCs occurring in 2018 (2,834 [3]), resulting in an annual economic value of 2.865 billion yen (approximately 25.93 million dollars) for Hokkaido's Yezo sika deer.



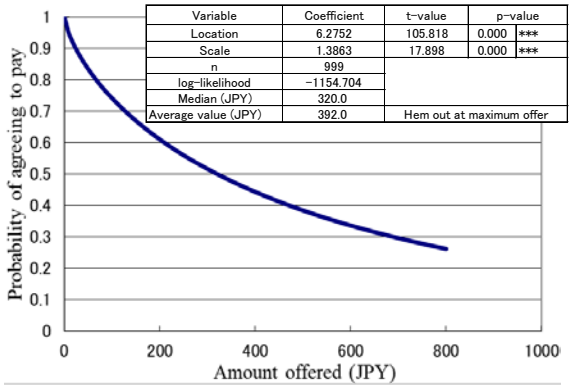
Variable	Coefficient	t-value	p-value	
Location	6.3018	23.952	0.000	***
Scale	2.3991	11.333	0.000	***
n	999			
log-likelihood	-878.687			
Median (JPY)	226			
Average value (JPY)	58.6	Hem out at maximum offer		

Fig. 3 Survival rate curve for 1 Ezo deer.



Variable	Coefficient	t-value	p-value	
Location	6.0766	70.010	0.000	***
Scale	1.6325	16.987	0.000	***
n	999			
log-likelihood	-1128.469			
Median (JPY)	239.0			
Average value (JPY)	229.0	Hem out at maximum offer		

Fig. 4 Survival rate curve for 5 Ezo deer.



Variable	Coefficient	t-value	p-value	
Location	6.2752	105.818	0.000	***
Scale	1.3863	17.898	0.000	***
n	999			
log-likelihood	-1154.704			
Median (JPY)	320.0			
Average value (JPY)	392.0	Hem out at maximum offer		

Fig. 5 Survival rate curve for 10 Ezo deer.

Table 3 Estimated economic value of Ezo sika deer in Hokkaido in 2018.

Economic value per 1 Ezo deer (JPY/person)	Number of DVCs in 2018	Number of households in Hokkaido	Estimated economic value of Ezo sika deer in Hokkaido
32.0	2,834	31,594	2.865 billion yen

Analysis of factors influencing WTP

An analysis of factors affecting the WTP of Ezo sika deer was conducted based on the personal attributes obtained from the questionnaire. The objective variable was the WTP of Ezo sika deer, and the explanatory variables were the following personal attributes: "area of residence," "awareness of the protection of the natural environment and living things," "frequency of participation in activities to protect the natural environment and living things," "knowledge of Ezo sika deer," "knowledge of roadkill," "frequency of seeing wild Ezo sika deer in the area of daily living," "occupation," "annual household income," "gender," and "age. The full log-linear logit model was used to analyze the results. As a result, the four variables that met the 10% significance level were "awareness of the protection of the natural environment and living creatures," "frequency of participation in activities to protect the natural environment and living creatures," "annual household income," and "gender. Thus, these indicated the possibility of higher WTP. The results of the analysis are summarized below;

1) Those who have a high awareness of the protection of the natural environment and living things have a high awareness of the conservation of living things, and many of them think that the protection of Ezo sika deer is also important, so they are expected to pay a higher amount.

2) Those who participate more frequently in activities to protect the natural environment and living things are more likely to believe that it is important to protect Ezo sika deer because they are in contact with the natural environment and living things regularly, and thus pay a higher amount.

3) Those with higher annual household incomes are expected to pay higher amounts because they have more money and can pay for the conservation of Ezo sika deer.

4) Males of both sexes are more likely to be employed and to have higher incomes, and thus are expected to pay more for the conservation of Ezo sika deer.

Table 4 Results of analysis of factors affecting WTP

Variable	Coefficient	t-value	p-value
Constant	1.279	2.468	0.014 **
ln(Bid)	-1.13	-18.62	0 ***
Awareness of protecting the natural environment and living things (1: I don't think so at all to 5: I think so very much)	0.919	9.538	0 ***
Frequency of participation in activities to protect the natural environment and living things (1: I do not participate at all to 5: I participate frequently)	0.42	4.74	0 ***
Annual household income	0.095	1.989	0.047 **
Gender (1:male, 2:female)	0.351	2.654	0.008 ***
n	999		
log-likelihood	-1069.741		

ESTIMATING EXTERNAL COSTS OF OCCURRING DVCS

The total social cost of DVCs was estimated by calculating the economic loss due to Ezo sika deer killed, loss due to vehicle damage, loss due to occupant health damage, Ezo sika deer treatment cost, and other external social costs in 2018 and summing them up. The economic loss due to roadkill of Ezo sika deer was calculated as 2.579 billion JPY by multiplying the estimated economic value of Ezo sika deer in Hokkaido (2.865 billion JPY: approximately 23.3 million dollars) by the 90% [15] probability of death of deer due to the occurrence of DVCs.

For the amount of social loss due to damage to vehicles caused by DVCs, we used data published by the Hokkaido Branch of the General Insurance Association of Japan [4]; the annual vehicle insurance payment due to DVCs occurrence in 2018 was 1.366 billion yen (approximately 12.34 million dollars).

The amount of loss due to physical damage to the occupants was calculated using the data on Ezo sika deer accidents from 2012 to 2018 provided by the Hokkaido Police and the amounts of "human loss" and "casualty loss" in the research report on the economic analysis of traffic accident damage and loss (2011) published by the Policy Management Bureau of the Cabinet Office [16]. The probability of occurrence of fatal and injury accidents was calculated based on the DVCs data for the past seven years (Table 5), and this was multiplied by the "amount of human loss" and "amount of casualty loss" per case to calculate the respective loss amounts per DVC. The result was 15,799 JPY (approximately 142.8 dollars) per incident (Table 6), and this amount was multiplied by the number of DVCs [3] occurring in 2018, resulting in an annual loss of 0.45 billion JPY (approximately 407,000 dollars).

Table 5 Ezo deer accident data from 2012-2018

	Personal Accidents		Property damage incidents	Total
Number of accidents for 7 years (2012-2018)	Fatal accidents	Injury Accidents		
	1	9	14,767	14,777

Table 6 Results of calculation of economic loss due to physical damage to occupants

	Fatal accidents	Injury Accidents	Property damage incidents
Probability of the number of accidents over 7 years (n=14,777)	0.01%	0.06%	99.93%
Death and injury loss + injury loss (JPY / case)	229,025,000	493,000	-
Economic loss per DVC (JPY/case)	15,499	300	-

The disposal cost of Ezo sika deer by road administrators was estimated based on the results of an interview with the Kushiro Development and Construction Department, Hokkaido Development Bureau, Ministry of Land, Infrastructure, Transport and Tourism. Under the conditions of processing carcasses with a processing time of 1.5 hours, two processing personnel, a 4-ton uniq processing machine, and a deer weight of 100 kg, the approximate result was 35,000 JPY (approximately 314 dollars) per case. This value was multiplied by the number of DVCs generated in 2018, resulting in an annual cost of 0.99 billion JPY (approximately 889,000 dollars).

As other external costs, we calculated the costs of public institutions such as emergency services and police at the time of the accident, as well as the amount of loss due to loss of worker personnel. As a result of the calculation using the Ezo Deer accident data provided by the Hokkaido Police [4] and the amounts for "Losses of various public institutions" and "Losses of business entities" in the Research Report on Economic Analysis of Traffic Accident Damage and Losses [16], the amount was 4,604 JPY (approximately 41.3 dollars)/incident. This amount was multiplied by the number of DVCs generated in 2018 [4], resulting in an annual amount of 0.13 billion JPY (approximately 117,000 dollars).

Table 7 Calculation results for other external costs

	Fatal accidents	Injury Accidents	Property damage incidents
Probability of the number of accidents over 7 years (n=14,777)	0.01%	0.06%	99.93%
Death and injury loss + injury loss (JPY / case)	2,822,000	682,000	4,000
Economic loss per DVC (JPY/case)	191	415	3,997

Estimated total external costs due to DVCs occurrence

As a result of summing up the estimates of social external costs, the estimated social external cost due to the occurrence of DVCs in 2018 was 4.102 billion JPY (approximately 36.774 million dollars).

Among the social external costs due to the occurrence of DVCs in 2018, the highest proportion of losses due to Ezo sika deer killed was 62.9%. This indicated that the occurrence of DVCs caused significant social losses due to roadkill of Ezo sika deer. Loss due to vehicle damage was also relatively high at 33.3%. These results indicate that a large amount of external costs is incurred annually in Hokkaido due to the occurrence of DVCs.

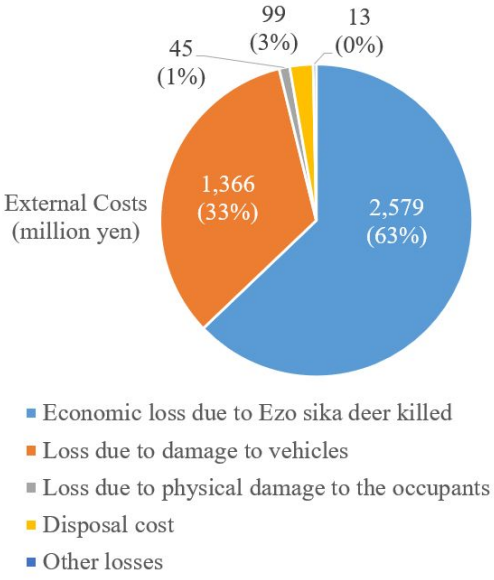


Fig. 6 Total external cost of DVCs.

CONCLUSIONS

In this research, we estimated the economic value of Ezo sika deer in Hokkaido using CVM, and then estimated the external costs due to the occurrence of DVCs. The results showed that approximately 60% of the social external costs were losses due to the roadkill of Ezo sika deer, which accounted for a high percentage of the total costs. Since the economic value of 32.0 JPY per Ezo sika deer was multiplied by the number of households in Hokkaido and the number of accidents, the external cost due to the occurrence of DVCs per year was estimated to be 4.102 billion yen, which is considered to be a large proportion. However, as a large amount of social costs are incurred every year, it is necessary to promote countermeasures against accidents involving Ezo sika deer.

As a future issue, it is necessary to examine the cost effectiveness of Ezo sika deer accident countermeasures based on the social costs estimated in this research. Also, a questionnaire survey was conducted on Hokkaido residents, but it needs to verify the economic value of Ezo sika deer when a questionnaire survey was conducted in other regions.

ACKNOWLEDGMENTS

We would like to express our gratitude to the Kushiro Development and Construction Department, Hokkaido Development Bureau, Ministry of Land, Infrastructure, Transport and Tourism, and the Hokkaido Prefectural Police for their cooperation in conducting this research. This research was supported by JSPS Grant-in-Aid for Scientific Research JP19K04671.

REFERENCES

[1] Teruyuki Komiya, Field's Best Illustrated Book: Mammals of Japan, Gakken Plus, 2002, 256pp.
[2] Estimated Population of Ezo Deer in 2019, Hokkaido Prefectural Government http://www.pref.hokkaido.lg.jp/ks/skn/est/R2/seisokusuu3.pdf (last access: June 16, 2021)
[3] Hokkaido Police: Deer Management Section and Utilization Section http://www.pref.hokkaido.lg.jp/ks/skn/est/index.htm (last access: June 16, 2021)
[4] The General Insurance Association of Japan, https://www.sonpo.or.jp/news/branch/hokkaido/index.html (last access: June 16, 2021)
[5] Shinya K and Atsuo K., External Costs of Road Transport in Japan, Transport policy studies' review, Vol.4 No.2, 2001, pp.19-30.
[6] Hiroki N and Soushi S., Evaluation of Economic Losses Caused by Yezo Deer Based on Contingent Valuation Method and Cluster Analysis: Proposal of a New System for Mitigating Economic Losses, Studies in Regional Science, Vol.46(1), 2016, pp.1-19.
[7] Ministry of the Environment, Ministry of the Environment's Biodiversity website: Examples of economic value evaluation Economic value evaluation of the Tsushima cat conservation and propagation project, http://www.biodic.go.jp/biodiversity/activity/policy/valuation/pdf/t1_03-2_140311.pdf (last access: June 16, 2021)
[8] Reed, F. D., Beck, D. T., and Woodard, N. T.: Methods of Reducing Deer-Vehicle Accidents: Benefit-Cost Analysis, Wildlife Society Bulletin, Vol.10, No.4, 1982, pp.349-354.
[9] Kurt A. Schwabe and Peter W. Schuhmann, Deer-Vehicle Collisions and Deer Value: An Analysis of Competing Literatures, Wildlife Society Bulletin, Vo.30, No.2, 2002, pp.609-615.

[10] A. Bissonette, Christine A. Kassar, Lawrence J. Cook, Assessment of costs associated with deer-vehicle collisions: human death and injury , vehicle damage, and deer loss, Human-Wildlife Conflicts, Vol.2, No.1, 2008, pp.17-27.

[11] Chambers, C. N., and Whitehead, J. C., A contingent valuation estimate of the benefits of wolves in Minnesota, Environmental and Resource Economics, Vol.26, No.2, 2003, pp.249-267.

[12] R. Bandara and C. Tisdell, The economic value of conserving the Asian elephant: contingent valuation estimates for Sri Lanka, Journal of the Asian Elephant Special Group 22, pp.22-29, 2003.

[13] Hokkaido Prefectural Government website: Population and Households in the Basic Resident Ledger. http://www.pref.hokkaido.lg.jp/ss/tuk/900brr/index2.htm (last access: June 16, 2021)

[14] K. Kuriyama, CVM in Excel Version 4.0 http://kkuri.eco.coocan.jp/research/introtxt/index.html (last access: June 16, 2021)

[15] Noriyuki Ootaishi and Tsuyoshi Hirata, Ezo deer are a blessing to the forest Coexistence of people, forest, and deer, Hokkaido newspaper company, 2011, 176pp.

[16] Director-General for Policy Management, Cabinet Office, Government of Japan: 2011 Survey Report on Economic Analysis of Traffic Accident Damage and Loss https://www8.cao.go.jp/koutu/chou-ken/h23/houkoku.html (last access: June 16, 2021)

7th Int. Conf.on Structure, Engineering & Environment (SEE),
Pattaya, Thailand, Nov.10-12, 2021, ISBN: 978-4-909106070 C3051

CHARACTERIZATION OF PHYSICALLY AND CHEMICALLY ACTIVATED CARBON FROM OIL PALM KERNEL SHELLS

Hisbullah[1], Siti Kana[1], Nabila[1], Muhammad Faisal[1,2*]
[1]Department of Chemical Engineering, Universitas Syiah Kuala, Banda Aceh, Indonesia
[2]Halal Research Center, Universitas Syiah Kuala, Banda Aceh, Indonesia

ABSTRACT

This research aimed to characterize the activated carbons from charcoal of Palm Kernel Shells by physical and chemical activation. The charcoal was synthesized by pyrolysis of palm kernel shells at a temperature of 400°C for 3 hours in a slow pyrolysis-batch reactor. The resulting products were liquid smoke, charcoal, and tar. In the physical activation, the charcoal was carbonized at a temperature of 600°C for 3 hours in a furnace, while in the chemical activation, NaOH 0.1 M, HCl 0.1 M, and 3% liquid smoke as activators were used (impregnation time: 24 hours). The activated carbons were then characterized by Fourier Transform Infra-Red (FTIR), Scanning Electron Microscope (SEM), and X-Ray Diffraction (XRD). The results indicated that all activated carbons were in accordance with the SII (Indonesian Industry Standard) No. 0258-88. The best result was obtained from the chemical activation with NaOH (moisture content: 4.7%; ash content: 7%; SiO_2 composition: 93.8%; pore sizes: 287.9 nm – 3.965 μm). The XRD analysis showed the broad peak at $2\theta = 22.76°$ and the appearance of SiO_2 amorphous structure. FTIR analysis identified all the activated carbons had the absorption pattern represent the functional group of O-H, C=O, C-H, and C=C, the presence of O-H and C-O functional groups showed that the activated carbons produced were polar.

Keywords: Activated Carbon, Palm Kernel Shells, Activation, SEM, XRD, FTIR

INTRODUCTION

Activated carbon is a microcrystalline adsorbent with a pore structure that has been developed to increase its internal porosity. Activated carbon has a high porosity, a large surface area, and a high degree of surface reactivity, with a specific surface area which then affects its adsorption capability.

A variety of materials can be used to produce activated carbon. The materials are generally fossil-based hydrocarbons (coal, lignite), natural biomass (lignocellulosic materials), biomass waste, polymers and carbon waste [1]. Biomass commonly used as activated carbon includes corn cobs [2], wheat straw [3], zeolites [4], bagasse [5], tea factory waste, almond shells, tomato stems and leaves [1], *Moringa oleifera* [6], oyster shells [7], coconut shells [8], coconut husks [9], and pistachio shells [10]. The utilization of natural biomass for activated carbon is more common because not only it is the most abundant renewable raw material, but it is also cheaper and easier to obtain.

Palm kernel shells derived from oil palm trees (*Elaeis guineensis*) have been widely used for the production of activated carbon as they contain lignocellulose known to be a good source of raw material and is proven to be a good precursor to produce high quality activated carbon [11]. The characteristics of activated carbon products are strongly influenced by the material content, activation method (physical or chemical activation), activating agent, and heat-treatment process.

Activated carbon from oil palm kernel shells can be prepared through pyrolysis with either physical or chemical activation. Pyrolysis is considered an important technology in all biomass utilization processes in which the biomass is heated to obtain such products as gas, liquid smoke, tar and charcoal. Liquid smoke from biomass pyrolysis has been used in various applications. Until today, however, charcoal as pyrolysis residue has not been used properly despite its huge amount produced. Once the charcoal is turned into activated carbon, it becomes a high value-added product.

The methods generally used in activating carbon include physical, chemical and physicochemical activations. Various studies found that chemical activation is better than physical activation in terms of the pore structure obtained, showing that the carbon is good for adsorption. This method is one of the most widely used. Sodium hydroxide (NaOH), zinc chloride ($ZnCl_2$), potassium hydroxide (KOH), phosphoric acid (H_3PO_4) are chemical reagents often used for carbon activation processes. Activation of charcoal is expected to improve its properties, thereby increasing the adsorption capability. However, detailed characterizations of carbon from palm kernel shells activated by various methods have not been widely carried out as yet. This study aims to characterize the active carbon

from palm kernel prepared by physical activation (heating at 600°C) and chemical activation (using NaOH, HCl and liquid smoke).

MATERIALS AND METHODS

Palm kernel shells were pyrolyzed using a pyrolysis reactor at 400°C. The charcoal produced was crushed using a ball mill to make it finer and was put through a sieve up to 80-100 mesh in size. Detailed procedures for making charcoal can be seen in another study by Faisal et al. [12]. Furthermore, the activation process was carried out as follows:

1. Physical activation was carried out by heating the charcoal at 600°C in a furnace (Muffle furnace Nabertherm, LV/ T/3/HA) for three hours.

2. Chemical activation was carried out using 0.1 M NaOH, 0.1 M HCl and 3% liquid smoke as an activator, into which charcoal was immersed for 24 hours. The activated carbon was filtered and washed in distilled water until it reached a neutral pH, then dried using an oven dryer (MEMMERT Drying Oven, GE-171 32 L)) at 105°C for an hour.

The resulting activated carbon was then characterized using SEM (Carl Zeiss Evo MA 10 Netherlands), XRD (XRD-7000, Shimadzu) and FTIR (IR Prestige 21, Shimadzu).

RESULTS AND DISCUSSION

Moisture and Ash Content

Table 1 shows that the moisture content in each sample is relatively low, namely, 4% - 6.5%, meeting the quality standard of activated carbon as required by the Indonesian Industry Standard No. 0258-88, which sets the maximum moisture of 10%. This result is also consistent with a previous study by Harahap et al. [13] that obtained a moisture content of 4.5% - 10%.

The analysis showed that activated carbons of AH, AN, AA and non-activated carbon of NA each had an ash content of 6.8%, 7%, 8.8% and 9.7% respectively and have met the standard. The highest ash content was found in AF, at 14%, which was probably caused by heating at 600°C. High ash content has a high amount of organic matter and can reduce the carbon capability in removing gas or liquid [14]. Meanwhile, activated carbon AH has the lowest ash content (6.8%). This is because HCl dissolves minerals by degrading cellulose in carbon [15].

Compound and Size Analyzes on X-Ray Diffraction

XRD characterization was carried out to determine the level of composition and crystallinity of the activated carbon which was marked by peaks at an angle of 2θ. The X-ray diffraction patterns are presented in Fig. 1.

Table 1 Moisture and ash content of the activated carbon

Parameter	Quality Standard (SII No. 0258-88)	Adsorbent	Analysis Results (%)
Moisture content	Max. 10%	NA	6.5
		AN	4.7
		AH	5.2
		AA	5.8
		AF	4.0
Ash content	Max. 10%	NA	9.7
		AN	7
		AH	6.8
		AA	8.8
		AF	14.0

Note: the carbon produced in this study included non-activated carbon (NA), NaOH-activated carbon (AN), HCl-activated carbon (AH), liquid smoke-activated carbon (AA) and physically activated carbon using a furnace (AF).

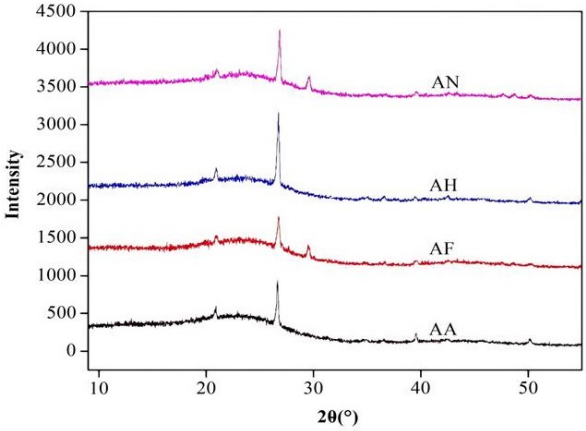


Fig. 1 X-ray diffraction patterns of AN, AH, AF, and AA activated carbons

Figure 1 shows the XRD diffractogram data from the analysis of the presence of SiO_2 for each sample at 2θ, namely, (activated carbon AF: 12.28° and 18.74°, activated carbon AA: 20.28° and 21.43°, activated carbon AH: 26.71° and 20.92°, and activated carbon AN 22.76° and 20.76° for SiO_2 and 25.60° for AI_2O_3). SiO_2 composition for each type of activated carbon is presented in Table 2.

Table 2 SiO_2 composition in each of the activated carbon from pyrolyzed oil palm kernel shells

Activated carbon	SiO_2 composition (%)
AN	93.8
AH	81.0
AA	79.4
AF	76.2

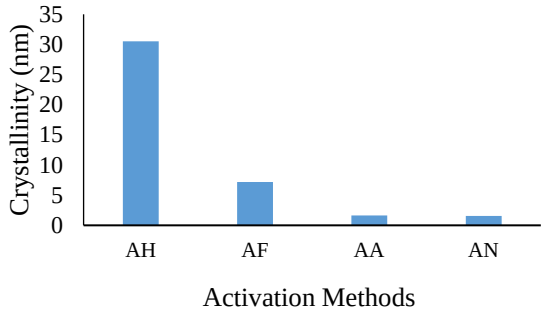
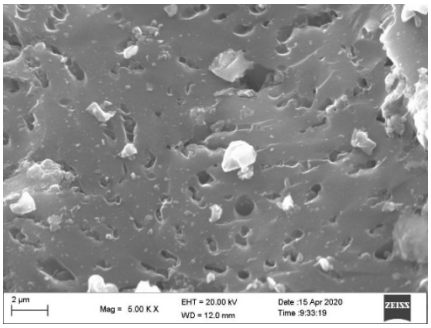


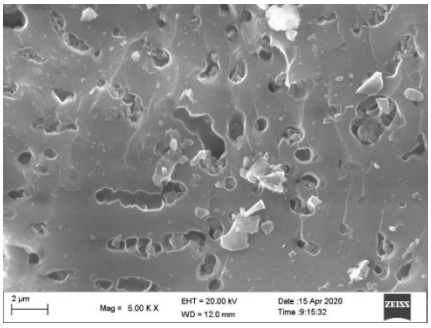
Fig. 2 Crystallinity of the activated carbon in various activation methods

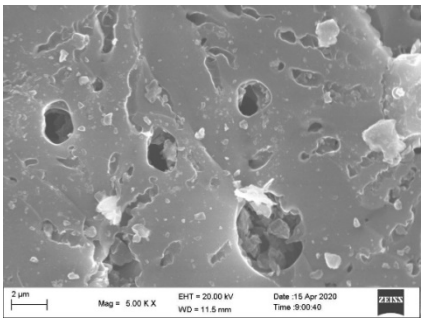
Figure 2 shows the crystallinity of the activated carbon from pyrolyzed palm shells in various activation methods, which was calculated using the Scherrer equation [16]. The crystallinity of activated carbons AH, AF, AA and AN were 30.51 nm; 7,18 nm; 1.64 nm and 1.55 nm. The analysis on activated carbon AN showed that it has lower crystallinity and the presence of amorphous SiO_2 is visible in the X-ray spectrum $2\theta = 20.76°$. This result confirms a previous study by Simatupang and Devi [17], that silica with a peak widened around $2\theta = 20° - 22°$ showed an amorphous structure (low crystalline degree). In addition, activated carbon AN showed a 2θ shift and caused a slight irregular sharp peak for the observed crystal structure. This is because the NaOH activation process changed the palm shell crystals. The characteristics of amorphous silica are shown from the sloping peaks in the range of $2\theta = 22°$ [18].

Structural and Morphological Analysis Using Scanning Electron Microscope (SEM)

The surface morphology of the activated carbon was identified by magnifying the object 5,000 times. The results are presented in Fig. 3. SEM analysis showed that activated carbons AH, AA and AF have particle sizes of (389.6 nm - 1.329 µm; 481.2 nm - 985.4 nm; 733.7 nm - 3.863 µm). The pore structure was formed as the non-carbon compounds in the palm shells evaporated and dissolved due to the pyrolysis process, leaving empty spaces that form pores [19].


(a) AH


(b) AA


(c) AN

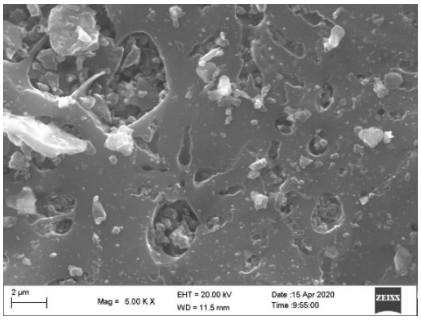

(d) AF

Fig. 3 SEM analysis of the palm kernel shell carbon with various activation at 5,000-time magnification.

The three activated carbons have irregular particle shapes and impurities are present, covering the pore surface. This is because the activated

carbons can easily dissolve in an acidic atmosphere [20] so that activation in an acidic atmosphere reduced the particle size of activated carbon, while furnace activation has a high ash content and these impurities clogged the pores of the activated carbon, resulting in the reduced surface area.

SEM analysis results for the non-activated carbon (NA), as also seen in an earlier study by Faisal et al. [21], showed that the carbon prepared from oil palm shells has a particle size below 500 nm and a rough and irregular pore surface. The AN activated carbon has a particle size of 287.9 nm – 3.965 μm and open pores with a cleaner surface compared to the other activated carbons. This is because NaOH activation could minimize tar formation and dissolve impurities. In addition, NaOH activation reduces hydrocarbons, which made the AN carbon surface more visible. Good pore formation can increase the ability of activated carbon to adsorb heavy metals [22]. This is in line with a study by Faisal et al. [21,23], that liquid smoke activated carbon particles have a smaller size than the activated carbon NaOH under the same conditions and activation method (immersed in a solution for 24 hours) with a particle size below 500 nm.

Functional Group Analysis Using Fourier Transform Infrared (FTIR)

The chemical functional groups of adsorbents NA, AN, and AA were identified using FTIR with a range of 500-4000 cm^{-1}.

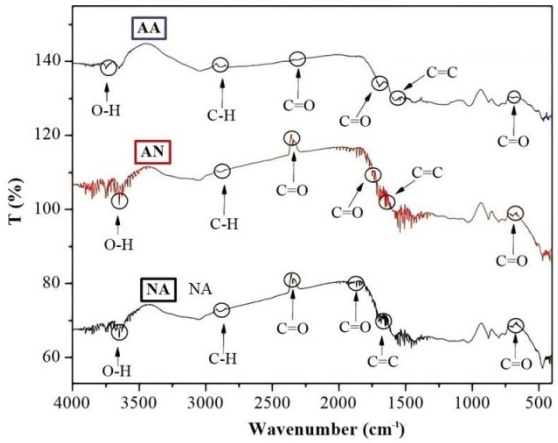


Fig. 4 Results of FTIR analysis of NA and activated carbons of AN and AA

Figure 4 shows that in the NA sample at a wavelength of 1791.87 cm^{-1}, there were peaks containing aldehyde, ketone and carboxylate groups. Meanwhile, in the AN sample, the presence of these groups decreases while the intensity increases in the AA sample. This is because NaOH is alkaline and liquid smoke contains more acid, resulting in a decrease in adsorption peak which is an indication of the formation of aromatic compounds [24]. The effect of adsorption intensity in the wavelength region will result in a change in the functional group structure.

Table 3 FTIR spectrum of carbon from pyrolyzed palm kernel shells

Functional group	Bonds	Reference	Wavenumber (cm^{-1})
			Before activated
Hydroxyl	O-H	4000-3400	3743.83
Aromatic Alkyls	C-H	3000-2700	2837.29
Aldehydes, Ketones, Carboxyl Acids	C=O	1900-1650	1791.87
Aromatic Alkenyl	C=C	1690-1450	1543.05
			NaOH activated
Hydroxyl	O-H	4000-3400	3751.55
Aromatic Alkyls	C-H	3000-2700	2839.22
Aldehydes, Ketones, Carboxyl Acids	C=O	1900-1650	1766.80
Aromatic Alkenyl	C=C	1690-1450	1560.41
			Liquid smoke activated
Hydroxyl	O-H	4000-3400	3745.76
Aromatic Alkyls	C-H	3000-2700	2879.72
Aldehydes, Ketones, Carboxyl Acids	C=O	1900-1650	1915.31
Aromatic Alkenyl	C=C	1690-1450	1575.84

The FTIR analysis of palm kernel shell activated carbon for each type of activator showed that the absorption of O-H, C-H, C=O and C=C groups dominated the three samples. The presence of O-H and C-O bonds indicates that the activated carbon produced is polar. The O-H functional group has a

negative charge which is highly reactive to metals, while the C=O group is a typical group found in activated carbon which increases the adsorbent performance in the adsorption process [19]. This confirms a previous study by Razi et al. [25] that the presence of OH group as the main functional group on NaOH-activated carbon from palm shells contributed to the reduction of pollutants from water. Table 3 presents the results of the FTIR spectra of NA, AN and AA adsorbents.

CONCLUSION

The results show that the activation method affected the characteristics of the activated carbon produced. Activated carbon with NaOH has a moisture content of 4.7% and an ash content of 7% and is the best activated carbon by SII standard. This activated carbon has a clean and even surface and has a crystalline value of 1.55 nm, which indicates the presence of amorphous SiO_2 and SiO_2 composition of 93.8%. FTIR analysis showed that all activated carbon had the dominant adsorption of O-H, C-H, C=O and C=C groups and that the activated carbon was polar. These results suggest that further research is needed to evaluate the performance of each activated carbon for the adsorption of various chemical compounds, especially those in industrial waste.

ACKNOWLEDGMENTS

The authors acknowledge Universitas Syiah Kuala and the Ministry of Education and Culture for funding and provided research facilities.

REFERENCES

[1] Tiryaki B., Yagmur E., Banford A., and Aktas Z., Comparison of Activated Carbon Produced from Natural Biomass and Equivalent Chemical Compositions. Journal of Analytical and Applied Pyrolisis, Vol. 105, 2014, pp. 276-283.

[2] Feng P., Li J., Wang H., and Xu Z., Biomass-based Activated Carbon and Activators: Preparation of Activated Carbon from Corncob by Chemical Activation with Biomass Pyrolysis Liquids. ACS Omega, Vol. 5, Issue 37, 2020, pp. 24064-24072.

[3] Naeem M.A., Imran M., Amjad M., Abbas G., Tahir M., Murtaza B., Zakir A., Shahid M., Bulgariu L., and Ahmad I., Batch and Column Scale Removal of Cadmium from Water Using Raw and Acid Activated Wheat Straw Biochar. Journal of Water, Vol.11, Issue 7, 2019, pp. 1-17.

[4] Barragan-Pena P., Marcedo-Miranda M.G., and Olguin M.T., Cadmium Removal from Wastewater in a Fixed-Bed Column System with Modified-Natural Clinoptilolite-Rich Tuff. Chemical Papers, Vol. 75, 2020, pp. 485-491.

[5] Xavier A.L.P., Adarme O.F.H., Furtado L.M., Ferreira G.M.D., Silva L.H.M., Gil L.F., and Gurgel L.V.A., Modelling Adsorption of Copper (II), Cobalt (II) And Nickel (II) Metal Ions from Aqueous Solution onto a New Carboxylated Sugarcane Bagasse. Part II: Optimization of Monocomponent Fixed-Bed Column Adsorption. Journal of Colloid and Interface Science, Vol. 516, 2018, pp. 431-445.

[6] Rajeshwari M., Agrawal P., Pavithra S., Priya, Sandhya G.R., and Pavithra, G.M., Continuous Biosorption of Cadmium by *Moringa olefera* in a Packed Column. Biotechnology and Bioprocess Engineering, Vol. 18, Issue 2, 2013, pp. 321–325.

[7] Yan-jiao G., Cadmium and Cobalt Removal from Heavy Metal Solution Using Oyster Shells Adsorbent. Asian Journal of Chemistry, Vol. 25, Issue 15, 2011, 1098-1101.

[8] Sousa F.W., Oliveira A.G., Ribeiro J.P., Rosa M.F., Keukeleire D., Nascimento R.F., Green Coconut Shells Applied as Adsorbent for Removal of Toxic Metal Ions Using Fixed-Bed Column Technology. Journal of Environmental Management, Vol. 91, Issue 8, 2010, pp. 1634-1640.

[9] Amarasinghe, B.M.W.P.K., Lead and Cadmium Removal from Aqueous Medium Using Coir Pith as Adsorbent: Batch and Fixed Bed Column Studies. Journal of Tropical Forestry and Environment, Vol. 1, Issue 1, 2011, pp. 36-47.

[10] Banerjee M., Bar N., Basu R.K., and Das R.K., Removal of Cr(VI) from Its Aqueous Solution Using Green Adsorbent Pistachio Shell: A Fixed Bed Column Study and GA-ANN Modeling. Water Conservation Science and Engineering, Vol. 3, Issue 1, 2018, pp. 19-31.

[11] Faisal M., Abubakar, Kelana S.P, and Nanda D.E., Removal of Cu^{2+}Ions Using Activated Carbon from Palm Kernel Shell Waste By Liquid Smoke Activation. International Journal on Advanced Science Engineering Information Technology, Vol. 10, Issue 6, 2020, pp. 2560-2566.

[12] Faisal M., Gani A., Husni and Daimon H., A Preliminary Study of the Utilization of Liquid Smoke from Palm Kernel Shells for Organic

Mouthwash. International Journal of GEOMATE, Vol. 13, Issue 37, 2017, pp. 116-120.

[13] Harahap H.H., Malik U., and Dewi R., Pembuatan Karbon Aktif dari Cangkang Kelapa Sawit dengan Menggunakan H_2O sebagai Aktivator untuk Menganalisis Proksimat, Bilangan Iodine dan Rendemen. Jurnal Online Mahasiswa Universitas Riau, Vol. 1, Issue 2, 2014, pp. 48-54.

[14] Laos L. E., and Selan A., Pemanfaatan Kulit Singkong sebagai Bahan Baku Karbon Aktif. Jurnal Ilmu Pendidikan Fisika, Vol. 1, Issue 1, 2016, pp. 32-36.

[15] Setiyoningsih L.A., Dwi I., and Tri M., Pembuatan dan Karakterisasi Arang Aktif Kulit Singkong Menggunakan Aktivator ZnCl2. Jurnal Kimia Riset, Vol. 3, Issue 1, 2018, pp. 13-19.

[16] Silas K., Ghani W.A.W.A.K., Choong T.S.Y., and Rashid U., Activated Carbon Monolith CO_3O_4 Based Catalyst: Synthesis, Characterization and Adsorption Studies. Environmental Technology and Innovation, Vol. 12, Issue 4, 2018, pp. 273-285.

[17] Simatupang L., and Devi, The Preparation and Characterization of Sinabung Volcanic Ash as Silica Based Adsorbent. Jurnal Pendidikan Kimia, Vol. 8, Issue 3, 2016, pp. 159-163.

[18] Su Y., Liu L., Zhang S., Xu D., Du H., Cheng Y., Wang Z., and Xiong Y., A Green Route for Pyrolysis Poly-Generation of Typical High Ash Biomass, Rice Husk: Effects on Simultaneous Production of Carbonic Oxide-Rich Syngas, Phenol-Abundant Bio-Oil, High-Adsorption Porous Carbon and Amorphous Silicon Dioxide. Bioresource Technology, Vol. 295, 2019, pp. 122243.

[19] Mentari V.A., Handika G., and Maulina S., Perbandingan Gugus Fungsi dan Morfologi Permukaan Karbon Aktif dari Pelepah Kelapa Sawit Menggunakan Aktivator Asam Fosfat (H_3PO_4) dan Asam Nitrat (HNO_3). Jurnal Teknik Kimia USU, Vol. 7, Issue 1, 2018, pp. 16–20.

[20] Wu Z.C., Wang Z.Z., Liu J., Yin J.H., and Kuang S.P., A New Porous Magnetic Chitosan Modified by Melamine for Fast and Efficient Adsorption of Cu(II) Ions. International Journal of Biological Macromolecules, Vol.81, 2015, pp. 838-846.

[21] Faisal M., Gani A., and Fuadi Z., Utilization of Activated Carbon from Palm Kernel Shells as the Bioadsorbent of Lead Waste. International Journal of GEOMATE, Vol. 20, Issue 78, 2021, pp. 81-86.

[22] Verayana, Paputungan M., and Iyabu H. Pengaruh Aktivator HCl dan H_3PO_4 Terhadap Karakteristik (Morfologi Pori) Arang Aktif Tempurung Kelapa Serta Uji Adsorpsi Pada Logam Timbal (Pb). Jambura Journal of Educational Chemistry, Vol. 13, Issue 1, 2018, pp. 67-75.

[23] Faisal M., Gani A., and Abubakar, Removal of Copper Ions from Aqueous Solution Using Palm Shell Charcoal Activated By NaOH. International Journal of GEOMATE, Vol. 15, Issue 48, 2018, pp. 143-147.

[24] Mohideen M.F, Faiz M., Salleh H., Zakaria H., and Raghavan V., Drying of Oil Palm Frond Via Swirling Fluidization Technique. In Proceedings of the World Congress on Engineering, Vol. 3, 2011, pp. 2375-2380.

[25] Razi M.A.M, Al-Gheeti A., Al-Qaini M., and Yousef, A., Efficiency of Activated Carbon from Palm Kernel Shell for Treatment of Greywater. Arab Journal of Basic and Applied Sciences, Vol. 25, Issue 3, 2018, 103–110.

IMPROVEMENT OF ETHANOL PRODUCTION FROM THE PALM OIL MILL EFFLUENT WASTEWATER TREATMENT

Andri Gumilar[1], Mindriany Syafila[1], Marisa Handajani[1] and Syarif Hidayat[1]

[1] Water and Wastewater Engineering Research Group, Faculty of Civil and Environmental Engineering, Institut Teknologi Bandung, Indonesia

ABSTRACT

Ethanol is an alternative energy that can be considered to replace energy sources derived from fossils. Ethanol can be produced at the acidogenesis stage of the anaerobic conversion process of palm oil mill effluent wastewater. The efficiency of bioethanol formation is influenced by several factors, including the presence of micronutrients such as molybdenum and nickel. The purpose of this study was to determine the effect of the presence of molybdenum and nickel in the anaerobic wastewater treatment process on the formation of ethanol. Palm oil mill effluent was used as a substrate which was added with Mo with a concentration of 1 and 3 mg/L and Ni of 0.25 and 0.5 mg/L. Mixed culture bacteria as biomass was used in the reactor. CBR reactor is used with an operational time of 72 hours. The reactor performance was investigated by measuring ethanol production, volatile fatty acids, VSS, pH and soluble COD. It was found that in the reactor with the addition of variations of Mo 3 mg/L and Ni of 0.25 mg/L ethanol production was higher than the other reactor about 578.44 mgCOD/L, while the higher COD removal occurs in the reactor with the addition of Mo and Ni variations of 1 mg/L and 0.25 mg/L respectively, which was 23.4%. These results show that the anaerobic product formation was influenced by the presence of molybdenum and nickel.

Keywords: Anaerobic processes, Ethanol, Palm oil mill effluent, Volatile fatty acids.

INTRODUCTION

The utilization of renewable energy is an alternative that can be developed to replace dependence on energy sources originating from fossils. Currently, the main energy sources come from fossil fuels consisting of petroleum (35%), coal (29%) and natural gas (24%) [1]. There are at least three main problems with the use of fossil fuels, including the depletion of known petroleum reserves, the instability of world oil prices due to a higher demand rate from oil production itself, and the emergence of greenhouse gases as a result of burning fossil fuels.

Ethanol is an alternative energy that can substitute fossil fuels. The advantages of ethanol used as fuel were supporting a sustainable economy by reducing the use of fossil fuels, reducing CO_2 accumulation and leading to zero net CO_2 output into the atmosphere [2]. Ethanol production capacity in 2005 and 2006 was about 45 and 49 billion liters respectively and it increased in 2015 by more than 115 billion liters [3].

The previous research indicated that high organic content wastewater can be used as a substrate for ethanol production using anaerobic processes. Palm oil mill effluent (POME) had a high concentration of organic, such as carbohydrate, protein, nitrogen compounds, oil and grease, high mineral content, and other organic compounds, such as cellulose, hemicellulose, and starch [4]. BOD and soluble COD concentration of POME were about 12,450 mg/L and 17,300 mg/L respectively [5]. Bioconversion of the high organic content wastewater can be used for biofuels production such as ethanol, hydrogen, methanol and ethanol [6]. The anaerobic process pathway proceeds in four stages, that are hydrolysis, acidogenesis, acetogenesis and methanogenesis [7]. The ethanol formation process is formed in the acetyl-CoA/Wood-Ljungdahl pathway for the production of acetyl-CoA, a precursor of cellular biomass, acetate, and ethanol. Key enzymes of this pathway include format dehydrogenase (FDH), bifunctional carbon monoxide dehydrogenase/acetyl CoA synthase (CODH/ACS), and hydrogenase (H_2ase), all of which are metalloenzymes [8].

Ethanol and other intermediate products are formed during the acidogenic phase. The anaerobic fermentation process involves cell metabolism influenced by micronutrients, such as metal ions even though the amount of it may be very low [9]. Some research has been reported the influence of metal addition to ethanol production. The addition of iron (II) concentration of 200 mg/L produced ethanol equal to the control (without iron addition), while addition of iron concentration of 400 mg/L produced ethanol 122 times lower than control and 600 mg/L of iron (II) could not produce the ethanol [10]. The combination of iron (II) and other metals also influenced ethanol production. For another

combination of iron (II) and magnesium (II) with the concentration are 0.5 mg/L-Fe + 0.5 mg/L-Mg; 1.5 mg/L-Fe + 0.5 mg/L-Mg and 2.5 mg/L-Fe + 0.5 mg/L-Mg produced ethanol with the concentration are 463.7; 572.3 and 689.7 mg/L respectively [5]. The experimental efficiency of ethanol yield under optimal conditions enhances the efficiency of ethanol yield by 5.63% by the addition of Mn^{2+} [9]. The addition of combination Mn^{2+} and Mg^{2+} can increase ethanol concentration from 93.45 g/L to 120.58 g/L sweet sorghum juice media [11]. Ethanol concentration increases from 64,53 g/L to 85,62 g/L in the addition of Cu^{2+} and Mn^{2+} from cane molasses. Cu^{2+} acts as a cofactor of some enzymes, such as cytochrome c oxidase, Cu, Zn-superoxide dismutase. Regarding Mn^{2+}, it is important in the metabolism of *S. cerevisiae* as a part of some enzymes relating to ethanol fermentation such as pyruvate carboxylase [11]. Mg^{2+} involves in physiological function, growth, metabolism and enzyme activity. Mg^{2+} had a positive effect on ethanol production. Mg^{2+} reduces the proton, especially anion permeability of the plasma membrane by interacting with membrane phospholipids, resulting in stabilization of the membrane bilayer. Therefore, it relates to the improvement of ethanol tolerance of microorganisms. According to Lettinga [12], the chemical composition of the methanogenic microorganisms is Fe, Ni, Co, Mo, Zn, Mn and Cu.

This research aimed to determine the effect of metal ion (Ni and Mo) addition on the ethanol formation from the POME treatment under anaerobic conditions. Metal ions have been found to maintain structural integrity and functionality of intracellular organelles, induce cell-cell interaction such as flocculation, govern gene expression and nutrient uptake mechanisms, activate arrays of enzymes intimately involved in metabolism, and also, acting as stress-protectants. Metal ions can affect the rate of glycolysis and conversion of pyruvate to ethanol and other volatile organic acids [13], increased fermentability and ethanol yield, improved yeast viability and vitality [14]. The products of the acidogenesis phase indicate a shifting of the fermentation pathway. This shifting was interfered with by the enzyme availability. The enzyme that contains iron and zinc that are usually available in Gram-negative bacteria are the main factor for ethanol production [15]. Alcohol dehydrogenase enzyme (ADH) was the main enzyme for ethanol production. Iron addition increased the activity of the alcohol dehydrogenase enzyme therefore the ethanol production could be increased [16].

RESEARCH SIGNIFICANCE

The novelty and originality of this research is the effect of the metal addition to increasing the production of ethanol in the anaerobic processing of palm oil mill effluent wastewater. The metal addition to the wastewater can be used as a basis for consideration in a strategy to control the formation of bioenergy towards such as ethanol. It is hoped that this research can make a scientific contribution and can provide information related to the use of palm oil mill effluent wastewater as a substrate for the formation of ethanol as alternative energy.

MATERIAL AND METHODS

Wastewater and Bioreactor

This research conducted on a laboratory scale. The wastewater, for substrate, was collected from the palm oil industry, PT Condong Garut, Indonesia. Biomass was taken from the sludge of pome mixed by cow rumen with the ratio of 50:50 (v/v) and acclimated to the wastewater. The concentration of biomass in terms of mixed liquor suspended solid (MLSS) and mixed liquor volatile suspended solid (MLVSS), were about 6.34 g ss/L and 4.72 g vss/L respectively.

Anaerobic batch reactor with the working volume of 5l was operated with the flushing n_2 1L/min for the first 24 h for purging O_2 in the headspace and continued with internal biogas circulation until 72 h (Fig. 1).

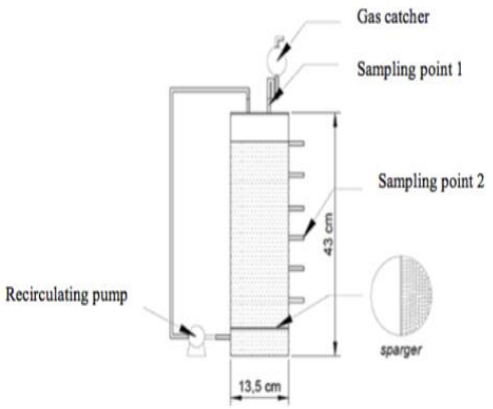


Fig. 1 Anaerobic batch reactor

The reactor was operated at room temperature (25°C ± 2°C). In the beginning, pH was adjusted to 6.5-7.0. Reactor filled by POME as a substrate and biomass with the ratio 4:1 (v/v). The concentration of the nickel addition was 0.25; 0.50 mg/L and 0 mg/L as a control and the concentration of molybdenum addition were 1; 3 mg/L and 0 mg/L as a control. $NiSO_46H_2O$ (p.a) was used as a source of nickel and $(NH_4)_6Mo_7O_244H_2O$ as a source of molybdenum. The addition of the metal ion was supplemented into POME at concentrations

indicating in Table 1. Samples were collected every 6 h and analyzed for soluble COD, pH, VSS, ethanol and volatile fatty acid.

Table 1 Experimental design for study effect of trace metal on ethanol production

Run	Ni (mg/L)	Mo (mg/L)	Notes
1		0	Control
2	0	1	Reactor A
3		3	Reactor B
4		0	Reactor C
5	0.25	1	Reactor D
6		3	Reactor E
7		0	Reactor F
8	0.5	1	Reactor G
9		3	Reactor H

Analytical Method

Soluble COD, pH and VSS was analysed refer to Standard Method for the Examination Water and Wastewater 23rd edition 2017. Volatile fatty acids were analyzed using HPLC type Hitachi Interface D-7000 HSM (UV-Vis detector Hitachi L-7400 and L-7100 Hitachi pump) with analytical column Aminex HPX-87H, and ethanol was analyzed using GC Shimadzu 17-A with column Analytic DB-Wax (propylene glycol).

Calculation

The units of each product are uniformized by using the following equation [17].

Acidogenic product equation:

$$COD_{theoritical}=8(4x+y-2z)/(12x+y+16z)gCOD.g^{-1}CxHyOz \quad (1)$$

Note: x = C; y =H and z = O

Significant differences in the ethanol production were analyzed by ANOVA two-factors, with H0 there is no significant difference in adding trace elements.

RESULTS AND DISCUSSION

Characteristics of Palm Oil Mill Effluent (POME)

The characteristic of POME which was used for ethanol production was presented in Table 2. POME had the high concentration of organic material, as soluble COD and BOD was a concentration of 18,433 mg/L and 14,500 mg/L respectively. Both COD and BOD reflect the high concentration of organic and it will potentially environmental problem for any untreated discharged. POME also contained macro and micronutrients such as nitrogen, potassium, magnesium, calcium, cadmium, copper, chromium and iron. Carbohydrates, lipids and minerals found in POME [18]. POME is one of the wastewaters which difficult to treat due to its massive and unproper treatment [19]. The processing carried out at this time is still unable to remove the hazardous compounds contained in palm oil mill effluent [20]–[22]. Currently, most of the processes that are carried out to treat POME are in open ponds which are relatively low cost and easy to do. However, this processing has the potential to pollute the environment, for example, the emergence of the greenhouse gas effect [23]–[25], also takes a fairly large area [26]. Ethanol can be produced through the proper processing of high concentrations of organic wastewaters. It means that POME could be used as a substrate for ethanol production under anaerobic conditions. The products produced in this processing are strongly influenced by the conditions of the processing itself.

Table 2 Characteristic of palm oil mill effluent

Parameter	Conc
Total COD	30367
BOD	14500
Soluble COD	18433
pH	4,3
Oil and grease	630
Ammonia (NH_3)	26,77
Nitrogen total	265,67
Total suspended solids (TSS)	6200
Volatile suspended solids (VSS)	3967
Ethanol	44,4
Volatile fatty acids (VFA's)	566,67
Iron (Fe)	14,96
Manganese (Mn)	2,09
Molybdenum (Mo)	< 0,001
Nickel (Ni)	0,025
Cooper (Cu)	0,073
Zinc (Zn)	0,051

Note: All units in mg/L, pH without unit

Effects of trace metals on the ethanol production

In this study, nickel and molybdenum were added to the reactor with different concentration variations. These trace elements were added individually or a combination of several concentrations, with one control reactor without adding trace elements.

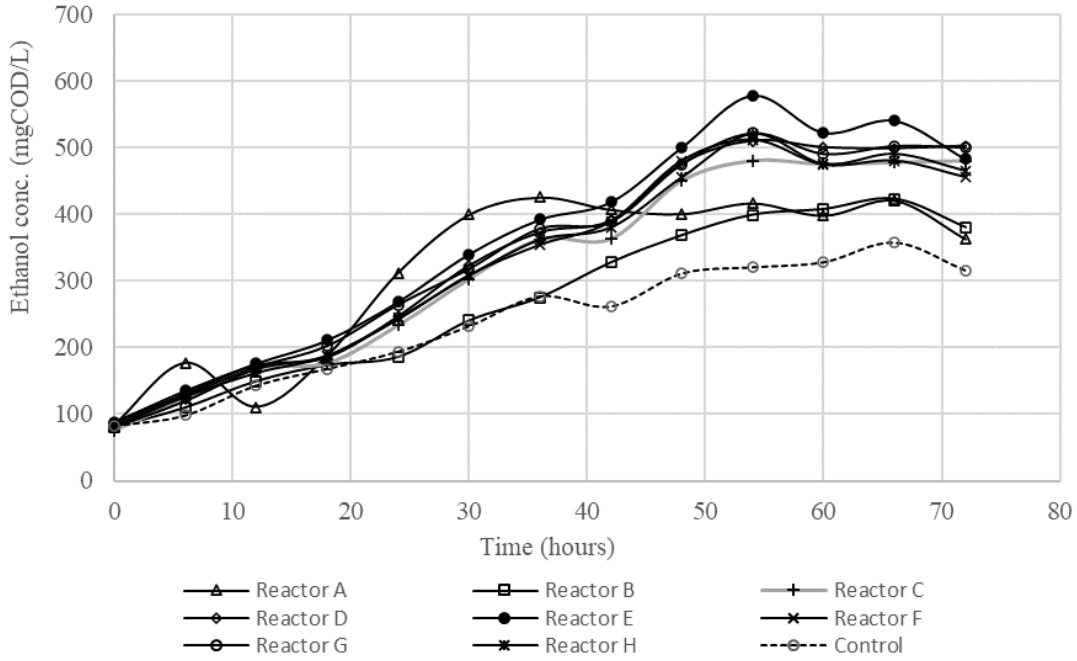


Fig. 2 Ethanol concentration in the reactor during the processes.

In Fig. 2, it can be seen that an increase in the concentration of ethanol occurred in almost all reactors from the beginning to the 54th hour. After 54 hours, the ethanol concentration tended to be stable and even decreased. Compared to the control, the increment of Ni and Mo addition improved ethanol production. The experiment indicated that the concentration of Ni and Mo addition influenced the lag and the exponential phase of ethanol production. The addition of Ni and Mo at a concentration of 3 and 0.25 mg/L (reactor E) can produce ethanol in a larger amount compared with the addition of other concentrations of 578.44 mgCOD/L. Reactor G and H with the addition of Ni and Mo respectively 0.5; 1 mg/L and 0.5; 3 mg/L produced almost similar ethanol at 521.68 mgCOD/L and 520.88 mgCOD/L. Reactors A and B which only added 1 and 3 mg/L of Mo (without Ni addition) respectively, could produce the ethanol with the concentration 416.78 mgCOD/L and 399.39 mgCOD/L respectively. The addition of trace metal at the optimum concentration was increased ethanol production by about 63.6%. Demirel and Scherer [27] reported that the addition of trace elements such as Fe, Mo, Ni, Co etc. can have a positive influence on the anaerobic process, which otherwise does not substrate. A trace element is an essential part of enzymes as a co-factor in the anaerobic process stage which directly affects the performance of microbes and can increase the efficiency in the anaerobic system [28].

The significance test was carried out to see the effect of adding trace elements to the formation of ethanol. The ANOVA results of trace elements added to improving ethanol production presented in Table 3. Based on the results of two-way ANOVA factorial statistics on ethanol formation, all H0 for each variation is rejected, meaning that all factors at various levels have a significant effect to increase ethanol formation in the anaerobic process.

Table 3 The results of two-way ANOVA calculation on ethanol formation

Variation	SS	Df	MS	F-value	F-table 5%	F-tables 1%	Results
A (Ni)	63266.5049	2	31633.252	48.406186	3.11	5.06	H0 rejected
B (Mo)	6622.54453	2	3311.2723	5.0670118	3.11	5.06	H0 rejected
AB	81864.481	4	1523.4917	3.3312944	3.11	5.06	H0 rejected
Error	5881.4646	9	653.49607				
Total	6093.96693	17					

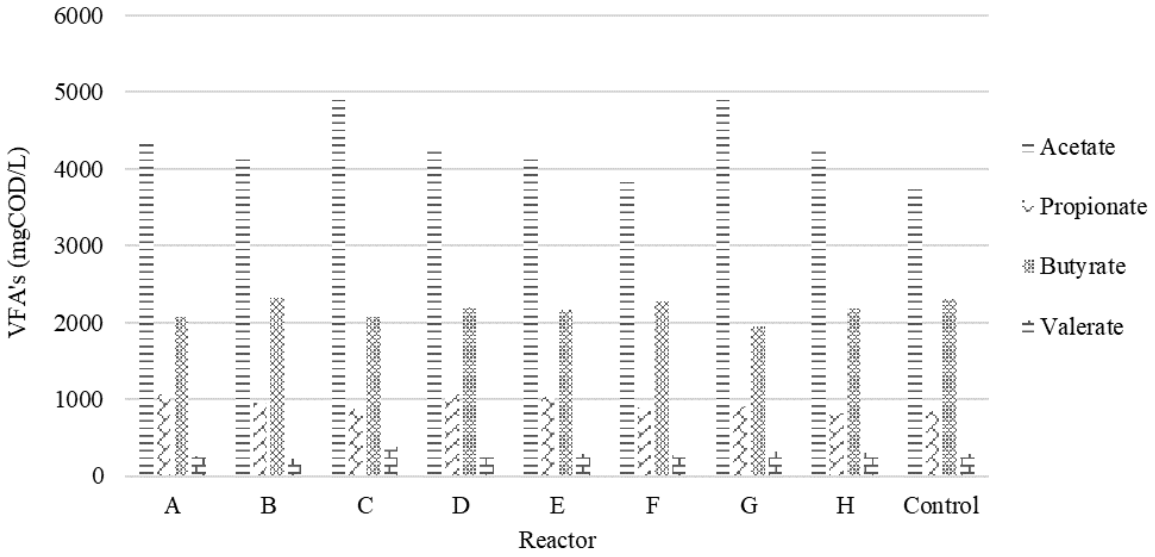


Fig. 3 Volatile fatty acid production during anaerobic processes

Acidogenesis product formation

Another product produced during the anaerobic process is the formation of volatile fatty acids (VFA). The optimum conditions for ethanol formation were chosen to study the effect of adding trace elements to the formation of other acidogenesis products. During anaerobic processes, volatile fatty acids such as acetate, propionate, butyrate and valeric produced with a concentration higher than ethanol concentration. The dominant of VFA's species were acetate, with the concentration of about 4972.57 mg COD/L in the reactor with the addition Ni 0.5 mg/L and Mo 1 mg/L. The formation of VFA's shown in Fig. 3.

The presence of trace elements can increase the optimization of the reaction rate at the hydrolysis and acidogenesis stages so that the production of organic acids will increase [29]. In other words, hydrolysis and acidogenesis bacteria got the benefit from the presence of nickel and molybdenum. In a study conducted by Evranos and Demirel [30], it was found that the presence of Ni can increase the performance of the hydrogenase enzyme and can increase bacterial growth, meanwhile, the presence of Mo can only increase bacterial growth. Table 3 shows that in this study, the addition of Mo did not have much effect on the growth of biomass, this can be seen from the VSS concentration between the control and the addition of Mo and Ni did not have much impact on increasing the VSS concentration. The products produced in the anaerobic processing of POME shown in Table 4. To compare the concentration of acidogenic products during the process, the units of each product are uniformized using Eq. 1.

Table 4 Anaerobic product formation during anaerobic processes

	A	B	C	D	E	F	G	H	Control
Ethanol *	416.78	399.39	480.11	510.21	578.44	511.24	521.68	520.88	320.52
Acetate *	4315.81	4118.81	4961.03	4228.45	4199.52	3819.33	4972.57	4281.65	3815.73
Propionate *	1056.53	962.12	878.25	1056.62	1037.44	886.73	916.28	821.73	844.81
Butyrate *	2073.49	2319.98	2078.94	2202.60	2168.87	2274.72	1954.31	2175.13	2305.08
Valerate *	251.66	231.83	382.51	248.33	283.61	272.62	318.5	300.25	291.66
TVFA's *	7697.49	7632.74	8300.73	7736.00	7689.44	7253.40	8161.66	7578.76	7257.28
VSS	4222	4192	4371	4491	4264	4517	4291	4028	4296
COD	14368	14886	14953	14119	14368	15027	14892	15120	16520
pH	5.13	5.66	4.98	5.19	5.28	5.21	4.89	5.36	4.79

Note: (*) units in mgCOD/L; VSS and soluble COD in mg/L; pH without unit.

The main acidogenesis products can be seen in Fig. 2 and Fig. 3. Based on Fig. 2, the largest ethanol can be produced in reactor E, namely with the addition of Mo 3 mg/L and Ni of 0.25 mg/L. With the addition of these metal ions, the amount of TVFA's was 7689.44 mgCOD/L. The TVFA's produced in other reactors ranged from 7253-8300 mgCOD/L with the largest production occurring in reactor C with the addition of Ni 0.25 mg/L. As for the control reactor, the amount of ethanol and TVFA's produced is less than the reactor with the addition of Mo and Ni. In other words, the addition of Mo and Ni ions added to the reactor can affect the resulting acidogenesis product.

CONCLUSION

The results showed that the presence of the micronutrients, such as nickel (Ni) and molybdenum (Mo) had a significant effect on ethanol formation. The control variation without the addition of Ni and Mo resulted in ethanol of 320.52 mgCOD/L. The concentration of 0.25 mg/L Ni and 3 mg/L Mo gave the highest ethanol production about 578.44 mgCOD/L. Based on the results of this study, the addition of nickel (Ni) and molybdenum (Mo) can increase the formation of ethanol greater than the formation of ethanol without the addition of metal ions.

ACKNOWLEDGMENTS

This research was funded by the Research, Community Development and Study Group Innovation Program (*Program Penelitian, Pengabdian kepada Masyarakat dan Inovasi* /P2MI), ITB 2021.

REFERENCES

[1] A. Ahmad, A. Buang, and A. H. Bhat, "Renewable and sustainable bioenergy production from microalgal co-cultivation with palm oil mill effluent (POME): A review," *Renew. Sustain. Energy Rev.*, vol. 65, 2016, pp. 214–234.

[2] Y. Yamashita, C. Sasaki, and Y. Nakamura, "Development of efficient system for ethanol production from paper sludge pretreated by ball milling and phosphoric acid," *Carbohydr. Polym.*, vol. 79, no. 2, 2010, pp. 250–254.

[3] F. Talebnia, D. Karakashev, and I. Angelidaki, "Production of bioethanol from wheat straw: An overview on pretreatment, hydrolysis and fermentation," *Bioresour. Technol.*, vol. 101, no. 13, 2010, pp. 4744–4753.

[4] N. K. N. Al-Shorgani *et al.*, "Process optimization of butanol production by Clostridium saccharoperbutylacetonicum N1-4 (ATCC 13564) using palm oil mill effluent in acetone–butanol–ethanol fermentation," *Biocatal. Agric. Biotechnol.*, vol. 4, no. 2, 2015, pp. 244–249.

[5] M. Handajani, A. Gumilar, and M. Syafila, "Effect of iron and magnesium addition for ethanol production from the conversion of palm oil mill effluent by anaerobic processes," *IOP Conf. Ser. Earth Environ. Sci.*, vol. 106, no. 1, 2018.

[6] A. Salihu and M. Alam, "Palm oil mill effluent: A waste or a raw material?," *J. Appl. Sci. Res.*, vol. 8, 2012, pp. 466–473.

[7] S. Sharma, S. Basu, N. P. Shetti, M. Kamali, P. Walvekar, and T. M. Aminabhavi, "Waste-to-energy nexus: A sustainable development," *Environ. Pollut.*, vol. 267, 2020, p. 115501.

[8] H. L. Drake, K. Küsel, and C. Matthies, "Acetogenic prokaryotes," *Prokaryotes Prokaryotic Physiol. Biochem.*, 2013, pp. 3–60.

[9] W. Cao and R. Liu, "Screening and optimization of trace elements supplement in sweet sorghum juice for ethanol production," *Biomass and Bioenergy*, vol. 50, 2013, pp. 45–51.

[10] Y. Yamashita, A. Kurosumi, C. Sasaki, and Y. Nakamura, "Ethanol production from paper sludge by immobilized Zymomonas mobilis," *Biochem. Eng. J.*, vol. 42, no. 3, 2008, pp. 314–319.

[11] O. Deesuth, P. Laopaiboon, P. Jaisil, and L. Laopaiboon, "Optimization of Nitrogen and Metal Ions Supplementation for Very High Gravity Bioethanol Fermentation from Sweet Sorghum Juice Using an Orthogonal Array Design," *Energies* , vol. 5, no. 9. 2012.

[12] G. Lettinga, "Sustainable integrated biological wastewater treatment," *Water Sci. Technol.*, vol. 33, no. 3, 1996, pp. 85–98.

[13] M. Azenha, M. T. Vasconcelos, and P. Moradas-Ferreira, "The influence of Cu concentration on ethanolic fermentation by Saccharomyces cerevisiae," *J. Biosci. Bioeng.*, vol. 90, no. 2, 2000, pp. 163–167.

[14] C. Xue, X.-Q. Zhao, W.-J. Yuan, and F.-W. Bai, "Improving ethanol tolerance of a self-flocculating yeast by optimization of medium composition," *World J. Microbiol. Biotechnol.*, vol. 24, no. 10, 2008, p. 2257.

[15] Y. F. Li, N. Qi Ren, Y. Chen, and G. Xiang Zheng, "Ecological mechanism of fermentative hydrogen production by bacteria," *Int. J. Hydrogen Energy*, vol. 32, no. 6, 2007, pp. 755–760.

[16] J. Saxena and R. S. Tanner, "Effect of trace metals on ethanol production from synthesis gas by the ethanologenic acetogen, Clostridium ragsdalei.," *J. Ind. Microbiol. Biotechnol.*, vol. 38, no. 4, 2011, pp. 513–521.

[17] P. M. B. T.-B. E. P. Doran, Ed., "A - Conversion Factors," London: Academic Press, 1995, pp. 395–397.

[18] E. I. Ohimain and S. C. Izah, "A review of biogas production from palm oil mill effluents using different configurations of bioreactors," *Renew. Sustain. Energy Rev.*, vol. 70, 2017, pp. 242–253.

[19] Z. S. Lee, S. Y. Chin, J. W. Lim, T. Witoon, and C. K. Cheng, "Treatment technologies of palm oil mill effluent (POME) and olive mill wastewater (OMW): A brief review," *Environ. Technol. Innov.*, vol. 15, 2019, p. 100377.

[20] M. H. Alhaji *et al.*, "Photo-oxidation of pre-treated palm oil mill Effluent using cylindrical column immobilized photoreactor," *Process Saf. Environ. Prot.*, vol. 117, 2018, pp. 180–189.

[21] C. K. Cheng, M. Rizauddin Derahman, and M. R. Khan, "Evaluation of the photocatalytic degradation of pre-treated palm oil mill effluent (POME) over Pt-loaded titania," *J. Environ. Chem. Eng.*, vol. 3, no. 1, 2015, pp. 261–270.

[22] U. Hasanudin, R. Sugiharto, A. Haryanto, T. Setiadi, and K. Fujie, "Palm oil mill effluent treatment and utilization to ensure the sustainability of palm oil industries," *Water Sci. Technol.*, vol. 72, 2015.

[23] T. Fujihira, S. Seo, T. Yamaguchi, M. Hatamoto, and D. Tanikawa, "High-rate anaerobic treatment system for solid/lipid-rich wastewater using anaerobic baffled reactor with scum recovery," *Bioresour. Technol.*, vol. 263, 2018, pp. 145–152.

[24] M. Gozan, N. Aulawy, S. Rahman, and R. Budiarto, "Techno-Economic Analysis of Biogas Power Plant from POME (Palm Oil Mill Effluent)," *Int. J. Appl. Eng. Res.*, vol. 13, 2018.

[25] Y. J. Chan, M. F. Chong, and C. L. Law, "Effects of Temperature on Aerobic Treatment of Anaerobically Digested Palm Oil Mill Effluent (POME)," *Ind. Eng. Chem. Res.*, vol. 49, no. 15, 2010, pp. 7093–7101.

[26] A. K. M. Omar *et al.*, "Implementation of the supercritical carbon dioxide technology in oil palm fresh fruits bunch sterilization: A review," *J. CO2 Util.*, vol. 25, 2018, pp. 205–215.

[27] B. Demirel and P. Scherer, "Trace element requirements of agricultural biogas digesters during biological conversion of renewable biomass to methane," *Biomass and Bioenergy*, vol. 35, no. 3, 2011, pp. 992–998.

[28] P. M. Thanh, B. Ketheesan, Z. Yan, and D. Stuckey, "Trace metal speciation and bioavailability in anaerobic digestion: A review," *Biotechnol. Adv.*, vol. 34, no. 2, 2016, pp. 122–136.

[29] M. Kim, Ç. Yangın-Gömeç, Y. Ahn, and R. Speece, "Hydrolysis and acidogenesis of particulate organic material in mesophilic and thermophilic anaerobic digestion," *Environ. Technol.*, vol. 24, 2003, pp. 1183–1190.

[30] B. Evranos and B. Demirel, "The impact of Ni, Co and Mo supplementation on methane yield from anaerobic mono-digestion of maize silage," *Environ. Technol.*, vol. 36, no. 12, 2015, pp. 1556–1562.

7th Int. Conf. on Structure, Engineering & Environment (SEE), Pattaya, Thailand, Nov.10-12, 2021, ISBN: 978-4-909106070 C3051

THE RISE OF RAINBOW VILLAGE: OPTIMIZING AESTHETICAL PROGRAM TO ACCELERATE SANITATION ACCESS (CASE STUDY: KAMPUNG CIBUNUT BERWARNA AND KAMPUNG PELANGI 200, BANDUNG CITY, INDONESIA)

L P Defi[1], I Kusumayanti[1], W M Fatimah[2], P W Sarli[3], and P Soewondo[2]

[1]Water Supply and Sanitation Infrastructure Management, Institut Teknologi Bandung, Indonesia; [2]Water and Wastewater Engineering Research Group, Institut Teknologi Bandung, Indonesia; [3]Civil Engineering, Institut Teknologi Bandung, Indonesia

ABSTRACT

Fulfilling basic needs for clean water and sanitation is still a challenge faced by Indonesia in achieving SDGs targets. In 2019, national access to basic sanitation was 77.83%, where in West Java Province only reached 66.25% of its population. The high rate of urbanization increases the number of slum areas in big cities in Indonesia. One of the problems commonly found in slum areas is the lack of sanitation facilities and infrastructure including clean water, wastewater, drainage, and waste management. Improving access of sanitation in slum areas has faced notable financial challenges. Meanwhile, in the past few years the making of rainbow village or colorful village is becoming a trend as an effort to improve the visuals of slum areas by painting houses. In further development, village visual improvement may convert the area into tourism destination. The increase in social and economic value from being a tourism destination is expected to help stimulate improvement of sanitation management in the village. Thus, the need to study rainbow village optimizing factors emerge. There are several rainbow villages in Bandung including Kampung Pelangi 200 and Kampung Cibunut Berwarna. Descriptive research design is used to compare and understand how the villages respond to the program. Survey research method is used to gather data. Based on the discussion, factors to be considered to optimize aesthetical program and enables sanitation access acceleration are: 1) Legality, 2) Institutional scheme, 3) Financial, and 4) Social.

Keywords: Kampung Pelangi 200, Kampung Cibunut Berwarna, Rainbow village, Sanitation, Visual improvement

INTRODUCTION

Rapid and unplanned population growth is often associated with population demands that outstrip infrastructure and service capacity and leading to environmental degradation [1]. In 2050, it is estimates that 70% of the world population will inhabit in urban areas [2]. The increase in population will certainly put pressure on cities. Cities must provide adequate basic infrastructure, if the cities cannot fulfill the basic infrastructure, the increasing number of populations will cause decreased resident's welfare, which may lead to exclusive and unhabitable urban areas.

In 2016, around 1.6 billion people live in inadequate housing globally, of which 1 billion live in slums and informal settlements [3]. In Indonesia, the rapid population growth and urbanization cause slum area to more than double in the last five years. According to the data from the Ministry of Public Works and Public Housing (PUPR) of Indonesia, the overall slum area in 2014 was 38,000 hectares and increased to 87,000 hectares in 2019.

According to SDGs, slum households are households whose members suffer from one or more of the following 'household deprivations': 1) Lack of access to improved water source, 2) Lack of access to improved sanitation facilities, 3) Lack of sufficient living area, 4) Lack of housing durability and, 5) Lack of security of tenure. Sanitation infrastructure is critical for public health and environment. Lack of sanitation is linked to reduced health and environmental degradation [4]. The importance of sanitation is reflected in Sustainable Development Goals (SDGs) 6. In slum areas, economic limitations as well as socio-cultural factors and lack of knowledge cause low-income people to have a low level of concern for the quality of their housing, including water and sanitation infrastructure.

Fulfilling basic needs for clean water and sanitation is still a challenge faced by Indonesia in achieving SDGs targets. In 2019, national access to basic sanitation was 77.39%, where in West Java Province only reached 69.64% of its population [5]. Improving access of sanitation in slum areas has faced notable financial challenges [6]. Meanwhile, in the past few years the making of rainbow village or colorful village is becoming a trend as an effort to improve the visuals of slum areas by painting houses.

In further development, village visual improvement may convert the area into tourism destination. The increase in social and economic value from being a tourism destination is expected to help stimulate improvement of sanitation management in the village. There have been several

rainbow villages studied which yield different outcomes from the village visual improvement in the long run. Sustainable visual and tourism practice by Jodipan-Ksatrian in Malang reflect a successful program to boost the village both in social standpoint and environmental standpoint [7]. In Bandung, there are several rainbow villages with different characteristics. One of the villages, Kampung Pelangi 200, was not able to retain the visual quality and tourism practices due to unclear management and minimum involvement by the village chief and government, compared with how it is managed in Jodipan and Ksatrian Village [8]. However, another rainbow village in Bandung, namely Kampung Cibunut Berwarna, seems to be able to match the success of Jodipan-Ksatrian in Malang.

The rise of rainbow village due to the increasing village aesthetic improvement programs gives an opportunity to start accelerating sanitation access in slum areas. However, the result differences in one village to another indicates that the program is not yet optimized. Thus, to ensure that the program can result in its best potential, a study related optimizing factors of aesthetical improvement program in rainbow villages is needed. This research will study rainbow villages with different characteristics in Bandung, namely Kampung Pelangi 200 and Kampung Cibunut Berwarna. In this study, qualitative research method is used to gather data and compare characteristics to obtain suspected associations between caused and effect to the desired conditions in Kampung Pelangi 200 and Kampung Cibunut Berwarna.

DESCRIPTION OF AESTHETICAL PROGRAM

The research locations are located in Bandung city and their location respective to each other can be seen in Figure 1.



(a) (b) (c)

Fig. 1 (a) Kampung Cibunut Berwarna and Kampung Pelangi 200 relative to each other on Bandung City; Existing Condition of (b) Kampung Cibunut Berwarna and (c) Kampung Pelangi 200.

Research Area Description

Kampung Cibunut Berwarna, Bandung

Kampung Cibunut Berwarna is a village located in Sumur Bandung district, Bandung City, West Java. Geographically, this village is located alongside the downstream area of Cikapundung River. There are several ways to access Kampung Cibunut Berwarna, but the most commonly used entrance can be accessed through Sunda Street (Figure 2). Kampung Cibunut Berwarna consist of 9 neighborhood/*Rukun Tetangga* (RT) under 1 hamlet/*Rukun Warga* (RW) with around 550 households. Details of the area distribution of each RT can be seen on Figure 3.



Fig. 2 Research location: Access to Kampung Cibunut Berwarna



Fig. 3 Research location: Area distribution of each RT in Kampung Cibunut Berwarna

Kampung Pelangi 200, Bandung

Kampung Pelangi 200 is a village located in Cidadap District, northern Bandung, West Java. Along with Kampung Cibunut Berwarna, Kampung Pelangi 200 also located alongside Cikapundung River. But in different, Kampung Pelangi 200 specifically located on the upstream area of the river, near the Cikapundung Riverspot facility. Kampung Pelangi consist of 4 RT with the total number of households around 225.

Description of Aesthetical Improvement Program

Kampung Cibunut Berwarna, Bandung

Kampung Cibunut Berwarna was initiated in 2016 by Kampung Cibunut inhabitants to participate in “Adu Geulis” competition held by Bandung Forum

for Waste-Free Champion to make proposals containing ideas of structuring residential areas (villages). Kampung Cibunut proposed to create a mural that has educational value, called "Edu Wall". Edu Wall is planned to have a different theme for each RT ranged from local culture, local figure, world insight, to environment and peace. In addition to making edu walls, stakeholders are also planning to paint all houses in Cibunut Village where each RT has a different color from the other RTs.

Various stakeholders were also involved in the making of the proposal, from karang taruna (youth organizations), community organizations, Institut Teknologi Bandung Alumni Association, to Senior High School State 3 Bandung Alumni Association. Kampung Cibunut managed to become 1st place in the competition and received paint procurement assistance from PT. ICI Paints Indonesia. The village painting process was carried out from 2016 to 2017. In November 27, 2017, Kampung Cibunut Berwarna (Colored Cibunut Village) was inaugurated by the Mayor of Bandung as a creative village with an environmental perspective.

Kampung Pelangi 200, Bandung

In Kampung Pelangi 200, the aesthetical program was a collaboration between chief of RW 12 and PT. Rajawali Hiyoto that produces paint branded "Sanlex". The initial idea from the chief was to turn Kampung 200 into a colorful village as a tourist destination inspired by Jodipan-Ksatrian in Malang. The chief then contacted Sanlex's public relations division to get information on their Corporate Social Responsibility (CSR) program, as Sanlex has conducted multiple CSR-related activities such as painting school, villages, etc. The painting process was conducted by the end of 2017 until early 2018. By March 2018, residents were given 2 to 3 can of 25 kg paint of the residents' preferred colors. Painting was carried out with the lead of the chief, in which the residents were responsible for their own respective houses and were encouraged to help their neighbors as well. Sanlex in collaboration with the subdistrict government held multiple public events and activities in the form of fun walk media exposure to introduces the village as a new tourist destination in Bandung.

Response After the Program

Kampung Cibunut Berwarna, Bandung

In Kampung Cibunut Berwarna, response after the project was positive. The inauguration of Kampung Cibunut Berwarna attracts many tourists to visit, take pictures, and share their experiences in managing waste in Kampung Cibunut Berwarna. Since 2017 until now, the visual appearance of the village is still notably vibrant, despite fading colour in some houses. Kampung Cibunut Berwarna actually still has an allocation for painting the village one more time from PT. ICI Paints Indonesia. However, until now this allocation has not been used because there is no desire from the community to use the paint allocation from the company.

Kampung Pelangi 200, Bandung

In Kampung Pelangi 200, response after the project was considerably quiet. This was due to the absence of further active involvement of the paint company (Sanlex) and also the individualistic nature of the residents. Even with publicity and acknowledgement from local government, no significant move was taken to ensure the achievement of the initial goal: to turn Kampung Pelangi 200 into a tourist destination. The initiator of the project was the chief of hamlet (RW); however, the plan was considerably one-sided and the residents' involvement were minimum, thus residents' eagerness was also minimum. Based on the collaboration contract, the residents can acquire paints from Sanlex until 3 years after the initial painting. However, not many of the residents are aware of or utilize this opportunity. Some of the residents who are still willing to follow the colorful village theme conducted maintenance from their own pockets (e.g., buying paint, paint thinner, brush, etc.).

METHODOLOGY

This research is a part of a series of studies on rainbow villages in Indonesia. Descriptive research is used to describe the characteristics of the population and the phenomenon studied. This research design is used to understand how 2 different groups (Kampung Berwarna Cibunut and Kampung Pelangi 200) respond to village aesthetic improvement program. Primary and secondary data is used to obtain thorough understanding. Survey method is used to gather primary data, where a mixed of open-ended and close-ended question is used as the tool.

Data Collection

Primary data collection was conducted in Kampung Cibunut Berwarna using random sampling method to ensure equal probability of respondents in the group being chosen. The questionnaire was built to attain information about demographic condition, social and economic aspects, water supply sources and the existing sanitation infrastructure. Yamane method was used to determine sample size with the formula as follows:

$$n = \frac{N}{1 + Ne^2}$$

n = sample size (85 households)
N = population size (550 households)
e = margin of error (10%)

Secondary data is used to describe Kampung Pelangi 200 which was obtained from the previous study.

Data Analysis

Close-ended questions data were analyzed using descriptive statistics, processed and illustrated using Microsoft Excel. Open-ended questions data were analyzed using conventional content analysis. The information gained, supported with documentation from direct observation, will be used to describe the existing condition of Kampung Cibunut Berwarna.

RESULTS AND DISCUSSION

Primary data analysis result regarding Kampung Cibunut Berwarna will be briefly explained. Subsequently, strategic thinking to discuss optimizing factors will be thoroughly discussed by comparing Kampung Cibunut Berwarna (Through primary data) and Kampung Pelangi 200 (Through secondary data).

Kampung Cibunut Demographic Characteristic

Household economy status is defined referring to Central Bureau of Statistics of Indonesia (BPS) categorizing the amount of household monthly income. Using this approach, household with monthly income below Rp. 1.500.000 is categorized as poor; Rp. 1.500.000 – Rp. 2.500.000 as middle, Rp. 2.500.000 – Rp. 3.500.000 as upper middle and above Rp. 3.500.000 as upper class [9]. The result shown that the amount of household monthly income in Kampung Cibunut Berwarna can be categorized as poor and middle class with both percentage on 36.6%. While the rest of the households can be categorized as upper middle and upper class with percentage around 22% and 4.9%. Data regarding household's occupations support the classification of the household status of economy as the dominant occupation is self-managed small merchant shop. However, because the majority of the households are self-employed, during this pandemic even the highest-earning households are vulnerable to fragile economic situations.

Education level from the majority of Kampung Cibunut Berwarna households are relatively high compared to the average of the national education level. While the average of the national education level is on second grade of middle school, 61% from the total households in research area education level are on high school level or equivalent.

There are many newcomers who live amongst the former residents in Kampung Cibunut Berwarna who mainly lived either in rented house or boarding houses. However, the households in research area still dominated by former residents who used to live in the area for more than 10 years with the percentage of 82.9%. Most of the residents (80.5%) in research area are living in their own house or in the house they inherit from their parents.

Sanitation Infrastructure and Sanitation Related Behavior

There are 2 main water sources that are used in Kampung Cibunut Berwarna, water pipes from regionally owned water supply company (PDAM), using either subsidized or non-subsidized connection, and groundwater. The ratio of water sources used by the residents can be seen on Figure 4.

The majority of the residents discharge their wastewater to the existing sewerage system that was built by the government in 1987 under the "Bandung Urban Development Project (BUDP)" program. The rest of the residents that are not connected to the system, usually houses located along the riverbanks, tend to discharge their wastewater directly to the river. After coloring program, there has not been significant changes in wastewater sector mainly due to the invisible nature of wastewater infrastructure (located underground). The ratio of residents' wastewater management is shown on Figure 4.

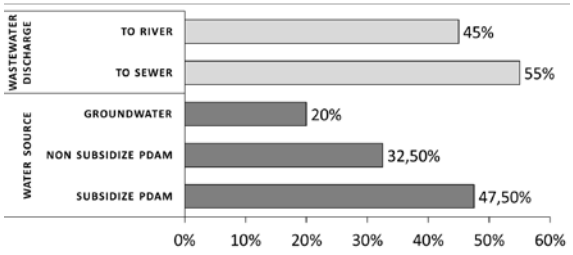


Fig. 4 Ratio of clean water sources and wastewater discharge in Kampung Cibunut Berwarna.

Before the program, majority of the residents has not done waste segregation and most of the waste produced are directly collected by waste worker. After the program, supported by the new local waste bank, the number of waste segregation done by the residents are rising quite high. Later, the collected segregated solid waste from the local waste bank is going to be sold to the central waste bank. The ratio of solid waste segregation done by the households before and after the visual improvement program can be seen on Figure 5.

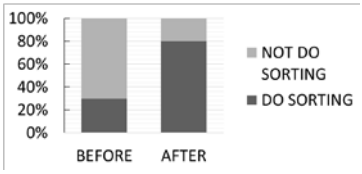


Fig. 5 Ratio of solid waste sorting activities before and after program. Do waste sorting (black) and not do waste sorting (grey).

Economic Impact of The Project

There is no specific purpose to make Kampung Cibunut Berwarna into a tourism village. The initial concept of the visual improvement project was only for aesthetic purposes. Tourists who visit Kampung Cibunut Berwarna come because they see the beauty of the village through the @cibunutfinest social media account and attracted to take pictures with the aesthetic mural background. There is no entrance fee for tourists who come in small numbers (1-5 people). However, for large group of tourists (>20 people) whose arrivals are usually on the recommendation of the Bandung City Government, the village provide tour packages for Rp. 45,000 per pax. The tariff is allocated for meals, snacks and incentives for speaker to share about waste management in Kampung Cibunut Berwarna. Hamlet (RW) chief collaborates with family welfare empowerment organization (PKK) and residents who have businesses in the culinary field to provide food and snacks for tourists. From the stakeholders of the Kampung Cibunut Berwarna, there is no special financial scheme to turn Kampung Cibunut Berwarna into a tourism village. The initial purpose of making Instagram social media account was only as a documentation of residents' activities and communication media for the Kampung Cibunut Berwarna community, not for the purpose of branding as tourism villages.

Strategic Thinking on Optimizing Factors

Strategic thinking to improve the quality of the visual improvement project in context to accelerate sanitation access is closely related to some aspects. Table 1 list and compare aspect of characteristics found between the village.

Legality – Kampung Pelangi 200 was constructed on a land owned by university, even though many have resided for more than 10 years. On the contrary, Kampung Cibunut Berwarna house and land ownership are the residents (although some are being contracted). Legality of the settlement area is important regarding further involvement from formal stakeholders, as legal settlements are more preferred to be chosen due to sustainability concerns.

Table 1. Comparison of aspects on the project's implementation in Kampung Pelangi 200 and Kampung Cibunut Berwarna, Bandung

Factors	Kampung Pelangi 200	Kampung Cibunut Berwarna
Legalilty	**Illegal**, settlement constructed on university owned land.	**Legal,** House and land ownership are true to the residents
Institutional scheme	• **Aim of program;** Corporate Social Responsibility (CSR) • **Initiators;** Paint company - PT. Rajawali Hiyoto (Sanlex) • **Internal stakeholders;** None.	• **Aim of program;** Government program on making "Zero Waste Area" • **Initiators;** Dinas Lingkungan Hidup dan Kebersihan Kota Bandung (Bandung City Environment Services and Cleanliness) • **Internal stakeholders;** RW, youth organization, PKK/family welfare empowerment organization), Kelompok Swadaya Masyarakat (community-based organization)
Financial	• **Retribution tariff**; No. • **Entrance Fee**; No	• **Retribution tariff**; Yes, there are 2 monthly retribution tariffs consist of (1) Solid waste retribution (Rp.5.000) (2) Iuran Gotong Royong (Community Retribution) (Rp. 5.000 - Rp. 7.000; depend on each RT). • **Entrance Fee**; Yes, but only applied to the group of visitors (≥ 20 people)
Social	• **Household engagement;** No. • **Public engagement through social media;** No	• **Household engagement;** Yes, through door-to-door pre-program socialization by internal stakeholders. • **Public engagement through social media;** Yes, using Instagram platform

Institutional Scheme – The purpose of visual improvement program in two research location is different. Kampung Pelangi 200 main purpose was the implementation of 'Corporate Social Responsibility' (CSR) from a paint company, Sanlex. In Kampung Cibunut Berwarna the main purpose was to participate in 'Waste-Free Area" program that was held by the government. Programs implemented in line with program held by the government are considered beneficial in supporting the successfulness of the programs. This is related to the ease in terms of branding and also in establishing relationships with external stakeholders who can be involved in the program.

Financial – There is no significant change in financial scheme before and after program in both of the research area. Before the program, Kampung Pelangi 200 has no community retribution fee and the same thing goes even though the program already done after. In Kampung Cibunut Berwarna, there is community retribution fee before the program implemented and still continue after the program implemented. In this case, even though there aren't any difference in the financial case on both of the research area, community retribution fee contributes in supporting the community livelihood. Community retribution fees can trigger community independence in maintaining and managing their environment, so the residents will not depend solely on assistance provided by external parties.

Social – There are two different perspective that can be used to analyze the sustainability of the program in term of social aspect. On internal perspective, community engagement plays a very important role to support the sustainability of the program. A proper approach method should be done to the residents to achieve a successful community engagement. Kampung Cibunut Berwarna took a door-to-door approach to the residents so the residents would understand completely about the purpose and goal of the program. This approach aids in engaging the community with the program. On external perspective, public outreach has a very important role in maintaining village tourism tourism potential. In this digital area, social media can be used to gain public engagement, as already implemented by the local community in Kampung Cibunut Berwarna. These internal and external perspective fulfillments were absent in Kampung Pelangi 200.

CONCLUSIONS

The majority of households is in poor-middle income (36,6%) and upper middle income (22%), where only 55% of households connected to sewer system. Coloring program significantly affect solid waste system (sorting activities increased by 60%) and does not significantly affect wastewater system. The difference in sanitation conditions as coloring project result between the villages studied is influenced by 1) Legality of house and land ownership which will be considered by donors and governments before planning on long term intervention, 2) Institutional scheme of village programs management and the involvement of stakeholders and community, 3) Financial plan from the community to keep programs going, and 4) Social aspects in the form of public outreach to promote and introduce the villages. These factors need to be considered not only for project sustainability but also other additional impacts that could be achieved from the project, one of which is sanitation development.

ACKNOWLEDGEMENTS

The authors would like to extend their gratitude toward the Research, Community Development and Study Group Innovation Program (Program Penelitian, Pengabdian Masyarakat dan Inovasi Kelompok Keahlian - P2MI) 2021 of Institut Teknologi Bandung (ITB) for funding this research. The study was carried out with the help of Water and Wastewater Engineering Research Group of the Faculty of Civil and Environmental Engineering, ITB.

REFERENCES

[1] G. W. N. Asoka, A. D. M. Thuo, and M. M. Bunyasi, "Effects of Population Growth on Urban Infrastructure and Services: A Case of Eastleigh Neighborhood Nairobi, Kenya," *J. Anthropol. Archaeol.*, vol. 1, no. 1, pp. 41–56, 2013

[2] E. Birch, A. Meleis, and S. Wachter, "The Urban Water Transition: Why We Must Address the New Reality of Urbanization, Women, Water, and Sanitation in Sustainable Development," *wH2O J. Gend. Water*, vol. 1, no. 1, Oct. 2017

[3] UN-Habitat, *Urbanization and Development: Emerging Futures*. 2016.

[4] G. Hutton and M. Varughese, *The Costs of Meeting the 2030 Sustainable Development Goal Targets on Drinking Water, Sanitation, and Hygiene*. World Bank, Washington, DC, 2016.

[5] R. Andiyanti, S. Mardiyah, W. S. Purba, and Y. Yunarsih, *Environment Statistics of Indonesia: Water and Environment 2020*. Jakarta, Indonesia: Badan Pusat Statistik/BPS – Statistics Indonesia, 2020.

[6] M. Roberts, F. Gil Sander, and S. Tiwari, *Time to ACT: Realizing Indonesia's Urban Potential*. Washington, DC: World Bank, 2019.

[7] P. W. Sarli and P. Soewondo, "Strategic Thinking to Change Behaviour and Improve Sanitation in Jodipan and Kesatrian, Malang, East Java, Indonesia," *Int. J. Urban Civ. Eng.*, vol. 10, p. 1438, 2017.

[8] W. M. Fatimah, P. W. Sarli, P. Soewondo, and N. M. Zakiyya, "Strategic thinking to improve sanitation in Kampung Pelangi 200, Bandung City: In comparison with Kampung Jodipan-Ksatrian, Malang City," *IOP Conf. Ser. Earth Environ. Sci.*, vol. 592, no. 1, 2020, doi: 10.1088/1755-1315/592/1/012018.

[9] R. Jaya, A. S. Rijal, and I. R. Mohamad, "Karakteristik Sosial Ekonomi Masyarakat Sub Das Alo Terhadap Perilaku Pemanfaatan Fisik Lahan," *J. Humanit. Soc. Justice*, vol. 2, no. 1, pp. 53–67, Jan. 2020, doi: 10.38026/journalhsj.v2i1.33.

7th Int. Conf. on Structure, Engineering & Environment (SEE), Pattaya, Thailand, Nov.10-12, 2021, ISBN: 978-4-909106070 C3051

DEGRADATION OF POLYETHYLENE TEREPHTHALATE (PET) AS SECONDARY MICROPLASTICS UNDER THREE DIFFERENT ENVIRONMENTAL CONDITIONS

Ansiha Nur[1], Prayatni Soewondo[1], Ahmad Soleh Setiyawan[1], Katharina Oginawati[1]
[1]Faculty of Civil and Environmental Engineering, Institut Teknologi Bandung, Indonesia

ABSTRACT

Polyethylene terephthalate (PET) bottles have been widely used as biofilm media for residential scale Wastewater Treatment Plants (WWTP) in Indonesia because of their advantages such as inert. PET bottles can also be degraded as secondary microplastic contaminants during operation of WWTPs. The aim of this study was to investigate the possibility of degradation of PET as secondary microplastics. The research was carried out in distilled water under three different environmental conditions (indoor laboratory scale, outdoor laboratory scale and field scale). The abundance, size, color, and shape of microplastics were observed through a light binocular microscope with a 100x magnification combined with Image Raster 3.0 software. Data of environmental properties (i.e., DO, temperature and pH) were collected. The solubility potential of PET as microplastics was identified after 7 months indoor and outdoor laboratory experiments with concentrations of 18.67 ± 7.02 MP/L and 44.00 ± 12.77 MP/L, respectively. Experiments on UV irradiation showed faster degradation of PET and the presence of microplastics increased along with the exposure period with concentration at the first month, the second month, the third month, and seventh month were 15.33 ± 7.09 MP/L, 51.67 ± 9.61 MP/L, 54.33 ± 8.39 MP/L and 248.67 ± 29.09 MP/L, respectively. The major microplastic characteristics were fragments (92.37%), fiber (7.63%), transparent particle color (82.85%) and particle size of 10 μm (61.04%).

Keywords: Degradation, Environmental conditions, Microplastics, Polyethylene terephthalate

INTRODUCTION

Polyethylene terephthalate (PET) plastic bottle waste has become a low-cost solution for biofilm media that had already applied in residential scale wastewater treatment plants (RC-WWTPs) in Indonesia. This is based on its advantages, first, it is widely available, cheap, and easy to obtain as plastic waste. Indonesia is a country with the 4th highest consumption of PET bottles in the world [1]. Second, it has the desired properties as a supporting media, namely lightweight, inert (not easily biodegradable), high cavity volume fraction, large surface area, durable, not easy to rot, resistant, able of attaching microorganisms well in large numbers [1] – [4]. Third, "waste treat waste" [5]-[6] as well as a solution to reduce the plastic bottle waste in Indonesia.

Although studies on PET as a supporting media in attached growth systems are globally limited, in Indonesia this studies raised attention since 2014, because of its advantages. PET as a low-cost media has been applied on a field scale at RC-WWTPs in Indonesia. PET are easy to form in various variations of shape and surface area. For this purpose, PET is cut, folded, and shaped in such away.

However, behind its advantages, the impact of using PET as a microplastic in the WWTP is still unknown, thus raising concerns about the presence of microplastics in the WWTPs. Microplastics are novel contaminants, plastic particles smaller than 5 mm [7] are of global concern today because they are persistent in the environment for hundreds of years or even thousands of years due to their stability and durability [8] and its negative impact that allows it to enter the food chain and lead to humans as top predators in the food chain [9]. Microplastics in the environment in two forms, primary (plastics of microscopic size that are purposefully used) and secondary (fragmentation and degradation from larger plastic items).

PET is a thermoplastic polymer have a slow rate of natural decomposition [10]. Physical processes (UV light, heat, photo-oxidation, reducing polymer size); chemical processes (use of chemical compounds to break polymer chains), and biological/degradation processes (bacteria and fungi activity) contribute to the fragmentation and degradation of plastics in the environment [11]. In addition, knowing the degradation process of PET plastics as secondary microplastics is critical for evaluating the status of PET bottle as supporting media in a WWTP. This study focuses to investigate the possibility of the degradation of PET as secondary microplastics under three different environmental conditions (indoor laboratory scale, outdoor laboratory scale, and field-scale). Thus, data on different exposure times in three different environments was carried out.

MATERIAL AND METHODS

Experimental setting

The experiment was carried out in three different environmental conditions; indoor laboratory scale (Laboratory A; Lab-A), outdoor (Laboratory B; Lab-B, and field-scale (field), as shown in Figure 1. The laboratory scale is carried out at the Water Quality Laboratory of Environmental Engineering ITB and the field scale is carried out in exposed outdoor directly to the sunlight.



Fig.1 Exeperiment in three different environmental conditions; a) Lab-A, b) Lab-B, and c) Field

Lab-B used a UVA340 lamp, selected as a simulated of natural sunlight [12], and will then be compared with field conditions with direct exposure to sunlight. First, the 330 ml PET plastic bottles are cleaned, cut the top and bottom, filled with 2 other PET plastic bottles. The size of the bottle pieces is 6 cm in diameter and 8 cm in height. The samples were placed on 250 ml glass beaker and submerged in the distilled. Second, each variation of samples Lab-A, Lab-B and filed was equipped with a blank, which only used distilled water, without any PET. Each variation was made triple. Total of each 72 samples. Beaker glasses (sample Lab-B) were put into a handmade chamber (50 cm x 35 cm x 20 for length, width, height, respectively) made of styrofoam coated with a zinc plate on the inside, equipped with a UV lamp, and tightly closed. who observed plastic pellets exposed to UV light on a laboratory scale. Sample Field used a glass jar, exposed to UV irradiation all day. The **e**xperiment was conducted 7 months observation. Each variation as long the observations were three repetitions, as shown in Table 1.

Table 1 The experiment matrix

Sample	Experiment	Observation (month)	Total sample
Lab-A	Laboratorium indoor		
	Blank (DW)	1,2,3,7	12
	PET dan DW	1,2,3,7	12
Lab-B	Laboratorium outdoor (UV lamp)		
	Blank (DW)	1,2,3,7	12
	PET dan DW	1,2,3,7	12
Field	Field (UV light)		
	Blank (DW)	1,2,3,7	12
	PET dan DW	1,2,3,7	12
	Total		72

DW = distilled water

Data analysis

Observations of Lab-A, Lab-B dan Field were carried out at months 1, 2, 3, and 7. The parameters of DO, pH, and temperature were measured at each observation. DO was measured using a DO-meter, pH, and temperature using a pH-meter.

All suspected microplastics particles were categorized by size, shape (fiber, fragments, microbeads, and others), and color [13]. All suspected microplastics identified by three rules that distinguish plastic from non-plastic [14]: 1) the particle should not have an organic or cellular structure, 2) the color appears homogeneous as a whole; 3) fiber should be similarly thick all through the whole length; and 4) fiber particles do not break when pressed.

The quantification and identification of microplastics by filtering all the samples using a 0.45 µm cellulose acetate filter and 45 mm in diameter (Sartorius stedim) with a Buchner funnel and a vacuum pump. Then the filter paper was dried using an oven at 105 ^{0}C [15] for 30 minutes. Visual observation of filter paper using an Olympus CX-21 light microscope with a magnification of 100x coupled with Optilab Viewer 3.0 software and measurements of particle size using Image Raster 3.0 software.

RESULTS AND DISCUSIONS

There were no microplastics found in the blank samples until 7th month. After 1 month UV irradiation exposure, microplastics began to occur in field conditions although in small quantities, while in laboratory conditions they were only identified in third month, although the addition was very small until third month to seventh month (shown in Fig. 2).

During the microplastics solubility test from first month to seventh month, it was found that the temperature factor from the sun's heat and UV irradiation greatly affected the solubility of PET as a secondary microplastics in distilled water. The

temperature under field conditions was higher than the temperature under laboratory conditions. The average temperature measured under field conditions was 36.0 ± 0.19 ^{0}C in the blank and 35.9 ± 0.28 ^{0}C in the sample, with the highest temperature measured 38.6 ± 0.26 ^{0}C and the lowest 34.4 ± 0.31 ^{0}C. Field samples were exposed in the sunlight from 7 am until 5 pm, and measurements were taken around 11 AM to 1 PM at noon on a sunny day. Meanwhile, the average temperature in the blank indoor laboratory was 25.6 ± 0.11 ^{0}C and the sample was 25.4 ± 0.10 ^{0}C with a temperature range between 25.2 ± 0.06 ^{0}C until 25.5 ± 0.17 ^{0}C in the blank and 25.1 ± 0.06 ^{0}C until 25.7 ± 0.06 ^{0}C in the sample. The outdoor laboratory was recorded at 25.8 ± 0.12 ^{0}C in the blank and 25.8 ± 0.20 ^{0}C in the sample with a temperature range between 25.8 ± 0.06 ^{0}C until 26.2 ± 0.25 ^{0}C in the blank and 25.5 ± 0.06 ^{0}C until 26.1 ± 0.26 ^{0}C in the sample. There were no many differences in the temperature of the outdoor and indoor environmental conditions on a laboratory scale. DO environmental conditions ranged from 8.33 ± 0.20 mg/L to 8.64 ± 0.07 mg/L under laboratory conditions and 6.06 ± 0.17 under field conditions and pH ranged from 5.57 ± 0.04 to 5.62 ± 0.02 did not have a significant effect on the solubility of PET in distilled water.

The temperature and duration of UV exposure affect the photo-oxidation process [12],[16]. In laboratory conditions, the presence of microplastics began to be identified in the third month as much as 13.67 ± 5.69 MP/L at indoor and 24.33 ± 12.90 particles/L at outdoor. In the 7th month, the identified microplastic particles in indoor and outdoor were 18.67 ± 7.02 particles/L and 44.00 ± 12.77 MPl/L. Different from the case with field conditions that were directly exposed to UV light, the presence of microplastics in the first month was immediately identified as much as 15.33 ± 7.09 particles/L, then began to increase in the second, third and seventh months by 51 .67 ± 9.61, 54.33 ± 8.39 and 248.67 ± 29.09 MP/L.

This study has similarities with Song [16], in that the first 2 months of exposure to UV light did not show the presence of microplastics. Another similar study by Cai et al (2019) who observed three types of pellets exposed to UV light in 3 different environments on a laboratory scale on plastic pellets, showed that in the third month there was surface damage and fragmentation. The mechanism of plastic pellets in their research was photo-oxidation caused by a free radical chain reaction [12].

This study had a similar duration of exposure UV light until microplastics was occurred [16], in that the first 2 months of exposure to UV light did not show the presence of microplastics. Another similar study by Cai [12] who observed three types of pellets exposed to UV light in 3 different environments on a laboratory scale on plastic pellets, showed that in the third month there was surface damage and fragmentation. The mechanism of plastic pellets in their research was photo-oxidation caused by a free radical chain reaction [16].

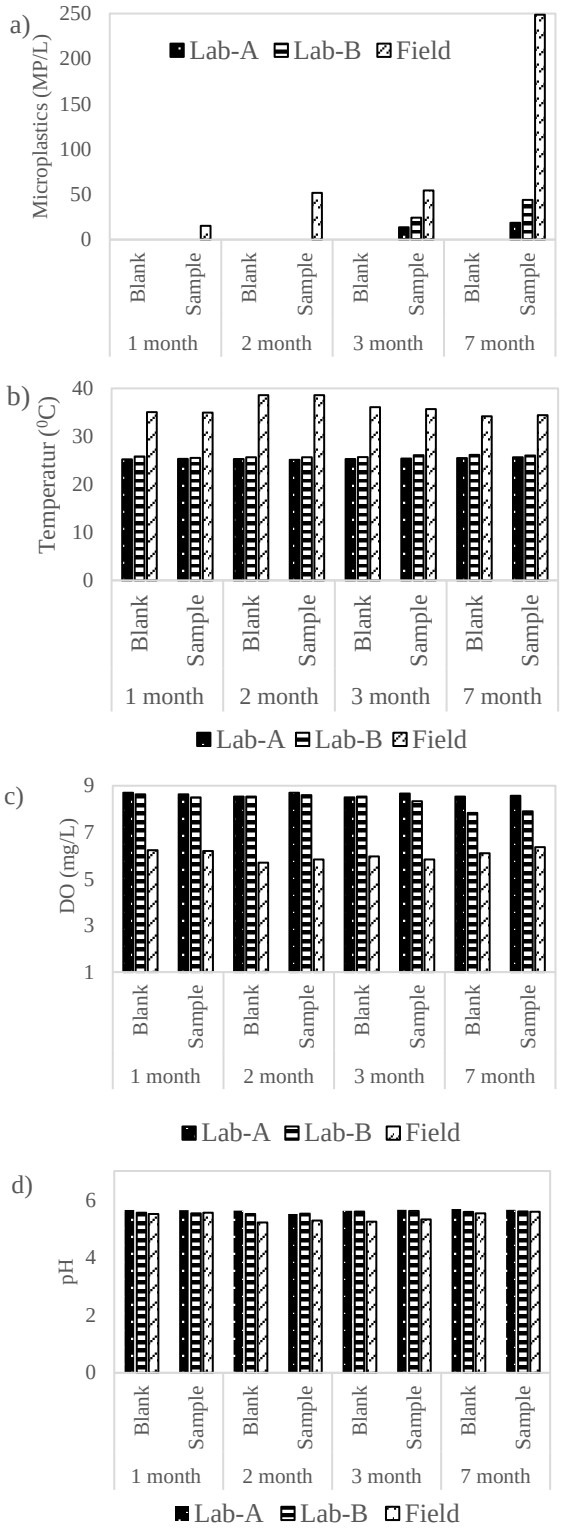


Fig.2 The conditions during the periode of observation: a) the occurrence of microplastics, environmental conditions, b) temperatur, c) DO, and d) pH

UV light has sufficient energy to generate initial free radicals as the main photochemical product and cause C C (375 kJ/mol) and C H (420 kJ/mol) bonds regardless of the main polymer or equivalent to 320 and 290 nm UV radiation [17]-[18]. It caused one or more chemical changes, resulting in the breakdown of the polymer surface, visible as cracks and fractures. UV oxidation results in damage to the polymer surface to a depth of more than 100 μm caused by cross-linking and chain reactions [19]. This brittle surface layer easily forms cracks and becomes clearer and thicker with increasing exposure time. Interestingly in the research of Song [16], brittle surfaces and cracks from photo-oxidation (or weathering) did not directly result in polymer "fragmentation". Although many large and small cracks were observed on the surface of the PE and PP pellets, no fragments were detected only by UV exposure by SEM. This implies that physical forces affect the breakdown of brittle plastics.

However, in the absence of heat from the sunlight/ UV irradiation under indoor conditions in the laboratory, the presence of microplastics was also identified in the third month although a litlle. This means that microplastics identified in distilled water under no UV exposure condition. Physical processes such as UV, heat, photooxidative, and size reduction were affected for large plastics degrade to microplastics in the environment [20]. The solubility test of PET into microplastics during this research came from a physical process and no influence of chemical or biological factors. Other factors such as molecular weight, density, thickness, polymer morphology were other important factors in the degradation of a polymer into monomers [21].

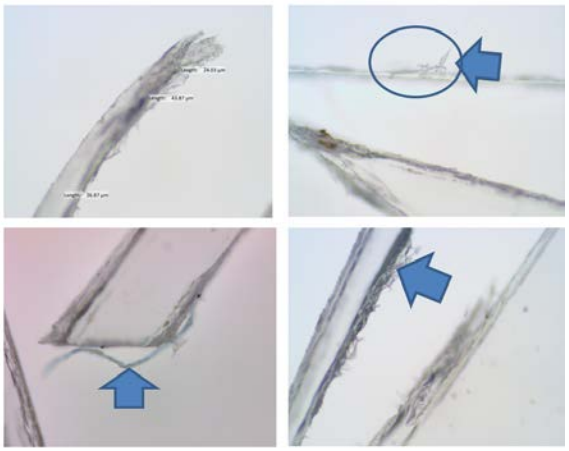


Fig.3 Observations of PET scrap under microscope with a magnification 100 times

Xiao [22], PET depolymerization could be through hydrolysis. PET hydrolysis using water produces terephthalic acid and ethylene glycol. Terephthalic acid is soluble in water at 0.0015 mg/100 mL at 20 ^{0}C. The PET pieces under a microscope with 100x magnification (Fig. 3), shows that the PET scrap have the potential to fragment into secondary microplastics. Many ends and pieces of PET plastic of various sizes are ready to be released into the water. Cracks and fractures as a form of fragmentation. The presence of UV light accelerates the process of dissolving PET into distilled water by breaking the main PET polymer chain.

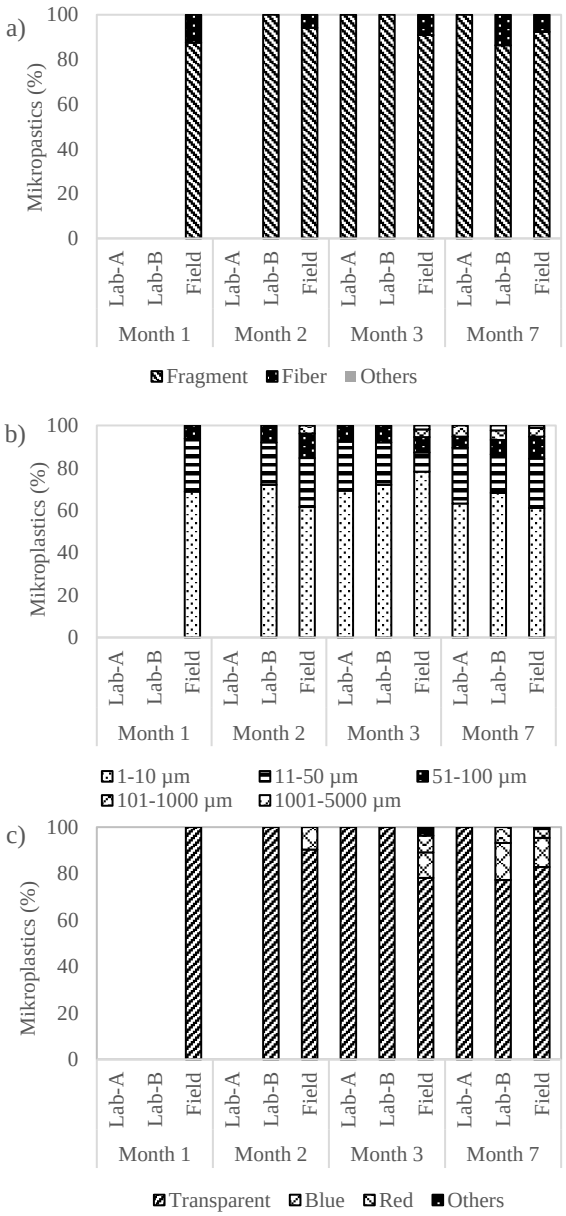


Fig. 4 Shape, size and color of PET as secondary microplastics

Based on Fig.4, the presence of microplastic particles due to the solubility/fragmentation of PET in distilled water were dominated by size < 50 μm, the form of fragments with transparent color. The number of microplastics in the first, second, third to seventh month in the field samples were 15.33 ± 7.99, 51.97 ± 9.62, 54.33 ± 8.39, and 248.67 ± 29.09 MP/L.

Meanwhile, the indoor (Lab-A) and outdoor (Lab-B) samples in the third month were identified as 13.67 ± 5.69 MP/L and 24.33 ± 12.90 MP/L and in the seventh month as many as 13.67 ± 5.69 MP/L and 24.33 ± 12.90 MP/L. 18.67 ± 7.02 and 44.00 ± 12.77 MP/L. Only two forms of microplastics were identified in this study, namely fragments and fibers, where fragments predominated from fibers. Fragments ranged from 87.50-94.12% and fiber 5.88-12.5%. Similar results in the study of Song [16] found the microplastics size as resulting fragmentation of larger plastic less than 100 μm were 73%.

As shown in Fig.4c, transparent microplastics were dominant. Another color were red and blue. In addition, the presence of red and blue colors as log as the observation was suspected from the various PET bottle brand used. All microplastic particles in this studi were very thin, the thickness less than 7 μm. Even though they were more than 500 μm in length, but the limitation on picking up the particle from filter paper for further FTIR analysis. Fig. 5 showed shape of secondary microplastics of PET under 100x magnifiction of microscope.

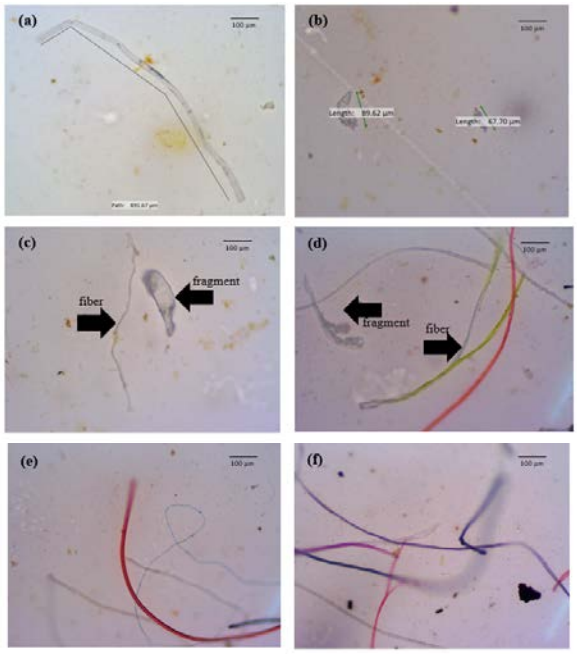


Fig. 5 Shape of secondary microplastics as effect of PET degradation. (a-b) fragment, (c-d) fragment and fiber, and (e-f) fiber.

CONCLUSIONS

Experiments under three environmental conditions for 7 month showed that physical and chemical factors were the main factors of PET degradation in WWTPs. Physical factors as effect of PET scraps and chemical factors as effect of PET duration submerged in WWTPs. PET as secondary microplastics increased over time. Transparent fragments with 50 μm in size were the dominant shape found. Thus, more investigations on the degaradation process of PET in WWTPs are need, this would help increase our understanding of predict the fate of microplastics in the environment.

ACKNOWLEDGMENTS

This work was supported by Riset Unggulan ITB, 2021.

REFERENCES

[1] PT. Chandra Asri Petrochemical, 2017, Analyst Meeting. Cilegon.

[2] Ahn, K.H., Hwang, J. H., Song, K. G., Jung, H.Y., Cho, E. S., Lim, B. R., Dezotti, Kim, K. S., Nitrogen Removal Using Recycled Polystyrene Bottles as Biofilm Media. Metals and Materials International, Vol. 10, 2004, pp. 167-170.

[3] Espinoza, K., Fernandez, C., Perez, J., Benalcazar, D., Romero, D., Lapo, B., Support materials of fixed biofilm based on solid plastic wastes for domestic wastewater treatment. Rev. Tec. Ing. Uviversitas Zulia, Vol. 42, Issue 2, 2019, pp. 67-75.

[4] di Biase, A., Maciej S. Kowalski, Tanner R. Devlin, Jan A. Oleszkiewicz., Moving Bed Biofilm Reactor Technology in Municipal Wastewater Treatment: A Review. Journal of Environmental Management, Vol. 247, 2019, pp. 849–866.

[5] Carrasco, R.M., Correa, E.M.C., Franco, M.F.A., Preparation of High-Quality Activated Carbon from Polyethyleneterephthalate (PET) Bottle Waste. Its Use in The Removal of Pollutants In Aqueous Solution. Journal of Environmental Management. Vol. 181, 2016, pp. 522-535.

[6] El Essawy, N. A., Ali, S. M., Farag, H. A., Konsowa, A. H., Elnouby, M., & Hamad, H. A., Green Synthesis of Graphene from Recycled PET Bottle Wastes for Use in The Adsorption of Dyes in Aqueous Solution. Ecotoxicology and Environmental Safety. Vol. 145, 2017, pp. 57–68.

[7] Eerkes-Medrano, D., Leslie, H.A., Quinn, B., Microplastics in Drinking Water: A Review and assessment of an emerging concern. Curr. Opin. Environ. Sci. Health. Vol. 7, 2018, pp. 69–75.

[8] Gewert, B., Plassmann, M.M., Macleod, M., Pathways for Degradation of Plastic Polymers Foating in The Marine Environment. Environ. Sci.: Processes Impacts. Vol. 17, 2015, pp. 1513–1521.

[9] Revel, M., Châtel, A., Mouneyrac, C., Micro(nano)plastics: A Threat to Human Health? Curr. Opin. Environ. Sci. Health. Vol. 1, 2018., pp. 17–23.

[10] Edge, M., Hayes, M., Mohammadian, M, Allen, N. S., Jewitt, T. S., Brems, K., Jones, K. Aspects of Poly (ethylene Terephthalate) Degradation for Archival Life and Environmental Degradation Polymer Degradation and Stability 32 (2) 1991: pp. 131 – 53.

[11] Moharir, R.V., Kumar, S., Challenges Associated with Plastic Waste Disposal and Allied Microbial Routes for Its Effective Degradation: A Comprehensive Review. Journal of Cleaner Production, Vol. 208, 2019, pp. 65-76.

[12] Cai, L., Wang, J., Peng, J., Wu, Z., Tan, X., Observation of The Degradation of Three Types of Plastic Pellets Exposed to UV Irradiation in Three Different Environments. Science of the Total Environment. Vol. 628-629, 2018, pp. 740-747.

[13] Crawford, C. B dan Quinn, B., Microplastic pollutants 1st edition e-Book Elsivier Science, 2017.

[14] Hidalgo-Ruz, V., Gutow, L., Thompson, R.C., Thiel, M., Microplastics in the Marine Environment: A Review of the Methods Used for Identification and Quantification. Environmental Science & Technology, Vol. 46, 2012, pp. 3060-3075.

[15] Alam, F., Sembiring, E., Muntalif, B. S., Suendo, V., Microplastic Distribution in Surface Water and Sediment River Around Slum and Industrial Area (Case Study: Ciwalengke River, Majalaya Distric, Indonesia). Chemosphere. Vol. 224, 2019, pp. 637 – 645.

[16] Song, Y. K., Hong, S. H., Jang, M., Han, G, M., Jung, S, W., Shim, W. J., Combined Effects of UV Exposure Duration and Mechanical Abrasion on Microplastic Fragmentation by Polymer Type. Environmental Science & Technology. Vol. 51, 2017, pp. 4368-4376.

[17] Singh B., and N. Sharma., Mechanistic implications of Plastic Degradation. Polymer Degradation and Stability. Vol. 93, 2008, pp. 561–584.

[18] Plotnikov, V. G., Effect of Mechanical Stresses on Photochemical Degradation of Polymeric Molecules. Dokl. Akad. Nauk SSSR. Vol. 301, 1988., pp. 376–379.

[19] Feldman, D., Polymer weathering: Photooxidation. J. Polym. Environ, Vol. 10, Issue 4, 2002, pp. 163−173.

[20] Cooper, D.A., Corcoran, P.L., Effects of Mechanical and Chemical Processes on the Degradation of Plastic Beach Debris on The Island Oo Kauai, Hawaii. Mar. Pollut. Bull. Vol. 60, 2010, pp. 650–654.

[21] Gu, J. D., Ford, T. E., Mitton, R., Microbial Degradation and Deterioration of Polymeric Materials. The Uhlig Corossion Book, second edition, 2000, pp. 439-460.

[22] Xiao, Y. Luo, W.-P. Zhang, X.-Y. Guo, C.-C.; Liu, Q. Jiang, G.-F. Li, Q.-H., Aerobic Oxidation of *p*-Toluic Acid to Terephthalic Acid over T(*p*-Cl) PPMnCl/ $Co(OAc)_2$ under Moderate Conditions. Catalysis Letters. Vol. 134, No, 1–2, 2010, pp. 155–161.

7th Int. Conf. on Structure, Engineering & Environment (SEE), Pattaya, Thailand, Nov.10-12, 2021, ISBN: 978-4-909106070 C3051

FORMULATION AND ANTIOXIDANT ACTIVITY OF LIP BALM ENRICH BY BIDARA LEAF EXTRACT (*Ziziphus spina-christi* L.)

Hendrawati[1], Siti Aidina[1], Maulidia[1], Nurhasni[1], Yulyani Nur Azizah[1]
[1]Faculty of Science and Technology, State Islamic University Syarif Hidayatullah Jakarta, Indonesia

ABSTRACT

Bidara leaf (*Ziziphus spina-christi* L.) are known for their high antioxidant activity. It can be used as an additional active component in preparation of lip balm formula. The purpose of this research is to get lip balm formula that enriched with Bidara leaf extract and to know its antioxidant activity. The antioxidant activity of Bidara leaf extract was tested using DPPH (1,1-diphenyl-2-picrylhydrazil) method and the active component was identified using GCMS (Gass Chromatography and Spectrometry Mass). The result showed that the antioxidant activity of Bidara leaf has an IC50 value 25.22 ppm. The GCMS analysis showed that Bidara leaf extract contained phytol component which have potentially as an antibacterial. The preparation formula of lip balm used 0; 1; 2; and 3% of Bidara leaf extract expressed by F0, F1, F2, and F3 respectively. The most optimum Bidara lip balm product based on general panelists preference level was F1 which content with 1% of Bidara leaf extract with a score of 4.37. All lip balm product tested have met the requirements for SNI 16-4769-1998 criteria encompass melting point range 53.50 – 54.50 ºC; pH value 4.43 – 4.53; homogeneous; and negative microbial contamination. The antioxidant activity result of the best formula has an IC50 value 339.23 ppm.

Keywords: Antioxidant, Bidara leaf, Cosmetic, Lip balm, SNI

INTRODUCTION

Bidara leaves (*Ziziphus spina-christi* L.) are very beneficial for the skin because they contain natural antioxidants. Antioxidant is an inhibitors that used to inhibit free radicals by forming a relatively stable reaction [1]. Secondary metabolite compounds present in the content of a material are responsible for the antioxidant content of the material. Bintoro et al. [2] analyzed Bidara leaf extract with GCMS and reported that phytol compounds were the most abundant in Bidara leaves. Kusriani et al. [3] determined the phenolic content of the ethanol extract of bidara leaves by 7.19% and has antioxidant activity with IC50 value of 127.87 ppm.

The research was strengthened by Heria et al. [4] which states that the ethanol extract of Bidara leaves has a flavonoid content of 1.53% and antioxidant activity with an IC50 value 90.96 ppm. The ethanol extract of bidara leaves has been studied also by Hendrawati et al [5] and was formulated in cosmetic preparations in the form of a peel-off-gel mask and has been tested to contain antioxidants. Based on the research sources above, Bidara leaves contain antioxidants that have the potential to be additional active ingredients in the manufacture of cosmetic preparations. In this study, Bidara leaf extract was added to lip balm cosmetics.

Lip balm cosmetics needed by many people in order to protect their lips from the sun and prevent the diseases of the lips [6]. Lips are part of the body that more delicate and sensitive than the other skin because the skin on the lips tends to be thinner and smoother [7]. Sun exposure causes free radical reactions that result in dry and cracked lips, darken lips, premature aging and skin cancer [8].

Using lip balm will protect the lips from sun exposure [9]. The addition of antioxidants to the lip balm formulation is better for protecting the lips because free radicals are neutralized with the active substances content. Lip balm is used by applying it evenly on the lips. The use of lip balm generally only leaves a glossy or transparent impression on the lips so that the application of lip balm is suitable for both women and men [10].

The formulation of lip cosmetic that enriched with Bidara leaf extract has been carried out. The lip balm made using cacao oleum base [11], added with various concentrations of Bidara leaf extract as much as 0; 1; 2; and 3% (w/w). Lip balm characteristics were tested with the parameters of melting point value, pH value, and total microbial contamination in accordance with the quality requirements of SNI 16-4769-1998, followed by a preference level test by 30 panelists. The antioxidant activity of the best lip balm preparation was tested and its stability was measured for 20 days.

MATERIAL AND METHODS

The tools used in this study include lip balm containers, glassware (*pyrex*), analytical scales (*Ohaus*), magnetic stirrer, rotary evaporator (*Heidolph-Lborota 4000*), pH meter (*Mettler Toledo*),

Perkin Elmer's Lambda 25 UV-Vis spectrophotometer, GCMS spectroscopy (*Shimadzu*), melting point, blender, and filter paper.

The main ingredient in this research is Bidara leaves obtained from the Bidara garden in Sumenep (East Java) and has been determined at the Center for Biology for Botany, Biology Research Center-LIPI Cibinong. The solvent used technical ethanol. The test material for determining antioxidant activity used DPPH (*Sigma*) and methanol (p.a *Merck*). The ingredients in the lip balm formulation used were cacao oleum, vaseline album (*Brataco*), glycerin (*Moon K*), sunflower seed oil (*Mazola*), and orange essence.

Preparations and Extraction of Bidara Leaf Samples

The Bidara leaves that have been cleaned with water were dried in the air. The dried leaf samples were mashed with a blender to obtain Bidara leaf powder. The extraction process was carried out by soaking 200 g of Bidara leaf powder with 96% ethanol (v/v) until the sample was completely submerged, then stirred using a magnetic stirrer for 30 minutes and stored for 24 hours in a place protected from sunlight. The results of the Bidara powder immersion are filtered and then the solvent was evaporated using a vacuum rotary evaporator to obtained a concentrated Bidara leaf extract [12].

Physical Evaluation of Bidara Leaf Extract Lip Balm Preparations

Melting point test

The lip balm sample is inserted into a capillary tube and then placed in a melting point apparatus. The temperature recorded is the temperature at which the sample first began to melt [13].

PH check

The pH meter was first standardized by dipped a pH meter electrode in standard solution pH 6.86 and washed with distilled water. Lip balm samples were made in 1% (w/v) concentration by melting 1 gram of the preparation in 100 mL of distilled water. The electrode is immersed in the solution and the examination was carried out 3 times for each formula [13].

Smear test

The greased test was carried out by applying a lip balm preparation 5 times on the observer's hand, then the color attached was observed after being left for 15 minutes. A good preparation does not leave color marks evenly with several application at a certain pressure [13].

Homogeneity examination

The homogeneity check was carried out by applying a certain amount of lip balm preparation on a transparent glass. Homogeneous preparations do not show coarse grains [13].

Stability check

Stability checks were carried out by storing the preparation at room temperature for 20 days. After the interval of 5 days, the preparation was observed for its changes in shape, color and odor [14].

Total Plate Number

Plate Count Agar (PCA) media was weighed as much as 5.3 g then dissolved with 250 mL of aquadest. Lip balm samples (on day 3) were diluted with sterile dilution to 10^{-3} then homogenized. One mL of each sample dilution was pipetted into sterile petri dishes in duplicate and then 12 mL of liquid Plate Count Agar (PCA) media was poured. The petri dish was shaken gently until the sample was well mixed. The mixture was allowed to solidify before being put into the incubator (35^{o}C) in an inverted position for 48 hours. The number of microbial colonies was observed and calculated using the formula Eq. 1 [13].

$$AL = \Sigma C \; x \frac{1}{fp} \quad (1)$$

Note: AL = number of colonies, C= number of colonies from each petri, fp = dilution factor

Preference Test for Lip Balm of Bidara Leaf Extract

The parameter of the preference test includes texture, color, scent, homogeneity, and general preference that was resulting from 4 lip balm formulations. 30 untrained panelists were taken randomly (questionnaire sheet is attached in Appendix 11) with a rating scale presented in Table 3. The data from the preference test results were analyzed using the SPSS application including the one-way test ANOVA and Duncan's test [15].

RESULT AND DISCUSSION

Bidara Leaf Extract

Determination of leaf samples species where carried out at LIPI Cibinong showed that the type of Bidara leaf used in this study was *Ziziphus spina-christi* (L.) The extraction of Bidara leaves was carried out by maceration method using ethanol. It

was chosen as a solvent because of its neutral, good absorption, non-toxic, not easily overgrown by microbes and molds [16]. The yield of Bidara leaf extract produced after concentrated using vacuum rotary evaporator was 16.3063%. That result did not significantly different from previous studies [5]. The extract obtained is thick in texture and dark green in color with a distinctive scent of Bidara leaf.

Phytochemical Test of Bidara Leaf Extract

Phytochemical identification is a qualitative test to determine the presence of secondary metabolites contained in the extract. Based on phytochemical testing on Table 1, the sample of Bidara leaf was confirmed contains compounds as listed below, that reinforced by the previous research [5].

Table 1 Phytochemical test result

Compound Group	Discoloration	Conclusion
Steroids	Green	+
Flavonoids	Orange	+
Triterpenoids	Brown Ring	+
Alkaloids	Chocolate	+
Phenolates	Black	+
Tannins	Blackish Green	+
Saponins	Foaming	+

The results indicated that Bidara leaves have antioxidant activity because they showed positive results for the flavonoid, phenol, and tannin group tests [17,18].

Active Compound of Bidara Leaf Extract Using GCMS

Identification of active compounds using Gas Chromatography Mass Spectrometry (GC-MS) was carried out to determine the active compounds contained in Bidara leaf extract. In this analysis, the stationary phase is used in the form of a DB-5MS UI column with a length of 30 m, a diameter of 0.250 mm, and a film thickness of 0.25.m. The results of the chromatogram are shown in Fig 1.

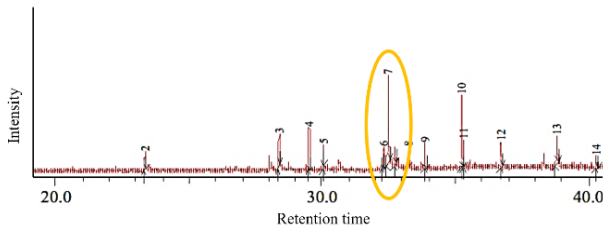


Fig. 1 Bidara leaf extract chromatogram

The results of the GCMS analysis obtained 14 chemical compounds with different retention times, abundances and peak segments. Based on the results of the similarity to the literature, the highest peak was at the 7th peak which suspected to be a phytol compound (Fig. 2) with a retention time of 32.471 minutes, a concentration of 21.98% and a molecular weight (m/z) of 296.

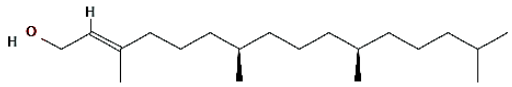


Fig. 2 Structure of phytol

Based on Bintoro et al [2], one of the phytochemical components in Bidara leaves is phytol compounds. Phytol is a diterpene compound that plays a role in the synthesis of vitamin E. This role allows this compound to function as an antimicrobial. In this study, quercetin and rutin were not identified which are responsible as antioxidants in Bidara leaves [5]. On research of Putri [19], analyzing the content of Bidara leaf extract using LCMS found the content of quercetin and rutin compounds that are responsible as antioxidants.

Antioxidant Activity of Bidara Leaf Extract

The antioxidant activity test of Bidara leaf extract (*Z. spina-christi* L.) was carried out using the DPPH (1,1-diphenyl-2-picrylhydrazil) method because it was accurate, effective and quantitative. The IC_{50} values obtained in Bidara leaf extract was 25.224 ppm (Table 2), these results showed a smaller value when compared to the research Kusriani et al [3] which has an IC_{50} value of 127.87 ppm and research Haeria et al [4] which has an IC_{50} value of 90.9548 ppm.

Table 2 Antioxidant activity of Bidara leaf extract

No	Conc. (ppm)	% Inhibition (SD)	IC_{50} (ppm)
1	0	0	
2	2.5	28.35 ± 0.0028	
3	5	33.33 ± 0.0014	
4	10	40.23 ± 0.0028	25,224
5	20	47.13 ± 0.0028	
6	40	62.45 ± 0.0014	
7	80	93.49 ± 0.0007	

The smaller of IC50 value, the stronger was its antioxidant activity, therefore the Bidara leaf sample in this study has strong antioxidant activity [1]. Nevertheless, compared with a standard used in antioxidant activity test, the IC50 result of Bidara leaf

extract was still higher than ascorbate (IC50 4.03 ppm) which categorized as very strong antioxidant.

Lip Balm Preparation Result

The lip balm formulation process was carried out by melting cacao oleum, vaseline album, beeswax, and oil at 85ºC as mixture A. Bidara leaf extract which has been added to glycerin is mashed with a mortar as mixture B. Mixture B was added to mixture A and then stirred until homogeneous. This mixing is carried out in a state of warm mixture A to minimize damage to the active substances in the bidara leaf extract. The orange essence was added also to disguise the characteristic odor of the preparation. The formulation was carried out with the addition of Bidara leaf extract as much as 0; 1; 2; and 3% (w/w).

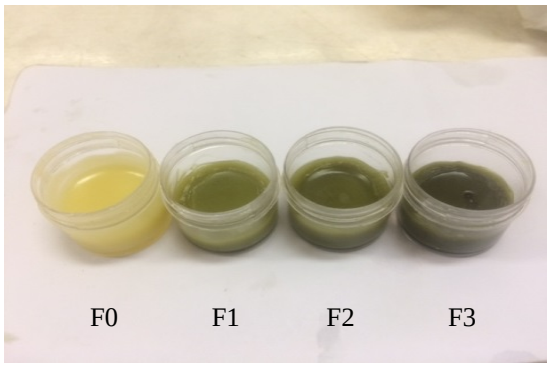


Fig. 3 The result of the formulation of Bidara leaf extract lip balm

Lip balm preparations formed different colors (Fig. 3). F0 with 0% extract concentration was yellow because it did not contain Bidara leaf extract, F1 with 1% extract concentration had light green preparation, while both F2 (2%) and F3 (3%) had dark green preparation. Bidara leaf extract has a green color due to the presence of chlorophyll compounds, so that variations of Bidara leaf extract added to lip balm preparation will produce an intense green color as increasing extract added.

Physical Quality Analysis of Lip Balm Preparations

Analysis of the lip balm formula preparation of Bidara leaf extract includes melting point, pH value, smear test, homogeneity test, stability test and microbial contamination test to determine the characteristics of each lip balm preparation. Standardization of lip balm preparation products refers to the physical quality requirements of SNI 16-4769-1998.

Melting point

The melting point of lip balm preparations is influenced by the components that make up the lip balm, such as the concentration of hardener, fat, and emollient. This research uses beeswax as hardener which has melting point of 62-64ºC, cocoa fat which has a melting point of 35ºC and emollients, namely sunflower seed oil and glycerin. Good mixture of wax is not more than 50% because it will produce a lip balm with a hard texture while the concentration of oil can lower the melting point of the lip balm [20]. Table 3 showed that the four lip balm formulations had identical melting points in the range of 53.5 – 54.5 ^{0}C, so therefore the melting point range according to SNI 16-4769-1998.

pH value

Recommended lip balm has an acidity value that close to the physiological pH value of the lip skin, which is 3.8-4.7, because if the pH value is too low it will cause skin irritation or if the pH is too high it will cause dry skin [14]. Table 3 was the result of pH examination which shows that the four lip balm preparations have a pH value in the range of 4.43-4.53, due to the presence of acidic sunflower seed oil content. The results of the pH test indicate that the preparations made are safe and do not cause irritation to the lips and met the pH range of skin acceptance according to SNI 16-4769-1998.

Dosage grease test

Lip balm preparations are said to have good greasing power if the preparation does not provide color (transparent), evenly, and homogeneous when applied. The results of the smear test for the preparation of lip balm preparations of Bidara leaf extract showed that all preparations had good smearing power (Table 3). Although the preparation of Bidara leaf lip balm was green physically, the whole preparation gives a transparent smear test result and indicated that the extract was well dispersed in the lip balm formula so that it does not leave a green color.

Homogeneity

Parameters of homogeneity testing of lip balm preparation were carried out to see the presence or absence of coarse grains. Coarse grains indicated that the lip balm preparation was not homogeneous because it was not dispersed between the components of the lip balm to form a homogeneous composition.

The results of the homogeneity examination on table 3 showed that all lip balm preparations of Bidara leaf extract did not show any coarse grains when applied to transparent glass which means the Bidara leaf lip balm had a homogeneous composition. The formation of good homogeneity will affect the even distribution of lip balm doses at the time of use. Homogeneous lip balm will give good results because

the medicinal ingredients are evenly dispersed in the base material so that when applied, the applied dose was evenly distributed and the use of lip balm will be effective in protecting the lips.

Stability

Stability observation was carried out to determine the occurrence of changes in color, scent, and texture or dosage form. The preparations that were stored for 20 days at room temperature did not experience drastic changes in both color and scent. All lip balm preparations began to change in texture on day 15 of storage with the appearance of white spots and increased in number on day 20. This was probably due to the absence of preservatives that can maintain the stability and durability of the lip balm so that the texture of the lip balm was damaged, meanwhile the color and scent of the lip balm did not change.

Microbial contamination

Microbial contamination test is one of the tests required by SNI 16-4769-1998. This test was important because microorganism contamination can cause phase separation, sample weight loss, affect shelf life, unpleasant odor even more cause irritation. Cosmetic products contaminated with microorganisms were usually seen from the formation of colored fungal colonies, changes in odor, changes in viscosity that damage the quality of cosmetic preparations [6]. According to Buckle et al [21], factors that can affect the growth of microorganisms include pH, water activity, temperature, and oxygen content.

The calculation of microbial contamination was carried out using the Total Plate Count (TPC) method where all colonies that grew in petri dishes were counted and to meet the statistical requirements, the petri dish selected in the calculation has a colony count of 30-300 in several dilutions [22]. The maximum amount of microbial contamination in mask products according to SNI is 102 colony/gram. The results of the microbial contamination test on all lip balm preparations did not show the number of microbial colonies in the range of 30-300 colonies so that the calculation of microbial contamination was considered non-existent. Therefore, all lip balm preparations meet the standards based on SNI 16-6070-1999 and safe to use.

Preference Test Result

The preference test is one type of acceptance test to obtain the most preferred lip balm variety preparations by the panelist. The panelists consisted of 21 women and 9 men aged 22 years and over, had knowledge of lip balm and were willing to become panelists. The level of preference was referred to a hedonic scale which can be stretched according to the desired scale range. The hedonic scale can be converted into a numeric scale with quality scores according to the level of preference, with this numerical data, parametric data analysis can be performed [23].

Based on table 3, the results of general level of preference for lip balm ranged from a score of 2.53-

Table 3. Characteristic of lip balm preparations of Bidara leaf extract

Parameter	F0	F1	F 2	F3	SNI
Melting point (º C)	54,50	53,50	53,50	53,50	50 - 70
pH	4,53	4,48	4,43	4,45	3,8 – 4,7
Smear test	Colorless, even	Colorless, even	Colorless, even	Colorless, even	
Homogeneity test	Homogeneous	Homogeneous	Homogeneous	Homogeneous	Homogeneous
Microbial contamination (colony/g)	Nothing	Nothing	Nothing	Nothing	Maximal 102
Texture preference test	$4,03^{b} \pm 0,615$	$3,97^{b} \pm 0,809$	$3,70^{a,b} \pm 0,794$	$3,33^{a} \pm 0,922$	
Color preference test	$4,07^{c} \pm 0,944$	$4,00^{c} \pm 0,743$	$3,50^{b} \pm 0,900$	$2,67^{a} \pm 0,994$	
scent preference test	$4,07^{b} \pm 0,177$	$3,90^{b} \pm 0,913$	$3,30^{a} \pm 0,988$	$3,03^{a} \pm 1,217$	
Homogeneity preference test	$4,40^{b} \pm 0,563$	$4,23^{a,b} \pm 0,504$	$4,00^{a} \pm 0,643$	$4,00^{a} \pm 0,371$	
General preference	$4,23^{c} \pm 0,626$	$4,37^{c} \pm 0,556$	$3,43^{b} \pm 0,774$	$2,53^{a} \pm 0,937$	

Note: F0 = lipbalm without the addition of Bidara leaf extract; F1 = lipbalm with the addition of 1% Bidara leaf extract; F2 = lipbalm with the addition of 2% Bidara leaf extract; F3 = lipbalm with the addition of 1% Bidara leaf extract

4.37, which means that the panelists stated their level of preference from dislike to like. The results of lip balm preparations that have the highest level of preference are F1 with an average score of 4.37 and the lowest level of preference is F3 with a score of 2.53. Both light green (F1) and yellow (F0) preparation of lip balm were more accepted by panelists compared to the dark green preparation left (F2, F3). The effect of smooth texture, light color and scent that covers the smell of the extract and other compositions, conclude that the F1 preparation was chosen as the best formula on the preference test.

The results of the one-way ANOVA statistical test with a 95% confidence level had a significant value of 0.000 which indicated that there was a significant difference ($P<0.05$) between the addition of Bidara leaf extract to the lip balm formulation and the panelists' preference level. The entire score generated is considered as a parameter that represents the assessment of the panelists, so the best formulation chosen is lip balm with the addition of 1% extract.

The best formula for lip balm

The lip balm product in this study had a melting point, pH and microbial contamination in the range of SNI 16-4769-1998. Based on the requirements of SNI 16-4769-1998 and the general highest level of panelist preference test, F1 was chosen as the best formula preparation of Bidara leaf extract lip balm which has a melting point of 53.5^{o}C, pH value 4.48 and homogeneous texture.

Antioxidant Activity of Lip Balm Preparations

The addition of natural ingredients in the form of extracts in cosmetics has the potential to maintain the physiological balance of human skin with a low or safe level of toxicity [25]. Determination of the antioxidant activity of the best lip balm preparations was carried out to determine how much influence the antioxidant compounds had on the ethanol extract of Bidara leaves which were added to the lip balm formulation.

The lip balm formula of F1 has a considerable IC50 value compared with Bidara leaf extract, which is 25.224 ppm. The heating process in the formulation and the addition of lip balm composition considered degrade the antioxidant activity of lip balm Bidara leaf extract.

Tabel 4. Antioxidant activity of F1 lip balm preparation

No.	Conc. (ppm)	% Inhibition (SD)	IC50 (ppm)
1	0	0	
2	12.5	1.82±0.0014	
3	25	7.27 ± 0.0028	
4	50	9.55±0.0014	339,234
5	100	18.64 ± 0.0028	
6	200	31.14 ± 0.0007	
7	400	57.50 ± 0.0035	

The results of this antioxidant activity showed that the lip balm formula F1 had weak antioxidants, in contrast to the IC50 of Bidara leaf extract, which had strong antioxidants. This can occur because the extract content is lower than other lip balm component, it also due to the heating process when formulating the lip balm which damaged the active substance in the extract, hence the antioxidant activity tends to be weak. Nurhaida et al [26] had formulated lipstick from dragon fruit extract with basic ingredients consisted of oil, cetyl alcohol, cacao oleum and beeswax, yet the antioxidant results of the lipstick showed a higher IC50 than its extract.

CONCLUSIONS

The entire lip balm formula meet the standards of SNI 16-4769-1998 which has melting point 53.5 – 54.5 ^{o}C, pH value of 4.43 – 4.53, all preparations were homogeneous, and negative for microbial contamination. The result of the most preferred lip balm preparation by panelists is the F1 formula which meets the physical quality requirements based on SNI 16-4769-1998 and has antioxidant activity with an IC50 of 339.234 ppm. The ethanol extract of bidara leaf identified through GCMS analysis did not show any compounds thought to be responsible as antioxidants, but the results of the analysis of its antioxidant activity showed an IC50 value of 25.224 ppm.

ACKNOWLEDGMENTS

I would like to thank the Rector of State Islamic University for research funding project through the LP2M Research Centre for 2021.

REFERENCES

[1] Molyneux P. The Use of the Stable Free Radical Diphenylpicryl-Hydrazyl (DPPH) for Estimating Antioxidant Activity. Songklanakarin Journal of Science and Technology, 2004, pp. 211–19.

[2] Bintoro A., Ibrahim A.M., and Situmeang B. Analysis and Identification of Saponin Compounds from Bidara Leaves." ITEKIMA, Vol. 2, Issue 1, 2017, pp. 84–94.

[3] Kusriani R.H., Nawawi A., and Machter E. Determination of Total Phenolic Compound Levels and Antioxidant Activity of Leaf, Fruit and Seed Extract of Bidara (Ziziphus *Spina-Christi* L.). Proceedings of SNaPP2015 Health, 1(1), 2015, pp. 311–18.

[4] Haeria H. Determination of Total Flavonoid Levels and Antioxidant Activity of Ethanol Extract of Bidara Leaf (Ziziphus Spina-Christi L.). Journal of Pharmaceutical and Medicinal Sciences, Vol. 1, Issue 2, 2016, pp. 57–61.

[5] Hendrawati, Aziza, La O.S., and Yulyani N.A. Formulation, Antioxidant And Antibacteria Activities Of Peel-Off Gel Mask, Enriched With Bidara Leaf (*Ziziphus Spina-Christi* L.) Extract. International Journal Of GEOMATE, Vol. 18, Issue 68, 2020, pp. 66 – 72.

[6] Tranggono R.I., and Latifah F. Handbook of Cosmetic Science. Jakarta: Main Library Publisher, 2007.

[7] Wibowo, D.S. Anatomy of the Human Body. Jakarta: Grasindo, 2008.

[8] Draelos Z.D., and Thaman L.A. Cosmetic Formulation of Skin Care Products. New Jersey: Taylor and Francis Group, 2006.

[9] Jacobsen P.L., Denis P.L., Michael A.S., Drore E., and Barbara D.W. The Little Lip Book. USA: Carma Laboratories Inc. Thing, 2011, pp. 27-29.

[10] Sulastomo E. Beautiful and Healthy Skin: Knowing and Caring for the Skin. Jakarta: Compass, 2013.

[11] Ratih H., Titta H., and Puri R.C. Formulation of Cananga Oil (Cananga Oil) Lipbalm as an Emollient. Proceedings of the Synopsis for Research on Natural Medicinal Ingredients (SPBOA) XVI, 2014.

[12] Ashri N.H. Activity Test and Identification of Antibacterial Chemical Compounds Ethanol Extract of Bidara Leaves (*Ziziphus Spina-Christi* L.) Against Several Pathogenic Bacteria [Thesis]. Makassar: Alauddin State Islamic University Makassar, 2016.

[13] [BSN] National Standardization Agency. SNI 16-4769-1998 Lipstick Quality Requirements. Jakarta: National Standardization Agency, 1998.

[14] Vishwakarma B., Dwivedi S., Dubey K., and Joshi H. Formulation and Evaluation of Herbal Lipstick. International Journal of Drug Discovery & Herbal Research, 2011.

[15] [BSN] National Standardization Agency. SNI 01-2346-2006 Instructions for Organoleptic and/or Sensory Tests. Jakarta: National Standardization Agency, 2006.

[16] Saadah H., and Nurhasnawati H. Comparison of Ethanol and Water Solvents in the Preparation of Tiwai (*Eleutherine Americana Merr*) Tuber Extract. Manutung Scientific Journal, Vol. 1, Issue 2, 2015, pp. 149–53.

[17] Salmiyah S., and Bahruddin A. Phytochemicals and Antioxidants in Tome-Tome Fruit (*Flacourtia Inermis*), Vol. 10, Issue 1, 2018, pp. 43–50.

[18] Khanahmadi M., Rezazadeh S.H., and Taran M. In Vitro Antimicrobial and Antioxidant Properties of Smyrnium Cordifolium Boiss (*Umberlliferae*) Extract. Asian Journal of Plant Science 9, 2010.

[19] Putri R.A.Z. Activity Test of Arabic Bidara Leaves (*Ziziphus Spina-Christi* L.) As Anticancer In Colon Cancer Cells (WiDr) Through MTT Method And Identification Of Active Compounds With LC-MS Method [Thesis]. Poor. Maulana Malik Ibrahim State Islamic University, 2017.

[20] Ansel H.C. Introduction to Pharmaceutical Dosage Forms. Jakarta: UI Press, 2008.

[21] Buckle K.A., Edwards R.A., Fleet G.H., and Wotton M. Food Science. Jakarta : University of Indonesia Press, 2010.

[22] Waluyo L. Basic Techniques and Methods in Microbiology. Malang: University of Muhammadiyah Malang Press, 2008.

[23] Setyaningsih D., Apriyantono A., and Sari M.P. Sensory Analysis for the Food and Agro Industry (DS Sard). Bogor: IPB Press, 2010.

[24] Mitsui T. New Cosmetic Science. Tokyo: Elsevier, 1997.

[25] Chancal D., and Swarnlata S. Novel Approaches in Herbal Cosmetics. Journal of Comestic Dermatol, Vol. 7, 2008, pp. 89–95.

[26] Nurhaida A., Susilo H., and Sari B.L. Antioxidant Activity of Lipstick Preparations With Natural Coloring Extract Of Super Red Dragon Fruit (Hylocereus Costaricensis L.). Pakuan University, 2017.

7th Int. Conf. on Structure, Engineering & Environment (SEE), Pattaya, Thailand, Nov.10-12, 2021, ISBN: 978-4-909106070 C3051

MORPHOLOGICAL RESPONSES AND TISSUE ADAPTATIONS OF GAMMA-IRRADIATED BANANA TO STANDING SUBMERGENCE CONDITION

Pimpan Pimonrat[1]and Seyha Kong[2]

[1]Faculty of Agricultural Technology, Rajamangala University of Technology Thanyaburi, Thailand; [2]Paper Tree Cambodia CO., Ltd., Cambodia

ABSTRACT

Water is considered as main factor for growth, development and fruit production of banana. Submergence condition (excessive amount of water) affects its nutrient uptake, photosynthesis and physiological metabolism. Objectives of this research were to study morphological responses and tissue adaptations of gamma-irradiated banana to submergence condition. *In vitro* suckers were exposed to gamma rays at doses of 10, 20, 30, 40 or 50 Gy and regenerated on MS medium with period of submergence condition for 15, 30 or 45 days. Plant height, leaf number, root number, sucker number, leaf width, leaf length and root and leaf cross section were recorded and analyzed. Results showed that growth parameters of banana plants analysis decreased by irradiating with high dose rate (50 Gy). Plant height (1.03±0.04 cm), leaf width (0.55±0.07 cm) and leaf length (3.05±0.07 cm) of irradiated suckers at dose of 20 Gy cultured with period of submergence condition for 15 days were higher than 10 and 30 Gy. Highest sucker number (1.38±0.63) was found after culturing 20 Gy irradiated shoot under period of submergence condition for 45 days. Cross sectional results of 20 Gy irradiated root showed that aerenchyma structure was strongly formed. In addition, 40 Gy of gamma rays highly promoted leaf number of banana cultured with period of submergence condition for 15 days. Our results were indicative that the dose of 20 Gy was an appropriate dose for enhancing tolerance of banana cultured in standing submergence condition.

Keywords: Gamma Irradiation, Banana, Submergence condition, Flooding tolerance

INTRODUCTION

Banana is one of crucial fruit crops originated in Indochina and Southeast Asia [1]. Banana has been using around the world for at least 7,000 years in Papua New Guinea [2], possibly 6,000 years in Uganda [3] and 2,500 years in Cameroon [4]. Today, banana is economically grown in about 130 countries [5]. Growth and development of banana are influenced by climate change which means weather expressed by properties such as temperature, wind, humidity, cloudiness and rainfall. Over a decade climate has been started to change driven by natural mechanisms or human activation processes. Changes in climate affect agriculture in many ways including lengthening of growing season, more drought land, salinization or more rainfall [6].

In Thailand, the climatic condition is suitable for production of banana therefore banana is seen in all areas from coastal plain to the highland [7]. Suitable climate for banana growth is warm moist weather without strong winds throughout the year. The water requirement for total growth period of banana is high, as it is an herbaceous and long-duration crop [8], [9]. In the humid tropics, it is 1,200 mm and 2,200 mm per year in the dry tropics [5]. However, excessive amount of water during the growth period generates damage and oxygen deficit to banana plant. 24 hours with a high level of water is enough to kill roots and high level of water that continues for several days makes the color of leaves turn pale [10].

Damage from submergence condition is more severe when water is standing than flowing [11]. Banana could tolerate 72 h of flooding with flowing water [12]. Floods in Thailand are regular natural disasters which happen nearly every year during the monsoon season which causes 100% of the production lost. So, it is important to improve submergence tolerance in banana. As bananas are recalcitrant to conventional breeding approaches, gamma irradiation and clonal selection are the major sources to address the submergence tolerance banana.

Gamma irradiation has been proven to be used as physical mutagen in breeding program that may result for new traits in crop plants called mutant [13], [14]. Mutation induction with gamma rays is the most powerful method to develop varieties with less time consuming and more genetic variation which may not located in desired plant germplasm [15]-[17]. In the recent year, there was submergence tolerance rice mutant has been developed by using gamma rays [18]. There were no reports on submergence tolerance banana.

Objectives of this present research were to study the morphological responses and tissue adaptations of banana that would differentiate submergence tolerance after investigation the induction of genetic variability using gamma irradiation.

METHODOLOGY

Plant materials and culture conditions

The commercial banana Hom Thong was used as the experimental material. The sucker of mature plant was harvested from field-grown plant. After removal of the outer leaves, the innermost suckers were cut into 3-5 cm pieces and firstly washed in tap water and then 5 min in sterile distilled water for 3 times. Surface decontamination was performed with 95% ethanol (v/v) for 5 min and 0.1 % mercury chloride (W/V) for 5 min, followed by three washed with sterile distilled water for 15 min each. Suckers were aseptically inoculated onto MS [19] medium supplemented with 2 mg/L BA and 3% Sucrose. The pH of culture medium was adjusted to 5.8 before autoclaving. This medium is referred to as sucker induction medium. Cultures were incubated inside sterile room at 25±2 °C at relative humidity 70-80% under photoperiod of 16 h for 4-5 weeks until 1 cm-height suckers appeared.

Gamma irradiation and treatment with submergence condition

Gamma irradiation was acutely carried out with a Cs^{137} sources by a Mark I Gamma Irradiator at the Nuclear Technology Research Center. 1 cm-height suckers were irradiated with different doses of gamma rays (5 level; 10, 20, 30, 40 and 50 Gy). For the selection of submergence tolerance, irradiated-suckers were transferred onto fresh MS medium with 3 cm of standing water layer for 15, 30 and 45 days. The morphological parameters of irradiated banana which were plant height, root number, leaf number, sucker number, leaf width and leaf length were recorded at the vegetative stage after treatment to analyze tolerance ability.

Tissue adaption analysis

Root and leaf samples were taken from cultured bottles to carry out cross-sectioning. Cassava corks were used to embed the plant samples. A small, deep hole on the center of the cork that fit with the size of the root and leaf samples was created and then put the root and leaf samples into the hole carefully. Several transversal slices were done to produce material that is as thin as possible. The most transparent, thinnest and intact slice of the material was chosen. Tissue adaptation was observed under the microscope by putting the selected cross sectioned samples on a slide with 1-2 drops of preservation liquid to avoid sample dehydration, then covering them with a cover glass.

Statistical analysis

Analytical measurements and all data were presented by mean value with standard deviation. Each parameter was analyzed by analysis of variance (ANOVA) by using completely randomized design (CRD) as experimental design. Duncan's multiple range test was used as determining of differences between the treatment at the 95% confidential ($p \leq 0.05$).

RESULT AND DISCUSSION

The results of the effect of gamma irradiation on the plant height and root number are shown in Table 1. Banana exposed to 20 Gy of gamma ray and cultured under period of submergence condition for 15 days had the highest plant height (1.03 cm), while high doses (40 and 50 Gy) of gamma rays were completely inhibited growth of banana. Plant high of banana irradiated with low dose (10 and 20 Gy) and cultured under period of submergence condition for 45 days was higher than high dose irradiating. It is indicated that severity of submergence condition for 45 days was reduced by low dose of gamma ray irradiation. This result is in agreement with the work of [20] who reported a decrease in plant height as doses increase. Low dose of gamma rays may change carbohydrate and energy metabolism and maintenance required for further growth during submergence.

Highest root number was found after irradiating banana sucker with 20 Gy gamma rays and cultured under period of submergence condition for 30 days. Increasing of root number is one of the flooding tolerance parameters which increase air flowing process to banana by aerenchyma structure. The impact of aerenchyma formed in root is to increase the amount of air available to banana tissues.

The most important parameters of banana production are leaf and sucker number. Banana exposed to 40 Gy and cultured under period of submergence condition for 15 days had the highest leaf number (4.29 leafs), while high dose (50 Gy) of gamma rays were completely inhibited growth of banana as shown in Table 2. The highest sucker number was found in treatment of exposure to 20 Gy and cultured under period of submergence condition for 45 days (1.38 suckers). Highest leaf width and leaf length were found in treatment of banana exposed to 20 Gy and cultured under period of submergence condition for 15 days as shown in Table 3. These results showed that lower doses of gamma irradiation have stimulatory effects on morphological responses of banana whereas higher doses had inhibitory as reported by many researchers [21], [22].

Table 1 Plant height and root number of irradiated banana exposed to different gamma radiation dose rates and cultured under different period of submergence condition

Treatment	Plant height (cm)	Root number (root)
10 Gy 15 days	0.39 ± 0.23 ^{de}	0.38 ± 0.18 ^{bcd}
30 days	0.58 ± 0.36 ^{cde}	0.83 ± 0.63 ^{abc}
45 days	0.67 ± 0.24 ^{bcd}	0.58 ± 0.38 ^{abcd}
20 Gy 15 days	1.03 ± 0.04 ^{a}	0.26 ± 0.01 ^{cd}
30 days	0.59 ± 0.19 ^{cde}	1.00 ± 0.43 ^{a}
45 days	0.76 ± 0.17 ^{abc}	0.88 ± 0.32 ^{ab}
30 Gy 15 days	0.44 ± 0.27 ^{cde}	0.26 ± 0.01 ^{cd}
30 days	0.92 ± 0.14 ^{ab}	0.26 ± 0.01 ^{cd}
45 days	0.28 ± 0.04 ^{ef}	0.00 ± 0.00 ^{d}
40 Gy 15 days	0.55 ± 0.07 ^{cde}	0.27 ± 0.02 ^{cd}
30 days	0.0 0± 0.00 ^{f}	0.00 ± 0.00 ^{d}
45 days	0.00 ± 0.00 ^{f}	0.00 ± 0.00 ^{d}
50 Gy 15 days	0.00 ± 0.00 ^{f}	0.00 ± 0.00 ^{d}
30 days	0.00 ± 0.00 ^{f}	0.00 ± 0.00 ^{d}
45 days	0.00 ± 0.00 ^{f}	0.00 ± 0.00 ^{d}
F-test	*	*
CV%	42.05	78.76

All the data are expressed as mean ± standard deviations. Means with the different superscript letters in a column are differ significantly ($p \leq 0.05$).

Table 2 Leaf and sucker number of irradiated banana exposed to different gamma radiation dose rates and cultured under different period of submergence condition

Treatment	Leaf number (leaf)	Sucker number (sucker)
10 Gy 15 days	0.75 ± 0.50 ^{cd}	0.75 ± 0.43 ^{abc}
30 days	1.83 ± 1.53 ^{bc}	0.67 ± 0.52 ^{abc}
45 days	1.42 ± 0.29 ^{bcd}	0.67 ± 0.29 ^{abc}
20 Gy 15 days	1.38 ± 0.18 ^{bcd}	0.95 ± 0.07 ^{ab}
30 days	1.92 ± 0.58 ^{bc}	0.81 ± 0.63 ^{abc}
45 days	2.38 ± 1.13 ^{b}	1.38 ± 0.63 ^{a}
30 Gy 15 days	1.42 ± 0.63 ^{bcd}	0.75 ± 0.50 ^{abc}
30 days	2.63 ± 1.16 ^{b}	0.44 ± 0.13 ^{bc}
45 days	0.00 ± 0.00 ^{d}	0.26 ± 0.01 ^{bc}
40 Gy 15 days	4.29 ± 0.05 ^{a}	0.63 ± 0.18 ^{abc}
30 days	0.00 ± 0.00 ^{d}	0.00 ± 0.00 ^{c}
45 days	0.00 ± 0.00 ^{d}	0.00 ± 0.00 ^{c}
50 Gy 15 days	0.00 ± 0.00 ^{d}	0.00 ± 0.00 ^{c}
30 days	0.00 ± 0.00 ^{d}	0.25 ± 0.00 ^{bc}
45 days	0.00 ± 0.00 ^{d}	0.25 ± 0.00 ^{bc}
F-test	*	*
CV%	58.43	67.51

All the data are expressed as mean ± standard deviations. Means with the different superscript letters in a column are differ significantly ($p \leq 0.05$).

Table 3 Leaf width and leaf length of irradiated banana exposed to different gamma radiation dose rates and cultured under different period of submergence condition

Treatment	Leaf width (cm)	Leaf length (cm)
10 Gy 15 days	0.25 ± 0.00 ^{bcd}	1.08 ± 0.52 ^{cde}
30 days	0.28 ± 0.16 ^{bc}	0.92 ± 0.19 ^{cde}
45 days	0.17 ± 0.07 ^{bcd}	1.17 ± 0.14 ^{bcd}
20 Gy 15 days	0.55 ± 0.07 ^{a}	3.05 ± 0.07 ^{a}
30 days	0.35 ± 0.17 ^{ab}	2.25 ± 0.25 ^{ab}
45 days	0.36 ± 0.19 ^{ab}	1.25 ± 0.41 ^{bcd}
30 Gy 15 days	0.15 ± 0.04 ^{bcd}	1.75 ± 1.52 ^{bc}
30 days	0.26 ± 0.18 ^{bc}	1.13 ± 0.57 ^{cde}
45 days	0.06 ± 0.01 ^{cd}	0.50 ± 0.00 ^{de}
40 Gy 15 days	0.26 ± 0.01 ^{bcd}	2.25 ± 0.01 ^{ab}
30 days	0.00 ± 0.00 ^{d}	0.00 ± 0.00 ^{e}
45 days	0.00 ± 0.00 ^{d}	0.00 ± 0.00 ^{e}
50 Gy 15 days	0.00 ± 0.00 ^{d}	0.00 ± 0.00 ^{e}
30 days	0.00 ± 0.00 ^{d}	0.00 ± 0.00 ^{e}
45 days	0.00 ± 0.00 ^{d}	0.00 ± 0.00 ^{e}
F-test	*	*
CV%	57.27	49.03

All the data are expressed as mean ± standard deviations. Means with the different superscript letters in a column are differ significantly ($p \leq 0.05$).

Tissue adaptation analyses showed that aerenchyma was formed in both root and leaf cross-sectional area of irradiated banana with 20 Gy gamma rays (Fig 1). Aerenchyma has been formed in root and leaf of submergence plant to obtain oxygen from shoot to root, sufficient oxygen will diffuse through aerenchyma to maintain growth and respiration of waterlogged root [23]. Aerenchyma can develop in the root cortex as well as in stem and leaves [24]. Long-term survival of banana in submergence condition results of porosity formation of aerenchyma by gamma ray irradiation.

CONCLUSION

The genetic variation induced by gamma ray irradiation of the studied banana genotypes might have resulted in more adaptation under submergence condition. Our results confirm that using 20 Gy gamma irradiation could introduce directly or indirectly a submergence tolerance trait as a new source of germplasm in breeding program for banana.

ACKNOWLEDGMENTS

We express our gratitude to Division of Crop Production in Rajamangala University of Technology Thanyaburi.

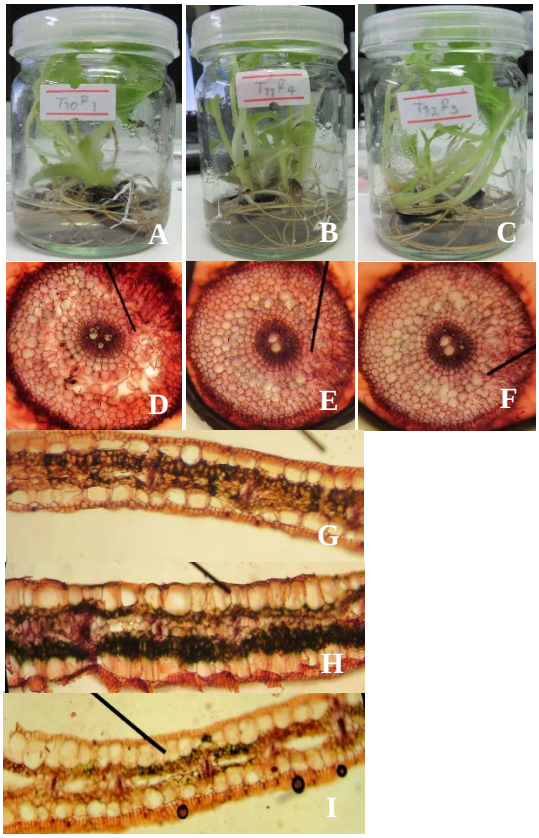


Fig. 1. Aerenchyma formation of root and leaf banana exposed to 20 Gy gamma ray and cultured under difference period of submergence condition; A, D, G for 15 days; B, E, H for 30 days; C, F, I for 45 days.

REFERENCES

[1] Simmonds N. W., The evolution of the bananas, Longman, London, 1962, pp. 167.

[2] Denham T. P., Haberle S. G., Lentfer C., Fullagar R., Field J., Therin M., Porch N., and Winsborough B., Origins of agriculture at Kuk Swamp in the highlands of Papua New Guinea. Science, Vol 301, 2003, pp. 189-193.

[3] Leijiu B. J., Robertshaw P., and Tayler D., Africa's earliest bananas?. J. Archaeol. Sci, Vol 33, 2006, pp. 102-113.

[4] Mindzie C. M., Doutrelepont H., Vrydaghs L., Swennen R., Swennen R. J., Beekman H., de Langhe E., and de Maret P., First archaeological evidence of banana cultivation in central Africa during the third millennium before present. Veg. Hist. Archaeobot, Vol 10, 2001, pp. 1-6.

[5] Ravi I. and Vaganan M. M., Abiotic stress tolerance in banana. Abiotic Stress Physiology of Horticultural Crops, DOI 10.1007/978-81-322-2725-0_12.

[6] Bosello F. and Zhang J., The effect of climate change on agriculture. FEEM, QA-Rivistadell' Associazione Rossi-Daria. 2006.

[7] Pimonrat P. and Yi C., Effect of gamma irradiation and salt stress on survival rate and growth of Hom Thong banana. Journal of Agricultural Technology, Vol 13, Issue 7.3, 2017, pp. 2387-2391.

[8] Popenoe W., Banana culture around the Caribbean. Tropical Agriculture, Trinidad, Vol 18, 1941, pp. 8-12.

[9] Turner D. W., Fortescue J. A., and Thomas D. S., Environmental physiology of the bananas (*Musa* spp.). Braz. J. Plant Physiol, Vol 19, Issue 4, 2007, pp. 463-484.

[10] Perming E., Paddy and banana cultivation in Sri Lanka-A study analysing the farmers' constraints in agriculture with focus on Sooriyawewa D.S. division. Seminar series nr 307. Department of Physical Geography and Ecosystem Science. Physical Geography and Ecosystem Analysis Lund University. 2013.

[11] Israeli Y. and Lahav E., Injuries to banana caused by adverse climate and weather. In: Jones D. R. (Ed) Diseases of banana, abaca and enset. CAB international, Wallingford, UK, 2000, pp. 351-369.

[12] Robinson J. C., Bananas and plantains (Series 5), Institute for tropical and sub-tropical crops, South Africa, CAB International Crop Production Science in Horticulture, Wallingford, UK, 1992, pp. 229.

[13] Lamseejan S., Jompuk P., Wongpiyasatid A., Deeseepan S., and Kwanthammachart P., Gamma-rays induced morphological changes in Chrysanthemum (*Chrysanthemum morifolium*). Kasetsart J (Nat. Sci.), Vol 34, 2000, pp. 417-422.

[14] Hanafiah D. S., Trikoesoemaningtyas., Yahya S., and Wirnas D., Induced mutations by gamma ray irradiation to Argomulyo soybean (*Glycine max*) variety. Bioscience, Vol 2, Issue 3, 2010, pp. 121-125.

[15] Van Harten A. M., Mutation breeding, theory and practical application. University of Cambridge, Cambridge, UK, 1998.

[16] Yaqoob M. and Rashid A., Induced mutation studies in some mungbean (*Vigna radiata* L.) Wilczek cultivars. J. Biol. Sci, Vol 1, 2001, pp. 805-808.

[17] Khan S. and Goyal S., Mutation genetic studies in mungbean IV. Selection of early maturing mutants. Thai Journal of Agricultural Science, Vol 42, Issue 2, 2009, pp. 109-113.

[18] Jiya M., Olamide F., Yusuf D. O. A., Abdulhakeem A., Muhammad M. L., Zulukanaini S. B., and David T. S., Effects of gamma irradiation on submergence tolerance of two selected varieties of low land rice (*Oryza sativa* L.). GSC Biological and Pharmaceutical Science, Vol 2, Issue 3, 2018, pp. 031-037.

[19] Murashige T. and Skoog F., A revised medium for rapid growth and bioassays with tobacco tissue

culture. Physiol. Plant, Vol 15, 1962, pp. 473-497.
[20] Mushtaq A. K. and Rakesh C. V., Assessment of the effect of gamma irradiation on various morphological and agronomic traits of common wheat (*Triticum aestivum* L.) var.WH-147. European Journal of Experimental Biology, Vol 5, Issue 7, 2015, pp. 6-11.
[21] Sikder S., Biswas P., Hazra P., Akhtar S., Chattopadhyay A., Badigannayar A. M., and D'Souza S. F., Induction of mutation in tomato (*Solanum lycopersicum* L.) by gamma irradiation and EMS. Indian Journal of Genetics, Vol 73, Issue 4, 2013, pp. 392-399.
[22] Salve K. M. and More A. D., Effect of gamma radiation on seed germination, seedling height and seedling injury in *Coriandrum sativum* Linn. International Journal of Life Sciences, 2014.
[23] Armstrong W., Brandle R., and Jackson M. B., Mechanisms of flood tolerance in plants. Acta Bot. Neerl, Vol 43, Issue 4, 1994, pp. 307-358.
[24] Mustroph A., Improving flooding tolerance of crop plants. Agronomy, Vol 8, 2018, pp. 1-25.

7th Int. Conf. on Structure, Engineering & Environment (SEE), Pattaya, Thailand, Nov.10-12, 2021, ISBN: 978-4-909106070 C3051

PASSIVE DESIGN ENERGY SAVING HOUSE BY NATURAL VENTILATION IN THAILAND.

Niran Watchrodom[1]
[1] Department of Mechanical Engineering, Faculty Industrial Education, Rajamangala University of Technology Suvarnabhumi; Suphanburi, Thailand.

ABSTRACT

This paper reports the experimental investigation and designing of Energy saving House by natural ventilation. The Gypsum Wall (GW) with to Metal Sheet Roof (MSR). Tinted Glass with Gypsum Wall (TGGW) with to Metal Sheet Roof with Perforated Ceiling (MSRPC). And the Solar Chimney Wall with Daylighting (SC-WD) with to Solar Chimney Metal Sheet Roof with Perforated Ceiling (SC-MSRPC)developed by Faculty Department of Mechanical Engineering, Faculty Industrial Education Rajamangala University of Technology Suvarnabhumi. The experimental study of three test houses. The dimension of the testing boxes is 120 X 120 cm with 120 cm height and the length of roof along slope is 160 cm. The wall houses were made of white painting gypsum board. The GW & MSR is single layer normal metal sheet. The TGGW & MSRPC uses Perforated Ceiling and open void for ventilation. The SC-WD & SC-MSRPC same TGGW & MSRPC but developed panels along the roof degrees. The slope of the angle roof is 30°.The experimental results were showed the room temperature of GW & MSR is always higher than the TGGW & MSRPC and SC-WD & SC-MSRPC, respectively. Observe that, during 12:00 - 18:00 the temperature difference between the attics space with room temperatures from ambient temperature of GW & MSR higher than TGGW & MSRPC and SC-WD & SC-MSRPC respectively due to the effect of attic space cannot ventilated. The average indoor illuminance of SC-WD & SC-MSRPC was higher than the standard illuminance by about 310 -910 lux. The air flow rate and number of air change by about 0.0025- 0.004 m^3/s (9-14 m^3/hr) and 2-8.5 ACH, respectively. The SC-WD & SC-MSRPC should be promoted for architectural and engineering designs.

Keywords: Passive Designing, Energy saving house, Natural ventilation

INTRODUCTION

Thailand is in a humid tropical climate. This affects the environment almost all year round. Depending on the architectural and engineering design, solar energy is one of the creating effects that will increase the cooling load of a home. Decades ago in Thailand The residence was designed using Solar chimneys to integrate building envelopes to reduce heat transfer and increase ventilation. The Building Science Research Center (BSRC) has proposed a residential performance by reconfiguring the Trombe wall [1]. Renovation of the Trombe Wall (PG-MTW) partial glazing, comprising masonry walls. with glass blocks on the outside Gypsum type aluminum foil and acrylic sheet on the inside. Open the vent of the size PG-MTW was tested against modified Trombe Wall (MTW). Results suggest that it is used in residential homes to reduce heat transfer and luminance in the home, after that BSRC. Offered homes using solar flue walls (GSCW) [2] consist of double glazing with Air gap area and vent openings at the top and bottom of the glass Test results obtained Confirmed to be suitable for countries with hot and humid climates. There is an increased rate of ventilation. In the summer of 2009, a performance test was conducted. The operation of the Solar Chimney Window (SCW) has been Installed on the school building [3] SCW consists of glass louvers on the outside. Inside is a clear glass pane which The gap between the glass is 0.065 m. By comparison, two types of louvered glass (clear glass and translucent glass) were used in the exterior. The inner sheet is also clear glass. The results of the experiment were confirmed in use. Solar chimney ideas for home improvement SCW optimization by installing Curtains in the gaps between the air gaps. Between the two model houses using synthetic blinds [4] and natural hemp curtains [5], SCW was presented with synthetic blinds comprising exterior louvered glass and inside is clear glass, surface area is 0.77 sq m, air gap area is 0.065 m, test results can be Reduce room temperature and ventilation by approximately 2.5 ˚C and 55 m^3/h SCW with hemp curtains. Nature was monitored for reducing heat transfer and ventilation. Research results show that high efficiency for heat dissipation, giving you the comfort of your home. by fact Various configurations of double glazing panels and theoretical studies and tests [6-7] show details. Further for the effect of natural light was carried out in the investigation of double clear glass wall (DCGW) and double light glass wall (DTGW) developed by the Faculty of Architecture and Design, King Mongkut's University of Technology. Klao

Bangkok North (KMUTNB) [8] The study validated the performance of both DCGW thermal configurations consisting of double glazing panels. The outside and inside are clear glass, different from DTGW which the outside is. translucent glass The clear glass and translucent glass are the same size, width 60 cm., length 200 cm. and thickness 6 mm., opening the air vents below (inside the room) and above (outside the room). Open the channel to 0.14 x 0.60 m. Test results show that the DTGW and DCGW home illuminance is higher than the illuminance standards by approximately 1,500 lux and 2,000 lux respectively. air flow rate and amount of air change about 0.0025 - 0.004 m^3/sec (9 - 14.4 m^3/hr) and 2 - 14 ACH, respectively. [9] Sahabuddin Latif *et al* Computational studies using Solidworks Flow Simulation software from heat vents in the attics of traditional Buginese houses in hot and humid tropical climates have been carried out. This research has proposed inclined chimney 45º with horizontal output, to cool the bedroom air for free. The triangular roof of Buginese houses can store large hot stock all day long throughout the year. This solution can improve weather conditions in the attic by modifying how to increase the airflow in it by utilizing the stack effect that occurs due to differences in attic temperature and the environment. In this study, the air intake area is thought to originate from the bedroom window.This flow creates two circulation zones on the inner surface of the roof, which then empties into horizontal channels at the top of the attic. The airflow increases as it passes through the horizontal triangular tube located at the top of the attic. These results present an interesting idea for building thermal energy using a solar chimney system

Human comfort issues in most tropical wellings is the amount of heat from the daily radiation from the sun that enters the house almost all year round Both the roof, walls and other parts that receive solar radiation. Therefore, in response to human comfort, commercial energy is used through electrical machinery such as fans, air conditioners. used to adjust the conditions in the home to be appropriate which will cause A huge waste of commercial energy, especially in countries that have to import commercial energy, will result in trade deficits. It also causes environmental pollution problems. This research project will design energy-saving homes based on natural ventilation. This will cause ventilation and reduce the amount of heat entering the building. which is a guideline to study how to reduce building electricity consumption.

OBJECTIVES OF THE RESEARCH

To study the comparative study of the temperature reduction caused by heat transfer into the building in the design of energy-saving houses by using natural ventilation that can reduce heat entering the building. and ventilate through the building frame in a natural way.

METHODS OF CONDUCTING RESEARCH

The design of energy-efficient houses based on natural ventilation was conducted in small-scale houses to compare thermal performance. The test is in the summer. The mock house for the test shown in Figure 1 is as follows.

EXPERIMENTAL PROCEDURE

Table 1. Different styles of walls and roofs of 3 model houses.

model house	Wall type	Roof type
model 1	Gypsum Wall (GW)	Metal Sheet Roof (MSR)
model 2	Tinted Glass with Gypsum Wall (TGGW)	Metal Sheet Roof with Perforated Ceiling (MSRPC)
model 3	Solar Chimney Wall with Daylighting (SC-WD)	Solar Chimney Metal Sheet Roof with Perforated Ceiling (SC-MSRPC)

Wall and roof tests facing south. The dimensions of the chamber are 1.20 x 1.20 x 1.20 m, as shown in Fig. 2 - 4. The walls and ceiling are using 9 mm thick gypsum. The small test chamber is raised with a steel stand 0.20 m from the floor. Located at Rajamangala University of Technology Suvarnabhumi Suphanburi Center, District 2, on the rooftop of Building 10, 3rd floor, with the coordinates being 13 0 54'N 100 038E.

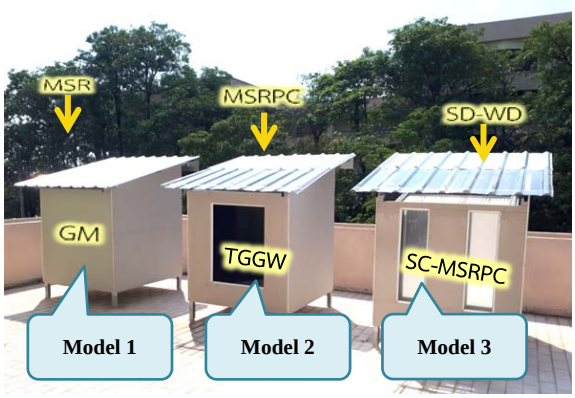


Figure 1. Shows the house for testing.

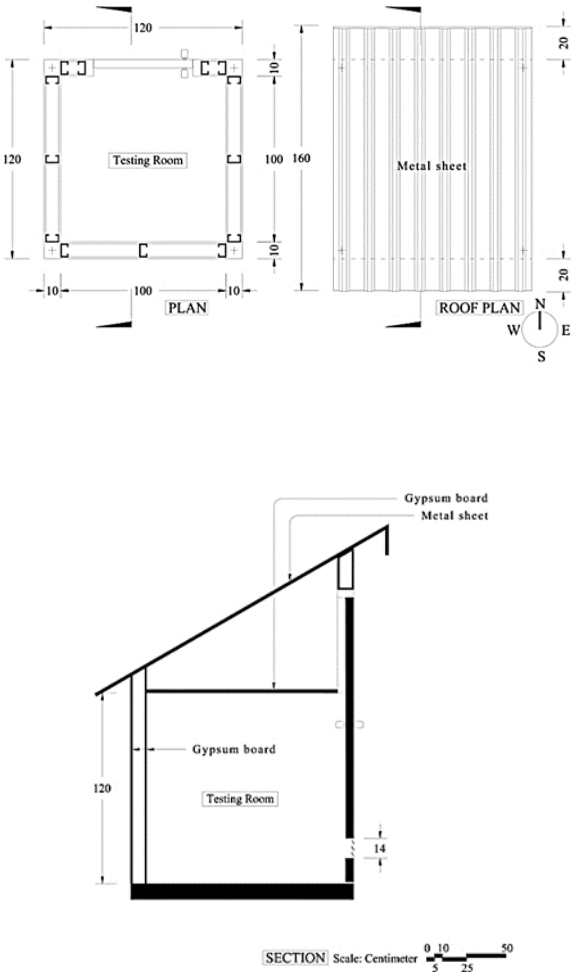
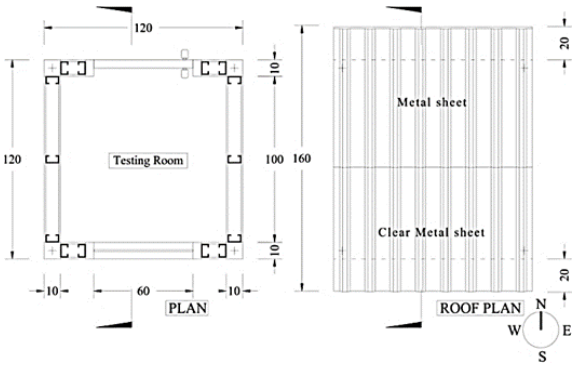


Figure 2. Show Model of the first house, Gypsum Wall (GW) tested together with Metal Sheet Roof (MSR).



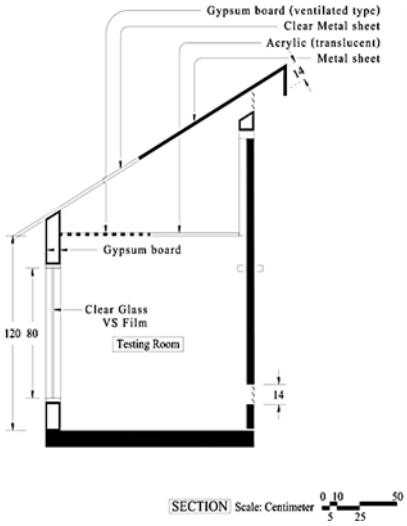


Figure 3. Show Model 2 house model, Tinted Glass with Gypsum Wall (TGGW) tested together with Metal Sheet Roof with Perforated Ceiling (MSRPC)

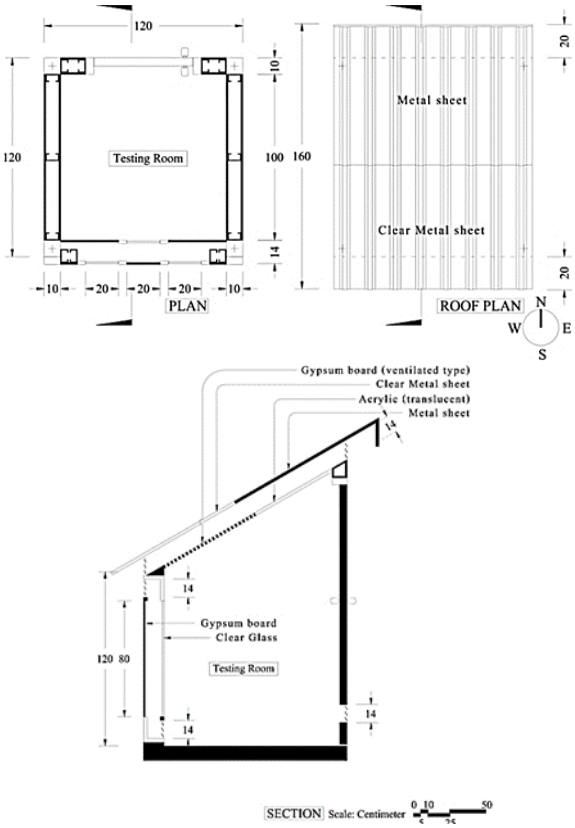


Figure 4. Show Model of the 3rd house model, Solar Chimney Wall with Daylighting (SC-WD), tested with Solar Chimney Metal Sheet Roof with Perforated Ceiling (SC-MSRPC)**.**

The model house testing with Thermocouples (Type K) are installed for temperature testing in different locations at GW & MSR, TGGW & MSRPC

and SC-WD & SC-MSRPC.

Model of the first house, Gypsum Wall (GW) tested together with Metal Sheet Roof (MSR).

- T wall 1 = Outside GW
- T wall 2 = Inside GW
- T roof 1 = Outside MSR
- T roof 2 = Inside MSR

Model 2 Tinted Glass with Gypsum Wall ; TGGW tested together with Metal Sheet Roof with Perforated Ceiling ; MSRPC

- T wall 1 = Outside TGGW
- T wall 2 = Inside TGGW
- T roof 1 = Outside MSRPC
- T roof 2 = Inside MSRPC

Model 3 Solar Chimney Wall with Daylighting ; SC-WD tested together with Solar Chimney Metal Sheet Roof with Perforated Ceiling ; SC-MSRPC

- T wall 1 = Outside SC-WD
- T wall 2 = Inside SC-WD
- T roof 1 = Outside SC-MSRPC
- T roof 2 = Inside SC-MSRPC

Experiments began from 6:00 a.m. to 6:00 p.m., with data recording every 30 minutes.

Results

Wall temperature:

The temperature at the different measurement locations of GW, TGGW and SC-WD is caused by a continuous increase in heat transfer from solar thermal radiation through the wall. The figure 5 shows that the temperature of the inner surface of the wall (Twall 1) of GW was higher compared to (Twall2) TGGW and (Twall 3) SC-WD, respectively, because the solar vent wall caused air retardation of the inner surface of the wall are therefore lower respectively.

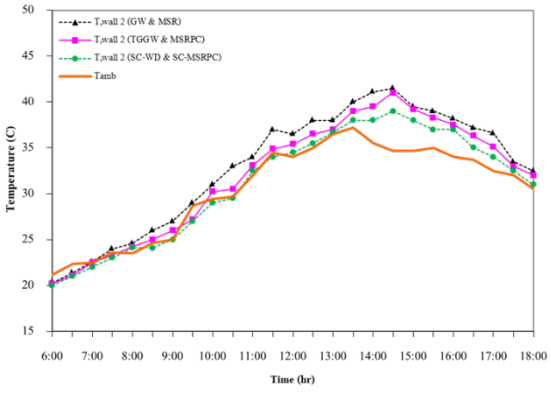


Figure 5. Show the different temperature variations of the walls GW , TGGW and SC-WD

Roof temperature:

The temperature at different measurement locations of the MSR, MSRPC and SC-MSRPC is due to the continually increased heat transfer from solar radiation through the roof. The figure 6 shows that the temperature of the inner surface of the roof (Troof 1) of MSR was higher compared to (Troof 2) MSRPC and (Troof3) SC-MSRPC, respectively, because the roof chimney caused air retardation. The temperature of the inner surface of the roof is therefore correspondingly lower.

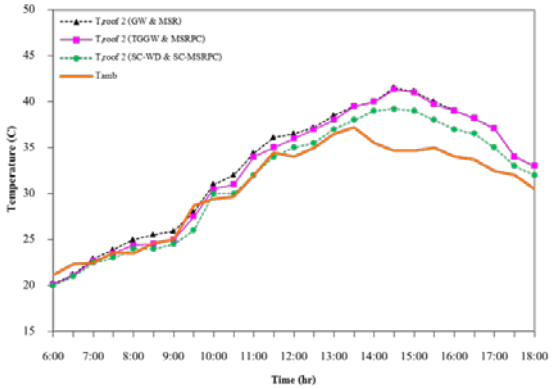


Figure 6. Show the different interior temperatures of MSR, MSRPC and SC-MSRPC

CONCLUSIONS

Energy-efficient house design based on natural ventilation. The third house that has installed a solar chimney wall to provide natural light, combined with a corrugated steel solar roof chimney and SC-WD & SC-MSRPC ventilation panels were designed in this research to be the most efficient. Compared to the 2nd house that has installed gypsum walls and tinted glass together with the rolled steel roof and ventilation ceiling TGGW & MSRPC and the 1st house that has installed the gypsum wall together with the roof. Rolled Steel GW & MSR .The 3rd house field tests showed that no overheating was observed at room temperature, it was often close to or below room temperature, which is of great interest to ventilation and airborne changes. Consistently quite high that varies between 2.8 and 8.5 watts per 1.44 sq m of surface area of the 3rd house SC-WD & SC-MSRPC. Observe that, during 12:00 - 18:00 the temperature difference between the attics space with room temperatures from ambient temperature of GW & MSR higher than TGGW & MSRPC and SC-WD & SC-MSRPC respectively due to the effect of attic space cannot ventilated. The average indoor illuminance of SC-WD & SC-MSRPC was higher than the standard illuminance by about 310 -910 lux. The air flow rate and number of air change by about 0.0025- 0.004 m3/s (9-14 m3/hr) and 2-8.5 ACH, respectively. The SC-WD & SC-MSRPC should be promoted for architectural and engineering designs.

ACKNOWLEDGEMENT

The results of this experiment. Can be accomplished with great help. From the consultation of the Faculty of Mechanical Engineering, thank you

to Research and Development Institute. Rajamangala University of Technology Suvarnabhumi for the budget for the research and thanks to the Faculty of Mechanical Engineering. Faculty of Industrial Education Suphanburi Center Providing facility, tools and support. In the research. The researcher highly appreciates.

REFERENCES

[1] Khedari J,Pongsathirat C., Puangsombut W., Hirunlabh J., Experimental performance of apartially-glazed Modified Trombe Wall. The International Journal of AmbientEnergy, Vol. 26, 2005, pp.27-36.

[2] Chantawong P., Hirunlabh J., Zeghmati B., Khedari J, Teekasap S., Win M. M.Investigationon thermal performance of solar chimney wall. Solar Energy, Vol. 80, 2006, pp.288-97.

[3] Puangsombut W., Experimental performance of solar chimney window on school building. Research and Development Journal of The Engineering Institute of Thailandunder H .M. The King's Patronage, Vol.20, 2009, pp.70-5.

[4] Ananacha T., Puangsombut W., Heat gain reduction through double window by naturalventilation with curtain. Proceedings of 24th Conference of the Mechanical Engineering Network of Thailand (ME-NETT), Ubon Ratchathani, Thailand; 2010.

[5] Sakdapipanich S., Puangsombut W., Heat gain reduction by hempen curtain with naturalventilation. Proceedings of 7th Conference on Energy Network of Thailand(E-NETT),Phuket, Thailand; 2011.

[6] Ananacha T., Puangsombut W., Hirunlabh., Shading Effects on the winter of the ThaiModern Façade Wall. Proceedings of 3th International Conference on SustainableEnergy and Green Architect (SEGA), Bangkok, Thailand; 2012.

[7] Ananacha T., Puangsombut W., Hirunlabh J., Khedari J. Field Investigation of the ThermalPerformance of a Thai Modern Façade Wall. The International Journal of Ventilation Vol.12, 2013, pp.223-34.

[8] Ananacha T., Daylighting and Thermal Performance of Double Glass Wall. InternationalConference on Advances in Science & Technology (ICAST), Chonburi,Thailand; 2014.

[9] Sahabuddin Latif , Baharuddin Hamzah, Ramli Rahim, Rosady Mulyadi, and Andi Erwin Eka Putra Study of the heat ventilation with inclined chimey in the attic. International Journal of GEOMATE, Vol. 17, Issue 64, 2019, pp. 178-184.

7thInt. Conf. on Structure, Engineering & Environment (SEE), Pattaya, Thailand, Nov.10-12, 2021, ISBN: 978-4-909106070 C3051

EFFECTS OF HIGH TEMPERATURE ON POLLEN VIABILITY AND TUBE GROWTH OF SOME INDIGENOUS PLANTS AND THE INFLUENCE OF GA3 ON TUBE GROWTH PROMOTION

Pornanan Boonkorn[1]
[1]Science Faculty, Lampang Rajabhat University, Lampang, Thailand

ABSTRACT

In summer, temperature in almost parts of Thailand increases around 38-43°C, which can affects fruit set rate of some indigenous fruit plants. This research divided into two experiments. The first experiment, effects of temperature (25 and 40°C) and sucrose concentration in pollen culture medium (0, 5, 10, 15, and 20%) on pollen morphology, viability and tube growth in 13 plants including *Citrus aurantifolia* Swing, *Dimocarpus longan* Lour., *Psidium guajava* L., *Punica granatum* L., *Solanum virginianum* L., *Tamarindus indica* L., *Capsicum annuum* L., *Vigna unguiculata* Verdc., *Luffa acutangula* Roxb., *Annona squamosa* L., *Cucumis sativus* L., *Momordica charantia* L. and *Mangifera indica* L. were tested. The results showed that sucrose concentrations and temperatures did not affect shape and size of all 13 pollen species. However, increasing the temperature from 25°C to 40°C gave lowering percentage of viability and germination of pollen tubes. The second experiment, effects of Gibberellic acid (GA3) at the concentrations of 0, 300, 600, 900 and 1200 mg/L on promoting pollen viability, pollen germination and the length of the pollen tube of longan raised under 25 and 40°C were studied. At 25°C, high value of pollen viability, pollen germination and pollen tube length were found in 300 mg/L GA3 treatment (93.87%, 81.81% and 100.04 µm, respectively). While at 40°C, which was an inappropriate temperature for pollen growth, GA3 at 300 mg/L also significantly ($p<0.05$) promoted pollen viability, pollen germination and pollen tube length of longan (91.99%, 51.93% and 80.96 µm, respectively) when compared to other treatments.

Keywords: Pollen viability, Pollen germination, High temperature, Indigenous plants, GA3

INTRODUCTION

Climate Change rises global temperature and affects all living organisms. For plants, it has both direct and indirect effects including changing rainfall patterns, distribution of pests and metabolism processes in a whole lifetime of plants. Hedhly, Hormaza and Herrero [1] stated the vulnerable of sexual reproductive phase in plants to the effects of global warming. In summer of almost parts of Thailand, temperature increases around 38-43°C and tended to increase gradually every year, which may affects fruit set rate of some indigenous fruit plants. Because viability and germination of pollen is a vital step in plant fertilization and any effect on their germination may have corresponding effect on the fertility and as well as yield production, a number of studies were carried out to determine the effects of high temperature on pollen germination and pollen tube growth. They found variation effects of temperature on among plant species and cultivars [2] - [5]. It also has long been known that some plant regulators can alleviate adverse effects on plants those encounter stresses. The objective of this research was to determine the effects of temperature and gibberellins (GA) on pollen grain morphology, viability, germination and tube length of thirteen indigenous fruit-bearing plants those grown in northern part of Thailand.

MATERIALS AND METHODS

The experiment was done in April-May, 2020. The first experiment, effects of temperature and sucrose concentration in pollen culture medium on pollen grain morphology, viability and tube growth in 13 plants including *Citrus aurantifolia* Swing, *Dimocarpus longan* Lour., *Psidium guajava* L., *Punica granatum* L., *Solanum virginianum* L., *Tamarindus indica* L., *Capsicum annuum* L., *Vigna unguiculata* Verdc., *Luffa acutangula* Roxb., *Annona squamosa* L., *Cucumis sativus* L., *Momordica charantia* L. and *Mangifera indica* L. were tested. Anthers of the thirteen plants were randomly collected from nearly-opened blossoms, fifty flowers per plant. The pollen grains were collected under the laminar air flow by pressing anther lightly on sterile glass slides and pollen suspensions were made in an appropriated concentration for each plant. The pollen germination media with various concentrations of sucrose at 0, 5, 10, 15 and 20% were autoclaved and cooled to ambient temperature. After pollen culture with each

concentration of sucrose medium by hanging drop technique in cavity slides, they were incubated in the dark at 25 or 40°C for 12 hours. The viable pollen grains were identified by staining with 1% 2,3,5-Triphenyl tetrazolium chloride, viable pollen was painted in red color after determined by light microscope. The germination percentage and morphological characteristics of pollen grains were also inspected. Pollen grains which produced a tube at least equal to their own diameter were counted as germinated. Fifteen fields of view per treatment were done. Germination percentage was determined by dividing the number of germinated pollen grains per field of view by the total number of pollen grains per field of view.

The second experiment, effect of GA3 (commercial type of Giberellin hormone) on promoting pollen germination of longan 'E Daw' cultivar was studied. Anthers and media with 15% sucrose were prepared just the same as in experiment one. GA3 was added to the germination medium to make a final concentration of 0, 300, 600, 900 and 1200 mg/L. Pollen culture were incubated in the dark at 25 or 40°C for 12 hours. Pollen viable, germination percentage and tube length of the pollen in each treatment were examined and calculated. All data analysis were done by ANOVA and mean differences were analyzed by least significant difference at $P < 0.05$.

RESULTS

Pollen grains morphology under light microscope of the tested plants was shown in Figs.1 and 2. The pollen grains were divided into 2 groups according to their size including small size (10 species, Fig.1A, B, C, D, E, F, I, J, L and Fig 2A) and big size (3 species, Fig1G, H and K), with round or triangle shape. After culture in various sucrose concentration and temperatures (Table 1), the results pointed out that viability percentage of the almost pollen grains those incubated in 25°C was significantly ($P<0.05$) higher than those incubated in 40°C. While no significantly effect of different temperatures and sucrose concentration on viability percentage was found in *P. granatum* L., *L. acutangula* Roxb., *C. sativus* L. and *M. indica* L. In *M. charantia* L., it was surprisingly that the pollen grains incubated in 40°C had higher viability percentage than in 25°C. In Table 2, the effect of temperature gave responses on pollen germination in almost plants just the same way as pollen viability (ie. high temperature gave low germination rate). Except two plants, *C. sativus* L. and *M. charantia* L. that high germination percentage was found at high incubation temperature. No significantly effect of different temperatures and sucrose concentration on germination percentage was found in *L. acutangula* Roxb. In this study, the variable effects of sucrose concentration on viable and germination of pollen were found, depended on plant species.

In the second experiment, pollen grains of longan were treated with GA3 at various concentrations; 0, 300, 600, 900 and 1200 mg/L (Table 3). Longan was chosen for the second experiment because of their high commercial value and their high vulnerable to temperature as was shown in the first experiment. Pollen grains in all treatments germinated with normal straight tube (Fig. 2) but with various percentages and length depended on GA3 concentrations and incubation temperatures.

The results in table 3 were shown that averaged percentage of pollen viability, pollen germination and tube length after GA3 treatment at a concentration of 300 mg/L were higher than other treatments (93.87%, 81.81% and 100.04 µm at 25°C and 91.99%, 51.93% and 80.96 µm, respectively). The obviously statistically improvement from 300 mg/L GA3 application was found in those incubated at 40°C in all measurements. However, higher concentration of GA3 (600, 900 and 1200 mg/L) decreased all measurements gradually.

DISCUSSION AND CONCLUSIONS

The germination of pollen is an important step in plant fertilization, any effect on their viable and germination may affect on their fertility and as well as yield production. Low pollen viability and pollen germination percentage were almost observed in high temperature incubation group (40°C), except for pollen grains from *P. granatum* L., *L. acutangula* Roxb., *C. sativus* L., *M. indica* L. and *M. charantia* L. which may be the reason from that these plants had high ability in adaptation to wide-range of temperatures because the plants can be found in various geographical areas range from temperate to tropical zone. The results were in accordance with reported from Lin [6] whom studied in litchi and found that the highest percentage of pollen germination was at 25°C. Choo [7] reported that the best temperature on flowering and fruit set for most cultivars of longan those growth in Thailand is 20-25°C.

In this study, neither effect of temperatures nor sucrose concentrations on morphology of pollen grains on any study plants was found (data not shown). Responses of pollen grains to various concentrations of sucrose were different between plants. Most of pollen grains germinated better at 10-15% concentrations than other concentrations. As Jayaprakash [8] stated that there are many germination media formulas for pollen germination, which depend on plant species and plant cultivars.

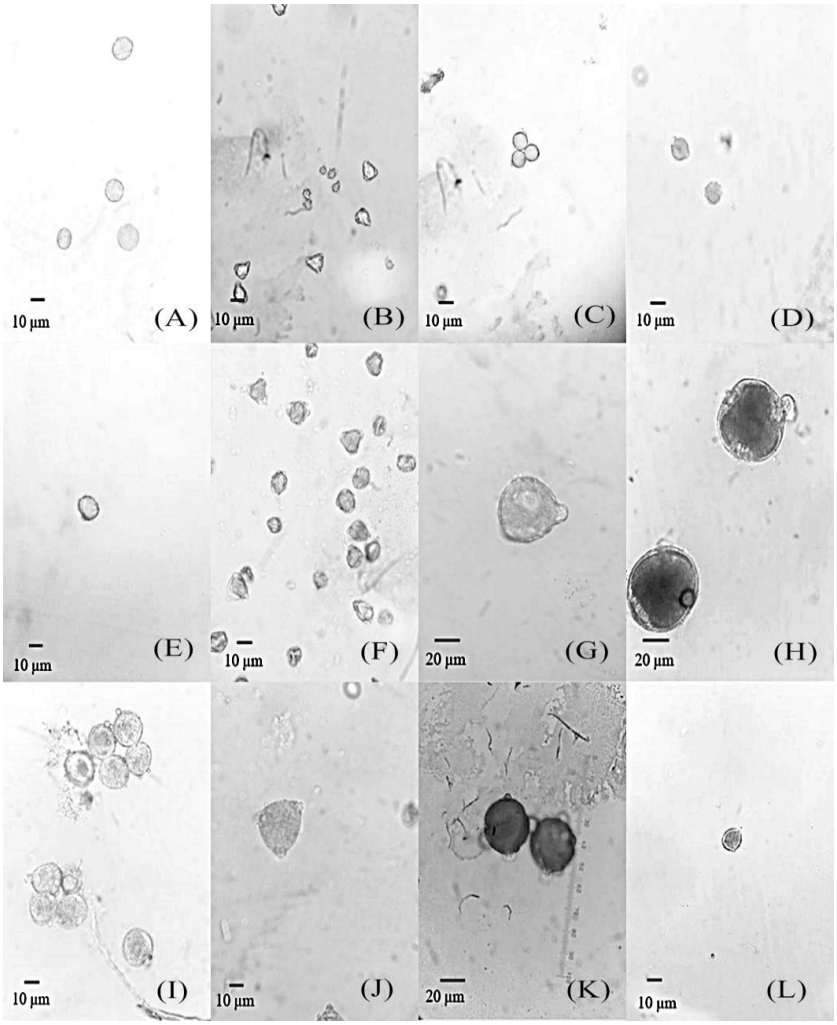


Fig. 1 The pollen grains of *C. aurantifolia* Swing (A), *P. guajava* L. (B), *P. granatum* L. (C), *S. virginianum* L. (D), *T. indica* L. (E), *C. annuum* L. (F), *V. unguiculata* Verdc. (G), *L. acutangula* Roxb. (H), *A. squamosa* L. (I), *C. sativus* L. (J), *M. charantia* L (K). and *M. indica* L (L)., inspected by light microscope.

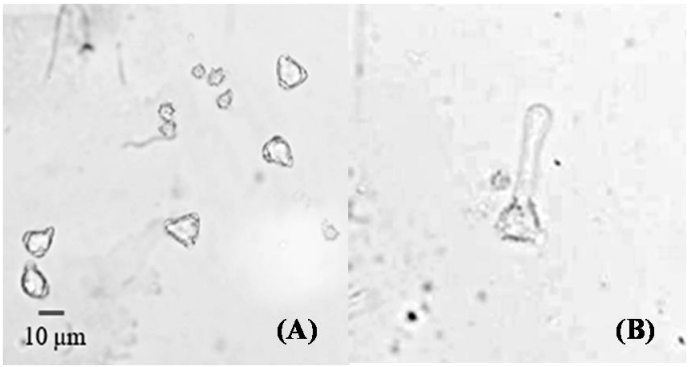


Fig. 2 The pollen grains of longan before incubation (A) and after incubated in various GA3 concentration and temperatures (B).

Table 1 Pollen viability percentage of 13 indigenous flowering plants incubated in various sucrose concentrations and temperatures

	0% suc		5% suc		10% suc		15% suc		20% suc		
Plant species	25°C	40°C	25°C	40°C	25°C	40°C	25°C	40°C	25°C	40°C	F-test
C. aurantifolia Swing	97.74	78.28	96.76	68.14	96.94	78.59	95.16	75.20	95.94	73.98	*
D. longan Lour.	93.28	91.08	92.09	87.70	90.33	89.10	93.20	87.62	93.36	89.55	*
P. guajava L.	95.24	79.51	95.88	81.95	95.14	84.65	94.16	83.25	95.73	83.63	*
P. granatum L.	93.20	93.11	91.57	92.26	96.04	94.67	96.12	95.10	92.25	92.61	ns
S. virginianum L.	94.30	85.68	91.93	86.50	92.17	81.47	93.58	86.96	94.50	89.82	*
T. indica L.	92.75	85.92	93.43	75.22	82.74	85.96	87.99	89.00	90.48	87.12	*
C. annuum L.	92.59	88.21	92.15	88.58	87.80	81.80	90.67	86.82	88.34	89.43	*
V. unguiculata Verdc.	88.26	27.30	56.73	48.47	67.19	40.47	56.21	31.08	60.50	47.93	*
L. acutangula Roxb.	81.51	76.40	83.85	81.40	75.06	74.62	69.70	69.54	81.55	80.56	ns
A. squamosa L.	47.91	31.20	48.17	37.49	46.58	41.83	60.97	44.04	61.32	48.10	*
C. sativus L.	97.08	97.34	96.74	95.20	94.45	94.98	94.91	96.18	93.18	95.87	ns
M. charantia L.	87.24	93.76	69.86	90.53	62.57	92.26	49.42	76.39	60.77	88.49	*
M. indica L.	91.04	90.25	92.00	90.21	90.17	93.09	91.96	90.48	92.62	93.44	ns

Note: Mean separation within rows by Duncan's multiple range test was at P‹0.05

Table 2 Pollen germination percentage of 13 indigenous flowering plants incubated in various sucrose concentrations and temperatures

	0% suc		5% suc		10% suc		15% suc		20% suc		
Plant species	25°C	40°C	25°C	40°C	25°C	40°C	25°C	40°C	25°C	40°C	F-test
C. aurantifolia Swing	32.00	18.74	36.65	16.02	29.15	17.00	28.03	16.54	28.15	15.32	*
D. longan Lour.	2.04	0.00	52.30	29.43	50.10	46.17	70.71	48.11	49.45	43.92	*
P. guajava L.	1.14	0.00	58.90	58.65	59.95	56.65	60.03	59.55	59.92	50.65	*
P. granatum L.	0.00	0.00	74.35	3.80	85.10	17.25	76.30	9.23	72.91	36.03	*
S. virginianum L.	41.40	41.23	54.23	41.79	41.61	40.88	41.79	41.24	43.50	42.13	*
T. indica L.	0.00	0.00	15.36	16.56	17.42	17.23	16.39	11.59	22.12	12.30	*
C. annuum L.	60.81	44.35	64.41	52.41	60.19	30.32	45.53	11.50	20.36	5.26	*
V. unguiculata Verdc.	30.32	15.13	51.31	22.64	55.44	24.32	50.63	20.66	48.66	17.43	*
L. acutangula Roxb.	63.49	64.18	64.84	64.40	63.19	67.79	66.45	64.54	63.69	63.20	ns
A. squamosa L.	0.00	0.00	41.13	40.91	40.25	36.25	40.11	38.42	35.23	22.63	*
C. sativus L.	42.40	54.88	50.32	50.15	40.19	41.22	20.36	30.19	1.10	3.02	*
M. charantia L.	33.54	46.25	50.92	55.28	53.99	71.57	48.69	79.51	46.60	62.48	*
M. indica L.	5.32	1.46	45.41	43.32	56.33	40.23	77.41	50.61	60.53	30.66	*

Note: Mean separation within rows by Duncan's multiple range test at P‹0.05

Table 3 Percentage of pollen viability, pollen germination and tube length of longan incubated in various GA3 concentrations and temperatures

GA3 concentration (mg/L)	Incubation temperature (°C)	Pollen viability percentage (%)	Pollen germination percentage (%)	Pollen tube length (µm)
0	25	85.05	77.67	80.02
	40	75.12	49.03	68.01
300	25	93.87	81.81	100.04
	40	91.99	51.93	80.96
600	25	93.15	70.19	41.98
	40	86.00	48.61	55.37
900	25	90.49	63.69	56.98
	40	70.20	43.34	70.42
1200	25	88.68	52.71	48.36
	40	70.02	31.74	57.83
F-test		*	*	*

Note: Mean separation within columns by Duncan's multiple range test at P‹0.05

The effects of various concentrations of GA3 on pollen viability, pollen germination and tube length at the two incubation temperatures for longan pointed out that the optimum concentration of GA3 for longan pollen grains was at 300 mg/L. Malik and Chhabra [9] treated pollens of groundnuts with IAA, GA3, ABA, ETH, CCC or MH at the concentration of 1-25 mg/L. They found that GA3 at the concentration of 10 mg/L promoted pollen tube elongation better than other treatments. Dhingra and Varghese [10] studied in maize pollen grains and found that GA3 at the concentration of 1mg/L could alleviated the disadvantage of salinity stress by promoting the germination of pollen tube. The reason behind a promoting effect of GA3 on pollen tube growth and their elongation is that the activation of GA3 on amylase enzyme those located in the cell wall of the germinated areas of the pollen. Amylase enzyme loose the fiber component of the cell wall and thinner it, make pollen tube easily to germination and elongation [11]. However, inappropriate concentrations of GA may also decrease or inhibit the pollen germination processes as was seen in this study. Singh, Jermakow and Swain [12] stated that GA3 can either activated or inhibit growth of pollen tubes, depend on optimum dose of GA3 for each plant species or cultivars.

It can be concluded that there were no effect of sucrose concentrations, incubation temperatures or GA3 concentrations on shape of pollen grains and shape of pollen tubes from the 13 indigenous plant species in this study, but high temperature seriously decreased pollen viability and pollen germination in almost studied plants, except for two plants, *C. sativus* L. and *M. charantia* L. Incubation temperatures and GA3 concentrations affected pollen viability, pollen germination and tube length of longan. The application of GA3 at 300 mg/L could promote viability and tube growth of pollen grains from longan those incubated, especially at high temperature (40°C(.

ACKNOWLEDGMENTS

I would like to thank the Faculty of Science, Lampang Rajabhat University, Lampang, Thailand, for supporting grant of the study. Research in the laboratory and equipment were supported by The Botanical Laboratory, Science faculty, Lampang Rajabhat University.

REFERENCES

[1] Hedhly A., Hormaza, J.I., and Herrero, M., Global Warming and Sexual Plant Reproduction. Trends in Plant Science, Vol.14, 2008, pp. 30-36.

[2] Acar, I., and Kakani, V.G., The Effects of Temperature on *In Vitro* Pollen Germination and Pollen Tube Growth of *Pistacia* spp. Scientia Horticulturae, Vol.125, 2010, pp. 569-572.

[3] Sorkheh, K., Shiran, B., Rouhi, V., Khodambashi, M., Wolukau, J.N., and Ercisli, S., Response of In Vitro Pollen Germination and Pollen Tube Growth of Almond (*Prunus dulcis* Mill.) to Temperature, Polyamines and Polyamine Synthesis Inhibitor. Biochemical Systematics and Ecology, Vol. 39, 2011, pp. 749-757.

[4] Pham, V.T., Herrero, M., and Hormaza, J.I., Effect of Temperature on Pollen Germination and Pollen Tube Growth in Longan (*Dimocarpus longan* Lour.). Scientia Horticulturae, Vol.197, 2015, pp. 470-475.

[5] Hebbar, K.B., Rose, H.M., Nair, A.R., Kannan, S., Niral, V., Arivalagan, M., Gupta, A., Samsudeen, K., Chandren, K.P., Chowdappa, P., and Prasad, P.V.V., Differences in *In Vitro* Pollen Germination and Pollen Tube Growth of Coconut (*Cocos nucifera* L.) Cultivars in Response to High Temperature Stress. Environmental and Experimental Botany, Vol.153, 2018, pp. 35-44.

[6] Lin, M.W., Studies on preharvest fruit dropping of litchi cv. Yu-Her-Pao. Hort. Abst., Vol.65(2), 1995, pp. 207.

[7] Choo, W.K., Longan Production in Asia. Food and agriculture organization of the united nations regional office for asia and the pacific Bangkok, Thailand. 2000, 14 pp.

[8] Jayaprakash, P., Pollen Germination *In Vitro*. IntechOpen, 2018, pp. 81-96.

[9] Malik C. P., and Chhabra, N., Hormonal Regulation of Pollen Gemination and Pollen Tube Elongation in *Arachis hypogea* Reitz. Proceeding of Indian Acadamy of Science, Vol. 84(3), 1976, pp. 101-108.

[10] Dhingna H.R., and Varghese T.M., Effect of Growth Regulators on the *In Vitro* Germination and Tube Growth of Maize)*Zea mays* L.(Pollen From Plants Raised Under Sodium Chloride

Salinity. New Phytology, Vol.100, 1958, 563-569.

[11] Kumar K.S., Khanduri V.P., Sharma C,M., and Kumar M., Effect of Growth Regulators and Time on *In Vitro* Pollen Germination in Three Ornamental Tropical Tree Species. Journal of Agricultural Science and Technology, Vol.18, 2016, pp. 1247-1255.

[12] Singh D.P., Jermakow, A.M., and Swain S.M., Gibberellins are Required for Seed Development and Pollen Tube Growth in Arabidopsis. The Plant Cell, Vol.14, 2002, pp. 3133-3147.

7thInt. Conf. on Structure, Engineering & Environment (SEE), Pattaya, Thailand, Nov.10-12, 2021, ISBN: 978-4-909106070 C3051

THERMAL PERFORMANCE OF THE CLEAR BLOCK WALL FOR VENTILATION

Thana Ananacha[1]

[1] Faculty of Architecture and Design, King Mongkut's University of Technology North Bangkok
1518 Pracharat 1 Road,Wongsawang, Bangsue, Bangkok 10800, Thailand

ABSTRACT

This research proposes a new type of Clear Block Wall based on natural ventilation with the objective of comparing the temperature reduction caused by heat transfer into the building, increasing the ventilation efficiency. The experimental comparative thermal performance between the two houses with Single Glass Wall (SGW) and the house with Clear Block Wall (CBW) on the equal size at 1.60 m^2. The dimension of the testing houses is 1.20 X 1.20 m^2 with 2.20 m height. Measurements were made in rooms of temperature (profile temperatures of Material). The wall facing to the south to obtain the most sunlight in the afternoon period. The experimental was conducted during the winter season in December for a period of 3 days. Data was corrected every 15 minutes. Test result show that the average room temperature during afternoon in the house model with CBW can reduce by 1.9°C and up to 2.9°C while receiving the natural light and reduce glare.

Keywords: Clear block, Daylighting, Performance, Ventilation

INTRODUCTION

Nowadays, Thailand uses energy from many air conditioning systems for reducing the heat from tropical weather. It is found that the energy consumption of air conditioning systems is up to 65 percent of total energy use in the building. In line with the trend of electrical energy consumption in residences which tend to increase every year [1] due to the design of residences in Thailand that should be consistent with the tropical environment. but has been modified by applying the modern style as the era changed. Which is an increasing in the proportion of transparent or glass material in the building. Allow the natural light but less ventilation affect the heat inside the houses due to direct solar radiation that entering through the glass. The design guidelines for energy conservation stats [2] that the amount of heat transferred trough glass is 5-10 times higher than opaque materials. Therefor there is the study of transparent material such as glass block or glass to prevent the heat accumulation inside the houses with natural ventilation by the performance of solar chimney that has been promote for the last decade in Thailand, The study the performance of a partially-Glazed Solar Chimney Wall [3] by testing the area of transparent material that affect the system by using glass blocks on the outer side with gypsum aluminum foil board and acrylic panel, And the opening vent of the wall are equal sizes. Test result show that the area of three row glass blocks affect the most to the ventilation of solar chimney, and can reducing the heat accumulation inside the house while still allows the natural light into the house. Investigation on thermal performance of glazed solar chimney walls (GSCW) [4] that is consisted of double glass pane, each glass thickness was 6 mm with an air layer in the middle compare to single glass wall the study confirmed that GSCW is highly suitable for hot country ,had the lower of room temperature and can reduce heat gain trough glass walls, Also allows the natural light into the house. after that there is the develop of double material with the air gap in the middle by using material other than glass for saving the material cost, The design the trombe wall using concrete block [5], that is the hollow material, study the ventilate of the system by simulate sun heat with halogen bulbs, the result show that the highest of thermal performance is 52 percent. from the above literature review it can be concluded that transparent material can prevent the heat accumulation by natural methods of solar chimney, also the hollow material that suit for this methods. This paper presents thermal performance of the clear block wall for ventilation with solar chimney methods.

Glass block are materials that provide light transmission, there is Air insulation in the blocks, as shown in Fig 1. It is mainly used for decorating walls, as masonry walls, therefore it does not allow air to flow through the block.



Fig. 1 The physical characteristics of glass blocks.

In this paper clear blocks wall are used as a prototype in designing by using translucent acrylic sheet that has the similar transparent property as glass block, the design allows the block to prevent heat by solar chimney, and still have the ability to provide light transmission, Investigate and make comparison of thermal performance between clear block wall and single glass wall.

METHODOLOGY

Solar chimney

A solar chimney is type of passive solar heating and cooling system that can be used to regulate the temperature of a building as well as providing ventilation, The process to prevent the heat by solar chimney is to bring heat from the sun to the building by heat transferred to the chimney, When the solar radiation hits the side of the chimney is heated and make the air less dense, then floats higher to the outlet vent according to the convection principle and the cooler air that is more dense will flow into the chimney capacity through the inlet vent create the natural ventilation. As shown in figure 2

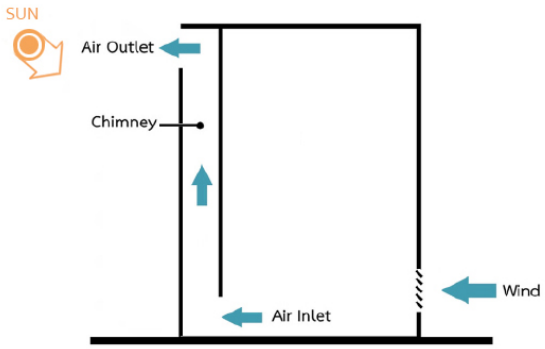


Fig. 2 This is the solar chimney diagram.

Materials Process

The materials process of design development was to provide the property of stack air flow to the blocks by making the cavity to allow stack air flow, design joint between the block instead of using masonry, provide the property of solar chimney performance by adding the inlet and outlet vent with equal sizes base on the air gap sizes in the block, The CBW has three block types have a translucent upper block that serves to ventilate the outside, the middle block serves as the vent gap and the lower block acts as an air vent from the test house. The clear blocks are the same size at 0.20x0.20x0.08 m. Air gaps and block openings are the same width of 0.068 m. and can be designing as shown in figure 3.

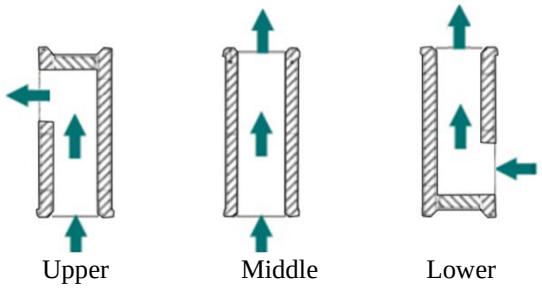


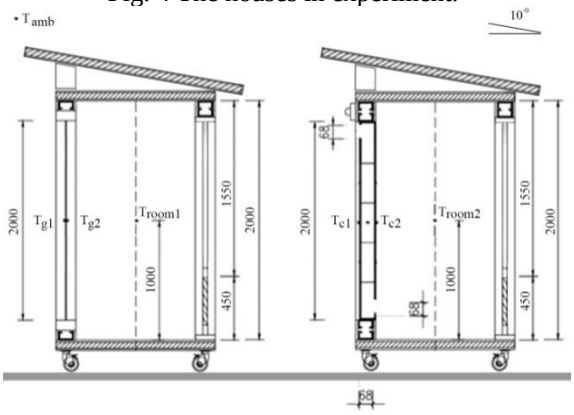
Fig. 3 Make the cavity between the block to allows stack air flow.

Experimental Process

The experimental set-up was built in the Rajamangala University of Technology Suvarnabhumi Suphanburi Campus, 450 Moo 6 Suphanburi - Chainat rd. Yanyaw, SamchookSuphanburi 72130, Thailand as shown in figure 4. The coordinates are 14°720’64” N 100°110’01” E to comparative thermal performance in the environment during 1-3 October 2020. Data was collected continuously every 15 minutes for a period of 3 days.



Fig. 4 The houses in experiment.



SGW (H1) CBW (H2)

Fig. 5 Detector positions at outside and inside house models.

The Installation of a thermal detector, measuring range 0-80 °C, accuracy ±0.5 °C, on the surface of the outer and inner walls. The center point of the chimney and the test house is 1.00 m. from the floor as shown in Figure 5. Temperature data was collected through the Micro Controller Arduino every 15 minutes into the Micro SD Card. Solar Intensity Meter Model EKO ML-01 Pyranometer (Measurement range 0-2000 W/m^2, tolerance ±3.07%) Record data in Heat Flow Logger HIOKI LR8432-20.

RESULT AND DISCUSSION

Room Temperature

Figure 6 show the temperature variation in house model (H1), It can be seen that the temperature on the surface of SGW always the highest at 15.00 in 3 days of experimental, while the room temperature (Troom1) were higher than outside during day, At night all the temperature positions on the inside house model are similar to outside temperature. And on the cloudy sky conditions day on 1, Oct It's can be seen that the gap temperature between each sensor are low but still higher than outside temperature.

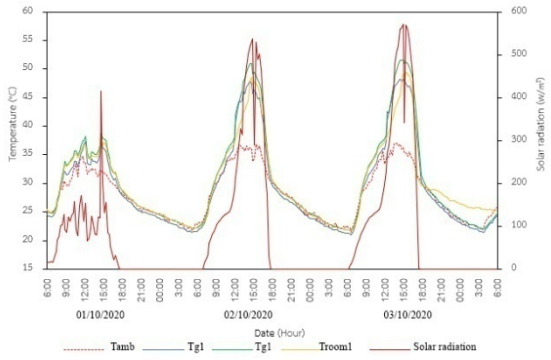


Fig. 6 Temperature variations in house model (H1).

Figure 7 show the temperature variation in house model (H2), It can be seen that the temperature on the inside surface of CBW(Tc2) had the highest temperature on clear sky conditions day(2-3,Oct) due to heat accumulation on the material, while air gap temperature was higher than Tamb and Troom2 on clear sky conditions day due to the working principal of solar chimney, and all the temperature positions were always higher than outside temperature during day and similar at night, On the cloudy sky conditions day(1, Oct) It's can be seen that the CBW performance are lower than other day with clear sky conditions.

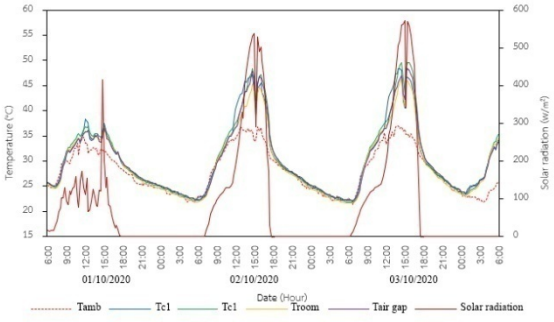


Fig. 7 Temperature variations in house model (H2).

Figure 8 show the comparison of room temperature variations in house model, It can be seen that the room temperature of SGW (Troom1) was always higher than room 1 temperature of CBW (Troom2) during 3 days, the gap temperature between two house model were highest during 15.00 because of the heat accumulation in the afternoon affect to solar chimney performance

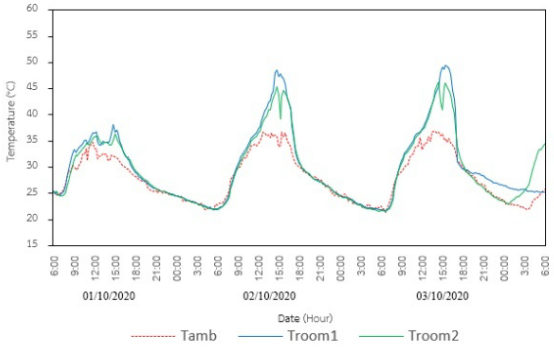


Fig. 8 The comparison of room temperature variations in house model.

Figure 9 show the comparison of surface temperature of SGW and CBW both inside (SGW; Tg3, Tg4 and CBW; Tc3, Tc4) and outside surface (SGW; Tg1 and CBW; Tc1) on 3 October 2020 it can be seen that the highest temperature is Tg4 that is located on the inside surface that affect by the sunlight and heat accumulation in the evening period while in the same located on CBW surface (Tc4) is lower by 2 °C, The lowest temperature is Tc1 that is located on the outside surface of CBW due to the outside air flow while the temperature at the same located on SGW surface (Tg1) is higher by only 0.1 °C

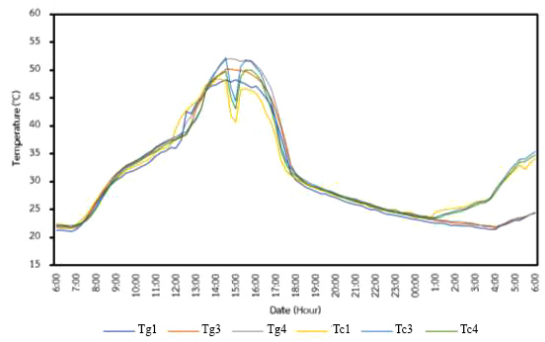


Fig. 9 The comparison of surface temperature of SGW and CBW on 03/10/2020.

Figure 10 show the comparison between room temperature (Troom1, Troom2) and CBW air gab temperature(Tair gab) it can be seen that Temperature of CBW including Tair gab and Troom2 is always lower than Troom1 due to the air flow ventilation of the chimney while Tair gab has the nearest temperature to Troom1 on 48 °C and 49 °C at 15.00 and the different temperature between Tair gab and Troom2 is 3°C due to the accumulation inside the chimney.

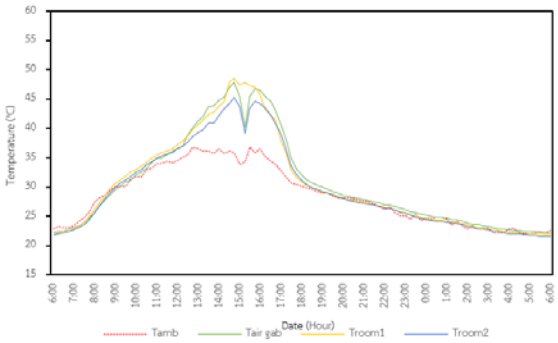


Fig. 10 The comparison of room temperature variations in house model and CBW air gab temperature.

Table 1 show all the temperature of testing and the average thermal in each house models at the outside and inside surface of material, room temperature, and CBW air gap temperature for a period of 3 days continuously, It can be seen that the highest average temperature was on the inside of single glass widow surface while the SGW average room temperature was higher than CBW at 2.9 °C

CONCLUSION

The experimental results were presented the thermal performance of single glass window (SGW) and clear block wall (CBW). The room temperature of CBW was always lower than SGW, It can be confirm that CBW can be prevent the heat accumulation inside the house model in term of solar chimney performance, obviously, the CBW provided well performance during 14.00-17.00 while still allow the natural light into the space room

Table 1 The summay of measure temperatures.

Outside / Inside	Temp. (°C)		Date			Temp. (°C)
	Min/Max		1	2	3	Avg. (°C)
Tamb	Min		21.6	22.2	21.5	21.6
	Max		34.6	36.6	37.1	36.2
	Avg.		.272	.284	.280	27.9
SGW	T_{g1}	Min	21.5	21.3	21.0	21.1
		Max	37.3	47.5	48.2	44.3
		Avg.	.275	30	.302	.291
	T_{g2}	Min	22.1	21.5	21.7	21.9
		Max	38.8	51.1	51.5	47.1
		Avg.	.287	.312	31.3	.304
	T_{g3}	Min	21.8	21.7	21.6	21.6
		Max	38.4	49.5	50.1	45.8
		Avg.	.284	30.7	.307	30.1
	T_{g4}	Min	22.1	22.0	21.8	21.8
		Max	38.8	50.2	52.1	47.1
		Avg.	.287	31	.311	.303
	T_{room1}	Min	22.1	21.9	21.9	21.8
		Max	38.1	48.5	49.5	45.4
		Avg.	28.4	30.3	31.3	30.1
CBW	T_{c1}	Min	22.7	22.3	22.1	22.3
		Max	38.4	47.1	48.7	44.4
		Avg.	.286	30.7	.314	.303
	T_{c2}	Min	22.2	21.9	21.9	21.8
		Max	37.1	48.4	49.7	45.1
		Avg.	.288	30.6	.318	.302
	T_{c3}	Min	22.1	21.1	22.1	21.6
		Max	38.2	50.2	51.3	46.4
		Avg.	.288	.308	32.1	.305
	T_{c4}	Min	22.2	21.8	21.7	21.8
		Max	37.7	48.2	50.1	45.4
		Avg.	28.7	30.7	.315	.301
	T_{room2}	Min	21.8	21.8	21.5	21.5
		Max	36.4	45.5	46.4	42.7
		Avg.	28.1	29.6	30.6	29.6
	$T_{air\ gap}$	Min	22.2	22.1	22.2	22.3
		Max	36.3	47.8	48.2	44.3
		Avg.	28.4	30.4	.312	.302

ACKNOWLEDGMENT

The authors are grateful to the Faculty of Architecture and Design, and the King Mongkut's University of Technology North Bangkok (KMUTNB) for the experimental equipment to do the research work.

REFERENCES

[1] Randazzo, T., De Cian, E., Mistry, M.N. (2020). Air conditioning and electricity expenditure: The role of climate in temperate countries. Journal: Economic Modeling, Vol.90, 273-287. https://doi.org/10.1016/j.econmod.2020.05.001.

[2] Sharda, A., Kumar, S. (2009) Heat Transfer Through Windows: a Review, International Conference on Advances in Mechanical Engineering, August 3-5, National Institute of Technology, Surat-395 007, Gujarat India, 1-25.

[3] Chingchai Pongsatirat. (2000). Experimental Performance of a Partially-Glazed Solar Chimney Wall. Master of Engineering, KMUTT from https://www.thaiscience.info/Article%20for%20ThaiScience/Article/3/10013668.pdf.

[4] Chantawong, P., Hirunlabh, J., Zeghmati, B., Khedari, J., Teekasup S., Win M.M., Investigation on thermal performance of glazed solar chimney walls, Solar Energy Vol.80, Issue 3, 288-297.

[5] Suntontam, T., Damrongsak, D., and Vorayos N. (2008). Design of Trombe Wall using Concrete Block. Engineering Journal Chiang Mai University, 15(1), 25-34. https://www.thaiscience.info/Journals/Article/EJCM/10343641.pdf

7th Int. Conf. on Structure, Engineering & Environment (SEE), Pattaya, Thailand, Nov.10-12, 2021, ISBN: 978-4-909106070 C3051

CONSOLIDATION OF INTERNATIONAL MARINE CONTAINER TERMINAL PORTS IN TOKYO BAY USING A MEGAFLOAT: A PROPOSAL

Shinji Sato[1] and Yusuke Miyajima[2]

[1]Department of Oceanic Architecture and Engineering, College of Science and Technology, Nihon University, Japan; [2]Plantec Architects, Inc., Japan

ABSTRACT

Currently, ports and harbors around the world are being upgraded to accommodate large ships, large quays with great water depths, and logistics facilities integrated with ports and harbors for efficient international logistics. In Japan, approximately 950,000 tons of cargo are imported and exported yearly, and more than 99.7% of them are transported by sea. Therefore, developing, maintaining, and upgrading ports and harbors are necessary to quickly respond to changes in their surrounding environment. Tokyo Bay, where the Port of Tokyo (the main gateway to Japan) is located, has the geographical problems of a narrow entrance and extremely shallow water. This plan provides a solution to a next-generation port logistics hub using a megafloat. A megafloat is a large rectangular floating body constructed by connecting steel cuboid floating blocks to each other. This floating body block has a hull (shell) structure similar to that of a vessel. It is constructed at a shipyard, towed by a ship on the sea, and joined/connected at the sea area where it is needed. A megastructure can be constructed in a shorter time than that required for a vessel. To solve the abovementioned problems of the Japanese ports, we propose to consolidate the container ports in Tokyo Bay at a single location and build a floating port that can accommodate large container ships.

Keywords: Logistics-type ports Mega floats Environmental impact of ships Ecological mixing Ports as tourism resources

INTRODUCTION

The ports located in Tokyo Bay are trading ports, which have supported Japan since the Meiji era to date. These ports played a significant role in import and export during the postwar high economic growth period as a doorway to Japan. In island nations such as Japan, ports are essential to maintain trade. Therefore, a perennial need to quickly resolve changes in the environmental surrounding of ports exists to overhaul, maintain, and update them.

Japan's position in international logistics continues to fall, and an urgent need exists to enlarge the ports to maintain the industries in Japan. However, the ports in Tokyo Bay have the following three major problems.

First, the development of ports (e.g., dredging concerning ports and overhauling routes) in Japan is regulated by Port and Harbor Act. However, a port is managed by the local authority where the port is located, and the local government with a limited budget cannot implement a large-scale overhaul. At Tokyo Bay, six ports are present, i.e., Tokyo, Kawasaki, Yokohama, Yokosuka, Chiba, and Kisarazu, even when only the major ports are counted.

The geographical characteristics of Tokyo Bay are as follows: urban areas press its hinterland, and the landscape hinders the expansion of the port sites.

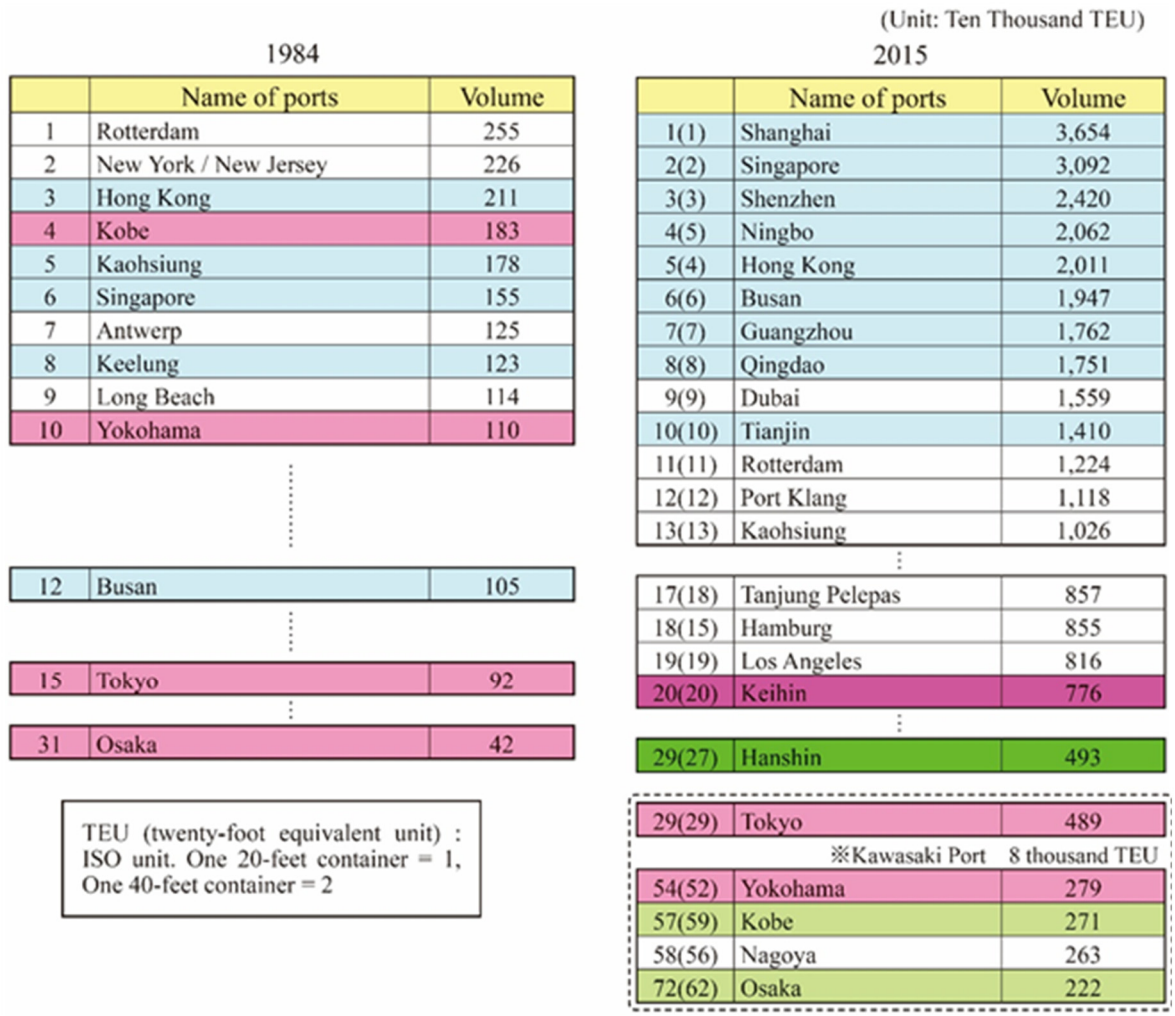
Recently, in areas surrounding a port, which have traditionally been used for industrial applications, waterfronts have been reevaluated as a place for citizen's entertainment and marine recreation. However, in the port area, a berth portion engaging mainly in freight transportation and a public space close to water are intricately entwined and are not utilized effectively.

The current proposed plan is in conjunction with the ongoing Tokyo Wanko-Road project [1] at the mouth of Tokyo Bay with a long-term perspective to solve the abovementioned challenges faced by the Japanese ports. The plan is to consolidate the container ports in Tokyo Bay to enable them accommodate containerships ever increasing in size.

BACKGROUND OF THE PLAN

Japan in the International Logistics

Container volumes are increasing worldwide, including in Japan. However, Japan's ranking based on container numbers is falling considerably. The Kobe Port, which was ever proud at the fourth place in the world, is now at the 57th place, and the Tokyo, Kawasaki, and Yokohama ports combined (so called the Keihin Port) are ranked 20th. The position of Japan in international logistics is relatively declining. Moreover, ports located in the Asian countries rank



	Name of ports	Volume
1	Rotterdam	255
2	New York / New Jersey	226
3	Hong Kong	211
4	Kobe	183
5	Kaohsiung	178
6	Singapore	155
7	Antwerp	125
8	Keelung	123
9	Long Beach	114
10	Yokohama	110
12	Busan	105
15	Tokyo	92
31	Osaka	42

	Name of ports	Volume
1(1)	Shanghai	3,654
2(2)	Singapore	3,092
3(3)	Shenzhen	2,420
4(5)	Ningbo	2,062
5(4)	Hong Kong	2,011
6(6)	Busan	1,947
7(7)	Guangzhou	1,762
8(8)	Qingdao	1,751
9(9)	Dubai	1,559
10(10)	Tianjin	1,410
11(11)	Rotterdam	1,224
12(12)	Port Klang	1,118
13(13)	Kaohsiung	1,026
17(18)	Tanjung Pelepas	857
18(15)	Hamburg	855
19(19)	Los Angeles	816
20(20)	Keihin	776
29(27)	Hanshin	493
29(29)	Tokyo	489
54(52)	Yokohama	279
57(59)	Kobe	271
58(56)	Nagoya	263
72(62)	Osaka	222

Fig. 1 Ranking of container volumes by the port worldwide [2].

high (Fig. 1). Japan currently lags behind the Asian countries considering the preparation of ports and is losing international competitiveness.

Upsizing of Vessels and Preparedness of Quays in Japan

The forms of vessels have evolved. Recently, in particular, vessels have been upsized. For example, containerships with a total length of 400 m and a beam of 59 m having the container-loading capacity of more than 18,000 twenty-foot equivalent units (TEU) have been put into service.

When the status of the preparation of quays for vessels with deep drafts in the Japanese and worldwide ports are compared, Japanese ports lag in both scale and preparedness.

Topography of Tokyo Bay and Current Conditions of the Container Ports

In Tokyo Bay, six ports (Tokyo, Yokohama, Kawasaki, Yokosuka, Chiba, and Kisarazu) are scattered in a narrow area. Among them, Tokyo, Yokohama, and Kawasaki ports combined are called the strategic international container port (so called the Keiyo Port). As such, many ports are crowded in Tokyo Bay, and approximately 500 vessels currently come in and go out of the ports in a day, even when only containerships are counted.

Moreover, considering its geography, the mouth of Tokyo Bay open to the Pacific Ocean is narrow, and many shallow spots, rock reefs, sunken rocks, and abandoned batteries are present inside the gulf. Therefore, two routes, i.e., Uraga-suido and Nakanose, are set up in Tokyo Bay. They are one of the well-known maritime transportation congestion areas. Furthermore, a mandatory pilotage system is established in the bay, and many port districts require pilots, thereby making the ports in Tokyo Bay inferior to ports in other countries regarding effectiveness and convenience. Therefore, traffic congestion always exists on the sea among vessels awaiting arrival to the ports.

Issues in the Logistics Network of Japan

Freights, such as container cargos unloaded at a

port, are sent to various destinations using ground transportation. At this time, the effect of delay due to traffic congestion should be considered. Most of the container cargos unloaded at the Tokyo and Yokohama ports are transported using trucks and mainly go through the areas around Tokyo and Kanagawa, which are prone to traffic congestion. Therefore, it is hard to say that there is an efficient logistics network prepared. When this congestion is compared domestically, the lost time due to traffic congestion in Tokyo is considerably high, approximately 1.6 times than the national average (Fig.2).

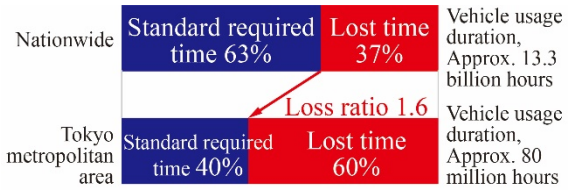


Fig. 2 Lost time for traffic congestion [3]
(The lost time expresses by nature the time lost in traffic congestion, and an increase in the lost time not only obstruct economic activities but also increase the release of greenhouse gases, such as carbon dioxide and nitrogen oxide.)

Issues of Traffic Congestion and Working Environment Due to Waiting Time for Cargo

With the increase in the number of containers, traffic congestion on neighboring roads has worsened. On the site, a line of trucks waiting for container loading has become common, and the on-duty hours of truck drivers have increased (Fig. 3).

This waiting time is a major issue in the logistics industry as it affects not only traffic congestion but also the working environment, and eventually, the global environment.

On-Port Logistics Hub

Moreover, at container terminals, the volume of container cargo has increased due to the upsizing of vessels, and congestion in the terminal has become an issue. Thus, there is a need to construct an effective transportation network to transport goods to the consumption area by performing devanning, processing for logistics, and inventory management in a location close to the container terminal.

POLICY OF THE PLAN

Consolidation of Container Terminals in the Tokyo Bay

To solve these issues and focus on more effective ports, we propose the following.

First, the container terminals at Tokyo, Yokohama, and Kawasaki ports in Tokyo Bay should be consolidated. A container port that can receive more containers should be constructed to consolidate containers received in three ports and enhance international competitiveness. Thus, various problems of the ports and logistics can be resolved, and environmental issues, such as traffic, inside Tokyo Bay and Tokyo metropolitan area can be improved [4], [5].

Reorganization of Logistics Network by Logistics-Type Port

To develop a logistics-type port in Japan, the traffic condition and its hinterland should be considered. It should be connected to the Metropolitan Inter-City Expressway (hereinafter Ken-O Expressway), around which the construction of factories and logistics facilities has increased

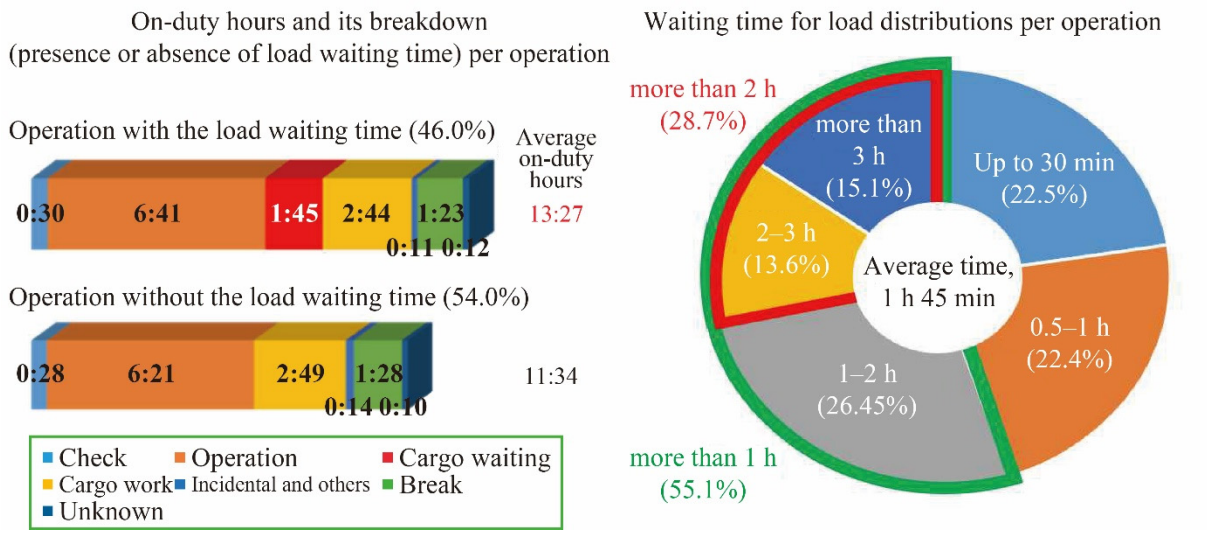


Fig. 3 Current conditions of on-duty hours and load waiting per one operation [2].

recently as development progresses, to form a more effective logistics network. By connecting the port directly to Ken-O Expressway, traffic congestion in the downtown area can be resolved, and an effective logistics network can be formed. Therefore, if Ken-O Expressway is opened, forming an effective logistics network in the whole Kanto zone may become possible in cooperation with factories and distribution bases located in Saitama Prefecture in the northern part of the Ken-O Expressway. To this end, constructing the "Tokyo Baymouth Road" proposed between the Miura Peninsula and Cape Futtsu is essential. The proposed route is at the entrance of Tokyo Bay, and it crosses over the Uraga-suido Route, which has the most ship traffic with a suspension bridge. By connecting the Ken-O Expressway, which encircles Tokyo Bay in a circle, and the Tokyo Bay Aqualine Link Road (hereafter, Aqualine) in the center of the Ken-O Expressway, made it possible to form Tokyo Bay ring road network that circles Tokyo Bay in a figure of eight (Fig. 4).

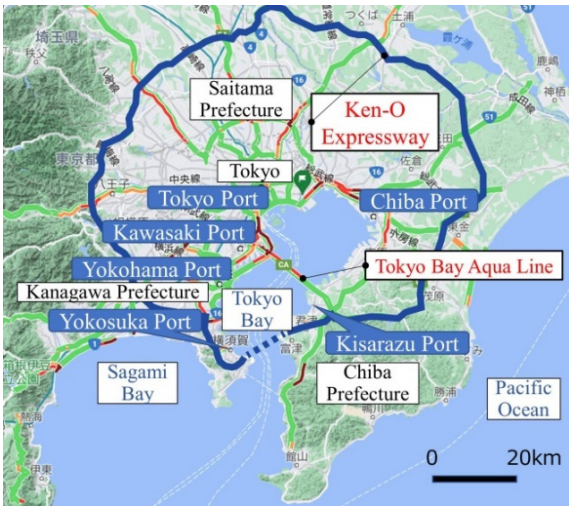


Fig. 4 Relationship between Tokyo Bay and ports in the gulf and Ken-O Expressway [6].

Port Plan as the Outpost for Festivity

Thus, this plan would open the areas occupied by warehouses and terminals to revitalize them as places for waterfront festivity. We should open the areas to public while utilizing the characteristics of the ports and also expect that they become tourist complex areas that can accommodate the rapidly increasing foreign visitors to Japan.

The summary of the abovementioned concept is as follows:

i. Response to the upsizing of the vessel: Possible to accept containerships with 18 m or more draft.
ii. Reducing the number of arrivals to the ports in the bay: By relocating and consolidating the ports near the entrance of Tokyo Bay, the number of ships entering the bay is reduced.
iii. Moderating traffic congestion in the metropolitan area: Consolidate the terminals next to the congested areas to reduce the number of trucks in the metropolitan area.
iv. Opening the waterfront: Consolidate the container ports and open the warehouses and terminals along the coastal line to public.

BASIC PLAN

This plan provides a solution to a next-generation port logistics hub using a megafloat. A megafloat is a large rectangular floating body constructed by connecting steel cuboid floating blocks to each other. This floating body block has a hull (shell) structure similar to that of a vessel. It is constructed at a shipyard, towed by a ship on the sea, and joined/connected at the sea area where it is needed. A megastructure can be constructed in a shorter time than that required for a vessel [7], [8].

Selection of Sea Area

Based on the background and policy of the plan, we propose the following plan: (1) the area where the water depth is 18 m or more and where large vessels can enter easily; (2) the area where the connection with the Ken-O Expressway is easy, and it can access a wider area; (3) the area where it can be accessed without going along the complicated routes in Tokyo Bay and entering deep into the gulf can be avoided.

Based on these conditions, it would be appropriate to install the megafloat in the sea area that connects Yokosuka, Kanagawa, Futtsu, and Chiba located on the boundary line between the inner and outside Tokyo Bay.

Tokyo Wanko-Road

To connect Ken-O Expressway at the Chiba and Kanagawa sides, it must pass through the Metropolitan Expressway Bayshore route and Aqua Line. Moreover, as the surrounding sea is a good fishing ground, the outflow of sediment due to reclamation work should be avoided. Thus, road planning with bridges is appropriate to maintain ecosystems in Tokyo Bay. A plan exists to link Futtsu, Chiba, Yokosuka, and Kanagawa in the sea area through an expressway and a bridge called the Tokyo Baymouth Road. Elaborating the plan, including the plan of the Baymouth Road bridge, forming a more effective logistics network becomes possible (Fig. 5).

Scale of the Plan

Considering the scale, the number of berths to be moored is calculated based on the container volumes at the ports in the Asian countries and Keihin Port.

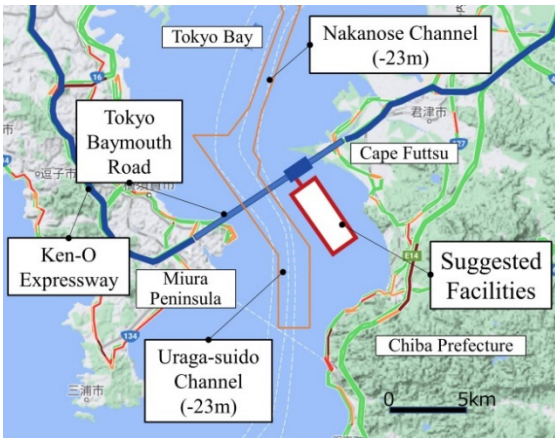


Fig. 5 Location of the proposed facilities on the Tokyo Wanko-Road.

The Port of Busan in South Korea has 23 quay berths with water depths of 16 meters or more, and its annual container volume is about 2.6 times of Keihin Port [3]. Based on this, the plan is to install 10 berths with a depth of 18 m or more at the following three areas (*Port area*, *Logistics area, Sightseeing complex area*) under the current conditions with the view of future expansion. Furthermore, assuming the flowing in and out of the seawater due to the tide, as it is located at the bay mouth, a dolphin method is adopted as the mooring method for the megafloat (Fig. 6).

Port area

The port area is the area receiving the containerships and where container berths, landing areas, and seaport warehouses are installed. The proposed plan meets the specifications defined by the Ministry of Land, Infrastructure, Transport, and Tourism in the superhub port project (three continuous berths, each measuring 1,000 m or more in length and 500 m or more in depth with an integral extension).

Logistics area

The logistics area is the area that supports the distribution ability and efficiency of the container terminal as a hinterland. In Tokyo Bay, trucks waiting for freights cause traffic congestion. This plan proposes enough parking lots in cooperation with the adjacent sightseeing complex area to minimize the effect of waiting for freights.

Sightseeing complex area

The plan includes a sightseeing complex area that utilizes the characteristics of both a waterfront area and a port. It serves as a venue for festivity without minding the noise, tourist facilities surrounding the sea, and a function as a commercial facility for exhibition and sales (because various products come and go at the port).

CONSTRUCTION PLAN FOR THE SIGHTSEEING COMPLEX AREA

Functions to be Introduced

In the logistics port, attaching the sightseeing complex area for the indigenes and tourists and enhancing the distribution function are also essential. This is to improve the availability of the Baymouth road away from the downtown area by utilizing holidays other than business days. Because it is located on the road connecting the Ken-O Expressway, the following functions are introduced

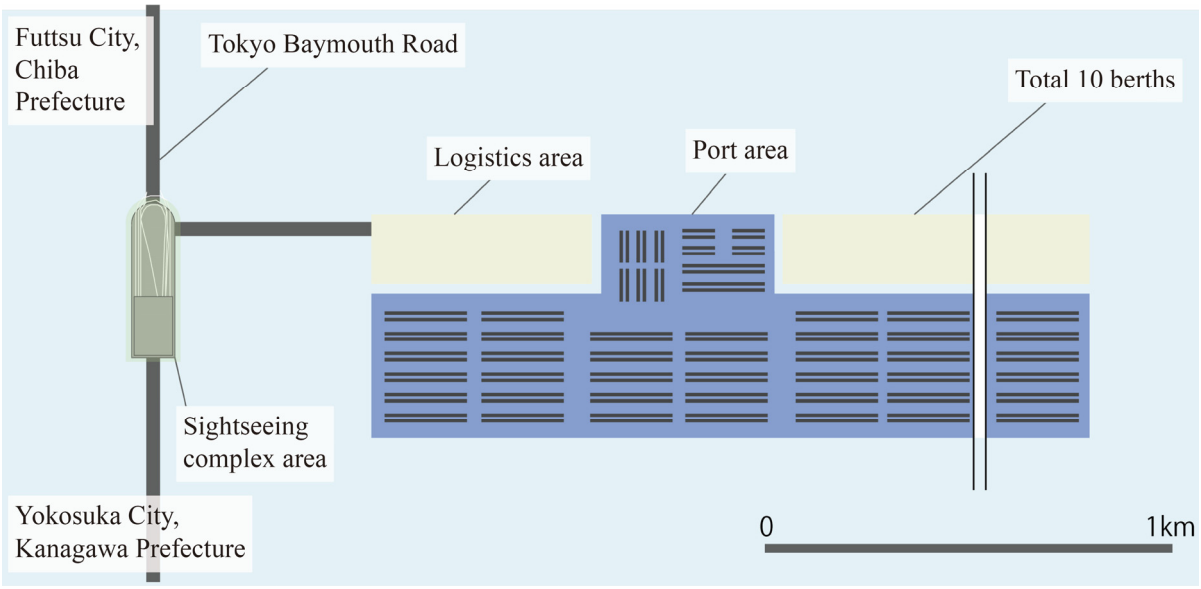


Fig. 6 Layout of each area.

to the sightseeing complex: (1) a lodging function as the base of sightseeing; (2) a parking area function; (3) an entertainment function, including a large-scale event venue; and (4) an exhibition/commerce function to utilize the characteristics of the ports where various goods come in and go out.

CONCLUSIONS

To solve the problem of seaports in Japan, we propose the following:

i. To control ships that enter and leave Tokyo Bay and create a safe port. The ships coming in and going out of Tokyo Bay include energy-carrying vessels (such as oil and LPG tankers), cargo vessels, passenger boats, warships, and pleasure boats. Among them, cargo vessels account for 42% of the traffic, and if their traffic inside the bay can be reduced considerably by preventing them from entering the bay, it would improve safety.
ii. To construct a port that can reduce greenhouse gas emissions. To enter each port in Tokyo Bay, carefully navigating through the narrow Uraga-suido Channel and introducing the pilot's guidance are necessary. Going through these complicated procedures cause wasteful consumption of fuels, temporal loss, and could lead to accidents. In particular, the inefficient consumption of ship fuels directly increases greenhouse gases. This proposed plan can reduce the emission of such gases.
iii. To construct a port that considers the response to the change in water quality due to the ballast water from cargo ships. Recently, issues related to the ballast water from cargo ships have attracted worldwide attention. Such issues include the release of hull drawn in other countries at the port, which moves and mixes organisms from different ecosystems. By transshipping freights at the bay mouth, the mixing of seawater in the gulf can be reduced.
iv. To make the port responsive to disasters, such as earthquakes. In constructing the megafloat, making sufficient calculations under high surf conditions is necessary. As the proposed site is located in an area with a water depth of 15–20 m at the bay mouth, it is hardly affected by an earthquake, and the long and big body absorbs long period waves as well. Moreover, the proposed megafloat would be installed at the bay mouth. Thus, external forces can easily escape as the structure is away from the shore. Therefore, it can withstand tsunamis.
v. To construct a port that would position Tokyo as an attractive resort town of the 21st century. Tokyo Bay used to be a sea with abundant fisheries, which are materials for sushi called "Edo style." Without blocking the bay mouth with reclamation to allow seawater to come in and go out naturally, Tokyo Bay can enhance rich fisheries.

REFERENCES

[1] The Chiba Bank. Ltd., Traffic Infrastructure Expansion in the Tokyo Area and a Survey of Regional Revitalization, 2000, 10, pp. 126. https://www.crinet.co.jp/economy/pdf/20201020.pdf.
[2] Ministry of Land, Infrastructure, Transport and Tourism, Current Situation Surrounding Distribution, 2016, https://www.mlit.go.jp/common/001173035.pdf.
[3] Ministry of Land, Infrastructure, Transport and Tourism, Policy on International Strategic Container Port, 2016, https://www.mlit.go.jp/common/001125138.pdf.
[4] Takizawa H., Takechi S., and Akimoto H., Selection and Evaluation of Network and Hub Ports for International Container Transportation Around Japan. Journal of the Japan Society of Naval Architects and Ocean Engineers, Vol.11, 2010, pp. 173-179.
[5] Domae K. and Matsumoto H., Current Conditions of the Ports in Japanese and Discussion Regarding the Development Thereof – Consolidation or Dispersion for International Container Distribution Function. Viewpoint to the East Asia, Vol. 27, Issue. 1, 2016, pp. 50-71.
[6] Central Nippon Expressway, Kanto Regional Development Bureau, Ministry of Land, Infrastructure, Transport and Tourism, Route 468, Metropolitan area center accessway (from Ebina to Atsugi), 2011, https://www.ktr.mlit.go.jp/ktr_content/content/000042945.pdf.
[7] Sato C., Principal Characteristic of Mega-Float and It's Structure Planning Flow. Journal of the Japan Welding Society, Vol. 69, Issue.4, 2000, pp. 304-308.
[8] Yamashita Y. and Kinoshita Y., Accuracy Management of Very Large Floating Structures. Preprint of the National Meeting of Japan Welding Society, Vol. 67, 2000, pp. F-40-F-45.

7th Int. Conf. on Structure, Engineering & Environment (SEE), Pattaya, Thailand, Nov.10-12, 2021, ISBN: 978-4-909106070 C3051

EVALUATING RESOURCE EFFICIENCY FOR PRINTED CIRCUIT BOARD WASTE SORTING AND TRANSFER PLANT USING MATERIAL FLOW COST ACCOUNTING

Supanisara Wanwong[1,2], Suphaphat Kwonpongsagoon[1,2] and Kanokwan Kingphadung[3]

[1]Department of Sanitary Engineering, Faculty of Public Health, Mahidol University, Thailand;
[2]Center of Excellence on Environmental Health and Toxicology (EHT), Thailand;
[3]Department of Food Technology, Faculty of Engineering and Industrial Technology, Silpakorn University, Thailand

ABSTRACT

The aim of this paper was to evaluate the resource efficiency of a printed circuit board waste (PCBW) sorting and transfer plant by identifying quantities of production loss and theirs associated true costs using the Material Flow Cost Accounting (MFCA) technique. The results of this study are based on data gathered in 2019. The 5 types of waste material input transferred directly to the production system are, namely wastewater sludge, PCB border, PCB scrap, drilling PCB and punching PCB powder. The findings showed that a positive and negative product cost were identified as 94% and 6% of the total cost, respectively. The greatest portion of the negative product cost resulting from system cost (SC) was 50% of the negative product cost or 3% of the total cost. Punching PCB waste was found to be the highest loss cost, about 54%. Regarding waste management loss cost (WC), all costs of waste handling and disposal were attributable to two material losses, namely punching PCB residue and PCB scrap. Based on the overall results of this study, the resource efficiency of the PCBW sorting and transfer plant in terms of the ratio of the recoverable precious metal – copper (Cu) could be quantified as 0.94 which was in accordance with the positive product cost of MFCA technique.

Keywords: MFCA, PCB waste, Sorting and transfer, Resource, Efficiency

INTRODUCTION

Electronic waste (e-waste) or waste from electrical and electronic equipment (WEEE) is one of the fastest-growing waste streams in the world both in terms of volume and growth rate. In 2016, the report of global e-waste monitor stated that one Thai citizen produces 7.4 kg of e-waste per year and increased to 9.2 kg per year in 2019, making Thailand the fourth largest e-waste generator among ASEAN countries [1], [2]. In addition to domestic generation, it has been reported that Thailand received imports of various kinds of electronic waste scraps from other developed countries, e.g., the US, China, Japan, Belgium, France, and the UK, around 64,437 tons in 2017 and 52,221 tons during the first half of 2018 [3]. As a result, the increasing volume of the e-waste has become a serious concern in this country.

Printed circuit board (PCB) waste is an essential component of all electrical and electronic equipment (EEE), used to connect electronic devices on the circuit board, making the devices connected and able to work as designed. About 3% by weight of the WEEE are printed circuit board (PCB) consisting of around 30% metals and 70% non-metallic materials [4]-[6]. In general, the major economic driving force for recycling printed circuit board waste (PCBW) is the high value of metallic materials, i.e., gold (Au), palladium (Pd), silver (Ag) and copper (Cu). In Thailand, only copper is feasibly recovered from wastes of PCB production and post-consumer waste PCB [7].

According to Thailand's 20 years' national strategy, the government has set a national goal to handle and reduce all waste types properly by 2037 [8], which makes the recycling business serve an important role. In 2018, a total of 3,102 recycling businesses were newly registered, with a tendency to continually rise, and around 57% (or 1,761 factories) were e-waste recycling businesses [9], [10]. Among these e-waste recyclers, about 70% were registered as waste collectors and transporters, which were classified as Factory type 105, and the rest were e-waste recyclers, classified as Factory type 106 – both factory types prescribed in the Thailand Ministerial Regulation No.2 B.E. 2535 (1992) issued pursuant to the Factory Act B.E. 2535 (1992). In addition, Krung Thai Bank Research Center [11] reported that the overall recycling market increased around 5.7% yearly or 1.2% of the total GDP, with a value of 1.7 billion Thai baht (THB) in 2019, and estimated to be 2.24 billion THB in 2024. It appears that the increasing trend of recycling businesses generally corresponds to the high waste generation of the country.

Material flow cost accounting (MFCA) (ISO standard 14051) is one of the environmental management tools, developed in Germany in the late

1990s and widely applied in the domestic industry of Japan by the Asian Productivity Organization (APO). MFCA is helpful in increasing the transparency of the material flow of production processes, which is a key to successful problem solving and industrial process improvement. The MFCA technique can identify quantities of production loss in physical units and identify quantities of true costs associated with production loss in monetary units [12]. By focusing on both the costs of products and the costs associated with materials losses, the ultimate purpose of MFCA is beneficial to identify opportunities to reduce materials use and losses, to improve the efficiency of materials and energy use, and to reduce adverse environmental impacts [13]. To date, MFCA has been widely applied in an extensive variety of industries including food, automotive, metal, chemicals and textile industries [14]-[24]. Among these MFCA applications, the method has also been extended to combine other techniques such as Lean, life cycle assessment and costing (LCA/LCC), enterprise resource planning systems and cause-effect diagram [14], [15], [20], [23].

Therefore, this study constitutes the first time to evaluate resource efficiency of an e-waste recycling business in Thailand, focusing on a printed circuit board waste sorting and transfer plant by applying the Material Flow Cost Accounting (MFCA) technique. Ultimately, the results will highlight improvable hotspots where waste management costs and inefficiency of processes occur and imply reduced environmental impacts (air pollution, water pollution, health problems etc.).

METHOD

System Boundary and Data Collection

The study was conducted in a small to medium sized (SME) printed circuit board waste (PCBW) sorting and transfer plant located in Suphanburi Province, Thailand. The plant is classified as Factory type 105, a factory engaged in businesses related to sorting and/ or landfill facility for wastes with characteristics and qualifications as prescribed in Thailand Ministerial Regulation no. 2 B.E. 2535 (1992) issued under the regulations in the Factory Act B.E. 2535 (1992). As can be seen in Fig. 1, the system boundary starts by transporting various waste types to the plant, followed by waste receiving, checking, sorting, sun drying, packing process, and transporting waste products out to another recycling plant. It covered seven activities/processes of the PCBW sorting and transfer plant, including transportation.

The data used in this study were primary data collected from the plant, representing a one-year period, in 2019. These collected data included inputs, outputs, and cost information, for example, amount of waste received, other materials/energy/fuel used, waste rejected, and costs associated with various processes across the target plant as described in Fig. 1.

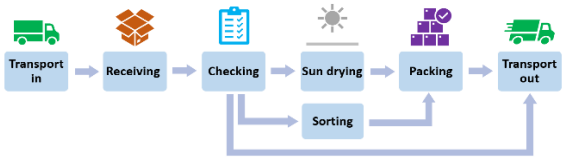


Fig. 1 System boundary of the study

Creation of Material and Copper Flow Model

According to the MFCA, a flow diagram of production process or material was firstly created, showing input material, product and waste of each subprocess and the entire process of the system boundary. Concerning the PCBW plant in this study, attention was drawn to the high value substances embedded in waste PCBs. As mentioned above, because Cu is one of the substances that is feasible to recover in the next stage of the recycling facility, the model of Cu flow was then created here along with the material flow model. The flow diagrams can trace all input materials and substance (Cu) that flowed through production processes and measure products and material/substance loss (waste) in kg.

The physical flow results for both material and Cu are based on the law of mass conservation. It could be explained that the mass of a material or substance never changes. Thus, all input materials and substances (Cu) equal the amount of output products (positive products) added to that of generated waste (negative products). The equation represents the identification of material/substance balance and measures products and material/substance loss (waste) in physical units using the following Eq. (1):

$$\frac{dMar(i)}{dt} = \sum(inputs) - \sum(outputs) \quad (1)$$

where Mar(i) = mass changed with respect to time (one year in this study).

Each material or substance (Cu) that goes in and out of the production process flow should be balanced. Thus, the target product in the MFCA analysis, the material/substance input and output need to be confirmed while comparing the quantities of material inputs to outputs and to identify any data gaps. The missing materials/substances or other data gaps could lead to identifying missing points resulting in areas of improvement [12].

Calculation of MFCA-Based Costs

The material balance of inputs and outputs obtained from the material model in physical units (or

weight) is linked to monetary units, by allocating costs to all products and material losses. The costs are measured in Thai Baht (THB). Under MFCA, four types of costs are generally considered quantifiable, namely, material costs, (MC) energy costs (EC), system costs (SC) and waste management costs (WC). Details of each cost analyzed in this study are defined as described below.

- Material cost: costs for raw materials and subsidiary materials, e.g., packaging, canvas
- Energy cost: costs for energy sources such as electricity and automotive fuel (for trucks and forklifts)
- System cost: costs incurred by labor and transportation
- Waste management cost: costs for handling material losses

RESULTS AND DISCUSSION

Material and Copper Flows

In 2019, the five input materials of waste PCB collected and transported to the PCBW sorting and transfer plant included wastewater sludge, PCB border, PCB scrap, drilling PCB powder, and punching PCB powder. Each type of waste has different characteristics and properties as follows: wastewater sludge is a sludge with an initial moisture content of 59% (wet weight basis) obtained from the wastewater treatment plant of PCB manufacture where wastewater generated from the cleaning process of drilled holes; PCB border and scrap are waste PCBs collected from the PCB cutting process; and drilling and punching PCB are PCB powder residues, generated from both drilling and punching processes. All five waste inputs contain different amounts of valuable metals, particularly Cu. It was estimated that the Cu content in drilling PCB residue, wastewater sludge (dry weight), and PCB border and scrap is around 30 to 40%, 10 to 30%, and 3 to 5%, respectively. For the punching PCB residue, too little Cu content was reported and infeasible to recover further, and is normally sent to another waste recycling plant for treatment. In 2019, PCBW input materials were picked up from different PCB manufacturing sources a total of 64 times, and transported to the PCBW sorting and transfer plant, while PCBW products were transported out from the PCBW sorting and transfer plant a total of 61 times to a recycling plant located in another province. The analyzed process of PCBW sorting and transfer plant can be separated in seven units: transporting in, receiving, checking, sun drying, sorting, packing and transporting out, as illustrated in Fig. 2.

In Fig. 2, all material flow results were estimated by excluding the amount of water in wastewater sludge. Based on the material flow model, total waste inputs (initial waste PCBs) transported to this plant was 694,363 kg yearly which ultimately yielded (positive products) 480,644 kg yearly or 69% of all waste inputs), and generated material loss (waste PCB or negative products) totaled 157,510 kg yearly or 23% of all waste inputs. As presented in Fig. 2, in terms of material flow, the results indicated that the highest material loss occurred during the receiving process (111,862 kg yearly), followed by sun drying, sorting and checking processes.

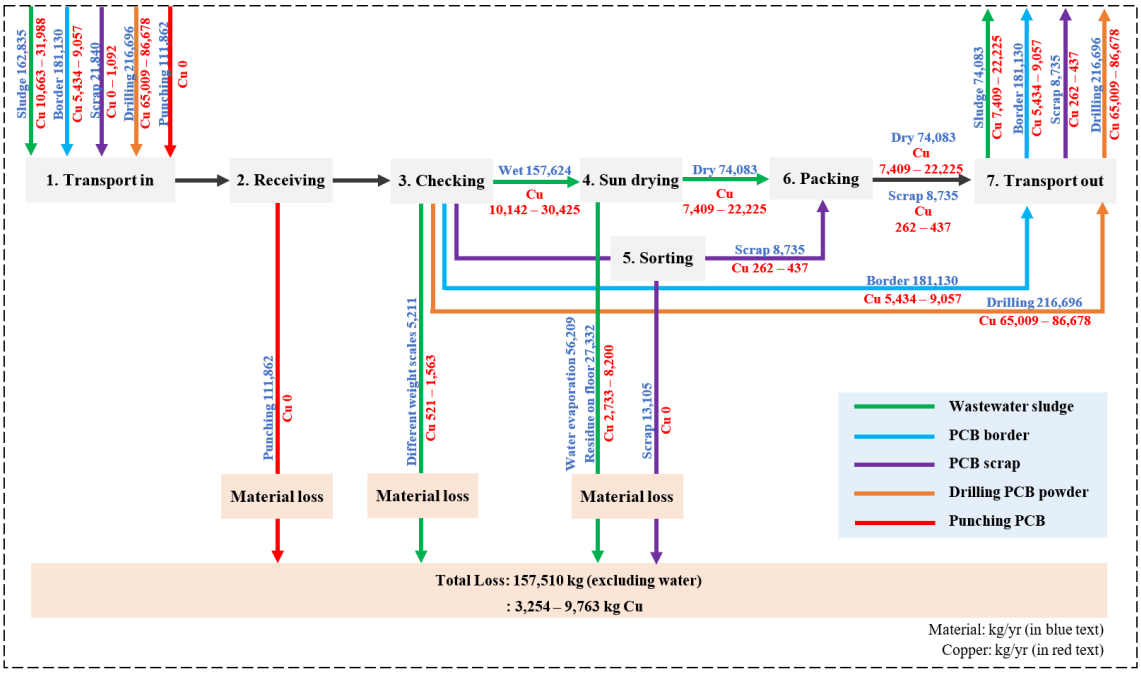


Fig. 2 Flow results of materials (in blue text) and copper (in red text) for a PCBW sorting and transfer plant in Thailand

Nevertheless, when considering the Cu flow model (see also Fig. 2) the total loss of Cu was 3,254 to 9,763 kg yearly depending on the Cu content from waste PCB inputs, with the highest Cu loss occurred during sun drying activity. Among those material losses, punching PCB powder was obviously identified as the most negative product, around 71% derived from the receiving process. Although Cu content was hardly found in punching PCB residues as mentioned above, the PCBW sorting and transfer plant had to handle and transfer this residue for further disposal as a complimentary waste because of the request by PCB manufacturers. The second and third material losses were wastewater sludge, which can be blown away to the air and left over on a concrete floor during and after open-air sun drying process, and PCB scraps from sorting activity about 17% and 8% of the total loss, respectively. The loss of these PCB scraps was about 60% of the initial scrap inputs and assumed to be Cu-free scraps. These scraps were separated out manually using simply invented sorting equipment. The last material loss was calculated based on the difference in weighting scales used between the waste generator (using a digital scale) and the PCBW sorting and transfer plant (using a mechanical or iron cast balance beam scale), around 3% of the total loss.

Concerning evaluating conventional resource efficiency of the PCBW sorting and transfer plant in terms of the ratio of material outputs to inputs, it could be estimated at 0.69 (excluding water). Regarding this estimation, the resource efficiency was not likely in this case and underestimated for the plant operation. In case of waste PCB, the prioritization of waste recovery focused on precious metals. Thus, the resource efficiency here should look at the ratio of the weight of the final precious metal – Cu embedded in the sorted PCB wastes (outputs) to the initial Cu contained in waste PCB inputs, rather than the conventional ratio of material outputs to inputs as reported above. Therefore, the resource efficiency of the PCBW sorting and transfer plant by considering Cu flow results (Fig. 2) could be quantified as high as 0.94 instead of 0.69.

TABLE 1 Material flow cost matrix for five PCB waste types

Cost type	Total Cost THB (%)	PCB waste type in THB (%)				
		Sludge	Border	Scrap	Drilling	Punching
Material Cost	**6,022,381 (77)**	**307,253 (4)**	**2,898,080 (37)**	**0 (0)**	**2,817,048 (36)**	**0 (0)**
Positive product	5,960,976 (76)	245,848 (3)	2,898,080 (37)	0 (0)	2,817,048 (36)	0 (0)
Negative product	61,405 (1)	61,405 (1)	0 (0)	0 (0)	0 (0)	0 (0)
System Cost	**1,052,322 (14)**	**282,619 (4)**	**174,219 (2)**	**270,858 (4)**	**174,658 (2)**	**149,968 (2)**
Positive product	823,683 (11)	245,012 (3.5)	174,219 (2)	197,051 (3)	174,658 (2)	32,743 (0.5)
Negative product	228,639 (3)	37,607 (0.5)	0 (0)	73,807 (1)	0 (0)	117,225 (1.5)
Energy Cost	**646,576 (8)**	**140,363 (2)**	**220,227 (3)**	**24,651 (0)**	**180,591 (2)**	**80,744 (1)**
Positive product	569,544 (7)	120,870 (2)	220,227 (3)	16,356 (0)	180,591 (2)	31,500 (0)
Negative product	77,032 (1)	19,493 (0)	0 (0)	8,295 (0)	0 (0)	49,244 (1)
Waste management Cost	**91,377 (1)**	**0 (0)**	**0 (0)**	**13,074 (0)**	**0 (0)**	**78,303 (1)**
Positive product	0 (0)	0 (0)	0 (0)	0 (0)	0 (0)	0 (0)
Negative product	91,377 (1)	0 (0)	0 (0)	13,074 (0)	0 (0)	78,303 (1)
Total Cost THB (%)	**7,812,656 (100)**	**730,235 (10)**	**3,292,526 (42)**	**308,583 (4)**	**3,172,297 (40)**	**309,015 (4)**

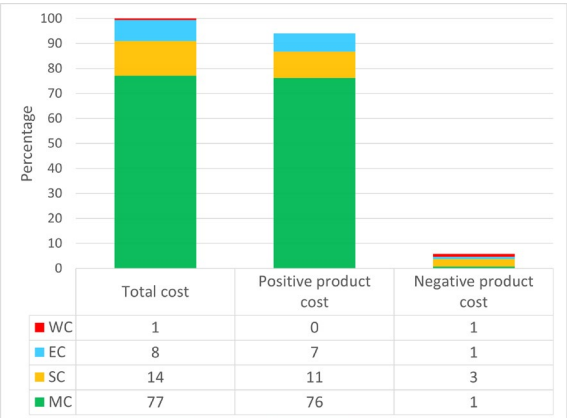
Note: all figures shown in this table based on a one-year period

Material Flow Cost Accounting

As a result of detailed cost allocation following the mass balance concept applied to the material flow model above, a material flow cost matrix for five different PCB wastes is presented in Table 1, and a summary of the cost ratio of total positive and negative products is depicted separately in Fig 3.

In Table 1, apparently 82% of the overall manufacturing costs come from two waste types – PCB border and drilling PCB which were allocated mostly to material costs. When focusing on the negative product cost, the major portion results from system costs (SC) about 50% or 3% of the total costs. These system loss costs, mainly labor and transportation costs, were generated from punching PCB residue accounting for 26% of the negative product cost, followed by PCB scrap (16%) and wastewater sludge (8%). Waste management loss cost was generated from two material losses, namely, punching PCB residue (17% of the total negative cost) and PCB scrap (3%). Among these five different waste types, punching PCB residue contributed the highest negative product cost, approximately 54% comprising system (26%), waste management (17%), and energy loss costs (11%).

As shown in Fig. 3, based on the MFCA, the overall cost can be summarized in positive and negative product costs 94% and 6%, respectively. Using the MFCA technique, the resource efficiency of the plant was 0.94, agreeing with the estimation in the previous section of this study.



	Total cost	Positive product cost	Negative product cost
WC	1	0	1
EC	8	7	1
SC	14	11	3
MC	77	76	1

Fig. 3 Summary of cost ratio in the MFCA

In determining resource efficiency, the estimation based on a recoverable precious metal (Cu) and its flow model is obviously compatible with the MFCA technique as described above (both calculated at 0.94). As the results of this study indicated, two processes were analyzed as high Cu losses, particularly Cu from wastewater sludge, at sun drying and weight checking processes that should be the focus for further improvement. A recommendation regarding the sun drying process was that improved cost savings and reduced air pollution could be achieved by switching from drying on an open-air floor to a closed drying system such as a greenhouse solar dryer. For the inefficiency of the weight checking process, changing to using a digital weighting scale was recommended for this plant. In terms of material loss costs, although punching PCB residue clearly produces significant costs for this manufacturing process, reducing such cost was deemed impossible because of the complimentary waste requested for handling by the PCB manufacturers.

CONCLUSIONS

To address losses and cost saving potentials of the PCBW plant, not just materials of the production process should be traced, but also precious metals (Cu) present in waste PCBs. Evidently, the results of this study highlight improvable hotspots where waste management costs and inefficiency of processes occurred. It could be concluded that the greatest portion of the negative product cost resulting from SC was 50% of the negative product costs (or 3% of the total cost). Regarding WC, all costs of waste handling and disposal were attributable to two material losses, namely, punching PCB residue (17% of the total negative costs) and PCB scrap (3%). Punching PCB waste was a main contributor of negative product costs. Overall, the resource efficiency of the plant could be evaluated at 0.94. All these helpful results are expected to lead to the improved and reduced environmental and health impacts of the plant.

ACKNOWLEDGMENTS

This research work was financially supported by the Center of Excellence on Environmental Health and Toxicology (EHT), Science & Technology Postgraduate Education and Research Development Office (PERDO), Ministry of Education, Thailand.

REFERENCES

[1] Baldé C.P., Forti V., Gray V., Kuehr R., and Stegmann P., The Global E-waste Monitor – 2017, United Nations University (UNU), International Telecommunication Union (ITU) & International Solid Waste Association (ISWA), 2017, pp.107.

[2] Forti V., Baldé C.P., Kuehr R., and Bel G., The Global E-waste Monitor 2020: Quantities, flows and the circular economy potential. United Nations University (UNU)/United Nations Institute for Training and Research (UNITAR) – co-hosted SCYCLE Programme, International Telecommunication Union (ITU) & International Solid Waste Association (ISWA), 2020, pp.114.

[3] Thai Customs Department, Situation and

Measures on the Import-Export of Electronic Scrap and Plastic Scrap [Internet]. 2018 [cited 2020 April 4]. Available from https://www.customs.go.th.

[4] Kanchanapiya P., E-waste: Printed circuit board scrap management technology, National Science and Technology Development Agency, 2011.

[5] Sohaili J., Muniyandi S., and Suhaila S., A review on printed circuit boards waste recycling technologies and reuse of recovered nonmetallic materials. International Journal of Scientific & Engineering Research, 2012, Vol. 3(2), pp. 1-7.

[6] Coombs C. F. Jr., Printed circuit handbook, 6th ed. McGraw-Hill, 2018.

[7] Tesanan S., Kwonpongsagoon S. and Kanchanapiya P., Solidification/stabilization of nonvaluable residue from waste printed circuit board assembly. International Journal of GEOMATE, 2016, Vol. 11, Issue 24, pp. 2307-2313.

[8] Strategy and Planning Division Office of the Permanent Secretary, Twenty-Year National Strategic Plan (2017-2036). Bangkok. Thailand: National Library of Thailand, 2017.

[9] Prachachat News, Recycling business over a hundred billion in revenue [Internet]. 2018 [cited 2020 April 5]. Available from https://www.prachachat .net/columns/news-205219

[10] Naewna News, 'Department of Industrial Works' controls tightening E-waste recycling plants [Internet]. 2018 [cited 2020 April 5]. Available from https://www.naewna.com/business/341446

[11] Krung Thai Bank Research Center, Marketing Strategy Department, Krung Thai points out the waste recycling business via digital platform to increase the potential to tackle environmental challenges [Internet]. 2020 [cited 2020 May 11]. Available from https://krungthai.com/th/krung thai-update/news-detail/484.

[12] Tachikawa H., Manual on Material Flow Cost Accounting ISO 14051. Asian Productivity Organization, 2014.

[13] Nakajima M., The New Management Accounting Field Established by Material Flow Cost Accounting (MFCA). Kansai University Review of Business and Commerce, Vol. 8, 2006, pp. 1-22.

[14] Chattinnawat W., Teeratanasombut M. and Kammoon C., Development of analysis method of material flow cost accounting using lean technique in food production: A case study of Universal Food Public (UFC) Co., Ltd., KKU Engineering Journal, Vol. 42(2), 2015, pp. 155-172.

[15] Chaiwan W., Boonmee C. and Kasemset C., Waste Reduction in Meat Processing Industry: the application of MFCA (ISO 14051). Toward Sustainable Operations of Supply Chain and Logistics Systems, 2015, pp. 183-193.

[16] Fakoya M.B., and Margaretha van der Poll H., Integrating ERP and MFCA systems for improved waste-reduction decisions in a brewery in South Africa. Journal of Cleaner Production, Vol. 40, 2013, pp. 136-140.

[17] Kurdve M., Shahbazi S., Wendin M., Bengtsson C. and Wiktorsson M., Waste flow mapping to improve sustainability of waste management: a case study approach. Journal of Cleaner Production, Vol. 98, 2014, pp. 304-315.

[18] Chang S., Material Flow Cost Accounting System for Decision Making: The Case of Taiwan SME in the Metal Processing Industry. Asian Journal of Finance & Accounting, Vol. 7(1), 2015, pp. 117-134.

[19] Behnami A., Benis K.Z., Shakerkhatibi M., Fatehifar E., Derafshi S. and Chavoshbashi M.M., Integrating data reconciliation into material flow cost accounting: the case of a petrochemical wastewater treatment plant. Journal of Cleaner Production, Vol. 218, 2019, pp. 616-628.

[20] Kasemset C., Chernsuporncha J. and Pala-ud W., Application of MFCA in waste reduction: case study on a small textile factory in Thailand. Journal of Cleaner Production, Vol. 108, 2014, pp. 1342-1351.

[21] Schaltegger S., Bennett M., Burritt R.L. and Jasch C., Environmental Management Accounting for Cleaner Production. Springer, Vol. 5, 2008.

[22] Nakano K. and Hirao M., Collaborative activity with business partners for improvement of product environmental performance using LCA. Journal of Cleaner Production, Vol. 19, pp. 1189-1197.

[23] Bierer A., Götze U., Meynerts L. and Sygulla R., Integrating life cycle costing and life cycle assessment using extended material flow cost accounting. Journal of Cleaner Production, Vol. 108, 2014, pp. 1289-1301.

[24] Wan Y.K., Ng R.T.L., Ng D.K.S. and Tan R.R., Material flow cost accounting (MFCA)-based approach for prioritisation of waste recovery. Journal of Cleaner Production, Vol. 107, 2015, pp. 602-614.

7th Int. Conf. on Structure, Engineering & Environment (SEE), Pattaya, Thailand, Nov.10-12, 2021, ISBN: 978-4-909106070 C3051

PHYLOGENETIC ANALYSIS OF ENDOPHYTIC *Colletotrichum* spp. FROM QUINA MEDICINAL PLANT (*Cinchona calisaya* Wedd.) BASED ON ITS rDNA AND ACTIN GEN AND ITS POTENTIAL AS QUINA PRODUCTION

Nani Radiastuti[1], Dwi Ningsih Susilowati[2], Siti Nurbayti[3], Zhaira Amila Haqqa[4], Wiwid Wiladatul Solihah[5]

[1,4,5]Departement of Biology, Faculty of Science and Technology, State Islamic University Syarif Hidayatullah Jakarta, Indonesia;
[3]Departement of Chemistry, Faculty of Science and Technology, State Islamic University Syarif Hidayatullah Jakarta, Indonesia;
[2]Indonesian Center for Agricultural Biotechnology and Genetic Resources Research and Development, Bogor, Indonesia

ABSTRACT

Endophytic fungi are microorganisms that can live inside plant tissues without harming the host. In this study seven endophytic *Colletotrichum* spp. were isolated from quina plants *(Cinchona calisaya* Wedd*).* The identification of endophytic fungi required combination of morphological characters and molecular methods. The purpose of this research was to identify seven isolates of endophytic fungi *Colletotrichum* spp. from *C. calisaya* based on phylogenetic tree. The method used phylogenetic analysis of maximum parsimony (MP) by PAUP 4.0b10 with bootstrap analysis 1000 random sequence additions. The analysis of the phylogenetic tree based on phylogenetic tree ITS rDNA, ACT and the combination of both ITS−ACT. The result showed that *Colletotrichum* M5 formed a monophyletic with *Colletotrichum karstii* with bootstrap value 89% and identified as *Colletotrichum karstii* M5. The endophytic *Colletotrichum* M2, M3, M4, M7, and M8 identified as *Colletotrichum* sp. The *Colletotrichum* sp. M30 formed a clade with *Colletotrichum camelliae* and *Gromerella cingulata* f sp. *camelliae* with bootstrap value 87% and identified as *Colletotrichum camelliae* M30. The identification of *Colletotrichum* spp. in this research needed another gen e.i. *glyceraldehyde-3-phosphate* (GDPH), *Calmodulin* (CAL), *Glutamine Synthetase* (GS), *β-tubulin* (TUB2), and *Elongation Factor1-α* (EF1-α) to be identified to species level. This research will rich up information on endophytic fungi from quina medicinal plant (*C. calisaya)* can produce quinine as antimalaria.

Keywords: Cinchona calisaya, Colletotrichum, Endophytic fungi, Phylogenetic tree

1. INTRODUCTION

The presence of endophytic is very abundant and diverse, mostly found in all plant species. The endophytic fungi have been isolated from a variety of plant species, including woody plants e.i. *Podocarpaceae, Fagaceae, Winteraceae* [1], palm [2], seaweed [3], as well as lichen crust [4]. The endophyte *Phomopsis* spp., *Diaporthe* spp., *Schizophyllum* spp., *Penicillium* spp., *Fomitopsis* sp. and *Arthrinium* sp. isolated from *Cinchona ledgeriana* successfully [5]. In addition to these endophytic species, *Colletotrichum* species have been widely isolated, such as from orchid plants [6], almonds [7], grasses and serelia [8]. However, the new endophytic *Colletotrichum* was first found in quina plants (*Cinchona calisaya*) [9].

The endophytic *Colletotrichum* is unique, because *Colletotrichum* is known as a pathogenic fungus in plants that can be found in various parts of the world, which can cause the anthracnose diseases, such as in almond plants in Australia by *C. acutatum* and *C. gloeosporioides* [7]. Both species are also found in tomatoes and mangoes [10, 11], while [12] found *C. phormii* in the *Phormium tenax* plant. The endophytic *Colletotrichum* were isolated from leaves of *Bletilla ochracea* (*Orchidaceae*) as much as thirty-six strains and collected from 5 sites in Guizhou,

China [6]. The *Colletotrichum* species were isolated as endophytes, but some of them have been known as pathogens on same or different hosts. Species such as *C. boninense, C. destructivum, C. karstii, C. miscanthi,* and *C. musae* have been known as causal agents of anthracnose of other host plants [13]. The *Colletotrichum coccodes* is a important for black dot disease on potato and anthracnose disease on many plants [14]. Some species of *Colletotrichum* have been known to evolve by forming endosymbiosis interactions with several plant species. One example is *C. gloeosporioides* that live on the plant *Artemisia annua* [15, 16]. [17] found that endophytic shell originating from the leaves of *Acalypha indica* was *C. gloeosporioides.* Based on previous study have found 7 endophytic *colletotrichum* from quina plant (*Cinchona calisaya* Wedd.) and second genus were found after *Phomopsis* [18]. The first report of seven *Colletotrichum* were found in the *C. calisaya* because several researcher e.i [19], [20], [21] were found some endophytic fungi namely *Arthrinium*, *Diaporthe*, *Phomopsis*, *Penicillium* and *Xylaria*. Therefore, the *Colletotrichum* in this study need to species identification.

The diversity of endophytic *Colletotrichum* were obtained from quina plant and has not been fully identified. This is due to the limitations of morphological characters. The most of the morphological observations of endophytic *Colletotrichum* have problematic, for example have form of a conidia almost same between genus *Colletotrichum*. Beside morphological identification, it is necessary to perform faster and more accurate molecular identification. According to [22] problems associated with identification of morphological characters could be solved using DNA-based analysis, even though molecular analysis alone has its own limitations. Beside that some of sequences down loaded from GenBank for comparative analysis may not be accurate in the identification. [23] said that type specimens are essential for molecular analysis when diagnosing *Colletotrichum* species as a large amount of sequences deposited in GenBank are shown to be derived from probably wrongly named strains. Therefore, the molecular approach and phylogenetic analysis are chosen for endohpytic fungi identification.

This study used multigen markers of ITS Deoxyribose Nucleic Acid ribosomal (rDNA) and Actin (ACT). The use of ITS rDNA to reestablish the seven isolate endophytes of *Colletotrichum* spp., This is because the rDNA ITS marker genes are universal for the fungi. [9] have identified *Colletotrichum* only used ITS rDNA regon. Beside used ITS rDNA, in this study used ACT gene, because the more specific ACT to identify up to the species level. Actin is the most globular protein in eukaryotic cells of 5% of all cell proteins, plays an important role in maintaining cell shape and generating cell motion. Although some previous research used some genes to identify of the *Colletotrichum* e.i. [24] used nine genes and ITS region, [6] used ITS region, TUB, ACT and GDPH gene, [25] used six genes namely ITS region, GC, TUB, ACT, CAL and GDPH gene The objective of this study to identify the seven endophyte *Colletotrichum* spp. from quina plant with ITS region and ACT gene. The phylogenetic analysis can be reconstructed of relationships by phylogenetic tree of ITS, ACT, and combination of ITS and ACT.

2. MATERIALS AND METHODS

2.1 Time and Place

This research was conducted at the Integrated Laboratory Center, Faculty of Science and Technology at State Islamic University Syarif Hidayatullah Jakarta and the Microbiology Laboratory at Indonesian Center for Agricultural Biotechnology and Genetic Resources Research and Development (ICABIOGRAD) Bogor.

2.2 Isolation of DNA

The molecular identification of endophytic isolates was carried out from the preparation stage of culture with PDB media. A total of 7 endophytic *Colletotrichum* spp. were derived from various quina plant organs. The *Colletotrichum* spp were grown in 5 mL of medium PDB for 4-7 days on a rotary shaker at 100 rpm at room temperature. The DNA isolation used the Phytopure Kit according to the manufacturer protocol

2.3 PCR Amplification and DNA Sequencing

The amplification of the ITS rDNA region and ACT conducted in the reaction mixture consisting of 9.5 mL Nuclease free water, go taq green master mix 12.5 mL, forward and reverse primer 1 mL then added 1 mL of the templete DNA. The forward ITS 4 (5'-TCCTCCGCTTATTGATATGC-3'), reverse ITS 5 (5'-GGAAGTAAAAGTCGTAACAAGG-3'), ACT-512-F(5'-ATGTGCAAGGCCGGTTTCGC-3') and ACT- 783-R (5'-TACGAGTCCTTCTGGCCAT -3') [25]. The mixture was amplified by a PCR machine (Biometra™ Thermal Cycler). Protocols PCR ITS rDNA and ACT were conducted 3 minutes initial denaturation at a temperature 95^{o}C followed by 34 cycles covering 1 minute with the temperature 95^{o}C, annealing 30 seconds at a temperature 52^{o}C, extensions 1 minute with the temperature 72^{o}C, and the last cycle with the extension late for 10 minutes with 72 °C. The PCR products were checked for quality by running on DNA electrophoresis devices. DNA sequencing of ITS rDNA and ACT was performed by the laboratory of First Base (1st Base).

2.4 Phylogenetic Analysis

The sequence results in an each isolate were aligmnent with Basic Local Allignment Search Tools (BLAST) against the GenBank gene database at the National Center for Biotechnology Information (NCBI) based on the ITS region and ACT gene. The sequence data was obtained from GenBank as much as 60 taxa *Colletotrichum* were selected and referred to the literature [26] and [27]. The alignment was done using the Molecular Evolutionary Genetics Analysis (MEGA) program.

The phylogenetic analysis was performed using Maximum Parsimony (MP) method in PAUP 4.0.b10 [28] base on combine ITS rDNA and ACT dataset. The heuristic method using tree bisection reconstruction (TBR), with the addition of 1000 random sequence algorithms to obtain the optimal tree. Tree length (TL), consistency endex (CI), retention index (RI), related consistency index (RC), and homoplasy index (HI) were calculated. The internal branch strength of the phylogenetic tree was tested by Bootstrap (BS) analysis with Value> = BS 50% using 1000 replications [29]. Homogeneity partition was tested using 1000 replications.

2.5 Fermentation

The endophytic were fermented with a liquid medium of 200 ml of PDB. The cultures were incubated with static methods for 21 days in room temperature. The product fermented from the biomass and filtrate were extracted with solvent addition of 100 mL chloroform pa ($CHCl_3$) and 0.1N NaOH 1 mL [5] with two time extractions by ratio: solvent (1: 0,5). The extract was silenced for 1 day to form 2 layers. Each fraction was collected and concentrated by rotary evaporator at a temperature of 45 °C and 60 rpm rotation.

2.6 HPLC Analysis

The extraction of the the endophytic fungi were analyzed quantitatively by using the Shimadzu brand high-performance liquid chromatography (KCKT) by using 5C18-MS-II (4.6 X 150 mm) cosmocil, aqueous phase: acetonitrile: glacial acetic acid (81: 18: 1), flow rate 0.6 mL/minute, 30°C and 5 µL injection volume. The detector used was a UV-Vis spectrophotometer with 250 nm wavelength. The concentration of chinchona alkaloid (mg/L) was calculated by the formula = sample area / standard area x standard.

3. RESULTS AND DISCUSSION

3.1 The Phylogenetic tree of ITS rDNA

Base on ITS rDNA of the Phylogenetic tree analysis that was obtained 608 characters, covering 477 characters constant, 53 characters were parsimony unformative and 78 characters were parsimony informative. The parsimony analysis resulted based on the phylogenetic tree of in a most parsimonious tree 68, with the value of consistency index (CI) = 0.630, the value retention index (RI) = 0,900, related consistency index (RC) = 0.567, and homoplasy index (HI) = 0.320. The phylogram showed that seven isolates asosiated with the quina plant formed 4 distinct big clade namely clade I, II, III, and IV with bootstrap support (Fig 1). This is as representative different *Colletotrichum* species.

A total of six endophytes *Colletotrichum* M1, M2, M3, M4, M6, and M7 were presented in clade I and *Colletotrichum* M5 was presented in clade II. *Colletotrichum* M2 formed a close related with the group together with *C. siamanse* strain C1255.1, *C. aenigma* strain C1253.4, *C. aenigma* strain C1256.6 and *C. aenigma* strain C1253T with supported low bootstrap values (≤50%). *Colletotrichum* M2 could be identified as *Colletotrichum* sp. M2, therefore it couldn't be identified until the species level using the primary ITS rDNA.

The endophytes *Colletotrichum* M3, M4, M7 and M6 formed the same cluster sisters with *C. gloeosporioides* strains TSG001, *C. gloeosporioides* strains TSG002, *C. horii* strains C1264, *C. horii* strains C1272.14, and *C. horii* strains C1180T with bootstrap values 51%, so it can be interpreted that the four isolates of *Colletotrichum* spp. were closely related with *C. gloeosporioides* and *C. horii* and they were one common ancestor. Moreover, *Colletotrichum* sp. M8 forms a monophyletic group but was supported with bootstrap value (≤50%). *Colletotrichum* sp. M4 and M7 formed one clade equal to 66% bootstrap value, therefore they were the same species. Endophytes *Colletotrichum* M3, M4, M7 and M8 couldn't be identified until species level with ITS rDNA and they were only closely related to *C. gloeosporioides* and *C. horii.*

The *Colletotrichum* sp. M5 formed a monophyletic group with *C. karstii* strain CGMCC 3.15123, *C. karstii* strain CBS 127552, *C. karstii* strain CBS 129822, and *C. karstii* strain CBS 128550 with 76% bootstrap value. The *Colletotrichum* sp. M5 was identified as *Colletotrichum karstii* M5 based on ITS rDNA region. The *Colletotrichum* M30 formed sister group with *C. kahawae* subsp. Cinggoro UWS124T strain with a low bootstrap value (≤50%). The *Colletotrichum* sp. M30 has not been identified to the species level using the rDNA ITS and was known only to be associated with *C. kahawae.*

The nuclear ribosomal internal transcribed spacer (ITS) has been chosen as the universal barcode for the Kingdom of Fungi [30]. In this study used to the ITS region for the identification of endophytic *Colletotrichum* but ITS sequence data can provide adequate resolution to determine and differentiate *Colletotrichum* species. The use of ITS sequences also has limitations in phylogenetic analysis, such as this noncoding ITS sequence is fast evolving with



Fig. 1 The *Colletotrichum* phylogenetic tree with related species sequences based on ITS rDNA sequences. Boostrap value> 50% (1000 replicates) are shown at the branch nodes *Monilocaetes infuscans* CBS 869 96 as outgroup

many variable characters. It is usually difficult to achieve a perfect sequence alignment at high taxonomic levels. The internal transcribed spacer (ITS) region conventionally includes the entire ITS5, 5.8S gene and ITS4 portion of the nuclear rDNA. The phylogenetic reconstructions based on ITS rDNA provide more clarification at both genus and species level than other gene markers. ITS2 had been suggested as a standard marker for fungi and integrating ITS2 based phylogenetic analysis with the morphological characters of their primary sequences has been the recent trend, which has significantly enhanced the resolution and stability of the clades [31]. It is suggested that using different gene sequences can resolve in the phylogenetic analysis of the endophytic *Colletotrichum* spp.

3.2 The Phylogenetic Tree of ACT Gene

The analysis phylogenetic tree of ACT region could be obtained 316 characters, consisting of 175 characters were constant, 42 were not informative and 99 characters were informative. Based on the parsimonies criterion was obtained 59 phylogenetic tree, with consistency index value (CI) = 0.627, retention index value (RI) = 0.602, related consistency index (RC) = 0.567, and homoplasy index (HI) = 0.372.

The phylogenetic tree formed 4 clade namely clade I, II, III, and IV. A total of 6 endophyte *Colletotrichum* M2, M3, M4, M7, M8, and M30 were present in clade I, while one isolate *Colletotrichum* M5 included in the clade III (Fig 2). Based on the ACT genes the *Colletotrichum* M2 form a clade sister with a group of *C. siamanse* strains C1255.1, *C. siamanse* strains C1258.5, *C. queenslandicum* strains ICMP 1778T, and *C. aeschynomenes* strains 313T with the supported bootstrap values of 65%. The isolate M2 was not accurately correlated to their corresponding species, so could be identified as *Colletotrichum* sp M2.

The endophytic *Colletotrichum* M3, M4, M7 and M8 formed the same cluster sisters as *C. gloeosporioides* strains TSG001, *C. gloeosporioides* strains TSG002, *C. horii* strains C1264, *C. horii* strains C1272.14, and *C. horii* strains C1180T with values Bootstrap 91%. This suggests that the four isolates with *C. gloeosporioides* and *C. horii* were closely related and fromed one common ancestor. The endophytic *Colletotrichum* M3, M4, M7 and M8 still couldn't be identified with ACT to species level and they were only closely related to *C. gloeosporioides* and *C. horii*. The isolate M3, M4, M7 and M8 identified as *Colletotrichum* sp.

The *Colletotrichum* M5 forms a monophyletic group with *C. karstii* strain CGMCC 3.15123, *C. karstii* strain CBS 127552, *C. karstii* strain CBS 129822, and *C. karstii* strain CBS 128550 with bootstrap value 68%, so *Colletotrichum* sp. M5 and *C. karstii* were closely related. The endophytic *Colletotrichum* M5 could be identified as *Colletotrichum karstii* M5 based on ACT gene.

The *Colletotrichum* M30 form a sister group with *Gromerella cingulata* f sp. *Camelliae* srain ICMP 10643, *Gromerella cingulata* f sp. *Camelliae* srain ICMP 10646, *C. camelliae* strain CBS 125502, *C. clidemiae* strain C1317T, and *C. kahawae* subsp. Cinggoro UWS124T strain with a bootstrap value of 97%. Nevertheless *Colletotrichum* sp. M30 has not been identified to the species level using ACT and is known to be closely related to *C. camelliae, C. clidemiae* and *C. kahawae*

Based on the phylogenetic tree ACT, only isolates M5 could be identified as *Colletotrichum karstii,* while others were still identified as *Colletotrichum* sp. Nevertheless ACT Primer has been widely used in molecular identification, such as [6] used ACT in identifying *Colletotrichum* endophytes from *Bletilla ochracea*, [26] identified *Colletotrichum* from *Annona muricata* using a partial actin region. [27] used ACT gene to introduce of the phylogenetic tree. The topology phylogenetic tree of ITS and ACT does not change the position of the isolates analyzed, since they formed in the same position. Using actin gene not yet help to identify the seven *Colletotrichum* spp. were analyzed.

3.3 Phylogenetic Tree Combine of ITS gene rDNA and ACT

Based on the results alignment DNA base sequence obtained 860 combinations of characters, including the 597 characters is constant, 92 are uninformative and 171 characters is very informative, then with PAUP program code and is very informative constant is analyzed to reconstruct the phylogenetic tree. Results obtained parsimony analysis based on the criteria of the phylogenetic tree 231, with a value of consistency index (CI) = 0.640, the value retention index (RI) = 0.905, related consistency index (RC) = 0.580, and homoplasy index (HI) = 0.360. Consensus tree of 231 phylogenetic tree formed in Fig 3. It is the best tree showing the phylogenetic relationship between isolates with taxa included in the analysis.

The endophytic *Colletotrichum* M3, M4, M7 and M8 included the fisrt clade and formed a sister clade with *C. gloeosporioides* strain TSG001*, C. gloeosporioides* strains TSG002, *C. horii* strain C1264, *C. horii* strain C1272.14, and *C. horii* strain C1180T with the bootstrap value is 98%. They could be interpreted that the four isolates were very close to *C. gloeosporioides* and *C. horii.* The *Colletotrichum* sp. M4 and M7 form one clade equal to 62% bootstrap value, making it possible of the same species. The endophytic *Colletotrichum* sp. M3, M4, M7 and M8 could not be identified by a combine of ITS and ACT yet and only closely related to *C.*

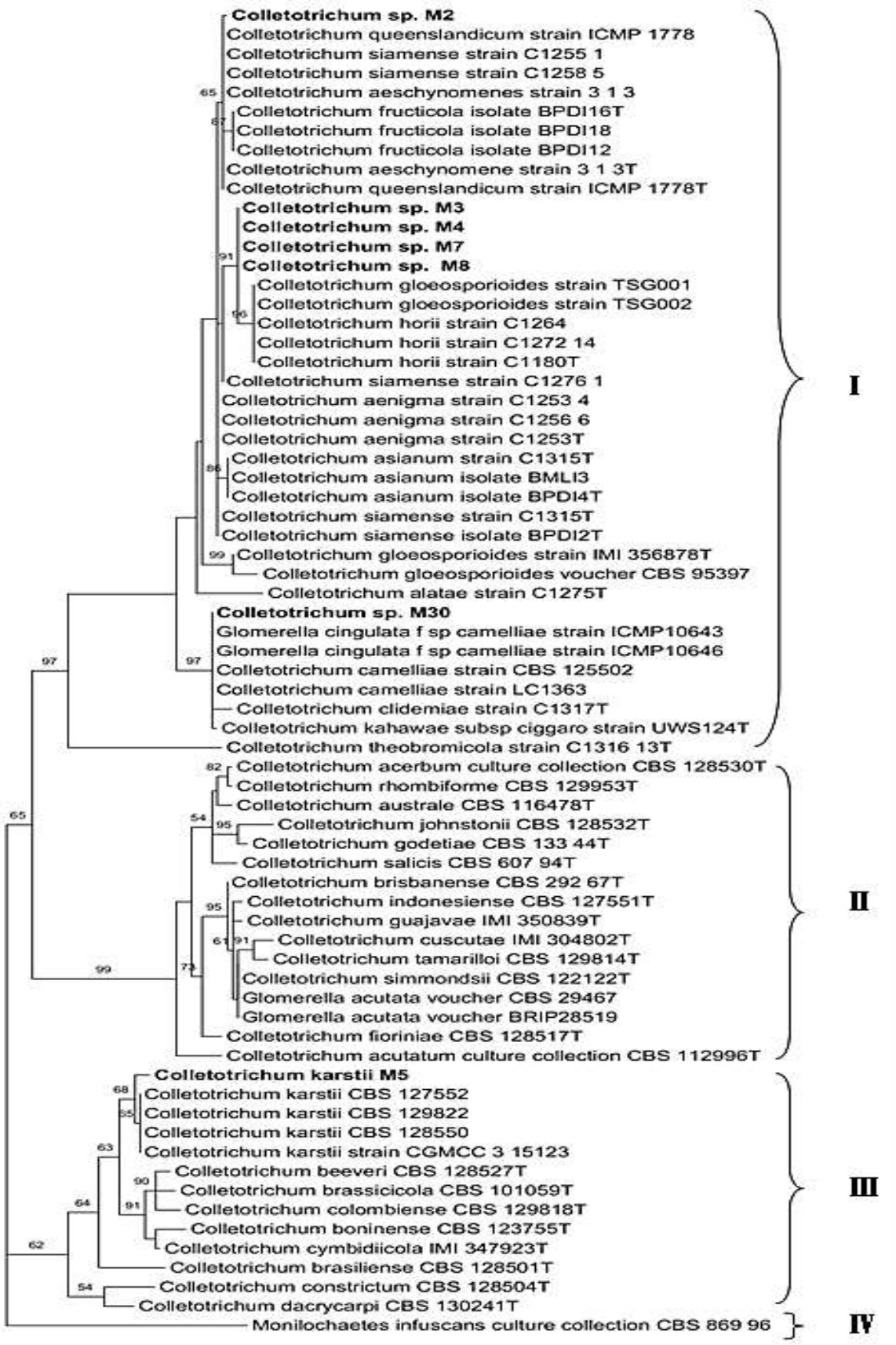


Fig. 2 The *Colletotrichum* phylogenetic tree with related species sequences based on ACT sequences. Boostrap value> 50% (1000 replicates) are shown at the branch nodes. *Monilocaetes infuscans* CBS 869 96 as outgroup.

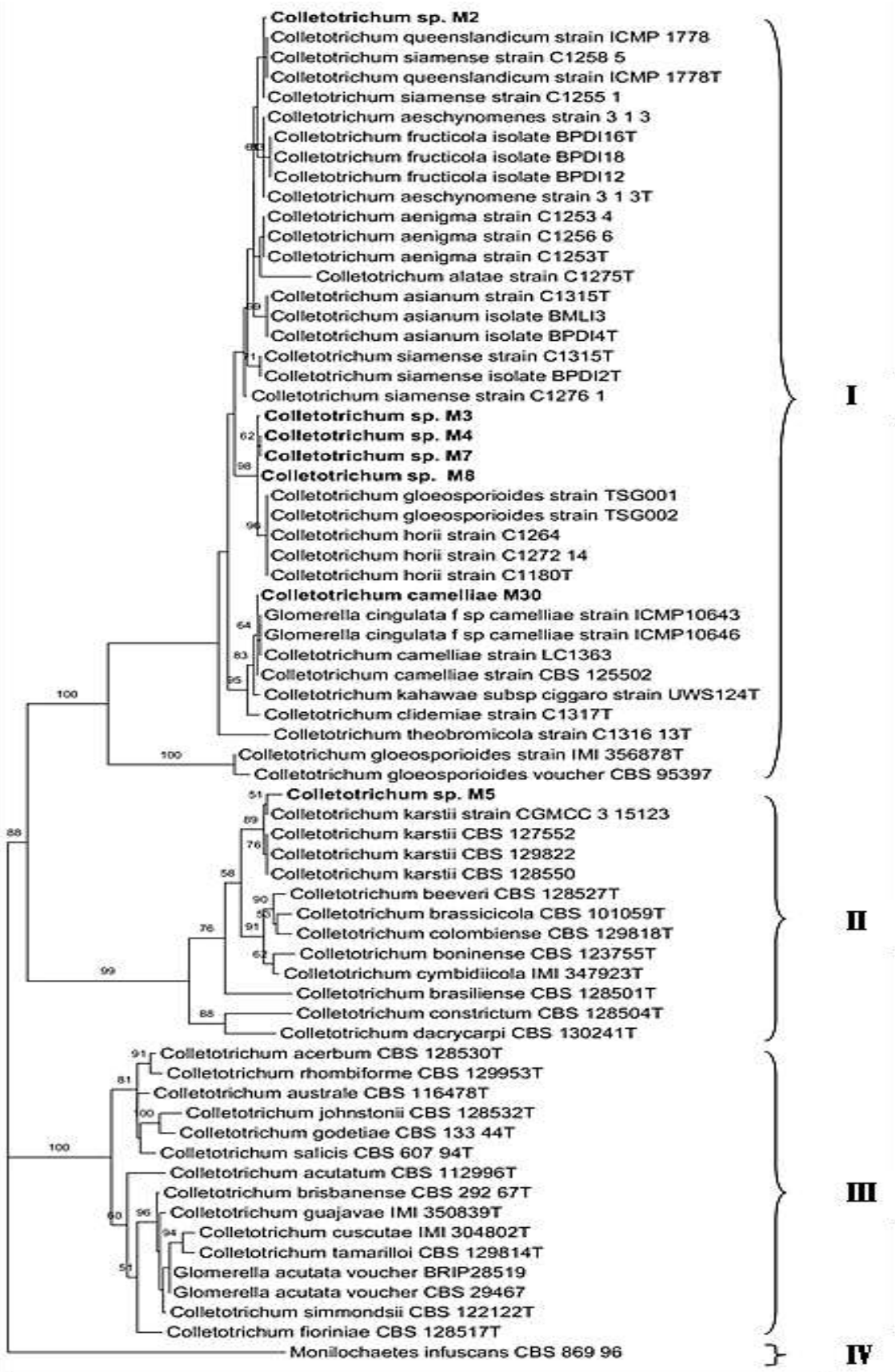


Fig. 3 The *Colletotrichum* phylogenetic tree with related species sequences based on combine ITS rDNA and ACT sequences. Boostrap value> 50% (1000 replicates) are shown at the branch nodes. *Monilocaetes infuscans* CBS 869 96 as outgroup

gloeosporioides and *C. horii*. The fourth of these isolates still need another gene to separate whether they are monophyletic with *C. gloeosporioides* or *C. horii.* According to [27] that it takes the ITS gene rDNA, ACT, TUB, GDPH, GS and CAL to identify the genus *Colletotrichum.* [32] *Colletotrichum* belongs to a large number of species, about 900 species in this genus, requiring multiple genes for identification. In addition, *Colletotrichum* belongs to a complex species requiring at least about 5 or more genes for its identification [27, 6, 26].

The clade II included *Colletotrichum* sp. M5 forms a monophyletic group with *C. karstii* strain CGMCC 3.15123, *C. karstii* strain CBS 127552, *C. karstii* strain CBS 129822, and *C. karstii* strain CBS 128550 with high bootstrap value 89%. The *Colletotrichum* sp. M5 and *C. karstii* were closely related and could be named as *Colletotrichum karstii* M5 based on a combination of ITS and ACT

The endophytic *Colletotrichum* sp M30 form a sister clade with *Gromerella cingulata* f sp. camelliae srain ICMP 10643, *Gromerella cingulata* f sp. *Camelliae* srain ICMP 10646, *C. camelliae* strain LC1363, and *C. camelliae* strain CBS 125502 with a bootstrap value of 64%. The *Colletotrichum* sp. M30 and *C. camelliae* were very close and come from the same ancestor. The *Colletotrichum* sp. M30 could be identified as *C. camelliae* based on a combination of ITS and ACT. The *C. camelliae* as anamorph and *Gromerella cingulata* f sp. *Camelliae* as teleomorph.

The three phylogenetic trees based on ITS, ACT or combination form a phylogenetic tree topology are relatively similar but in combination trees. The data set is better because using a combination of marker genes, it can be seen the value of bootstrap on each clade formed. Bootstrap analysis is a method to test how well the data model set, the bigger the predictions of the branches formed the more reliable. Phylogenetic trees have been helpful in the identification of one *Colletotrichum* sp. M5 such as forming a monophyletic group with *C. karstii* it can be said that the isolates can be classified in *C. karstii* M5 and *Colletotrichum* sp. M30 as *C. camelliae* M30. Resulting phylogenetic tree can be translated into a classification system, and for that only a monophyletic group can be used In this study, the seven endophytic *Colletotrichum* could be identified to species level only two strain namely *C. karstii* M5 and *C. camelliae* M30. Therefore the analyses of phylogenetic tree need to another beside ITS rDNA region and ACT. The systematics of *Colletotrichum* have been problematic for a long time, as there are few distinctive morphological characters useful for species discrimination [24]. The systematics of *Colletotrichum* have been problematic for a long time, as there are few distinctive morphological characters useful for species discrimination [25]. The multi-gene phylogenies were also successfully applied to resolve the relationships among *Colletotrichum* species with curved conidia from herbaceous hosts [8, 13]. Multi-gene phylogenetics is an accurate and reliable way for the identification of *Colletotrichum* species, but is not economical and efisiency. It is currently impractical to apply multiple gene phylogenetics to every *Colletotrichum* species,as different research groups use different gene regions. Multilocus molecular phylogenetic analysis involving nucleotide sequences generated from other gene regions. Beside the multilocus, the identification of *Colletitrichum* was better used to polyphasic characters (morphology, physiology, pathogenicity, infection processes, cultural characteristics and secondary metabolites) [23, 33]. [24] have listed all the multi-gene sequences derived from the type or epitype cultures of *Colletotrichum.* This provides an excellent for data analysis for study the relationships among species. A six genes e.i. ITS, ACT, CHS, GPDH, histone 3, beta-tubulin were used for studying *Colletotrichum* species [13]. Using gene for separating *Colletotrichum* in the phylogenetic analysis was different gene for each *Colletotrichum* species for example *Colletotrichum gloeosporioides sensu lato* GPDH, CAL, and ACT are better for barcodes, while ITS, CHS, and EF1α are poor candidates [23]. To solve the problem of few morphologically informative characters, researchers have utilised other characters such as nucleic acid sequence data, physiology, secondary metabolites and pathogenicity, as part of a polyphasic approach [27].

3.4 HPLC Analysis

The HPLC results showed that M7 isolate was capable of producing quinine compounds with concentration 0.12 ppm. The content of quinidine compounds was obtained by M5 and M30 isolates in 5.27-13.25 ppm. The cinchonidine compounds were capable of producing M2, M3, M4, M7, M8 and M30 isolates by 2.16-29.67 ppm. Furthermore, the cinchonine compounds could be produced only isolate M2 with concentration in 1.04-11.21 ppm. The differences in the content of the cinchona alkaloid in each isolate were due to the ability of each strain to adapt in using nutrition and enviroment in the synthetic medium for producing secondary metabolites. [21] found that the *Diaporthe* isolated from *C. ledgeriana* were able to produce 60-110 ppm quinine, 3-5 µm quinidine, 10-15 ppm cinchonine, and 15-20 ppm cinchonidine. Based on research conducted, LMC-29 endophytic fungi isolated from *C. ledgeriana* rod organ were capable to produce 0, 312 ppm medium cinchonine GDP and 23.656 ppm quinine. Meanwhile, research conducted by [9] found endophytic *F. incarnatum* strain IPBCC 15.1253, strain IPBCC 15.1252, and strain IPBCC 15.1251; *F. oxysporum* strain IPBCC 15.1250; and *F. solani* strain IPBCC.15.1249 IPBCC 15.1248 and strains isolated from quinine plant (*Cinchona calisaya*

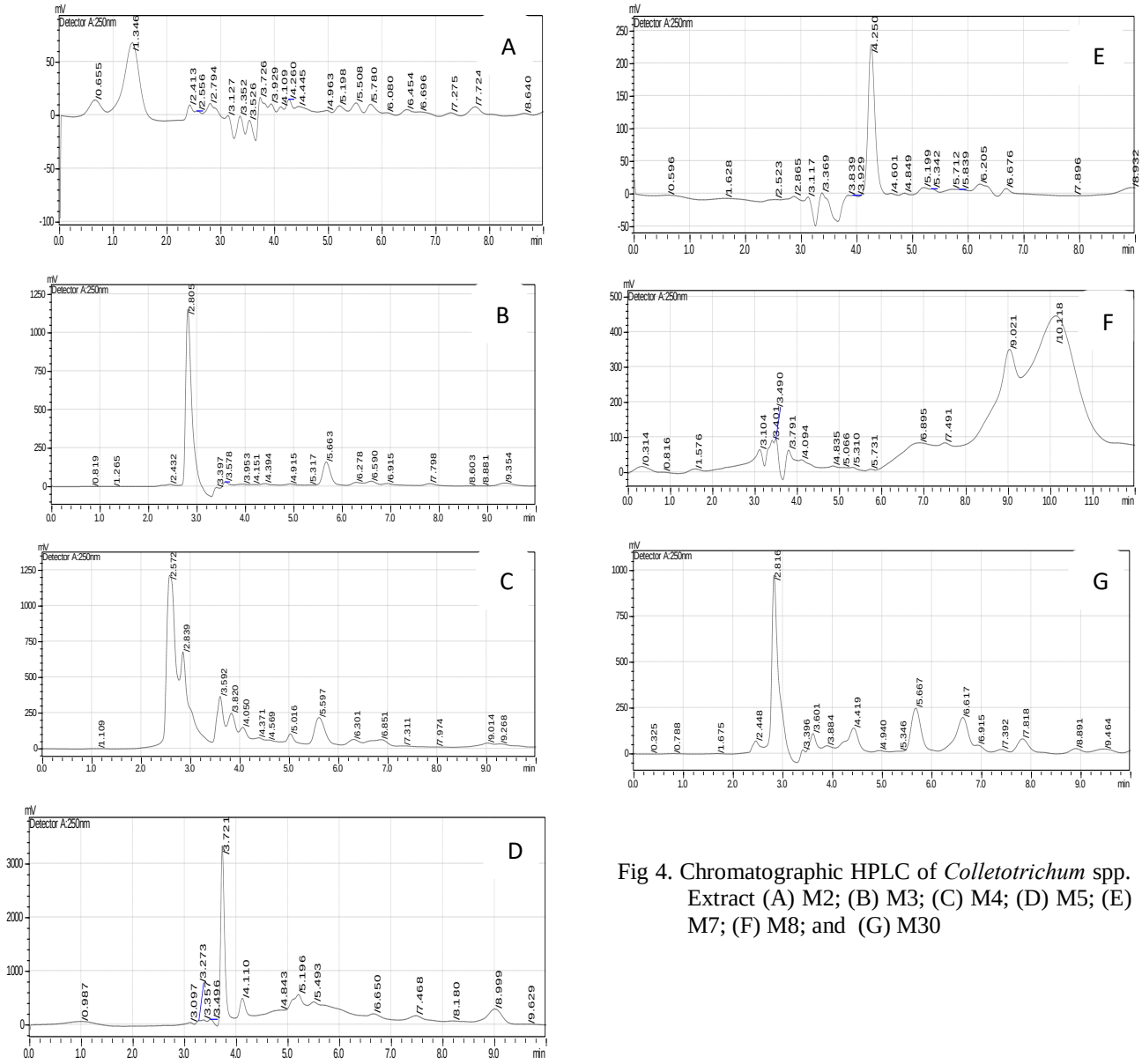


Fig 4. Chromatographic HPLC of *Colletotrichum* spp. Extract (A) M2; (B) M3; (C) M4; (D) M5; (E) M7; (F) M8; and (G) M30

Table 4. The concentration of cinchona alkaloid compounds from *Colletotrichum* spp.

Strain	Retention time (Minute)	Area (%)	Cinchona alkloid	Concentration (ppm)
M2	3.72	5.17	Cinchonine	5.17
	4.10	2.99	Cinchonidine	2.99
M3	3.58	3.85	Cinchonidine	3.85
M4	3.59	7.98	Cinchonidine	7.98
M5	3.60	5.27	Quinidine	5.27
M7	4,25	29,67	Cinchonidine	1,04
	6,20	7,78	Quinine	0,12
M8	3,79	2,12	Cinchonine	31,13
	4,09	2,16	Cinchoinidine	4,73
M30	3,72	19,46	Quinidine	13,25
	4,11	6,61	Cinchonidine	7,54

note: eluent H2O : acetonitrile : asetat glasial acid (18:18:1); rate flow 0,6 ml/minute λ= 250n

Wedd.) compounds containing quinine around 0.7-0.9 ppm. Meanwhile, *F. incarnatum* strain IPBCC 15.1253 and strain IPBCC 15.1251; *F. oxysporum* strain IPBCC 15.1250; and *F. solani* strains IPBCC.15.1249 were capable to produce cinchonine.

The results of secondary metabolites of *Colletotrichum* spp. have compounds with host plants (quina plants), namely quinine compound. The same result was found by Numonov et al. [34] that *Colletotrichum* isolated from the *Artemisia annua* plant is able to stimulate the production of artemisinin which is a compound in antimalarial activity [34].

4. CONCLUSIONS

The endophytic *Colletotrichum* from *C. calisaya* could be identified as *Colletotrichum* sp. M2, *Colletotrichum* sp. M3, *Colletotrichum* sp. M4, *Colletotrichum* sp. M7, and *Colletotrichum* sp. M8, *C. karstii* M5 and *C. camilliae* M30 based on combine ITS rDNA region and ACT gene. The phylogenetic study of the endophyte of *Colletotrichum* in this research will rich up information on endophytic fungi from quina medicinal plant (*Cinchona calisaya)*.

5. REFERENCES

[1] Oses R., Valenzuela S., Freer J., Sanfuentes E., and Rodriguez J., Fungal Endophytes In Xylem of Healthy Chilean Trees and Their Possible Role in Early Wood Decay, Fungal Diversity, Vol. 33, 2008, pp. 77─86.

[2] Frohlich J., Hyde K.D., and Petrini O., Endophytic Fungi Associated with palms, Mycological Research, Vol. 104, Issues 10, 2000, pp. 1202–1212.

[3] Alva P., McKenzie E.H., Pointing S., Pena-Muralla R., and Hyde K., Do Sea Grasses Harbour Endophytes, Fungal Diversity Research Series, 2002, pp. 167–178.

[4] Li W.C., Zhou J., Guo S.Y., and Guo L. D., Endophytic Fungi Associated with Lichens in Baihua Mountain of Beijing, China, Fungal Diversity, Vol. 25, 2007, pp. 69–80.

[5] Maehara S., Simanjuntak P., Kitamura C., Ohashi K., and Shibuya H., Cinchona Alkaloid are also Produced by An Endophytic Filamentous Fungus Living in Cinchona Plant. Chemical and Pharmaceutical Bulletin, Vol. 59, Issues 8, 2012, pp. 1073–1074, Available from: do1.

[6] Tao G., Liu Z.Y., Liu F., Gao Y.H., and Cai L., Endophytic *Colletotrichum* Species from *Bletilla Ochracea* (Orchidaceae), with Descriptions of Seven New Speices, Fungal Diversity, Vol. 61, Issues 1, 2013, pp. 139–164, Available from: doi:10.1007/s13225-013-0254-5.i:10.1248/cpb.59.1073.

[7] McKay S.F., Freeman S., Minz D., Maymon M., Sedgley M., Collins G.C., and Scott E.S., Morphological, Genetic, and Pathogenic Characterization of *Colletotrichum Acutatum*, The Cause of Anthracnose of Almond in Australia, *Ecology and Epidemiology*, Vol. 99, Issues 8, 2009, pp. 985–995. Available from: doi:10.1094/PHYTO-99-8-0985.

[8] Crouch J.A., Clarke B.B., and Hillman, B.I., What is The Value of ITS Sequence Data in Colletotrichum Systematics and Species Diagnosis? A Case Study using The Falcate-Spored Graminicolous *Colletotrichum* Group, Mycologia, Vol. 101, Issues 5, 2009, Taylor & Francis, pp. 648–656.

[9] Hidayat I., Radiastuti N., Rahayu G., Achmadi S., and Okane I., Endophytic Fungal Diversity from *Cinchona Calisaya* Based on Phylogenetic Analysis of The ITS Ribosomal DNA Sequence Data, Curr Res Environ Appl Mycol, Vol. 6, Issues 2, 2016, pp. 132–142, Available from: doi:10.5943/cream/6/2/7.

[10] Martínez E. P., Hío J. C., Osorio J. A., and Torres M. F., Identification of *Colletotrichum* Species Causing Anthracnose on Tahiti Lime, Tree Tomato and Mango, *Agronomia Colombiana*, Vol. 27, Issues 2, 2009, Universidad Nacional de Colombia, Facultad de Agronomía, pp. 211–218.

[11] Zivkovic S., Stojahovic S., Ivanovic Z., Trkulja N., Dolovac N., Aleksic G., and Balaz J., Morphological and Molecular Identification of *Colletotrichum Acutatum* from Fruit Tomat, Pesticides and Phytomedicine (Belgrade), Vol. 25, 2010, pp. 231-239.

[12] Golzar H., and Wang C., First Report of *Colletotrichum Phormii* The Cause of Anthracnose on *Phormium Tenax* in Australia, Australasian Plant Disease Notes, Vol. 5, Issues 1, 2010, Springer, pp. 110–112.

[13] Damm U., Woudenberg J.H.C., Cannon P.F., and Crous P.W., *Colletotrichum* Species with Curved Conidia from Herbaceous Hosts, Fungal Diversity, Vol. 39, 2009, pp. 45–87.

[14] Prihastuti H., Cai L., Crouch J.A., Phoulivong S., Moslem M.A., McKenzie E.H.C., and Hyde K.D., Neotypification of *Colletotrichum Falcatum*, The Causative Agent of Red-Rot Disease in Sugarcane, *Sydowia*, Vol. 62, Issues 2, 2010, Verlag Ferdinand Berger & Söhne, pp. 283–293.

[15] Zou W. X., Meng J. C., Lu H., Chen G. X., Shi G.X., Zhang T.Y., and Tan R. X., Metabolites of *Colletotrichum Gloeosporidies* and Endophytic Fungus in *Artemisia Mongolica*, Journal of Natural Products, Vol. 63, 2000.

[16] Agusta A., Maehara S., Ohashi K., Simanjuntak P., and Shibuya H., Stereoselective Oxidation at C-4 of Flavans by The Endophytic Fungus *Diaporthe* sp. Isolated from a Tea Plant.

Chemical and Pharmaceutical Bulletin, Vol. 53, Issues, 12, 2005, pp. 1565–1569, Available from: doi:10.1248/cpb.53.1565.

[17] Gangadevi V., and Muthumary J., Isolation of *Colletotrichum Gloeosporioides*, A Novel Endophytic Taxol-Producing Fungus from The Leaves of A Medicinal Plant, *Justicia Gendarussa*, *Mycologia Balcanica*, Vol. 5, 2008, pp. 1–4, Available from: doi:10.1.1.457.1000&rep=rep1&type=pdf.

[18] Radiastuti N., Rahayu G., Okane I., Hidayat I., and Achmadi S., Alkaloid Profile of Endophytic *Diaporthe* spp. from *Cinchona Calisaya,* Jurnal Penelitian Teh & Kina, Vol. 18, Issues 1, 2015, pp. 81-93.

[19] Simanjuntak P., Parwati T., Bustanussalam., Prana T. K., Wibowo S., Shibuya H., Isolasi dan Kultivasi Mikroba Endofit Penghasil Senyawa Alkaloid Kinkona dari *Cinchona* spp, Jurnal Mikrobiologi Indonesia, Vol. 7, 2002, pp. 27–30.

[20] Shibuya H., Kitamura C., Maehara S., Nagahata M., Winarno H., Simanjuntak P., Kim H. S., Wataya Y., Ohashi K., Transformation of *Cinchona* Alkaloids Into 1–N–Oxide Derivatives by Endophytic *Xylaria* sp. Isolated from *Cinchona Pubescens*, Chemical and Pharmaceutical Bulletin, Vol. 51, 2003, pp. 71–74.

[21] Maehara S., Simanjuntak P., Ohashi K., Shibuya H., Composition of Endophytic Fungi Living in *Cinchona ledgeriana* (Rubiaceae), Journal of Natural Medicines, Vol. 64, 2010, pp. 277–230. doi: 10.100/s11418-009-0380-2.

[22] Hyde K. D., Understanding Microfungal Diversity-A Critique, *Cryptogamie* Mycology, Vol. 28, 2007, pp. 281–289.

[23] Cai L., Hyde K. D., Taylor P. W. J., Weir B. S., Waller J., Abang M. M., Zhang J. Z., Yang Y. L., Phoulivong S., Liu Z. Y., Prihastuti H., Shivas R. G., McKenzie E.H.C., and Johnston P. R., A Polyphasic Approach for Studying *Colletotrichum*, Fungal Diversity, Vol. 39, Issues 1, 2009, pp. 183–204.

[24] Hyde K. D., Cai L., Cannon P. F., Crouch J. A., Crous P. W., Damm U., Goodwin P. H., Chen H., Johnston P. R., Jones E. B. G., Liu Z. Y., McKenzie E. H. C., Moriwaki J., Noireung P., Pennycook S. R., Pfenning L. H., Prihastuti H., Sato T., Shivas R. G., et al., Colletotrichum - Names in Current use, Fungal Diversity, Vol. 39, Issues 2, 2009a, pp. 147–183.

[25] Hyde K. D., Cai L., McKenzie, E. H. C., Yang Y. L., Zhang J. Z., and Prihastuti H., Colletotrichum: a Catalogue of Confusion, Fungal Diversity, Vol. 39, Issues 1, 2009b, pp. 1–17.

[26] Alvarez E., Ganan L., Rojas Trivino A., Mejia J. F., Llano G. A., and Gonzalez A., Diversity and Pathogenicity of *Colletotrichum* Species Isolated from Soursop in Colombia, European journal of plant pathology, Vol. 139, Issues 2, 2014, pp. 325–338, Available from: doi:10.1007/s10658-014-0388-7.

[27] Prihastuti H., Cai L., Chen H., McKenzie E.H.C., and Hyde K.D., Characterization of *Colletotrichum* Species Associated with Coffee Berries in Northern Thailand, Fungal Diversity, Vol. 39, Issues 1, 2009, pp. 89–109.

[28] Swofford D.L., PAUP*: Phylogenetic Analysis using Parsimony (*and other methods), Version 4, Sinauer Associates, Sunderland, Massachusetts, 2002.

[29] Felsenstein J., Confidence Limits on Phylogenies: an Approach using The Bootstrap, *Evolution*, Vol. 39, Issues 4, 1985, pp. 783–791, Available from: doi:10.1111/j.15585646.1985.tb00420.x.

[30] Schoch C. L., Seifert K. A., Huhndorf S., Robert V., Spouge J. L., Levesque C. A., Chen W., Bolchacova E., Voigt K., and Crous P. W., Nuclear Ribosomal Internal Transcribed Spacer (ITS) Region as A Universal DNA Barcode Marker for Fungi, Proceedings of the National Academy of Sciences, Vol. 109, Issues 16, 2012, National Acad Sciences, pp. 6241–6246.

[31] Schultz J., Maisel S., Gerlach D., Muller T., and Wolf M., A Common Core of Secondary Structure of The Internal Transcribed Spacer 2 (ITS2) Throughout The Eukaryota. RNA, Vol. 11, 2005, pp. 361-364, Available from: doi:10.1261/rna.7204505.

[32] Hodkinson T. R., and Parnell J. A. N., *Reconstructing The Tree of Life: Taxonomy and Systematics of Species Rich Taxa*, CRC Press, 2006.

[33] Frisvad J. C., Andersen B., and Thrane, U., The use of Secondary Metabolite Profiling in Chemotaxonomy of Filamentous Fungi, Mycological Research, Vol. 112, Issues 2, 2008, pp. 231–240, Available from: doi:10.1016/j.mycres.2007.08.018.

[34] Numonov, Sodik, Farukh Sharopov, Aminjon Salimov, Parviz Sukhrobov, Sunbula Atolikshoeva, Ramazon Safarzoda, Maidina Habasi, and Haji Aisa. "Assessment of Artemisinin Contents in Selected Artemisia Species from Tajikistan (Central Asia)." *Medicines*. vol 6, Issues 1, 2019, pp. 23

7th Int. Conf. on Structure, Engineering & Environment (SEE), Pattaya, Thailand, Nov.10-12, 2021, ISBN: 978-4-909106070 C3051

ANALYSIS OF SOIL QUALITY INDEX AT POTATO PRODUCTION CENTER IN THE UPSTREAM OF LEMBANG WATERSHED

Aprisal [1], Bambang Istijono [2], Irwan Darpis[1], Mimin Harianti[1], and Teguh Huria Aditia[3].

[1] Soil science of Agriculture Faculty Andalas University, Padang Indonesia
[2] Hydrology laboratory technique Faculty Andalas University Padang Indonesia
[3] Postgraduate of Soil Science of Agriculture Faculty Andalas University Padang, Indonesia

ABSTRACT

Potato is considered as one of the primary agricultural commodities in the upstream of Lembang watershed. Rotation cropping system using shallots is occasionally adopted, due to market price influence and higher profitability. This cultivation process typically instigates soil degradation devoid of conservation measures. The land survey approach was employed as the research method, while proportional random sampling was used to select the sample. Subsequently, the soils were categorized into intact and disturbed portions to analyze the physical (texture, specific gravity, C-organic and permeability) as well as chemical (nitrogen, phosphorus, potassium, calcium, magnesium, pH, and CEC) properties, respectively, at the Soil Laboratory of Agriculture Faculty, Andalas University. These data were processed using Minitab 17 to determine the soil quality index. The results showed the existence of three primary components (PC) termed, PC1, PC2 and PC3, believed to influence the alternating index state by 80%. Furthermore, the dominant variables of these components include exchanged potassium, organic C and clay fraction texture. Based on the calculation of component factors and soil properties, the soil quality index (SQI) was classified into moderate, good and very good conditions.

Key words: soil quality index, production center areas, soil properties. conservation, degradation. potato

INTRODUCTION

Extreme exploitation of agricultural resources without considering the consequences, significantly contributes to soil quality degradation. In conventional farming systems, suitable conservation methods, including the deposition of harvest remnants are less applied. This results to the loss of several useful nutrients absorbed in the plant. Also, the rigorous application of chemical fertilizers greatly influenced certain soil properties, including pH decline and other related rapid changes. Therefore, agricultural management devoid of conservation measures triggers a decrease in terms of soil quality and environment. This circumstance continues to adversely affect productivity, eventually leading to a diminished potato grade [1]. In another study, the product quality was strongly influenced by genetic factors and soil ecosystems [2]. Meanwhile, in advanced farming, artificially engineered soil ecosystems include field, water and fertilizer management, responsible for regulating soil microenvironment. This ecosystem serves as a plant growth carrier and also provides the necessary nutrients for effective development [2], [3]. [1], further stated that without adequate cultivation control, the income from potato farming tends to decline. In several instances, farmers prefer to cultivate other commodities, including onions. This situation threatens the research location as a viable potato production base. There is a crucial need to examine the soil quality, in an effort to overcome the prevalent challenge. This property appears very essential in terms of agricultural management [5]. Soil system refers to the change in the properties and the dynamic nature of soil management is potentially due to the complex technical structure in plant cultivation. Also, the concept of soil quality is associated to effective sustainability and management, with a primary focus on contaminated land. Previous report stated that the notion of soil quality is expected to include productivity, fertility, and degradation, as well as environmental values. Therefore, by this definition, the main activity is devoted to the evaluation of a sustainable soil management system alongside the development of a related soil quality assessment. This research is aimed at determining the soil quality status for potato cultivation in various forms within the upstream of Lembang sub-watershed.

Location and Research Methodology

Research Location

The research location is situated in the upstream of Lembang sub-watershed, in close proximity to Talang mountain, a known active volcano in Solok

regency, and also adjacent to Dibawah Lake. In addition, the sample soil containing several volcanic residues was nominated by Andisol and Inseptisol orders. This region shows a rainfall estimate of approximately 2,333 mm/year and also serves as a potato production centre in Solok. Furthermore, the research was conducted on five farmer groups, termed I, II, III, IV and V, on the basis of the land physiography. Group I and IV appeared flat, while II was described as slightly sloping. However, III and V showed a sloping pattern. These structures confirmed the sample location as a viable center for potato production.

Soil sample collecting

Field survey was employed to obtain the secondary and primary data at pre-determined locations (Figures 1, 2 and 3). The primary data involves soil sampling at several locations of the five farmer groups. This sample was acquired at a depth of 20 cm, using purposive random technique. Furthermore, the intact portions were applied to analyze the physical properties, while the disturbed samples were used to determine the chemical and biological features.

Table 1. Groups, soil types and sampling points

Location	Soil type	Soil sampling	Plan type
I	Andisol	3	Potatoes
II	Andisol	2	Potatoes
III	Inceptisol	4	Potatoes
IV	Inceptisol	2	Potatoes
V	Inceptisol	2	Potatoes

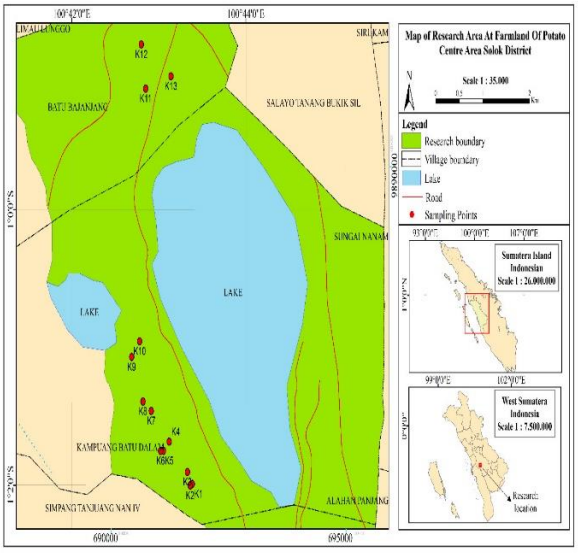


Figure 1. Research location in the potato production area at the upstream of Lembang sub-watershed, Solok regency.

Table 2. Parameters to be observed as minimum data set (MDS) for soil quality analysis in potato production areas.

Observation Variable	Variable	Method
Soil Physical Properties	Soil texture (%)	Pipette
	Bulk density (g/cm3)	Volumetric
	Total pore space (%)	Volumetric
	C-organic (%)	Walkley and black
Soil Chemical Properties	pH	pH meter
	N-Total (%)	Khjedal
	Available-P soil (ppm)	Bray II
	Ca (cmol/kg)	
	Mg (cmol/kg)	
	CEC (cmol/kg	Washing with Ammoniu m
	Available-K soil (cmol/kg)	Washing with Ammoniu m
	KB (cmol/kg)	
	DHL (electrical conductivity) µs/cm	



Figure 2. Observations on the potato plant conditions.



Figure 3. Performance of potato land.

Also, the sampling technique was conducted in four potato farmland groups around the Dibawah lake. (2) The secondary data encompassed the land conditions and the aspects of potato cultivation.

Data analysis with PCA

The preferred data analysis method was based on the lowest characteristics with optimal influence on soil quality or the minimum data set (MDS) using Minitab 17.0. Also, the MDS was generated with the principal component analysis (PCA), while the soil quality evaluation was achieved by multiplying the MDS weight and the soil analysis value, followed by the addition of scores obtained for individual land use. This data analysis value was obtained within the range of 1-5. Consequently, higher variables triggered a corresponding increase in the soil quality [7]. Furthermore, the systematic assessment of soil quality was calculated by the soil quality index (SQI) formula:

$$SQI = \sum_{i=1}^{n} Wi \; x \; Si$$

Description:
IKT = soil quality index
Wi = Weight factor in PC
Si = score index (soil quality indicator score).

Table 3 represents the soil quality classification after obtaining the index value.

Soil Quality	Scale	Class
Very Good (SB)	0.8 – 1	1
Good (B)	0.6 – 0.79	2
Moderate (S)	0.35 – 0.59	3
Low (R)	0.20 – 0.34	4
Very Low (SR)	0 – 0.19	5

RESULT AND DISCUSSION

Soil properties

Table 4 represents the analysis of the physical, chemical and biological soil properties. This depiction also indicate a relative satisfactory criteria for these characteritics, including pH, C-organic, phosphorus, CEC and K-dd. Based on Table 5, the research location showed a soil dominance with dusty loam texture and crumb structure, as well as high suitability for potato cultivation. Table 6 shows the soil fertility status was based on soil characteristics variables, including C-organic, phosphorus, potassium, CEC, and K-dd, ranging from low to high. This demonstrates a high ability as a cultivation medium and provides root nutrients. In a sustainable carrying capacity, the plants tend to develop optimally. Based on the key variables, soil fertility status, termed C-organic appeared relatively high, due to a value above 2%. This condition also resulted from excessive application of organic fertilizers e.g manure. [8]. According to Cation exchange capacity (CEC) refers to a major soil chemical properties closely related to plant nutrient availability and also serves as a fertility indicator. This parameter describes the potentials of clay to bind and exchange cations depending on the clay content and types as well as the organic matter. Furthermore, CEC also defines the soil cations, including Ca, Mg, and Na. These elements are exchanged or absorbed by plant roots.

In determining the extent of dominant soil properties, the quality index is evaluated from the principal component analysis (PCA) results (Tables 7 and 8). As a consequence, three primary components, termed PC1, PC2 and PC3 occurred as the factors in evaluating the diversity of soil quality indices.

Table 4. Biophysical properties of research soil from potato production centers

Sampling	pH	C-org	N	C/N	P	KTK	K-dd	Ca	Mg	Kj.KB	DHL	Pasir	Debu	Liat
		(%)	(%)		(ppm)		cmol/kg			%	µs/cm		%	
1	3,7	6,94	1,32	5,26	479,16	61,33	0,26	3,22	0,47	6,75	86,4	6,26	68,86	24,84
2	4,85	7,08	0,83	8,53	11,6	54,52	0,16	0,96	0,11	2,57	66,4	13,07	70,1	16,7
3	5,89	4,45	1,2	3,71	64,73	41,79	0,53	6,02	0,51	17,37	53,9	20,58	57,87	18,26
4	5,1	6,99	1,41	4,96	8,12	43,22	0,29	0,8	0,15	3,22	70,4	7,91	62,94	26,1
5	5,58	8,31	0,99	8,39	31,21	37,68	0,6	3,05	0,21	10,59	50,2	11,66	62,48	22,23
6	5,47	9,26	0,59	15,53	25,75	37,4	0,19	1,92	0,32	7,65	27,5	16,07	57,83	33,25
7	4,3	7,56	1,4	5,4	47,35	46,22	0,32	1,24	0,27	4,24	188,3	8,82	61,52	23,9
8	5,16	9,9	0,96	10,31	14,82	36,55	0,55	1,37	0,23	6,01	66,6	14,58	51,51	23,9
9	5,8	10,18	0,55	18,51	9,36	31,24	0,51	3,93	0,38	15,65	58,2	25,5	66,48	8,02
10	5,67	9,4	0,72	13,06	7,87	43,03	0,51	2,96	0,41	9,46	51,9	17,39	67,44	15,17
11	7,11	11,59	0,98	11,83	237,8	19,75	1,47	7,17	0,42	46,68	66,1	24,67	51,13	24,21
12	6,87	11,74	0,31	37,87	230,85	43,96	1,24	7,86	0,74	22,68	58,6	13,2	44,73	42,07
13	6,77	8,62	0,34	25,35	673,58	17,34	1,65	6,59	0,55	51,5	133,4	34,7	47,38	17,92

Table 5. Soil texture classes based on the USDA texture triangle in the potato production area.

Sampling	Sand	Dust	Clay	Texture class
1	6.26	68.86	24.84	Silt loam
2	13.07	70.1	16.7	Silt loam
3	20.58	57.87	18.26	Silt loam
4	7.91	62.94	26.1	Silt loam
5	11.66	62.48	22.23	Silt loam
6	16.07	57.83	33.25	Silty clay loam
7	8.82	61.52	23.9	Silt loam
8	14.58	51.51	23.9	Silt loam
9	25.5	66.48	8.02	Silt loam
10	17.39	67.44	15.17	Silt loam
11	24.67	51.13	24.21	Silt loam
12	13.2	44.73	42.07	Silty clay
13	34.7	47.38	17.92	Clay loam

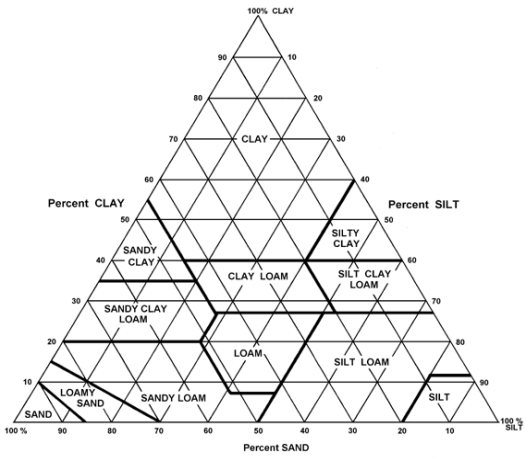


Figure 2. Soil Texture Triangle (USDA).

Table 6. Soil fertility status based on key variables of fertility in potato production centers in the upstream of Lembang sub-watershed.

Sample	C-org (%)	P (ppm)	CEC cmo/kg	K-dd cmol/kg	Kj.KB %	Fertility Status
1	6.94 st	479.16 st	61.33 st	0.26 rd	6.75 sr	t
2	7.08 st	11.6 st	54.52 st	0.16 rd	2.57 sr	t
3	4.45 t	64.73 st	41.79 st	0.53 t	17.37 sr	sd
4	6.99 st	8.12 r	43.22 st	0.29 sd	3.22 sr	sd
5	8.31 st	31.21 t	37.68 t	0.6 t	10.59 sr	t
6	9.26 st	25.75 sd	37.4 t	0.19 r	7.65 sr	sd
7	7.56 st	47.35 st	46.22 st	0.32 sd	4.24 sr	sd
8	9.9 st	14.82 rd	36.55 t	0.55 sd	6.01 sr	r
9	10.18 st	9.36 sr	31.24 t	0.51 sd	15.65 sr	r
10	9.4 st	7.87 sr	43.03 st	0.51 sd	9.46 sr	sd
11	11.59 st	237.8 st	19.75 sd	1.47 st	46.68 sd	t
12	11.74 st	230.85 st	43.96 st	1.24 st	22.68 r	t
13	8.62 st	673.58 st	17.34 sd	1.65 st	51.5 t	t

Description: r = low, sr = very low, sd = moderate, t = high, st = very high.

Principal Component Analysis (PCA)

Table 7. The results of the eigenvalue calculation on the soil biophysical property variable in the potato production centre in the upstream of Lembang sub-watershed.

Eigenvalue	7.4477	1.9673	1.7146	0.9875	0.8250	0.3841	0.3671	0.1526	0.0800	0.0417
Proportion	0.532	0.141	0.122	0.071	0.059	0.027	0.026	0.011	0.006	0.003
Cumulative	0.532	0.673	0.795	0.866	0.924	0.952	0.978	0.989	0.995	0.998

Table 7 represents the eigenvalues from PCA analysis and indicates the influence of a variable on soil characteristics. The determining factor is retained in the model with values above 1, but absent at estimates below 1. Also, the eigenvalue expresses the element contributing to the variance in the entire variables. However, only factors with variance greater than 1 are included, while no importance is attached to values less than 1, as the original variable has been standardized. This means the average is 0 and the variance is 1 [9].

The soil analysis data obtained three factors (PC), termed PC1, PC2 and PC3, with eigenvalues above 1. Each PC describes a certain amount of variation (%) in the total data set needed to generate a value for the selected variable. Also, three factors significantly influence the soil quality index. The first, PC1, obtained an eigenvalue of 7.44%, with a 53.2% proportion of influence on variables, including pH and K-dd. Subsequently, the second factor, PC2, attained an eigenvalue of 19.67%, with C-org, C/N ratio, CEC and clay fraction content. These parameters were used to determine the soil quality at 14.1%. Meanwhile, the third factor, PC3, showed an eigenvalue of 17.14 %, comprising phosphorus (P) and DHL. Furthermore, the three factors, PC1, PC2 and PC3, contributed to the overall cumulative variance of approximately 80%. This result indicates the variables of components 1, 2 and 3 were able to separately comprehend the influence on the soil quality diversity.

Table 8 represents the loading matrix values from soil property analysis. A high variable estimate on PC1, in the form of potassium (K-dd) was specified at 0.345. Meanwhile, the maximum element on PC2 referred to the clay fraction, or soil texture, with a loading value of 0.565. Finally, the third parameter, PC3, represented the optimal variable as C-organic. Ultimately, the three greatest estimates were applied in the analysis of soil quality index (Table 9).

Soil quality index

Table 9 represents the soil quality indices obtained by multiplying the weight index and the score indicator. These SQI values ranged between 0.51-0.97, where a higher estimate instigates an increase in soil quality. In addition, the research location generated a scale of moderate to very good. The dominant determining factors in the sample soil quality index refer to the availability of potassium (K-exchangeable) and soil texture, including the clay fraction and organic carbon content. Several studies reported the potassium content in potassium-based fertilizer tends to increase tuber accumulation, dry matter, crude starch synthesis and dissolved vitamin C [10]. Meanwhile, the application of NPK fertilizers significantly improved the potato tuber quality. Furthermore, organic carbon matter greatly influences the soil structure, as the soil remained loose. Increasing soil organic matter enhances the physical properties and the nutrients, leading to extensive crop biomass and yield [11].

Table 8. The loading matrix value from analysis of soil biophysical properties

Variable	PC1	PC2	PC3
pH	0.328	0.020	0.228
C-org	0.222	0.295	0.232
N	-264	-0.183	-0.273
C/N	0.289	0.316	0.018
P	0.207	-0.191	-0.468
CEC	-0.276	0.265	-0.259
K-dd	0.345	-0.105	-0.106
Ca	0.319	-0.002	-0.139
Mg	0.267	0.144	-0.287
KB	0.331	-0.253	-0.071
DLH	-0.006	-0.319	-0.482
Sand	0.279	-0.364	0.239
Dust	-0.294	-0.150	0.153
clay	0.068	0.565	-0.320

The physical, chemical and biological soil properties are important considerations in determining soil quality. This is due to the very dynamic state prevalent in intensive potato farming. [12]. In addition, a significant aspect of the biophysical properties refers to organic matter. This variable serves as an essential indicator for soil health and also shows a high influence on crop yields [13].

Table 9. Soil quality index in potato production centers area

Group	S1 K-exchangable	W1 Weight	S2 Soil texture (clay fraction)	W2 Weight	S3 Organic carbon	W3 Weight	SQI	SQI Class
I	0.25		1		1		0.88	sb
	0.1		1		1		0.83	sb
	0.5		0.5		0.25		0.51	sd
II	0.25		1		1		0.88	sb
	0.5		0.75		0.75		0.77	b
III	0.25		1		1		0.88	sb
	0.5	0.345*	0.5	0.565*	1	0.232*	0.69	b
	0.5		1		1		0.97	sb
IV	0.5		1		1		0.97	sb
	0.5		0.5		1		0.69	b
	0.75		0.5		1		0.77	b
V	0.75		0.5		1		0.77	b
	0.75		0.75		1		0.91	sb

Description: S ; score index, W ; weights, SQI ; soil quality index, sb ; very good, b ; good, sd; medium.

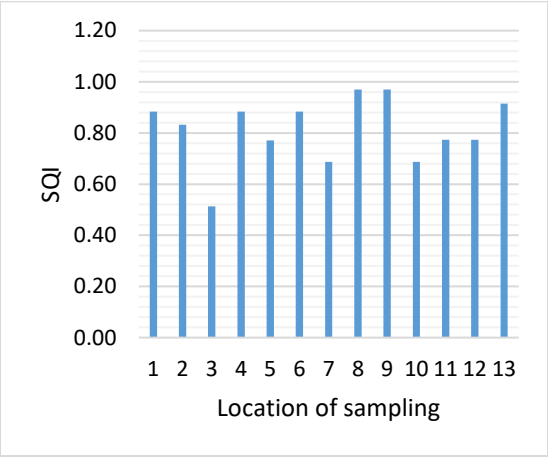


Figure 3. Histogram of SQI comparison from research location in the potato production center

Figure 4 shows the comparison of SQI between soil sample locations. Based on the histogram, the diversity of SQI in the potato production centre in the upstream of Lembang sub-watershed, Solok regency, was significantly influenced by the landform variation and land management.

CONCLUSION

Based on the results on the soil quality index in the potato production centre, the soil quality index was dominated by good and very good classes, while only one location was specified in the moderate class in soil group 1. Furthermore, the dominant factors influencing the soil quality index included the properties of potassium availability, organic C, and texture from the percentage of clay fraction.

ACKNOWLEDGMENTS

This research was funded by Andalas University under Research Grant No SP DIPA 023.017.2.677513/2021, 23 Novemver 2020

REFERENCES

[1]. Aprisal. Istijono, B ., Mimin, H., Juniarti. 2018. Soil quality index analysis under horticultural farming in Sumani Upper Watershed. International Journal of Geomate, April 2019, Vol.16, Issue 56, pp. 191 - 196 ISSN: 2186-2982 (P), 2186-2990 (O), Japan.

[2]. Qi Hu, Ning Yang, Feifei Pan, Xuebiao Pan, Xiaoxiao Wang and Pengyu Yang. 2017. Adjusting Sowing Dates Improved Potato Adaptation to Climate Change in Semiarid Region, China. Journal Sustainability 2017, 9, 615.

[3] Bhandaria,K.B., Charles P. Westa, Veronica Acosta-Martinezb , Jon Cottonb , and Amanda Cano. 2018. Soil health indicators as affected by diverse forage species and mixtures in semi-arid pastures. Applied Soil Ecology 132 (2018) 179–186

[4]. Karlen, D.L., M.J. Mausbach, J.W. Doran, R.G. Cline, R.F. Harris, and G.E. Schuman. 1997. Soil quality: A concept, definition, andframework for evaluation. Soil Science of America Journal 61: 4- 10

[5]. SQI, 2001. Guidelines for Soil Quality Assessment in Conservation Planning. Soil Quality Institute. Natural Resources Conservation Services. USDA

[6]. Doran, J.W. and T.B.Parkin. 1999. Quantitative Indicators of Soil Quality: A Minimum Data Set. In:

Doran, J.W. and A.J. Jones (Eds). 1999. Methods for Assessing Soil Quality. Soil Science Society of America, Inc. Wisconsin.

[7]. Pratono, S. A. C., Supriyadi, and Purwanto. 2011. Zoning of Rice Field Quality in Industrial Area of Bengawan Solo Watershed Area of Karanganyar Regency. Journal of Soil Science and Agroklimatologi 8 (1) : 1-12

[8]. Herawati Soekamto. 2015. Study on the status of soil fertility in cocoa land, Kampung Klain, Mayamuk District, Sorong Regency, Miraculous Agriculture, Muhammadiyah University, Sorong.

[9]. Santoso,S. 2002 "SPSS Multivariate Statistics", Jakarta: PT. Elex Media Kompitundo.

[10].Yingying Xing , Xiaoli Niu , Ning Wang, Wenting Jiang , Yaguang Gao and Xiukang Wang. 2020. The Correlation between Soil Nutrient and Potato Quality in Loess Plateau of China Based on PLSR. Journal Sustainability 12(4) 1588

[11].Liu, S.J. Herbert2, A.M. Hashemi2, X. Zhang1, G. Ding. 2006. Effects of agricultural management on soil organic matter and carbon transformation – a reviewX. Journal of plant soil environ., 52, 2006 (12): 531–543

[12]. Ball, A., & De la Rosa, D. (2006). Modeling possibilities forthe assessment of soil systems. In: N. Uphoff, A. Ball, E. Fernandes, H. Herren, O. Husson, M. Laing, Ch. Palm, J. Pretty, P. Sanchez, N. Sanginga, & J. Thies (Eds.), Biological approaches to sustainable soil systems (pp. 683–692). Boca Raton, FL: Taylor & Francis/CRC Press.

7th Int. Conf. on Structure, Engineering & Environment (SEE), Pattaya, Thailand, Nov.10-12, 2021, ISBN: 978-4-909106070 C3051

EFFECTS OF BA ON IN VITRO CALLUS DEVELOPMENT FROM LEAVES OF EUPHORBIA MILII

Pantipa Limsanguan, Teerayut Klumchaun, Pennapha Suphatphol, Jutamas Taosanosieng and Onpreeya Chana-in
Faculty of Agricultural Technology, Rajamangala University of Technology Thanyaburi, Thailand

ABSTRACT

The callus induction from *Euphorbia milii* leaves on solid MS medium containing NAA at 3 mg/l in concerted with 1 mg/l BA was performed for 4 weeks. The calli were then subjected to solid MS medium containing 0, 1, 3, 5, 7 and 9 mg/l BA. The tissue was cultured under 50 µmole/m^2/s, 16 hr. light and 25±2°C for 8 weeks. The experimental design was completely randomized design (CRD) with 10 replications, each of 2 pieces. The results revealed that the difference in responses to BA concentration of callus was statistically significance ($p \leq 0.05$). The 1 mg/l BA yielded the highest weight and size of callus were 4.86 g and 7.00 cm^2 followed by 3 mg/l BA the weight and size of callus 4.26 g and 6.69 cm^2 were obtained respectively. For root induction it was found that 5 mg/l BA yielded the highest number of roots 20.00 roots followed by 9 mg/l BA as 17.50 roots was obtained respectively.

Keywords: Euphorbia milii, Micropropagation, Callus, Leaves

INTRODUCTION

Euphorbia milii is native to the forests of North Africa, Commonly named “crown of thorns”, it is a colorful flowers, many colors, woody shrub, very spiny, with milky latex that can reach a height of 1.5 m with an equal spread. It is usually grown as a flowered pot plant but can also be used in the landscape. [1] When flowering, the flowers will have a distinctive color. It is generally considered that Poysean is an auspicious plant. The term Poysean is derived from a Chinese legend and means “eight saints”; it is believed that taking care of these plants could bring good luck, money and gold.

The plants of *Euphorbia* can be grown year round in dry, high temperature and high solar radiation areas as potted, bedding, or garden plants [2]. *Euphorbia milii* is a much esteemed plant for pot culture owing to its brilliant inflorescences. Crown of thorns is commercially propagated by tip cuttings [3], but slow-growing and limited-branching habit is a major hurdle for propagation. As a result, plant tissue culture techniques play a role. In order to increase the knowledge of the propagation techniques, a micropropagation trial has been carried out with the aim to investigate the effects of BA on callus development from leaves of *Euphorbia milii*.

MATERIAL AND METHODS

Plant Materials and Surface Sterilization

The plant material in this research is cultivar of commercial grown *Euphorbia milii* (Terd Thai). These leaves were first washed in tap water with liquid detergent (Sunlight®), and then rinsed with tap water 2-3 times. The explants were surface sterilized with 70 % ethanol for 2 min, followed by immersion 20 min in a sterilization solution of 20 % (v/v) Haiter® containing 2-3 drops Sunlight® emulsifier per 100 ml solution. Leaves were then rinsed 2 times with sterile distilled water.

Callus Induction and Callus Development

The leaves were surface sterilized and then leaves were cut into 0.5x0.5 cm long segments and cultured on solid Murashige and Skoog medium (MS) [4] containing NAA at 3 mg/l in concerted with 1 mg/l BA was performed 4 weeks for callus induction. The calli were then subjected to solid MS medium containing 0, 1, 3, 5, 7 and 9 mg/l BA. The tissue was cultured under 50 µmole/m^2/s, 16 hr. light and 25±2°C for 8 weeks. *In vitro* plantlets were subcultured at monthly. The experimental design was completely randomized design (CRD) with 10 replications, each of 2 pieces. The development of callus was observed for callus weight, number of roots and size of callus.

Statistical Analysis

The callus was examined by analysis of variance. The differences among the mean values of treatments were compared using Duncan's multiple range test (DMRT) at $P<0.05$.

RESULTS AND DISCUSSIONS

Callus Induction

The callus induction from *Euphorbia milii* leaves on solid MS medium containing NAA at 3 mg/l in concerted with 1 mg/l BA was performed for 4 weeks. It was found that in the first week the leaf plates began to bend. After 2-3 weeks, the callus developed in the beginning a light green compact callus starting from the adaxial surface and the cut end of the explants. At the 4th week the callus proliferation increased, resulting in a callus clump that covered the entire explants surface (Fig. 1). Callus formation from leaves segments of *Euphorbia milii* was studied. MS medium was used throughout the experiments. The medium containing a concentration of BA and NAA gave callus production. This may be due to two main factors. The first is internal factors such as the concentration level of plant growth regulators. And the second is external factors such as medium composition, temperature and cultured conditions.

However, as observed in the present study, only one species in this result requires supplementary cytokinin along with auxin for optimum response and in some cases to prevent necrosis of callus. This requirement for exogenous cytokinin could be related to the maintenance of a proper balance between auxin and cytokinin, which act synergistically to regulate cell division [5], a process essential for callus formation. Moreover, [6] reported that appropriate auxin and cytokinin levels are required for callus induction from each species or variety.

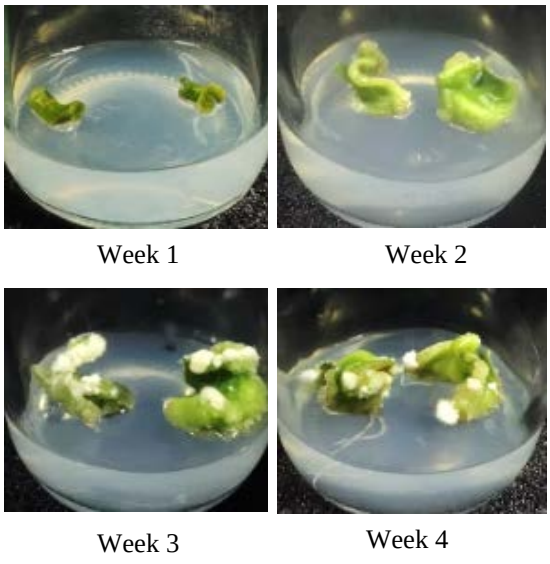


Fig. 1 Time course development of callus induction from *Euphorbia milii* leaves on solid MS medium containing NAA at 3 mg/l in concerted with 1 mg/l BA

The Effect of BA on Callus Development

When the callus transferred to solid MS medium supplemented with 0, 1, 3, 5, 7 and 9 mg/l BA. The statistical analysis of variance showed that callus weight, number of roots and size of callus were significantly difference ($p \leq 0.05$) and data are presented in Fig. 2 and Fig. 3. The results revealed that the difference in responses to BA concentration of callus. The 1 mg/l BA yielded the highest weight and size of callus were 4.86 g and 7.00 cm^2 followed by 3 mg/l BA the weight and size of callus 4.26 g and 6.69 cm^2 were obtained respectively. For root induction it was found that 5 mg/l BA yielded the highest number of roots 20.00 roots followed by 9 mg/l BA as 17.50 roots was obtained respectively. Many factors are important for callus development; genotype, composition of the nutrient medium, physical growth factors (light, temperature, ect.).The MS [4] mineral medium or modification of this are often used. Sucrose or glucose (2-4%) is usually employed as the sugar source. The effect of light on callus development is dependent on the plant species; light may be required in some case and darkness in other cases. A temperature of 22-28 °C is normally advantageous for callus development.

When the callus was cultured on MS medium supplemented with various concentration of BA. The results revealed that, the difference effect on the development concentration of callus was in terms of weight, number of roots and size of callus. This formula of solid MS medium was not yet able to induce a shoot, possibly because the balance of the plant growth regulator was not suitable for plant formation. Our results are in disagreement with the finding of [7] who reported that Kinetin was the most effect agent for regenerating shoots from callus of *Panicum maximum* Jacq. They reported that 3-4 mg/l kinetin significantly promoted shoot induction. And this finding was not similar to the study by [8]. They studied the effect of NAA and BA on callus and shoot formation of *Asparagus racemosus* Wild. The result revealed that Shooting was 100 from leaves cultured on medium added with 1 and 2 mg/l BA. [9] Postulated that the increment in branch number as a result of BA application may be attributed to its influence on counteracting or eliminating the apical dominance. [10] Mentioned that cytokinins are derivatives of the nitrogenous base adenine and are noted primarily for their capacity to stimulate cell division in tissue culture. Cytokinins also influences a number of other developmental responses, including shoot and root differentiation in tissue culture. Benzyladenine (BA) is an aromatic cytokinin that is found in only a few species. It is most commonly used in micropropagation work.

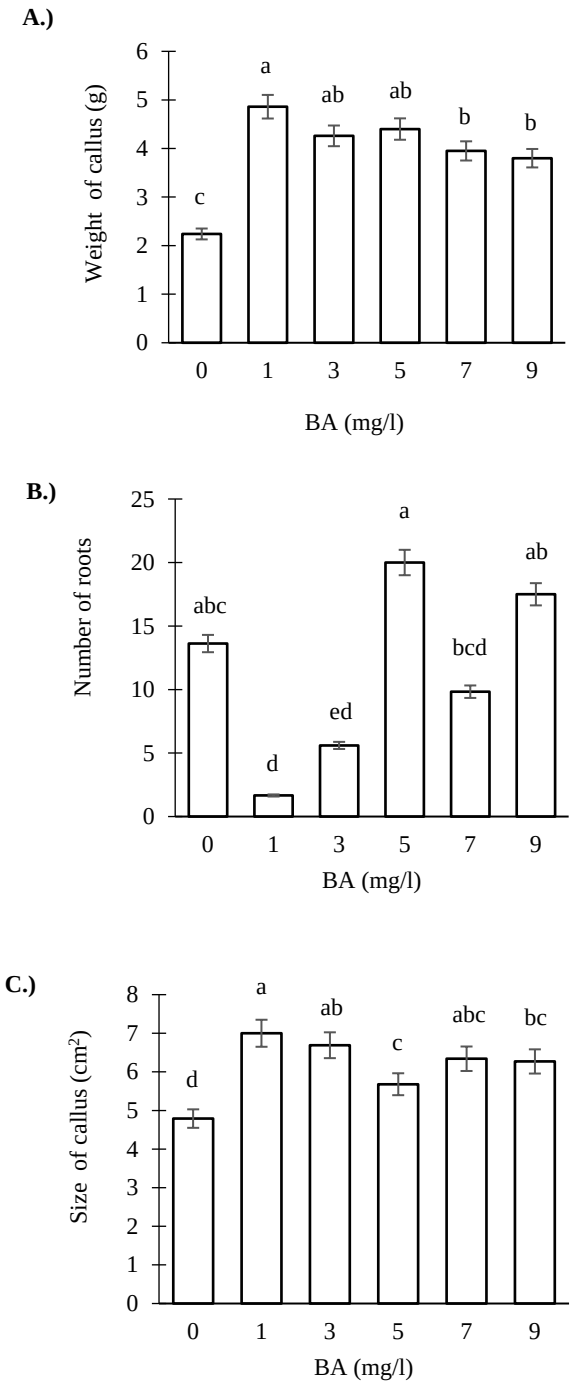


Fig. 2 The average callus weight (A), number of roots (B) and size of callus (C) derived from *Euphorbia milii* leaves cultured on solid MS medium containing 0, 1, 3, 5, 7 and 9 mg/l BA for 8 weeks, where columns with different superscripts are significantly different at $p<0.05$ and error bars indicate standard deviation of data.

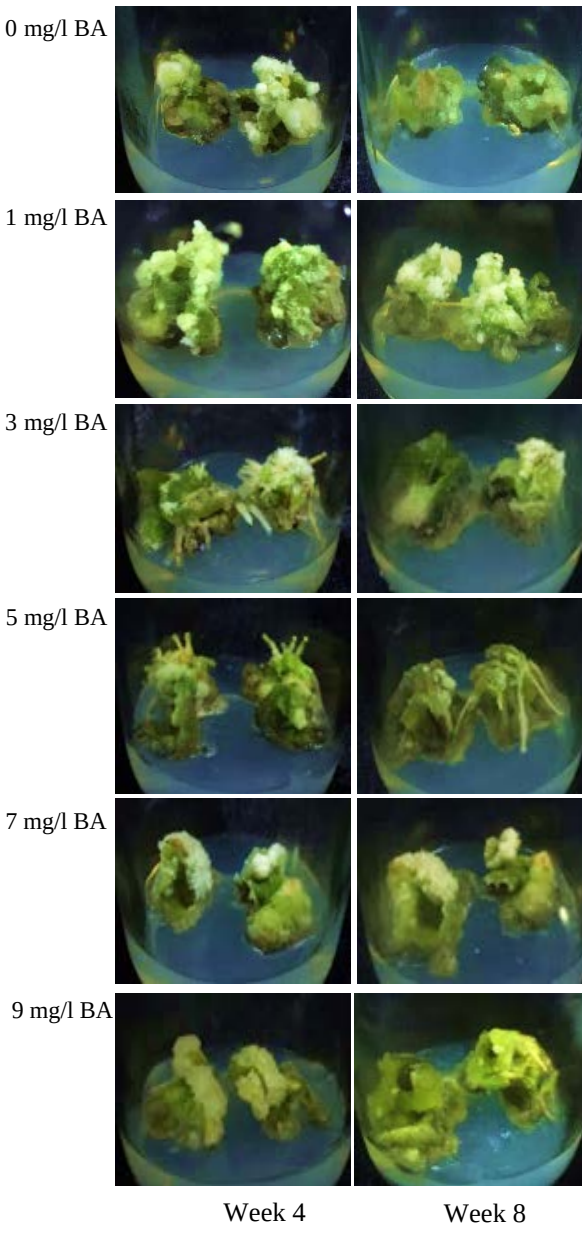


Fig. 3 Callus development from *Euphorbia milii* leaves cultured on solid MS medium containing 0, 1, 3, 5, 7 and 9 mg/l BA for 4 and 8 weeks

CONCLUSIONS

The research was carried out answer the question regarding the effect of BA on callus development from leaves of *Euphorbia milii*. The 1 mg/l BA yielded the highest weight and size of callus followed by 3 mg/l BA. For root induction it was found that 5 mg/l BA yielded the highest number of roots followed by 9 mg/l BA respectively.

ACKNOWLEDGMENTS

The author would like express thanks to The Division of Crop Production, Faculty of Agricultural Technology, Rajamangala University of Technology Thanyaburi for equipment and laboratory used in the experiment.

REFERENCES

[1] Airo M., Zizzo G.V. and Ruffoni B., *In Vitro* Propagation of an *Euphorbia milii* Hybrid. Acta Horticulturae. Vol. 748, 2007, pp. 241-246.

[2] Jankalski S. Crown of Thorns hybrids- Past and present. Cactus Succulent Journal. Vol. 72, Issue 4, 2000, pp. 202-204.

[3] Smoley R. Giant-flowered *Euphorbia milii* hybrids. Cactus Succulent Journal. Vol. 72, 2000, pp. 198-201.

[4] Murashige T. and Skoog F. A revised medium for rapid growth and bioassays with tobacco tissue cultures. Plant Physiology. Vol. 15, 1962, pp. 473-497.

[5] Johri M.M. and Mitra D. Action of plant hormones. Current Science. Vol. 80, 2001, pp. 199-205.

[6] Rout G.R. and Das P. Recent trends in the biotechnology of chrysanthemum: A critical review. Scientia Horticulturae. Vol. 69, 1997, pp. 239-257.

[7] Saura C., Martin Z., Prieto M. and Santana K. Plant regeneration from tissue culture in guinea grass, *Panicum* maximum Jacq. Pastosy Forrajes. Vol. 10, Issue 3, 1987, pp. 199-202.

[8] Saensouk P. and Suddee N. Effects of NAA and BA on callus and shoot formation of *Asparagus racemosus* Wild. KKU Research Journal. Vol. 9, Issue 2, 2004, pp. 31-39.

[9] Sachs R. M., Hield H. and Debic J. Dikegulac, a promising new foliar applied growth regulator for woody species. Horticultural Science. Vol. 10, 1975, pp. 367-369.

[10] Hopkins W. G. and Huner N. P. A., Introduction to Plant Physiology, 4th ed. John Wiley & Sons, Inc, 2009, pp. 68- 76, 330-331 and 339-344.

7th Int. Conf. on Structure, Engineering & Environment (SEE),
Pattaya, Thailand, Nov.10-12, 2021, ISBN: 978-4-909106070 C3051

THE MITIGATION PRIORITY OF ORGANIC RICE FARMING RISK IN LOCAL FARMER PERSPECTIVE

Ujang Maman,[1] Arif Sumantri,[2] Dwi Purwoko,[3] Muksin,[4] and Lukman Effendy[5]

[1]Faculty of Science and Technology, Universitas Islam Negeri Syarif Hidayatullah Jakarta, Indonesia
[2]Faculty of Health Science, Universitas Islam Negeri Syarif Hidayatullah Jakarta, Indonesia,
[3]Center for Society and Culture, The Indonesian Institute for Science (LIPI), Jakarta, Indonesia,
[4]State Polytechnic of Jember, East Java, Indonesia
[5]Polytechnic of Agricultural Development, Bogor, Indonesia

ABSTRACT

Organic rice farming system is valuable for healthy food and environmental sustainability. However, the process of organic farming has a high risk which could probably jeopardize the organic status, in which it needs mitigation. But, unfortunately, the risk control is frequently top down and elite judgment. This research, therefore, aims to identify attributes mitigation, determine mitigation priority, and maintain the has-been-implemented organic rice farming attributes in pre-cultivation phase based on local farmer experience. By these objectives, this research adopts IPA (Importance Performance Analysis) model, which begins with collection of organic rice farming mitigation attributes from farmers' perspective, which is followed by exploration of farmers' experiences regarding the urgency and performance of these attributes. Based on sample farmer in West Java whose size is determined by Slovin formula with below-eight-percent error probability, this study found five attributes as the action to mitigates the risk of organic rice farming; and the main priority of risk mitigation – from the five -- is the farmer group association should provide rice seeds themselves; and the achievement that should be maintained is the seeds to be planted should come from organic seedbeds.

Keywords: Mitigation Attributes, Importance, Performance, and Priority of Action

INTRODUCTION

The question of how to optimize the availability of healthy and safe food – in which it is free-chemical input residue – is strongly valuable. The food security, according to The Economist [4], is not merely indicated by food availability and affordability, but it strongly depends on the food health and safe. For Muslim society, the healthy food availability is not merely physical need, but it is part of their faith which could not be separated. The halal and *thayyib* is united concept as Allah told: "O mankind! Eat of that which is halal and *thayyib* on earth…" (Al-Baqarah [2]: 168). Quoting Ibn al-Arabi, Nafis [11] explained, "Thayyib" indicates the thing appropriate for mankind.

The food contaminated by chemical residue of course disturbs the *thayyib.* The literature study pointed out pesticide consists of poisoning effect [14]. The pesticide residue is strongly resistant on leave, fruit and vegetable. The research in several markets of twin cities of R.R. District and Hyderabad, India proved pesticide residues have a strong resistance, and by aids of instrument lab analysis, it could easily be found [3]. Pyne [16] emphasized less than 0.1% of pesticide spraying reaches target properly to attack pest; the major rest contaminates air, water, soil, vegetable, and fruit.

The pesticide's harmful, unfortunately does not become the common farmer's awareness yet. The 95.2% of Indonesian farmers use chemical pesticides to protect plant from plant-disturbing organism [18]. But, unpleasantly, the farmer commonly sprays pesticide regularly without consideration of insect and pest level [5]. The pesticide, for several farmers, is not poison but medicine to increase the yield [15].

The high dependence on pesticide use describes farmer's habit in Indonesia. The other side presents the awareness of pesticide harmful and steps to decrease dependence on this "poison." Fortunately, the organic farming system (OFS) has been widely disseminated. The OFS is a production system to sustain the health of soil, people, and ecosystem [8]

In the Indonesian context, however, the development of OFS gets high challenge as well as high risk which probably nullify the organic status. The ORF practice is not adopted by all farmers yet. Many of them oppositely still depend on chemical input. The two ways of this farming is frequently neighbor, has the same flow of water and area. In addition, the paddy field which has different way of farming is also often line up from upper to lowland. The water which flows from the conventional farming could probably bring the pesticide residue.

The above condition raises the question of how to maintain the status of OFS, and how to mitigate the risk jeopardizes the status of organic product. This research focuses to answer this question based on farmer's traditional practice in Tasikmalaya, West

Java, Indonesia. This area, geographically, is mostly similar with above mentioned illustration.

FRAMEWORK ANALYSIS

The major aims of this research is to make a proper planning in mitigating the risk of organic rice farming system (ORFS) to yield real organic rice. However, this planning is not simply formulated on top down way or based on elite judgment. The action of mitigation is expected does not experience of elite biased. Therefore, this research does not adopt the logic and flow model of house of risk (HOR) -- in which it is frequently implemented in identifying and prioritizing the actions of mitigation -- but follows the Importance Performance Analysis (IPA) model. By adopting the HOR model, Maman *et al*. [9]– for example – started the research by identifying the risk event, the risk agent, and determining the agent that should be prioritized to mitigate by performing the HOR-1's analysis. The next stage of research is exploring the potential of proper action to mitigate the risk. The research finally concluded – by adopting the HOR-2's model -- the 1st, 2nd, 3rd, 4th priority and so on regarding the action of mitigation. But, unfortunately, this identification is based on "the top" decision, which could not properly avoid the elite bias and judgment.

In fact, the planning should be diverse in line with variety of people who will execute the action. The people could probably think the subject planned is important and they have implemented it or even the action has become their habit. The planning for this people should completely be different with the people who think the case is important but they could not perform it yet; and also different with the people who perceives that the item is not strongly important, and they also do not perform it.

By this reason and assumption that farmer is an expert who has many experience and achievement, this research adopt the IPA. The IPA is originally developed by Martilla and James at seventies, which is created to measure customer satisfaction as well as to detect the necessary improvement of a services or product [13]. Fortunately, on the basis of perception on the importance vs performance, the IPA model has been adopted in many fields. Since initial introduction of this model, there are at list 1075 paper with key words of importance and performance in various fields [13].

The basic principle of IPA is confronting between importance vs. performance. A research has adopted the IPA model to present the customer satisfaction of after sale service (ASS) of home appliances [10]. In this context, the researchers identified twenty attributes relating to the satisfaction of ASS. Based on IPA, these twenty attributes have been divided into four categories: (a) high expectation vs high satisfaction; (b) high expectation vs low satisfaction; (c) low expectation vs low performance; and (d) low expectation vs satisfaction. This category practically indicates different implication for management strategy.

In the light of above discussion, this research aims to identify attributes of risk mitigation; categorize the attributes and arrange the planning on the basis of importance and performance.

The risk consists of uncertainty affects unexpected result [2]. The unsuccessful target is a risk indicated by unpleasant result [17]. The risk is a condition that has a possible adverse effect [1]. The risk level is frequently based on people's view, in which the yield is not the same with planned [17].

The ORFS has single risk in cultivating process, namely the probability of organic status loss. The overview on risk inspection in EU organic certification found the farmer's non-compliance (NC) is the main factors for the risk [7]. The EOCC [6] has also emphasized the keyword of NC in certification process of organic farming. Gambelli *et al*. [7] elaborated the NC into farmer's NC attitude, non-organic land, and processing activity. In Indonesian context, by the case of Yogyakarta region, the most of organic farmer is still uncertified, and farmer's awareness of organic farming is relatively low leads to uncomplete implementation of organic principle [19].

The above mentioned risk of organic farming process could probably happen in each step in farming process in pre-cultivation activity, such as in land preparation, irrigation, nursery process, and source of seeds. The mitigation is of course should be explored deeply in this steps.

RESEARCH METHODS

By the aim of exploring farmer's view and practice in mitigating risk of organic rice farming risk (ORFR), this research methodologically adopts importance performance analysis (IPA) model, in which this model is a combination between qualitative and quantitative approach as well as a composite between a grounded exploration and survey sample. Therefore, this research process was started by exploring attributes mitigation of ORFR in pre-planting phase based on local wisdom, farmer's practice, and written as well as unwritten guidance owned by a farmer group association of *Simpatik* in Tasikmalya, Wet Java,.

Although the attribute mitigation is acquired from farmer's view, the research measures quantitatively the importance and performance level of each attribute in Likert scale. Thus, the research is a survey. The population is organic rice practitioner gather in in *Simpatik* farmer group association in Tasikmalaya, West Java; and sample size is 109 farmers based on Slovin formula taken from 236 organic rice farmer with error probability is less than

7%. The research respondents are determined by a proportional stratified random sampling. The research variable is the importance and performance of each ORFR's mitigation attributes.

Following the survey requirement, prior to data collecting, this research performs a validity and reliability test of instruments. Fortunately, in line with Cronbach alfa criteria, this research questionnaire gets 0.942 score of reliability.

Data analysis based on IPA logic and flow adopts following stages. *The first*, categorizing the degree of importance and performance of each ORFR mitigation attribute into high, moderate, and low in the light of this formula [1]:

$$Interval = \frac{\text{The higher Score} - \text{The lower Score}}{\text{Amount of Alternative Category}}$$

Second, counting total score and average of importance and performance level of each attributes based on total of respondents. *Third*, assigning suitability and gap between importance and performance level by adopting following formula:

$$Tki = \frac{\overline{Xi}}{\overline{Yi}} \times 100\% \quad [2]$$

In which:
Tki = Level of suitability
$\overline{Xi}$ = Performance score
$\overline{Yi}$ = Importance score

Forth, providing the matric of importance and performance level, and dividing it into four columns of quadrants by this formula of [3]:

$$\overline{\overline{X}} = \frac{\sum_{i-1}^{N} \overline{xi}}{k}$$

$$\overline{\overline{Y}} = \frac{\sum_{i-1}^{N} \overline{yi}}{k}$$

Where:
$\overline{\overline{X}}$ = Average of the average of performance score
$\overline{\overline{Y}}$ = Average of the average of importance score
K = The number of ORFR attributes

The fifth, presenting each ORFR attributes in Cartesians diagram determining level of priority in quadrant matric based on below formula;

$\bar{X} = \frac{\sum Xi}{n}$ $\bar{Y} = \frac{\sum Yi}{n}$ [4]

Where:
$\bar{X}$ = Average of performance score
$\bar{Y}$ = Average of importance score
n = Amount of respondent

This formula [4] divides all ORFR attributes into four quadrants in a Cartesian diagram. The first (A) presents high importance and low performance indicates high priority of mitigation program. The second (B) identifies high importance and performance indicates the achievement to maintain. The third (C) represents low importance and low performance as a second priority; and the fourth (D) presents high performance but low importance, proving the unimportant attributes to plan.

RESULT AND DISCUSSION

The Attributes of Risk Mitigation

Based on in-depth interviews with organic farmer; and according to Internal Control System (ICS) owned by this *Gapoktan*, this research found five mitigations attributes of organic rice farming, in which the five attributes are coded M1 to M5.

In land preparation, the attribute mitigation is how to make an agreement with all organic farmers not to use agricultural tools and machines that are no longer suitable to use (M1). This is intended to make the prepared land completely sterile from chemical input. In terms of irrigation, the risk mitigation is to create a filter tube in the upstream water -- flow and enter to the organic farming rice area -- by placing water hyacinth above the filter basin (M2). The water hyacinth is -- traditionally and has been become a farmer local wisdom -- able to naturally neutralize chemical residue in water stream.

The next mitigation, in nursery process, the risk mitigation is the farmer should participate in the training of seedling and making organic fertilizers (M3). The training is intended to support the farmers to understand thoroughly organic seeding process; to make them able to provide and produce independently farming material. The training is also useful for the farmers to monitor the pre-planting process in accordance with organic farming standards. The risk mitigation in selection of seed sources, first the seeds should be from organic nurseries (M4), carried out directly by farmer independently as well as by other parties, but the farmers should know the process, which it means that farmers know the origin of the seeds. Second, the *Gapoktan* should provide seeds from independent nurseries as well as the seeds are purchased with an organic label (M5) (Table 1.)

The Importance Level of Attributes Mitigation

The farmer's view of the importance of the attribute of organic farming mitigation is averagely 3.51, indicates high expectations of farmers to implement this attributes. From five mitigation items, the attribute with the code M4, in which the seeds to be planted should be from organic nursery, obtained the highest value of expectation with a score of 3.61, indicates this item is the most important in farmer perspective.

The score of farmers' expectations to implement the attributes spreads between 3.39-3.61 shows the

farmers consider all attributes are important. However, the M3-attributes which encourage farmer to participate in a training to make nursery and organic fertilizer get merely the score of 3.39. It means the farmer has low expectation for this attributes, because making a nursery and organic fertilizer has become a habit of farmer.

The Performance of Attributes Mitigation

This performance is to identify the extent to which the implementation of risk mitigation attributes is practically adopted by the farmer. This performance is measured by a four-level of Likert scale with the keywords according to the context of the question, such as never, often and always. Based on this measurement, the average score of performance of risk mitigation range from 2.55 to 3.52. There are four attributes get high performance, and an attribute gets lower performance.

The performance of risk mitigation attributes – for more clearer – gets an average of average score of 3.20, the medium category. While, based on measurement results regarding the level of importance, the farmers consider the mitigation attributes are important with an average of average score is 3.51 (Table 1.). Indeed, the gap between expectations and performance cannot completely be avoided yet. The gap averagely obtains 0.31. Although it is relatively low, it should get pay seriously attention. Therefore, the gap should be identified for each mitigation attribute.

The attribute that *Gapoktan* must provide organic seeds (M5) get the lowest score compared to other attributes with an average performance's score is 2.55, below the average of average of performance, (3.20). The hope that *Gapoktan* should provide organic seeds is not yet implemented. The farmers in contrary have not utilized the organic rice seeds provided by *Gapoktan*. The other attribute (M1, M2, M3, and M4) obtain relatively high score (Table 1.). The M5-attribute, therefore, should get special attention as the main planning to perform.

The attribute regarding the necessity that the seeds to be planted should come from organic nurseries got the highest average score (3.52). The farmers do not merely consider the high importance of this item, but they also have completely performed this attribute. This attribute could also be considered as the most implementable; and has become a local wisdom and common practice independently to prevent chemical contamination of seeds. This is probably the farmer achievement.

The Compatibility of Expectations and Performance

The compatibility – as well as the gap – is essential following the next stage of IPA analysis model. This presentation is actually providing the asymmetry between expectation and performance. The lower gap attributes hypothetically is the achievement to hold; while the higher gap of attributes could probably the main action to remediate the ORFS. The mapping of the attributes is actually based on this compatibility and gap.

The level of conformity of expectations and performance averagely gets a high percentage, (91 %). This means that in general there is a match between expectations and performance. The highest suitability level of attribute is "participating in a training to make a nursery and organic fertilizer" (M3), which its percentage of compatibility reaches 98 %. The next high suitability is "the seed to be planted comes from organic seedbeds" (M4) which gets percentage of 98. The attribute regarding the suggestion to make a filter tub upstream into organic rice field, topped with water hyacinth (M2) get merely 96 % of suitability. The attribute of provision to make an agreement with all organic farmer not to use agricultural production tool that is not suitable for use or contaminated by chemical input (M1) get merely rank of fourth (93 %). This relatively high gap indicates the difficulty of farmer to perform this provision. The cooperation between farmer is most likely is a very serious problem in farming practice.

The attribute that should get a high attention, in this context, is the item that the *Gapoktan* should provide organic seed independently (M5). The farmer views this provision as the strongly high important item, indicated by the high expectation of farmer in which the average score gets 3.59 from the 108 respondents. But, unfortunately, the performance is strongly low, the score is merely 2.55. The compatibility level between the expectation and performance is also low, merely 71 %. The asymmetry is high, reaches almost 29% (Table 1). Compared with the average of compatibility -- which gets 91 % and the average gap is 9 % -- this attribute should also get a serious attention; and hypothetically the mitigation of ORFS risk should focus on this item; while the other attributes should be hold as an achievement.

Mapping of Risk Mitigation Plan

This mapping is carried out using a quadrant approach, based on the expected value (Y) and performance (X). The results of IPA will properly form a matrix consisting of four quadrants, which each describes the priority scale. The Cartesian diagram matrix consisting of four quadrants is formed by two perpendiculars intersecting lines at the points (Y) and (X). The average value of the average level of performance appraisal can be symbolized by (X), while the average value of the average level of expectation is symbolized by (Y). These two points intersect into four quadrants. The first (I) is located

on the upper left, the second (II) is located on the upper right, the third (III) is located on the lower left, and the fourth (IV) is located on the lower right. These quadrants will bring up which attributes should be a main and low priority, the attributes that should not be planned, and the achievement to hold.

Table 1. The Risk Mitigation Attributes of ORFS

Source of Risk	Attribute Mitigation	Imp Score	Imp Average	Perf Score	Perf Average	Comp (%)
Land Preparation	M1	376	3.45	350	3.21	93
Watering	M2	381	3.50	366	3.36	96
Nursery	M3	370	3.39	364	3.34	98
Source of	M4	393	3.61	384	3.52	98
Seed	M5	391	3.59	278	2.55	71
Av of Av			3.51		3.20	91

Note:
X1: Making agreement with all organic farmers not to use agricultural production tool that is no longer suitable for use or contaminated by chemical input.
X2: Making a filter tub upstream into organic rice fields, topped with water hyacinth;
X3: Participating in a training to make a nursery and organic fertilizers
X4: The seeds to be planted come from organic seedbeds;
X5: Farmer group associations provide organic seeds

The coordinates obtained from the intersect points on (Y) and (X), which is the result of average value of the average level of farmer performance appraisal with the symbol (X) is 3.20. Meanwhile, the average level of expectations symbolized by (Y) is 3.51. The Cartesian diagram matrix obtained based on this intersection is presented in Figure 1, which describes a map of attributes of mitigation of ORFS based on the difference between expectations and performance, which is divided into four quadrants, namely quadrants I, II, III, and IV.

In the light of quadrant, the research concludes the M5 attribute should be priority of the planning in which the farmer group associations provide organic seeds by themselves (Table1). This attributes gets high expectation and low performance. Adopting the IPA's sentence "be concentrate here" to make planning to remediate this attribute. The average of importance level of M5 attribute is 3.59, while the rate of its implementation is merely 2.55. In line with this average score, the compatibility level is also low (merely 71 %), and the gap is high (29%). This attribute places the quadrant I, which concludes that the *Gapoktan* should provide the organic seed for the whole farmer of rice organic farmer. The all sides should support the *Gapoktan* to perform this serious task.

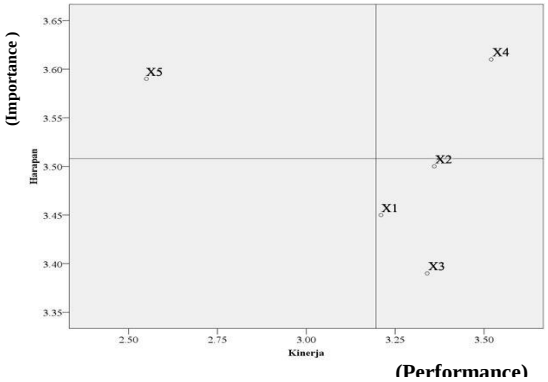


Figure 1. Cartesian Diagram of Risk Mitigation

If the M5 could be considered as the lack of ORS practice, the M4 and M2 should be perceived as the farmer's achievement in performing their local wisdom relating to ORFS. In the IPA's sentence, the seeds to be planted comes from organic seedbeds (M4), has to be "kept up as the good work." This achievement has actually been predicted by the high score of importance within the farmer of ORF as well as the high score of its performance (Table 1). The IPA's rule suggests, the high score of importance level as well as its implementation will let the attributes to be achievement to hold.

The attribute of M2 – although a little less – could be placed at this achievement position. The score of importance level and performance is relatively comparable (Table 1), which indicates that making a filter tube upstream into organic rice field, top with water hyacinth is not merely a farmer's local wisdom but has become a farmer's daily habit.

Regarding the M1 and M3 attributes, it should furtherly be explored. These attributes actually take the third quadrant, in which the IPA's rule insists "the possibly overkill" of these items, indicates the unnecessary to consider in arranging the development planning. The conclusion is not amazing because the average score of the M1 and M2 is lower than the average of the average score of its importance; while, the average score of its performance is higher than the average of the average score of its performance (Table 1). However, the average score of the importance of these two items (M1 and M2) could actually be categorized into high, in which the average is above three (3). The performance also obtains a high score category (above 3). Therefore, these items could also be regarded as farmer's achievement.

In addition, the provision to make an agreement with all organic farmer not to use agricultural production tool that is no longer suitable to for use (M1) has become a part of their custom in performing the OFS. Therefore, the suggestion to participate in a training to make a nursery and organic fertilizer (M3) is not strongly important for the farmer, because making organic nursery and fertilizer for them has been part of their habit.

Based on this reason, this mapping has actually proved two categories of planning about the rice organic farming mitigations: one attribute as the main program to remediate, and four items as farmer achievement. Fortunately, the mapping does not find the low priority and unimportant attributes to plan.

CONCLUSION

Based on the IPA approach the mitigation planning should be based on assumption the farmer is expert, experienced, and innovative in performing the ORFS mitigation. In the light of this assumption, the research finds at least four achievements in mitigation of ORFS that had become their local wisdom, includes: (a) Making an agreement with all organic farmers not to use agricultural production tool that is no longer suitable for use or contaminated by chemical input; (b) Making a filter tube upstream into organic rice field, topped with water hyacinth; (c) Participating in a training to make a nursery and organic fertilizer; and (d) The seeds to be planted come from organic seedbed. In this assumption, the research merely finds a mitigation attribute as a lack that should be a main planning to remediate, namely the provision that the farmer group association provides organic seeds.

REFERENCE

[1] Ajupov, A.A., M.A. Beloborodova, M.G. Sorokina, M.G., and A.A. Sherstobitova (2016). Risk-Management in Economic and Financial System. *International Business Management*, Vol. 10 (22), 5227-5231

[2] Baranoff, E., P.L. Brockett and Y. Kahane, WY. Enterprise and Individual Risk Management (Unnamed Publisher)

[3] Dasika, R.. Tangirala, R. and Naishadham, P., (2012), "Pesticide residue analysis of fruits and vegetables," Journal of Environmental Chemistry and Ecotoxicology Vol. 4(2):19-28.

[4] The Economist (2019), *Global Food Security Index 2019: Strengthening Food Systems and The Environment Through Innovation And Investment*, The Economist Intelligent Unit, London, UK

[5] Eliza, T. Hasanuddin. T Suriaty Situmorang (2013) Farmers' Behavior In Chemical Pesticides Use: Case of Chili Crop Farmers at Gisting Atas Village, Gisting District, Tanggamus Regency," JIIA 1(4): 334-342.

[6] EOCC (2016), Risk-assessment in organic certification: A snapshot of the current implementation and further perspectives, EOCC Task Force Risk Assessment Final report, EOCC, Belgium

[7] Gambelli, D., Solfanelli, Francesco., and Zanoli, R., (2014), Risk assessment in EU organic certification system: a systematic literature review, Proceedings of 4th ISOFAR Scientific Conference. Istanbul, Turkey

[8] IFOAM (2007), The IFOAM basic standards for organic production and processing, IFOAM, Germany

[9] Maman, U., Mahbubi, A. and Jie, F. (2018), Halal Risk Mitigation in The Australian-Indonesian Read Meat Supply Chain, *Journal of Islamic Marketing*, Vol 9(1), 60-79.

[10] Murali, S., and Pugazhendhi, S. (2015), An Importance and Performance analysis of ASS attributes for home appliances manufacturing firms, *Vels Journal of Mechanical Engineering*, Vol-2 (2), 7-13.

[11] Nafis, Muhammad Cholil (2019), The Concept of Halal and Thayyib and Its Implementation in Indonesia, *Journal of Halal Product and Research*, Vol. 2(1), 1-5

[12] Omar R. and J. Din (2017), Risk Assessment Tool for Software Project in Malaysian Public Sector. *Journal of Engineering and Applied Science* , Vol. 12(3):527-533.

[13] Ormanović, Semso., Alen Ćirić , Munir Talović, Haris Alić , Eldin Jelešković , Denis Čaušević (2017), Importance-Performance Analysis: Different Approaches, *Acta Kinesiologica*, Vol. 11 (2), 58-66

[14] Pamungkas, Oktofa Setia (2016) Bahaya Paparan Pestisida terhadap Kesehatan Manusia, *Bioedukasi* 14(1): 27-31

[15] Puspitasari and Marendra Kiloes, WY, Perilaku Petanidalam Menggunakan Pestisida di Sentra Produksi Bawang Merah Kabupaten Brebes, Proceedings of the National Location-Specific Agroinovation Seminar for Food Security in the Era of the ASEAN Economic Community.

[16] Pyne, Erin (2015), Occurrence and Distribution of Pesticide Residues in Soil as a Result of Long-Term Application, Thesis in Utrecht University, Wageningen.

[17] Sotic, A., and R. Radenko (2015), The Review of Definition of Risk. *Online Journal of Applied Knowledge Management*. Vol. 3(3):17-26.

[18] Sumiati, Astri, and Julianto, Reza Prakoso Dwi (2018), Analisa Residu Pestisida di Wilayah Malang dan Penanggulanganya untuk Keamanan Pangan Buah Jeruk, *Buana Sains*, 18(2): 125-130.

[19] Sriyadi (2018), The Risks of Organic Rice Farming: A Case Study in The Kebonagung Village Imogiri District and Wijirejo Village Pandak District Bantul Regency, Special Region of Yogyakarta, 4th International Conference on Food and Agriculture esources (FANRes 2018) Published by Atlantis Press

7th Int. Conf. on Structure, Engineering & Environment (SEE), Pattaya, Thailand, Nov.10-12, 2021, ISBN: 978-4-909106070 C3051

IMPACTS OF SEVEN INSECTICIDES ON THREE MAJOR NATURAL ENEMIES IN THE NORTHEASTERN THAILAND

Ruchuon Wanna[1] and Mongkol Wongsawas[1]
[1]Faculty of Technology, Mahasarakham University, Thailand

ABSTRACT

Insecticides are considered the first line of protection for the control of insect pests. At least in the short and medium period, the use of insecticides will remain an important tactic for insect pest management, allowing farmers to produce crops of sufficient quality at low costs. Because of the negative impacts cause by insecticides on agriculture and their harmful effects on natural enemies. The purpose of this research was to determine the impacts of the seven insecticides including carbosulfan 20%EC, cypermethrin 35%EC, beta-cyfluthrin 2.5%EC, amitraz 20%EC, imidacloprid 10%SL, thiamethoxam 25%WG and dinotefuran 10%WP, used to control sucking insect pests in the northeastern region of Thailand on the three important natural enemies, *Sycanus collaris*, *Eocanthecona furcellata* and *Anagyrus lopezi*. Experiment was conducted in CRD with 4 replications by residue film test at 24 hours. Recommended concentrations of insecticides were used in the experiments. It was found that all insecticides caused the mortality of three natural enemies was significantly different ($p < 0.01$). They were toxic to three natural enemies with 12.5-100 %mortality. All insecticides were moderately to severe toxic on *A. lopezi* and *E. furcellata*. However, they were slightly toxic to *S. collaris*. The results indicated that the use of insecticides has brought losses, such as, negative impacts on natural enemies. When these beneficial insects reduce cause the eruption of pests and resurgence it's more common. Thus, principles of conservation these arthropods are extremely important in the biological control of pests, so that these natural enemies may present a high performance.

Keywords: Insecticides, Toxicity, Predator, Parasitoid, Thailand

INTRODUCTION

Globally, large-scale agricultural enterprises, particularly in western agriculture, rely predominantly upon prophylactic chemical control and host plant resistance/tolerance to reduce invertebrate pest populations [1], [2]. This has resulted in an over-reliance on chemicals and the emergence and spread of pesticide resistance in a wide range of pest species across an array of agricultural ecosystems [3], [4].

The goal of Integrated Pest Management (IPM) is to shift from the traditional use of prophylactic pesticide treatments towards more sustainable farming approaches. One of the pillars of IPM is the utilization and preservation of arthropod natural enemies (predators and parasitoids) in agricultural ecosystems to biologically control pest species [5]–[8]. Strategies exist that permit farmers to manipulate and augment predator and parasitoid densities by releasing mass-reared commercially available species (augmentative biological control) [9], [10] or to conserve existing populations through landscape diversification by including or conserving non-crop and resource-rich habitat (conservation biological control) [7], [11]–[12]; however, the application of these strategies within a broadacre context can have varying success [6]. Sustainable management strategies such as the choice of selective chemicals that are less harmful or disruptive towards natural enemies further complement these systems.

Reduviidae a large family belongs to the order Hemiptera, found to be efficient predators of different insect pest, preferably lepidopteran larvae [13]. *Sycanus collaris* (Fabricius) (Hemiptera: Reduviidae), known as assassin bug, all of its life stage efficiently feed on the target insect. It mainly distributed in Southeast Asia [14]. Depending on the feeding on different insect the developmental period and fecundity rate is also different when fed on different hosts [15]. Among them, some arthropods are considered as pest and some are considered as biological control agents. The sequential predatory behavior of the Genus *Sycanus* on its prey is very active [16].

Eocanthecona furcellata Wolff. (Hemiptera: Pentatomidae) is a native generalist predator that is easily reared in the laboratory and regarded as a potential larval predator. It is an effective predatory species widely distributed and has been reported from Southeast Asia, Japan, India, Taiwan, China and Indonesia on Lepidopteran, Coleopteran and Heteropteran insect [17]–[20]. In Thailand, *E. furcellata* had been considered as an important predator on several important lepidopteran pests [21].

Anagyrus lopezi were first imported to Thailand

in the year 2009 in order to control the outbreak of cassava mealybugs in the infested cassava fields because they attack cassava mealybugs specifically. However, there are various instructions on how to release wasps *A. lopezi* when a spread of cassava mealybugs occurs [22].

Use of chemical pesticides having residual problem in made crop besides the negative impact on the environments a concern for crop growers. The objectives of this study were to investigated the impacts of the seven insecticides on adult stage of two predators (*S. collaris* and *E. furcellata*) and parasitoid (*A. lopezi*), the major important natural enemies in the northeastern Thailand, of filed crops such as sugarcane, cassava, soybean insect pests etc.

MATERIALS AND METHODS

Insect Rearing

Predators rearing, *Sycanus collaris* and *Eocanthecona furcellata* used in the study were obtained from Khon Kaen Agricultural Technology Promotion Center (Plant Protection) in Khon Kaen, Thailand. Initially all predators (adults and nymphs) were maintained under laboratory conditions at 30±5°C, 70±5% relative humidity, and a photoperiod of 8 h: 16h (L:D) with a third to fifth stadium larvae of *Corcyra cephalonica*. Water was provided with a wet piece of sponge. The males and females were allowed to mate in the rearing containers. The eggs laid by the females were collected on folded paper towels. After egg hatching were obtained. To avoid cannibalism, twenty newly hatched nymphs were separated in a new plastic container (21.5 x 30.5 x 11.7 cm) covered with ventilated lid. Each nymph was provided with larvae of *C. cephalonica* and a moistened sponge every 2-3 days. There were kept under the same environmental conditions described above. Adult stage of predators was used for test.

Parasite rearing, A laboratory colony of cassava mealybugs (*Phenacoccus manihoti*) initiated from cassava fields in Mahasarakham, was maintained on the cassava seedlings into the plastic cages. Colonies of *Anagyrus lopezi* were obtained from Khon Kaen Agricultural Technology Promotion Center (Plant Protection) in Khon Kaen, Thailand. Parasitoids were mass-reared supporting the third instar nymphs of *P. manihoti*. Fifty pairs of adult parasitoids were introduced into the plastic cage and a cotton ball soaked with 10% honey solution was put into the small cup, as a food source. After the release of the parasitoids about two weeks, mummies (parasitized mealybugs) were collected and put into plastic containers. The emerged parasitoids were used for experiment and mass rearing. The rearing conditions were maintained at 30±5°C, 70±5% relative humidity, and a photoperiod of 8 h: 16h (L:D).

Insecticides

The seven commercial insecticides were trade grade insecticides in Table 1. Their formulations were carbosulfan 20%EC (Pitsulin Co., Ltd., Thailand), cypermethrin 35%EC (Chia Tai Co., Ltd., Thailand), beta-cyfluthrin 2.5%EC (Bayer Thai Co., Ltd., Thailand), amitraz 20%EC (Extra Agrochemical Co., Ltd., Thailand), imidacloprid 10%SL (Millennuim Farm Co., Ltd., Thailand), thiamethoxam 25%WG (Syngenta Crop Protection Co., Ltd., Thailand) and dinotefuran 10%WP (Sotus International Co., Ltd., Thailand). Depending on the application technique, aqueous solutions, were prepared prior to the experiments. The stock solutions of seven insecticides were prepared by dissolving in distilled water and were only applied at their maximum field recommended concentrations (MFRC) as registered in Thailand, are shown in Table 2.

Table 1 Type of seven insecticides.

Insecticides[1/]	chemical groups
carbosulfan 20% EC	carbamate
cypermethrin 35% EC	pyrethroid
beta-cyfluthrin 2.5% EC	pyrethroid
amitraz 20% EC	amidine
imidacloprid 10% SL	neonicotinoid
thiamethoxam 25% WG	neonicotinoid
dinotefuran 10% WP	neonicotinoid

[1/]insecticide formulations: EC = emulsifiable concentrate, SL = soluble concentrate, WG = water dispersible granules, WP = wetable power

Table 2 Application rate of seven insecticides.

Insecticides[1/]	MFRC[2/]
carbosulfan 20% EC	50 mL/20 L
cypermethrin 35% EC	20 mL/20 L
beta-cyfluthrin 2.5% EC	40 mL/20 L
amitraz 20% EC	30 mL/20 L
imidacloprid 10% SL	10 mL/20 L
thiamethoxam 25% WG	4 g/20 L
dinotefuran 10% WP	10 g/20 L

[1/]insecticide formulations: EC = emulsifiable concentrate, SL = soluble concentrate, WG = water dispersible granules, WP = wetable power

[2/]MFRC = maximum field recommended concentrations.

Toxicity Bioassay

Toxicity bioassays were conducted at 30±5°C, 70±5% relative humidity, and a photoperiod of 8 h: 16h (L:D). Residue film test was used for the female adult stage of three major natural enemies to evaluate contact toxicity because male longevity is shorter than that of females, a modified from the methods of Snodgrass [23] and Snodgrass [24].

The toxicity bioassay for *S. collaris* and *E. furcellata* were used for adult stage of predators. The prepared various treatments were poured into test tubes (30 mm in diameter x 200 mm length) and swirled for 1 minute. The excess quantity was poured off and the residue was air-dried for 2 h. In the control treatment, the prepared concentration was replaced with distilled water. Five adults of predator were released in the individual treated a tube. The top of the test tube was closed with a cotton plug. A larva of C. *cephalonica* was supplied as food. The experiments were replicated many times until the total number counted was 100 individuals of each predator per treatment. The mortalities of adults of each predator were recorded 24 h after the treatments.

A toxicity bioassay for *A. lopezi* was used for adult stage of parasitoid. The prepared various treatments were poured into test tubes (15 mm in diameter x 125 mm length) and swirled for 1 minute. The excess quantity was poured off and the residue was air-dried for 2 h. In the control treatment, the prepared concentration was replaced with distilled water. Two newly emerged adults of parasitoid were released in the individual treated a tube. The top of the test tube was closed with a cotton plug. Diluted honey was supplied as food through the cotton wool pellet. The experiments were replicated many times until the total number counted was 100 individuals of parasitoid per treatment. The mortalities of adults of parasitoid were recorded 24 h after the treatments.

Data Analysis

The mortalities obtained in the control treatment were used to correct the mortalities obtained with each an application rate of the seven commercial insecticides according to Abbott [25]. Data were analyzed using a one-way analysis of variance (ANOVA). The means were separated by the least significant differences (LSD) multiple range test ($p < 0.05$). It was performed using the SPSS statistical package. All percentage data were transformed (square root arcsine) before analysis. Means presented are back-transformed and where appropriate changed from proportions to percentages.

For the toxicity rating of insecticides (based in the total effect caused in the enemy), the International Organisation for Biological Control (IOBC) classification for laboratory standard tests (residual exposure) [26]: 1 (harmless, < 30%), 2 (slightly harmful, 30-79%), 3 (moderately harmful, 80-99%), 4 (harmful, > 99%), was also used for the other exposure routes used in this study in order to have a common scale for comparison.

RESULTS

Toxicity on *Sycanus collaris*

Effects of insecticides on the female adults of *S. collaris* after 24 h of in vitro insecticide exposure. All tested insecticides caused the highest significantly difference ($p < 0.01$) in mortality for *S. collaris*, compared to the distilled water (negative control) and acetone (positive control) (Table 3). Thiamethoxam had the highest mortality of *S. collaris* with 75%, but there was no the significantly difference ($p > 0.05$) when compared with imidacloprid, cypermethrin, and dinotefuran. Their mortality of 70, 60 and 60%, respectively, followed by carbosulfan with the mortality of *S. collaris* (47.5%), and no significantly difference was observed when compared with beta-cyfluthrin.

Table 3 Mortality (mean ± SD) of *S. collaris* exposed to seven insecticides

Treatments	%Mortality of *S. collaris*
carbosulfan	47.50 ± 12.58 bc
cypermethrin	60.00 ± 8.16 ab
beta-cyfluthrin	40.00 ± 14.14 c
amitraz	12.50 ± 5.00 d
imidacloprid	70.00 ± 14.14 a
thiamethoxam	75.00 ± 10.00 a
dinotefuran	60.00 ± 8.16 ab
distilled water[1/]	0.00 ± 0.00 e
acetone[2/]	0.00 ± 0.00 e
F-test	**
CV (%)	13.25

[1/]distilled water was negative control.
[2/]acetone was positive control.
** represents significant difference at $p \leq 0.01$.
Means within the same column followed by the same letter were not significantly different (LSD: $p > 0.05$).

Table 4 Laboratory IOBC toxicity ratings of seven insecticides impact on the female adult stage of *S. collaris*.

Treatments	% Mortality	IOBC[1/] toxicity classes
carbosulfan	47.50	2
cypermethrin	60.00	2
beta-cyfluthrin	40.00	2
amitraz	12.50	1
imidacloprid	70.00	2
thiamethoxam	75.00	2
dinotefuran	60.00	2
distilled water	0.00	1
acetone	0.00	1

Natural enemy response classified using the IOBC laboratory scale [26]:
1 = harmless (mortality < 30%),
2 = slightly harmful (mortality 30-79%),
3 = moderately harmful (mortality 80-99%),
4 = harmful (mortality > 99%)

Amitraz was the lowest mortality *S. collaris* with 12.5% and the significantly differences compared to the six insecticides; thiamethoxam, imidacloprid, cypermethrin, dinotefuran, carbosulfan, and beta-cyfluthrin. Residual effects of amitraz studied were negligible against the female adults of *S. collaris* and its could be classified as IOBC class1. In addition, residues of other 6 insecticides were slightly toxic to *S. collaris* (IOBC class 2) (Table 4).

Toxicity on *Eocanthecona furcellata*

E. furcellata was exposed to in vitro insecticide after treatments at 24 h. It was found the highest significantly difference ($p < 0.01$) in the female adult mortality of *E. furcellata* when compared with the two control treatments (Table 5).

Table 5 Mortality (mean ± SD) of *E. furcellata* exposed to seven insecticides

Treatments	%Mortality of *E. furcellata*
carbosulfan	100.00 ± 0.00 a
cypermethrin	100.00 ± 0.00 a
beta-cyfluthrin	95.00 ± 10.00 a
amitraz	65.00 ± 17.32 b
imidacloprid	95.00 ± 10.00 a
thiamethoxam	100.00 ± 0.00 a
dinotefuran	100.00 ± 0.00 a
distilled water[1/]	0.00 ± 0.00 c
acetone[2/]	0.00 ± 0.00 c
F-test	**
CV (%)	5.99

[1/]distilled water was negative control.
[2/]acetone was positive control.
** represents significant difference at $p \leq 0.01$.
Means within the same column followed by the same letter were not significantly different (LSD: $p > 0.05$).

Carbosulfan, cypermethrin, thiamethoxam and dinotefuran had the highest mortality of *E. furcellata* with 100% and no significantly difference was observed when compared with carbosulfan, cypermethrin, thiamethoxam and dinotefuran. Beta-cyfluthrin and imidacleprid were high mortality with 95%. For amitraz, the mortality of *E. furcellata* was 65%. There were significantly different comparisons with six other insecticides; carbosulfan, cypermethrin, beta-cyfluthrin, imidacloprid, thiamethoxam and dinotefuran. Carbosulfan, cypermethrin, dinotefuran and thiamethoxam were in general more toxic to the female adult of *E. furcellata*. (IOBC classes 4). For beta-cyfluthrin and imidacloprid could be classified as IOBC class 3 and only amitraz was slightly toxic to *E. furcellata* and then classified as IOBC class 2 (Table 6).

Table 6 Laboratory IOBC toxicity ratings of seven insecticides impact on the female adult stage of *E. furcellata*.

Treatments	%Mortality	Assessment
carbosulfan	100.00	4
cypermethrin	100.00	4
beta-cyfluthrin	95.00	3
amitraz	65.00	2
imidacloprid	95.00	3
thiamethoxam	100.00	4
dinotefuran	100.00	4
distilled water	0.00	1
acetone	0.00	1

Natural enemy response classified using the IOBC laboratory scale [26]:
1 = harmless (mortality < 30%),
2 = slightly harmful (mortality 30-79%),
3 = moderately harmful (mortality 80-99%),
4 = harmful (mortality > 99%)

Toxicity on *Anagyrus lopezi*

Effects of insecticides exposure allowed on the *A. lopezi* after 24 h in vitro insecticide. It was found that the results showed the same trend as the toxicity bioassay in *E. furcellata.* The insecticides caused the highest significantly difference ($p < 0.01$) in the newly emerged female adult mortality of *A. lopesi* when compared to both in control treatments (Table 7).

Table 7 Mortality (mean ± SD) of *A. lopezi* exposed to seven insecticides

Treatments	%Mortality of *A. lopezi*
carbosulfan	100.00 ± 0.00 a
cypermethrin	100.00 ± 0.00 a
beta-cyfluthrin	100.00 ± 0.00 a
amitraz	67.50 ± 9.57 b
imidacloprid	100.00 ± 0.00 a
thiamethoxam	100.00 ± 0.00 a
dinotefuran	100.00 ± 0.00 a
distilled water[1/]	0.00 ± 0.00 c
acetone[2/]	0.00 ± 0.00 c
F-test	**
CV (%)	2.53

[1/]distilled water was negative control.
[2/]acetone was positive control.
** represents significant difference at $p \leq 0.01$.
Means within the same column followed by the same letter were not significantly different (LSD: $p > 0.05$).

Carbosulfan, cypermethrin, beta-cyfluthrin, imidacleprid, thiamethoxam and dinotefuran were the highest mortality of *A. lopezi* with 100% and no significantly difference was observed. However, there was a significantly difference compared to amitraz with the lowest mortality of 67.5%. Carbosulfan, cypermethrin, beta-cyfluthrin, thiamethoxam and

dinotefuran were the most toxic to the newly emerged female adult of *A. lopezi*. (IOBC classes 4). Only amitraz could be classified as IOBC class 2 (Table 8).

Table 8 Laboratory IOBC toxicity ratings of seven insecticides impact on the female adult stage of *A. lopezi*.

Treatments	%Mortality	Assessment
carbosulfan	100.00	4
cypermethrin	100.00	4
beta-cyfluthrin	100.00	4
amitraz	67.50	2
imidacloprid	100.00	4
thiamethoxam	100.00	4
dinotefuran	100.00	4
distilled water	0.00	1
acetone	0.00	1

Natural enemy response classified using the IOBC laboratory scale [26]:

1 = harmless (mortality < 30%),
2 = slightly harmful (mortality 30-79%),
3 = moderately harmful (mortality 80-99%),
4 = harmful (mortality > 99%)

Copyright Form

Copyright form signed by all authors is necessary for GEOMATE. It should be submitted along with the paper submission. Copyright form can be downloaded from geomate web site.

DISCUSSIONS

Adult of the parasite *A. lopezi* should be considered as a susceptible natural enemy because demonstrated in this study. It was very exposed to seven insecticides due to high mortality. In contrast, *S. collaris* showed moderately resistance to these insecticides. Residue toxicity of amitraz studied was expoured adult of three major natural enemies and its could be classified as IOBC classes 1-2. In contrast, four insecticides as carbosulfan, cypermethrin, thiamethoxam and dinotefuran were very toxic to adut of *E. furcellata* and *A. lopezi* (IOBC class 4) but the harmful effect was greatly decreased in *S. collaris* with slight harmful as IOBC class 2. For beta-cyfluthrin and imidacloprid showed since classified as IOBC classes 2-4. Carbosulfan, cypermethrin, thiamethoxam and dinotefuran were very harmful to adult of *S. collaris*, *E. furcellata* and *A. lopezi*. Therefore, it was concluded that the most of insecticides in this study was highly harmful to three majaor natural enemies in the northestern Thailand. It consider, that these insecticides cannot be recommended for use in the Integrate Pest Management (IPM) programs in these regions, mainly where the species *E. furcellata* and *A. lopezi* are dominant.

Results from these experiments should help to integrate chemical and biological control in agroecosystems where this enemy is present, because many attempts to suppress pest populations by biological measures have failed because of deleterious effects of chemicals on beneficials.

CONCLUSIONS

The new challenge for research in this field (pesticide selectivity to natural biological control agents) is the description of lethal and sub lethal effects of pesticides on natural control agents, and also to consider the ecological structure within agricultural ecosystems. In practice, growers have to consider a comprehensive evaluation of pesticide impacts. Therefore, we require a better knowledge of the diversity of biological control species in agroecosystems and of the different ways pesticides can affect their efficacy. An in-depth knowledge on how chemical compounds impact beneficial organisms is essential to overcome the challenges and constraints for research of pesticide effects on natural enemies and resulting field recommendation.

ACKNOWLEDGEMENTS

The authors thank the Department of Agricultural Technology, Faculty of Technology, Mahasarakham University for providing instruments. Research assistance from Miss Phanthiwa Kwang-Ngoen ana laboratory assistance from Miss Jiraporn Krasaetep are gratefully acknowledged.

REFERENCES

[1] Hoffmann A. A., Weeks A. R., Nash M. A., Mangano G. P., and Umina P. A., The Changing Status of Invertebrate Pests and the Future of Pest Management in the Australian Grains Industry. Australian Journal of Experimental Agriculture, Vol. 48, 2008, pp.1481-1493.

[2] Reisig D. D., Bacheler J. S., Herbert D. A., Kuhar T., Malone S., Philips C., and Weisz R., Efficacy and Value of Prophylactic Vs. Integrated Pest Management Approaches for Management of Cereal Leaf Beetle (Coleoptera: Chrysomelidae) in Wheat and Ramifications for Adoption by Growers. Journal of Economic Entomology, Vol. 105, 2012, pp.1612-1619.

[3] Umina P. A., McDonald G., Maino J., Edwards O., and Hoffmann A. A., Escalating Insecticide Resistance in Australian Grain Pests: Contributing Factors, Industry Trends and Management Opportunities. Pest Management Science, Vol. 75, 2019, pp.1494-1506.

[4] Huseth A. S., Chappell T. M., Chitturi A., Jacobson A. L., and Kennedy G. G., Insecticide Resistance Signals Negative Consequences of Widespread

Neonicotinoid Use on Multiple Field Crops in the U.S. Cotton Belt. Environment Science and Technology, Vol. 52, 2018, pp.2314-2322.

[5] Fiedler A. K., Landis D. A., and Wratten S. D., Maximizing Ecosystem Services from Conservation Biological Control: The Role of Habitat Management. Biological Control, Vol. 45, 2008, pp.254-271.

[6] Holloway J. C., Furlong M. J., and Bowden P. I., Management of Beneficial Invertebrates and Their Potential Role in Integrated Pest Management for Australian Grain Systems. Australian Journal of Experimental Agriculture, Vol. 48, 2008, pp.1531-1542.

[7] Jonsson M., Wratten S. D., Landis D. A., and Gurr G. M., Recent Advances in Conservation Biological Control of Arthropods by Arthropods. Biological Control, Vol. 45, 2008, pp.172-175.

[8] Torres J. B. and de Bueno A. F., Conservation Biological Control Using Selective Insecticides–A Valuable Tool for IPM. Biological Control, Vol. 126, 2018, pp.53-64.

[9] Collier T. and van Steenwyk R. A, Critical Evaluation of Augmentative Biological Control. Biological Control, Vol. 31, 2004, pp.245-256.

[10] Crowder D. W., Impact of Release Rates on the Effectiveness of Augmentative Biological Control Agents. Journal of Insect Science, Vol. 7, 2007, pp.1-11.

[11] Cullen R., Warner, K. D., Jonsson M., and Wratten S. D., Economics and Adoption of Conservation Biological Control. Biological Control, Vol. 45, 2008, pp.272-280.

[12] Gagic V., Paull C., and Schellhorn N. A., Ecosystem Service of Biological Pest Control in Australia: The Role of Non-Crop Habitats Within Landscapes. Austral Entomology, Vol. 57, 2018, pp.194-206.

[13] Ambrose D. P., Rajan X. J. S., Nagarajan K., Singh V. J., and Krishnan S. S., Biology, Behaviour and Functional Response of *Sphedanolestes variabilis* Distant (Insecta: Hemiptera: Reduviidae: Harpactorinae), a Potential Predator of Lepidopteran Pests. Entomologia Croatica, Vol. 13, Issue 2, 2009, pp.33-44.

[14] De Clercq, P., 2000. Predaceous Stinkbugs (Pentatomidae: Asopinae), In Heteroptera of Economic Importance. Schaefer C. W. and Panizzi A. R., Eds. CRC Press, Boca Raton, Florida, 2000, pp.758-761.

[15] George P. J. E., Life Tables and Intrinsic Rate of Natural Increase of the Three Morphs of *Rhynocoris marginatu*s (Fab.) on *Corcyra cephalonica* Stainton. Journal of Experimental Zoology, Vol. 3, Issu 1, 2000, pp.59- 63.

[16] Ambrose D. P., Assassin Bugs. Oxford and IBH Publishing Company Private Limited, New Delhi, India and Science Publishers, Incorporation, Enfield, New Hampshire, U.S.A., 1999, pp.337.

[17] Prasad D., Singh K. M., Singh R. N., and Mehto D. N., A New Predator of New Pest of Jasmine in Delhi. Bull. Entomol., Vol. 24, 1983; pp.140-141.

[18] Ahmad M., Singh A. P., Sharma S., Mishra R. K., and Ahmad M. J., Potential Estimation of the Predatory Bug *Canthecona furcellata* Wolff (Hemiptera: Pentatomidae) Against Popular Defoliator *Clostera cupreata* (Lepidoptera: Notodontidae). Annals of Forestry, Vol. 4, 1996, pp.133-138.

[19] Chang C. P., Mass Rearing and Utilization of the Predatory Stink Bug *Eocanthecona furcellata.* Formosan Entomologist, Vol. 3, 2002, pp.175-181.

[20] Shylesha A. N. and Sravika A., Natural Occurrence of Predatory Bugs, *Eocanthecona furcellata* (Wolff) and *Andrallus spinidens* (Fabr.) on *Spodoptera frugiperda* (Smith) (Hemiptera: Pentatomidae) in Maize and Their Potential in Management of Fall Army Worm. Journal of Biological Control, Vol. 32, Issue 3, 2018, pp.209-211.

[21] Hutacharern C. and Choldumrongkul S., Survey on the natural enemies of teak defoliator *Hyblaea puera* Cramer. Thai Journal of Forestry, Vol. 14, 1995, pp.9-16.

[22] Aekthong S. and Rattanakul C., Investigating the Use of Wasps *Anagyrus lopezi* as a Biological Control Agent for Cassava Mealybugs: Modeling and Simulation. Advances in Difference Equations, Vol. 2019, Article number 237.

[23] Snodgrass G. L., Glass-Vial Bioassay to Estimate Insecticide Resistance in Adult Tarnished Plant Bugs (Heteroptera: Miridae). Journal of Economic Entomology, Vol. 89, 1996, pp.1053-1059.

[24] Snodgrass G. L., Adamczyk J. J., and Gore J., Toxicity of Insecticides in a Glass-Vial Bioassay to Adult Brown, Green and Southern Green Stink Bugs (Heteroptera: Pentatomidae). Journal of Economic Entomology, Vol. 98, 2005, pp.177-181.

[25] Abbott W.S., A Method of Computing the Effectiveness of An Insecticide. Journal of Economic Entomology, Vol. 18, 1952, pp.265-267.

[26] Hassan S. A., Activities of the IOBC/WRPS Working Group "Pesticides and Beneficial Organisms". IOBC/WPRS Bulletin, Vol. 17, Issue 10, 1994, pp.1-5.

7th Int. Conf. on Structure, Engineering & Environment (SEE), Pattaya, Thailand, Nov.10-12, 2021, ISBN: 978-4-909106070 C3051

BIOMASS FUEL POTENTIAL FROM AGRICULTURAL PRODUCT WASTES IN SOUTHERN BORDER PROVINCES, THAILAND

Saudee Maprasit, Piyaruk Pradabphetrat, Romsan Madmanang, Ratchada Boonkaew and Sidthipong Sathawong
Department of Environmental Science, Faculty of Science Technology and Agriculture, Yala Rajabhat University, Thailand

ABSTRACT

The aim of this research is to study the properties and economic value of biomass briquette from various agricultural product wastes such as bagasse, rice husks, corn husks with cob, peanuts husks and Durian peel in order to reduce air pollution from burning wastes and use as alternative energy in biomass power plants and communities. The biomass sticks in this study was produced by hand-press machine mixing with pasty tapioca starch at the best ratios. The fuel properties of briquette were analyzed according to ASTM standards. The study results showed that the heating value of the various briquette is in the range between 3,299 (husks) - 4,661 (peanut husks) Kcal/g. The moisture, volatile, ash, and fixed carbon content are 7.24 (corn husks with cob) - 11.64 (bagasse), 61.65 (husks) - 75.91 (corn husks with cobs), 0.72 (bagasse) - 13.21 (husks) and 12.74 (corn husks with cob) - 16.97 (Durian peel and bagasse) %, respectively. The proper proportion for pressing fuel briquette is dry agricultural product wastes 1,000 g: pasty tapioca flour 150 g which produced from heated mixed tapioca flour 100 g with water 180 g. The economic value of biomass briquette production was analyzed using net present value (NPV), internal rate of return (IRR) and payback period (PB). The analysis results show that the biomass briquettes production from wastes of agricultural product is economically feasible. Moreover, the results show that the most influential risk factors of the biomass production are fuel price and number of fuel production daily, followed by specification and price of machines and number of agricultural productions.

Keywords: *biomass potential; agricultural product wastes; southern border provinces*

INTRODUCTION

Garbage is a major problem that all sectors have to take action to resolve and deal with in the area. Due to the impact on people living in the area directly year 2014-2018, Thailand has a total amount of waste 28.14 million tons. They are from the waste generated by the sanitary method, only 28.5 per cent, with unsanitary disposal and 31 per cent smuggled in unsuitable locations and 26 per cent are recycled. The residual waste in areas that are not collected or disposed of 32 percent of the increasing amount of waste each year, causing waste management problems in many communities. Some communities use a participatory waste management process has set up a waste bank Waste management is done by making organic compost. Waste is processed into renewable energy in the form of biogas and waste fuel and etc [1].

Using municipal waste to produce fuel pellets in addition is helping to solve the problem of municipal waste, it can also be used as a substitute for household cooking fuels as another form because the process is simple and for community is easy to do. Especially rural communities that have a way of life and behavior of using wood and charcoal for cooking. And using pellet fuel is another option for the community. In addition, the use of pellet fuel is developed at the industrial level and is the main fuel in power plants. There are more education and development but not suitable in this border area. The researcher expected that this would be another large channel for community development at a macro level while being able to manage community waste at the same time [2]. From the model of using pellet fuel as a renewable energy, many kinds of agricultural waste and waste materials have been researched into the production of pellet fuel such as durian husks, mangosteen peel, rice straw, twigs, leaves and corn cobs. The properties of this pellet fuel can be used as a substitute for firewood and wood charcoal as well. But the efficiency of using as fuel potential in southern biomass power plants has not been studied. Due to the southern area is quite a large amount of agricultural product, thus high agricultural residues and waste are disposed and burned. It also destroys the environment [3].

This research is to study experiments to develop pellet fuel from organic waste of agricultural products. Which is a waste that occurs in the community to produce pellet fuel for use as a renewable energy in the community. Especially for use in southern biomass power plants. As well as fuel to sell to power plants because the above agricultural residue contains cellulose, hemicellulose and flax with combustible properties [4]. And it is also another process that helps solve the problem of rubbish in the community.

STUDY AREA

The southern border consists of three provinces: Pattani, Yala and Narathiwat, located at the southern end of the country and bordering Malaysia. It has a border to the south and west with Malaysia. Total distance between Thailand - Malaysia 258 kilometers with mountains Sankalakiri ridge as a barrier. North and East Next to the Gulf of Thailand, a distance of 172.31 kilometers. The southern border has a total area of 6.84 million rai. Topography in the central and southern part of the region has the Sankalakiri mountain range (Yala and Narathiwat) resting in the east-west line and a border between Thailand and Malaysia in the east, it is a river plain along the Thai Gulf coast in Pattani and Narathiwat provinces.

Southern border is located near the equator. It is characterized by hot, humid, monsoon weather. The average temperature is 28 degrees Celsius. It is influenced by the southwest monsoon. During the period from mid-May to mid-October This causes a lot of rain in the western part of the region and is influenced by the northeast monsoon wind that prevails in mid-October to mid-February. Causing a lot of rain around the area East side of the region the average number of rainy days is 148.7 days per year and the average rainfall is 1,781.7 millimeters per year [5].

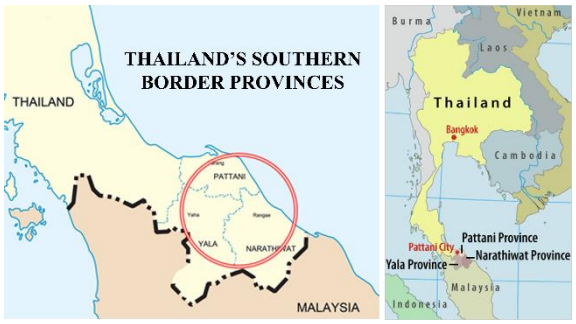


Fig.1 The southern border Provinces (https://www.thailand-business-news.com/wp-content/uploads/2011/09/thailandsouthmaplegend) (http://www.pbs.org/frontlineworld/rough/roughimages/thai_map_sm.gif)

In 2018-2019, there was a total area of 6.8 million, with land utilization classified as a forestry area, not 1.7 million rai or 25.0 percent of the total area. Mangrove area 0.22 hundred thousand or 0.33 percent of agricultural area 3.4 million rai (rubber, palm, fruit and rice fields) or 50.0 percent of the total area. And other utilization areas 1.66 million rai or 24.5 percent of the area of the region. In 2018, the agricultural sector accounted for 31.1 percent of the region's products. The agricultural sector's economic activity is important as the majority of people work in agriculture. However, the share of the agricultural sector is likely to decline compared to 38.1% in 2013. This is because the prices of major agricultural products, especially rubber, have continued to decline. Industry sector is relatively stable. The percentage of production was 10.1 percent, while the service sector tended to increase. In particular, the education service and government service sector have an increasing trend from allocating government budgets to develop and improve the quality of life of the people and resolve the unrest in the border provinces in the Deep South.

The agricultural production of the southern border is still the same as it has been processed. In 2017, agricultural products were valued at 44,048 million baht that accounting for 31.1 percent of the region's product value. Decreased from the year 2013 with a value of 50,192 million baht. The expansion of the agricultural sector contracted by 7.9 percent compared to the previous year [5].

The amount of solid waste tends to increase slightly in the period 2013 - 2017, the southern border region, the rate of solid waste has increased by an average of 2.20 percent per year, with the year 2017 the amount of waste generated 0.74 million tons or 2,030. Tons per day or equivalent to 2.70% of the total amount of waste generated in the country. An increase from 2016 in the amount of 13,518 tons or 0.1% increase [6].

The development of strategy 1: Develop agro industry and agricultural processing industry to stabilize the manufacturing sector encourage smallholder farmers to adjust their production systems to be self-sufficient and to promote sustainable agriculture such as new theory agriculture, integrated agriculture, organic agriculture. It is a safe and environmentally friendly agriculture.

The southern border provinces of Thailand are Yala, Pattani and Narathiwat with fertile areas and natural resources. There is a forest, hills, trees. Animal species also in the area of Pattani and Narathiwat, adjacent to the Gulf of Thailand

Such fertility conditions, therefore, the southern border provinces are areas which is very conducive to farming Whether it is growing both short-term biennial crops and Perennial plants, animal husbandry, both terrestrial and aquatic animals Agricultural service or even a business agricultural related trade.

There are 247,090 farmers households out of the total 329,255 households.

Which accounts for 75.00 percent of the total number of households living in the three southern border provinces.

The economic structure of these provinces depends on Agricultural production is the main in which 72.00 percent of the total agricultural area is planted rubber [7] But dealing with agricultural waste

in the southern regions Most often, use a simple and easy way. That is, burning in the open air which tends to burn more every year especially the higher the price of agricultural products, the higher the incineration of agricultural waste.

MATERIAL AND METHODOLOGY

Agricultural waste-pellets preparation

The fuel pellets in this research were used cold-press technique by using tapioca starch water as a binder. Because tapioca starch is a binder with high thermal value and can bind the material to homogenize and enhance physical properties [8] At this stage, the properties of the raw materials used in it are analyzed. Fuel briquettes include Para-rubber wood, bagasse, corn husks with cobs, rice husks, bean husks and agricultural waste with durian husks which is the main raw material of fuel and tapioca starch which acts as a binder and heat (heating value) of all raw materials according to ASTM D7582 Standard [8].



Fig. 2 waste-pellets material preparation

Waste pellets properties analysis

Fuel Properties Analysis of Fuel Bars by using briquettes of biomass fuel to analyze the fuel properties by analyzing different quantities as follows:

(1) Heating value is analyzed according to BSEN14918 standard.

(2) Moisture content was analyzed according to ASTM D7582 standard method.

(3) Ash content was analyzed in accordance with ASTM D7582 standard method.

(4) Volatile matter content was analyzed in accordance with ASTM D7582.

(5) Fixed carbon analyzed in accordance with ASTM D7582.

Waste pellets Economical analysis

This research analyzes the reduction in greenhouse gas emissions, net received energy and economic cost-effectiveness of biomass briquette production from agricultural waste. Considerable environmental benefits, in this research, the amount of greenhouse gases that can be reduced in the form of carbon dioxide equivalent (CO2e) using kilograms This quantity can be calculated is obtained from the following equation [9],

$$ER = BE\text{-}PE \quad (1)$$

Where ER is the reduction in greenhouse gas emissions from activities (greenhouse gas emission reduction) (kgCO2eq)

BE is the amount of greenhouse gas emissions in base case or amount of greenhouse gas emissions when No activity (baseline emission) (kgCO2eq)

PE is the amount of greenhouse gas emissions in the event that the project or business (project emission) (kgCO2eq)

In case of net received energy

It is calculated from the following equation [10],

$$Enet = E0\text{-}Ei \quad (2)$$

where Enet is net energy (kcal/kg)

Eo is the energy received (kcal/kg)

Ei is the energy required for the activity (kcal/kg).

This analysis was to assess the suitability in practice The project yield was analyzed to assess whether the benefits from agricultural waste disposal to produce briquettes, is it worth the cost of investment and management? Can it be an alternative for farmers to use as a way to manage agricultural waste and be able to operate sustainably? In addition, project risks were analyzed in order to identify the risk factors for the implementation of the project in practice with the steps project return analysis and sensitivity analysis.

1) project return analysis such as net present value, NPV), internal rate of return (IRR), and payback period, PB).

1.1) Net present value (NPV) is the net present value of the net cash flows over the project life at the desired rate of return or the cost of investment in the NPV project. can be calculated from the following equation.

$$NPV = \sum_{t=1}^{n} \frac{CF_t}{\left(1+\frac{i}{100}\right)^t} \quad (3)$$

Where *n* is the age of the project (years), *t* is the year index over the project period (years), t =1, 2, 3, …, n, and CF_t is the project's net cash flow in year *t* equal to cash inflow in year *t* - cash outflow in year t (Baht), i is the discount rate or the desired rate of return (%)

The criterion for making decisions is investment. is a project that yields value when NPV ≥ 0, and Not worth when NPV < 0

1.2) Internal rate of return (IRR) refers to the rate of return made. Let the present value of net cash flows over the project life be zero. represents the rate of return. The average project life cycle IRR can be calculated from the following equation.

$$NPV = \sum_{t=1}^{n} \frac{CF_t}{\left(1+\frac{IRR}{100}\right)^t} \quad (4)$$

Where *n* is the age of the project (years), *t* is the year index over the project period (years), t =1, 2, 3, …, n, and *CFt* is the net cash flow of the project in year *t* equal to cash inflows in year *t* - cash outflows in year *t* (Baht), IRR is the internal rate of return (%).

1.3) The simple payback period (PB) refers to the period during which the accumulated cash inflows equal the cash outflows from investments. It is a measure of the project's risk profile. The decision criterion is to accept the project when PB ≤ target payback period.

2) sensitivity analysis to analyze project risks with the following steps;

2.1) Determine the variables with uncertainty to be studied.

2.2) Specify the scope of possible values or the range of interest for each variable.

2.3) Change the value of the variable of interest one by one with the remaining variables fixed, and calculate the NPV, IRR and PB values of each case to analyze the relationship of NPV, IRR and PB with the changes of each variable. In this research, the sensitivity of four factors affecting project returns is analyzed: the amount of fuel produced per day; machine price Labor cost and number of days of production per year [10].

RESULTS AND DISCUSSION

Prepared Agricultural Waste-Pellets

Appropriate ratio between crushed agricultural waste and binder with ratio between tapioca starch and water at 1:1.8 is obtained. Mixture of shredded material and binder at 100 g per 15 g. By specifying that the fuel obtained must not exceed the size of the biomass fuel rod used in the biomass power plant (not more than 10 centimeters in length and not more than 1 centimeter in diameter).



Fig.3 Agricultural Waste-Pellets

Waste pellets properties

Table 1 The physical properties of Waste pellets

Waste pellets Type	Density	Moisture content	Volatile
Para rubber wood	0.85	9.05±0.04	74.82±0.47
bagasse	0.82	11.64±0.07	74.90±0.09
rice husks	0.84	10.64±0.03	61.65±0.12
bean husks	0.99	10.03±0.02	67.84±0.12
corn husks with cobs	0.74	7.24±0.04	75.91±0.59
Agri-waste with durian husks	0.67	8.47±0.02	69.54±0.47

The moisture content test showed that corn husks with cobs and Agri-waste with durian husks had the lowest moisture content, while bean husks, rice husks and bagasse had similar and higher moisture content than the rubberwood fuel used in power plants but still had the highest moisture content. within the standard of the power plant. Therefore, the development of biomass fuels in terms of moisture should consider adding corn husks with cobs as they can reduce the amount of moisture remaining after drying. which will directly affect the heat value Because if the waste has a lot of moisture, there will be a loss of heat due to the evaporation of moisture during combustion. lower the heat value.

Volatile Matters testing showed that corn husks with cobs and bagasse had a high content of volatile waste. When heated, waste with such high volatile content tends to have a high calorific value. However, it is necessary to study the properties of certain volatile substances that may cause problems for materials or equipment that use fuel materials, such as alkaline substances in palm bunches. Will become sticky rubber sticks to the water pipes in the combustion chamber. causing the efficiency of the radiator to decrease [10], [11]

Table 2 The chemical properties of Waste pellets

Waste pellets Type	Fixed carbon	Ash	Heating value
Para rubber wood	14.73±0.52	1.40±0.02	4,039±64
bagasse	12.74±0.17	0.72±0.04	3,618±18
rice husks	14.50±0.09	13.21±0.00	3,299±16
bean husks	14.00±0.25	8.13±0.35	4,661±92
corn husks with cobs	15.11±0.55	1.74±0.02	3,907±12
Agri-waste with durian husks	16.97±0.48	5.02±0.01	3,932±108

Fixed Carbon Test which is a difficult volatile compound which will remain in the waste after incineration of volatile substances at 750 degrees Celsius. Agri-waste with durian husks and corn husks with cobs have the highest amount of Fixed Carbon and higher than Para rubber wood fuel. So it has a long burning time. Therefore, to develop biomass fuels that provide a long and consistent combustion period. Consideration should be given to increasing the content of corn husks with cobs and durian husks with high carbon content [11]

However, when using Agri-waste with durian husks, there may be a problem of ash content or the ash content of inorganic substances in the sample which has been burned at high temperatures so that the substance is Organic (Organic substance) burns out. which from the test It was found that the fuel from rice husks, bean husks and the addition of durian husks produced the most ash. And it will be a problem to burn and complicate the removal of the ash produced but using corn husks with cobs and bagasse can help reduce the amount of ash.

The heat value test found that bean husks provide higher heat value than rubber wood fuel. and the development of fuels using the proportions of different components of agricultural waste. It will help to increase the heat as well. In particular, corn husks with cobs and bagasse are used as a major component of at least 40% of biomass fuels combined with other feedstocks. It helps to increase the efficiency of fuel in terms of low humidity. high heat It burns for a long time and reduces the amount of ash. in the durian peel Which parts of the bark need to be further studied (outer or inner) that can increase fuel efficiency in terms of humidity Long burning and low ash content. including other improvements Including the development of compression and drying processes of fuel rods before use. will cause the water in the waste to be removed. Increase efficiency and value for biomass fuels from the agricultural sector [10], [11].

Waste pellets economy

Table 3 The comparison of energy production

Management approach	Net Power (kgCO2eq/kg dry agricultural waste)		
	Eo	Ei	Enet
Biomass briquettes (This research)	2,740	7,425	4,685
Biogas production	285	0	285

The development of biomass pellets could give more energy than method of another one like biogas production.

Table 4 The comparison of greenhouse gas reduction

Management approach	Greenhouse Gas Reduction (kgCO2eq/kg dry agricultural waste)		
	BE	PE	ER
Biomass briquettes (This research)	15.75	0.073	15.677
Biogas production	5.53	0	5.53

The development of biomass pellets could reduce more greenhouse gas than method of another one like biogas production.

Table 5 The economical description

Indicators	Value	Description
NPV	9,798 Baht	NPV > 0 Show that the project investment is worthwhile.
IRR	7.6 %	IRR > The interest rate of 6.15% indicates that the project investment is worthwhile.
PB	7 years	The payback period is less than or equivalent to the service life of the machine. Shows that the project has an acceptable level of risk.

CONCLUSION

The Results of a study on the use of agricultural waste to produce biomass briquettes by cold compression method using cassava oil as a binder. It was found that the fuel rods could be extruded well when the mixture ratio by weight of tapioca starch after the measurement of agricultural waste was 100 g: 15 g or more. The resulting fuel had

calorific value in the range of 3,299-4,661 kcal/kg. which is sufficient for use as an alternative fuel for biomass power plants and communities Compared to the use of rubber wood fuel used in the area. Which is a biomass fuel that is widely used in power plants in the three southern border provinces today. And the moisture, ash, volatile matter and carbon content were stable in the range similar to that of the green fuels made from other raw materials compared. Which is enough to conclude that In case of wanting to increase the heat value of briquette fuel May consider using waste material or husks from legumes. In case of wanting to reduce humidity Increasing the heating power should consider the waste material from corn and sugar cane. The use of durian peel material will help the fire last longer. But further studies may be needed to reduce the amount of ash feeding.

The comparison of the energy production and environmental benefits of management approaches in this research with agricultural waste measurements for biogas production. It was found that the net energy of 4,685 kcal/kg by using agricultural waste to compress fuel rods was able to reduce greenhouse gas emissions by 15.677 kCO2eq/kg, which was higher than other management approaches.

The economic cost-effectiveness study found that the production of biomass briquettes from agricultural waste It is economically worthwhile, with NPV = 9,798 > 0 and IRR = 7.6 % > 6.15 %, indicating that the return is worth the investment. can be implemented in practice In addition, the project has a payback period (PB) = 7 years, which is not very long compared to the average service life of the machines. This makes the project have a low risk of loss.

The results of a sensitivity analysis show that project returns are the most sensitive to fuel prices. and the maximum amount of fuel produced per day followed by workers' wages Number of production days and machine prices, respectively.
Therefore, the management of production of this fuel to be the main alternative fuel in power plants. Therefore, raw materials should be gathered in sufficient quantities. and then began to compress the fuel rods would be more appropriate than frequent small fuel briquette operations.

Processing agricultural waste into briquette biomass fuel is one of the most useful and efficient methods of agricultural waste disposal. Can be used as an alternative energy to replace the main fuel for biomass power plants and help reduce environmental impact at the same time.

.

ACKNOWLEDGMENTS

The authors are extremely grateful to the faculty of science technology and agriculture of Yala Rajabhat University. The southern farmers for agricultural material and finally we would like to thank to the Yala Gulf Green, a biomass power plant for comparison data with my research and consulting information.

REFERENCES

[1] Energy Policy and Planning Office, 2013, Thailand Energy Statistics Report 2013, Ministry of Energy, Bangkok, 335 pages.
[2] Department of Alternative Energy and Efficiency, 2013, Energy in Thailand: Facts & Figures 2013, Ministry of Energy, Bangkok, 21 pages.
[3] Department of Alternative Energy and Efficiency Ministry of Energy, Biomass Potential in Thailand, Source : http://www.dede.go.th/dede/index.php?option=com_content&view=article&id= 130:2010-05-07-08-10- 57& catid=58&Itemid=68, 18 September 2019.
[4] Department of Alternative Energy and Efficiency, 2012, Alternative Energy Development Plan 25% in 10 Years (2012-2021), Ministry of Energy, Bangkok.
[5] Southern Border Group Plan 2020. Strategic Management Group of Southern Border Provinces.
[6] Pollution Control Department. (2016). The National Solid Waste Management Master Plan (2016 - 2021).
[7])Information technology & Communication Center, Department of Agricultural Extension, 2014; Ministry of the Interior, 2014(
[8] Ministry of agriculture and cooperatives and The Japan Institute of Energy, Asia Biomass Handbook
[9] Greenhouse Gas Management Organization, 2013, Carbon Footprint Assessment Guidelines of Organization, Greenhouse Gas Management Organization (Public Organization), 72 pages.
[10] Thanapol Tantisattayakul, Kachamard Saidam, Sujitra Phusongsri and Sivaporn Ngernruengroj. Feasibility Study of Biomass Briquettes Production from Pineapple Peel, Thai Science and Technology Journal, 23, pp.754-773.
[11] Vacharaporn Yubolket and Dariwan Settheetham, Quality Comparison of Leaf-Trash Chunk-Compressed Fuel by Compressor and Hand, KKU Research Journal, Vol.17, No.4, pp.85-96.

INDONESIA'S ESSENTIAL OILS IN THE GLOBAL MARKET

Lilis Imamah Ichdayati[1], Rizki Adi Puspita Sari[2] and Ratdin Cahyaning M. Warahmah[3]

[1,2] Agribusiness Department, State Islamic University Syarif Hidayatullah Jakarta, Indonesia; [3] State Islamic University Syarif Hidayatullah Jakarta, Indonesia

ABSTRACT

Indonesian essential oil demands are not very stable, including the trade deficit, due to price fluctuations and quality concerns. These materials have a wide range of application across perfumery, food and beverages, flavor, pharmaceuticals as well as cosmetic industries. The objectives of this study are to analyze the market structure and position of trade specialties of Indonesian essential oils in the global market. As a consequence, the research scope encompasses essential oils in HS code 3301 and also focuses on the 5 main export destinations, comprising the United States, Singapore, India, Spain and France. Secondary or panel data, a combination of time series and cross section records between 2009-2018, were subsequently applied. In addition, the analytical tools involve the use of HHI (Herfindahl-Hirschman Index) and TSI (Trade Specialization Index). The HHI test showed an oligopoly market structure for the exports in Singapore and India, while, the United States, Spain and France experienced a monopolistic state. Furthermore, the TSI analysis indicated the product specialties in the expansion stage in 4 global markets, including the United States, India, Spain and France, while specializing as a net exporter in Singapore.

Keywords: Essential Oils, Market Share, Trade Specialization, Oligopoly, Monopolistic

INTRODUCTION

Essential oils are derived from aromatic plants, with widespread application in the non-oil and gas industries, chemical, pharmaceutical and orthodox medicine sub-sectors [1]. These oils also serve as a foreign exchange earner for several countries, including Indonesia.

There are 80 essential oils traded in the global market. Indonesia tends to produce 40 types where 12 have already accessed the international market, including patchouli, vetiver (aromatic root), cananga, cajuput (eucalyptus), lemon grass, clove, sandalwood, nutmeg, cinnamon, cubeb or Javanese pepper and regular pepper [2]. In this paper Indonesian essential oil uses HS code 3301 with various derivatives or subheadings.

The country's primary export destinations between 2013-2016 included Singapore, India, China, United States of America, France, Spain, Switzerland, Germany, England and the Netherlands [3]. Furthermore, the European Union is recognized as the world's largest importer of essential oils, with France, Germany and Great Britain as the dominant market [4].

Table 1 represents the increase in the demand for Indonesian essential oils over the past 5 (five) years from 2014-2018.

Table 1. Volume Balance and Exports and Imports Value of Indonesian Essential Oils.

Year	Export of Essential Oils				Import of Essential Oils			
	Volume (ton)	Growth (%)	Value (x1000 US$)	Growth (%)	Volume (ton)	Growth (%)	Value (x 1.000 US$)	Growth (%)
2013	4,358	-	123,048	-	7,559	-	137,456	-
2014	3,988	-8.5	156,301	27	7,619	1	122,403	-11
2015	5,199	30.4	179,905	15.1	7,581	-0.5	114,912	-6.1
2016	30,767	491.8	166,381	-7.5	8,482	11.9	129,440	12.6
2017	4,897	-84.1	160,369	-3.6	7,986	-5.9	136,213	5.2
2018	6,630	35.4	199,267	24.3	9,668	21.1	211,109	55
Average Growth		118.4		7.1		6.7		16.7

Noted :[5]

Based on the above table, the average growth of the export volume was obtained at 118.37%. The outcome was due to a surge in 2016 of approximately 30,766 tons, although normalcy reverted the subsequent year. This circumstance essentially lowered the export value, as prices also reduced (Table 2). Meanwhile, overall growth in export value remained positive at 7.06%.

Table 2. List of Average World Essential Oil Prices for 2014-2018

Year	Price (US$/Kg)	Growth (%)
2013	0.028	-
2014	0.039	38.82
2015	0.035	-11.72
2016	0.005	-84.37
2017	0.033	505.52
2018	0.030	-8.22
Average	0.028	73.34

Noted :[5]

The average global price of essential oils between 2014-2018 was reportedly USD 0.028/kg with a positive growth of 73.34%. However, in 2016, the value significantly declined to USD 0.005/kg, but eventually was restored the subsequent year. This drastic decrease caused a instant increase in export volume to match the value equivalent of the previous year. The condition showed a high dependency of the country's foreign exchange from essential oil exports on world demand and price fluctuations.

Table 1 indicates an extensive essential oil imports in Indonesia, compared to exports. This circumstance is due to the high demand by the domestic food and cosmetic industries, in an effort to obtain the derivatives [6]. However, local processing is barely capable of producing crude essential oils with limited by products. This situation forces the government to only export the raw materials and import the refined products, including citronellal esters, menthol, eugenol and vanillin.

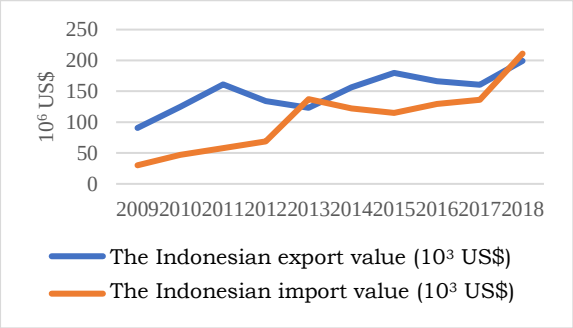


Fig.1.The Essential Oil Trade Flow, 2009-2018 [5]

Figure 1 shows the occurrence of two trade deficits between 2009–2018, where the import value was greater, compared to the exports in a 5-year cycle, including in 2013 and 2018. This outcome was caused by a gradual decline in global economic growth and prices. However, the dwindling purchasing power also pressured the international market, resulting to a decreasing export value.

Figure 2 shows the global demand for essential oils is also influenced by competing countries, including Indonesia. In 2018, Brazil was reportedly the largest global exporter with a volume of 54,501 tons [7]. This ranking was followed by India, while America held the third position. Indonesia occurred as the 11th spot, with an export volume of 6,630 tons.

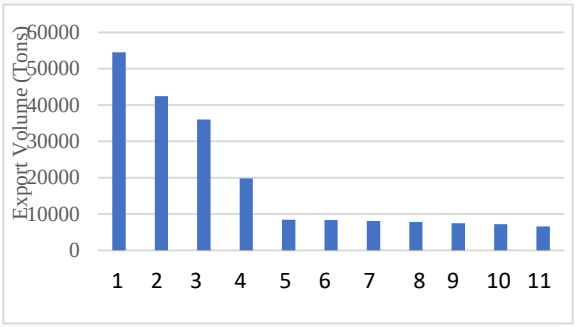


Fig. 2 World Essential Oil Exporting Countries in 2018 [7]

Note: 1 = Brazil; 2= India; 3= USA; 4= China; 5= Mexico; 6=England; 7= Spain; 8= France; 9=Argentina; 10= Germany, 11=Indonesia.

Based on the above description, particularly on export-import and trade balance, there is a crucial need to conduct research on the market structure and analyze the unique position of Indonesian essential oil trade in the global market.

METHODOLOGY

This research employed a descriptive approach using cross section and time series data to determine individual variable value, where the market conditions of the primary exporting countries of essential oils are systematically and accurately described. The time series analysis was conducted using the interval from 2009-2018, while cross section research focused on the 5 main export destinations earlier mentioned. Furthermore, the commodities analyzed include HS code 3301 for essential oils.

Panorama [8] and Hayes [9] calculated the market share of each essential oil producer in the main export destination countries. Subsequently, the market structure of a country in the global essential oil trade was measured using Herfindahl-Hirschman Index [10] as follows:

$$HHI = \sum_{i=1}^{n} p_i^2 \qquad (1)$$

Where the Herfindahl-Hirschman index is a proportion or market share of Indonesian essential oils (p) in export destination countries (n). This parameter ranges from 0-1 and for values adjacent to zero, the market structure indicates a competitive state, while with values above 1, then the shift tends towards monopoly, with irregular market share distribution [9].

Furthermore, the competitive advantage of a product is possibly determined using the trade specialization index (TSI) [11]. This framework has the capacity to describe a commodity, in terms of ascertaining the position of a country, either as an exporter or an importer [12]. The equation is generally expressed as follows:

$$TSI_{ij} = (X_{ij} - M_{ij})/(X_{ij} + M_{ij}) \quad (2)$$

Where X_{ij} and M_{ij} are the export and import of good i by country j, respectively. The standard value of the index ranged from -1 to 1. However, with a positive TS value between 0 and 1 ($0 < TSI \leq 1$), the commodity then demonstrates a robust competitiveness or the country in question tends to be the exporter, as domestic supply appears greater than demand. Conversely, with a negative TSI value between -1 to 0 ($-1 \leq TSI < 0$), the commodity obtains low competitiveness or tends to be the importer, as local supply become lesser.

RESULTS AND DISCUSSION

Indonesian Essential Oil Export Destination Countries

Based on available data between 2009-2018, about 62 destinations were recorded for Indonesia's essential oil exports, comprising 20 regular routines, while the remaining were incidental [5]. The 5 main export domains, include Spain, France, India, Singapore and USA. Essential oil trading analysis followed the harmonized system (HS) nomenclature with HS code 33.01. Majority of the main destinations are developed nations. Figure 3 shows the average growth in the product value to recipient countries.

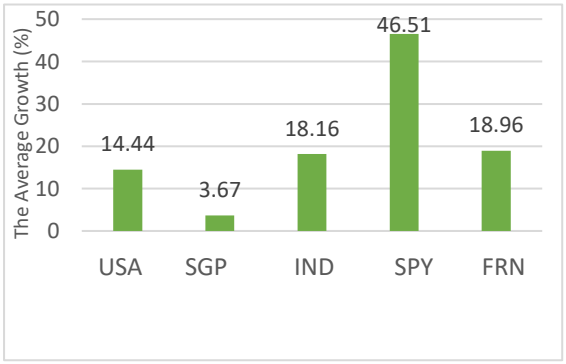


Fig. 3: The Average Growth (%) of Indonesia's Essential Oil Export Destination Countries, 2009-2018 [5].
Note: SGP = Singapore; IND= India; SPY = Spain; FRN = France

Market Structure

Herfindahl-Hirschman Index (HHI) is a type of concentration model used to measure the market structure to obtain an overview of the dominant essential oil market share for each participating country. Also, by realizing HHI value, the characteristics of the essential oil market structure are possibly identified. These properties include the number of producers, barriers to market entry, power to determine prices or profits generated, efficient use of products, and shared market information [8].

In entirety, the average HHI estimate in terms of the 5 main export destinations, exhibited the maximum and the minimum values in the Indian and French markets, respectively (Table 3).

The market structure in the United States with an average HHI of 826.2 indicates a monopolistic outcome and is characterized by product differentiation in the form of quality variations, product grouping, less competitions, and barriers to market entry [13]. In terms of the determining power of prices and profits, the market tends appears insignificant. The absorption of essential oils is massive, according to USA population. Furthermore, in terms of market information, several celebrity endorsements and the use of internet are very common.

The market structure in Singapore shows a state of oligopoly, based on the average HHI of 1622.8. Essential oil exporting countries show a high degree of dependence on each other. Therefore, the ability to influence the market also exists. Several players in Singaporean market are becoming more intense, with the increasingly high competition.

Barriers to market entry are relatively high with strict procedures [14]. Singapore's imported essential oils occur in the form of crude oil. The country refines for export to other states that serve industrial needs [15]. The product efficiency appears relatively poor as Singapore re-exports. In addition, low absorptions are based on limited information. Therefore, the aromatherapy products and essential oil fragrances are less popular.

The market structure in India is oligopoly and is characterized by price decision from one exporting country to another. There is a non-price competition, including advertising wars. However, HHI average value of 1692.5 indicates relatively lesser triggers on the level of competition. Trade barriers are also referred as barriers to trade and investment [16]. These constraints occurring as import tariffs, risk of bureaucratic delays, risk of bribery/corruption, and inadequate infrastructure, significantly impacted distribution and logistics, including essential oil

exports. Furthermore, the Indian market demands new additions to flavors and fragrances as a creative innovation.

Table 3. HHI Value of Indonesia's Essential Oils in Main Export Destination Countries.

Year	**USA**	Exporter	**SGP**	Exporter	**IND**	Exporter	**SPY**	Exporter	**FRN**	Exporter
2009	940.7	79	1853.4	57	2260.3	59	1138.1	65	531.5	104
2010	858.8	86	2053.2	59	1751.7	65	1001.7	73	479.1	107
2011	884.5	87	1924.6	71	1726.9	82	1073.5	67	498.9	115
2012	1015.1	89	1928.3	62	1418.9	73	1020.7	70	522.9	120
2013	926.7	91	1731.3	64	1736.6	64	953.1	75	492.5	124
2014	776.5	96	1427.7	76	1685.9	66	926.6	77	459.1	114
2015	758.8	92	1338.6	80	1220.6	63	1063.9	82	471.1	115
2016	735.2	100	1284.9	86	1365.4	61	917.8	87	467.4	122
2017	672.1	105	1369.0	86	1749.3	68	958.9	89	469.6	116
2018	693.4	105	1317.3	77	2009.2	66	1005.9	86	463.8	115
Average	**826.2**		**1622.8**		**1692.5**		**1006.0**		**485.6**	

Note: SGP = Singapore; IND= India; SPY = Spain; FRN = France

Another obstacle is limited market information, due to the risk of bribery / corruption of data accumulation.

The Spanish market structure with an average HHI value of 1006.1 represents a monopolistic market, where product differentiation exists, although similar products can be replaced. Therefore, varying commodities are needed among exporting countries to increase competition. In comparison to the market structure of Singapore and India, Spanish market has a larger number of players, indicating a higher competition.

Furthermore, the characteristic of entry barriers is relatively low [17], and European Union buyers, including the perfume industry, tends to search for unique essential oils. New players from developing countries are required to compete in terms of quality, price and reliability, sustainability as well as meet ISO, IFRA, Organic, FSC, Fair Trade and Fair wild standards. Participants have virtually no power to negotiate prices, resulting to profits at normal levels. Essential oil products are absorbed relatively high in the Spanish market, due to open information where celebrity endorsements are employed to promote trademarks, despite adding to production costs.

Finally, the structure of the French market, with an average HHI value of 485.6, indicates a monopolistic state and is characterized by product differentiation possibly replaceable by similar competing commodities. Judging from the vast number of actors, there is a relatively high consumption potential for essential oils among the French population. In addition, no serious trade barriers exist [18], except the growth of particular plant types in certain seasons. Furthermore, market information is accessible with the internet as a distribution network.

The Singaporean market has the largest contribution of Indonesian essential oil exports, particularly the leading patchouli oil, compared to the other major destinations. However, based on limited available players, low competition is prevalent in the producing country. In the ASEAN region, Singapore subsequently exports to industry and final customers, resulting to a minimal sales value. This experience varies from destination countries in Europe as the final end users. Therefore, a higher added value is observed. However, to significantly expand the European market, it is necessary to meet the legitimate requirements [19].

Essential Oils Trading Specialization Position

TSI analysis is used to determine the Indonesia's essential oils as an import or export nation to global destinations, including the United States, Singapore, India, Spain and France. The results are represented in Figure 4 and Table 4 below.

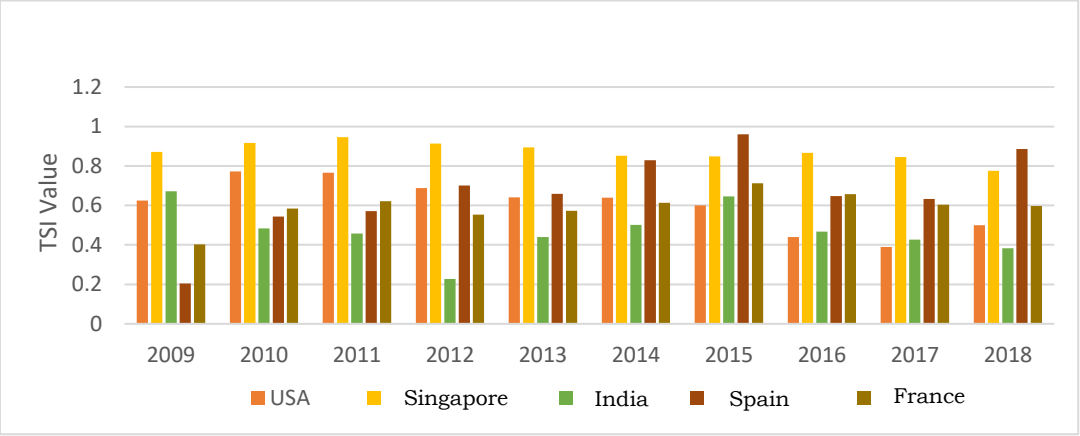


Figure 4. The TSI Value of Indonesia's Essential Oils in Main Destination Countries

The distribution of TSI value in tandem each year of Indonesian essential oils shows that USA and India tend to decrease. In contrast to the case in Spain and France there was an increase in the TSI value. Meanwhile in Singapore, the TSI value was relatively stable throughout 2009-2018.

Table 4. The Average TSI Value of Indonesia's Essential Oils in Main Destination Countries

Description	USA	Singapore	India	Spain	France
Average TSI Value	0.61	0.87	0.47	0.66	0.59

Indonesia's essential oil trade to the United States attained a growth stage with an average TSI value of 0.61. Under this circumstance, the domestic market conditions showed a greater supply, compared to demand, where strong competitiveness possibly exists. In addition, the import value from the United States continues to increase every year and the highest rate obtained in 2018 was estimated at USD 13 million.

Similarly, the trade to Singapore achieved a maturity stage with an average TSI value of 0.87. This shows a standardizing level using technology and substantial competitiveness. Under this condition, Indonesia is globally recognized as a net exporter of essential oil commodities in the Singaporean market.

The export to India reached a growth stage with an average TSI value of 0.47. Despite obtaining the smallest estimate, it also shows that the product is within the export expansion stage, where strong competitiveness exists. However, the import value was relatively high in 2018, indicating a massive India exports of essential oils to Indonesia in the form of processed products. Meanwhile, the local downstream sector employs this derivative nature as raw materials. Consequently, Indonesia needs to import essential oils from other countries, particularly from India.

The average TSI value of Indonesian essential oils in Spain is 0.66, indicating a growth stage. Under this circumstance, the domestic market conditions for the product showed a higher supply than demand. This implies that similar samples in Spain occur in the expansion stage, also with robust competitiveness. In addition, the export value tends to increase, while the imports possibly declined. Furthermore, the value of essential oil imports in Spain increased rapidly from 2015-2016 with an estimate of 85%, but decreased to USD 1 million in 2018.

The average TSI value of Indonesian essential oils in France is 0.59, indicating a growth stage. Similar to the other three main export destination countries for Indonesia's essential oils, the growth stage indicates that Indonesia's essential oil trade in France is in the stage of expanding exports which has strong competitiveness. Meanwhile, the export and import value of Indonesian essential oils to France tend to increase in tandem each year.

The four main export destinations, including the United States, India, Spain and France, attained a growth stage, with strong product competitiveness. Meanwhile, the Singaporean market observed a maturity stage, indicating an already existing position as a net exporter. However, to maintain and increase competition, sufficient maintenance is required. Purchasing countries are able to receive essential oil products from Indonesia with 3Q standards in quality, quantity and continuity.

CONCLUSION

This research showed a monopolistic market structure of Indonesian essential oils, with high competition in the 2 main export destinations, United States of America and France. Meanwhile, the other 3 countries, termed Spain, India and Singapore obtained a state of oligopoly, with relatively low competition.

Furthermore, the commodities occurred in the growth stage in the United States of America, India, Spain and France, with potentials to support expansion. However, the maturity stage only exist in Singapore, with a trade specialization position as a net exporter.

REFERENCE

[1] Julianto, Tatang S. 2016. Indonesia's Flower Essential Oil. Deepublish Publisher: Yogyakarta

[2] Ministry of Trade, Republic of Indonesia. 2011. Indonesian Essential Oil: The Scents of Natural Life. Handbook of Commodity Profile. Published by: Trade Policy Analysis and Development Agency (Trecyda), Ministry of Trade, Republic of Indonesia.

[3] Indonesian Essentials Council. 2018. Essential Data, Essential Plants, Export Destination Countries. http://www.atsiri-indonesia.com/. Accessed on 12 March 2020 at 19.30 WIB

[4] Barbieri, Cinzia & Borsoto, Patrizia. 2018. Chapter 6. Essential oils: Market and Legislation. In Potential of Essential Oils. http://dx.doi.org/10.5772/intechopen.77725

[5] UN Comtrade. 2019. United Nations Statistics Division-Commodity Trade Statistics Database (COMTRADE). http://comtrade.un.org/db. Accessed on March 20, 2020 at 17.00 WIB

[6] Center for Chemical Research, Indonesian Institute of Sciences (LIPI). 2019. Essential Oil Fraction Products as Chemical Raw Materials. Indonesian Institute of Science Research (LIPI): Jakarta

[7] International Trade Statistics (TRADEMAP). 2019. Trade Statistics For International Business Development. http://trademap.org. Accessed on February 25, 2020 at 13.00 WIB

[8] Panorama, Maya. 2016. Market Structure: Analysis Using Curves. Idea Press Yogyakarta: Yogyakart

[9] Hayes,Adam. 2021. Herfindahl-Hirschman Index(HHI).Investopedia. https://wwwinvestopedia.com/terms/h/hhi.asp

[10] Dumičić, Ksenija, Jošić, Hrvoje and Žmuk, Berislav. 2018. Investigating Export Market Concentration For Developed, Developing And Transition Countries. International Journal - VALLIS AUREA • Volume 4 • Number 1 • Croatia, June 2018

[11] Yusefzadeh, Hassan et.al. 2015. A Study of Comparative Advantage and Intra-Industry Trade in The Pharmaceutical Industry of Iran. Global Journal of Health Science, vol 7, No 6,2015, ISSN 1916-9736; E-ISSN 1916-9744

[12] Ekananda, Mahyus. 2014. International Economics. Erlangga: Jakarta

[13] Food and Drug Administration (FDA). 2019. United States Essential Oil Quality Requirements. http://fda.gov. Accessed on December 10, 2020 at 10.30 WIB

[14] Health Science Authority (HSA). 2017. Import Procedure to Singapore Market. http://hsa.gov.sg. Accessed on 12 December 2020 at 13.00 WIB.

[15] International Trade Promotion Center Singapore (ITPC Singapore). 2016. Market Brief Essential Oil HS 3301. http://itpc-singapura.es. Ministry of Trade: Jakarta

[16] International Trade Promotion Center Chennai (ITPC Chennai). 2016. Essential Oil HS 3301. http://itpc-chennai.es. Ministry of Trade: Jakarta.

[17] International Trade Promotion Center Barcelona (ITPC Barcelona). 2016. Trade With Remarkable Indonesia. http://itpc-barcelona.es. Ministry of Trade: Jakarta

[18] International Trade Promotion Center Lyon (ITPC Lyon). 2016. Market Brief Essential Oil HS 3301. http://itpc-lyon.es. Ministry of Trade: Jakarta.

[19] United Nations Globally Harmonized System (GHS) of Europe. 2018. Classification and Labeling (CLP / GHS). http://ec.europe.eu. Accessed on 15 November 2020 at 08.00 WIB

7th Int. Conf. on Structure, Engineering & Environment (SEE), Pattaya, Thailand, Nov.10-12, 2021, ISBN: 978-4-909106070 C3051

AN *IN SITU* VOLCANIC GASEOUS EMISSIONS CONCENTRATION MEASUREMENT SYSTEM: A CASE STUDY FOR WELIRANG VOLCANO, MALANG, INDONESIA

Arinto Yudi Ponco Wardoyo[1], Hari Arief Dharmawan[1], Muhammad Nurhuda[1], Arif Budianto[1], and Azarine Aisyah Widhowati[1]

[1]Faculty of Mathematics and Natural Sciences, University of Brawijaya, Indonesia

ABSTRACT

Gaseous emissions and particulate matter in different aerodynamic diameters can be derived from many sources, such as volcanic activities. According to previous studies, gaseous emissions, such as sulfur dioxide, carbon monoxide, and carbon dioxide, may affect human health. Furthermore, there is a significant correlation between exposure to gaseous emissions and cell deformation, indicating the organ system's abnormalities. Therefore, there is a need to mitigate and identify volcanic gaseous emissions as an identification system. Thus, this study conducted an *in situ* volcanic gaseous emissions concentration measurement system collected directly from areas near the plume of Welirang volcano, Malang, East Java Province, Indonesia (7°43'59" S 112°34'29" E). The measurement system consisted of several gases and particulate matter sensors. The measurements were conducted on ten areas surrounding the Welirang volcano's plume to identify the highest volcanic emission dispersion. The emission concentrations were measured for five minutes every 30 seconds as the interval time. The results show that emission consisted of several gases and particulate matters in different concentrations, such as carbon monoxide, carbon dioxide, methane, and toluene. In addition, the concentrations were influenced by the distance of the measurement sites to the plume. Therefore, the system works well with a response time of fewer than two seconds and the sensitivity of 0.56 Volt/ppm and 0.63 Volt/ppm, respectively, for methane and toluene. The range of the system measurement is 0-100 ppm (carbon monoxide), 400-1,000 ppm (carbon dioxide), and 0-100 ppm (methane), and 0-100 ppm (toluene).

Keywords: Gaseous emission, in situ measurement, Volcanic gaseous emission, Welirang volcano

INTRODUCTION

Volcanic activities are natural sources of air pollutant emissions in the form of gaseous and particulate emissions. They may release gaseous emission consisted of carbon monoxide (CO), carbon dioxide (CO_2), methane (CH_4), sulfur dioxide (SO_2), mercury (Hg), and hydrogen sulfide (H_2S). Metals, including As (arsenic), Pb (lead), Sb (antimony), Se (selenium), and Tl (thallium), can also be found in the mixture substances [1] [2]. This activity also generates volcanogenic particulate matter that varied in composition, shape, and size. Both internal and external factors influence the composition's variety. The internal factor is related to the magmatic activity, while the external one is associated with the deposited dust in the magma pathway's surface [3]. Both volcanogenic gaseous and particulate emissions are formed from crustal rocks, fluid, and magma originating from the earth's mantle.

Carbon monoxide is considered an indirect greenhouse gas and contributes to the chemical reaction that produces other greenhouse gases, such as carbon dioxide and methane. Both are the two most important greenhouse gases, resulting in the acceleration of the global warming process [4][5]. However, besides global warming, volcanism can cause the exact opposite of it. Volcanism has a cooling effect when there is a major eruption. The particles of the materials from the eruption float to the earth's atmosphere and block the solar radiation. This case happened in 1815 when Mt. Tambora (Indonesia) massively erupted, which cause prolonged winter that led to famine [6].

Besides having impacts on the environment, volcanic emissions can also bring adverse impacts on humans. The impact of particulate emissions for humans ranges from respiratory to cardiovascular disease, cognitive decline, and stroke [3], [7]. These adverse impacts are then classified based on their diameter, determining their deposition efficiency in the human body. Large particles (> 2.5 μm in diameter) are deposited in the trachea, bronchi, and bronchioles. At the same time, small particles (<2.5 μm in diameter) are deposited in the lung area that can penetrate deeper into the respiratory system to the blood circulation and the heart and kidneys [8]. The deposited particulate matter in the respiratory tract will directly impact the inhalation capacity of the lungs and may cause many negative cell deformation [9], [10]. In contrast, it can induce

changes in skin morphology and oxidative stress that lead to inflammatory cytokines on the skin. The greater the surface area of a particulate matter that enters the body causes a higher ability to produce oxidative stress. Moreover, research in the Azores (Portugal) found a severe increase in chronic bronchitis from volcanic emissions. Furthermore, volcanic emissions exposure can lead to cancers of the mouth and larynx [11].

Air quality measurement systems that consist of gas and PM measurement are always in constant development to produce the nearest value to the actual value, especially volcanic emission measurement systems. Previous research has developed a portable DOAS (Differential Optical Absorption Spectroscopy) system for scanning SO_2 concentrations. This instrument measures the solar radiation that reaches the CCD (Charge-Coupled Device) detector to generate a spectral signal from the spectrometer then uses the DOAS algorithm [12], [13]. Gas measurement using satellites or atmospheric chemistry experience (ACE) has a similar principle to DOAS using solar radiation. It is done by measuring the composition of pollutants in the atmosphere, one of which is volcanic emissions using the solar occultation method. An occultation occurs when another object covers an object as it passes through between the observed object and the observer. Measurements are taken when the sun rises and sets. The center of solar radiation will be tracked, and the decrease in light intensity is measured using a near-sight infrared spectrophotometer [14]. PM and gas measurement systems can also be carried out using a satellite-based sensor system. The sensors are mounted on the satellite so that they can measure various pollutant gases. Near real-time air, pollutant measurement can detect PM, CO, SO_2, NH_4, CO_2, etc. Sensors such as the Cloud-Aerosol Lidar with Orthogonal Polarization (CALIPSO) provide 3D information regarding air pollution [15], [16].

MATERIALS AND METHODS

System Circuit

The minimum system circuit has a step-down switching regulator IC (integrated circuit) LM2596. This circuit converts the input voltage (12 V) to 5 V output voltage (V_{cc}) up to 3 A of continuous current *I*. The input voltage is used to power up the microcontroller board, suction pump, and cooling fan. The output voltage is connected to the sensor's V_{cc} (common voltage collector) and *G* (ground) pins. This circuit is added with a safety switch to cut off the current (Fig. 1).

For sensing and signal processing purposes, the study uses an Arduino UNO microcontroller and six different sensors. In contrast, a Sensirion SHT-31D (I2C – Inter-Integrated Circuit - pins are connected to *SDA-SCL* pins of the microcontroller) is used to monitor the temperature (T) and relative humidity (RH). The toluene (C_7H_8) concentration is detected using a Figaro TGS2600 (connected to the analog pin A_0 of the microcontroller). In addition, a metal oxide CCS811 sensor is installed on the system to measure equivalent carbon dioxide (eCO_2) (equivalent carbon dioxide) concentrations (connected to *SDA* and *SCL* pins of the microcontroller). Another sensor, MQ-9, is connected to the A_1 pin of the microcontroller to measure methane (CH_4) and carbon monoxide (CO) concentrations. The measured concentrations are then displayed on a 20 x 4 I2C LCD (liquid crystal display).

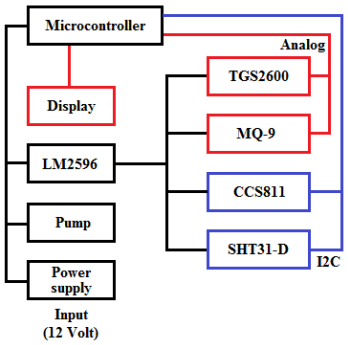


Fig. 1 The schematic diagram of the minimum circuit.

System Calibration and Measurement

The system was calibrated using a TSI Q-Trak model 7575x (CO, eCO_2, T, and RH) and a TVOCs meter (Total of Volatile Organic Compounds) inside an experimental chamber with a volume of 12,000 cm^3. This procedure was repeated three times (n = 3) for an hour. At the same time, the resulted resistance (R_s) and voltage output signals (V) were compared to the provided datasheet and the comparator devices (Fig. 2).

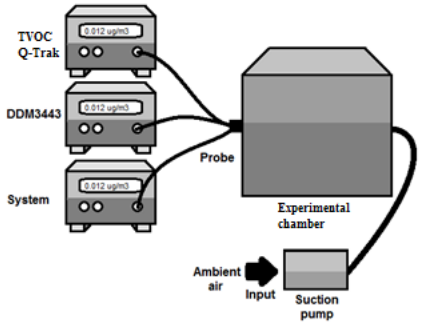


Fig. 2 The procedure of the system calibration inside an experimental chamber.

The resulted values were analyzed to obtain the sensitivity (S), the response time (t_r), and the range (r) [17]. Response time is calculated by repeating the measurement in eight sampling points. The difference duration (Δt) between the initial time (t_0) and the processing time of the microcontroller (t_e) is considered as the response time [17]. Sensitivity is obtained from the system output values, C_n, whose concentrations are increased stepwise from C_0 to C_{max} related to the datasheet (A), representing the effect of offset parameter (Eq. 2) [18]:

$$S = \frac{\Delta V}{\Delta C} \quad (1)$$

Sampling Sites

This research was conducted at the areas surrounding Welirang volcano's plume, Malang, East Java, Indonesia (7°43'58" S 112°34'29" E, elongation = 3,070 m a.s.l.). The measurement areas were divided into 12 sampling sites (A1 to A12 sites) to identify the dispersion of the volcanic emissions (Fig. 3). These site variations were varied based on the plume's distance (s) from the measurement areas [1], [12]. These sites are located 4 to 5 km away from the plume (measurement radius) with an elongation of 1,542 to 1,730 m a. s. l. (above the sea level) (Table 1).

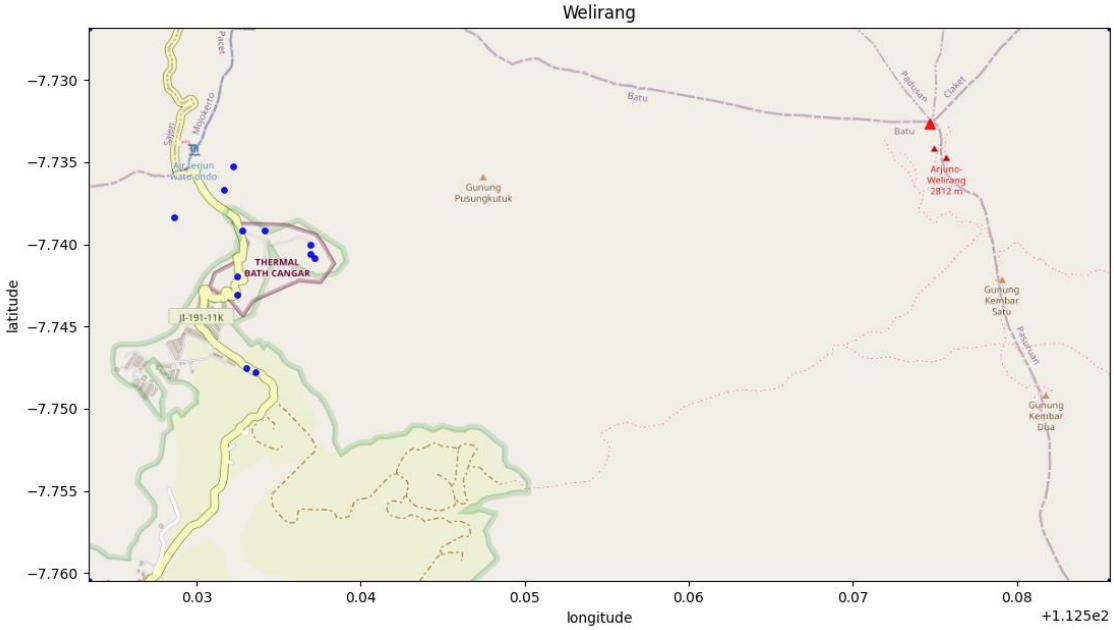


Fig. 3 The sampling sites (red dots) in the areas surrounding Welirang volcano.

Table 1 Sampling sites

Site	Radius (m)	Elongation (m a. s. l.)
A1	5,090	1,690
A2	4,310	1,730
A3	4,440	1,624
A4	4,230	1,590
A5	5,200	1,542
A6	4,190	1,590
A7	3,830	1,653
A8	3,770	1,650
A9	3,710	1,660
A10	5,330	1,600
A11	4,640	1,640
A12	5,630	1,727

Statistical Analysis

All data were written as the mean values ± standard error of the mean (SEM). A linear function regression was used to identify the measurement system performance to the filtered ambient air, including sensitivity, response time, and accuracy. At the end, $R^2 > 0.75$ was considered statistically significant [19]. The dispersion parameter of the emission was approximated by using a correlation between measurement radius and the measured concentrations (interpreted as the dispersion graph).

RESULTS AND DISCUSSION

CO and CO_2

The measured CO and CO_2 concentrations are presented in Fig. 4. There is no significant difference between CO concentrations from A1 to A12 ($p < 0.05$). The concentrations are in the range of 2 to 3 ppm. In contrast, there is a fluctuation in CO_2 concentrations related to the distance from the plume (the concentrations are 400.4 to 401.4 ppm). The inactive status of the plume may influence these differences. CO_2 shall be found as the volcanic activity output as major gas species [20], [21], even in a volcanic lake as the diffuse CO_2 [22]. Edwards et al. [1] reviewed this gas's existence may also serve as more tracer gas for other emissions, such as Hg. This gas also indicates the possibility of the geothermal prospect and other volcanic parameters [23]. Considering that there was no significant volcanic activity during the measurement time, it is possible to determine that the influencing factor of these gases is the distance (x). According to the secondary data obtained from the meteorology station, there is no significant difference in the wind speed.

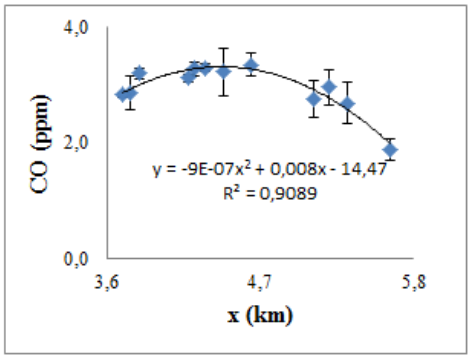


Fig. 4 Measured CO and CO_2 concentrations from different measurement radius: (a) upside: CO and (b) downside: CO_2.

Toluene (VOC Element)

Toluene concentrations are in the range of 1 to 6 ppm. The results show that volcanic activity may generate volatile organic compounds, such as toluene or C_7H_8 (Fig. 5). The developed system works well in measuring this gas, with a sensitivity of 0.63 Volt/ppm (0 to 100 ppm of the system range). The system needs <2 s to detect the toluene gas, as defined as the response time. As state in a previous study, there are many organic compounds from volcanic gases (more than 200 types) [26]. They are indeed derived from abiogenic gas-phase radical reactions, specifically at a high temperature [26]. However, there is limited information about the volatile compounds related to volcanic activity. As reported in a previous study, only bromine (either in volatile forms of condensed gas) was identified as the volatile compound emissions associated with the complex eruption in Puyehue-Cordon Caulle, 2011 [27].

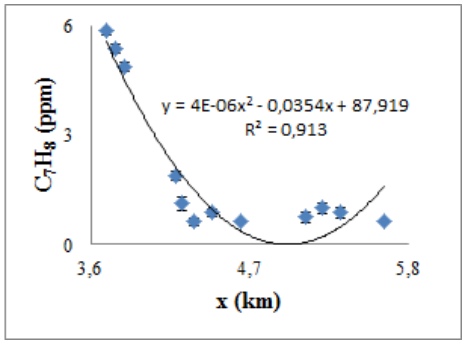


Fig. 5 Measured C_7H_8 concentrations from different measurement radius.

CH_4

Methane gas (CH_4) concentrations are interpreted in Fig. 6. The results show that the volcanic emission measurement has a value of 0 to 4 ppm, with a sensitivity of 0.56 Volt/ppm.

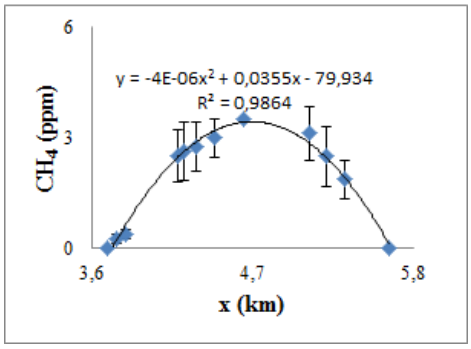


Fig. 6 Measured CH_4 concentrations from different measurement radius.

CONCLUSIONS

According to the results, it can be concluded that the system works well in measuring volcanic gas emissions. The system can measure methane, toluene, carbon monoxide, and carbon dioxide gasses in the range of 0 to 100 ppm. The developed system needs a response time of fewer than two seconds and a sensitivity of 0.56 Volt/ppm and 0.63 Volt/ppm, respectively, for methane and toluene. The resulted data are influenced by the distance of the measurement sites to the plume.

ACKNOWLEDGMENTS

The authors wish to acknowledge assistance or encouragement from colleagues Moch. Agung P. N., Eko Teguh P. A., Rizqi Amalia, and Maria Pramundhitya W. W. All authors thank the "Ministry of Research and Technology/ National Research and Innovation Agency Republic of Indonesia" for their financial contribution (contract number: 439.19//UN10.C10/TU/2021 and 023/ SP2H/LT/DRPM/2021, March 18th, 2021).

REFERENCES

[1] Edwards B. A., Kushner D.S., Outridge P. M., and F. Wang, Fifty years of volcanic mercury emission research: Knowledge gaps and future directions, Sci. Total Environ., Vol. 757, 2021, pp. 143800.

[2] Zelenski M. et al., Volcanic gas emissions from Taftan and Damavand, the Iranian volcanoes, J. Volcanol. Geotherm. Res., Vol. 397, 2020, pp. 106880,

[3] Trejos E. M. et al., "Volcanic emissions and atmospheric pollution: A study of nanoparticles," Geosci. Front., Vol. 12, no. 2, 2021, pp. 746–755.

[4] Dimitriou K. et al., Greenhouse gases (CO_2 and CH_4) at an urban background site in Athens, Greece: Levels, sources and impact of atmospheric circulation, Atmos. Environ., Vol. 253, 2021, pp. 118372.

[5] Liu S., Fang S., Liang M., Sun W., and Feng Z., Temporal patterns and source regions of atmospheric carbon monoxide at two background stations in China, Atmos. Res., Vol. 220, 2019, pp. 169–180.

[6] Fell H. G., Baldini J. U. L., Dodds B., and Sharples G. J., Volcanism and global plague pandemics : Towards an interdisciplinary synthesis, J. Hist. Geogr., Vol. 70, 2020, pp. 36–46.

[7] Ramírez O., Sánchez de la Campa A. M., Amato F., Moreno T., Silva L. F., and de la Rosa J. D., Physicochemical characterization and sources of the thoracic fraction of road dust in a Latin American megacity, Sci. Total Environ., Vol. 652, 2019, pp. 434–446.

[8] O. Mazuryk et al., "Influence of aqueous extracts of urban airborne particulate matter on the structure and function of human serum albumin," Environ. Pollut., Vol. 263, 2020.

[9] Wardoyo A. Y. P., Juswono U. P., and Noor J. A. E., The association between the diesel exhaust particle exposure from bus emission and the tubular epithelial cell deformation of rats, Environ. Sci. Pollut. Res., Vol. 27, 2020, pp. 23073–23080.

[10] Wardoyo A. Y. P., Juswono U. P., and Noor J. A. E., How exposure to ultrafine and fine particles of car smoke can alter erythrocyte forms of male mice, Polish J. Environ. Stud., Vol. 28, no. 4, 2019, pp. 2901–2910.

[11] Heaviside C., Witham C., Vardoulakis S., and et al, Potential health impacts from sulphur dioxide and sulphate exposure in the UK resulting from an Icelandic effusive volcanic eruption, Sci. Total Environ., Vol. 774, 2021, pp. 145549.

[12] Raponi M. et al., First portable scanning-DOAS system developed in Latin America for volcanic SO2 monitoring, J. South Am. Earth Sci., Vol. 108, 2021.

[13] Li X. et al., Study of aerosol characteristics and sources using MAX-DOAS measurement during haze at an urban site in the Fenwei Plain, J. Environ. Sci. (China), Vol. 107, 2021, pp. 1–13.

[14] Bernath P. F., Crouse J., Hughes R. C., and Boone C. D., The Atmospheric Chemistry Experiment Fourier transform spectrometer (ACE-FTS) version 4.1 retrievals: Trends and seasonal distributions, J. Quant. Spectrosc. Radiat. Transf., vol. 259, 2021, pp. 107409.

[15] Tang Y. *et al.*, Air quality impacts of the 2018 Mt. Kilauea Volcano eruption in Hawaii: A regional chemical transport model study with satellite-constrained emissions, Atmos. Environ., vol. 237, 2020, pp. 117648,

[16] Singh D., Dahiya M., Kumar R., and Nanda C., Sensors and systems for air quality assessment monitoring and management : A review, J. Environ. Manage., Vol. 289, 2021, pp. 112510.

[17] Jin H. et al., "A humidity sensor based on quartz crystal microbalance using graphene oxide as a sensitive layer," Vacuum, Vol. 140, 2017, pp. 101–105.

[18] Pongsuttiyakorn T., Sooraksa P., and Pornchalermpong P., Simple effective and robust weight sensor for measuring moisture content in food drying process, Sensors Mater., Vol. 31, no. 7, 2019, pp. 2393–2404.

[19] Alfano B. et al., "A review of low-cost particulate matter sensors from the developers' perspectives," Sensors (Switzerland), vol. 20, no. 23, 2020, pp. 1–56.

[20] Yang X. et al., The impact of volcanic activity on the deposition of organic-rich shales: Evidence from carbon isotope and geochemical compositions, Mar. Pet. Geol., vol. 128, 2021, pp. 105010.

[21] Zelenski M., Simakin A., Taran Y., Kamenetsky V. S., and Malik N., "Partitioning of elements between high-temperature, low-density aqueous fluid and silicate melt as derived from volcanic gas geochemistry, Geochim. Cosmochim. Acta, Vol. 295, 2021. pp. 112–134.

[22] Andrade C., Cruz J. V., Viveiros F., and Coutinho R., Diffuse CO_2 emissions from Sete Cidades volcanic lake (São Miguel Island, Azores): Influence of eutrophication processes, Environ. Pollut., Vol. 268, 2021.

[23] Taussi M., Nisi B., Vaselli O., Maza S., Morata D., and Renzulli A., Soil CO_2 Flux and Temperature From a New Geothermal Area in the Cordón De Inacaliri Volcanic Complex (Northern Chile), Geothermics, Vol. 89, 2021, pp. 101961.

[24] Aroskay A. et al., Multi O- and S-isotopes as tracers of black crusts formation under volcanic and non-volcanic atmospheric conditions in Sicily (Italy), Sci. Total Environ., vol. 750, 2021. pp. 142283.

[25] Henley R. W. and Fischer T. P., Sulfur sequestration and redox equilibria in volcanic gases, J. Volcanol. Geotherm. Res., Vol. 414, 2021, pp. 107181,

[26] Schwandner F. M., Seward T. M., Gize A. P., Hall K., and Dietrich V. J., Halocarbons and other trace heteroatomic organic compounds in volcanic gases from Vulcano (Aeolian Islands, Italy), Geochim. Cosmochim. Acta, Vol. 101, 2013, pp. 191–221.

[27] Bubach D., Pérez Catán S., Arribére M., and Guevara S. R., Bioindication of volatile elements emission by the Puyehue-Cordón Caulle (North Patagonia) volcanic event in 2011, Chemosphere, Vol. 88, no. 5, 2012, pp. 584–590.

7th Int. Conf. on Structure, Engineering & Environment (SEE),
Pattaya, Thailand, Nov.10-12, 2021, ISBN: 978-4-909106070 C3051

INVESTIGATION OF WATER-RESERVOIRS IMPACT MECHANISM ON GROUNDWATER AND INDICATOR SCHEME OF ASSESSMENT

Matchavariani Lia[1], Metreveli Giorgi[1] and Gulashvili Zaza[1]

[1]Faculty of Exact and Natural Sciences, Ivane Javakhishvili Tbilisi State University, Georgia

ABSTRACT

All water-reservoirs play a unique role in determining the mechanism of reservoir impact on groundwater. The goal of our study was to develop a modern option of an impact mechanism and indicator scheme to assess reservoirs impact on groundwaters. For this purpose, the methods of mathematical statistics and stochastic hydrology were used. Different types of reservoirs with different durations of exploitation were selected as a study object. As per the updated impact mechanism, the filtration regime and yield are the function of properties of water-reservoir level and the bed constituent rocks and responds to the level fluctuation with a certain delay. One of the main determinants of the delay time is the distance from the reservoir to the filtrate monitoring station. It was found that filtration decreases in proportion to the bed silting, while the time of delay increases in proportion to silting. As silting reaches its maximum, the filtration regime is determined only by the filtrate of the derivation tunnel and other structures, as well as by the level of reservoir. The indicator scheme selected to evaluate the reservoir impact on the ground waters is as follows: debit of streams, range of underground waters' horizon fluctuation, infrastructure affected by the landslide and bogged plots of field. The criteria to assess the efficiency of water-reservoir are: if the filtrate is used for any purpose, its value augments the efficiency of the reservoir; if the filtrate is harmful for the infrastructure and environment, it undermines the importance of reservoir.

Keywords: Environment Impact Assessment, Filtration, Groundwater, Indicator, Water reservoirs

1. INTRODUCTION

The issues of using and design of water-reservoirs, their positive and negative aspects, sedimentation-siltation, expected risks of infrastructure and population safety, as well as estimation of reservoir impact on the environment, have been multiple times and comprehensively studied by many scientists from different regions of the world [1]–[7]. There are also many publications related to the management, planning, forecasting, solution, seashore protection, assessment of water resources in the environment generally in the scientific literature [8]–[19]. The impact of reservoirs on environmental components, has been repeatedly studied. With respect to ground-water, it is a special exception. As a rule, the impact of climate change on groundwater, or vice versa, and such other issues were studied. However, the impact of reservoirs on groundwater has been studied minimally and is practically not reflected in the scientific literature. Exactly this has led us to focusing our interest for studying the reservoirs impact on groundwater as well. This issue is especially relevant in the case of mountain reservoirs, where due to the large slope, water flows into the layers of inclined rocks. In conditions of plain terrain, such impacts on groundwater are not taken into account.

Mountain reservoirs formed on mountain rivers within the limits of geographical elements vertical zoning with volume >0.1 mln m^3. Their main features are: big bed depth (h), high amplitude of level variation (A), intense sanding-up (mostly with coarse sediment) and strong impact on groundwaters. The latter feature is especially noticeable in the regions where the reservoir is formed in the valleys built with sedimentary and dislocated volcanic rocks. The Caucasus Mountains are one such region. Chirkey, Jvari, Zhinvali, Sarsang, Irganai and other dams with the depth of 50-250 m are found there. They are characterized with a high amplitude and speed of level variation. Such features define the peculiarities of the groundwater regime in both races.

The water from a water reservoir penetrates the ground through the reservoir bed and slopes, as well as from dam and derivation tunnel. Consequently, the volume of filtered water is the function of the area of the wetted bed surface (f) and the hydrostatic pressure (p), created by the dammed-up water on the reservoir bed and slopes. These factors change depending on the level of the dammed-up water (H). With H value, it is possible to monitor and describe the regimes of underground waters with certain accuracy as well.

The bed geo-geomorphological features (water permeability – i, gradient – φ) and dammed-up water level regime (H) define the type and degree of a reservoir impact on underground waters.

$$\Phi = f(i, \varphi, H)$$

Certain volume of filtered water increases the horizon of local streaks of the underground waters, while the remaining volume outcrops as springs at

some distance from the reservoir, or forms swamps or landslides. These objects are visible indicators of a reservoir impact on groundwaters. Some of them are positive, while others are negative. Estimating a reservoir impact on the groundwaters means studying the said indicators and selecting relevant measurement parameters for each of them.

The type of impact differs depending on both stream of the reservoir (upstream and downstream). The impact indicators in the headrace are: landslides (m) and deformed areas (Φ) by damming up the groundwaters. The filtrate in the tailrace forms streaks and basins of underground waters and increases their horizons. Such waters are positive indicators when they outcrop on the surface and are used for any aim (irrigation, public water supply, power supply, etc.). The indicator is negative if when the areas of infrastructure, buildings and premises deformed due to landslide and piping processes are bogged or salinated. These indicators are estimated by relevant features: a) variability of the groundwater reserve – by their spatial-temporal oscillation amplitude (A, cm) of their horizon; b) the variability of springs is evaluated by their yield (q, l/sec., m^3/sec) and the variability of landslides – by their area (f, m^2, ha).

The goal of the present paper is to provide an up-to-date version of the mechanism of the reservoir impact on groundwaters and develop an indicated plan to estimate the impact based on monitoring of the regimes of active reservoirs and available data.

2. METHODOLOGY

The above-said goal was reached by means of the methods of mathematical statistics and stochastic hydrology – the least squares and analogy. For the water reservoirs where filtration is proportionate to the principal members of the water balance (river runoff, evaporation, atmospheric precipitations, etc.), an empirical water balance method was used. This method considers the filtration losses (Φ) as a principal member of the equation of the water balance of a reservoir, to which the expression must be realized. A plan of local indicators was necessary to develop in order to evaluate the impact outcomes.

3. RESULTS AND DISCUSSION

The water reservoirs of different types and duration of the Caucasus Mountains were selected as a study object, including Jvari dam (R.Enguri) with the highest-level variation amplitude; Tbilisi Reservoir, with its filtrate causing certain problems to the capital; highest Aparan Reservoir (1835 m asl) and Tsalka dam characterized by large volumes of filtrate and long operation (75 years). The filtration of the listed dams is high and their indicators are clearly presented, while the monitoring and field study materials are quite reliable.

Jvari dam is a regulating reservoir of Enguri HPP (normal filling level – 510 above sea level, volume – 1.1 m^2, range of level fluctuation – 70 m, greatest depth – 20 m). The dam is used for power generation purposes and has a significant touristic, recreational, fishing and industrial potential.

The dam occupies the part of the R.Enguri gorge built with carbonate rocks. There is a tectonic crack spread across the given section of the gorge. The crack is filled with sands and calcite cemented with dolomite clay. The hard rocks have a dense and vast network of tectonic faults. Most of them (>60 %) are narrower than 1 cm, but all of them are a potential filtrate duct. The water absorption of the constituent rocks of the bed of the dam is 0.17 l/sec and 0.07 l/sec for the right and left slopes respectively. During the construction, anti-filtration screens were provided in some of such water-permeable areas. However, their efficiency is less than the normal value during the high levels (H≥500 m asl) of the water reservoir. The area of the wetted slopes and bed, with which the dam affects the ground waters, is approximately 15 km^2. The maximum amplitude of its level fluctuation is 70 m. This means that the pressure difference, with which the impounded water acts on the cracks and fissures in the bed constituent rocks, reaches 7 Atmosphere. Such a pressure fluctuation expands the water ducts gradually and increases filtration losses.

This phenomenon partially explains the fact that despite the anti-filtration works, the losses across the slopes and bed of the reservoir is proportionate to the principal members of the water balance. The trend approved to explore this problem is the water balance calculations by using the following expressions:

$$\Sigma\Pi - \Sigma P = A \pm N, \quad \Sigma P - \Sigma\Pi = -A \pm N$$

here ΣΠ – is the balance revenue; ΣP – is the balance expenditure, with the filtration being one of its essential members (Φ); A – is the volume fluctuation in the reservoir; N – is the balance error. The latter is an occasional value with a variable sign, if all members of the balance are registered with an admissible accuracy. In other case, N>0 and N= ΣΦ and it is the function of the reservoir level and varies in different seasons of the year:

$$\Sigma\Phi = \Sigma\Pi - (\Sigma P + A)$$

As per the field and theoretical studies, accomplished for Jvari dam in 1980-2020, average filtration volume is 100 mln m^3. A certain amount of this water flows as springs on the land surface. Due to intense mudding of Jvari dam in 1980-2020, the filtration reduced and its role in supplying the dam decreased proportionally as well.

By 2020, the indicators of impact of Jvari dam on the underground waters are springs and submarine waters flowing out in the tailrace. At the initial stage of the dam operation (1970-80s), the filtrate formed

local landslide hearths in the tailrace. Currently, the hearths are stable, while the filtrate flows out onto the surface as springs. Such springs may be assessed as a positive indicator, as they are used by the population.

As of today, the role of the waters filtrated from the dam in supplying the underground reserve is determined by the volume and regime of the derivation tunnel filtrate. The derivation tunnel (length 16.0 km) operates under complex natural conditions. Consequently, there is a quite reliable system in place to register its condition and filtration losses. The data of the system were used to plot a polynomial curve of dependence between the dam levels and the filtration losses – filtrate (fig.1).

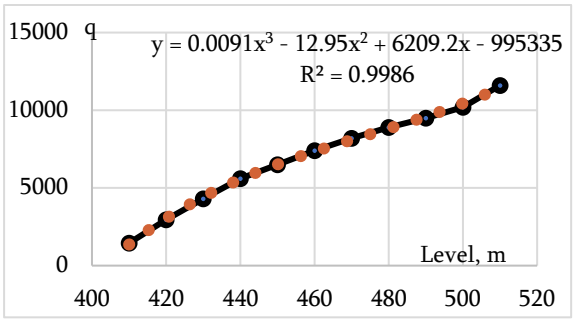


Fig. 1 Dependence curve of the filtrate output of Enguri HPP derivation tunnel (l/sec) and the dam levels

Dependencies of type Φ_d=Ғ(H) are most precisely expressed by a polynomial equation:

$y = ax^3 + bx^2 + cs + d$

At some locations, the filtrate in the derivation tunnel is localized in concrete tunnels (fig.2) and flows into the nearest valleys and rivers. Such an indicator, unless it is harmful, must be assessed as neutral, whose nature will determine the outcome of its action in the future. As an example, we can cite the filtrate from Tsalka dam, which flow out as springs in the R.Khrami valley.



Fig. 2. The spring with the highest yield of filtrate in the derivation tunnel

One of the major issues of the study of the impact of a water reservoir on the ground waters is the spatial-temporal association between the reservoir level (H), yield of the ground waters (q, l/sec., m^3/sec) and time (τ) needed for the filtrate to cover the distance from the reservoir to the point of outcrop onto the ground surface. The richest information to study this issue can be obtained from the results of monitoring of Sioni, Tsalka and Aparani dams.

The normal inundation level of Sioni dam is 1068.3 m; volume – 0.325 km^3; the maximum range of the level fluctuation – 55 m; the greatest depth is 67 m and the wetted surface area about 15.8 km^2. The dam is multi-functional (irrigation, communal water supply, power generation, tourism and recreation).

The bed of dam is built with conglomerates and sandstones. These rocks are almost totally covered with impermeable alluvial and diluvial deposits. An exception is the bank adjoining the left wing of the dam, from where the filtrated water outcrops on the river bank, 0.5 km down. Here, with the purpose of monitoring the filtration regime, the sections to measure its output were provided. The results of their monitoring clearly describe the association of the filtration output with the dam level (fig.3).

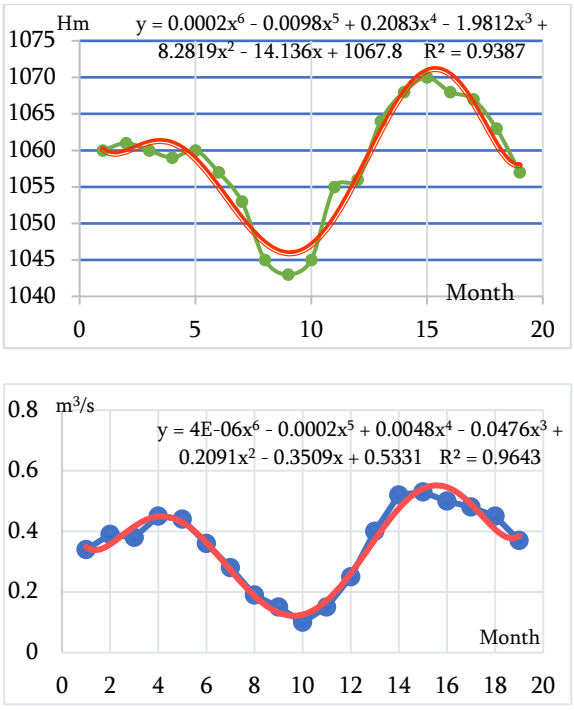


Fig. 3. Association between the average levels (A) and the filtration (B) of Sioni dam in the initial phase of the dam operation (VI.1964-XII.1965).

In 2016-2020, this system did not function and the measurements were done in the field. As the results show, there is a strong association between the dam levels and the filtrate output, according to which, the maximum average levels of the dam surpass filtrate maximum by 12-15 days. This means that the average filtrate motion rate is 35 m/day.

As per the monitoring results, filtration was highest (q≥0,5 m^3/sec) in the initial phase of the dam operation (1964-1970 years). As the episodic measurements of 2020 evidence, the filtration output was 0.05 m^3/sec and the Dam level did not exceed 1025 m asl. Consequently, for 66 years of the dam operation, sanding and mudding of the dam bed and slopes increased so much that the filtration decreased by almost ten times at the low and average levels (1015-1025 m). In the dam tailrace, the filtrate has formed landslide hotspots and made the residential area adjacent to the dam uninhabitable. Currently, the filtrate here forms a swampy massif, the area of which is as much as 1.5 ha. Consequently, the indicator of impact of the given dam on the groundwater in terms of swampy lands is definitely negative.

Tsalka dam is located in the R.Ktsia gorge, in a flat-bottomed cave with the same name. Its characteristics are as follows: normal flooding level 1512 m, volume 0.313 km^3, range of maximum fluctuation 14.5 m, length 30.6 m, greatest depth 25 m, area of wetted surface ~43,0 km^2. Its bed is built with dislocated volcanic rocks – mostly fissured dolerites, which have the tuff and volcanic ash aquifers of different thicknesses at some spots. Tsalka cave was formed in the Tertiary period. In this period, the paleo-volcanic currents of Korsus lavas blocked the cave from the south and created a funnel-like depresssion, in the center of which a water-bearing funnel-like depresssion remained open for lava. This geological formation is immediately associated with an alluvial water-bearing layer spread below it, which outcrops in gorge R.Khrami 3-6 km away. The water filtrated flew out as Dashbash springs at the same location even before the dam construction; however, its maximum flow did not exceed 3 m^3/sec. Since the dam commissioning, as per the monitoring data of these springs [20], its flow rate has been varying within the range of 4.5-9.5 m^3/sec and responds to the dam level fluctuations with a 7-10-day delay (fig.4). Consequently, as these data suggest, the filtration flow velocity is 400-600 m/day.



Fig. 4. Dashbash Springs in the River Khrami gorge in summer and winter.

The yield of Dashbash springs is assessed by using the dependence curve Φ=J(H) of the dam average levels (H) and the flow of the springs (Φ).

The observations over the Tsalka dam filtrate are done episodically, in 2010-2020, for the scientific and energetic purposes. The series of such measurements was done in autumn of 2015. This season of the year was preferred, as the yield of the underground waters and dam level are the least during it.

A reference measurement of this series was done on 17.11.2015. It was preceded by a two-week period without precipitations and low air temperatures 0.0≤T C0≤7.0, while the dam level varied within the range of 1503-1502 m asl. As per the measurement data, the yield of the springs reached 3.54 m^3/sec. As per the data of the studies, Tsalka dam filtrate reaches approximately 82.4 mln m^3 annually, with a maximum value of 147.7 mln m^3 and minimum value of 54.8 mln. m^3 (fig.5, fig.6). The given data evidence that Dashbash springs, as an indicator of impact of Tsalka dam on the ground waters must be assessed as negative since the Dam construction.

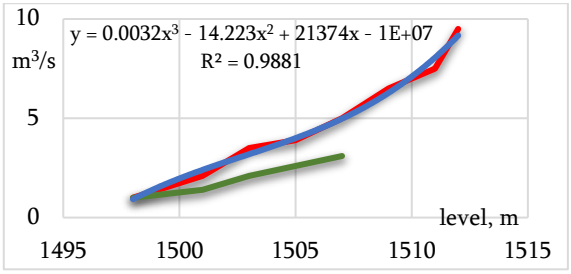


Fig. 5. Dependence curves of Tsalka Dam levels and filtration in terms of open (upper) water and ice cover.

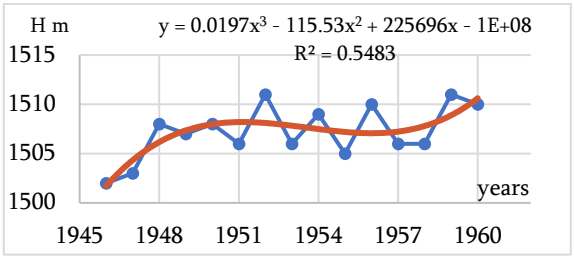


Fig. 6. Fluctuation of the maximum levels of Tsalka dam and maximum filtrate flow in the first decades of the dam operation.

Aparan Reservoir was built across R.Kasagh in 1966, in the volcanic mountains of the South Caucasus. Its normale filling level is 1835 m; its volume is 0.09 km^3; level fluctuation range is 20 m; the greatest depth is 45 m; the area of the wetted bed surface is 10 km^2. Its bed is formed in the dislocated andesite-basalt rocks, which are intensely fissured. After the Reservoir was put to operation, the filtrate flowing out of the said fissures, flow into the R.Kasagh as strong springs, like Dashbash springs.

With the aim of monitoring the reservoir safety and its filtrate, a hydrometric section operated on the said springs in 1967-1970, where the filtrate flow was measured regularly.

Reservoir contributes much to the groundwater reserves and the filtrate volume is proportional to main constituents of its water balance. In the first years of the water reservoir operation, during the monitoring of the spring flow, the value of the filtrate in the water balance was recorded with the highest accuracy with dependence curve Φ_d=Ғ(H) (fig.7). In the current decade, when this monitoring system is no longer operational, it is possible to determine this component by using the expression of the water balance method. According to the calculations, the groundwater basin receives an average of 70 mln m^3 of filtrate per year from the reservoir, with a volume of 56 to 177 mln m^3 in the abundant- and low-water years respectively. The given volume of filtrate is distributed across the irrigation channels in the lower reaches of the R.Kasagh and is consumed by the population. Consequently, this indicator of Aparan Reservoir can be evaluated positively.

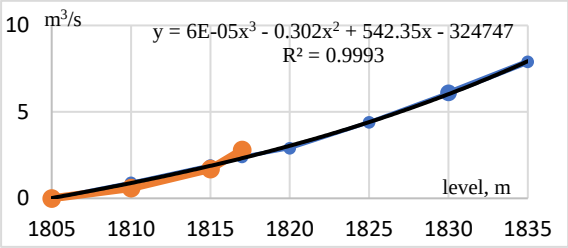


Fig. 7. Dependence curves of Aparan Reservoir levels and filtration in terms of open water and ice cover.

Sanding and mudding of the bed of the given water body, like Tsalka Reservoir, is much slower than the same processes on Caucasus southern slope, where the reservoirs regulate the rivers with bulk drift.

Particularly interesting is the impact of Tbilisi and Zhinvali dams on the groundwaters, as they immediately affect the stability of the buildings in the adjoining micro-districts and living conditions of the people. Tbilisi Reservoir was provided in the old bed of R.Mtkvari, which is separated from the settlement districts with concrete dams. Its bed constituent rocks (gypsum sandstones) are inclined towards the city and as a result, during the high reservoir levels (H≥535 m asl), the filtrate flows towards the populated areas through underground channels.

The design filing level of the Reservoir was 548 m asl. At present, due to the mentioned reasons, the level is decreased to 540 m. The corresponding volume of the Reservoir is 0.22 km^3; the fluctuation range of levels is up to 7 m; the greatest depth is 37 m; the area of the wetted bed surface does not exceed 14 km.

10 years following the commissioning of the reservoir, the water started to seep into the basements and foundations of the newly built houses in Gldani, Avchala and Avlabari Districts. In the following years, the process activated so much that it became necessary to reduce the filing level to 540 m. However, this action is not sufficient to stop filtration, as the bedrocks towards Gldani and Avlabari districts are found at lower heights, while the weirs fail to protect the city from the filtrate. This is evidenced by the streams of filtrated waters with 2-3 l/sec yield flowing on the contact surface of the loose ground and the bedrocks towards the R.Mtkvari bed.

As there is not a network to monitor filtration and groundwaters around the reservoir, it was assessed by using the water balance method and episodic information gathered during the construction works in the areas of the Reservoir. With such data, the average annual volume of the filtrate is 2.0-2.5 mln m^3, and 1.5 and 3.0 mln m^3 in the abundant- and low-water years, respectively.

The means to reduce the filtrate is the further decrease in the reservoir level. However, such a measure would badly deteriorate the water-economic and recreational importance of the reservoir. Therefore, it would be more beneficial to establish a filtrate monitoring network in the said districts and to take the given house-building data in the micro-districts into account. According to the results of the studies, Tbilisi (the capital of the country) water reservoir has a strong impact on the ground waters and its indicator is definitely negative.

The normal corrected inundation level of Zhinvali dam is 800 m asl; the level fluctuation range is 30 m; the volume is 0.4 km^3; the greatest corrected depth is 83 m; the area of wetted bed surface is about 15 km^2. The impact of Zhinvali dam on the tailrace under-ground waters is important in that it flooded the currents flowing out in the R.Pshavi bed. This phenomenon activated an old landslide on the right slope and formed new hearths. Dam in the tailrace increased the filtrate towards Bulachauri significantly (by 10-15%). Besides, such phenomena are important in that the filtrate increases the underground water reserves even during the seasons distinguished by low-water periods of the R.Aragvi. According to such results of study, the impact of Zhinvali dam on the underground waters is strong and the filtrate indicator is negative in the headrace and is positive in tailrace.

4. CONCLUSION

1. According to the corrected mechanism of impact of a water reservoir on the ground waters, the filtrate, under the impact of hydrostatic, gravitational and capillary forces, follows the pores, cracks and tectonic faults in the rocks until it merges with the underground waters, or flows out on surface. The filtrate flow rate is determined by the gravitation in the volcanic rocks and by the capillary forces in the sedimentary rocks.
2. Filtration decreases in proportion to sanding and mudding processes and as the reservoir is sanded to the limited volume, it virtually stops. In this phase the “water reservoir-ground waters” relation is determined

by the filtrate of the derivation tunnel and the auxiliary structures.

3. The visible indicators are: the springs, bogged and salinized plots of field and deformed infrastructure. Invisible indicators are: submarine waters and the waters flowing across the adjoining basins.

4. The indicative plan to assess the filtrate is a quite efficient tool to evaluate a water reservoir efficiency, as it refines and simplifies the given operation.

5. ACKNOWLEDGMENTS

This work was supported by Shota Rustaveli National Science Foundation of Georgia (SRNSFG) [FR-18-009].

6. REFERENCES

[1] Dewals B, Rulot F, Erpicum S, Archambeau P, Pirotton M, Long-term sediment management for sustainable hydropower. Comprehensive Renewable Energy. 2012, vol. 6, pp. 355-376.

[2] Bennett SJ, Dunbar JA, Rhoton FE, Allen PM, Bigham JM, Davidson GR, Wren DG, Assessing sedimentation issues within aging flood-control reservoirs. Reviews in Engineering Geology, 2013, 21, pp. 25-44.

[3] Caputo M, Carcione JM, A memory model of sedimentation in water reservoirs. Journal of Hydrology, Elsevier, 2013, 476, pp. 426-432.

[4] Garg V, Jothiprakash V, Evaluation of reservoir sedimentation using data driven techniques. Applied Soft Computing, Elsevier, 2013, 13(8), 3567-3581.

[5] Detering M, Schuettrumpf H, Reservoir Siltation and Ecological Life Span of Dams. Wasser Wirtschaft, Springer, 2014, 104 (1-2), pp. 30-33.

[6] Matchavariani L, Metreveli G, Lagidze L, Gulashvili Z, Svanadze D, Positive Aspects of Studying the Sedimentation in Reservoirs through the Natural Experiment. Journal of Environmental Biology. 2017, vol. 38(5), pp. 1155-1159.

[7] Metreveli G, Matchavariani L, Research Method of Silting the Mountain Reservoirs Under the Current Climate Change. Journal of Water Resources and Ocean Science. SP Group, 2016, vol. 5, #2, pp. 22-27.

[8] Jain SK, Singh VP, Water Resources Systems Planning and Management. Elsevier, 2003, 882p.

[9] Motiee H, McBean E, An Assessment of Long-term Trends in Hydrologic Components and Implications for Water Levels in Lake Superior. Hydrology Research, 2009, 40 (6), pp. 564-579.

[10] Marco JB, Harboe R, Salas JD (Ed.), Stochastic Hydrology and its Use in Water Resources Systems Simulation and Optimization. Springer Science & Business Media, NATO ASI Series E: Applied Science, 2012, vol. 237, 483p.

[11] Andredaki M, Georgoulas A, Hrissanthou V, Kotsovinos N, Assessment of reservoir sedimentation effect on coastal erosion in the case of Nestos River, Greece. International Journal of Sediment Research, 2014, 29(1), pp. 34-48.

[12] Gopinath G, Ashitha MK, Jayakumar KV, Sedimentation assessment in a multipurpose reservoir in Central Kerala, India. Environmental Earth Sciences, 2014, 72(11), pp. 4441-4449.

[13] Hosseinjanzadeh H, Hosseini K, Kaveh K, Mousavi SF, New proposed method for prediction of reservoir sedimentation distribution. Int. J. of Sediment Research, 2015, 30(3), pp. 235-240.

[14] Matchavariani L, Metreveli G, Lagidze L, Svanadze D, Gulashvili Z, Solution of Reservoirs' Siltation Problem for Hydropower Development and Coastal Protection. International Journal of GEOMATE, Japan, 2017, vol. 13(39), pp. 206-212.

[15] Loucks Daniel P, Eelco van Beek, Water Resource Systems Planning and Management: An Introduction to MethodsModels and Applications, Springer, 2017, 624 p.

[16] Moeeni H, Bonakdari H, Ebtehaj I, Monthly reservoir inflow forecasting using a new hybrid SARIMA genetic programming approach. J Earth Syst Sci, 2017, 126: 18.

[17] Metreveli G, Matchavariani L, Gulashvili Z, Method for Hydrological Parameters Definition of Silting Prism and Equilibrium Bed in Water Reservoirs. Proceedings of the 19th Intern. Multidisciplinary Scientific GeoConference SGEM, Bulgaria, 2019, vol. 19(3.1), pp. 363-368.

[18] Patriadi A, Soemitro RAA, Warnana DD, Wardoy W, Mukunoki T, Tsujimoto G, The Influence of Sembayat Weir on Sediment Transport Rate in the Estuary of Bengavan Solo River, Indonesia. Intern. Journal of GEOMATE, vol. 20, Issue 81, 2021, pp. 35-43

[19] Nozaki S, Onodera SI, Tomozawa Y, Saito M, Spatial Distributions in Groundwater Discharge on Various Tidal Flats in a Small and Steep Island, Western Japan. Intern. Journal of GEOMATE, vol. 20, issue 81-82, 2021, pp. 66-71

[20] Gvelesiani L, Sediment Regime of Mountain Rivers and Siltation of Reservoirs. Hydrology of Lakes and Reservoirs. Part 2. Water Reservoirs. MGD, International Higher Hydrological Courses of UNESCO, 5th Session, 1973, pp. 38-48.

7th Int. Conf. on Structure, Engineering & Environment (SEE), Pattaya, Thailand, Nov.10-12, 2021, ISBN: 978-4-909106070 C3051

STRENGTH AND MICROSTRUCTURE DEVELOPMENT OF RICE HUSK ASH WITH CEMENT STABILIZED SOIL

Sayful Kabir Khan[1, 2], Najmun Nahar[1, 3], Alex Otieno Owino[1], Zakaria Hossain[1] and Noma Tamaki[4]

[1]Graduate School of Bioresources, Mie University, Japan,
[2]Directorate of Food, Dhaka, Bangladesh
[3]Life and Earth Science, Jagannath University, Bangladesh,
[4]Make Integrated Technology Company, Osaka, Japan

ABSTRACT

Rice husk ash (RHA) is an agricultural by-product, contains a high amount of amorphous silica, and acts as secondary cementitious material. It can partially replace the cement amount in ground improvement that is environmentally and economically feasible. In this study, ten combination types were prepared, including untreated soil with a comparatively considerable amount of RHA (5%, 10%, and 15%) and nominal dosages of cement (0.2%, 0.4%, and 0.6%). A series of laboratory tests were conducted to identify the soil type. The standard proctor test was conducted to measure the mixtures' optimum moisture content (OMC) and maximum dry density (MDD). The unconfined compression strength (UCS) test and scanning electron microscopy (SEM) test were conducted considering seven days of moist curing. The results showed that the increase of RHA and cement led to increased OMC and decreased MDD. There was an increase in UCS with RHA and cement percentage increase compared to the control specimens (180 kPa). The maximum UCS value (205.2 kPa) was observed for soil with 5% RHA and 0.6% cement. The results were validated using the microstructure development of the SEM images. The outcomes of this study can be used in many geotechnical engineering applications.

Keywords: Compactibility, Stress-strain relationship, Deformation modulus, Scanning electron microscopy

INTRODUCTION

The demand for construction materials is increasing day by day for building new houses, roads, and other engineering projects with the increase of urbanization rate by the pressure of the growing world population [1]. Consequently, the per capita consumption of cement is also increasing as the critical binding material in the construction sector [2]. An enormous amount of carbon dioxide (CO_2) releases into the atmosphere, which contributes about 8% of CO_2 emissions of the world during cement production [3], causes environmental problems and human health hazards [4]. Cement manufacturing has escalated to 0.5% CO_2 intensity directly every year during 2014-2018, and it is essential to stay on track by a 0.8% yearly reduction of CO_2 with the Sustainable Development Strategy (SDS) through 2030 [5]. Environmental scientists always recommend the usage of various cementitious recycled wastes as cement alternatives [6]. The utilization of agricultural and industrial wastes, including bagasse ash (BA), blast furnace slag, fly ash (FA), metakaolin, rice husk ash (RHA) are increasing in construction industries since the last couple of decades [7]. Currently, a significant number of investigations have been conducted on the integration of rice husk ash (RHA) as the obtainability of a high quantity of reactive and amorphous silica in RHA among all agricultural wastes [8]. The pozzolanic reactions of RHA enhance the unconfined compressive value and durability of soil [7].

Rice husk ash (RHA) is a renewable agricultural bi-product. Annually about 500 million tons of paddy rice is produced in developing countries. About 100 million tons of rice husk are obtainable after milling, and only 20% rice husk ash (RHA) is made after burning rice husk in these countries [9]. An enormous amount of RHA is discarded at riverside and landfill sites for transportation and management problems as having a microporous structure with lightweight [10]. About 80-95% amorphous silica is obtained in RHA [8]. Various types of soil have been improved significantly by using RHA in many countries in the world [11], but RHA is commonly used with cement and lime, as only RHA cannot provide adequate soil strength [12]. When RHA is mixed with cement and water in the soil, it mechanically captivates the massive amount of water, diminishes the bleed water, and improves the inter-particle bonding among soil, RHA and cement particles. Simultaneously, the amorphous silica in RHA chemically combines with calcium hydroxide ($Ca(OH_2)$) in the secondary hydration process and produce calcium silicate hydrate (C-S-H) gel, developing the strength and durability of soil [13].

For soil stabilization, many studies have used about 5-15% RHA with 2-10% cement in different soil types. Only Hossain and Sakai [14] mixed minimal dosage of cement (0.2%, 0.4%, 0.6% cement) for clay soil stabilization and found the improvement of California bearing ratio (CBR) and

unconfined compressive strength (UCS) values. There are no or very few studies that have been conducted using RHA with a nominal dosage of cement. Soil addition with RHA and a small amount of cement can ensure environment-friendly structures such as rural roads, pedestrian roads, ridges between paddy fields, etc. Therefore, the current study investigates soil's strength and microstructure development using rice husk ash with a nominal cement dosage. Unconfined compressive strength tests and scanning electron microscopy (SEM) tests evaluated all specimens of soil-RHA-cement combination types, considering 7-day curing. The test results on the stress-strain relationship, UCS value, modulus of deformation, UCS specimens' failure pattern, and soil microstructure changes with 5%, 10%, 15% RHA, and 0.2%, 0.4% 0.6% cement are illustrated in the study.

MATERIALS AND METHODS

Materials

Soil, natural RHA, and ordinary Portland cement were used in this investigation. The soil samples were collected from the Handa area, Tsu City, Mie Prefecture, Japan. The soil was light brown. The basic properties of soil were settled through a series of laboratory tests and presented in Table 1. The particle size distribution curve of soil and RHA is exhibited in Fig. 1.

Table 1 Basic properties of soil

Parameters	Values
Specific gravity (ρs)	2.701 g/cm^3
Maximum dry density ($\gamma_{dry\ max}$)	1.696 g/cm^3
Optimum Moisture Content (W_{opt})	17.50%
Sand (75μm – 2 mm)	88.00%
Silt (5 - 75 μm)	9.00%
Clay (<5 μm)	3.00%
Liquid Limit (LL)	37.50%
Plastic Limit (PL)	29.70%
Plasticity Index (PI)	7.80%
Coefficient of gradation (c_u)	9.841
Coefficient of curvature (c_c)	1.024
AASHTO classification	A-2-4
USCS classification	SM

Readymade RHA was collected from Make Integrated Technology (MIT) company, Osaka, Japan. The physical and chemical properties of RHA are presented in Table 2.

The properties of ordinary Portland cement are available in other studies.

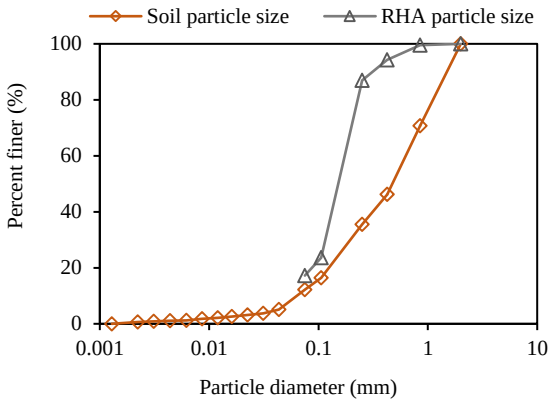


Fig. 1 Particle size distribution curve of soil and RHA

Table 2 The major properties of RHA

Parameters	Values
Average Particle size	0.001-0.3 mm
Specific gravity	2.12 g/cm^3
Burning temperature	650-700°C
Burning time	27 hours
Silica (SiO_2)	91.10%
Alumina (Al_2O_3)	0.03%
Potassium Oxide (K_2O)	2.40%
Calcium Oxide (CaO)	0.57%
Carbon dioxide (CO_2)	4.35%

Mix Design and Specimen Preparation

The soil sample was air-dried at room temperature (25°C) and sieved by JIS sieve No. 4 for removing unwanted roots and leaves from the soil. A total of 1o combinations including control (Soil only), RHA 5%, 10%, 15%, with nominal doses of cement 0.2%, 0.4%, 0.6%. The mix types, materials proportions, and indices of the soil-RHA-cement combinations types are shown in Table 3.

Table 3 Investigated mixtures and indices of soil-RHA-cement admixtures

Sl. No.	Mix types	Material types (% by weight)			Index
		Soil (%)	RHA (%)	Cement (%)	
1	Soil (Control)	100	0	0	Control
2	Soil + 5% RHA + 0.2% Cement	100	5	0.2	S+5R+0.2C
3	Soil + 5% RHA + 0.4% Cement	100	5	0.4	S+5R+0.4C
4	Soil + 5% RHA + 0.6% Cement	100	5	0.6	S+5R+0.6C
5	Soil + 10% RHA + 0.2% Cement	100	10	0.2	S+10R+0.2C
6	Soil + 10% RHA + 0.4% Cement	100	10	0.4	S+10R+0.4C
7	Soil + 10% RHA + 0.6% Cement	100	10	0.6	S+10R+0.6C
8	Soil + 15% RHA + 0.2% Cement	100	15	0.2	S+15R+0.2C
9	Soil + 15% RHA + 0.4% Cement	100	15	0.4	S+15R+0.4C
10	Soil + 15% RHA + 0.6% Cement	100	15	0.6	S+15R+0.6C

Around 3500 gm dry soil was used for each mix of the standard Proctor compaction test, and 2000 gm

dried soil was taken to prepare three specimens for each mixture for conducting an unconfined compression strength (UCS) test and triaxial test. The needed soil, RHA, and cement were manually mixed with plastic gloves in a big tray for 10 to 15 minutes. The water was mixed slowly into the dry mixture to be equally distributed in the mix. Before samples were mixed, the standard proctor test (compaction test) was performed on soil RHA-cement mixtures to determine each optimum moisture content (OMC). The amount of water added was either 2% below the OMC of each sample. The UCS test specimens were 7-day moisture-cured.

Standard Proctor Compaction Test

According to Japanese Industrial Standards (JIS-A-1210), the Standard Proctor compaction test was conducted to determine the optimum moisture content (OMC) and maximum dry density (MDD) of soil control and other mix types [15]. The applied apparatus for performing the test was a 10 cm diameter cylindrical compaction mold equipped with a base and a collar, rammer mass of 2.5 kg, and a falling height of 30 cm. The RHA mixed soil was compacted in three layers in the compaction mold with 25 blows for each layer. For each mix type, soil-RHA-cement was manually mixed homogenously in dry conditions. Subsequently, different moisture contents were added homogeneously by manual mixing like the previous step for getting the expected moisture content.

Unconfined compressive strength (UCS) test

In this research, the mixtures of soil-RHA-cement were compacted in three layers in a mold using a 4.9 cm diameter hand-rammer with a rammer mass of 1.0 kg and a falling height of 30 cm. Each layer was compacted by 20 blows. UCS at a loading rate of 0.1 mm/min and recorded every 0.5 mm displacement applied in this research. These tests were performed according to Japanese Industrial Standards (JIS-A-1216) [16]. The maximum value of compressive stress was defined as the unconfined compressive strength (UCS) (q_u) in kPa, and the strain at that time was defined as the fracture strain. The deformation coefficient (E_{50}) in MPa was calculated using from the following Eq. 1.

$$E_{50} = \frac{\frac{q_u}{2}}{\varepsilon_{50}} / 10 \qquad (1)$$

Where, ε_{50} is the compressive strain, and q_u is the maximum value from stress.

RESULTS AND DISCUSSIONS

Compactability of Soil-RHA-Cement Admixtures

The optimum moisture content OMC of control was 17.5%, and maximum dry density (MDD) was 1.696 g/cm^3. The OMC increased with the increase of RHA and cement percentages in the soil-RHA-cement combination types. The OMC of the combination of S+5R+0.2C, S+5R+0.4C, S+5R+0.6C was 21.0%, 21.3%, 21.5%; the OMC of S+10R+0.2C, S+10R+0.4C, S+10R+0.6C was 25.1%, 25.3%, 25.5%, and for S+15R+0.2C, S+15R+0.4C, S+15R+0.6C was 28.8, 29.0%, 29.2% (Fig. 2). It specifies that the surplus amount of RHA and cement significantly affect the OMC of the mix types. Conversely, with the increase of RHA content and cement in the soil-RHA-cement combination types, MDD decreases. The MDD of the admixture of S S+5R+0.2C, S+5R+0.4C, S+5R+0.6C was 1.538, 1.536, 1.534 g/cm^3; for S+10R+0.2C, S+10R+0.4C, S+10R+0.6C was 1.436, 1.435, 1.434 g/cm^3; and for S+15R+0.2C, S+15R+0.4C, S+15R+0.6C was 1.323, 1.318, 1.312 g/cm^3 (Fig. 2). Due to RHA's higher microporous structure and lower specific gravity than soil and cement, the fine particles of RHA occupied the pore space in the soil and lessened the MDD of the mix types [17, 18].

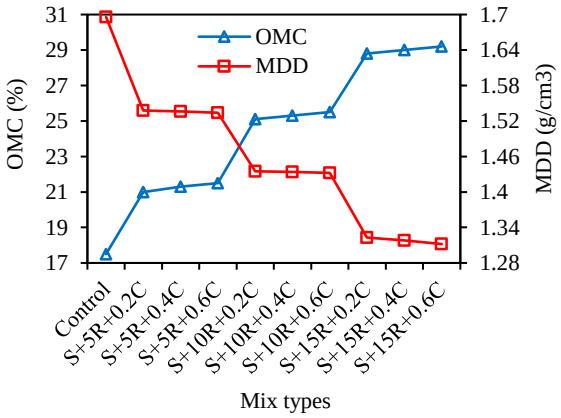


Fig. 2 Variation of OMC and MDD of control and soil-RHA-cement combinations

Unconfined Compressive Strength (UCS) Test Results of Soil-RHA-Cement Admixtures

The UCS test results of the untreated soil and other soil-RHA-cement combination types are displayed in Fig. 3. For each curve, there is a peak or ultimate stress (termed as compressive strength), and then, after the peak value, there is a softening behavior. It is observed that the compressive stress increases with the increase of displacement until appearing the peak value, naturally, but the increment rate varies depending on the different quantities of RHA and cement.

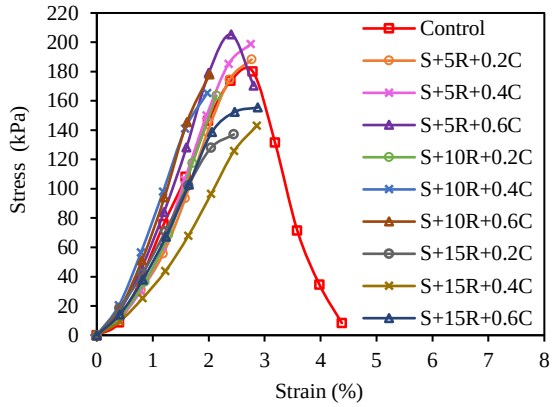


Fig. 3 The stress-strain relationship curve of control and various soil-RHA-cement combinations.

Fig. 4 shows the average of the three samples variation of the unconfined compressive strength (UCS, q_u) with different combinations of soil-RHA-cement types. It is noticed that an increase in the compressive strength with the addition of cement content with RHA 5%. The increase of strength is due to the pozzolanic action between the silica from RHA and calcium release by cement. The addition of the 10% RHA causing to a drop in the compressive strength of the composite. It is interesting to note that further addition of RHA to 15% showing a continuous decrease in the strength due to the unbalance of silica and calcium reaction.

With the further rise of RHA with cement, the UCS value decreases noticeably. The UCS value of the control is 180 kPa. The highest UCS value was observed from the S+5R+0.6C combination (205.2 kPa). Only soil with 5% RHA with different ratios of cement content shows the increment of UCS value compared to the control specimen.

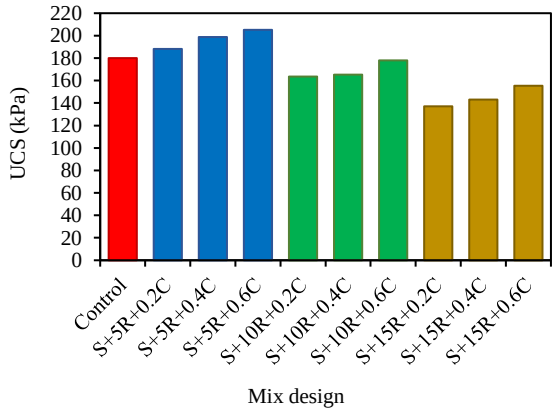


Fig. 4 Variation of UCS of control and various soil-RHA-cement combinations.

The modulus of elasticity (E_{50}) of various mixtures of soil, RHA, and cement are illustrated in Fig. 5. It is observed that the modulus of deformation increased with the addition of cement content, and the highest modulus of deformation observed the S+5R+0.6C combination. Then it decreased for further addition of cement with 10% and 15% RHA [20]. Similar to the case of UCS, the reduction in the modulus of elasticity value after adding 10% and 15% RHA with the different nominal dosages of cement may be due to the extra RHA weaken the bonding between soil, cement, and pozzolanic materials in the mixtures [19].

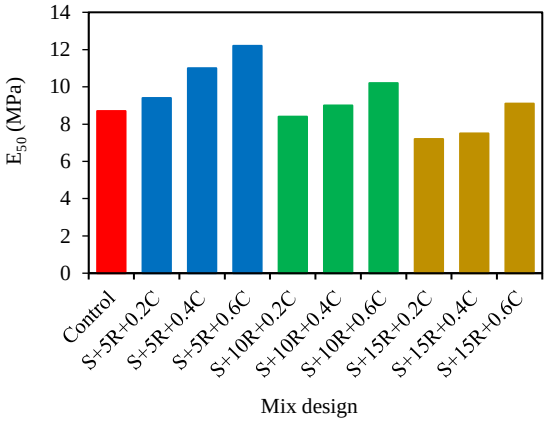


Fig. 5 The modulus of deformation of control and various soil-RHA-cement combinations.



Fig. 6 Failure modes of control and soil-RHA-cement combinations under UCS test

Fig. 6 represents the failure modes of control and soil-RHA-cement combination types. It can be

seen that the control has a primary diagonal failure pattern. In contrast, soil with cement and RHA addition has various slip lines showing the potential discontinuity due to the addition of RHA and cement. It is known that both RHA and cement particles would have altered the failure modes of soil. Interestingly, most of the failures are simple shear, but some are wedges failures observed as well.

Scanning Electron Microscopy (SEM) Test Results of Soil-RHA-Cement Admixtures

The SEM images of control and soil with 5%, 10%, 15% RHA, and 0.6% combinations types are exhibited in Figs. 7-10. The best strength and microstructural improvement were noticed in the S+5R+0.6C combination compared to the control specimen. The soil showed a closed structure after adding 5% RHA and 0.6% cement content due to the pozzolanic reaction among RHA, cement content with water, and simultaneously, the interlocking of RHA and cement particles in the soil (Fig. 8). This point of SEM results agrees well with the strength development as discussed in the previous sections.

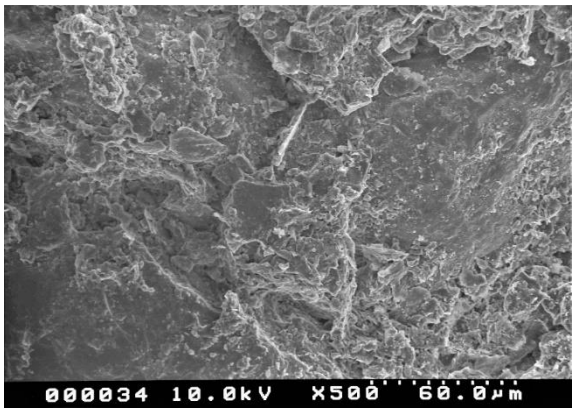


Fig. 7 SEM images of compacted control specimen

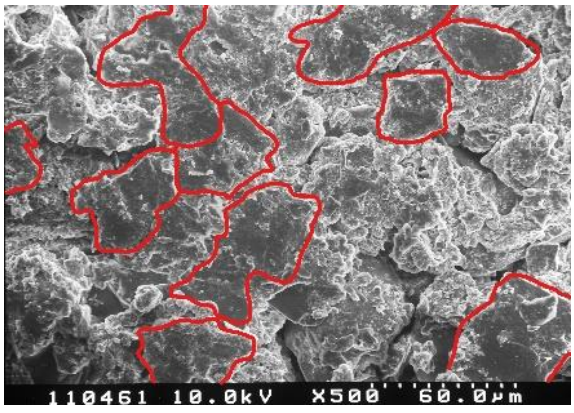


Fig. 8 SEM images of S+5R+0.6C specimen

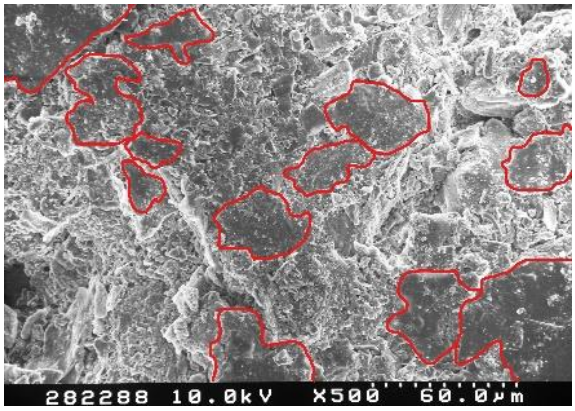


Fig. 9 SEM images of S+10R+0.6C specimen

The decrease in the strength with 10% and 15 % RHA that was observed in the case of UCS and E50 are validated using the soil microstructure analysis as shown in Fig.9 and Fig.10. The SEM images clearly showed weakened bonding phenomena with the increment of RHA with the same amount of cement content. The surplus RHA inhibited the chemical reaction of silica to calcium.

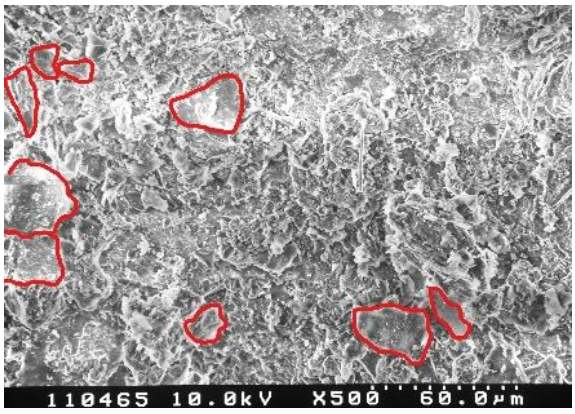


Fig. 10 SEM images of S+15R+0.6C specimen

CONCLUSIONS

The experimental investigation on the addition of RHA with the nominal dosages of cement in soil showed an improvement of geotechnical properties of soil, and it can be concluded that

- The S+5R+0.6C showed the improvement of unconfined compressive strength (205.2 kPa) and modulus of deformation (12.2 MPa) compared to control (UCS =180.0 kPa and E_{50} = 8.7 MPa) considering 7 days of curing.
- The SEM image on the S+5R+0.6C combination showed the best microstructural development for 7 days.
- It is recommended that the S+5R+0.6C mixture can be used in ground improvement for environmental and economic benefit, particularly in the rural areas of developing countries.

REFERENCES

[1] Koncept Analytics. (2019). Global Cement Market (Production, Consumption, Imports & Exports): Insight, Trends, and Forecast (2019-2021).

[2] Rodgers, L. (2018). Climate change: The massive CO2 emitter you may not know about. BBC News. 17 December 2018. https://www.bbc.com/news/science-environment-46455844.

[3] Andrew, R. M., Global CO_2 emissions from cement production. Earth System Science Data, Vol. 10, Issue 1, 2018, pp. 195-217.

[4] Khan, R., Jabbar, A., Ahmad, I., Khan, W., Khan, A. N., and Mirza, J., Reduction in environmental problems using rice-husk ash in concrete. Construction and Building Materials, Vol. 30, 2012, pp.360-365.

[5] IEA (2020), Cement, IEA, Paris https://www.iea.org/reports/cement

[6] Khan, M. N. N., Jamil, M., Karim, M. R., Zain, M. F. M., & Kaish, A. A., Utilization of rice husk ash for sustainable construction: a review. Research Journal of Applied Sciences, Engineering and Technology, Vol. 9, Issue 12, 2015, pp. 1119-1127.

[7] Kuntikana, G., & Singh, D. N. Contemporary issues related to utilization of industrial by-products. Advances in Civil Engineering Materials. Vol. 6, Issue 1, 2017, pp. 444-479.

[8] Thomas, B. S. Green concrete partially comprised of rice husk ash as a supplementary cementitious material–A comprehensive review. Renewable and Sustainable Energy Reviews, Vol. 82, 2018, pp. 3913-3923.

[9] Jongpradist, P., Homtragoon, W., Sukkarak, R., Kongkitkul, W., & Jamsawang, P. Efficiency of rice husk ash as cementitious material in high-strength cement-admixed clay. Advances in Civil Engineering, 2018.

[10] Pode, R., Potential applications of rice husk ash waste from rice husk biomass power plant, Renewable and Sustainable Energy Reviews, Vol. 53, 2016, pp. 1468-1485.

[11] Alhassan, M., & Alhaji, M. M. Utilisation of rice husk ash for improvement of deficient soils in Nigeria: a review. Nigerian Journal of Technology, Vol. 36, Issue 2, 2017, pp. 386-394.

[12] Choobbasti, A. J., Samakoosh, M. A., & Kutanaei, S. S. Mechanical properties soil stabilized with nano calcium carbonate and reinforced with carpet waste fibers. Construction and Building Materials, Vol. 211, 2019, pp. 1094-1104.

[13] Singh, B. Rice husk ash. In Waste and Supplementary Cementitious Materials in Concrete, 2018, pp. 417-460, Woodhead Publishing.

[14] Hossain, M. Z., and Sakai, T., The effectiveness of nominal dosage of ordinary cement on strength and permeability of clayey soil, Journal of the Japanese Society of Soil Physics, Vol. 110, 2008, pp. 25-35.

[15] JIS A 1210, 2010. Test method for soil compaction using a rammer. Japanese Industrial Standard, Guidance and Basic - Soil Test, The Japanese Geotechnical Society (in Japanese), 71-78.

[16] JIS A 1216, 2010. Method for unconfined compression test of soils. Japanese Industrial Standard, Guidance and Basic - Soil Test, The Japanese Geotechnical Society (in Japanese), 151-158.

[17] Phai, H., Eisazadeh, A., Geotechnical properties of rice husk ash-lime-stabilised Bangkok clay, Journal of Engineering Science and Technology, Vol. 15, Issue 1, 2020, pp. 198-215.

[18] Nahar, N., Hossain, Z., Tamaki, N., Optimum utilization of rice husk ash waste for ground improvement. International Agricultural Engineering Journal, Vol. 30, Issue 1, 2021, pp. 1-10.

[19] Alhassan, M., Potentials of rice husk ash for soil stabilization. Assumption university journal of technology, Vol. 11, Issue 4, 2008, pp. 246-250.

[20] Sharma, M., & Soni, D. K. Effect of Rise Husk Ash and Cement Mixtures on Unconfined Compressive Strength of Cohesive Soil. Indian Journal of Science and Technology, Vol. 9, Issue 44, 2016.

SEE-Mie 2022

The Eighth International Conference on

Structure, Engineering & Environment

10-12 November 2022

Mie, Japan

- The "International Journal of GEOMATE" is a Scientific Journal of the GEOMATE International Society that encompasses a broad area in Geotechnique, Construction Materials and Environment.
- The key objective of this journal is to promote interdisciplinary research from various regions of the globe.
- The editorial board of the journal is comprised of extensively qualified researchers, academicians, scientists from Japan and other countries of the world.
- It is peer-reviewed Journal that is published quarterly till 2015 and now monthly. All articles published in this journal are available online.
- Contributors may download the manuscript preparation template for submitting paper or contact to the Editors-in-Chief

[editor@geomatejournal.com]

